Marc Dewey

Cardiac CT

Second Edition

Springer

Cardiac CT

Marc Dewey

Cardiac CT

Second Edition

Springer

Marc Dewey, Prof. Dr. med.
Charité – Universitätsmedizin Berlin
Heisenberg Professor of Radiology
Institut für Radiologie
Charitéplatz 1
10117 Berlin
Germany
e-mail: dewey@charite.de

ISBN 978-3-642-41882-2 ISBN 978-3-642-41883-9 (eBook)
DOI 10.1007/978-3-642-41883-9
Springer Heidelberg New York Dordrecht London

Library of Congress Control Number: 2014936307

Foreword

Computed tomography (CT) has been going through a dramatic evolution of technology in the past years. Cardiac CT has become reliably possible and benefits to a large extent from the continuous development. The technical advances directly translate into improved image quality, lower radiation exposure, and more versatile applications. CT angiography of the coronary arteries – often referred to as coronary CT angiography – has received tremendous interest and is now an established clinical tool in selected patients. In fact, it has the potential to greatly alter the way in which many patients with suspected coronary artery disease will be worked up. However, the technique requires special knowledge and experience and it is important to keep abreast with the newest developments, protocols, technology, and clinical results in order to optimally apply this diagnostic tool.

This is why the second edition of this textbook edited by Dr. Dewey is just as welcome as the first edition in 2011. It provides insight into the basics of cardiac CT and at the same time includes all relevant new developments. May it be a useful resource to its readers and may it contribute towards the further development of this exciting field.

Erlangen, Germany — Stephan Achenbach
Baltimore, MD, USA — Elliot K. Fishman
August 2013

Acknowledgments

Together with my team I would like to thank our patients, without whom we would not be able to conduct our clinical work and studies to continuously increase our understanding of the clinical utility of cardiac CT.

We are indebted to our technicians, assistants, and nurses at the Department of Radiology of the Charité – Universitätsmedizin Berlin for their contributions to the success of our clinical cardiovascular imaging program. Without their support, this book would not have been possible. The editorial assistance of Bettina Herwig and Deborah McClellan has been instrumental in writing this book. Stephanie Kreutzer has created beautiful artwork to illustrate essential concepts and approaches.

The excellent collaboration with the Department of Cardiology and Angiology at the Charité (Chairman: Prof. Gert Baumann, Vice Chairman: Prof. Karl Stangl) has tremendously facilitated this work. We thank Prof. Wolfgang Rutsch (former head of the cardiac catheterization laboratory at the Charité Campus Mitte) and his successor Dr. Michael Laule as well as their coworkers Dr. Adrian Borges, Dr. Hans-Peter Dübel, Dr. Christoph Melzer, Prof. Verena Stangl, and Prof. Heinz Theres for providing the majority of the conventional invasive angiograms presented in this book.

I wholeheartedly thank Drs. Martina and Charles Dewey.

Berlin, Germany
August 2013

Marc Dewey

Contents

Contributors

Editor

Marc Dewey, Prof. Dr. med.
Institut für Radiologie, Charité – Universitätsmedizin Berlin, Charitéplatz 1, 10117 Berlin, Germany
dewey@charite.de

Contributors

Gerhard Adam, Prof. Dr. med.
Klinik und Poliklinik für Diagnostische und Interventionelle Radiologie, Universitätsklinikum Hamburg-Eppendorf, Diagnostikzentrum, 20246 Hamburg, Germany
g.adam@uke.uni-hamburg.de

Katharina Anders, Priv.-Doz. Dr. med.
Radiologisches Institut, Universitätsklinikum Erlangen, Maximiliansplatz 1, 91054 Erlangen, Germany
katharina.anders@uk-erlangen.de

Raoul Arnold, Dr. med.
Klinik III: Angeborene Herzfehler/Pädiatrische Kardiologie, Zentrum für Kinderheilkunde und Jugendmedizin, Universitätsklinikum Freiburg, Mathildenstr. 1, 79106 Freiburg, Germany
raoul.arnold@uniklinik-freiburg.de

Hans-Christoph Becker, Prof. Dr. med.
Institut für Klinische Radiologie, Klinikum der Universität München, Marchioninistraße 15, 81377 Munich, Germany
christoph.becker@med.uni-muenchen.de

Philipp G. C. Begemann, Priv.-Doz. Dr. med.
Röntgeninstitut Düsseldorf, Kaiserswerther Strasse 89, 40476 Düsseldorf, Germany
p.begemann@roentgeninstitut.de

Matthew J. Budoff, MD
Los Angeles Biomedical Research Institute, 1124 W Carson Street, 90502 Torrance, CA, USA
mbudoff@labiomed.org

Jean Nicolas Dacher, Prof.
Département d'Imagerie Médicale, Imagerie Cardiaque non Invasive, University Hospital of Rouen, 1, Rue de Germont, 76031 Rouen, France
jean-nicolas.dacher@univ-rouen.fr

Victoria Delgado, MD, PhD
Department of Cardiology, Leiden University Medical Center, Albinusdreef 2, 2300 RC Leiden, The Netherlands
v.delgado@lumc.nl

Andrejs Erglis, Prof. MD, PhD
Insititute of Cardiology, Latvian Centre of Cardiology, Pauls Stradins Clinical University Hospital, University of Latvia, Pilsonu 13, LV1001 Riga, Latvia
a.a.erglis@stradini.lv

Gudrun Feuchtner, Ao. Univ.-Prof. Dr. med.
Institut für Radiologie II, Medizinische Universität Innsbruck, Anichstr. 35, A-6020 Innsbruck, Austria
gudrun.feuchtner@i-med.ac.at

Oliver Gaemperli, Priv.-Doz. Dr. med.
Andreas Grüntzig Cardiac Catheterization Laboratories and Cardiac Imaging, University Hospital Zurich, Ramistrasse 100, CH-8091 Zurich, Switzerland
oliver.gaemperli@usz.ch

Jacob Geleijns, PhD
Afdeling Radiologie, Leids Universitair Medisch Centrum, Postbus 9600, 2300 RC Leiden, The Netherlands
k.geleijns@lumc.nl

Thomas Gerber, MD, PhD
Division of Cardiovascular Diseases, Mayo Clinic, 4500 San Pablo Road, 32224 Jacksonville, FL, USA
gerber.thomas@mayo.edu

Benoît Ghaye, MD
Department of Radiology, Cliniques Universitaires St-Luc, Catholic University of Louvain, Brussels, Belgium
benoit.ghaye@uclouvain.be

Philip Greenland, MD
Northwestern University Feinberg School of Medicine, 680 North Lake Shore Drive, Suite 1400, 60611 Chicago, IL, USA
p-greenland@northwestern.edu

Maria Grigoryev, Dr. med.
Institut für Radiologie, Charité – Universitätsmedizin Berlin, Charitéplatz 1, 10117 Berlin, Germany
maria.grigoryev@charite.de

Bernd Hamm, Prof. Dr. med.
Institut für Radiologie, Charité – Universitätsmedizin Berlin, Charitéplatz 1, 10117 Berlin, Germany
bernd.hamm@charite.de

B. Kelly Han, MD
Minneapolis Heart Institute, The Children's Heart Clinic at the Children's Hospitals and Clinics of Minnesota, Suite 500, 2530 Chicago Ave South, 55404 Minneapolis, MN, USA
khan@chc-pa.org

Martin K. Hoffmann, Prof. Dr. med.
Leiter Interventionelle Radiologie, Luzerner Kantonsspital, 6000 Luzern 16, Luzern, Switzerland
martin.hoffmann@luks.ch

Martin Jeltsch, Dr. med.
Kliniken der Kreisspitalstiftung Weißenhorn, Weißenhorn, Germany
m.jeltsch@stiftungsklinik-weissenhorn.de

Masahiro Jinzaki, Dr.
Department of Diagnostic Radiology, Keio University School of Medicine, 35 Shinanomachi, Shinjuku-ku, 160-8582 Tokyo, Japan
jinzaki@rad.md.keio.ac.jp

Philipp A. Kaufmann, Prof. Dr. med.
University Hospital Zurich, Ramistrasse 100, CH-8091 Zurich, Switzerland
pak@usz.ch

Kakuya Kitagawa, MD, PhD
Department of Radiology, Mie University Hospital, Tsu, Japan
kakuya@clin.medic.mie-u.ac.jp

Oliver Klass, Priv.-Doz. Dr. med.
MediaPark-Klinik, Im Mediapark 3, 50670 Köln, Germany
oliver.klass@arcor.de

Christian Klessen, Dr. med.
Institut für Radiologie, Charité – Universitätsmedizin Berlin, Charitéplatz 1, 10117 Berlin, Germany
christian@klessen.net

Lucia J.M. Kroft, Dr.
Afdeling Radiologie, Leids Universitair Medisch Centrum, Postbus 9600, 2300 RC Leiden, The Netherlands
L.J.M.Kroft@lumc.nl

Muhammad A. Latif, MD
Stanford University School of Medicine, 800 Welch Road, FC2C51, 94304 Stanford, CA, USA
draamirlatif@gmail.com

Lukas Lehmkuhl, Dr. med.
Diagnostische und Interventionelle Radiologie, Universität Leipzig – Herzzentrum, Strümpellstrasse 39, 04289 Leipzig, Germany
lukas.lehmkuhl@med.uni-leipzig.de

Jonathon Leipsic, MD
Department of Radiology, St. Paul's Hospital, 1081 Burrard St, V6Z 1Y6 Vancouver, BC, Canada
JLeipsic@providencehealth.bc.ca

John R. Lesser, MD
Minneapolis Heart Institute, 920 E. 28th Street, Suite 300, 55407 Minneapolis, MN, USA
jrlesser1@gmail.com

Sebastian Ley, Priv.-Doz. Dr. med.
Diagnostische und Interventionelle Radiologie, Chirurgische Klinik Dr. Rinecker, Am Isarkanal 30, 81379 Berlin, Germany
ley@gmx.net

Gunnar Lund, Priv.-Doz. Dr. med.
Klinik und Poliklinik für Diagnostische und Interventionelle Radiologie, Universitätsklinikum Hamburg-Eppendorf, Diagnostikzentrum, 20246 Hamburg, Germany
g.lund@uke.uni-hamburg.de

Eugenio Martuscelli
Department of Internal Medicine, Division of Cardiology, University of Rome "Tor Vergata", Viale Oxford 81, 00133 Rome, Italy
e.martuscelli@libero.it

Koen Nieman, MD, PhD
Departments of Cardiology and Radiology, Erasmus Medical Center, Thoraxcenter Bd 116, 's-Gravendijkwal, 3015 CE Rotterdam, The Netherlands
koennieman@hotmail.com

Hiroyuki Niinuma, MD, PhD
Memorial Heart Center, Iwate Medical University, 1-2-1 ChuoDori, 020-8505 Morioka, Iwate, Japan
h_niinuma@imu.ncvc.go.jp

Fabian Plank, MD
Institut für Radiologie II, Medizinische Universität Innsbruck, Anichstr. 35, A-6020 Innsbruck, Austria
magolin@gmail.com

Rodrigo A. Salgado, MD
Department of Radiology, Cardiovascular Imaging, Antwerp University Hospital, Wilrijkstraat 10, 2650 Edegem, Belgium
rodrigo.salgado@uza.be

Paul Schoenhagen, MD
Division of Radiology, Cardiovascular Imaging and Department of Cardiovascular Medicine, The Cleveland Clinic Foundation, Cleveland, USA
schoenp1@ccf.org

Florian Wolf, Priv.-Doz. Dr. med.
Abteilung für Kardiovaskuläre und Interventionelle Radiologie, Medizinische Universität Wien, Universitätsklinik für Radiodiagnostik, Währinger Gürtel 18-20, A-1090 Wien, Austria
florian.wolf@meduniwien.ac.at

Elke Zimmermann, Dr. med.
Institut für Radiologie, Charité – Universitätsmedizin Berlin, Charitéplatz 1, 10117 Berlin, Germany
elke.zimmermann@charite.de

Introduction

B. Hamm

The advent of multislice computed tomography (CT) was a quantum leap for CT technology. When this technical innovation was first introduced, the radiological community was faced with the task of putting its advantages to use for diagnostic patient management and optimizing its clinical applications. One of the major clinical challenges was to develop this new tool for noninvasive cardiac imaging applications ranging from coronary angiography, to ventricular function analysis, to cardiac valve evaluation and myocardial perfusion analysis.

Marc Dewey and the authors of the book have closely followed the development of this new generation of CT scanners in the clinical setting, in scientific studies, and in experimental investigations. The team of authors has gained a wealth of experience spanning CT from 16-row technology to the most recent dual-source and 320-row CT scanners. In their scientific investigations, the authors have always placed great emphasis on a critical appraisal of this emerging imaging modality in comparison to well-established diagnostic tests such as coronary angiography, magnetic resonance imaging, and echocardiography, also including the socioeconomic perspective. The close cooperation with the Departments of Cardiology and Cardiac Surgery of the Charité – Universitätsmedizin Berlin was pivotal for obtaining valid results in both clinical examinations and scientific studies and also led to many improvements of the diagnostic workflow.

This book focuses on how to integrate cardiac CT into routine practice. Readers will learn how to perform noninvasive imaging of the heart using CT and how to interpret the images. A clear overview of the essentials is given, and numerous clinical cardiac CT cases are presented for illustration.

All steps involved in cardiac CT examination are described in detail, including patient preparation, the actual examination, and analysis and interpretation of the findings. Just 3 years after its first edition, *Cardiac CT* is published with updates of all previous chapters that focused on facilitating the practical implementation of the technology. The revised chapters deal with pivotal topics such as technical and personnel requirements, clinical indications, patient preparation, radiation exposure, clinical practice, examination and reconstruction, reading and reporting, coronary artery stents, bypass grafts, coronary anomalies, and congenital heart disease. Because of relevant developments over the last years the second edition also includes completely new chapters on prognostic implications of coronary calcium, CT for aortic valve replacement and interventions of the mitral and pulmonic valve as well as the left atrium, myocardial CT perfusion, hybrid imaging of anatomy and perfusion, and electrophysiology applications. Several revised chapters discuss other upcoming clinical applications of cardiac CT – plaque imaging and assessment of cardiac function and valves.

Another important asset of the book in terms of practical clinical application is that the authors present and discuss the specific features of the CT scanners from all four major vendors including all novelties as they relate to cardiac CT. In the final three chapters, relevant clinical examples, a summary of study results, and an outlook on conceivable future technical and clinical developments are given.

I congratulate the team of 41 authors on an excellent book that focuses on the practical clinical aspects of cardiac CT and offers its readers an easy to follow introduction to this promising new diagnostic tool. However, the book also provides useful tips and tricks for those already familiar with this imaging modality, which will help them further improve their diagnostic strategy for the benefit of their patients.

M. Dewey, *Cardiac CT*,
DOI 10.1007/978-3-642-41883-9_1,

Technical and Personnel Requirements

M. Dewey

Abstract

In this chapter, the requirements for setting up a cardiac CT practice are summarized. At least a 64-row CT scanner should be present from a technical perspective, and the personnel needs to be adequately und continuously trained in performing, reconstructing, and reading cardiac CT datasets.

List 2.1. Technical requirements for cardiac CT

1. CT scanner with at least 64 simultaneous rows
2. CT scanner with a gantry rotation time of below 400 ms
3. Adaptive multisegment reconstruction or dual-source CT
4. ECG for gating or triggering[a] of acquisitions
5. Dual-head contrast agent injector for saline flush
6. Workstation with automatic curved multiplanar reformation and three-dimensional data segmentation and analysis capabilities

[a] This refers to the acquisition method: retrospective (ECG gating) or prospective (ECG triggering). See Chap. 7 for details on radiation exposure reduction using ECG triggering

2.1 Technical Requirements

Noninvasive coronary angiography is the major clinical application of computed tomography (CT) that requires very high spatial and temporal resolution. Thus, CT scanners with multiple detector rows (multislice CT), short gantry rotation times, and thin-slice collimation are essential for establishing a successful cardiac CT practice. Because 64-row CT is relevantly superior to 16-row CT in terms of image quality and diagnostic accuracy, at least 64-row technology should be used for noninvasive coronary angiography (**List 2.1**). CT with 64-row technology not only increases the quality of the images (**Figs. 2.1**, **2.2** and **2.3**) but also improves the workflow because scanning and breath-hold times are shorter (**Table 2.1**). Even greater improvements can be achieved with imaging during a single heartbeat (**Table 2.1** and **Figs. 2.2** and **2.3**), which is feasible with 320-row volume CT and second-generation dual- source CT (Chaps. 9a and 9b). The shorter breath-hold time of 64-row CT and single-beat imaging is also very relevant for patients after coronary bypass grafting (**Fig. 2.4**, Chap. 12). The faster gantry rotation speed of recent CT scanners (**List 2.1**) improves temporal resolution and dramatically reduces the likelihood of relevant motion artifacts.

Temporal resolution can be significantly improved by using two simultaneous X-ray sources (dual-source CT, Siemens) and adaptive multisegment reconstruction (Toshiba, Philips, and GE). We believe that one of these two approaches should be implemented on cardiac CT scanners to reduce the influence of heart rate on image quality (**List 2.1**).

M. Dewey, *Cardiac CT*,
DOI 10.1007/978-3-642-41883-9_2, © Springer-Verlag Berlin Heidelberg 2014

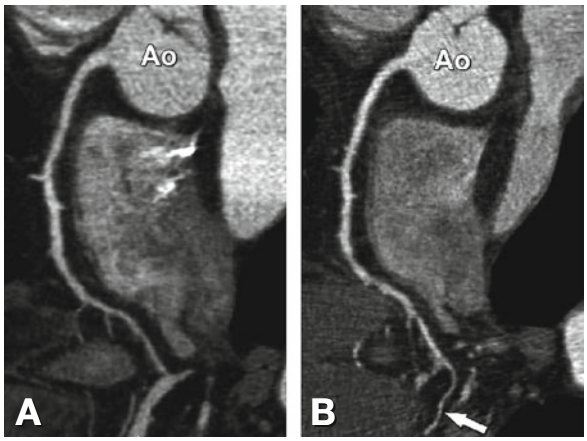

Fig. 2.1 Comparison of 16-row (**Panel A**) and 64-row CT coronary angiography (**Panel B**) of the right coronary artery (curved multiplanar reformation) in a 61-year-old male patient. 64-row CT shows longer vessel segments, especially in the periphery (*arrow*). This enhanced performance can be explained by fewer motion artifacts (due to breathing, extrasystoles, or variations in the length of the cardiac cycle) and the better contrast between arteries and veins resulting from the faster scan and consequently better depiction of the arterial phase. The improved depiction of the arterial phase using 64-row CT is also demonstrated in **Fig. 2.2**. **Panel B** also illustrates the slightly higher image noise with 64-row CT, which can be compensated for by the better depiction of the arterial phase and the higher intravascular density. *Ao* aorta

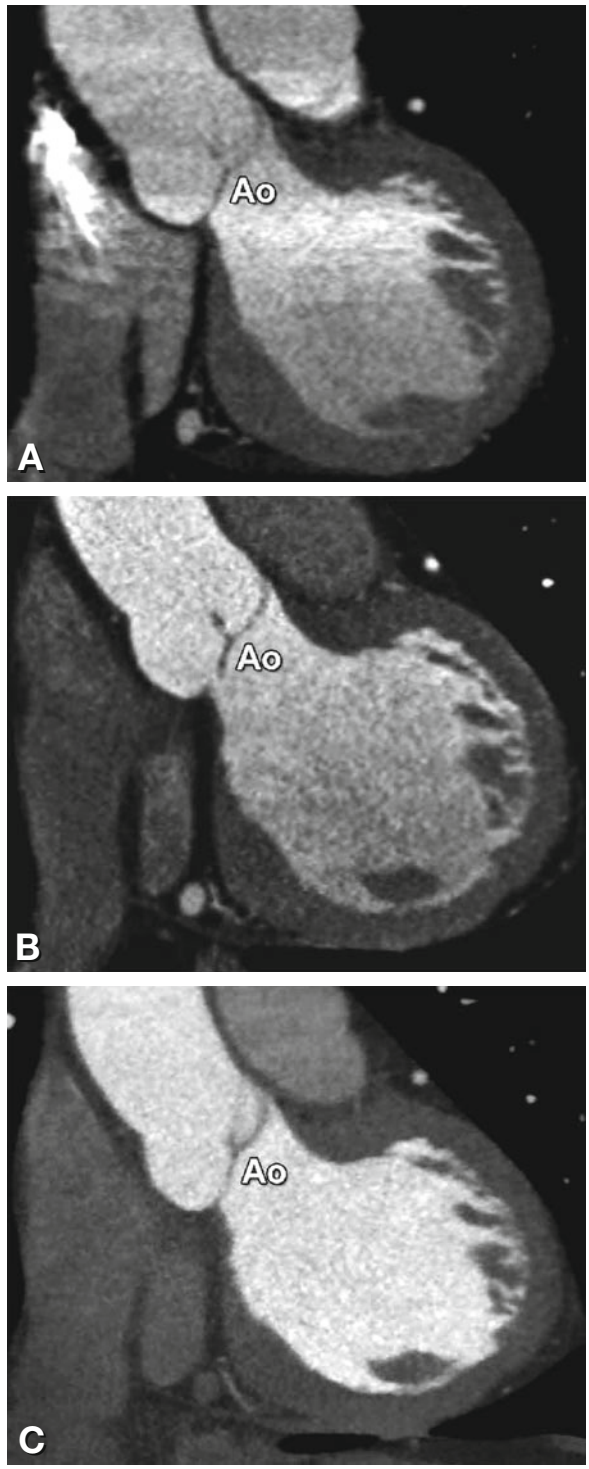

Fig. 2.2 The improved depiction of the arterial phase using 64-row CT (**Panel B**) and even further using 320-row CT (**Panel C**) when compared with 16-row CT (**Panel A**) is illustrated by a double oblique coronal slice along the left ventricular outflow tract, with the aortic valve nicely depicted (*Ao*). In the craniocaudal direction, the density in the aorta and left ventricle shows less variation and decline when 64 simultaneous detector rows are used (**Panel C**) and almost no difference with 320-row CT acquired during a single heartbeat. Use of 64- and 320-row CT thus improves image quality and facilitates the application of automatic coronary vessel and cardiac function analysis tools

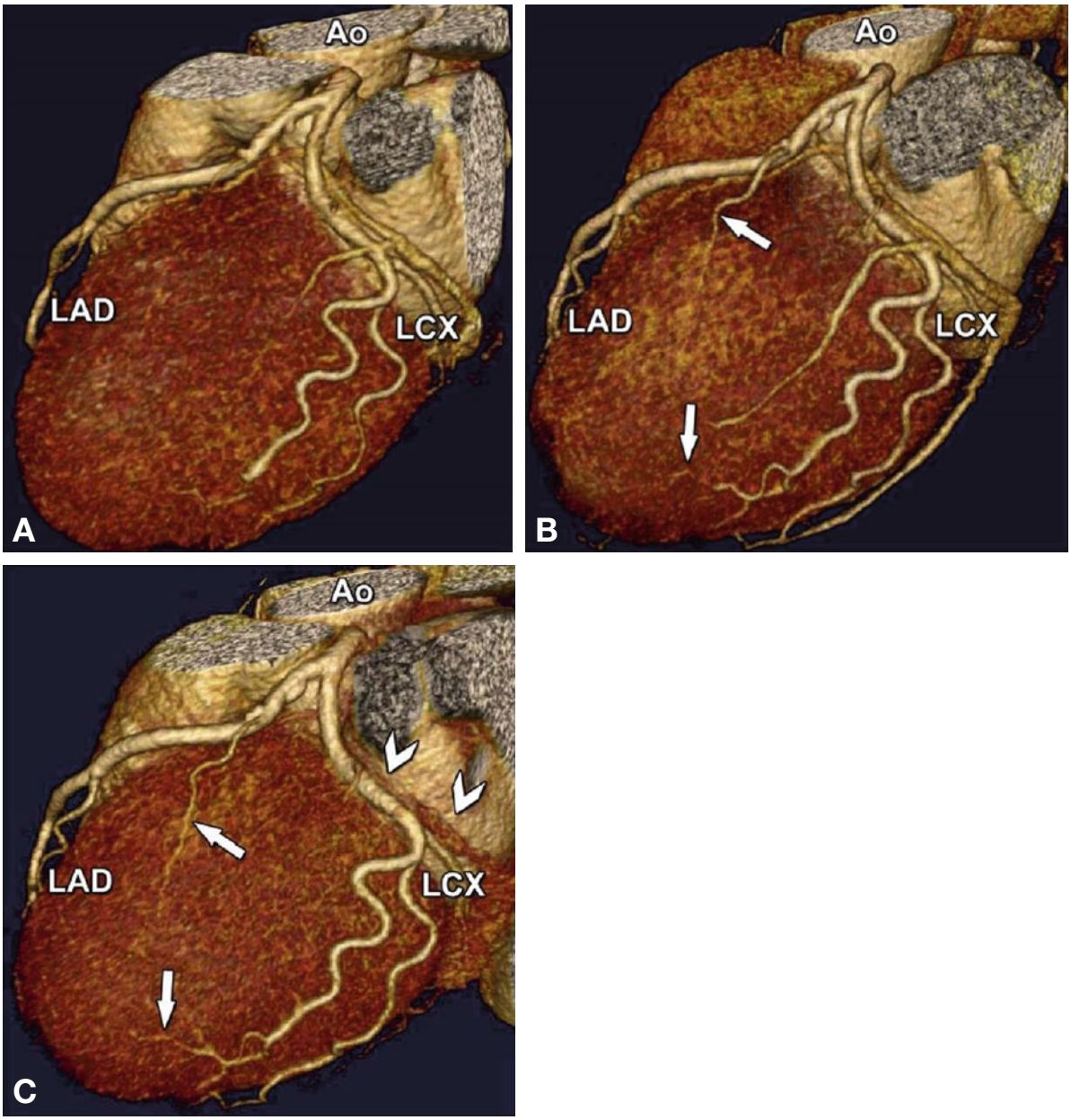

Fig. 2.3 Example illustrating the improved depiction of distal coronary artery branches using 64-row (**Panel B**) and 320-row CT (**Panel C**) in a 58-year-old female patient. Three-dimensional volume-rendered reconstructions of the left coronary artery with the left anterior descending (*LAD*) and left circumflex coronary artery (*LCX*) examined using 16-row (**Panel A**), 64-row (**Panel B**), and 320-row CT coronary angiography (**Panel C**). Note the improved depiction of smaller side branches with the 64-row (*arrows* in **Panel B**) and 320-row technology (*arrows* in **Panel C**) when compared with the same segments in 16-row CT (**Panel A**). Also, there is best depiction of the arterial phase (with less venous overlap, *arrowheads* in **Panel C**) using 320-row CT. Single-beat imaging using 320-row CT or second-generation dual-source CT with a fast prospective spiral also greatly reduces radiation exposure (Chap. 7). *Ao* aorta

Table 2.1 Typical characteristics of 16- and 64-row as well as single-heartbeat CT scanners

	16-row	64-row	Single heart beat CT[a]
Slice collimation			
Coronary arteries	0.5–0.75 mm	0.5–0.75 mm	0.5–0.6 mm
Coronary bypass grafts	0.5–1.25 mm	0.5–0.75 mm	0.5–0.6 mm
Gantry rotation time			
Coronary angiography	0.4–0.6 s	0.27–0.4 s	0.28–0.35 s
Scan length			
Coronary arteries	9–13 cm	Increase by 15%[b]	9–13 cm
Coronary bypass grafts	12.5–22 cm	Increased by 5–10%	12.5–22 cm[c]
Effective radiation dose			
Coronary arteries	5–15 mSv	10–20 mSv[d]	1–5 mSv
Coronary bypass grafts	10–30 mSv	20–40 mSv[d]	2–10 mSv
Contrast-to-noise ratio			
Coronary angiography	15–25	Similar	Similar
Vessel lengths free of motion			
Coronary angiography		Improved by 10–30%[e]	Further improvements expected
Breath-hold time[f]			
Coronary arteries	25–30 s	8–12 s	3 s
Coronary bypass grafts	40–50 s	12–15 s	5 s
Contrast agent amount			
Coronary arteries	90–130 ml	60–90 ml	40–70 ml
Coronary bypass grafts	130–160 ml	80–110 ml	50–80 ml

[a] CT of the heart during a single beat can be performed using 320-row volume CT (Chap. 9a) and second- or third- generation dual-source CT with a fast spiral acquisition (Chap. 9b)

[b] This increase is due to the larger overranging effect of 64-row CT, which in turn also increases radiation exposure by 15%

[c] Bypass grafts are scanned with 320-row CT in two heartbeats and with dual-source CT in the caudocranial direction with the proximal parts of the bypass grafts covered during the next R-wave and early systole of the next beat

[d] The values given here are for retrospectively acquired data. The increase in effective dose with 64-row CT can be explained by the larger overranging effect, the fact that scanning cannot be stopped as abruptly once the lower border of the heart has been reached because of the faster table speed, and the higher mA settings necessary (because of the increased scattered radiation and noise with 64-row CT). Using prospectively acquired data with 64-row CT, effective dose can be drastically reduced to below 5 mSv in nearly all patients with stable and low heart rates (<65 beats per minute). See Chap. 7

[e] The increase in the visible vessel length free of motion that can be obtained for the three coronary arteries with 64-row CT scanners is approximately 10% for the left anterior descending, 20% for the left circumflex, and 30% for the right coronary. Most notably, in more than one-third of all cases, the length of the right coronary free of motion is increased by more than 5 cm when 64-row CT is used

[f] This includes a 2–3 s wait period after the breathing command before scanning to assure normalization of heart rate after inspiration

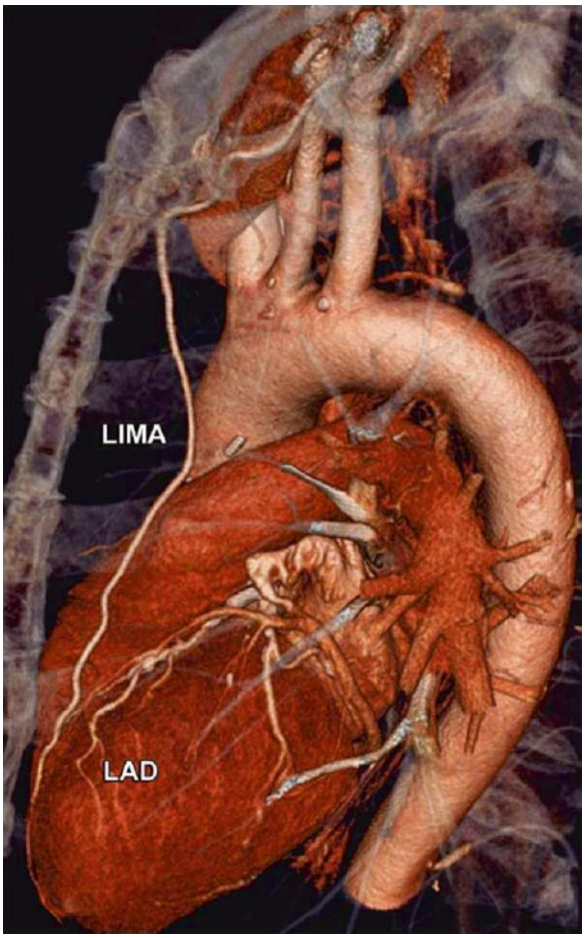

Fig. 2.4 Arterial bypass graft (left internal mammary artery, *LIMA*), which extends all the way down to the LAD and was scanned in less than 15 s, using a 64-row CT scanner. With this technology, preoxygenation is no longer necessary for bypass imaging. With 16-row technology, the scanning took an average of 40–50 s, and preoxygenation was almost always required. Note that CT nicely depicts the distance between the sternum and coronary bypass graft, which can be of relevance if repeat cardiac surgery is considered. Bypass imaging time can be further shortened with 320-row CT and second-generation dual-source CT (**Table 2.1**)

In addition to these technical improvements, beta blocker administration should be used whenever possible to lower the heart rate to below approximately 60 beats per min, because slowing the heart rate to this level further improves both the image quality and the diagnostic accuracy (Chaps. 6 and 8) while also reducing radiation exposure because ECG triggering can be used (Chap. 7). Finally, an ECG, a dual-head contrast agent injector, and an automatic three-dimensional analysis workstation are required for cardiac CT (**List 2.1**).

2.2 Purchasing a Scanner

The purchase costs of CT scanners still differ enormously. For applications other than cardiac imaging, 16-row CT scanners are clearly sufficient to answer the vast majority of clinical questions. For cardiac applications, however, at least 64-row technology is clearly needed. The decision to purchase a scanner from any particular manufacturer not only depends on its meeting the relevant technical criteria, such as those mentioned earlier, but will definitely also be influenced by local pricing policies and, more important, by the quality of the maintenance and service support (**List 2.2**). How to perform cardiac CT exams using scanners from the four main vendors is explained in Chaps. 9a, 9b, 9c and 9d.

List 2.2. Factors to consider in deciding to purchase a particular CT sanner

1. Local situation and mixture of different examination types
2. Quality of technical and maintenance support
3. Availability of high temporal and spatial resolution
4. Quality and durability of the application support
5. Integration into existing picture archiving and communication systems
6. Local pricing policies

Multislice CT has a variety of other applications in addition to cardiac imaging, and CT scanners used solely for cardiac applications are very unlikely to reach the break-even point. Thus, we believe that a mixture of different CT applications is a prerequisite for clinical and economic success. In the USA, the Center for Medicare and Medicaid Services (CMS) decided after an extensive review that no Medicare national coverage of coronary CT angiography was appropriate in 2008. In the decision memo, it is concluded that no adequately powered study has established that improved health outcomes can be causally attributed to coronary CT angiography for any well-defined clinical indication. Thus, coverage will be determined by local contractors through the local coverage determination process or case-by-case adjudication. The local coverage decisions are variable in extent. Effective January 1, 2010, the American Medical Association (AMA) released the new Current Procedural Terminology (CPT) Category I codes for cardiac CT with four new

codes. These replace the previous Category III CPT codes for cardiac CT, which listed cardiac CT examinations as "emerging technology." Coverage is a local issue that is quickly changing and needs to be looked into before setting up a cardiac CT practice anywhere. Chapter 4 discusses cardiac CT in clinical practice and Chap. 5 presents clinically most relevant indications for cardiac CT. In some countries, such as Japan, there is national coverage of cardiac CT, whereas in others such as Germany cardiac CT is reimbursed as a chest CT only.

2.3 Personnel Requirements

Having well-trained technicians who are knowledgeable in cardiac CT applications is a prerequisite for success (**List 2.3**). It is better to have a limited number of specialized technicians who perform cardiac CT than to have all technicians perform this test. On the one hand, having specialized staff members can ensure a consistently high level of image quality, and these experienced technicians can assist in further educating other coworkers about the entire scanning and reconstruction procedure. On the other hand, if more technicians are involved in performing cardiac CT, coronary CT angiography can easily be offered at night; doing so, however, also requires a physician trained in reading the images 24 by 7. What we consider most helpful in terms of training is to give constant feedback to the technicians about good as well as bad examinations. This approach ensures that a high level of quality is maintained, and small mistakes are prevented from creeping in. Moreover, providing positive feedback about high-quality examinations is very motivating, and sufficient hands-on training should be provided to anyone involved in performing or reading cardiac CT scans.

List 2.3. Personnel requirements for cardiac CT

1. Well-trained and experienced CT technicians
2. Physician knowledgeable in CT and radiation exposure
3. Physician knowledgeable in cardiac anatomy and pathophysiology
4. Team focused on quality assurance

There are two major prerequisites for physicians, in addition to good anatomical, technical (incl. radiation issues), and clinical knowledge: (1) a clear understanding of the entire examination procedure, and (2) the ability to independently interpret three-dimensional cardiac CT datasets on workstations.

Chapters 6 and 8 discuss how to prepare the patient for cardiac CT and how to perform the procedure. Being present during examinations is the key to understanding the work of the technicians and the special requirements of cardiac CT. It is also enlightening for physicians to perform examinations themselves, because doing so can yield important insights into the procedural steps and problems that can be encountered during scanning. This hands-on training also strengthens the position of the physician as an educator of other physicians or technicians. In larger centers, it is good to identify two to three doctors who will be considered the primary contacts for cardiac CT imaging for the technicians as well as the referring physicians.

2.3.1 Hands-on Courses, Learning Curve, and Accreditation

Competence in image interpretation is best achieved by correlating conventional coronary angiograms with CT angiography results. How to read and interpret cardiac CT scans is explained in Chap. 10. To understand and gain skill in using the workstations, physicians should practice operating them without time pressure. The time necessary to feel comfortable with the workstations will depend on an individual's general computer skills, but 2–4 continuous weeks should be sufficient, and attending one of the true hands-on courses is a good way to begin the learning process. Such courses should ideally offer direct comparison of CT findings (on interactive workstations) with conventional coronary angiography and/or the results of cardiac stress tests. This is the only way of acquiring a thorough understanding of coronary and cardiac pathology. Good cardiac CT courses and fellowships also offer active participation in patient preparation and scanning. Nevertheless, the learning curve for centers with some prior experience has been shown to last at least 6 months before the diagnostic accuracy stabilizes, and the learning curve of individuals with little prior exposure is considerable (at least about 12 months).

Moreover, learning does not stop after a few weeks of intensive familiarization with the workstations or a

short course: Even in a team of experienced readers, certain coronary lesions will sometimes be misinterpreted (over- called or even overlooked). Thus, continuous learning efforts with comparison of CT to the invasive coronary angiography findings, e.g., in joint interdisciplinary conferences, are necessary to maintain high quality.

There is also a formal accreditation of the physicians' skills and knowledge. The American College of Radiology (ACR) and the American College of Cardiology (ACC) have established guidelines for assessing clinical competence in performing and interpreting cardiac CT. These guidelines play an increasing role in obtaining certification and claiming reimbursement in the US. Those outside the US may find it useful to study these guidelines as a basis for starting discussions about certification of cardiac CT readers and centers in their own countries.

In Germany, for instance, the law requires that every physician performing CT (of any organ) hold the *Fachkunde* ("technical qualification") for CT, which requires having conducted 1,000 examinations over a period of at least 12 months and participating in a course on radiation protection. Such regulations offer promise for reducing patient radiation exposure and they emphasize the relevance of the ongoing discussion on requirements for cardiac CT.

2.3.2 Guidelines of the ACR

Several ACR guidelines are relevant to coronary CT angiography. Most important is the "ACR Practice Guideline for the Performance and Interpretation of Cardiac Computed Tomography" (http://www.acr.org/~/media/ACR/Documents/PGTS/guidelines/CT_Cardiac.pdf). Other important guidelines are the "ACR Clinical Statement on Noninvasive Cardiac Imaging," "ACR Practice Guideline for the Performance and Interpretation of CT Angiography," and the "ACR Practice Guideline for Performing and Interpreting Diagnostic Computed Tomography." Later we briefly outline and discuss the recommendations arising from the guidelines that directly relate to coronary CT angiography.

The ACR defines cardiac CT as a chest CT performed primarily for the evaluation of the heart (including the cardiac chambers, valves, myocardium, aorta, central pulmonary vessels, pericardium, coronary arteries, and veins). However, noncardiac structures are included and must be evaluated by a trained physician. Trained physicians are defined in the "ACR Practice Guideline for Performing and Interpreting Diagnostic Computed Tomography" as board-certified radiologists who have interpreted and reported at least 100 CT examinations over each of the past 3 years and interpret and report at least 100 CT examinations per year to maintain

Table 2.2 ACR physician requirements for coronary CT angiography

	Not trained in general or thoracic CT	Board-certified radiologists[a]
CME (category I)	Completion of an ACGME approved training program in the specialty practiced 200 h in cardiac CT[b]	Training in cardiac CT in an ACGME approved training program 30 h in cardiac anatomy, physiology, pathology, and cardiac CT
Interpretation, reporting, and/or supervised review[c]	500 CT examinations[d]	50 contrast-enhanced cardiac CT examinations
Maintaining competence	75 contrast-enhanced cardiac CT examinations every 3 years 150 h of CME every 3 years	

ACGME Accreditation Council for Graduate Medical Education

[a] In addition, at least 100 CT examinations are required during each of the past 3 years, as also at least 100 CT examinations per year to maintain competence according to the ACR practice guideline for performing and interpreting diagnostic CT

[b] Including at least 30 h in cardiac anatomy, physiology, pathology, and cardiac CT

[c] Examinations (noncontrast examinations do not count) in a supervised environment during the past 3 years; supervising physician needs to meet the ACR requirements

[d] At least 100 must be a combination of thoracic CT or thoracic CT angiography (exclusive of calcium scoring exams). At least 50 contrast-enhanced cardiac CT examinations must also be included

competence. These physicians can achieve competence in the performance and interpretation of coronary CT angiography by at least 30 h of CME in cardiac anatomy, physiology, pathology, and cardiac CT, plus the interpretation, reporting, and/or supervised review of at least 50 cardiac CT examinations during the past 3 years (**Table 2.2**). Physicians who are not defined in this guideline as trained physicians in diagnostic CT can achieve competence in the performance and interpretation of coronary CT angiography by at least 200 h of CME in the performance and interpretation of cardiac CT, plus the interpretation, reporting, and/or supervised review of at least 500 chest CT examinations (including 50 cardiac CT examinations) during the past 3 years (**Table 2.2**). The ACR stresses that all physicians performing cardiac CT need to be knowledgeable about the administration, risks, and contraindications of beta blockers and nitroglycerin.

2.3.3 Guidelines of the ACC

The "ACC Clinical Competence Statement on Cardiac Imaging with Computed Tomography and Magnetic Resonance" (http://www.cbcct.org/resources/ CT_CMRcompetency.pdf) states that it is intended to be complementary to the recommendations of the ACR on noninvasive cardiac imaging. Cardiac CT is defined in this guideline as the imaging of anatomy, function, coronary calcium, noncalcified plaque, and congenital heart disease. The guideline defines three levels of competence in coronary CT angiography, of which two are relevant here. Level 2 allows independent performance and interpretation of cardiac CT and requires 8 weeks (each consisting of at least 35 h) of cumulative training in a clinical cardiac CT laboratory plus 150 contrast-enhanced and 50 noncontrast cardiac CT examinations. A physician willing to achieve level 2 competence needs to be physically present and involved in the acquisition and performance of 50 of the 150 contrast-enhanced cardiac CT examinations (**Table 2.3**). Level 3 allows serving as a director of an independent cardiac CT center and requires 6 months of cumulative training in a clinical cardiac CT laboratory plus 300 contrast-enhanced and 100 noncontrast cardiac CT examinations. A physician willing to achieve level 3 competence needs to be physically present and involved in the acquisition and performance of 100 of the 300 contrast-enhanced cardiac CT examinations (**Table 2.3**). An additional recommendation for "Training in Advanced Cardiovascular Imaging (Computed Tomography)" has been released by the ACC. The ACC stresses that all physicians performing cardiac CT need to be knowledgeable about radiation risks and noncardiac findings on coronary CT angiography. Interestingly, Pugliese et al. have recently shown that it may take more than 12 months of full-time training in cardiac CT for a novice to acquire moderate expertise and they conclude that the levels of training suggested by the ACC may thus be insufficient to become an independent practitioner of cardiac CT. However, the debate is ongoing and further recommendations are expected.

Table 2.3 ACC physician requirements for coronary CT angiography

	Level 2[a]	Level 3[b]
CME (category I)	20 h in cardiac CT	40 h in cardiac CT
Training[c]	8 weeks	6 months
Interpretation, reporting, and/or supervised review	50 noncontrast and 150 contrast- enhanced cardiac CT examinations[d]	100 noncontrast and 300 contrast-enhanced cardiac CT examinations[d]
Maintaining competence	50 contrast-enhanced cardiac CT examinations every year, 20 h of CME in cardiac CT every 3 years	100 contrast-enhanced cardiac CT examinations every year, 40 h of CME in cardiac CT every 3 years

[a] Allows independent performance and interpretation of cardiac CT

[b] Allows serving as a director of an independent cardiac CT center

[c] Training must be conducted under the supervision of a level 3 physician. Each week consists of at least 35 h. The time commitment does not go into effect until July 2010

[d] Physically present and involved in the acquisition, performance, and interpretation of 50 (level 2) or 100 (level 3) contrast-enhanced cardiac CT examinations. The noncontrast examinations can be performed in the same patients who undergo contrast-enhanced CT

Recommended Reading

Achenbach S, Chandrashekhar Y, Narula J (2008) Computed tomographic angiography and the Atlantic. JACC Cardiovasc Imaging 1:817–819

Budoff MJ, Achenbach S, Berman DS et al (2008) Task force 13: training in advanced cardiovascular imaging (computed tomography) endorsed by the American Society of Nuclear Cardiology, Society of Atherosclerosis Imaging and Prevention, Society for Cardiovascular Angiography and Interventions, and Society of Cardiovascular Computed Tomography. J Am Coll Cardiol 51:409–414

Budoff MJ, Cohen MC, Garcia MJ et al (2005) ACCF/AHA clinical competence statement on cardiac imaging with computed tomography and magnetic resonance. J Am Coll Cardiol 46:383–402, The guideline of the ACC (Budoff et al.) can be accessed at: http://content.onlinejacc.org/article.aspx?articleid=1136771

Chin S, Ong T, Chan W et al (2006) 64 row multi-detector computed tomography coronary image from a centre with early experience: first illustration of learning curve. J Geriatr Cardiol 3:29–34

Dewey M, Hamm B (2007) Cost effectiveness of coronary angiography and calcium scoring using CT and stress MRI for diagnosis of coronary artery disease. Eur Radiol 17:1301–1309

Dewey M, Hoffmann H, Hamm B (2007) CT coronary angiography using 16 and 64 simultaneous detector rows: intraindividual comparison. Rofo 179:581–586

Hamon M, Morello R, Riddell JW (2007) Coronary arteries: diagnostic performance of 16- versus 64-section spiral CT compared with invasive coronary angiography-meta-analysis. Radiology 245:720–731

Hausleiter J, Meyer T, Hadamitzky M et al (2007) Non-invasive coronary computed tomographic angiography for patients with suspected coronary artery disease: the Coronary Angiography by Computed Tomography with the Use of a Submillimeter resolution (CACTUS) trial. Eur Heart J 28:3034–3041

Jacobs JE, Boxt LM, Desjardins B, Fishman EK, Larson PA, Schoepf J (2006) ACR practice guideline for the performance and interpretation of cardiac computed tomography (CT). J Am Coll Radiol 3:677–685, The ACR practice guideline for the performance and interpretation of cardiac CT (update of Jacobs et al.) can be accessed at: http://www.acr.org/~/media/ACR/Documents/PGTS/guidelines/CT_Cardiac.pdf

Pannu HK, Alvarez W Jr, Fishman EK (2006) Beta-blockers for cardiac CT: a primer for the radiologist. AJR Am J Roentgenol 186:S341–S345

Pugliese F, Hunink MG, Gruszczynska K et al (2009) Learning curve for coronary CT angiography: what constitutes sufficient training? Radiology 251:359–368

Weinreb JC, Larson PA, Woodard PK et al (2005) ACR clinical statement on noninvasive cardiac imaging. J Am Coll Radiol 2:471–477

Further Recommended Websites

The ACR practice guideline for the performance and interpretation of cardiac CT (update of Jacobs et al.) can be accessed at: http://www.acr.org/~/media/ACR/Documents/PGTS/guidelines/CT_Cardiac.pdf

The guideline of the ACC (Budoff et al.) can be accessed at: http://content.onlinejacc.org/article.aspx?articleid=1136771

http://www.escr.org

http://www.nasci.org

http://www.scct.org

http://cccvi.org/cbcct/

Anatomy

M. Dewey and L.J.M. Kroft

Abstract

This chapter reviews coronary and myocardial anatomy and stresses its relevance to cardiac CT. It is important that physicians interpreting cardiac CT use the same coronary artery segmentation scheme as the interventional laboratories with which they are working together. Myocardial segmentation should follow the standardized 17-segment model.

3.1 Coronary Arteries

The major coronary arteries, together with their second-order branches, can usually be well-visualized by CT. Third-order branches may be visualized, but smaller branches are generally not visible because of their small size and the limitations of the scanner with regard to spatial and temporal resolution.

In the normal situation, the coronary arteries arise from the proximal aorta. The right and left coronary arteries arise from the right and left sinus of Valsalva, respectively. The noncoronary sinus of Valsalva is usually the posterior one. The main coronary artery segments run in the left and right atrioventricular grooves between the atria and ventricles, and then perpendicularly in the anterior and posterior interventricular grooves between the left and right ventricles (**Fig. 3.1**). The coronary arteries and their side branches vary greatly in terms of their presence or absence and their size, shape, and length. A pragmatic approach that can help understand the relationship between the heart and the three-dimensional coronary artery anatomy uses the demonstrator's left and right hand for illustration (**Fig. 3.2**).

The right coronary artery (RCA) arises from the aorta at the right sinus of Valsalva and courses in the right atrioventricular groove. Along its course, it first gives off the conus artery (in 50% of all individuals; in the other 50%, the conus artery arises directly from the aorta). It then gives off the sinoatrial node artery (in roughly 60%; in the remaining individuals, it arises from the left circumflex coronary artery [LCX]). Acute marginal branches arise from the mid-segment and posterior right ventricular branches from the distal segment. In case of a right-dominant circulation, the RCA gives rise to the posterior descending artery (PDA) at or near the crux cordis (where the left and right atrioventricular groove and posterior interventricular groove join), from where it courses in the posterior interventricular groove, and the RCA gives rise to posterolateral artery branches as it continues in the left atrioventricular groove beyond the crux. In case of a left-dominant circulation, the LCX gives rise to the PDA. The RCA supplies both the myocardium of the right atrium and ventricle and inferior portions of the left ventricle and interventricular septum.

The left main coronary artery (LM) arises from the aorta at the left sinus of Valsalva and has a length that varies from 0 to 15 mm. The LM usually bifurcates into the left anterior descending coronary artery (LAD) and LCX; however, in a third of the population, the LM ends as a trifurcation with an intermediate branch (IMB, also called ramus medianus) arising between the LAD and the LCX (**Fig. 3.3**). An IMB can be regarded as a diagonal branch or as an obtuse marginal branch, depending on its course along the left ventricle.

M. Dewey, *Cardiac CT*,
DOI 10.1007/978-3-642-41883-9_3,

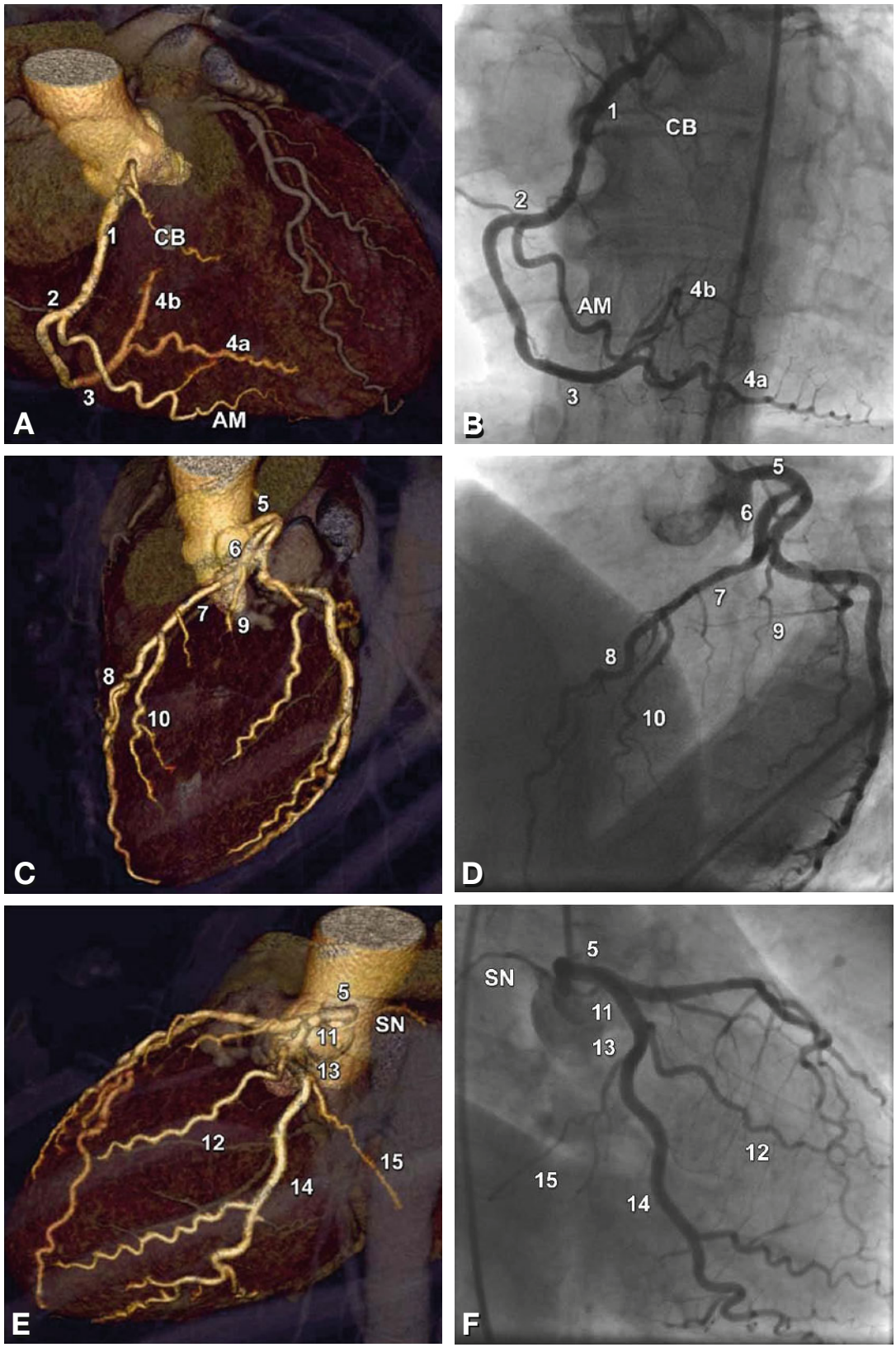
A
1
CB
2
4b
4a
3
AM
B
1
CB
2
AM
4b
4a
3
C
5
6
7
9
8
10
D
5
6
7
9
8
10
E
5
SN
11
13
12
15
14
F
5
SN
11
13
12
15
14

Fig. 3.1 Direct comparison of segmental coronary artery anatomy, as depicted by CT (*left panels*, three-dimensional reconstructions) and conventional coronary angiography (*right panels*). If an intermediate branch is present (about 30% of patients) this segmentation model consists of 17 segments. The RCA with its five segments is shown in **Panels A** and **B**, and the left coronary artery with its two main branches – the left anterior descending and the left circumflex – in **Panels C**–**F**. The RCA (**Panels A** and **B**) is composed of segments 1–4, with the distal segment (4) being further subdivided into 4a (posterior descending artery, PDA) and 4b (right posterolateral branch). The left main coronary artery (**Panels C**–**F**) is referred to as segment 5, and the left anterior descending coronary artery (**Panels C** and **D**) is composed of segments 6–10, with the two diagonal branches being segments 9 and 10. The LCX (**Panels E** and **F**) is composed of segments 11–15, with the two (obtuse) marginal branches being segments 12 and 14. Note that the distal left circumflex (segment 15) is rather small in this patient with a right-dominant coronary circulation. The sinus node artery (SN) is the first branch of the LCX in this patient (**Panels E** and **F**) but is more commonly one of the first branches of the RCA. *AM* acute marginal branch, *CB* conus branch. **Table 3.1** gives an overview of all coronary artery segment numbers and names

Table 3.1 Coronary artery anatomy using a 17-segment model

Segment no.	Vessel name	Segment name
1	Right coronary artery (RCA)	Proximal right coronary
2		Mid right coronary
3		Distal right coronary
4a		Posterior descending artery[a]
4b		Right posterolateral branch[a]
5	Left main coronary artery (LM)	Left main coronary artery
6	Left anterior descending artery (LAD)	Proximal left anterior descending
7		Mid left anterior descending
8		Distal left anterior descending
9		First diagonal branch
10		Second diagonal branch
11	Left circumflex artery (LCX)	Proximal left circumflex
12		First (obtuse) marginal
13		Mid left circumflex
14		Second (obtuse) marginal
15		Distal left circumflex[a]
16	Intermediate branch[b]	Intermediate branch[b]

This segmentation is based on the AHA segmentation published in 1975 by Austen et al.

[a] In case of RCA dominance, at least one right posterolateral branch (segment 4b) is present and supplies the inferolateral myocardial segments. If the left coronary artery is dominant, the distal LCX ends as the posterior descending coronary artery (segment 4a). In case of codominance, segment 4a is part of the RCA, and the distal left circumflex ends as a posterolateral branch after giving off two marginal branches

[b] An intermediate branch (ramus intermedius) is present in approximately 30% of patients and is the 17th segment in this model (note that the RCA has five segments with segment 4 being subdivided into 4a and 4b)

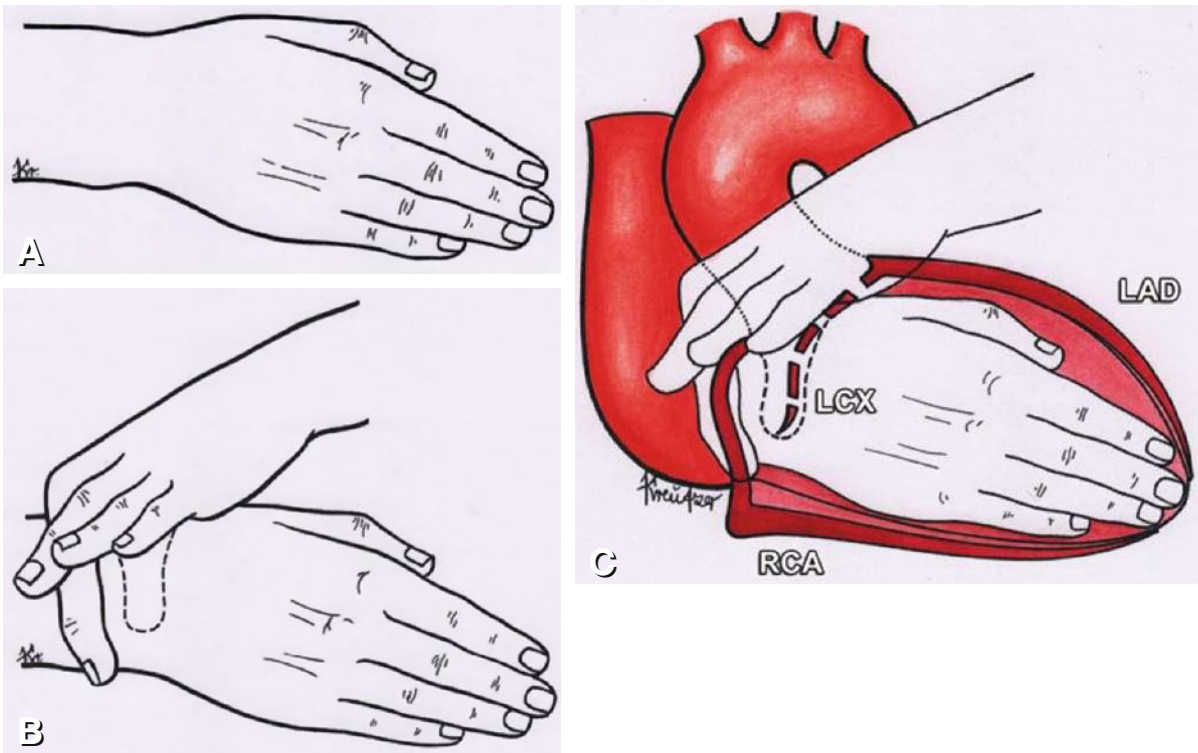

Fig. 3.2 Simple method of teaching three-dimensional coronary artery anatomy. The technique utilizes the concept of two imaginary circles around the interventricular and atrioventricular grooves, which are indicated by the position of the demonstrator's right and left hand, respectively. **Panel A** shows the right hand which demonstrates the position of the interventricular septum with its margins, the posterior and anterior interventricular groove. In **Panel B** the atrioventricular groove is represented by the thumb and index finger of the added left hand, which encircle the right wrist. The superimposed cardiac structures with the coronary arteries are shown in **Panel C**. *LAD* left anterior descending artery, *LCX* left circumflex coronary artery, *RCA* right coronary artery (Adapted from Sos and Sniderman, *Radiology*, 1980)

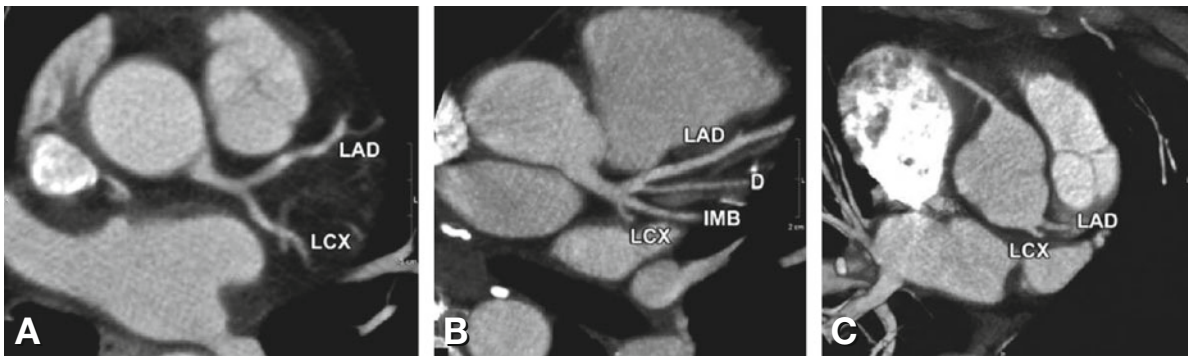

Fig. 3.3 Different types of left main coronary artery bifurcation. Oblique transverse thin-slab maximum-intensity projection images. The left main coronary artery is shown bifurcating into the left anterior descending coronary artery (*LAD*) and left circumflex coronary artery (*LCX*, **Panel A**), the left main with trifurcation into the LAD and the LCX, and in between an intermediate branch (*IMB*, **Panel B**). Note the high diagonal branch (*D*) from the LAD (**Panel B**). An absent left main coronary artery, with separate origins for the LAD and LCX (**Panel C**)

In about 1% of the population, the LM is absent, and there are separate ostia for the LAD and LCX (**Fig. 3.3**).

The LAD courses in the anterior interventricular groove. The major branches of the LAD are the septal branches that pass downward into the interventricular septum and the diagonal branches (usually one to three are present) that pass over the anterolateral aspect of the heart. The LAD and its side branches supply the anterior as well as the anteroseptal and anterolateral left ventricular segments. The septal branches, in particular, serve as important collateral pathways.

The LCX courses in the left atrioventricular groove, where the major side branches are the obtuse marginal branches (usually one to three are present) that supply

the lateral free wall of the left ventricle. The left atrial circumflex branches that supply the lateral and posterior aspect of the left atrium also arise from the LCX.

3.1.1 Coronary Artery Dominance

The circulation is right-dominant in about 60–85% of the population (the RCA gives rise to the posterior descending and at least one posterolateral branch). Left coronary dominance (the LCX gives rise to the PDA) is found in 7–20% of the population, whereas a balanced (or co-dominant) distribution is seen in 7–20% (the RCA gives rise to the PDA, and the LCX gives rise to posterolateral branches). In the case of a left-dominant circulation, the RCA is small and does not supply blood to the left ventricular myocardium. Recognizing the dominancy of the circulation is important, so as to avoid confusing this situation with branch occlusion (e.g., a short RCA in a left-dominant circulation, **Fig. 3.4**). Although it is

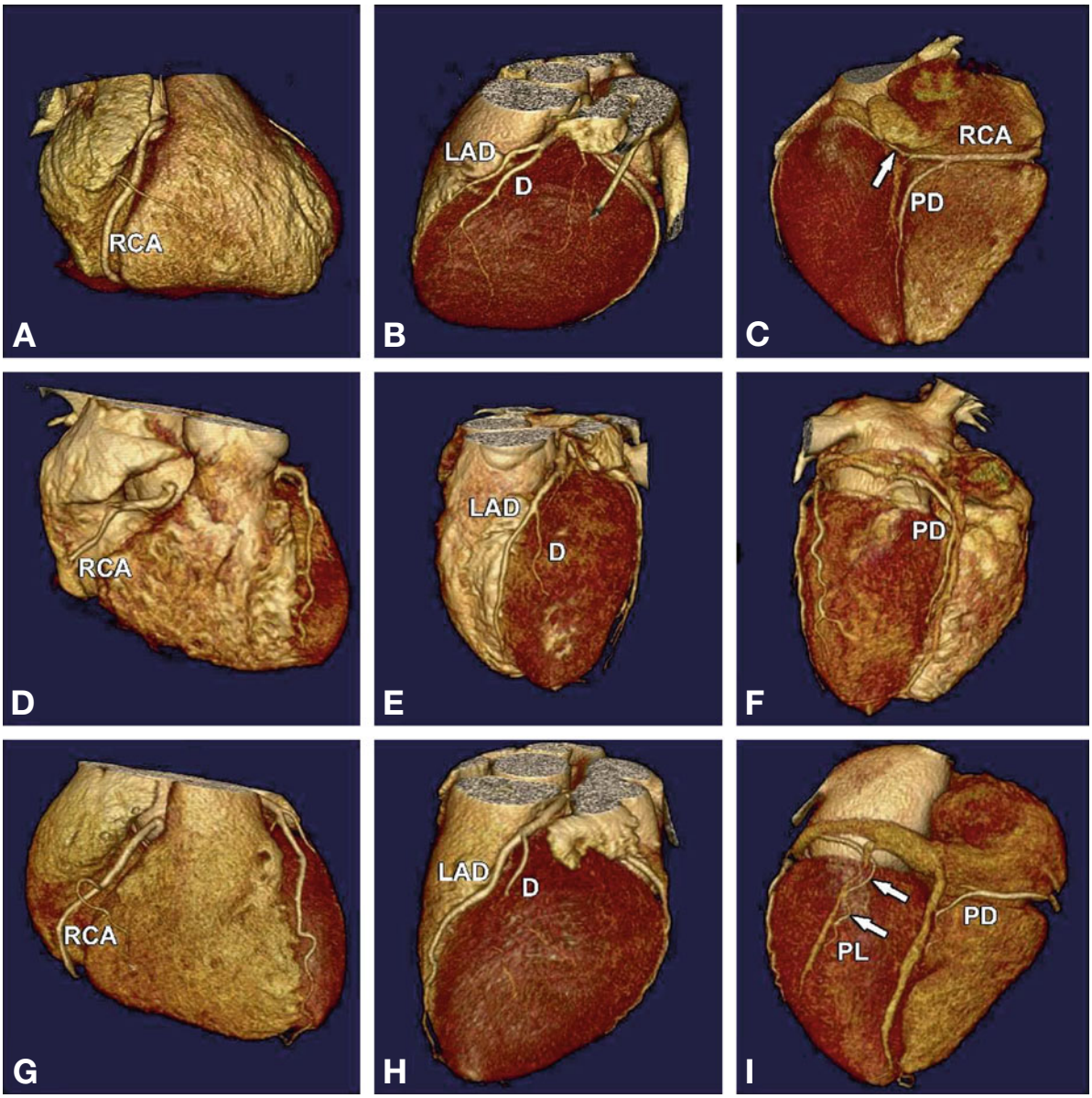

Fig. 3.4 Different coronary artery distribution types on three-dimensional volume-rendered images. **Panels A–C**: Right-dominant circulation. The RCA is dominant and gives rise to the posterior descending artery (*PD*), and also continues in the left atrioventricular groove (*arrow* in **Panel C**). **Panels D–F**: Left-dominant circulation. The LCX is dominant and gives rise to the posterior descending artery (*PD* in **Panel F**). Note the small RCA in the left-dominant coronary artery system (**Panel D**). **Panels G–I**: Balanced circulation (codominant circulation), where the RCA gives rise to the PD and the LCX gives rise to a posterolateral branch (*PL* in **Panel I**). *D* diagonal branch; *LAD* left anterior descending artery

the RCA that is typically dominant, it is usually the left coronary artery that supplies the major part of the left ventricular myocardium as well as the anterior and mid portions of the interventricular septum.

3.1.2 Coronary Artery Segments

The coronary arteries with their side branches can be further subdivided and classified (**Figs.** 3.1, 3.5, 3.6, and 3.7 and **Table** 3.1). These segments are of importance in describing the location of significant coronary stenoses found on noninvasive imaging and correlating them with possible myocardial ischemia, as well as for accurately guiding subsequent revascularization. Use of the 17-segment model further described in **Table** 3.1 and **Figs.** 3.1, 3.5, 3.6, and 3.7 is recommended for this purpose; in the case of pathology (i.e., the presence of stenoses), it is recommended that the location be reported either by segment name or by number. The 17-segment model has advantages over its competitor segmentation schemes, the foremost being its simplicity and conciseness.

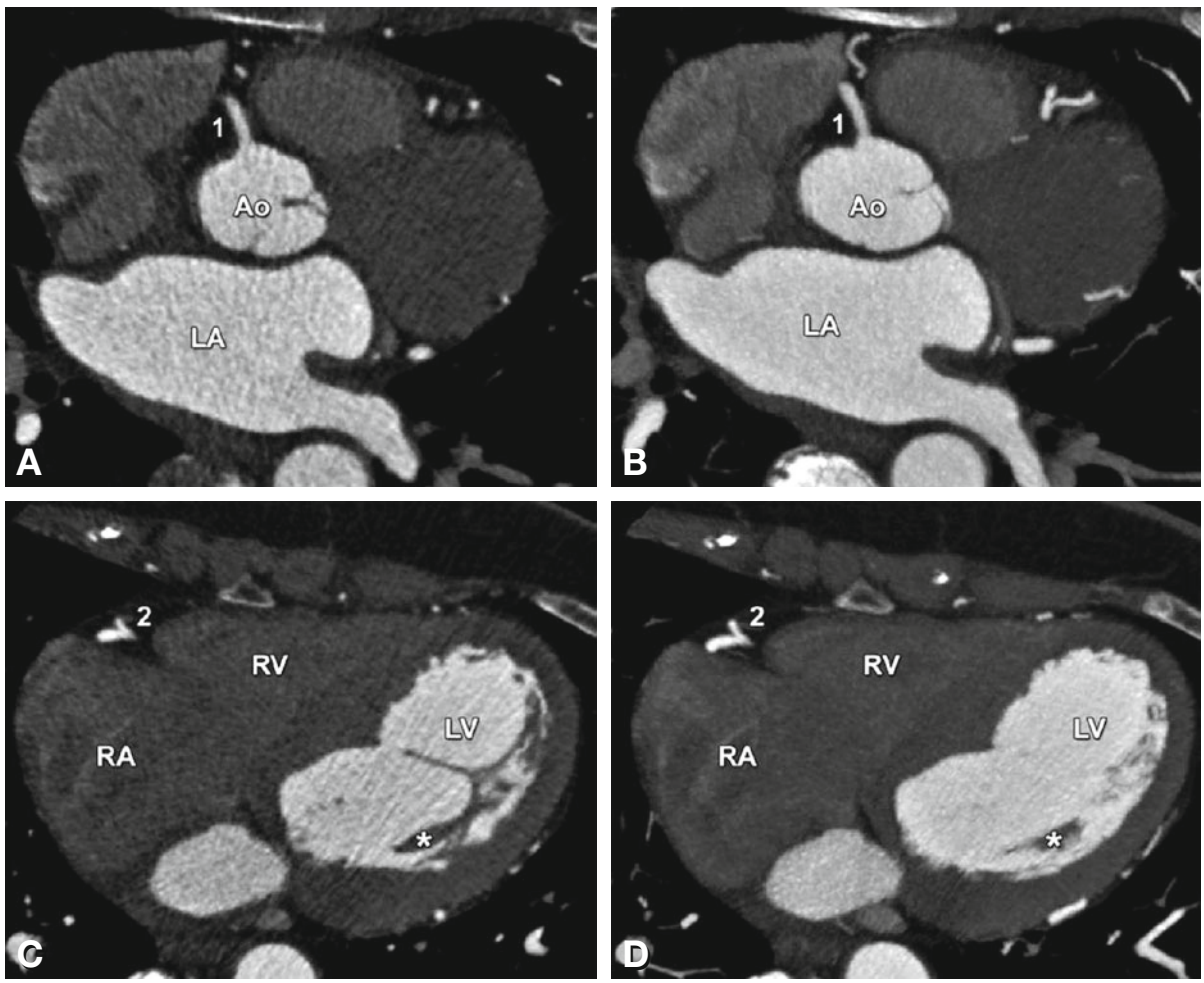

Fig. 3.5 The RCA with all its segments in axial slices (*left panels*), and the corresponding maximum-intensity projections of 5-mm thickness in the axial orientation for comparison (*right panels*). The proximal segment of the RCA (1) comes off the aorta, arising from the right sinus of Valsalva (**Panels A** and **B**). It first moves anteriorly and then (as segment 2) caudally in the right atrioventricular sulcus (**Panels C** and **D**) to the posterior surface of the heart (**Panels E** and **F**)

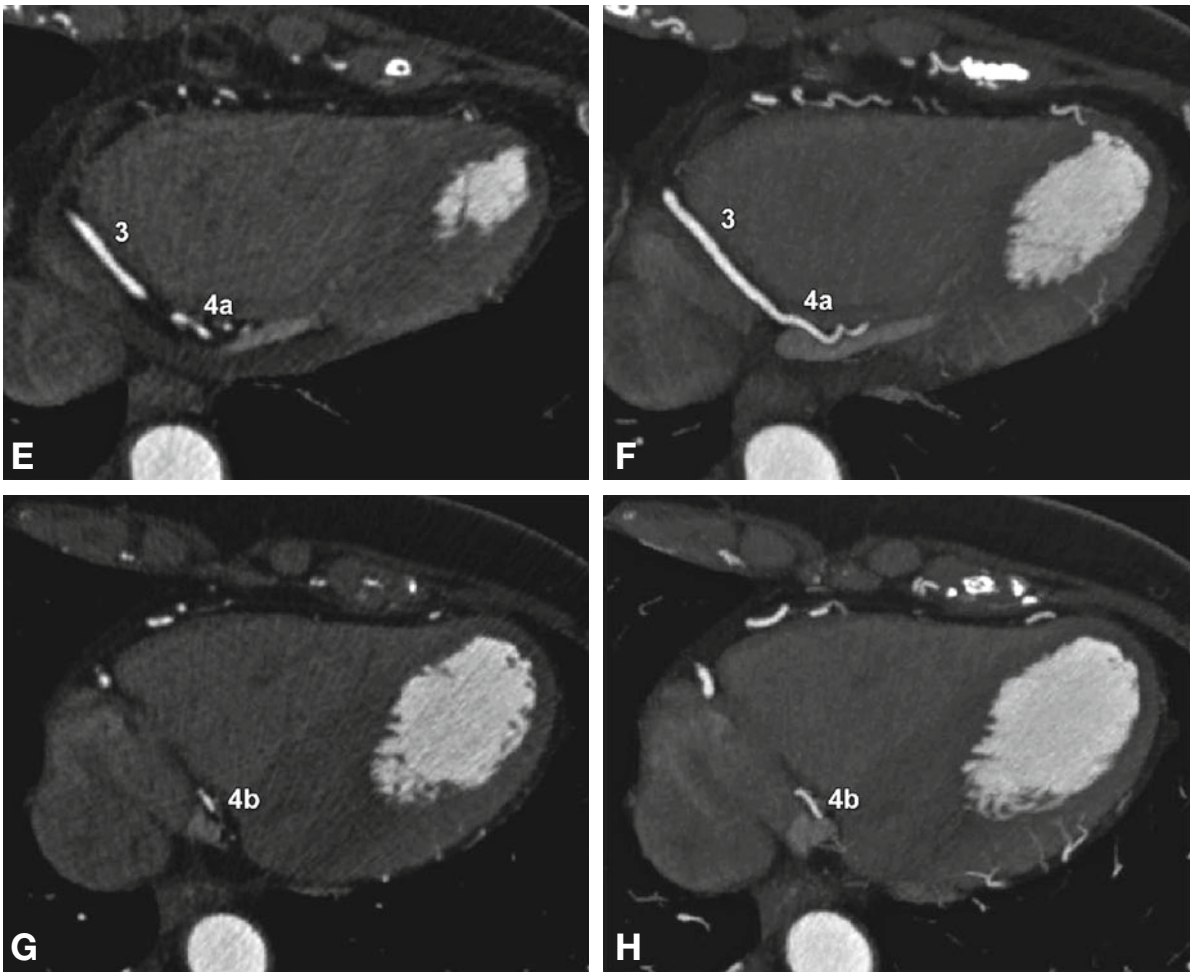

Fig. 3.5 (continued) where it again moves in the horizontal plane on the diaphragmatic face of the heart as segment 3. At the crux cordis, segment 3 bifurcates into the posterior descending artery (4a) and the right posterolateral branch (4b in **Panels G** and **H**). In cases of dominance of the RCA (as in this case), segments 4a and b are side branches of the RCA. In case of left coronary artery dominance, the posterior descending artery (4a) is part of the LCX. *Ao* aorta, *Asterisk* papillary muscles, *LA* left atrium, *LV* left ventricle, *RA* right atrium, *RV* right ventricle

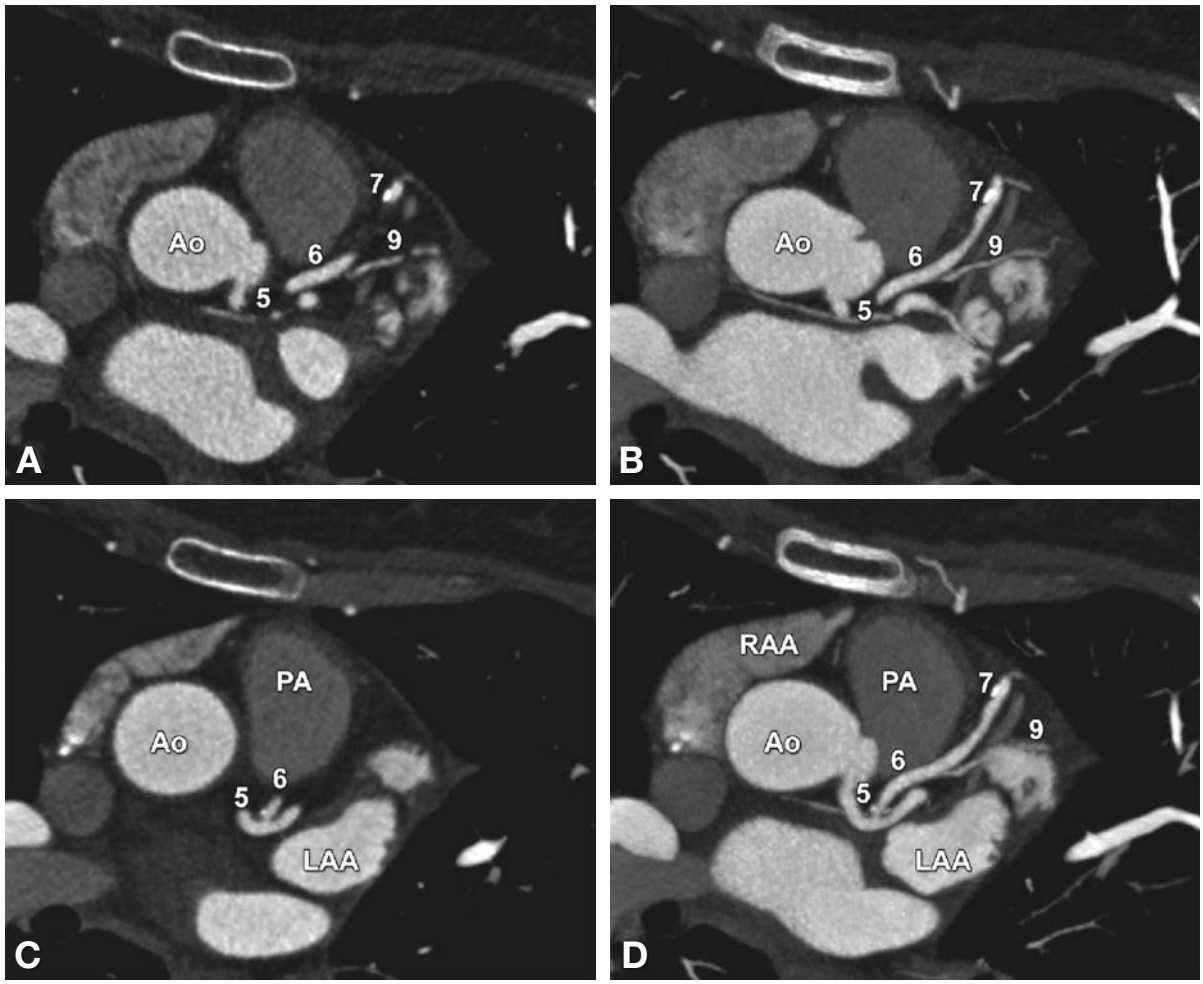

Fig. 3.6 The left anterior descending coronary artery with all its segments in axial slices (*left panels*), and the corresponding maximum-intensity projections of 5-mm thickness in the axial orientation for comparison (*right panels*). The proximal left anterior descending coronary artery segment (6) is the anterior branch of the left main coronary artery (5, **Panels A**–**D**).

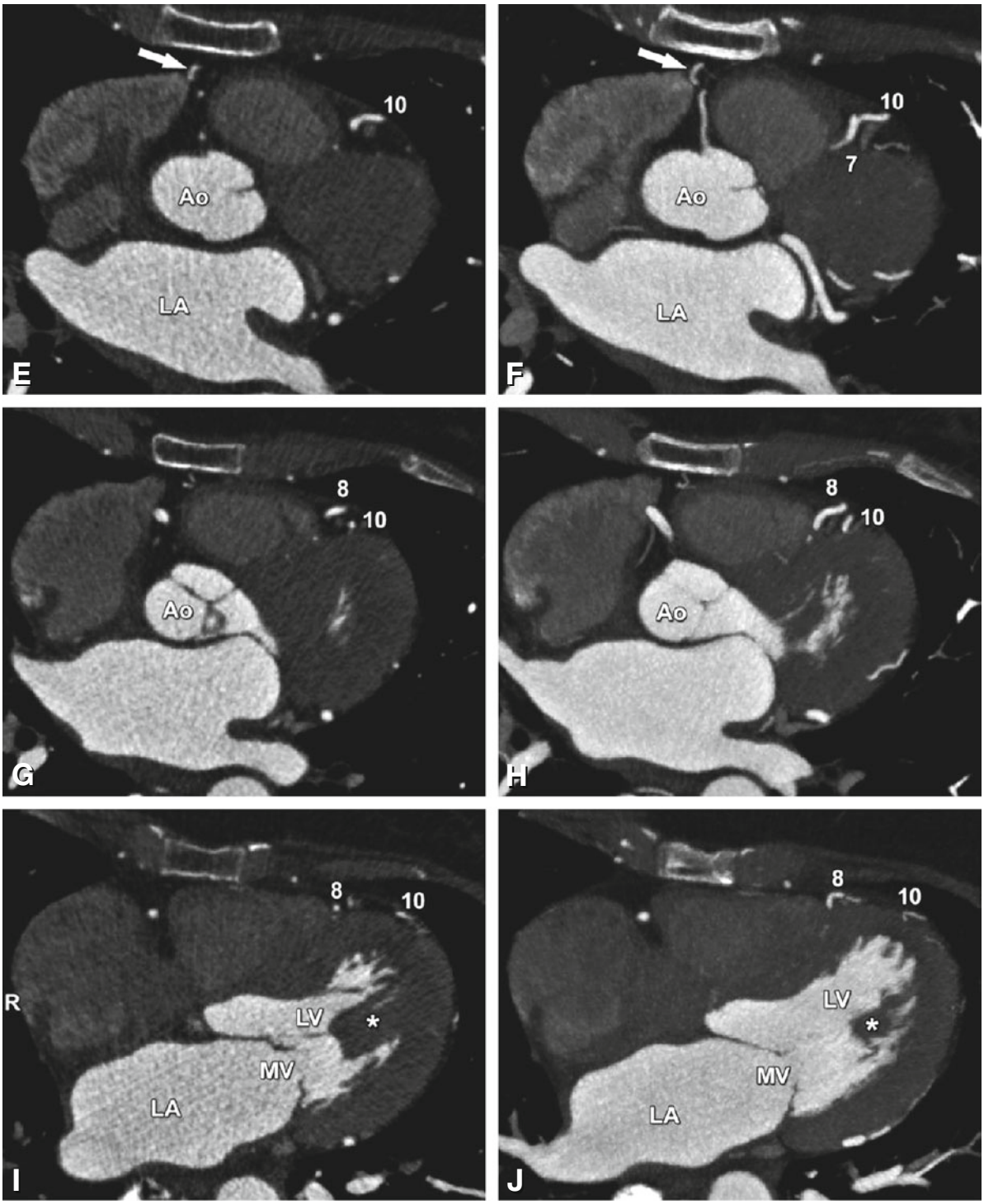

Fig. 3.6 (continued) Segment 6 of the left anterior descending coronary artery then bifurcates into the mid-left anterior descending (7) and the first diagonal branch (9, **Panels A–D**). Further caudally, the mid-left anterior descending coronary artery gives off the distal segment (8) and the second diagonal (10, Panels E–J) In **Panels E** and **F**, the conus branch (arrows, first side branch of the RCA), which travels cranial to the proximal RCA segment, is also visible. Ao aorta, Asterisk papillary muscles, LAA left atrial appendage, LA left atrium, LV left ventricle, MV mitral valve, PA pulmonary artery, RAA right atrial appendage

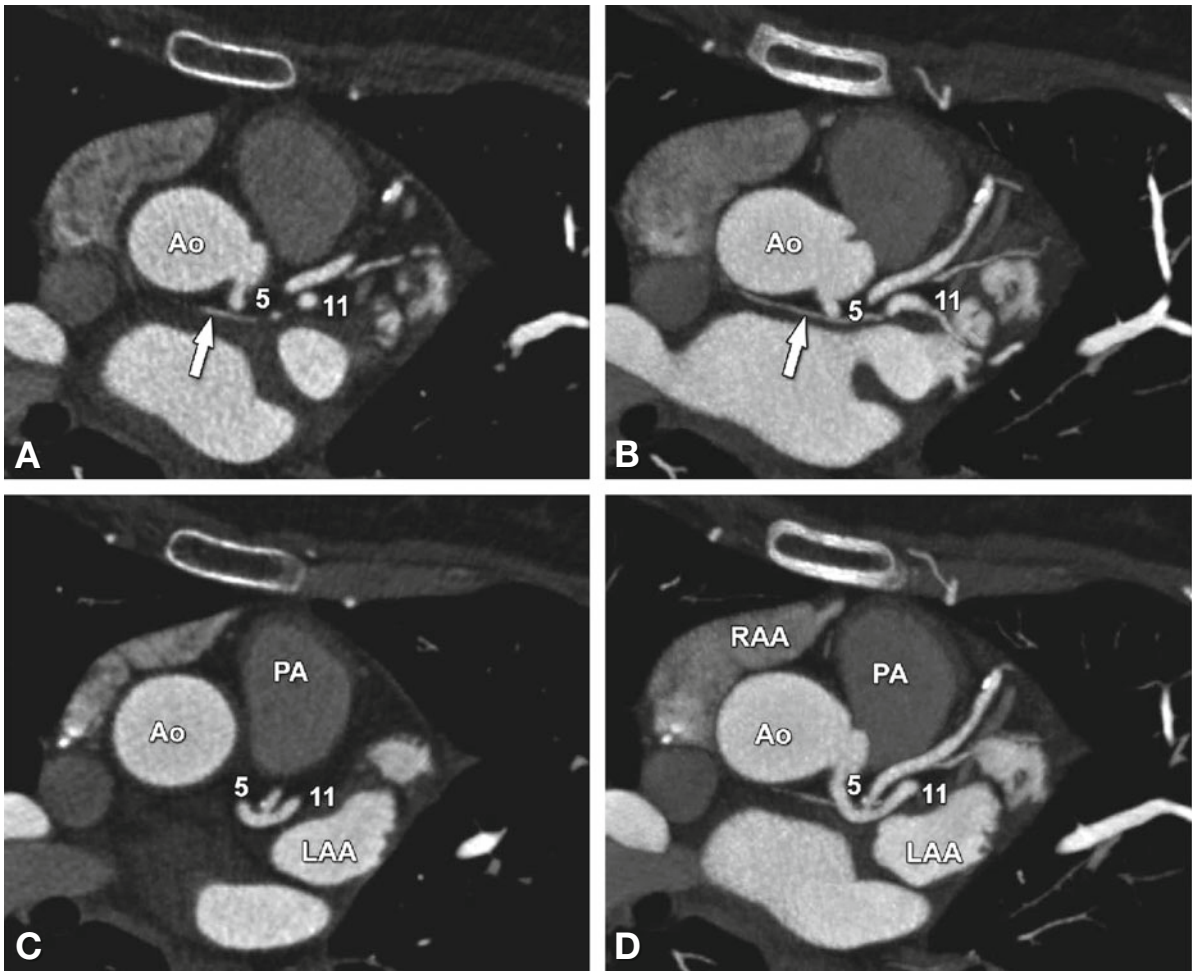

Fig. 3.7 The LCX with all its segments in axial slices (*left panels*), and the corresponding maximum-intensity projections of 5-mm thickness in the axial orientation for comparison (*right panels*). The proximal LCX segment (11) is the posterior branch of the left main coronary artery (5, **Panels A**–**D**).

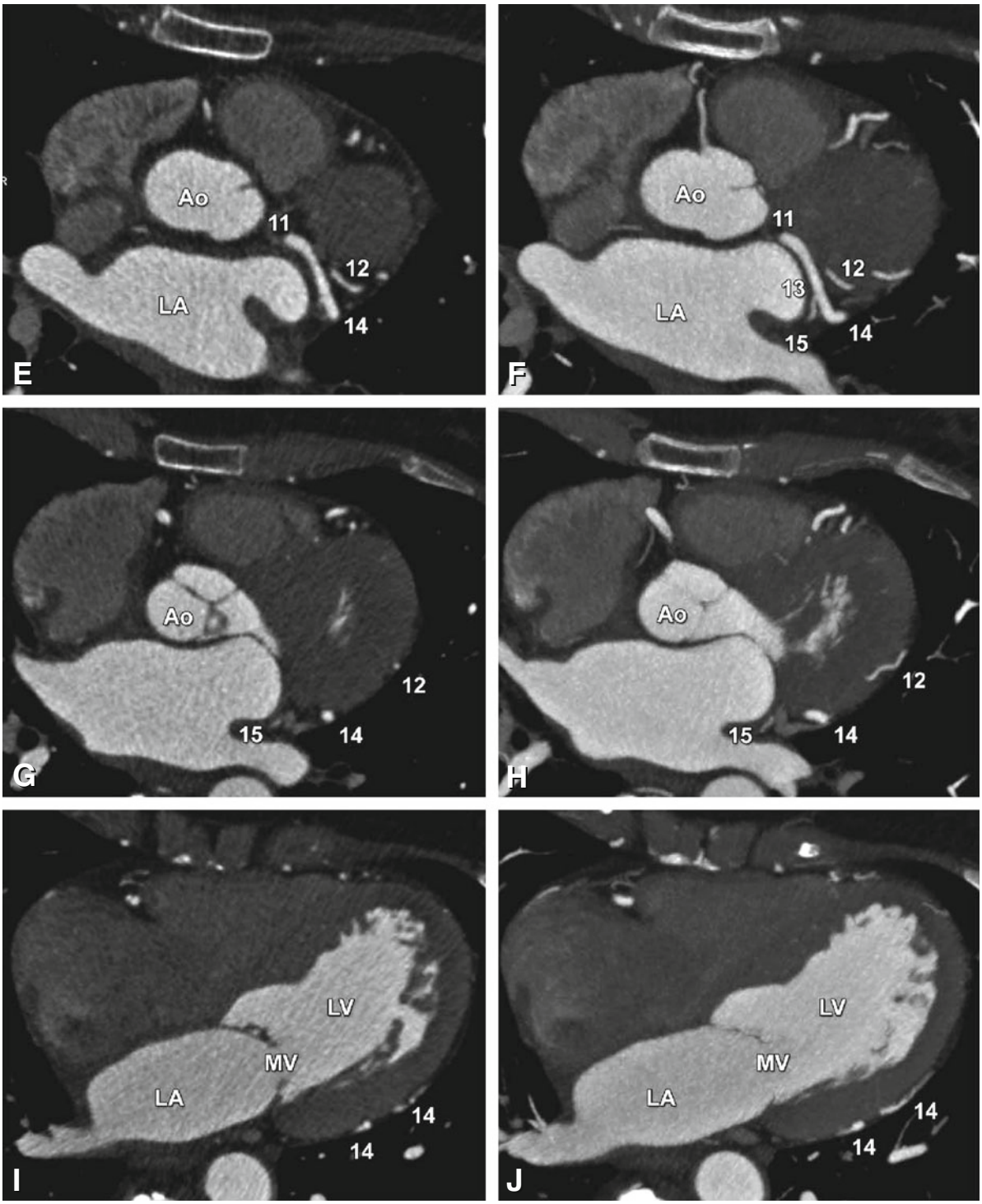

Fig. 3.7 (continued) Further down, the proximal left circumflex splits into the mid-left circumflex (13) and the first (obtuse) marginal branch (12, **Panels E–H**). The mid-left circumflex (13) then gives off the distal left circumflex (15, **Panels F–H**) (obtuse) marginal branches (14, **Panels E–J**), which supply the inferolateral myocardial segments. In the case of left coronary artery dominance, the distal circumflex (15) ends as the posterior descending artery (4a), whereas in right coronary dominance, as in this case, the RCA gives rise to the posterior descending and at least one posterolateral branch. The sinus node artery (arrow in **Panels** A and B) is the first branch of the LCX in this patient. Ao aorta, LAA left atrial appendage, LA left atrium, LV left ventricle, MV mitral valve, PA pulmonary artery, RAA right atrial appendage

3.1.3 Frequent Coronary Artery Variants

In addition to the variation in normal anatomy caused by left or right dominance, there are other variations, such as myocardial bridging and anomalous origin, as well as variability in the course of the coronary arteries.

In less than 5% of patients, interventional coronary angiography identifies myocardial bridging. This term refers to the descent of a portion of the coronary artery into the myocardium (**Fig. 3.8**). Because of the improved imaging of myocardial tissue that can be achieved with cardiac CT, myocardial bridging can be observed in about 25–30% of patients, a figure that is consistent with most pathological reports. Myocardial bridging is usually confined to the LAD, diagonal or IM branches. At systole, the overlying bridge of myocardial tissue contracts and may cause systolic compression of the coronary artery segment. At diastole, the caliber is generally normal. Because most of the flow through the coronary arteries occurs at diastole, myocardial bridging does not usually cause symptoms. Thus, myocardial bridging should not be considered an anomaly but a variant. However, incidental cases have been associated with ischemia (Chap. 23).

The anomalous origin or course of a coronary artery is less frequently encountered (<1%). The existence of separate origins for the LAD and LCX has already been discussed. The two most frequent other anomalies are an RCA with an anomalous origin from the LM or the left sinus of Valsalva, and an LCX with an anomalous origin from the RCA or the right sinus of Valsalva.

In the case of an anomalous origin of the RCA from the left sinus of Valsalva or LM, the RCA commonly courses anteriorly between the aorta and the pulmonary trunk (**Fig. 3.9**). This inter-arterial course is also called "malignant course," because these patients have a high risk for exercise-induced ischemia and sudden death. At exercise, more blood is present in the aorta and pulmonary artery, causing the anomalous segment to be squeezed between these large arteries and potentially inducing ischemia. Also, the anomalous artery is usually somewhat narrowed at the origin and forms an acute angle with the aorta that may be pinched off by exercise. Other (left coronary artery) anomalies with an interarterial course between the aorta and pulmonary trunk can also cause ischemia.

The most frequent LCX anomaly is an LCX having its origin from the RCA or right sinus of Valsalva, where the LCX courses posterior to the aorta to enter its normal location in the left atrioventricular groove (**Fig. 3.10**). This is a benign condition that is not associated with ischemia. For details on coronary artery anomalies see Chap. 22.

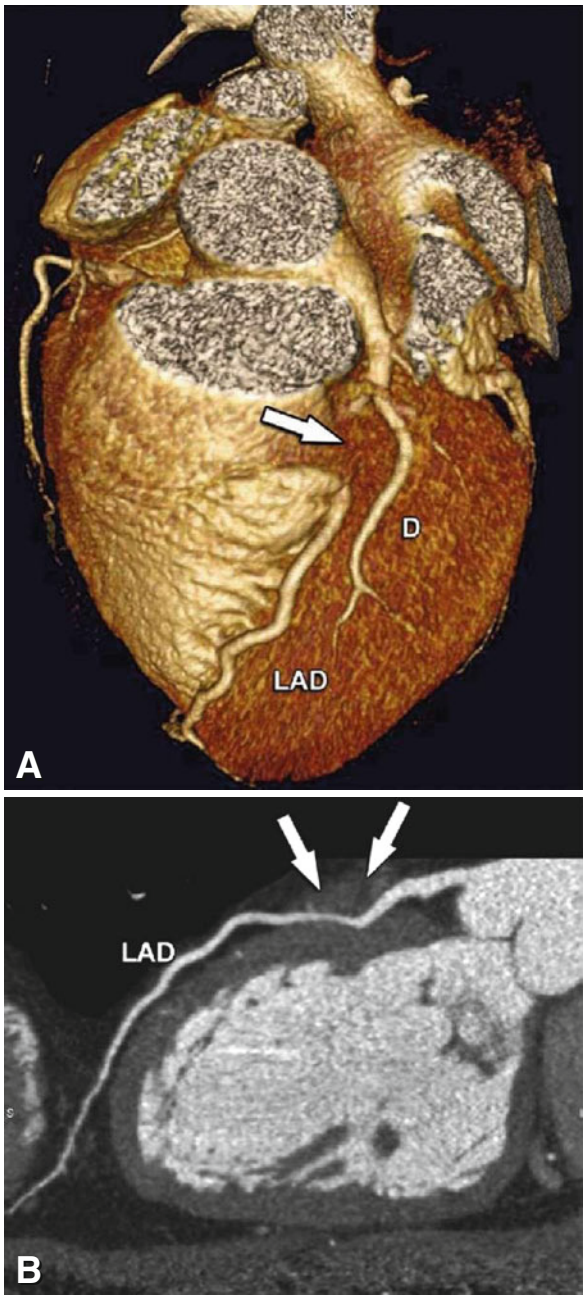

Fig. 3.8 Myocardial bridging of a proximal left anterior descending coronary artery (*LAD*) segment (*arrows*). Three-dimensional volume-rendered image (**Panel A**) and curved multiplanar reformation (**Panel B**). Note the bridge of myocardial tissue overlying the LAD segment (*arrows*, **Panel B**). *D* diagonal branch

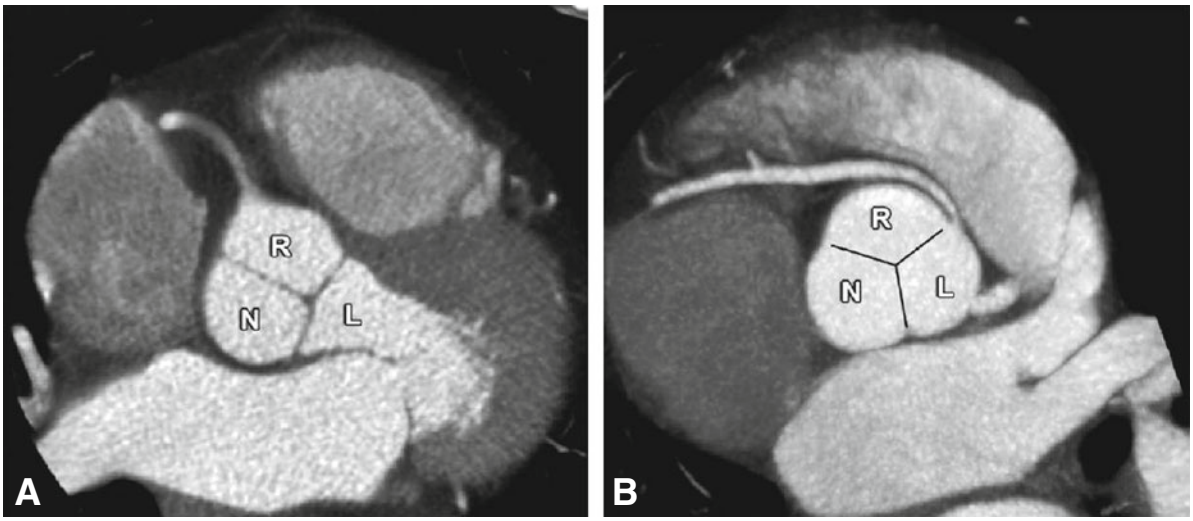

Fig. 3.9 Normal origin of the RCA, arising from the right sinus of Valsalva (**Panel A**), in an oblique transverse thin-slab maximum-intensity projection image. Anomalous origin of the RCA, arising from the left sinus of Valsalva, with an inter-arterial course between the aorta and pulmonary trunk (**Panel B**). *L* left sinus of Valsalva, *R* right sinus of Valsalva, *N* non-coronary sinus

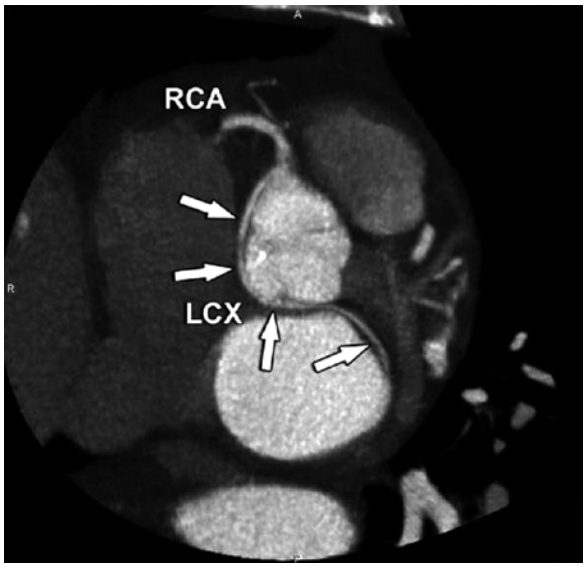

Fig. 3.10 LCX with an anomalous origin, arising at the origin of the RCA, as shown in an oblique transverse thin-slab maximum-intensity projection image. The LCX follows a retro-aortic course to its normal position in the left atrioventricular groove (*arrows*). This is a benign variant that is not associated with ischemia

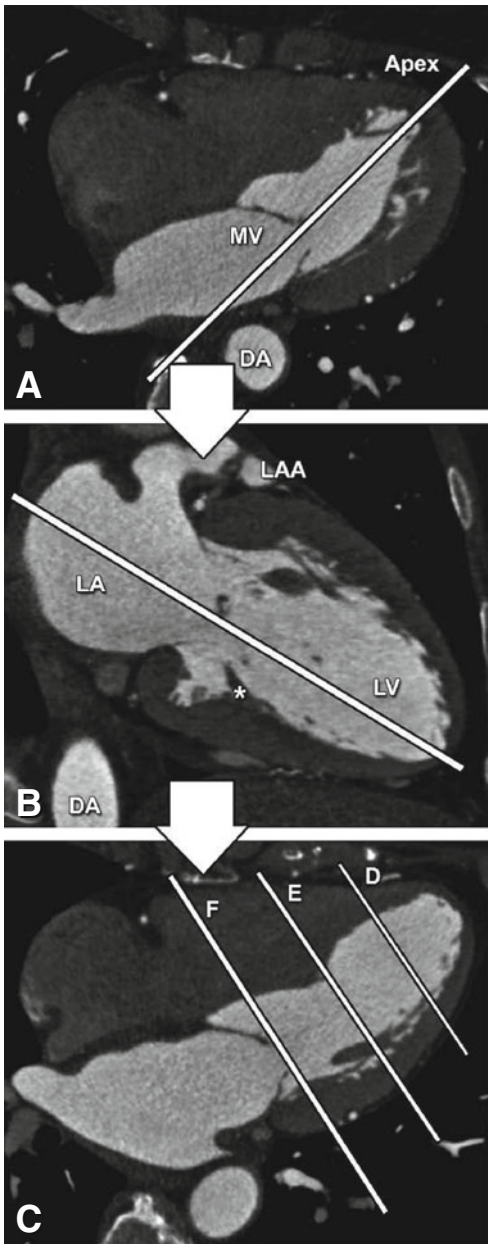

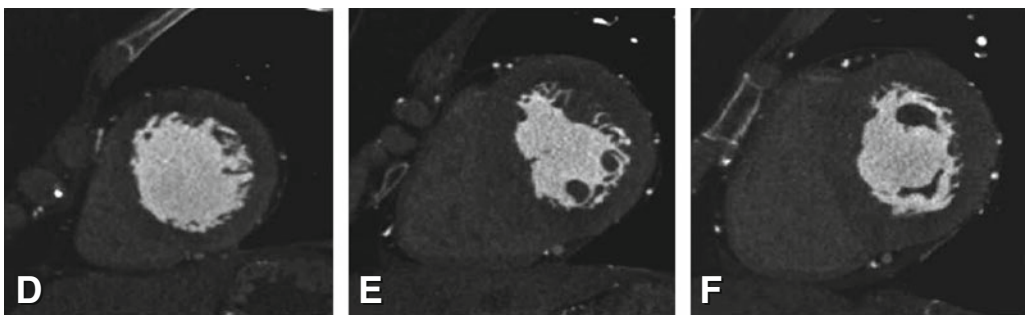

Fig. 3.11 Generating short and long-axis views for cardiac function analysis. On the basis of an axial CT slice (**Panel A**), a two-chamber view (**Panel B**) along the left ventricle (*LV*) and left atrium (*LA*) is created by connecting the apex of the left ventricle with the mitral valve (*MV*; *white line* in **Panel A**). From this two-chamber view, a four-chamber view is generated (**Panel C**) by again connecting the apex of the left ventricle with the mitral valve (MV). In this way, the individual double-oblique cardiac long axes can be identified. True cardiac short-axis slices are created by further reformations orthogonal to the interventricular septum (**Panels D**–**F**). In this way, apical (**Panel D**), mid-cavity (**Panel E**), and basal (**Panel F**) short-axis slices are created, for instance, to assess global and regional cardiac function; they can be viewed as cine loops throughout the cardiac cycle. *Asterisk* papillary muscles, *DA* descending aorta, *LAA* left atrial appendage, *LA* left atrium, *LV* left ventricle

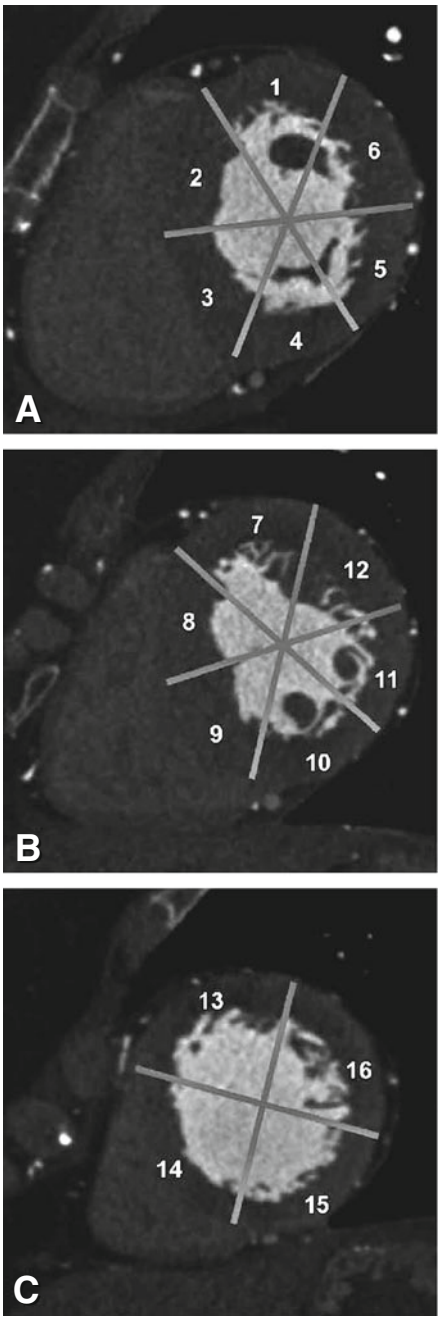

Fig. 3.12 Segmental myocardial anatomy, as shown in true cardiac short-axis slices. The basal short axis is divided into segments 1–6, in counter-clockwise order (**Panel A**). The mid-cavity (**Panel B**) and apical segments (**Panel C**) are also numbered in counter-clockwise order with the numbers 7–12 and 13–17, respectively. Segment 17 is not displayed in the apical short-axis slice because it represents the apex, which is nicely seen in the long-axis views in **Panels B** and **C** of **Fig. 3.11**. The myocardial segment names and numbers are given in **Table 3.2**

3.2 Myocardium

In addition to the coronary artery anatomy described in the previous section, a basic understanding of gross cardiac anatomy is necessary for reporting cardiac function analysis (Chap. 15) using CT. **Fig. 3.11** describes how short and long axes orthogonal to the cardiac structures can be reconstructed from axial CT data sets. We recommend using the 17-segment model for reporting myocardial findings (**Fig. 3.12**), and for practical purposes it seems more convenient to use the myocardial segment names instead of the segment numbers (**Table 3.2**).

Table 3.2 Myocardial segmental anatomy

Segment no.	Location	Segment name
1	Basal	Anterior
2		Anteroseptal
3		Inferoseptal
4		Inferior
5		Inferolateral
6		Anterolateral
7	Mid-cavity	Anterior
8		Anteroseptal
9		Inferoseptal
10		Inferior
11		Inferolateral
12		Anterolateral
13	Apical	Anterior
14		Septal
15		Inferior
16		Lateral
17	Apica	Apex

AHA segmentation published in 2002 by Cerqueira et al.

Recommended Reading

Austen WG, Edwards JE, Frye RL et al (1975) A reporting system on patients evaluated for coronary artery disease. Report of the Ad Hoc Committee for Grading of Coronary Artery Disease, Council on Cardiovascular Surgery, American Heart Association. Circulation 51:5–40

Boxt LM (2005) CT anatomy of the heart. Int J Cardiovasc Imaging 21:13–27

Cerqueira MD, Weissman NJ, Dilsizian V et al (2002) Standardized myocardial segmentation and nomenclature for tomographic imaging of the heart: a statement for healthcare professionals from the Cardiac Imaging Committee of the Council on Clinical Cardiology of the American Heart Association. Circulation 105:539–542

Kini S, Bis KG, Weaver L (2007) Normal and variant coronary arterial and venous anatomy on high-resolution CT angiography. AJR Am J Roentgenol 188:1665–1674

Konen E, Goitein O, Sternik L, Eshet Y, Shemesh J, Di Segni E (2007) The prevalence and anatomical patterns of intramuscular coronary arteries: a coronary computed tomography angiographic study. J Am Coll Cardiol 49:587–593

Krakau I, Lapp H (2005) Das Herzkatheterbuch. Thieme, Stuttgart

Leschka S, Koepfli P, Husmann L et al (2008) Myocardial bridging: depiction rate and morphology at CT coronary angiography – comparison with conventional coronary angiography. Radiology 246:754–762

Levin DC, Harrington DP, Bettmann MA, Garnic JD, Davidoff A, Lois J (1982) Anatomic variations of the coronary arteries supplying the anterolateral aspect of the left ventricle: possible explanation for the "Unexplained" anterior aneurysm. Invest Radiol 17:458–462

O'Brien JP, Srichai MB, Hecht EM, Kim DC, Jacobs JE (2007) Anatomy of the heart at multidetector CT: what the radiologist needs to know. Radiographics 27:1569–1582

Popma J (2005) Coronary angiography and intravascular ultrasound imaging. In: Zipes DP (ed) Braunwald's heart disease: a textbook of cardiovascular medicine. Elsevier, Philadelphia

Saremi F, Abolhoda A, Ashikyan O et al (2008) Arterial supply to sinuatrial and atrioventricular nodes: imaging with multidetector CT. Radiology 246:99–107; discussion 108–109

Schmitt R, Froehner S, Brunn J et al (2005) Congenital anomalies of the coronary arteries: imaging with contrast-enhanced, multidetector computed tomography. Eur Radiol 15:1110–1121

Sos TA, Sniderman KW (1980) A simple method of teaching three-dimensional coronary artery anatomy. Radiology 134:605–606

Yamanaka O, Hobbs RE (1990) Coronary artery anomalies in 126, 595 patients undergoing coronary arteriography. Cathet Cardiovasc Diagn 21:28–40

Zimmermann E, Schnapauff D, Dewey M (2008) Cardiac and coronary anatomy in CT. Semin Ultrasound CT MR 29:176–181

Cardiac CT in Clinical Practice

K. Nieman

Abstract

Cardiac CT applications include restratification of cardiovascular risk and rule-out of obstructive coronary artery disease in patients with stable, unstable, or atypical chest discomfort before, during, and after coronary revascularization.

4.1 Introduction

Over the past decade multislice computed tomography (CT) has seen an unparalleled technical development, and we are now able to image the small coronary arteries. While there are many potential indications for noninvasive coronary imaging, investigation of its benefit compared with other techniques has not kept pace with the enthusiasm of its adoption into cardiovascular medicine. In this chapter we will discuss some of the most frequent applications of ECG-synchronized cardiac CT in clinical practice.

4.2 Cardiovascular Risk Refinement in Asymptomatic Individuals

Calcium detected by CT is a visible measure of coronary atherosclerosis. The amount of coronary calcium measured by CT correlates with the overall coronary plaque burden and predicts cardiovascular events (see Chap. 11). In routine clinical practice, cardiovascular risk is assessed using traditional risk factors and models derived from large population studies such as the Framingham Heart study or the European Systemic Coronary Risk Evaluation (SCORE). Coronary calcium scoring independently improves the prediction of adverse events and is incremental to the traditional risk factors. Whether performing a calcium scan is meaningful and will change a patient's medical management depends on the pretest cardiovascular risk estimated using the traditional risk factors (**Table 4.1**). Patients with a history of cardiovascular disease, diabetes mellitus, or a high estimated cardiovascular risk should receive the highest level of prevention (**Fig. 4.1**). A calcium scan is generally not recommended for patients at low risk, i.e., those who have no more than one risk factor, but may be useful in patients with an intermediate estimated risk of major adverse events (10–20% Framingham risk score) or cardiovascular mortality (SCORE 5–10%). A meta-analysis suggests that intermediate risk individuals with a low calcium score would have an event rate comparable to those at low risk by conventional risk assessment. The ability to restratify patients has been prospectively demonstrated in two large population studies [Heinz-Nixdorf

M. Dewey, *Cardiac CT*,
DOI 10.1007/978-3-642-41883-9_4, © Springer-Verlag Berlin Heidelberg 2014

Table 4.1 Traditional cardiovascular risk estimation

High CVD risk	Intermediate CVD risk	Low CVD risk
Estimated 10-year cardiovascular mortality (SCORE > 10%)	SCORE 5–10%	SCORE <5%
Established cardiovascular disease Diabetes mellitus II Diabetes mellitus type I with microalbuminuria Markedly elevated single risk factor	Two or more risk factors (e.g., nicotine abuse, hypertension, low high-density lipoprotein cholesterol, family history of premature coronary artery disease, and age)	0–1 risk factors

CVD cardiovascular disease, *SCORE* Systemic Coronary Risk Evaluation

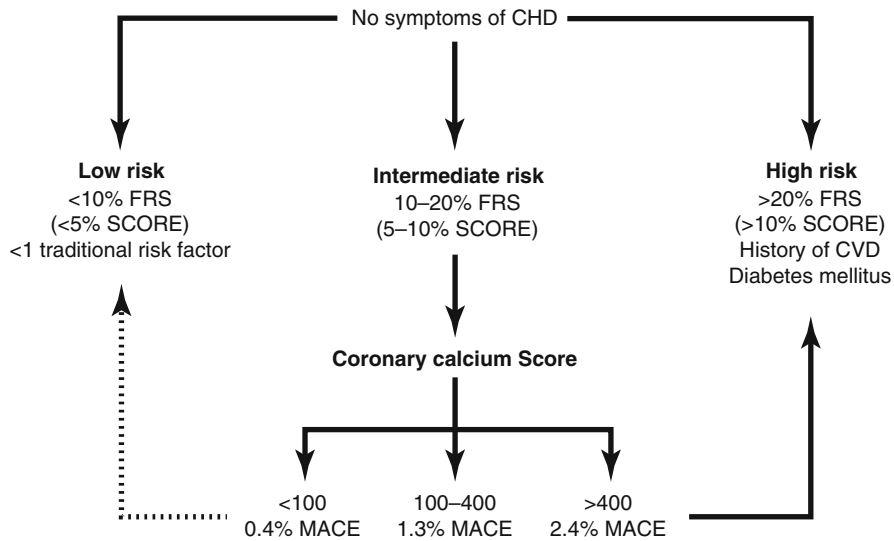

Fig. 4.1 Use of coronary calcium imaging in asymptomatic intermediate-risk individuals. Coronary calcium score can reclassify individuals at intermediate risk of coronary artery disease (10–20% 10-year risk by Framingham Risk Score, FRS) or cardiac death (5–10% 10-year by SCORE) into low, intermediate and high risk (major adverse cardiac events per year). While more intensive preventive measures are warranted in patients reclassified to high risk, there are no recommendations to decrease preventive measures in patients reclassified to low risk. This scheme follows the recommendations by Greenland et al. in the ACCF/AHA 2007 Expert Consensus Document. *CHD* coronary heart disease, *MACE* major adverse cardiovascular events

Recall Study; MESA Study]. A high calcium score is associated with an event rate comparable to that of patients in the highest conventional risk category. These patients might benefit from more intensive preventive measures, including medical treatment with statins, aspirin, and/or ACE inhibitors. Whether patients at intermediate risk and a negative calcium score should be managed as low risk is still debated. A substantial number of asymptomatic patients with a very high calcium score will have (silent) obstructive coronary artery disease. In these patients a low threshold to ischemia detection seems reasonable. Although calcium scoring in patients at intermediate risk seems reasonable, there is currently no data showing that this approach improves outcome (in a cost-effective manner).

Contrast-enhanced CT angiography is currently not recommended in patients who do not have symptoms. While radiation exposure may become less of a concern with the development of low-dose scan protocols, there is still the need for intravenous injection of potentially harmful contrast media. Coronary CT angiography has the potential to identify patients with severe but noncalcified coronary artery disease, which would be missed by unenhanced CT. Finding severely obstructive disease is rare, and the overall prognosis of asymptomatic patients without detectable coronary calcium is excellent (<1% annual event rate). CT angiography in an asymptomatic Korean population resulted in more coronary interventions, but no increased hard event rate in patients with silent CAD. Whether identification of the small number

of patients with significant noncalcified plaque justifies the higher radiation exposure and contrast agent administration is unclear and heavily debated.

4.3 Patients with Stable Chest Discomfort

In Europe exercise electrocardiography remains the most frequently used initial test in patients with suspected coronary artery disease, whereas in the USA single-photon emission computed tomography is more frequently used. Exercise electrocardiography has a high specificity but a low sensitivity, using invasive angiography as a reference (**Fig. 4.2**). Myocardial perfusion imaging, using single-photon emission computed tomography, positron emission tomography, or magnetic resonance imaging (MRI), is more accurate but also more expensive in comparison to exercise electrocardiography. They are therefore considered secondary diagnostic modalities in the majority of patients (**Table 4.2**) by the European guidelines. The British NICE guidelines have removed conventional exercise testing and suggest that stress imaging should be the first choice technique in patients with an intermediate pretest likelihood of CAD.

Coronary angiography by CT represents an attractive means to noninvasively assess patients with suspected coronary artery disease. The high sensitivity and negative predictive value of coronary CT angiography allow confident visual exclusion of coronary artery disease. Myocardial ischemia is very unlikely in the absence of obstructive coronary artery disease on CT. However, angiographic disease (by CT or catheter angiography) may exist without causing ischemia or symptoms and may not need revascularization. Additionally, stenosis severity cannot be assessed with the same level of accuracy as compared to conventional angiography and will often be overestimated when severe calcification is present. Therefore, coronary CT angiography appears most useful to exclude coronary artery disease in patients with a low-to-intermediate pretest likelihood of disease. Whether CT angiography should be used as the initial test in these patients or after an inconclusive stress test, is still under investigation. Most registries show a very low prevalence of significant obstructive disease in patients with stable chest symptoms without detectable calcium. Therefore, a calcium scan may be an appropriate first step and function as a gatekeeper to further testing, including contrast-enhanced CT angiography. In fact, the British NICE criteria recommend a calcium scan as the first test in patients with chest pain of recent onset and a low pretest likelihood of CAD (10–29%). Only if the calcium scan is 1–400 do they recommend CT angiography. To avoid unnecessary revascularization, we

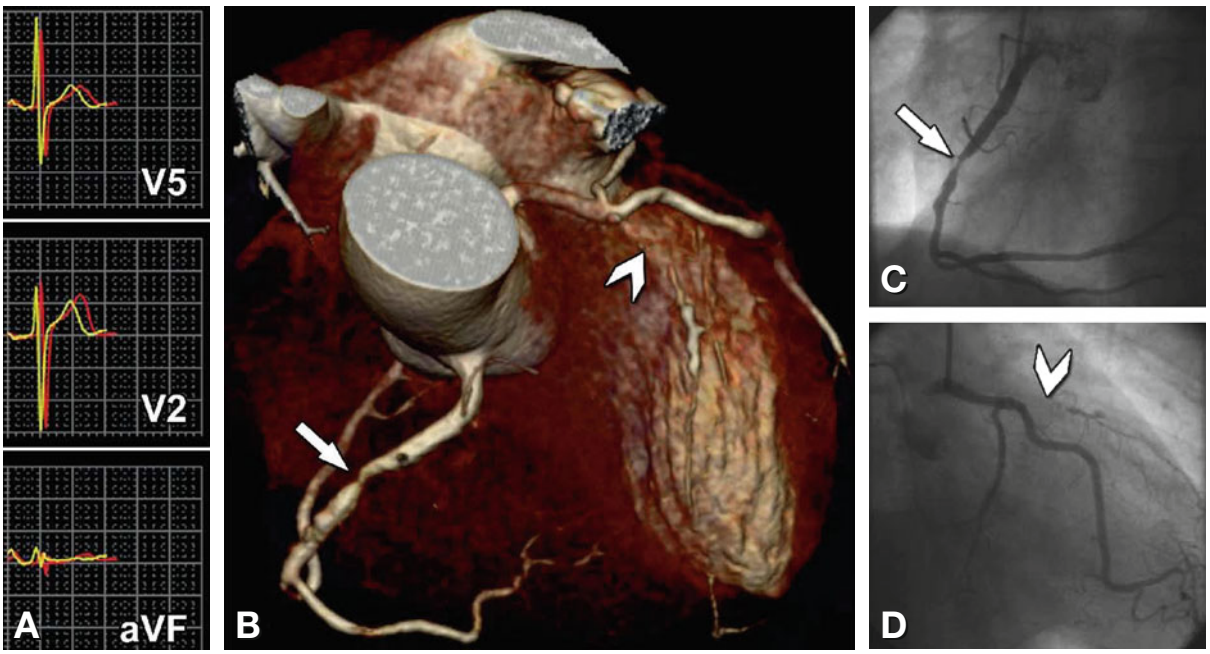

Fig. 4.2 False-negative exercise ECG and true-positive coronary CT angiography. Exercise ECG without significant ECG changes in a 57-year-old patient with stable angina symptoms (**Panel A**). Severely stenotic right coronary artery (*arrow*) and occluded left anterior descending coronary artery (*arrowhead*) on coronary CT angiography (**Panel B**), confirmed by conventional coronary angiography (**Panel C** and **D**)

Table 4.2 Diagnostic accuracy for noninvasive detection of coronary artery disease

Modality	Diagnostic performance	
	Sensitivity (%)	Specificity (%)
Exercise electrocardiography	68	77
Exercise stress echocardiography	80–85	84–86
Dobutamine stress echocardiography	40–100	62–100
Vasodilator stress echocardiography	56–92	87–100
Exercise perfusion scintigraphy	85–90	70–75
Vasodilator perfusion scintigraphy	83–94	64–90
Dobutamine stress MRI	83 (79–88)	86 (81–91)
Vasodilator perfusion MRI	91 (88–94)	81 (77–85)
CT coronary calcium score (>0 threshold)	>95	≈50
CT coronary angiography	100 (98–100)	89 (85–92)

Reported diagnostic performance is derived from the 2006 ESC Guidelines on the management of stable angina, the ACCF/AHA 2007 Experts consensus document on calcium scoring, and Nandalur et al. (for MRI) and Von Ballmoos et al. (for coronary CT angiography). Numbers in parentheses give the 95% confidence intervals for CT and ranges for the other tests

currently prefer to perform stress testing when CT shows moderate obstructive disease to assess hemodynamic significance. As a matter of fact, if coronary CT angiography identifies obstructions of moderate severity at prognostically less important sites, a physician may be more confident in maintaining medical treatment rather than immediately sending the patient for revascularization. Methods to assess functional significance of coronary stenosis by computed tomography are under investigation, which include vasodilator mediated myocardial perfusion imaging and computed simulated fractional flow reserve estimation based on CT angiograms. While statistical modeling of registry data suggests that CT angiography can be cost-effective, prospective data in comparison with other techniques has not yet become available.

In patients with suspected coronary anomalies, CT angiography is the most accurate imaging technique for assessment of the origin, course, and termination of abnormal coronary arteries in relation to surrounding structures (Chap. 17).

In conclusion, cardiac CT (including calcium scanning and CT angiography) has an expanding role in the assessment of suspected coronary artery disease. Whether the technique should be used as the initial test in low-to-intermediate risk patients followed by functional testing in patients with obstructive disease or secondary to functional tests that cannot be performed or produce equivocal results, is yet unresolved. Just as there are patients who are unsuitable to undergo stress testing, CT angiography should only be performed in patients in whom diagnostic image quality can be expected.

4.4 Acute Chest Pain

Cardiac CT may have various advantages over the current diagnostic approach in patients presenting to an emergency department with acute chest pain. Particularly when symptoms have subsided the ECG may be normal, while biomarkers could still take hours to convert in case of an acute coronary syndrome. Stress testing may exclude severe stenosis, but will neglect the presence and extent of coronary atherosclerosis. CT can visualize coronary artery atherosclerosis, identify severe obstructions, detect myocardial hypoperfusion (secondary to myocardial infarction), and allow detection of other potentially life-threatening conditions presenting with acute chest discomfort including aortic dissection, pulmonary emboli, pericardial effusions, and pulmonary disease.

A simple calcium scan may allow exclusion of severe disease in a substantial number of patients and is associated with excellent outcome. However, because of the potentially devastating consequences and the possibly

higher incidence of noncalcified disease in patients with an acute presentation, many prefer contrast-enhanced CT angiography instead (**Fig. 4.3**). CT angiography can exclude an acute coronary syndrome with a high negative predictive value, whereas the positive predictive value appears to be somewhat lower in acute patients. Additionally, the absence of coronary stenosis on CT does not entirely rule out an acute coronary stenosis. A number of randomized trials in low-risk patients with acute chest discomfort can be safely discharged based on CT, reducing hospital stay and overall expenses (**Fig. 4.4**). The applicability of these results and limited to low risk patients. No clinical benefit was demonstrated and cost-effectiveness will be affected by local logistics and practices of both CT and standard practice, and may change with widespread implementation of high-sensitive troponin measurements. Use of cardiac CT in the emergency ward requires technicians and physicians

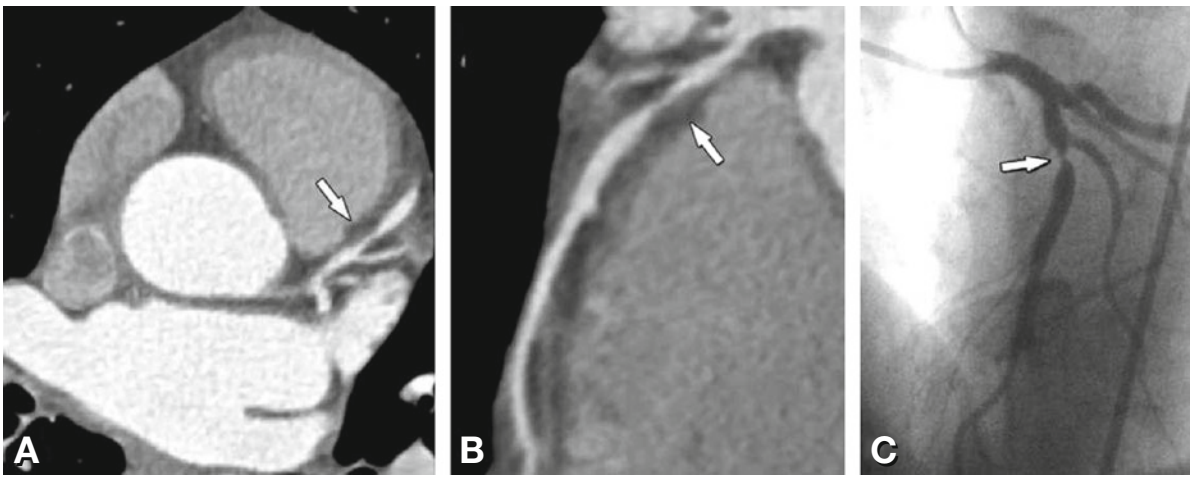

Fig. 4.3 Acute presentation of a 43-year-old man with progressive angina pectoris (without elevated troponin). Coronary CT angiography shows an outwardly (positively) remodeled, noncalcified, stenotic lesion (*arrow*) in the left anterior descending coronary artery (**Panel A**, axial image; **Panel B**, curved multiplanar reformation), confirmed on conventional coronary angiography (**Panel C**)

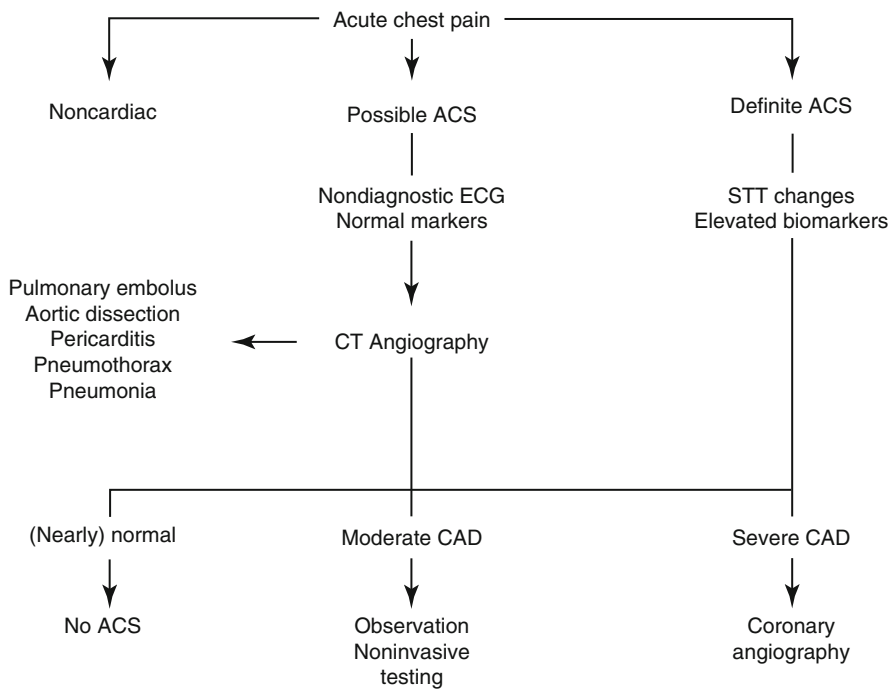

Fig. 4.4 Potential implementation of cardiac CT in patients with a suspected acute coronary syndrome. *ACS* acute coronary syndrome, *CAD* coronary artery disease, *STT* ST trace

experienced in coronary CT, a service few clinics can provide 24 by 7.

Cardiac CT can exclude several potentially life threatening conditions during a single examination, including an acute coronary syndrome, a pulmonary embolism or an acute aortic syndrome (as well as pericardial effusion, pneumothorax, etc.). Routine performance of a so-called triple rule-out scan for exclusion of myocardial infarction, pulmonary embolism, and aortic dissection has been investigated, but shows limited benefit. The frequency by which pulmonary embolisms and dissections are found is much lower compared to an acute coronary syndrome, and clinically significant pathology may still be identified on "simple" coronary CT angiograms. In fact, performing a more complicated scan in a patient suspected of an acute coronary syndrome to simultaneously image the pulmonary arteries, may negatively affect the interpretability of the coronary arteries (Chap. 6).

4.5 Rule-Out of Coronary Artery Disease in Specific Situations

In certain clinical situations coronary artery disease needs to be excluded, even when concrete symptoms of ischemia are absent. Conventional coronary angiography is routinely performed in patients scheduled for (noncoronary) cardiac surgery, such as valve surgery. Except perhaps for patients with degenerative aortic valve disease, which is often associated with calcified coronary disease, coronary artery disease can be excluded in the majority of the presurgical patients using cardiac CT. In case of aortic valve endocarditis or aortic dissection, CT may in fact be preferred over manipulation of catheters in the affected region (Chap. 16). A small proportion of patients with heart failure, assumed to be nonischemic, will have obstructive coronary artery disease. Calcium scanning and/or CT angiography can be a useful alternative to rule out coronary arty disease in most of these patients.

4.6 Noninvasive Angiographic Follow-Up After Coronary Revascularization

Follow-up of patients after revascularization is more complicated than assessing patients without stents or bypass grafts, by any modality. Cardiac CT is limited by specific imaging complications of the stent material (Chap. 13), artifacts from surgical clips in the vicinity of grafts (Chap. 12), but mostly by the presence of (native) coronary artery disease, which is often diffuse. In particular the more abundant presence of calcified plaque reduces the reliability of cardiac CT angiography. Moreover, CT angiography does not have the ability to determine the hemodynamic significance of lesions, which may be unpredictable in the presence of collateral perfusion of the myocardium. Therefore, complementary functional information will often be needed in these populations. The introduction of non-metal (bioresorbable) devices may expand the role of cardiac CT after intervention.

After stenting, cardiac CT can be used to exclude in-stent obstruction of large-diameter stents (≥3.5 mm) in proximal coronary arteries (Chap. 13). In-stent restenosis in an (unprotected) left main stent may have serious consequences. Because stress testing is considered less reliable, conventional coronary angiography is routinely performed after 3–6 months. Cardiac CT can exclude significant disease in the majority of patients with large stents, thereby avoiding recatheterization in a substantial number of patients, particularly when "simple" stenting (i.e., no bifurcation stenting) has been performed

After bypass graft surgery, CT can be of use to exclude graft obstruction. As subclinical occlusion may exist for years, because of competitive antegrade or collateral flow, assessment of the significance of an occluded graft late after revascularization requires some kind of functional imaging. Occasionally, the exact anatomy of the bypass graft procedure is unknown, or grafts cannot be located or engaged by catheter for other reasons, in which case CT can be very useful.

4.7 CT-Assisted Cardiac Interventions

Cardiac CT can provide unique three-dimensional information of the heart, which can benefit complex cardiac procedures such as electrophysiological ablation (Chap. 21), coronary revascularization procedures (Chaps. 12 and 13) and valvular procedures (Chaps. 17 and 18).

Cardiac CT can provide potentially valuable information supplementing the angiographic projections obtained by invasive means. Information on the angulation of vessels or the presence and location of plaques at ostial or bifurcation sites is useful in complex coronary procedures. In chronic total occlusion, CT can provide information regarding the length and content of the occluded segment, proximal vessel tortuosity and stump morphology, and the presence of side branches

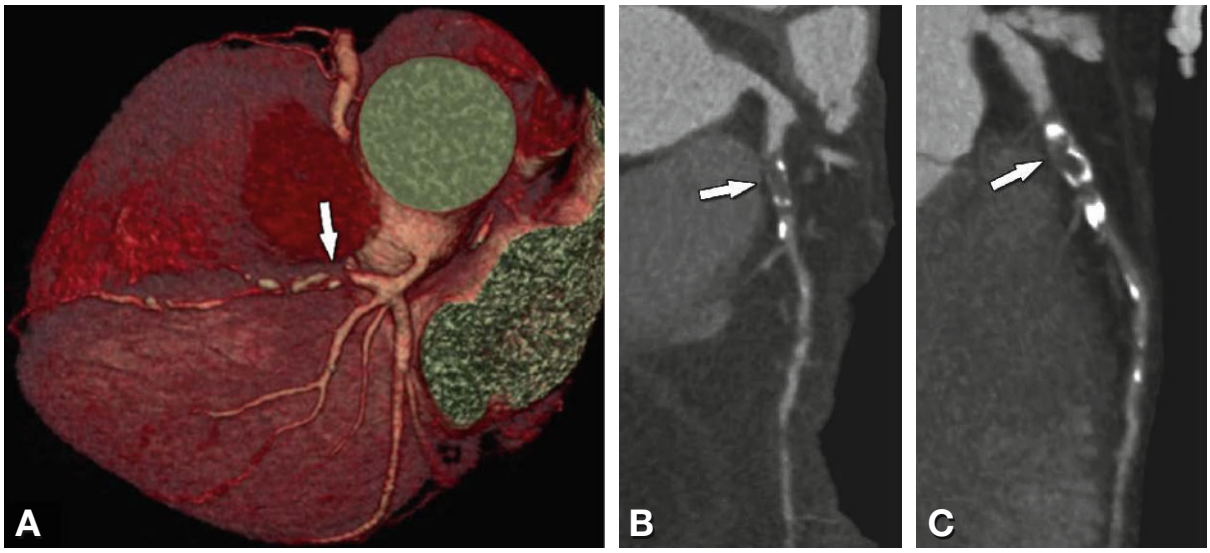

Fig. 4.5 Chronic total occlusion in the left anterior descending coronary artery of a 55-year-old woman with anginal symptoms. Short occlusion (*arrow*) with moderate amounts of calcium in the left anterior descending coronary artery. **Panel A** is a volume-rendered reconstruction, **Panels B** and **C** are curved multiplanar reformations and maximum-intensity projections

List 4.1. Predictors of revascularization failure in chronic total occlusion

1. Longer duration of the occlusion
2. Absence of antegrade collateral filling
3. Blunt rather than a tapered proximal stump
4. Occlusion length >15 mm[a]
5. Severe calcification[a]
6. Side branch at the occlusion site
7. Vessel tortuosity proximal to the occlusion

[a] Predictive value confirmed by CT

(**Fig. 4.5** and **List 4.1**). Severe calcification and long occlusion predict a poorer outcome of revascularization procedures. These images may also be integrated in advanced catheter registration and navigation systems.

In patients undergoing electrophysiological procedures, three-dimensional imaging of the cardiac chambers is performed to assess (abnormal) anatomy, select the most optimal technique and equipment, avoid complications (by localization of the esophagus), guide catheters, and record proceedings (Chap. 21).

In many centers cardiac CT has become a routine pre-procedural examination prior to percutaneous implantation of aortic valves. Measurement of the aortic outflow tract dimensions are important to assess suitability, select the optimal device size, predict procedural outcome. In addition, imaging of the peripheral vasculature is important to select the most optimal vascular access (Chap. 17).

4.8 Ventricular Function, Myocardial Infarction, and Valvular Heart Disease

The clinical mainstay of cardiovascular imaging is echocardiography. The technique is quick, inexpensive and can be performed at the bedside. When an acceptable echocardiographic window is available, echocardiography is the first choice for functional imaging of the heart. For more accurate or reproducible assessment of left ventricular function, MRI or nuclear imaging are generally performed (**Table 4.3**). While assessment of global left ventricular function by ECG-gated CT is possible, with good correlation to echocardiography, MRI, and nuclear imaging, it is not solely performed for this purpose unless other modalities are unavailable (Chap. 15). Dynamic display of cardiac CT can be used for assessment of segmental wall motion or valvular mobility, although CT has poorer temporal resolution than echocardiography and MRI and does not provide all functional parameters that can be determined with the latter two techniques. It should also be mentioned that full-cycle data is often unavailable with current

Table 4.3 Left ventricular function

Modality	Advantages	Disadvantages
Echocardiography	Easy, real-time, portable, low cost, safe and repeatable Velocity measurement	Acoustic accessibility Operator dependence Geometric assumptions[a]
Nuclear imaging	Accurate and reproducible No geometric assumptions	Radiation exposure Limited anatomy Arrhythmia No wall thickening[b] Hypoperfused myocardium delineation[c]
Magnetic resonance imaging	No ionizing radiation Flexible and reproducible	Limited availability and relatively time-consuming Pacemaker devices, claustrophobia, etc. Patient motion
Computed tomography	Available as part of conventional ECG-gated spiral CT High spatial resolution High contrast-to-noise ratio No geometric assumptions Reproducible	Not routinely available with prospectively ECG-triggered axial scan protocols Contrast agent and radiation exposure Limited temporal resolution (wall motion)

[a] Largely overcome by three-dimensional echocardiography

[b] Radionuclide ventriculography

[c] Gated single-photon emission computed tomography

dose-saving CT protocols (prospective acquisition, Chap. 8). CT provides detailed information on valve morphology during end-systole or mid-diastole but lacks the functional information afforded by Doppler measurement, often crucial in decision making. Aortic valve planimetry can be helpful in patients with poor acoustic windows (Chaps. 16 and 17).

Myocardial infarction may be recognized as low myocardial attenuation on (coronary) CT angiograms. Chronic myocardial infarction may be differentiated from acute perfusion defects based on the lower myocardial attenuation resulting from the presence of fat tissue within the scar tissue. However, acute infarction within an area of subendocardial scarring will be difficult to recognize based on these attenuation values. The area of early hypoenhancement may underestimate the total volume of infarcted myocardium, and late imaging after contrast injection ("delayed enhancement") is more accurate in quantifying myocardial infarction. Late-enhancement imaging by CT, like MRI, allows transmural infarction sizing, which is an advantage over nuclear techniques. However, current delayed-imaging CT techniques require more contrast agent to compensate for the generally lower contrast-to-noise levels and additional X-ray exposure, making it a second choice to MRI for myocardial viability assessment.

Recommended Reading

Achenbach S, Delgado V, Hausleiter J et al (2012) SCCT expert consensus document on computed tomography imaging before transcatheter aortic valve implantation (TAVI)/transcatheter aortic valve replacement (TAVR). J Cardiovasc Comput Tomogr 6:366–380

Arad Y, Goodman KJ, Roth M, Newstein D, Guerci AD (2005) Coronary calcification, coronary disease risk factors, C-reactive protein, and atherosclerotic cardiovascular disease events: the St. Francis heart study. J Am Coll Cardiol 46:158–165

Budoff MJ, Achenbach S, Blumenthal RS et al (2006) AHA Committee on Cardiovascular Imaging and Intervention; AHA Council on Cardiovascular Radiology and Intervention; AHA Committee on Cardiac Imaging, Council on Clinical Cardiology. Assessment of coronary artery disease by cardiac computed tomography: a scientific statement from the AHA Committee on Cardiovascular Imaging and Intervention, Council on Cardiovascular Radiology and Intervention, and Committee on Cardiac Imaging, Council on Clinical Cardiology. Circulation 114:1761–1791

Cho I, Chang HJ, Sung JM et al (2012) Coronary computed tomographic angiography and risk of all-cause mortality and nonfatal myocardial infarction in subjects without chest pain syndrome from the CONFIRM Registry (coronary CT angiography evaluation for clinical outcomes: an international multicenter registry). Circulation 126:304–313

Choi EK, Choi SI, Rivera JJ et al (2008) Coronary computed tomography angiography as a screening tool for the detection of occult coronary artery disease in asymptomatic individuals. J Am Coll Cardiol 52:357–365

Dedic A, Ten Kate GJ, Neefjes LA et al (2013) Coronary CT angiography outperforms calcium imaging in the triage of acute coronary syndrome. Int J Cardiol 167(4):1268–1275

Fox K, Garcia MA, Ardissino D et al (2006) Task force on the management of stable angina pectoris of the European Society of Cardiology; ESC Committee for Practice Guidelines (CPG). Guidelines on the management of stable angina pectoris: executive summary: The task force on the management of stable angina pectoris of the European Society of Cardiology. Eur Heart J 27:1341–1381

García-García HM, van Mieghem CA, Gonzalo N et al (2009) Computed tomography in total coronary occlusions (CTTO registry): radiation exposure and predictors of successful percutaneous intervention. EuroIntervention 4:607–616

Graham I, Atar D, Borch-Johnsen K et al (2007) European guidelines on cardiovascular disease prevention in clinical practice: full text. Fourth joint task force of the European society of cardiology and other societies on cardiovascular disease prevention in clinical practice. Eur J Cardiovasc Prev Rehabil 14(Suppl 2):S1–S113

Greenland P, Bonow RO, Brundage BH et al (2000) Society of Atherosclerosis Imaging and Prevention; Society of Cardiovascular Computed Tomography. ACCF/AHA 2007 clinical expert consensus document on coronary artery calcium scoring by computed tomography in global cardiovascular risk assessment and in evaluation of patients with chest pain: a report of the American College of Cardiology Foundation Clinical Expert Consensus Task Force (ACCF/AHA Writing Committee to Update the 2000 Expert Consensus Document on Electron Beam Computed Tomography) developed in collaboration with the Society of Atherosclerosis Imaging and Prevention and the Society of Cardiovascular Computed Tomography. J Am Coll Cardiol 49:378–402

Hoffmann U, Bamberg F, Chae CU et al (2009) Coronary computed tomography angiography for early triage of patients with acute chest pain: the ROMICAT (Rule Out Myocardial Infarction using Computer Assisted Tomography) trial. J Am Coll Cardiol 53:1642–1650

Hoffmann U, Truong QA, Schoenfeld DA et al (2012) Coronary CT angiography versus standard evaluation in acute chest pain. N Engl J Med 367:299–308

Knez A, Becker A, Leber A et al (2004) Relation of coronary calcium scores by electron beam tomography to obstructive disease in 2, 115 symptomatic patients. Am J Cardiol 93:1150–1152

Lardo AC, Cordeiro MA, Silva C et al (2006) Contrast-enhanced multidetector computed tomography viability imaging after myocardial infarction: characterization of myocyte death, microvascular obstruction, and chronic scar. Circulation 113:394–404

Lee HY, Song IS, Yoo SM et al (2011) Rarity of isolated pulmonary embolism and acute aortic syndrome occurring outside of the field of view of dedicated coronary CT angiography. Acta Radiol 52:378–384

Litt HI, Gatsonis C, Snyder B et al (2012) CT angiography for safe discharge of patients with possible acute coronary syndromes. N Engl J Med 366:1393–1403

Maintz D, Seifarth H, Raupach R et al (2006) 64-slice multidetector coronary CT angiography: in vitro evaluation of 68 different stents. Eur Radiol 16:818–826

McClelland RL, Chung H, Detrano R, Post W, Kronmal RA (2006) Distribution of coronary artery calcium by race, gender, and age: results from the Multi-Ethnic Study of Atherosclerosis (MESA). Circulation 113:30–37

Meijboom WB, van Mieghem CA, Mollet NR et al (2007) 64-slice computed tomography coronary angiography in patients with high, intermediate, or low pretest probability of significant coronary artery disease. J Am Coll Cardiol 50:1469–1475

Mollet NR, Hoye A, Lemos PA et al (2005) Value of preprocedure multislice computed tomographic coronary angiography to predict the outcome of percutaneous recanalization of chronic total occlusions. Am J Cardiol 95:240–243

Nandalur KR, Dwamena BA, Choudhri AF, Nandalur MR, Carlos RC (2007) Diagnostic performance of stress cardiac magnetic resonance imaging in the detection of coronary artery disease: a meta-analysis. J Am Coll Cardiol 50:1343–1353

Nieman K, Galema TW, Neefjes LA et al (2009) Comparison of the value of coronary calcium detection to computed tomographic angiography and exercise testing in patients with chest pain. Am J Cardiol 104:1499–1504

Serruys PW, Ormiston JA, Onuma Y et al (2009) A bioabsorbable everolimus-eluting coronary stent system (ABSORB): 2-year outcomes and results from multiple imaging methods. Lancet 373:897–910

Skinner JS, Smeeth L, Kendall JM et al (2010) Chest Pain Guideline Development Group. NICE guidance. Chest pain of recent onset: assessment and diagnosis of recent onset chest pain or discomfort of suspected cardiac origin. Heart 96:974–978

Soon KH, Cox N, Wong A et al (2007) CT coronary angiography predicts the outcome of percutaneous coronary intervention of chronic total occlusion. J Interv Cardiol 20:359–366

Taylor AJ, Cerqueira M, Hodgson JM et al (2010) ACCF/SCCT/ACR/AHA/ASE/ASNC/NASCI/SCAI/SCMR 2010 Appropriate Use Criteria for Cardiac Computed Tomography. J Cardiovasc Comput Tomogr 4:407.e1–407.e33

Von Ballmoos MW, Haring B, Juillerat P, Alkadhi H (2011) Meta-analysis: diagnostic performance of low-radiation-dose coronary computed tomography angiography. Ann Intern Med 154: 413–420

Clinical Indications

M. Dewey

Abstract

The clinically most relevant indications for cardiac CT are presented. CT angiography for ruling out coronary artery disease in patients with low-to-intermediate pretest likelihood of disease is the most common appropriate indication. Assessing myocardial viability by CT and performing coronary CT angiography in asymptomatic individuals and patients with typical symptoms and high likelihood of coronary artery disease are not recommended.

5.1 Suspected Coronary Artery Disease

The most obvious indication for cardiac CT is to exclude coronary artery disease (CAD) in symptomatic patients with stable chest pain and low-to-intermediate pretest likelihood of disease, which is defined as a likelihood of approximately 20–70% (**Fig. 5.1**). This group includes patients with inconclusive findings in previous stress tests and those presenting with atypical angina. On the one hand, patients with a higher pretest likelihood of CAD (>70%; e.g., with typical angina, risk factors, and a positive stress test) should not undergo cardiac CT as the first-line modality, because more patients in this subgroup will require subsequent conventional coronary angiography as the negative predictive value of CT is reduced (making a negative CT result less reliable). On the other hand, the positive predictive value is rather low in patients with a very low pretest likelihood of CAD

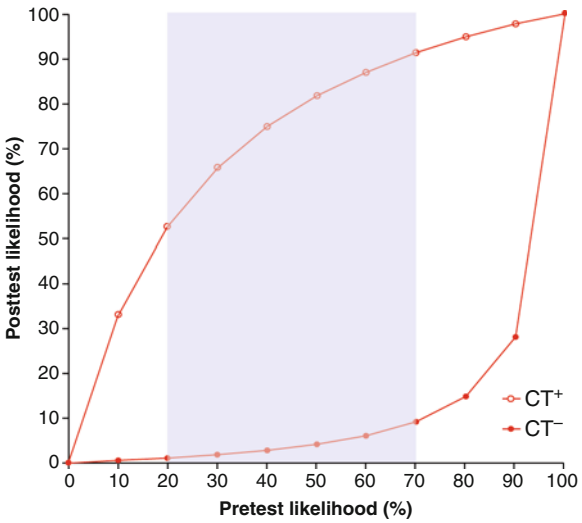

Fig. 5.1 The patient population with suspected CAD that is clinically most suitable for undergoing coronary CT angiography is highlighted in *blue* and has a pretest likelihood of disease of 20–70%. CT coronary angiography is very accurate in ruling out disease over a wide range of clinical presentations, as can be seen in the very low posttest likelihood after a negative CT (below 10% for pretest likelihoods of up to 70%). Thus, coronary CT angiography allows reliable exclusion of disease. However, patients with a likelihood of less than 20% may not benefit from noninvasive testing because of the very low positive predictive value in this group, which may lead to a rather high rate of unnecessary conventional coronary angiographies. This calculation, made according to the Bayes' theorem, is based on the overall sensitivity and specificity of coronary CT angiography in patients with suspected CAD, as specified in Chap. 25 and modified from Schuetz et al. *Ann Intern Med* 2010

M. Dewey, *Cardiac CT*,
DOI 10.1007/978-3-642-41883-9_5, © Springer-Verlag Berlin Heidelberg 2014

Table 5.1 Likelihood (in %) of CAD according to sex, age, and symptoms[a]

Men				Women			
Age (years)	Nonanginal chest pain[b]	Atypical angina[c]	Typical angina[d]	Age (years)	Nonanginal chest pain[b]	Atypical angina[c]	Typical angina[d]
30–39	0.8	4	26	30–39	5	22	70
40–49	3	13	55	40–49	14	46	87
50–59	8	32	79	50–59	22	59	92
60–69	19	54	91	60–69	28	67	94

[a] The range of patients who are most likely to benefit from coronary CT angiography is highlighted in blue (those with a likelihood of 20–70%). In the 30–69-year age range, all men with atypical symptoms would be expected to benefit from CT, whereas women with atypical angina pectoris would be suitable candidates for coronary CT angiography only if they were older than 50 years of age. Modified from Diamond and Forrester *New Engl J Med* 1979

[b] Only one of the three characteristics of angina pectoris is present (either retrosternal localization of pain, pain precipitated by exercise or decreased at rest, or on nitrate medication)

[c] Only two of the three characteristics of angina pectoris are present

[d] All of the three characteristics of angina pectoris are present

(<20%; e.g., with nonanginal chest pain and a negative stress test), and the CT findings would lead to many unnecessary conventional coronary angiographies.

Thus, the preferred patient population for CT coronary angiography has a pretest likelihood of CAD of 20–70%. In **Tables 5.1, 5.2,** and **5.3,** patients with a pretest likelihood in this range are highlighted in blue. The markings in the tables make it easy to identify those patients who are most likely to benefit from coronary CT angiography and to simultaneously exclude others who should not undergo this test. These tables may also be helpful in increasing the cost-effectiveness of coronary CT angiography, as costly and unnecessary secondary examinations, which are more likely in very low (<20%) and high-likelihood patients (>70%), can potentially increase societal costs related to the diagnosis of CAD.

5.2 Other Appropriate Clinical Indications

Other justified indications for cardiac CT angiography in addition to suspected CAD are summarized in **Table 5.4**. The most common of these indications is in patients presenting with acute low-risk chest pain (with normal enzymes and without ECG changes) to the emergency department; a subgroup of patients for whom evidence in favor of CT has accumulated over the last years from single-center studies and several multicenter trials including CT-STAT by Raff et al., ACRIN-PA 4005 by Litt et al., and ROMICAT II by Hoffmann et al.. It is important to note that a zero CT calcium score had upper 95% confidence intervals for a subsequent acute coronary syndrome of above 2% in these trials. Thus, calcium scoring alone does not allow reliable rule-out of subsequent events in patients with acute chest pain. These studies suggest that management of low-risk patients with acute chest pain might be streamlined using CT (greater cost-effectiveness and a significant reduction in the length of hospital stay of 25–60%) in comparison to standard of care. Interestingly, Hoffmann et al. recently reported, in a substudy of the ROMICAT II trial, that CT results in an even stronger reduction in length of stay, fewer hospital admissions, and lower radiation dose in the CT group compared with standard of care. As a consequence of these research findings, the current guideline of the European Society of Cardiology for the management of acute coronary syndrome concludes that CT should be considered an alternative to invasive angiography to exclude acute coronary syndrome when there is a low to intermediate likelihood of CAD and when troponin and ECG are inconclusive (Class IIa, Level B indication).

In contrast, the so-called "triple rule-out" CT (to exclude coronary stenosis, pulmonary embolism, and aortic dissection) in acute patients is still limited by the fact that no generally accepted scanning protocols are available, and the patient population that might benefit from such a comprehensive examination remains to be clearly defined (**Table 5.6**). A nonrandomized study by Madder et al. found similar clinical outcomes of triple

Table 5.2 Posttest likelihood (in %) of CAD in women after an electrocardiographic stress test (ST depression), according to age and symptoms[a]

Women					
ST depression (mm)	Age (years)	Asymptomatic	Nonanginal chest pain[b]	Atypical angina[c]	Typical angina[d]
0–0.5	30–39	0.1	0.2	1	7
	40–49	0.2	0.7	3	22
	50–59	0.8	2	10	47
	60–69	2	5	21	69
0.5–1.0	30–39	0.3	0.7	4	24
	40–49	0.9	3	12	53
	50–59	3	8	31	78
	60–69	7	17	52	90
1.0–1.5	30–39	0.6	2	9	42
	40–49	2	6	25	72
	50–59	7	16	50	89
	60–69	15	33	72	95
1.5–2.0	30–39	1	3	16	59
	40–49	4	11	39	84
	50–59	12	28	67	94
	60–69	25	49	83	98
2–2.5	30–39	3	8	33	79
	40–49	10	24	63	93
	50–59	27	50	84	98
	60–69	47	72	93	99.1
>2.5	30–39	11	24	63	93
	40–49	28	53	86	98
	50–59	56	78	95	99.3
	60–69	76	90	98	99.7

[a] The range of women who are most likely to benefit from coronary CT angiography is highlighted in blue (20–70%). Modified from Diamond and Forrester *New Engl J Med* 1979

[b] Only one of the three characteristics of angina pectoris is present (either retrosternal localization of pain, pain precipitated by exercise or decreased at rest, or on nitrate medication)

[c] Only two of the three characteristics of angina pectoris are present

[d] All of the three characteristics of angina pectoris are present

Please note that 1.0 mm is equal to 0.1 mV

Table 5.3 Posttest likelihood (in %) of CAD in men after an electrocardiographic stress test (ST depression), according to age and symptoms[a]

		Men			
ST depression (mm)	Age (years)	Asymptomatic	Nonanginal chest pain[b]	Atypical angina[c]	Typical angina[d]
0–0.5	30–39	0.4	1	6	25
	40–49	1	4	16	61
	50–59	2	6	25	73
	60–69	3	8	32	79
0.5–1.0	30–39	2	5	21	68
	40–49	5	13	44	86
	50–59	9	20	57	91
	60–69	11	26	65	94
1.0–1.5	30–39	4	1	38	83
	40–49	11	26	64	94
	50–59	19	37	75	96
	60–69	23	45	81	97
1.5–2.0	30–39	8	19	55	91
	40–49	20	41	78	97
	50–59	31	53	86	98
	60–69	37	62	90	99
2.0–2.5	30–39	18	38	76	96
	40–49	39	65	91	99
	50–59	54	75	94	99.2
	60–69	61	81	96	99.5
>2.5	30–39	43	68	92	99
	40–49	69	87	97	99.6
	50–59	81	91	98	99.8
	60–69	85	94	99	99.8

[a] The range of men who are most likely to benefit from coronary CT angiography is highlighted in blue (20–70%). Modified from Diamond and Forrester *New Engl J Med* 1979

[b] Only one of the three characteristics of angina pectoris is present (either retrosternal localization of pain, pain precipitated by exercise or decreased at rest, or on nitrate medication)

[c] Only two of the three characteristics of angina pectoris are present

[d] All of the three characteristics of angina pectoris are present

Please note that 1.0 mm is equal to 0.1 mV

Table 5.4 Appropriate clinical indications for cardiac CT

	Pros	Cons
Exclusion of CAD in symptomatic patients with low to intermediate pretest likelihood	High negative predictive value of CT Noninvasive CT is highly accepted by patients	Only little data available on possible advantages of CT over other modalities such as stress ECG, and on possible advantages for patient management
Patients with suspected CAD and equivocal stress-test results	High negative predictive value of CT Noninvasive CT is highly accepted by patients	Only little data available on possible advantages for patient management
Acute chest pain with negative ECG and borderline enzymes	Reliable exclusion of CAD in these patients is possible Patients can be discharged earlier	An outcome benefit over the standard of care has not been shown. However, very large and long-term studies may be needed to show this
Follow-up of symptomatic patients with coronary artery bypasses	Reliable visualization of the entire bypass, including the proximal and distal anastomoses Noninvasive CT is highly accepted by patients	Only little data available on possible advantages for patient management Numerous studies, but in small patient populations
Exclusion of or delineation of the course of coronary artery anomalies	Excellent evaluation of the course of anomalous coronaries (malignant vs. benign) Unlike MRI, CT allows reliable visualization of the entire course of the vessel	Its competitor, MRI, is to be preferred, especially in younger patients, because it does not involve radiation exposure Unreliable in visualizing coronary collaterals
Assessment of pulmonary vein anatomy prior to and after electrophysiology procedures (e.g., in patients with atrial fibrillation)	CT has high spatial resolution Data can be acquired without ECG gating and thus with lower radiation exposure	MRI does not require radiation exposure and is able to visualize scar tissue after ablation using delayed-enhancement techniques
Analysis of global and regional cardiac function and valvular function[a]	CT has high spatial resolution[b] All data needed for functional analysis can be derived from CT coronary angiography without the need for an additional scan	Temporal resolution of CT is limited MRI and echocardiography are the established scientific and clinical gold standards

[a] Analysis of cardiac function is very fast and easy to perform using recent software tools, and because of its clinical importance, it should be performed and reported in every patient undergoing cardiac CT with retrospective gating. In only rare cases there is a clinical indication for cardiac function analysis alone. Functional analysis is nearly always done as part of coronary CT angiography performed for other clinical indications

[b] CT performs better than echocardiography and cineventriculography

rule-out CT as compared with standard cardiac CT but higher overall radiation exposure, downstream utilization, and invasive testing. Further larger studies investigating the benefit of CT in this respect are necessary before its general use can be considered and we regard the triple rule-out indication as inappropriate at this point in time. Another important argument against routine triple rule-out CT is that, according to Stillman et al., only two of the three diseases are actually suspected and need to be ruled out in most of the acute chest pain patients. Thus, the technical approach may better individually focus on two of the vascular beds ("double-rule out"), which will increase practicality and image quality.

Imaging and follow-up of symptomatic patients with coronary artery bypass grafts (e.g., recurrent chest pain; Chaps. 12 and 20) is an important appropriate indication. There is good evidence that CT allows highly accurate assessment of both the native coronaries and the bypass grafts in a single examination. However, the

Table 5.5 Potential clinical indications for cardiac CT

	Pros	Cons
Ruling out CAD prior to noncoronary cardiac surgery	Reliable exclusion of CAD in these patients may be possible Conventional coronary angiography may be avoided	There are as yet no results from studies in larger patient populations Unclear outcome benefit over established tests
Follow-up of patients with coronary artery stents	High negative predictive value for some stents Can be used for non-invasive follow-up	Evaluation of stents with an internal diameter <3.0–3.5 mm is still limited Current CT technology does not provide functional information on blood flow direction
Prior to reoperative cardiac surgery	Important pathology (such as sternal wire near bypasses) and dimensions (e.g., distance of sternum to bypass) can be detected prior to operation	There are as yet no results from studies in larger patient populations
Assessment of cardiac tumors	CT has high spatial resolution and best allows assessment of calcifications	MRI does not require radiation exposure and due to better soft tissue contrast enables better differentiation of certain tumor types
Suspected pericardial disease	Excellent depiction of calcified pericarditis ("armored heart") and pericardial effusion	CT provides only limited functional information MRI and echocardiography yield good results without radiation exposure

native coronary arteries in patients after bypass grafting are not as easily assessed as are the bypasses themselves (Chap. 12), and only a few studies have addressed the combined reading of coronaries and bypasses. Thus, scientific evidence most strongly supports the use of CT for exclusion of CAD in patients with low-to-intermediate pretest likelihood (e.g., patients with suspected CAD and inconclusive findings and complaints).

The presence of coronary artery anomalies (Chap. 22) is also readily ruled out with CT, which is superior to magnetic resonance imaging (MRI) in depicting the distal parts of the coronaries and visualizing the entire course of anomalous vessels. Moreover, CT is well suited for follow-up of coronary aneurysms; however, in young patients, such as those with Kawasaki syndrome, MRI should be the first-line imaging tool because it does not involve radiation exposure, and there is no need for contrast agent administration.

CT is also highly accurate in analyzing global and regional cardiac function (Chap. 15). Coronary CT angiography has the crucial advantage that the images necessary for cardiac function analysis are inherently part of a standard retrospectively acquired dataset, and no additional injection of contrast agent or radiation exposure is required. Therefore, because of the importance of global as well as regional cardiac function for the patient's prognosis and further management (Chap. 10), we strongly encourage the inclusion of cardiac function analysis in the reports of all patients undergoing retrospectively gated coronary CT angiography. Nevertheless, because of the radiation exposure and the need for a contrast medium, CT is rarely indicated for analysis of cardiac function alone, but rather for use in combination with other clinical questions to be answered.

5.3 Potential Clinical Indications

CT coronary stent imaging is one of the potential clinical indications (**Table 5.5**). However, the available evidence (Chaps. 13 and 25) clearly indicates a reduced diagnostic accuracy and increased nondiagnostic rates in stents with a diameter of less than 3.5 mm. Also, because such stents represent 70–80% of all implanted coronary stents, in patients with more than two coronary stents the diagnostic accuracy will very likely be limited. Thus, there is no general indication for follow-up using currently available CT technology in patients after stent placement (**Table 5.5**). Also, the positive predictive value of CT is limited in coronary stent imaging (Chap. 25). The decision for or against CT should be made individually on the basis of the stent material and diameter; however, selected patients with low and stable heart rates and proximal large stents can successfully be analyzed using CT angiography. CT

Table 5.6 Currently no clinical indications for cardiac CT

	Pros	Cons
Screening of asymptomatic individuals	May conceivably be more accurate than other noninvasive modalities in reliably excluding disease	The positive predictive value is unacceptably low in screening patients with a very low pretest likelihood of CAD (**Fig. 5.1**) Study results are not yet available
High pretest likelihood of CAD based on typical symptoms or positive results of other noninvasive tests	High negative predictive value	The negative predictive value is unacceptably low in patients with high pretest likelihood of CAD (**Fig. 5.1**) Intervention is likely required
Triple rule-out (to exclude coronary stenoses, pulmonary embolism, and aortic dissection)	Comprehensive examination	Generally accepted scanning protocols, and the target population remain to be defined No outcome studies
Assessment (including characterization and quantification) of coronary plaques	CT has reasonable accuracy in detection and characterization of plaques	Interobserver variability of CT is considerable and exact analysis of plaque dimension is limited Analysis is rather time-consuming Clinical implications have not been fully explored
Analysis of myocardial viability and perfusion	CT has higher spatial resolution than MRI Quantification of perfusion by CT is theoretically feasible	Stress echocardiography and MRI have good clinical accuracy without involving radiation exposure Analysis of myocardial vitality and perfusion by CT requires an additional scan after coronary angiography

perfusion may provide an adjunct to CT angiography when stented coronary segments are considered non-diagnostic (Chap. 19).

5.4 Currently No Clinical Indications

Besides triple rule-out CT, screening is another application that we currently do not consider an established clinical indication for coronary CT angiography (**Table 5.6**) because its predictive value for the presence of significant stenoses is too low in this patient population (**Fig. 5.1**). In contrast, the negative predictive value is very low in patients with typical symptoms and/or positive results of noninvasive tests (high pretest likelihood), so that CT is also not reliable enough to exclude coronary stenoses in this group.

Visualization and analysis of myocardial viability and perfusion is likewise not an accepted clinical indication for CT (**Table 5.6**). The main drawback of myocardial viability imaging by CT is that extra scans with additional radiation exposure are necessary, whereas MRI yields excellent results without radiation exposure (Chap. 26). Myocardial CT perfusion imaging has great potential, while from a clinical perspective it is still in its infancy and widespread use cannot be recommended at present (Chap. 19).

5.5 Patient Referral

We recommend using a special referral form, to be completed by physicians referring a patient for cardiac CT (**Fig. 5.2**). The information provided in the form makes it easier to decide whether the patient will benefit most from CT or another test. It also helps standardize and facilitate communication with referring physicians. Moreover, possible contraindications (Chap. 6) can be identified before an appointment is made, and the radiologist can choose in advance the most appropriate kind of coronary CT angiography (Chaps. 7 and 8) to be performed in the patient (**Fig. 5.2**).

In summary, the decision as to whether there is a clinical indication for coronary CT angiography should

CHARITÉ

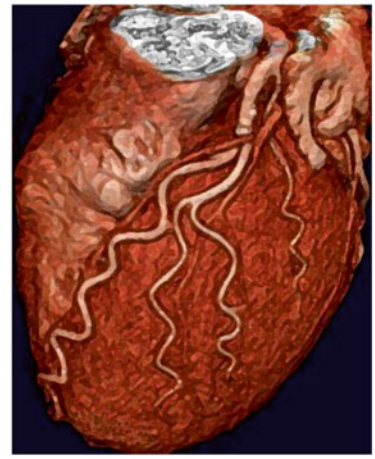

Referred by

Name: .....

Phone: .....

Address: .....

Referral for Cardiac CT (Coronary Arteries)

5

Charité Campus Mitte
Dept. of Radiology
Charitéplatz 1
10117 Berlin, Germany

❍ **FAX:**
+49 (0)30/450 527 911

I request a **cardiac CT** for the following patient:
Last name: ..... First name: ..... D.O.B.: . . .
Address: .....Phone: .....

Reason for exam: ❍ Suspected CAD ❍ Follow-up bypass ❍ Follow-up stent ❍ Other: .....
Indication/Question/Risk factors:
.....
.....

If the patient has undergone previous tests: Which? **(please attach reports)**
❍ ECG ❍ Stress ECG ❍ Echo ❍ Stress echo ❍ Cardiac scintigraphy ❍ PET ❍ MRI ❍ CT

In patients with bypasses: No. of bypasses: ..... Date of operation: .....
❍ LIMA to ..... ❍ RIMA to ..... No. of veins to: ❍ LAD: ..... ❍ LCX: ..... ❍ RCA: .....❍ Other: .....

Provision of the following information is **mandatory** in patients with stents to decide whether CT is reasonable: No. of stents: ..... Stent diameter (mm): ...../...../...../.....
Stent length (mm): ...../...../...../..... Stent site: ...../...../...../.....

Did the patient have a prior conventional coronary angiography? Date : . . .
Findings: .....

We ask for the following information so that we can exclude contraindications to CT:
Creatinine: ..... (mg/dl) ❍ Hyperthyroidism (TSH: .....) ❍ Allergic reaction to iodinated contrast agent
❍ Irregular heart rate (e.g. atrial fibrillation): ..... ❍ Severe asthma (if high heart rate)
Please contact us by phone (+49 (0)30 450 527 133) if your patient has a contraindication or if you have further questions.

Fig. 5.2 Example of a referral form that can be used for coronary CT angiography

always be made on an individual basis and should take into account the patient's pretest likelihood and possible contraindications.

Recommended Reading

Achenbach S (2006) Computed tomography coronary angiography. J Am Coll Cardiol 48:1919–1928

Bluemke DA, Achenbach S, Budoff M et al (2008) Noninvasive coronary artery imaging: magnetic resonance angiography and multidetector computed tomography angiography: a scientific statement from the American Heart Association Committee on Cardiovascular Imaging and Intervention of the Council on Cardiovascular Radiology and Intervention, and the Councils on Clinical Cardiology and Cardiovascular Disease in the Young. Circulation 118:586–606

Cademartiri F, Schuijf JD, Pugliese F et al (2007) Usefulness of 64-slice multislice computed tomography coronary angiography to assess in-stent restenosis. J Am Coll Cardiol 49:2204–2210

Chinnaiyan KM, Raff GL, Goraya T et al (2012) Coronary computed tomography angiography after stress testing: results from a multicenter, statewide registry, ACIC (Advanced Cardiovascular Imaging Consortium). J Am Coll Cardiol 59:688–695

Cordeiro MA, Lima JA (2006) Atherosclerotic plaque characterization by multidetector row computed tomography angiography. J Am Coll Cardiol 47:C40–C47

Cury RC, Feuchtner GM, Batlle JC et al (2013) Triage of patients presenting with chest pain to the emergency department: implementation of coronary CT angiography in a large urban health care system. AJR Am J Roentgenol 200:57–65

de Roos A, Kroft LJ, Bax JJ et al (2007) Applications of multislice computed tomography in coronary artery disease. J Magn Reson Imaging 26:14–22

Dewey M, Hamm B (2007) CT coronary angiography: examination technique, clinical results, and outlook on future developments. Fortschr Röntgenstr 179:246–260

Dewey M, Müller M, Eddicks S et al (2006a) Evaluation of global and regional left ventricular function with 16-slice computed tomography, biplane cineventriculography, and two-dimensional transthoracic echocardiography: comparison with magnetic resonance imaging. J Am Coll Cardiol 48:2034–2044

Dewey M, Teige F, Schnapauff D et al (2006b) Noninvasive detection of coronary artery stenoses with multislice computed tomography or magnetic resonance imaging. Ann Intern Med 145:407–415

Diamond GA, Forrester JS (1979) Analysis of probability as an aid in the clinical diagnosis of coronary-artery disease. N Engl J Med 300:1350–1358

Ehara M, Kawai M, Surmely JF et al (2007) Diagnostic accuracy of coronary in-stent restenosis using 64-slice computed tomography: comparison with invasive coronary angiography. J Am Coll Cardiol 49:951–959

Feuchtner GM, Dichtl W, Friedrich GJ et al (2006a) Multislice computed tomography for detection of patients with aortic valve stenosis and quantification of severity. J Am Coll Cardiol 47:1410–1417

Feuchtner GM, Dichtl W, Schachner T et al (2006b) Diagnostic performance of MDCT for detecting aortic valve regurgitation. AJR Am J Roentgenol 186:1676–1681

Garcia MJ, Lessick J, Hoffmann MH (2006) Accuracy of 16-row multidetector computed tomography for the assessment of coronary artery stenosis. JAMA 296:403–411

Gaspar T, Halon DA, Lewis BS et al (2005) Diagnosis of coronary in-stent restenosis with multidetector row spiral computed tomography. J Am Coll Cardiol 46:1573–1579

Gasparovic H, Rybicki FJ, Millstine J et al (2005) Three dimensional computed tomographic imaging in planning the surgical approach for redo cardiac surgery after coronary revascularization. Eur J Cardiothorac Surg 28:244–249

Gilard M, Cornily JC, Pennec PY et al (2006) Assessment of coronary artery stents by 16 slice computed tomography. Heart 92:58–61

Goldstein JA, Chinnaiyan KM, Abidov A et al (2011) The CT-STAT (Coronary Computed Tomographic Angiography for Systematic Triage of Acute Chest Pain Patients to Treatment) trial. J Am Coll Cardiol 58:1414–1422

Hamon M, Biondi-Zoccai GG, Malagutti P et al (2006) Diagnostic performance of multislice spiral computed tomography of coronary arteries as compared with conventional invasive coronary angiography: a meta-analysis. J Am Coll Cardiol 48:1896–1910

Hamon M, Champ-Rigot L, Morello R et al (2008) Diagnostic accuracy of in-stent coronary restenosis detection with multislice spiral computed tomography: a meta-analysis. Eur Radiol 18(2):217–225

Hendel RC, Patel MR, Kramer CM et al (2006) ACCF/ACR/SCCT/SCMR/ASNC/NASCI/SCAI/SIR 2006 appropriateness criteria for cardiac computed tomography and cardiac magnetic resonance imaging. J Am Coll Cardiol 48:1475–1497

Hoffmann MH, Shi H, Schmitz BL et al (2005) Noninvasive coronary angiography with multislice computed tomography. JAMA 293:2471–2478

Hoffmann U, Pena AJ, Cury RC et al (2006) Cardiac CT in emergency department patients with acute chest pain. Radiographics 26:963–978; discussion 979–980

Hoffmann U, Truong QA, Schoenfeld DA et al (2012) Coronary CT angiography versus standard evaluation in acute chest pain. N Engl J Med 367:299–308

Jones CM, Athanasiou T, Dunne N et al (2007) Multi-detector computed tomography in coronary artery bypass graft assessment: a meta-analysis. Ann Thorac Surg 83:341–348

Leber AW, Johnson T, Becker A et al (2007) Diagnostic accuracy of dual-source multi-slice CT-coronary angiography in patients with an intermediate pretest likelihood for coronary artery disease. Eur Heart J 28(19):2354–2360

Litt HI, Gatsonis C, Snyder B et al (2012) CT angiography for safe discharge of patients with possible acute coronary syndromes. N Engl J Med 366:1393–1403

Madder RD, Raff GL, Hickman L et al (2011) Comparative diagnostic yield and 3-month outcomes of "triple rule-out" and standard protocol coronary CT angiography in the evaluation of acute chest pain. J Cardiovasc Comput Tomogr 5:165–171

Mahnken AH, Muhlenbruch G, Gunther RW et al (2007) Cardiac CT: coronary arteries and beyond. Eur Radiol 17:994–1008

Malagutti P, Nieman K, Meijboom WB et al (2006) Use of 64-slice CT in symptomatic patients after coronary bypass surgery: evaluation of grafts and coronary arteries. Eur Heart J 28:1879–1885

Martuscelli E, Romagnoli A, D'Eliseo A et al (2004) Evaluation of venous and arterial conduit patency by 16-slice spiral computed tomography. Circulation 110:3234–3238

Maurer MH, Zimmermann E, Schlattmann P et al (2012) Indications, imaging technique, and reading of cardiac computed tomography: survey of clinical practice. Eur Radiol 22:59–72

Meijboom WB, Mollet NR, Van Mieghem CA et al (2006) Pre-operative computed tomography coronary angiography to detect significant coronary artery disease in patients referred for cardiac valve surgery. J Am Coll Cardiol 48:1658–1665

Meijboom WB, van Mieghem CA, Mollet NR et al (2007) 64-slice computed tomography coronary angiography in patients with high, intermediate, or low pretest probability of significant coronary artery disease. J Am Coll Cardiol 50:1469–1475

Meyer TS, Martinoff S, Hadamitzky M et al (2007) Improved noninvasive assessment of coronary artery bypass grafts with 64-slice computed tomographic angiography in an unselected patient population. J Am Coll Cardiol 49:946–950

Mollet NR, Cademartiri F, Nieman K et al (2004) Multislice spiral computed tomography coronary angiography in patients with stable angina pectoris. J Am Coll Cardiol 43:2265–2270

Poon M, Rubin GD, Achenbach S et al (2007) Consensus update on the appropriate usage of cardiac computed tomographic angiography. J Invasive Cardiol 19:484–490

Raff GL, Chinnaiyan KM, Berman DS et al (2009) Coronary Computed Tomography for Systematic Triage of Acute Chest Pain Patients to Treatment – (The CT-STAT Trial). Circulation 120:2160

Rixe J, Achenbach S, Ropers D et al (2006) Assessment of coronary artery stent restenosis by 64-slice multi-detector computed tomography. Eur Heart J 27:2567–2572

Ropers U, Ropers D, Pflederer T et al (2007) Influence of heart rate on the diagnostic accuracy of dual-source computed tomography coronary angiography. J Am Coll Cardiol 50:2393–2398

Schoepf UJ, Zwerner PL, Savino G et al (2007) Coronary CT angiography. Radiology 244:48–63

Schuetz GM, Zacharopoulou NM, Schlattmann P et al (2010) Meta-analysis: noninvasive coronary angiography using computed tomography versus magnetic resonance imaging. Ann Intern Med 152:167–177

Stillman AE, Oudkerk M, Ackerman M et al (2007) Use of multidetector computed tomography for the assessment of acute chest pain: a consensus statement of the North American Society of Cardiac Imaging and the European Society of Cardiac Radiology. Eur Radiol 17:2196–2207

Truong QA, Hayden D, Woodard PK et al (2013) Sex differences in the effectiveness of early coronary computed tomographic angiography compared with standard emergency department evaluation for acute chest pain: the Rule-Out Myocardial Infarction with Computer-Assisted Tomography (ROMICAT)-II trial. Circulation 127:2494–2502

van der Vleuten PA, Willems TP, Gotte MJ et al (2006) Quantification of global left ventricular function: comparison of multidetector computed tomography and magnetic resonance imaging. a meta-analysis and review of the current literature. Acta Radiol 47:1049–1057

Van Mieghem CA, Cademartiri F, Mollet NR et al (2006) Multislice spiral computed tomography for the evaluation of stent patency after left main coronary artery stenting: a comparison with conventional coronary angiography and intravascular ultrasound. Circulation 114:645–653

Weustink AC, Meijboom WB, Mollet NR et al (2007) Reliable high-speed coronary computed tomography in symptomatic patients. J Am Coll Cardiol 50:786–794

Patient Preparation

M. Dewey

Abstract

Patient preparation is the key to success in cardiac CT, and the relevant aspects of this step are discussed in detail in this chapter. Standardized information sheets should be used to make every patient understand the nature of the procedure. Informed consent is pivotal to ensure that patients avoid movements that can cause artifacts and that no patients with contraindications undergo cardiac CT.

6.1 Patient Information Sheets

As patient preparation is the cornerstone of a successful cardiac CT, a well-trained nurse, physician assistant, technician, or a physician (according to state and/or federal legal regulations) should discuss the entire procedure with the patient and obtain written informed consent. Patient education can be facilitated by sending the patient an information sheet and questionnaire before the appointment (**Figs. 6.1** and **6.2**). The information asked in the questionnaire also serves to verify the patient's clinical indication for cardiac CT (Chap. 5) and exclude possible clinical contraindications to the examination.

6.2 General Information

The patient should be assured that CT is a noninvasive diagnostic procedure and that it does not take long to perform the examination. The short duration of the CT examination (about 15 min in the scanner room) and the comfortably wide and short gantry (in contrast to the narrow, claustrophobia-inducing bore in MRI) are major advantages of CT over MRI and should be stressed while talking to the patient. On the one hand, clearly explaining these aspects before the patient enters the scanner room reduces psychological stress and may relax the patient as well as reduce heart rate in some cases. On the other hand, the patient must also be given explicit information about the radiation exposure, which is the most important disadvantage of cardiac CT. As it does not mean much to a layperson that the effective exposure of a typical retrospectively gated exam is approximately 10–20 mSv, meaningful comparisons should be used, such as "the radiation exposure of cardiac CT angiography is five to ten times the annual background radiation" or "the effective radiation dose is the same as that of 100–200 chest X-rays." Using prospective gating ("step-and-shoot") will dramatically reduce the effective dose of cardiac CT to below 5 mSv in nearly all patients with low and stable heart rates (Chap. 7). Such effective doses are lower than necessary for nuclear myocardial perfusion imaging (about 8–12 mSv) and conventional coronary angiography (about 8 mSv). Thus, in patients with low and stable heart rates, the radiation exposure of CT is lower than that of alternative diagnostic tests. Nevertheless, especially in younger patients with a higher lifetime risk of cancer induced by CT, it is essential to carefully consider alternative imaging tests that might yield the same clinical information without radiation exposure.

M. Dewey, *Cardiac CT*,
DOI 10.1007/978-3-642-41883-9_6, © Springer-Verlag Berlin Heidelberg 2014

CHARITÉ

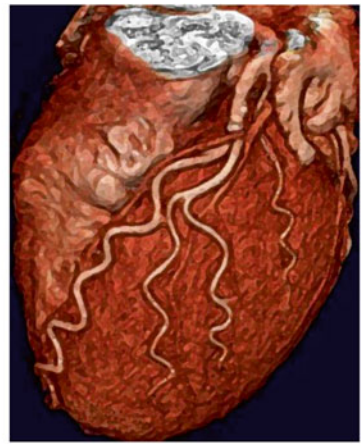

Patient Information
Cardiac CT

Dear Ms./Mr. ……,
Your doctor has referred you for an examination of your heart vessels (coronary arteries) to look for narrowings (stenoses) and deposits (plaques). The examination is performed on a computed tomography (CT) scanner. CT identifies stenosis in the coronary arteries with a reliability of over 90% and we expect that the information gained by the examination will help improve your further treatment.

You should fast for four hours before the examination (most importantly, you should not drink coffee or tea) and should continue to take your usual medications. If you take the antidiabetic drug called metformin, you may have to stop taking this medication for 48 hours after cardiac CT if you renal function is impaired (calculated eGFR ranging from 30-60 ml/min). Please contact us in case of questions about eGFR and metformin ahead of time.

Please carefully complete the questionnaire provided with this information sheet (see **Fig. 6.2**). The details about your symptoms and other tests that you have had in the past will help us make the correct diagnosis by CT. A written report of the CT findings together with representative images will be sent to your doctor after the examination.

Please send the completed form to the address or fax number given below or bring it along when you come in for your examination on day: …… at: ……

Address:
Charité
Department of Radiology, CT
Luisenstr. 7
10117 Berlin

FAX No.:
+49 (0)30/450 527 911

Phone:
+49 (0)30/450 527 133

Most patients with one of the following conditions cannot undergo a CT scan of the heart:

1. Irregular heart beat (e.g., atrial fibrillation)
2. Severe bronchial asthma (if high heart rate is present)
3. Intake of certain erectile dysfunction pills (e.g., Viagra)
4. Reduced kidney function (creatinine level > 1.5 – 2.0 mg/dl)
5. Allergic reactions to X-ray contrast media
6. Manifest thyroid overactivity (hyperthyroidism)

If one of these conditions applies in your case, please contact us before the examination

Fig. 6.1 Example of an information sheet that is sent out to the patient prior to the examination. Patients are asked to inform us in case contraindications to coronary CT angiography might be present that have been overlooked during the prior referral procedure (Chap. 5)

Patient Questionnaire

Name: ..... Address: ..... Phone No.: .....

FAX: .....Email: .....@.....

1. **D.O.B.**: . . . **Height**: . m/inches **Weight**: ..... kg/pounds **male** ❍ **female** ❍
2. Do you have **pain** in the chest? yes ❍ no ❍, If yes, please describe the location and type of pain:

.....

Does the pain increase when you **exercise**? yes ❍ no ❍ How long does the pain last? .....

Does the pain decrease **at rest or after nitro spray**? yes ❍ no ❍

3. Do you **smoke**? yes ❍ no ❍ If yes, for how long? .... years, how many cigarettes per day? .....
4. **Did you smoke**? yes ❍ no ❍ If yes, for how long? .... years, how many cigarettes per day? .....
5. Do you have **high blood lipid levels** (hyperlipidemia)? yes ❍ no ❍

Total cholesterol: .....(p≥200 mg/dl) **LDL**: ..... (p≥120 mg/dl) **TG**: .....(p≥200mg/dl)

6. Do you take **statins** or other drugs to lower cholesterol? yes ❍ no ❍ - for how long? ..... years
7. Do you have **high blood sugar** (diabetes mellitus)? yes ❍ no ❍
8. Do you have **high blood pressure** (hypertension)? yes ❍ no ❍
9. Do you take **beta blockers** to lower blood pressure? yes ❍ no ❍ - for how long? ..... years
10. Have you had a **heart attack** (myocardial infarction)? yes ❍ no ❍, If yes, please bring the report with you.
11. Do you have **stents** that keep the heart vessels open? yes ❍ no ❍, If yes, please bring the report with you.
12. Have you had **widening of a vessel** with a catheter? yes ❍ no ❍, If yes, please bring the report with you.
13. Do you have any cardiac **bypasses**? yes ❍ no ❍, If yes, please bring the report with you.
14. Have you had an **electrocardiogram** (ECG)? yes ❍ no ❍, If yes, please bring the report with you.
15. Have you had an **exercise (treadmill) ECG**? yes ❍ no ❍, If yes, please bring the report with you.
16. Have you had an **echocardiogram**? yes ❍ no ❍, If yes, please bring the report with you.
17. Have you had a **stress echocardiogram**? yes ❍ no ❍, If yes, please bring the report with you.
18. Have you had **myocardial scintigraphy**? yes ❍ no ❍, If yes, please bring the report with you.
19. Have you had a **cardiac catheter examination**? yes ❍ no ❍, If yes, please bring the report(s) with you.
20. Have you had a **CT scan/MRI** of the heart? yes ❍ no ❍, If yes, please bring the reports with you.
21. Which **medications** are you taking? Please list, **with doses**:

- .....
- .....
- .....
- .....
- .....
- .....

Fig. 6.2 Example of a medical history questionnaire that is also sent out to the patient prior to the examination. This questionnaire elicits information about the patient's entire cardiovascular medical history and is very valuable for diagnostic procedures in the outpatient setting

Patients should know that lower heart rates (<60 beats per min) are associated with longer cardiac rest periods and thus improve image quality and diagnostic accuracy while they also help to reduce radiation dose. Informing them about the entire procedure prevents inadvertent reactions to unexpected events that might increase their heart rate. Hence, patients should be informed that they might experience a sensation of warmth when the contrast medium is injected and should also be told beforehand about the expected duration and number of breath-hold periods. Patients who are aware that the target structures are just a few millimeters in size will better understand that any motion during the breath-hold periods may severely degrade the images and may even result in a nondiagnostic scan. They also need to be informed that they should hold their breath after submaximal inspiration (ca. 75% of maximum inspiration), a maneuver that should be taught either prior to the examination or during scanning as part of the training related to the breath-hold commands (Chap. 8). The submaximum depth of inspiration is important, because maximal inspiration may increase intrathoracic pressure (Valsalva maneuver) and reduce inflow of the contrast medium.

The length of the breath-hold periods varies between 3 and 30 s, depending on the scanner used and the examination performed (Chap. 2). Breath-hold training on the scanner table is therefore also important to determine whether a patient is able to hold his or her breath for the required duration, or whether oxygen administration is needed to improve compliance. Preoxygenation is rarely required when the examination is performed on a 64-row CT scanner, with scan times of only 8–12 s. Using wide-volume scanning (320-rows) or fast prospective spiral acquisitions with second-generation dual-source CT, the scanning time is greatly reduced to just a single heart beat and breath-hold time is about 3–5 s (Chap. 2).

6.3 Contraindications

When informing the patient about cardiac CT, the examiner should make sure that the patient is in sinus rhythm. This assessment is most easily accomplished by feeling the radial pulse when meeting the patient. In the case of patients with atrial fibrillation or frequent extrasystoles (at least one or two within the expected scanning period), the per-patient diagnostic accuracy is still unsatisfactory; for this reason, it is advisable that the examination be performed at a later time, for example after medical or electrical cardioversion.

At the same time, the patient should also be questioned about general contraindications to contrast agents (**List 6.1**), as well as contraindications to nitroglycerin (**List 6.2**) and beta blockers (**List 6.3**). The considerable radiation exposure involved precludes coronary CT angiography in young and pregnant women. It is usually safe to administer nitroglycerin and/or beta blockers for the CT scan to patients who are taking these two medications on a regular basis without problems. Whether CT can be performed without nitroglycerin and/or beta blocker administration in patients with contraindications must be decided on an individual basis and depends on the clinical question and the patient's heart rate. It is generally desirable to administer nitroglycerin because of the beneficial vasodilatory effect. The CT scan should be postponed by at least 24 h in patients who have taken phosphodiesterase inhibitors (**List 6.2**).

List 6.1. Contraindications to iodinated contrast agents

1. Renal insufficiency (creatinine level >1.5–2.0 mg/dl, absolute contraindication unless evidence-based measures to prevent contrast-induced nephropathy can be taken)
2. Intake of metformin-containing medications (metformin needs to be discontinued for 48 h after contrast injection)[a]
3. Prior allergic reactions to iodinated contrast agents (switching to a different contrast agent and antiallergic premedication may enable imaging in those patients)
4. Manifest hyperthyroidism

[a] In patients with abnormal renal function, metformin also needs to be discontinued for 48 h prior to elective examinations, according to the ESUR guideline.

List 6.2. Contraindications to nitroglycerin

1. Intake of phosphodiesterase inhibitors (such as sildenafil, tadalafil, and vardenafil)
2. Arterial hypotension (systolic blood pressure below 100 mmHg)
3. Severe aortic stenosis
4. Hypertrophic obstructive cardiomyopathy
5. Nitroglycerin intolerance (e.g., severe headache)

List 6.3. Contraindications to beta blockers

1. Severe asthma
2. Severe obstructive lung disease
3. Bradycardia (below 50 beats per min)
4. Second or third degree atrioventricular block
5. Beta blocker intolerance (e.g., psoriasis)

Recommended Reading

Achenbach S (2006) Computed tomography coronary angiography. J Am Coll Cardiol 48:1919–1928

Achenbach S, Rost C, Ropers D, Pflederer T, von Erffa J, Daniel WG (2007) Non-invasive coronary angiography: current status and perspectives. Dtsch Med Wochenschr 132:750–756

Dewey M, Hamm B (2007) CT coronary angiography: examination technique, clinical results, and outlook on future developments. Fortschr Röntgenstr 179:246–260

Dewey M, Hoffmann H, Hamm B (2006) Multislice CT coronary angiography: effect of sublingual nitroglycerine on the diameter of coronary arteries. Fortschr Röntgenstr 178:600–604

Einstein AJ, Henzlova MJ, Rajagopalan S (2007) Estimating risk of cancer associated with radiation exposure from 64-slice computed tomography coronary angiography. JAMA 298:317–323

Hoffmann U, Ferencik M, Cury RC, Pena AJ (2006) Coronary CT angiography. J Nucl Med 47:797–806

Mahabadi AA, Achenbach S, Burgstahler C, Dill T, Fischbach R, Knez A, Moshage W, Richartz BM, Ropers D, Schröder S, Silber S, Möhlenkamp S, Working Group "Cardiac CT" of the German Cardiac Society (2010) Safety, efficacy, and indications of beta-adrenergic receptor blockade to reduce heart rate prior to coronary CT angiography. Radiology 257(3):614–623

Maurer M, Maurer MH, Zimmermann E, Schlattmann P, Germershausen C, Hamm B, Dewey M (2012) Indications, imaging technique, and reading of cardiac computed tomography: survey of clinical practice. Eur Radiol 22:59–72

Pannu HK, Alvarez W Jr, Fishman EK (2006) Beta-blockers for cardiac CT: a primer for the radiologist. AJR Am J Roentgenol 186:S341–S345

Schoepf UJ, Zwerner PL, Savino G, Herzog C, Kerl JM, Costello P (2007) Coronary CT angiography. Radiology 244:48–63

Schönenberger E, Schnapauff D, Teige F, Laule M, Hamm B, Dewey M (2007) Patient acceptance of noninvasive and invasive coronary angiography. PLoS ONE 2:e246

Schuetz GM, Zacharopoulou NM, Schlattmann P, Dewey M (2010) Meta-analysis: noninvasive coronary angiography using computed tomography versus magnetic resonance imaging. Ann Intern Med 152:167–177

Weigold WG (2006) Coronary CT angiography: insights into patient preparation and scanning. Tech Vasc Interv Radiol 9:205–209

Further Recommended Websites

The ESUR guideline on contrast media can be accessed at: http://www.esur.org/esur-guidelines/contrast-media-70/

Physics Background and Radiation Exposure

J. Geleijns and M. Dewey

Abstract

This chapter outlines the physical background of cardiac CT and different scanning approaches including aspects of radiation exposure. Several measures are instrumental for reducing radiation exposure from cardiac CT: prospective ECG triggering of acquisitions, short scan lengths, reduction of tube voltage as much as feasible, and individual adjustment of tube current to each patient. Raw-data-based iterative reconstruction has potential to improve image quality, which can be used to reduce radiation output.

7.1 Physics of CT

The mathematical principle underlying computed tomography (CT) was formulated by the Austrian mathematician Johann Radon in 1917. The inverse Radon transform can be used to calculate tomographic reconstructions from line integrals of the attenuation of X-rays. In CT, the Radon transform is often visualized as a sinogram. The sinogram represents the raw data space of a CT scan. It took until the early 1970s before Allan Cormack and Sir Godfrey Hounsfield were able to generate the first 2D reconstructions of a human brain in preclinical laboratory experiments. This lead to the clinical introduction of CT in 1974 with the installation of 60 head scanners. Allan Cormack and Sir Godfrey Hounsfield shared the Nobel Prize in Physiology or Medicine in 1979 for their pioneering work in the development of CT.

The first CT scanners were manufactured exclusively for CT examinations of the brain (**Fig. 7.1**) since the bore was too small to fit the trunk of an adult patient. An impressive milestone for the development of cardiac imaging of the heart was reported by Harell and his research group as early as June 1976. They used a new whole-body CT scanner and a rotation time of 6 s to perform what they termed "stop-action computed tomography." Their total scan time of 18 s consisted of two 6-s rotations separated by 6 s, allowing imaging of the heart within one breath-hold. The resulting 12-s data acquisition included 13% heartbeats. By simultaneously recording the raw data and the ECG, combined with a sophisticated reconstruction technique, they were able to reconstruct images corresponding to any phase of the

M. Dewey, *Cardiac CT*,
DOI 10.1007/978-3-642-41883-9_7,

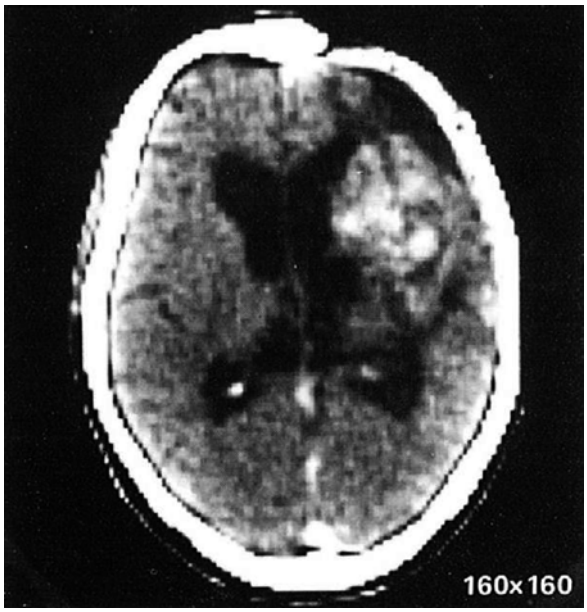

Fig. 7.1 Early brain image from a CT head scanner. Reconstruction performed on a 160^2 matrix

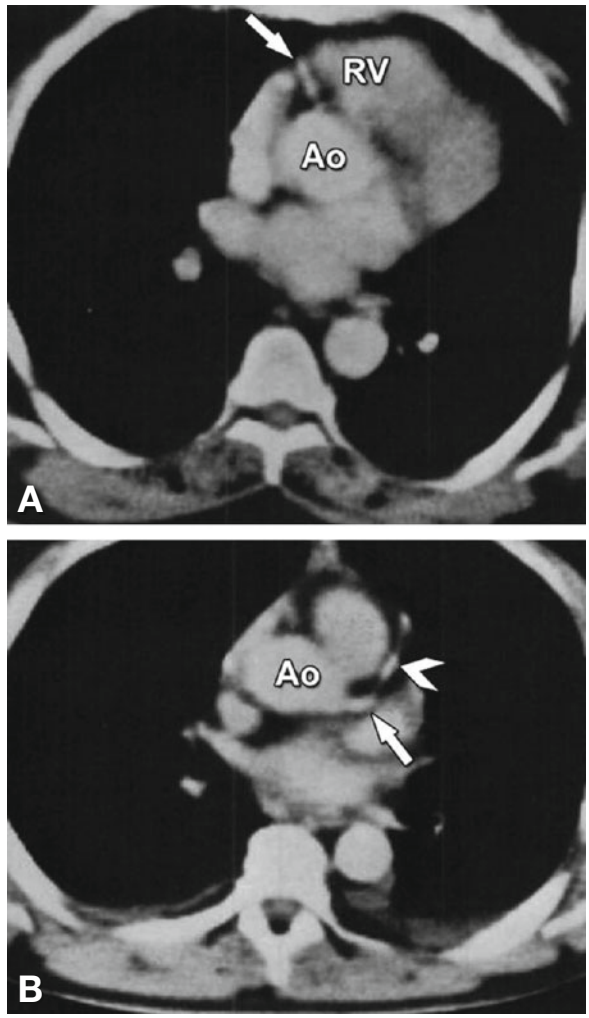

Fig. 7.2 First images of coronary CTA. (**Panel A**) shows the proximal right coronary artery (*arrow*) and (**Panel B**) the left main (*arrow*) and left anterior descending coronary artery in another patient (*arrowhead*). *Ao* aorta, *RV* right ventricle (With permission from Guthaner et al. *AJR* 1979 (American Roentgen Ray Society))

cardiac cycle with a temporal resolution of 250 ms. However, a serious limitation of the technique developed by Harell was that they could only reconstruct images of a single plane of the heart. The same research group presented their first results on coronary CT angiography (CTA) in 1979 (**Fig.** 7.2). The basic principles of their reconstruction technique and particularly their method of obtaining a short snapshot of the heart are still applied today in what is now known as multisegment reconstruction.

It took about 25 years of research and development after Harell's initial experiment to develop CT scanners suitable for routine cardiac imaging. Good in-plane spatial resolution and good low-contrast resolution were already accomplished with the single detector row CT axial scanners available in 1976. Volume acquisitions became feasible with the introduction of helical single-row CT in 1989, and a small slice thickness of about 1 mm was available as early as 1981. However, it took the introduction of helical 4-row CT scanners with rotation times below 1 s in 1998 to combine small slice thickness and sufficient volume coverage within one breath-hold. With the 4-row CT scanners it became possible for the first time to assess cardiac function and coronary arteries in a clinical setting. Further developments leading to 16- and 64-row CT scanners provided considerable improvements in image quality (Chap. 2). Even more sophisticated performance in cardiac CT is offered by recent achievements, such as second-generation dual-source CT (Somatom Definition Flash, Siemens;

Table 7.1 Attenuation values of different tissues and materials

Substance	Hounsfield unit (HU)	Range of HUs
Compact bone	+1,000	(+300 to +2,500)
Contrast-enhanced blood[a]	+400	(+200 to +600)
Calcified plaque	+400	(+130 to +1,000)
Noncalcified fibrotic plaque	+80	(+30 to +130
Noncalcified lipid plaque	+10	(−40 to +40)
Liver	+60	(+50 to +70)
Blood	+55	(+50 to +60)
Kidneys	+30	(+20 to +40)
Muscle	+25	(+10 to +40)
Brain, gray matter	+35	(+30 to +40)
Brain, white matter	+25	(+20 to +30)
Water	0	
Fat	−90	(−100 to −80)
Lung	−750	(−950 to −600)
Air	−1,000	

[a]Enhanced aorta, ventricle or coronary artery

Chap. 9b) and volumetric second-generation cone-beam CT (Aquilion ONE, Toshiba; Chap. 9a).

CT images are typically reconstructed using a 512 × 512 axial image matrix. The numerical value assigned to each pixel represents the average linear X-ray attenuation coefficient of the tissues within the associated voxel relative to the attenuation coefficient of water, and are given in Hounsfield units, see **Table 7.1**. The Hounsfield unit for a voxel that contains different tissues expresses the average attenuation within the voxel; this averaging is referred to as the partial volume effect.

The basic acquisition parameters for a CT scan are the number of active detector rows, slice thickness (mm), X-ray tube rotation time (s), tube current (mA), and tube voltage (kV). In axial scans, the table translation between axial acquisitions is referred to as the table increment, in helical CT the pitch factor defines the table increment per rotation. These parameters must be optimized to achieve contradictory goals such as minimal motion artifacts, coverage within one breath-hold, good spatial resolution, good contrast resolution, and minimal radiation exposure. The parameters relevant for high-quality reconstruction in CT are the reconstruction field of view, the reconstructed slice thickness, the reconstructed slice increment, and the reconstruction filter.

7.2 Physics of Cardiac CT

Users of CT scanners aim at producing images of good diagnostic quality whilst maintaining the radiation exposure of the patient as low as reasonably achievable. In cardiac CT it is crucial to achieve excellent spatial resolution (to be able to visualize the small coronaries), excellent temporal resolution (to avoid motion-induced blurring), and short scan time (to avoid breathing artifacts). In addition, image noise should be low enough and the contrast-to-noise ratio high enough for visualization of the coronary arteries. What distinguishes cardiac CT from most other CT applications is the need for appropriate synchronization of the image reconstruction with the simultaneously recorded ECG.

7.2.1 Spatial Resolution

Spatial resolution plays an important role in coronary CTA, particularly in the visualization of distal segments with diameters down to less than 1 mm. A voxel size of about 0.5 × 0.5 × 0.5 mm or smaller in combination with an intrinsic spatial resolution (expressed as FWHM[1]) of about 0.5–0.7 mm is sufficient for coronary imaging. However, for accurate visualization of very small

[1]Physicists measure spatial resolution as the point spread function (PSF) and express the performance of CT scanners with regard to spatial resolution as the full width half maximum (FWHM) of the PSF. The FWHM defines whether or not two adjacent structures will be represented separately in the images; two structures separated by at least one FWHM can in general be distinguished from each other, two structures separated by less than one FWHM are bound to merge together in the reconstructed image.

structures, such as early atherosclerotic lesions within the coronary wall, even better spatial resolution is required but not possible with current CT scanners. Spatial resolution in the reconstructed images also depends on the reconstruction filter used; in cardiac CT for example a dedicated stent or coronary reconstruction filter. Small objects such as stents and calcifications may also be visualized inappropriately due to artifacts related to motion, partial volume effect, and beam hardening.

7.2.2 Temporal Resolution

Good temporal resolution is required in cardiac CT to guarantee that the motion of the fast moving coronary arteries does not lead to substantial artifacts. This can be achieved by hardware that allows fast data acquisition, e.g., a fast rotating gantry and/or a gantry equipped with two X-ray tubes. The rotation time of the X-ray tube should be as short as possible, but is limited by engineering since short rotation times lead to very high g-forces, up to 20–30 g, on all components mounted on the rotating gantry. Rotation times of current CT scanners are in the range of 0.27–0.35 s. Optimal temporal resolution can also be enhanced by dedicated reconstruction algorithms. CT images are generally reconstructed from one full (360°) rotation. In cardiac CT, images are reconstructed from half (180°) rotations because, according to the mathematics of CT, this yields the minimum required amount of information. **Fig. 7.3** illustrates that hundreds of views are required to reconstruct artifact-free images. Temporal resolution can be further improved by a factor of two with the incorporation of two X-ray tubes (dual-source CT). Improved temporal resolution can also be achieved by including attenuation profiles acquired during two or more heartbeats in the reconstruction. In this latter case, raw data from multiple heartbeats are combined during the reconstruction. This is referred to as a multisegment reconstruction, i.e., more than one RR interval is used for image reconstruction.

7.2.3 Tube Voltage and Tube Current

Low image noise provides better image quality. Image noise may be decreased by raising the tube current (mA), but this comes at the cost of increased patient exposure. Currently, the choice of tube current in cardiac CT acquisitions is based on clinical experience and provides a balance between low patient dose and sufficient image quality (Chap. 10). Computer simulations of the image quality of cardiac CT resulting from a lower tube current can be performed and may provide an evidence base for selection of the most appropriate tube current (**Fig. 8.11**). In addition, image quality, and the contrast-to-noise ratio, in cardiac CT may be enhanced by selecting a lower tube voltage (e.g., 100 or 80 kV), which improves the visualization of iodine. Particularly in patients with a normal or low body mass index, a lower tube voltage can be used to achieve better image quality at the same radiation exposure or to reduce the dose whilst maintaining image quality.

7.2.4 Retrospective ECG Gating and Prospective ECG Triggering

Essential in cardiac CT is synchronization of the image reconstruction with the patient's ECG and selection of the best cardiac phase. Current cardiac CT scanners only provide good image quality, without motion artifacts, when the reconstructed images correspond to the optimal rest phase of the coronary arteries. The principles of retrospective ECG-gated reconstruction and prospective ECG-triggered reconstruction are illustrated in **Fig. 7.4**.

Reconstruction based on retrospective cardiac phase selection requires helical registration of the raw data and the ECG during several complete cardiac cycles. **Figure 7.4A** shows that retrospective ECG gating allows reconstruction of the scanned volume at any cardiac phase. Effective dose can be reduced using ECG-triggered tube current modulation (**Fig. 7.4B**). **Figure 7.4C** shows that at higher heart rates, there is less opportunity to reduce the tube current during helical acquisitions.

An alternative to retrospective helical ECG-gated reconstruction is prospective axial ("step-and-shoot") acquisition (**Fig. 7.4D**). Axial scans have the advantage of reducing patient dose, but the required stitching of several volumes is prone to artifacts at the borders of the prospectively acquired slabs, especially in arrhythmic patients. Of course, prospectively acquired axial scans (step-and-shoot) do not allow assessment of cardiac

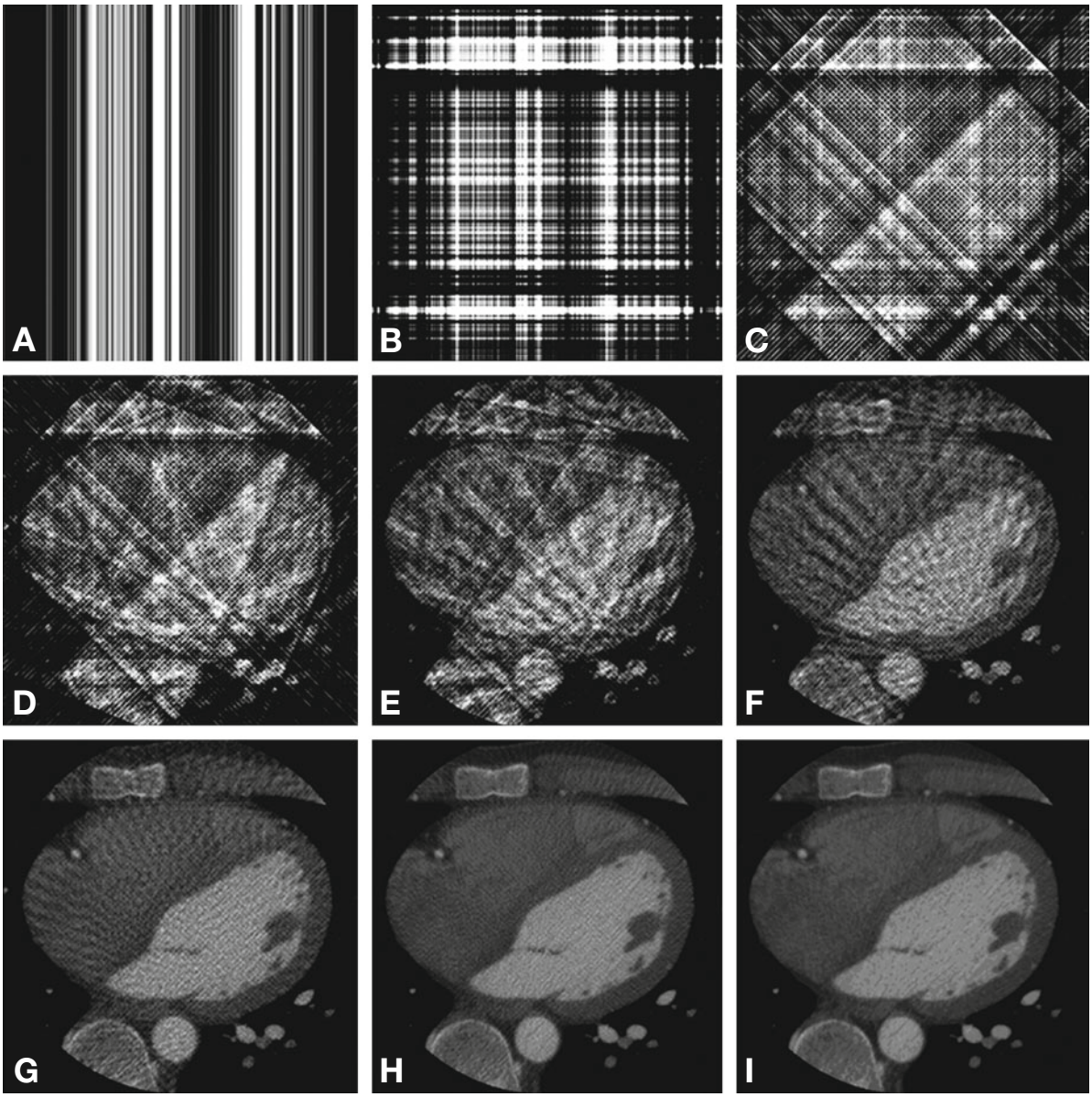

Fig. 7.3 Simulation of the effect of the number of backprojections on image quality. Reconstructed axial cardiac CT images are shown using 1, 2, 4, 8, 16, 32, 64, 128, and 1,024 backprojections in (**Panels A–I**), respectively

function since they only cover the (assumed) best cardiac phase. Also, prospective ECG triggering is preferred in patients with low and stable heart rates, in whom the center of the acquisition window is located at approximately 70–80% of the RR interval. Some CT scanners allow prospective scanning of the entire heart within a single heartbeat: a fast dual-source CT scanner is capable of performing a helical acquisition of the entire heart (Siemens Definition Flash), and a wide cone beam CT scanner performs an axial acquisition of the entire heart

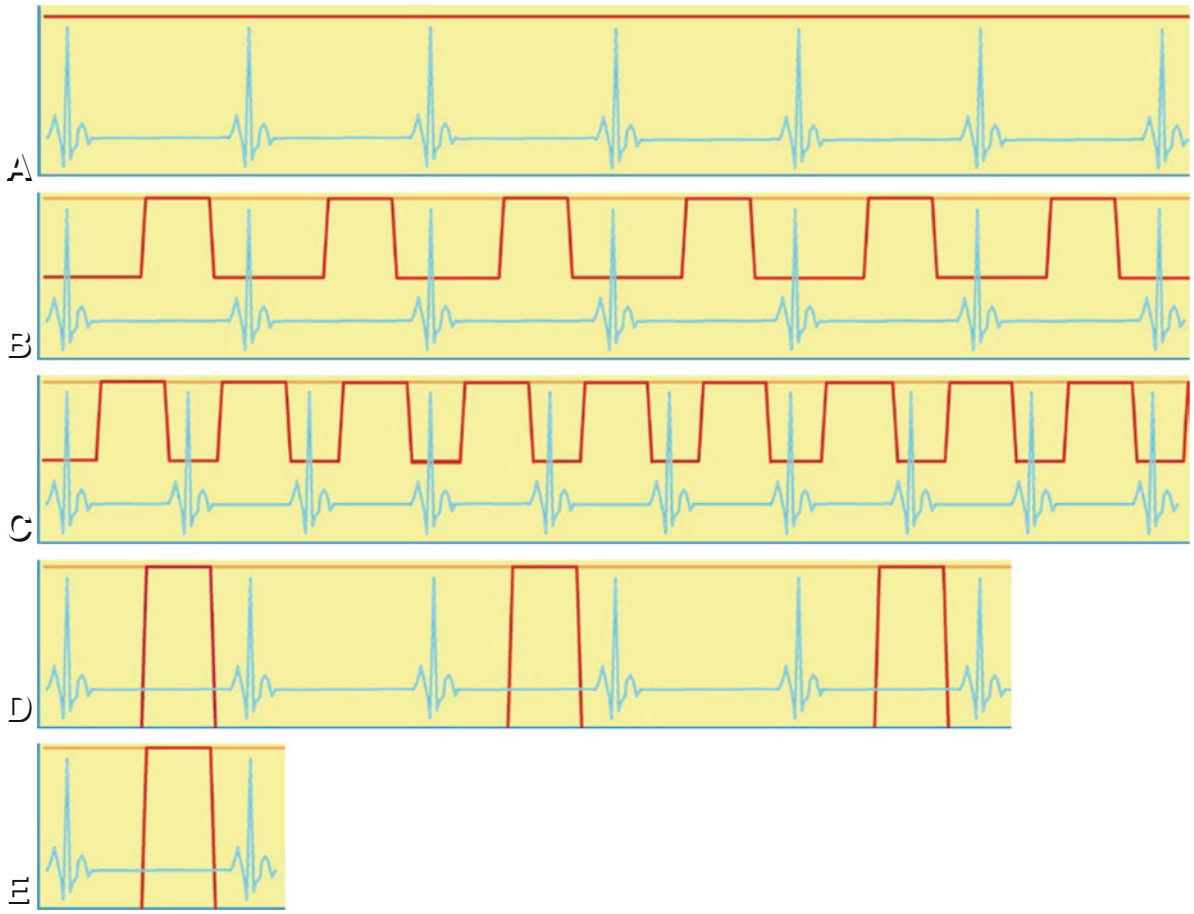

Fig. 7.4 ECG (*blue lines*) and tube current during different acquisitions (*red lines*). (**Panel A**) shows that during a retrospective helical acquisition with a 64-row CT scanner, the tube current remains constant during six RR intervals. (**Panel B**) shows how the tube current can be modulated during a helical acquisition based on the recorded ECG to achieve good image quality for assessment of the coronary arteries (where the tube current remains high, peaks of the *red line*) and at the same time sufficient image quality for assessment of cardiac function (where the tube current is reduced). (**Panel C**) shows that at a higher heart rate, there is less opportunity to reduce tube current during the helical acquisition and less opportunity to reduce patient exposure. All helical acquisitions depicted in (**Panels A**–**C**)allow assessment of cardiac function. (**Panel D**) shows how an acquisition on a 64-row CT scanner is done in five heartbeats with axial scans ("step-and-shoot") covering the entire heart with lower dose at the assumed coronary rest phase. Different axial scans are separated by at least one heartbeat to allow for translation of the patient. (**Panel E**) shows that some CT scanners allow prospective scanning of the entire heart within a single heartbeat: a fast dual-source CT scanner is capable of performing a helical acquisition of the entire heart within one heartbeat (Siemens Definition Flash), and a wide cone beam CT scanner performs an axial acquisition of the entire heart (Toshiba Aquilion ONE) within one heartbeat. Such novel "single heartbeat" techniques carry the promise of further dose reduction and image quality improvement

(Toshiba Aquilion ONE) within one heartbeat (**Fig.** 7.4E). Such novel "single heartbeat" techniques carry the promise of further dose reduction. The appearance of helical and axial scans on film that is exposed on the CT table is shown in **Fig.** 7.5.

Scans that require image acquisition during more than one cardiac cycle are inherently sensitive to arrhythmia, this is true for both retrospective and prospective acquisitions. But even CTA scans acquired within a single heartbeat are prone to artifacts caused by arrhythmia, since it is not possible to predict if the subsequent heartbeat will be stable or irregular. A volume CT scanner covering the entire heart in an axial snapshot (Aquilion ONE, Toshiba) may be more robust with regard to arrhythmia due to the lack of table movement (**Fig.** 7.6).

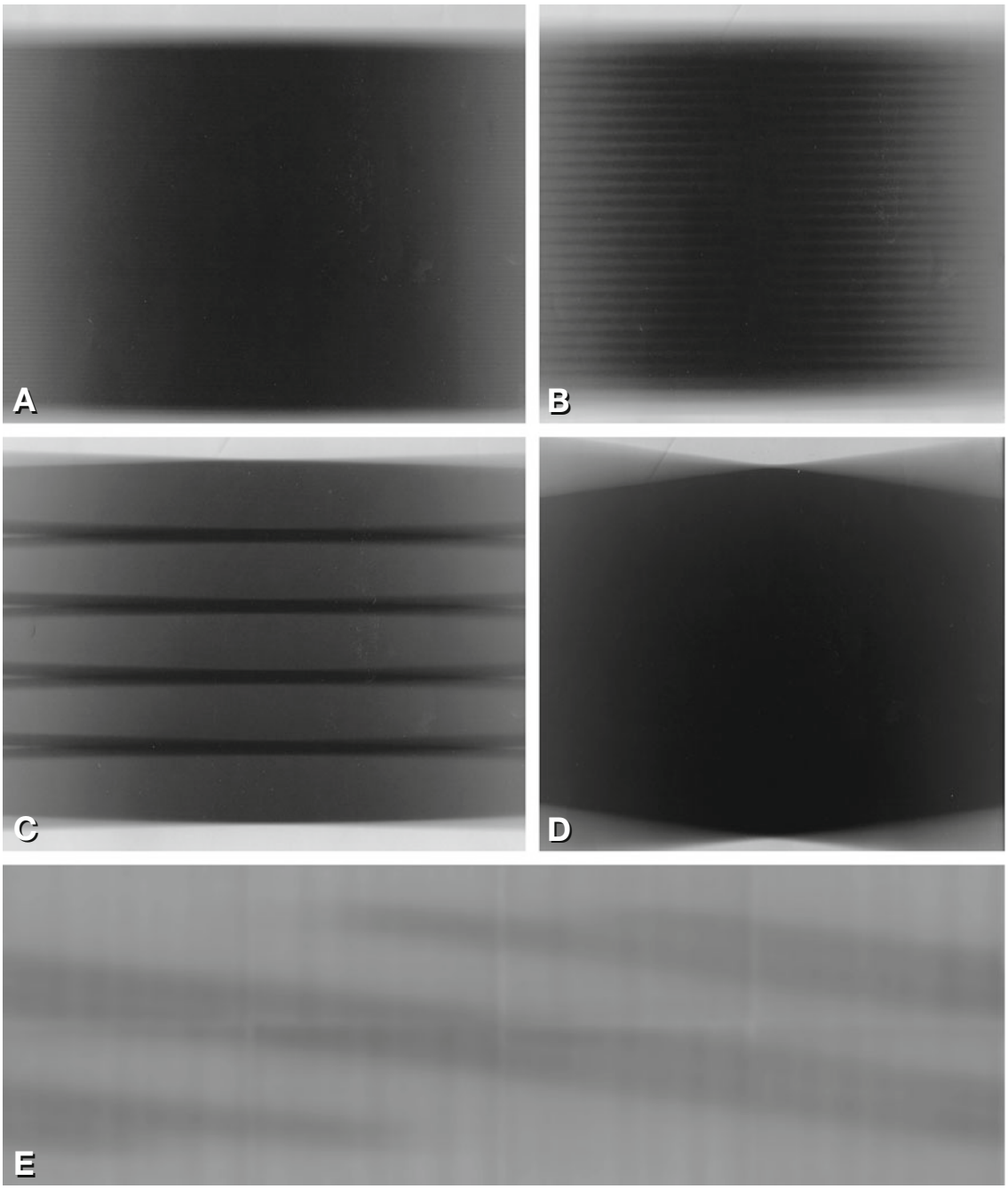

Fig. 7.5 Appearance of coronary scans covering 16 cm in the Z-axis with different collimations on films exposed on the CT table. (**Panel A**) shows a retrospectively ECG-gated helical scan performed using 16-row CT whereas (**Panel B**) shows retrospectively ECG-gated scanning using 64-row CT. There is significant overscanning visible on the films exposed using these approaches. Prospectively ECG-triggered scanning using 5 axial acquisitions in the step-and-shoot mode is shown in (**Panel C**) with the overlapping areas of the prospectively acquired slabs clearly visible. Nevertheless, there is relevant reduction of overscanning. (**Panel D**) is a representation of a single shot with volume CT using 320 simultaneous detectors. Because of the low radiation exposure of high-pitch (3.4) spiral acquisition on second-generation dual-source CT scanners, there was no visible blackening using conventional films as for (**Panels A**–**D**). Thus, for this scanner, we used a very sensitive film (GafChromic) that was circularly placed around a body phantom and gave the results shown in (**Panel E**). In this example, 16 cm were covered in the Z-axis and the resulting effective dose was below 1 mSv; however, one should note that 25 cm were radiated along the Z-axis because the adaptive dose shield is currently not fast enough to completely avoid over-ranging in high-pitch spiral scans (We are thankful to R. Juran M.Sc., U. Heimann, M.Sc., and J. Mews RT for their assistance with this figure and to T. Flohr, PhD for discussions about dual-source CT)

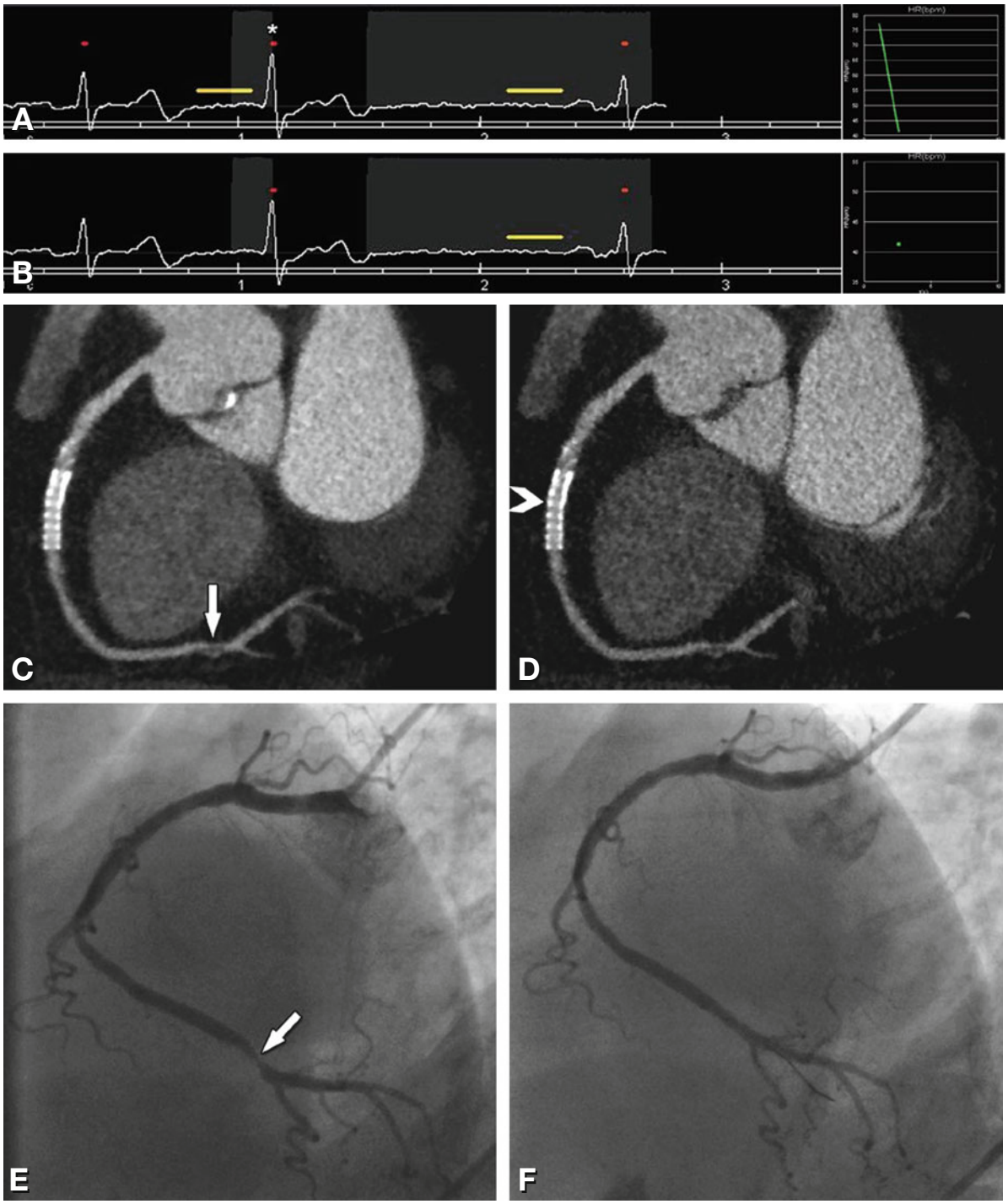

Fig. 7.6 Advantage of volume coronary CTA in arrhythmia. Example of a 66-year-old woman who had a premature atrial contraction during the heartbeat intended for volumetric scanning (*asterisk* in (**Panel A**). Scanning was immediately stopped when the arrhythmia occurred and was continued during the subsequent beat with a safety window (**Panel A**). These two beats had a rate of 77 and 41 beats per min (**Panels A** and **B**). Only the second, nonarrhythmic beat was used for reconstruction of images (**Panel B**). Reconstructions with a soft filter showed a significant (70% diameter) stenosis of segment 3 of the right coronary artery (RCA, *arrow* in **Panel B**), whereas significant in-stent restenosis of the 3.0-mm mid-RCA stent was excluded in reconstructions with a stent filter (**Panel D**). Conventional coronary angiography confirmed the significant distal RCA stenosis (*arrow* in **Panel E**), which was treated during the same interventional session (**Panel F**)

7.3 Patient Dosimetry and Radiation Exposure

7.3.1 Dosimetry

Dosimetry is used to measure the energy imparted by ionizing radiation to matter. Physicists provide the basis for radiation dosimetry with the definition of the fundamental physical quantity for radiation dosimetry, being the quantity absorbed dose (D). Absorbed dose is the quotient of the energy imparted by ionizing radiation (energy (E); unit Joule (J)) and the mass of the exposed matter (mass (m); unit kilogram (kg)). The unit of absorbed energy is Joule per kilogram (J/kg), but in radiation dosimetry absorbed dose is expressed as gray (Gy). Dose levels that occur in CT are generally much lower than 1 Gy, therefore doses are usually expressed in milligray (1 mGy = 0.001 Gy).

Dose measurements must be performed during installation, acceptance testing, and constancy testing of CT scanners. During such tests the normalized output of the scanner is generally established as the CT dose index per unit of tube charge (CTDI/Q; unit mGy/mAs). The radiation exposure of specific CT acquisition protocols is expressed either as CTDI (mGy) or as dose length product (DLP, Gy.cm). The CTDI represents the radiation output of the CT scanner during one full rotation of the X-ray tube; and the DLP represents the radiation exposure during a complete helical or axial acquisition and takes into account the total number of tube rotations during the CT scan. Both CTDI and DLP are very useful for comparing the radiation exposure of different CT acquisition protocols.

Dosimetric quantities that are most often used in the context of biomedical dose assessment are the equivalent organ dose[2] (H_T, mSv) and the effective dose (E, mSv). The effective dose is the pragmatic weighted sum of equivalent organ doses, where the tissue weighting factors (w_T) are used to take into account the relative sensitivity of organs to carcinogenic and hereditary effects. Tissue weighting factors are regularly revised on the basis of new scientific insights (**Table 7.2**). Particularly relevant for cardiac CT are the changes in the tissue weighting factor for breast tissue. It was 0.15 in 1972 and was decreased to 0.05 in 1991. Since 2007, the tissue factor breast has been 0.12 according to the most recent ICRP recommendation. As a result of this latest change, effective doses for cardiac CT calculated according to the most recent ICRP publication are generally higher compared to effective doses calculated according to the previous ICRP publication.

Table 7.2 Tissue weighting factors published by the ICRP in 1972 (ICRP publication 26), 1991 (ICRP publication 60), and 2007 (ICRP publication 103)

Organ	ICRP 26, 1972	ICRP 60, 1991	ICRP 103, 2007
Breast	0.15	0.05	0.12
Bone marrow	0.12	0.12	0.12
Lung	0.12	0.12	0.12
Colon	–	0.12	0.12
Stomach	–	0.12	0.12
Thyroid	0.03	0.05	0.04
Bone surface	0.03	0.01	0.01
Gonads	0.25	0.20	0.08
Other	0.30	0.05	0.12

7.3.2 Computed Tomography Dose Index (CTDI) and Dose Length Product (DLP)

The computed tomography dose index (CTDI, mGy) applies to one 360° rotation of the X-ray tube and is defined as the integral of the dose profile along the Z-axis divided by the nominal beam width. Measurements are performed with a 100 mm long pencil ionization chamber (**Fig. 7.7**). A derivative of the CTDI has been defined that is based on weighting of the five CTDIs measured at central and peripheral positions of the phantoms, yielding the weighted CTDI (CTDIw, mGy). The CTDIw can be conveniently applied to axial "step-and-shoot" CTA. For helical CTA acquisitions it is common practice to correct the CTDIw by dividing it by the pitch factor, yielding the volume CTDI (CTDIvol, mGy). Both the CTDIw and the CTDIvol are approximations of the average dose in a cross section of the cylindrical CT dose phantom. The dose length product (DLP, mGy.cm) is calculated by multiplying the CTDIw (axial acquisition) or CTDIvol (helical acquisition) by the actual scan range. Modern CT scanners give the weighted CTDI or volume

[2]The equivalent dose is the product of absorbed dose (D, mGy) and a radiation weighting factor (wR, mSv/mGy). The radiation weighting factor for X-rays is 1, so absorbed dose and the equivalent dose are numerically equal.

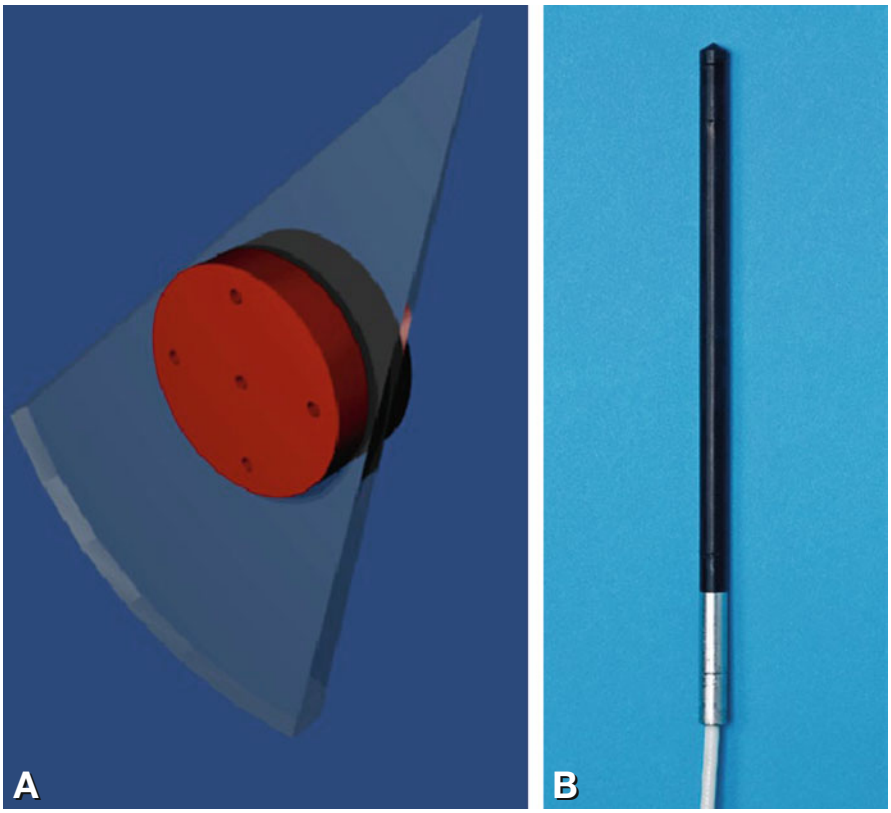

Fig. 7.7 Measurement of CTDI. (**Panel A**) shows in red the CT dose body phantom with five positions for inserting a CT ionization chamber (one in the center, four at the periphery of the phantom). (**Panel B**) shows a pencil CT ionization chamber, which was specifically developed for CT dosimetry. The length of the ionization chamber is 100 mm

CTDI and DLP on the scanner console for each acquisition. Generally these dose values are also stored in, and can be retrieved from, the DICOM header of the CT examination.

7.3.3 Organ and Tissue Doses

Organ doses cannot be measured directly during clinical CT examinations. An exception is the entrance skin dose, which can be measured with small dosimeters that can be attached safely to the skin. Particularly relevant in cardiac CT is the assessment of the exposure of organs such as breast, lung, liver, esophagus, and stomach. There is software available for calculating organ doses incurred during a CT scan. An example is the generic ImPACT CT Patient Dosimetry Calculator (ImPACT, http://www.impactscan.org/ctdosimetry.htm). These software applications do not require special user skills, it is sufficient to specify the scanned range, the type of CT scanner, and some basic acquisition parameters such as tube voltage, tube current, rotation time, pitch (helical) or table increment (axial), slice thickness, and number of active detector rows. These generic computer applications are suitable for solving most clinical dosimetric questions in CT (**Fig. 7.8**). A disadvantage is that they may not be updated for new types of scanners, only provide dose estimations for standard sized patients (adults), and do not integrate tube current modulation schemes in their dose calculation.

Figure 7.9 shows the contours of a virtual patient model (MIRD phantom) represented as a voxel phantom that can be used for Monte Carlo computer simulations, which are more accurate than generic software calculations. Accurate organ doses can easily be estimated from the calculated dose distribution of these more sophisticated models. Rough estimates of organ doses resulting from cardiac CT in average-sized patients are presented in **Table 7.3**. Clearly, female breast tissue and lung tissue receive the highest doses. Organs in the upper abdomen are also exposed to substantial levels of radiation, and exposure is usually highest for retrospective helical

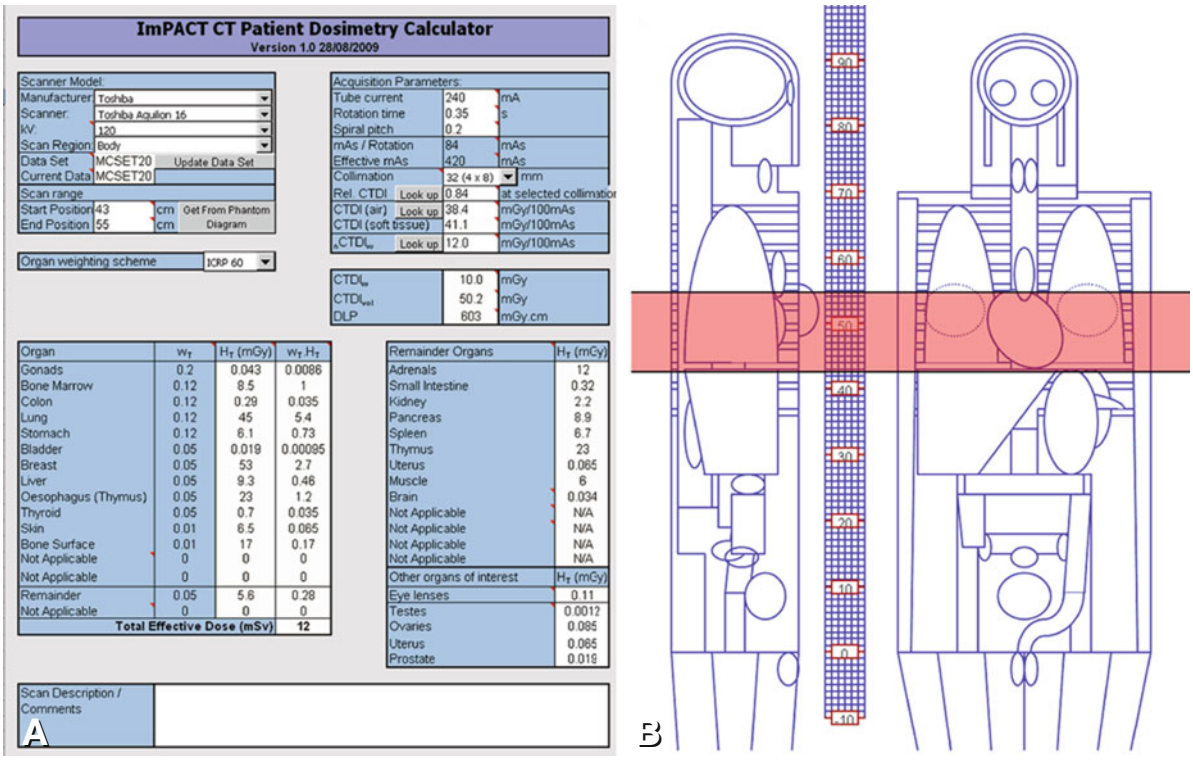

Fig. 7.8 Two screenshots of the ImPACT CT Patient Dosimetry Calculator (http://www.impactscan.org/ctdosimetry.htm). (**Panel A**) shows the worksheet for entering the scan details, in this example a retrospectively ECG-gated helical cardiac CT, and the dosimetric results, equivalent organ dose, and effective dose. (**Panel B**) shows a drawing of the patient model with the scan range in *red*

acquisitions. A modest dose reduction in helical CT can be achieved using tube current modulation. Substantial dose reduction can be achieved with prospectively triggered axial acquisitions; these can be performed either in one single acquisition if the X-ray beam width covers the entire heart (volumetric or fast dual-source CT) or in two to five shots for scanners that cover part of the heart. Clinical studies are necessary to identify the clinical indications for which ultra-low-dose protocols are best used.

7.3.4 Effective Dose

The most pragmatic approach for calculating effective dose is to record the DLP and to multiply this value with a conversion factor. This conversion factor expresses the effective dose (mSv) per unit of dose length product (mGy.cm). Such conversion factors have been published for CT scans of different parts of the body. For general chest CT (120 kV, entire chest CT scan) conversion factors in the range of 0.014–0.017 mSv/mGy.cm have been published (effective dose according to ICRP 60). These conversion factors are also frequently used for calculating effective dose for cardiac CT but may not be the most accurate choice here. More appropriate for typical cardiac CT scans (120 kV, 120–140 mm range) are conversion factors of about 0.020 mSv/mGy.cm (according to ICRP 60) and 0.030 mSv/mGy.cm (according to ICRP 103). Even more accurate estimates of the effective dose for patients undergoing coronary CTA can be derived from the generic software applications, which take into account the actually exposed range (see Sect. 7.3.3).

Table 7.4 provides typical effective dose values for chest and cardiac imaging. The effective dose values clearly show that radiation exposure from chest radiography is negligible compared to nuclear medicine, conventional coronary angiography, and CT. There is also a trend towards lower effective doses in cardiac CT, from up to 20 mSv for retrospective acquisitions to less than 2 mSv for ultra-low-dose protocols. The order of magnitude of the effective dose for established cardiac imaging tests such as SPECT, PET, and conventional coronary angiography is about 8 mSv.

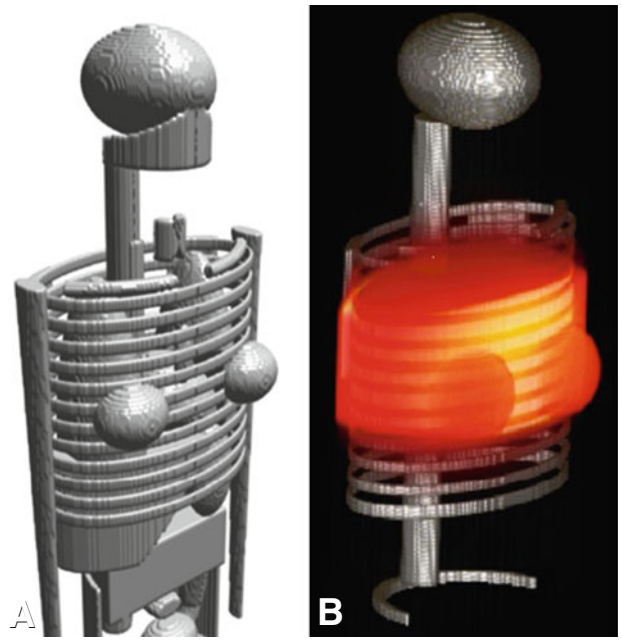

Fig. 7.9 Organ doses and effective dose are often derived from computer simulations. (**Panel A**) shows the contours of some organs of a virtual, average-sized patient (phantom). (**Panel B**) shows the dose distribution (colors) in this virtual patient; the dose distribution is calculated for a single-shot cardiac acquisition using a 320-row CT scanner. Note the lighter the color, the higher the absorbed dose; the contours of the skeleton are shown in *gray* in (**Panel B**)

Table 7.3 Typical equivalent organ doses (mGy) for different acquisition techniques

	Equivalent organ dose, mGy			
	Retrospectively ECG-gated reconstruction, no tube current modulation'	Retrospectively ECG-gated reconstruction with tube current modulation[a]	Prospectively ECG-triggered axial acquisition	Ultra-low-dose technique (volumetric CT, dual source CT)
Breast	40	32	10	5
Lung	35	28	9	5
Liver	30	24	8	4
Esophagus	25	20	7	3
Stomach	25	20	7	3
Bone surface	20	16	5	3
Red bone marrow	15	12	4	2
Skin	5	4	1	0.7
Colon	1.5	1	0.4	0.2
Bladder	0.1	0.1	0.03	0.01
Ovaries	0.1	0.08	0.03	0.01
Testes	0.01	0.008	0.003	0.001

Note that only retrospectively ECG-gated acquisition allows assessment of cardiac function in addition to coronary CTA

Table 7.4 Typical exposure values according to ICRP 60

Chest radiography	
PA chest radiograph	0.02 (0.01–0.04) mSv
LAT chest radiograph	0.04 (0.02–0.0S) mSv
SPECT, myocardial perfusion	
Rest; technetium Tc-99m tetrofosmin, 500 MBq	3.S mSv
Stress; technetium Tc-99m tetrofosmin, 500 MBq	3.5 mSv
PET, myocardial viability	
ISF-Fluorodeoxyglucose (FDG), 400 MBq	7.6 mSv
Conventional coronary angiography	
Diagnostic catheterization	S.0 (4.0–16) mSv
Percutaneous coronary intervention	12.0 (S.0–20) mSv
Cardiac CT	
CT radiography, planscan	0.05 (0.02–0.10) mSv
Bolus tracking	0.15 (0.10–0.20) mSv
Calcium scoring	2.0 (1.0–2.0) mSv
Coronary CTA	
Retrospectively ECG-gated reconstruction, no tube current modulation	15.0 (10.0–20.0) mSv
Retrospectively ECG-gated reconstruction, ECG-triggered tube current modulation	12.0 (5.0–15.0) mSv
Prospectively ECG-triggered axial acquisition	4.0 (2.0–S.0) mSv
Ultra-low-dose (volumetric CT, fast dual-source CT)	<2.0 mSv

SPECT single photon emission computed tomography, *PET* positron emission tomography

Recommended Reading

Achenbach S, Marwan M, Ropers D et al (2010) Coronary computed tomography angiography with a consistent dose below 1 mSv using prospectively electrocardiogram-triggered high-pitch spiral acquisition. Eur Heart J 31:340–346

Buzug TM (2008) Computed tomography: from photon statistics to modern cone-beam CT. Springer, Berlin

Cody DD, Mahesh M (2007) AAPM/RSNA physics tutorial for residents: technologic advances in multidetector CT with a focus on cardiac imaging. Radiographics 27:1829–1837

Dewey M, Zimmermann E, Deissenrieder F et al (2009) Noninvasive coronary angiography by 320-row CT with lower radiation exposure and maintained diagnostic accuracy: comparison of results with cardiac catheterization in a head-to-head pilot investigation. Circulation 120:867–875

Dirksen MS, Bax JJ, de Roos A et al (2002) Usefulness of dynamic multislice computed tomography of left ventricular function in unstable angina pectoris and comparison with echocardiography. Am J Cardiol 90:1157–1160

Earls JP, Berman EL, Urban BA et al (2008) Prospectively gated transverse coronary CT angiography versus retrospectively gated helical technique: improved image quality and reduced radiation dose. Radiology 246:742–753

Geleijns J, Joemai RM, Dewey M, de Roos A, Zankl M, Cantera AC, Artells MS (2011) Radiation exposure to patients in a multicenter coronary angiography trial (CORE 64). AJR Am J Roentgenol 196(5):1126–1132

Guthaner DF, Wexler L, Harell G (1979) CT demonstration of cardiac structures. AJR Am J Roentgenol 133:75–81

Harell GS, Guthaner DF, Breiman RS et al (1977) Stop-action cardiac computed tomography. Radiology 123:515–517

Hsieh J (2002) Computed tomography: principles, design, artifacts, and recent advances, vol PM114. SPIE Press Monograph, Bellingham

Kak AC, Slaney M (1988) Principles of computerized tomographic imaging. IEEE Press, New York. Free PDF at http://www.slaney.org/pct/

Kalender W (2005) Computed tomography: fundamentals, system technology, image quality, applications. Publicis Corporate Publishing, Erlangen

Kobayashi Y, Lardo AC, Nakajima Y, Lima JA, George RT (2009) Left ventricular function, myocardial perfusion and viability. Cardiol Clin 27:645–654

Kroft LJ, de Roos A, Geleijns J (2007) Artifacts in ECG-synchronized MDCT coronary angiography. AJR Am J Roentgenol 189: 581–591

Lell M, Marwan M, Schepis T et al (2009) Prospectively ECG-triggered high-pitch spiral acquisition for coronary CT angiography using dual source CT: technique and initial experience. Eur Radiol 19:2576–2583

McNitt-Gray MF (2002) AAPM/RSNA physics tutorial for residents: topics in CT. Radiation dose in CT. Radiographics 22(6):1541–1553

Nieman K, Oudkerk M, Rensing BJ et al (2001) Coronary angiography with multi-slice computed tomography. Lancet 357:599–603

Rybicki FJ, Otero HJ, Steigner ML et al (2008) Initial evaluation of coronary images from 320-detector row computed tomography. Int J Cardiovasc Imaging 24:535–546

Valentin J (ed) (2007a) Annals of the ICRP, Publication 102. Managing patient dose in multi-detector computed tomography (MDCT). Oxford, UK

Valentin J (ed) (2007b) Annals of the ICRP, Publication 103. The 2007 recommendations of the international commission on radiological protection. Oxford, UK

Examination and Reconstruction

M. Dewey

Abstract

In this chapter, the examination- and reconstruction-related procedures are described. The preparation of patients with nitroglycerin as well as with oral and/or intravenous beta blockers is explained. How to avoid pitfalls during scanning and reconstruction is the final part of this chapter.

8.1 Examination

The CT examination should be performed in a calm and comfortable atmosphere (e.g., lights should be dimmed, and the staff should speak quietly), avoiding anything that might affect the patient's heart rate, because a constant rate is crucial for image quality and diagnostic accuracy in coronary CT angiography. Patients should likewise avoid anything that can increase their heart rate, such as talking during the scan or moving too much. The steps involved in cardiac CT are summarized in **List 8.1**. The entire examination procedure takes approximately 15–20 min.

List 8.1. Steps in performing cardiac CT

1. Reassure the patient that the examination will be short and uncomplicated – consider oral beta blockers
2. Place the patient in a comfortable supine position
3. Place ECG electrodes to obtain good R-wave signals
4. Check heart rate and rhythm – consider injecting beta blockers
5. Plan scan range, and adjust scan and contrast agent parameters individually
6. Administer nitroglycerin sublingually
7. Provide breath-hold training
8. Repeat beta blocker injection if necessary
9. Inject the contrast agent – adjust scan delay individually
10. Perform the scan, and make sure that the patient is feeling fine afterward

M. Dewey, *Cardiac CT*,
DOI 10.1007/978-3-642-41883-9_8,

8.1.1 Calcium Scanning

Unlike coronary CT angiography, coronary calcium scanning is always performed with prospective triggering and without contrast administration (Chap. 11), typically using 3-mm slice collimation, and can help reduce radiation exposure by allowing exact determination of the scan range required for subsequent cardiac CT (from about 1 cm above to 1 cm below the coronaries). The clinical benefit of calcium scoring is not in detecting or ruling out coronary artery disease (Chap. 4), but in risk stratification of individual patients (Chap. 11). Combined coronary calcium scanning and coronary CT angiography can be easily performed, and it prolongs the examination by only 3–5 min.

However, in symptomatic patients, especially young ones, with low-to-intermediate pretest likelihood of coronary artery disease, calcium scoring should not be performed alone, since angiography will demonstrate significant coronary stenoses in a considerable number of patients without coronary calcium or a low coronary calcium score. Very high calcium scores (above 600 or 1,000) are considered by some groups to preclude reliable reading of coronary CT angiography and may be used as a gatekeeper prior to noninvasive angiography. This approach, however, requires calculating or estimating the score during the examination and may reduce workflow. In our experience, neither image quality nor diagnostic accuracy is significantly reduced in patients with somewhat higher calcium scores, and patients with atypical angina pectoris and a 20–70% pretest likelihood of coronary disease only rarely have very high calcium scores. Therefore, on our 64-row scanner, we did not routinely perform calcium scanning in patients with low-to-intermediate pretest likelihood of coronary artery disease. For single heart beat imaging with the 320-row CT scanner or fast prospective spiral acquisition using dual-source CT, we now always perform coronary calcium scanning to adjust the scan range to individual heart size (Chaps. 9a and 9b). To sum up, the decision whether to perform coronary CT angiography alone or in combination with calcium scanning in symptomatic patients largely depends on the local situation and the individual patient's needs, whereas in asymptomatic intermediate-risk individuals without known cardiovascular disease, the calcium score provides incremental risk stratification.

8.1.2 Positioning and ECG

Once the patient has been placed on the table in the supine position with the arms above the head (**Fig. 8.1**), he or she should not move, in order to ensure that the planned scan region matches the region actually scanned and that the entire coronary tree is imaged (**Fig. 8.2**). Spatial resolution is highest in the center of the scan field, which is why the patient should be shifted slightly to the right side of the table, so that the heart is as close to the center as possible (**Fig. 8.1**). The ECG electrodes should be placed so that they do not disturb the patient (**Fig. 8.1**), while ensuring optimal identification of R-wave signals (**Fig. 8.3**). The optimal electrode position is as close as possible to the heart but outside the anatomic scan field (**Fig. 8.4**), in order to avoid artifacts. If the electrodes are too far away from the chest (e.g., near the biceps or deltoid muscles), involuntary muscle shivering may be superimposed on the cardiac electrical activity (**Fig. 8.5**).

8.1.3 Nitroglycerin

Sublingual nitroglycerin administration increases the diameter of the coronary arteries (**Fig. 8.6**) and therefore facilitates image interpretation and comparability of the results (percent diameter stenosis) with those of cardiac catheter examination (which is often performed with intracoronary nitroglycerin administration). The onset of action of sublingual nitroglycerin spray (**Fig. 8.7A**) is about 10–20 s after administration, and its effect lasts for about 10 min. Patients should be given two to three sprays of sublingual nitroglycerin (corresponding to a dose of about 0.8–1.2 mg). Complications of nitroglycerin administration include tachycardia and hypotension (which may cause headaches). Relevant reflex tachycardia is rare, and this unlikely event should not prevent physicians from taking advantage of the beneficial vasodilatory effect of nitroglycerin (**Fig. 8.6**).

8.1.4 Beta Blockade and I_f Channel Blockade

The heart rate can be reduced (**Fig. 8.8**) by oral administration of a beta blocker about 1 h before CT scanning (e.g., 50–150 mg atenolol, **Fig. 8.7B**), or intravenous administration of an agent with rapid onset of action and shorter duration of action (e.g., esmolol at a dose of 25–50 mg min^{-1} [0.5 mg kg^{-1} bodyweight per min], **Fig. 8.7C**; or metoprolol at 2.5–5 mg min^{-1}, **Fig. 8.7D**) with the patient on the table. All intravenous beta blockers should be injected slowly, and the examiner must wait and see how the patient reacts to the initial dose (e.g., 20–30 mg of esmolol) before determining

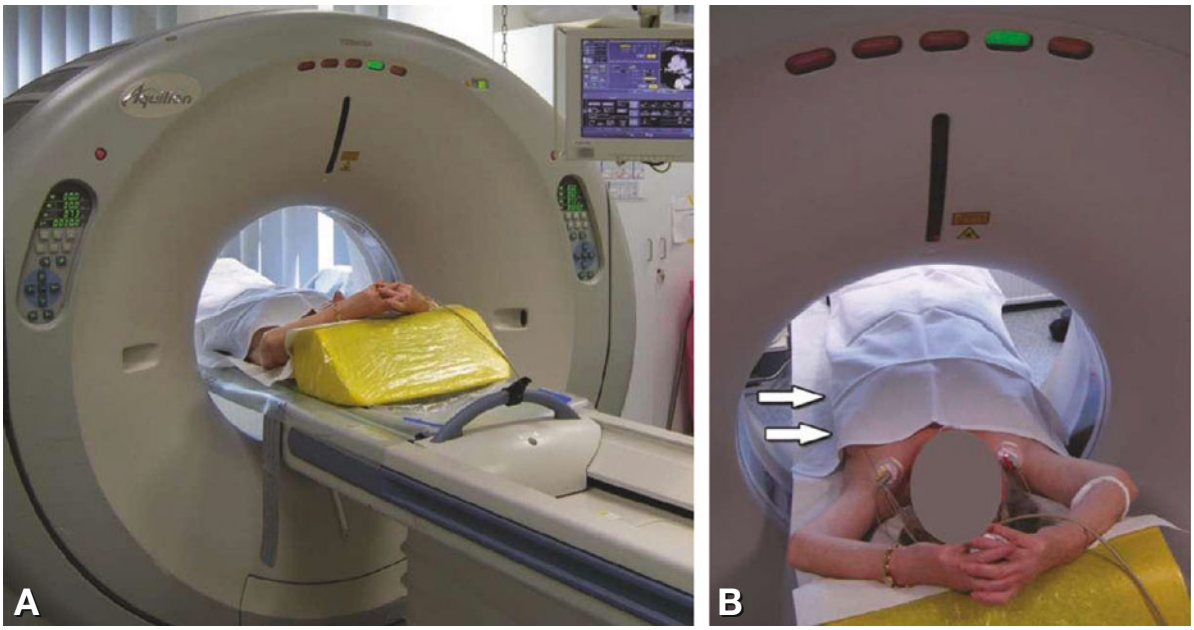

Fig. 8.1 Patient positioning for cardiac CT. Examining the patient feet-first (**Panel A**) has the advantage of providing better access to the patient than with head-first positioning. The arms are comfortably placed above the head to improve penetration of the chest by the X-rays, thereby reducing artifacts and radiation exposure. The patient is placed in an offset position, slightly to the right side of the table (*arrows*, **Panel B**), to ensure that the heart is as close as possible to the center of the scan field. ECG electrodes are attached in the area of the supraclavicular fossa after the patient has elevated his or her arms. The ECG electrodes should not be attached near the biceps or deltoid muscles, in order to minimize the effects of muscle tremor on the ECG (**Fig. 8.5**)

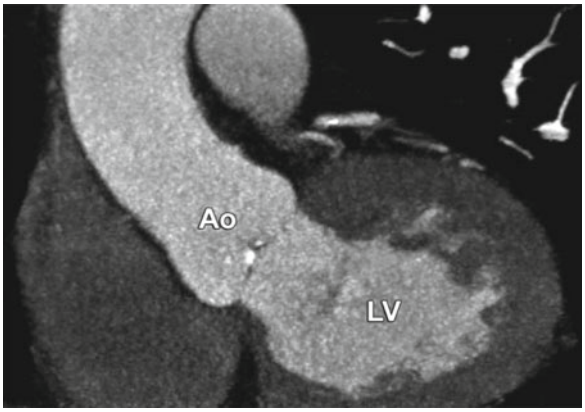

Fig. 8.2 Motion of the patient between planning of the scan and the actual scan resulted in a scan range that extended too far cranially, and therefore the caudal portions of the heart were missed. Oblique coronal maximum-intensity projection in the left ventricular outflow tract view. *Ao* aorta, *LV* left ventricle

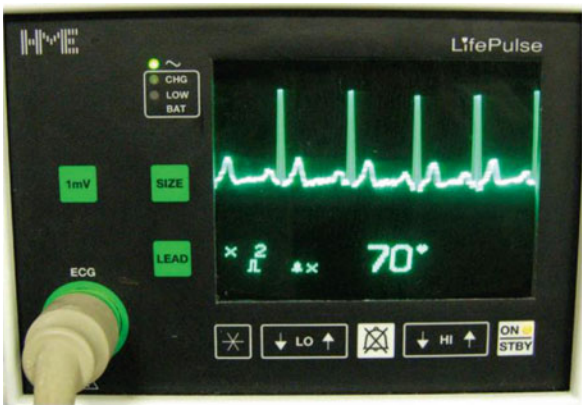

Fig. 8.3 ECG monitor with regular ECG and sufficiently high R waves for gating of the examination. However, heart rate reduction using beta blockade should be considered

the further injection protocol. The onset of action of esmolol is approximately 2–5 min, and the half-life is only 9–10 min. Therefore, a lower risk of complications such as bradycardia can be expected with intravenous beta blockade, while oral beta blockers tend to lower heart rate more effectively. Thus, beginning with oral beta blockade and adding intravenous beta blockers if needed is the most common approach to lowering the heart rate. Another important effect of beta blockers is the reduction of heart rate variability, which significantly improves image quality.

In our experience, a resting heart rate of 60 beats per min is a good threshold above which to give oral beta blockers. Up to a threshold of about 65 beats per min, good image quality can almost always be achieved and

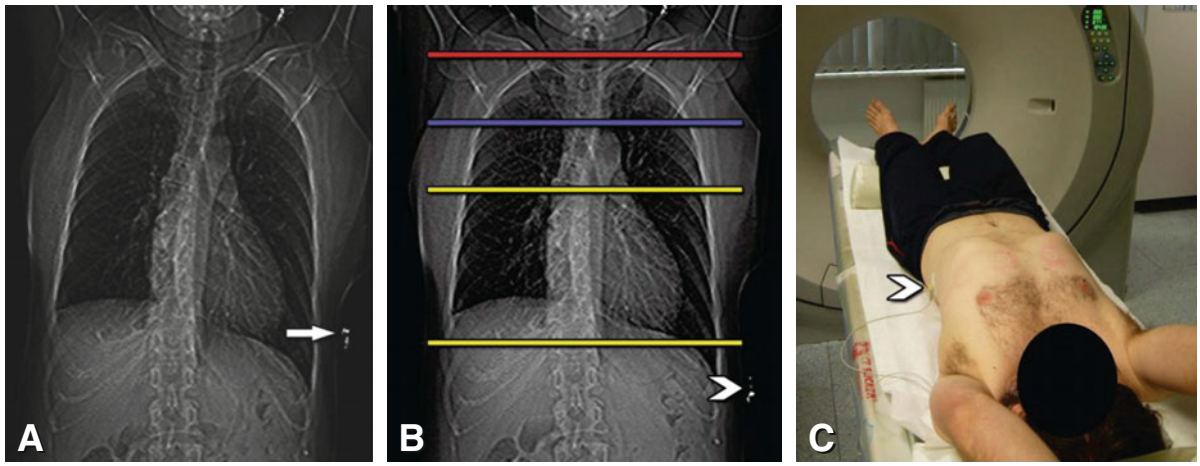

Fig. 8.4 Positioning of ECG leads and planning of the scan. A typical anterior scanogram (**Panel A**) with a too-high electrode (*arrow*) on the left side of the chest, which can lead to artifacts over the cardiac structures. Such artifacts can be easily avoided by lower placement of the electrode (*arrowhead* in **Panels B** and **C**). The typical anatomic scan range for patients with suspected or known coronary artery disease is indicated by the *yellow lines* and extends from above the left atrium to immediately below the heart (**Panel B**). Because of the high effective dose, the scan range should be as short as reasonably achievable. For imaging of venous (*blue line*) or internal mammary artery bypass grafts (*red line*), the beginning of the scan range needs to be extended (**Panel B**)

8

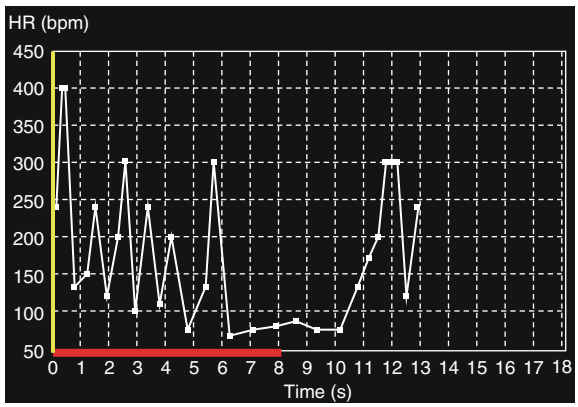

Fig. 8.5 Unconscious muscle shivering led to a highly variable (between 60 and 400 beats per min) and unreliable heart rate recording. Covering the patient with a blanket will reduce shivering, and the ECG will very likely become normal

prospective acquisitions protocols ("step-and-shoot") with reduced effective dose can be applied. In patients with heart rates of more than 80 beats per min, a combination of oral and intravenous beta blockers is very likely needed to reduce the heart rate sufficiently. A potent alternative that avoids the contraindications of beta blockers (Chap. 6) is the oral administration of ivabradine (e.g., 5 mg 1 h before CT). This drug is a selective I_f channel blocker and has been shown very effective in achieving target heart rates, either alone or in combination with beta blockers.

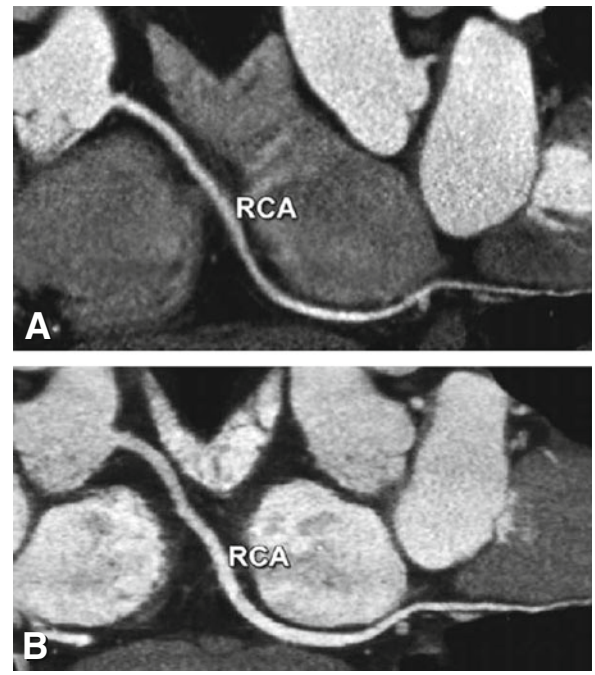

Fig. 8.6 Effect of sublingual nitroglycerin on the coronary vessel diameters. Curved multiplanar reformation of the right coronary artery (*RCA*) in a patient who underwent coronary CT angiography without (**Panel A**) and after sublingual nitroglycerin (**Panel B**). Nitroglycerin administration leads to a relevant increase in the coronary diameter (on average 12–21%), which also improves visibility of the distal vessel segments

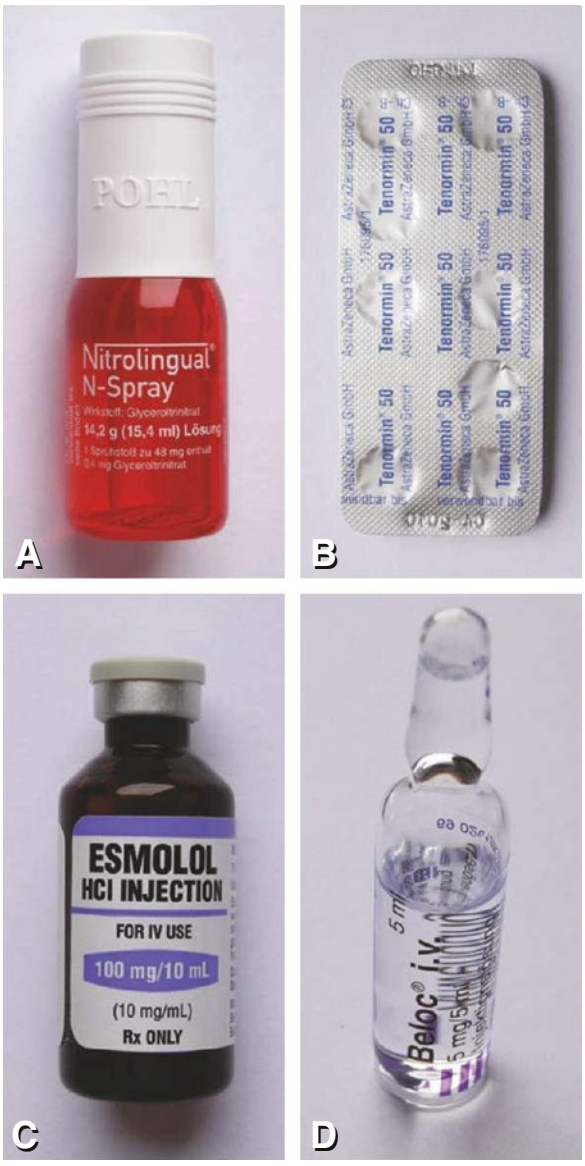

Fig. 8.7 Drugs for premedication in patients undergoing coronary CT. Sublingual nitroglycerin (**Panel A**) increases coronary vessel diameters and facilitate comparison of the findings to conventional coronary angiography. Oral (**Panel B**, metoprolol or atenolol) and/or intravenous beta blockade (**Panels C** and **D**, esmolol or metoprolol) is important to reduce heart rate in order to improve image quality and increase diagnostic accuracy as much as possible

In general, beta blockers should be administered in accordance with local practice and guidelines where applicable. Note that atropine must be available as an antidote whenever beta blockers are given. Complications of beta blockers are bradycardia, hypotension, and acute

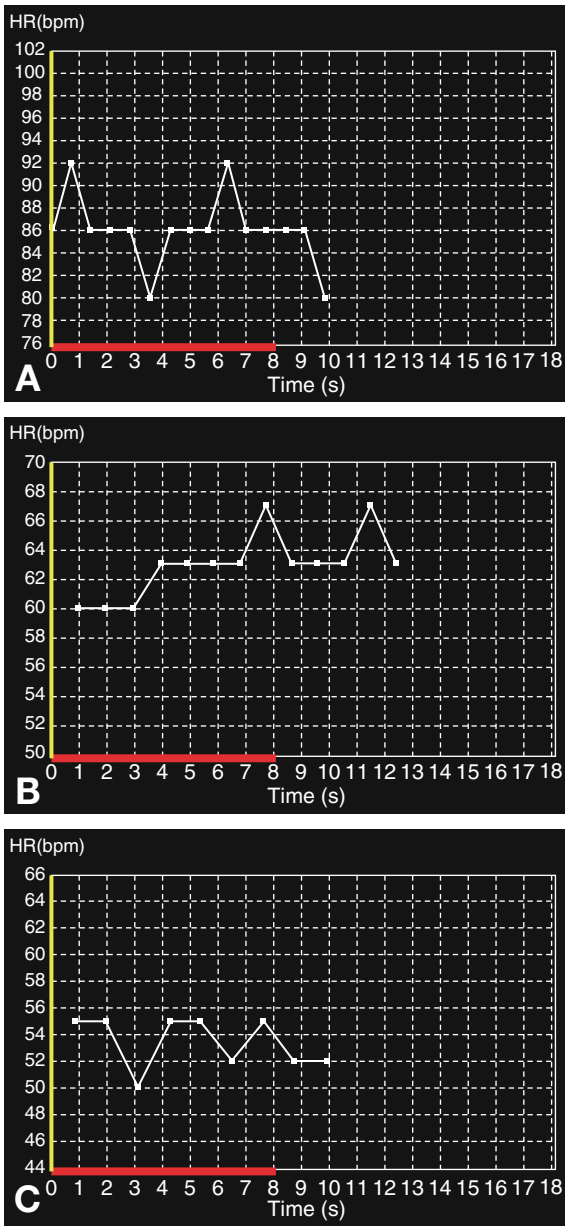

Fig. 8.8 Heart rate reduction using intravenous beta blockade. The patient (90 kg) had an initial heart rate of 80–92 beats per min during breath-hold training (**Panel A**). An initial dose of 10 mg metoprolol (equivalent to approximately 100 mg esmolol) reduced the heart rate to 60–67 beats per min (**Panel B**). After a second injection of 10 mg metoprolol, the patient's heart rate was adequately reduced to 50–55 beats per min during the final breath-hold training period (**Panel C**). Following contrast injection, the heart rate remained stable at 55 beats per min. In this case, the dose of intravenous beta blockers might have been reduced if oral beta blockers had been administered before the patient entered the scanner room

asthmatic episodes. The foremost measure to alleviate the initial symptoms of bradycardia and hypotension is to elevate the patient's legs and administer saline intravenously. In case of severe hypotension, 0.5–1.0 mg atropine should be given intravenously. Nevertheless, serious complications of beta blockers are very rare and, in patients with high heart rates, should not prevent us from making use of the positive effects of beta blockers in terms of improved image quality and diagnostic accuracy at a markedly decreased effective dose. In case of an insufficient effect of beta blockade, intravenous conscious sedation (e.g., 1 mg of midazolam or lorazepam) is a very effective alternative to slow heart rate and may improve image quality in selected patients.

8.1.5 Planning the Scan

When a CT scan is performed for suspected coronary disease or follow-up of coronary artery stents, the scan range extends from above the left atrium to immediately below the heart (**Figs. 8.4** and **8.9**). As 1 cm of a retrospective helical scan is equal to an effective dose of 1–2 mSv, every effort should be made to limit the scan range as much as possible. For imaging of the ascending aorta or the aortic and/or pulmonic valve, the start of the scan range needs to be extended above the aortic arch (**Fig. 8.4**). This scan range is also sufficient for patients who have undergone sole venous coronary bypass grafting, whereas in patients with left or right internal mammary artery grafts, the scan should start approximately in the middle of the clavicle (**Fig. 8.4**) to include the full length of these grafts. These different scan lengths highlight the importance of taking into account clinical information about previous treatments and diagnostic tests to tailor the examination to the individual patient's needs.

The scan field of view (axial extension of the radiated area) should be as small as possible to reduce the radiation exposure and, most important, to increase the spatial resolution (since small focus spots are used). We use, for instance, 320-mm scan fields of view (medium size) for coronary imaging, which reduces radiation exposure by 20–25% when compared with large scan fields of view (**Fig. 8.9**). The scan field of view needs to be differentiated from the smaller reconstruction field of view, which determines the size of the images to which the standard 512 × 512 CT matrix is applied. If the scanner allows the determination of this reconstruction field of view during the scanning procedure, it is clearly advisable to do so (**Fig. 8.9**), as this precaution will avoid potential mistakes, such as forgetting to reduce the reconstruction field of view afterward and reconstructing the coronary images on large fields of view.

8.1.6 Breath-Hold Training

Temporal resolution can be improved by testing the patient's heart rate before the examination using the same breathing instructions ("Please breathe in and then hold your breath") as during the actual scan (**Fig. 8.9**). The information on the individual patient's heart rate range during the trial breath-hold can be used on some scanners to automatically adjust scan parameters such as pitch and gantry rotation time to the individual heart

Fig. 8.9 Planning and conducting the scan. The scan range for a typical coronary CT extends from above the left atrium to immediately below the heart (*dotted lines* in **Panel A**). We then perform a single axial scan at the level of the largest diameter of the heart (**Panel B**), which is indicated by a *yellow line* in **Panel A**. We use this axial image to determine the 180–200 mm reconstruction field of view (*yellow circular region* in **Panel C**) to make optimal use of the maximum resolution provided by CT scanners (10 line pairs per cm). Breath-hold training not only familiarizes the patient with the breathing instructions for the actual coronary scans but also allows monitoring of heart rate and variability during this period (**Panel D**). If the heart rate variability is above 10% (43–60 beats per min), as shown in **Panel D**, either further relaxation of the patient or beta blockade is necessary to reduce the RR interval variability to less than 10%, as shown in **Panel E** (55–57 beats per min). By obtaining another axial scan at the level of the planned beginning of the helical coronary acquisition (**Panel F**), we can make sure that no coronary vessels are visible on this axial image (**Panel G**) that might not be included in the planned scan region. Alternatively, the unenhanced calcium scan can be used to define the start and end of the coronary scan. This axial image (**Panel G**) is also used to define a circular region of interest (*arrowhead*) in the descending aorta. This region of interest is subsequently used to track the arrival of the contrast agent bolus (**Panel H**) and to start the helical scan at a threshold of 180 Hounsfield units. Once the threshold has been reached, a simple, 5-s breathing instruction is given ("Please breathe in and then hold your breath"). The helical scan is then started with a delay of 3 s, to allow the heart to return to normal after inspiration. During the subsequent helical acquisition, the moving position of the online images is indicated by a *yellow line* on the scanogram (**Panel I**). These online images (**Panel J**, in this case showing an example at the level of the largest diameter of the heart) can be used to stop the acquisition once the caudal border of the heart has been reached, in order to reduce radiation as much as possible. The results of this coronary CT angiography are shown in **Panel K**

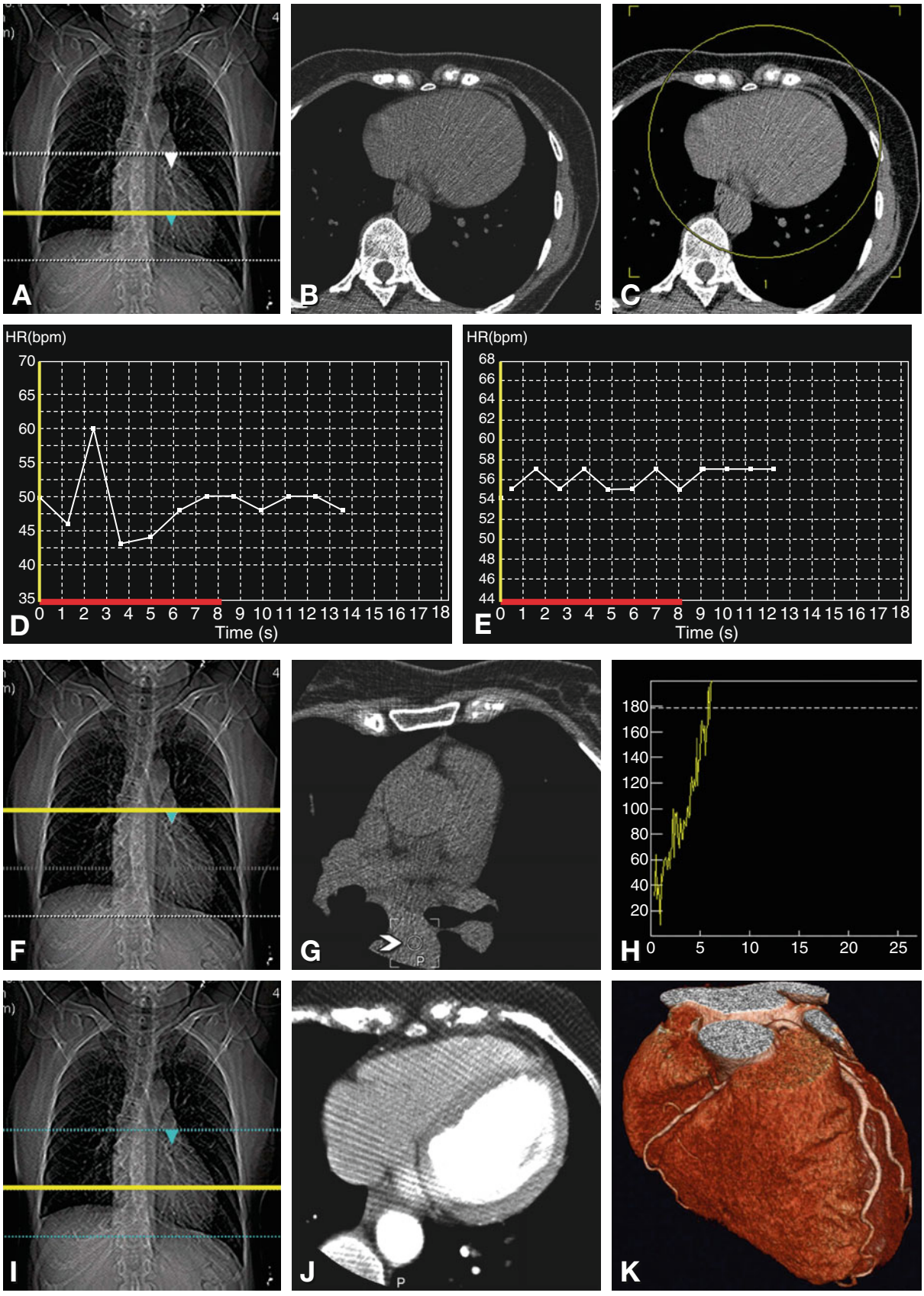
A
B
C
HR(bpm)
70
65
60
55
50
45
40
35
0 1 2 3 4 5 6 7 8 9 10 11 12 13 14 15 16 17 18
Time (s)
D
HR(bpm)
68
66
64
62
60
58
56
54
52
50
48
46
44
0 1 2 3 4 5 6 7 8 9 10 11 12 13 14 15 16 17 18
Time (s)
E
F
G
P
180
160
140
120
100
80
60
40
20
0 5 10 15 20 25
H
I
J
P
K

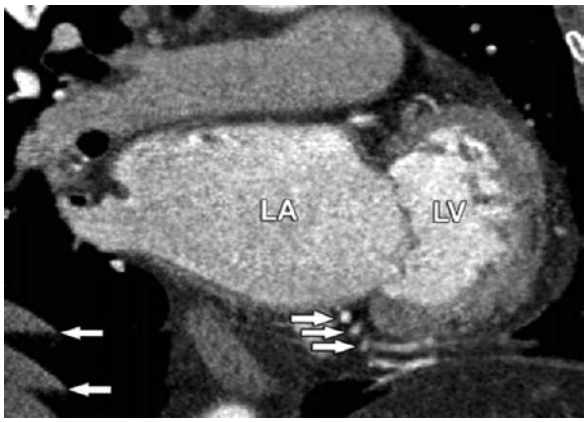

Fig. 8.10 Breathing-related motion artifacts leading to multiple visualizations of the right coronary artery and diaphragm and degraded images of the caudal portions of the heart (*arrows*). Such artifacts can be avoided in most patients by breath-hold training to ensure that the patient can hold his or her breath as long as is required for scanning. If the patient is unable to do so, breath-hold capacity can be improved by preoxygenation. *LA* left atrium, *LV* left ventricle

rate and heart rate variability. Even more importantly, breath-hold training ensures that a patient can actually hold his or her breath as long as necessary for the scan (**Fig. 8.10**). Heart rate variability during breath-hold training should be less than 10% (**Fig. 8.9**), because greater variability will degrade image quality. Breath-hold training is also a good opportunity to remind the patient that scanning is not performed at full inspiration but at about 75% of maximum inspiration, because the increased intrathoracic pressure at full inspiration (Valsalva maneuver) might reduce inflow of the contrast agent.

8.1.7 Scanning Parameters

Tube current should be adjusted to the patient's body weight or dimensions to ensure a constant high image quality regardless of body mass, while keeping the effective radiation dose to a minimum (**Table 8.1** and **Fig. 8.11**). The effective dose can be reduced effectively by choosing the smallest possible scan, since a range of about 1 cm of a retrospective scan corresponds to the effective radiation dose of 5–10 mammographies (each an effective dose of approximately 0.2 mSv). A further significant reduction of 10–40% and 60–90% can be achieved by ECG-gated tube current modulation and prospective ECG triggering ("step-and-shoot"), respectively. Nevertheless, these techniques should only be used in patients with slow heart rates (≤65 beats per min) and low heart rate variability to maintain

Table 8.1 Scanner settings for CT coronary angiography

Body weight	kV	mA	
		Pitch of 0.2 to <0.225[a]	Pitch of >0.225
<60 kg (<132 lb)	120	300	300
60–80 kg (132–176 lb)	120	340	360
>80 kg (>176 lb)	120	360	400

[a] The pitch can be adjusted according to the heart rate and heart rate variability during breath-hold training (see Sect. 8.1.6). The mA settings above are valid for Toshiba's Aquilion 64 scanner only. Optimal mA settings may be different on other scanners (Chap. 9). As a general rule, the mA should always be reduced in patients with lower body weight or body mass index and increased in heavier patients. An increase in kV (e.g., to 140) may be considered in very heavy patients (above 100 or 120 kg)

adequate image quality. In patients with a slim chest, use of a lower tube voltage of 80 or 100 kV is another useful approach to reduce effective dose without a loss of image quality. Whether or not such a situation is present can be decided using the attenuation information on the scanogram and the area of the thoracic solid tissue. Whether the best kV setting can be automatically predicted by scanner software is under clinical investigation. Simply using a low body mass index or body weight of patients to predict kV settings is arguably less accurate than measuring the attenuation on the scanogram because of great interindividual variations in thoracic tissue and body mass index or weight. In selected patients with small chest dimensions and low and stable heart rates, recent approaches to dose reduction can result in very small effective doses (**Fig. 8.12**).

8.1.8 Contrast Agent

The flow of contrast agent, and thus its amount, should also be adjusted to the patient's body weight (**Table 8.2**) in order to compensate for the greater attenuation of X-rays in heavier patients and to achieve comparable contrast between the contrast-filled coronary lumen and the surrounding tissue over a wide range of body weights (**Table 8.2**). When coronary artery stents are being imaged, a higher density in the vessel lumen is beneficial (Chap. 13), whereas for coronary plaque imaging, the density should not be too high (to avoid influencing of plaque density values, and potentially also plaque volumes, Chap. 14). Thus, contrast agent flow may also have to be adapted to reflect the clinical question to be answered by cardiac CT.

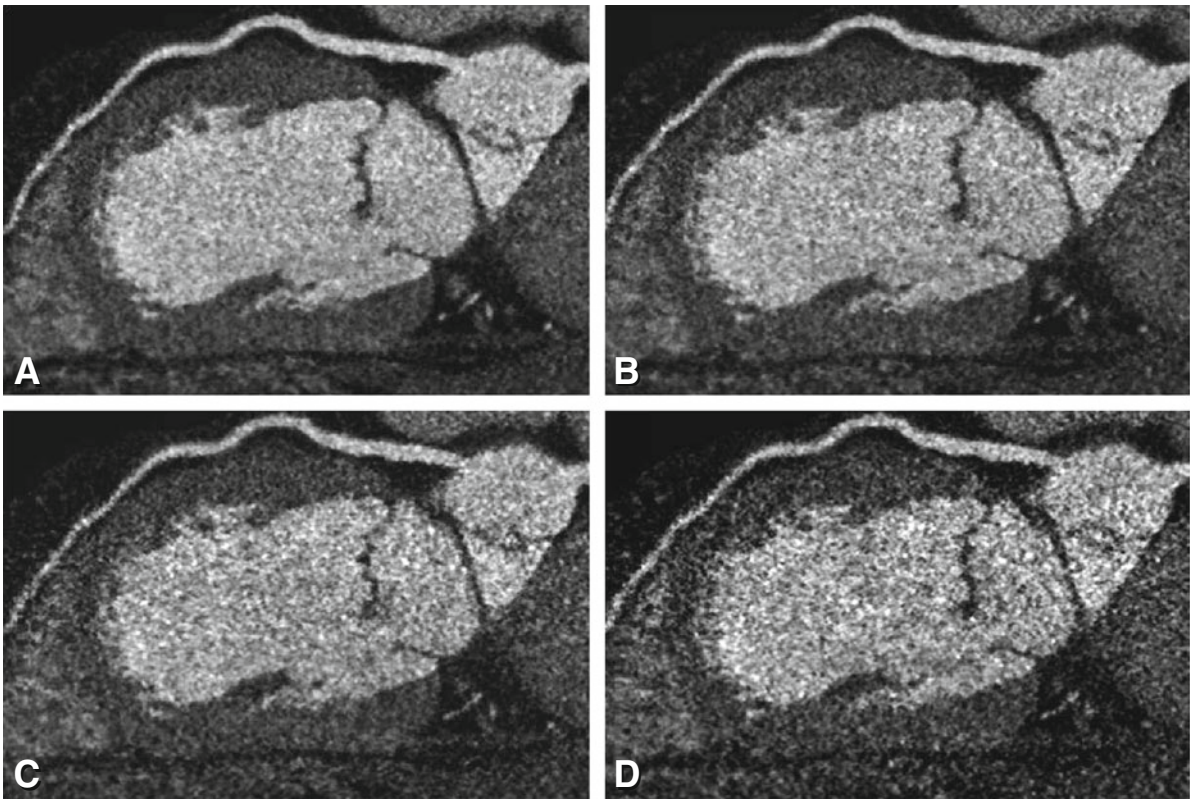

Fig. 8.11 Effect of tube current on image quality. Curved multiplanar reformations along the left anterior descending coronary artery in a patient with a body weight of 110 kg and a body-mass index of 32. The scan was acquired with a mA of 360 and is shown in **Panel A**. Using the raw data for this patient, we simulated (**Panels B**–**D**) what the images would look like with lower mA settings (performed in cooperation with Toshiba; Okumura-san and Noshi-san). These panels represent mA settings of 300 (**Panel B**), 250 (**Panel C**), and 200 (**Panel D**). Already at 300 mA (**Panel B**), the curved multiplanar image looks much grainier (salt-and-pepper appearance). At the lowest mA settings (**Panel D**), it becomes impossible to rule out significant stenoses and plaques in the mid-segment of this vessel. This situation illustrates the importance of adjusting the tube current to the size of each patient. It is important to note that these images represent simulations, and the differences would be even larger in actual repeated scanning (which would be unethical)

Injection of the contrast agent followed by a saline flush (using a dual-head injector) results in a more compact contrast bolus in the heart and ensures that only little contrast medium is left in the right ventricle and atrium when the coronary scan is started with an adequate delay. Ensuring this washout of the right ventricle and atrium significantly reduces the likelihood of streak artifacts arising from the right cardiac chambers, which can otherwise severely degrade the capacity to assess the right coronary artery. This simple bolus of contrast agent followed by saline is sufficient for coronary artery imaging. Because of the very low density in the right cardiac chambers, however, the septal wall might not be easily discernible, making it difficult to evaluate both regional and global left and right ventricular function. Thus, whenever cardiac function assessment is pivotal, two injection protocols can be used to improve the images: (1) dual-phase contrast agent injection (e.g., 5 ml s^{-1} for 80% of the contrast agent, and 2 ml s^{-1} for the rest) followed by saline, or (2) after the first contrast agent injection phase, injection of a mixture of contrast agent and saline (second phase), again followed by saline (third phase). In most "rule out coronary disease" patients, however, such sophisticated contrast agent injection techniques are not a must, and simple contrast agent administration followed by a saline flush is sufficient.

What is clearly more important than these issues is that at least a 20-gauge intravenous line is used for contrast agent injection. The right cubital veins are clearly preferable over the left side or hand veins, because the distance to the cardiac chambers is shortest this way and the contrast bolus is the least diluted. Moreover, using the right cubital vein is preferable because this approach avoids problems with streak artifacts from contrast agent in the left subcla-

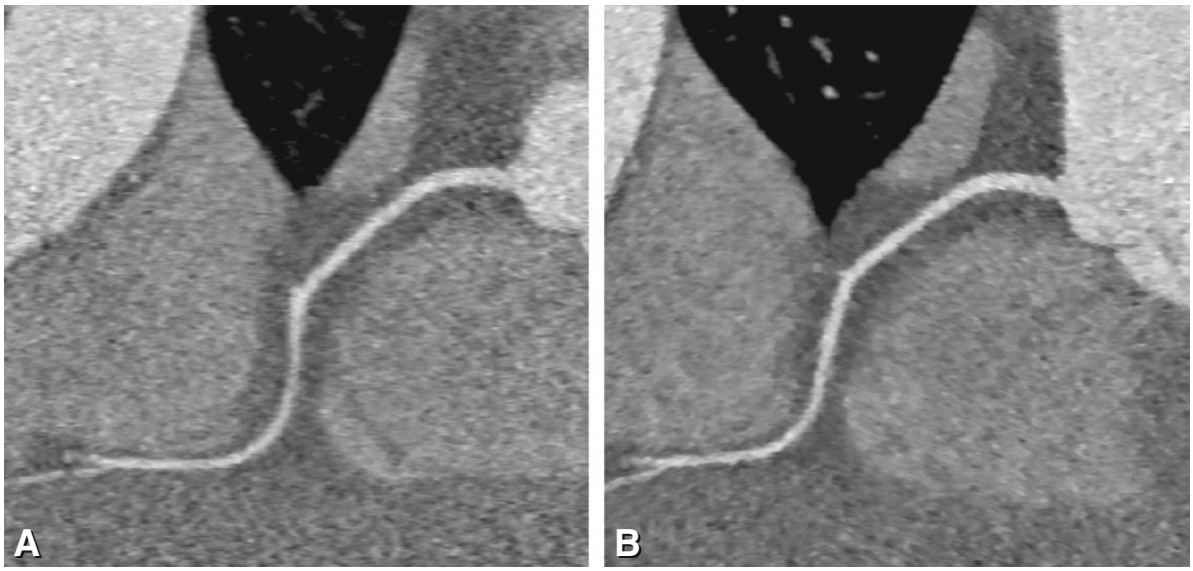

Fig. 8.12 Dramatic reduction of effective radiation dose is possible in selected patients. Example of a curved multiplanar reformation of the right coronary artery reconstructed using filtered backprojection (**Panel A**) and sonogram-affirmed iterative reconstruction (**Panel B**) in a patient with a slow and stable heart rate of 53 beats per min and a weight of 62 kg at a height of 170 cm. Scanning was done by using 80 kV and 50 mAs, resulting in a dose-length product of only 4 mGy.cm (Used with permission from Schuhbaeck et al. *Eur Radiol* 2013a)

8

Table 8.2 Contrast agent injection rates

Body weight	Rate (ml/s)[a]
<60 kg (<132 lb)	3.5
60–80 kg (132–176 lb)	4.0
>80 kg (>176 lb)	5.0

[a] The amount of iodine injected should be about 1.3–2.0 g s^{-1} to ensure adequate opacification of the coronary arteries. The flow rates given in the table are thus valid for contrast agents with an iodine concentration of 350–400 mg ml^{-1}. For contrast agents with a lower iodine concentration (e.g., 320), the flow needs to be increased to achieve the same iodine influx of 1.3–2.0 g s^{-1}. Higher flow rates can also be used with 350–400 mg ml^{-1} contrast agents to make the bolus more compact and increase vessel lumen density (e.g., for stent assessment), but this will also increase the risk of adverse reactions. We feel that the suggestions above are a reasonable compromise between image quality and patient safety

vian vein that might obscure the most common arterial bypass graft (left internal mammary artery).

Another area of concern is how to estimate and standardize the contrast agent amount that is injected for cardiac CT. The following formula can be used to calculate the amount of contrast agent for CT angiography on a 64-row scanner according to the individual helical scan duration:

Contrast agent amount [ml] = (10 s + scan duration in seconds) × contrast agent flow in ml/s[a]

First example: 70 kg patient undergoing a 10-s coronary helical scan

$(10\ s + 10\ s) \times 4\ ml\ s^{-1} = 80\ ml$

Second example: 105 kg patient undergoing a 15-s coronary bypass scan

$(10\ s + 15\ s) \times 5\ ml\ s^{-1} = 125\ ml$

[a]See **Table 8.2** for calculating contrast agent injection rates. The 10 s is a constant.

8.1.9 Starting the Scan

Properly connecting the contrast agent line to the patient's intravenous access and making sure that there is no air in the injection system are essential to preventing air from being injected into the cardiac chambers or pulmonary arteries (**Fig. 8.13**). Before starting the contrast agent injection, it is important to reassure the patient that the next breath-hold is the last one and that it takes as long as the one during breath-hold training. Again, mentioning that the patient might feel some warmth can

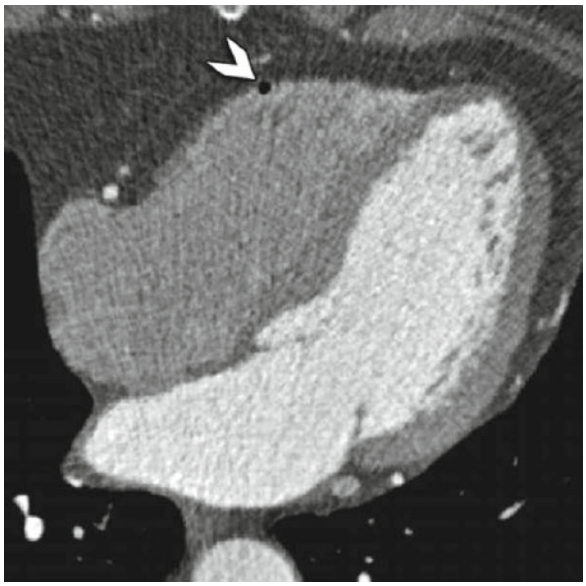

Fig. 8.13 Four-chamber view showing a very small air bubble at the ventral wall of the right ventricle (*arrowhead*). The bubble was most likely introduced when the contrast agent line was connected to the patient's intravenous line. Such small amounts are unlikely to harm the patient. Care must be taken not to inject relevant amounts of air into the cardiac chambers or pulmonary arteries, by properly connecting the contrast agent line and excluding any air that is in the injection system

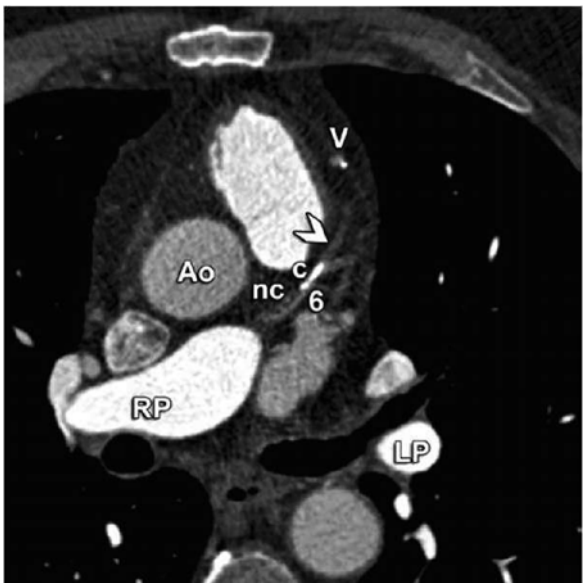

Fig. 8.14 Too-early initiation of the coronary acquisition, with most of the contrast agent still in the pulmonary arteries (LP and RP). As a result, there is very little contrast in the aorta (*Ao*) and the coronary arteries (*arrowhead*) in this patient with a history of venous coronary bypass grafting (*V*). Because of the poor opacification, it is very difficult to identify the stenosis in segment 6 of the left anterior descending coronary artery caused by noncalcified (*nc*) and calcified (*c*) plaques. In this patient, a test bolus was used to calculate the appropriate delay time for initiation of the coronary scan, but a heart-rate change after contrast agent administration led to incorrect timing of the coronary helical scan. *LP* left pulmonary artery, *RP* right pulmonary artery

be important for those who are nervous. It is always a good idea to have someone on site to monitor the injection of the contrast agent for at least a few seconds to avoid extravasation.

Immediately prior to injecting the contrast agent, make a "final check" to ensure that the heart rate is still in an acceptable range and the ECG is detected by the system. There are two options for timing the start of the helical scan after intravenous contrast administration: (1) monitoring the arrival of the contrast agent during the injection of the main bolus and starting the helical scan once a threshold has been reached ("bolus tracking"), and (2) injecting a test bolus to determine the individual patient's circulation time and adjusting the scanning parameters accordingly ("test bolus"). The second approach has the disadvantage that any changes between the test bolus and the actual bolus used for coronary opacification (such as relevant heart rate changes) can alter the patient's circulation time. We think that the test bolus approach more commonly leads to mistiming of the coronary helical scan (**Fig. 8.14**), and it has also been shown that the coronary enhancement is less homogenous when this approach is used. We therefore strongly recommend the bolus tracking approach (for 64-row CT), which also reduces the total amount of contrast agent injected, as no test bolus is needed.

We perform bolus tracking (which should be initiated 10–15 s after the start of contrast injection) by analyzing Hounsfield unit density in a region of interest in the descending aorta (**Fig. 8.9**). The spiral scan at a threshold of 180 Hounsfield units is then initiated. We use the descending aorta, as opposed to the ascending aorta, for example, for bolus tracking because it is less likely for early-enhancing vessels such as the superior vena cava to affect this region of interest. As soon as the threshold for initiation of the scan has been reached, a simple 5-s breathing instruction is given ("Please breathe in and then hold your breath"). Since there is often a brief increase in heart rate after inspiration, there is an additional gap of 3 s before the scan is started, so that the heart rate can normalize after submaximal inspiration.

8.1.10 After the Scan

As soon as the prospectively or retrospectively gated coronary scan is completed, we return to the scanning room to make sure that the patient has tolerated the contrast agent well. Because of the nitroglycerin and possible beta blockade, it is advisable that the patient gets up slowly to avoid orthostatic reactions. Most patients are eager to know the results of the examination immediately, which is difficult because a single cardiac CT can easily produce as many as 4,000–5,000 images.

The patient can be offered the opportunity to wait in the seating area after the scan is completed and to meet with the interpreting physician to discuss the results as soon as he or she has finished reading and interpreting the images. This offer is highly appreciated by some patients and many of our referring physicians. In addition, sending reconstructions of the coronary arteries to the referring physician together with the report not only improves further management of the patient but is also a strong marketing tool.

8.2 Reconstruction

Image reconstruction is an integral component of the examination. The parameters for coronary and lung reconstructions are compiled in **Table 8.3**, and typical results of these reconstructions are shown in **Fig. 8.15**. The reconstruction of cardiac CT is summarized in **List 8.2**.

8.2.1 Slice Thickness and Fields of View

For analysis of the small and tortuous coronary arteries, it is of utmost importance to keep the reconstructed slice thickness for the axial slices as thin as possible. A slice thickness of 3 or 2 mm is clearly inadequate for coronary imaging, but there is also a remarkable difference between 0.5 and 1.0-mm reconstructions (**Fig. 8.16**). The reconstructed slice thickness is different from the reconstruction increment. This increment between the centers of adjacent slices can be thinner (e.g., 0.4 mm) than the slice thickness (e.g., 0.5 mm) to improve the

Table 8.3 Reconstruction settings

	FOV (mm)	Slice thickness (mm)	Reconstruction increment (mm)	Kernel	RR intervals
Coronary images	180–200	0.5–0.75	0.3–0.5	Coronary, possibly stent kernel	0–90% at 10% increments[a] and/or minimal cardiac motion phases
Lung and mediastinal images	Scan field of view[b]	3–5	3–5	Lung and mediastinum	80%[c]

[a] Alternatively, one can reconstruct images at 5% increments around 70–80% of the RR interval

[b] Adapted to include the entire chest in the xy-plane

[c] This percentage refers to the center of the reconstruction window (as on Toshiba, Philips, and General Electric scanners). On other scanners (Siemens), the percentage phase given denotes the beginning of the reconstruction phase (which would be equal to approximately 65% or 70% instead)

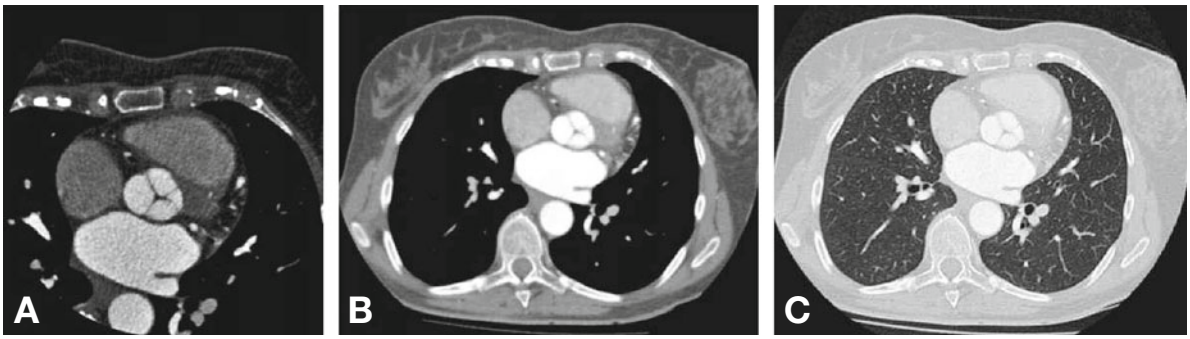

Fig. 8.15 Typical axial images of coronary (**Panel A**), mediastinal (**Panel B**, soft tissue), and lung reconstructions (**Panel C**) at the level of the aortic valve. Please note that the coronary reconstructions here (**Panel A**) were performed on smaller fields of view in order to maximize spatial resolution. The mediastinal (**Panel B**) and lung (**Panel C**) reconstructions are less noisy because of the greater slice thickness (3–5 mm)

List 8.2. Steps in the reconstruction of cardiac CT images

1. Check whether the heart rate was regular throughout scanning
2. Perform ECG editing if necessary – consider automatic identification of minimal cardiac motion phases
3. Reconstruct coronary axial slices using specific kernels on small fields of view (180–200 mm) – consider stent kernels
4. Reconstruct lung and mediastinal axial slices using specific kernels on large fields of view to cover the entire chest width
5. Archive all reconstructed coronary images or only those indicated by the reading physician
6. Archive all lung and mediastinal images

three-dimensional reconstructions by spatial interpolation. However, the true spatial resolution is defined by the actual slice thickness, and a reduction in the slice increment may impose too large a burden on the local picture archiving and communication system. Thus, it clearly depends on the local situation whether it is advisable to use this spatial interpolation approach or not.

What is much more important than slice interpolation is the use of a minimally small reconstruction field of view (ca. 180–200 mm) to make optimal use of the maximal spatial resolution of the scanner (10 line pairs per cm) using a 512×512 image matrix (**Table 8.3**). With this image matrix, a 180-mm field of view results in a pixel size of 0.35×0.35 mm^2 (0.12 mm^2). If one inadvertently uses a 320-mm field of view for reconstruction, the resulting pixel size is about 0.625×0.625 mm^2 (0.4 mm^2), which is almost four times larger. The effect on image quality is significant and is illustrated in **Figs. 8.17** and **8.18**. In contrast to the situation for coronary axial slices, it is ethically desirable to use the entire scanned field for reconstruction of the lung, the mediastinum, and the chest wall (**Fig. 8.15** and **Table 8.3**) to avoid overlooking any pathology in this area.

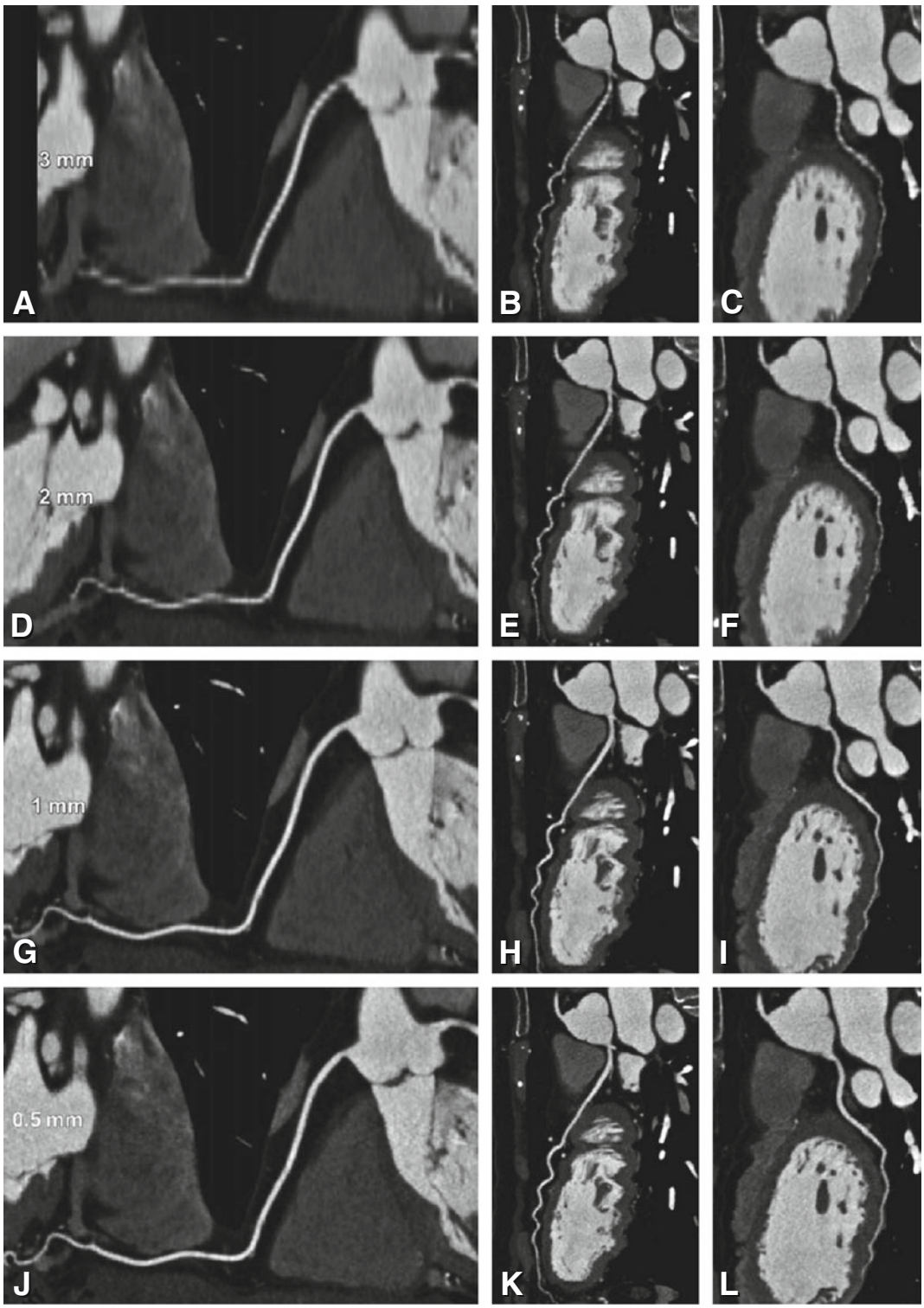

Fig. 8.16 Importance of slice collimation for image quality, as shown in curved multiplanar reformations along the right coronary artery (*first column*), left anterior descending coronary artery (*middle column*), and left circumflex coronary artery (*third column*). Slice thicknesses of 3 mm (**Panels A**–**C**) and 2 mm (**Panels D**–**F**) are clearly inadequate for coronary imaging, as can be seen in the step-like appearance of the vessel on curved multiplanar reformations. These slice thicknesses were commonly used with electron-beam CT and 4-row CT. But there is also an image-quality difference (step-like appearance) between 0.5 and 1.0-mm slice thickness reconstructions available on different 16 and 64-row CT scanners (**Panels G**–**I** and **Panels J**–**L**). All reconstructions were performed using raw data that were acquired with 64 × 0.5-mm detector collimation in a single patient

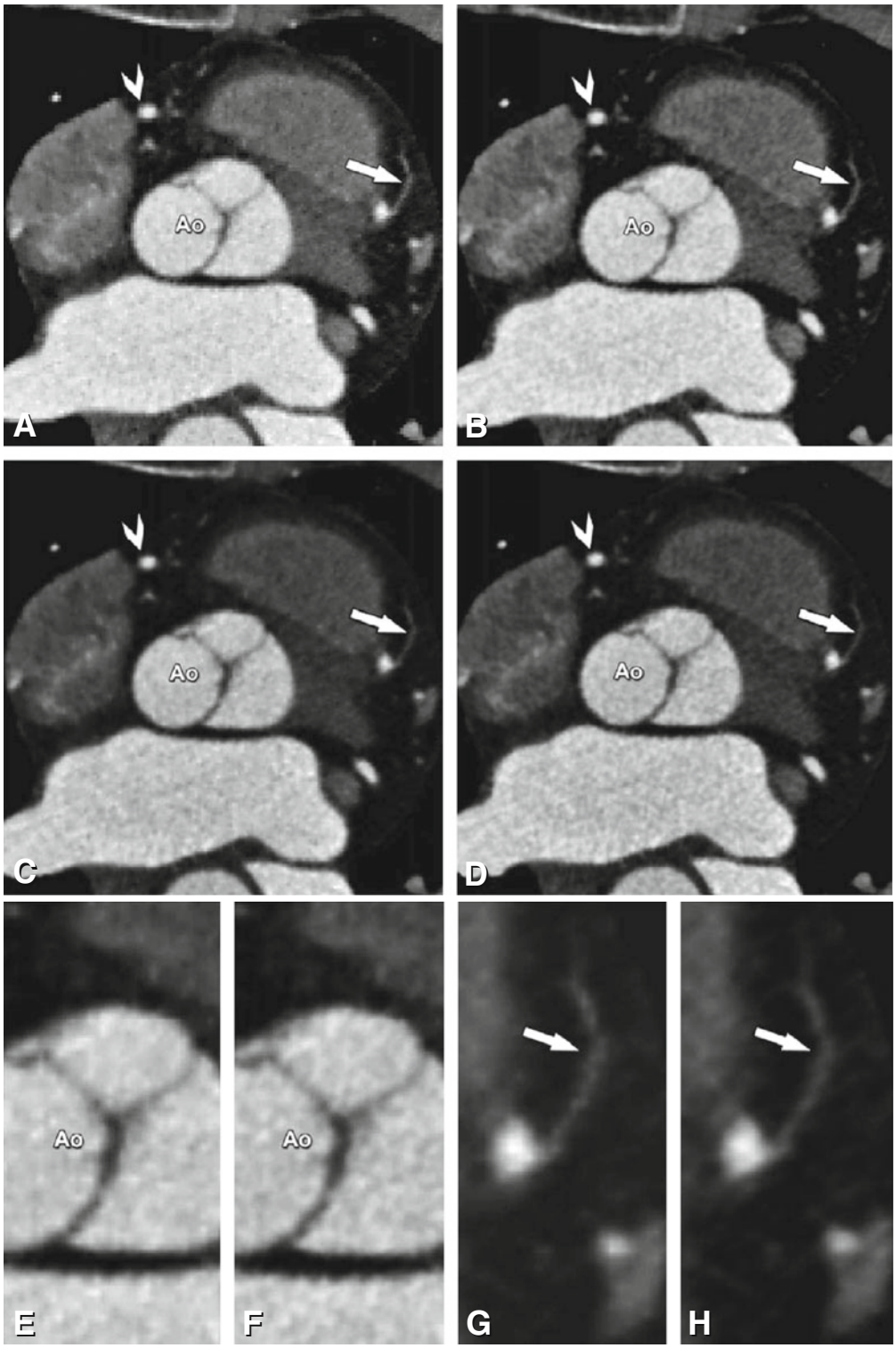

Fig. 8.17 Effect of the reconstruction field of view (320 vs. 180 mm) on the image quality of coronary artery reconstructions. The original axial images of the 320-mm reconstruction field of view (**Panel A**) are compared with the 180-mm reconstruction fields of view (**Panel B**). The 320-mm reconstructions (**Panel A**) have markedly poorer spatial resolution with coarser pixels (ca. 0.625×0.625 mm^2 vs. 0.35×0.35 mm^2), as illustrated by the right coronary artery (*arrowhead*) and a rather small side branch of the LAD (*arrow*). On workstations this difference appears to be somewhat blurred but is still present, as can be seen in the images at exactly the same anatomic level (**Panel C** vs. **D**). Magnified views of the aortic valve cusps (**Panel E** vs. **F**) and the small side branch of the LAD (**Panel G** vs. **H**) clearly show the considerable advantage of using small 180-mm reconstruction fields of view (**Panels F** and **H**). *Ao* aorta

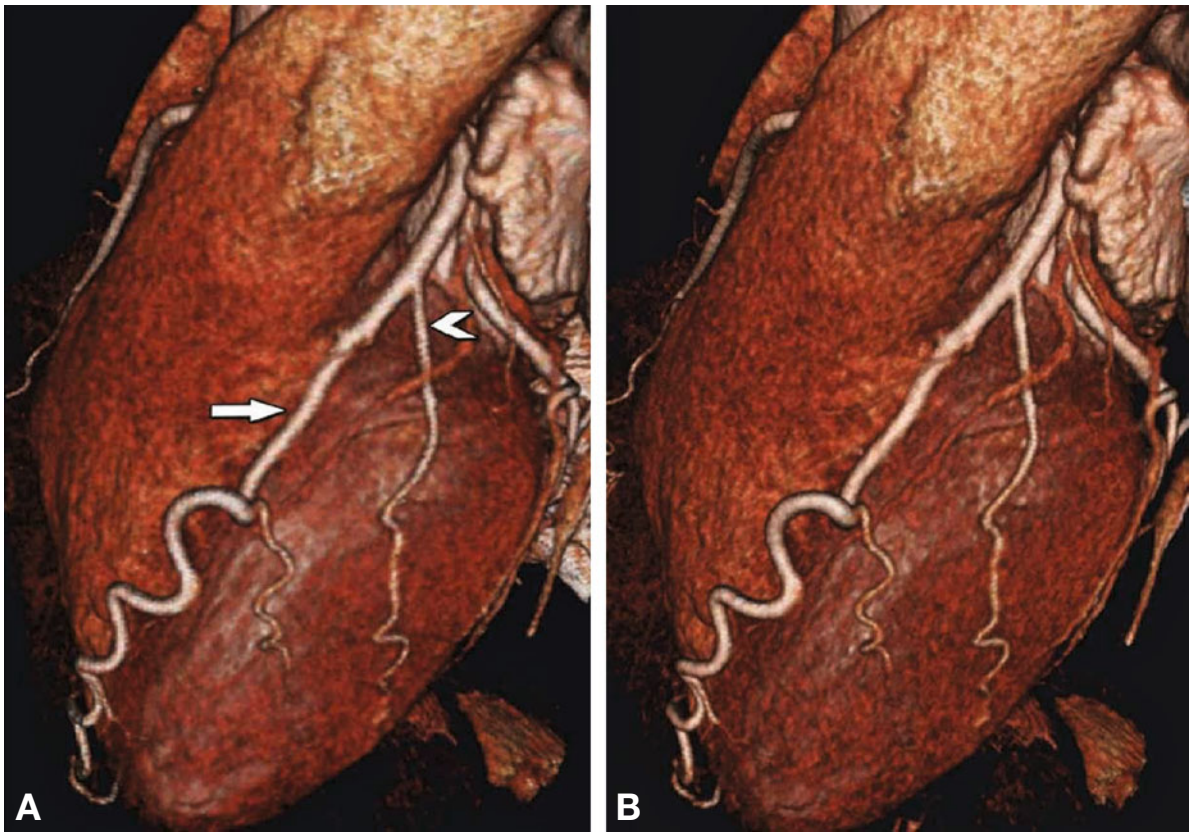

Fig. 8.18 Effect of the reconstruction field of view (320 vs. 180 mm) on the image quality of coronary artery reconstructions. Three-dimensional reconstructions of the LAD (of the same patient as in **Fig. 8.17**) show the relevantly lower spatial resolution obtained using the 320-mm reconstruction field of view (**Panel A**), when compared with the smaller 180-mm reconstruction field of view (**Panel B**), as illustrated by the mid-LAD (*arrow*) and the first diagonal branch (*arrowhead*)

8.2.2 Temporal Resolution and the Cardiac Reconstruction Phase

Temporal resolution is still the major limitation of coronary CT and the main cause of nondiagnostic images, and therefore all possible measures must be taken to improve this parameter. One such measure is adaptive multisegment reconstruction, which should be used whenever available for patients with heart rates greater than about 60 beats per min (**Figs. 8.19** and **8.20**). An alternative approach that markedly improves temporal resolution is dual-source CT, which allows a 50% reduction in the length of the reconstruction window, regardless of the heart rate (**Fig. 8.21**). In this way, dual-source CT markedly reduces heart-rate dependence.

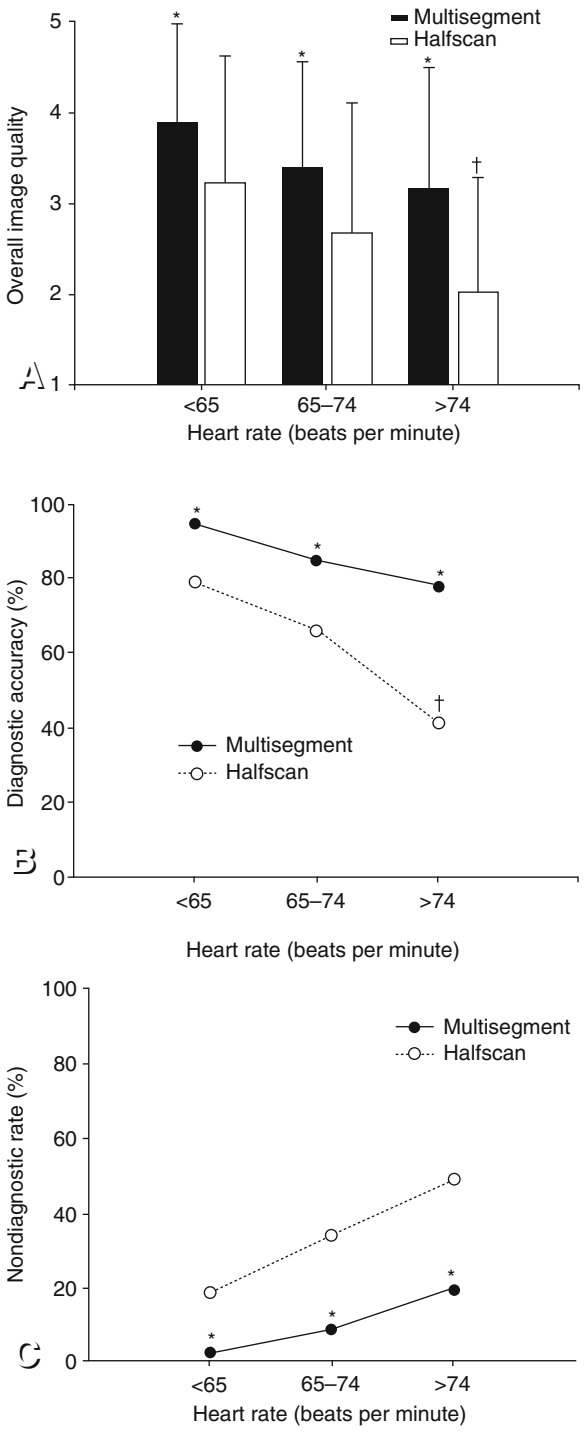

Reconstruction can be done throughout the cardiac cycle at 10% intervals, resulting in 10 phases, or around a mid-diastolic interval at 5% increments (about 70–80% of the RR interval) (**Table 8.3**). Most of the suitable reconstruction phases (intervals) within the cardiac cycles are mid-diastolic phases (e.g., 75%) and end-systolic phases (e.g., 40%). The latter are especially suitable for analysis in patients with higher heart rates. Reconstruction of several phases throughout the RR interval has the advantage that the resulting data can be used for high-resolution analysis of regional and global cardiac function without having to perform any additional reconstructions. It is important to note that the designations of the phases are not defined consistently by the different vendors. The percentage of the RR interval refers either to the center of the reconstruction

Fig. 8.19 Comparison of overall image quality (**Panel A**), per-patient diagnostic accuracy (**Panel B**), and per-patient nondiagnostic rate (**Panel C**) of CT coronary angiography obtained using adaptive multisegment and standard halfscan reconstructions in three heart rate groups. There is a trend toward reduced overall image quality and accuracy at higher heart rates, which was significant in the case of the halfscan reconstructions when the 65–74 and above 74 beats-per-min groups were compared (*dagger*). Nevertheless, regardless of whether multisegment reconstruction is available or not, the heart rate should be reduced to below 65 beats per min by beta blocker administration whenever possible. For all three heart rate groups, overall image quality, diagnostic accuracy, and nondiagnostic rate are significantly superior for multisegment reconstruction than for standard halfscan reconstruction (*asterisk*). Therefore, whenever available, adaptive multisegment reconstruction should be used instead of halfscan reconstruction. A very recent important alternative to improve temporal resolution is DSCT (**Fig. 8.21**). Note that the image quality and accuracy obtained with multisegment reconstruction at high heart rates (>74 beats per min) are comparable with the results obtained using standard halfscan reconstruction at slow heart rates (<65 beats per min) (From Dewey et al. *Eur Radiol* 2007)

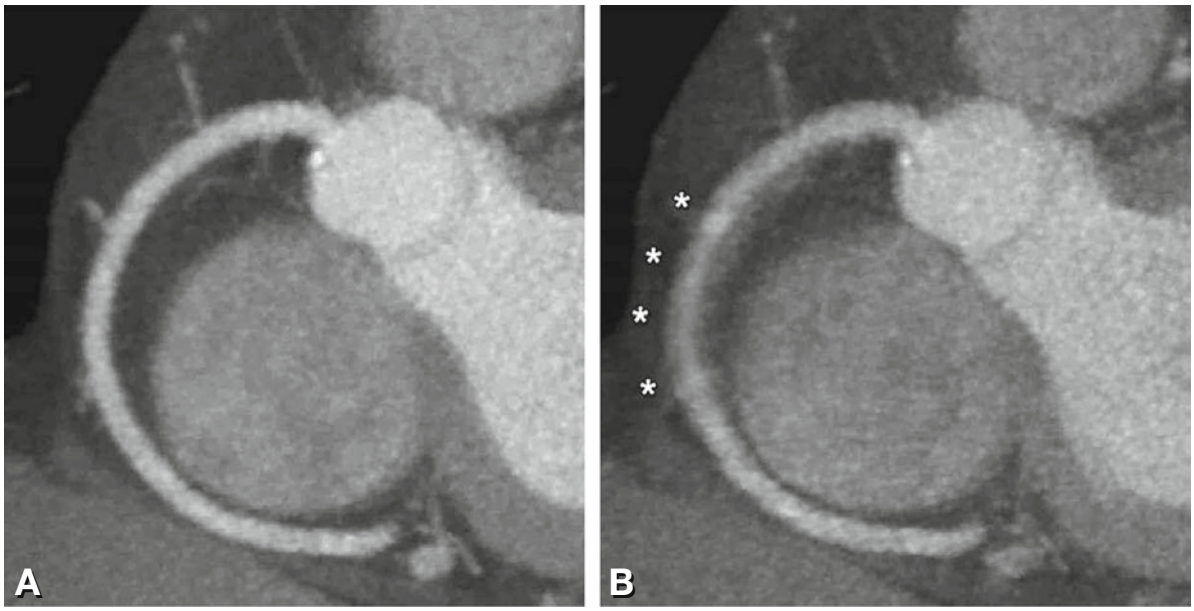

Fig. 8.20 Advantages of multisegment reconstruction (**Panel A**) over halfscan reconstruction (**Panel B**), as illustrated by a cath view along the right coronary artery in a patient with a heart rate of 66–68 beats per min during 320-row CT scanning. There are multiple motion artifacts resulting from insufficient temporal resolution with halfscan reconstruction, which cause blurring of the vessel wall (*asterisks*, **Panel B**)

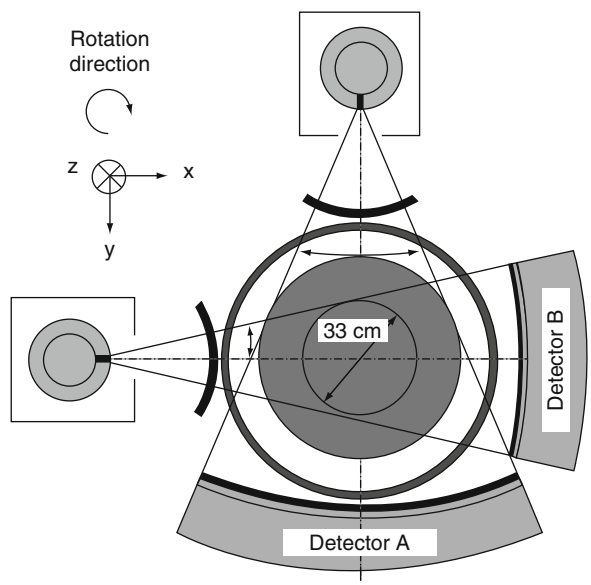

Fig. 8.21 Technical realization of second-generation dual-source computed tomography (DSCT). One detector (*A*) covers the entire scan field of view with a diameter of 50 cm, while the other detector (*B*) is restricted to a slightly smaller field (33 cm). With first-generation DSCT the second field of view was restricted to 26 cm and the two gantries were mounted at a 90° angle. With second-generation DSCT this space limitation was reduced by having a 95° off-set between the gantries. Using DSCT, the length of the image reconstruction window can be reduced by a factor of 2 when compared with standard halfscan reconstruction using a single X-ray source, to one-fourth of the gantry rotation time. Thus, temporal resolution is significantly improved (Image courtesy of Thomas Flohr)

phase (Toshiba, Philips, and General Electric) or the beginning of the reconstruction phase (Siemens). As a result, there are different recommendations regarding minimal cardiac motion phases, but these can be matched (thus, the start of the reconstruction phase at about 65–70% of the RR interval corresponds to a center of the phase at about 75–80%). In patients with severe arrhythmias (e.g., atrial fibrillation) an absolute temporal reconstruction approach (in ms) might be superior to relative reconstruction intervals (% of the RR interval).

In discussing the number of phases to be reconstructed and the distance between phases, one must bear in mind that the reconstruction window in coronary CT angiography is about 50–175 ms long, corresponding to about 8–20% of the RR interval. Therefore, there will not be great differences between reconstructions at intervals ≤2%.

Heart rate is crucial in determining the position of the minimal cardiac motion phase that is most suitable for reconstruction. In patients with higher heart rates, end-systolic phases (e.g., 30–40%) are often superior to diastolic phases in terms of image quality. Selection of the reconstruction phase has considerable influence on the diagnostic accuracy of coronary CT angiography. It has been shown, for example, that a single reconstruction phase (typically with the center of the reconstruction window at 80%) results in optimal quality and diagnostic accuracy in only half of the patients. Two reconstruction phases are necessary in 40% of patients, and at least three phases in 10%, to optimally evaluate the entire coronary artery tree by CT angiography. Automatic determination of minimal cardiac motion using software approaches based on the raw data (e.g., "Best Phase") using motion maps (**Fig. 8.22**) is likely to considerably simplify identification of the optimal cardiac phase for coronary artery analysis (Chap. 10).

8.2.3 Iterative Reconstruction

Recently, several vendors have introduced iterative reconstruction for routine clinical use. This reconstruction takes slightly longer than standard filtered back projection but also reduces image noise significantly. Thus the mA during scanning may be lowered while image quality is maintained and effective dose relevantly reduced (**Fig. 8.23**).

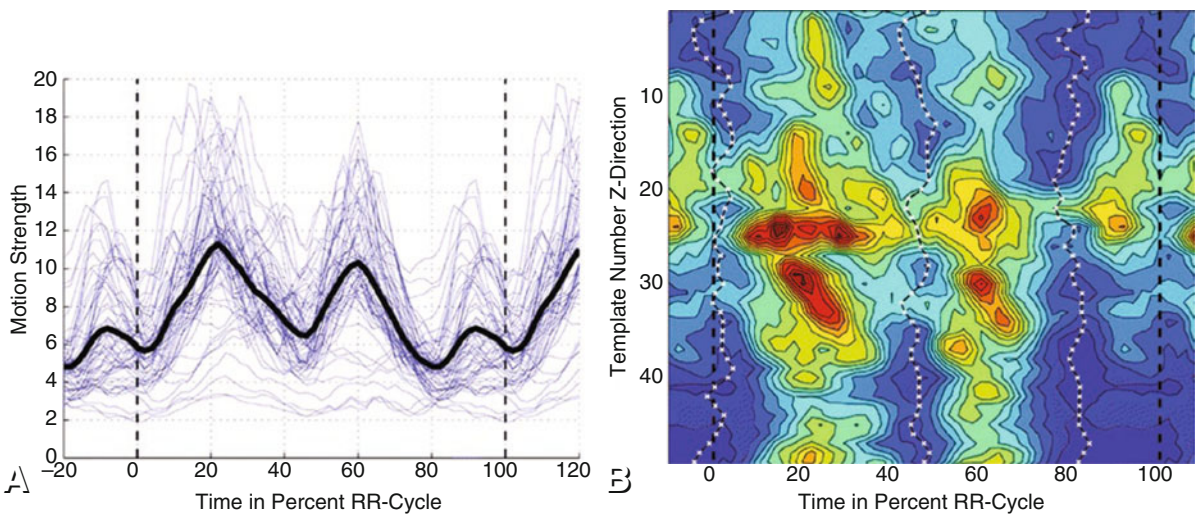

Fig. 8.22 Motion strength curve and motion map samples. **Panel A** shows a representative mean curve of the motion strength function for all voxels within a single axial plane. Motion strength (corresponding to inverse similarity) is plotted against phase point propagation of one cardiac cycle. The *curve* shows low motion troughs for the end-systolic phase (~46%) and the mid-diastolic or diastasis phase (~80%). **Panel B** shows the corresponding motion map, with color-coded (*blue*, low motion; *red*, high motion) motion strength curves plotted against the cardiac phase (x-axis) and against z-axis propagation of the helical scan (y-axis truncated at a value of 50 to confine the coverage to aortic root position, y-axis value = 0, down to the diaphragmatic surface of the heart, y-axis value = 49). A low-motion phase becomes apparent as a *blue valley* between *red-colored* systolic contraction (0–40% longitudinally) and rapid diastolic filling (50–70% longitudinally). Atrial contraction is apparent as a hump around 90%. *Lines with crosses* track the valleys of lowest motion; *dashed vertical lines* mark the beginning and the end of the cardiac cycle (R to R peak) (Used with permission from Hoffmann et al. *Eur Radiol* 2006)

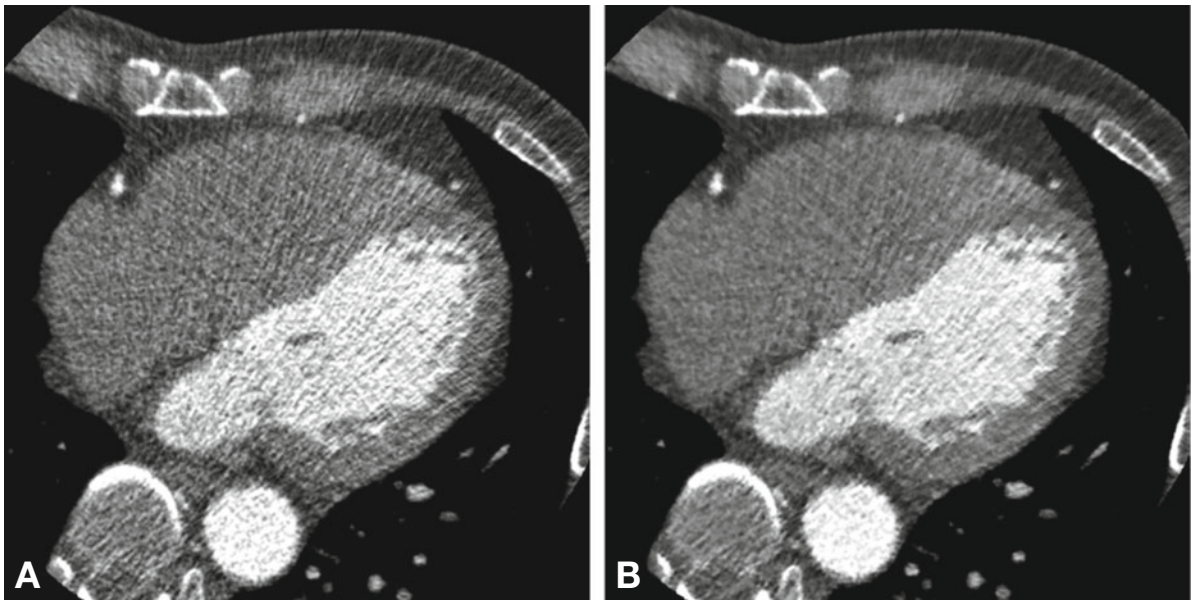

Fig. 8.23 Example of cardiac CT reconstructed with standard filtered back projection (**Panel A**) and iterative reconstruction (**Panel B**). Imaging was performed on a 320-row CT using 120 kV and 60 mA translating into an effective dose of about 0.6 mSv. There is significant reduction in image noise using adaptive iterative dose reduction reconstruction (**Panel B**) in comparison to standard filtered back projection (**Panel A**) on these axial images (Images courtesy of Kazuhiro Katada, Fujity University)

Recommended Reading

Achenbach S (2006) Computed tomography coronary angiography. J Am Coll Cardiol 48:1919–1928

Cademartiri F, Luccichenti G, Marano R, Runza G, Midiri M (2004a) Use of saline chaser in the intravenous administration of contrast material in non-invasive coronary angiography with 16-row multislice computed tomography. Radiol Med (Torino) 107:497–505

Cademartiri F, Nieman K, van der Lugt A et al (2004b) Intravenous contrast material administration at 16-detector row helical CT coronary angiography: test bolus versus bolus-tracking technique. Radiology 233:817–823

Cademartiri F, Mollet NR, Runza G et al (2005a) Influence of intracoronary attenuation on coronary plaque measurements using multislice computed tomography: observations in an ex vivo model of coronary computed tomography angiography. Eur Radiol 15:1426–1431

Cademartiri F, Runza G, Mollet NR et al (2005b) Impact of intravascular enhancement, heart rate, and calcium score on diagnostic accuracy in multislice computed tomography coronary angiography. Radiol Med (Torino) 110:42–51

Cademartiri F, Mollet NR, Runza G et al (2006) Improving diagnostic accuracy of MDCT coronary angiography in patients with mild heart rhythm irregularities using ECG editing. AJR Am J Roentgenol 186:634–638

Cademartiri F, Maffei E, Palumbo AA et al (2008) Influence of intracoronary enhancement on diagnostic accuracy with 64-slice CT coronary angiography. Eur Radiol 18:576–583

Chun EJ, Lee W, Choi YH et al (2008) Effects of nitroglycerin on the diagnostic accuracy of electrocardiogram-gated coronary computed tomography angiography. J Comput Assist Tomogr 32:86–92

Dewey M, Hamm B (2007) CT coronary angiography: examination technique, clinical results, and outlook on future developments. Fortschr Rontgenstr 179:246–260

Dewey M, Laule M, Krug L et al (2004) Multisegment and halfscan reconstruction of 16-slice computed tomography for detection of coronary artery stenoses. Invest Radiol 39:223–229

Dewey M, Hoffmann H, Hamm B (2006) Multislice CT coronary angiography: effect of sublingual nitroglycerine on the diameter of coronary arteries. Fortschr Rontgenstr 178:600–604

Dewey M, Teige F, Laule M, Hamm B (2007) Influence of heart rate on diagnostic accuracy and image quality of 16-slice CT coronary angiography: comparison of multisegment and halfscan reconstruction approaches. Eur Radiol 17:2829–2837

Dewey M, Teige F, Rutsch W, Schink T, Hamm B (2008) CT coronary angiography: influence of different cardiac reconstruction intervals on image quality and diagnostic accuracy. Eur J Radiol 67(1):92–99

Earls JP, Berman EL, Urban BA et al (2008) Prospectively gated transverse coronary CT angiography versus retrospectively gated helical technique: improved image quality and reduced radiation dose. Radiology 246:742–753

Einstein AJ, Moser KW, Thompson RC, Cerqueira MD, Henzlova MJ (2007) Radiation dose to patients from cardiac diagnostic imaging. Circulation 116:1290–1305

Engelken F, Lembcke A, Hamm B, Dewey M (2009) Determining optimal acquisition parameters for computed tomography coronary angiography: evaluation of a software-assisted, breathhold exam simulation. Acad Radiol 16:239–243

Flohr TG, McCollough CH, Bruder H et al (2006) First performance evaluation of a dual-source CT (DSCT) system. Eur Radiol 16: 256–268

Recommended Reading

Guaricci AI, Schuijf JD, Cademartiri F, Brunetti ND, Montrone D, Maffei E, Tedeschi C, Ieva R, Di Biase L, Midiri M, Macarini L, Di Biase M (2012) Incremental value and safety of oral ivabradine for heart rate reduction in computed tomography coronary angiography. Int J Cardiol 156:28–33

Hoffmann MH, Lessick J, Manzke R et al (2006) Automatic determination of minimal cardiac motion phases for computed tomography imaging: initial experience. Eur Radiol 16:365–373

Horiguchi J, Shen Y, Hirai N et al (2006) Timing on 16-slice scanner and implications for 64-slice cardiac CT: do you start scanning immediately after breath hold? Acad Radiol 13:173–176

Horiguchi J, Fujioka C, Kiguchi M et al (2007) Soft and intermediate plaques in coronary arteries: how accurately can we measure CT attenuation using 64-MDCT? AJR Am J Roentgenol 189:981–988

Hur G, Hong SW, Kim SY et al (2007) Uniform image quality achieved by tube current modulation using SD of attenuation in coronary CT angiography. AJR Am J Roentgenol 189:188–196

Husmann L, Valenta I, Gaemperli O et al (2008) Feasibility of low-dose coronary CT angiography: first experience with prospective ECG-gating. Eur Heart J 29:191–197

Kim DJ, Kim TH, Kim SJ et al (2008) Saline flush effect for enhancement of aorta and coronary arteries at multidetector CT coronary angiography. Radiology 246:110–115

Leber AW, Johnson T, Becker A et al (2007) Diagnostic accuracy of dual-source multi-slice CT-coronary angiography in patients with an intermediate pretest likelihood for coronary artery disease. Eur Heart J 28:2354–2360

Leschka S, Wildermuth S, Boehm T et al (2006) Noninvasive coronary angiography with 64-section CT: effect of average heart rate and heart rate variability on image quality. Radiology 241:378–385

Maffei E, Palumbo AA, Martini C et al (2009) "In-house" pharmacological management for computed tomography coronary angiography: heart rate reduction, timing and safety of different drugs used during patient preparation. Eur Radiol 19(12):2931–2940

Mahesh M, Cody DD (2007) Physics of cardiac imaging with multiple-row detector CT. Radiographics 27:1495–1509

Morin RL, Gerber TC, McCollough CH (2003) Radiation dose in computed tomography of the heart. Circulation 107:917–922

Paul JF, Abada HT (2007) Strategies for reduction of radiation dose in cardiac multislice CT. Eur Radiol 17:2028–2037

Ropers U, Ropers D, Pflederer T et al (2007) Influence of heart rate on the diagnostic accuracy of dual-source computed tomography coronary angiography. J Am Coll Cardiol 50:2393–2398

Schnapauff D, Zimmermann E, Dewey M (2008) Technical and clinical aspects of coronary computed tomography angiography. Semin Ultrasound CT MR 29:167–175

Schuetz GM, Zacharopoulou NM, Schlattmann P, Dewey M (2010) Meta-analysis: noninvasive coronary angiography using computed tomography versus magnetic resonance imaging. Ann Intern Med 152:167–177

Schuhbaeck A, Achenbach S, Layritz C, Eisentopf J, Hecker F, Pflederer T, Gauss S, Rixe J, Kalender W, Daniel WG, Lell M, Ropers D (2013a) Image quality of ultra-low radiation exposure coronary CT angiography with an effective dose <0.1 mSv using high-pitch spiral acquisition and raw data-based iterative reconstruction. Eur Radiol 23(3):597–606

Schuhbaeck A, Schaefer M, Marwan M, Gauss S, Muschiol G, Lell M, Pflederer T, Ropers D, Rixe J, Hamm C, Daniel WG, Achenbach S (2013b) Patient-specific predictors of image noise in coronary CT angiography. J Cardiovasc Comput Tomogr 7(1):39–45

Shapiro MD, Pena AJ, Nichols JH et al (2008) Efficacy of pre-scan beta-blockade and impact of heart rate on image quality in patients undergoing coronary multidetector computed tomography angiography. Eur J Radiol 66(1):37–41

Yoshimura N, Sabir A, Kubo T, Lin PJ, Clouse ME, Hatahu H (2006) Correlation between image noise and body weight in coronary CTA with 16-row MDCT. Acad Radiol 13:324–328

Toshiba Aquilion 64 and Aquilion ONE

E. Zimmermann

Abstract

This chapter outlines how the heart is examined and reconstructed on Toshiba CT scanners.

9a.1 Examination

9a.1.1 Preparation

The patient is positioned on the scanner table in a comfortable supine position with the arms raised above the head and feet first. To image the heart in the isocenter of the scanner, the patient should be positioned slightly to the right side of the table. It is recommended that the 20 or 18-gauge cannula be checked by means of a physiologic saline flush immediately before scanning to avoid contrast extravasation. Care must be taken to remove all foreign materials that can cause image artifacts (e.g., electrocardiography electrodes/cables and other metal-dense foreign bodies) from the scan field. It is also important to make sure that the ECG electrodes make good contact with the patient's skin and that a good R-wave is displayed on the monitor (**Fig**. 9a.1). Details of patient preparation for coronary CT angiography on all scanner types are presented in Chaps. 6 and 8.

9a.1.2 Defining the Scan Range

A low-dose planning scan (scanogram with 50 mA) is obtained on the Aquilion 64, Toshiba's 64-row CT, to define the start and end of the spiral scan, identify the widest dimension of the heart, and place the SureStart (**Figs**. 9a.2, 9a.3, and 9a.4). The start position is placed just above the origins of the coronary arteries, using the left atrial appendage for orientation. The scan ends just below the heart, and can be stopped manually. The SureStart is placed at the start of the spiral scan, by positioning the active line exactly over the upper boundary of the scan as illustrated in **Fig**. 9a.2. The SureStart should not contain the coronary arteries or be placed too high (**Fig**. 9a.4). Careful planning of the scan is essential for achieving an optimal result while minimizing radiation exposure.

M. Dewey, *Cardiac CT*,
DOI 10.1007/978-3-642-41883-9_9,

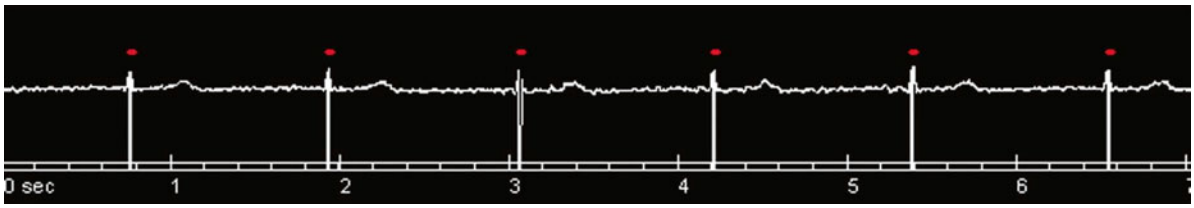

Fig. 9a.1 Illustration of optimal ECG recordings. A clear R-wave and sinus rhythm are essential for reconstruction of the image data. Here, the *red dot* indicates identification of the R-wave. An incorrect R-wave can be removed by clicking on the *red dot* (ECG editing). In patients with arrhythmia, it may be helpful to add "virtual R-waves" by clicking on additional *red dots* or to remove incorrectly identified R-waves. The goal is to obtain a highly regular ECG in order to minimize image artifacts

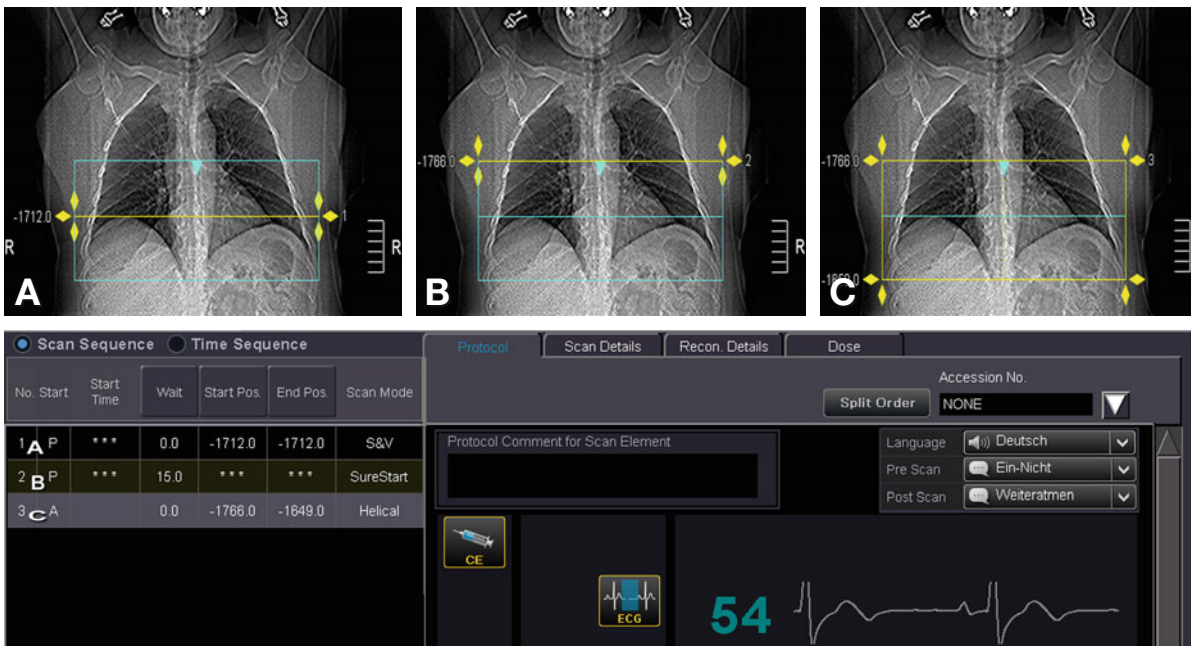

Fig. 9a.2 Planning the acquisition. A planning scan (scanogram) is acquired to identify the greatest circumference of the heart (**Panel A**), position the SureStart (**Panel B**), and define the scan length (**Panel C**) for the subsequent helical coronary examination. *Yellow* indicates the active area, while *blue* indicates inactive areas. As anatomical structures may be displaced as a result of respiratory motion, we recommend defining the start of the scan about 1 cm above the assumed coronary artery origins and the end of the scan about 1 cm below the heart base. **Panel A** shows the positioning of a single slice (low-dose scan, 50 mA) that defines the greatest circumference of the heart. **Panel B** shows the position of another low-dose single slice (50 mA) (**Fig. 9a.4**) that defines the SureStart, which serves to trigger the spiral scan once the desired density threshold has been reached. The scan is automatically started after 15 s. **Panel C** defines the scan length. The start of the spiral scan corresponds to the SureStart position. The tube current for the spiral scan is selected according to the patient's weight and is higher in obese patients to ensure an adequate image quality

9a.1.3 SureStart

Planning the individual scan delay on the Aquilion 64 using the SureStart bolus tracking tool is illustrated in **Fig. 9a.4**. The selected scan plane, just above the origin of the coronary arteries, is chosen to start the scan at the optimal time by monitoring the arrival of the contrast bolus in a region of interest (ROI) placed in the descending aorta (**Fig. 9a.5**). Important landmarks in this plane are the sternum anteriorly and the descending aorta posteriorly. Also seen in this plane are a segment of the pulmonary trunk and a portion of the anterolateral chest wall. The ROI in the descending aorta is used to monitor the increase in Hounsfield units (HU) after initiation of contrast injection.

The scan delay after contrast injection can be determined in one of the two ways: (1) by injection of a test bolus to determine the patient's individual circulation time and optimize the spiral scan parameters accordingly, or (2) by bolus tracking, with automatic

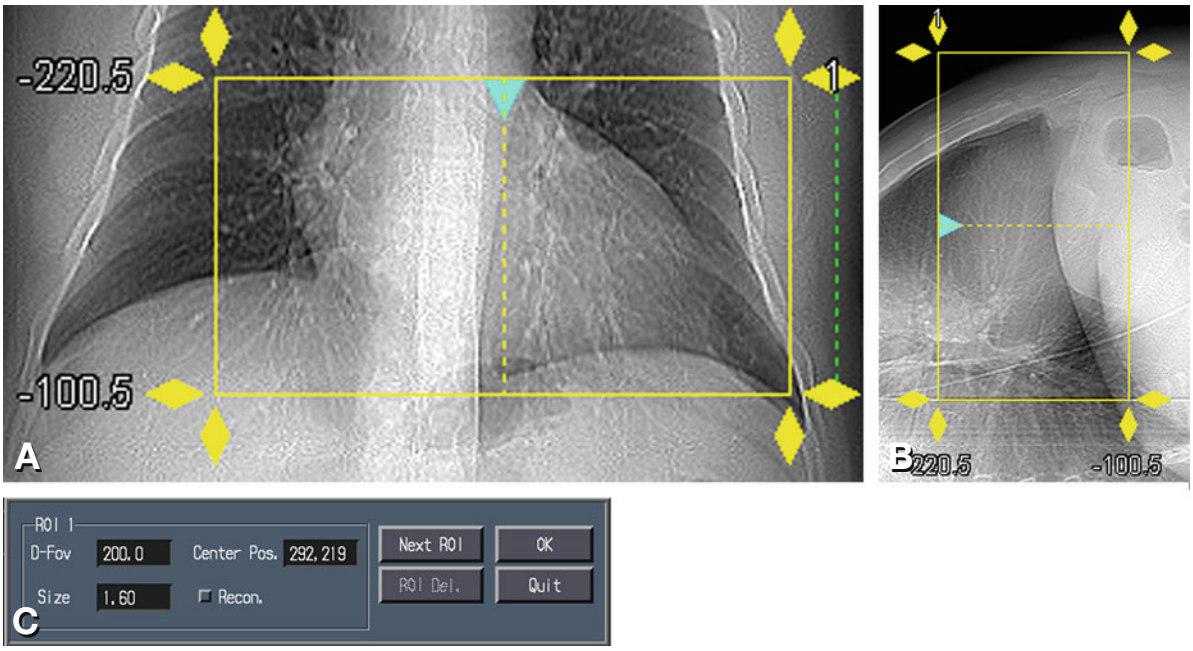

Fig. 9a.3 Defining the FoV. The scan depicting the greatest circumference of the heart seen on the anteroposterior and lateral scanogram (**Panels A** and **B**) is used to define the FoV according to individual heart size, ensuring good image quality at the highest possible spatial resolution. In the majority of patients, the FoV should be about 180 mm (**Panel C**)

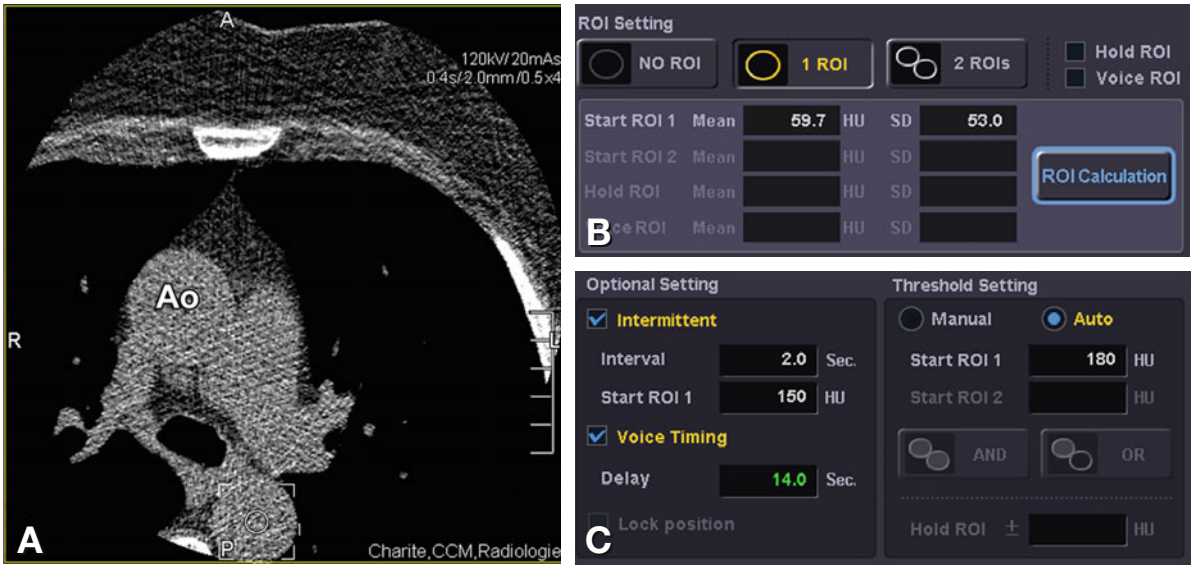

Fig. 9a.4 Planning of the SureStart. Using the SureStart (**Fig. 9a.2**), a ROI is identified in the descending aorta (*circle* in **Panel A**); this region should be neither too large nor too small to avoid mistriggering the spiral scan. The ROI is placed in the descending aorta because there are fewer motion artifacts than in the ascending aorta (Ao). In this way, it is possible to avoid mistriggering of the scan as a result of effects of the superior vena cava, which is opacified very early. Another safeguard is checking attenuation in the ROI (**Panel A**) by clicking on "ROI Calculation" (**Panel B**). An attenuation of about 40–60 HU is optimal. Next, the threshold of 180 HU for starting the scan is defined (**Panel C**), and "Auto" is selected from the menu as the start position. The scan is then automatically started once the 180 HU threshold has been reached. Alternatively, the scan can be started manually by the examiner, on the basis of visual identification of the time of optimal contrast enhancement. Starting the scan manually results in considerable variation in coronary opacification, since the start is influenced by various factors such as individual reaction time and the examiner's level of experience

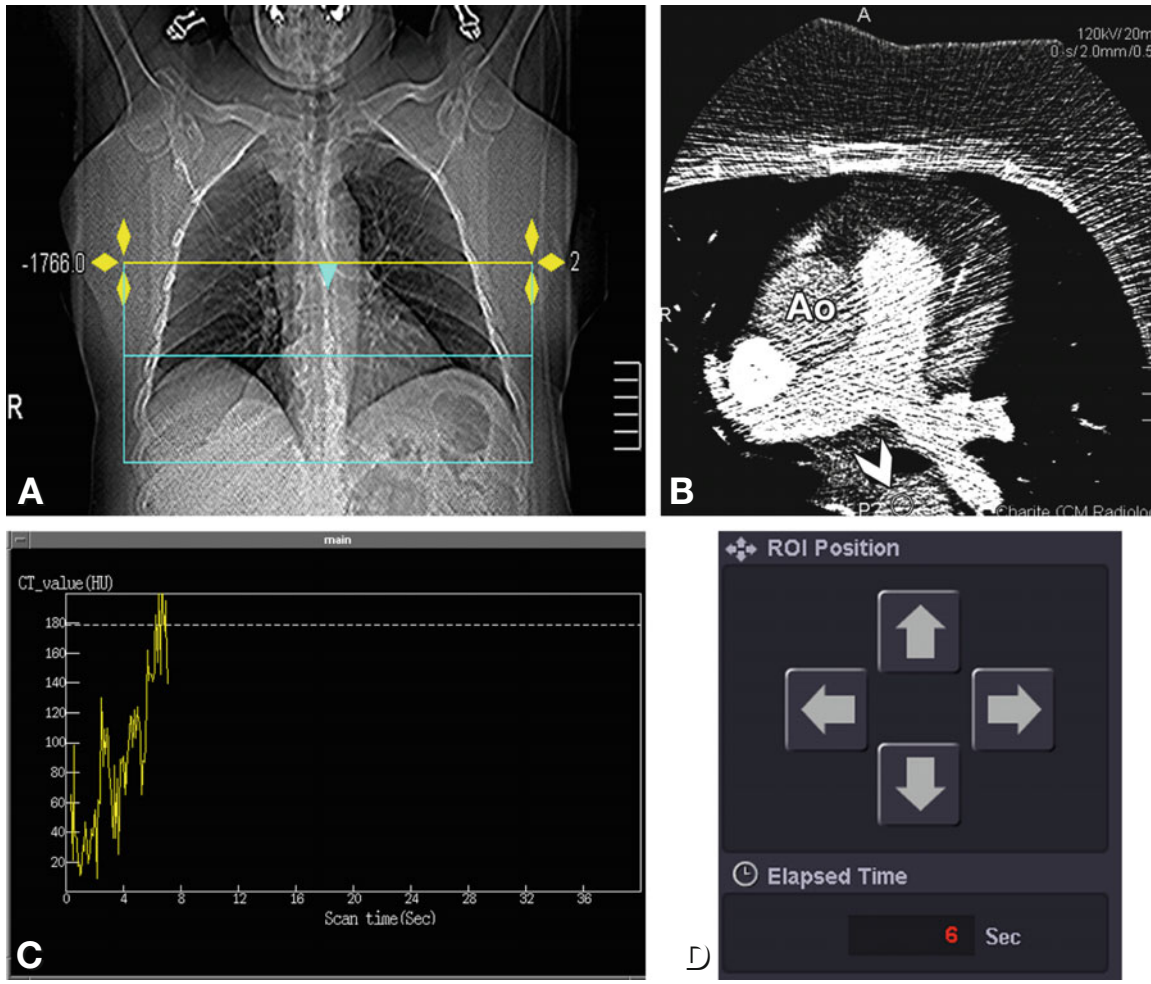

Fig. 9a.5 Start of the helical coronary examination. The position of the SureStart has been defined on the basis of the planning scan (**Panel A**). Next, a continuous low-dose scan (30–50 mA) is acquired at the level of the start of the spiral scan for triggering the spiral scan after IV contrast administration (**Panel B**). Contrast arrival can be tracked in real time. The continuous scan is started not earlier than 15 s after initiation of contrast administration for reasons of radiation protection and to ensure optimal opacification of the target vessels. Contrast arrival is measured in an ROI in the descending aorta (*arrowhead* and *small circle* in **Panel B**). The continuous increase in HU in the ROI over time is represented in **Panel C** in the form of a **graph.** The breathing command starts once the defined threshold of 180 HU has been reached. The scan then starts with a 3-s delay to allow the heart rate to normalize after inspiration. The *arrows* in **Panel D** represent cursor movements and can be clicked to correct the position of the ROI in the descending aorta if necessary and also displayed the elapsed time. *Ao* ascending aorta

triggering of the scan once a predefined Hounsfield threshold has been reached (**Figs.** 9a.4 and 9a.5). Use of the test bolus method increases the total amount of contrast injected and may be inaccurate because the circulation time may vary. Contrast agent injection is usually followed by an automatic 40-ml intravenous saline flush administered at a flow rate of 4 ml s^{-1}, which serves to wash out the right ventricle and improve coronary artery visualization.

Precontrast baseline attenuation is also measured in the descending aorta. In our experience, good results are achieved using a threshold of 180 HU when baseline attenuation is in the range of approximately 30–60 HU. On the basis of our experience, we recommend the use of the SureStart bolus tracking option because it consistently yields good-quality images.

9a.1.4 Breath-Hold Training and Premedication

We recommend sublingual nitroglycerin administration (0.8–1.2 mg) before the breath-hold training. Nitroglycerin dilates the coronary arteries and improves the comparability of the CT findings with those of cardiac catheterization. The effect of nitroglycerin lasts for about 10–30 min. Although nitroglycerin is usually well tolerated, patients should be monitored for the occurrence of possible hemodynamic side effects (e.g., hypotension).

Fig. 9a.6 Breath-hold examination. Breath-hold training is performed by selecting "Breath Ex." from the Scan Details menu. As can be seen in **Panel A**, the default breath-hold time should be 10–12 s for scanning of the coronary arteries. When bypasses are scanned, longer breath-hold periods are needed according to the scan length. The test is started by clicking on "Breath Ex."; the breathing commands that will also be used during the actual scan are then heard. The computer automatically calculates heart rate variability (which should be <10%), the optimal helical pitch (HP), and gantry rotation time. **Panel B** shows a case in which heart rate variability is in the upper normal range (80–92 beats per min). **Panel C** shows the results of a second test at a later time after intravenous beta blocker administration. The result is good, with a heart rate of 50–55 beats per min, and the examination can proceed. **Panel D** shows the results of the breath-hold test: a breath-hold time of 10.8 s, total scan time of 6.4 s, heart rate of 50–55 beats per min, and a recommended HP of 17.1. Other recommended scan parameters are shown in **Panel E**

In our department, we use an automatic speech system for the breathing commands ("Please breathe in and hold your breath"). The required breath-hold period is about 6–30 s, depending on the scanner used and the scan volume. Breath-hold training is done without radiation exposure, and the physician or technician should stand next to the patient to verify that the patient can hold his/her breath in submaximal inspiration for the required period and also to check for possible ECG alterations during inspiration. Toshiba scanners have a special function for breath-hold training. Heart rate variability should be less than 10% to achieve good results (**Fig. 9a.6**). Breath-hold training can be repeated if the ECG is suboptimal. If intravenous beta blocker injection is deemed necessary, it can be done at this stage. Heart rate variability is determined for individual adjustment of scan parameters such as pitch and gantry rotation time. A consistent image quality is achieved in all patients if the tube current is adjusted according to body weight (Chap. 8).

9a.2 Reconstruction

Following acquisition of the CT dataset, a few more steps are necessary to ensure good image quality as a basis for a reliable diagnosis. Motion of the individual coronary arteries, and even of their segments, varies during the different phases of the cardiac cycle. A number of reconstruction algorithms are available to depict the entire coronary arteries without motion. A basic prerequisite, as already mentioned, is sinus rhythm and low heart rate variability during data acquisition. Whether this has been the case during scanning should be verified by checking the ECG before proceeding to the next steps (**Fig. 9a.7**).

Image reconstruction starts automatically after completion of the examination, if this option has been selected in the scan protocol. In our department, we use adaptive multisegment reconstruction in increments of 10 from 0 to 90% of the RR interval if retrospective data have been acquired (**Fig. 9a.7**). Instead of percent-related or millisecond-related reconstructions, one can opt for so-called "BestPhase" and "Systole/Diastole" reconstructions. The "BestPhase" always corresponds to either "Systole" or "Diastole." For "Systole" reconstruction, the systolic phase with the least coronary motion is reconstructed. The same holds true for "Diastole" reconstruction. To reduce storage requirements, one can select "Systole/Diastole" reconstruction alone as the standard option and then, after reviewing the images, retrospectively select individual phases for repeat reconstruction. On the basis of the scan field of view (FoV) selected before the examination, one should then reconstruct the so-called lung and soft tissue windows on large FoVs (**Fig. 9a.8**). It is quite common that accessory pulmonary, soft-tissue, or vascular changes are detected on the noninvasive coronary angiography scans. We use Vitrea workstations for the evaluation of noninvasive coronary angiography and generation of representative images for the patient and referring physician (**Fig. 9a.9**).

9a.3 Aquilion ONE and Aquilion ONE ViSION EDITION

The Aquilion ONE and the Aquilion ONE ViSION EDITION are the 1st and 2nd generation systems of Toshiba's 320-row CT, respectively. The 1st and 2nd generations have a gantry rotation time of 350 and 275 ms, respectively. Both systems enable 16-cm coverage along the Z-axis making them extremely well suited to perform CT examinations of the heart. Since nearly all hearts are smaller than 12 cm, the entire heart can be scanned with a single gantry rotation in the prospective acquisition mode (**Fig. 9a.10**), for the first time enabling scanning of the entire coronary tree with uniform enhancement along the Z-axis at one point in time.

Fig. 9a.7 The reconstruction procedure. **Panel A** shows the ECG, the heart rate [HR (bmp)], and hear rate variability (in this case zero) during scanning. The *red dots* indicate the R-waves identified. In **Panel B**, the reconstruction algorithm can be seen. In our example, we use adaptive multisegment reconstruction and Phase Xact using Best Phase (*arrow*). The "Slice thickness" is 0.5 mm, and the reconstruction interval ("Interval") is 0.5 mm. In addition, "Systole/Diastole" reconstruction can be selected separately using Phase Xact and reconstruction in percentages or ms in the RR interval using CTA. The effective slice thickness and reconstruction interval are the same. The reconstruction FoV should be 180–220 mm for the coronary arteries and 320 mm for lung/soft tissue reconstruction (**Panel B**, *bottom right*). To send the images to the archive or a workstation, click on the "Transfer off" button to activate the transfer ("Transfer on") and select the target. The reconstructed segment is indicated in **Panel C** (*bottom right*), and any reconstructed image can be selected from a list (**Panel C**, *left part*). Finally, click on "Reconstruction" (*arrow*) to start the reconstruction (**Panel D**)

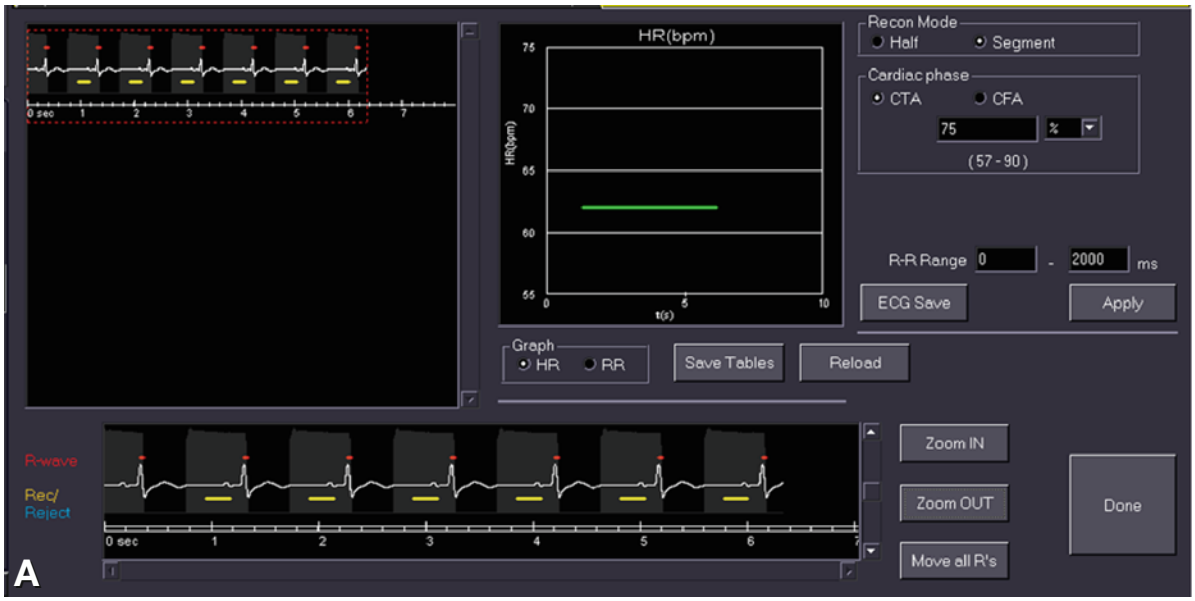
HR(bpm)
Recon Mode
Half
Segment
Cardiac phase
CTA
CFA
75
%
(57 - 90)
R-R Range
0
2000
ms
ECG Save
Apply
Graph
HR
RR
Save Tables
Reload
R-wave
Rec/
Reject
Zoom IN
Zoom OUT
Move all R's
Done
A

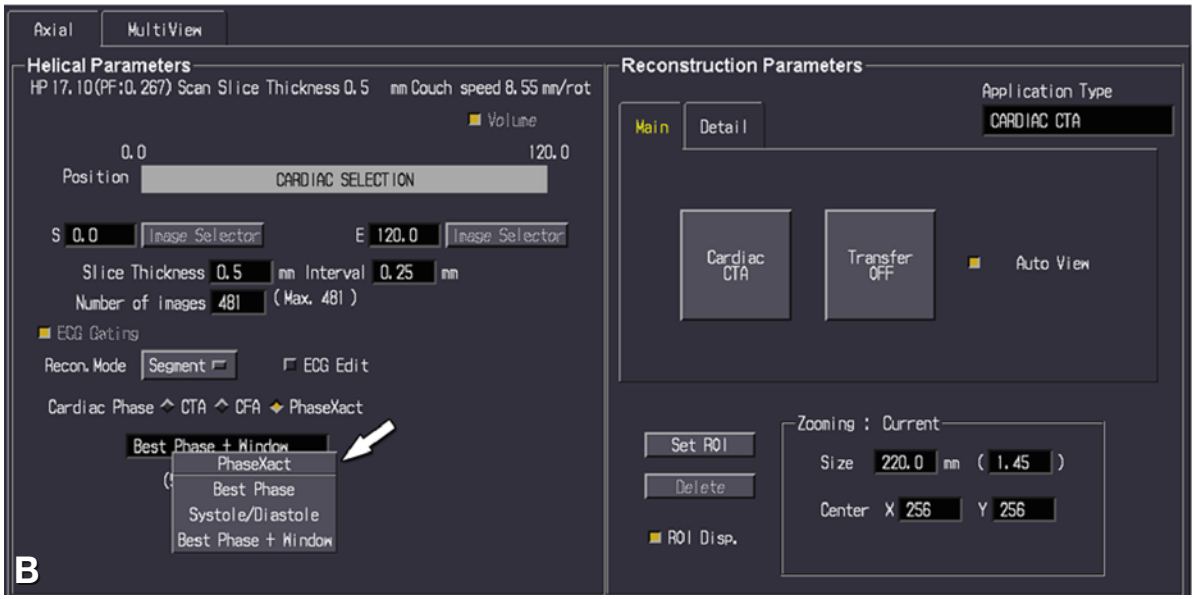
Axial
MultiView
Helical Parameters
HP 17.10(PF:0.267) Scan Slice Thickness 0.5 mm Couch speed 8.55 mm/rot
Volume
0.0
120.0
Position
CARDIAC SELECTION
S 0.0
Image Selector
E 120.0
Image Selector
Slice Thickness 0.5 mm Interval 0.25 mm
Number of images 481 (Max. 481)
ECG Gating
Recon. Mode
Segment
ECG Edit
Cardiac Phase CTA CFA PhaseXact
Best Phase + Window
PhaseXact
Best Phase
Systole/Diastole
Best Phase + Window
Reconstruction Parameters
Main
Detail
Application Type
CARDIAC CTA
Cardiac CTA
Transfer OFF
Auto View
Set ROI
Delete
ROI Disp.
Zooming : Current
Size 220.0 mm (1.45)
Center X 256 Y 256
B

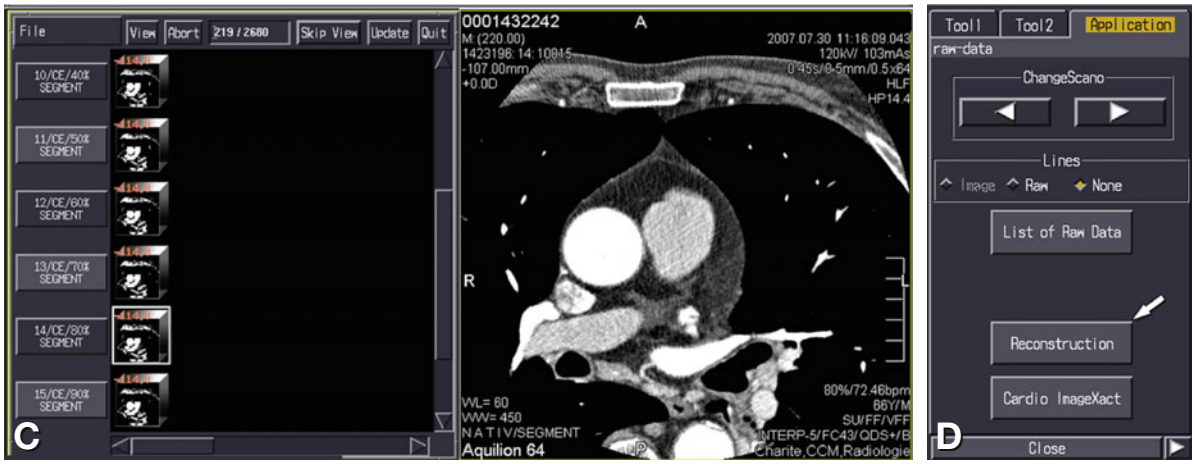
File
View
Abort
219 / 2680
Skip View
Update
Quit
10/CE/40% SEGMENT
11/CE/50% SEGMENT
12/CE/60% SEGMENT
13/CE/70% SEGMENT
14/CE/80% SEGMENT
15/CE/90% SEGMENT
C
0001432242
A
2007.07.30 11:16:09.043
120kV/ 103mAs
HP14.4
R
WL= 60
WW= 450
NATIVE/SEGMENT
Aquilion 64
Tool1
Tool2
Application
raw-data
ChangeScano
Lines
Image
Raw
None
List of Raw Data
Reconstruction
Cardio ImageXact
Close
D

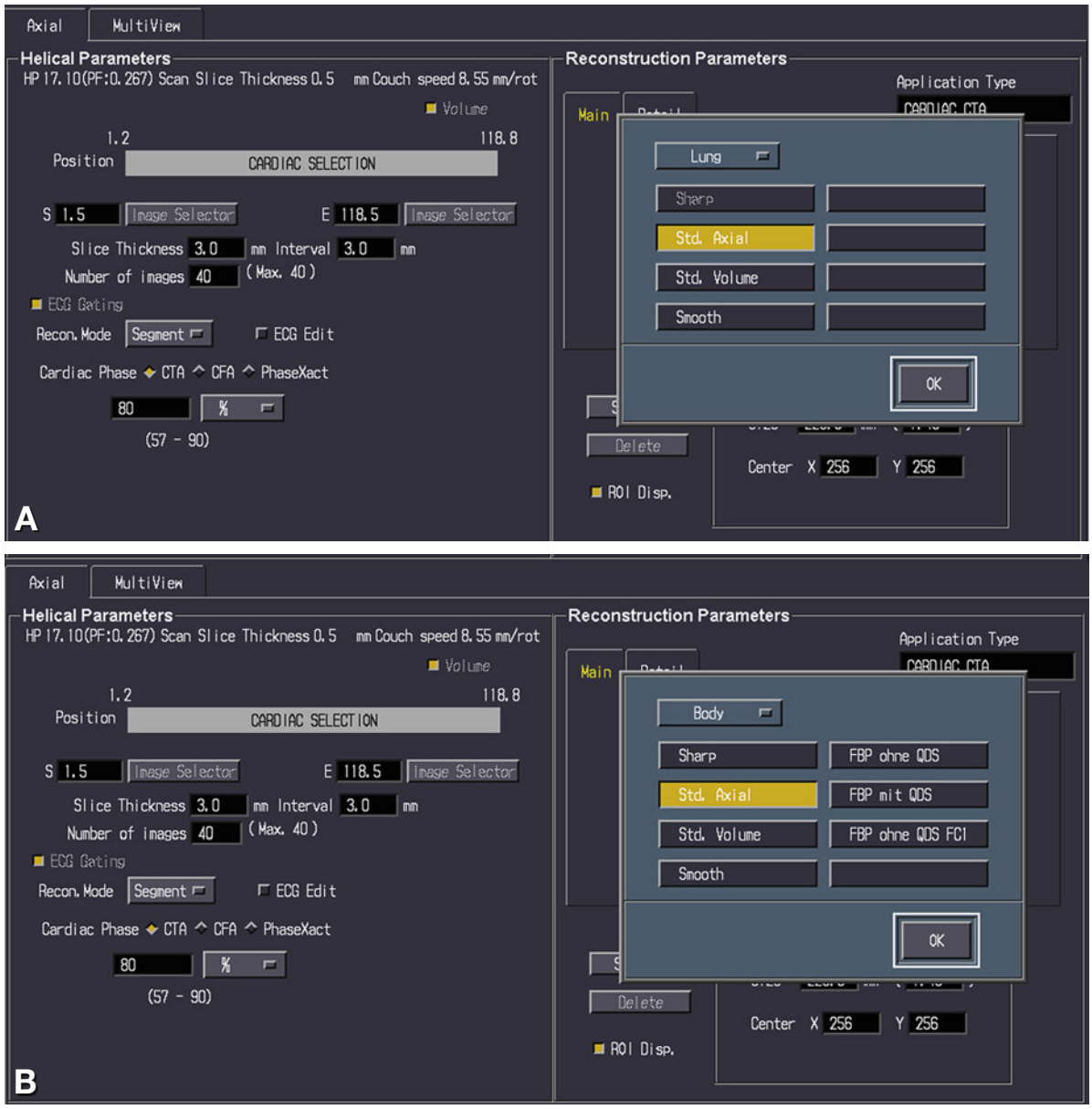

Fig. 9a.8 Reconstruction of lung and soft tissue windows. The lung window (**Panel A**) and soft tissue window (**Panel B**) are reconstructed on large FoVs with a "Slice thickness" of 3 mm and an "Interval" of 3 mm at 80% of the RR interval and are selected by clicking on "Lung Std. Axial" and "Body Std. Axial," respectively. Again, reconstruction is started by clicking on "Reconstruction" (**Fig. 9a.7**)

9a.3.1 Preparation

Patient preparation is nearly the same as described above and is of crucial importance for obtaining a good scan with low effective dose with the 320-row CT system as well. As with other CT scanners, a low heart rate is pivotal for good image quality. The 320-row system enables acquisition of a cardiac CT scan in a single heartbeat, which minimizes radiation exposure.

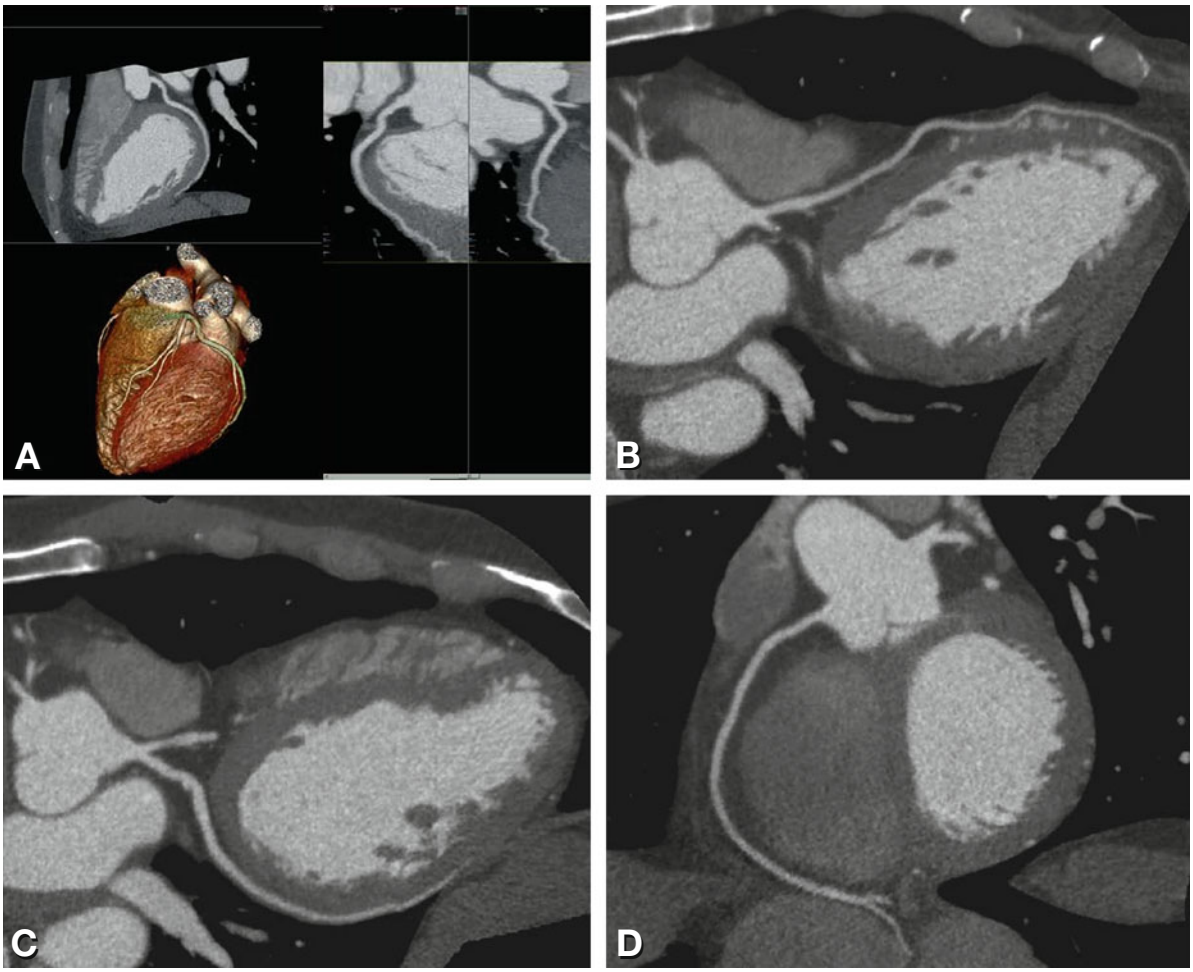

Fig. 9a.9 Reconstruction examples: Three-dimensional reconstructions of the heart are well suited for demonstrating the most important findings. The heart can be rotated to allow viewing from any direction (**Panel A**). An automatic tool identifies a vessel and traces a path along its course for generation of a curved multiplanar reformation (MPR, *right upper corner* in **Panel A**) or cath view (*left upper corner* in **Panel A**). On both the MPR and the cath view, the vessel is straightened and displayed in one plane. **Panel B** shows the curved MPR of the left anterior descending coronary artery (LAD). MPR is a fast and easy reconstruction method that provides good image quality and is very helpful in detecting and quantifying coronary stenosis. **Panel C** shows the curved MPR of the left circumflex coronary artery (LCX). **Panel D** shows the MPR of the right coronary artery (RCA)

9a.3.2 The Role of the Cone Beam for Defining the Scan Range

The 15.2° cone angle of 320-row CT and the resulting cylindrical shape of the acquired volume makes it more difficult to plan the CT angiogram scan range from the scanogram alone (anteroposterior and lateral) compared with conventional CT scanners. The heart must lie in the center of the scan field (Chap. 8). The volume acquired with the 15.2° scan angle does not cover the cranial and caudal portions of the heart with a maximal axial field of view (**Fig. 9a.10**). The effects of the cone angle are best illustrated with the aid of coronal reconstructions (**Fig. 9a.11**). The resulting truncation of the volume was reduced with the software VolumeXact+by 75% (**Fig. 9a.12**) which greatly facilitates planning of the coronary acquisition.

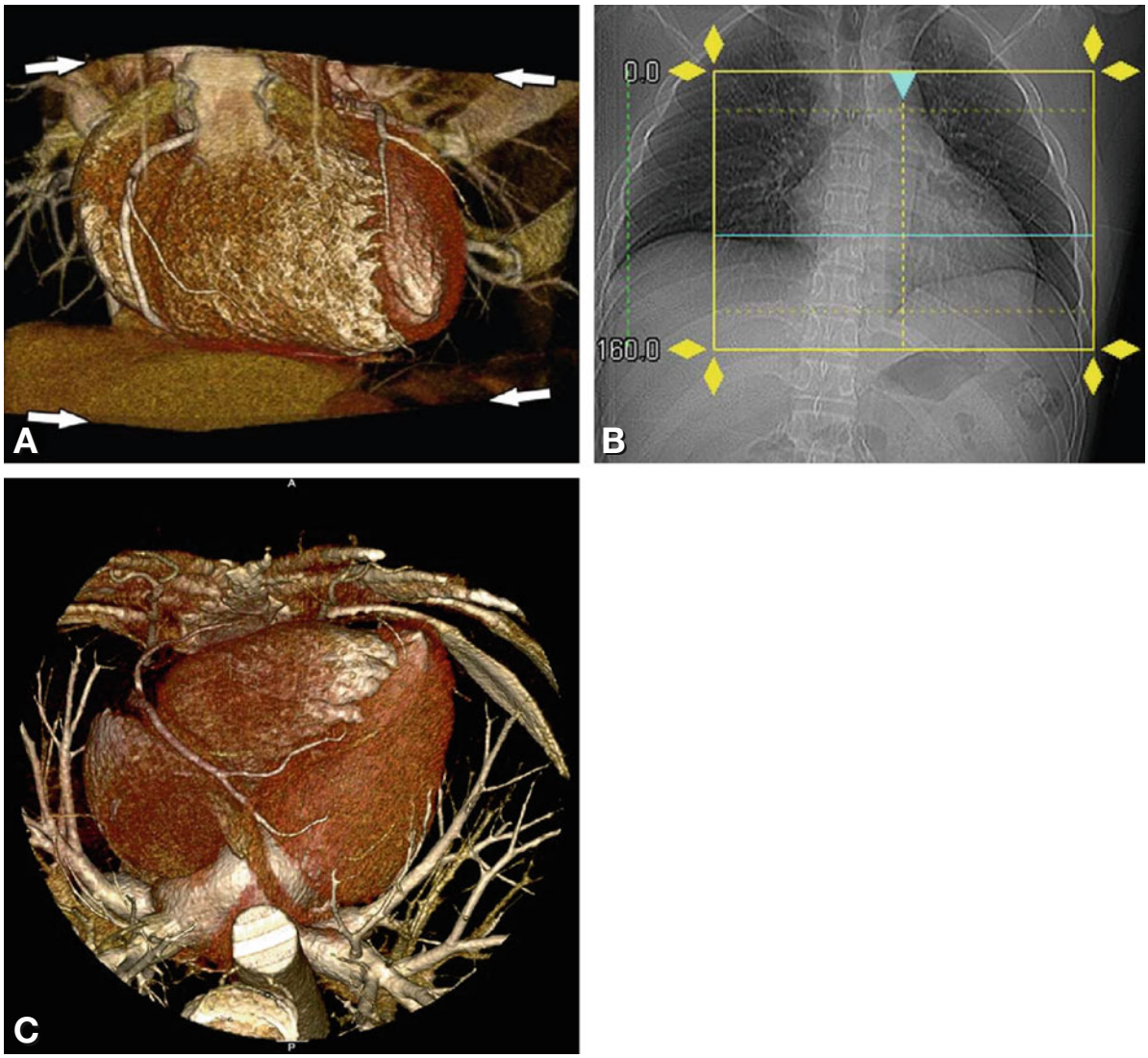

Fig. 9a.10 Imaging of the entire heart with a single gantry rotation using 320-row CT. Nearly all hearts are smaller than 12 cm and can be completely scanned with a single gantry rotation using less than 320 simultaneous rows. The challenge of coronary CT angiography is to obtain good image quality with a minimum of radiation exposure. If the heart is not positioned in the center of the scan field (**Panel A**), there is the risk of "cutting off" cranial or caudal cardiac or coronary portions, and a stenosis of the left main coronary artery, for example, may be overlooked. **Panel A** is an anterior three-dimensional reconstruction of the heart, showing narrowing of the scan volume at the cranial and caudal ends (*arrows*) using 320-row CT; these portions cannot be reconstructed with the maximum axial FoV. **Panel B** shows a caudal three-dimensional reconstruction of the same heart. **Panel C** is the corresponding anteroposterior scanogram, illustrating the difficulty of exactly determining the heart size using only this image. The yellow rectangle indicates the scan range in the Z-axis. Note the two vertical broken yellow lines, which outline the scan length imaged with the maximum axial FoV

Fig. 9a.11 Effects of the 15.2° cone angle of 320-row CT. The 16-cm detector width of 320-row CT results in a cone angle of 15.2° (*arrows* in **Panel A**). It is important to correctly position the patient to preclude incomplete visualization of the target anatomy. **Panels A**, **C**, and **E** show coronal reconstructions of a properly positioned heart. The red horizontal lines in **Panels A**, **C**, and **E** indicate the positions of the corresponding axial slices (**Panels B**, **D**, and **F**). The left main coronary artery is depicted in the center in one of the cranial slices with a maximum axial FoV (**Panel B**). As a result, all four cardiac chambers are fully depicted at the level of the widest dimension of the heart in coronal (**Panel C**) and axial (**Panel D**) planes. The basal portions are also depicted in the center and with a maximum FoV (**Panels E** and **F**). *Ao* aorta, *DA* descending aorta, *LV* left ventricle, *RV* right ventricle

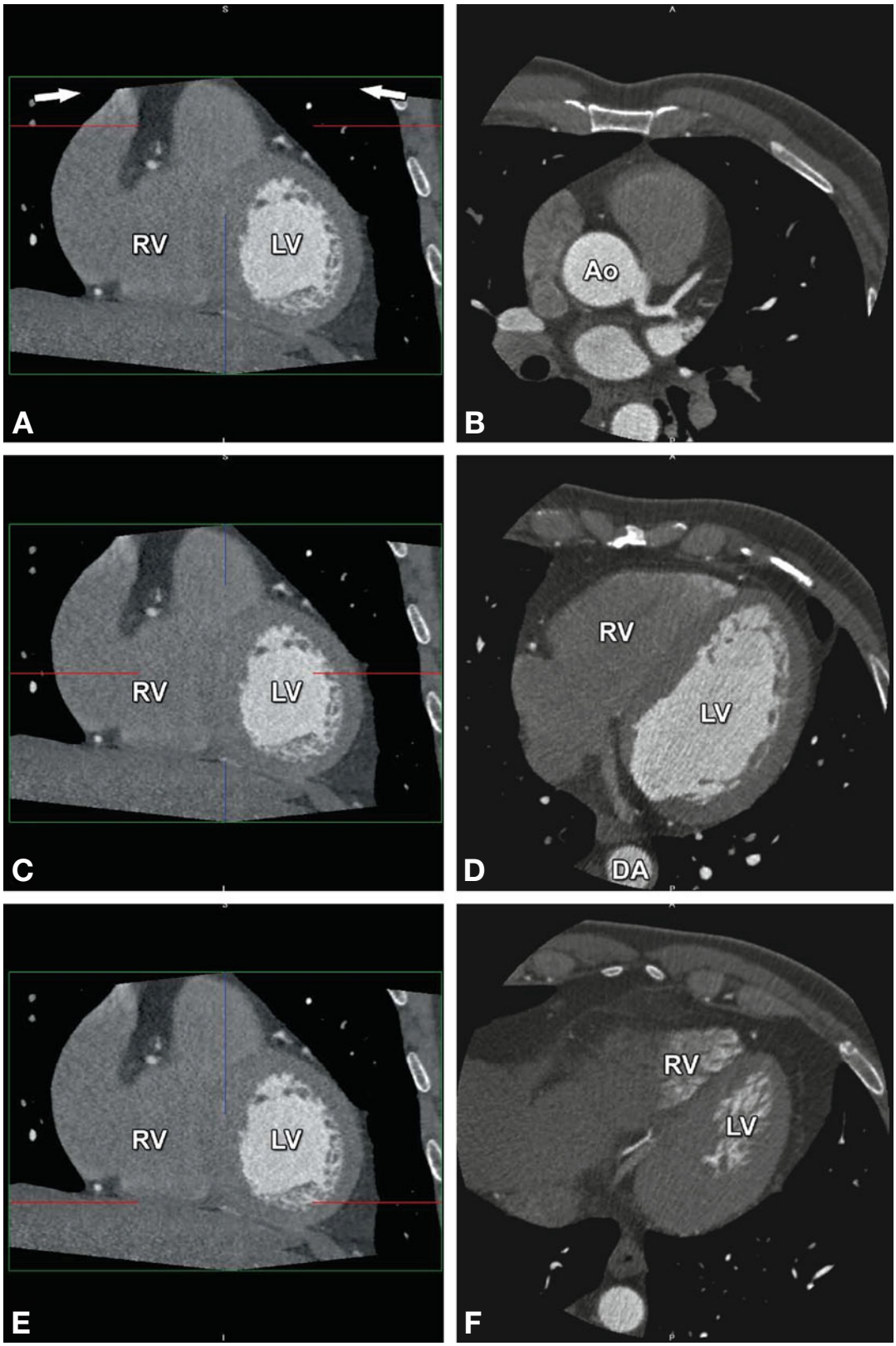
RV
LV
A
Ao
B
RV
LV
C
RV
LV
DA
D
RV
LV
E
RV
LV
F

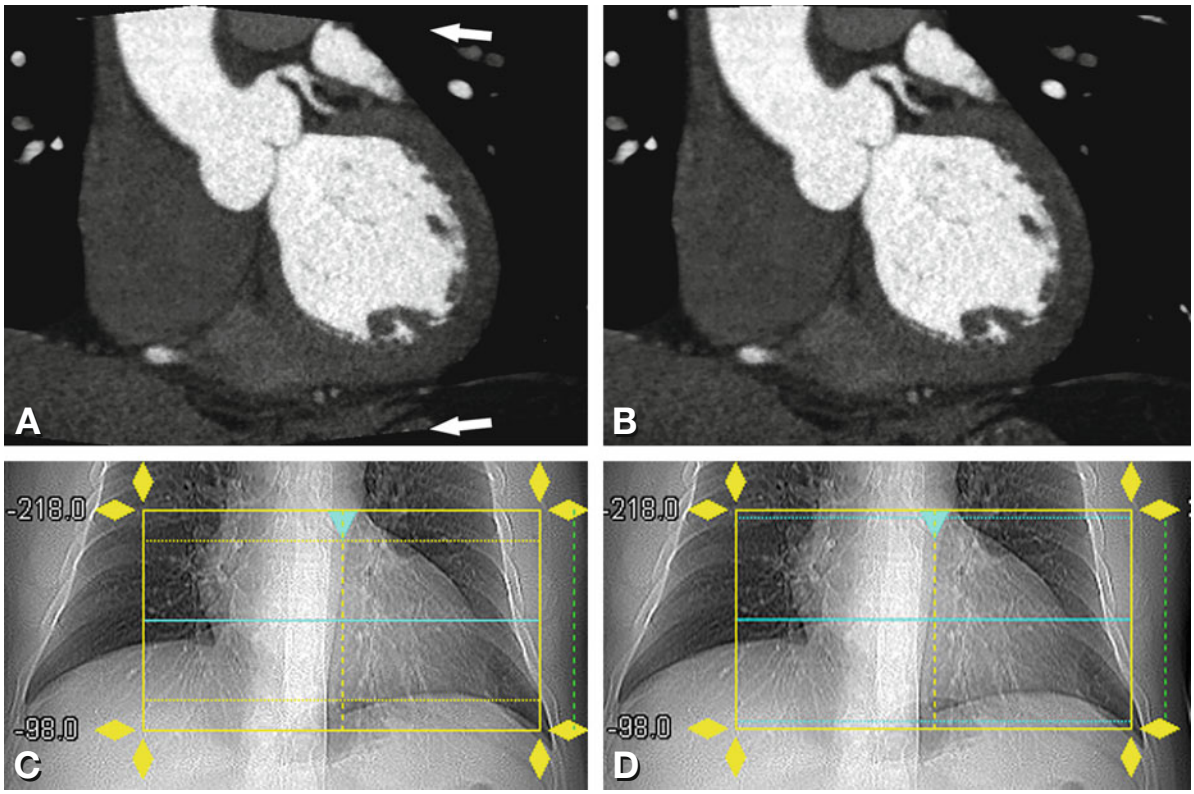

Fig. 9a.12 Reduced truncation of the cylindrical volume obtained with 320-row CT shown on coronal reformations. Using VolumeXact + for reconstruction it is possible to reduce the truncation (**Panel A**) of the volume dataset (which occurs with the ConeXact reconstruction based on the cone angle of 15.2° *arrows*, see **Fig. 9a.11**) by about 75% (**Panel B**). VolumeXact + with less truncation therefore greatly facilitates the planning process based on the scanograms (**Panels C** and **D**)

9a.3.3 Planning the Scan Range Using a Calcium Scan

A low-dose scanogram in two planes is acquired to define the proximal and distal ends of the low-dose calcium scan (**Fig. 9a.10**). The unenhanced axial slices of the calcium scan are used to individually plan the final length of the cardiac CT angiogram (**Fig. 9a.13**). Estimating individual heart size and planning the length of the CT scan in the Z-axis are much more difficult from the scanogram. Errors in planning may result in overestimation of the scan range required to cover the target anatomy, which may lead to unnecessary radiation exposure, or in underestimation with failure to capture the proximal or distal portions of the coronary arteries. **Fig. 9a.14** illustrates how the scan range is adjusted to the patient's heart size.

Fig. 9a.13 Planning the 320-row CT angiogram from a low-dose calcium scan. Individual adjustment of the scan length of a cardiac CT angiogram to the patient's heart size can reduce the radiation exposure compared with the full 16-cm scan range in the z-direction. The heart size is determined from the axial slices of the calcium scan. The slice containing the most cranial segment of the coronary arteries, typically the left main coronary artery, is identified (**Panel A**). **Panel B** shows the slice with the anatomic landmark (aortic root with the left main coronary artery and the proximal segments of the left anterior descending and left circumflex coronary arteries) coded in green. The widest dimension of the heart is shown in **Panel C**. **Panel D** shows the four cardiac chambers, which are difficult to delineate on unenhanced scans, in green. The red dot is a cross-section of the RCA (**Panel D**). Next, the slice containing the most caudal portion of the heart is identified (**Panel E**), which is typically the apex of the heart (**Panel F**). To accommodate variations in the position of the heart with the phase of the respiratory cycle at which a patient holds his or her breath, an additional 10–15 mm are added at either end of the calculated scan length for the CT angiography. If the variation in inspiration depth is not taken into account, there is a risk of missing portions of the target anatomy despite accurate planning of the scan length. *Ao* aorta, *DA* descending aorta, *LV* left ventricle, *RV* right ventricle

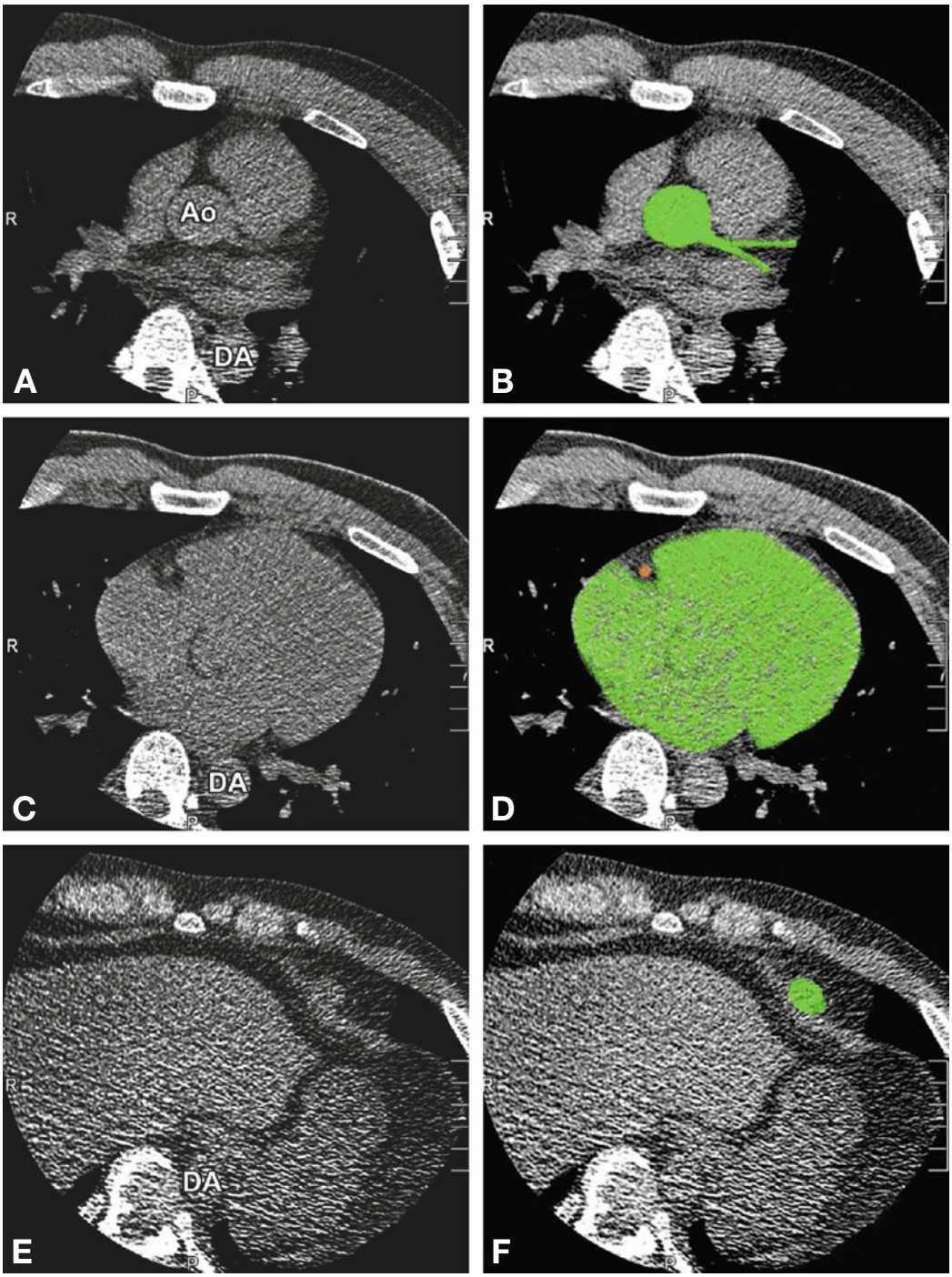
Ao
DA
A
B
DA
C
D
DA
E
F

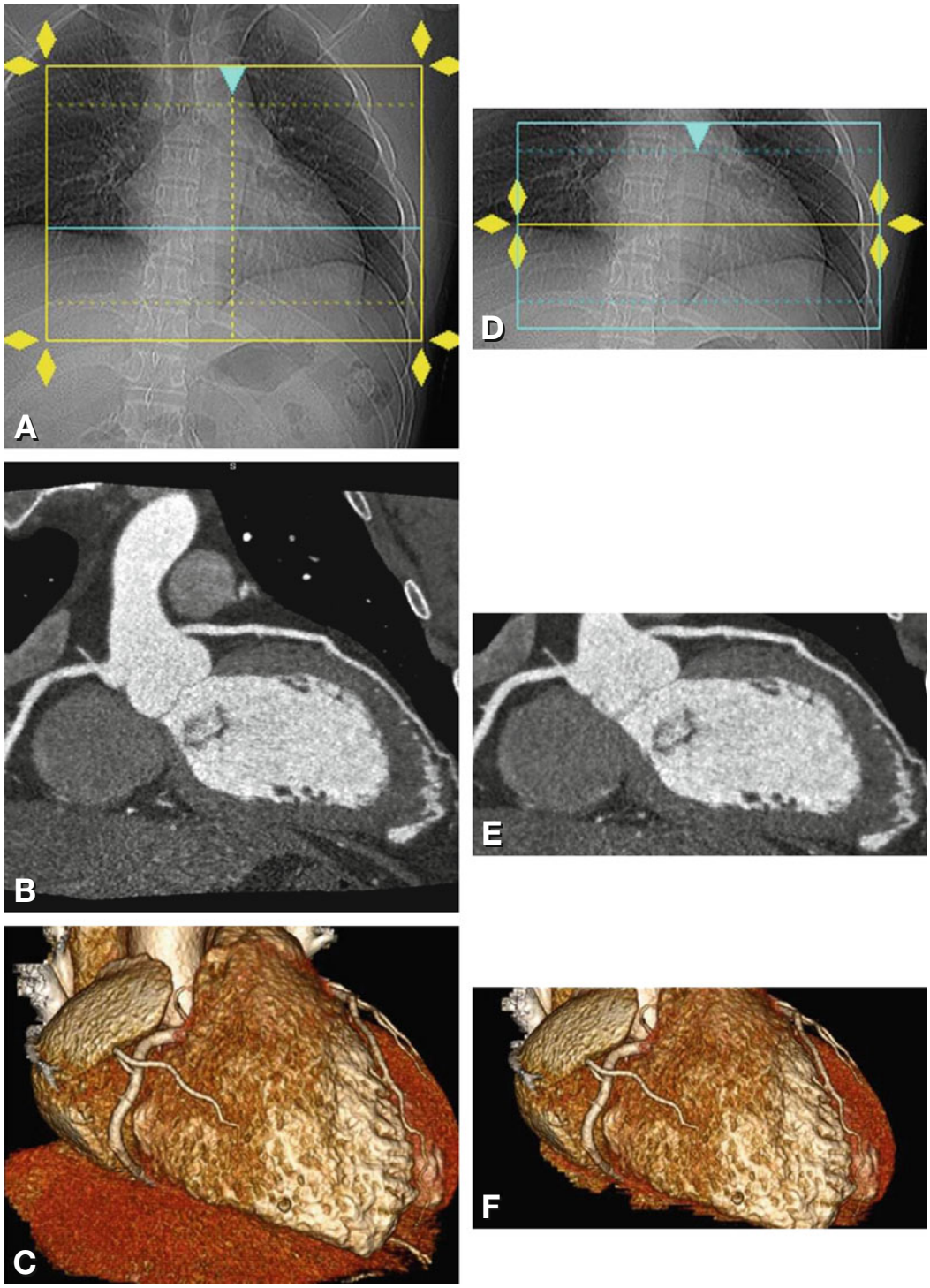

Fig. 9a.14 Comparison of the full 16-cm scan range of 320-row CT angiography with the scan range adjusted to individual heart size. **Panel A** shows how the 16-cm scan range is planned using a scanogram. In the same patient, the scan range was also planned on the basis of the actual heart size determined using a low-dose calcium scan (**Panel D**). The coronal (**Panels B** and **E**) and three-dimensional reconstructions (**Panels C** and **F**) nicely illustrate the effects of a meaningful limitation of the scan range, which allows a marked reduction of the radiation exposure

9a.3.4 SureStart

The 320-row CT system has the so-called Fast SureStart option (**Fig. 9a.15**) which allows initiation of the cardiac CT scan within 1 s after reaching the predefined threshold in the descending aorta. The SureStart protocol and contrast agent injection are started simultaneously, and acquisition of a low-dose monitoring scan starts after 10 s and is presented online. After another 4 s, the breathing command is given ("Please breathe in and

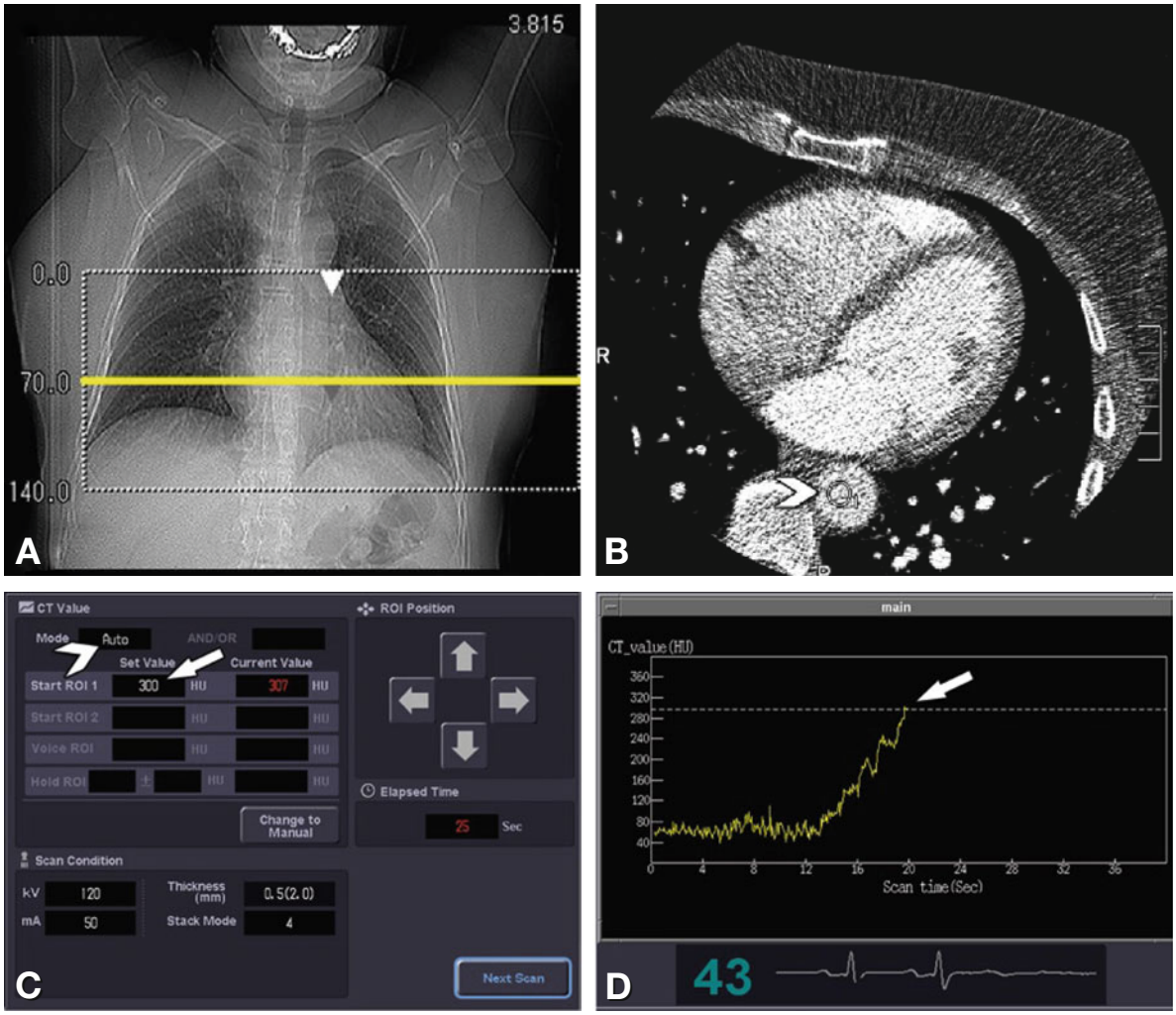

Fig. 9a.15 SureStart for 320-row CT. The low-dose scanogram is used to position the axial monitoring slice (**Panel B**) in the center of the scan area (Z-axis) (**Panel A**). This slice (**Panel B**) is used for real-time monitoring of the inflowing contrast agent, which can be followed on its passage from the right atrium and ventricle to the left atrium and ventricle, and to the thoracic aorta. The CT angiogram can be started automatically or manually. (1) Automatically starting the CT angiogram after a predefined attenuation threshold (HU) has been reached. Arrival of the contrast agent is measured in a region of interest (ROI) in the descending aorta (*arrowhead*) (**Panel B**). The ROI can be displaced from the aorta by respiratory motion while the SureStart scan is running, which must be corrected in order not to miss the optimal time for starting the CT angiogram. The position of the ROI (**Panel B**, *arrowhead*) can be corrected with the cursor (**Panel C**, *right*). When the predefined threshold is exceeded (**Panel C**, *arrow*), the scan is started automatically. The increase in HU measured in the descending aorta is presented online in the form of a Hounsfield unit curve, which serves as a control of contrast administration (**Panel D**). If the threshold is not reached, the scan can be started manually by clicking on the "Next Scan" button (**Panel C**). (2) Alternatively, the manual start option can be selected. When this option has been chosen, the user visually follows the inflow of the contrast agent on the monitor (**Panel B**) to start the scan. For this option, no threshold or ROI need to be defined. The scan mode is selected via the "Mode" button ("Auto" or "Manual," **Panel C**, *arrowhead*). In the manual mode, the CT angiogram is started by clicking on the "Next Scan" button (**Panel C**). The manual start option depends on the skills and experience of the operator but has a greater potential for reducing the amount of contrast agent administered. An optimal time point for starting the scan (automatically or manually) has been reached when there is good enhancement of the left ventricle and aorta and most of the contrast agent has been washed from the right ventricle (**Panel B**)

hold your breath"), which lasts 4 s. The breathing command is followed by a 2-s delay, which is necessary to allow the heart rate to normalize following the slight increase that may be induced by inspiration. This means that there is a delay of at least 20 s after the start of contrast injection before the cardiac CT scan can be started. In patients with a normal circulation time, optimal enhancement of the cardiac chambers will be seen after about 20–25 s. The amount of contrast agent is adjusted to the patient's body weight and ranges from 60 to 80 ml (administered at a flow rate of 3.5–5 ml/s), followed by a 40-ml saline chaser administered at the same flow rate, which serves to accelerate washout from the right ventricle.

The axial contrast agent monitoring slice for the SureStart protocol is defined on the basis of a scanogram. This axial slice provides an overview and is presented on the screen for real-time monitoring of the inflow of contrast agent into the right atrium and ventricle and its further passage into the left atrium and ventricle and the thoracic aorta. The optimal time for starting the CT angiogram is when most of the contrast agent has left the right ventricle and there is good enhancement of the left ventricle and aorta. Two options are available for starting the CT angiogram: (1) automatic start after a predefined Hounsfield threshold has been reached in the descending aorta (e.g., 300 HU) or (2) manual start based on visual assessment of enhancement in the cardiac chambers. **Fig. 9a.15** illustrates the individual steps of planning the CT scan and using the SureStart option.

9a.3.5 Scan Modes

The scan mode (**Fig. 9a.16**), so-called "Target CTA," allows the user to determine the radiation exposure before the scan by defining the number of beats to be used for data acquisition. However, this scan mode does not allow automatic arrhythmia control. The user also defines the center position of the exposure window in relation to the RR target phase in Target CTA (e.g., 75% of the RR interval) before the scan starts. The exposure window defines the duration of radiation exposure.

Unlike Target CTA, "Prospective CTA" allows arrhythmia control, which is why a maximum radiation exposure threshold cannot be defined beforehand. The individual heart rate registered during breath-hold training (SureCardio) serves to define the number of beats to be used for the prospective CTA scan, the exposure time, and the center position of the exposure window in relation to the RR interval.

Cardiac function analysis (CFA) can be done using one of two scan modes: (1) identical mA (CTA/CFA Cont.) for the entire scan, ensuring a constant image quality for both CTA and CFA or (2) modulated scan mode (CTA/CFA Mod.) with variable mA (high during diastole and 25% of this value during the other cardiac phases), resulting in a reduction of the effective dose (**Fig. 9a.16**).

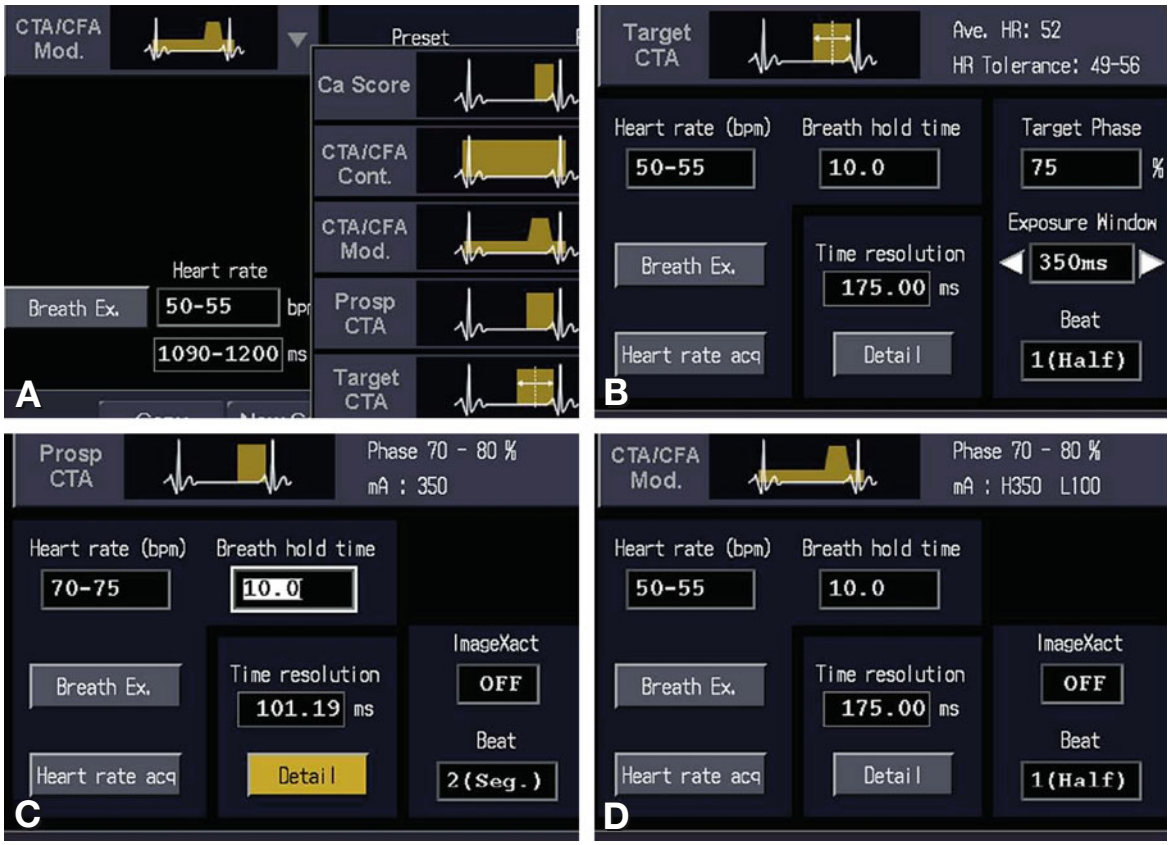

Fig. 9a.16 Scan modes available on the 320-row CT system. Select "Scan details" from the menu to make changes to the scan modes for each examination (**Panel A**). "Target CTA" (**Panel B**) is a scan mode allowing the user to define the number of beats and the target phase (position of the exposure window in relation to the RR interval) before the examination. Heart rate tolerance refers to the range of heart rates for which image reconstruction will be possible. Target CTA does not provide automatic arrhythmia control but sets an upper limit for radiation exposure. In contrast, "Prospective CTA" (**Panel C**) is a scan mode that automatically adjusts the examination to individual variations in heart rate and allows arrhythmia control. The number of beats (2 in the example in **Panel C**) depends on the heart rate recorded during breath-hold training (70–75), and the exact position of the triggered phase (70–80%) is determined online on the basis of the last five heartbeats (real time beat control). Cardiac function analysis (CFA) modulates radiation exposure during different phases of the RR interval (**Panel D**). For the phase of the RR interval deemed favorable for CT angiography, a higher mA is used to ensure good image quality, while mA is reduced to 25% for the remainder of the RR interval. This mode allows evaluation of the coronary arteries with simultaneous functional analysis at a reduced radiation exposure. The number of beats for CFA also depends on the patient's heart rate

9a.3.6 Selection of mA and kV

Using recent software on the 320-row CT scanners both optimal mA and kV are suggested by the Sure Exposure 3D based on patient size information derived from the scanogram (**Fig. 9a.17**). This suggestion incorporates whether filtered back projection or iterative reconstruction (AIDR) will be used and helps to better individually adjust the scan parameters to the patient dimensions.

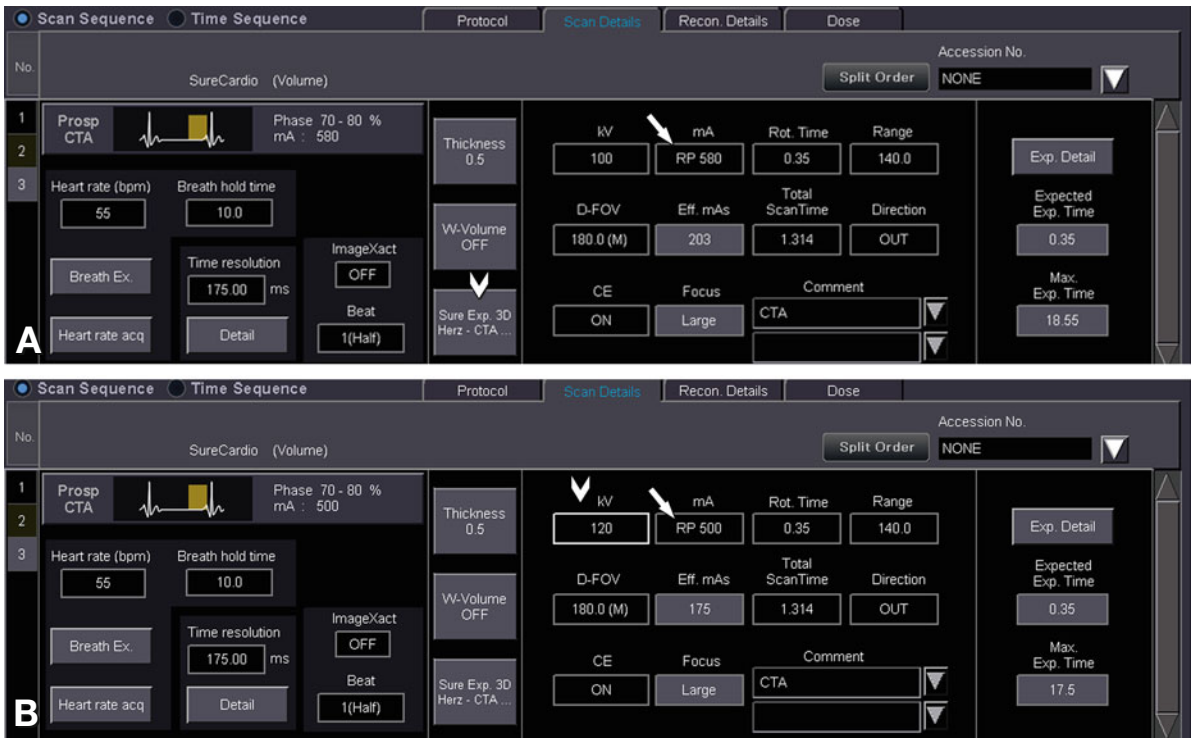

Fig. 9a.17 Selection of mA and kV. After selecting a cardiac CTA protocol, which regularly contains all parameters to ensure optimal image quality for this examination, i.e. an automatic exposure control (Sure Exp. 3D, *arrowhead* in **Panel A**) and the appropriate reconstruction algorithm (AIDR 3D standard, FC03), 100 kV can be used as the standard voltage. The resulting mA (580) for this patient is displayed in the mA field (*arrow* in **Panel A**). If the mA value reaches 580 mA (for Aquilion ONE, and 900 mA for Aquilion ONE ViSION) the operator should change the tube voltage setting manually to 120 kv (*arrowhead* in **Panel B**) to ensure that the current (now 500 mA at 120 kV) is not limited by the generator (*arrow* in **Panel B**). This will guarantee a constant signal-to-noise ratio. Is the suggested mA value rather low using 100 kV, also manually entering 80 kV is possible in order to reduce dose as low as reasonable achievable

Siemens Somatom Sensation, Definition, and Definition Flash

H.-C. Becker, C. Klessen, and K. Anders

Abstract

This chapter describes the scan acquisition and image reconstruction of cardiac CT data sets on Siemens scanners.

9b.1 Preparing the Examination

The vendor recommends performing coronary angiography with the patient in a supine head-first position. Nevertheless, scanning the patient in feet-first position has some advantages: The patient is easier to monitor and can be accessed more quickly in case of an emergency (e.g., contrast medium intolerance or extravasation). Moreover, it is easier to administer intravenous beta blockers or nitroglycerin spray and other medications. Note, however, that the speakers for giving any instructions are at the back of the gantry. Thus, the volume must be turned up when examining patients in the feet-first position, especially if they are hard of hearing.

It is important to place the ECG electrodes outside the scan area to reduce image artifacts. Correct electrode placement is illustrated in **Fig. 9b.1**. Moreover, with the Somatom Sensation as well as the Definition CT scanners the ECG electrodes must be in place before the scan protocol is called up in order for the software to recognize the ECG signal. Particular attention should be paid to placing the connector of the ECG leads outside the scan range. Else, there is a potential risk of inducing currents in the connector while the X-ray beam is passing over it. As such induced currents are excessively higher in voltage than the signal from the heart, the ECG trace may be degraded by artificial spikes, making it useless for image reconstruction.

Details of patient preparation for coronary CT angiography on all scanner types are presented in Chaps. 7 and 9.

9b.2 Image Acquisition

Acquisition of a conventional chest topogram (**Fig. 9b.2**) may be followed by planning and acquiring two axial control scans (**Fig. 9b.3**). The first control scan is acquired in the plane with the largest transverse extension of the heart and serves to optimize the field of view for the subsequent CT angiogram (**Fig. 9b.3**). Bi-plane topograms in the anteroposterior and lateral projections allow adjustment of the table height to make sure that the patient's heart is positioned in the center of the gantry, where the spatial and temporal resolution in the image are highest.

The second control scan is obtained to select the scan position for test bolus acquisition (**Fig. 9b.3**). The subsequent test bolus scan consists of a series of images acquired at a rate of one image every 1–2 s (**Fig. 9b.4**). The test bolus consists of 10–15 ml of iodine-based contrast medium, followed by a 30–50-ml saline flush (injection rate: 5 ml s^{-1}) in normal-weight patients. Radiation exposure is minimized by starting the scan 10–15 s after injection and stopping acquisition once the contrast medium peak has been reached. A dedicated software

M. Dewey, *Cardiac CT*,
DOI 10.1007/978-3-642-41883-9_10, © Springer-Verlag Berlin Heidelberg 2014

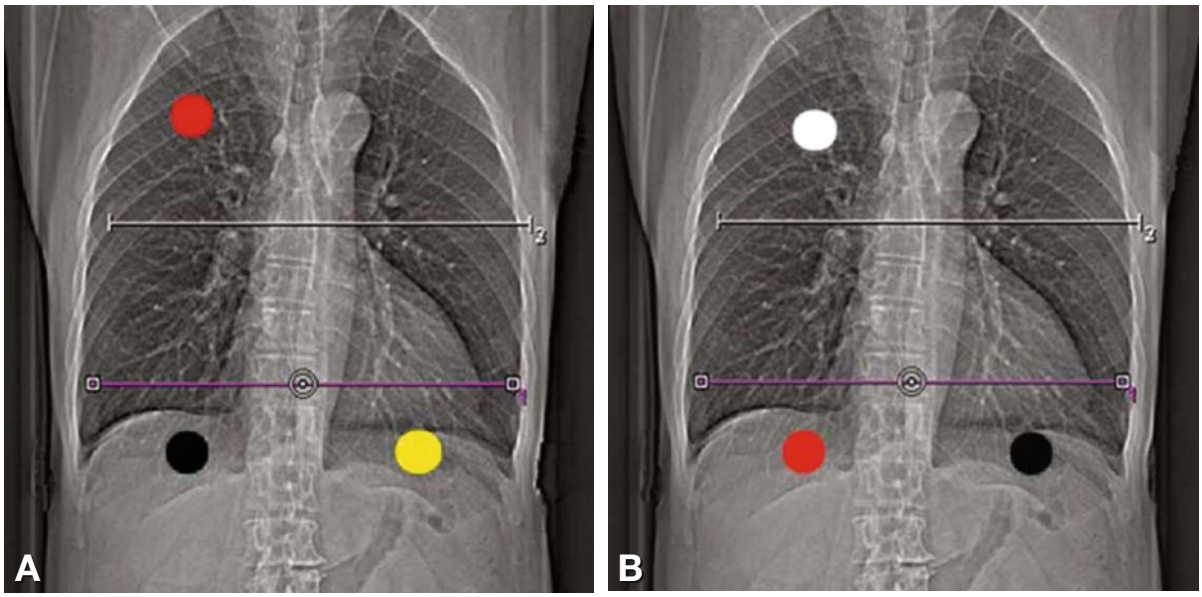

Fig. 9b.1 Optimal positioning of the ECG electrodes on the chest. **Panel A** shows the IEC standard and **Panel B**: the USA standard

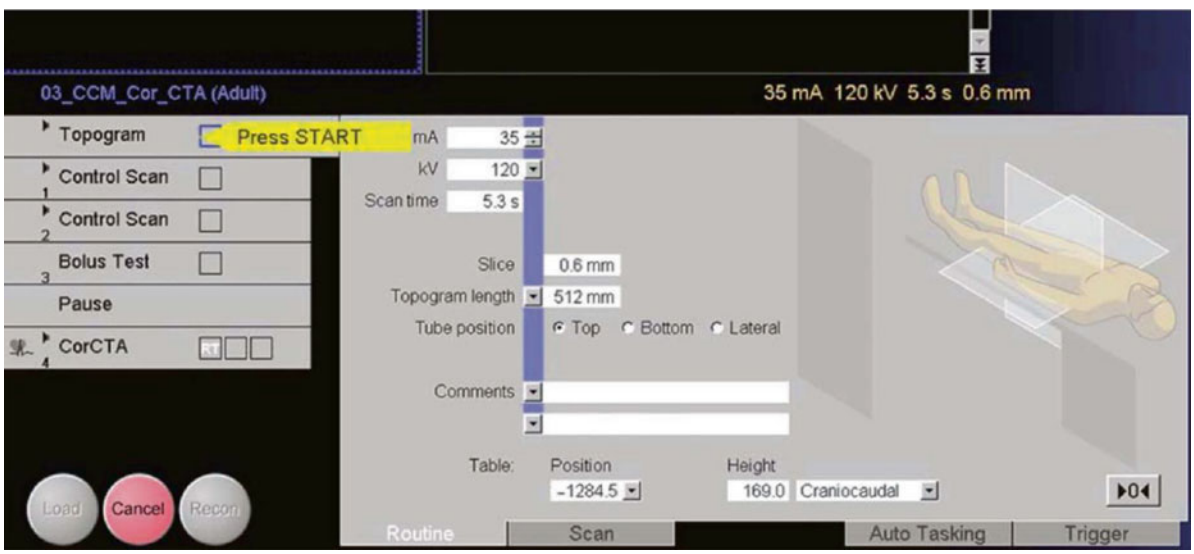

Fig. 9b.2 The first step is the acquisition of a chest topogram (scanogram), typically acquired from *top* to *bottom*. To minimize the scan area, the acquisition can be stopped as soon as the entire heart has been scanned

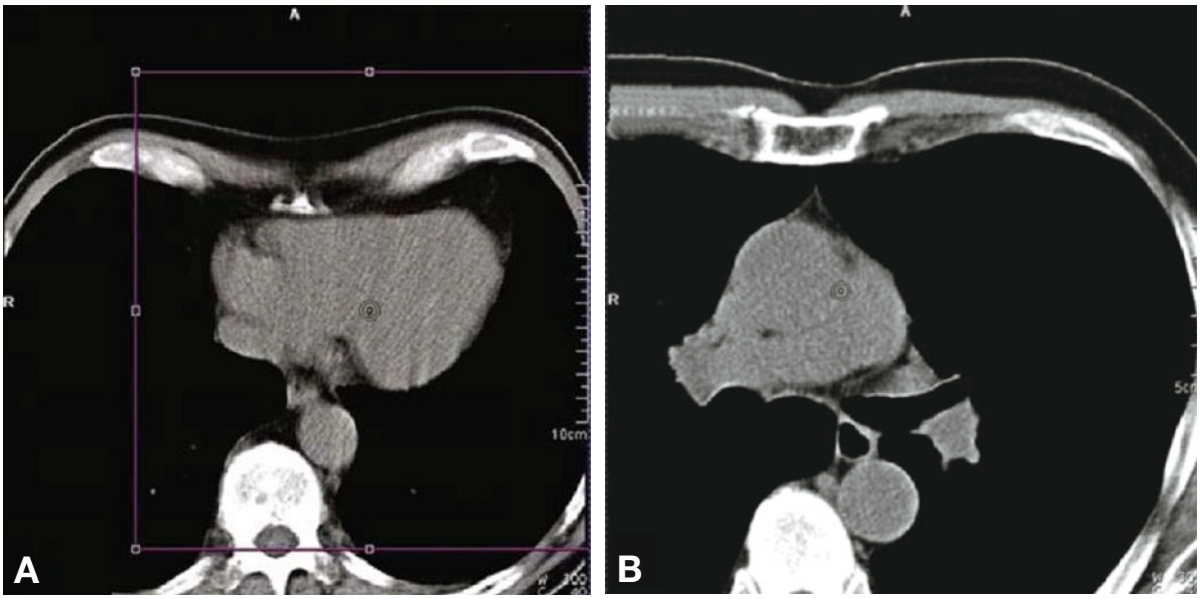

Fig. 9b.3 Acquisition of two control scans. The first control scan (**Panel A**) is positioned at the level of the greatest transverse extension of the cardiac silhouette on the topogram and serves to plan the field of view "*violet box*" for the coronary CT angiography scan. The second control scan (**Panel B**) is obtained about 1–2 cm below the tracheal bifurcation to identify the position for test bolus acquisition

tool, DynEva, is available for semiautomatic analysis of the test bolus series. The scan delay (the time interval between the start of the test bolus injection and image acquisition) is calculated as the individual test bolus arrival time plus an additional 3 s. The additional 3 s delay is necessary to achieve optimal arterial contrast in the ascending aorta and the coronary arteries while ensuring low contrast in the right ventricle and the right atrium in order to avoid inflow artifacts, which may hamper the evaluation of the right coronary artery.

Alternatively, all current Siemens CT systems have contrast bolus tracking software, used as the preferred option in many centers. A reference image is acquired at the level of the aortic root. A region of interest is then placed within the aorta. Repetitive scans are acquired at the same level to follow the arrival of the contrast medium. The consecutive cardiac scan is initiated once enhancement surpasses a predefined threshold in the ascending aorta.

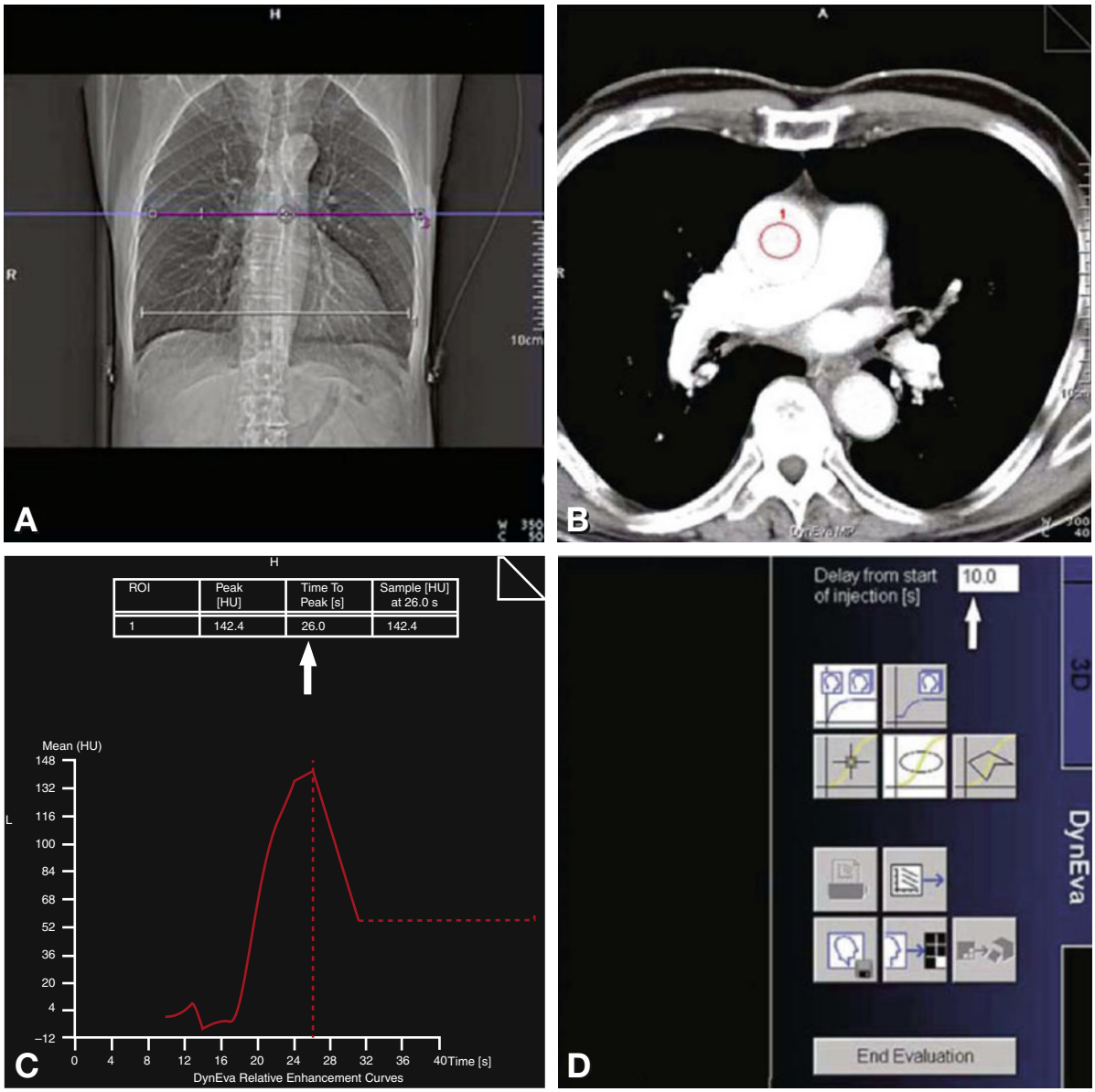

Fig. 9b.4 Bolus test scan. The test scan (*redline* in **Panel A**) comprises a maximum of 40 images. It is started 10–15 s after the beginning of the contrast medium injection. The test bolus series can be analyzed visually or with the DynEva software (**Panels B**–**D**). A region of interest (ROI) is defined in the ascending aorta for analysis (**Panel B**). The time to peak can be read in a table (*arrow* in **Panel C**) after entering the delay used for image acquisition (*arrow* in **Panel D**)

Next, the CT angiography scan, planned to cover the entire heart is acquired from top to bottom (**Fig. 9b.5**). To minimize the inferior extension of the scan field, scanning can be manually discontinued as soon as the real-time images show the entire heart.

With a single-source Somatom Sensation scanner, prospective ECG dose modulation (ECG pulsing) should be used for all retrospectively gated spiral scans in patients with a regular sinus rhythm, as it can reduce radiation exposure by up to 40–50%. In slender patients,

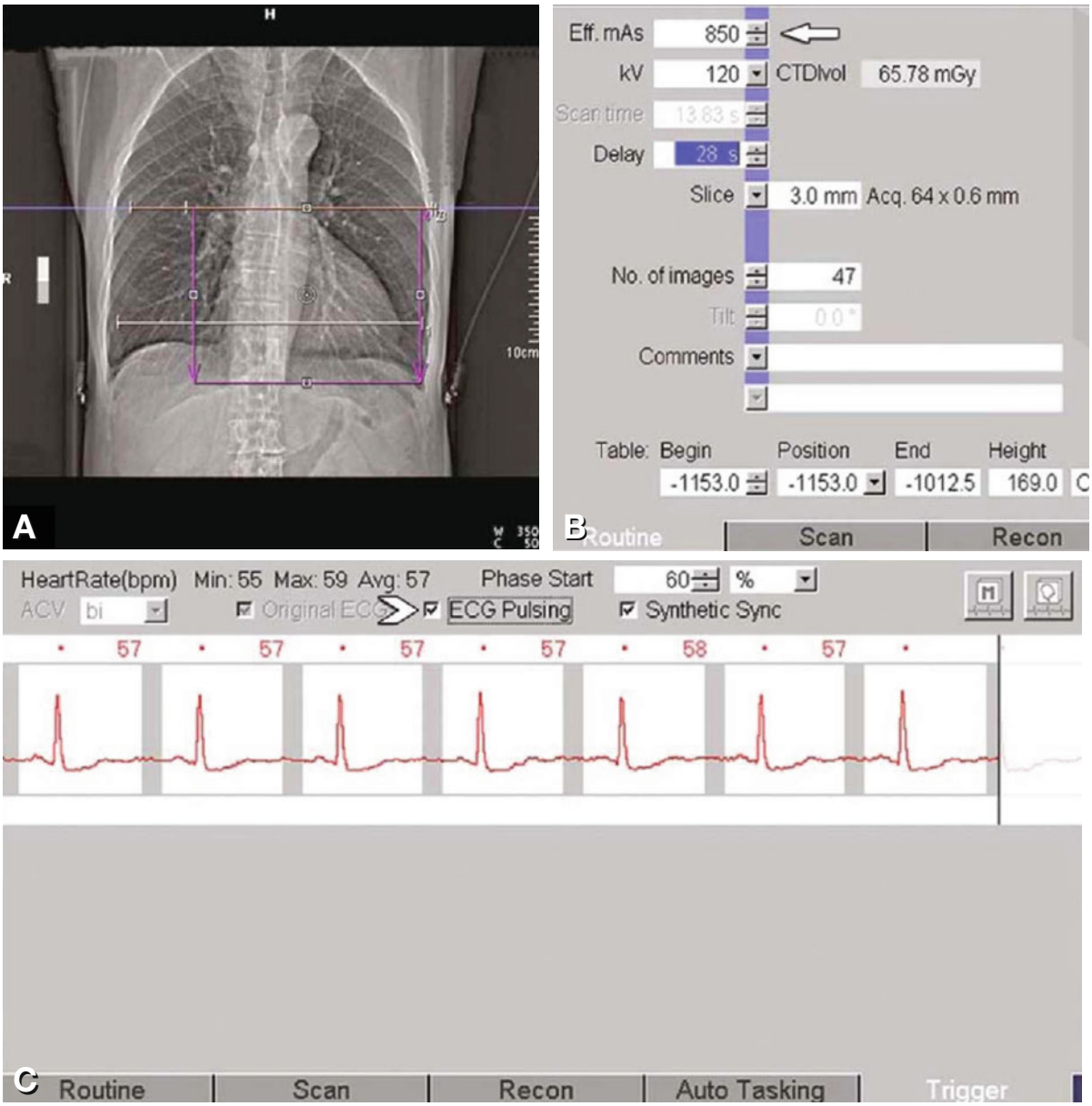

Fig. 9b.5 Planning of the coronary CT angiography scan (**Panel A**). For normal-weight patients, the manufacturer recommends 850 eff. mAs (*arrow* in **Panel B**). In slender patients, radiation exposure can be considerably reduced by using a 100 kV protocol. The highest possible eff. mAs value may be required in obese patients. Finally, prospective ECG dose modulation (ECG pulsing) can be activated from the trigger card of the Syngo menu (*arrowhead* in **Panel C**)

radiation exposure is furthermore reduced considerably by using a 100 kVp or even 80 kVp scan protocol. Recent CT systems from Siemens are equipped with an automated exposure control ("CAREkV") for adjusting both tube current and voltage to the patient's body habitus. This tool uses reference imaging parameters (kVp and mAs) for the desired contrast-to-noise ratio. These adjustments can be refined further by specifying the tissue of interest (e.g., vasculature in the case of cardiac CT), optimizing acquisition parameters for CT angiography, or aiming at lower X-ray tube voltage with high signal-to-noise ratio (**Fig. 9b.6**).

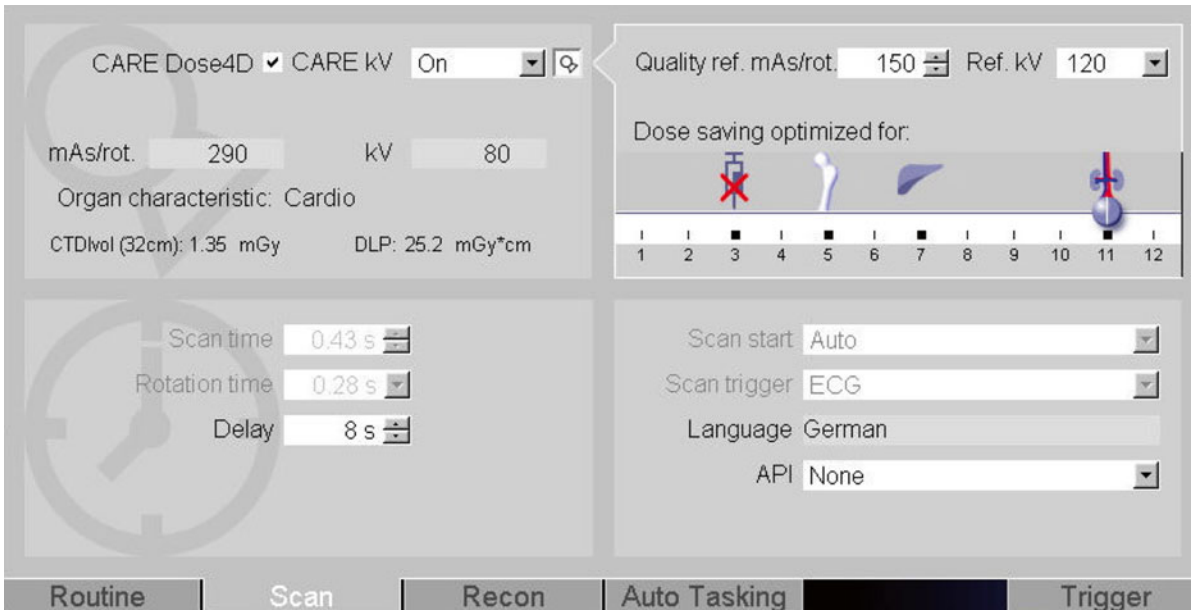

Fig. 9b.6 Based on quality reference mAs and kVp the effective imaging parameters are calculated according to the intended investigation (CTA selected by the slider on the right, *arrow*) and the body habitus of the patient. In this example exposure was set to 290 mAs with 80 kVp, resulting in a CTDI and DLP of 1,35 mGy and DLP of 25,2 mGy · cm for a high-pitch spiral CT scan

9b.3 Image Reconstruction

The first step in image reconstruction is to check the recorded ECG (**Fig. 9b.7**). If there are isolated extrasystoles, the corresponding reconstruction intervals can be deactivated or deleted for image reconstruction. It is recommended to generated a preview series based on a reference image at the level of the mid-RCA (segment 2) to identify the most suitable phase for image reconstruction (**Fig. 9b.8**). Next, thin-slice data sets (0.6–0.75 mm) are reconstructed at the optimal phase of the RR interval determined in this way (**Fig. 9b.9**).

A software option called "best diastole" and "best systole" automatically creates images at a minimal cardiac motion during diastole and systole, with reasonable good success. However, one must bear in mind that arrhythmic patients have a variable length of diastole, whereas the systole remains constant regardless of the length of the individual heart beat. In order achieve acceptable image quality in arrhythmia, the options should be set to "best systole" in combination with "ms" instead of "%" within the RR interval.

Optimal spatial resolution is achieved by selecting a small field of view (ca. 180 mm in square). Reconstruction is usually done using a soft-tissue reconstruction algorithm (B26f smooth), while a sharper kernel (B 46f) may be used to improve the evaluation of calcified plaques and stents. With the newest software available on the most recent scanner generation, iterative reconstruction, marketed as "SAFIRE" (Sinogram Affirmed Iterative Reconstruction), is available for image reconstruction (I26, I46). So called iteration loops (calculation of image data from raw data and back, with generation of synthetic raw data that are compared with the acquired ones) are used to identify and reduce noise while maintaining resolution. Consequently, reference tube settings can be reduced in order to achieve adequate image quality with reduced patient exposure.

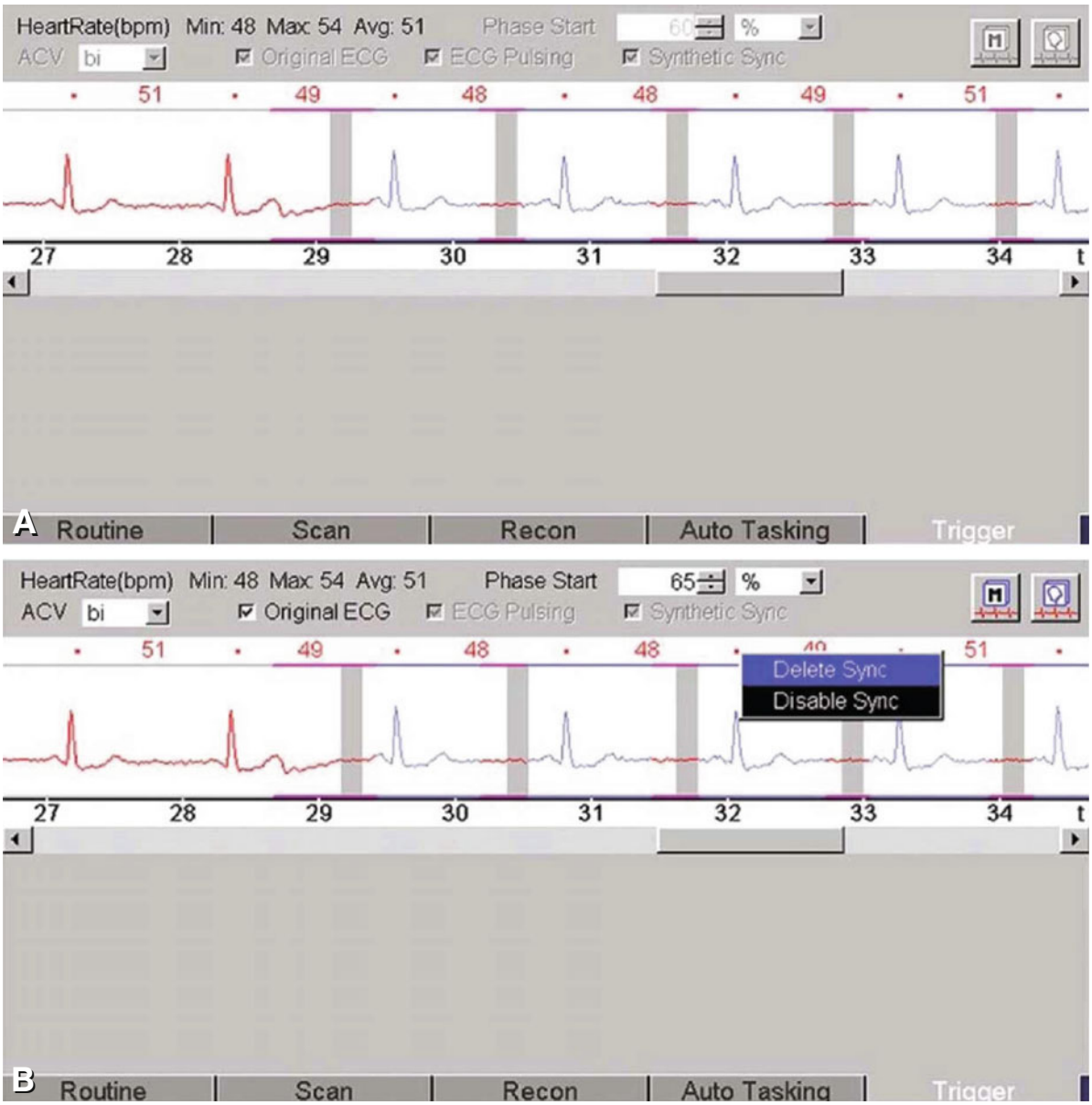

Fig. 9b.7 As a first step in image reconstruction, the ECG signal recorded during scanning is checked in the trigger card (**Panel A**). The minimum, maximum, and average heart rate during the acquisition are displayed on the top of the trigger card. If isolated extrasystoles are present, the corresponding reconstruction intervals can be deactivated or deleted (**Panel B**)

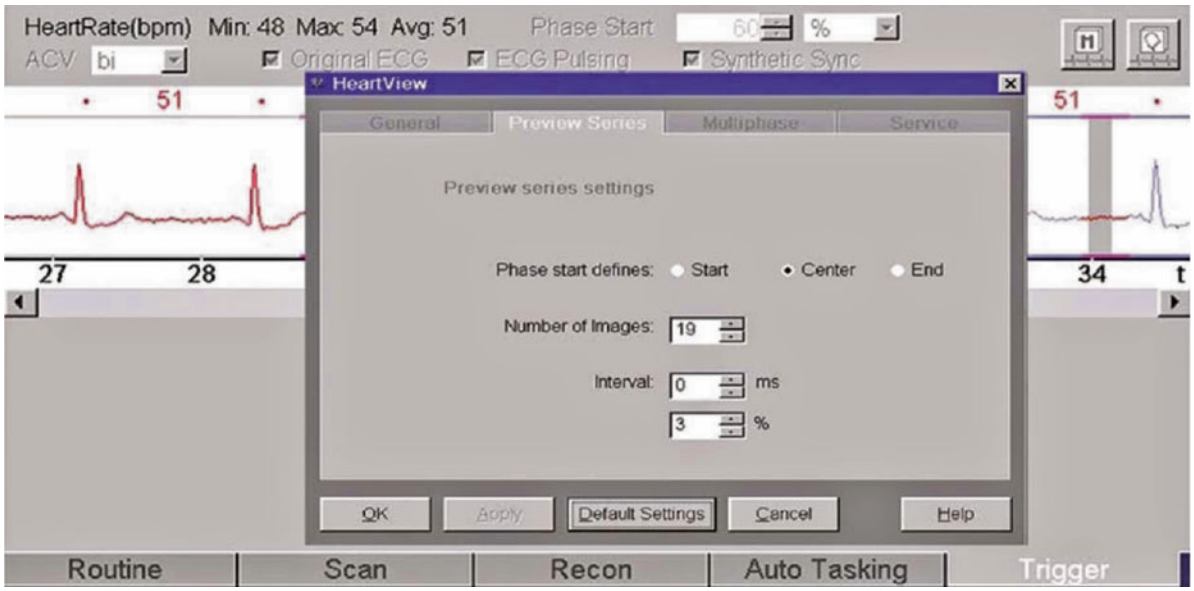

Fig. 9b.8 The user can identify the best time point in the RR interval for image reconstruction by clicking on the "Preview Series" button to generate a series of preliminary images. Such a series may consist for example of 19 images reconstructed at 3% intervals around the start phase. The image selected for generation of the preview series should contain the middle portion of the RCA (segment 2), which is highly susceptible to degradation by motion artifacts

Multiphasic reconstructions (i.e., automatic reconstruction of multiple phases of the RR interval) can be performed whenever the entire cardiac cycle has been covered. Multiphasic reconstructions (e.g., 0–90% in 10% intervals) are especially useful if the diagnostic question includes the assessment of ventricular and/or valvular function. In contrast to the situation for the scanners from the other three vendors, the percentage that determines the position of the phase within the RR interval indicates the start, and not the center, of the image reconstruction window (phase).

Finally, reconstruction series with a large field of view are computed for assessment of the soft tissue and lungs (**Fig. 9b.10**).

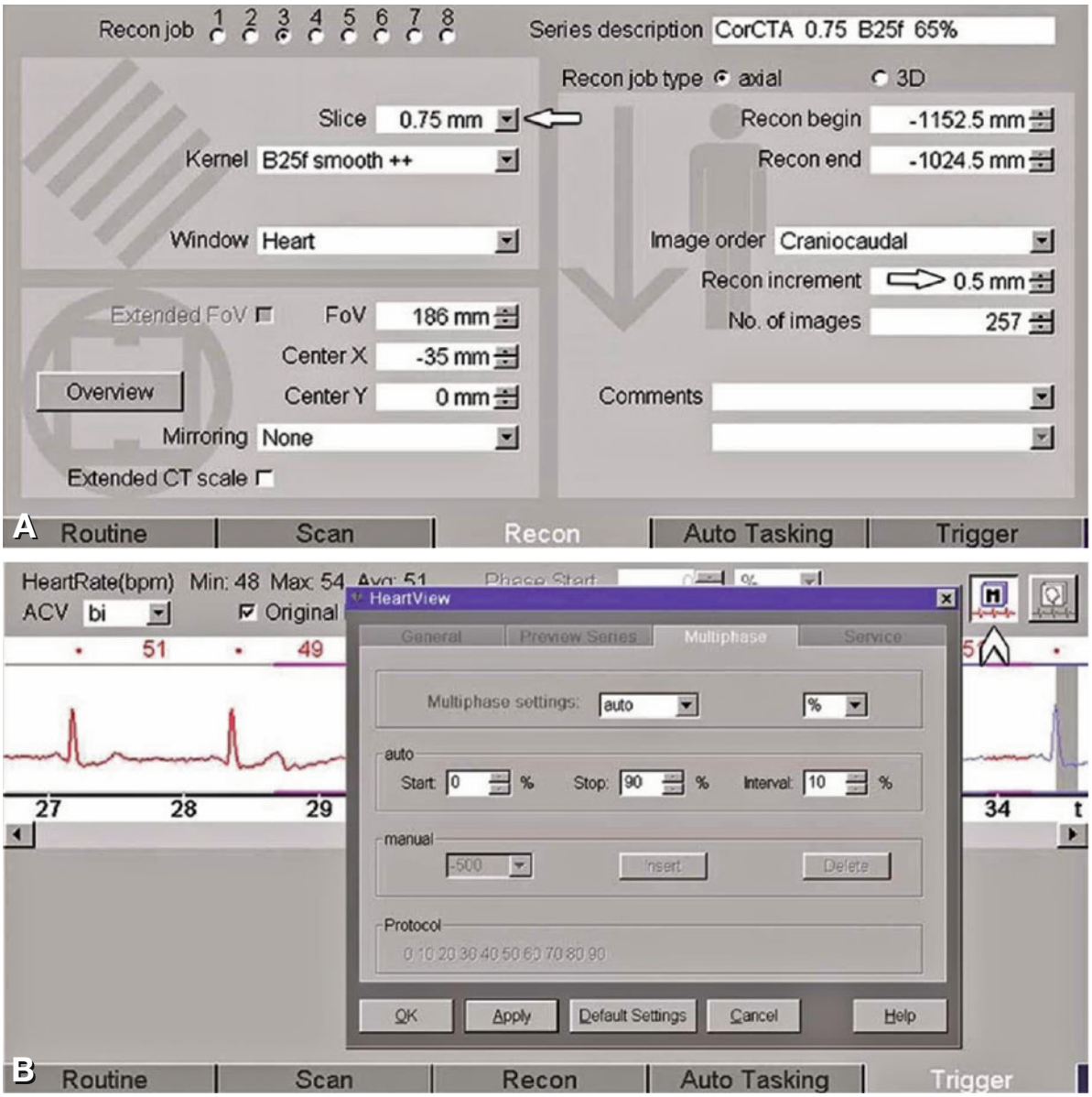

Fig. 9b.9 Next, image series are reconstructed at specific times in the RR interval (**Panels A** and **B**). The time is preselected in the trigger card. As a rule, 0.75 mm images are reconstructed at overlapping intervals (*arrows* in **Panel A**). Alternatively, multiple phases can be automatically reconstructed (in the example shown, from 0 to 90% of the RR interval at 10% increments). The automatic reconstruction mode is activated by clicking on the multiphase button (*arrowhead* in **Panel B**) and selecting the desired start and stop points as well as the reconstruction interval. Note, however, that the automatic mode generates a large number of images, especially when small intervals are preselected

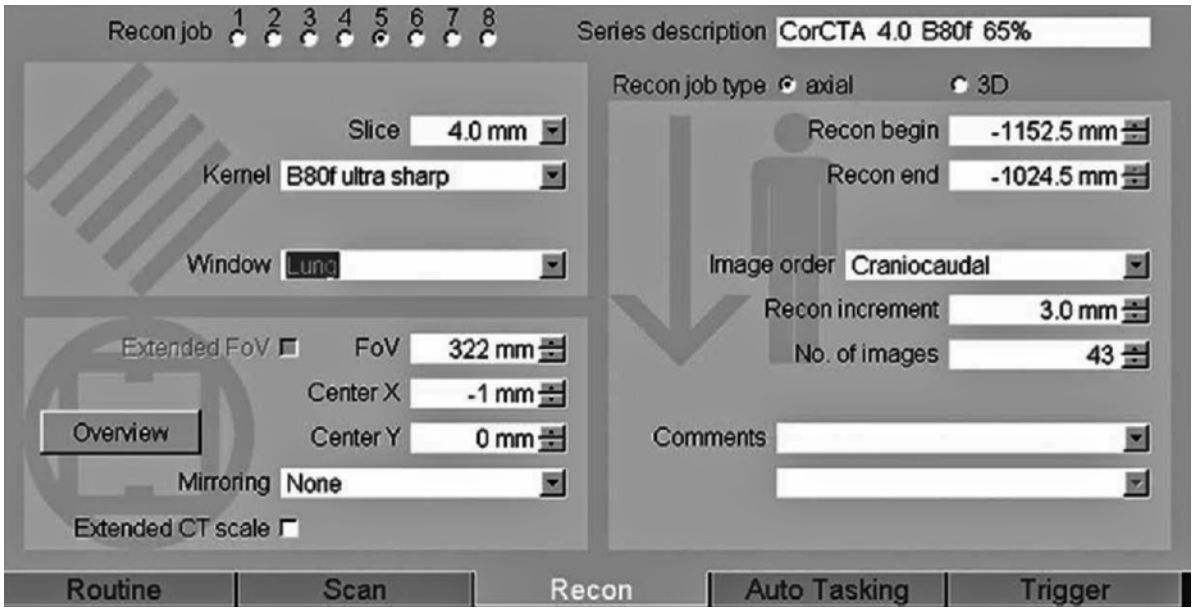

Fig. 9b.10 For evaluation of the lungs, a reconstruction series is generated with a large field of view and thicker slices, using a lung kernel

9b.4 Dual-Source CT ("Somatom Definition")

The technical background of dual-source CT (DSCT) has been described in Chap. 8. The most important practical advantage of DSCT is the improved temporal resolution resulting in better image quality in patients with higher heart rates and arrhythmia (**Fig. 9b.11**) as well as the potential to relevantly reduce radiation exposure (**Fig. 9b.12**). Although beta blockade is recommended to lower heart rates for DSCT as well, the threshold up to which very good image quality can be expected in the diastole is increased to about 70 beats per min (in contrast to the 60 beats per min threshold with half-scan reconstruction and 64-row CT). The workflow of scanning using DSCT (Somatom Definition) and the scanner's software is not significantly different from that of the Somatom Sensation 64. It should be noted that the field of view is limited with dual-source CT because the second gantry has a scan field of only 25 cm. Typical image acquisition parameters are listed in Table **9b.1**.

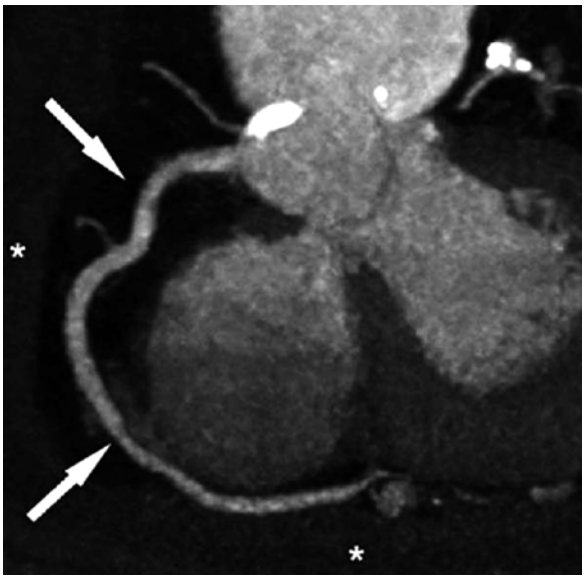

Fig. 9b.11 Example of an examination with dual-source CT in a patient with a heart rate of 125 beats per min. Maximum-intensity projection of the right coronary artery (*arrows*). Note the surrounding pericardial effusion (*asterisks*) that caused the high heart rate (Used with permission from Achenbach et al. *Eur Radiol* 2008)

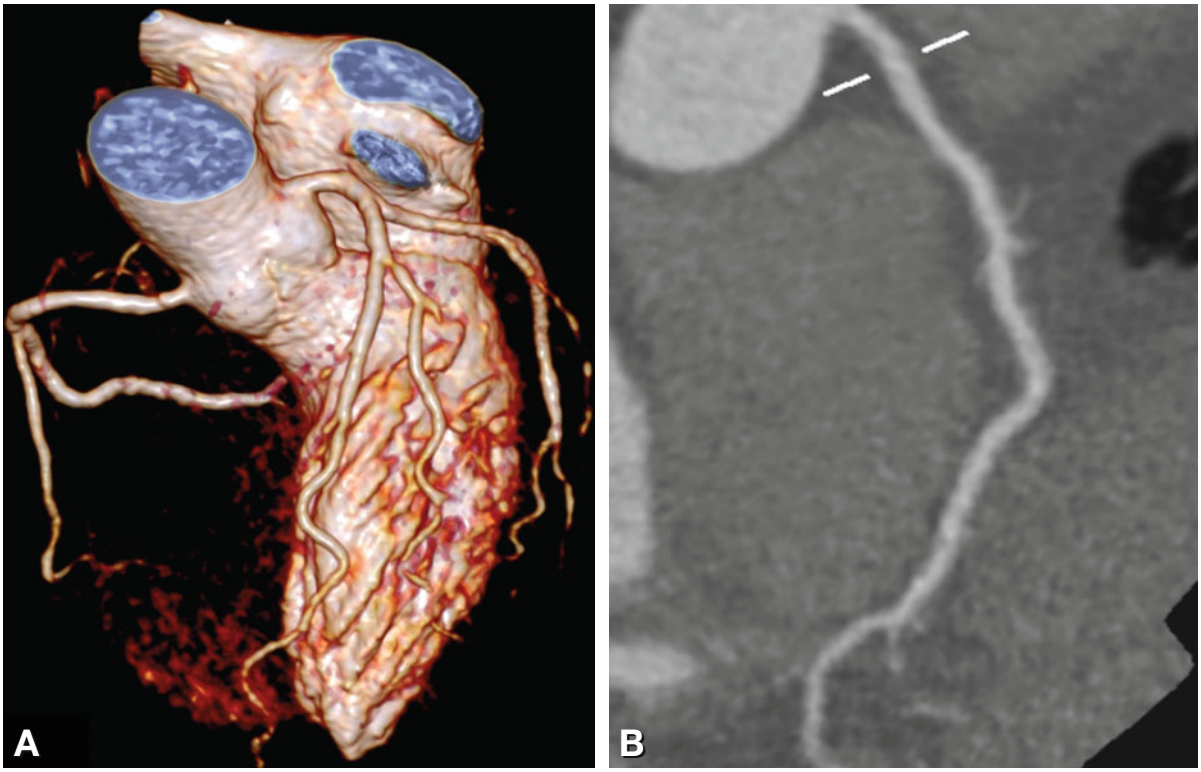

Fig. 9b.12 Example of an examination with reduced radiation exposures using ECG-triggered high-pitch spiral acquisition with 80 kVp and 50 mAs in a 52-year-old male patient with 62 kg body weight. High injection rate and iterative reconstruction compensate for high image noise in the dataset. No evidence of coronary artery disease is apparent in the three-dimensional volume rendering (**Panel A**) or curved multiplanar reformation (**Panel B**)

Table 9b.1 Typical data acquisition parameters for first-generation dual-source CT coronary angiography

Parameter	Value
Gantry rotation time	330 ms
Total scan time	7–10 s
Slice width	0.6 mm
Collimation	19.2 mm
Pitch	0.20 for heart rate <50 beats per min 0.22 for heart rate 50–59 beats per min 0.28 for heart rate 60–69 beats per min 0.33 for heart rate 70–79 beats per min 0.39 for heart rate 80–89 beats per min 0.44 for heart rate 90–99 beats per min 0.50 for heart rate >100 beats per min
Tube voltage	120 kV (adapted to body habitus by CarekV) 100 kV for patients <85 kg 80 kV for very slim patients
Tube current	e.g., 400 + 400 mA
mAs value per rotation	e.g., 264 mAs (=800 × 0.33); the resulting value is relevant for image quality considerations (modulated by CareDose)
Effective mAs value	e.g., 528 mAs (=267 × 0.6/0.3); in this example, a pitch of 0.3 and an ECG pulsing efficiency factor of 0.6 were assumed; the resulting value is relevant for dose considerations
Contrast agent	40–80 ml at 5 ml s^{-1} (consider 6 ml s^{-1} in patients >100 kg)
Contrast timing	Test bolus or bolus tracking

Modified and used with permission from Achenbach et al. *Eur Radiol* 2008

9b.5 Second Generation Dual-Source CT ("Somatom Definition FLASH")

The second generation dual-source CT scanner ("Somatom Definition FLASH") has a wider detector (38.4 mm) and an increased rotational speed of 280 ms. The acquisition window per axial image thus is 75 ms. Furthermore, both X-ray tubes and detectors are arranged at a 95° offset (instead of the previous 90°), which enables the use of a larger detector for the second tube (B-tube) and thus a larger scan field of view (33 cm, Chap. 8). The faster gantry rotation speed, the novel detector arrangement, and finally the use of a larger detector (64 × 0.6 mm, doubled by the use of a dual focal spot) allow cardiac scanning in a non-overlapping, prospectively triggered spiral mode (FLASH mode) with a pitch of 3.4. Data acquisition can thus be completed within a single heartbeat in patients with stable heart rates below about 60 beats per min. Starting this type of scan at 55% of the RR interval using a craniocaudal scan direction is recommended. This entails visualization of the distal right or left coronary artery branches at a slightly later cardiac phase, e.g., around 80%. Planning of the scan range of coronary CT angiography in the FLASH mode is facilitated by obtaining a non-contrast coronary artery calcium scan (also acquired using a high-pitch spiral). Prior to any FLASH mode scan, a so-called FLASH check has to be performed, which analyzes the patient's ECG recording (obtained during breath-hold) for heart rate stability and RR intervals to determine whether high-pitch scanning is likely to be successful. However, the scan can be initiated regardless of a positive flash check, which only checks for heart rate variability, and, in clinical practice, the flash check has not been found to guarantee successful image acquisition. It should be noted, however, that a recent publication by Neefjes et al. (*Eur Radiol* 2013) has found the axial scan mode ("sequence") to be the most robust scan

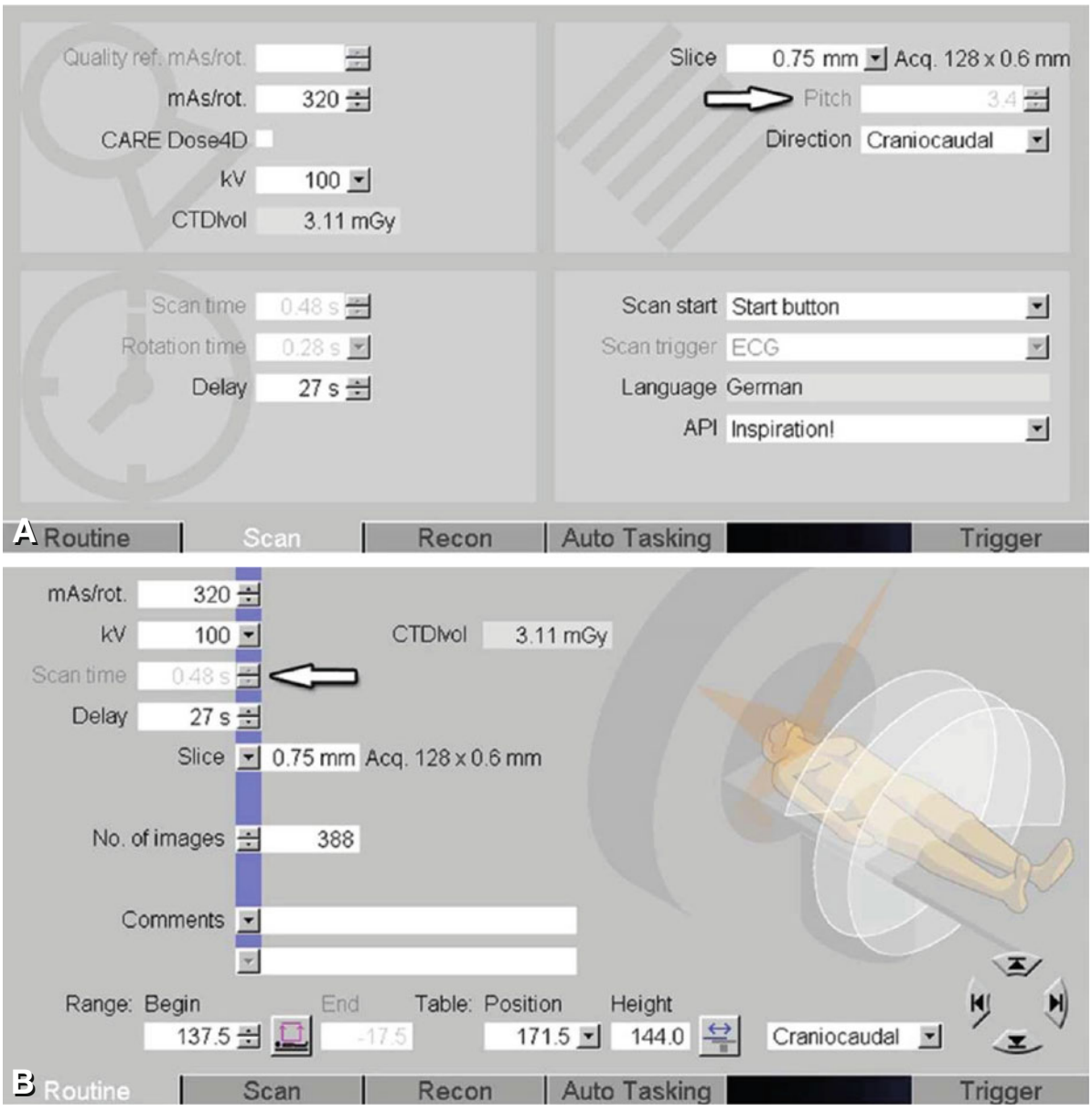

Fig. 9b.13 Cardiac scan user interface of the Definition FLASH. In slim patients, a 100 kV protocol can be used. Note the CTDI of 3.11 mGy (**Panel A**) and the pitch of 3.4 (*arrow* in **Panel A**). For a scan range of 15.5 cm (Begin: 137.5 mm and End: −17.5 mm), the resulting scan time is 0.48 s (*arrow* in **Panel B**)

technique with second generation dual-source CT not only in patients with heart rates above but also those below 65 beats per min.

Furthermore, the FLASH mode cannot be used for functional analysis since, as with sequential scan modes, only samples of the cardiac cycle are recorded. Functional imaging requires overlapping spiral acquisition with ECG gating, which of course is also possible – albeit with a higher effective dose. **Figure 9b.13** shows the scan parameters as displayed by the user interface. **Figure 9b.14** shows the acquisition window placed according to the patients' recorded ECG with a scan start at 60% of the RR interval. Resulting images of a low-dose examination to rule out relevant coronary artery disease are displayed in **Fig. 9b.15**.

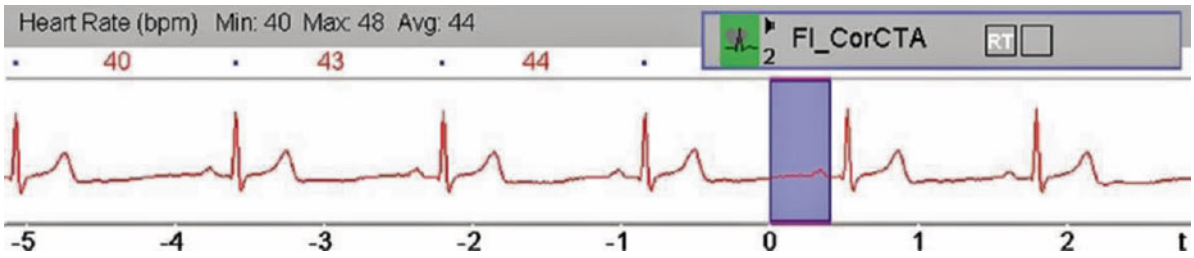

Fig. 9b.14 Cardiac FLASH scan ECG file and data acquisition window. The *blue box* within the ECG file indicates the tube-on time, during which the entire heart was scanned. Prior to scanning the FLASH check symbol turns green (*inset*)

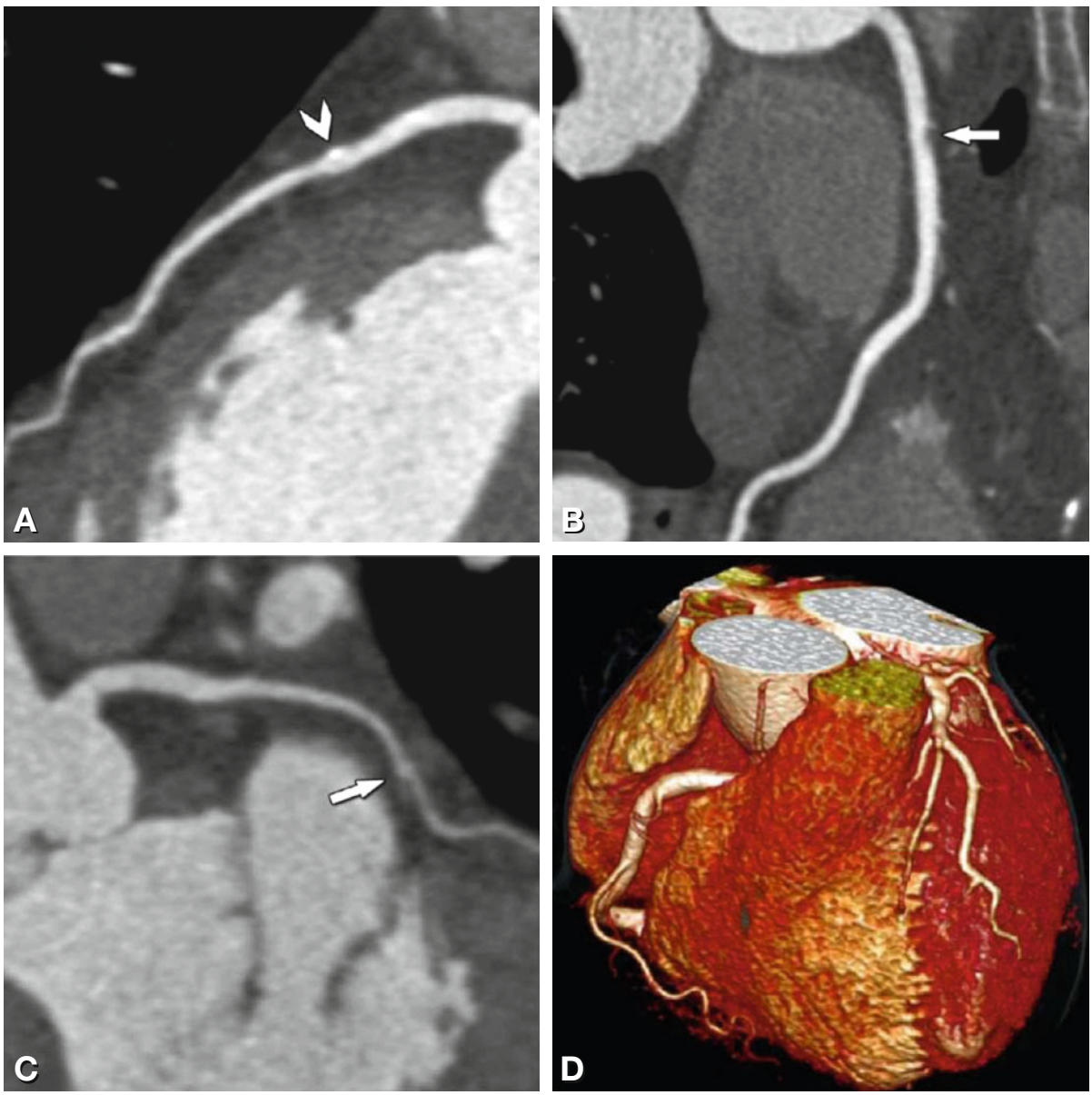

Fig. 9b.15 Cardiac FLASH scan in a 52-year-old female patient with atypical angina at a heart rate of 56 beat per min using the following scanner settings: 100 kV, 320 mAs/rot, CTDIvol 3.10 mGy, resulting DLP 49 mGycm, and scan start at 60% of the RR interval. Small calcified plaque in the left anterior descending artery (**Panel A**, *arrowhead*) and noncalcified, nonstenotic plaque in the right coronary artery (**Panel B**, *arrow*). The small left circumflex artery shows no relevant lesions (**Panel C**); the origin of a side branch (*arrow*) mimics focal wall irregularities on a curved multiplanar reformation. A three-dimensional overview of the case is given in **Panel D**, showing that no relevant motion artifacts are present. No invasive angiography was performed

List 9b.1. Which protocol to choose?

1. Beta blockers are always advisable unless contraindications exist
2. Patients with low and regular sinus rhythm (<60 bpm) may be investigated with prospectively ECG-triggered highpitch spiral acquisition unless functional information is required
3. Patients with regular sinus rhythm and a heart rate between 60 and 70 beats per min may be investigated with prospectively ECG-triggered sequential scan modes with diastolic image acquisition, when the examination is performed on a dual-source scanner
4. Any patient with a heart rate above 70 beats per min and regular sinus rhythm should be investigated with a spiral scan using retrospective ECG gating with ECG pulsing, allowing reconstruction of high quality images in both diastole and systole
5. Patients in whom functional assessment of the valves and the myocardium is required as well as patients with arrhythmia are best investigated with the retrospective ECG-gated scan mode with ECG pulsing turned off. Although this scan mode may go along with a comparably high amount of radiation, it will allow reconstructing images at any time point to achieve the best image quality

Single source scanners from the "Definition" family (Definition AS, Definition AS+) provide inferior temporal resolution (rotation/2) for half scan reconstruction. However, due to their larger detector size compared to the "Sensation" scanners, they allow axial data acquisition ("sequence") in patients with well-controlled, low heart rates.

9b.6 Which Protocol for Whom?

The follow general advice can be given to choose the most appropriate scan protocol for an individual patient (**List 9b.1**).

Philips Brilliance 64 and iCT

O. Klass, M. Jeltsch, and M.K. Hoffmann

Abstract

Performing cardiac CT on Philips scanners is described.

9c.1 Preparing and Starting the Examination

After entering the patient's ID, the examiner should select table position, age group, and the desired exam protocol group (**Fig**. 9c.1). The patient is then placed on the CT table in a supine position, and ECG leads are attached. The automatically started ECG viewer enables permanent registration of heart rate and rhythm including calculation of standard deviation and mean heart rate. Details of patient preparation for coronary CT angiography on all scanner types are presented in Chaps. 7 and 9.

Each examination starts with a surview (scanogram) to determine the position of the heart. The localizer scan should be as small as possible while covering the entire heart and is acquired during a single inspiratory breath-hold. The scan area for a standard coronary CT angiography is often determined using the tracheal bifurcation as the upper reference point. It is also the level of the plane in which the tracker for the bolus timing algorithm is placed. The scan ends about 1–2 cm below the heart (**Fig**. 9c.2). The scanner gantry isocenter line should be properly placed in the center of the heart. Finally, the entire heart is examined with ECG gating during a single inspiratory breath-hold.

The scan is timed to coincide with peak contrast enhancement, derived from the preceding bolus tracking. Bolus tracking is performed by a Locator and a Tracker scan, positioned on the level of the tracheal bifurcation. Pressing "Go" starts the Locator scan, and the system automatically shows the tracker window. A region of interest (ROI) is positioned in the descending aorta (**Fig**. 9c.2). Now bolus tracking and injection of contrast medium must be started at the same time. After a start delay, several transverse sections are successively acquired at the defined level. The scan starts automatically once attenuation enhancement values in Hounsfield units reach a predefined threshold.

9c.2 Prospective Axial Acquisition ("Step & Shoot")

Since the introduction of the new scanner generation (Brilliance iCT) with a rotational speed of 270 ms and a detector width of 8 cm (128 rows), the majority of patients (80–90%) can be scanned with prospective axial acquisition ("Step & Shoot") with helical retrospective gating being reserved for data acquisition in patients with arrhythmia and high heart rates. As a prospectively gated scan mode, "Step and Shoot" requires a stable heart rate below 70 beats per min. This scan type combines the

M. Dewey, *Cardiac CT*,
DOI 10.1007/978-3-642-41883-9_11, © Springer-Verlag Berlin Heidelberg 2014

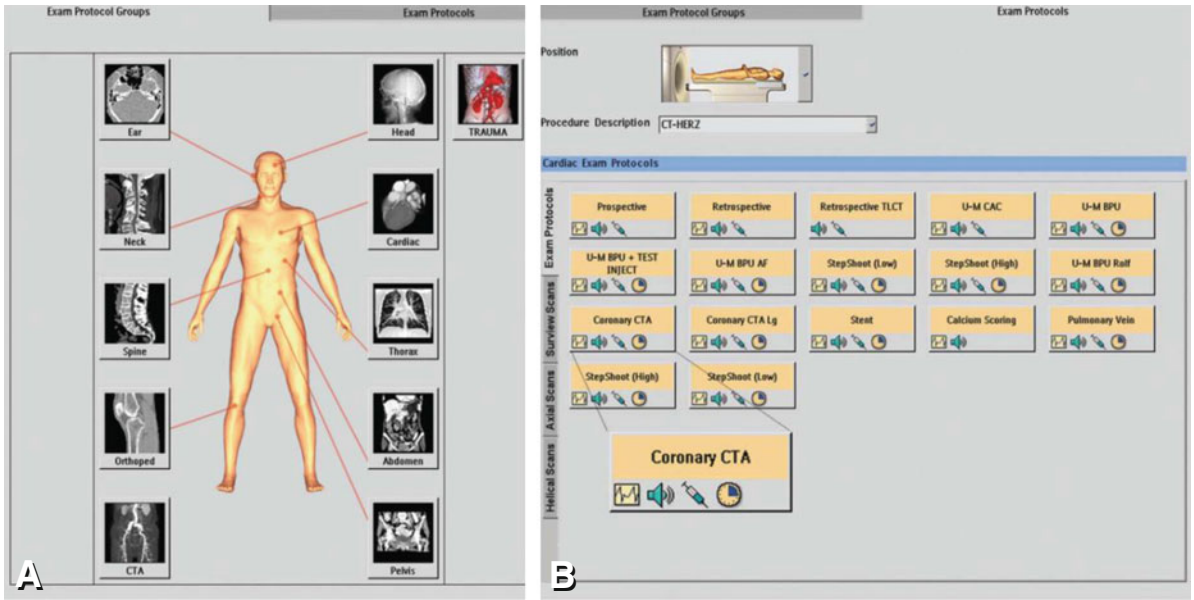

Fig. 9c.1 Setting up the scan protocol. The different "Exam Protocol Groups" are shown in **Panel A** while **Panel B** details the "Cardiac Exam Protocols" such as "Coronary CTA". Depending on the planned examination, you can select between different protocols (e.g., standard helical "Coronary CTA," "Step & Shoot" mode, or "Calcium Scoring")

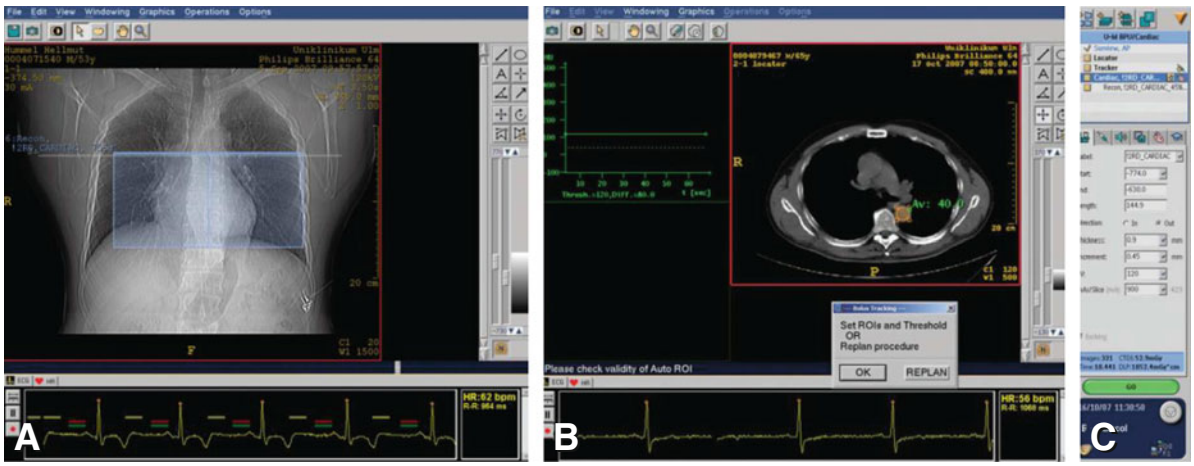

Fig. 9c.2 The user interface for a standard retrospective helical scan, including the defined field of view and an ECG viewer, is shown in **Panel A**. The *blue box* indicates the preselected scan area and range. For bolus tracking, the ROI is positioned in the descending aorta (**Panel B**). The dose indication box shows the expected dose exposure and scan time (**Panel C**)

advantages of axial and helical scans and relies on sequential axial acquisition. Generally, "Step & Shoot" involves a typical scan sequence that is based on volume acquisition ("Shoot") and table movement ("Step"). Depending on the system used, the heart is covered in four to six (Brilliance 64) or two to three (iCT) axial rotations, combined with prospective triggering (**Fig. 9c.3**). The main advantages of "Step & Shoot" scanning are summarized in **List 9c.1**.

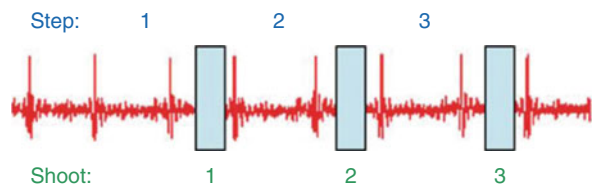

Fig. 9c.3 The principle of sequential axial acquisition after table movement (Step), combined with prospective ECG gating (triggering)

List 9c.1. Advantages and disadvantages of prospective coronary acquisition

Advantages:

1. Provides a low-dose scan with a dose reduction to one-fourth of that of standard helical scans
2. Image quality is comparable (*or even better with the iCT*) to that of standard helical scans
3. Improved rotational speed of the iCT enables coverage of the whole chest in one breath-hold with "Step & Shoot"; e.g., to image coronary artery bypass grafts or to perform a triple rule-out scan
4. Allows each volume to be reconstructed from a single cardiac cycle resulting in a better edge depiction of the coronary arteries
5. Includes an online arrhythmia handling mechanism (**Fig. 9c.4**)

Disadvantages:

1. Limited to patients with stable heart rates below 70 beats per min
2. Lower temporal resolution when compared to helical scans
3. Geometric distortion at the borders of the prospectively acquired slabs (**Fig. 9c.5**)

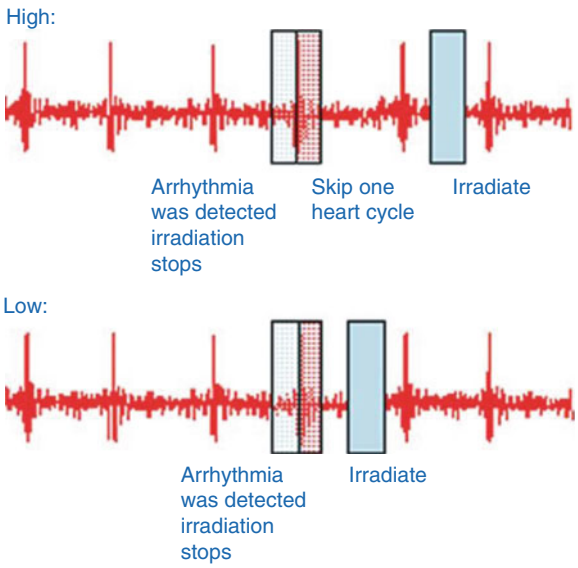

Fig. 9c.4 Two options are available for online arrhythmia handling in the "Step & Shoot" mode. "High" arrhythmia tolerance: When an arrhythmia is detected, irradiation stops immediately; the system waits for one cardiac cycle and then continues exposure in the same table position after the next cycle. "Low" arrhythmia tolerance: When an arrhythmia is detected, irradiation stops immediately; the system continues exposure in the same table position in the cycle immediately following. To prevent excessively long scan times (in the "High" tolerance mode), in a sequence of more than two irregularities, the "High" strategy is automatically changed to "Low"

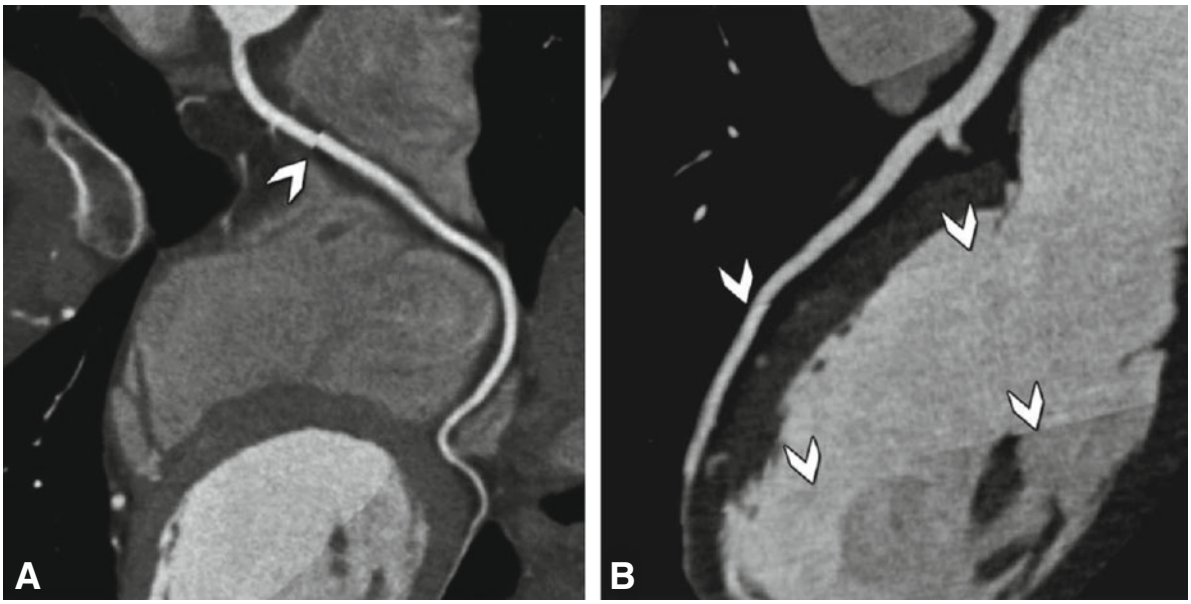

Fig. 9c.5 Drawbacks of the "Step & Shoot" approach. Curved multiplanar reformations of the right coronary artery with "steps" (*arrowhead* in **Panel A**) and of the left anterior descending coronary artery showing "bands" (*arrowheads* in **Panel B**) as artifacts resulting from geometric distortion at borders of the prospectively acquired slabs

9c.2.1 Scan Protocol

A standardized protocol is used for prospective acquisition (**Table 9c.1**) with 64 × 0.625 mm collimation and a tube rotation time of 400 ms on the Brilliance 64 and 128 × 0.625 mm collimation and a tube rotation time of 270 ms on the iCT. The tube voltage is 120 kV or 100 kV using an iterative reconstruction algorithm (iDose) for image reconstruction for a standard patient weighing up to 90 kg (range 80–140 kV), and tube current typically 190–210 mAs. Data are acquired for a full rotation (360°) instead of a half scan plus fan angle, providing greater flexibility in compensating for changes in heart rate.

Table 9c.1 Typical scan parameters

	Helical scan	Step & Shoot
Total collimation (mm)	64 × 0.625	64 × 0.625
Rotation time (ms)	400	400
Tube voltage (kV)	120–140	
Current time product/tube load (mAs)	600–900[a]	150–210[a]
Pitch	0.2	NA
$^{C}T^{DI}$vol (mGy)	34–75[b]	11–22
Maximum field of view (mm)	500	250
Scan duration	Approximately 10 s	Approximately 10 s
ECG synchronization	Retrospective ECG gating	Prospective ECG gating (triggering)
Cycles	NA	4–5
Threshold for bolus tracking (HU)	150	150
Postthreshold delay (s)	5–7	7

NA not applicable

[a] True mA = electrical mA; effective mA = electrical mA divided by pitch

[b] Without temporal dose modulation ("ECG gating")

The planning on the scanogram of the "Step & Shoot" scan is similar to the helical scan with the following differences: the field of view is limited to 250 mm (in both standard and detailed resolutions). This limitation is indicated by a "gray box" that is displayed on the surview image (**Fig. 9c.6**). To make sure that the optimal phase is acquired even under changing conditions, the "Step & Shoot" application has a built-in mechanism that analyzes the patient's heart rate online during the scan, and, if arrhythmia occurs, it responds accordingly. The new reconstruction capabilities of "Step & Shoot" allow the user to select any reconstructed slice thickness and slice increment as in equivalent helical scans. These characteristics are reflected in the values that are defined in the dropdown menus for both "Increment" and "Thickness" fields (**Fig. 9c.6**).

9c.2.2 Dose Indication Box

Since the "Step & Shoot" scan time and irradiation profile are not known in advance (because of potential online arrhythmia handling), the dose indication box is different from that for retrospective image acquisition (**Fig. 9c.2**) to reflect this uncertainty (**Fig. 9c.6**).

9c.2.3 Injection Protocol

The injection protocol for "Step & Shoot" acquisition is identical to that used for current helical acquisition. It is important to emphasize that the minimal post-threshold delay is 7 s, which is the amount of time needed to reach the initial scan position and to build up adequate tube voltage. Another important drawback is that only one cardiac phase can be acquired when using prospective acquisition. The cardiac phase needs to be selected beforehand, and the center of the phase can vary from 40 to 85% of the RR interval. An innovation of the iCT is the option to choose a reconstruction window with a surrounding phase variance of 3 or 5% ("padding"), meaning that reconstructions of a preselected phase of 78% can also be done at 75 and 81% or 73 and 83%.

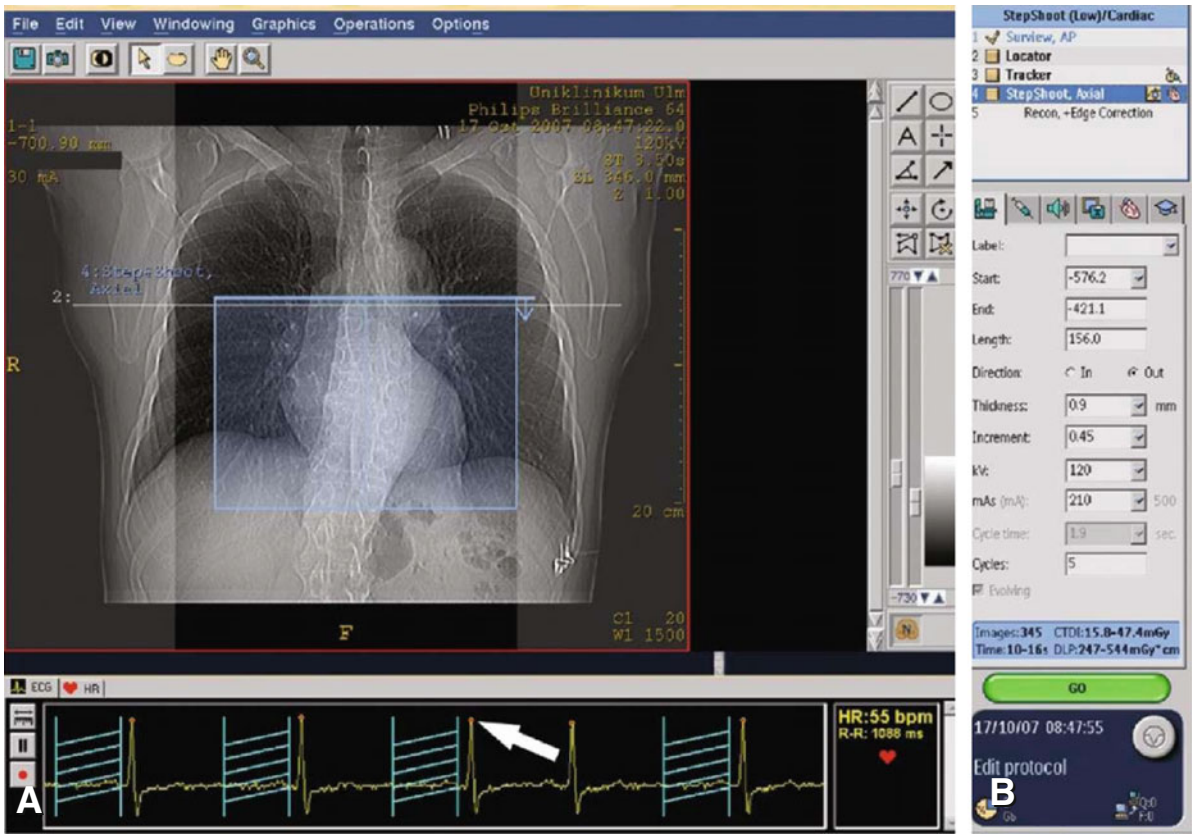

Fig. 9c.6 Limited field of view with "Step & Shoot". The "gray stripes" on both sides of the patient in the scanogram (**Panel A**) reflect the limited field of view (250 mm). To avoid unnecessary radiation exposure an additional lateral scanogram should be obtained only in patients with above-average thoracic diameters. Additionally, prospective ECG triggering with online arrhythmia handling is also shown skipping one RR cycle (*arrow* in **Panel A**). **Panel B** shows the dose indication box, displaying CTDI and DLP values as ranges (e.g., CTDI 15.8–47.4 mGy and DLP 247–544 mGy × cm), where the lowest value represents a case without any arrhythmia, and the highest value a case with severe continuous irregularities. The "Time" field in this box gives the scan time range without irregularities (minimum) and the scan time in the case of continuous irregularities (maximum). The slice increment and thickness are the same as with the helical protocol

9c.3 Retrospective Helical Image Acquisition

The retrospectively gated helical acquisition mode, which used to be the standard scan mode for coronary CT angiography, has become the scan mode for "difficult" patients with high heart rates, a wider range of heart rate variations, and arrhythmias. With the improved temporal resolution of up to 67 ms of the current CT generation, the helical scan mode even allows scanning patients with atrial fibrillation with more or less stable image quality. This is due to the fact that retrospective gating allows multisegment image reconstruction at any arbitrary phase of the cardiac cycle.

9c.3.1 Scan Protocol

A standardized examination protocol (**Table 9c.1**) with 64 × 0.625 mm collimation and a tube rotation time of 420 ms on the Brilliance 64 and 128 × 0.625 mm collimation and a tube rotation time of 270 ms on the iCT is used. The typical tube voltage is 120 kV with a tube current of 600–900 mAs, depending on patient size, body

mass index, and thoracic diameters in the scan area. A standard patient with 75 kg body weight is scanned with 120 kV and a tube voltage of 800 mAs. A separate dose indication box gives the expected dose exposure and scan time (**Fig. 9c.2**).

After the scan is completed, preview images are presented and can be centered and zoomed to the optimal size. Philips also offers an option for editing of the ECG wave as well as off-line arrhythmia handling prior to the start of reconstruction (**Fig. 9c.7**).

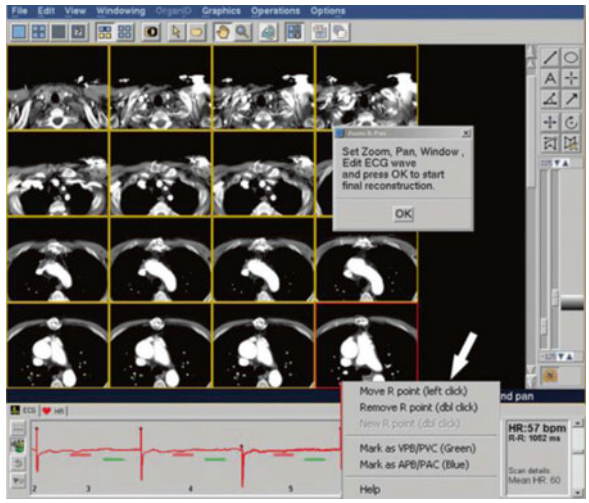

Fig. 9c.7 Preview images shown after completion of scan acquisition. Images can be centered and zoomed to the optimal size. Prior to starting final image reconstruction the ECG of the acquired scan can be manipulated using the off-line arrhythmia handling software as shown in the pop-up window (*arrow*)

9c.4 Reconstruction

Image reconstruction is performed using comparable parameters for retrospectively and prospectively acquired data (**Table 9c.2**), with cardiac standard filters XCA-D during mid-diastole and end-systole of the cardiac cycle (**Fig. 9c.8**). Philips uses an adaptive multisegment reconstruction algorithm for retrospectively acquired data integrating 3D voxel-based backward projection of the cone beam. Image reconstruction

Table 9c.2 Typical reconstruction parameters

	Prospective helical scan	Step & Shoot
Reconstruction filter kernel	Xres Standard (XCA-D)	Xres Standard (XCA-D)
Reconstruction field of view	Approximately 200 mm	Approximately 200 mm
Matrix	512×512	512×512
Slice thickness (mm)	0.9	0.9
Reconstruction increment (mm)	0.45	0.45
Reconstructed ECG intervals[a]	Normally 40 and 75%, for functional analysis 0–90% equally spaced by 10%	Normally 78% (40–85%)

[a] Percentages indicate the center of the image reconstruction interval

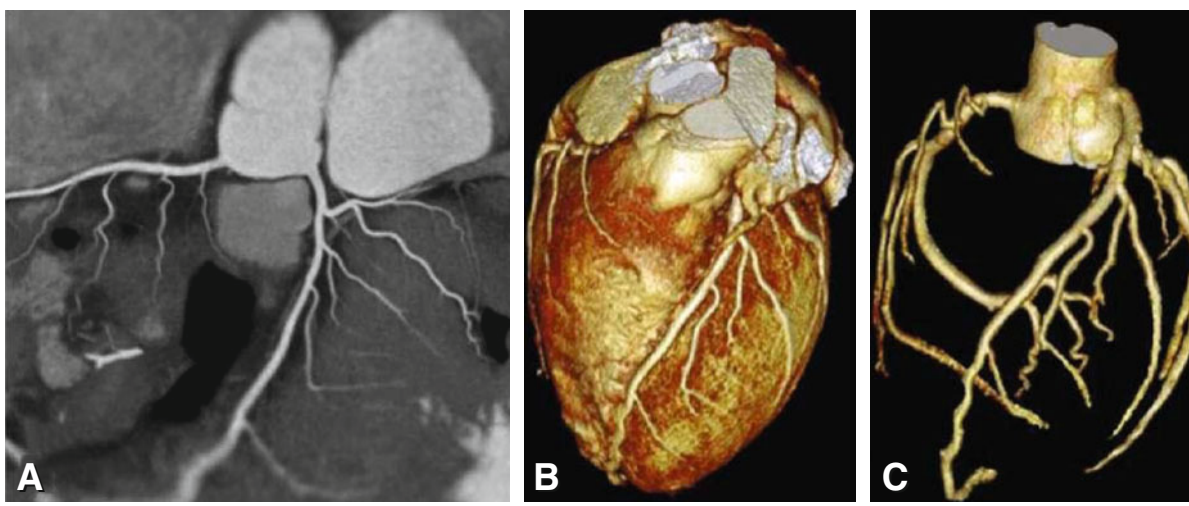

Fig. 9c.8 Reconstructions from a "Step & Shoot" examination: two-dimensional map (**Panel A**), volume-rendering of the heart (**Panel B**), and the extracted coronary tree (**Panel C**) reconstructed at 75% of the R-R cycle using an XCA-D filter

using the raw data from up to five segments from consecutive cardiac cycles improves the theoretical temporal resolution. A coronary artery will be reconstructed from partial raw data from several consecutive RR intervals. This reconstruction principle is applied separately for each voxel.

Left/right ventricular analysis requires ECG intervals equally spaced by a maximum of 10%. It is advisable to perform an additional reconstruction of the raw data in a lung-adapted window setting using maximum fields of view.

9c.5 Iterative Reconstruction Algorithm (iDose)

An iterative reconstruction algorithm (iDose) uses the raw data output from the Nano-Panel^{3D} detector to determine and remove noise resulting from low-dose scanning. This allows a further reduction of the effective dose (a standard patient can now be scanned with 100 kV instead of 120 KV) while optimizing image quality without losing image detail.

After acquisition of the raw data iDose can be used for additional image reconstruction on different levels of noise reduction (levels 1–7 corresponding to noise reductions of 20–80%). Selected levels of iDose can be implemented in standard reconstructions so that a standard filtered backprojection as well as a selected level of iDose reconstruction for the selected phase or phases is performed. To start this additional reconstruction job, select the "Reconstruction" drop-down menu and change from *Standard* to *iDose* (**Fig. 9c.9**).

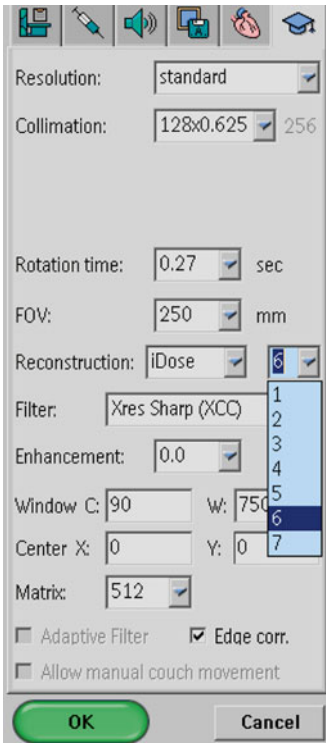

Fig. 9c.9 Reconstruction parameter box; displaying the option of changing from *Standard* to *iDose* reconstruction on different levels (levels 1–7). Usually level 6 (70% noise reduction) is used for coronary arteries

General Electric LightSpeed VCT, Optima CT660 and Discovery CT750 HD

L. Lehmkuhl, E. Martuscelli, and M. Jinzaki

Abstract

This chapter describes how cardiac CT is performed on General Electric scanners.

9d.1 Scanner Types

General Electronics has three types of 64-row multislice CT scanners: LightSpeed VCT, Opima CT660, and Discovery CT750.

LightSpeed VCT is the first 64-row CT with 100 kW X-ray tube power. Its capabilities include 350 ms gantry rotation time, adaptive statistical iterative reconstruction (ASiR), prospective ECG-gated step-and-shoot acquisition (SnapShot Pulse), and ECG editing.

Optima CT660 is the latest 64-row CT with 72 kW X-ray tube power, improved workflow including a gantry display monitor, and compact gantry design. It is identical to LightSpeed VCT with regard to gantry rotation speed, ASiR, SnapShot Pulse, and ECG editing. Additional features are temporal resolution enhancement (SnapShot Freeze) and cardiac acquisition parameter optimization (SnapShot Assist), similar to the Discovery CT750 HD.

Discovery CT750 HD is characterized by a better in-plane pixel size (0.23×0.23 mm^2). This improvement is due to (1) new detector material (gemstone) that provides a primary speed of 0.03 ms and an afterglow of only 0.001% and (2) a new data acquisition system, which allows acquiring 2.5 times more views. Also, this scanner features a new generator tube supporting ultrafast kV switching for dual-energy imaging and can reconstruct images using ASiR. The Discovery CT750 HD also has 350 ms gantry rotation time, SnapShot Pulse, ECG editor, SnapShot Freeze, SnapShot Assist, and Cardiac Spectral CT (Dual Energy Cardiac: GSI Cardiac).

M. Dewey, *Cardiac CT*,
DOI 10.1007/978-3-642-41883-9_12, © Springer-Verlag Berlin Heidelberg 2014

9d.2 Electrode Placement and ECG

9d.2.1 Electrode Placement

It is recommended that the electrodes not be placed over muscle, scar tissue, or hair; the proper placement is medially over the clavicle to avoid the muscle tissue when the arms are raised over the head. It is very important to ensure good skin contact. Details of patient preparation for cardiac CT and of the examination procedure on all scanner types are presented in Chaps. 7 and 9.

Figure 9d.1 shows proper lead placement using the IVY ECG monitor: First raise the patient's arms above the head, and then position the leads as shown. Place the two upper leads directly on the patient's clavicle. This placement provides the best signal for the IVY monitor. To avoid incompatibilities, do not use patient monitoring electrodes that may be available from other departments in your facility. The electrodes recommended by General Electric (GE) are Dyna/Trace 1500 by Conmed.

9d.2.2 ECG Monitor

Turn on the ECG machine and make sure that there are good connections to the gantry and leads. A good connection is confirmed if "CONNECTED" appears in the upper right display area of the monitor. Otherwise, check to make sure that the cable connecting the ECG machine to the backside of the gantry is plugged in properly and that the same cable is connected to the ECG machine. In case of low signal, check the electrode placement and choose an alternative position if needed (**Fig. 9d.1**). If there is "noise" within the ECG wave, it is recommended that you do not scan until this condition is corrected.

9d.3 Scan Preparation

9d.3.1 Breathing Instructions

Prior to the scan, have the patient practice the automatic breathing instructions. Scanning is sufficiently rapid that it is not necessary for the patient to hyperventilate. The scanning time should be no longer than 5–8 s on average. Let the patient take one breath in, blow it out, then take a breath in and hold it, while you watch the ECG monitor and take note of the patient's heart rate during breath-holding. A patient who has any difficulty holding his or her breath may be put on 2–4 l min^{-1} of oxygen via a nasal cannula. Oxygen administration may also help to lower the heart rate.

When recording the breathing instructions for cardiac CT that are programmed in the scanner, make sure to give the breathing instructions slowly. The breathing instructions should be no shorter than 10 s. When recording the instructions, and after you say, "take a breath in and hold it," be sure to wait for 3–5 s (of silence) prior to clicking on the "stop recording" button. This delay will give the patient enough time to hold his or her breath before the actual start of the scan and for the heart rate to stabilize; otherwise the patient may still be breathing in during the first several slices, which could lead to motion artifacts on the images.

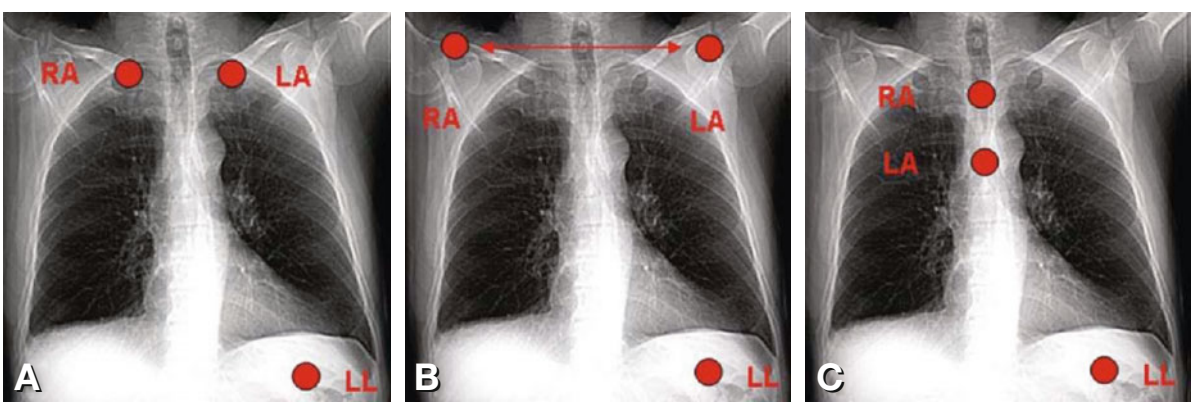

Fig. 9d.1 ECG electrode placement. **Panel A** shows a scanogram depicting the recommended ECG lead placement for best signal clarity. If the signal is low or the QRS peak is not noticeably stronger than the other ECG wave segments, using one of the two alternate positions (**Panels B** and **C**) may improve the ECG signal and its detection

9d.3.2 Scout Scans

The following steps, summarized in **List 9d.1**, should be performed to choose the correct scan protocol and to acquire the scout scans.

List 9d.1. Choice of protocol and scout acquisition

1. Landmark the patient at the sternal notch
2. Select "new patient" and enter patient data
3. Select the anatomical area (chest)
4. Select the snapshot (cardiac) protocol from the main menu
5. On the scout screen, check to make sure you are in "Active Gating" mode and that the gating is fine, then take the scout views
6. Use the cardiac breathing protocol for the scout scans and all subsequent scans (**Fig. 9d.2**)
7. Monitor the patient's heart rate during the breath-hold[a]
8. When the two scout scans are completed, select "next series" to display the next step of the protocol

[a] The body's natural physiologic response during breath-hold is to reduce the heart rate by approximately 5 beats per min. Knowing what the patient's heart rate does during the breath-hold will help you determine what scanning mode to use during the cardiac scan (**Fig. 9d.3**).

If the heart rate is not displayed on the screen and you have a "red" gating box, the scanner is not reading the patient's waveform. To correct this problem, try the following: (1) click on the red "Gating" box and turn off the gating, then turn it back on; (2) check all connections between the gantry and the ECG machine; and (3) check once again for proper placement of the leads on the patient.

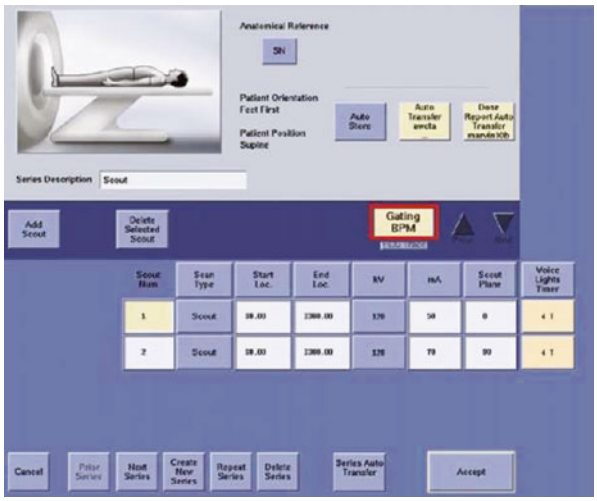

Fig. 9d.2 Planning the scout (scanogram) acquisition. Make sure that "Active Gating" (see *red frame*) has been selected when taking the two scout views (AP and lateral). The cardiac breathing protocol should be used for the scout scans and all subsequent scans

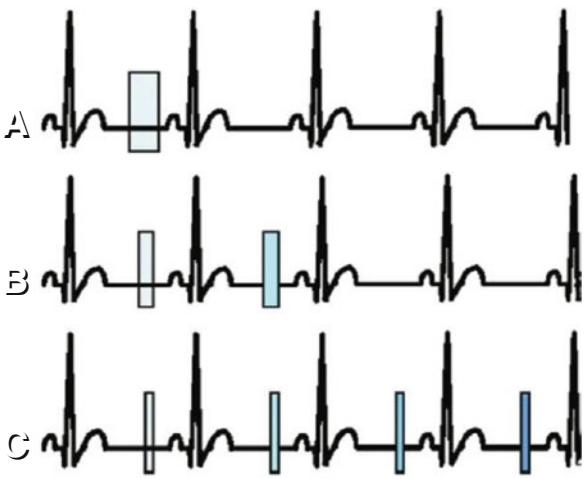

Fig. 9d.3 Alternative retrospective cardiac reconstruction methods. **Panel A** shows the "SnapShot Segment Mode" (halfscan): heart rate, 30–74 beats per min; one sector; reconstruction window, 175 ms; a retrospectively gated reconstruction using data from 2/3 of a gantry rotation to create an image from one cardiac cycle. **Panel B** shows the "SnapShot Burst Mode" (multisegment): heart rate, 75–113 beats per min; two sectors; reconstruction window, ~87 ms; a retrospectively gated reconstruction using data from up to two cardiac cycles within the same cardiac phase to create an image at a given table/anatomic location. **Panel C** shows the "SnapShot Burst Plus Mode" (multisegment): heart rate, >113 beats per min; two, three, or four sectors; reconstruction window, 44 ms; stable heart rates; a retrospectively gated reconstruction using data from up to four cardiac cycles within the same cardiac phase to create an image at a given table/anatomic location

9d.4 Scan Modes, Bolus Timing, and Image Acquisition

9d.4.1 CT Coronary Angiography Scan Modes

There are three different modes for retrospectively gated reconstruction that can be used for image acquisition, depending on the patient's heart rate. These modes are described in **Fig**. 9d.3. Alternatively, in patients with low and stable heart rates, prospectively ECG-gated (i.e., triggered) axial acquisitions (nonhelical) can also be performed; this approach has the advantage of reducing the radiation exposure.

9d.4.2 Bolus Timing

To calculate the exact arrival time of the contrast medium in the coronary arteries, the test bolus protocol described in **Table** 9d.1 is recommended. View the scout and place an axial monitoring scan 1 cm below the carina. If a non-contrast localizer series was previously done (e.g., for calcium scoring), you may also scroll through these images and determine the location for the axial monitoring scan by manually typing the location into the View/Edit screen.

If you have a dual-head injector, it is recommended that you follow the contrast test bolus with a 20-ml saline chaser. Scan the patient with the cardiac breathing protocol and note the heart rate during the scan.

Once all of the test bolus images are reconstructed, highlight the view port in which they are loaded, select the measurement icon on the "Exam Rx Desktop," then select "MIROI" (Multi-Image Region of Interest). Select the elliptic ROI from the pop-up box on the screen, and place the ROI in the ascending aorta and size it to fit completely within the aorta. Then click OK on the pop-up box and calculate the bolus arrival time as described in **Fig**. 9d.4. Click on "Next series" to display the gated cardiac helical acquisition protocol. Enter in the prep delay, based on the test bolus. Alternatively, a bolus tracking technique can be selected by clicking on "Smart Prep." For bolus tracking, a threshold of 120–150 HU is recommended for initiation of the subsequent helical scan (**Fig**. 9d.5).

Table 9d.1 Parameters of the test bolus scan

Parameter	Value
Rotation time	0.5 s
Interval	0
Thickness	5 mm
Prep delay	5 s
Interscan delay	1.5 s
SFOV	Large
DFOV	25 cm
kV	120
mA	40
No. of scans	14
Contrast agent amount	15 ml
Injection rate	5 ml s^{-1}, or the same injection rate as for the cardiac angiogram

DFOV display field of view. This term describes the central part of the scan field of view, which is chosen for image reconstruction. *SFOV* scan field of view. This term describes the maximum diameter of the acquired scan area that can be used for image reconstruction

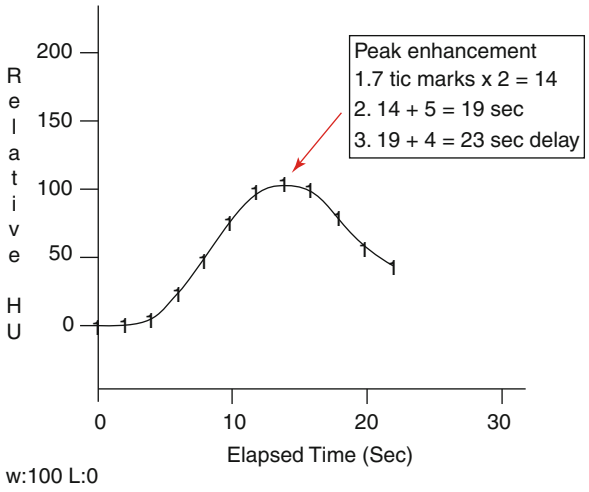

Fig. 9d.4 Time-to-peak curve derived from the test bolus acquisition. On the graph image, count each tic mark on the line graph to the peak of the curve, multiply the number of tic marks by 2, and then add 5 s. Remember that image no. 1 is at 5 s and the tic marks are 2 s apart. This time represents the time it takes for the contrast agent once injected to reach the root of the aorta, where the coronary arteries arise (time-to-peak enhancement). Once you have the time-to-peak enhancement, add an additional 4 s (to allow for filling of the distal coronary vessels); this number is now the pre-scan delay or prep group delay for the cardiac CT exam. In brief, prep delay is calculated as follows: (number of tic marks × 2) +5 s +4 s; alternatively, it can be expressed as: peak +9 s. This bolus time is a key parameter to use for the gated cardiac acquisition

9d.4.3 Image Acquisition

Prescribe the location of the scan on the scout using graphic Rx, or type in the start and end locations using explicit Rx, on the basis of the noncontrast localizer images. Use the scan parameters described in **Table 9d.2**. Choose detector coverage, helical thickness, and rotation time as shown in **Fig. 9d.6**.

Just prior to scanning the patient, it is very important to check the ECG trace on the scanner console and to ensure proper gating and that the scanner is triggering on the appropriate segment of the ECG wave. You should see a "RED" line on the R peak of the QRS complex on the patient's ECG wave. If you do not see the "RED" line on the R peak but rather somewhere else, make the appropriate adjustments to the electrode placement or monitor settings to ensure proper gating on the R peak. The "white" area represents the reconstruction window of 75% in the RR interval used for the reconstruction of the first set of images. The ECG trace on the console refreshes every 2 s.

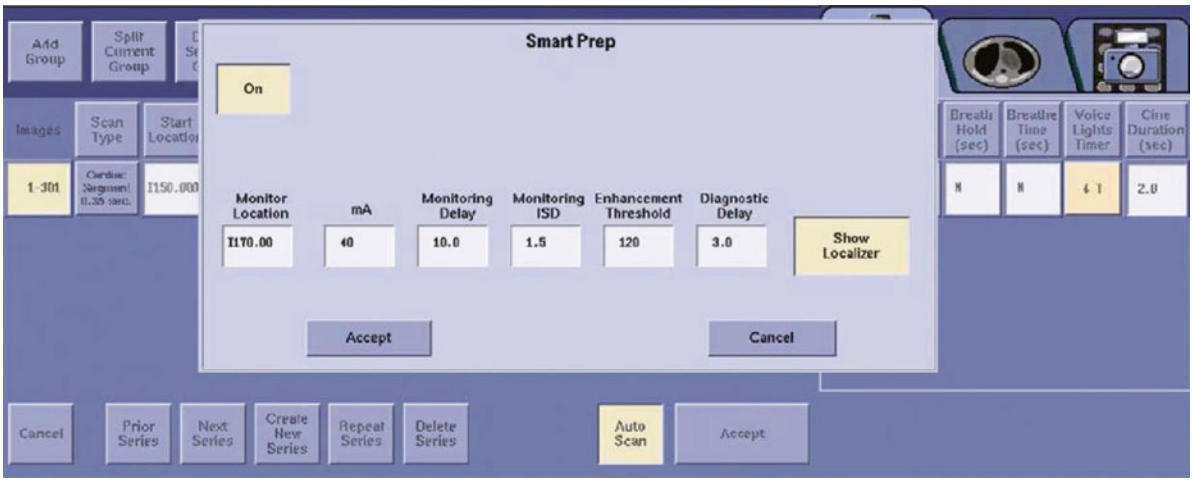

Fig. 9d.5 Choosing the parameters for bolus tracking ("Smart Prep"). An enhancement threshold of 120–150 HU is recommended

Table 9d.2 Image acquisition parameters

Scan parameter	Value	Comment
Scan type	Cardiac helical	
Rotation time	0.35 s	
Start location	–	Based on the scout scans
End location	–	Based on the scout scans
Coverage	Entire heart	
Slice thickness	0.625 mm	See **Fig. 9d.6**
Slice interval	0.625 mm	No overlap (overlap results in more artifacts)
SFOV	Cardiac large	See **Table 9d.3**
DFOV	25 cm	Adjustable as desired to contain coronaries
mA	See **Table 9d.4** and **Fig. 9d.7** for recommended values (adjust these as appropriate for your clinical needs)	ECG modulation can lead to a dose decrease of up to 50% in low stable heart rates; see **Fig. 9d.8** for further instructions
kVp	120	
Pitch	–	The pitch is automatically set by the software, based on the patient's heart rate
Reconstruction type	Standard	
Cardiac noise reduction filters	C1, C2, or C3	These filters allow dose reductions of up to 30% on top of the ECG modulation dose reduction while preserving image quality

DFOV display field of view, *SFOV* scan field of view

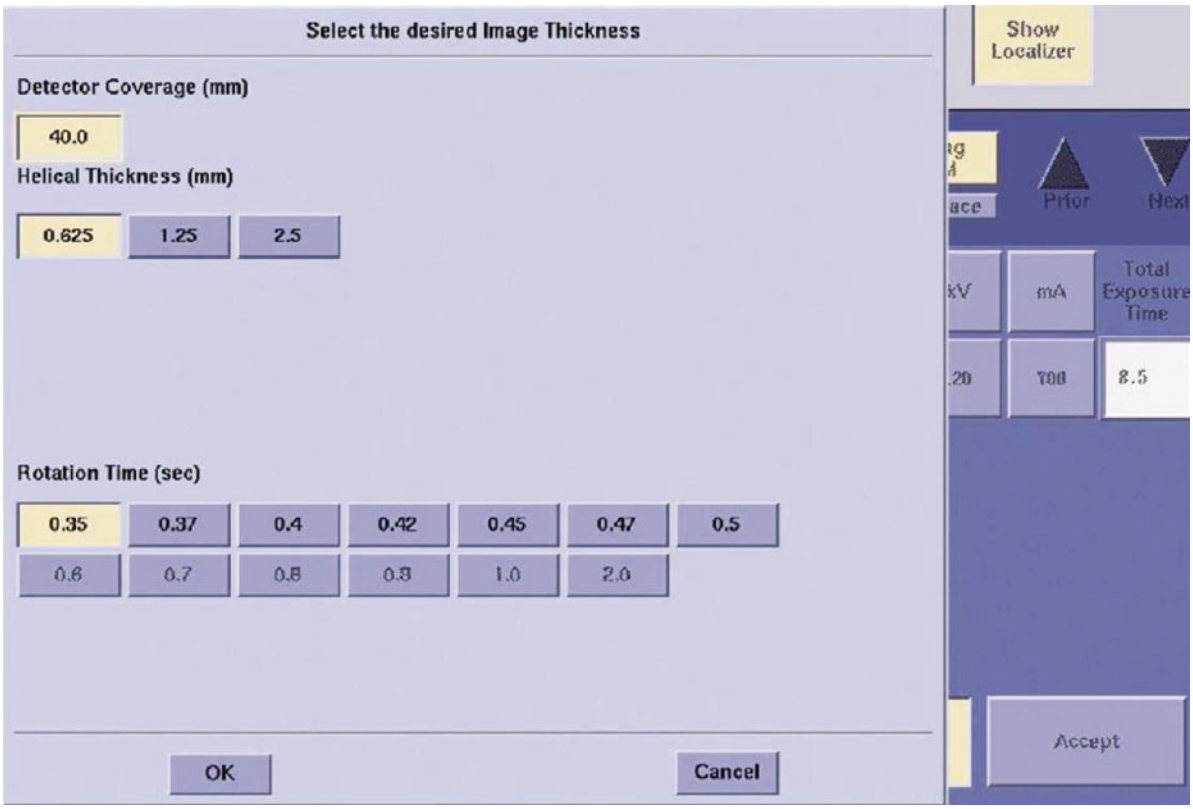

Fig. 9d.6 For cardiac scanning, choose the detector coverage, helical thickness, and rotation time as shown in this screenshot

Table 9d.3 Different cardiac scan fields of view

SFOV	Bowtie filter	DFOV (cm)[a]
Cardiac small	Small	9.6–32
Cardiac medium	Medium	9.6–36
Cardiac large	Large	9.6–50

DFOV display field of view, *SFOV* scan field of view

[a]The standard DFOV for cardiac CT using GE scanners is 25 cm

Table 9d.4 Recommended mA values for ECG modulation

Body weight	Minimum mA value	Maximum mA value
<60 kg (<132 lb)	100	450
60–80 kg (132–176 lb)	250	550
>80 kg (>176 lb)	400	750

If no modulation is desired, the scan should be acquired with the maximum mA value

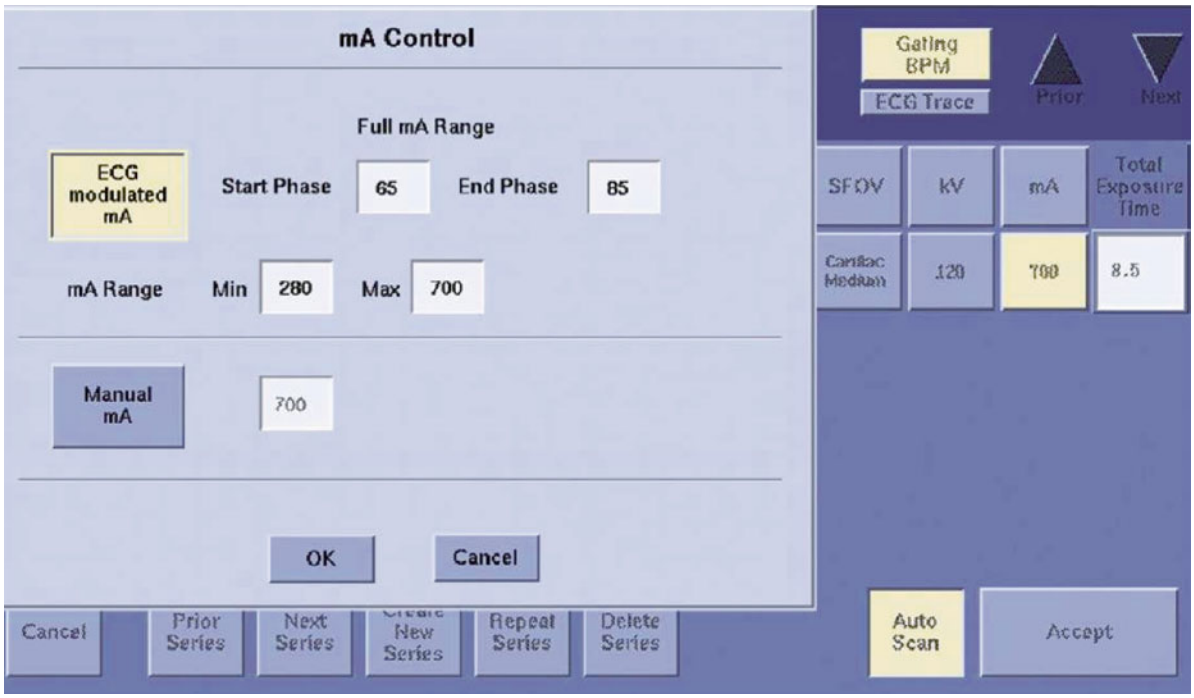

Fig. 9d.7 Adjusting the mA setting for cardiac CT. The full mA range phase and mA range can be chosen by clicking on the "mA" button. ECG modulation can be switched off by clicking on the "Manual mA" button. "Min" and "Max" define the mA range of the modulation, whereas "Start phase" and "End phase" describe the part of the RR interval to which the maximum mA is applied. Recommended mA values are listed in **Table 9d.4**

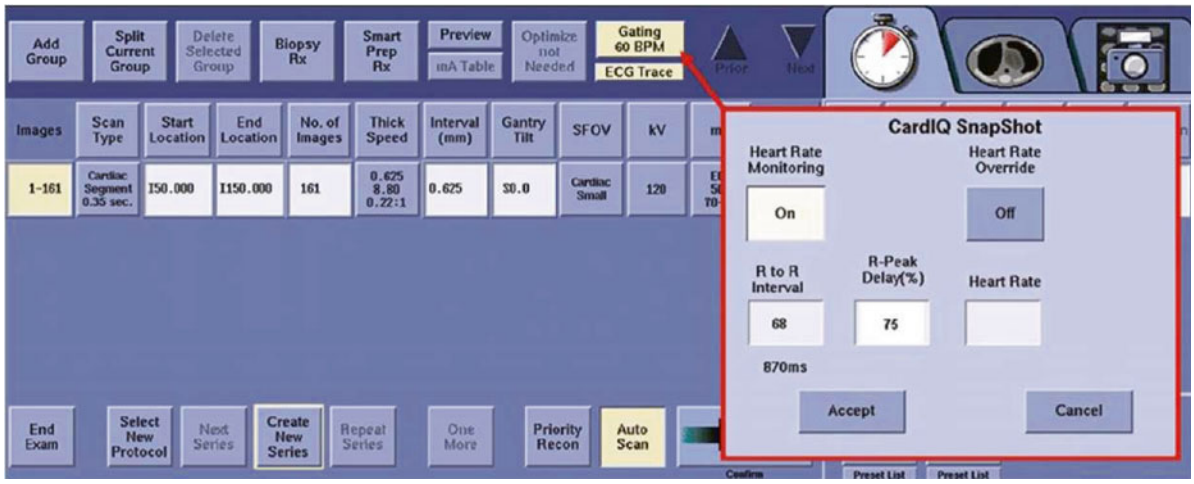

Fig. 9d.8 Before starting the scan, make sure that the reconstruction phase is centered at 75%. The "Heart Rate Override" button allows you to use a lower pitch than suggested by the software

9d.5 Image Reconstruction

Once the scan is completed, select "retro recon." Select the phase button and process the images from 70 to 80% of the RR interval with an incremental step of 10% in the mode in which the images were acquired. These images (displayed as complete series) will be used if the heart is not frozen at 75% of the RR interval from the initial scan. The images can also be processed from any other point within the RR interval (**Fig. 9d.9**) using percentages or milliseconds within the cardiac cycle. If the RCA is not frozen in the 70–80% phase range, it is best to reconstruct the phases centered at 40–55% (endsystole).

An iterative reconstruction technique (Adaptive Statistical Iterative Reconstruction, ASiR) is available with 0–100% blending rate in Slice and Volume mode at Recon Option (**Fig. 9d.10**). A clinical case example with ASiR is shown in **Fig. 9d.11**.

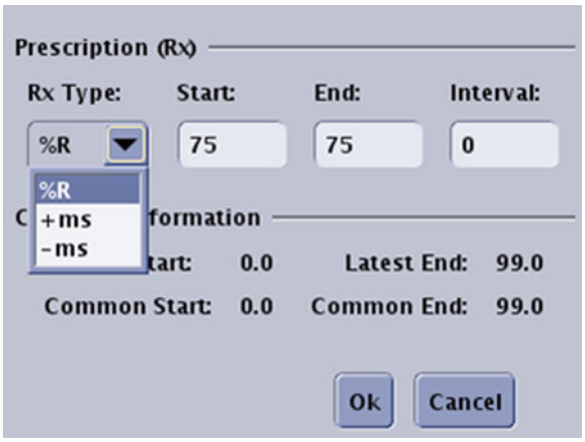

Fig. 9d.9 Reconstruction at different phases

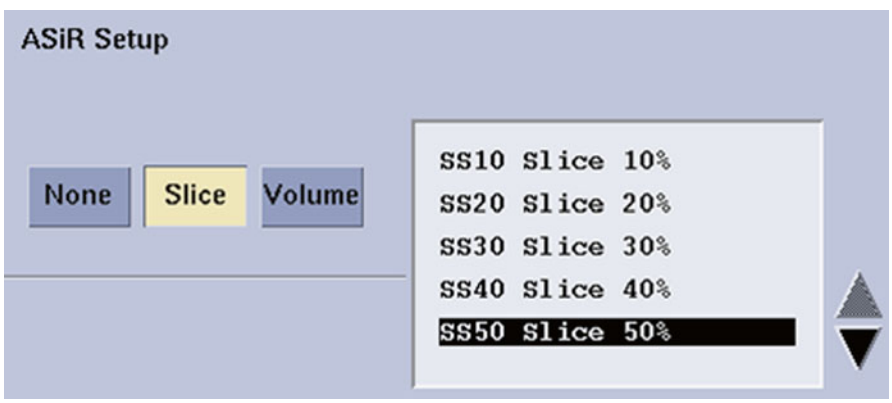

Fig. 9d.10 Choosing the ASiR mode and blending rate in Slice and Volume modes. ASiR 50% reduces the radiation dose by about 50%, while retaining image noise performance

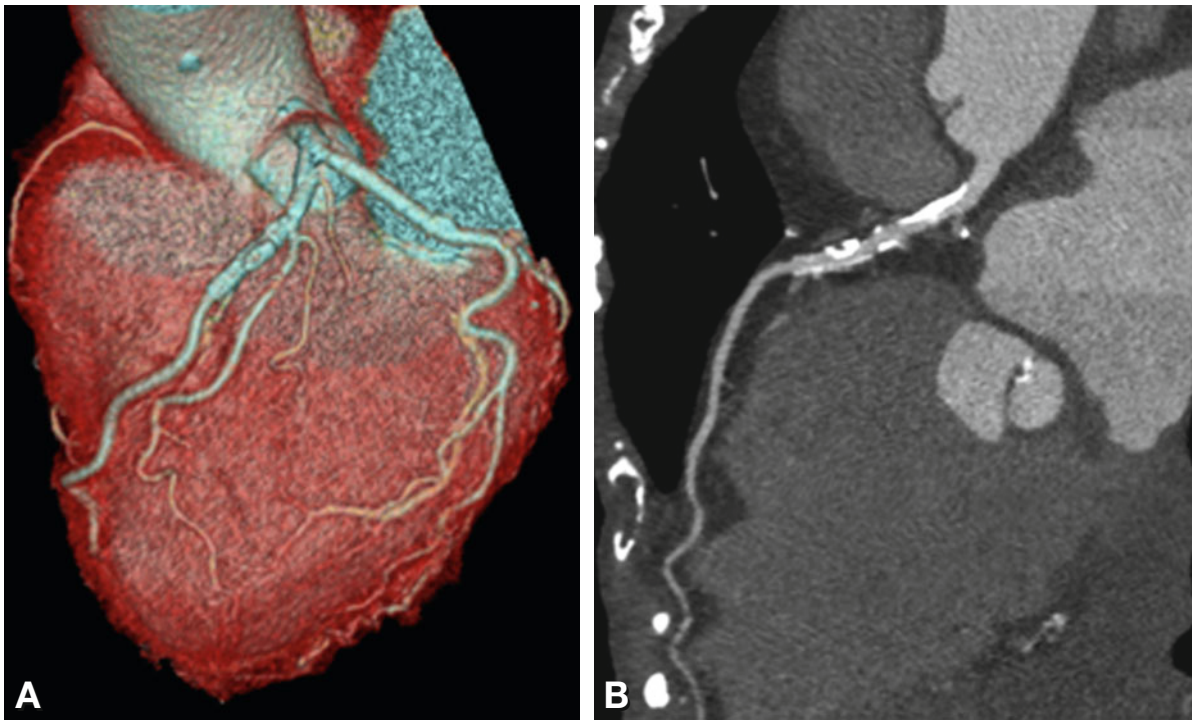

Fig. 9d.11 ASiR example with volume rendering (**Panel A**) and curved multiplanar reformation (**Panel B**) obtained by the Discovery CT750 HD scanner in a 91-year-old patient with a BMI of 15.7 for coronary evaluation. The scan technique was 100 kVp, 140 mA and 350 ms rotation with 105 mm scan range, and the radiation dose values were 22.24 mGy*cm (dose length product), corresponding to 0.38 mSv (Image courtesy of T. Keida, Edogawa Hospital, Japan)

9d.6 Discovery CT750 HD

9d.6.1 Technical Characteristics

The last-generation GE scanner is characterized by a better in-plane spatial resolution (0.23 mm). This improvement is due to (1) new detector material (gemstone) able to provide a primary speed of 0.03 ms and an afterglow of only 0.001% and (2) a new data acquisition system, which allows acquiring 2.5 times more views. Also, this scanner features a new generator tube supporting ultrafast kV switching for dual-energy imaging and can reconstruct images using adaptive statistical iterative reconstruction (ASiR), reducing noise by 50–70%. Recently, model-based iterative reconstruction (MBIR) has been introduced for clinical use, which will reduce noise by 80–90%. However, MBIR is not yet applicable to cardiac CT.

9d.6.2 Image Acquisition and Specific Reconstruction Kernels

Coronary CT should be done in the high-resolution mode (**Fig**. 9d.12). Prospective (axial) acquisition can be selected using the snapshot segment cine mode. Retrospective helical acquisitions with the HD 750 can also be done using (a) single segment (SnapShot), (b) dual-segment (SnapShot Burst), or (c) three to four segments (SnapShot Burst Plus, **Fig**. 9d.3 and 9d.12). The

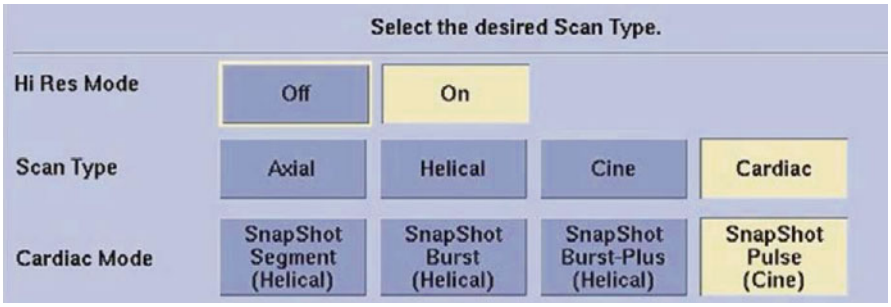

Fig. 9d.12 Choosing the high-definition option: the high definition is indicated as Hi Res Mod (high resolution modality) option. The label of the HD modality is right above the Scan Type. After choosing cardiac scanning, the axial reconstruction algorithm (step and shoot) can be selected with SnapShot Pulse (Cine). The helical reconstruction algorithm can be planned selecting "SnapShot Segment" (Helical), "SnapShot Plus" (Helical), or "SnapShot Burst-Plus" (Helical)

Table 9d.5 Image acquisition parameters with the 750HD CT scanner

Scan type	Helical	Axial
Rotation time (s)	0.350	0.350
Slice thickness (mm)	0.625	0.625
Slice interval (mm)	0.4	0.625
SFOV	Cardiac small	Cardiac small
DFOV	Adjust as small as possible	Adjust as small as possible
Pitch	0.16–0.24 (automatically selected by the scanner)	
Reconstruction type	HD standard	HD standard
ASiR	40%	40%
Padding		Automatic: based on heart rate Manual: 0–300 ms

DFOV display field of view, *SFOV* scan field of view

recommended scanning parameters and tube settings for the prospective and retrospective modes are summarized in **Table** 9d.5 and 9d.6. To take advantage of the high-definition mode the use of specific kernels (HD standard and HD details) is mandatory (**Fig.** 9d.13). Cardiac CT reconstruction should be done using the adaptive statistical iterative reconstruction (ASiR) algorithm although this takes slightly longer than standard filtered backprojections (35 s vs. 16 s for 10 images). The ASiR level should only be 40% since a combination of filtered backprojection and a certain level of ASiR provides a compromise between adequate noise reduction and retaining the more typical appearance of CT images.

Table 9d.6 Recommended kV and mA values with the 750HD CT scanner

Acquisition mode	Helical[a]		Axial	
	Tube current (mA)	Tube voltage (kV)	Tube current (mA)	Tube voltage (kV)
BMI <20	150–400	80–100	400	80–100
BMI 20 to <25	150–500	100	500	100
BMI 25–29	150–750	100	750	100
BMI >29	150–625	120–140	625	120–140

[a]Using tube current modulation

9d.6.3 Adaptive Gating and ECG Editor

One of the most important features of HD CT is the adaptive gating system in the SnapShot Pulse mode. When this prospectively gated acquisition mode is used, the scanner is able to stop and skip a premature heartbeat and wait for the next normal cardiac cycle to acquire data. Before scanning in the SnapShot Pulse mode, the operator can choose the maximum number of extrasystoles to be skipped during acquisition. In the cardiac retro recon, the HD scanner provides an ECG editor (**Fig**. 9d.14), which allows manipulating the position of the reconstruction window within the cardiac cycle in case of premature contractions. Typical images obtained using this scanner and reconstruction are shown in **Fig**. 9d.15.

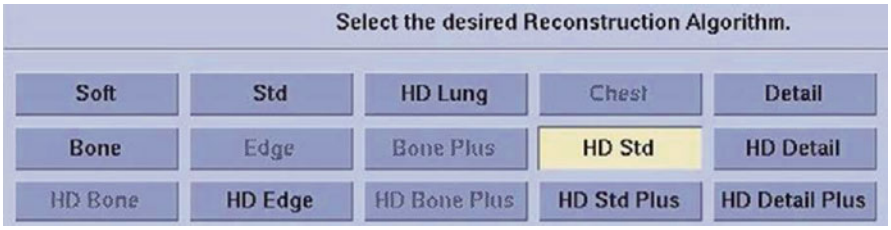

Fig. 9d.13 Choosing the cardiac scan type and the high-resolution option, the user can select the "HD Std" kernel or the "HD Detail" kernel. HD Detail allows having higher spatial resolution but is also noisier than HD Std and may thus be best suited for stent analysis and heavily calcified vessels

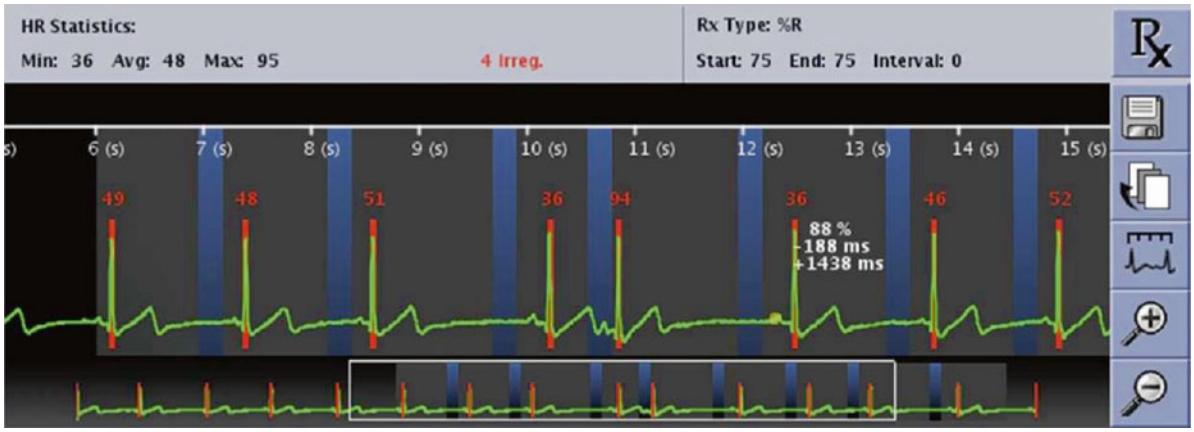

Fig. 9d.14 The ECG editor allows one to move the reconstruction window along the cardiac cycle to reduce artifacts and is available in both retrospective helical and prospective (pulse) acquisitions. In the pulse mode, the width of padding somewhat limits the range through which the reconstruction window can be moved. The position of the recon window can be adjusted by dragging the corresponding R peak (*red line*)

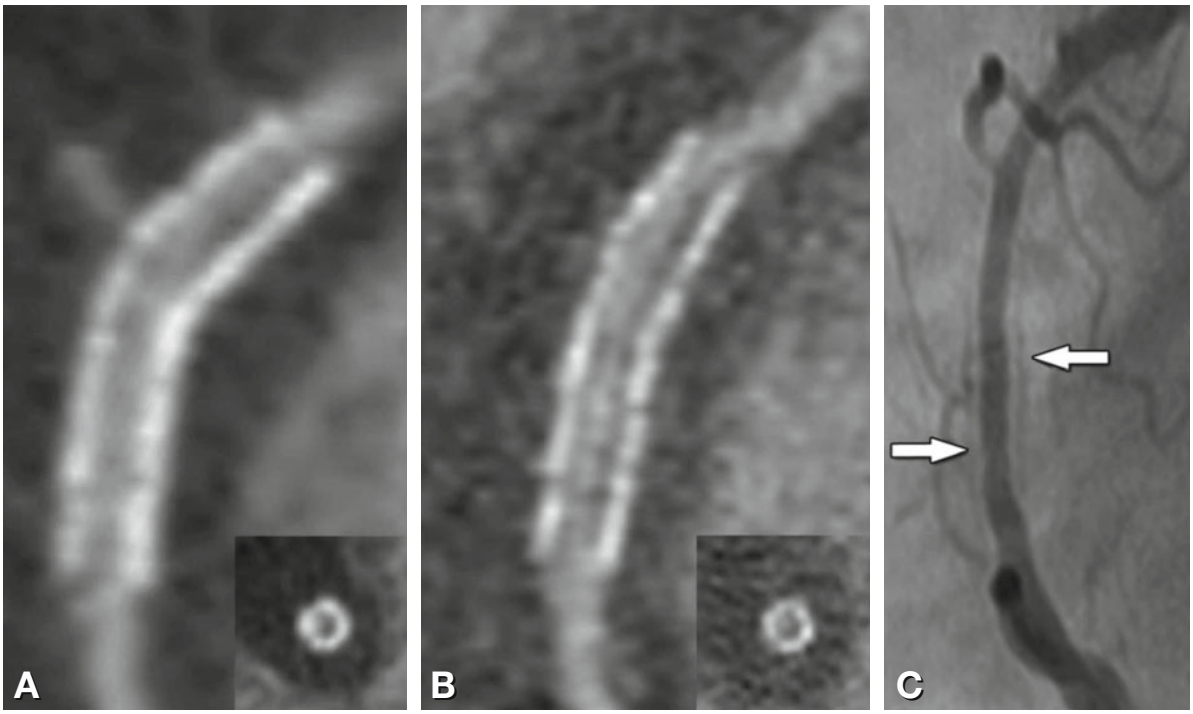

Fig. 9d.15 Typical images obtained with the Discovery CT750 HD in *a* 50-year-old male patient for stent patency evaluation. **Panel A** shows a curved multiplanar reformation of the initial examination with the Lightspeed VCT XT (cross-section, *inset*); after 7 months the study was repeated on the Discovery CT 750 HD (**Panel B**). With depiction of intimal hyperplasia without significant stenosis. Conventional coronary angiography confirmed the presence of intimal hyperplasia (*arrows* in **Panel C**) (Image courtesy of J.-L. Sablayrolles, Paris)

9d.6.4 Temporal Resolution Enhancement and Cardiac Acquisition Parameter Optimization

Temporal Enhancement (SnapShot Freeze) is an image reconstruction technique used to correct coronary artery motion artifacts that sometimes degrade image quality in patients with high heart rates. This technique specifically targets coronary motion, adaptively compressing the temporal window within those circumscribed regions where most needed. As this technique estimates motion within a single cardiac cycle and corrects that motion, it is not susceptible to beat-to-beat inconsistencies or heart period/gantry period resonance points, which may limit multisegment reconstruction. Based on phantom experiments, the motion reduction that can be expected is comparable to that from a gantry with 58 ms rotation time. Temporal Enhancement utilizes three phase datasets to perform coronary vessel detection, motion estimation, and motion correction (**Fig**. 9d.16).

Automatic activation of Temporal Enhancement for high heart rate patients is enabled by a cardiac scan parameter optimization feature called SnapShot Assist. SnapShot Assist analyzes a patient's ECG trace recorded during a breath-hold to estimate heart rate and variability. This information is used to determine the appropriate acquisition mode and settings (axial or helical mode, phase range, etc.) for the gated cardiac series (**Fig**. 9d.17). The feature also prescribes appropriate kV and mA values based on patient size (**Fig**. 9d.18). Optimizing cardiac scan settings based on a patient's size and heart rate characteristics enables ultra-low dose imaging. For smaller patients with stable heart rates, dose values less than 1 mSv can be routinely achieved (see **Fig**. 9d.11).

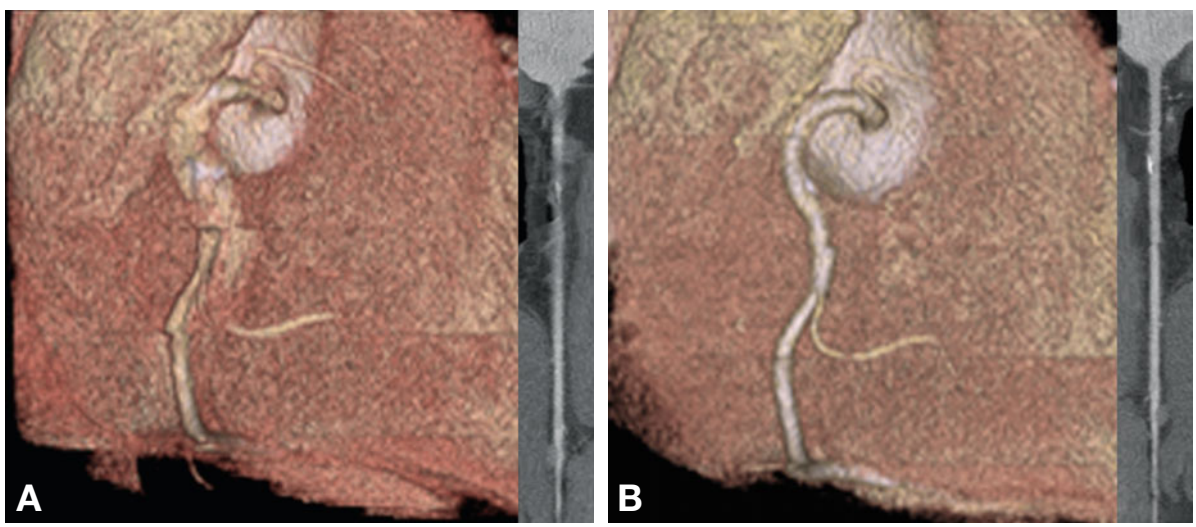

Fig. 9d.16 Improvement in image quality with temporal enhancement on the Discovery CT750 HD scanner using SnapShot Freeze in the right coronary artery of a 66-year-old patient who presented with chest discomfort. Heart rate during scanning was 70–73 beats per min. **Panel A** shows ASiR reconstruction without the Temporal Enhancement and **Panel B** shows the Temporal Enhancement using SnapShot Freeze. Comparison is done using a three-dimensional volume rendering and a curved multiplanar reformation of the right coronary artery

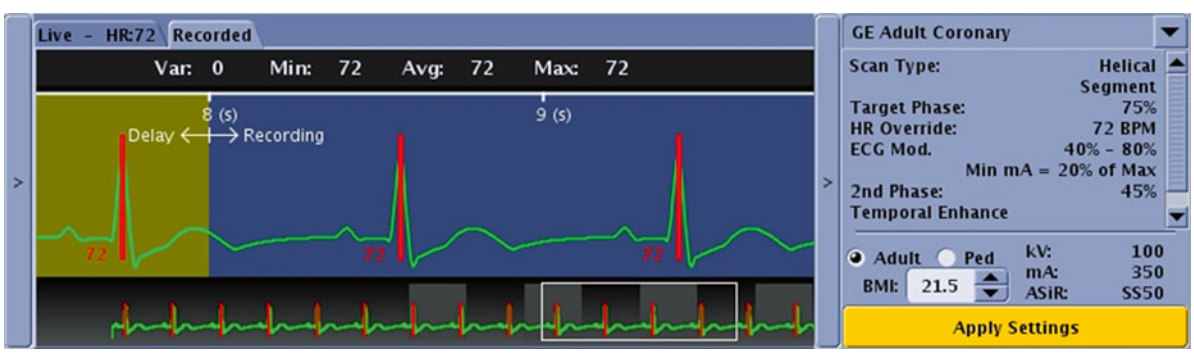

Fig. 9d.17 SnapShot Assist user interface. Based on the patient information (age and BMI) and data from ECG monitoring, optimal image acquisition and reconstruction parameters are recommended by SnapShot Assist before actually scanning the patient

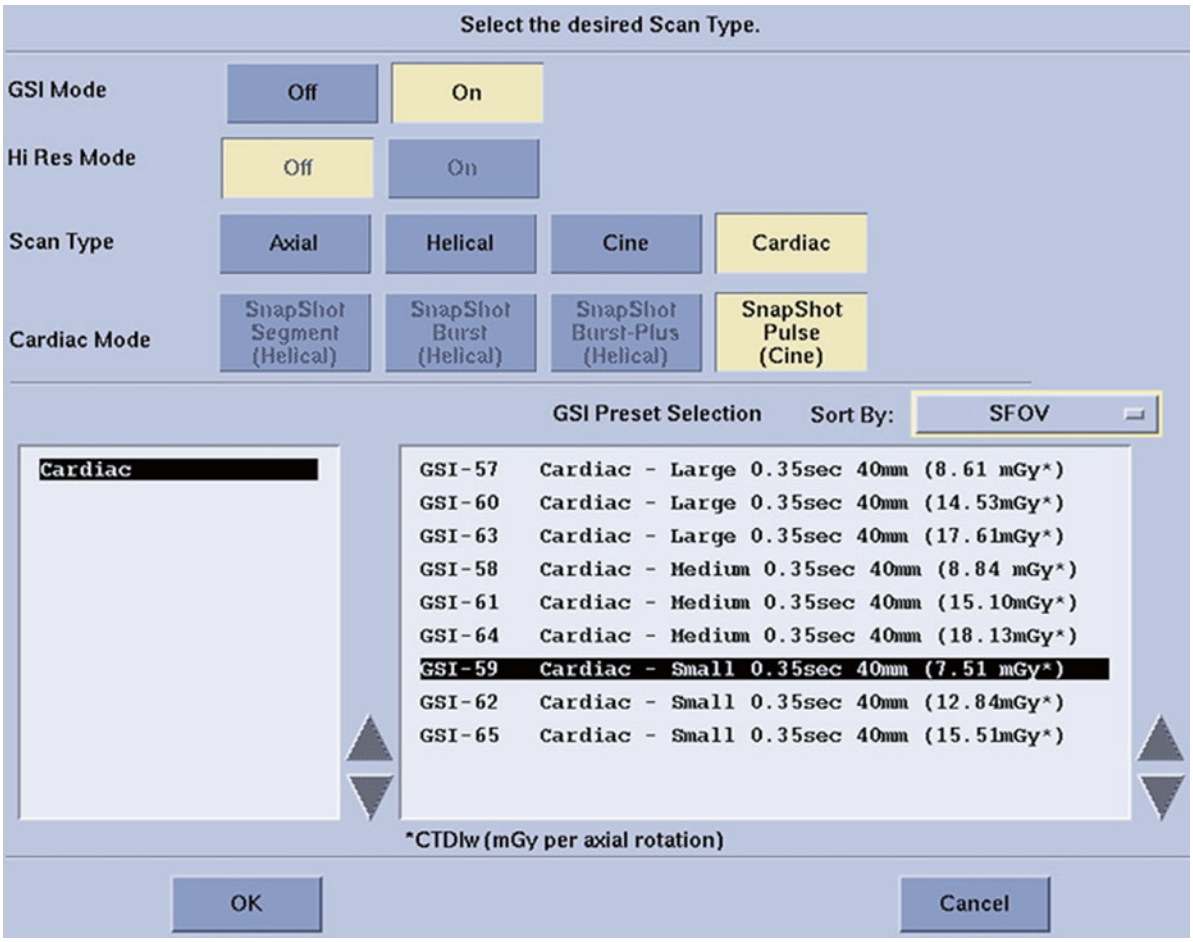

Fig. 9d.18 SnapShot Assist kV and mA table. Users can set kV, mA, ASiR blending values based on each BMI range

9d.6.5 Cardiac Spectral CT

The CT750 HD can scan using Dual Energy mode (Gemstone Spectral Imaging, GSI) with prospective ECG gating (GSI Cardiac). It uses ultrafast kV switching and projection-based image reconstruction, hence beam-hardening-corrected monochromatic imaging and material-decomposed density imaging methods are available. Choose GSI mode and Cardiac in the Scan Type, then select suitable scan preset. GSI cardiac has 9 presets with 3 different mA levels and 3 different scan field of view (FOV) settings (**Fig 9d.19**). A GSI-specific viewer and/or advantage workstation enable display of 40–140 keV in monochromatic images, and basis material density like iodine, water and calcium in material-decomposed density images. **Figure 9d.20** is a coronary artery imaging example with monochromatic images and material-decomposed density images. **Figure 9d.21** is a myocardial perfusion imaging example with monochromatic images using the advantage workstation perfusion feature.

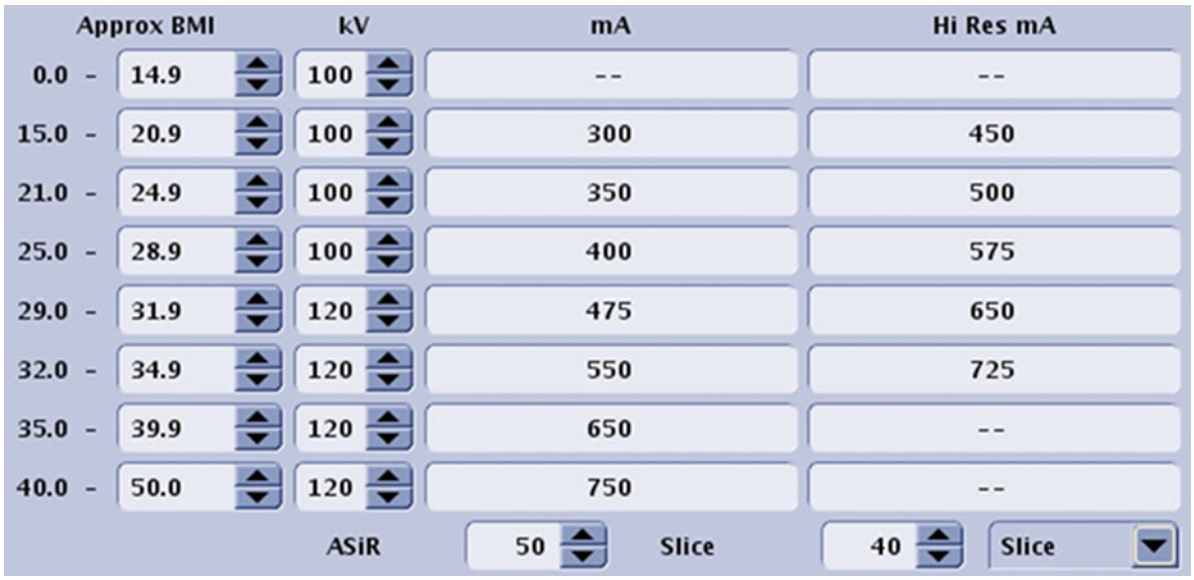

Fig. 9d.19 Choosing GSI Cardiac mode and GSI Cardiac image acquisition preset

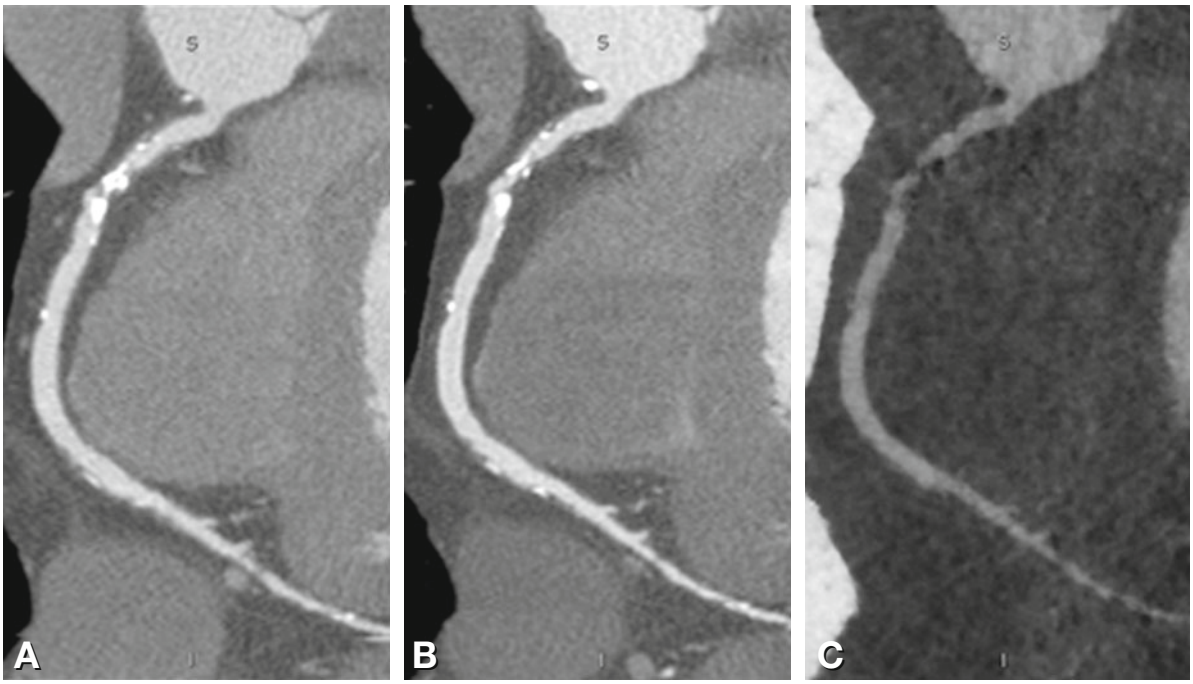

Fig. 9d.20 GSI of the right coronary artery obtained with the Discovery CT750 HD scanner. **Panel A** shows conventional 120 kVp and **Panels B** and **C** are the images generated by GSI cardiac acquisition. **Panel B** shows monochromatic 70 keV image, **Panel C** shows iodine material density image, This technique has the potential to improve the evaluation of severely calcified plaques

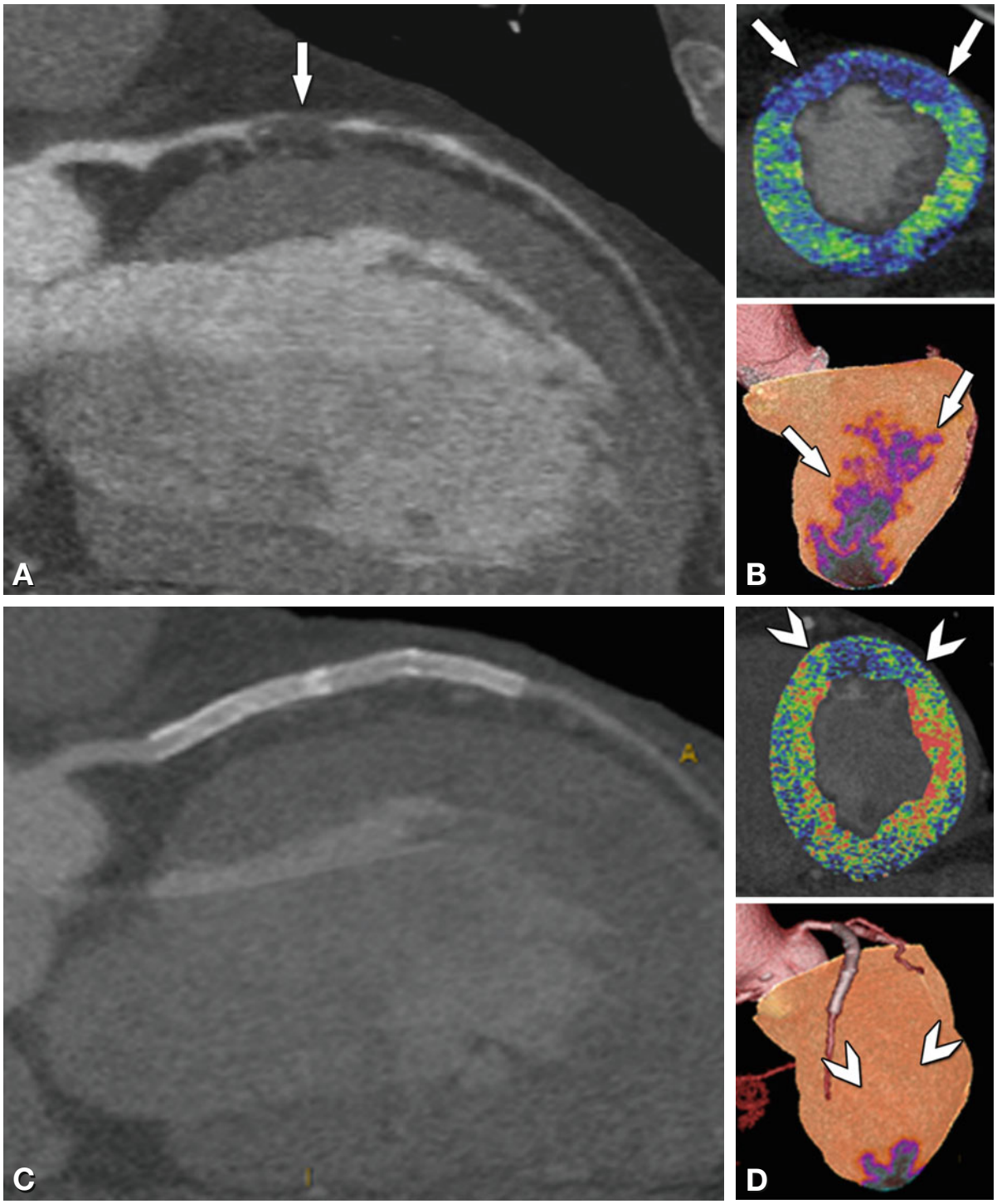

Fig. 9d.21 GSI of a left anterior descending coronary artery stenosis and adenosine-stress myocardial perfusion images in the short axis and a three-dimensional display obtained with the Discovery CT750 HD scanner before and after stent placement. **Panel A** shows a curved multiplanar reformation of the left anterior descending coronary artery with a 90% stenosis (*arrow*) and corresponding anterior ischemia (*arrows*) on stress myocardial perfusion with monochromatic imaging before stent implantation (**Panel B**). **Panels C** and **D** show the results after stent implantation with improved blood flow (*arrowheads*) (Image courtesy of G. Pontone, Milan, Italy)

Reading and Reporting

L.J.M. Kroft and M. Dewey

Abstract

In this chapter, we describe how to read and report cardiac CT studies. For reading it is recommended to use axial images together with coronal and sagittal slices complemented by curved multiplanar reformations and double-oblique maximum-intensity projections. Typical artifacts and how to avoid them is also discussed in this chapter. Structured reporting of findings has the advantage that it improves consistency.

10.1 Reading

10.1.1 Selecting Cardiac Phases

With current prospective electrocardiogram (ECG) gating techniques ("step-and-shoot") that substantially reduce patient dose, image acquisition is performed during a limited portion of the RR interval. Depending on the acquisition interval width (e.g., 70–80%, or 30–80%), "padding" for image reconstruction can be performed within the acquired range. It is important to select the phase(s) with the sharpest coronary artery depiction to maximize the number of coronary segments rendered without motion artifacts. If acquisition is restricted to the smallest acquisition interval possible for image reconstruction (e.g., center of the phase predefined at diastole at 75% of the RR interval for slow heart rates below 60 beats per minute), padding is not possible and image reconstruction can be performed at the predefined 75% phase only. With acquisition at a wider interval during the cardiac cycle, the best phase can be manually selected by visual inspection of different reconstructions from the acquired interval. Another approach that has recently become available is motion mapping, which automatically identifies the phases with the least overall motion (**Fig. 10.1**). Various automatic phase selection software tools are now available for use in clinical practice. If the phases reconstructed using any of these methods are not sufficient for making a reliable diagnosis, further reconstructions (e.g., from the 10 reconstructions rendered at 10% intervals throughout the RR interval) may be reviewed, although this requires acquisition of the full cardiac cycle (**Fig. 10.2**).

However, even after all the desired phases are reviewed, a coronary artery segment may occasionally still prove to be of nondiagnostic quality, e.g., because of artifacts resulting from very high or irregular heart rates or patient movement.

M. Dewey, *Cardiac CT*,
DOI 10.1007/978-3-642-41883-9_13, © Springer-Verlag Berlin Heidelberg 2014

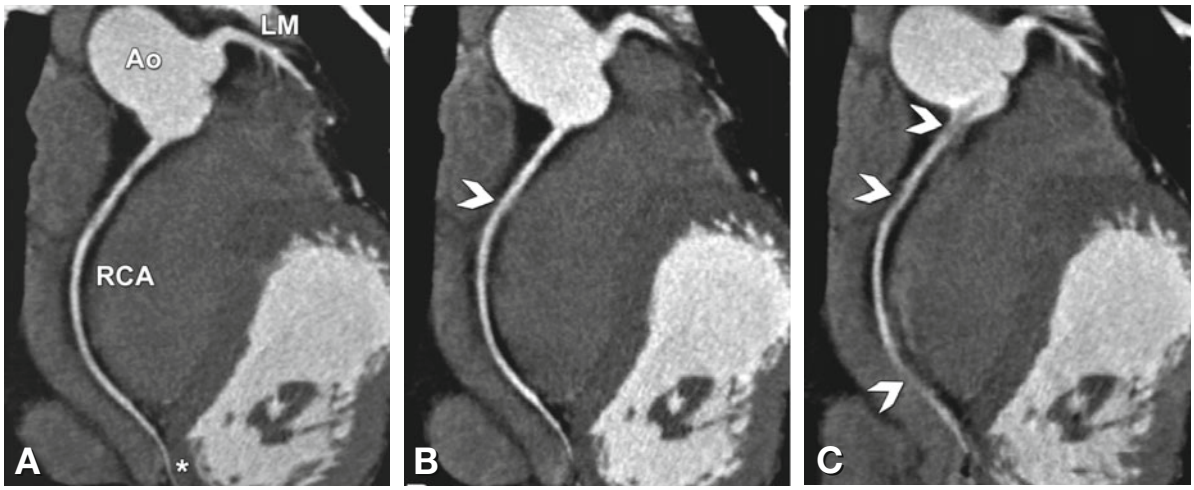

Fig. 10.1 Improved depiction of the right coronary artery (RCA) on curved multiplanar reformations using motion mapping with automatic identification of the phase with least motion during mid-diastole (**Panel A**), when compared with standard reconstructions centered at 70% (**Panel B**) and 80% (**Panel C**) of the cardiac cycle, which show minimal (**Panel B**) and more severe (**Panel C**) motion artifacts (*arrowheads*). Note the excellent visualization of the distal vessel segment with automatic phase selection (*asterisk* in **Panel A**). *Ao* aorta, *LM* left main coronary artery

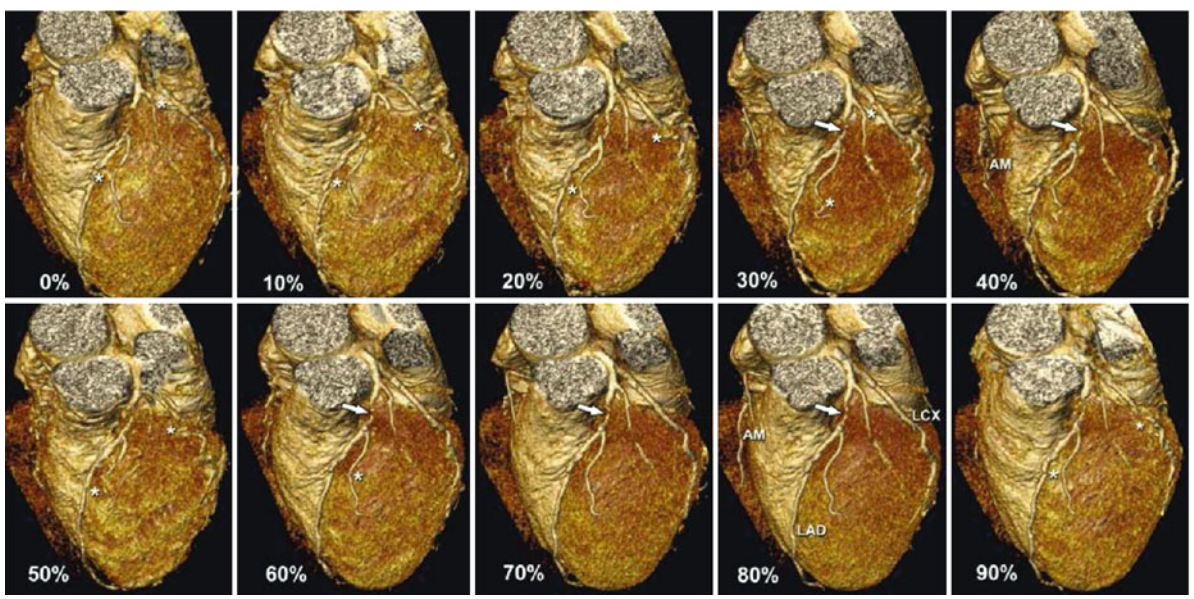

Fig. 10.2 Three-dimensional volume-rendered reconstructions of the coronary arteries (left anterosuperior views) shown for 10 image reconstruction intervals throughout the entire cardiac cycle (centered at 0–90%). There is a significant stenosis (*arrow*) of the proximal left anterior descending coronary artery (LAD), which is best seen at 70 and 80% but also at 40%. In comparison, however, the left circumflex coronary artery (LCX) is best seen at 70 and 80%. There are multiple motion artifacts in the other reconstruction intervals (marked with *asterisks*), rendering these phases nondiagnostic (artifacts were identified using the axial source images). Interestingly, the right coronary artery with its acute marginal (AM) branch is well depicted during mid-diastole (80%) as well as end-systole (40%). In many cases, the right coronary artery is best seen at end-systole (especially at higher heart rates)

If a stenosis is seen in any phase, this finding should be confirmed by excluding motion artifacts. This confirmation can be accomplished in two ways: (1) by correlating the results with those for the same coronary segment in another phase, and/or (2) by reviewing the axial images in lung window settings in order to detect potential motion in the image (e.g., at the heart-lung border). If no stenoses are seen and image quality is good, it is not necessary to go through all the reconstructed coronary artery phases. The comprehensive assessment of a cardiac CT study on a workstation takes time and concentration.

10.1.2 Systematic Approach

The review of a cardiac CT data set focuses on the coronary arteries but should also comprise assessment for other cardiac findings and extracardiac findings. As in all radiological examinations, a systematic approach is pivotal to a comprehensive evaluation of all anatomical regions (**List 10.1**). Easy evaluation of the coronary arteries is now possible by reading (semi) automatic curved multiplanar reformations, which are crucial for detecting pathology. However, the findings should always be confirmed on the original slices in axial, sagittal, and/or orthogonal orientations. Reading is improved when curved multiplanar reconstructions, double-oblique reconstructions, and source images can be evaluated simultaneously. Thin-slab (3–5 mm) maximum-intensity projections are usually very helpful in evaluating the continuity of the coronary arteries.

Among patients with suspected coronary artery disease, only 5% have obstructive (>50% diameter reduction) stenoses in distal segments or minor side branches without a more proximal stenosis (**Fig. 10.3**). Thus, major branches and side branches as well as bifurcations are first places to look when searching for significant stenoses. Prestenotic dilatation of the vessel lumen is an interesting indirect indicator of a significant stenosis located distally, and its recognition is critical. Furthermore, aneurysms of the coronary arteries are present in 5% of patients with atherosclerotic coronary artery disease but can also be present in patients without significant stenoses (**Fig. 10.4**).

If images look very poor on every reconstruction despite adequate contrast and compliance of the patient during the examination, one should inspect the recorded ECG tracing for irregularities, such as premature ventricular contraction, extrasystoles, or atrial fibrillation, or search for postprocessing errors by looking at the phases selected for image reconstruction. Using ECG editing, image degradation due to ECG irregularities can often be overcome by deleting or adding R waves for triggering and reconstructing image data without scanning the patient again (**Fig. 10.5**).

List 10.1. Systematic approach to reading cardiac CT studies[a]

1. Obtain a quick overview of the gross anatomy, e.g., by looking at three-dimensional renderings
2. Assess the individual coronary arteries and major side-branches by using reconstruction tools and viewing original slices, preferably simultaneously[b]
3. Evaluate the cardiac extracoronary structures[c]
4. Evaluate extracardiac organs[d]

[a] The approach may vary with the workstation used.

[b] Double-oblique reconstructions, thin-slab maximum-intensity projections, and curved multiplanar reformation are very helpful displays for evaluating the major coronary arteries and their large side-branches. Any pathology detected on such advanced reconstructions should be confirmed on original axial, coronal, or sagittal slices.

[c] This includes the cardiac valves, the myocardium, the atrial, and ventricular cavities (e.g., for presence of intracavitary thrombus), evaluation of (left) ventricular function, the pericardium, and the aortic root.

[d] This includes assessment of all organs other than the heart and has to be performed on large fields of view. Evaluate the large vessels (e.g., the aorta for dissection or aneurysm and the pulmonary arteries for presence of emboli), mediastinum, hila, lungs, chest wall and breasts, abdominal organs, and bones in organ-adapted window-level settings.

10.1.3 Source Images

Reading cardiac CT datasets requires knowledge of coronary and cardiac anatomy (Chap. 3). The axial source images represent the basic reconstructions that contain all information available in the three-dimensional dataset. Conclusions and final diagnoses should always be based on standard slices in the axial and orthogonal planes (which is possible because of isotropic voxel size in CT). Scrolling through the slices back and forth on a workstation is the best way to look at the source images. Additional information can be obtained from thin-slab maximum-intensity projections (see below) and interactive double-oblique positioning of slices along or orthogonal to lesions.

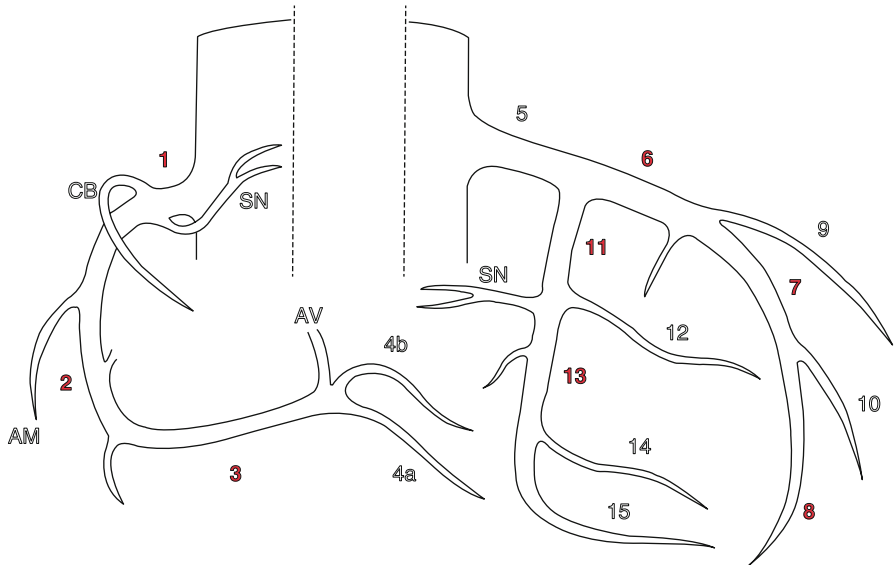

Fig. 10.3 Coronary artery model using 17 segments based on the AHA segmentation published in 1975 by Austen et al. The segments which account for more than 5% of percutaneous coronary interventions each and are thus of major relevance in reading cardiac CT have *pink numbers* (1–3, 6–8, 11, 13). The left main coronary artery (segment 5) is also of great relevance and in about 3% of cases obstructive stenoses are found here; they are mainly treated with bypass grafting (about two-thirds of cases) and less commonly with percutaneous coronary intervention. It is important to note that it is very rare to detect an isolated distal obstructive (>50%) stenosis without a significant proximal lesion in a patient. Nevertheless, also side branches and distal segments (as small as 2 mm in diameter) need to be searched for significant stenoses that might be amenable to treatment. Bifurcations are other important sites to look for stenoses when ruling out coronary artery disease. The right coronary artery consists of 5 segments (1-4a/b), with the distal segment (4) being further subdivided into 4a (posterior descending artery, PDA) and 4b (right posterolateral branch) in right-dominant circulation. The left anterior descending coronary artery consists of segments 6–10, with the two diagonal branches being segments 9 and 10. The left circumflex coronary artery consists of segments 11–15, with the two (obtuse) marginal branches being segments 12 and 14. In case of right-coronary dominance, at least one right posterolateral branch (segment 4b) is present and supplies the inferolateral myocardial segments. If the left coronary artery is dominant, the distal left circumflex ends as the posterior descending coronary artery (segment 4a). In case of codominance, segment 4a is part of the right coronary, and the distal left circumflex ends as a posterolateral branch (4b) after giving off two marginal branches. *AM* acute marginal branch, *Av* atrioventricular node branch, *CB* conus branch, *SN* sinus node artery (Modified from Austen et al. *Circulation* 1975)

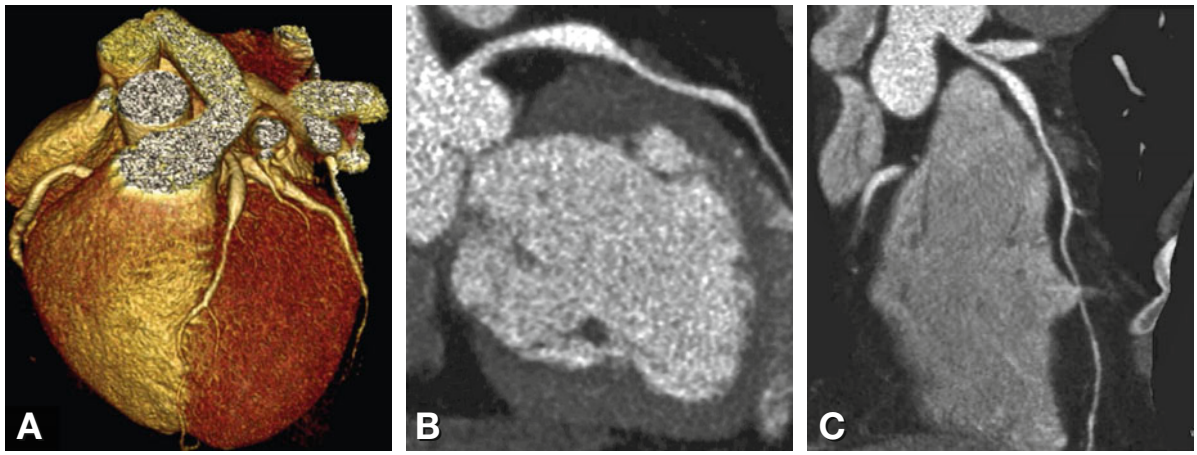

Fig. 10.4 Dilation without significant coronary stenosis. Volume-rendered image (**Panel A**) and multiplanar reconstructions (**Panels B** and **C**) of the left anterior descending coronary artery in a 47-year-old male with atypical chest pain. The patient had no coronary artery stenoses but did have dilating coronary artery disease. Note the dilation in the proximal left descending coronary artery. There is some focal myocardial bridging, and the right and left circumflex coronary arteries were also dilated (not shown)

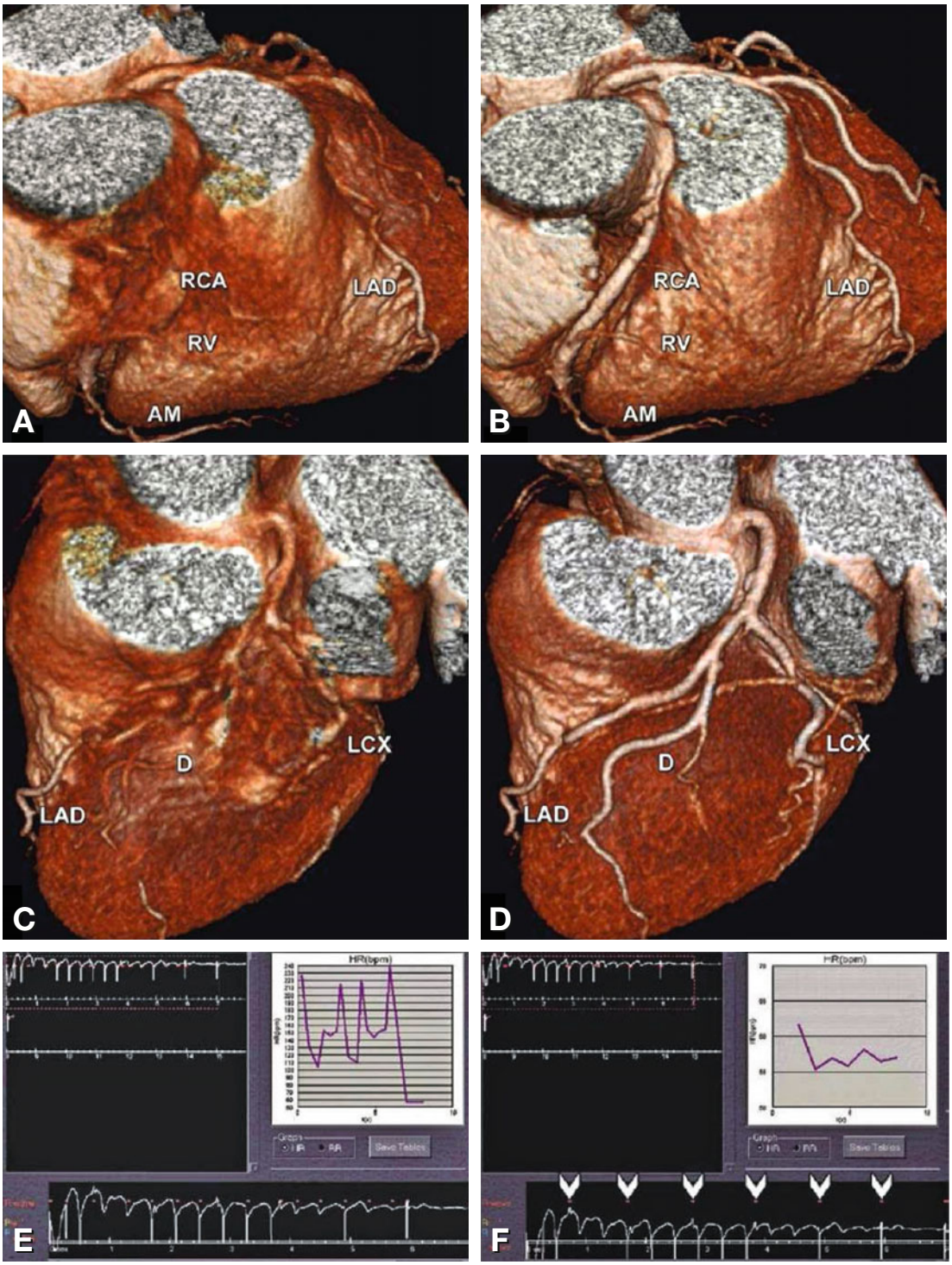

Fig. 10.5 Use of ECG editing significantly improves the image quality of reconstructions on the basis of the same raw data (without rescanning the patient). The left side (**Panels A**, **C**, and **E**) shows the results before editing, and the right side (**Panels B** and **D**) the three-dimensional reconstructions obtained after ECG editing. The entire course of the coronary arteries is blurred before ECG editing because of extrasystoles during scanning (**Panel E**, differentiating supraventricular and ventricular extrasystoles was not possible using this data and Holter ECG was recommended). Excluding the arrhythmic peaks and using only the typical R-wave peaks for editing (*arrowheads* in **Panel F**) greatly improves the images of both the right (**Panel B**) and the left (**Panel D**) coronary artery system. The right-hand corner *insets* in (**Panels E** and **F**) show the unedited and edited heart rate courses over time that were used for image reconstruction. *AM* acute marginal artery, *D* diagonal branch, *LAD* left anterior descending coronary artery, *LCX* left circumflex coronary artery, *RCA* right coronary artery, *RV* right ventricular branch

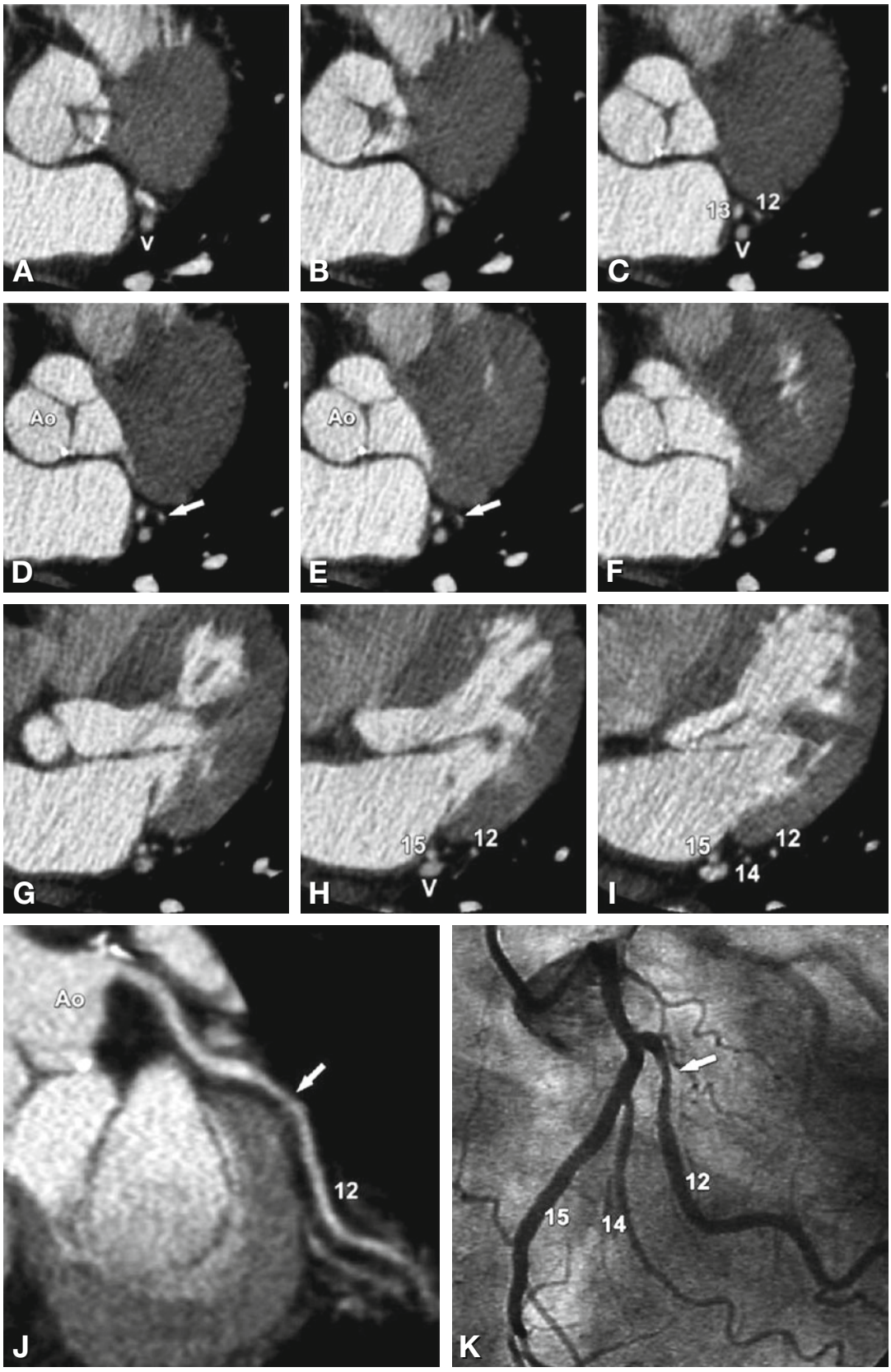
A
V
B
C
13
12
V
D
Ao
E
Ao
F
G
H
15
12
V
I
15
12
14
J
Ao
12
K
12
15
14

List 10.2. Reconstructions available for reading cardiac CT angiography studies

1. Axial, coronal, and sagittal images are the primary source of information
2. Curved multiplanar reformations are convenient for identifying stenoses
3. Maximum-intensity projections give a good overview of vessels and lesions but may obscure stenoses and overestimate calcified lesions
4. Angiographic emulations and three-dimensional renderings may be used for elegant display and presentation of findings

Compared with the source images, all other reconstructions such as curved reformations, maximum-intensity projections, angiographic emulations, and volume rendering (**List 10.2**) tend to reduce the information content and may even obscure relevant information. The main advantage of these reconstructions, which can be prepared by the technician, is that they make evaluation of the coronary arteries much easier because large vessel segments are displayed in a single image. This wide view can be beneficial in detecting abnormalities such as short coronary stenoses or wall irregularities (**Fig. 10.6**). Also, reconstructed images can be useful for demonstrating results during multidisciplinary team meetings. Printouts showing the reconstructed coronary arteries can be sent to the referring physicians as summaries of image findings and images stored in the picture archiving and communication system can be used for demonstration in interdisciplinary conferences.

10.1.4 Curved Multiplanar Reformations

Curved multiplanar reformations are generated using a centerline along the coronary vessel path and show large parts of the coronary vessel lumen in a single image (**Figs. 10.6** and **10.7**). Depending on the workstation used, the curved multiplanar reformations may be rotated around their centerlines, thereby rotating the coronary artery lumen around its longitudinal axis and greatly improving the visual estimation of the severity of the stenosis. The curved multiplanar reformations also allow rendering cross-sectional images orthogonal to the vessel course, which further facilitates the quantification of the percent diameter stenosis (based on reference and stenosis diameters, **Fig. 10.8**).

Continuously improving automatic vessel detection and segmentation tools are available for the creation of curved multiplanar reformations. These automatic software tools are currently available on all commercial workstations and allow diagnostic accuracy to be maintained while relevantly reducing analysis time. When using one of the currently available reconstruction tools, however, the user must be aware of two limitations of automatic segmentation that can lead to false-positive or false-negative lesions: First, the automatic vessel probing tools do not always entirely follow the course of the coronary vessels (especially if these are very tortuous). The resulting images may suggest stenoses on the curved multiplanar reformations that are, however, usually readily identified as artifacts (**Fig. 10.9**). The centerline should be checked (e.g., on three-dimensional renderings) when stenoses are suggested (**Fig. 10.9**), and the findings should be confirmed on the original images. Anders et al. have shown that, especially for less experienced readers, curved multiplanar reformations alone are not recommended but should be supplemented by interactive double-oblique reformations along the vessels. The second common limitation of automatic vessel detection is that the most proximal segment of the coronary artery may not be completely probed. Significant proximal stenosis can thus be missed if one looks only at the automatically probed vessel segments. However, this limitation is also easily overcome by manually or automatically adding the vessel portions that have been missed by the automatic tool (**Fig. 10.10**). Fully automated computer-aided diagnosis systems for coronary CT angiography have become available recently (**Fig. 10.11**). These are currently being validated for clinical use and may have the potential to be used as a second reader to increase sensitivity, especially when a less experienced reader is interpreting the scan.

In addition to motion artifacts resulting from a rapid or irregular heartbeat, heavily calcified coronary segments pose the greatest challenge because they obscure the coronary artery lumen (**Fig. 10.12**). Heavily calcified

Fig. 10.6 Short coronary artery stenosis of the first obtuse marginal artery (segment 12) that might be missed on axial images (**Panels A**–**I**), which show the stenosis on only two consecutive slices (*arrow* in **Panels D** and **E**). In contrast, this 75% diameter stenosis (as measured on quantitative coronary angiography) is easily detected on a curved multiplanar reformation (*arrow* on **Panel J**), demonstrating the advantage of such reconstructions along the vessel course. There is good agreement of the CT finding with conventional coronary angiography (**Panel K**). *V* cardiac vein

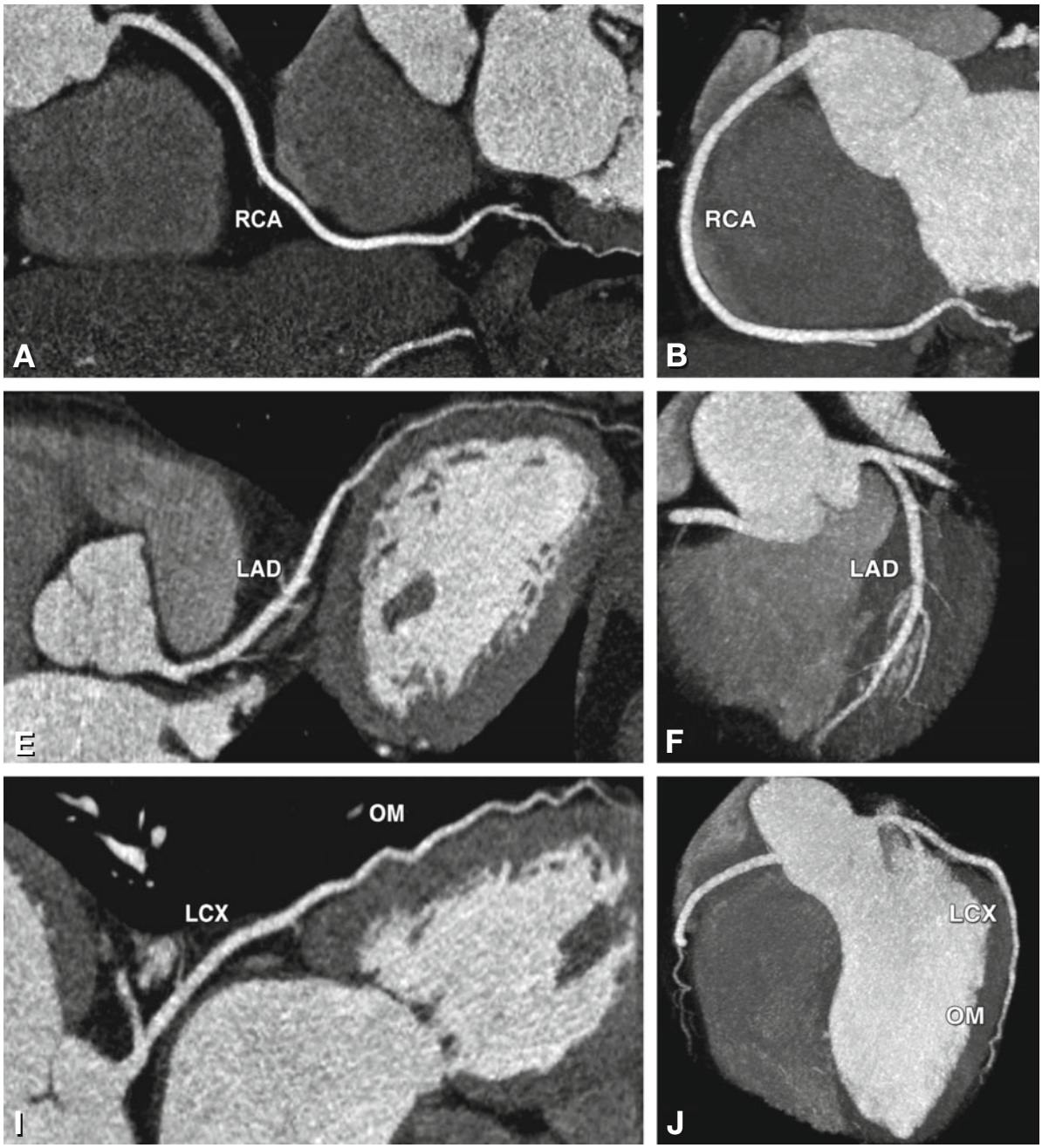

Fig. 10.7 Normal coronary arteries as seen on curved multiplanar reformations (*first column*), maximum-intensity projections(second *column*), and three-dimensional volume-rendered reconstructions (*third column*) of multislice CT using 64 simultaneous detector rows. There is good correlation with conventional coronary angiography (*last column*). The results are shown separately for the right coronary artery (RCA, **Panels A**–**D**), left anterior descending coronary artery (LAD, **Panels E**–**H**), and left circumflex coronary artery (LCX, **Panels I**–**L**). Curved multiplanar reformations allow estimation of the percent diameter stenosis from two perpendicular directions along the long axis or from orthogonal cross-sections and also the detection of coronary artery plaques, with evaluation of their composition. Maximum-intensity projections give a nice overview of the entire vessel but may obscure stenoses because of their projectional nature. Three-dimensional reconstructions provide an overview of long segments of the coronary arteries but should not be used for reading cases. Please note that there is right coronary artery dominance in this patient, with the right coronary giving off the posterior descending artery (PDA), as well as a large right posterolateral artery (RPL, inferior view of the heart in the *inset* in **Panel C**). *OM* obtuse marginal artery

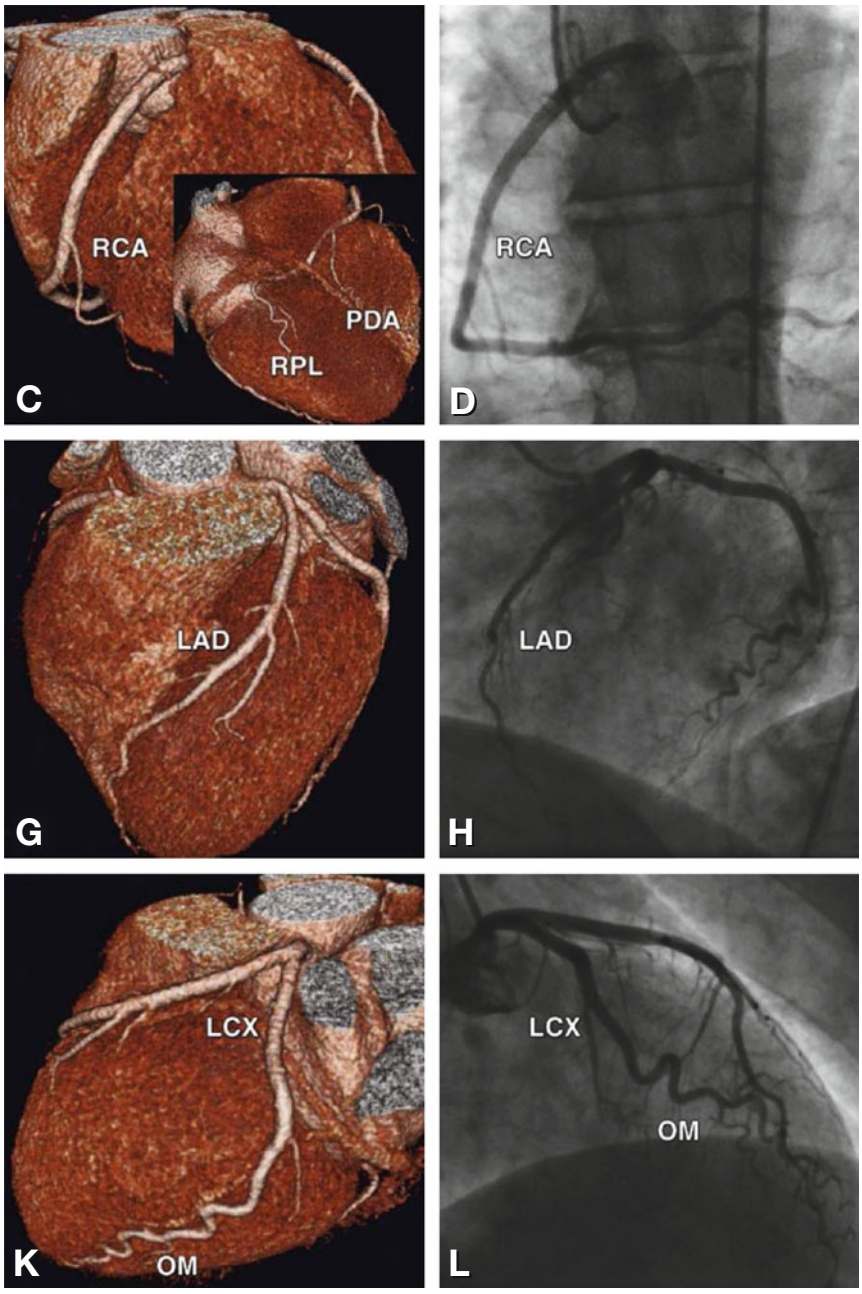
RCA
PDA
RPL
C
RCA
D
LAD
G
LAD
H
LCX
OM
K
LCX
OM
L

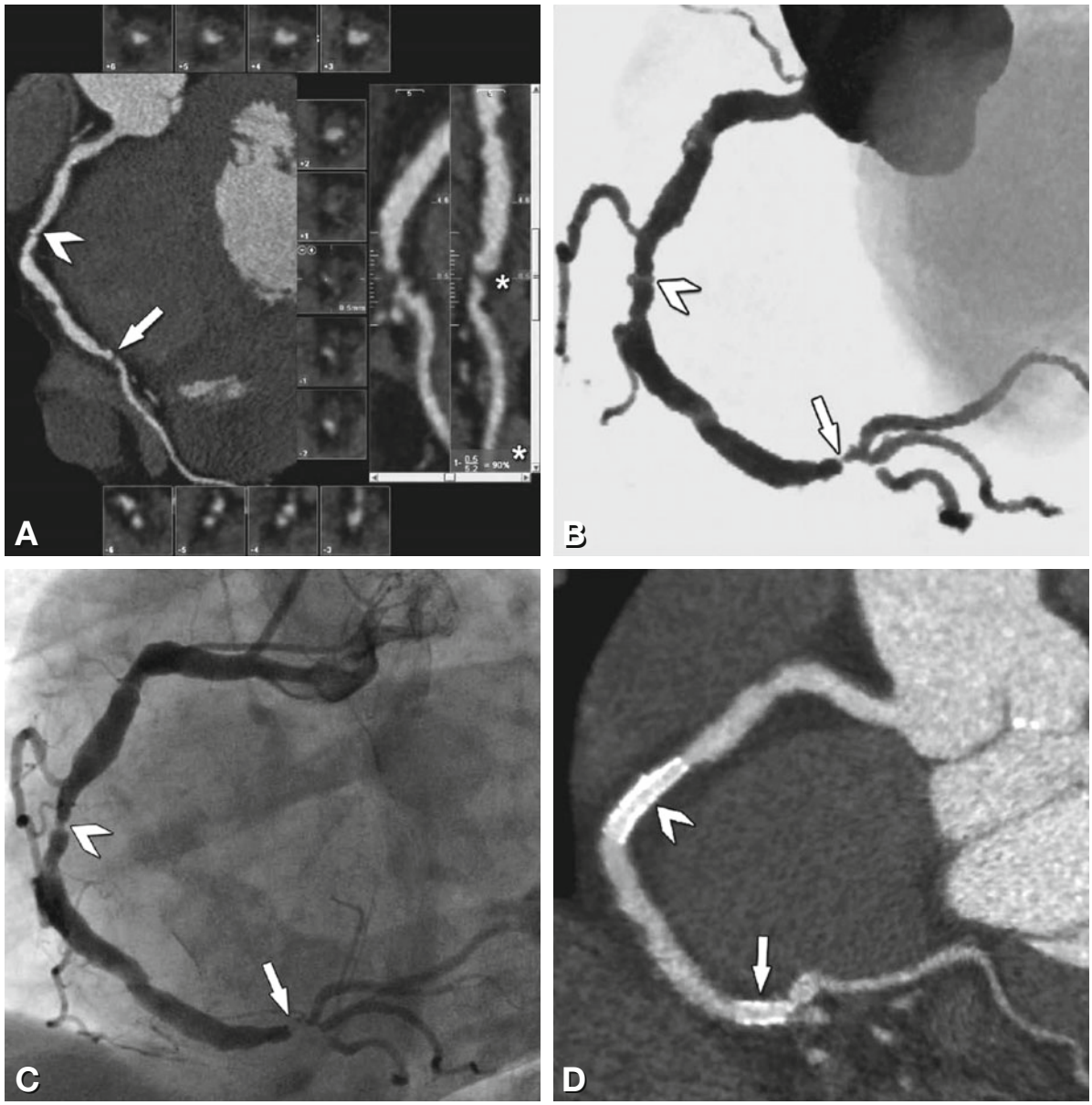

Fig. 10.8 Measurement of percent diameter stenosis using curved multiplanar reformations and orthogonal cross-sections. Right coronary artery with a high-grade stenosis at the crux cordis (*arrow* and *asterisk* in the perpendicular longitudinal views in **Panel A**). The reference vessel diameter is measured proximal and distal to the lesion, and the stenosis diameter is measured within the lesion on orthogonal cross-sections (*squared insets* in **Panel A**). From these measurements (automatic or by caliper) the percent diameter stenosis (in this case 90%) is calculated (*asterisk* in **Panel A**). There is good correlation with angiographic emulation of CT (**Panel B**) and conventional coronary angiography (**Panel C**) regarding this high-grade coronary artery stenosis. A second stenosis is present in segment 2 of the right coronary artery, which was calculated to be a 75% diameter stenosis on quantitative analysis (*arrowhead* in **Panels A**–**C**). Both stenoses were treated with stent placement and there was no significant in-stent restenosis on a cath view reconstruction of the follow-up CT (**Panel D**)

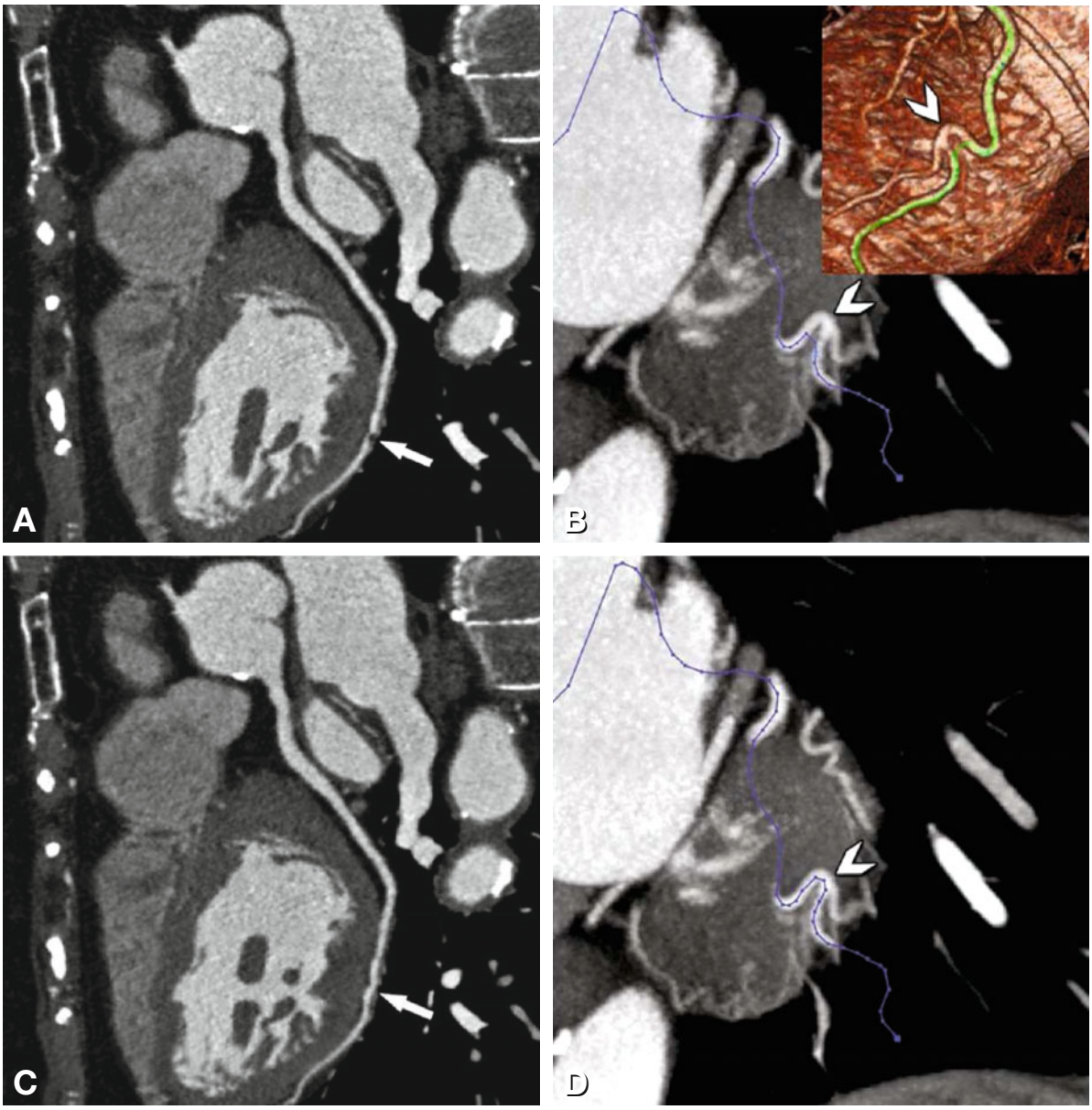

Fig. 10.9 Coronary artery pseudostenosis on a curved multiplanar reformation, caused by an automatic detection tool error. Pseudostenosis on the curved multiplanar reformation along the left circumflex coronary artery (*arrow* in **Panel A**) is caused by a short-track route of the automatic probing tool. This error in vessel tracking (*arrowhead*) is easily recognized on a maximum-intensity projection (*blue centerline* in **Panel B**) and in the *green centerline* on a three-dimensional reconstruction (*inset* in **Panel B**). After manual correction of the *centerline* (*arrowhead* in **Panel D**) the curved multiplanar reformation shows the actual course of the left circumflex coronary artery, which is unremarkable and continuous (**Panel C**)

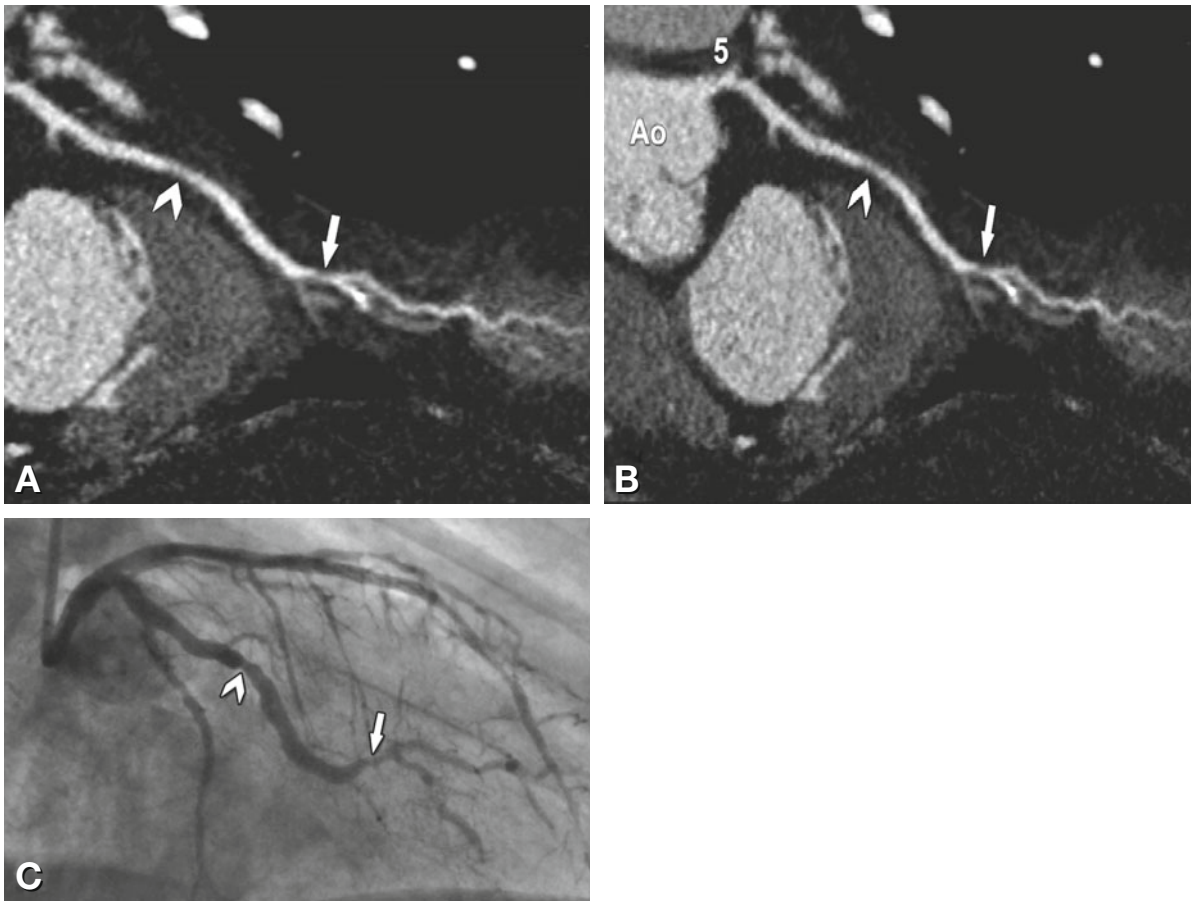

Fig. 10.10 The proximal vessel segment is sometimes missed by the automatic probing tool. Using such a curved reformation (**Panel A**), proximal stenoses cannot be excluded and, as illustrated here, manual extension of the *centerline* to the aorta (*Ao*) is necessary to visualize the entire vessel (**Panel B**) including segment 5 (left main coronary artery). There is a nonsignificant (*arrowhead*, 40%) and a significant stenosis in the first obtuse marginal branch (*arrow*, 70%), with good correlation with conventional coronary angiography (**Panel C**)

Fig. 10.12 Severe coronary calcifications can hamper the interpretation of CT coronary angiography. In this 82-year-old male patient, there are severely calcified plaques (*asterisks*) along the major course of the right coronary artery (**Panel A**) and left anterior descending coronary artery (**Panel B**). The resulting blooming artifacts obscure the coronary artery lumen, rendering the affected coronary artery segments nondiagnostic. These calcifications were found to cause only short significant stenoses (*asterisk*) in conventional coronary angiography (**Panels D** and **E**). There are additional less pronounced calcifications in the left circumflex coronary artery (*arrow* in **Panel c**), but these likewise preclude a definitive diagnosis regarding the presence of significant coronary artery stenosis. Conventional coronary angiography shows moderate stenosis of the left circumflex coronary artery (**Panel F**). Using stent kernels for severely calcified lesions might help to reduce the artifacts, although this approach results in higher noise levels that may also hamper evaluation. Specific window-level settings might be an option for analysis of both calcified and noncalcified plaques (**Fig. 10.13**). Note that there is also a short ostial stenosis of the right coronary artery (*arrow* in **Panels A** and **D**). *Ao* aorta

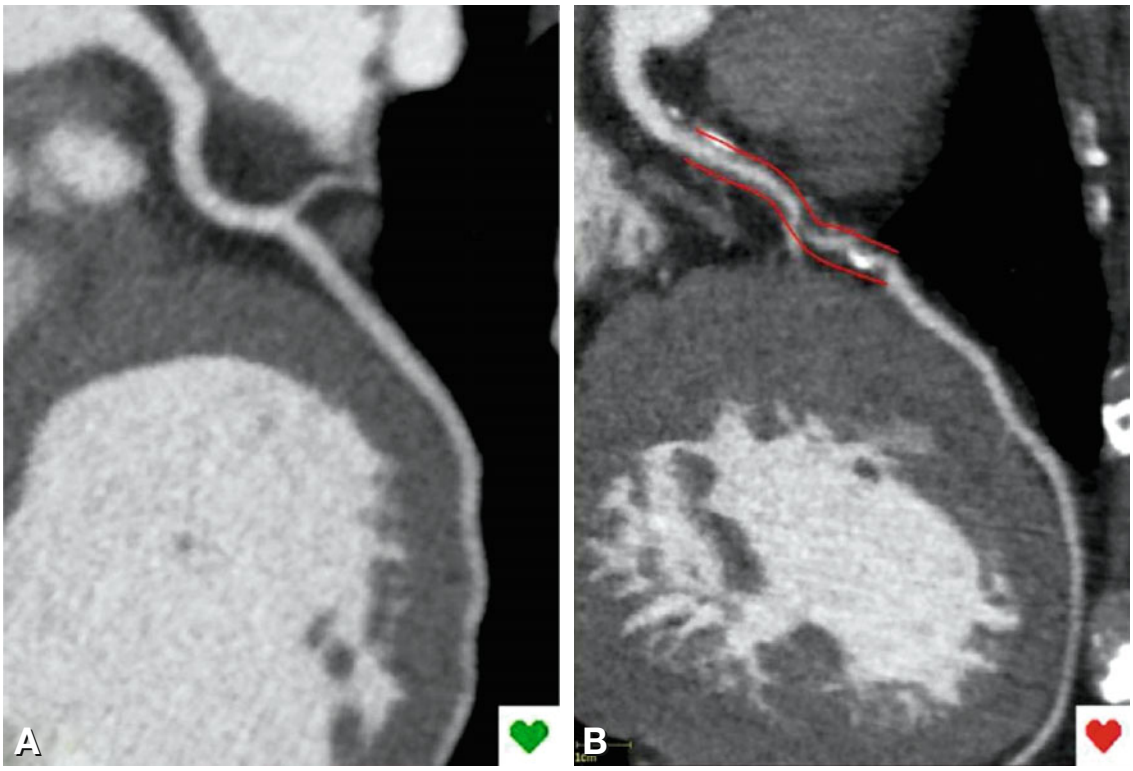

Fig. 10.11 Fully automated computer-aided diagnosis system for coronary CT angiography. This software (RCADIA, Cor Analyzer) allows automatic identification of patients without stenosis (**Panel A**) and with coronary stenosis (**Panel B**), who are indicated by green and red heart icons (*inset*), respectively

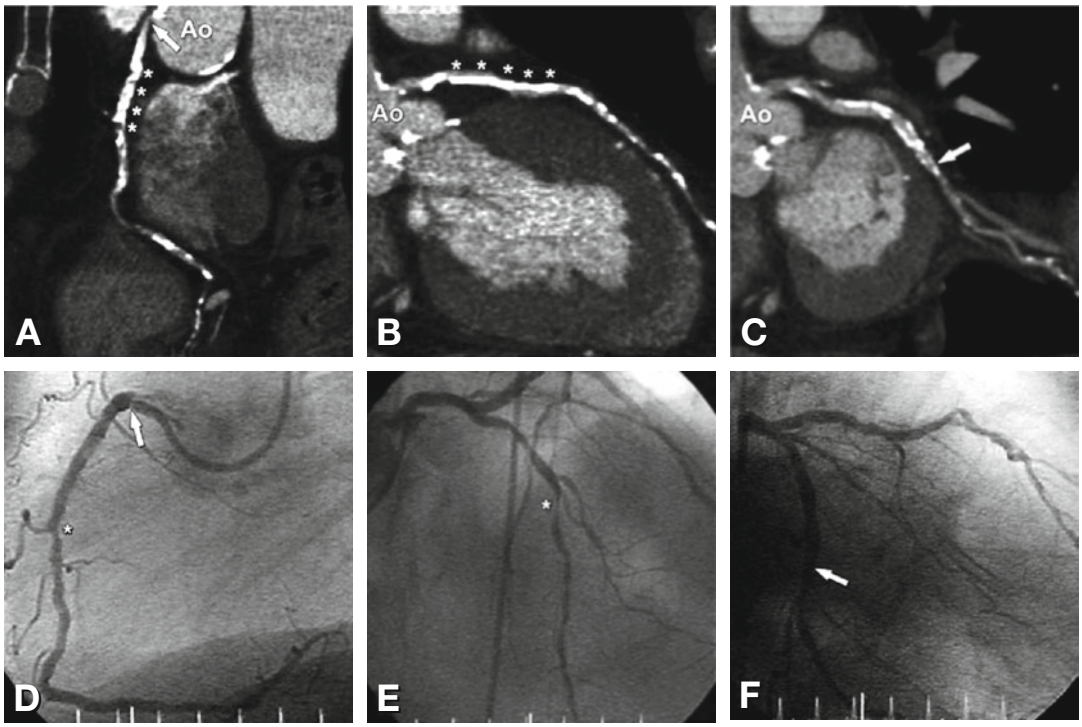

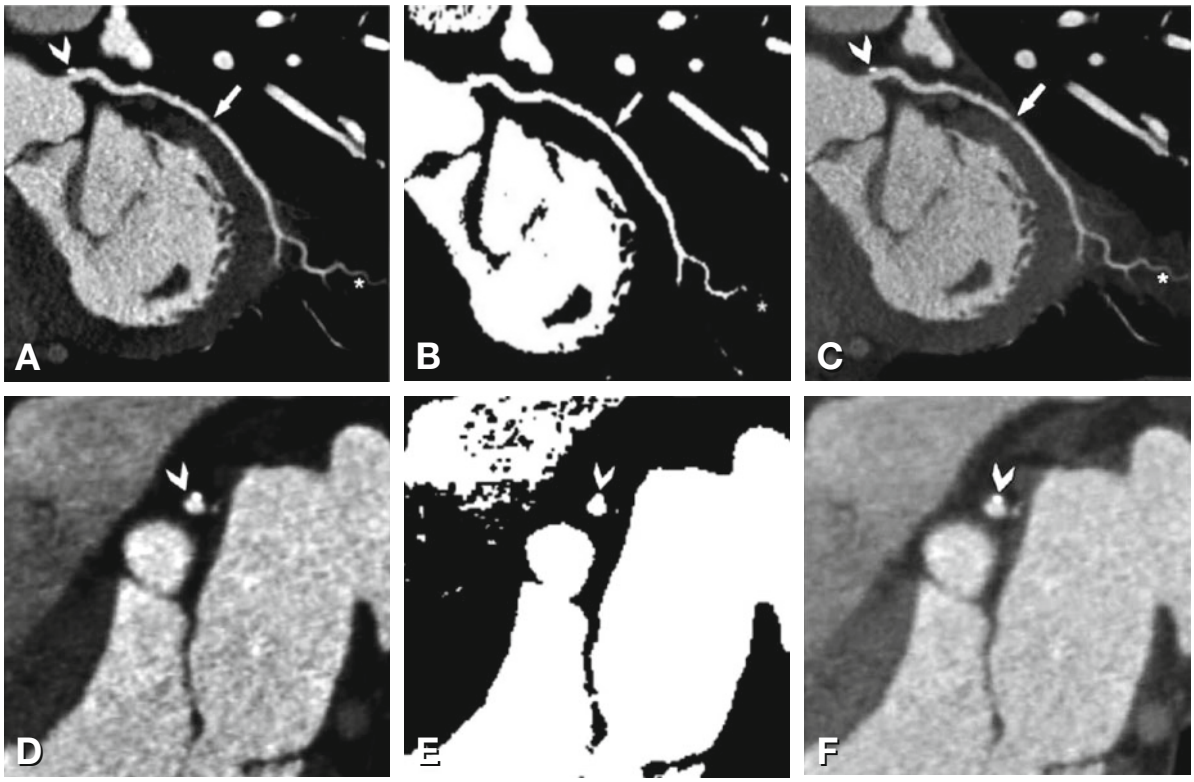

Fig. 10.13 Specific window-level settings may be used for different coronary artery plaques. The *upper row* presents curved multiplanar reformations along the left circumflex coronary artery, and the *lower row* presents cross-sections orthogonal to the left main coronary artery (as indicated by the direction of the *arrowhead* in **Panel A**). Noncalcified coronary plaques and outer vessel boundaries are best visualized using a window representing 155% of the mean density within the coronary lumen and a level representing 65% of the mean density within the lumen as described by Leber et al. (Chap. 14). (**Panels A** and **D**; this is very commonly equal to 600–700/250–300 HU settings). The noncalcified plaque in the left main coronary artery is nicely seen on the cross-section in **Panel D** (*arrowhead*), and distal vessel segments are depicted on the curved multiplanar reformation using these settings (*asterisk* in **Panel A**). Optimal measurement of the coronary lumen, however, is obtained by keeping the level constant at 65% of the mean lumen density while reducing the window width to 1 (**Panels B** and **E**). Using these settings yields the most accurate measurement of the diameter stenosis in comparison to intravascular ultrasound (in this case 55% diameter reduction) as shown by Leber et al. The drawbacks of these settings include the fact that distal vessel segments are not seen as well (*asterisk* in **Panel B**), and calcified plaques are no longer discernible from the lumen (*arrowhead* in **Panel E**). Using more bone-window-like settings (e.g., 1,300/300 HU here), as shown in the last column, reduces the artifacts caused by calcifications and results in less overestimation of calcified coronary plaques than when standard settings are used (*arrowhead* in **Panels C** and **F**)

segments may not be evaluable, although severe calcifications do not per se exclude evaluation. In this situation, visualization of coronary stenoses can be improved by using specific window-level settings (**Fig. 10.13**).

10.1.5 Maximum-Intensity Projections

Maximum-intensity projections can be varied in projection thickness and give a nice overview of vessel continuity and course in a single image (**Fig. 10.7**). In particular, thin-slab maximum-intensity projections (3–5 mm) are very useful for quickly depicting coronary artery disease. By scrolling through a dataset of thin-slab maximum-intensity projections (e.g., of axial source images), side branches are easily visualized and more side-branches can be recognized than on three-dimensional reconstructions. However, low-grade stenoses may be overlooked. The main drawback of reading maximum-intensity projections is that heavily calcified stenoses present with exaggerated blooming artifacts (**Fig. 10.14**).

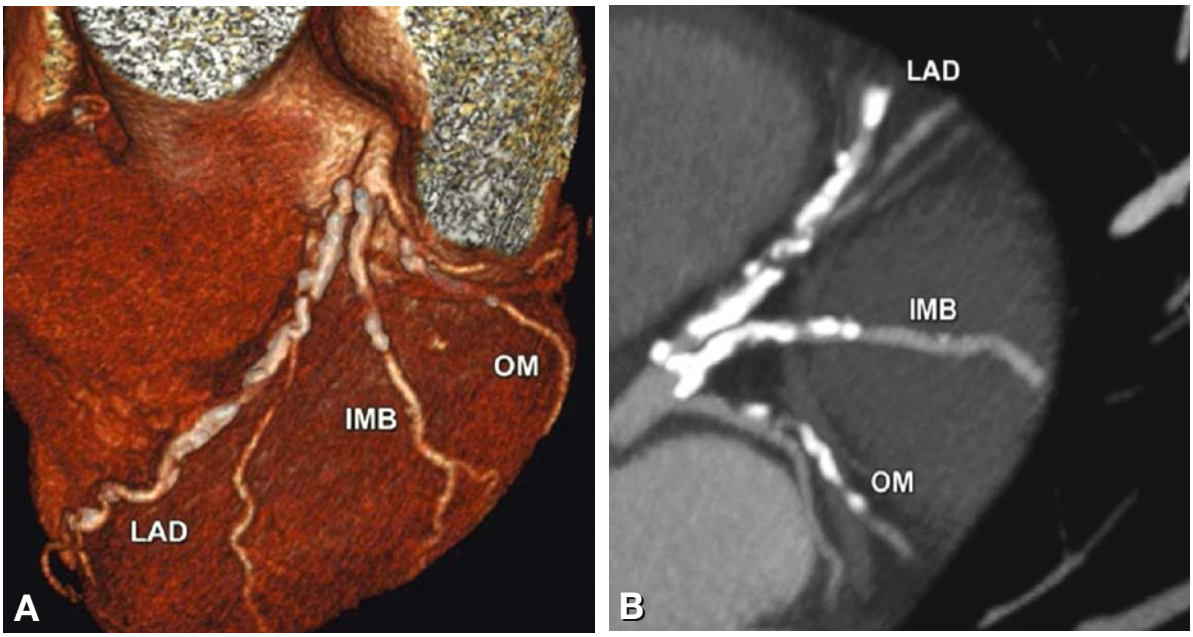

Fig. 10.14 Three-dimensional reconstructions (**Panel A**) and maximum-intensity projections (**Panel B**) do not allow the assessment of severely calcified coronary artery plaques, as shown here in the left anterior descending (LAD), intermediate branch (1 MB), and obtuse marginal branch (OM). Because of the projectional nature of maximum-intensity projections, calcified plaques can even be overemphasized (i.e., blooming; **Panel B**). Such blooming artifacts are less pronounced on curved multiplanar reformations and standard two-dimensional images with bone-window-type settings (**Fig. 10.13**). In this patient, conventional coronary angiography revealed significant stenoses in all three vessels

10.1.6 Volume Rendering and Angiographic Emulation

Volume-rendered and angiographic three-dimensional reconstructions are elegant methods for the display and presentation of findings (**Figs. 10.2**, **10.5**, **10.7**, **10.8**, and **10.15**) to referring physicians, patients, and colleagues during interdisciplinary meetings (Chap. 24). Interestingly enough, referring physicians have been reported to prefer angiographic emulations to standard curved multiplanar reformations, while simultaneously identifying the limited visibility and assessability of coronary plaques on these images as a main drawback. Coronary interventionalists may also prefer angiographic emulations of CT data, since they are used to viewing coronary arteries in predefined angiographic projections. Angiographic emulations look much like the interventional angiographic images, and if the desired angled projections are generated, these images may serve as improved anatomic roadmaps for guiding interventions. Making a diagnosis using only three-dimensional reconstructions is not recommended because of the abovementioned limitations.

10.1.7 Typical Artifacts

It is necessary to understand the technical limitations of CT that affect image quality in coronary angiography. The recognition of artifacts that can simulate coronary artery stenoses is particularly critical. The most important artifacts encountered in cardiac CT are summarized in **List 10.3**.

Artifacts have major implications for cardiac CT. Although spatial and temporal resolution has been greatly improved with 64-row CT scanners when compared with earlier scanners, artifacts are still a major problem. Such artifacts, which generally result from motion, can preclude the evaluation of parts of the coronary arteries, as is still the case in 3–12% of coronary

List 10.3. The most important artifacts in cardiac CT

1. Blooming artifacts caused by calcifications
2. Motion artifacts causing blurring
3. Low-contrast artifacts

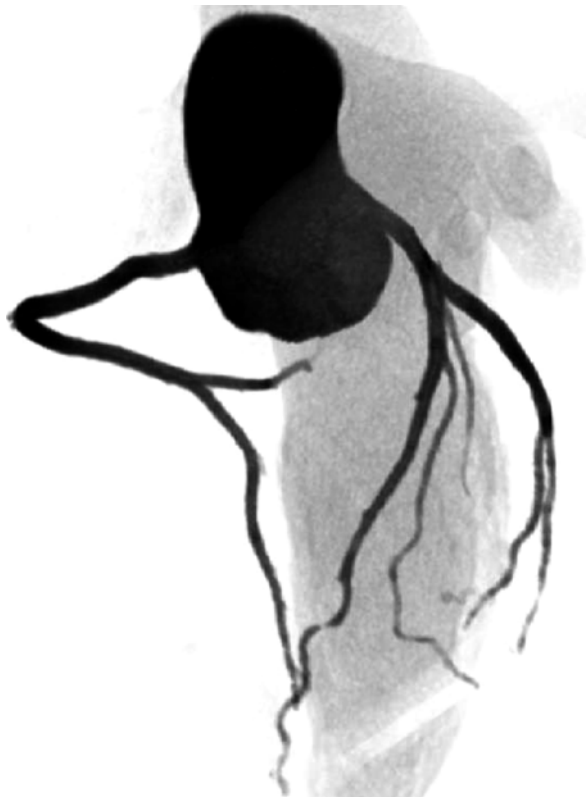

Fig. 10.15 An angiographic emulation of the entire coronary artery tree shows no significant stenoses. The advantage of this type of reconstruction is the striking similarity to conventional angiography, which helps interventionalists rapidly grasp the type and location of coronary lesions before performing invasive procedures. The drawback is that only the lumen and not the underlying plaque is seen on these images (**Fig. 10.8**)

artery segments imaged by 64-row CT scanners. Moreover, artifacts are the main cause of false-positive and false-negative diagnoses regarding the presence of coronary artery stenosis, with misinterpretation of stenosis grade being generally attributable to the presence of dense coronary artery calcifications (**Figs. 10.12** and **10.14**). Other important causes of misinterpretation are motion artifacts and poor contrast-to-noise ratio in obese patients.

Nearly all artifacts in CT are caused by limitations related to spatial resolution, temporal resolution, noise, and the reconstruction algorithms used. Artifacts cause blurring, blooming, streaks, missing data, discontinuities, and poor contrast enhancement.

Spatial resolution is the ability to visualize small structures in the scanned volume and is considered in three dimensions. Important parameters of spatial resolution are voxel size and geometric unsharpness. In the *x-y* plane, a pixel size of $0.35 \times 0.35\ mm^2$ can be obtained with a reconstructed field of view of 180 mm and a 512^2 pixel matrix. The greatest improvement introduced by the current generation scanners is that volumes with smaller section thickness in the Z-axis can be obtained. With 64-row CT, 64×0.6 mm or 64×0.5 mm collimations are achieved. Geometric unsharpness depends on factors such as focal spot size, detector size, and scanner geometry. Limitations in spatial resolution cause partial volume artifacts as a result of the attenuation coefficient in voxels that are heterogeneous in composition. Resulting artifacts include blooming and blurring, especially in the presence of calcifications (**Figs. 10.12** and **10.14**).

Temporal resolution is the ability to resolve rapidly moving objects and is strongly related to coronary artery size and motion. With the ECG-synchronized scanning techniques and rapid rotation times available today, it is possible to obtain "frozen" images by using half-scan or adaptive multisegment reconstruction at the cardiac phase with the least motion. If the cardiac rest phase is shorter than the scanner's image reconstruction window, motion artifacts occur, but images usually still have adequate diagnostic quality if the artifacts are slight (**Fig. 10.1**). Depending on the heart rate, image quality is generally best at mid-diastole or at end-systole (**Fig. 10.2**). Overall, image quality is better in patients with low and stable heart rates. For this reason, beta blocker administration is recommended to slow and stabilize the patient's heart rate. For heart rates <65 beats per min, image quality is usually best at mid-diastole, whereas for heart rates >75 beats per min, the best image quality shifts to end-systole. At low heart rate, a single time-phase reconstruction is usually enough to visualize all the coronary artery segments with diagnostic quality. At high heart rates, additional reconstructions may be necessary. In conclusion, limitations in temporal resolution cause blurring that may hamper coronary artery evaluation. The smaller the coronary artery size the greater the effect of motion on the diagnostic image quality.

Respiratory motion can seriously degrade the image quality (**Fig. 10.16**). With scan times of 8–12 s on current 64-row CT scanners, patients are usually able to hold their breath during scanning.

Image noise is mainly dependent on the number of photons used to make the image. Large chest sizes result in higher image noise, which can be reduced by adjusting the dose settings (kV, mA) to account for the patient's size (Chaps. 8 and 9). Contrast is improved by using iodinated contrast agents for lumen visualization. Patients need to be adequately instructed on how to hold their breath and the Valsalva maneuver should be avoided because it impairs contrast agent flow to the heart. At the workstation, window-level settings can optimize image contrast. Artifacts caused by noise and contrast-to-noise limitations result in poor overall image

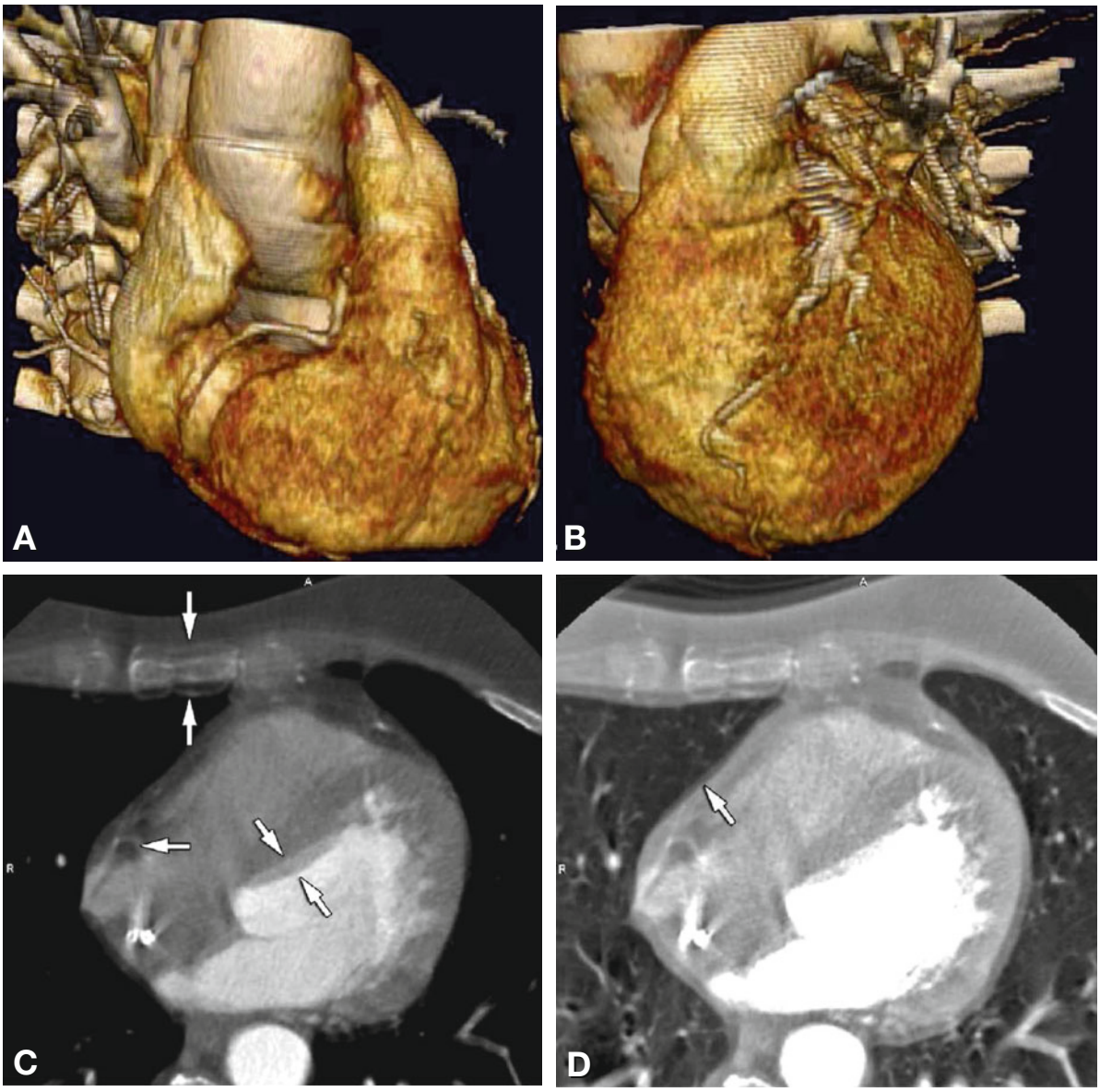

Fig. 10.16 Severe respiratory motion artifacts. Volume-rendered images (**Panels A** and **B**) and axial source images using soft tissue setting (**Panel C**) and lung window-level setting (**Panel D**) in a 46-year-old female patient who panicked during contrast agent injection and was then unable to hold her breath during scanning. The right coronary artery (**Panel A**) and left coronary artery (**Panel B**) were not evaluable. Note the motion visible in the area of the sternum, right coronary artery, and interventricular septum (*arrows* in **Panel C**). Breathing is also clearly indicated by blurring of the vascular structures and cardiac double contour in the lung setting (*arrow* in **Panel D**). Note that the coronary arteries are not well visualized (**Panels A**–**C**). The movement of body structures due to breathing resulted in a nondiagnostic scan

quality (high noise-level images) and images with low contrast (**Fig. 10.17**).

Reconstruction algorithms also cause artifacts. Spiral acquisition may cause geometric distortion, resulting in dark shadows near the coronary arteries that should not be confused with noncalcified plaques (**Fig. 10.18**). Other artifacts related to limitations in reconstruction algorithms are beam-hardening artifacts (e.g., resulting from high-density contrast agent injection) causing dark bands, as well as metal objects causing complex artifacts, including beam-hardening and partial-volume artifacts (**Fig. 10.19**). Fully automated reconstruction tools used during postprocessing can also result in image artifacts (**Figs. 10.9** and **10.10**). An irregular heart rate during scanning, such as that resulting from premature atrial contraction, can lead to erroneous phase selection during that abnormal heartbeat, which may cause blurring or even pseudostenosis (**Fig. 10.20**).

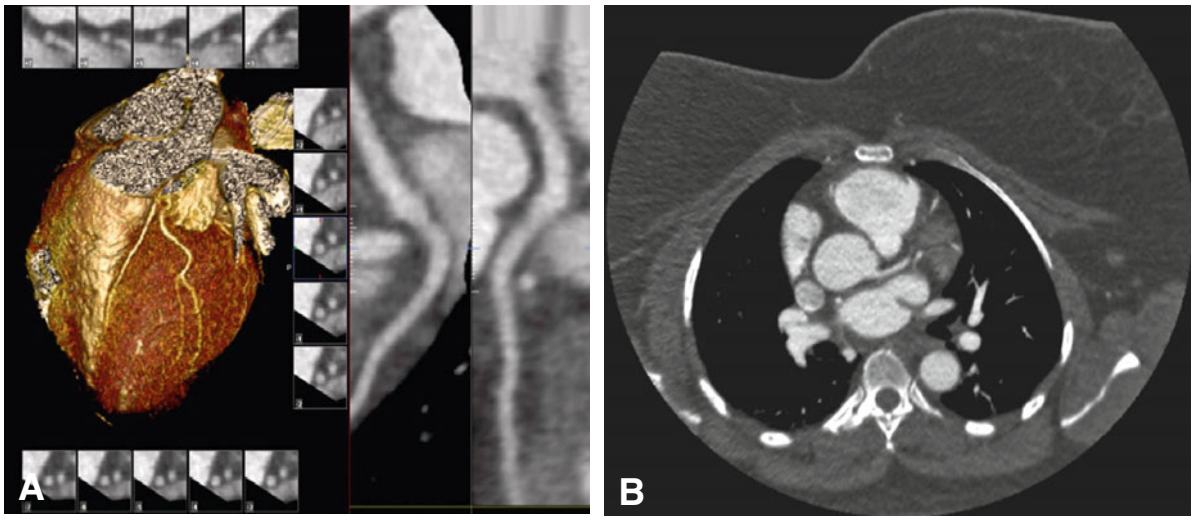

Fig. 10.17 Issues with high noise levels. A volume-rendered image with curved multiplanar reformations (**Panel A**) and axial source images using soft tissue setting (**Panel B**) in a 65-year-old very obese female patient. The image is noisy and of moderate quality despite the use of higher kV and mA settings (135 kV and 350 mA) to increase the radiation dose. Only the proximal parts of the coronary arteries can be evaluated well. Compare the image quality in **Panel A** with that of other figures (e.g., **Fig. 10.7**). Small side-branches are not visible in this overweight patient

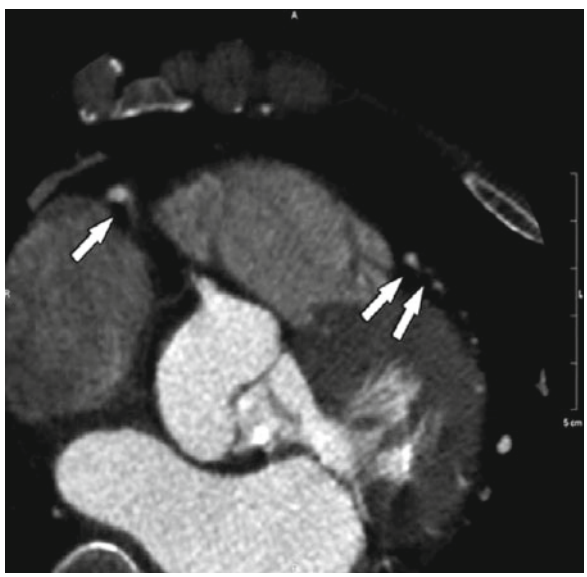

Fig. 10.18 Artifacts resulting from coronary artery motion and geometric distortion appear as *dark spots* adjacent to the right coronary artery and the left anterior descending coronary artery, including its diagonal branches (*arrows*). These artifacts should not be confused with noncalcified coronary artery plaques

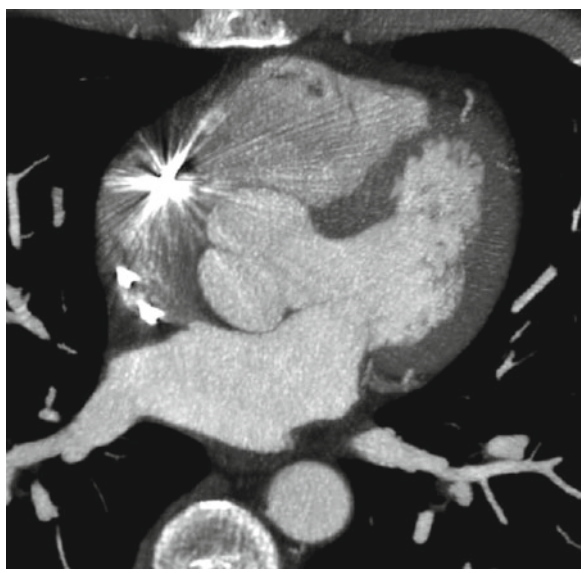

Fig. 10.19 Beam-hardening artifacts in a patient with a pacemaker lead (metal artifact) obscuring the right coronary artery. The patient had no coronary artery stenosis. Note the dilated aortic root with a maximum size of 4.7 cm

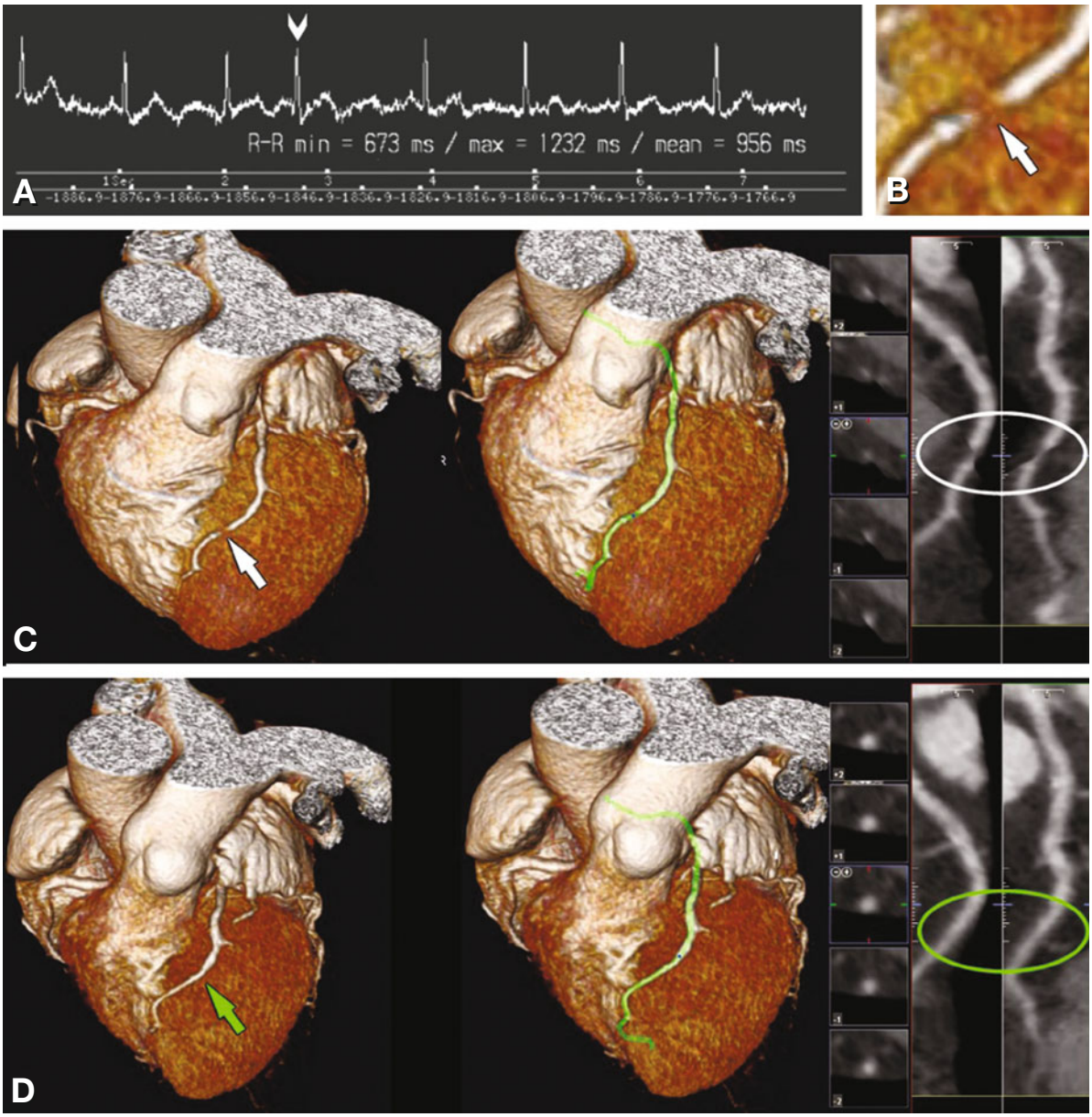

Fig. 10.20 Artifacts caused by irregular heart rate during scanning. CT coronary angiography in a 73-year-old female patient with suspected acute coronary artery syndrome. Premature atrial contraction after the third R-peak (*arrowhead*), followed by a compensatory long pause before the next R-peak (**Panel A**). Automatic reconstruction centered at 75% of the RR interval was performed with suboptimal time points relative to the R-peaks at the location of the short RR interval, giving rise to a coronary artery pseudostenosis (*arrow* in **Panels B** and **C**). Reconstruction at an optimal time point (ECG editing) resulted in normal image quality and elimination of the pseudostenosis (*green arrow* and *circle* in **Panel D**)

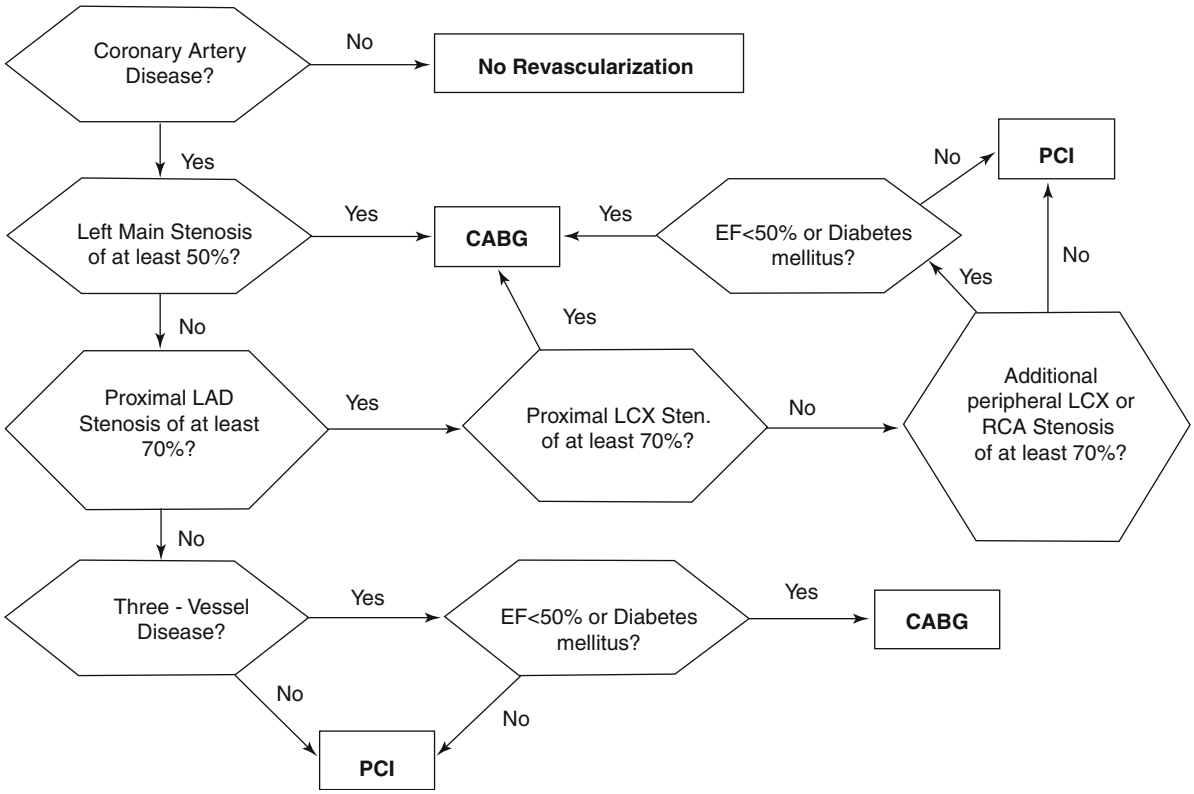

Fig. 10.21 Flowchart for the management of patients with suspected coronary artery disease, according to current guidelines. Interventional treatment is indicated when the percent diameter stenosis is at least 70%, or 50% for the left main coronary artery. Whether coronary artery bypass grafting (CABG) or percutaneous coronary intervention (PCI) should be performed is influenced by the presence of left main disease or left main equivalents as well as global left ventricular cardiac function (ejection fraction, EF) and the presence or absence of diabetes mellitus. This situation highlights the importance of locating coronary stenoses and assessing left ventricular global cardiac function by CT. The guidelines on which this flowchart is based were established by the American College of Cardiology/American Heart Association for conventional coronary angiography: (1) "For the Management of Patients With Chronic Stable Angina" (Gibbons et al. *Circulation* 2003), (2) "Update for Coronary Artery Bypass Graft Surgery" (Eagle et al. *Circulation* 2004), and (3) "For Percutaneous Coronary Intervention" (Smith et al. *JACC* 2001). Recommendations I and Level of Evidence A and B were included in creating the flowchart. *LAD* left anterior descending coronary artery, *LCX* left circumflex coronary artery, *RCA* right coronary artery (With permission from Hoffmann et al. *Acad Radiol* 2007)

We recommend checking the ECG during image interpretation to recognize heart rate irregularities that may cause these types of artifacts, which can be eliminated by manual ECG editing (**Figs.** 10.5 and 10.20). If pathology such as coronary artery stenosis is identified on postprocessed images, the findings should always be confirmed by reviewing the original data set (axial and/or orthogonal source images).

10.1.8 Cardiac Function

In addition to the location and severity of coronary artery stenoses as well as the presence of diabetes mellitus, left ventricular ejection fraction (above vs. below 50%) is of pivotal importance in determining the most suitable therapy for patients (percutaneous coronary intervention vs. coronary artery bypass grafting,

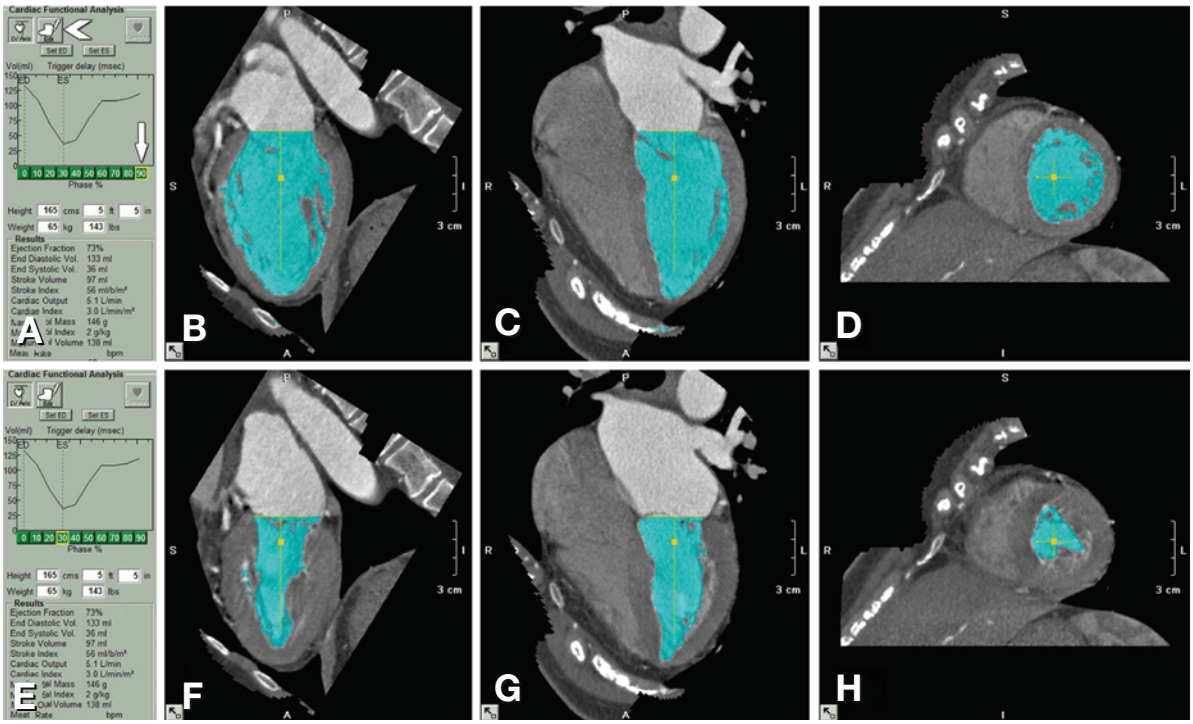

Fig. 10.22 Fully automated cardiac function analysis software (Vitrea, Vital Images). Diastolic frames are shown in the *upper row* (**Panels A**–**D**) and systolic frames in the *lower row* (**Panels E**–**H**). This software tool automatically identifies the cardiac axes with the two-chamber (**Panels B** and **F**) and four-chamber view (**Panels C** and **G**) as well as the cardiac short axis (**Panels D** and **H**). The orientation of the left ventricular cardiac axis (marked in *yellow*) and the level at the border of the left atrium and left ventricle can be manually changed. The left ventricular blood pool (excluding the papillary muscles) is also automatically identified and marked in *light blue*. Using the edit function (*arrowhead* in **Panel A**) makes it possible to manually change the automatically defined endo- and epicardial contours in the short-axis views. The end-diastolic time frame is mostly centered around 90% or 0% of the cardiac cycle (**Panel A**, *arrow* at 90%), whereas the end-systolic time frame is mostly at 30% or 40% (**Panel E**). Analysis of 10 image reconstruction intervals serves to calculate a left ventricular volume curve over time (**Panels A** and **E**). Ejection fraction, end-diastolic and end-systolic volumes, stroke volume, and myocardial mass are calculated automatically (**Panels A** and **E**). If the patient's weight and height and the heart rate are given, the software will also calculate stroke index, cardiac index, cardiac output, and myocardial index (**Panels A** and **E**)

Fig. 10.21). Also, left ventricular ejection fraction has been shown to be the most important prognostic factor for cardiac events and death that can be derived from diagnostic testing. Cardiac function analysis may be performed as part of cardiac CT, and is preferably done with using ECG-triggered dose modulation techniques to limit patient dose (Chap. 15). Automatic or semiautomatic software tools can be used to derive left ventricular volumes and ejection fraction (**Figs. 10.22** and **10.23**). Software tools allow manually adapting the contours if the automatically detected contours are not sufficiently accurate. Quantitative analysis of regional cardiac function may be facilitated by using bull's eye plots, which are available on many workstations (**Fig. 10.24**). Another convenient approach is to evaluate regional cardiac function by looking at cardiac short-axis and long-axis views in cine mode (using 10 reconstructions throughout the cardiac cycle). The cine mode is also useful for the assessment of cardiac valves (Chap. 16) in different orthogonal or long-axis views (**Figs. 10.25** and **10.26**).

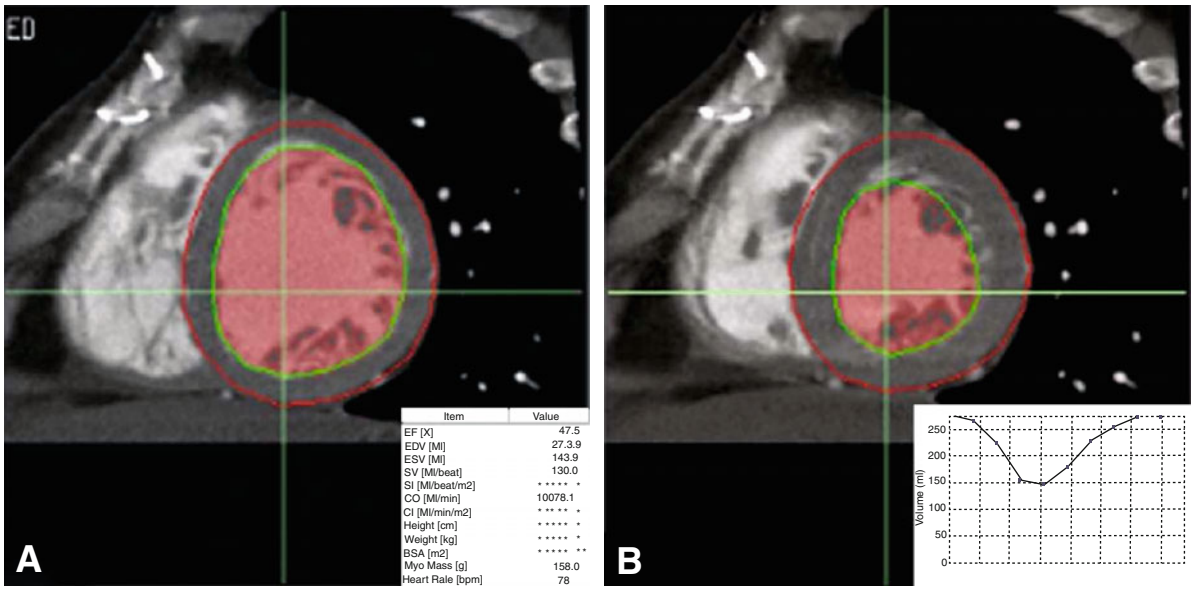

Fig. 10.23 Semiautomatic cardiac function analysis software (Toshiba) with a short-axis slice at end-diastole (**Panel A**) and end-systole (**Panel B**). The *green* and *red contours* in these images represent the automatically generated endo- and epicardial contours, respectively. Note that not all of the area surrounded by the *green line* is assigned to the left ventricular volume, as only pixels with a certain manually adjustable minimum Hounsfield unit density are recognized as part of the blood pool (colored *pink* in the images). In this way, the papillary muscles are excluded from the blood pool. In the *inset* in **Panel A**, the results of global left ventricular function analysis are displayed; the *inset* in **Panel B** shows a volume curve, with end-diastole and end-systole represented by the largest and smallest left ventricular volumes, respectively. This semiautomatic analysis tool, although not optimized for this purpose, is also easier to use for right ventricular function assessment than the current fully automated approaches

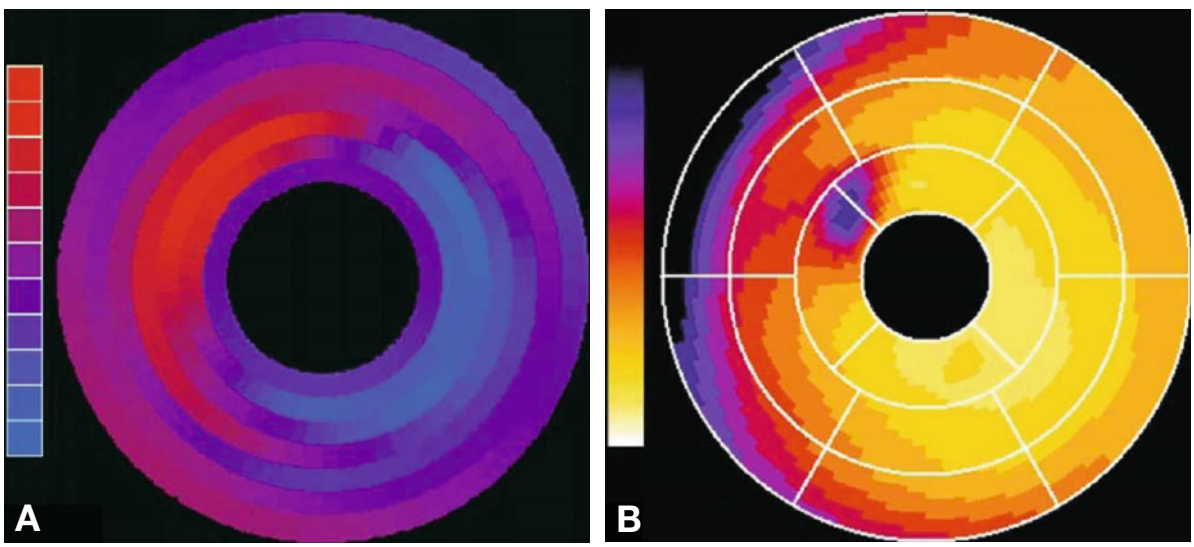

Fig. 10.24 Regional quantitative cardiac function analysis using bull's eye plots of cine magnetic resonance imaging (**Panel A**) and multislice CT (**Panel B**) in a patient with regional hypokinesia in the apical anteroseptal segments (segments 13 and 14, see Chap. 3). This regional wall motion deficit is identified by an analysis of relative wall thickening during systole, and is easily identified by the coloring (*red* in **Panel A** and *dark blue* in **Panel B**), which is different from that of normal segments. In CT (**Panel B**), the borders of the myocardial segments are used as an overlay to facilitate the assignment of findings

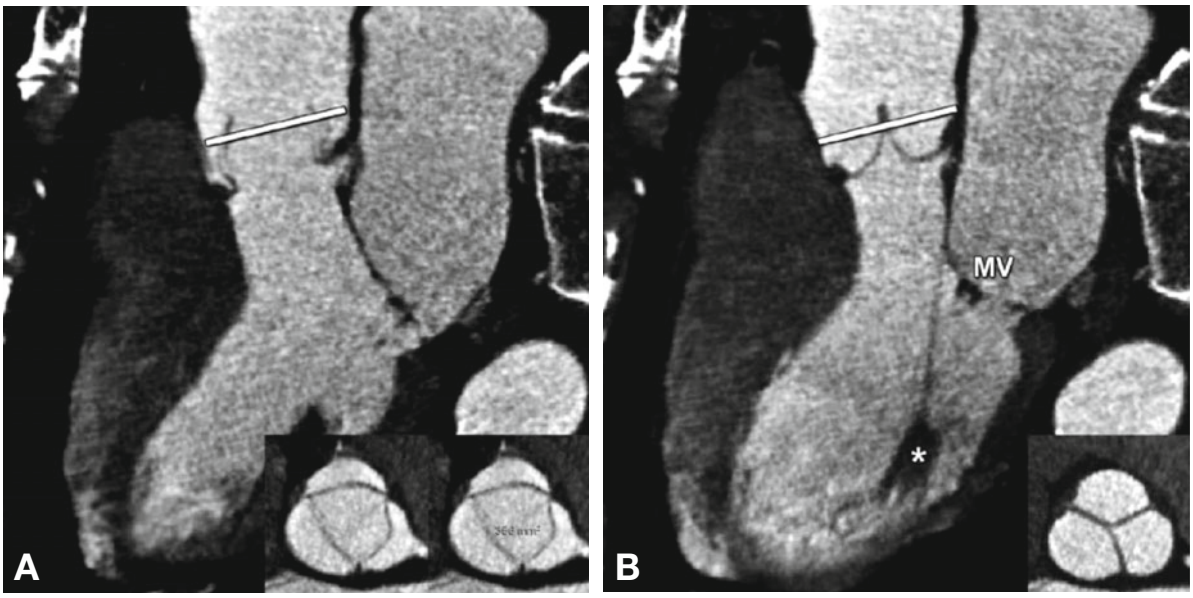

Fig. 10.25 Assessment of the aortic valve using CT in a long-axis three-chamber view during systole (**Panel A**) and diastole (**Panel B**). In this patient, the aortic leaflets are unremarkable; in particular there are no calcifications. During systole, the aortic valve area measures over 3.5 cm^2 (see *insets* in **Panel A**, which are oriented along the *white line* in **Panel A**). During diastole there is complete closure of the aortic valve leaflets (**Panel B**), and there is no aortic regurgitation area visible (*inset* in **Panel B**). Note the closed aortic leaflets showing the Mercedes-Benz sign in this *inset*. *Asterisk* papillary muscles, *MV* mitral valve

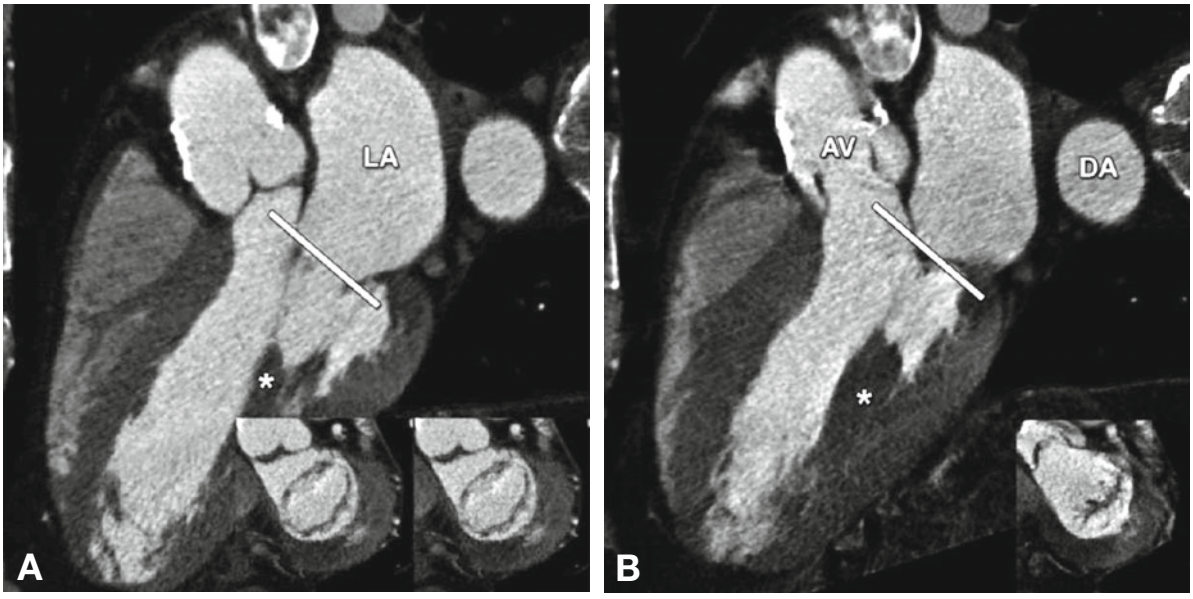

Fig. 10.26 Assessment of the mitral valve in a long-axis three-chamber view during mid-diastole (**Panel A**) and mid-systole (**Panel B**). In this patient, the mitral valve leaflets are unremarkable; in particular there are no calcifications. During mid-diastole, the mitral valve area measures over 6 cm^2 (see *insets* in **Panel A**, which are oriented along the *white line* in **Panel A**). During systole there is complete closure of the mitral valve (**Panel B**), and there is no mitral regurgitation area visible (*inset* in **Panel B**). Please note the calcifications of the ascending aorta. *Asterisk* papillary muscles, *AV* aortic valve, *DA* descending aorta, *LA* left atrium

10.2 Reporting

10.2.1 Structured Reporting

Reports of cardiac CT studies should be precise and concise. Using a structured reporting technique ensures that no important aspects are overlooked and also improves consistency (Stillman et al. *J Am Coll Radiol* 2008). The important elements of a cardiac CT report are summarized in **List 10.4**.

In 2006, the American College of Radiology (ACR) published a practice guideline (Jacobs et al. *J Am Coll Radiol* 2006) on the conduct and interpretation of cardiac CT studies. This guideline describes how cardiac CT studies should be interpreted and the findings documented. Another, more general ACR practice guideline (Kushner et al. *J Am Coll Radiol* 2005) describes the steps involved in reporting and communicating diagnostic imaging findings. In 2009, the SCCT published its guidelines for the interpretation and reporting of coronary CT angiography (Raff et al. *JCCT* 2009).

List 10.4. Pivotal elements of a cardiac CT report[a]

1. Clinical history, symptoms, and question to be answered[b]
2. Technical details of the CT protocol used and image quality
3. Description of findings
4. Overall impression and recommendations for further testing if necessary

[a] The elements are basically the same as for general radiological (CT) reports.

[b] To explain why an examination with radiation exposure was necessary.

10.2.2 Medical History, Symptoms, and Questions to Be Answered

Only the pertinent facts are stated. Also relevant are the patient's symptoms (such as angina, dyspnea, fatigue), risk factors for coronary artery disease, history of previous revascularization therapies, and results of prior ischemia testing. The question to be answered by cardiac CT should be included (e.g., "coronary artery disease?").

Examples of reports of cardiac CT studies are shown in **Figs. 10.27** and **10.28**.

10.2.3 Technical Approach and Image Quality

The report should state the detector collimation, the acquisition method (retrospective [ECG gating] or prospective [ECG triggering]), the amount and type of contrast agent used, and the doses of nitroglycerin or beta blocker given. Parameters relevant for radiation dose should be registered according to state or federal regulations. One may add which coronary artery reconstruction phase was used for analysis because doing so will facilitate comparison with future examinations. This kind of information may also be stored elsewhere (e.g., in the radiology-information and/or picture archiving and communication system). However, it should be stated in the report whether nondiagnostic (not evaluable) coronary artery segments and/or artifacts were present that may have limited the interpretation.

Cardiac CT

History:

-Suspected coronary disease, atypical angina pectoris, equivocal stress ECG

Technique:

64-row cardiac computed tomography with prospectively ECG-triggered acquisitions (at 75%) after IV bolus injection of 80 ml of Xenetix 350. Premedication with 0.8 mg sublingual nitroglycerin and an intravenous beta blocker (10 mg Beloc Zok). Reconstruction of 0.5 mm thick slices in 0.25 mm increments at 75% of the cardiac cycle. 3D and MPR postprocessing at 75% of the cardiac cycle.

Findings:

Very good image quality. Right coronary artery dominance.

LMA: No significant stenoses or plaques.

LAD: No significant stenoses or plaques.

LCX: No significant stenoses or plaques.

RCA: No significant stenoses or plaques.

Left ventricular EF 63%, EDV 113 ml, ESV 42 ml, SV 71 ml, LV MM 131 g. No regional wall motion deficits.
Unremarkable appearance of the regions of the lungs, mediastinum, and chest wall.

Overall impression:

Based on this CT of the heart, significant coronary stenosis can be excluded (images and CD attached).
Normal left ventricular function.

Fig. 10.27 Example of a report of a cardiac CT study in a patient in whom no significant stenoses were found and cardiac function was normal

Cardiac CT

History:

-Status post MI 20 years earlier, no angina pectoris, hypertension; obesity; nuclear stress test: anterior ischemia and posterior infarction; exercise ECG: normal; no invasive tests; coronary artery stenosis?

Technique:

320-row cardiac computed tomography with prospectively ECG-triggered (at 70-80%) acquisition after IV bolus injection of 60 ml of Xenetix 350. Premedication with 0.8 mg sublingual nitroglycerin and an intravenous and oral beta blocker (100 mg Esmolol and 50 mg Atenolol). Reconstructionof 0.5 mm thick slices in 0.25 mm increments at 70, 75, and 80% of the cardiac cycle. 3D and MPR postprocessing at 75% of the cardiac cycle.

Findings:

Good image quality. Balanced coronary distribution.
LMA: Noncalcified plaque that extends to the proximal LAD (segment 6), where it causes an 80% stenosis.
LAD: Significant stenosis 12 mm in length in segment 6 (ca. 60% diameter reduction) due to a noncalcified plaque. Additional noncalcified plaque with nonsignificant (30% diameter reduction) stenosisin segment 7.
LCX: Noncalcified plaque in segment 11 without significant stenosis. Segment 13 with proximal subtotal occlusion (about 95%) due to a noncalcified plaque.
RCA: Reliable evaluation down to the distal portion of segment 2: no significant stenosis. There are two motion artifacts affecting the proximal portion of segment 3, which degrade evaluation of a segment of about 10 mm. No stenoses and plaques further downstream.
Unremarkable appearance of the regions of the lungs, mediastinum, and chest wall.
Left ventricular myocardial function: EF35%, EDV 113 ml, ESV 73 ml, SV 40 ml, LV MM 118 g. Global hypokinesia, posteromedial akinetic areas (segment 10) after history of posterior MI.

Overall impression:

2-vessel coronary artery disease with suspected significant stenosis in segments 6 (LAD) and high-grade in 13 (LCX) (see attached images). The stenosis in the proximal LAD is likely responsible for the anterior ischemia found on nuclear imaging. Nondiagnostic portion of segment 3 of the RCA by motionartifacts. Reduced left ventricular EF in the presence of marked global hypokinesia and posterior akinesia. Consider invasive coronary angiography.

Fig. 10.28 Example of a report of a cardiac CT study in a patient in whom significant coronary stenoses were found. Global and regional left ventricular function were also markedly reduced

10.2.4 Description of Findings

If one is comparing two studies, this is the best place in a report to mention to which examination the current findings are being compared (e.g., "compared to the prior cardiac CT of December 15, 2009"). The coronary artery dominance type (right, left, codominant) should be mentioned. If stenoses or plaques are present, it is critical to provide the location (ostial, near side-branch) and/or segment name or number (**Fig. 10.3**). Also, the estimated percent diameter stenosis (**Fig. 10.8**) should be given. As the characteristics of coronary stenoses may determine the success rate of percutaneous coronary interventions, it may be helpful to provide details regarding the length of a stenosis and its eccentricity as well as the presence of calcification or thrombus (**Fig. 10.29**). In patients with chronic total occlusion, CT information can improve the success of subsequent percutaneous coronary intervention, e.g., by improving guidance of the catheter (**Fig. 10.30**). Further characteristics (e.g., plaque volume, Hounsfield units) may be given as well (Chap. 14).

Other cardiac findings such as global and regional cardiac function (Chap. 15) should be reported if imaging data have been acquired over the entire cardiac cycle. Further cardiac evaluation includes evaluation of the myocardial tissue, cardiac chambers, and pericardium. Myocardial perfusion defects or other structural myocardial abnormalities, thrombi, and valve-leaflet or annulus calcifications are described if present (Chap. 16).

Cardiac and coronary artery evaluation is performed on a small reconstruction field of view using small slice thickness (0.5–0.9 mm) with overlap for optimal spatial resolution. However, these small reconstruction field of views cover only about one-third of the total chest volume, whereas about two-thirds of the chest volume has been exposed, which can be covered in the maximum field of view. The maximum field of view should always be evaluated for extracardiac findings. Extracardiac abnormalities in the lungs, bones, chest wall, mediastinum, etc. should be reported. Extracardiac findings are frequently encountered and may explain the patient's chest pain and/or dyspnea, e.g., in the case of incidentally found large diaphragmatic hernia, pulmonary embolism, or emphysema.

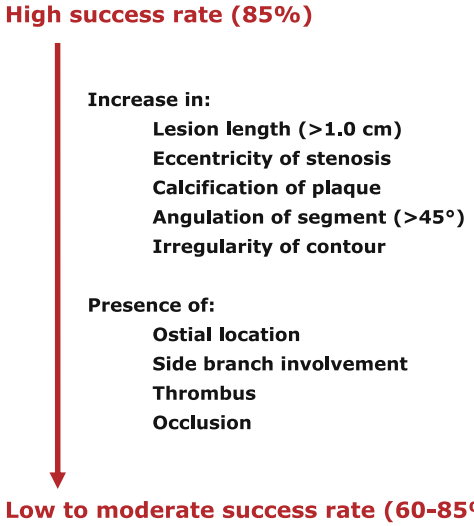

Fig. 10.29 Influence of different coronary artery stenosis characteristics on the success rate of percutaneous coronary interventions (Based on and modified from data provided in Ryan et al. *J Am Coll Cardiol* 1988 and Smith et al. *JACT* 2001). Success rates may be as low as 60% in patients with very long coronary lesions (>3.0 cm), lesions with severe angulation (>90°), or occlusions existing for more than 3 months. Other important characteristics that can be nicely evaluated with coronary CT are the eccentricity of the stenosis, degree of calcification, and presence of ostial or bifurcation lesions

10.2.5 Overall Impression and Recommendations

The major findings regarding coronary artery stenoses (e.g., "2-vessel coronary artery disease with significant stenoses in …"), ventricular function, and relevant cardiac and extracardiac findings should be summarized and the differential diagnoses listed. If the relevance of stenoses appears uncertain, one may recommend which test is indicated next (e.g., nuclear or any other ischemia test to further analyze a borderline stenosis). However, only further investigations that promise to be truly helpful are worth listing here in order to avoid the so-called "layering" of tests. In case of extracardiac findings, it can be stated whether or not these findings might explain the patient's complaints. Based on the reported improvement in lung cancer mortality by the National Lung Screening Trial Research Team it is recommended to have all cardiac CT studies read for the detection of lung nodules as identification of incidental lung cancer may improve patient outcome.

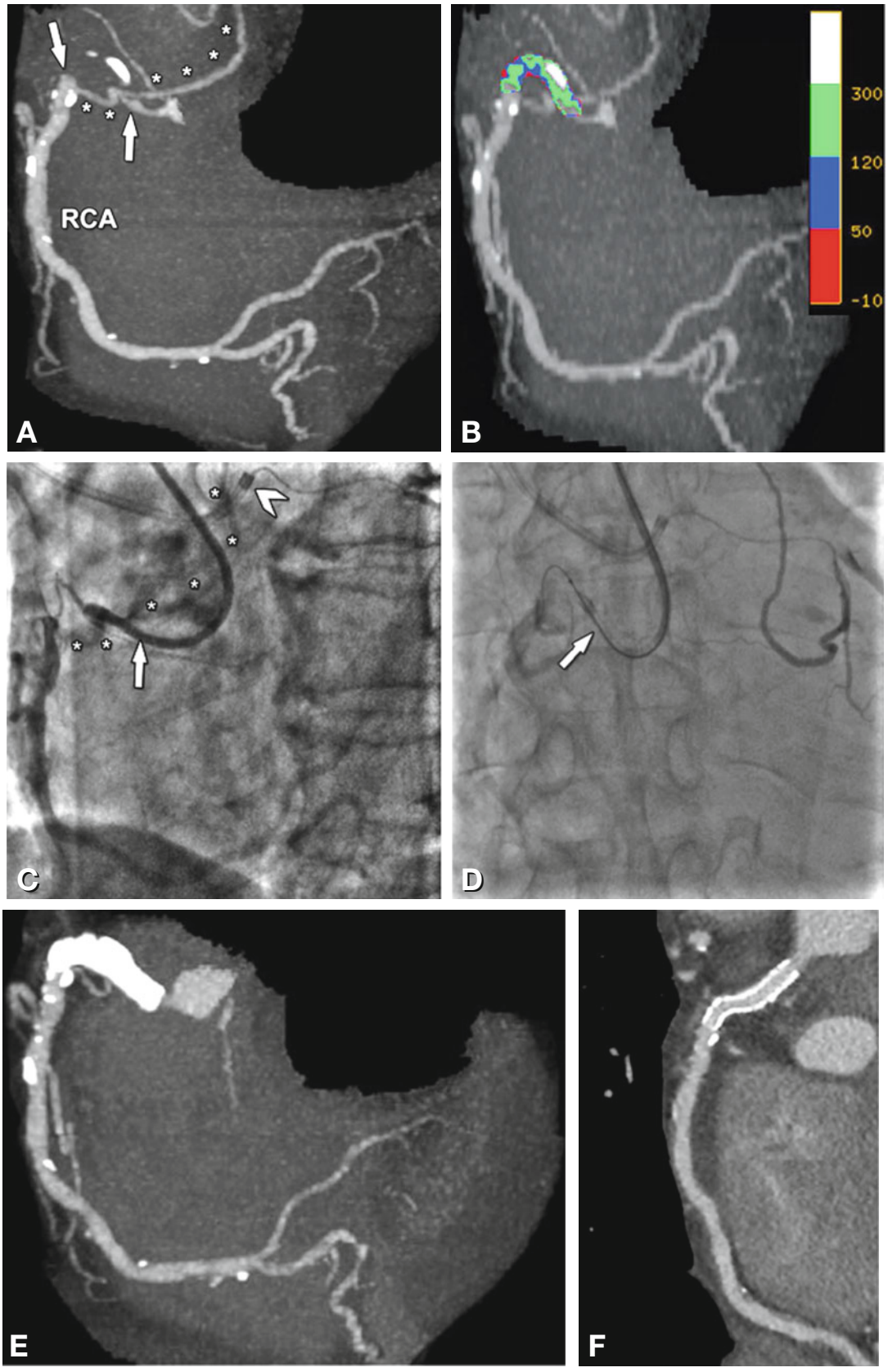
RCA
300
120
50
-10
A
B
C
D
E
F

Fig. 10.30 Chronic total occlusion (CTO) in the right coronary artery (RCA) of a 65-year-old man who presented for operation of an abdominal aortic aneurysm. Because of incidental ischemia on myocardial perfusion imaging, CT was performed. **Panel A** is an angiographic view that demonstrates the CTO of the RCA (*arrows*) and a collateral vessel from the left circumflex coronary artery and right sinus node artery (*asterisks*). However, this image doses not provide information on the plaque that resulted in the CTO. **Panel B** is the plaque-loaded angiographic view demonstrating the Hounsfield units of the different plaque components as an overlay (color-coded) in this tortuous CTO. **Panel C** is the corresponding conventional coronary angiogram for which double catheterization of the RCA and LCX was used to better characterize the CTO. One catheter was inserted at the RCA orifice (*arrow*), the other into the left circumflex (*arrowhead*), and the co-axial catheter was inserted via the LCX-loaded catheter into the collateral vessel to the right sinus node artery (*asterisks*, not as densely filled as the RCA), which connected to the distal portion of the CTO. The image obtained with this dual injection (**Panel C**) was similar to the angiographic view (**Panel A**), but did not provide insights into the plaque. **Panel D** shows how stenting was done by the interventionalist with the help of the CT data. The CT data indicated that the guidewire should be directed upwards in a 45° angle (*arrow* in **Panel D**). **Panel E** shows the angiographic view and **Panel F** is the curved multiplanar reformation of the RCA after stenting (Images courtesy of M. Jinzaki and S. Kuribayashi)

Recommended Reading

Anders K, Ropers U, Kuettner A, Wechsel M, Daniel WG, Uder M, Achenbach S (2011) Individually adapted, interactive multiplanar reformations vs. semi-automated coronary segmentation and curved planar reformations for stenosis detection in coronary computed tomography angiography. Eur J Radiol 80:89–95

Arnoldi E, Gebregziabher M, Schoepf UJ et al (2010) Automated computer-aided stenosis detection at coronary CT angiography: initial experience. Eur Radiol 20:1160–1167

Austen WG, Edwards JE, Frye RL et al (1975) A reporting system on patients evaluated for coronary artery disease. Report of the Ad Hoc Committee for Grading of Coronary Artery Disease, Council on Cardiovascular Surgery, American Heart Association. Circulation 51:5–40

Bonow RO, Carabello B, de Leon AC et al (1998) ACC/AHA guidelines for the management of patients with valvular heart disease. executive summary. A report of the American College of Cardiology/American Heart Association Task Force on Practice Guidelines (Committee on Management of Patients With Valvular Heart Disease). J Heart Valve Dis 7:672–707

Califf RM, Mark DB, Harrell FE Jr et al (1988) Importance of clinical measures of ischemia in the prognosis of patients with documented coronary artery disease. J Am Coll Cardiol 11:20–26

Chin S, Ong T, Chan W et al (2006) 64 row multi-detector computed tomography coronary image from a centre with early experience: first illustration of learning curve. J Geriatric Cardiol 3:29–34

Coakley FV, Liberman L, Panicek DM (2003) Style guidelines for radiology reporting: a manner of speaking. AJR Am J Roentgenol 180:327–328

de Roos A, Kroft LJ, Bax JJ, Geleijns J (2007) Applications of multislice computed tomography in coronary artery disease. J Magn Reson Imaging 26:14–22

Dewey M, Schnapauff D, Laule M et al (2004) Multislice CT coronary angiography: evaluation of an automatic vessel detection tool. Fortschr Röntgenstr 176:478–483

Dewey M, Müller M, Eddicks S et al (2006) Evaluation of global and regional left ventricular function with 16-slice computed tomography, biplane cineventriculography, and two-dimensional transthoracic echocardiography: comparison with magnetic resonance imaging. J Am Coll Cardiol 48:2034–2044

Eagle KA, Guyton RA, Davidoff R et al (2004) ACC/AHA 2004 guideline update for coronary artery bypass graft surgery: a report of the American College of Cardiology/American Heart Association Task Force on Practice Guidelines (Committee to Update the 1999 Guidelines for Coronary Artery Bypass Graft Surgery). Circulation 110:e340–e437

Feuchtner GM, Dichtl W, Friedrich GJ et al (2006a) Multislice computed tomography for detection of patients with aortic valve stenosis and quantification of severity. J Am Coll Cardiol 47:1410–1417

Feuchtner GM, Dichtl W, Schachner T et al (2006b) Diagnostic performance of MDCT for detecting aortic valve regurgitation. AJR Am J Roentgenol 186:1676–1681

Friedman PJ (1983) Radiologic reporting: the hierarchy of terms. AJR Am J Roentgenol 140:402–403

Gibbons RJ, Abrams J, Chatterjee K et al (2003) ACC/AHA 2002 guideline update for the management of patients with chronic stable angina-summary article: a report of the American College of Cardiology/American Heart Association Task Force on Practice Guidelines (Committee on the Management of Patients With Chronic Stable Angina). Circulation 107:149–158

Hall FM (2000) Language of the radiology report: primer for residents and wayward radiologists. AJR Am J Roentgenol 175:1239–1242

Hamon M, Morello R, Riddell JW (2007) Coronary arteries: diagnostic performance of 16- versus 64-section spiral CT compared with invasive coronary angiography-meta-analysis. Radiology 245:720–731

Herzog C, Ay M, Engelmann K et al (2001) Visualization techniques in multislice CT-coronary angiography of the heart. Correlations of axial, multiplanar, three-dimensional and virtual endoscopic imaging with the invasive diagnosis. Rofo 173:341–349

Hoe JW, Toh KH (2007) A practical guide to reading CT coronary angiograms-how to avoid mistakes when assessing for coronary stenoses. Int J Cardiovasc Imaging 23:617–633

Hoffmann H, Dübel HP, Laube H, Hamm B, Dewey M (2007) Triage of patients with suspected coronary artery disease using multislice computed tomography. Acad Radiol 14:901–909

Juergens KU, Fischbach R (2006) Left ventricular function studied with MDCT. Eur Radiol 16:342–357

Kelle S, Hug J, Kohler U, Fleck E, Nagel E (2005) Potential intrinsic error of noninvasive coronary angiography. J Cardiovasc Magn Reson 7:401–407

Kim TJ, Han DH, Jin KN, Won Lee K (2010) Lung cancer detected at cardiac CT: prevalence, clinicoradiologic features, and importance of full-field-of-view images. Radiology 255(2):369–376

Koonce J, Schoepf JU, Nguyen SA, Northam MC, Ravenel JG (2009) Extra-cardiac findings at cardiac CT: experience with 1,764 patients. Eur Radiol 19:570–576

Kroft LJ, de Roos A, Geleijns J (2007) Artifacts in ECG-synchronized MDCT coronary angiography. AJR Am J Roentgenol 189:581–591

Leber AW, Becker A, Knez A et al (2006) Accuracy of 64-slice computed tomography to classify and quantify plaque volumes in the proximal coronary system: a comparative study using intravascular ultrasound. J Am Coll Cardiol 47:672–677

Libby P (2007) Braunwald's heart disease: a textbook of cardiovascular medicine. Saunders, An Imprint of Philadelphia: Elsevier

MacMahon H, Austin JH, Gamsu G et al (2005) Guidelines for management of small pulmonary nodules detected on CT scans: a statement from the Fleischner Society. Radiology 237:395–400

National Lung Screening Trial Research Team, Aberle DR, Adams AM, Berg CD, Black WC, Clapp JD, Fagerstrom RM, Gareen IF, Gatsonis C, Marcus PM, Sicks JD (2011) Reduced lung-cancer mortality with low-dose computed tomographic screening. N Engl J Med 365(5):395–409

Rolf A, Werner GS, Schuhbäck A, Rixe J, Möllmann H, Nef HM, Gundermann C, Liebetrau C, Krombach GA, Hamm CW, Achenbach S (2013) Preprocedural coronary CT angiography significantly improves success rates of PCI for chronic total occlusion. Int J Cardiovasc Imaging 29(8):1819–1827

Ryan TJ, Faxon DP, Gunnar RM et al (1988) Guidelines for percutaneous transluminal coronary angioplasty. A report of the American College of Cardiology/American Heart Association Task Force on Assessment of Diagnostic and Therapeutic Cardiovascular Procedures (Subcommittee on Percutaneous Transluminal Coronary Angioplasty). Circulation 78:486–502

Schnapauff D, Zimmermann E, Dewey M (2008) Technical and clinical aspects of coronary computed tomography angiography. Semin Ultrasound CT MR 29:167–175

Smith SC Jr, Dove JT, Jacobs AK et al (2001) ACC/AHA guidelines of percutaneous coronary interventions (revision of the 1993 PTCA guidelines)–executive summary. A report of the American College of Cardiology/American Heart Association Task Force on Practice Guidelines (committee to revise the 1993 guidelines for percutaneous transluminal coronary angioplasty). J Am Coll Cardiol 37:2215–2239

Stillman AE, Rubin GD, Teague SD, White RD, Woodard PK, Larson PA (2008) Structured reporting: coronary CT angiography: a white paper from the American College of Radiology and the North American Society for Cardiovascular Imaging. J Am Coll Radiol 5:796–800

Vogel-Claussen J, Pannu H, Spevak PJ, Fishman EK, Bluemke DA (2006) Cardiac valve assessment with MR imaging and 64-section multidetector row CT. Radiographics 26:1769–1784

Vogl TJ, Abolmaali ND, Diebold T et al (2002) Techniques for the detection of coronary atherosclerosis: multi-detector row CT coronary angiography. Radiology 223:212–220

Further Recommended Websites

Jacobs JE, Boxt LM, Desjardins B, Fishman EK, Larson PA, Schoepf J (2006) ACR practice guideline for the performance and interpretation of cardiac computed tomography (CT). J Am Coll Radiol 3:677–685, The ACR practice guideline for the performance and interpretation of cardiac CT (Jacobs et al.) can be accessed at: http://www.acr.org/~/media/ACR/Documents/PGTS/guidelines/CT_Cardiac.pdf

Kushner DC, Lucey LL (2005) Diagnostic radiology reporting and communication: the ACR guideline. J Am Coll Radiol 2:15–21, The ACR practice guideline for communication of diagnostic imaging findings (Kushner et al.) can be accessed at: http://www.acr.org/~/media/C5D1443C9EA4424AA12477D1AD1D927D.pdf

Raff GL, Abidov A, Achenbach S et al (2009) SCCT guidelines for the interpretation and reporting of coronary computed tomographic angiography. J Cardiovasc Comput Tomogr 3:122–136, The SCCT guidelines for the interpretation and reporting of coronary computed tomographic angiography (Raff et al.) can be accessed at: http://www.scct.org/documents/SCCTGuidelinesforI&RofCCTA.pdf

Coronary Artery Calcium

M.A. Latif, M.J. Budoff, and P. Greenland

Abstract

This chapter reviews the role of coronary artery calcium scoring in clinical settings. Coronary calcium scoring appears most useful for risk stratification of asymptomatic patients with an intermediate risk of subsequent cardiac events.

11.1 Introduction

Coronary artery calcium scoring allows assessment of coronary atherosclerotic disease, even at an early stage. This is especially useful in understanding the pathology of vascular diseases in asymptomatic populations and also has prognostic implications.

When pathologists first began to perform autopsies on those who died of presumed coronary artery disease, they observed that a link existed between arterial deposits of calcium and cardiac death. With the development of x-rays, calcium associated with the heart was again recognized as an indicator of coronary artery disease. In fact, for most of the 20th century, calcium, because of its density, was the only feature that was apparent on radiographs of the heart. The observation that coronary artery calcification, with rare exceptions, is associated exclusively with intimal disease was made by Blankenhorn and Stern in 1959. Along with this insight came numerous studies on the ability of detecting calcifications in the coronary arteries with invasive coronary radiography.

No much progress relating to the significance of coronary calcification was made in the 1960s and 1970s with the widespread use of invasive coronary angiography and advances in the use of less invasive tests, such as stress thallium imaging. The advent of angioplasty and stent placement in the treatment of arterial stenosis contributed to the impression that calcium detection was not clinically important. The rise of coronary artery calcium detection in clinical medicine is related to both scientific and technical advances. First and foremost, coronary calcium has been shown to be a strong marker of atherosclerosis and has prognostic utility over and above traditional risk factors. Clinicians have also come to recognize that earlier treatment of atherosclerosis and an individual's global cardiovascular risk may be more important than the treatment of an individual high-grade stenosis. Equally important has been the revolution in CT technology itself. Electron-beam CT was the first technique to provide a real breakthrough in the quantitation of calcium in the coronary arteries. Although valuable in launching the field, electron-beam CT was hampered by cost and limited utility for noncardiac imaging.

Following on the heels of electron-beam CT, there have been many improvements in cardiac CT (Chap. 7).

M. Dewey, *Cardiac CT*,
DOI 10.1007/978-3-642-41883-9_14, © Springer-Verlag Berlin Heidelberg 2014

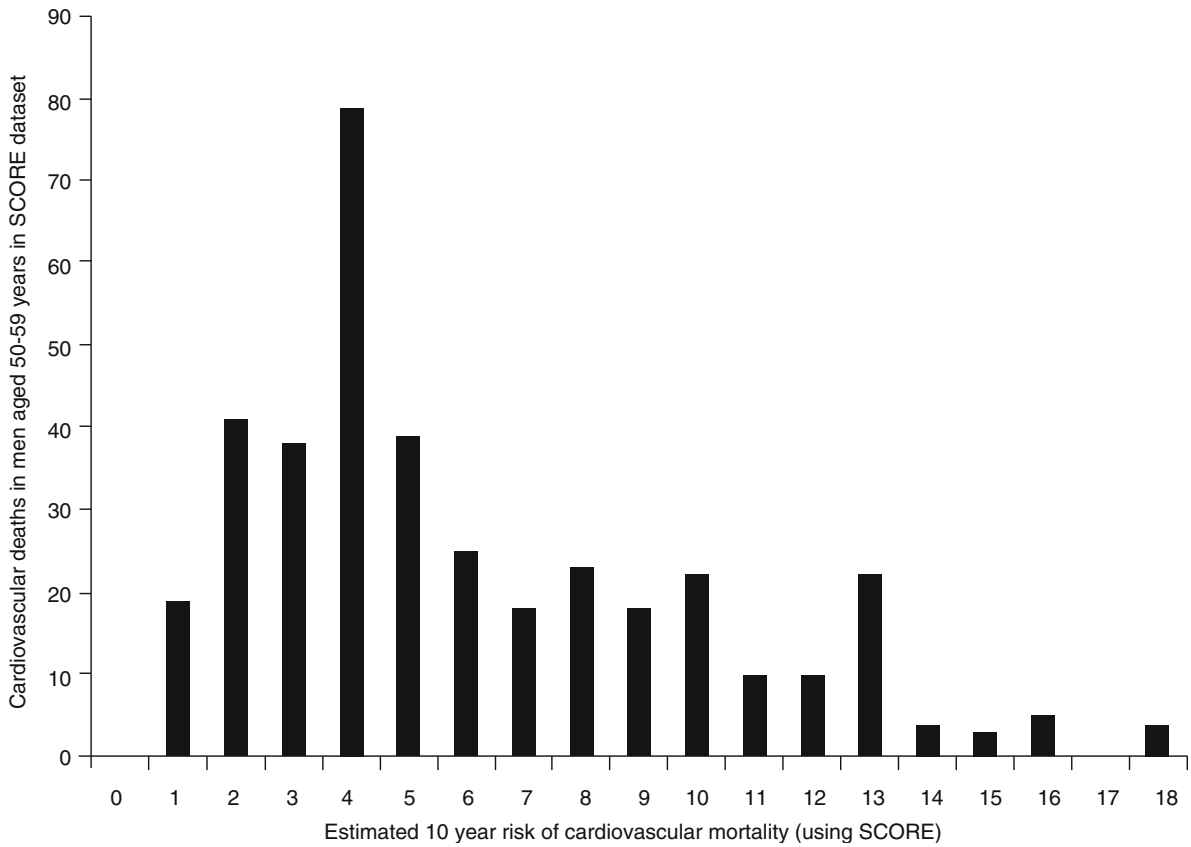

Fig. 11.1 This graph, from the *SCORE* (Systematic COronary Risk Evaluation) database, illustrates a key feature of prevention strategies. Known as the "Rose prevention paradox," the figure illustrates the seemingly contradictory situation that the majority of events from a disease occur in members of the population at low or moderate event risk, while only a minority of events occur in the highest-risk segment of the population. See text for additional details. *CVD* cardiovascular disease, *SCORE* Systematic COronary Risk Evaluation (With permission from Cooney et al., *European Journal of Preventive Cardiology* 2009)

With the advent of 16- and 64-row scanners, more attention was directed to coronary CT angiography, and calcium scoring also gained wider use. The latest technology includes volume-type 320-row (Chap. 9a) and dual-source CT scanners (Chap. 9b) that can acquire the data in a single heartbeat. At this point in time, the critical question is no longer "should we do calcium scoring?" but rather "when should we do it?"

Despite dramatic decreases in age-adjusted cardiovascular mortality over the past decades, cardiovascular diseases remain the most common cause of death worldwide. Nearly all cardiovascular events occur in persons without prior myocardial infarction or revascularization. Although this may seem paradoxical considering the higher cardiovascular risk of patients who have had prior cardiovascular events, it is explained by the fact that people without a previous event (primary prevention) represent the majority of the population. While the absolute risk in these asymptomatic people is lower, their greater number results in a higher overall population attributable risk. Therefore, the concept of risk stratification of asymptomatic individuals without previous cardiovascular events has been incorporated into prevention guidelines to identify people at high cardiovascular risk in whom prevention strategies, including drug therapy, are recommended.

The fact that a majority of events occur in people at low to intermediate risk is a phenomenon known as "the Rose prevention paradox". As Rose showed in his classic 1985 paper on the prevention paradox, the highest-risk individuals account for a minority of all coronary events. This concept has recently been revisited using data from 109,954 participants pooled from six European general population cohort studies from the high-risk cohorts of the SCORE (Systematic COronary Risk Evaluation) dataset as shown in **Fig. 11.1**. The conclusions regarding prevention strategies are: (1) An overall population strategy is needed to shift the entire population risk distribution to lower risk. (2) Among lower, intermediate, and

higher risk individuals, a clinical strategy might be implemented to try to identify the individuals with the highest risk. This is where coronary calcium scoring could be most useful.

11.2 Clinical Use

11.2.1 Measurement of Coronary Calcium

In the coronary arteries, calcifications almost always occur in the setting of atherosclerosis. The only known exception is renal failure, which may be associated with medial (non-atherosclerotic) calcification of the coronary artery wall along with atherosclerotic calcification. Even in renal failure patients, extensive intimal calcification is also present, contributing to the exceptionally high cardiovascular mortality. In fact, the coronary calcium score is considered to provide an estimate of vascular age in patients without renal failure. It has been shown that the amount of coronary artery calcium reflects the total atherosclerotic burden, including both calcified and noncalcified plaques. The quantitative relationship between calcified and noncalcified plaque components, however, is not uniform and, in some individuals, only noncalcified plaques are present.

Coronary artery calcium can be detected on noncontrast cardiac CT (**Figs.** 11.2 and 11.3). To quantify coronary artery calcium, the area and density, volume, or mass of calcified deposits is measured. Several quantification

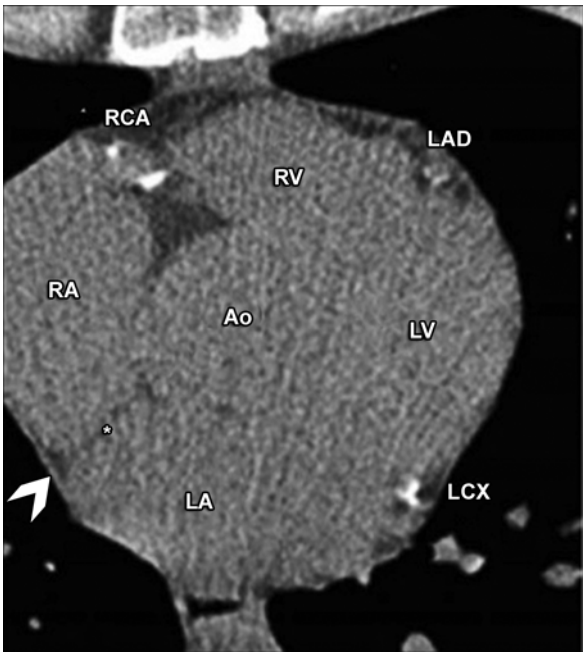

Fig. 11.2 Considerable information on cardiac structures can be garnered from noncontrast CT. The left anterior descending (*LAD*), left circumflex (*LCX*), right coronary artery (*RCA*), and the ascending aorta (*Ao*) can be seen, as labeled. The four chambers of the heart are also seen and labeled as *RA* (right atrium), *RV* (right ventricular outflow tract), *LA* (left atrium), and *LV* (left ventricle). Relative chamber sizes can be estimated from noncontrast CT. The pericardium is visible as a thin line (*arrowhead*). The inter-atrial septum is also seen (*asterisk*)

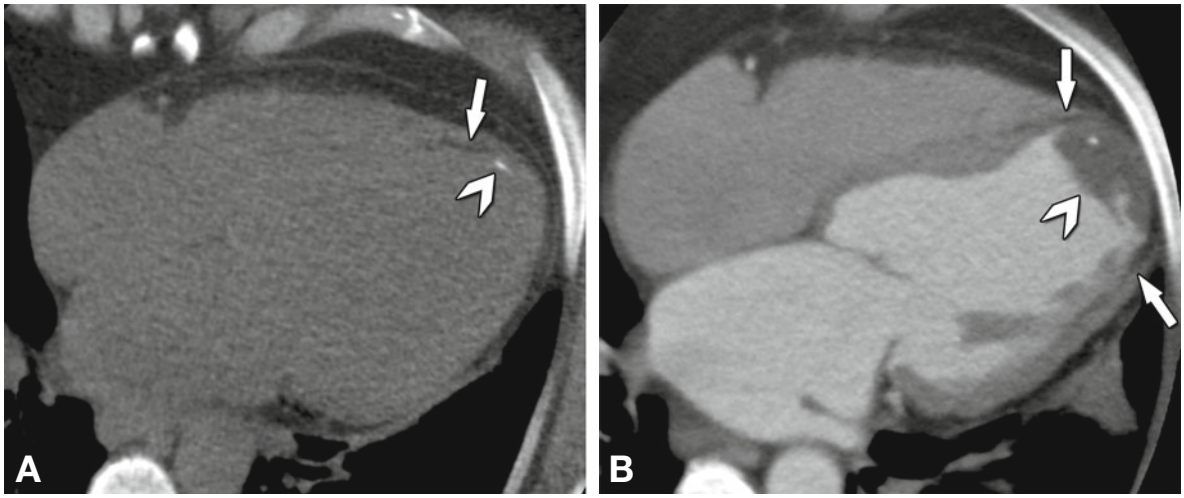

Fig. 11.3 Chronic apical infarction seen on a noncontrast scan as an incidental finding in a 50-year-old female patient with a calcium score of zero. **Panel A** shows the apical infarction with thinning and fatty degeneration of the myocardium (*arrow*), while a nearby calcification is also visible on a four-chamber view reconstructed from the non-contrast acquisition (*arrowhead*). **Panel B** shows a 5-mm average reconstruction in the four-chamber view from contrast-enhanced CT angiography in the same patient, delineating the thinned fatty myocardium (*arrows*) and an apical thrombus (*arrowhead*) that contains the calcification

Table 11.1 Classification of calcium scores using the Agatston method

Agatston units	Ranking
0	Absent
>0–10	Minimal
>10–100	Mild
>100–400	Moderate
>400–1,000	Severe
>1,000	Extensive

The thresholds shown here are empirical

methods exist: (1) the Agatston score (**Tables 11.1** and **11.2**), (2) the volume score, (3) the derived calcium mass, and (4) the calcium coverage score (**Table 11.2**).

The prevalence and extent of coronary artery calcium increases with age, and both are higher in men compared with women at any age. The prognostic value of absolute coronary artery calcium scores and calcium 'percentiles' – relative to age and gender – has been compared in the Multi-Ethnic Study of Atherosclerosis. In this study, although both scoring methods yielded effective risk stratification, the absolute measurement approach performed better than the percentile approach. Therefore, reporting the absolute coronary artery calcium score is currently recommended for clinical practice.

In cardiac CT imaging, certain noncardiac incidental findings may be seen such as thoracic and abdominal diseases including liver cysts, calcified lymph nodes, emphysema, and lung nodules. Other calcified tissues including cardiac valve leaflets can resemble coronary artery calcium and must be interpreted correctly in order not to falsely increase the total "coronary" calcium score (**Fig. 11.4**). Misinterpretation is highly unlikely in experienced centers, as these different entities are easy to distinguish from each other. Importantly, aortic valve calcification has independent prognostic value for risk stratification. It is important to distinguish all of these noncoronary findings so that they can be properly diagnosed and managed.

11.2.2 Scan Protocol

The standard imaging protocol is to acquire 40 consecutive 3-mm images at a rate of 100–200 ms per image from below the carina to the base of the heart. Images are obtained with prospective ECG-triggering during end-diastole over several heart beats (Chap. 8). There are two protocols for single-beat coronary artery calcium scanning: fast prospective spiral acquisition with 2nd generation dual-source CT and axial volumetric prospective acquisition with 320-row CT.

A reduction of tube voltage from120 to 100 kV results in higher Hounsfield units (HU) of calcified tissue (Chap. 7). Therefore, when lowering tube voltage from standard 120 to 100 kV, the 130 HU threshold for the coronary artery calcium score is no longer valid. Some noncalcified plaques, which at 120 kV would be below the 130 HU threshold, may now be scored. Scientific evidence is not sufficient to validate a new Hounsfield unit threshold or scoring system for 100 or 80 kV, and each scanner is expected to have some variation, so it is recommended to acquire coronary artery calcium scans only at 120 kV at this time. Lower tube current with iterative reconstruction can potentially preserve image quality at lower radiation doses without changing the calcium score. Such patient-specific protocols and limited scan lengths reduce radiation exposure. With currently available CT technology, the radiation exposure from a typical calcium scoring study is comparable to that of approximately five mammograms (each an effective dose of approximately 0.2 mSv). Images are reconstructed using a 512 × 512 matrix on a small field of view (Chap. 8), and scoring is done as shown in **Tables 11.1** and **11.2**.

11.2.3 Prognostic Value in Asymptomatic People

In asymptomatic individuals, the absence of detectable coronary artery calcium is associated with a very low (less than 1% per year) risk of major cardiovascular events over the next 5 years. At the other extreme, up to an 11-fold higher risk for major cardiac events has been reported for asymptomatic people with extensive coronary calcification (Agatston score >1,000), and results of several large population-based studies provide evidence for the incremental prognostic value of coronary artery calcium as quantified by CT. The population-based Multi-Ethnic Study of Atherosclerosis, conducted in 6,722 asymptomatic individuals from four racial groups and followed for 3.8 years, demonstrated significant variation in the prevalence of coronary calcium among ethnic groups (from 70% in white men to 52% in black men) but similar incremental prognostic value of coronary artery calcium scores over traditional risk factors,

Table 11.2 Comparison of four methods for coronary artery calcium (CAC) scoring

	Agatston score[a]	Volume score	Derived calcium mass	Calcium coverage score
Calculation of calcium score	$CS^b = W^c \times A^d$	$VS^e = Vnox^f \times Nvox^g$	$Cac^h \times Vcp^i$	Affected 5-mm segments/total number of 5-mm segments
Advantages	Most commonly used method for which substantial reference data exist	High reproducibility Useful for assessing progression of coronary calcium	Accurate and little variability	Helpful in conveying to the patient the percentage of his/her arteries that have calcified plaque
Disadvantages	Low interscanner agreement	Partial volume effects may impair accuracy	Difficult to measure	Requires accurate tracing of the coronary arteries, which adds more reading time
	Nonlinearity with respect to amount of calcium Dependence on noise Score does not correspond to a physical measure	Less clinical data available	Requires a phantom to be placed under the patient for calibration Less clinical data	Not well established clinically
Interscan variability	15–20%	10–12%	10–12%	No data
Unit	mm^2	mm^3	mg of calcium hydroxyapatite equivalence	Percentage (%)
Clinical use	Most commonly used	Can be used to measure progression of atherosclerosis	Best measure of the amount of calcium in coronary arteries	Too tedious for clinical practice

[a] The Agatston score was first described by Agatston et al. in 1990. The Agatston score is the traditional method of quantifying coronary artery calcium

[b] Calcium score by Agatston method for a single lesion, Agatston scores for each artery, each calcification, or the entire heart—sometimes called total calcium score (TCS)—are calculated by summing the respective values for the regions of interest

[c] Weighing factor, where W = 1 if 130 HU ≤ CT max <200 HU, W = 2 if 200 HU ≤ CT max <300 HU, W = 3 if 300 HU ≤ CT max <400 HU and W = 4 if 400 HU ≤ CT max

[d] Area of lesion in mm^2

[e] Volume score

[f] Volume of one voxel

[g] Number of voxels

[h] Calcium concentration

[i] Volume of calcified plaque

with a sevenfold increase in the occurrence of coronary events for Agatston scores > 100 compared with individuals without detectable coronary artery calcium.

For clinical decision-making, the additional risk of cardiac events associated with coronary artery calcium in each conventional risk category may be sufficient to reclassify individual risk. In a prospective population analysis of 1,461 individuals, it was observed that cardiac event rates increased with high coronary artery calcium scores in each Framingham risk category, including

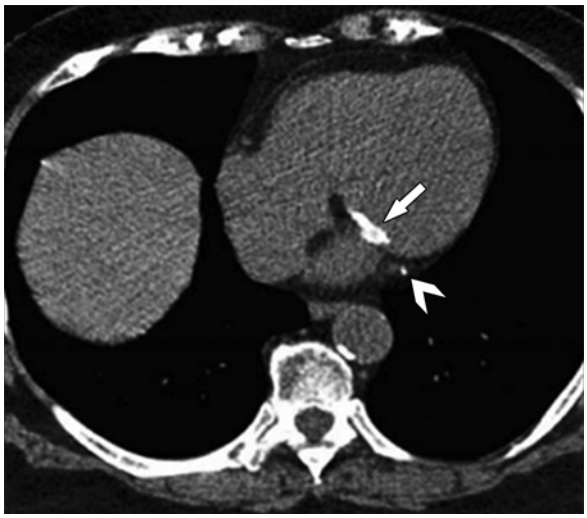

Fig. 11.4 Axial noncontrast CT showing a significantly calcified mitral annulus (*arrow*). This is important to distinguish from the calcification (*arrowhead*) in left circumflex artery, as this would substantially increase the coronary calcium score. Calcified plaque in the descending aorta is also seen

low-risk, intermediate-risk, and high-risk individuals (**Fig. 11.5**). However, in individuals classified as very low risk by the Framingham method (<6% 10-year risk), high coronary artery calcium scores (Agatston score > 400) are uncommon, and despite increased risk, this segment of the population remains below the current risk threshold for aggressive risk factor modification. Current clinical practice guidelines (see Sect. 11.3) do not recommend calcium scoring for patients at this very low global cardiovascular risk.

Several studies have shown the prognostic value of coronary calcium scoring for people with a low to moderate risk. The St. Francis Heart Study demonstrated that low-risk patients, especially those in middle age, can have increased cardiovascular risk associated with very high coronary calcium scores. The PACC study demonstrated an 11-fold increased risk of cardiovascular events among low- to moderate-risk active United States military personnel who had very high coronary calcium scores. Thus, the American College of Cardiology and American Heart Association both have included low-to-intermediate risk

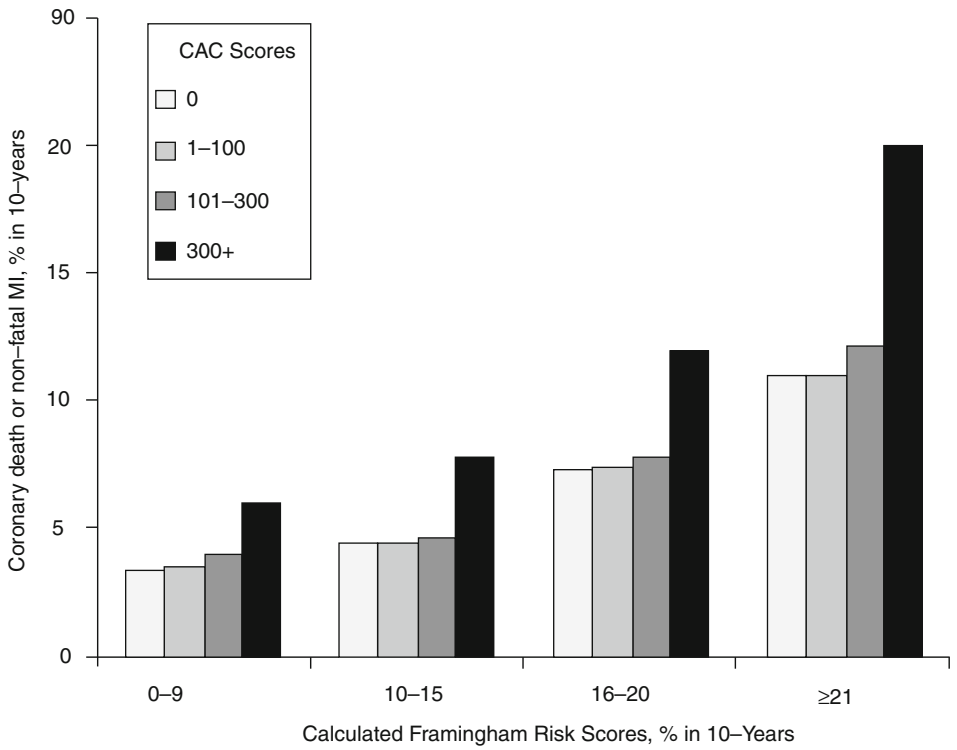

Fig. 11.5 Seven-year event rates for different coronary calcium scores within each of the Framingham risk categories in research participants without previous cardiovascular disease. In this population sample, participants with an estimated baseline Framingham risk of 16–20% who also had a calcium score of at least 301 Agatston units were reclassified to a much higher risk group. Note that thresholds of 100 and 400 for the Agatston score have been most widely used in clinical practice. Very few studies have utilized alternative thresholds, such as 300 or 600, and these alternative thresholds are not generally clinically employed (With permission from Greenland et al. (2004))

individuals (10 year risk of 6–10%) among those who may benefit from coronary calcium scoring (Class IIb recommendation).

Calcium scoring is one of many potential tests that have been proposed to improve risk assessment beyond traditional risk factors. In persons with an intermediate risk (>10–20% 10-year risk), coronary artery calcium scoring has been shown to be the most useful additional risk marker for risk classification compared to other markers such as carotid intima-media thickness and C-reactive protein.

11.2.4 Patients with Type 2 Diabetes

Patients with type 2 diabetes experience more diffuse, calcified, and extensive coronary artery disease, more often have left ventricular dysfunction, and more frequently have silent ischemia. They have substantially higher cardiovascular event rates than nondiabetic individuals without cardiovascular disease. Even in the absence of cardiac symptoms, type 2 diabetics are considered at high risk for coronary artery disease, and secondary prevention strategies are typically recommended. Further risk stratification in diabetic patients may help identify those with extensive coronary atherosclerosis and with significant inducible silent myocardial ischemia, who might potentially benefit from even more intensive treatment strategies, including coronary revascularization.

Coronary calcium scoring for risk stratification in asymptomatic diabetic patients is currently endorsed by the American College of Cardiology/American Heart Association recommendations. In addition, a meta-analysis published in a 2013 *BMJ* issue suggests that an Agatston CAC score of less than 10 may define an especially low-risk diabetic population. If a strategy of testing asymptomatic diabetics for the presence of silent ischemia is considered, preselection of individuals based on calcium scores >400 with the intent of performing subsequent functional imaging if a substantial atherosclerotic burden is identified might be reasonable.

11.2.5 Patients with Renal Disease

Impaired renal function is a major cardiovascular risk factor, and the risk gradually increases as the glomerular filtration rate decreases. Patients with impaired renal function have elevated coronary artery calcium scores, and the prevalence and extent of coronary calcium are especially high in dialysis patients, partly due to nonatherosclerotic mechanisms. Coronary artery calcium progresses more rapidly in dialysis patients, in whom it correlates with age, duration of dialysis, chronic renal failure, diabetes mellitus, alterations in mineral metabolism as well as use and dose of calcium-based phosphate binders. In addition to the amount of coronary calcium, calcification of the mitral annulus and noncoronary vascular calcification in dialysis patients have also been shown to be associated with incident cardiovascular events and increased mortality risk.

Coronary artery calcium scoring is advocated for chronic kidney disease patients by the KDIGO Clinical Practice Guideline for the Diagnosis, Evaluation, Prevention, and Treatment of Chronic Kidney Disease-Mineral and Bone Disorder (CKD-MBD). The guideline states "that patients with CKD stages 3–5D with known vascular/valvular calcification (can) be considered at highest cardiovascular risk (2A). It is reasonable to use this information to guide the management of CKD". Patients with any coronary artery calcium should switch to non-calcium-based phosphate binders, so the calcium score can directly influence clinical decision making. Coronary artery calcium scoring is not considered useful for cardiovascular risk stratification of patients with chronic kidney disease, who are already considered candidates for intensive cardiovascular risk modification. Patients with a high coronary calcium burden are recommended to avoid calcium-based phosphate binders.

11.2.6 Measurement of Coronary Calcium Progression

The ease of obtaining a coronary calcium score makes it an appealing tool for serial measurement and monitoring of atherosclerosis burden over time. Data relating to coronary calcium progression demonstrate that, while statins do not specifically slow progression in short-term randomized trials of low-dose statins versus placebo, calcification progression is consistently and strongly associated with poorer cardiovascular disease outcome.

There is no consensus on the most appropriate measure of progression, i.e., whether to use absolute score differences, percent changes, or square root changes. Progression of the absolute calcium score is dependent on the amount of calcium present at baseline. It is also related to patient age, sex, family history of premature coronary artery disease, ethnic background, diabetes, body mass index, elevated blood pressure, and renal insufficiency. Importantly, the reliability of measurement

in repeat calcium scans is relatively high and may be suitable to monitor the effect of preventive medications on clinical disease progression. A large substudy of the Multi-Ethnic Study of Atherosclerosis showed a fourfold increased risk in calcium score progressors versus non-progressors, independent of statin use. Therefore, serial assessment may have value in assessing plaque progression and identifying progressors, who are at increased risk of cardiovascular events. Practice guidelines from several countries do not currently recommend using serial coronary calcium scoring for assessment of disease progression in clinical routine.

11.3 Guidelines

There are several guidelines that have commented on coronary artery calcium scoring for risk assessment. We discuss guidelines from the USA, Canada, and Europe.

11.3.1 USA Guideline

The American College of Cardiology Foundation/American Heart Association Task Force on Practice Guidelines published a guideline on risk assessment for asymptomatic adults in 2010. This guideline identified two Class IIa indications for coronary artery calcium scoring. A Class IIa recommendation indicates that it is reasonable to perform the procedure because benefits outweigh risk. The Guideline states that coronary artery calcium scoring is reasonable as a risk assessment adjunct in asymptomatic individuals at intermediate risk (between 10 and 20% in 10 years) and for diabetics older than 40 years (both Class IIa recommendations). It further states that measurement of coronary calcium may be reasonable for cardiovascular risk assessment in persons at low to intermediate risk (6–10% 10-year risk; a Class IIb recommendation, meaning that there is less robust evidence for benefit but calcium scoring may be helpful in selected patients). A coronary artery calcium score greater than zero establishes the presence of underlying coronary artery disease and may be a rationale for more aggressive risk factor management. The risk for future events increases in direct proportion to the coronary artery calcium score. Patients with diabetes and high coronary artery calcium scores may be candidates for cardiac stress testing to rule out the presence of silent myocardial ischemia.

11.3.2 Canadian Guideline

The Canadian Risk Assessment guideline was updated in 2012 (published in 2013). The Guideline states: While not as sensitive as coronary angiography, coronary artery calcium scoring may be useful for the differential diagnosis of chest pain in highly selected patients. Coronary artery calcium scoring, according to the Canadian Guideline, is not recommended for screening asymptomatic people.

11.3.3 European Guideline

The Fifth Joint Task Force of the European Society of Cardiology and Other Societies on Cardiovascular Disease Prevention in Clinical Practice reviewed the role of coronary artery calcium scoring in risk assessment. This guideline, published in 2012, regards the Agatston score as an independent risk marker regarding the extent of coronary heart disease and prognostic impact. The Rotterdam calcification study showed that the upper percentile range reflects a 12-fold increased risk of myocardial infarction—independent of the classical risk factors—even in elderly people. This Guideline concludes that, although calcium scoring is widely applied today, it is especially suited for patients at moderate risk (Class IIa recommendation). Recent studies have also shown that multi-slice computed tomography coronary angiography with decreased radiation levels is highly effective in restratifying patients into either a low or high post-test risk group. Thus, the European Guideline comes to similar conclusions as the US Guideline.

11.4 Outlook

Substantial evidence indicates that measurement of coronary calcification provides effective, independent, and incremental risk stratification and is especially useful in asymptomatic intermediate-risk individuals without known cardiovascular disease. In addition, coronary calcium scoring provides prognostic information in asymptomatic type 2 diabetic patients without known coronary artery disease. Therefore, these specific patient groups may benefit from imaging strategies for risk stratification in primary prevention, and the use of coronary artery calcium scoring may be reasonable, after consideration of patient characteristics and the specific clinical situation.

With conventional risk factor testing alone, large numbers of coronary events occur in people thought to be at low to intermediate risk. Thus, calcium scoring has great potential for improving risk assessment. The results of the Rotterdam Heart Study, the Heinz Nixdorf Recall Study, and the Multi-Ethnic Study of Atherosclerosis indicate that coronary calcium is the best risk stratifier among current risk assessment algorithms. Further research is needed to define the clinical impact of coronary calcium testing for early detection. In addition, studies of the cost-effectiveness of such testing are needed.

Recommended Reading

Agatston AS, Janowitz WR, Hildner FJ, Zusmer NR, Viamonte M Jr, Detrano R (1990) Quantification of coronary artery calcium using ultrafast computed tomography. J Am Coll Cardiol 15(4):827–832

Anderson TJ, Grégoire J, Hegele RA, Couture P, Mancini GB, McPherson R, Francis GA, Poirier P, Lau DC, Grover S, Genest J Jr, Carpentier AC, Dufour R, Gupta M, Ward R, Leiter LA, Lonn E, Ng DS, Pearson GJ, Yates GM, Stone JA, Ur E (2013) 2012 update of the Canadian Cardiovascular Society guidelines for the diagnosis and treatment of dyslipidemia for the prevention of cardiovascular disease in the adult. Can J Cardiol 29(2):151–167

Blankenhorn DH, Stern D (1959) Calcification of the coronary arteries. Am J Roentgenol 81:772–777

Budoff MJ, McClelland RL, Nasir K, Greenland P, Kronmal RA, Kondos GT, Shea S, Lima JA, Blumenthal RS (2009a) Cardiovascular events with absent or minimal coronary calcification: the Multi-Ethnic Study of Atherosclerosis (MESA). Am Heart J 158(4):554–561

Budoff MJ, Nasir K, McClelland RL, Detrano R, Wong N, Blumethal RS, Kondos G, Kronmal RA (2009b) Coronary calcium predicts events better with absolute calcium scores than age-sex-race/ethnicity percentiles: MESA (Multi-Ethnic Study of Atherosclerosis). J Am Coll Cardiol 53:345–352

Cooney MT, Dudina A, Whincup P, Capewell S, Menotti A, Jousilahti P, Njølstad I, Oganov R, Thomsen T, Tverdal A, Wedel H, Wilhelmsen L, Graham I (2009) SCORE Investigators. Eur J Cardiovasc Prev Rehabil 16(5):541–549

Elias-Smale SE, Proença RV, Koller MT, Kavousi M, van Rooij FJ, Hunink MG, Steyerberg EW, Hofman A, Oudkerk M, Witteman JC (2010) Coronary calcium score improves classification of coronary heart disease risk in the elderly: the Rotterdam study. J Am Coll Cardiol 56(17):1407–1414

Elkeles RS, Godsland IF, Feher MD, Rubens MB, Roughton M, Nugara F, Humphries SE, Richmond W, Flather MD, PREDICT Study Group (2008) Coronary calcium measurement improves prediction of cardiovascular events in asymptomatic patients with type 2 diabetes: the PREDICT study. Eur Heart J 29(18):2244–2251

Erbel R, Möhlenkamp S, Moebus S, Schmermund A, Lehmann N, Stang A, Dragano N, Grönemeyer D, Seibel R, Kälsch H, Bröcker-Preuss M, Mann K, Siegrist J, Jöckel KH, Heinz Nixdorf Recall Study Investigative Group (2010) Coronary risk stratification, discrimination, and reclassification improvement based on quantification of subclinical coronary atherosclerosis: the Heinz Nixdorf Recall study. J Am Coll Cardiol 56(17):1397–1406

Greenland P, Alpert JS, Beller GA, Benjamin EJ, Budoff MJ, Fayad ZA, Foster E, Hlatky MA, Hodgson JM, Kushner FG, Lauer MS, Shaw LJ, Smith SC Jr, Taylor AJ, Weintraub WS, Wenger NK (2010) 2010 ACCF/AHA guideline for assessment of cardiovascular risk in asymptomatic adults: a report of the American College of Cardiology Foundation/American Heart Association Task Force on Practice Guidelines. J Am Coll Cardiol 56:50–103

Greenland P, LaBree L, Azen SP, Doherty TM, Detrano RC (2004) Coronary artery calcium score combined with Framingham score for risk prediction in asymptomatic individuals. JAMA 291:210–215

K/DOQI clinical practice guidelines for chronic kidney disease: evaluation, classification, and stratification. Kidney Disease Outcome Quality Initiative (2002) Am J Kidney Dis 39(2 Suppl 2):S1–246

Kramer CK, Zinman B, Gross JL, Canani LH, Rodrigues TC, Azevedo MJ, Retnakaran R (2013) Coronary artery calcium score prediction of all cause mortality and cardiovascular events in people with type 2 diabetes: systematic review and meta-analysis. BMJ 346:f1654

Kronmal RA, McClelland RL, Detrano R, Shea S, Lima JA, Cushman M, Bild DE, Burke GL (2007) Risk factors for the progression of coronary artery calcification in asymptomatic subjects: results from the Multi-Ethnic Study of Atherosclerosis (MESA). Circulation 115:2722–2730

Latif MA, Budoff MJ (2013) Coronary artery calcium scanning: a useful tool for refining heart failure risk prediction? Future Cardiol 9(1):1–3

McEvoy JW, Blaha MJ, DeFilippis AP, Budoff MJ, Nasir K, Blumenthal RS, Jones SR (2010) Coronary artery calcium progression: an important clinical measurement? a review of published reports. J Am Coll Cardiol 56:1613–1622

Perk J, De Backer G, Gohlke H et al (2012) European guidelines on cardiovascular disease prevention in clinical practice (version 2012). The fifth joint task force of the European Society of Cardiology and other societies on cardiovascular disease prevention in clinical practice (constituted by representatives of nine societies and by invited experts). Developed with the special contribution of the European Association for Cardiovascular Prevention and Rehabilitation (EACPR). Eur Heart J 33:1635–1701

Rose G (1985) Sick individuals and sick populations. Int J Epidemiol 14(1):32–38, PubMed PMID: 3872850

Yeboah J, McClelland RL, Polonsky TS, Burke GL, Sibley CT, O'Leary D, Carr JJ, Goff DC, Greenland P, Herrington DM (2012) Comparison of novel risk markers for improvement in cardiovascular risk assessment in intermediate-risk individuals. JAMA 308(8):788–795

Coronary Artery Bypass Grafts

E. Martuscelli

Abstract

This chapter provides practical information for optimizing scanning of coronary artery bypass grafts and reading the images. Reading the images is best done on axial and multiplanar reformations and should include the evaluation of graft anastomoses and run-offs as well as the native vessels. The thoracic aorta and cardiac function should be considered in the reporting.

12.1 Introduction

In patients who underwent coronary artery bypass grafting, recurrence of symptoms can be due to graft failure or progression of atherosclerosis in the native vessels. Conventional coronary angiography has so far been considered the reference standard for visualization of both native vessels and bypass grafts. With its inherent advantages and good diagnostic accuracy, noninvasive coronary angiography using CT is considered a viable alternative in symptomatic patients after coronary artery bypass grafting (Chap. 5).

CT was first proposed for noninvasive imaging of coronary artery venous bypass grafts by Brundage et al. in 1980. At that time the detection of flow-limiting stenoses was not possible. CT technology has since greatly improved (Chap. 7), which has important implications for the diagnostic evaluation of venous and arterial coronary bypass grafts since they are ideal vessels for visualization by CT because of their greater diameter, their reduced motion, and their relative freedom from calcification.

However, applicability of CT to all comers is limited by premature atrial or ventricular contractions, which can reduce image quality when occurring during scanning. Moreover, in patients with coronary artery bypass grafts, the investigation of the native vessels can pose a challenge because of the often times severe coronary calcifications present.

12.2 Vade Mecum of Coronary Surgery

There are two main approaches for performing coronary artery bypass grafting: (1) traditional on-pump surgery, the most common form of revascularization, which usually involves median sternotomy, a single period of aortic cross-clamping, intermittent infusion of cold cardioplegia, and use of cardiopulmonary bypass; (2) minimally invasive coronary artery bypass grafting. This includes four subtypes: (a) port access coronary artery bypass grafting performed with femoral-femoral cardiopulmonary bypass and cardioplegic arrest; (b) port access approach using a totally endoscopic robotically assisted technique with coronary artery bypass grafting in cardiac arrest; (c) off-pump surgery, performed using median sternotomy without cardiopulmonary bypass, stabilizing

M. Dewey, *Cardiac CT*,
DOI 10.1007/978-3-642-41883-9_15, © Springer-Verlag Berlin Heidelberg 2014

Table 12.1 Arterial and venous grafts in coronary surgery

Graft	Preparation	Direction
LIMA	Pedicled	LAD/Dia/OM
	Skeletonized	LAD/Dia/OM
	Free graft	LAD/Dia/OM
RIMA	Pedicled	LAD/Dia/OM/proximal RCA
	Skeletonized	LAD/Dia/OM/proximal RCA
	Free graft	LAD/Dia/OM/proximal RCA
RA	Free graft	Any vessel
GEA	Skeletonized	PDA
	Free graft	Distal LAD (prolonging LIMA)
GSV	Free graft	Any vessel

Dia diagonals, *GEA* gastroepiploic artery, *GSV* great saphenous vein, *LAD* left anterior descending artery, *LIMA* left internal mammary artery, *OM* obtuse marginals, *PDA* posterior descending coronary artery, *RA* radial artery, *RCA* right coronary artery, *RIMA* right internal mammary artery

the target vessel by specific devices; and (d) minimally invasive direct coronary artery bypass grafting via left anterior thoracotomy without a cardiopulmonary bypass.

Depending on the approach used for revascularization, the surgeon can utilize different types of arterial and venous grafts, which the physician performing the scan needs to be familiar with (**Table 12.1**). Despite the more complex harvesting procedure, arterial grafts are commonly used because of a better patency rate than venous coronary artery bypass grafts.

The left internal mammary artery is usually anastomosed to the left descending coronary artery, diagonals, and/or obtuse marginal branches both as a single graft (**Fig. 12.1**) or in a sequential arrangement. The right internal mammary artery is usually anastomosed to the left anterior descending coronary artery crossing the midline (**Fig. 12.2A**), to the proximal right coronary artery, to obtuse marginal branches or diagonals, via the transverse sinus (behind the aorta) (**Fig. 12.2B**), or to obtuse branches or diagonals (**Fig. 12.3**).

The great saphenous vein is usually directly anastomosed to the aorta to revascularize any coronary artery both in a single graft (**Figs. 12.4** and **12.5**) or in a sequential arrangement (**Fig. 12.6**). The radial artery is also used as free graft to all coronary arteries as a single graft (**Fig. 12.4C**) or in sequential arrangement. It is more frequently attached in a Y-configuration to left or right internal mammary grafts and less commonly to the aorta. The gastroepiploic artery is only rarely used to revascularize the posterior descending coronary artery; sometimes it is used as a free graft to extend a left internal mammary graft anastomosed to the very distal part of left anterior descending coronary artery (**Fig. 12.7**).

12.3 Technical Considerations

12.3.1 CT Scanner

CT of coronary artery bypass grafts requires a larger scan range (12.5–22.0 cm) and consequently a longer breath-hold. Due to the limited coverage of 4-row CT a very long, impractical breath-hold of over 50 s was required. 16-row CT slightly improved the situation, but it took the advent of 64-row systems to make CT of coronary artery bypasses a practical approach with a short breath-hold duration (12–15 s) and thin-slice imaging. Moreover, apart from enhancing diagnostic accuracy, 64-row scanners improved the applicability of the method in other ways as well. The latest generation of scanners with a very large detector coverage (320-row; Chap. 9a) or very fast table feed (Chap. 9b) promise a further reduction in radiation exposure and improvement in image quality. For clinical routine, at least 64 rows are recommended for follow-up of patients after coronary surgery.

12.3.2 Scan Range and Direction

The scan range depends on both the modality of grafting. Patients who have received a mammary artery bypass graft should be scanned starting at the subclavian arteries (about at the middle of the clavicle, Chap. 8). The scan usually ends at the inferior border of the heart with the exception of patients with a gastroepiploic artery graft, in whom the scan has to include the upper abdomen. Using 64-row CT the scan direction is usually craniocaudal.

12.3.3 Contrast Agent

Bolus tracking should be preferred for more consistent results and more homogeneous contrast in the coronary arteries (Chap. 8). An amount of approximately 60–100 ml of contrast agent followed by a saline flush is sufficient for bypass imaging using 64-row CT.

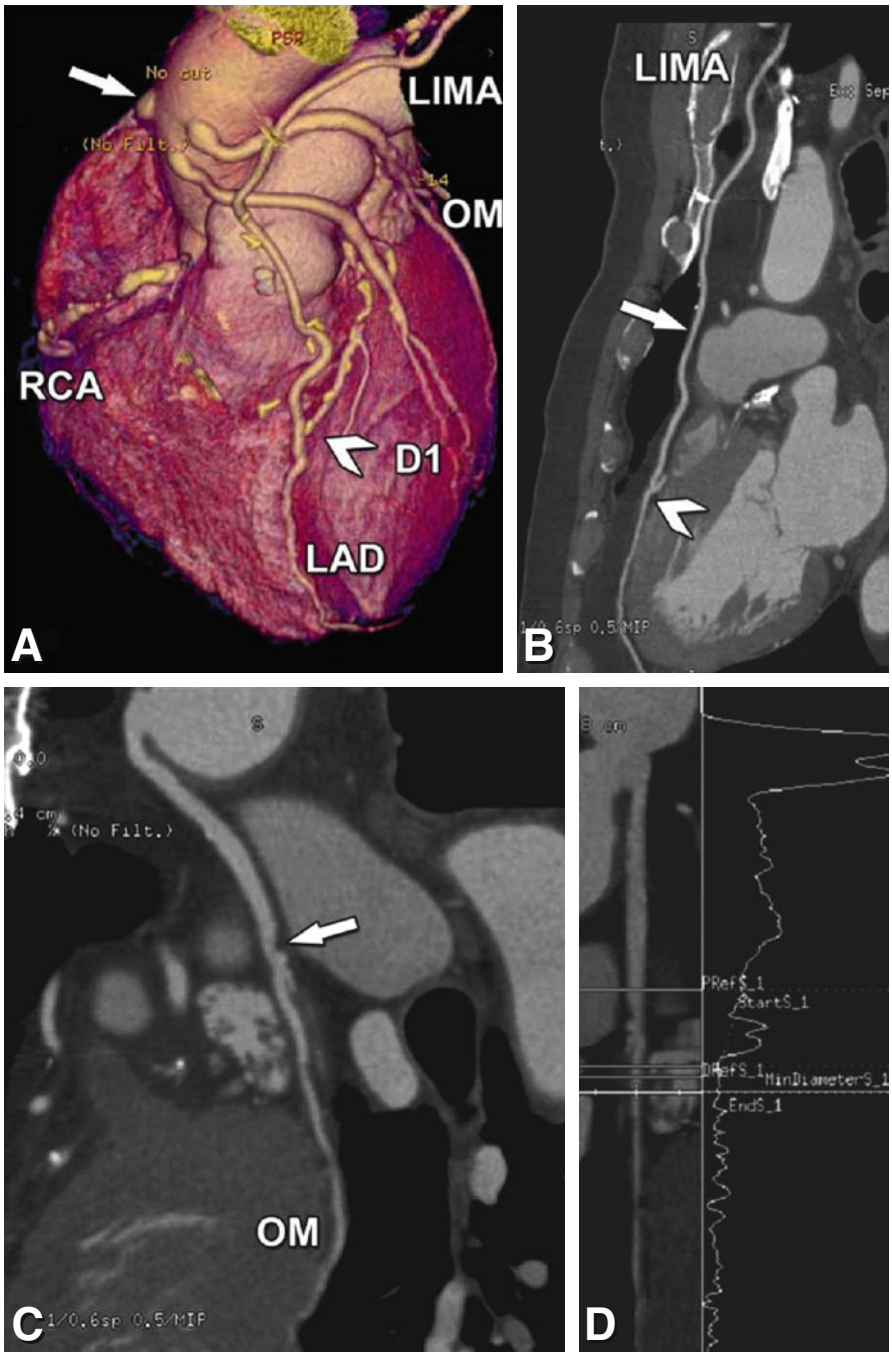

Fig. 12.1 64-year-old male patient who was underwent left internal mammary artery (*LIMA*, skeletonized) grafting to the left descending coronary artery and vein grafts to the right coronary artery (*RCA*), the diagonal branch (*D1*), and to the obtuse marginal branch (*OM*, **Panel A**, three-dimensional reconstruction) 14 years ago. CT was performed because of an inferior myocardial perfusion defect on single-photon emission computed tomography. The skeletonized LIMA graft is patent (*arrow* in **Panel B**, curved multiplanar reformation) with a normal distal anastomosis (*arrowhead* in **Panels A** and **B**) but the vein graft to the RCA is occluded (*arrow* in **Panel A**). The venous graft to the OM branch shows luminal narrowing (*arrow* in **Panel C**, curved multiplanar reformation), which was estimated to be not significant by quantitative analysis (14% diameter stenosis in **Panel D**, lumen stripe reformation)

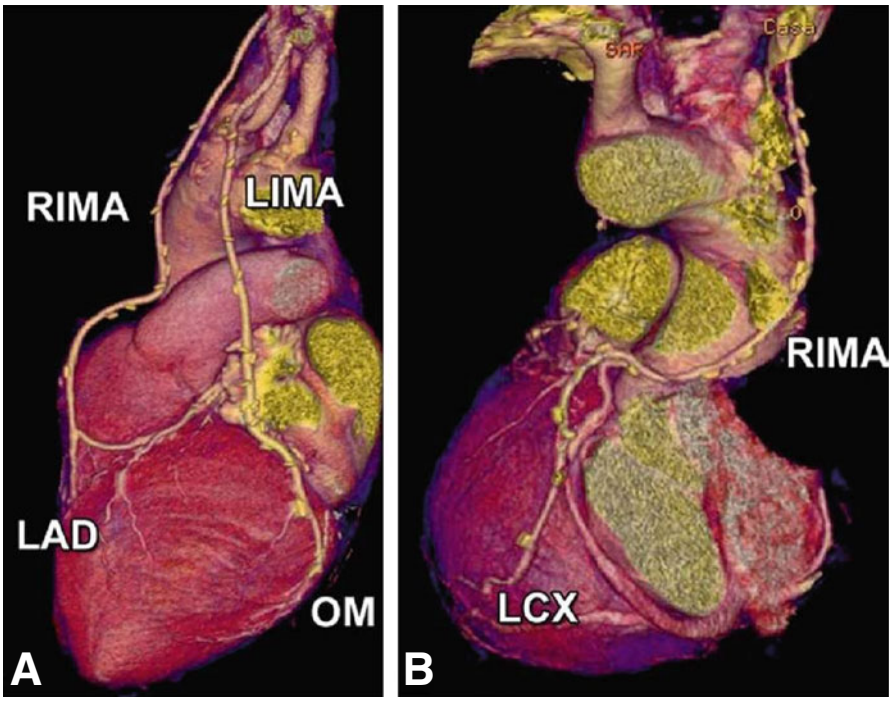

Fig. 12.2 Different examples of left and right internal mammary artery grafts. **Panel A** shows three-dimensional reconstructions of the CT in a 68-year-old female patient who underwent left internal mammary artery (*LIMA*, skeletonized) grafting to an obtuse marginal branch (*OM*) and right internal mammary artery (*RIMA*, also skeletonized) to the left anterior descending coronary artery (*LAD*) 6 years ago. The CT was performed because of atypical angina and shows that both arteries are patent (volume-rendered three-dimensional reconstruction). **Panel B** shows a RIMA (skeletonized) anastomosed to the left circumflex coronary artery (*LCX*) across the transverse sinus behind the aorta in a 58-year-old male patient who was operated on 8 years ago. CT was performed because of an inconclusive stress test. The grafts were patent in both patients

12.3.4 Acquisition Protocols

In case of a slow and stable heart rate (<65 beats per min), prospective ECG triggering is recommended because it can reduce the radiation dose by up to about 80–90% compared to retrospective spiral scanning. Since coronary artery bypass patients often have more irregular heart rates than patients scanned for suspected coronary artery disease, it may be wise to use some padding resulting in a somewhat lower radiation dose reduction (60–80%). The drawbacks of prospective acquisition are a lack of flexibility in reconstructing image data across the cardiac cycle and the impossibility to undertake functional analysis unless single-beat prospective triggering with tube current modulation is used. Retrospective ECG gating should be preferred in case of heart rate instability. Adjusting the tube current to body mass is a useful measure to reduce effective dose also in CT bypass imaging. For specific recommendations for scanners from different vendors see Chap. 9.

12.3.5 Reconstruction and Reading

Reconstruction of coronary artery bypass acquisitions is similar to standard coronary CT angiography protocols. Slice thickness and the reconstruction field of view should be as small as possible. Halfscan reconstruction is usually adequate in low heart rates (<65 beats per min), and dual-source CT and/or multisegment reconstruction are beneficial in higher heart rates. Sharp kernels (e.g., as used for stent imaging, see Chap. 13) may be used in heavily calcified vessels, which are common in patients after bypass grafting.

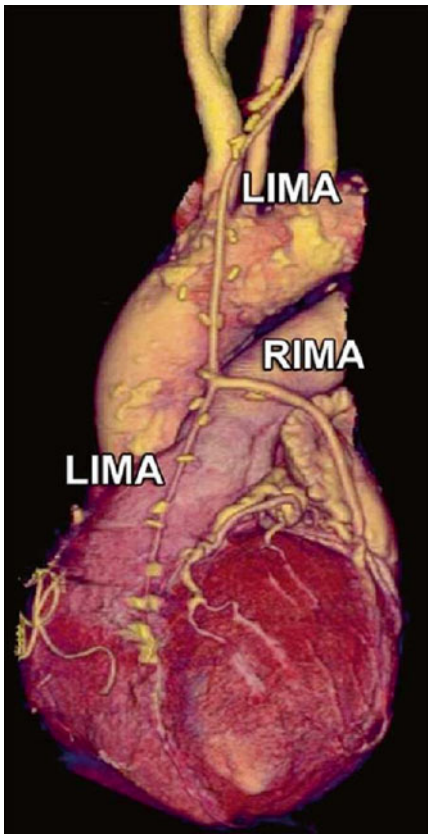

Fig. 12.3 66-year-old female who was operated on 7 years ago by left internal mammary artery (*LIMA*) to the left descending coronary artery, a right internal mammary artery (*RIMA*) used as free graft in Y configuration with the LIMA to revascularize an obtuse marginal branch. CT was carried out because of an inconclusive stress test. The grafts are patent without significant stenoses

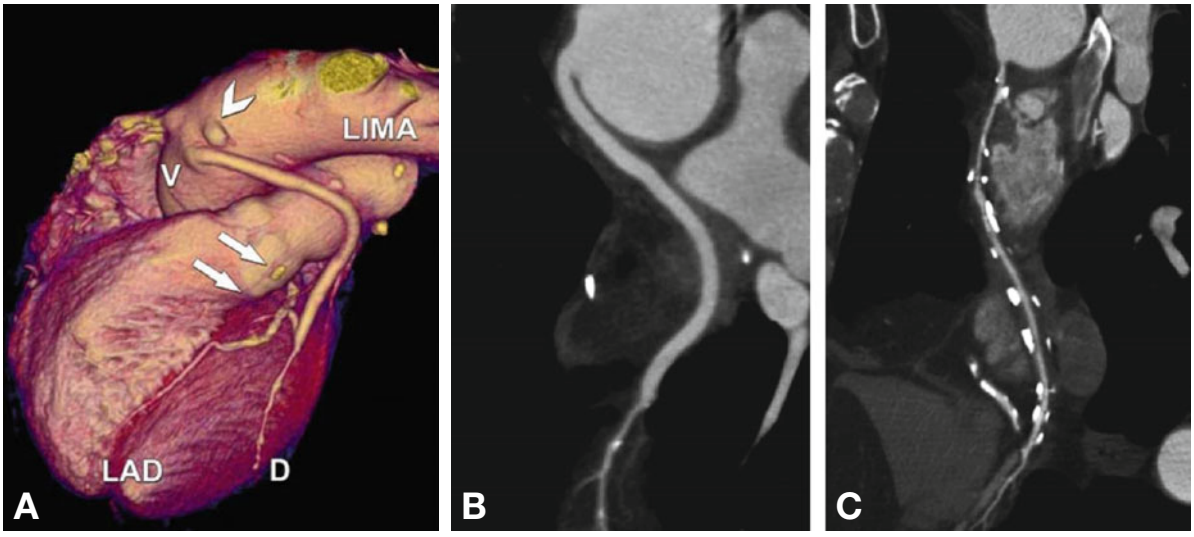

Fig. 12.4 63-year-old male patient who was underwent left internal mammary artery (*LIMA*) to the left descending coronary artery (*LAD*), two single vein (*V*) grafts to the obtuse marginal branch and diagonal (*D*) branch (**Panels A** and **B**) as well as radial artery (free graft) to the descending posterior coronary artery (**Panel C**) 10 years ago. CT was performed because of a positive perfusion stress test (lateral wall). The venous graft to the marginal branch *(arrowhead)* and the LIMA *(arrows)* is occluded (**Panel A**, volume rendering) whereas the venous graft to the D branch is patent (**Panel B**, curved multiplanar reformation). The assessability of the radial artery free graft is slightly impaired by the presence of the typical large number of metallic clips (**Panel C**, curved multiplanar reformation)

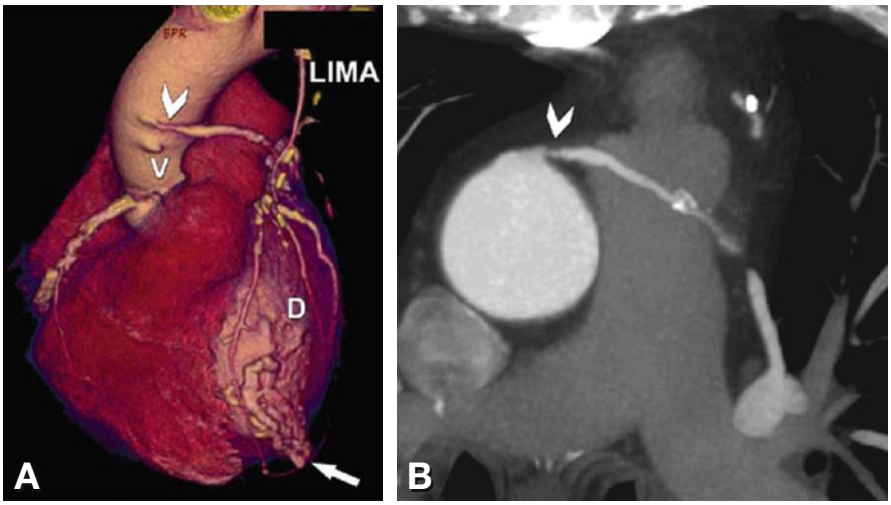

Fig. 12.5 65-year-old male patient who underwent left aneurysmectomy *(arrow)*, left internal mammary artery (*LIMA*, pedicled) to the first diagonal branch (*D*), and a vein graft to the first and second obtuse marginal branches (**Panel A**) 5 years ago. CT was performed because of recurrence of atypical angina. The LIMA graft is patent but the vein graft to the first OM is occluded (*V*) and the one to the second obtuse marginal branch is severely stenosed (*arrowhead* in **Panels A** and **B**); the latter was found to be unsuitable for revascularization

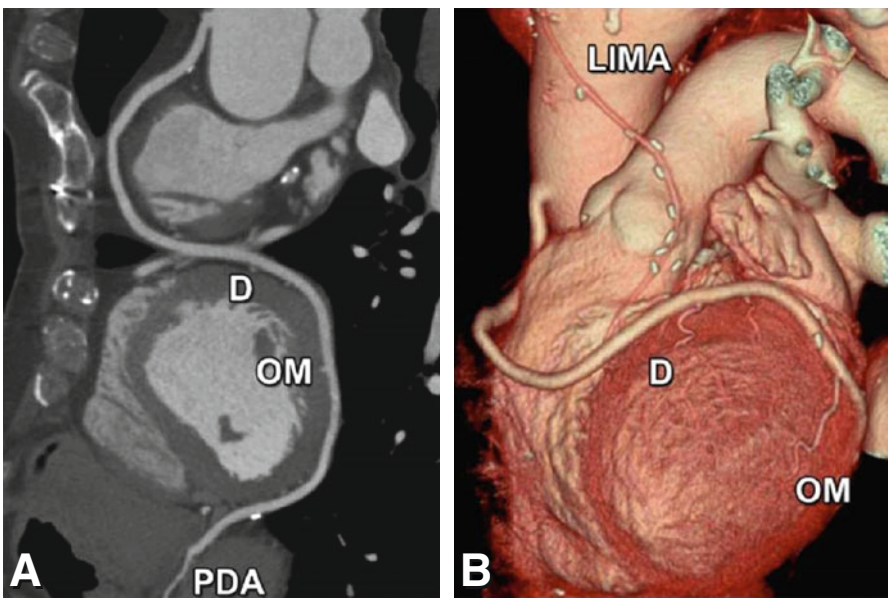

Fig. 12.6 68-year-old male patient who underwent venous circular (jump) grafting to the diagonal branch (*D* in **Panel A**, curved multiplanar reformation), obtuse marginal branch (*OM*), and the posterior descending coronary artery (*PDA*) 12 years ago. The left anterior descending coronary artery was revascularized by the left internal mammary artery (*LIMA* in **Panel B**). CT was carried out because of atypical angina and showed the venous circular graft to be patent

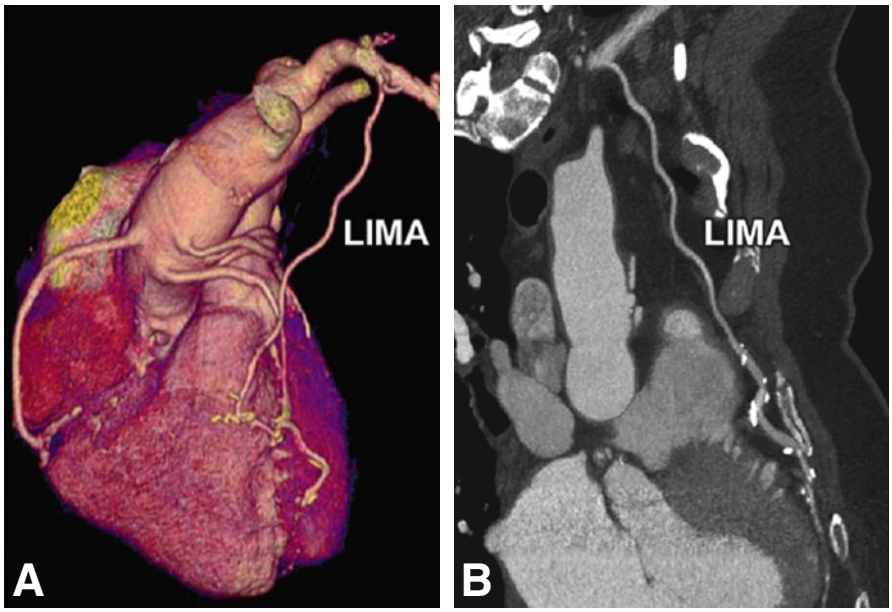

Fig. 12.7 62-year-old male patient who was operated on 15 years earlier with five venous bypass grafts. Because of an occlusion of the left anterior descending artery and typical angina pectoris (Canadian class III) the left internal mammary artery (skeletonized, *LIMA*) prolonged with the right gastroepiploic artery (free graft) was used to revascularize the left anterior descending artery 3 years ago. CT was now performed because of atypical angina pectoris and showed the vein grafts (**Panel A**) and the LIMA (**Panel B**) to be patent without significant stenosis

List 12.1 suggests a structured approach to reading coronary bypass CT datasets.

Three-dimensional volume rendering is particularly useful in patients who underwent surgical revascularization because it allows a quick overview of arterial and venous grafts and a quick evaluation of their anatomical condition. Significant stenoses are usually searched for by scrolling through axial images (with and without maximum-intensity projection). This should be supplemented by oblique multiplanar reformations and curved multi-planar reformations, which allows quantification of percent diameter stenosis on cross-sections along the vessel.

List 12.1. Systematic approach to reading coronary artery bypass CT

1. Volume-rendered images for a rapid overview of graft anatomy
2. Graft evaluation by axial scrolling and multiplanar reconstructions
3. Evaluation of graft anastomoses and run-off
4. Evaluation of native vessels
5. Anatomy of the thoracic aorta and left ventricle (diastolic dimensions)
6. Left ventricular and valve function in case of retrospective gating (Chaps. 15 and 16)

12.4 Diagnostic Accuracy of CT

Diagnostic accuracy and evaluability depend on the technical characteristics of the scanner available with a continuous improvement of performance from 4-row to 64-row (or more) scanners.

Four-row CT provided an anisotropic resolution, often times did not depict the distal anastomosis, and 38% of the patent grafts could not be evaluated because of respiratory/motion/metallic clip artifacts. The advent of 16-row CT improved assessment of occlusion/significant stenosis; however, about 20% were judged not assessable because of artifacts (**Table 12.2**).

Sixty-four-row CT improved the depiction of the distal anastomosis and showed excellent diagnostic results (**Table 12.2**) in the evaluation of arterial and venous grafts without excluding grafts from analysis. However, the investigation of native vessels showed somewhat mixed results with about 10% of coronary

Table 12.2 Meta-analysis of diagnostic performance of 16- and 64-row CT for detection of coronary artery bypass obstruction (stenosis and occlusion)

Scanner	Graft assessability	Sensitivity	Specificity	Positive predictive value	Negative predictive value
16-row	78%	96.9% (94.2–98.6%)	96.4% (94.8–97.6%)	91.3% (87.6–94.2)	98.8% (97.7–99.4%)
64-row	100%	98.1% (96.0–99.3%)	96.9% (95.3–98.1%)	94.1% (91.0–96.3%)	99.1% (98.0–99.7)

Adapted from Hamon et al. Radiology 2008.

Numbers in parentheses are 95% confidence intervals

segments being nondiagnostic, mostly because of severe calcifications. In evaluable native vessel segments, sensitivity and specificity are significantly lower than in patients with suspected coronary artery disease. Thus, image quality is important in coronary artery bypass patients to allow a comprehensive assessment of the grafts and the native vessels.

Recommended Reading

Achenbach S, Marwan M, Ropers D et al (2010) Coronary CT angiography with a consistent dose below 1 mSv using prospectively electrocardiogram-triggered high-pitch acquisition. Eur Heart J 31: 340–346

Brundage BH, Lipton MJ, Herfkens RJ et al (1980) Detection of patent artery bypass grafts by CT. Circulation 61:826–831

Dewey M, Zimmermann E, Deissenrieder F et al (2009) Non invasive coronary angiography by 320 row CT with lower radiation exposure and maintained diagnostic accuracy. Circulation 120:867–875

Hamon M, Lepage O, Malagutti P et al (2008) Diagnostic performance of 16 and 64 section spiral CT for coronary artery bypass grafts assessment. Radiology 247:679–686

Hermann F, Martinoff S, Meyer T et al (2008) Reduction of radiation estimates in cardiac 64-slice CT angiography in patients after coronary by artery bypass graft surgery. Invest Radiol 43:253–260

Martuscelli E, Romagnoli A, D'Eliseo A et al (2004) Evaluation of venous and arterial conduit patency by 16-slice spiral CT. Circulation 110:3234–3238

Nazeri I, Shahabi P, Tehrai M, Sharif-Kashani B, Nazeri A (2009) Assessment of patients after aortocoronary bypass grafting using 64-slice computed tomography. Am J Cardiol 103:667–673

Ropers D, Ulzheimer S, Orlov B et al (2001) Investigation of aortocoronary artery bypass grafts by multislice spiral CT with electrocardiographic-gated image reconstruction. Am J Cardiol 88:792

Ropers D, Pohle FK, Kuetter A et al (2006) Diagnostic accuracy of non invasive coronary angiography in patients after bypass surgery using 64-slice spiral CT with 330-ms gantry rotation. Circulation 114:2334–2341

Steigner M, Otero H, Mitsouras D et al (2009) Narrowing the phase window width in prospectively ECG gated single heart beat 320-detector row coronary CT angiography. Int J Cardiovasc Imaging 25:85–90

Coronary Artery Stents

K. Anders

Abstract

This chapter details the demands on coronary artery stent CT angiography and the typical challenges when reading these datasets.

13.1 Clinical Background

In most patients with relevant coronary artery disease (CAD), interventional treatment comprises placement of a coronary artery stent rather than angioplasty alone. Stent material, coating, drug-eluting properties, and anticoagulant drugs influence re-endothelialization rates, recurrent intimal hyperplasia, in-stent restenosis, and thrombosis. Conventional bare-metal stents have a clinically symptomatic restenosis rate of about 20–30%. Initial results for drug-eluting stents first published in 2002 and 2003 (sirolimus- and paclitaxel-eluting stents) were very favorable with significantly decreased restenosis rates at short- and mid-term follow-up (up to 1 year). However, more recent literature suggests that – possibly due to vessel wall inflammation in the vicinity of drug-eluting stents and reduced re-endothelialization – late in-stent thrombosis rates may be increased.

Multislice CT angiography has been contemplated as a noninvasive follow-up tool for detecting in-stent restenosis or occlusion in patients with coronary stents. The increasing number of stent implantations performed every year heightens our chances of having to report on stents in cardiac CT examinations performed for some other reason.

13.2 Challenges

Coronary stent sizes vary with the diameter of the artery treated and usually range between 2.5 and 5 mm. Depending on the skills of the interventionist involved, they might be found nearly anywhere within the coronary tree, including coronary artery bifurcations, rather distal segments, and bypass grafts. As most coronary segments take an oblique course relative to the scan axis, isotropic datasets with the best possible spatial resolution in any direction are desirable.

Most current stents are made of metal struts with a strut thickness between approximately 0.07 and 0.15 mm; mesh design can show considerable differences (e.g., sinusoidal ring, slotted tube, or multicell design), with different metal-to-surface ratios causing different degrees of attenuation. **Figure 13.1** shows an

M. Dewey, *Cardiac CT*,
DOI 10.1007/978-3-642-41883-9_16, © Springer-Verlag Berlin Heidelberg 2014

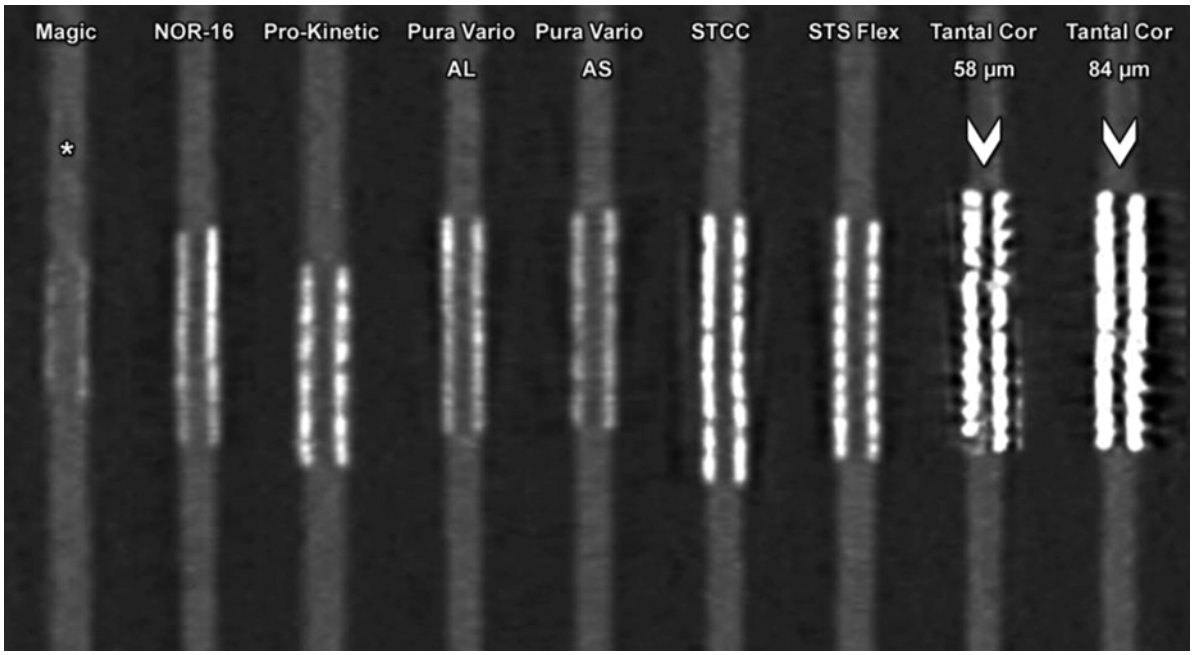

Fig. 13.1 Overview of different coronary stents using ex-vivo CT. Stent lumen visibility and artifacts differ greatly for the currently available coronary artery stents. This is mainly due to differences in material, strut size, and design. The visibility of the lumen of the Magic stent (*asterisk*), which is made of magnesium (plus less than 5% of zirconium, yttrium, and rare earth metals each), is far superior to that of tantalum-coated stents (strut thickness of 58 and 84 mm) with pronounced artificial lumen narrowing (*arrowheads*) (Modified and used with permission from Maintz et al. *Eur Radiol* 2009)

overview of stents used and their different appearances in ex-vivo CT scans. Drug-eluting stents are additionally covered with a polymer, storing the drug to be released to the vessel wall within 6–8 weeks following implantation. Over the last decade, several manufacturers have developed so-called biodegradable stents made of organic polymers or corrodible metals (e.g., poly-*l*-lactic acid, polytyrosine or absorbable magnesium), meant to resolve completely after a while. After having been evaluated for the treatment of peripheral atherosclerotic stenosis first, they are now investigated for the use in coronary artery stenosis (e.g., PROGRESS-AMS-trial, ABSORB trial).

In CT, any kind of metal will cause typical artifacts resulting from the pronounced attenuation due to its very high density. The severity of metal artifacts in the final image is determined by spatial resolution on the one hand and the use of noise filters and special reconstruction algorithms on the other. Residual motion artifacts due to high heart rates, irregular beats, or paradoxical ventricular motion patterns – conditions likely to be met in patients with manifest CAD – enhance the artifacts caused by the metal stents. Furthermore, decreased cardiac output, also common in patients with CAD, influences individual contrast dynamics.

13.3 Beam Hardening, Blooming, and Artificial Lumen Narrowing

13.3.1 Beam Hardening

Beam hardening refers to a shift in the X-ray spectrum to higher energy photons caused by absorption of lower energy photons within very dense structures such as metallic material. It may lead to a virtual loss of CT density in surrounding soft tissue (i.e., it may look "darker" than it should and black streaks may occur). This is because higher energy photons are less sensitive to soft tissue and iodine attenuation. **Figure 13.2** shows beam hardening with corresponding tissue or filling defects caused by high density contrast agent or metal. Dedicated image reconstruction algorithms (see below) may correct or even overcorrect for this effect and may thus eventually even exaggerate soft tissue densities.

13.3.2 Blooming and Artificial Lumen Narrowing

So-called blooming of stent struts is an apparent increase in strut size in x-, y-, and z-direction and is

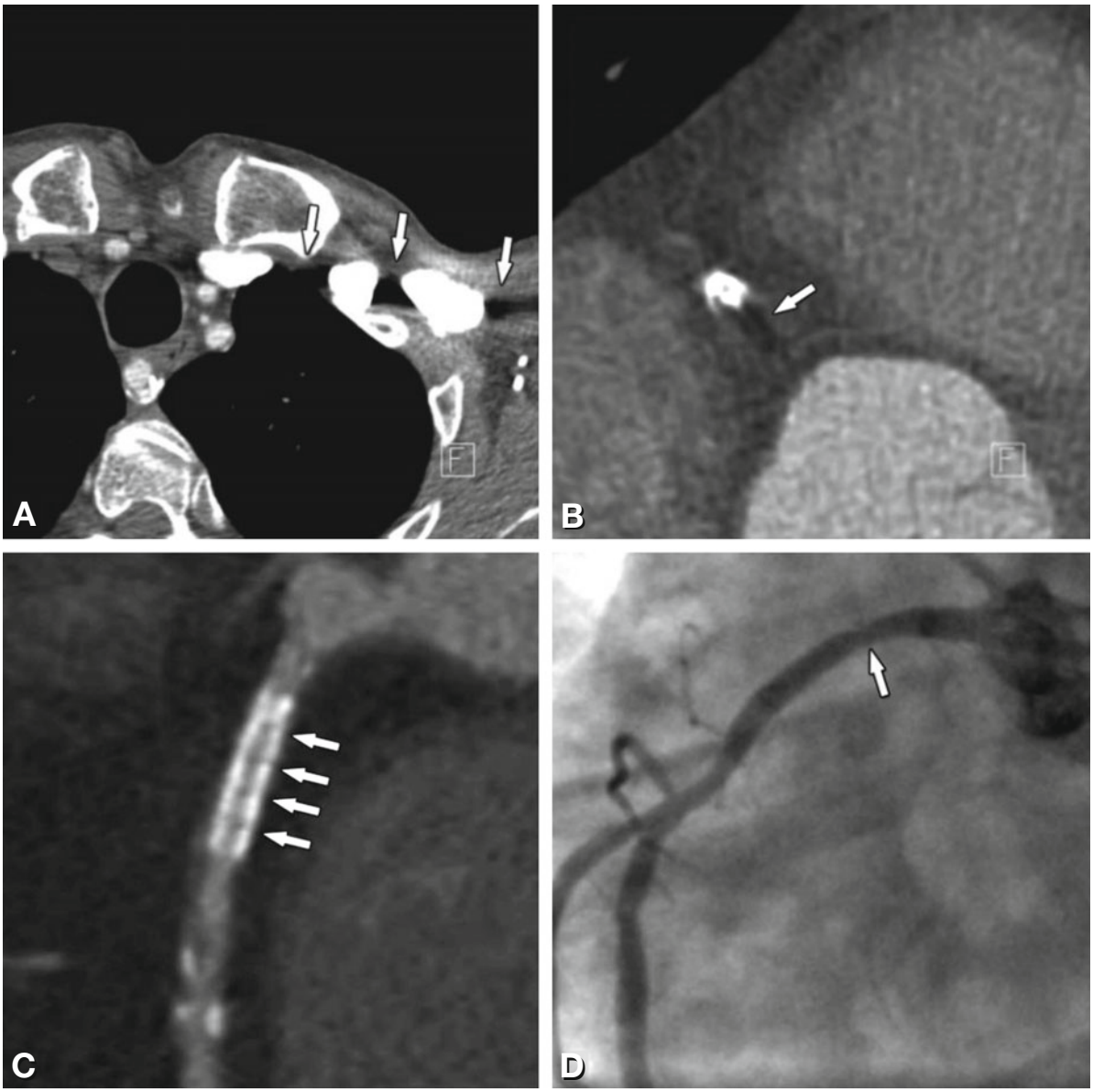

Fig. 13.2 Beam-hardening effects as caused by undiluted contrast agent (**Panel A**) or metal (**Panels B**, **C**)**.** Next to high-density inflowing contrast agent, the relative increase in X-ray energy decreases the visualization of low-density soft tissue, causing black streaks and artificial tissue defects (*arrows* in **Panel A**)**.** The same effect can be witnessed in surrounding tissue next to coronary stents (*arrow* in **Panel B)**. Within the stent, beam hardening artifacts depend on the individual stent structure and may look like repeated dark spots inside the stent lumen (*arrows* in **Panel C**)**.** They preclude rule-out of in-stent restenosis in this 56-year-old male patient, which thus had to be excluded by conventional coronary angiography. The corresponding angiogram in **Panel D** shows only mild focal wasting (*arrow*) but no relevant stenosis

mainly caused by partial volume effects. Its magnitude is influenced by the reconstruction algorithm used for image computation. Whenever a voxel includes two different densities (e.g., parts of stent struts as well as lumen), the average density of the two will be displayed. As CT density values of metal are extremely high, those average values will always be way above those of body tissue and – in the window-level settings used in CT angiography – will rather resemble those of the stent struts. Thus the better

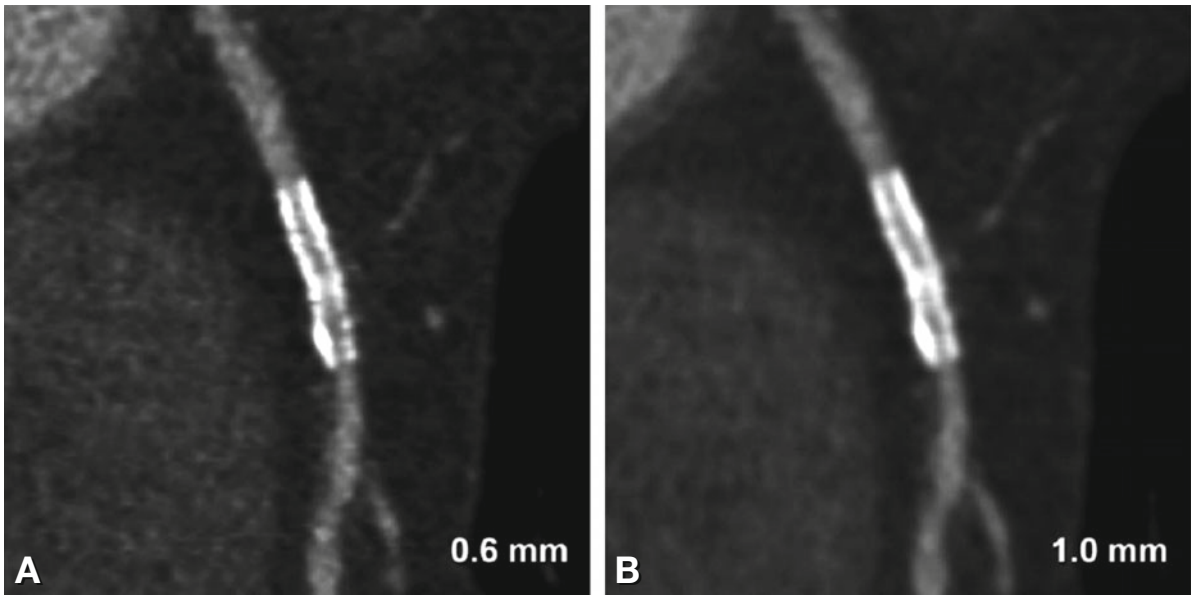

Fig. 13.3 Illustration of the effect of slice thickness on visibility of in-stent lumina. Curved multiplanar reformations of a 3.0-mm stent in the right coronary artery using a slice thickness of 0.6-mm (**Panel A**) and 1.0 mm (**Panel B**)**.** The improved resolution shows greater detail, but also increases noise (**Panel A**)**,** whereas there is pronounced blooming and reduced lumen visibility with thicker slices (**Panel B**). Both datasets were reconstructed at a slice increment equal to two thirds of the slice thickness (0.4 and 0.7 mm) with an intermediate sharp reconstruction kernel and are displayed with identical window-level settings (1,500/300)

spatial resolution gets, which means the smaller the voxels are, the fewer partial volume effects will be seen. However, even state-of-the-art high-end CT scanners do not provide a spatial resolution equivalent to current stent strut size (0.07–0.15 mm). One of the most bothersome effects of blooming is artificial lumen narrowing. The in-stent lumen is systematically underestimated in CT: artificial narrowing ranges from 20 to 100% depending on stent material. When using current 64-row CT with smaller slice thickness and dedicated reconstruction kernels, artificial narrowing is reduced (**Fig. 13.3**) but still considerable at about 30–40%.

13.4 Data Acquisition and Image Reconstruction

13.4.1 Temporal Resolution

Considering the general challenges of cardiac CT (motion) and the special challenges of imaging coronary artery stents (metal artifacts enhanced by motion), individualized contrast timing and premedication (e.g., beta blocker and nitroglycerin) as well as a fast gantry rotation speed and the use of the scanner's best possible temporal resolution are important. Please be reminded that a scanner's temporal resolution is best at the center of the scan field since the influence of the fan angle increases in off-center positions. So try to ensure optimal positioning of the heart by adjusting table height and patient position on the table accordingly (Chap. 9).

13.4.2 Spatial Resolution: Scanning

The scanner's detector size (e.g., 0.5 mm) determines the thinnest possible reconstructed slice thickness and thus spatial resolution in Z-direction. Coronary artery stent imaging demands submillimeter collimation. Yet, smaller detector elements will result in images with higher noise. Unfortunately, increased image noise degrades the depiction of fine details. Thus, the X-ray input needs to be increased when the smallest possible detector collimation is to be used, especially in larger individuals.

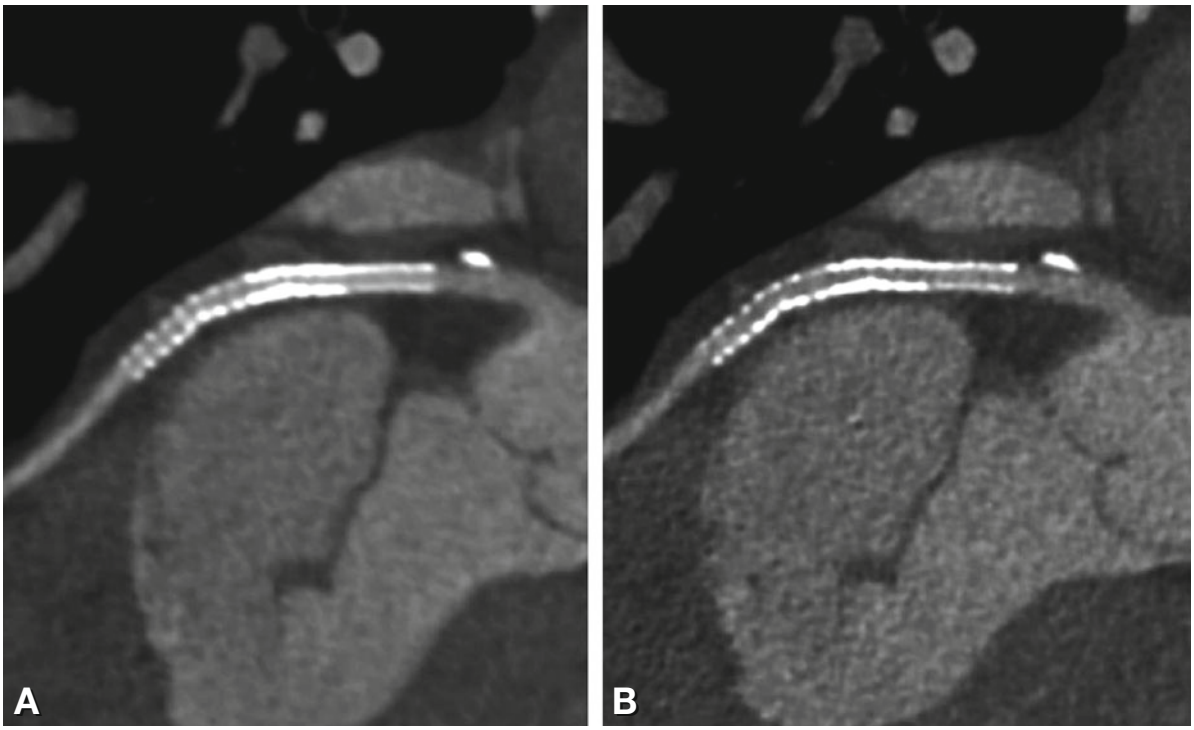

Fig. 13.4 Effect of reconstruction kernels on stent visibility. Curved multiplanar reformations (0.75 mm slice thickness) of a 3-mm stent in the left circumflex coronary artery using soft (**Panel A**) and intermediate sharp reconstruction kernels (**Panel B**). There is a smooth impression, but reduced stent lumen visibility using the soft kernel (**Panel A**) compared to the grainy appearance (higher image noise) of the sharper kernel in **Panel B,** which however allows better in-stent lumen assessment. Identical window-level settings (1,500/300) were used

13.4.3 Spatial Resolution: Image Reconstruction

The reconstruction field of view determines pixel size within the axial image. For coronary stent evaluation, the field of view should be just large enough to contain the entire heart, but small enough to take advantage of its 512 × 512 matrix (Chap. 9). Of course, a second reconstruction with a larger field of view to cover possible noncoronary findings is also needed.

The reconstruction algorithms used for image calculation from raw data can manipulate the original data in several ways. They can smoothen the overall image impression by stretching the transition between different tissues/densities over several voxels or emphasize tissue differences by sharpening the delineation of neighboring CT attenuation values. Unless confounded by additional filtering or iteration loops, smoothing algorithms will decrease and edge-enhancing filters will enhance background image noise. The different image impressions resulting from use of a soft vs. intermediate reconstruction kernel with identical window-level settings are shown in **Fig. 13.4**. The recommended reconstruction kernels for the evaluation of coronary artery stents are frequently identical to those used in the presence of heavy coronary calcifications. **Table 13.1** gives an overview of the reconstruction algorithms recommended for coronary artery stent imaging.

Table 13.1 Vendor-specific reconstructions kernels for coronary CT angiography

CT vendor	Reconstruction kernel recommended for routine coronary CT angiography	Reconstruction kernel recommended for calcium/coronary stents
GE	SOFT	Detail (DTL), Bone C2
Philips	CA	CD (calcium: CC)
Siemens	B26f(B30f)	B46f
Toshiba	Cardiac CTA (FC 3)	Cardiac stent (FC 5)

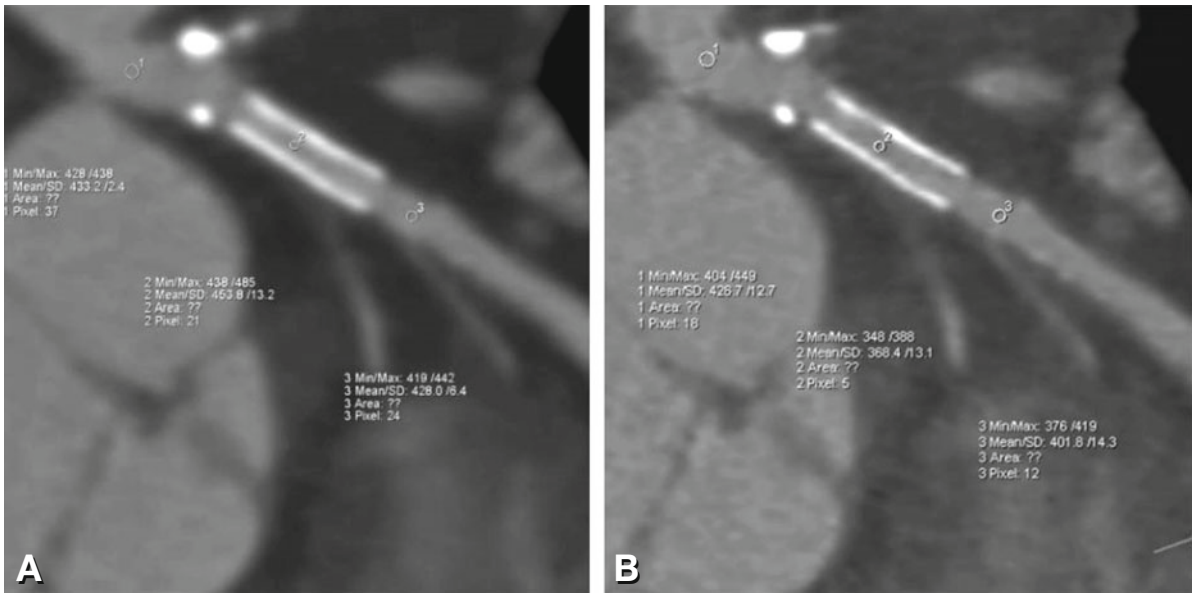

Fig. 13.5 Decrease of false-high in-stent HU values (**Panel A**) when using sharp reconstruction kernels (**Panel B**). A decrease in partial volume effects and different filtering techniques included in recommended reconstruction kernels lead to different in-stent HU values in the same LAD stent reconstructed with a soft (B26f) (**Panel A**) vs. a sharp (B46f) (**Panel B**) reconstruction kernel. Whereas in **Panel A,** in-stent values exceed those measured before and after the stent (mean of about 454 HU versus 433 and 428 HU), in-stent HU values in **Panel B** are not higher but slightly lower than those in the adjacent nonstented vessel (about 368 HU versus 427 and 402 HU). Of course, standard deviation as a surrogate of image noise shows higher values in **Panel B**

In addition, reconstruction algorithms may contain corrections for local artifacts such as beam hardening or weakening in the vicinity of high-density material. An increase in Hounsfield unit (HU) values within the stent lumen compared to lumen attenuation proximal and distal to the stented segment may result from both limited spatial resolution and overcorrection of the algorithm used. False-high in-stent densities can be reduced by using dedicated sharp reconstruction algorithms for coronary stent visualization (**Fig. 13.5**).

With increasing computational power of recent CT systems, so-called iterative reconstruction algorithms have become available in clinical practice. Unlike so-called weighted filtered back projection (WFBP) used in standard reconstruction algorithms, iterative reconstruction algorithms perform repeated calculations from raw data to image data and back (= iteration loops), generating retransferred raw data sets, which are compared with the originally scanned data in order to identify differences caused by noise. This can be repeated several times, as predefined by the user (two or more iteration steps) and finally be used to reduce noise *without* losing spatial resolution. Resulting images appear smoothened, yet detailed. However, as anything in life, iterative reconstruction can be overdone as well: as the number of iteration loops is increased (5 or more), the more the visual impression of our images deviates from what we are used to and deteriorates again (**Fig. 13.6**).

13.5 CT Wish List

The evaluation of the small coronary in-stent lumen, which may contain low-density soft tissue, e.g., neointima or plaque, demands higher spatial resolution because it is surrounded by high-density stent struts leading to artificial lumen narrowing. Also, datasets without motion artifacts and with optimal contrast are required. However, whenever wishes have to be put into practice, some trade-offs arise. At present, it is impossible to provide all of the above at once. **Table 13.2** gives an overview of the wish list and the issues involved.

13.6 Reading and Interpretation

A systematic approach to reading cardiac CT as described in Chap. 11 should also be used for evaluating coronary stents. Interactive multiplanar reading and curved multi-planar reformation using thin-slice isotropic datasets are recommended for evaluation of the stent lumen.

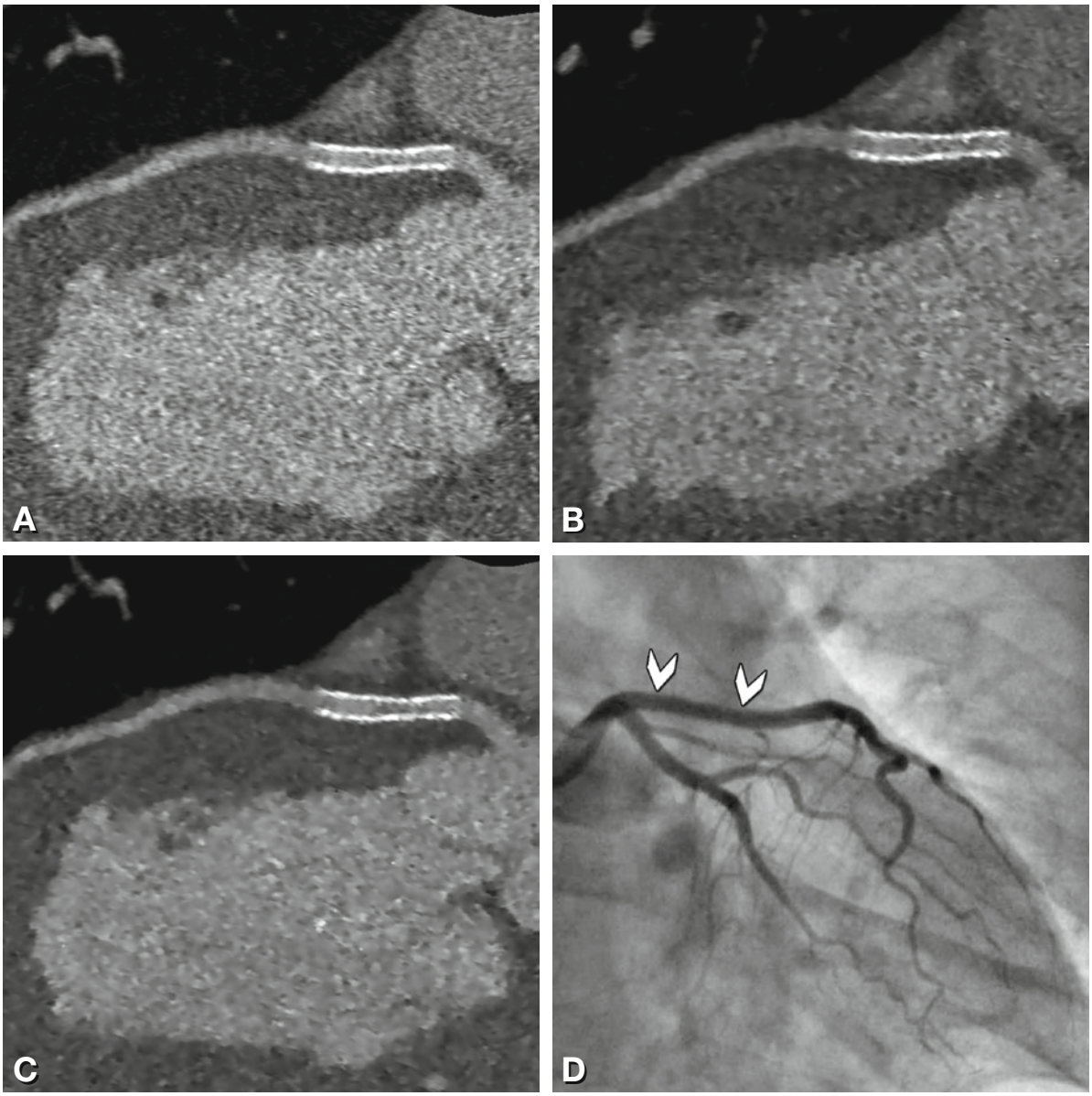

Fig. 13.6 Proximal LAD stent visualized by curved multiplanar reformation using a standard B 46f reconstruction kernel (**Panel A**) as opposed to 3 (I 46f 3, **Panel B**) or 5 (I 46f 5, **Panel C**) iteration steps. Note the reduction in overall image noise, whereas adequate delineation of the stent is preserved. However, when using 5 iteration steps, a course-grained image impression results. One might suspect in-stent intimal hyperplasia within the proximal two thirds of the stent in **Panel C**. However, no in-stent restenosis is demonstrated by invasive angiography (*arrowheads* in **Panel D**) (CT source data and angiogram courtesy of T. Pflederer, Erlangen)

Maximum-intensity projections or three-dimensional reconstructions merely provide an overview of stent locations while lumen information is always obscured by the dense stent struts on these images.. Attention should be paid to the window-level settings in reading stents. In order to not obscure vessel wall calcifications and overestimate vessel dimensions in case of high attenuation, standard mediastinal or abdominal settings (e.g., window/level 350/50 or 400/50) cannot be used. A CT angiography window-level preset (usually around 600/200) can be adapted for stents, depending on individual vessel contrast and calcium load. Whereas earlier studies used a 700/200 or 1,000/200 window-level setting, recent recommendations derived from phantom studies advise to go up to 1,500/300 for stent reading. **Figure 13.7** demonstrates the great influence of window-level settings on the visibility of the stent lumen.

Table 13.2 CT wish list for coronary CT angiography of stented arteries

What do we want?	Why don't we get it?	What is the remedy?
No blooming and no artificial lumen narrowing	Slice thickness and matrix are subject to technical limitations. We cannot go thinner than current detector elements. Noise reduction decreases visibility of details	Use the thinnest detector collimation available, and try to adapt X-ray input and image reconstruction (see kernels in Table 13.1) in order to get diagnostic images
No image noise	There is always image noise in CT – even when scanning just air (electronic noise); and in humans, the amount of photons cannot be deliberately increased. The demand for detailed images requires noisy reconstruction algorithms	As much X-ray as is required should be used. Noise in the final image is also determined by the reconstruction algorithm used, and here, unfortunately, noise and detail increase or decrease conjointly when using standard weighted filtered back projection. Iterative reconstruction algorithms will not eliminate this relationship, but may make it easier to live with it
Optimal vessel contrast	Circulation time, cardiac output, blood volume, and distribution determine contrast, but are not always easy to predict or control	We can get close to optimal contrast by using individual contrast timing and weight- or BMI-adapted flow rates (see Chap. 9)
Motion-free images	Heart rate acceleration during breath-hold, involuntary expiration, extrasystolic beats, and ECG misregistration cause motion artifacts	Thorough patient preparation (beta blockers), breath-hold instruction, and prescan ECG check will help (see Chap. 7)

Any in-stent finding should be confirmed by excluding motion artifacts, e.g., by comparison with the same stent in another cardiac phase. Unfortunately, low attenuation in-stent findings sometimes cannot be differentiated from beam hardening artifacts caused by the individual stent structure, calcium in the vessel wall next to the stent struts, radiopaque stent markers, or overlapping struts. If the presence of artifacts cannot be ruled out, the in-stent lumen becomes nondiagnostic and conventional coronary angiography has to be performed (see **Fig. 13.8**). Interestingly, the presence of contrast agent within a distal vessel segment does not rule out in-stent stenosis or even occlusion because of possible collaterals. **Figure 13.9** shows a true-negative as well as a true-positive coronary stent seen with CT.

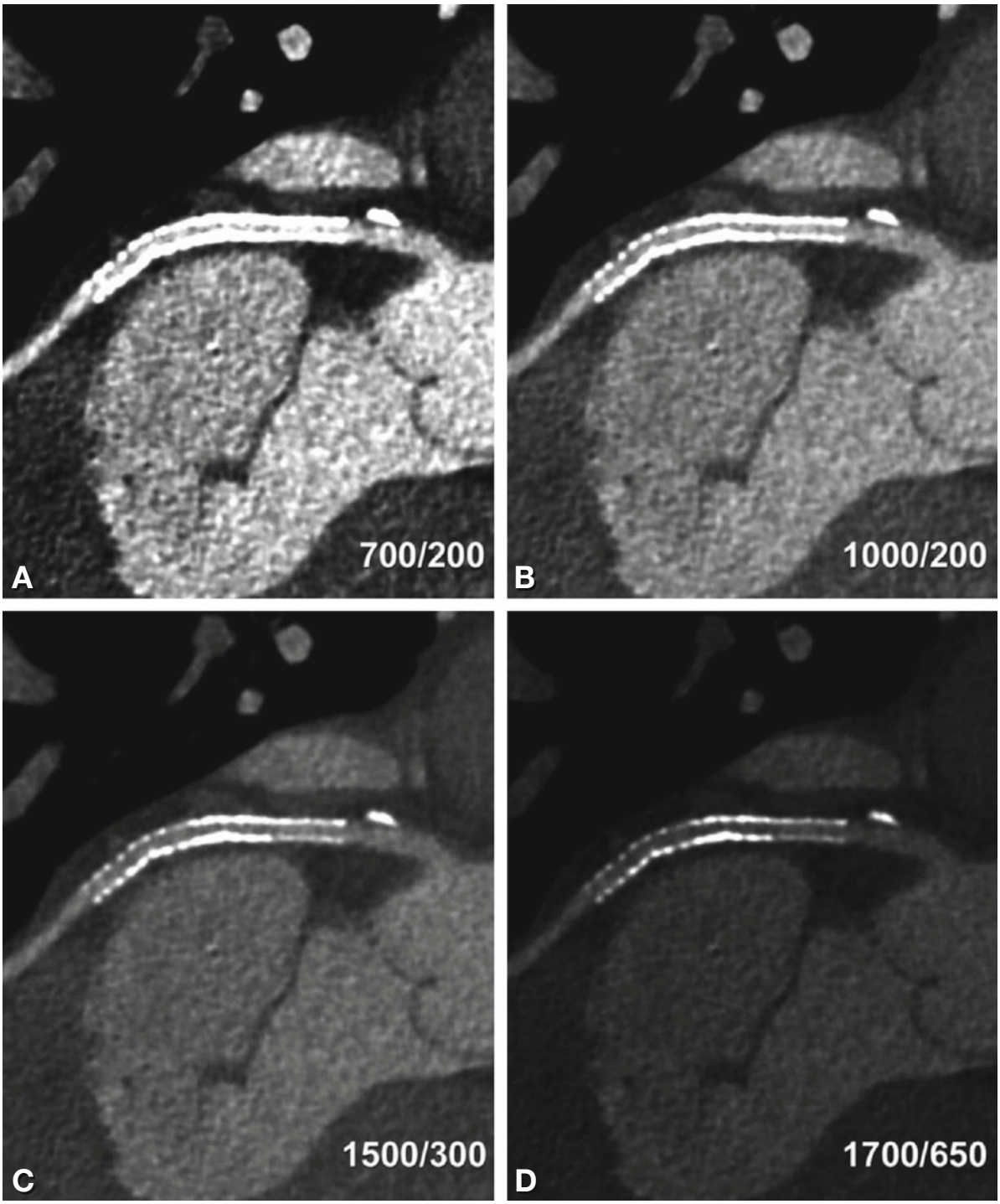

Fig. 13.7 Window-level settings influence the depiction of coronary stents. Curved multiplanar reformations (0.75-mm slice thickness) of the same stent as shown in **Fig. 13.4** displayed with different window-level settings: in **Panel A** with 700/200, which is often used for CT angiography and nicely displays contrast-filled vessels, but enhances stent blooming. In **Panel B** with 1,000/200, the increase in window width reduces blooming, but is still insufficient to adequately visualize the in-stent lumen. In **Panel C** with 1,500/300, which is a reasonable trade-off, blooming is greatly reduced while vessel contrast is maintained. In **Panel D** with 1,700/650, window values are shifted closer towards "bone-window"-like settings. Here, blooming becomes less significant but vessel contrast and the ability to depict noncalcified plaque decreases considerably. All images were reconstructed with a sharp kernel

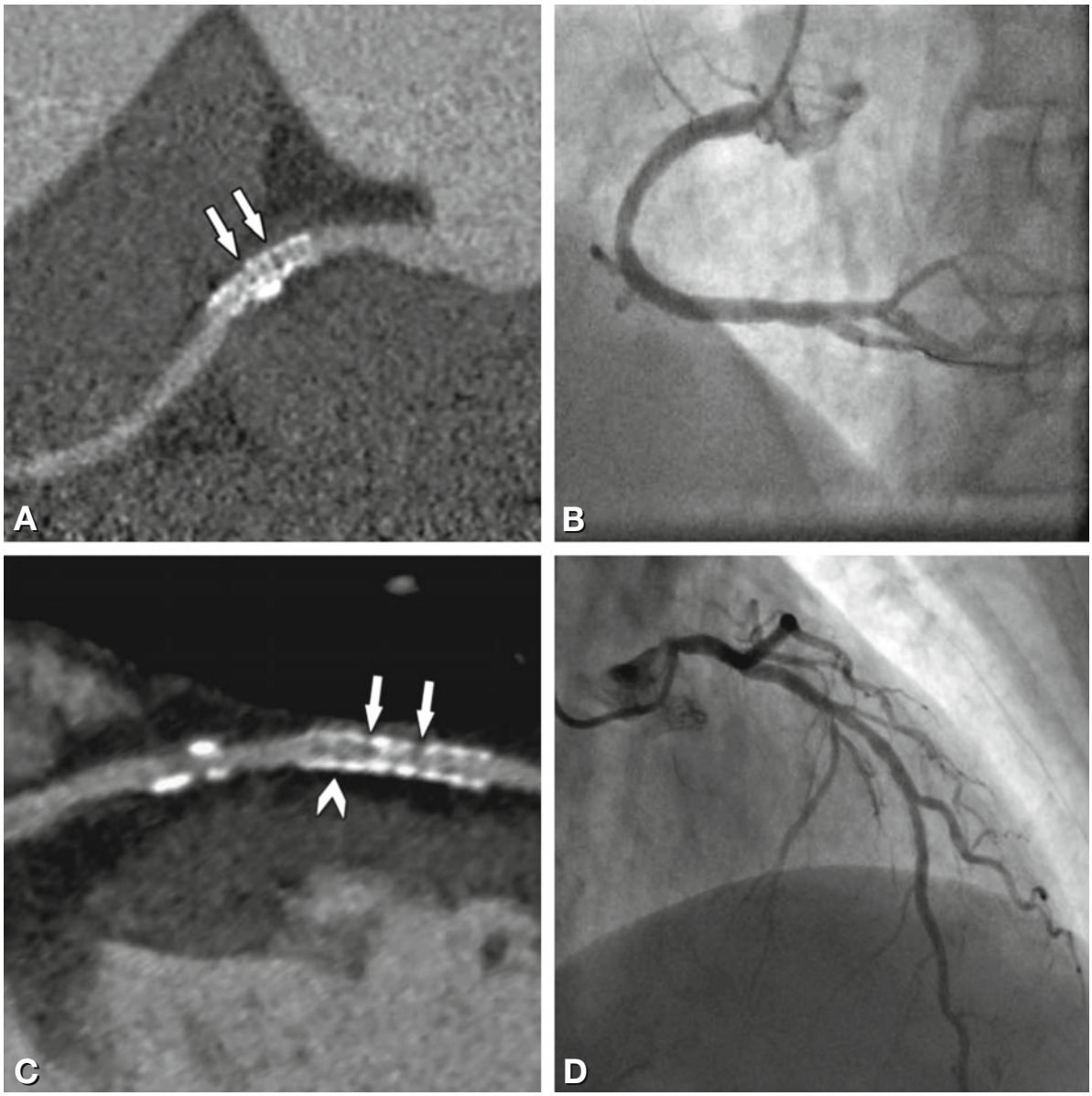

Fig. 13.8 Examples of nondiagnostic coronary artery stents. **Panel A** shows a proximal 3.5-mm stent in the right coronary artery in a 67-year-old female patient presenting with worsening shortness of breath. In this case multiple black streaks, most likely artifacts caused by the stent struts, cross the lumen, making it uninterpretable (*arrows* in **Panel A).** Thus, conventional coronary angiography had to be performed to rule out significant in-stent restenosis (**Panel B**)**.** In a 56-year-old male patient presenting with exercise-induced chest pain but with inconclusive stress ECG changes, blurry streaks (*arrows*) as well as reduced attenuation in the proximal third of the stent (*arrowhead*) preclude ruling out significant stenosis in a 3-mm stent in the mid left anterior descending coronary artery (**Panel C**). No significant stenosis is present in the corresponding conventional coronary angiogram (**Panel D**) (Images courtesy of S. Achenbach)

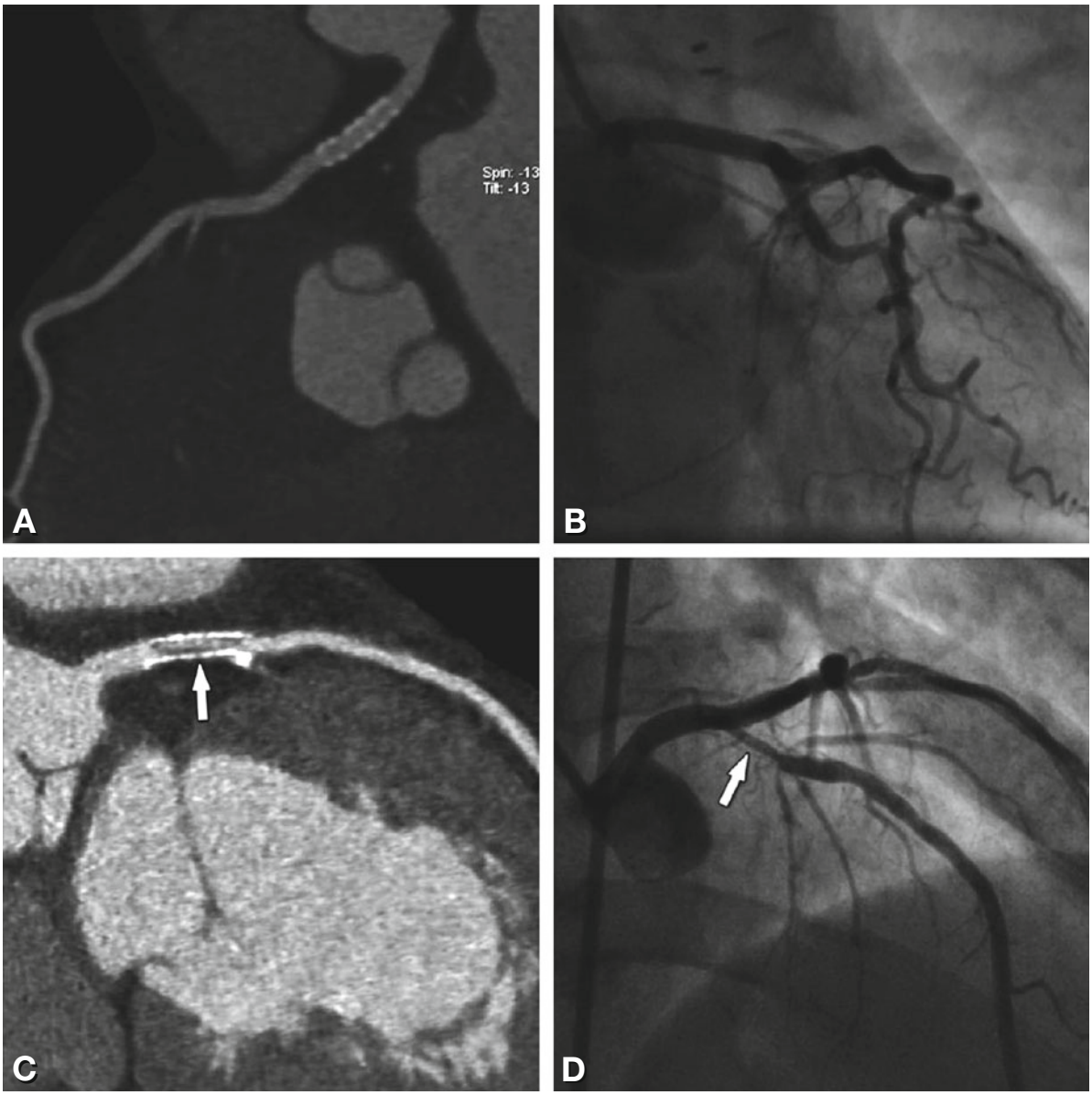

Fig. 13.9 Examples of true-negative and true-positive findings in coronary stent CT angiography. Significant stenosis is correctly ruled out (**Panel A**) using a curved multiplanar reformation along the left main and left anterior descending coronary artery in a 62-year-old female patient presenting with atypical angina pectoris. Absence of significant left main in-stent stenosis is confirmed on conventional coronary angiography (**Panel B**). True-positive significant in-stent restenosis in a proximal left anterior descending coronary artery stent in a 60-year-old male patient presenting with typical angina (**Panel C**). This curved multiplanar reformation along this proximal left anterior descending coronary artery stent with filling defects is suggestive of relevant in-stent stenosis (*arrow*). The corresponding conventional coronary angiogram in **Panel D** confirms this diagnosis (*arrow*, 65% diameter stenosis on quantitative coronary angiography) (Conventional angiograms courtesy of S. Achenbach)

13.7 Clinical Results and Recommendations

Four-row CT was shown to be inappropriate for the visualization of the coronary stent lumen due to pronounced artificial lumen narrowing (60–100%). Evaluation was mostly limited to determining patency vs. occlusion. Whereas 16- and 64-row in-vitro data suggested improved visualization of coronary artery stent lumen, clinical results remained very heterogeneous. In several single-center clinical trials, between 13% and 51% (16-row) and 0–40% (64-row) of all stents had to be excluded from analysis due to artifacts. The reported sensitivity values of 16- and 64-row CT ranged from 54 to 92% and 75–100%, respectively, with a negative predictive value of up to 97–99%. Meta-analyses summarizing clinical trials using 16-, 40- and 64-row CT confirmed the improved diagnostic accuracy, but clearly emphasized its limitations in unselected patients and its shortcomings in stents <3 mm. Despite improved temporal resolution, dual-source CT did not overcome the shortcomings in small stents, which are mainly due to insufficient spatial resolution. Thus, coronary CT angiography for in-stent lesion evaluation is regarded as inappropriate in asymptomatic individuals, whereas the benefit remains uncertain in symptomatic patients. First clinical studies investigating image quality with use of iterative reconstruction suggest improved delineation of the in-stent lumen, decreased image noise, and improved signal-to-noise ratios. Yet further and larger studies will have to determine whether current recommendations need to be revised. **List 13.1** summarizes current exclusion criteria.

List 13.1. Coronary stent CT angiography should not be performed in

1. Asymptomatic patients (if not part of an approved study protocol)
2. Arrhythmic patients
3. Patients with elevated heart rate and contraindications to beta blockers (see Chap. 7)
4. Stents with a diameter of below 3.0–3.5 mm
5. Tantalum stents or gold-coated stents (all sizes)

13.8 Outlook

13.8.1 Scanners

Further improvements in spatial resolution would help to reduce partial volume effects in coronary stent visualization. Flat-panel detector CT improves lumen visibility in ex-vivo coronary stents. However, inherent to flat-panel detector use with its smaller detector elements is a pronounced increase in image noise, which would have to be compensated for by raising X-ray input. Furthermore, currently available flat-panel scanners still have a rather long gantry rotation time and comparably slow data read-out and are of limited use for in-vivo cardiac examinations in clinical routine but might become a valuable alternative in the future.

13.8.2 Stents

An exciting alternative to current metal struts is the use of biodegradable material, dissolving within 4–6 months, leaving only the original vessel wall to be evaluated. The PROGRESS-AMS trial evaluated clinical results up to 1 year following coronary implantation of a biodegradable magnesium stent in de novo 50–99% coronary artery stenoses; according to intravascular ultrasound follow-up, stent struts were fully absorbed within the first 4 months and are also not visible in CT. However, the restenosis rate was relatively high with an overall target lesion revascularization rate of 45% at 1 year. Polymer drug-eluting stents as described in the ABSORB study (everolimus-eluting poly-l-lactic acid stent) are fully absorbed after 2 years with no target lesion revascularization required in the study cohort. Apart from radiopaque markers at the stent entry and exit, they seem to be virtually invisible in conventional coronary angiography and are thus compatible with follow-up coronary CT angiography (**Fig. 13.10**).

At present, both flat-panel CT and absorbable stents are not available in everyday clinical routine.

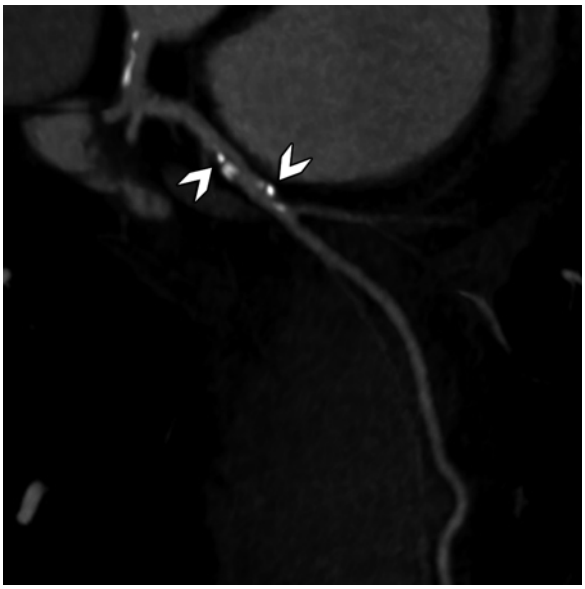

Fig. 13.10 Example of a poly-l-lactic acid biodegradable stent in the proximal LAD. Note the platinum markers indicating the distal edges of the stent (*arrowheads*). In addition, wall calcifications are present in the LM and the LAD artery (Courtesy of K. Nieman, Rotterdam)

Recommended Reading

Beohar N, Davidson CJ, Kip KE et al (2007) Outcomes and complications associated with off-label and untested use of drug-eluting stents. JAMA 297:1992–2000

Cademartiri F, Schuijf JD, Pugliese F et al (2007) Usefulness of multislice computed tomography coronary angiography to in-stent restenosis. J Am Coll Cardiol 49:2204–2210

Ebersberger U, Tricarico F, Schoepf UJ et al (2013) CT evaluation of coronary artery stents with iterative image reconstruction: improvements in image quality and potential for radiation dose reduction. Eur Radiol 23:125–132

Ehara M, Kawai M, Surmely JF et al (2007) Diagnostic accuracy of coronary in-stent restenosis using 64-slice computed tomography: comparison with invasive coronary angiography. J Am Coll Cardiol 49:951–959

Erbel R, Di Mario C, Bartunek J, PROGRESS-AMS (Clinical Performance and Angiographic Results of Coronary Stenting with Absorbable Metal Stents) Investigators et al (2007) Temporary scaffolding of coronary arteries with bioabsorbable magnesium stents: a prospective, non-randomised multicentre trial. Lancet 369:1869–1875

Hamon M, Champ-Rigot L, Morello R, Riddell JW, Hamon M (2008) Diagnostic accuracy of in-stent coronary restenosis detection with multislice spiral computed tomography: a meta-analysis. Eur Radiol 18:217–225

Kumbhani DJ, Ingelmo CP, Schoenhagei P (2009) Meta-analysis of diagnostic efficacy of 64-slice computed tomography in the evaluation of coronary in-stent restenosis. Am J Cardiol 103:1675–81

Lell MM, Panknin C, Saleh R et al (2007) Evaluation of coronary stents and stenoses at different heart rates with dual source spiral CT (DSCT). Invest Radiol 42:536–541

Mahnken AH, Buecker A, Wildberger JE et al (2004) Coronary artery stents in multislice computed tomography: in vitro artifact evaluation. Invest Radiol 39:27–33

Mahnken AH, Seyfarth T, Flohr T et al (2005) Flat-panel detector computed tomography for the assessment of coronary artery stents: phantom study in comparison with 16-slice spiral computed tomography. Invest Radiol 40:8–13

Maintz D, Seifarth H, Raupach R et al (2006) 64-slice multidetector coronary CT angiography: in vitro evaluation of 68 different stents. Eur Radiol 16:818–826

Maintz D, Burg MC, Seifarth H et al (2009) Update on multidetector coronary CT angiography of coronary stents: in vitro evaluation of 29 different stent types with dual-source CT. Eur Radiol 19:42–49

Morice MC, Serruys PW, Sousa JE, RAVEL Study Group et al (2002) Randomized study with the sirolimus-coated Bx velocity balloon-expandable stent in the treatment of patients with de novo native coronary artery lesions. A randomized comparison of a sirolimus-eluting stent with a standard stent for coronary revascularization. N Engl J Med 346:1773–1780

Moses JW, Leon MB, Popma JJ, SIRIUS Investigators et al (2003) Sirolimus-eluting stents versus standard stents in patients with stenosis in a native coronary artery. N Engl J Med 349:1315–1323

Oncel D, Oncel G, Tastan A, Tamci B (2008) Evaluation of coronary stent patency and in-stent restenosis with dual-source CT coronary angiography without heart rate control. AJR Am J Roentgenol 191:56–63

Ramcharitar S, Serruys PW (2008) Fully biodegradable coronary stents: progress to date. Am J Cardiovasc Drugs 8:305–314

Rixe J, Achenbach S, Ropers D et al (2006) Assessment of coronary artery stent restenosis by 64-slice multi-detector computed tomography. Eur Heart J 27:2567–2572

Schepis T, Koepfli P, Leschka S et al (2007) Coronary artery stent geometry and in-stent contrast attenuation with 64-slice computed tomography. Eur Radiol 17:1464–1473

Schlosser T, Scheuermann T, Ulzheimer S et al (2007) In vitro evaluation of coronary stents and in-stent stenosis using a dynamic cardiac phantom and a 64-detector row CT scanner. Clin Res Cardiol 96:883–890

Schuijf JD, Pundziute G, Jukema JW et al (2007) Evaluation of patients with previous coronary stent implantation with 64-section CT. Radiology 245:416–423

Seifarth H, Ozgun M, Raupach R et al (2006) 64- Versus 16-slice CT angiography for coronary artery stent assessment: in vitro experience. Invest Radiol 41:22–27

Serruys PW, Ormiston JA, Onuma Y et al (2009) A bioabsorbable everolimus-eluting coronary stent system (ABSORB): 2-year outcomes and results from multiple imaging methods. Lancet 373:897–910

Sun Z, Davidson R, Lin CH (2009) Multi-detector row CT angiography in the assessment of coronary in-stent restenosis: a systematic review. Eur J Radiol 69:489–495

Vanhoenacker PK, Decramer I, Bladt O et al (2008) Multidetector computed tomography angiography for assessment of in-stent restenosis: meta-analysis of diagnostic performance. Review BMC Med Imaging 8:14

Vermeersch P, Agostoni P, Verheye S et al (2006) Randomized double-blind comparison of sirolimus-eluting stent versus bare-metal stent implantation in diseased saphenous vein grafts: six-month angiographic, intravascular ultrasound, and clinical follow-up of the RRISC Trial. J Am Coll Cardiol 48:2423–2431

Vermeersch P, Agostoni P, Verheye S, DELAYED RRISC (Death and Events at Long-term follow-up AnalYsis: Extended Duration of the Reduction of Restenosis In Saphenous vein grafts with Cypher stent) Investigators et al (2007) Increased late mortality after sirolimus-eluting stents versus bare-metal stents in diseased saphenous vein grafts: results from the randomized DELAYED RRISC Trial. J Am Coll Cardiol 50:261–267

Veselka J, Cadova P, Tomasov P et al (2011) Dual-source CT angiography for detection and quantification of in-stent restenosis in the left main coronary artery: comparison with intracoronary ultrasound and coronary angiography. J Invasive Cardiol 23:460–464

Win HK, Caldera AE, Maresh K, EVENT Registry Investigators et al (2007) Clinical outcomes and stent thrombosis following off-label use of drug-eluting stents. JAMA 297:2001–2009

Coronary Artery Plaque

P. Schoenhagen, H. Niinuma, T. Gerber, and M. Dewey

Abstract

CT angiography allows assessment of plaque of the coronary artery wall before luminal narrowing develops. In symptomatic patients with suspected luminal stenosis, identification and characterization of nonobstructive plaque provides prognostic data incremental to the evaluation of luminal stenosis alone. This chapter describes the rationale and clinical approach to plaque imaging and evaluation.

14.1 Introduction

Plaque imaging describes the identification and characterization of atherosclerotic changes of the vessel wall. Atherosclerosis imaging research has significantly contributed to the understanding of disease progression/regression and the development of novel antiatherosclerotic treatment strategies. Successful translation into clinical practice requires reliable identification of plaque characteristics associated with a high risk for future cardiovascular events and ultimately demonstration of how atherosclerosis imaging contributes to preventive and therapeutic strategies and thus helps reduce the risk. Two principal strategies are pursued: (1) focal identification of individual unstable, vulnerable plaques with potential subsequent local/interventional treatment and (2) systemic assessment of the total plaque burden and activity with subsequent systemic/pharmacological treatment.

Local identification of the most vulnerable plaques is a fascinating theoretical concept derived from invasive imaging in the catheterization laboratory, with intravascular ultrasound (IVUS) and optical coherence tomography for example. If reliable identification were possible, such lesions could be treated locally ("plaque sealing") before causing clinical events. However, none of the current invasive or noninvasive imaging modalities can reliably identify vulnerable lesions. It is likely that such imaging will require molecular or genetic markers of lesion biology beyond simple anatomy. Moreover, there are no evidence-based data that local treatment of vulnerable lesions will be associated with clinical benefit.

A clinically more promising approach is to identify systemic vulnerability by assessing plaque burden,

M. Dewey, *Cardiac CT*,
DOI 10.1007/978-3-642-41883-9_17, © Springer-Verlag Berlin Heidelberg 2014

composition, and activity in the entire coronary tree. Similar to carotid intima-media thickness measurement by ultrasound and coronary artery calcium scoring by CT, there are solid data from coronary CT angiography demonstrating that both the extent and characteristics of plaque predict the risk of future cardiovascular events.

This information has been derived from symptomatic, intermediate-risk populations, in whom CT angiography (CTA) was indicated according to clinical guidelines. It probably does not apply to low- and high-risk populations. Based on these data, current clinical guidelines do not recommend CTA plaque screening of asymptomatic individuals. In contrast, assessment of nonobstructive changes is recommended in symptomatic patients undergoing CTA for suspected luminal stenosis (or other clinically supported indications).

14.2 CT for Plaque Identification, Characterization, Quantification, and Assessment of Remodeling

14.2.1 Plaque Identification

Coronary atherosclerotic plaque begins accumulating in the vessel wall long before the development of luminal narrowing (**Fig. 14.1**). The early stages of coronary atherosclerotic plaque accumulation are typically associated with expansion of the vessel wall (positive remodeling; Glagov et al. *N Engl J Med* 1987). The resulting enlargement of the vessel cross-section typically prevents or mitigates development of luminal narrowing until the plaque area exceeds about 40% of the vessel area. Because coronary CT angiography allows simultaneous assessment of luminal dimensions/stenosis and the vessel wall/plaque, it can identify these early disease stages, which are not well reflected by coronary angiography. Plaque identification with CT is possible with two types of acquisition/scanning protocols: (1) calcium scoring (no contrast agent, low radiation) and (2) contrast-enhanced angiography (IV contrast, higher radiation).

There are extensive evidence-based data in support of calcium scoring, in particular in asymptomatic, intermediate-risk populations, documenting that the amount of calcium predicts the risk of future events (Chap. 11).

The identification of noncalcified plaque and the assessment of the overall plaque burden are more complex and require outlining the lumen with contrast. Preclinical CT plaque imaging of ex-vivo arteries after static filling or perfusion of the lumen with contrast medium and in-vivo imaging of animal models with subsequent histologic verification have been performed for validation of plaque imaging. Plaque imaging using standard clinical contrast-enhanced CT protocols has been validated against IVUS. These studies have demonstrated reliable identification of calcified and noncalcified plaque (**Table 14.1**).

14.2.2 Plaque Characterization

Characterization of plaque components based on tissue attenuation in Hounsfield units (HU) allows differentiation into broad groups of noncalcified, mixed, and calcified plaque types (**Figs. 14.2**, **14.3**, **14.4**, and **14.5**). Comparison of the plaque types differentiated by CT with IVUS plaque characterization has revealed a correlation between IVUS echodensity and HU values, but significant overlap of attenuation values between the different noncalcified plaque types, in particular between lipid-rich and fibrous plaque components (**Table 14.2**). In addition, CT studies demonstrate that the attenuation of plaques is influenced by contrast density in the lumen and by contrast enhancement of the vessel wall itself. Furthermore, the visualization of relatively small HU differences between different plaque components is probably affected by the imaging technique used. The impact of low-dose CTA acquisition including imaging with lower tube voltage (kV), tube current (mA), and novel reconstruction algorithms, such as iterative reconstruction, on plaque imaging is incompletely understood. Importantly, it should be noted that IVUS echodensity has limited value as a reference standard because it correlates only modestly with histology.

14.2.3 Arterial Remodeling

The assessment of arterial remodeling is an important aspect of plaque identification and quantification. As described above, early atherosclerotic plaque accumulation is typically associated with expansion of the vessel wall, mitigating development of luminal narrowing. It is now well established that remodeling is related to plaque

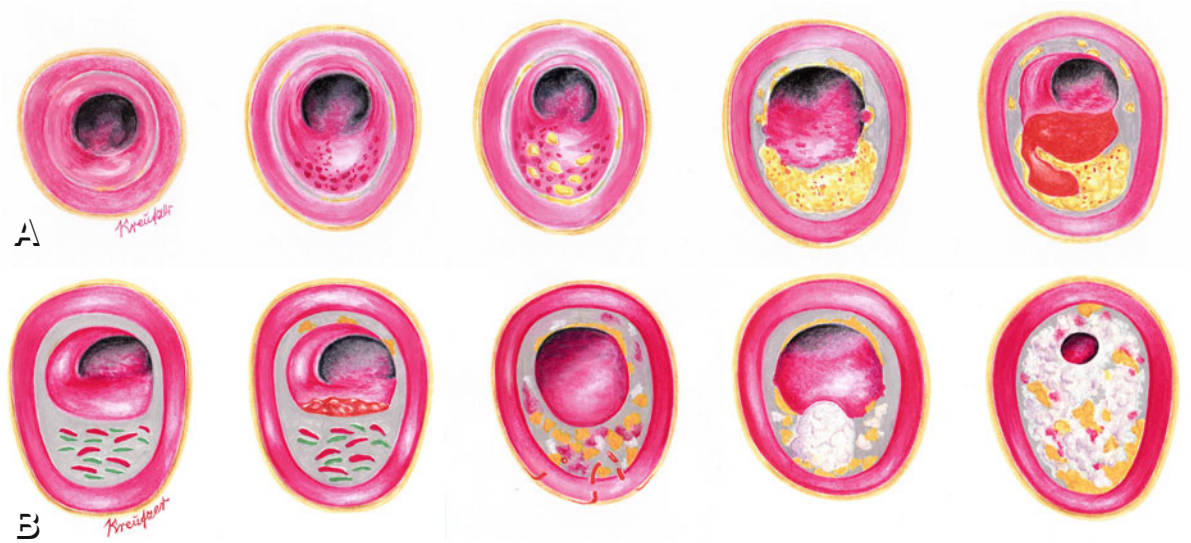

Fig. 14.1 Different types of atherosclerotic plaque. The leftmost image in Panel is a three-dimensional drawing of a normal vessel. The accumulation of macrophages and lipids can lead to large lipid cores and thin fibrous caps (further images in **Panel A**) and finally the rupture of the plaque cap and luminal clot formation (rightmost image in **Panel A**). The first image in **Panel B** show erosion-prone plaque with proteoglycan matrix in a smooth muscle cell-rich lesion. This can lead to plaque erosion and subocclusive thrombus formation (second image in **Panel B**). Intraplaque hemorrhage secondary to leaking vasa vasorum is shown in the plaque in the middle image in **Panel B**. The aforementioned plaque will be noncalcified on CT. Calcified nodules that only protrude into the lumen in the beginning can grow and become chronically stenotic plaques with severe calcification and old thrombus, resulting in an eccentric lumen (last two images in **Panel B**) (Adapted from Naghavi et al. *Circulation* 2003)

Table 14.1 Accuracy of plaque detection with CT in comparison to IVUS

Study	Scanner type	N	Sensitivity (%)	Specificity (%)
Achenbach et al. *Circulation* 2004	16-row	22	94	86
Leber et al. *JACC* 2004	16-row	58	85	92
Leber et al. *JACC* 2006	64-row	20	92	94
Sun et al. *AJR* 2008	64-row	26	96	90
Petranovic et al. *JCCT* 2009	64-row	11	96	89

stability, with outward/positive remodeling constituting a marker of vulnerability. Remodeling is described by relating the vessel size at the lesion site to that at the adjacent reference site. The remodeling index is a quantitative measure calculated by dividing the vessel diameter at the lesion site by that at the adjacent normal reference site. Values higher than 1 or 1.05 indicate outward (positive) remodeling. While remodeling can be assessed with CT (**Table 14.3**), assessment of remodeling in clinical routine is limited by the focal nature of plaque and the fact that it is dependent on the definition of the lesion and reference site.

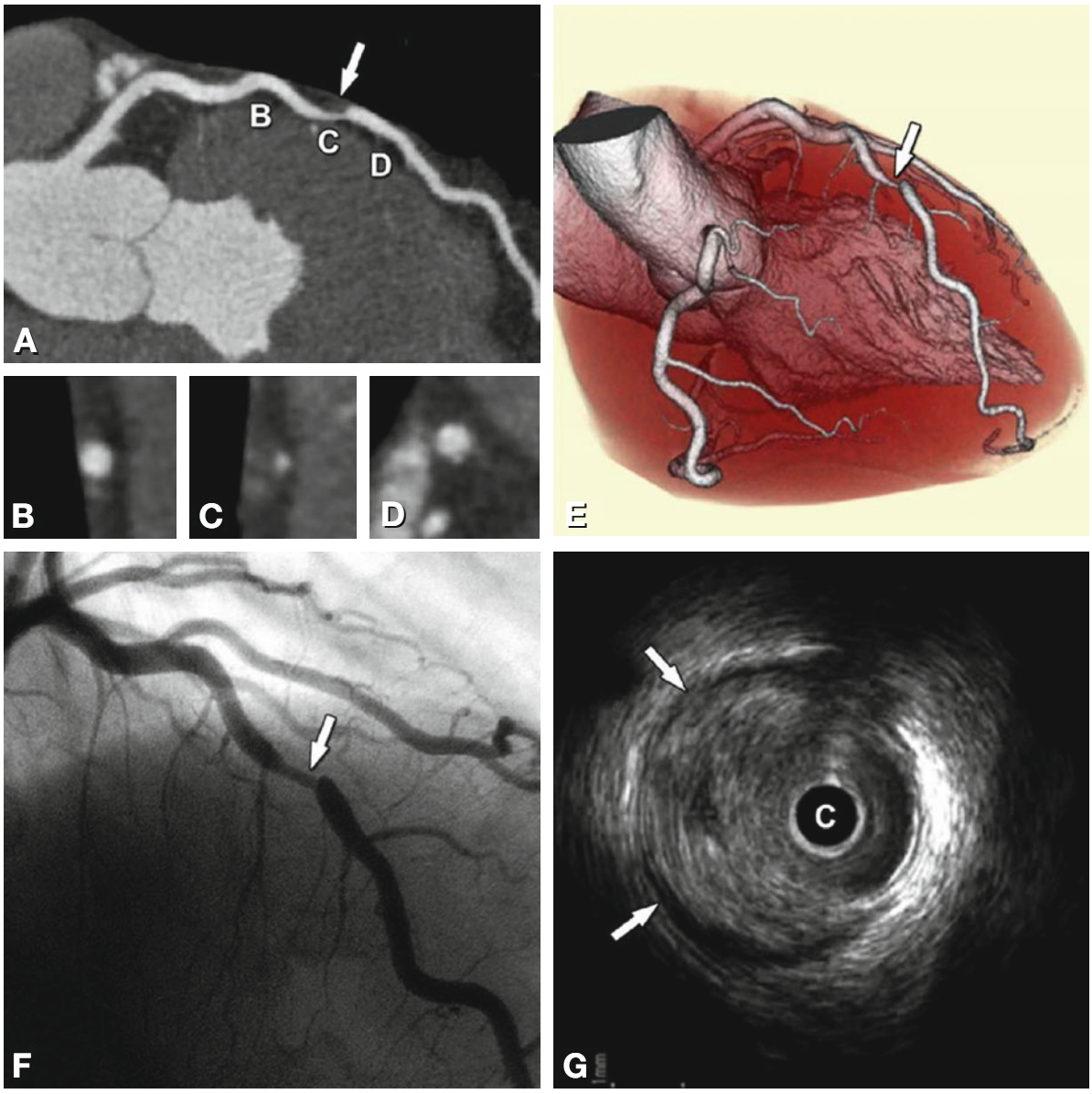

Fig. 14.2 Noncalcified plaque (*arrow*) in the proximal left anterior descending coronary artery associated with significant luminal stenosis in a 65-year-old male patient. **Panel A** shows a curved multiplanar reformation with cross-sections along the vessel in **Panels B**–**D**, and **Panel E** is a volume-rendered three-dimensional reconstruction of CT. **Panel F** is the conventional coronary angiography of this plaque, which resulted in a 70% diameter stenosis. **Panel G** is the intravascular ultrasound confirming the eccentric noncalcified plaque (*arrows*). *C* intravascular ultrasound catheter

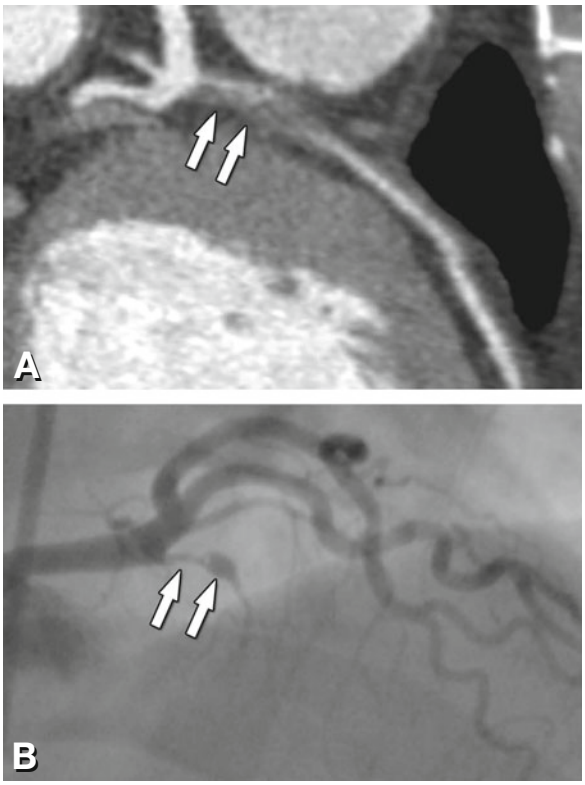

Fig. 14.3 Noncalcified plaque (*arrows*) of the proximal left anterior descending coronary artery associated with (subtotal) occlusion in a 48-year-old male patient presenting with a vague history of recent episodes of chest pain. **Panel A** shows a curved multiplanar reformation of CT. **Panel B** shows the corresponding conventional coronary angiogram

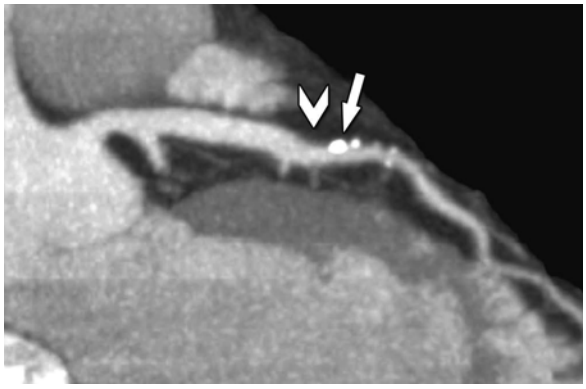

Fig. 14.4 Mixed plaque with calcified (*arrow*) and noncalcified components (*arrowhead*) in the mid left anterior descending coronary artery associated with mild luminal narrowing in a 55-year-old female patient presenting with atypical angina pectoris. The image shown here is a maximum-intensity projection along the vessel

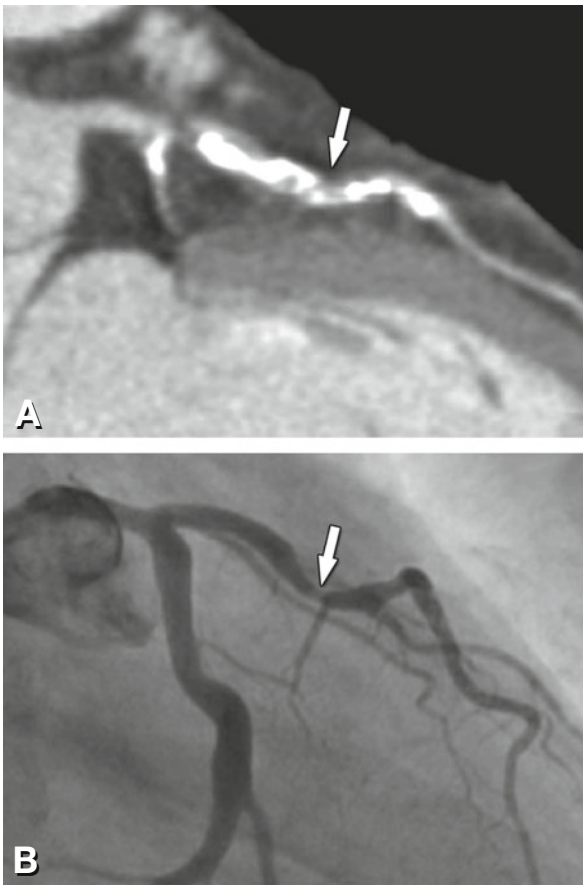

Fig. 14.5 Densely calcified plaque in the proximal and mid left anterior descending coronary artery (*arrow*) in a 65-year-old female patient presenting with chronic angina pectoris. **Panel A** shows a curved multiplanar reformation, while the corresponding conventional coronary angiogram (**Panel B**) shows a hazy stenotic lesion (75% diameter stenosis) in the mid part of the calcified plaque. Importantly, the densely calcified plaques in the proximal and distal segment show no evidence of significant angiographic stenosis

Table 14.2 Plaque characterization by CT in comparison to IVUS

Study	Lipid-rich (HU)	Fibrous (HU)	Calcified (HU)
Schroeder et al. *JACC* 2001	14 ± 26	91 ± 21	419 ± 194
Leber et al. *JACC* 2004	49 ± 22	91 ± 22	391 ± 156
Becker et al. *Eur Radiol* 2006	47 ± 9	104 ± 28	
Carrascosa et al. *AJC* 2006	72 ± 32	116 ± 36	383 ± 186
Pohle et al. *Atherosclerosis* 2007	58 ±43	121 ± 34	
Motoyama et al. *JACC* 2007	11 ± 12	78 ± 21	516 ± 198
Sun et al. *AJR* 2008	79 ± 34	90 ± 27	772 ± 251
Petranovic et al. *JCCT* 2009	100 ± 28	77 ± 39	608 ± 217

HU densities are given as mean ± standard deviation. There is considerable overlap between the HU measurements in lipid-rich and fibrous plaques. The reference standard classification into lipid-rich, fibrous, and calcified is based on IVUS criteria

Table 14.3 Assessment of arterial remodeling

Study	Scanner	N	Definition of remodeling
Schoenhagen et al. *Coronary Artery Disease* 2003	16-row	14	Qualitative assessment
Achenbach et al. *JACC* 2004	16-row	44	Quantitative Remodeling index
Imazeki et al. *Circ J* 2004	4-row	57	Quantitative Remodeling index
Motoyama et al. *JACC* 2007; 2009	16- and 64-row	71	Quantitative Remodeling index
Meijs et al. *Am J Cardiol* 2009	64-row	114	Quantitative Remodeling index

[a]Remodeling is assessed by relating lesion site and reference vessel site diameters to each other

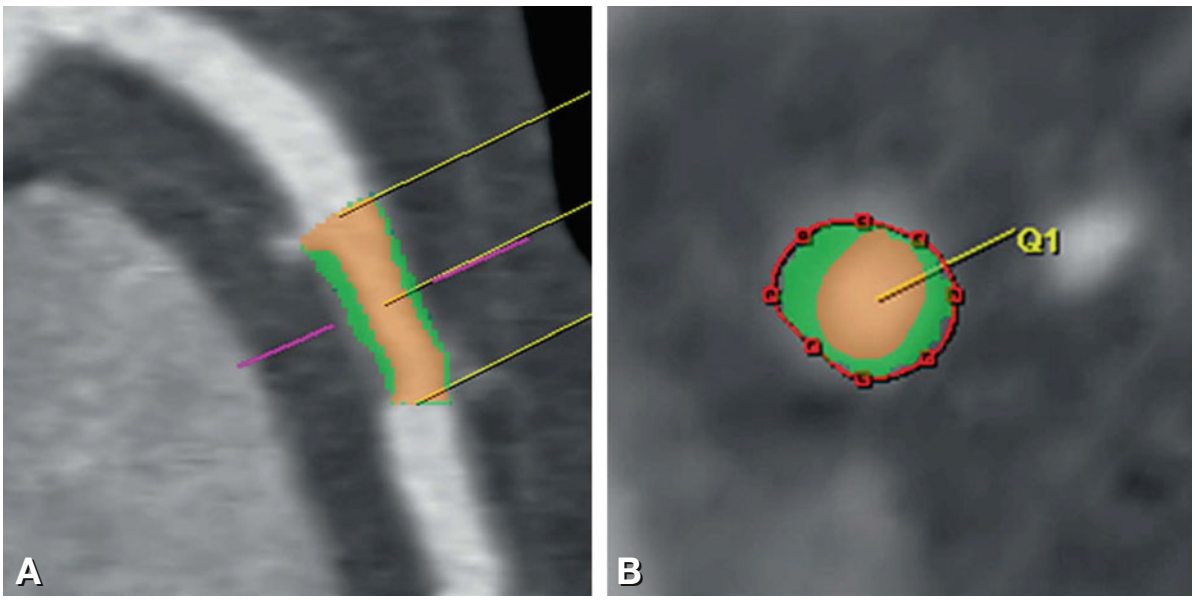

Fig. 14.6 Noncalcified plaque without significant diameter loss in the left anterior descending coronary artery in a 42-year-old male patient presenting with atypical angina pectoris. **Panel A** is a curved multiplanar reformation and **Panel B** is a corresponding cross-section. The semiautomated analysis of this noncalcified plaque is shown as a color overlay with the plaque colored in *green* and the lumen in *orange*, while a *red line* traces the endothelial-adventitial border

14.2.4 Plaque Quantification

Quantification of overall plaque burden and its components with CT requires outlining the lumen/vessel wall and vessel wall/adventitia borders for segmentation of the wall, including atherosclerotic plaque. Segmentation allows quantification of plaque area or volume, and in a second step, the vessel wall and plaque contained between these borders can be characterized based on HU (**Fig. 14.6** and **14.7**).

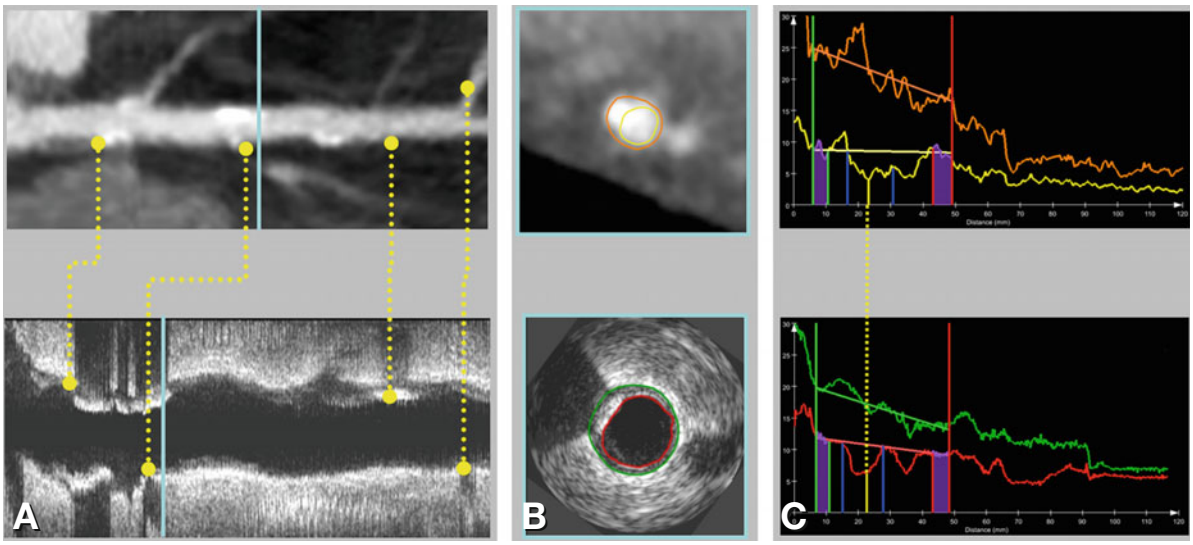

Fig. 14.7 Overview of validation setup for CTA plaque quantification using IVUS data. **Panel A** shows common landmarks (for example bifurcations and calcified plaques) in both CTA and IVUS data, which are used to register IVUS slices with slices from a stretched multiplanar reformation in CTA. **Panel B** presents an example of matched slices showing contours in both CTA and IVUS. **Panel C** presents matched quantification graphs of CTA and IVUS for the whole vessel. Lesion definitions obtained with both modalities can be compared this way. Software package QAngioCT Research Edition, Medis Medical Imaging Systems; Leiden, The Netherlands (With permission from Boogers et al. *Eur Heart J* 2012)

Limitations are the lower spatial resolution relative to IVUS and optical coherence tomography (>0.4 mm for each voxel edge with CT) and difficulties in defining intimal and adventitial borders. Clinical experience with CT in comparison to histology and IVUS for quantification of coronary artery plaque (**Table 14.4**), including reproducibility of plaque volume quantification is accumulating (**Table 14.5**). **Figure 14.8** outlines a systematic approach to plaque identification and semiquantitative grading.

It is important to be aware that these data originate from highly standardized, quantitative analysis of large patient populations in high-quality datasets; hence, the results reflect the special situation of clinical trials with data analysis by dedicated core laboratories. Quantification of plaque burden will eventually allow serial noninvasive examination in pharmacological studies, similar to other imaging modalities, such as IVUS. However, the clinical value of plaque quantification in individual patients is not well understood.

Table 14.4 Plaque quantification

Study	Scanner	n
Boogers et al. *EHJ* 2012	64-slice or 320 slice	51
Rinehart et al. *JCCT* 2011		30

Table 14.5 Interobserver variability of plaque quantification

Study	Segments	Interobserver variability (%)
Leber et al. *JACC* 2006	All	37
Pflederer et al. *Roefo* 2008	Proximal LAD	17
	Proximal LCX	29
	Proximal RCA	32
Petranovic et al. *JCCT* 2009	All	30

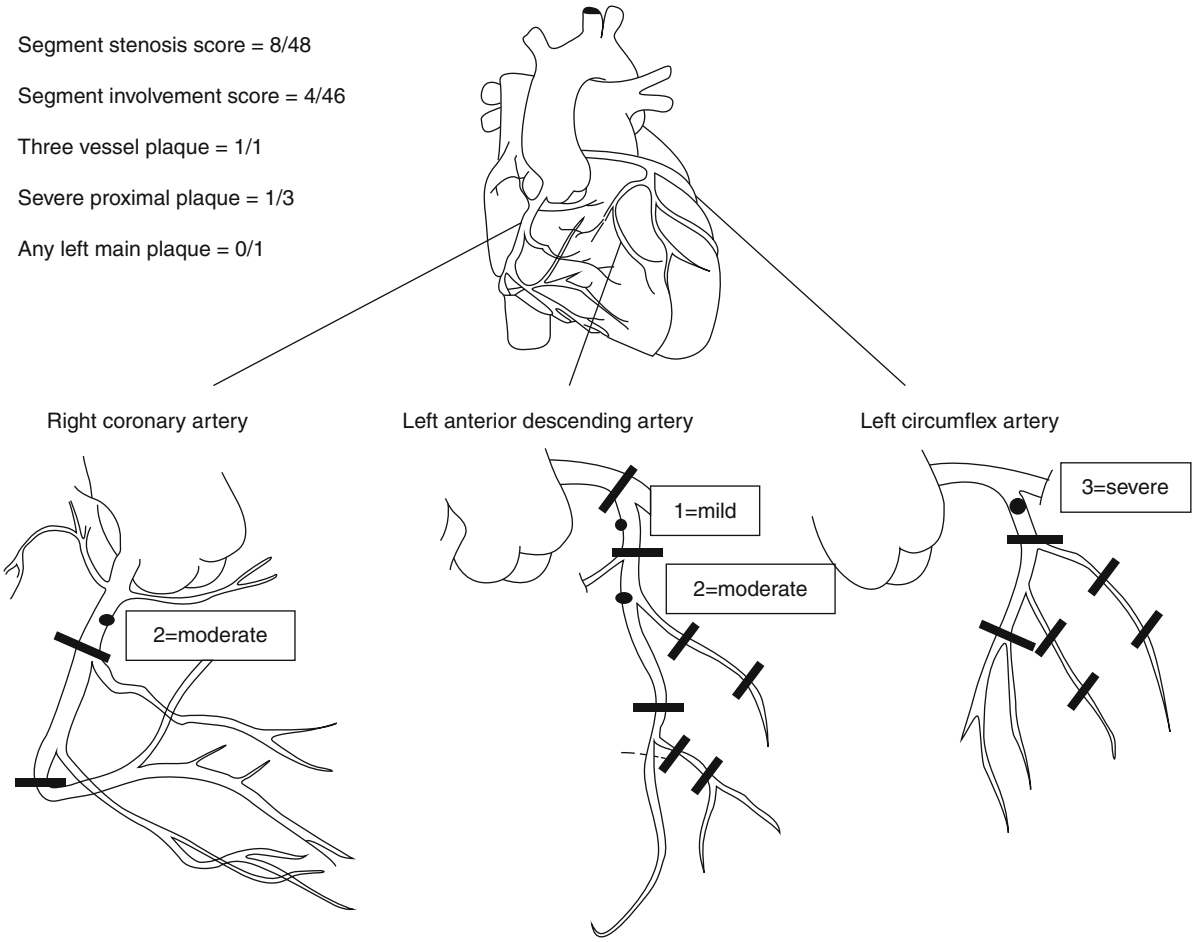

Fig. 14.8 Semiquantitative grading system, based on the angiographic Duke index, of atherosclerotic disease burden in a patient with mild narrowing in the proximal LAD, moderate narrowing in the mid LAD, severe narrowing in the proximal LCX, and moderate narrowing in the proximal RCA (Modified from Min et al. *J Am Coll Cardiol* 2007 with permission from Elsevier)

14.3 Relationship Between Composition of Individual Lesions and Clinical Presentation

14.3.1 Retrospective Data

Following the above-described validation of plaque imaging with CT, it was possible to retrospectively evaluate lesion criteria and their relationship to clinical presentation. A number of histologic criteria of vulnerable lesions (thin-cap fibroatheroma) have been derived from post-mortem studies (**List 14.1**).

Corresponding in-vivo imaging findings have been described with invasive modalities. In gray-scale IVUS studies, low echodensity, positive remodeling, and small "spotty" calcifications have been identified as high-risk criteria for culprit lesions in patients with acute coronary events. Based on further analysis with IVUS radiofrequency analysis, criteria for IVUS-derived thin-cap fibroatheroma are defined (**List 14.2**).

IVUS assessment of these criteria typically serves as the gold standard for the evaluation with CT. Note, however, that IVUS identification of lesion vulnerability is a limited gold standard with moderate correlation to histology.

As described above, CT allows identification of low-density plaques, pattern and extent of calcification,

List 14.1. Histologic criteria of lesion vulnerability

1. Large overall plaque burden
2. Necrotic core, separated from the lumen by a thin fibrous cap (<65 mm)
3. Positive arterial remodeling
4. Presence of cell populations associated with inflammatory response

List 14.2. IVUS criteria of lesion vulnerability

1. Significant plaque burden
2. Confluent necrotic core >10–20% of the total plaque volume
3. Amount of calcium >10% with a speckled appearance
4. No imaging evidence of a fibrous cap (i.e., thin cap is below spatial resolution)

and remodeling. In populations with intermediate risk for CAD examined with CT, noncalcified coronary plaque is found in about 30% of patients, often along with adjacent coronary calcifications. The prevalence of noncalcified plaques as the only manifestation of CAD is less than 10%. In patients with acute coronary syndromes, culprit lesions on coronary CT angiography are mostly noncalcified or mixed plaques, and less frequent densely calcified plaques (**Table 14.6**). Mixed plaques identified with CT appear to correspond to thin-cap fibroatheroma at IVUS. However, differentiation of noncalcified plaque components based on HU is limited, and there is overlap of the above high-risk criteria between stable and unstable lesions (Kitagawa et al. *JACC Cardiovasc Imaging* 2009).

These criteria were used in clinical trials comparing baseline plaque characteristics with outcome. For example, in a study analyzing 10,037 coronary segments in 1,059 patients (Motoyama et al. *J Am Coll Cardiol* 2007), low-attenuation plaque and positive vessel remodeling independently predicted subsequent development of acute coronary syndrome with a hazard ratio of 22.8 (95% confidence interval, 6.9–75.2).

The most rigorous data have accumulated regarding the prognostic value of plaque burden. In selected asymptomatic, intermediate-risk populations, CT calcium scoring was found to have an incremental predictive value for future coronary events over "traditional" multivariate risk assessment models (Chap. 11). In symptomatic patient populations with clinical indications for coronary CT angiography, several studies demonstrated the prognostic value of contrast-enhanced CT plaque imaging (**Table 14.7**). The data have been summarized in two meta-analyses of studies including patients with suspected or known CAD (**Table 14.8**). The pooled annualized event rate for obstructive (any vessel

Table 14.6 Characteristics of unstable plaques

Criteria	Suggested definition
Low density, noncalcified plaque	HU < 20–40
Positive arterial remodeling	Remodeling index >1.05
Spotty calcification	Calcium < 3 mm

Table 14.7 Prognostic value of plaque burden and composition

Study	n	Follow-up length	Score details	Endpoint
Min et al. *JACC* 2007	1,127	15 months	Luminal stenosis and plaque	All-cause mortality
Carrigan et al. *EHJ* 2009	227	28 months	Luminal stenosis and plaque	Composite: cardiac mortality, MI, revascularization
Motoyama et al. *JACC* 2009	1,059	27 months	Remodeling, low-attenuation	ACS
van Werkhoven et al. *EHJ* 2009	432	670 days	Luminal stenosis and plaque versus calcium score	Composite: all-cause mortality, MI, unstable angina

ACS acute coronary syndrome, *MI* myocardial infarction

Table 14.8 Plaque burden and clinical outcome

Study	N of studies	N of patients	FU months	MACE
Hulten et al. *J Am Coll Cardiol* 2011	18	9,592	20	449
Bamberg et al. *JACC* 2011	11	7,335	20	252
Chow et al. *Circ Cardiovascular Imaging* 2011	Multicenter registry	14,064	23	271

with >50% luminal stenosis) versus normal coronary CTA was about 3% versus 0.1% for death or myocardial infarction ($p < 0.05$). Strata of "absent CAD," "nonobstructive CAD" (worst stenosis <50%), or "obstructive CAD" demonstrated incrementally increased risk of future MACE.

The data demonstrate that adverse cardiovascular events are rare in patients with normal findings on coronary CTA, similar to the background event rate of healthy low-risk individuals (<1%). Nonobstructive plaque increases the risk to some extent. Lastly, the presence of "significant" stenosis (>50% luminal diameter stenosis) is associated with significantly higher risk than nonobstructive atherosclerotic changes, supporting earlier observations made with invasive coronary angiography. It is important to note that these data are derived from symptomatic patient populations evaluated for suspected obstructive CAD.

14.3.2 Prospective Data

Prospective data demonstrating the prognostic impact of plaque characteristics on future outcome are limited. Using invasive IVUS, the PROSPECT trial included 697 patients with acute coronary syndrome who underwent three-vessel coronary angiography and gray-scale and radiofrequency IVUS imaging after percutaneous coronary intervention (Stone et al. 2011). Subsequent major adverse cardiovascular events (death from cardiac causes, cardiac arrest, myocardial infarction, or rehospitalization due to unstable or progressive angina) were adjudicated to be related to either originally treated (culprit) lesions or untreated (nonculprit) lesions. The 3-year cumulative rate of major adverse cardiovascular events was 20.4%. Major adverse cardiovascular events were equally attributable to recurrence at the site of culprit lesions and to nonculprit lesions. Although nonculprit lesions that were responsible for unanticipated events were frequently angiographically mild, most were thin-cap fibroatheromas or were characterized by a large plaque burden, a small luminal area, or some combination of these characteristics, as determined by gray-scale and radiofrequency IVUS.

Data with CT are more limited. In a subanalysis of the prospective ROMICAT trial, the authors examined the association of clinical risk scores and coronary plaque burden as detected by CT with outcome in patients with acute chest pain (Ferencik et al. *Acad Emerg Med* 2012). The clinical risk scores and coronary plaque burden showed modest and good discriminatory capacity for the diagnosis of acute coronary syndrome (ACS) in patients with acute chest pain. The combined information of risk scores and plaque burden significantly improves the discriminatory capacity for the diagnosis of ACS.

The data were obtained in patients who presented with acute coronary syndrome and underwent percutaneous coronary intervention. Prospective data demonstrating the prognostic impact of plaque characteristics on future outcome are limited, both for invasive and noninvasive imaging modalities.

14.4 Clinical Recommendations

The data reviewed demonstrate that plaque imaging is feasible with CT. However, there is no evidence that screening asymptomatic patient with CT would have clinical benefit, and all major clinical guidelines therefore discourage use of CTA in asymptomatic persons. In contrast, plaque assessment as part of clinically indicated coronary CT angiography in symptomatic patients provides incremental information to the assessment of luminal narrowing in intermediate-risk populations. Semiquantitative plaque assessment in individual coronary segments is therefore recommended in consensus guidelines, including a position paper of the SCCT (Raff et al. *JCCT* 2009). Based on the current literature, preliminary clinical recommendations can be made (Tables **14.9** and **14.10**).

14.5 Future of Plaque Imaging

Rapid technical development of CT scanners and scanner software and the accumulating data from preclinical and clinical studies have greatly improved our understanding of the potential and the limitations of plaque imaging by cardiac CT. **List 14.3** summarizes some of the more recent developments.

Future large, prospective clinical trials will correlate diagnostic testing with clinical endpoints. One of the central questions will be whether downstream treatment

Table 14.9 Clinical approach and recommendations

Approach	Recommendations
Indication	Plaque imaging alone is not an indication for CT angiography. In other words, screening of asymptomatic patient cannot be recommended (Chaps. 6 and 21)
	The indication for CT is based on the need to exclude luminal stenosis in symptomatic patients with intermediate pretest probability (Chaps. 5 and 6)
	In patients in whom coronary CT angiography is clinically indicated, analyzing plaque burden for its prognostic value may be performed, but the implications for clinical management are not definitively established
Data acquisition	The data acquisition protocol should be determined by the primary indication for CT
	Standard coronary CT angiography scanning protocols should not be modified solely for the purpose of facilitating plaque imaging, especially if the modification will increase radiation dose to the patient
Data analysis - technique	General approach as described in Chap. 11
	Multiplanar reformations, maximum-intensity projections, and curved multiplanar reformations
	Adjust window-level setting to optimize differentiation between vessel wall and surrounding soft tissue (Leber et al. *JACC* 2006)
Data analysis - clinical aspects	Identification of obstructive and nonobstructive plaque in all visualized coronary segments
	Classification into noncalcified and calcified plaque
	Summarize plaque burden with semiquantitative scores (Table 14.8)
High-risk plaque criteria	Spotty calcification, mixed, and noncalcified plaque components
	Low-attenuation plaque components
	Positive (expansive) remodeling
Atherosclerosis research	Manual and semiautomated quantitative and volumetric analysis
	Dedicated plaque characterization beyond HU, including functional analysis with molecular imaging of plaque for cellular or humoral markers of inflammation

Table 14.10 Approaches to clinical scores of overall disease burden

Approach	Description	Study
Vessel stenosis/ involvement score	Major epicardial vessels (LM, LAD, LCX, RCA) with moderate (>50%) or severe (>70%) luminal diameter narrowing	Min et al.
Segment involvement score	Presence of plaque irrespective of the degree of luminal stenosis within each segment	Min et al.
	Yields a total score ranging from 0 to 16	Carrigan et al.
Segment stenosis score	Grade of luminal diameter stenosis (0 = none, 1 = <50%, 2 = ≥ 50%, 3 = >70%) in each coronary segment	Min et al.
	Yields a total score ranging from 0 to 48	Carrigan et al.
Vulnerability score	Low-density plaque and arterial remodeling in each segment	Motoyama et al.

List 14.3. Future of plaque imaging

1. Better detector material (e.g., k-edge imaging based on photon-counting detectors)
2. Dual-energy for plaque characterization
3. Improved reconstruction algorithm, e.g., iterative reconstruction
4. Volumetric analysis (with semiautomated software tools)
5. Contrast agents with specific binding (e.g., to intercellular adhesion molecules or cellular markers of inflammatory response)

decisions following the imaging test will be influenced by the CT findings and benefit our patients. Such trials are currently enrolling patients, some mandating treatment options and others not. Over the next several years, these data will define the relative role of invasive and noninvasive modalities and their cost effectiveness in coronary plaque assessment.

Recommended Reading

Achenbach S, Moselewski F, Ropers D et al (2004a) Detection of calcified and noncalcified coronary atherosclerotic plaque by contrast-enhanced, submillimeter multidetector spiral computed tomography: a segment-based comparison with intravascular ultrasound. Circulation 109:14–17

Achenbach S, Ropers D, Hoffmann U et al (2004b) Assessment of coronary remodeling in stenotic and nonstenotic coronary atherosclerotic lesions by multidetector spiral computed tomography. J Am Coll Cardiol 43:842–847

Bamberg F, Sommer WH, Hoffmann V, Achenbach S, Nikolaou K, Conen D, Reiser MF, Hoffmann U, Becker CR (2011) Meta-analysis and systematic review of the long-term predictive value of assessment of coronary atherosclerosis by contrast-enhanced coronary computed tomography angiography. J Am Coll Cardiol 57(24):2426–2436

Boogers MJ, Broersen A, van Velzen JE, de Graaf FR, El-Naggar HM, Kitslaar PH, Dijkstra J, Delgado V, Boersma E, de Roos A, Schuijf JD, Schalij MJ, Reiber JH, Bax JJ, Jukema JW (2012) Automated quantification of coronary plaque with computed tomography: comparison with intravascular ultrasound using a dedicated registration algorithm for fusion-based quantification. Eur Heart J 33(8):1007–1016

Carrigan TP, Nair D, Schoenhagen P et al (2009) Prognostic utility of 64-slice computed tomography in patients with suspected but no documented coronary artery disease. Eur Heart J 30:362–371

Chow BJ, Small G, Yam Y, Chen L, Achenbach S, Al-Mallah M, Berman DS, Budoff MJ, Cademartiri F, Callister TQ, Chang HJ, Cheng V, Chinnaiyan KM, Delago A, Dunning A, Hadamitzky M, Hausleiter J, Kaufmann P, Lin F, Maffei E, Raff GL, Shaw LJ, Villines TC, Min JK, CONFIRM Investigators (2011) Incremental prognostic value of cardiac computed tomography in coronary artery disease using CONFIRM: COroNary computed tomography angiography evaluation for clinical outcomes: an InteRnational Multicenter registry. Circ Cardiovasc Imaging 4(5):463–472

Cho I, Chang HJ, Sung JM, Pencina MJ, Lin FY, Dunning AM, Achenbach S, Al-Mallah M, Berman DS, Budoff MJ, Callister TQ, Chow BJ, Delago A, Hadamitzky M, Hausleiter J, Maffei E, Cademartiri F, Kaufmann P, Shaw LJ, Raff GL, Chinnaiyan KM, Villines TC, Cheng V, Nasir K, Gomez M, Min JK, CONFIRM Investigators (2012) Coronary computed tomographic angiography and risk of all-cause mortality and nonfatal myocardial infarction in subjects without chest pain syndrome from the CONFIRM Registry (coronary CT angiography evaluation for clinical outcomes: an international multicenter registry). Circulation 126(3):304–313

Ferencik M, Schlett CL, Bamberg F, Truong QA, Nichols JH, Pena AJ, Shapiro MD, Rogers IS, Seneviratne S, Parry BA, Cury RC, Brady TJ, Brown DF, Nagurney JT, Hoffmann U (2012) Comparison of traditional cardiovascular risk models and coronary atherosclerotic plaque as detected by computed tomography for prediction of acute coronary syndrome in patients with acute chest pain. Acad Emerg Med 19(8):934–942

Glagov S, Weisenberg E, Zarins CK, Stankunavicius R, Kolettis GJ (1987) Compensatory enlargement of human coronary arteries. N Engl J Med 316:1371–1375

Greenland P, Bonow RO, Brundage BH et al (2007) ACCF/AHA 2007 clinical expert consensus document on coronary artery calcium scoring by computed tomography in global cardiovascular risk assessment and in evaluation of patients with chest pain. J Am Coll Cardiol 49:378–402

Hendel RC, Patel MR, Kramer CM et al (2006) ACCF/ACR/SCCT/SCMR/ASNC/NASCI/SCAI/SIR 2006 appropriateness criteria for cardiac computed tomography and cardiac magnetic resonance imaging. J Am Coll Cardiol 48:1475–1497

Hulten EA, Carbonaro S, Petrillo SP, Mitchell JD, Villines TC (2011) Prognostic value of cardiac computed tomography angiography: a systematic review and meta-analysis. J Am Coll Cardiol 57(10):1237–1247

Imazeki T, Sato Y, Inoue F et al (2004) Evaluation of coronary artery remodeling in patients with acute coronary syndrome and stable angina by multislice computed tomography. Circ J 68:1045–1050

Kitagawa T, Yamamoto H, Horiguchi J et al (2009) Characterization of noncalcified coronary plaques and identification of culprit lesions in patients with acute coronary syndrome by 64-slice computed tomography. JACC Cardiovasc Imaging 2:153–160

Leber AW, Becker A, Knez A et al (2006) Accuracy of 64-slice computed tomography to classify and quantify plaque volumes in the proximal coronary system: a comparative study using intravascular ultrasound. J Am Coll Cardiol 47:672–677

Meijs MF, Meijboom WB, Bots ML et al (2009) Comparison of frequency of calcified versus non-calcified coronary lesions by computed tomographic angiography in patients with stable versus unstable angina pectoris. Am J Cardiol 104:305–311

Min JK, Shaw LJ, Devereux RB et al (2007) Prognostic value of multidetector coronary computed tomographic angiography for prediction of all-cause mortality. J Am Coll Cardiol 50:1161–1170

Motoyama S, Sarai M, Harigaya H et al (2009) Computed tomographic angiography characteristics of atherosclerotic plaques subsequently resulting in acute coronary syndrome. J Am Coll Cardiol 54:49–57

Nair A, Kuban BD, Tuzcu EM, Schoenhagen P, Nissen SE, Vince DG (2002) Coronary plaque classification with intravascular ultrasound radiofrequency data analysis. Circulation 106:2200–2206

Raff GL, Abidov A, Achenbach S, Berman DS, Boxt LM, Budoff MJ, Cheng V, DeFrance T, Hellinger JC, Karlsberg RP, Society of Cardiovascular Computed Tomography (2009) SCCT guidelines for the interpretation and reporting of coronary computed tomographic angiography. J Cardiovasc Comput Tomogr 3(2):122–136

Rinehart S, Vazquez G, Qian Z, Murrieta L, Christian K, Voros S (2011) Quantitative measurements of coronary arterial stenosis, plaque geometry, and composition are highly reproducible with a standardized coronary arterial computed tomographic approach in high-quality CT datasets. J Cardiovasc Comput Tomogr 5(1):35–43

Rodriguez-Granillo GA, García-García HM, Mc Fadden EP et al (2005) In vivo intravascular ultrasound-derived thin cap fibroatheroma detection using ultrasound radiofrequency data analysis. J Am Coll Cardiol 46:2038–2042

Schoenhagen P, Tuzcu EM, Stillman AE et al (2003) Non-invasive assessment of plaque morphology and remodeling in mildly stenotic coronary segments: comparison of 16-slice computed tomography and intravascular ultrasound. Coron Artery Dis 14:459–462

Schoenhagen P, Ziada KM, Kapadia SR, Crowe TD, Nissen SE, Tuzcu EM (2000) Extent and direction of arterial remodeling in stable versus unstable coronary syndromes. Circulation 101:598–603

Schroeder S, Kopp AF, Baumbach A et al (2001) Noninvasive detection and evaluation of atherosclerotic coronary plaques with multislice computed tomography. J Am Coll Cardiol 37:1430–1435

Springer I, Dewey M (2009) Comparison of multislice computed tomography with intravascular ultrasound for detection and characterization of coronary artery plaques: a systematic review. Eur J Radiol 71:275–282

Stone GW, Maehara A, Lansky AJ, de Bruyne B, Cristea E, Mintz GS, Mehran R, McPherson J, Farhat N, Marso SP, Parise H, Templin B, White R, Zhang Z, Serruys PW; PROSPECT Investigators (2011) A prospective natural-history study of coronary atherosclerosis. N Engl J Med 364(3):226–235

Cardiac Function

F. Wolf and G. Feuchtner

Abstract

In this chapter, clinical indications, examination techniques, and postprocessing methods for evaluation of cardiac function with CT are presented.

15.1 Performance of CT for Assessment of Cardiac Function

Global left ventricular function is an important parameter for defining clinical management of patients in the routine setting. Cardiac computed tomography (CT) enables evaluation of global left ventricular function and shows good agreement with magnetic resonance imaging (MRI), the gold standard (see Chap. 25). The agreement of CT with MRI is better than that of both cine-ventriculography and echocardiography with MRI. Evaluation of right ventricular function is feasible by CT, and initial study results are promising. Still, the complex geometry of the right ventricle makes its segmentation more difficult.

If a retrospectively gated CT scan is performed and images are reconstructed at 5% (or 10% at most) steps during the cardiac cycle, cardiac function can be analyzed as part of coronary CT angiography. The analysis can be performed on commercially available three-dimensional postprocessing workstations using automated or semiautomated software tools.

Regional left ventricular dysfunction occurs in various underlying diseases, e.g., ischemic heart disease (**Fig. 15.1**). A convenient approach for assessing regional left ventricular function is to evaluate wall motion abnormalities on cardiac short- and long-axis views (four-chamber, three-chamber, and two-chamber views) in the four-dimensional cine-mode. Datasets allowing four-dimensional cine viewing need to be acquired using retrospective ECG gating with image reconstruction at 5% or 10% intervals throughout the cardiac cycle. Regional

M. Dewey, *Cardiac CT*,
DOI 10.1007/978-3-642-41883-9_18, © Springer-Verlag Berlin Heidelberg 2014

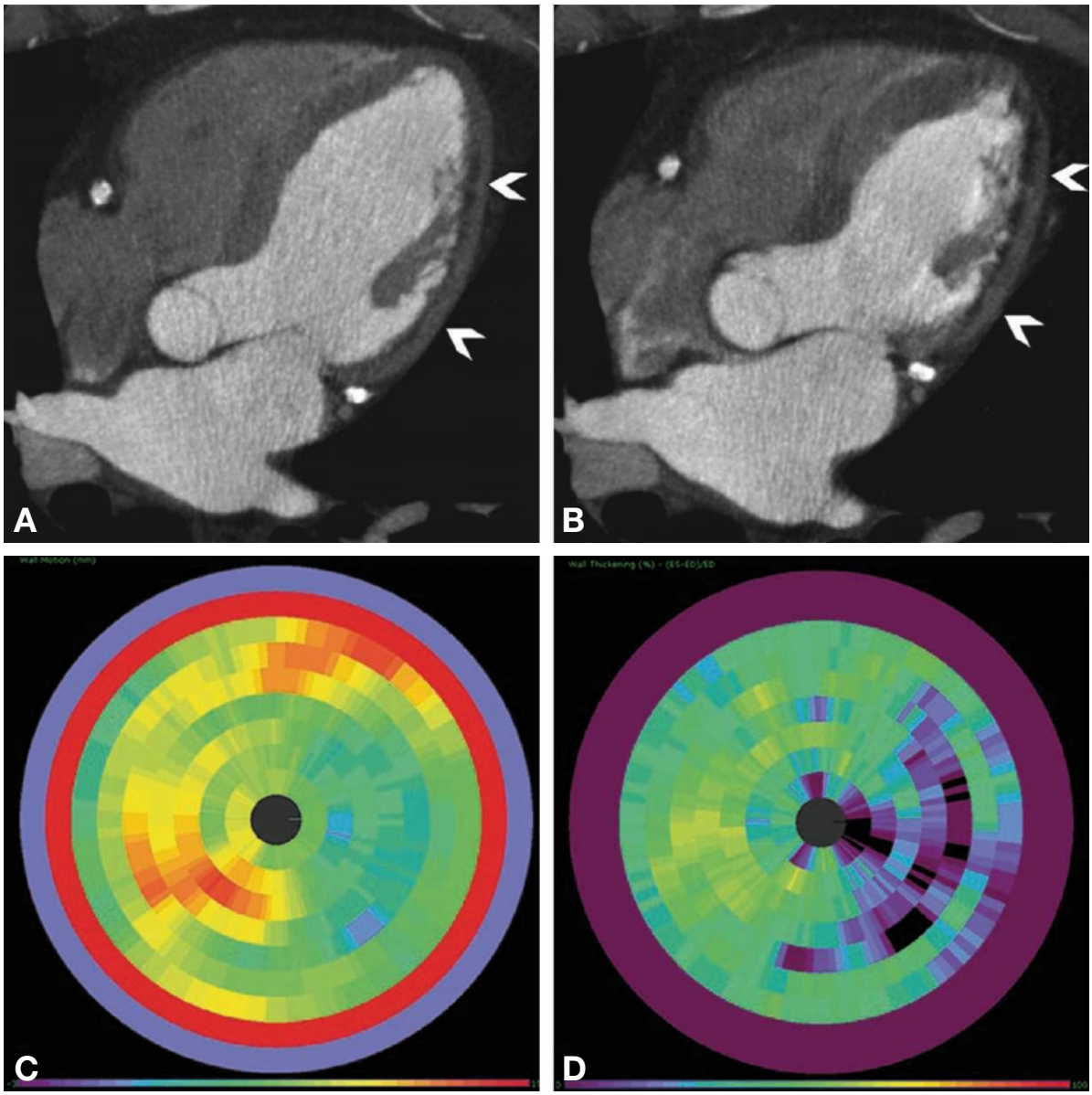

Fig. 15.1 Fifty-nine-year-old patient with regional akinesia after a large infarct in the lateral wall of the left ventricle. Note thinning of the lateral wall (*arrowheads*) during end-diastole (**Panel A**, four-chamber view) and end-systole (**Panel B**, four-chamber view). **Panel C** shows the colored bull's eye plot of wall motion in mm and **Panel D** shows wall thickening in percent

wall motion abnormalities and global left ventricular function can be evaluated from the same datasets.

In normal ventricles, left ventricular free wall thickness increases by more than 40% during systole (normokinetic myocardium) with a slightly smaller increase in the thickness of the ventricular septum. In patients with ischemic or nonischemic heart disease, wall motion abnormalities can be observed. Hypokinesia is defined as a systolic wall thickening of less than 30%, and akinesia as wall thickening of less than 10%. Dyskinesia is defined as outward myocardial motion during systole, usually in association with systolic wall thinning, and aneurysms are defined as distinct areas of abnormal left ventricular diastolic contour.

Wall motion abnormalities are systematically evaluated and reported using the 17-segment model of the

AHA (see Chap. 3). Each segment can be assigned a score on the basis of its contractility as assessed visually (normal = 1, hypokinesia = 2, akinesia = 3, dyskinesia = 4, and aneurysm = 5). A wall motion score index can be calculated to semiquantitatively describe the extent of regional wall motion abnormalities:

$$\textit{Wall motion score index} = \textit{sum of wall motion scores} / \textit{number of segments}$$

Normally contracting left ventricular myocardium has a wall motion score index of 1 (17/17 = 1). The evaluation of wall motion abnormalities can be performed automatically or semiautomatically on dedicated cardiac CT workstations (see Sect. 15.5).

If a myocardial segment with wall motion abnormalities is seen, the myocardium should be evaluated for morphologic abnormalities. Common causes are chronic myocardial infarcts/scars or acute ischemia in patients with acute chest pain. While myocardial infarcts show hypoperfusion (hypodense zones), thinning of the myocardium (<5 mm) or calcification, acute ischemia results in territorial perfusion defects due to hypoperfusion (Chap 19). Other reasons for hypokinetic, akinetic, or dyskinetic segments are cardiomyopathies or myocarditis. A common pitfall is left bundle branch block, which consistently leads to dyssynchronic movement of the anterior and inferior septal segments and does not indicate myocardial disease (**Fig. 15.2**). Paradoxical septum movement may be as well be seen on cine images in patients with left bundle branch block.

To summarize, although recent technical developments have improved the capabilities of CT, temporal resolution is still lower than that of cardiac MRI. Hence MRI should be preferred as first-line imaging modality in clinical practice. However, if retrospective ECG-gated datasets are available for coronary CT angiography, comprehensive evaluation of regional wall motion abnormalities or global left ventricular function may have added value.

15.2 Clinical Use of Cardiac CT

Current cardiac CT should not be used as first-line imaging modality for evaluation of left ventricular function because it involves radiation exposure. Cardiac MRI or echocardiography should be preferred for primary evaluation of right and left ventricular function. MRI is regarded as the gold standard method with the highest reproducibility.

Cardiac CT has the advantage that the datasets acquired for coronary CT angiography using retrospective ECG gating can also be used for evaluating cardiac function. No additional injection of contrast agent or exposure to further radiation is necessary. Because of the importance of global as well as regional cardiac function for a patient's individual prognosis and further clinical management, we thus strongly encourage to perform cardiac function analysis in all patients undergoing coronary CT angiography if datasets are acquired with conventional retrospective ECG gating.

15.3 Adjustment of CT Examination Protocols for Evaluation of Cardiac Function

15.3.1 Contrast Bolus Design

For evaluation of cardiac function, it is recommended to adjust the contrast agent injection protocol. Homogeneous enhancement of the right ventricle is desirable for better delineation of the interventricular septum. If a single bolus is injected for arterial phase at high flow rate (~5 ml/s), followed by a saline chaser, as commonly used for coronary CT angiography, most of the contrast agent will have left the right ventricle by the time the scan is taken. Hence, the interventricular septum and the right ventricle will not be delineated. If contrast bolus timing is suboptimal, e.g., if the injection time is too long, and/or if the bolus volume is too large, the right ventricle will appear inhomogeneous and show streak artifacts hampering image quality.

As mentioned before in Chap. 8, whenever assessment of cardiac function is required, biphasic injection of the contrast agent or injection of a mixture of contrast agent and saline have shown to improve image quality by providing low but homogeneous contrast attenuation of the right chambers. Streak artifacts, resulting from persisting flow of contrast agent, impair segmentation of the right chambers using fully automated software tools and degrade image quality of the right coronary artery. Therefore, the attenuation of the right chambers should be as homogeneous as possible.

Vrachliotis et al. describe a biphasic injection protocol including a first phase bolus of contrast at high flow

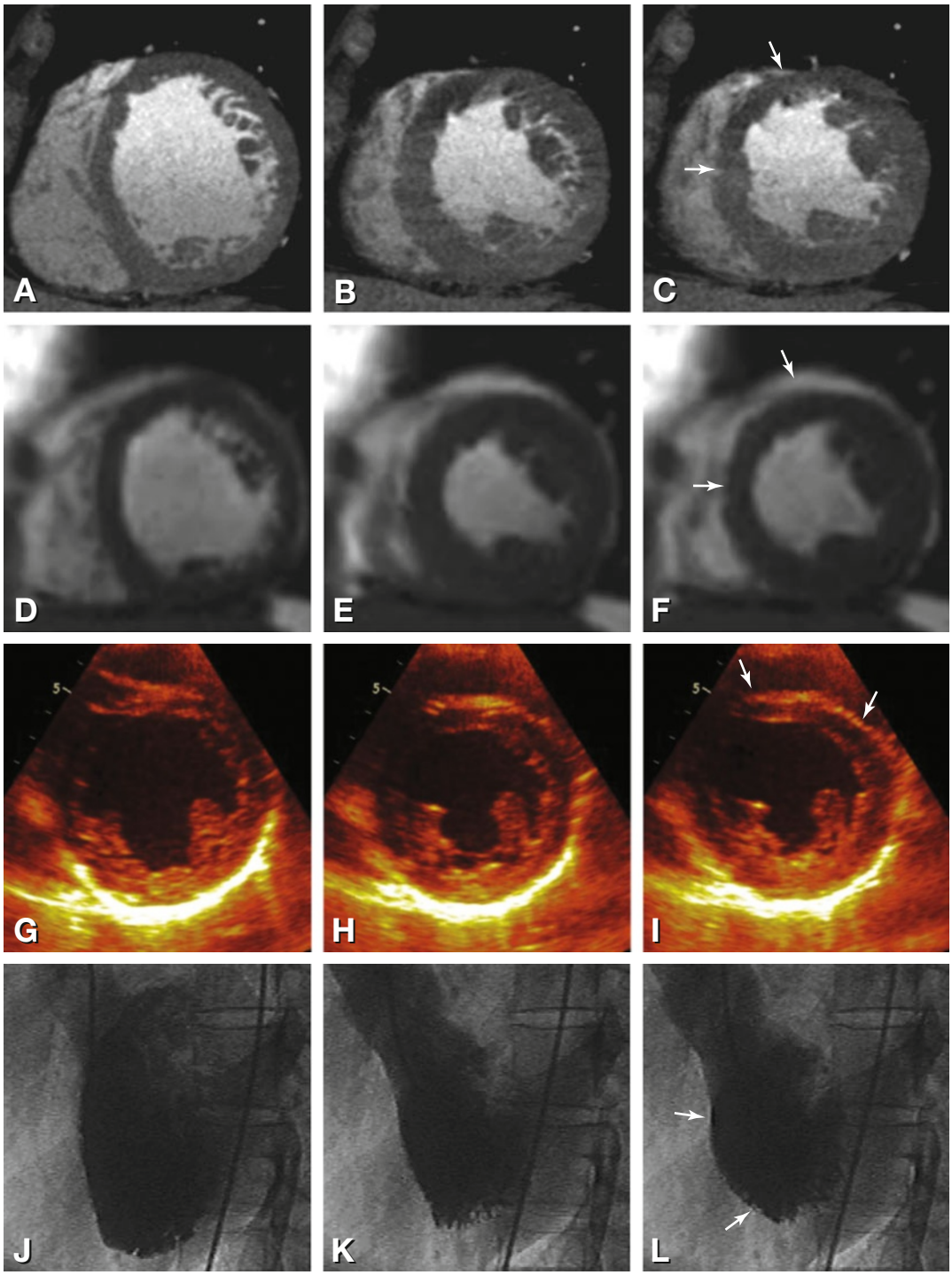

Fig. 15.2 Left-bundle branch block resulting in paradoxical movement of the anteroseptal segment in a 45-year-old female patients presenting with atypical angina pectoris. Results are shown in the short axis for CT (**Panels A**–**C**), magnetic resonance imaging (**Panels D**–**F**), and echocardiography (**Panels G**–**I**) and for cineventriculography in the left anterior oblique projection (**Panels J**–**L**). The diastolic images are shown in the *first column* for all techniques (**Panels A**, **D**, **G**, and **J**) while midsystolic images are shown in the *middle column* (**Panels B**, **E**, **H**, and **K**) without any wall-motion abnormalities. At endsystole (*right column*), all techniques show paradoxical outward motion and thinning of the anteroseptal segment (dyssynchrony, *arrows*, **Panels C**, **F**, **I**, and **L**), whereas all other segments exhibit further systolic inward motion. This is best seen on cine movies and is typical for left-bundle branch block but should not be mistaken for true dyskinesia. Conventional coronary angiography and coronary CT angiography did not show coronary artery stenosis in this patient

rate (100 ml at 5 ml/s) and a second phase at decreased flow (30 ml at 3 ml/s), resulting in an overall contrast agent volume of 130 ml. This protocol allows triple rule-out because it ensures rather homogenous enhancement in the coronary, aortic, and pulmonary vasculature as well as in the right ventricle using 64-row CT.

15.3.2 ECG-Gating Techniques

Retrospective ECG gating is required for assessment of cardiac function, which permits the acquisition of multiphase datasets over the entire cardiac cycle. ECG-dependent tube current modulation can be applied, resulting in diagnostic images in most cases despite higher image noise during systole.

Prospectively EGG-triggered datasets ("step-and-shoot") preclude evaluation of cardiac function if the padding window is placed at end-diastole.

The recently introduced prospective ECG-triggered adaptive sequential scan mode, with additional tube current modulation throughout the cardiac cycle enables estimation of cardiac function parameters and may provide a reasonable alternative in patients with stable heart rates.

15.3.3 Image Reconstruction

Reconstruction of the multiphase dataset covering the entire cardiac cycle should be performed in 5% or 10% steps from 0 to 90% of the RR interval. For detailed information on how to generate multiphase datasets on the different scanners, please see Chap. 9.

We recommend reconstructing a slice width of 1 mm (overlap, 70%) to ensure highest spatial resolution and highest accuracy of measurements; however, one needs to keep in mind that multiphase datasets produce large amounts of images. If one experiences difficulties in uploading large datasets, slice thickness may be increase to 1.5–2 mm to reduce the number of images.

Most of the commercially available workstations provide tools for automated detection of the maximum end-systolic and end-diastolic volumes. Using these tools, it is generally possible to automatically identify systole and diastole and reduce data volume and analysis time.

15.4 Definition of Cardiac Function Parameters

A large number of cardiac function parameters exist. **Table 15.1** presents clinically relevant parameters, which can be calculated with all commercially available postprocessing workstations equipped with cardiac software packages. **Table 15.2** lists other important cardiac parameters, which can be evaluated depending on the ECG-gating technique (retrospective or prospective ECG gating) and the specific workstation used.

15.5 Analysis of Cardiac Function on Different Commercial Workstations

Cardiac software packages from all major CT vendors and dedicated cardiac workstations allow evaluation of cardiac function. Most workstations have automated or semiautomated tools to facilitate and accelerate function analysis. All vendors have tools to evaluate left ventricular function; some of them also developed tools to evaluate right ventricular function.

Table 15.1 Clinically relevant cardiac function parameters

Parameter	Unit	Description
End-diastolic volume (EDV)	ml	Largest volume of the left ventricle during any cardiac phase. An increase in venous return to the heart increases the EDV, which stretches the muscle fibers and increases the preload. This leads to an increase in ventricular contraction in order to eject the additional blood, resulting in a higher SV
End-systolic volume (ESV)	ml	Smallest volume of the left ventricle during any cardiac phase
Stroke volume (SV)	ml/stroke	Blood volume ejected during systole (SV = EDV – ESV)
Ejection fraction (EF)	%	Percentage of blood in the left ventricle ejected during systole (EF = SV/EDV × 100%)
Cardiac output (CO)	l/min	Blood volume ejected from the heart per minute (CO = heart rate × SV/1,000). CO is regulated principally by the oxygen demand of the body cells and is increased during infection and sepsis and decreased in cardiomyopathy and heart failure

Table 15.2 Parameter unit description

Parameter	Unit	Description
Myocardial volume (MV)	Ml	Volume of myocardium of the left ventricle (inclusion or exclusion of the papillary muscles depending on the workstation)
Myocardial mass (MM)	G	MM = MV × 1.05 g/ml (1.05 g/ml = specific mass of the myocardium)
Myocardial mass index (MMI)	g/kg	MMI = MM (g)/body weight (kg)
Body surface area (BSA)	m^2	BSA = 0.007184 × body height $^{0.725}$ (cm) × body weight $^{0.425}$ (kg)
Stroke index (SI)	(ml/beat)/m^2	SI = SV/BSA
Cardiac index (CI)	(l/min)/m^2	CI = CO/BSA
Wall motion (WM)	mm	Maximum motion of the outer (epicardial) contours between systole and diastole
Wall thickening (WT)	%	WT = (ES wall thickness – ED wall thickness)/ED wall thickness × 100%

15.5.1 Vital Images (Vitrea Workstation)

After loading a multiphase dataset (**Fig. 15.3**), this software tool fully automatically identifies the cardiac axes, the endo- and epicardial contours as well as end-systole and end-diastole of the left ventricle. The cardiac axes as well as the endo- and epicardial contours should be checked in all phases to avoid false measurements of function parameters. If necessary, these parameters including the mitral valve plane can be adjusted manually. For evaluation of function parameters such as ejection fraction or stroke volume, the papillary muscles are excluded, whereas for the evaluation of myocardial mass, the papillary muscles are included. Regional wall motion analysis using this tool is shown in **Fig. 15.4**.

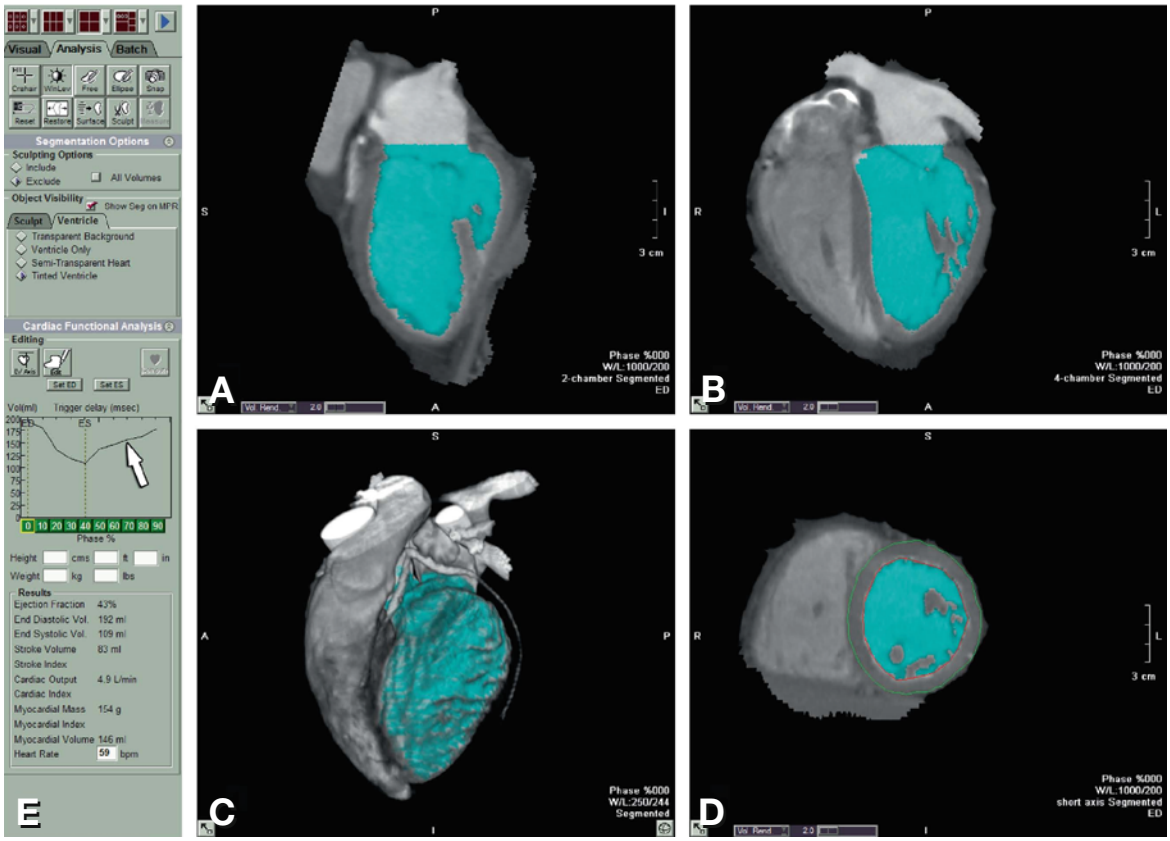

Fig. 15.3 Fully automated cardiac function analysis software (Vitrea, Vital Images) in a patient with reduced left ventricular ejection fraction (43%). Images are presented in two-chamber view (**Panel A**), four-chamber view (**Panel B**), three-dimensional display (**Panel C**), and short-axis view (**Panel D**). The blood pool of the left ventricle is marked in *blue*. The papillary muscles are excluded. The epicardial contours are indicated with *green lines*, the endocardial contours with *red lines* (**Panel D**). **Panel E** shows a volume curve of the left ventricle (*arrow*) over the cardiac cycle. End-diastole (ED, 0% of RR interval) and end-systole (ES, 40% of RR interval) are automatically recognized and marked. Moreover, results of the function analysis are shown. If the patient's weight and height and the heart rate are given, the software calculates stroke index, cardiac index, cardiac output, and myocardial index (Figure courtesy of Vital Images)

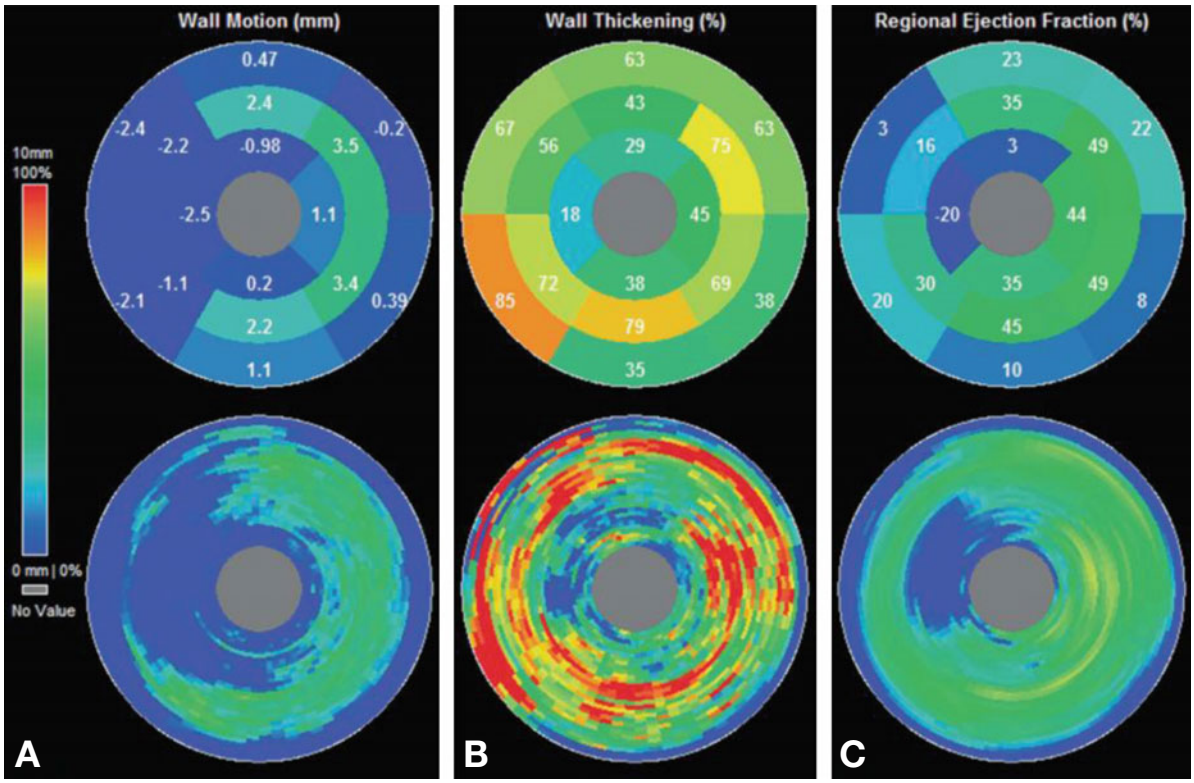

Fig. 15.4 Color-coded map (Vitrea, Vital Images) of the left ventricle using the 17-segment model of the American Heart Association (*AHA*) obtained with automated cardiac function analysis software (Vitrea, Vital Images). Wall motion is shown in mm (**Panel A**), while wall thickening and the regional ejection fraction are presented as percentages (**Panels B** and **C**). Images show that all three parameters are reduced in the anteroseptal segments in the apical third of the left ventricle in a patient with high-grade LAD stenosis (Figure courtesy of Vital Images)

15.5.2 Siemens (syngo.via™, Cardio-Vascular Engine)

After loading a multiphase dataset, automatic recognition of the left heart epi- and endocardial and the right heart endocardial contours is performed (**Fig. 15.5**). All contours can be adjusted manually, if necessary. Despite the use of maximal tube current modulation (**Fig. 15.6**) (MinDose™), endocardial and epicardial boarder contour tracking is feasible. Cardiac function results are presented for the left and right ventricle including a time-volume curve (**Fig. 15.5e**) and bull's eye plots for wall motion, wall thickening, and wall thickness (**Fig. 15.7b**). Hypoattenuated myocardium (e.g., myocardial infarction) is segmented based on Hounsfield units (**Fig. 15.7c**).

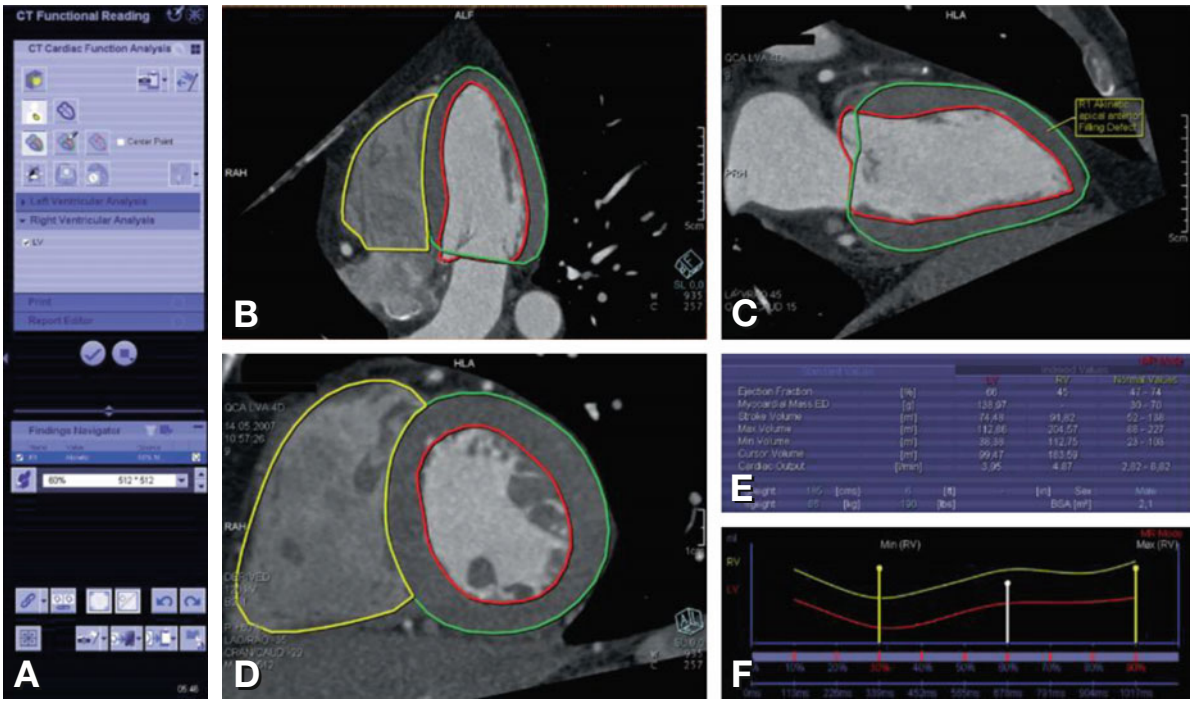

Fig. 15.5 Cardiac function analysis software (**Panel A**, syngo.via™, Cardio-Vascular Engine, Siemens). The inner endocardial borders of the left (*red*) and right (*yellow*) ventricle including the papillary muscles are traced automatically. Left ventricular function parameters are shown in four-chamber (**Panel B**), two-chamber (**Panel C**), and short-axis-view (**Panel D**). Cardiac function parameters are presented for the left and right ventricle and compared with the normal values (**Panel E**). **Panel F** shows a time-volume curve for the left (*red*) and right (*yellow*) ventricle (Figure courtesy of Siemens)

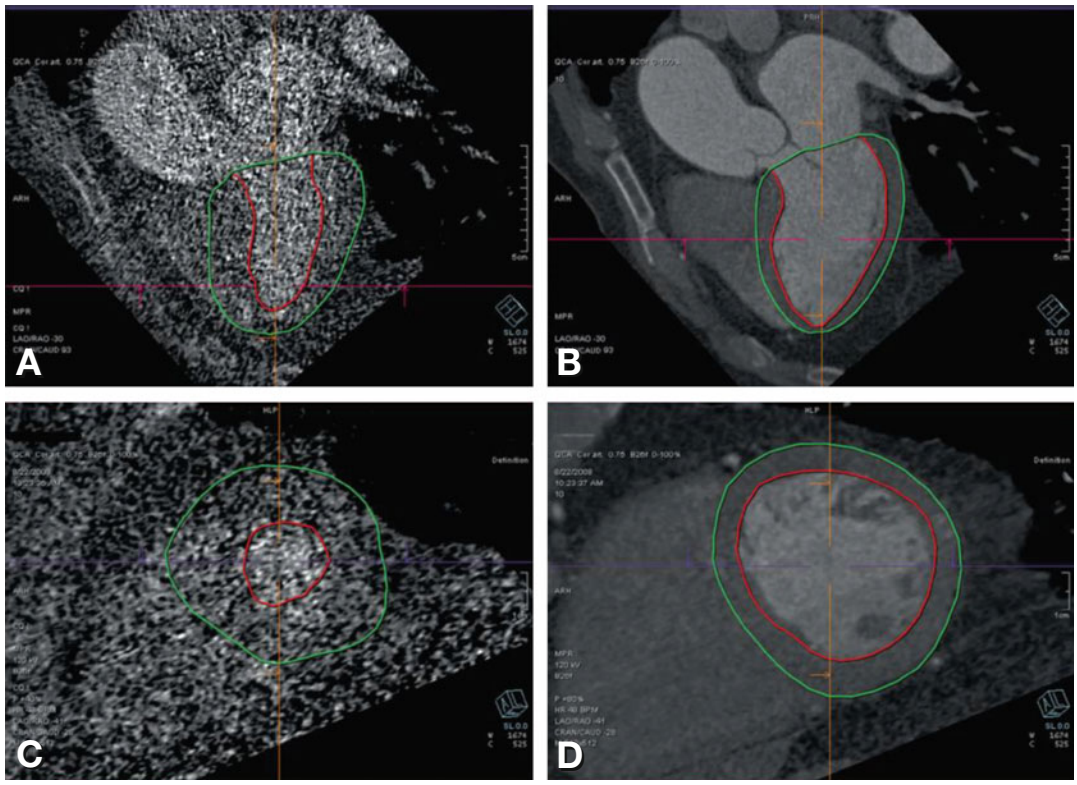

Fig. 15.6 Recently introduced software (syngo.via™, Cardio-Vascular Engine, Siemens) allows endo- and epicardial contour tracking despite high image noise during systole (**Panels A** and **C**) through the use of MinDose™ (Siemens). Note full tube current is applied during end-diastole (**Panels B** and **D**) only. Contour tracking results may be corrected manually if necessary (Figure courtesy of Siemens)

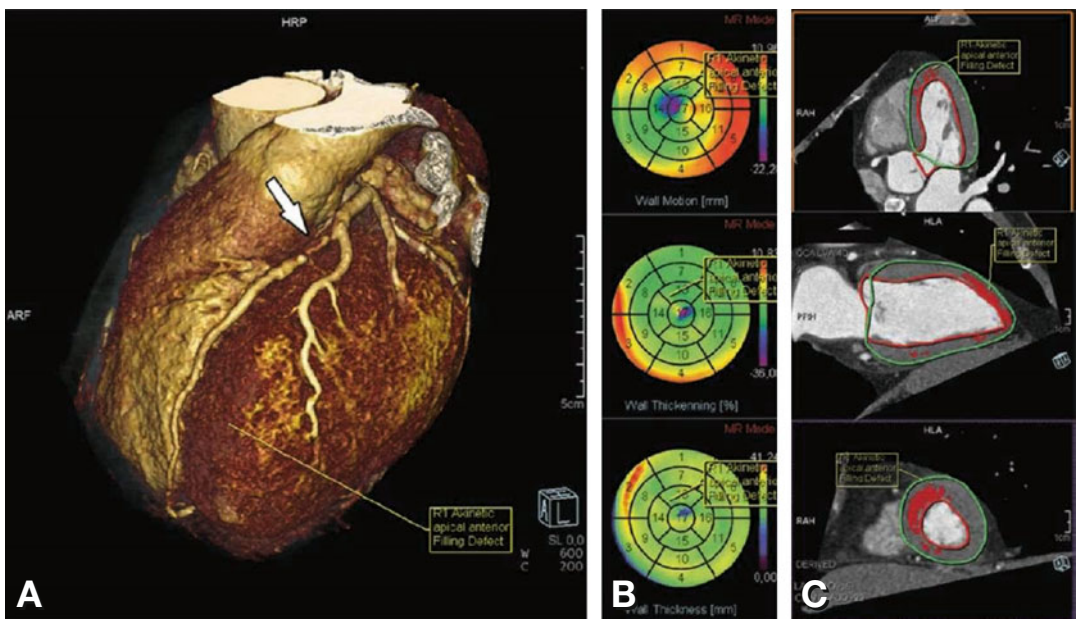

Fig. 15.7 Assessment of myocardial infarction using syngo.via™, Cardio-Vascular Engine (Siemens). This patient is the same as in **Fig. 15.4** and had a 90% LAD stenosis (*arrow* in **Panel A**), which matched with an anteroseptal perfusion defect (*colored red* in **Panel C**). The perfusion defect, defined as hypoattenuating region, is segmented automatically based on Hounsfield unit ratio. **Panel B** shows the corresponding wall motion deficit (segments 13, 14, and 17 in the bull's eye plot) (Figure courtesy of Siemens)

15.5.3 Philips (Brilliance Workspace, Comprehensive Cardiac)

At least two (end-systole and end-diastole) or more datasets (e.g., 0–90% in 10% steps) can be uploaded into the comprehensive cardiac tool. Cardiac function analysis works fully automated, and endo- and epicardial borders as well as cardiac axes and the position of the mitral valve can be adjusted manually if necessary. Function analysis can be performed using the conventional short-axis method (**Fig. 15.8**). Alternatively, the user can select the fully automated method allowing segmentation of all four cardiac chambers (**Figs. 15.9** and **15.10**)

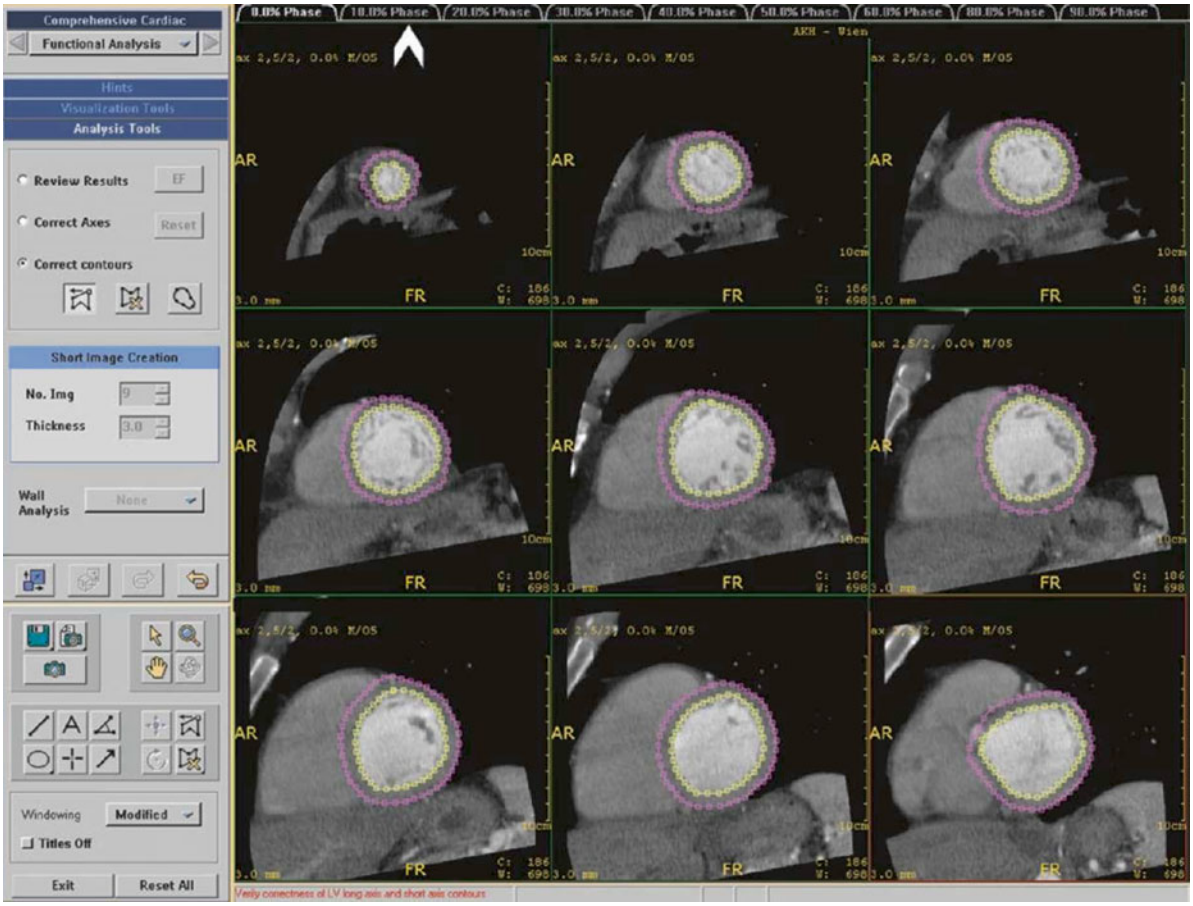

Fig. 15.8 Conventional cardiac function analysis tool (Comprehensive Cardiac, Philips) in a patient with normal left ventricular function. Multiple datasets (0–90%, at 10% steps) can be evaluated by clicking on the different phase cards (*arrowhead*). Endo- and epicardial contours of the left ventricle can be adjusted manually if necessary. Left ventricular function parameters are calculated using Simpson's method

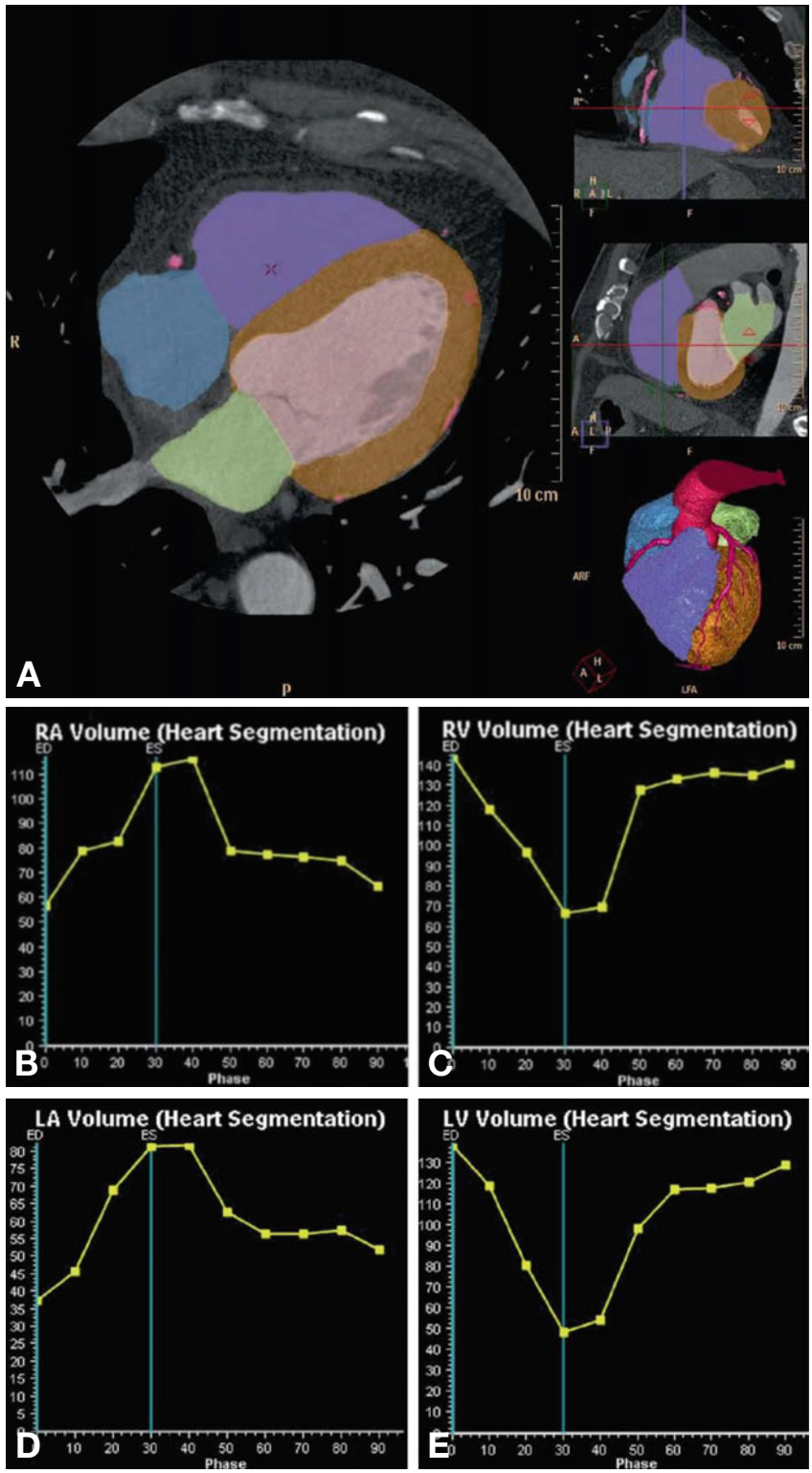

Fig. 15.9 Fully automated cardiac function analysis tool (Comprehensive Cardiac, Philips). All relevant cardiac structures are recognized and color-coded (**Panel A**). Volume-over-time curves for all four cardiac chambers (*LA* left atrium, *LV* left ventricle, *RA* right atrium, *RV* right ventricle) can be generated (**Panels B**–**E**)

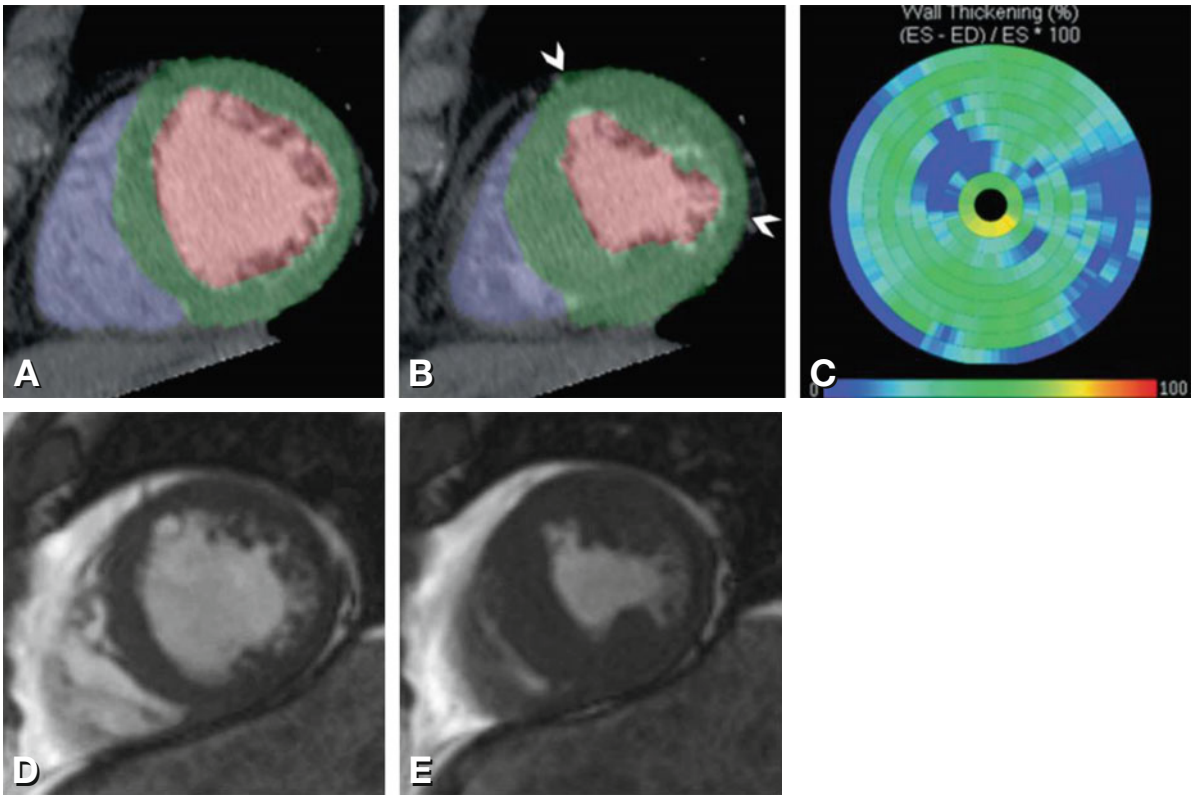

Fig. 15.10 Cardiac function analysis in a patient 2 years after myocardial infarction using a fully automated tool (Comprehensive Cardiac, Philips). **Panels A** and **B** show end-diastolic and end-systolic short-axis views, respectively. There is a small area of hypokinesia anteriorly and a larger area of akinesia inferolaterally (*arrowheads* in **Panel B**). **Panel C** presents a color-coded bull's eye plot of the CT examination showing the reduced wall thickening (*dark-blue areas*). **Panel D** shows end-diastolic and **Panel E** end-systolic short-axis images obtained in the same patient with MRI

15.5.4 GE (Advantage Workstation)

A three-dimensional model of the left ventricle at end-systole and end-diastole is segmented (**Fig. 15.11**). All function parameters are calculated and shown for each chamber. Automated endocardial (**Fig. 15.11**) and epicardial contour tracking (**Fig. 15.12**) of the left ventricle is feasible. The program allows measurement of left ventricular wall thickness and wall motion in the bull's eye view (**Fig. 15.12**).

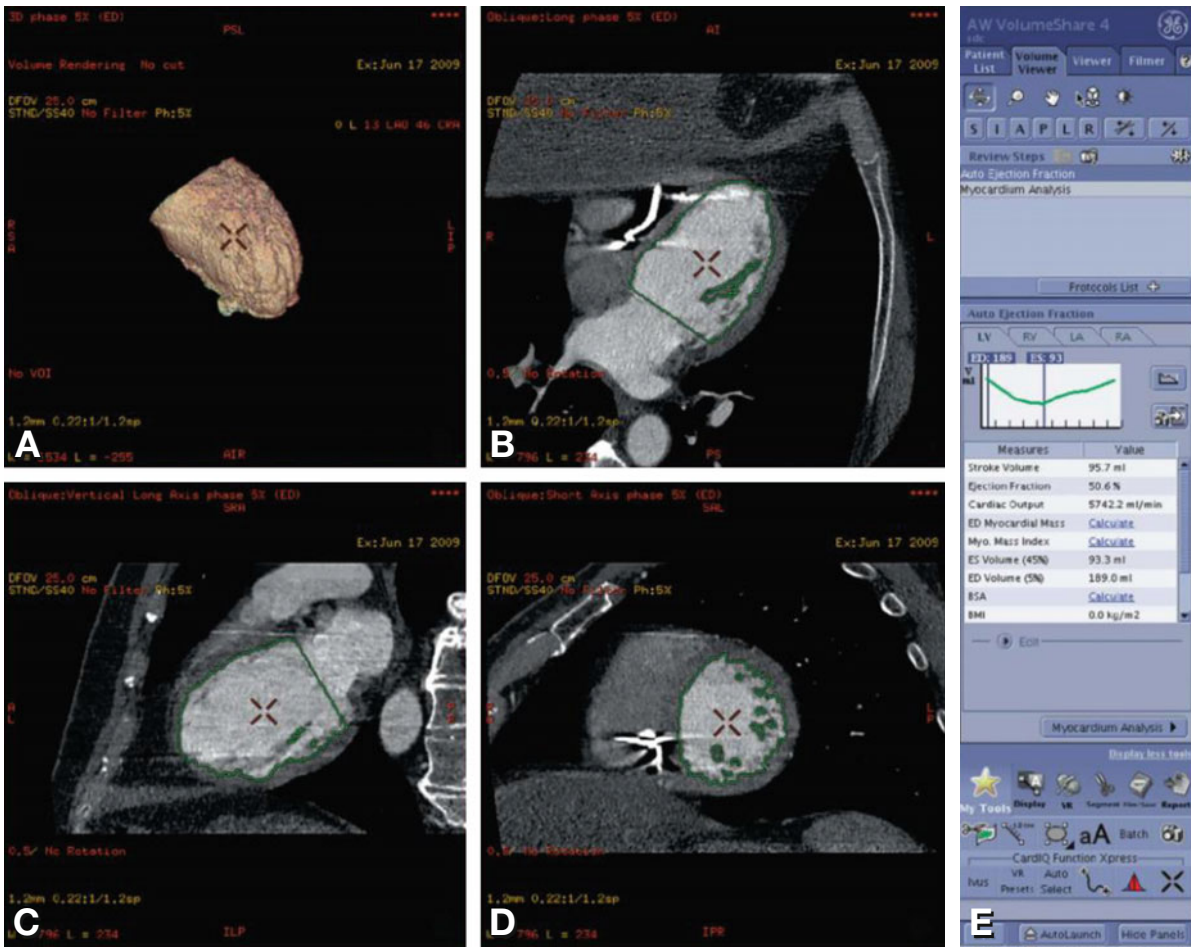

Fig. 15.11 Fully automated global left ventricular function evaluation tool (Advantage Workstation, GE) shown in a patient with normal function and a pacemaker lead in the right ventricle (artifacts). The data are shown as a three-dimensional model (**Panel A**), four-chamber view (**Panel B**), two-chamber view (**Panel C**), and a short-axis view (**Panel D**). The endocardial contours are traced in green color. **Panel E** shows a volume-over-time curve and the numerical results of the left ventricle analysis (Figure courtesy of E. Martuscelli)

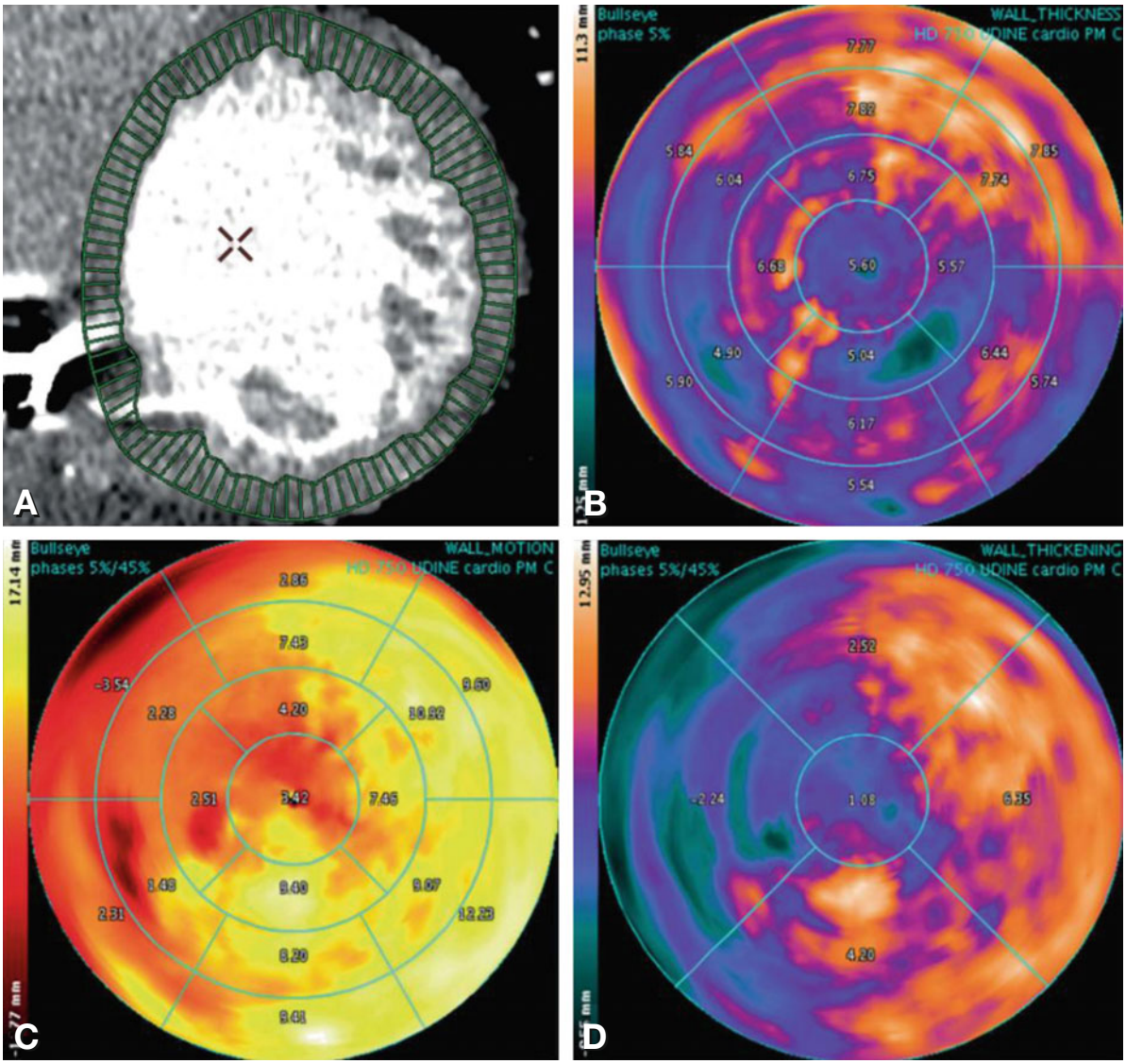

Fig. 15.12 By using "myocardium analysis" tool (Advantage Workstation, GE), the myocardial mass, the left ventricular wall thickness, wall motion, and systolic wall thickening can be measured. Epi- and endocardial contours are recognized automatically and can be adjusted manually if necessary (**Panel A**). Results are presented in the bull's eye view for left ventricular wall thickness (**Panel B**), left ventricular wall motion (**Panel C**), and systolic wall thickening (**Panel D**) (Figure courtesy of E. Martuscelli)

15.5.5 Terarecon (Aquarius iNtuition)

The cardiac function tool from Terarecon allows uploading datasets with multiple cardiac phases. Epi- and endocardial contours of the left ventricle are recognized automatically and can be adjusted manually (**Fig. 15.13**). The software recognizes end-systole and end-diastole.

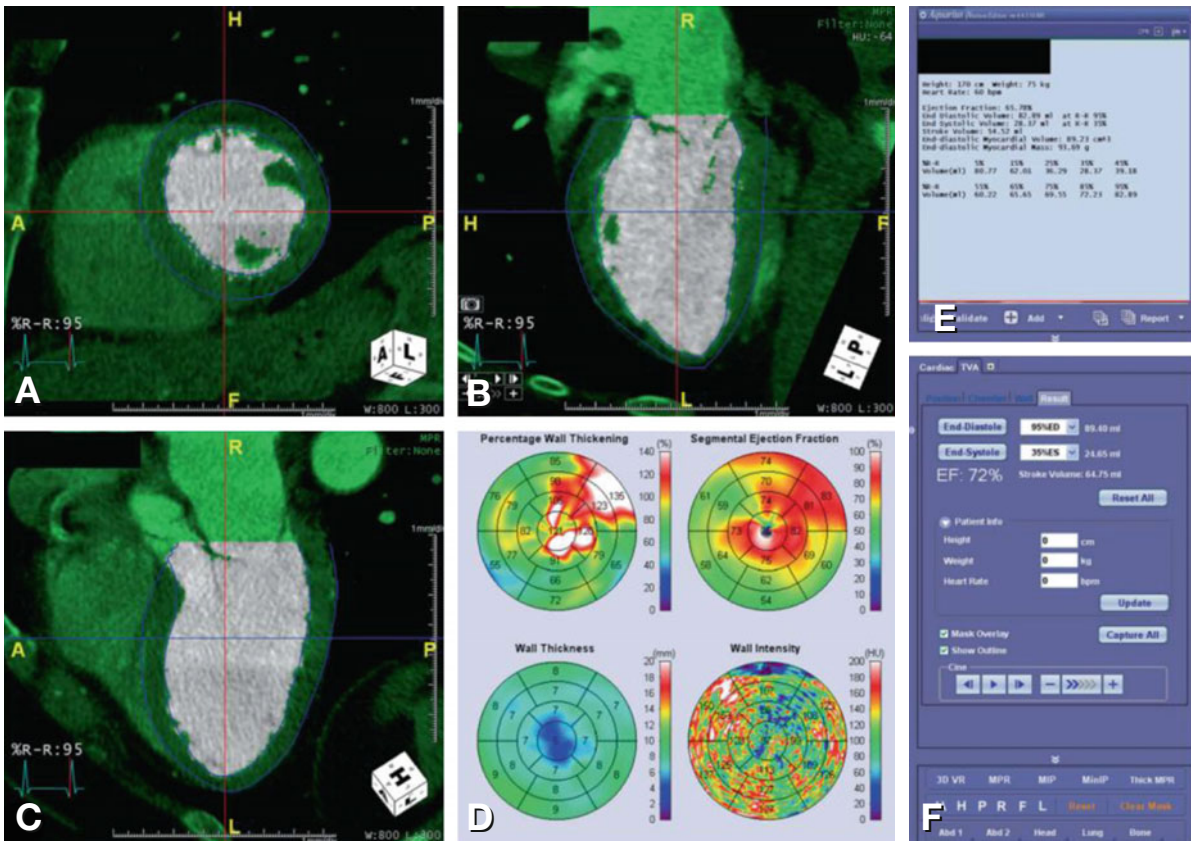

Fig. 15.13 Left ventricular function analysis with the software tool from Terarecon (Aquarius iNtuition). Epi- and endocardial contours of the left ventricle are recognized, the myocardium is colored in *green* and shown as short-axis view (**Panel A**) and long-axis views (**Panels B** and **C**). Results are presented numerically (**Panels E** and **F**) and also in the bull's eye view (**Panel D**). In addition to the standard values – percentage wall thickening, segmental ejection fraction and wall thickness – the wall intensity is also evaluated, which represents the segmental Hounsfield units of the left ventricle myocardium (Figure courtesy of Terarecon)

Recommended Reading

Bansal D, Singh RM, Sarkar M et al (2008) Assessment of left ventricular function: comparison of cardiac multidetector-row computed tomography with two-dimension standard echocardiography for assessment of left ventricular function. Int J Cardiovasc Imaging 24:317–325

Cury RC, Nieman K, Shapiro MD et al (2008) Comprehensive assessment of myocardial perfusion defects, regional wall motion, and left ventricular function by using 64-section multidetector CT. Radiology 248:466–475

Dewey M, Müller M, Eddicks S et al (2006a) Evaluation of global and regional left ventricular function with 16-slice computed tomography, biplane cineventriculography, and two-dimensional transthoracic echocardiography: comparison with magnetic resonance imaging. J Am Coll Cardiol 48:2034–2044

Dewey M, Müller M, Teige F et al (2006b) Multisegment and halfscan reconstruction of 16-slice computed tomography for assessment of regional and global left ventricular myocardial function. Invest Radiol 41:400–409

Dewey M, Müller M, Teige F, Hamm B (2006c) Evaluation of a semiautomatic software tool for left ventricular function analysis with 16-slice computed tomography. Eur Radiol 16:25–31

Feuchtner GM, Plank F, Pena C, Battle J, Min J, Leipsic J, Labounty T, Janowitz W, Katzen B, Ziffer J, Cury RC (2012) Evaluation of myocardial CT perfusion in patients presenting with acute chest pain to the emergency department: comparison with SPECT-myocardial perfusion imaging. Heart 98(20):1510–1517

Fischbach R, Juergens KU, Ozgun M et al (2007) Assessment of regional left ventricular function with multidetector-row computed tomography versus magnetic resonance imaging. Eur Radiol 17:1009–1017

Gilard M, Pennec PY, Cornily JC et al (2006) Multi-slice computer tomography of left ventricular function with automated analysis software in comparison with conventional ventriculography. Eur J Radiol 59:270–275

Jensen CJ, Jochims M, Hunold P et al (2010) Assessment of left ventricular function and mass in dual-source computed tomography coronary angiography influence of beta-blockers on left ventricular function: comparison to magnetic resonance imaging. Eur J Radiol 74:484–491

Juergens KU, Seifarth H, Range F et al (2008) Automated threshold-based 3D segmentation versus short-axis planimetry for assessment of global left ventricular function with dual-source MDCT. Am J Roentgenol 190:308–314

Kerl JM, Ravenel JG, Nguyen SA et al (2008) Right heart: split-bolus injection of diluted contrast medium for visualization at coronary CT angiography. Radiology 247:356–364

Kristensen TS, Kofoed KF, Moller DV et al (2009) Quantitative assessment of left ventricular systolic wall thickening using multi-detector computed tomography. Eur J Radiol 72:92–97

Mühlenbruch G, Das M, Hohl C et al (2006) Global left ventricular function in cardiac CT. Evaluation of an automated 3D region-growing segmentation algorithm. Eur Radiol 16:1117–1123

Müller M, Teige F, Schnapauff D, Hamm B, Dewey M (2009) Evaluation of right ventricular function with multidetector computed tomography: comparison with magnetic resonance imaging and analysis of inter- and intraobserver variability. Eur Radiol 19:278–289

Remy-Jardin M, Delhaye D, Teisseire A, Hossein-Foucher C, Duhamel A, Remy J (2006) MDCT of right ventricular function: impact of methodologic approach in estimation of right ventricular ejection fraction, part 2. Am J Roentgenol 187:1605–1609

Schepis T, Gaemperli O, Koepfli P et al (2006) Comparison of 64-slice CT with gated SPECT for evaluation of left ventricular function. J Nucl Med 47:1288–1294

Stolzmann P, Scheffel H, Trindade PT et al (2008a) Left ventricular and left atrial dimensions and volumes: comparison between dual-source CT and echocardiography. Invest Radiol 43:284–289

Stolzmann P, Scheffel H, Leschka S et al (2008b) Reference values for quantitative left ventricular and left atrial measurements in cardiac computed tomography. Eur Radiol 18:1625–1634

van der Vleuten PA, de Jonge GJ et al (2009) Evaluation of global left ventricular function assessment by dual-source computed tomography compared with MRI. Eur Radiol 19:271–277

Vrachliotis TG, Bis KG, Haidary A et al (2007) Atypical chest pain: coronary, aortic, and pulmonary vasculature enhancement at biphasic single-injection 64-section CT angiography. Radiology 243:368–376

Cardiac Valves

G. Feuchtner

Abstract

Information about cardiac valves is available from ECG-gated cardiac CT. This chapter reviews the current role of cardiac CT in valve imaging and outlines potential clinical applications and future developments. Aortic valve stenosis can be accurately assessed by CT which is also suitable for patients with suspected infective endocarditis and suspected dysfunctioning prosthetic valves.

16.1 Reading and Reporting

Through improvements in temporal resolution and the use of ECG gating during the entire cardiac cycle, four-dimensional cine imaging of cardiac valve function (**Fig. 16.1**) by computed tomography (CT) is feasible. The main advantage of cardiac CT is that the cardiac valves can be evaluated from the CT datasets acquired for assessment of the coronary arteries and left ventricular function.

The standard views for evaluation of the aortic valve and the mitral valve are summarized in **Table 16.1**. Please see also Chaps. 3 and 10 for details on anatomy and image interpretation.

Table 16.1 Standard views for cardiac valve evaluation

Aortic valve	Mitral valve
Left coronal oblique (**Figs. 16.2A**, **16.3B**, **16.4A**, **E**, **16.9A**, **B**, and **16.10A**, **D**)	Two-chamber view (**Fig. 16.9C**) Four-chamber view (**Fig. 16.10B**)
Three-chamber view (**Figs. 16.3A**, **D**, **16.4B**, **16.5A**, **16.8A**, **16.11C**, **d**, and **16.12A**)	
Cross-sectional LVOT (**Figs. 16.2C**, **16.3C**, **F**, **16.4C**, and **16.5B**)	Short-axis LV at the level of the mitral annulus (**Fig. 16.6B**)

LVOT left ventricular outflow tract, *LV* left ventricle

16.2 CT Examination Technique

For evaluation of valvular morphology, at least one cardiac phase is necessary (e.g., for imaging of the bicuspid valve, the end-diastolic phase is sufficient). Hence, low-dose techniques such as prospective ECG gating can be used for evaluation of morphology. Also, aortic regurgitation can be assessed on static end-diastolic phases.

For evaluation of valvular function, CT data need to be acquired during the entire cardiac cycle. To date, retro-

M. Dewey, *Cardiac CT*,
DOI 10.1007/978-3-642-41883-9_19, © Springer-Verlag Berlin Heidelberg 2014

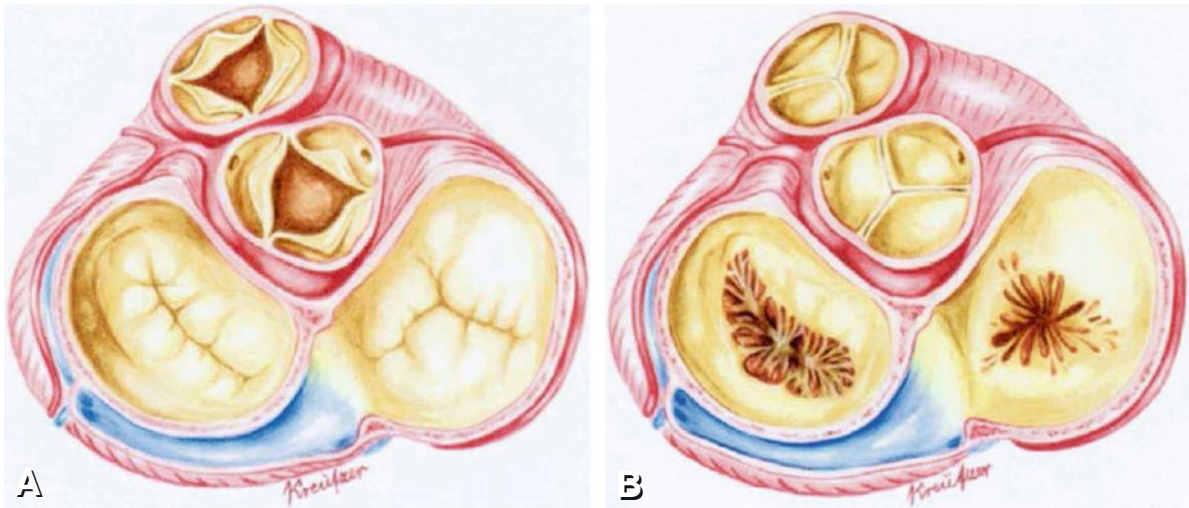

Fig. 16.1 Posterior view of all four cardiac valves (drawing) during systole with opening of the aortic and pulmonic valve (**Panel A**) as well as during early diastole (**Panel B**). Also shown are the left and right coronary artery arising from the left and right sinus of Valsalva, respectively, the posterior noncoronary sinus of Valsalva, and the great cardiac vein with the coronary sinus opening into the right atrium

spective ECG gating is the mode of first choice. ECG tube current modulation (with ~20% tube current reduction during systole) can be applied in the conventional mode, but leads to an increase in image noise, which can reach nondiagnostic levels, especially in morbidly obese patients. Special care needs to be taken when adjusting scan parameters for tube current modulation in obese patients (e.g., by tube current or tube voltage elevation). Very recently introduced prospective scan modes using dual-source and wide-area detector CT allow expansion of the scan window during the entire cardiac cycle, hence evaluation of cardiac function has become feasible.

A biphasic contrast agent injection protocol is advantageous over a monophasic injection for optimal timing of the contrast bolus to ensure right ventricular enhancement and adequate evaluation of all four cardiac valves and cardiac regional and global function. If only the aortic and mitral valves need to be assessed, a monophasic bolus injection as commonly applied for coronary CT angiography is appropriate.

16.3 Valvular Heart Disease

16.3.1 Aortic Stenosis

Degenerative aortic stenosis is very common with a prevalence of 2–5% in the elderly population >65 years. The pathomechanisms are similar to those in coronary heart disease, involving a degenerative process leading to aortic valve calcification and developing slowly during a lifetime. Rheumatic disease can cause aortic stenosis as well. Rarely, subaortic stenosis, defined as the presence of a congenital subaortic annulus membrane leading to narrowing of left ventricular outflow tract, may be present. These thin membranes are often well visualized by cardiac CT, and appear as hypodense flap-like lesions below the annulus.

Transthoracic echocardiography is the clinical reference modality to establish the diagnosis of aortic stenosis, based on measurement of transvalvular pressure gradients and calculation of the aortic valve orifice area using the Doppler-velocity time integral (continuity equation). This formula has some limitations and its accuracy for hemodynamic estimation of the effective aortic valve orifice is limited, e.g., in the presence of low-flow, low-pressure gradient aortic stenosis, or in case of reduced cardiac output. In addition, other factors such as eccentricity of left ventricular outflow tract (LVOT) influence these measurements. In contrast, the anatomic (= geometric) aortic valve area obtained directly from cross-sectional imaging techniques such as cardiac CT (**Fig. 16.2**) or magnetic resonance imaging (MRI) is not affected by external factors and flow phenomena. Several studies, with more than 300 patients enrolled, showed a high correlation of CT with transthoracic echocardiography. The size of the aortic valve area is used to classify

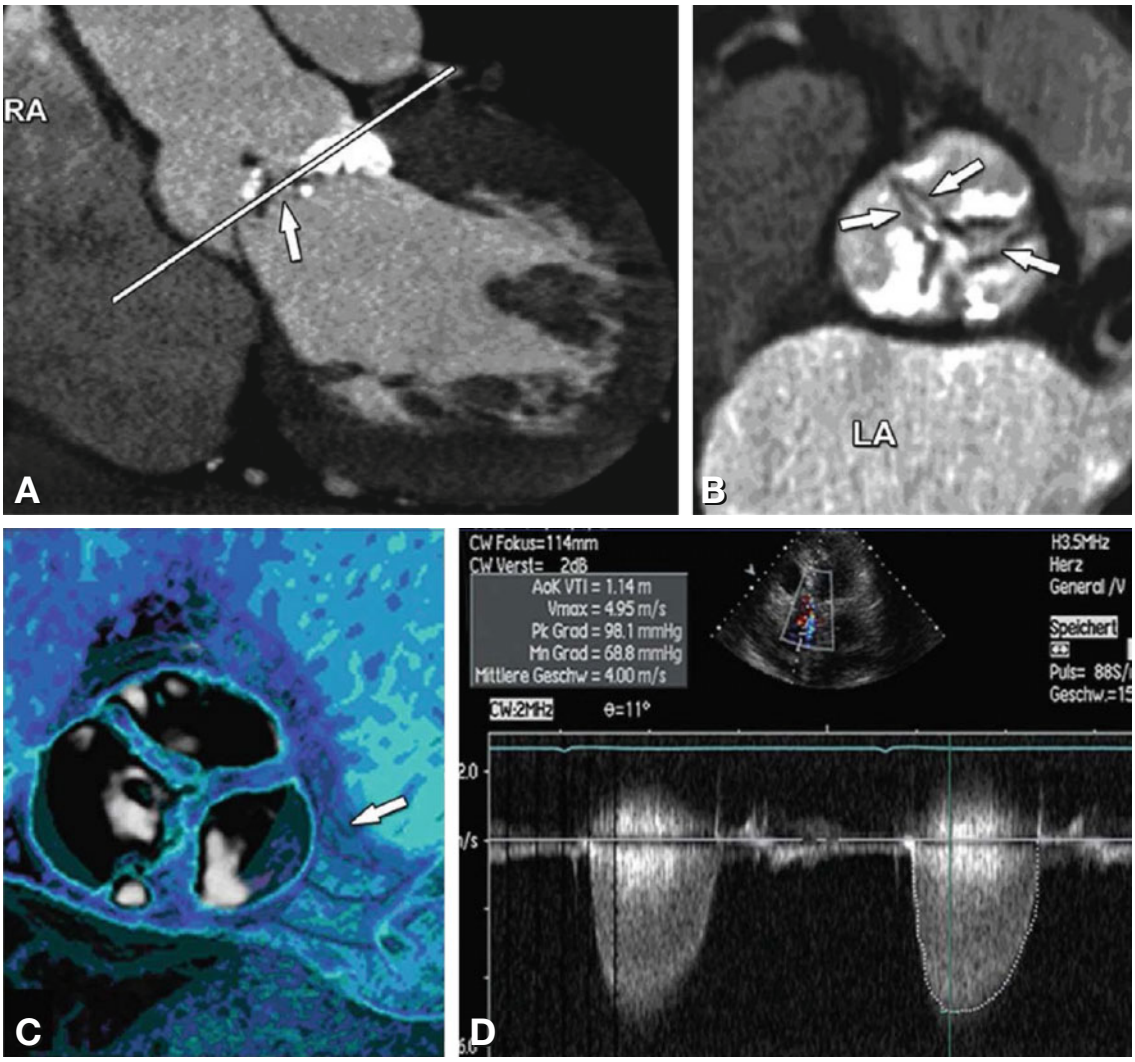

Fig. 16.2 Tricuspid aortic valve with severe calcification and stenosis. Left coronal oblique view of aortic root (**Panel A**). The white line in **Panel A** indicates the position of the cross-sectional image of the aortic root (**Panel B**) which allows measurement of the inner aortic valve orifice area (delineated with *arrows*). The calcifications are also nicely shown in a three-dimensional volume rendering (**Panel C**) with the *arrow* pointing at the left coronary ostium. Transthoracic echocardiography (**Panel D**) shows increased velocity of 4 m/s and transvalvular pressure gradient (*PK Grad* peak gradient, *Mn Grad* mean gradient) over the aortic valve. *RA* right atrium, *LA* left atrium

the severity of aortic stenosis as mild, moderate, and severe (**Table 16.2**). Images should be reconstructed at early/mid systole, which is the time point of maximal aortic valve opening, and depicted at 10–25% of the RR-interval pending on a patient's individual heart rate. Importantly, the phase with the best image quality should be selected for final sizing of the AVA. The best phase is also somewhat variable among various scanner generations. CT scanners with highest temporal resolution are advantageous for optimal image quality without motion artifacts during systole. The views for evaluation of the

Table 16.2 Staging of aortic stenosis (AS)

Classification	Staging	AVA
AS I	Mild	>1.5 cm^2
AS II	Moderate	1.0–1.5 cm^2
AS III	Severe	<1.0 cm^2
	Severe critical	<0.7 cm^2

AVA aortic valve area

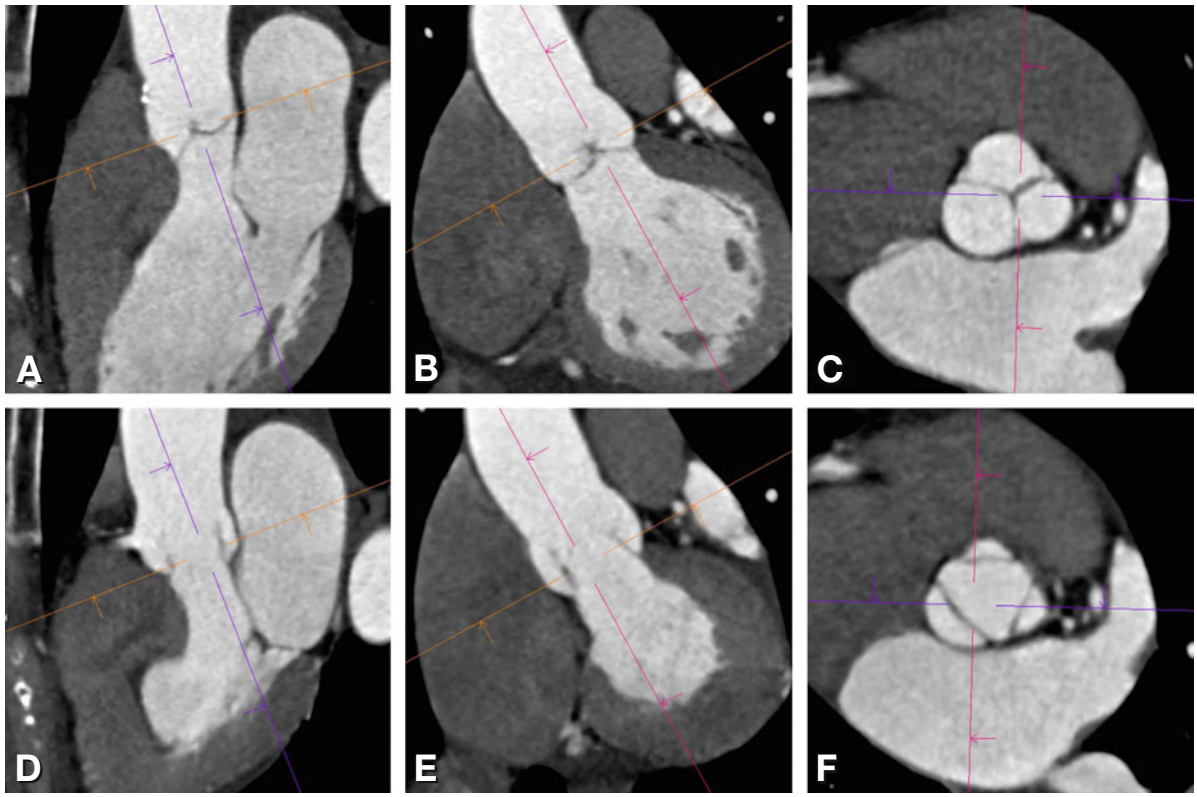

Fig. 16.3 Three standard views of the aortic valve during end-diastole (*above*) and mid-systole (*below*). Three-chamber view (**Panel A**) left coronal oblique (**Panel B**), and cross-sectional axial oblique (**Panel C**), reconstructed with double-oblique multiplanar reformations during end-diastole and during mid-systole (**Panels D**–**F**)

aortic valve are shown in **Fig. 16.3** and listed in **Table 16.1**. Multiplanar reformations should be applied, and left coronal oblique views, three-chamber views, and cross-sectional oblique axial views of the aortic valve should be reconstructed.

The following clinical applications for measurement of the aortic valve area are useful: first, in patients referred for coronary CT angiography, if valve calcification is present, the aortic valve area may be measure because these patients may have aortic stenosis or just non-stenotic valve calcification. Second, patients who require a second imaging modality for accurate sizing of the aortic valve area, e.g., in case of pending cardiac surgery, and/or if echocardiography has inherent limitations such as in low-flow low-gradient aortic stenosis. In these patients, CT can also yield information about the presence of coronary artery disease, left ventricular function, and the size of the aortic annulus. Left ventricular function is a valuable predictor of outcome in severe aortic stenosis. Accurate sizing of aortic root dimensions is required especially before minimally invasive aortic valve replacement or percutaneous transcatheter valve implantation.

16.3.2 Bicuspid Aortic Valve

CT can also identify bicuspid or tricuspid valve morphology (**Fig. 16.4**). The aortic valve can be congenitally bicuspid (without or with a fused raphe) or develop a secondary degenerative bicuspid shape due to calcification and adhesions. This information is of interest in clinical practice for cardiac surgeons to define the surgical approach (valve replacement versus possible surgical reconstruction) or to define further patient management. Congenital bicuspid valves are prone to developing dysfunction (regurgitation or stenosis), hence those patients may need to be followed up closer.

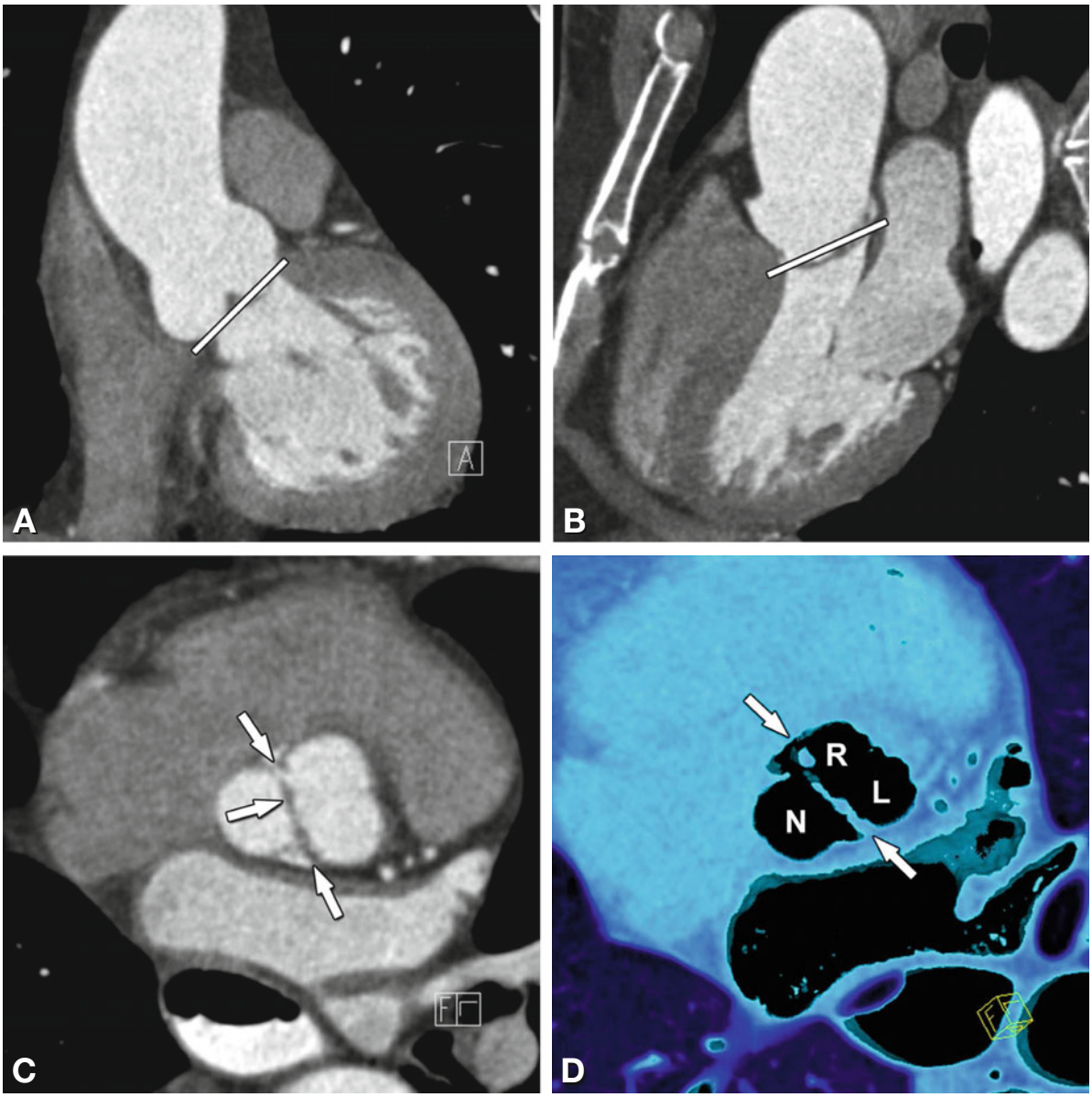

Fig. 16.4 Congenital bicuspid aortic valve reconstructed from standard views of the aortic valve during diastole. **Panels A** is a left coronal oblique and **Panel B** a three-chamber view. The *line* on **Panels A** and **B** indicates the plane of **Panel C**. **Panel C** is a cross-sectional axial oblique view and **Panel D** a corresponding volume rendering showing a bicupsid aortic valve consisting of two cusps only ("linear sign", *arrows*) during diastole. The left (*L*) and right (*R*) coronary cusp are fused (**Panel D**) and there is no raphe

16.3.3 Aortic Valve Calcification

CT allows quantification of aortic valve calcifications by using the same commercially available software as for coronary artery calcium scores. The aortic valve calcium score provides independent prognostic information in patients with asymptomatic aortic stenosis. Moreover, an aortic valve calcium score cut-off of 1,100 Agatston units is associated with a high likelihood of aortic stenosis. Thus all patients referred for nonenhanced coronary calcium scoring, in whom aortic valve calcification is an incidental finding, should be referred for transthoracic echocardiography for further evaluation.

16.3.4 Aortic Regurgitation

The onset of aortic regurgitation (AR) is either acute or chronic. Whilst acute aortic regurgitation is seen in fulminant infective endocarditis or ascending aortic dissection involving the valve, chronic aortic regurgitation can develop on the basis of several underlying diseases, the most common being aortic root dilatation and aneurysm formation (**Fig. 16.5**) as well as degenerative or rheumatic disease.

In patients with aortic regurgitation, cardiac CT allows visualization of the anatomic regurgitant orifice area. This area can be seen as central valvular leakage area, reflecting an incomplete co-adaption of cusps (**Fig. 16.5**), by selecting end-diastolic CT datasets, which are usually reconstructed

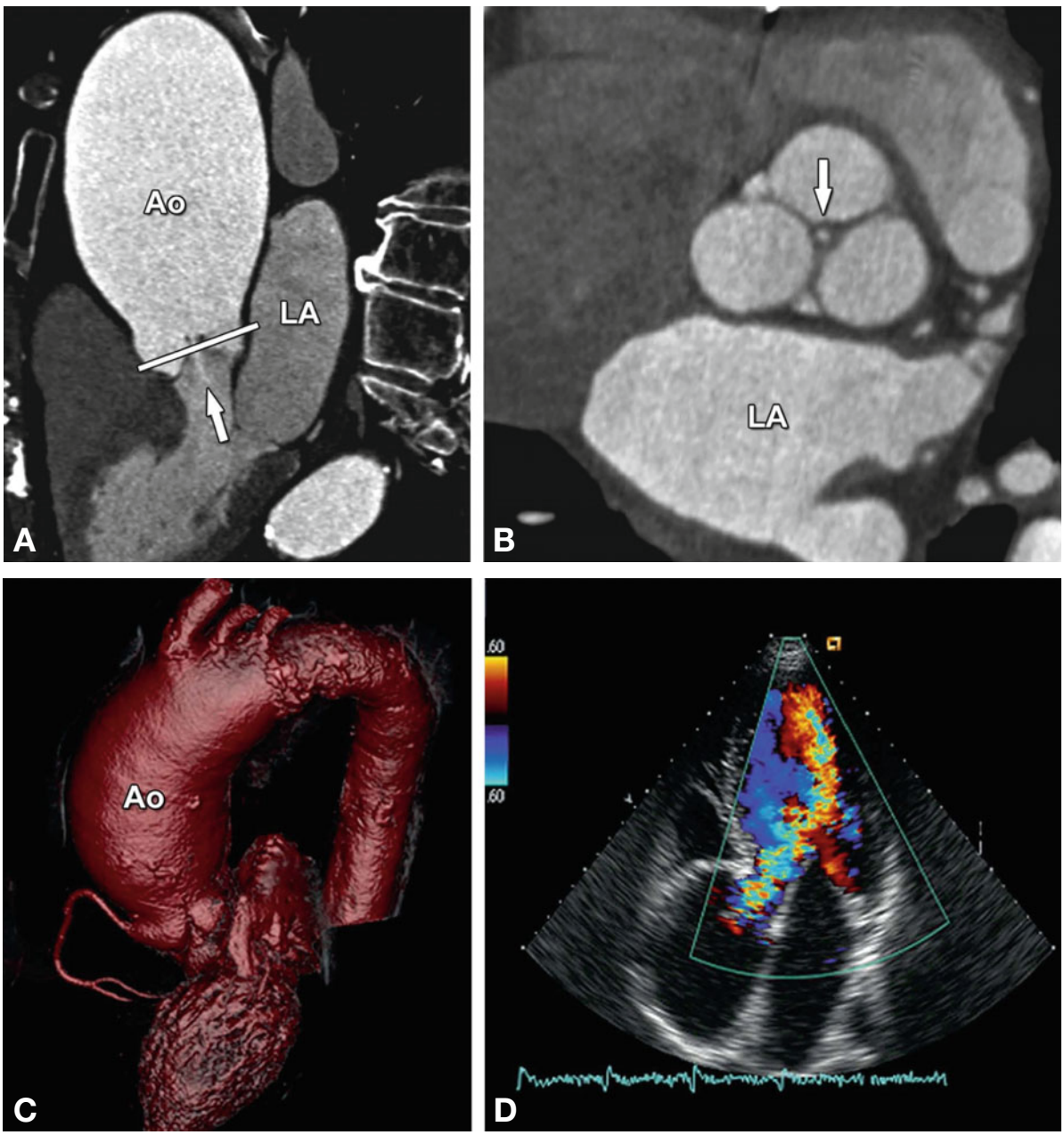

Fig. 16.5 Aortic regurgitation due to ascending aortic (*Ao*) aneurysm. The three-chamber view (**Panel A**) shows incomplete closure of the aortic leaflets during diastole with a regurgitant jet downstream into the left ventricular outflow tract (*arrow*). The *white line* in **Panel A** indicates the position of the cross-section through the aortic root (**Panel B**). This cross-section shows central valvular leakage (*arrow*, aortic regurgitant orifice area). The ascending aortic aneurysm is shown in a three-dimensional volume rendering in (**Panel C**) and the corresponding echocardiography (**Panel D**) shows a Doppler regurgitation jet ("vena contracts") towards the left atrium. *LA* left atrium

for coronary CT angiography. The regurgitant orifice area is a reliable diagnostic criterion for identifying aortic regurgitation. Several studies demonstrated the ability of CT to detect moderate and severe aortic regurgitation. Mild aortic regurgitation can be missed in the presence of dense valvular calcification or in patients with bicuspid valves. Contradictory data are available regarding the accuracy of CT in grading the severity of aortic regurgitation. One study mostly including patients with prevailing aortic root dilatation and rather mildly calcified valves, found a good performance of CT in differentiating moderate (cut-off: regurgitant orifice area >25 mm^2) and severe aortic regurgitation (cut-off: regurgitant orifice area >75 mm^2). Other studies recruited mainly patients with degenerative valve disease and observed a limited accuracy of CT in distinguishing the degrees of aortic regurgitation based on the regurgitant orifice area. Besides measurement of the regurgitant orifice area, newly introduced software modules enable right and left ventricular volume segmentation, hence they may provide a quantification tool for functional calculation of the aortic regurgitation fraction and volume, based on right and left stroke volume mismatch.

Preoperative triage is an important clinical application of cardiac CT in patients with aortic regurgitation. CT allows differentiation between bicuspid and tricuspid valve morphology and offers the advantage of simultaneous, accurate sizing of the aortic root and the ascending aorta as well as the evaluation of coronary arteries and left ventricular function within one scan.

The aortic valve should be evaluated in all patients undergoing CT angiography for possible concomitant underlying aortic regurgitation, in particular if no recent echocardiography exam was performed. In case of a visible regurgitation on CT, the patients should be further evaluated with echocardiography.

To summarize, echocardiography is the modality of choice for diagnosis and accurate graduation of severity of AR, however AR can be visualized by CT as well but CT does not allow flow measurement to-date.

16.3.5 Mitral Stenosis

The prevailing etiology of mitral stenosis is rheumatic disease, leading to leaflet thickening and structural degeneration of the valve apparatus including the chordae and causing obstruction of left ventricular inflow. Echocardiography is the imaging method of choice for grading mitral stenosis. Evaluation encompasses a combination of transvalvular pressure gradients, pulmonary artery systolic pressure, and an assessment of the mitral valve orifice area for differentiating between mild, moderate, and severe stages of disease. Mitral valve stenosis is regarded as significant if the mitral orifice area is less than 1 cm^2/m^2 body surface area. Only one study has assessed the value of CT in mitral stenosis, showing good correlation of planimetric measurement of the mitral valve orifice area (**Fig. 16.6**) with those obtained from

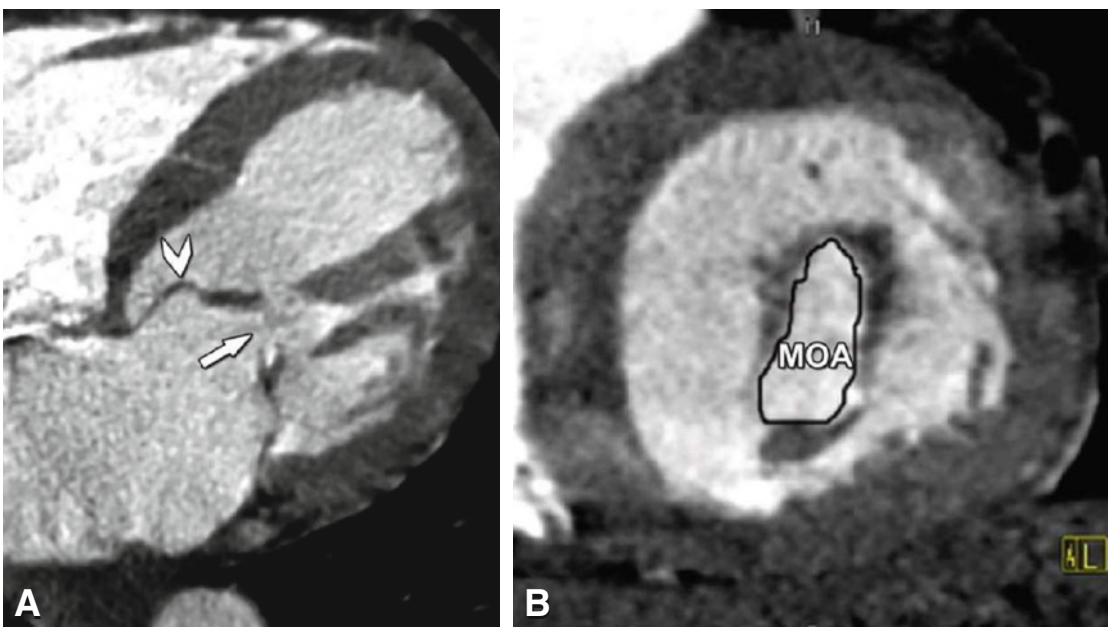

Fig. 16.6 Mitral stenosis with a four-chamber view (**Panel A**) showing the stenotic mitral valve orifice (*arrow*) and doming of anterior leaflet (*arrowhead*). The short-axis view of the left ventricle (**Panel B**) at the level of the mitral valve during diastole allows quantification of the mitral orifice area (*MOA*)

transesophageal echocardiography. Doming of mitral leaflets (**Fig. 16.6A**) is a further very typical imaging finding in mitral stenosis.

Left atrial dilatation, subsequently inducing atrial fibrillation, is common in advanced mitral stenosis. Hence, left atrial appendage thrombus, is a typical result. Importantly, cardiac CT allows accurate exclusion of left atrial thrombus. Care needs to be taken when filling defects are seen in the left atrial appendage, since these may represent either spontaneous echo contrast or artificial lack of contrast agent due to incomplete filling. A transesophageal echocardiography exam or a late-phase CT is required in case of uncertainty.

16.3.6 Mitral Regurgitation

The etiology of mitral regurgitation is variable. Mitral regurgitation may develop as a primary condition, such as in the course of rheumatic, degenerative or infectious disease, but also secondary to mitral annulus dilatation in ischemic or nonischemic cardiomyopathy. Another underlying disease is classic mitral valve prolapse. One study employed the potential of CT to quantify the degree of mitral regurgitation and showed good correlation of planimetric measurement of the regurgitant orifice area at CT with both echocardiography and ventriculography. However, an overlap between the different grades of mitral regurgitation as determined with CT was found. Thus, given few scientific data, accurate identification and quantification of the disease with CT seems not feasible at this time.

16.3.7 Mitral Annular Calcification

However, CT provides a valuable imaging modality for clarifying valvular morphology and masses that are unclear on echocardiography. Mitral annular calcification is a degenerative process, which typically shows slow circular progression from an initial U-shape or J-shape to O-shape in end-stage disease. On occasion, these calcifications appear mass-like with a mass effect, typically protruding into the adjacent myocardium from the base of the annulus (**Fig. 16.7**). A special subtype of mitral annular calcification is mitral caseous calcification,

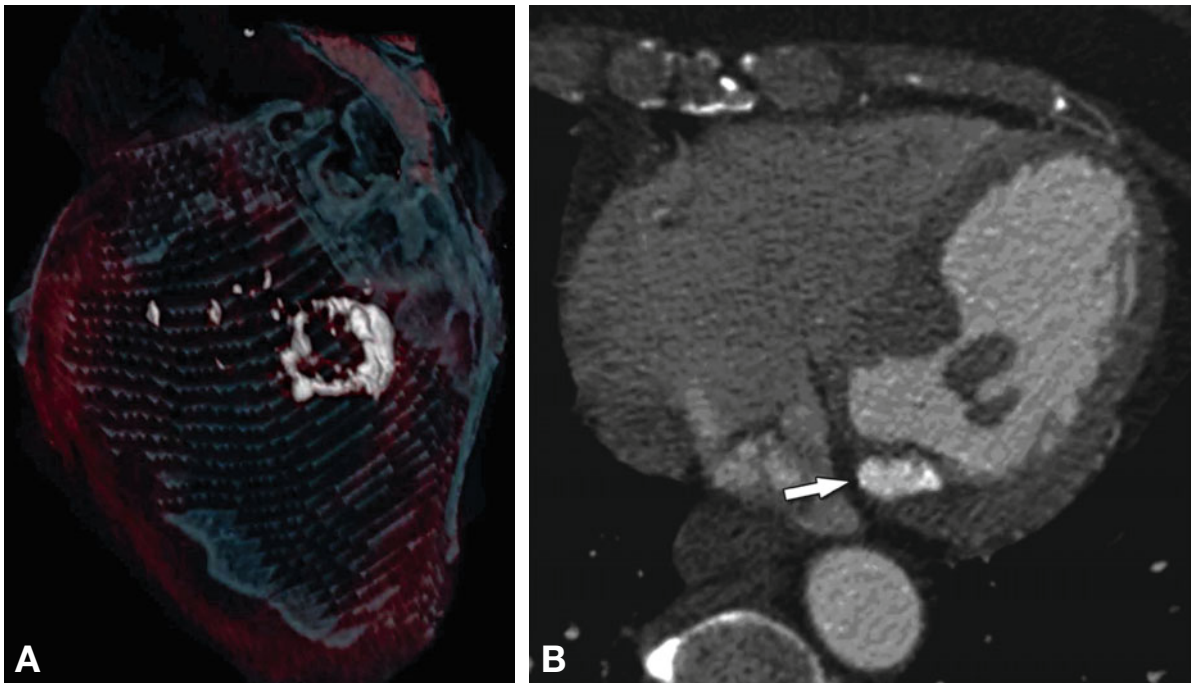

Fig. 16.7 Mitral annular calcification. Such an annulus calcification typically originates from the base of the annulus (U-shape) and progresses upstream in a circular fashion until involving the entire annulus, finally forming an O-shape (**Panel A**, three-dimensional reconstruction). Ovoid calcified mass (*arrow* in **Panel B**) at the base of the mitral annulus, which can mimic a fibrous mass on echocardiography. CT can help to clarify the exclusively calcific nature. Mitral annular calcification may serve as a marker for other cardiac structural abnormalities such as mitral regurgitation

which typically presents as a central echolucent mass on echocardiography which can be difficult to distinguish from other tumors. With cardiac CT, the diagnosis of mitral annular calcification can be easily established or confirmed based on a prevailing calcific component (**Fig. 16.7B**).

16.3.8 Mitral Valve Prolapse

Mitral valve prolapse is defined as systolic displacement of mitral valve leaflets below the mitral annulus plane (**Fig. 16.8**). The prevalence is 2.3% in the general population. There are two types of prolapsed. The first, *billowing*, (bowing of the leaflet), typically develops in the course of myxomatous degeneration and thickening due to redundant leaflets with increased thickness (>2–5 mm). A mid-systolic click murmur is characteristic.

In contrast, a *flail leaflet* (=free leaflet edge prolapse) is a result of chordal rupture, e.g., in the presence of rheumatic disease, infective endocarditis, or rarely of trauma or myocardial infarction, which is not necessarily associated with concomitant leaflet thickening. In general, a mitral leaflet is regarded as thickened if it measures more than 2 mm during diastole.

Transthoracic echocardiography is the reference method to establish the diagnosis of mitral valve prolapse. Three-dimensional transesophageal echocardiography is used for detailed preoperative characterization of the extent of involvement if surgical mitral reconstruction is planned. A recent study has shown that CT allows accurate diagnosis of prolapse, if three-chamber and two-chamber views reconstructed during systole are used in combination. The criterion used for definite diagnosis of mitral valve prolapse is leaflet displacement of more than 2 mm below the mitral annulus. However, the saddle-shape of the mitral valve leads to overestimation of the extent of prolapse on four-chamber views on CT, similar to echocardiography.

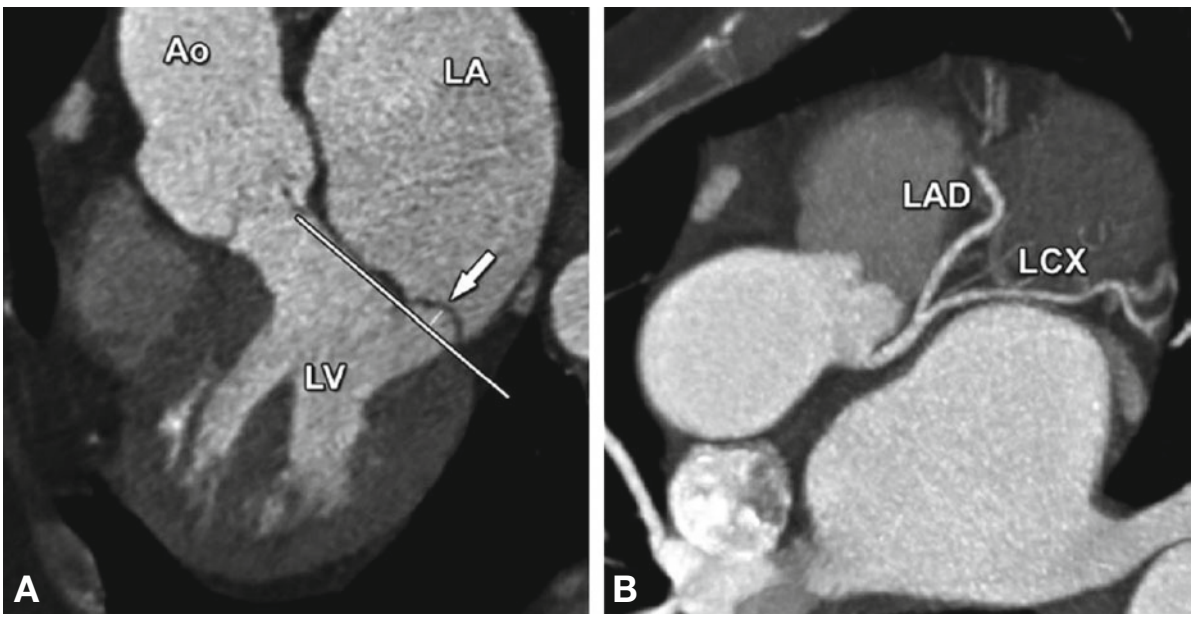

Fig. 16.8 Mitral valve prolapse. Billowing (=bowing) of posterior leaflet (*arrow*) below the annulus plane (*white line*) on a three-chamber view (**Panel A**). Note myxomatous thickening of anterior leaflet without prolapse (**Panel A**). The mitral valve is closed during systole. In this patient, also coronary artery disease could be excluded (**Panel B**). Note normal left anterior descending coronary artery (*LAD*) and left circumflex coronary artery (*LCX*). *Ao* ascending aorta, *LA* left atrium, *LV* left ventricle

16.3.9 Infective Endocarditis

Valvular involvement is most commonly found in infective endocarditits, however, the entire endocardium can become involved in inflammation. Notably, intracardiac devices such as prosthetic valves, pacemaker leads, or atrial septal defect occluders are prone to infections and subsequently, vegetations, which appear as masses attached to those devices. These infected masses must be distinguished from thrombi and pannus. A differentiation cannot always be made based on imaging findings stand-alone; and laboratory parameters are needed as evidence of infection.

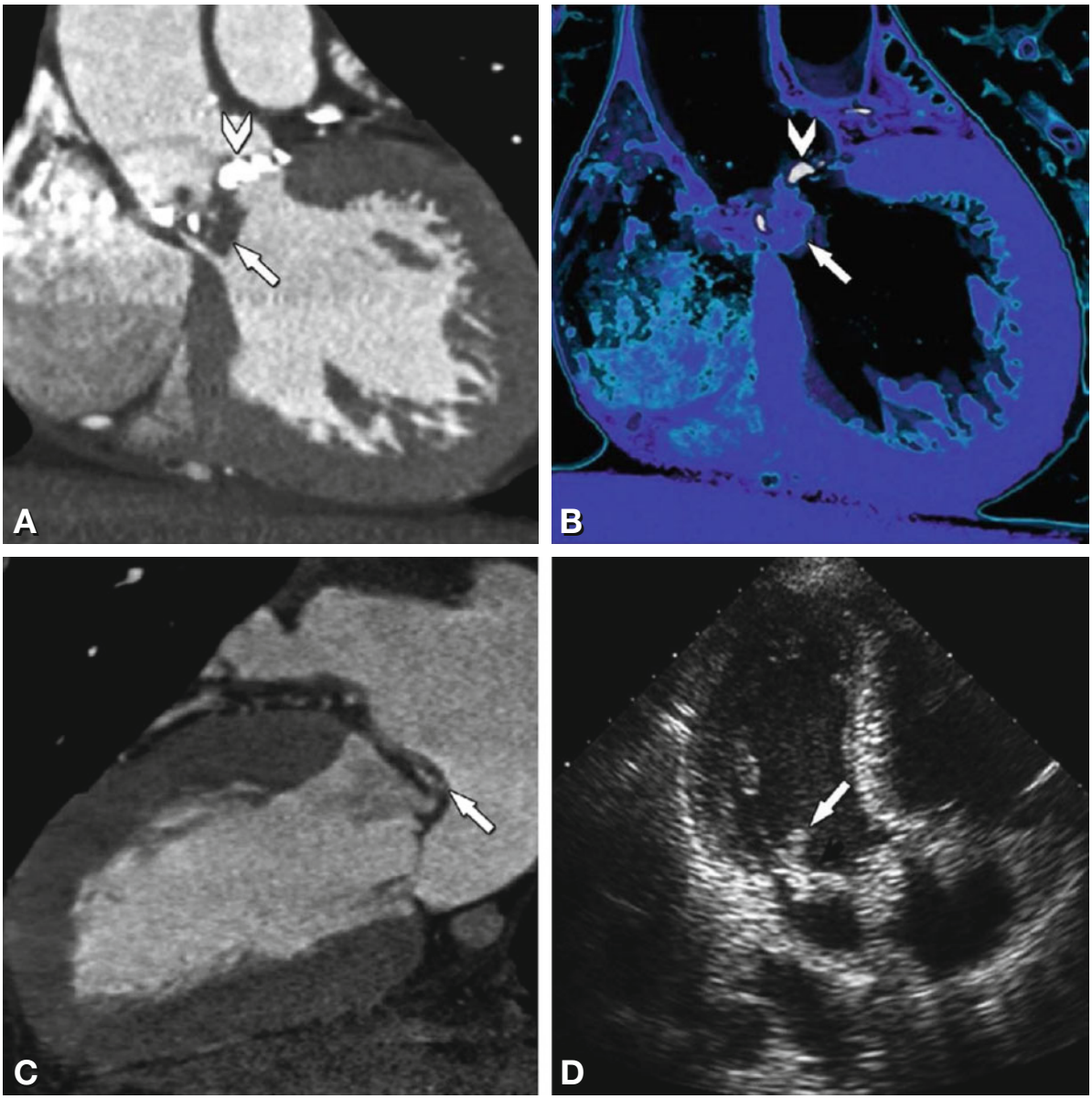

Fig. 16.9 Two examples of infective endocarditis. Aortic valve vegetation (**Panels A** and **B**, left coronal oblique view) that is hypodense and prolapses into the left ventricular outflow tract (*arrow*). Note calcified spots on the aortic valve, which can be clearly distinguished from the vegetation (*arrowhead* in **Panels A** and **B**). Mitral leaflet perforation and vegetation in another patient (*arrow* in **Panel C**) with contrast agent between the split two layers of thickened leaflets in a two-chamber view. The corresponding echocardiography with the mitral valve vegetation (*arrow*) is shown in **Panel D**

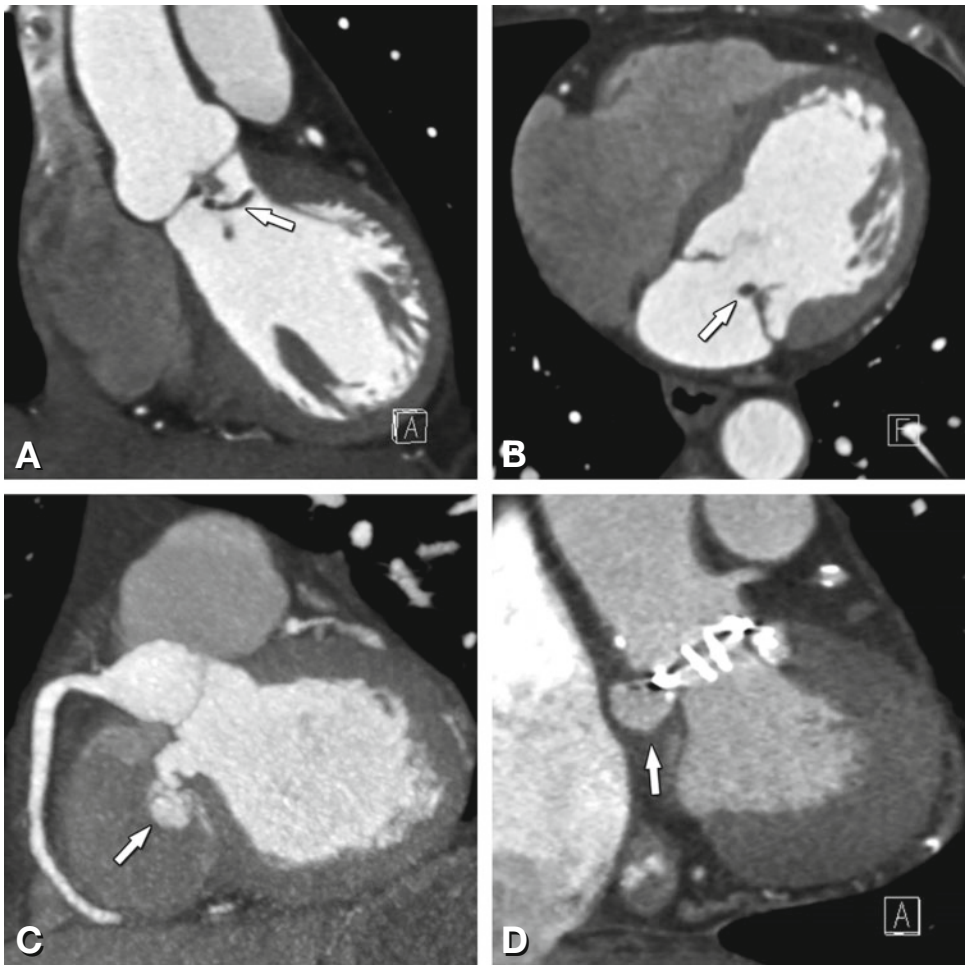

Fig. 16.10 Further examples of infective endocarditis in three different patients who all had clinical signs of infection with fever and elevated C-reactive protein. Mobile aortic valve vegetation floating into the left ventricular outflow tract (**Panel A**, left coronal oblique view, *arrow*) and a mitral valve vegetation on the posterior cusp that is hypodense and round (**Panel B**, four-chamber view, *arrow*). Fistula between the right and left ventricle with contrast agent filled space (*arrow* in **Panel C**). Paravalvular aneurysm of the aortic root and surrounding in a third patient with a mechanic aortic valve prosthesis abscess (*arrow* in **Panel D**)

Imaging findings are the key to establishing the diagnosis of infective endocarditis according to the modified Duke criteria, besides clinical parameters such as positive blood culture and signs of infections (major/minor criteria). Transesophageal echocardiography is the current reference method to assess imaging findings. Typical imaging findings are shown in **Figs.** 16.9 and 16.10 and recommendations for image reformation are summarized in **Table** 16.3. The most common imaging findings are vegetations, defined as hypodense irregular masses (**Figs.** 16.9A and 16.10A), typically located on the "downside" on the valve (thus floating into the left ventricular outflow tract in case of aortic valve involvement; or floating into the left atrium if mitral valve involvement). Their size ranges from few mm up to 1 cm and above. They can be mobile and non-mobile. Sometimes, vegetations appear as round-shaped (**Figs.** 16.9B and 16.10B) masses.

Exact morphological evaluation of vegetations and sizing defines further management of patients: small (<1 cm) and nonmobile lesions, without paravalvular involvement, can be treated conventionally with medication while cardiac surgery is rather considered for larger and mobile lesions. Importantly, vegetations may result in valve dysfunction, most frequently regurgitation, with a severity ranging from mild up to severe. Also, valvular stenosis may develop as a result of dense vegations narrowing the valve orifice.

Table 16.3 CT Imaging findings in infective endocarditis

CT findings	
Vegetations	Hypodense (~30 HU) soft tissue masses Varying in size and shape, ranging from well-defined masses (typically round, ovoid, or pedunculated) to rather diffuse irregular leaflet thickening
Cusp perforation	Discontinuation in cusps (= contrast agent between cusps)
Paravalvular involvement	
Abscess	Loss of perivascular/periaortic fatty tissue and diffuse infiltration (>0 HU, ca. 10–50 HU)
Aneurysm	Cavity filled with contrast agent
Valvular regurgitation	
Aortic	Incomplete closure of cusps during diastole
Mitral	Incomplete closure of cusps during systole
Fistula	Communication between chambers or extracardiac vascular system (e.g., aorta)
Dehiscence (prosthetic valve)	Displacement >5° above annulus plane

MPR multiplanar reformation, *VRT* volume rendering technique, *CH* chamber, *LV* left ventricle, *LVOT* left ventricular outflow tract, *SA* short axis

Further imaging findings in infective endocarditis include cusp perforation, defined as a discontinuation in cusps; or fistula, defined as a communication between cardiac chambers and/or the aortic root. These fistula may lead e.g. to a continuation between the left and right chamber (**Fig. 16.10C**), visualized as a contrast agent filled channel. Similarly, paravalvular pseudoaneurysm are a results of extensive inflammatory involvement. Pseudoaneurysms are typically found near the aortic valve annular plane, or the mitral valve annulus. On cardiac CT, pseudoaneuryms appear as contrast agent filled lesions. They are seen both in native valves or after prosthetic valve implantation as a result of chronic or acute severe inflammation. In case of acute inflammation, abscess may surround the pseudoaneuryms (**Fig. 16.10D**). Abscess is defined as paravalvular or periaortic root fluid-like infiltration or accumulation of fluid (**Fig. 16.10D**). Often, the aortic root perivascular fatty tissue is infiltrated thus loosening of periaortic root fatty tissue is seen and the HU increase above 0 (range, 0–30).

CT allows imaging of valvular abnormalities and extravalvular involvement in infective endocarditis. Its advantage is the differentiation between calcifying and soft-tissue masses, which can be difficult on echocardiography. Hence, CT can help to clarify uncertain echocardiography findings, in particular in patients with equivocal or contradicting clinical findings. Moreover, the main advantage of CT in those patients is comprehensive evaluation of coronary arteries before surgery. Thus, conventional coronary angiography, with the risk of embolization originating from valvular vegetations, may be avoided.

16.4 Prosthetic Valves

There are two different prosthetic valve types: mechanical and bioprosthetic valves. The St. Jude bileaflet mechanical valve (**Fig. 16.11**) is currently the most commonly implanted type. Cardiac CT allows dynamic four- dimensional cine imaging of leaflet motion. Thus, CT can assist echocardiography in defining the cause of prosthetic valve dysfunction such as broken metallic leaflets, or stuck valves. Masses attached to a prosthetic valve can represent either thrombus or pannus (=chronic organized thrombus) or vegetations in case of clinical signs of infection. While a thrombus is per-definition hypodense without iodine contrast agent uptake (approx 30–60 HU), a pannus may uptake contrast agent on a delayed scan (minimum >70 s post injection or longer).

Another type of dysfunction is dehiscence, a loose connection between the prosthesis and the annulus (**Table 16.3**). Paravalvular leakage and regurgitation can occur after prosthetic valve implantation, which may need intervention depending on severity of backflow. In contrast, bioprosthetic valves may tend to slowly develop structural degeneration over time, leading to leaflet thickening, calcification, and destruction of leaflets and the apparatus. Paravalvular leakage may occur as a result of a disconnection between the prosthesis and the annulus (=dehiscence or suture loosening).

Prosthesis mismatch, (= sizing mismatch of the device in relation to the annulus/aortic root) may also lead to prosthetic valve dysfunction. A “stuck-valve” is diagnosed if a mechanic leaflet does not open

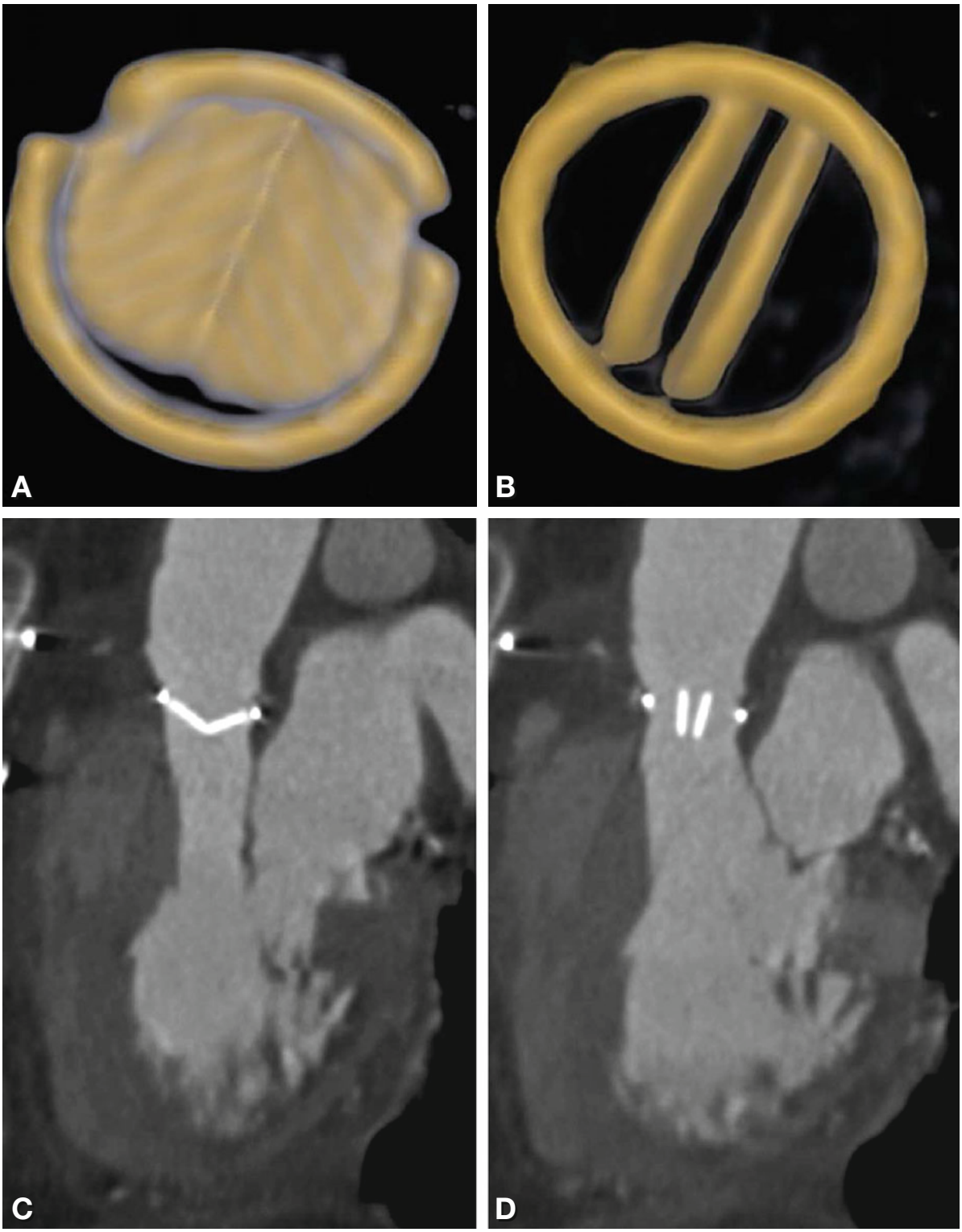

Fig. 16.11 Mechanical aortic prosthetic valve (bileaflet type, St. Jude). Closed valve during end-diastole (**Panels A** and **C**) and opened valve during systole (**Panels B** and **D**). Data are displayed using volume rendering (**Panels A** and **C**) and multiplanar reformations in the three-chamber view (**Panels C** and **D**)

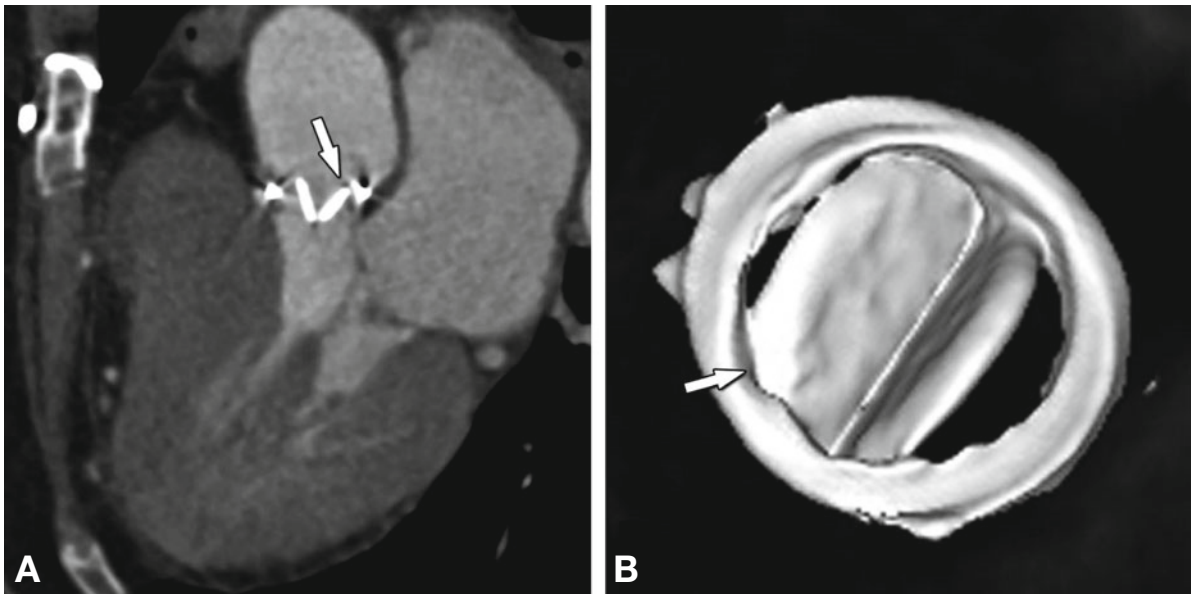

Fig. 16.12 Prosthetic valve dysfunction also called "stuck valve". The posterior mechanic leaflet of this St. Jude bileaflet mechanic valve prosthesis in the aortic position in a 49-year-old female patient does not open (*arrow*) appropriately during systole due to prosthesis-mismatch in relation to the patients aortic root size. **Panel A**, multiplanar reformation, three-chamber view, and **Panel B**, volume rendering view from above, show that the posterior leaflet does not open appropriately (*arrow*)

appropriately (**Fig. 16.12**) during systole. The reason may be thrombi, vegetations or pannus obstructing the device, but also prosthesis mismatch.

The detection rate of mechanical aortic valve dysfunction is low with ~51% by echocardiography, because metal artifacts hamper image quality. CT has shown to be a superior and valuable imaging modality in patients with suspected prosthetic valve dysfunction, particularly in prosthesis that induce may artifacts during echocardiography. Scientific data suggest that the diagnostic performance of CT may be better than that of echocardiography. Thus, CT may be considered as an additional modality in case of uncertain echocardiography findings in patients with suspected prosthetic valve dysfunction or infection. Further a combined 18FDG-PET/CT is useful to either reject or establish definite diagnosis of prosthetic valve infection.

To summarize, aortic valve disease is currently considered the main use of CT in the context of valvular disease. New promising clinical applications of cardiac CT include infective endocarditis, prosthetic valves, and the implementation of CT for planning of minimally invasive surgical or transcatheter valvular interventions.

Recommended Reading

Alkadhi H, Desbiolles L, Husmann L et al (2007) Aortic regurgitation: assessment with 64-Section CT. Radiology 245:111–121

Alkahdi H, Bettex D, Wildermuth S et al (2005) Dynamic cine imaging of the mitral valve with 16-MDCT: a feasibility study. AJR Am J Roentgenol 185:636–646

Bonow RO, Carabello BA, Chatterjee K et al (2006) ACC/AHA 2006 guidelines for the management of patients with valvular heart disease. J Am Coll Cardiol 48:e1–e148

Bouvier E, Logeart D, Sablayrolles JL et al (2006) Diagnosis of aortic valvular stenosis by multislice cardiac computed tomography. Eur Heart J 27:3033–3038

Dewey M, Müller M, Eddicks S et al (2006) Evaluation of global and regional left ventricular function with 16-slice computed tomography, biplane cineventriculography, and two-dimensional transthoracic echocardiography: comparison with magnetic resonance imaging. J Am Coll Cardiol 48:2034–2044

Feuchtner GM (2009) The utility of computed tomography in the context of aortic valve disease. Int J Cardiovasc Imaging 25:611–614

Feuchtner GM, Dichtl W, Friedrich GJ et al (2006) Multislice computed tomography for detection of patients with aortic valve stenosis and quantification of severity. J Am Coll Cardiol 47:1410–1417

Feuchtner GM, Dichtl W, Müller S et al (2008) 64-MDCT for diagnosis of aortic regurgitation in patients referred to CT coronary angiography. Am J Roentgenol 191:W1–W7

Recommended Reading

Feuchtner GM, Stolzmann P, Dichtl W et al (2009) Multislice computed tomography in infective endocarditis: comparison with transesophageal echocardiography and intraoperative findings. J Am Coll Cardiol 53:436–444

Feuchtner G, Alkadhi H, Karlo C et al (2010) Cardiac CT angiography for the diagnosis of mitral valve prolapse: comparison with echocardiography. Radiology 254:374–383

Habets J, Mali WP, Budde RP (2012) Multidetector CT angiography in evaluation of prosthetic heart valve dysfunction. Radiographics 32(7):1893–1905

Kim YY, Klein AL, Halliburton SS et al (2007) Left atrial appendage filling defects identified by multidetector computed tomography in patients undergoing radiofrequency pulmonary vein antral isolation: a comparison with transesophageal echocardiography. Am Heart J 154:1199–1205

Konen E, Goitein O, Feinberg MS et al (2008) The role of ECG-gated MDCT in the evaluation of aortic and mitral mechanical valves: initial experience. Am J Roentgenol 191:26–31

Lee AM, Beaudoin J, Thai WE, Wai B, Hui GC, Sidhu MS, Engel LC, Abbara S, Hoffmann U, Ghoshhajra BB (2013) Feasibility of aortic valve assessment with low dose prospectively triggered adaptive systolic (PTAS) cardiac computed tomography angiography. BMC Res Notes 6(1):158

Meijboom WB, Mollet NR, Van Mieghem CA et al (2006) Preoperative computed tomography coronary angiography to detect significant coronary artery disease in patients referred for cardiac valve surgery. J Am Coll Cardiol 48:1658–1665

Messika-Zeitoun D, Aubry MC, Detaint D et al (2004) Evaluation and clinical implications of aortic valve calcification measured by electron-beam computed tomography. Circulation 110:356–362

Messika-Zeitoun D, Serfaty JM, Laissy JP et al (2006) Assessment of the mitral valve area in patients with mitral stenosis by multislice computed tomography. J Am Coll Cardiol 48:411–413

Pouleur AC, le Polain de Waroux JB et al (2007) Aortic valve area assessment: multidetector CT compared with cine MR imaging and transthoracic and transesophageal echocardiography. Radiology 244:745–754

Saby L, Laas O, Habib G, Cammilleri S, Mancini J, Tessonnier L, Casalta JP, Gouriet F, Riberi A, Avierinos JF, Collart F, Mundler O, Raoult D, Thuny F (2013) Positron emission tomography/computed tomography for diagnosis of prosthetic valve endocarditis: increased valvular (18)F-fluorodeoxyglucose uptake as a novel major criterion. J Am Coll Cardiol 61(23):2374–2382

Shah RG, Novaro GM, Blandon RJ et al (2009) Aortic valve area: meta-analysis of diagnostic performance of multi-detector computed tomography for aortic valve area measurements as compared to transthoracic echocardiography. Int J Cardiovasc Imaging 25:601–609

Tops LF, Wood DA, Delgado V et al (2008) Noninvasive evaluation of the aortic root with multislice computed tomography implications for transcatheter aortic valve replacement. JACC Cardiovasc Imaging 1:321–330

Tsai IC, Lin YK, Chang Y et al (2009) Correctness of multi-detector-row computed tomography for diagnosing mechanical prosthetic heart valve disorders using operative findings as a gold standard. Eur Radiol 19:857–867

Transcatheter Aortic Valve Interventions

F. Plank, J.N. Dacher, G. Feuchtner, and J. Leipsic

Abstract

This chapter outlines the challenges of planning transcatheter aortic valve implantation (TAVI) and novel CT applications for optimizing patient outcome.

17.1 Clinical Background

Severe aortic stenosis is a common valve disease with increasing prevalence in an aging population. Conservative treatment has a poor prognosis, particularly in patients who are symptomatic (Chap. 16). Surgical aortic valve replacement is currently the standard of care; however, elderly patients with multiple comorbidities are often not suitable for conventional open-heart surgery, and it is estimated that up to 40% of patients are declined or refuse surgery. Since the advent of transcatheter aortic valve implantation (TAVI) in 2002, improvements in device technology and procedural management have resulted in high procedural success rates with fewer major complications to the point where TAVI has become the standard of care for inoperable and selected high-risk surgical patients.

The Placement of Aortic Transcatheter Valves (PARTNER) randomized controlled trials have found a strong survival benefit of TAVI over medical therapy in inoperable patients. Only four patients need to be treated with TAVI to save one life at 2 years (all-cause mortality of 67.6% in the medical arm vs. 43.3% in the TAVI arm). In addition, TAVI has been proven to be noninferior to surgical aortic valve replacement in high-risk patients with regard to all-cause mortality (33.9% vs. 32.7%).

Two different transcatheter systems, for which extensive data on feasibility, safety, and outcome are available, are currently in use. Several large registries have demonstrated excellent short- and mid-term results for both the Edwards SAPIEN and the Medtronic CoreValve (**Figs.** 17.1 and 17.2).

The balloon-expandable Edwards SAPIEN valve can be implanted using a transfemoral, transapical, or transaortic access, and the self-expanding Medtronic CoreValve is available for transfemoral, transaxillar, and transaortic access routes. Both devices utilize similar low-profile delivery systems and can be implanted in a conventional catheterization laboratory under fluoroscopic guidance. The different device sizes and delivery system specifications are outlined in **Table** 17.1.

M. Dewey, *Cardiac CT*,
DOI 10.1007/978-3-642-41883-9_20, © Springer-Verlag Berlin Heidelberg 2014

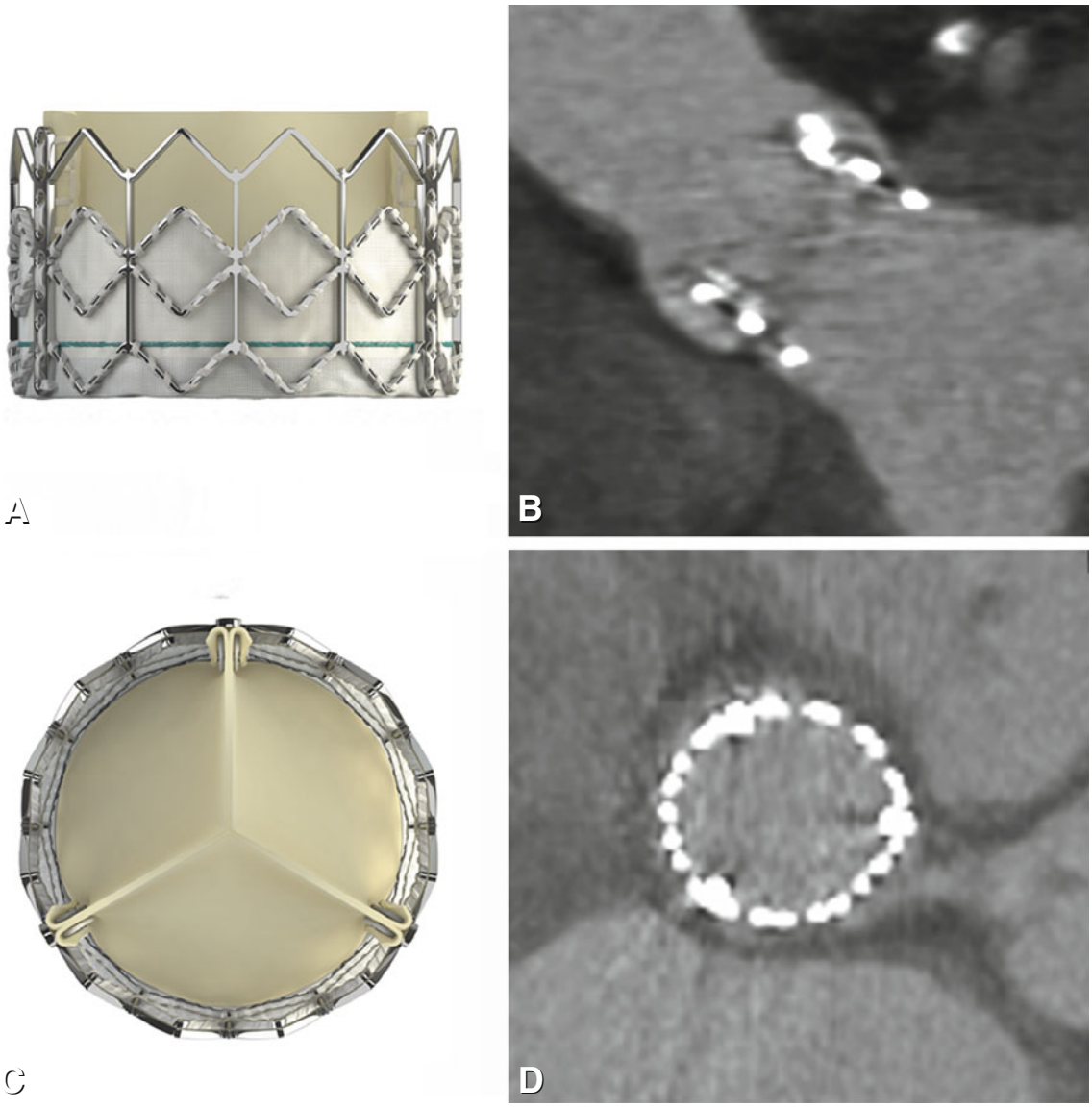

Fig. 17.1 Edwards SAPIEN (Edwards Lifesciences Corporation Irvine, CA). The balloon-expandable valve in a lateral view (**Panel A**) and the appearance on CT on a corresponding maximum intensity projection (**Panel B**) as well as on-top view (**Panel C**) and corresponding multiplanar reformation along the short axis from CT data (**Panel D**) (**Panels A** and **C** are reproduced with permission of Edwards Lifesciences)

Figures 17.1 and 17.2 show the currently used prostheses and their CT appearance. While the native annulus is directly visualized and sized in surgical replacement, TAVI relies exclusively on pre- and periprocedural imaging to size the aortic annulus for correct prosthesis selection. Therefore, precise preprocedural planning including sizing, access route selection based on individual anatomy and comorbidities, as well as three-dimensional evaluation of aortic annular structures are key to successful TAVI.

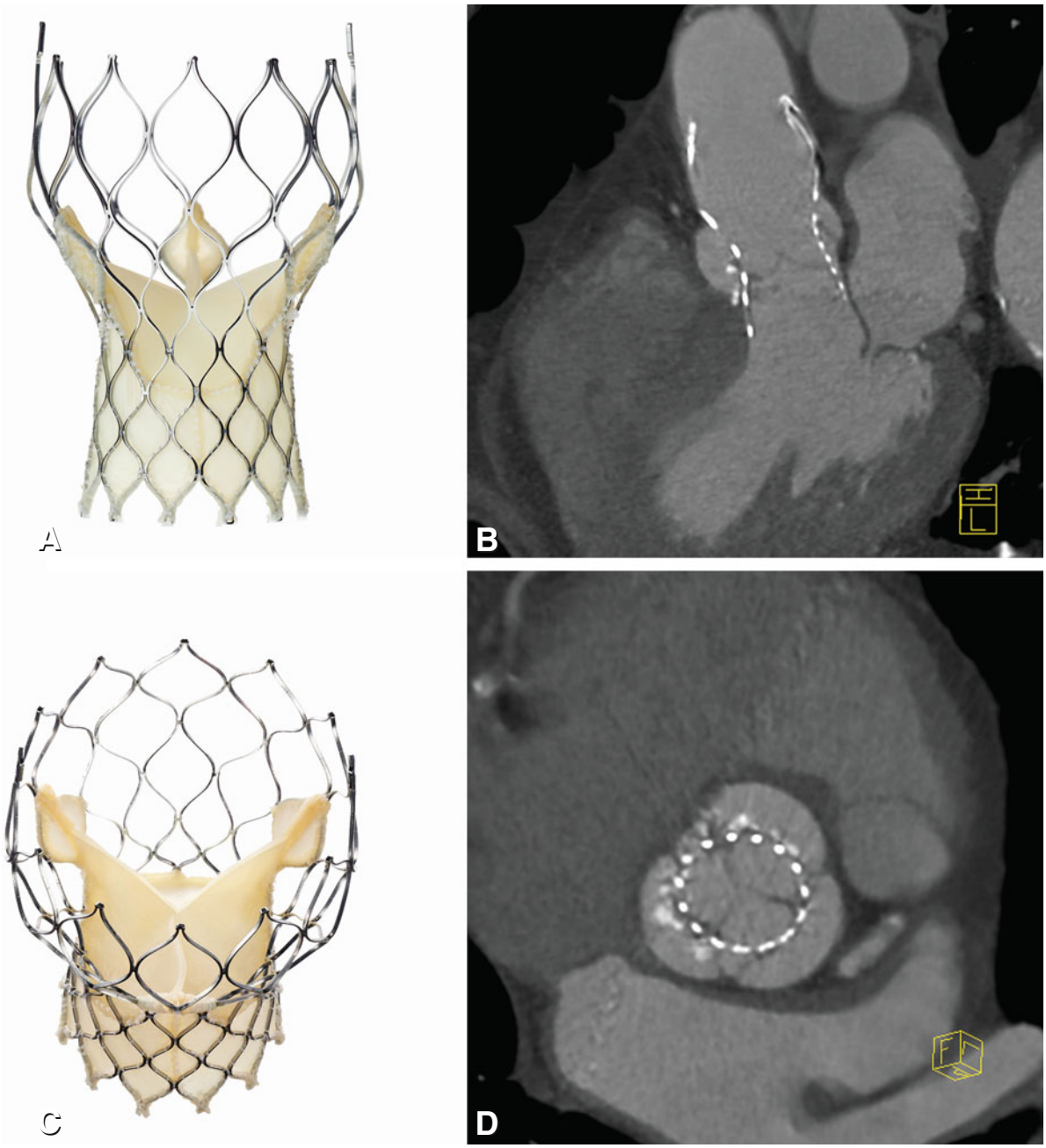

Fig. 17.2 Medtronic CoreValve (Medtronic, Minneapolis, Minnesota). The self-expandable valve on a lateral view (**Panel A**) and in CT (**Panel B**). **Panels C** and **D** show the CoreValve from above (**Panels A** and **C** are reproduced with permission of Medtronic)

Table 17.1 Characteristics of the available transcatheter devices

Device and valve size (mm)	Delivery system size (F)	Recommended vessel lumen diameter (mm)
Edwards Sapien transcatheter heart valve with Retroflex 3 delivery system		
23	22	≥7
26	24	≥8
Edwards Sapien XT Transcatheter heart valve with NovaFlex delivery system and eSheath		
23	16	≥6
26	18	≥6.5
29	20	≥7.0
Medtronic CoreValve revalving system		
26	18F	≥6
29	18F	≥6
31	18F	≥6

Current balloon-expandable (Edwards Sapien) and self-expanding (Medtronic CoreValve) devices are available in sizes ranging from 23 to 29 mm and 26 to 31 mm, respectively. External diameters of delivery catheters are given in F (French). Recommended minimal vessel diameters for each system to minimize vascular injury are also presented

17.2 Patient Preparation and CT Scan

Evaluation for TAVI is a crucial, high-risk, and complex process involving a multidisciplinary approach in the frail elderly candidates for this procedure. The overall preprocedural goals, according to a recent guideline by Bloomfield et al., are summarized in **List 17.1**.

17

List 17.1. Main goals of preprocedural CT evaluation

1. Ensure patient suitability for TAVI and the proposed access route
2. Ensure implantation safety and feasibility, based on the device characteristics and the anatomic relationships between the aortic valve, root, left ventricle (LV), and coronary ostia
3. Suggest appropriate valve size

Accurate planning to determine the best access route and vessel disposition is required. Transthoracic and/or transesophageal echocardiography is the cornerstone of evaluation of aortic stenosis severity including measurement of aortic stenosis jet velocity, mean transvalvular gradient, aortic valve orifice area, and left ventricular function. Echocardiography has also traditionally been the primary tool for measuring the aortic annulus diameter, which is required for selecting the transcatheter heart valve size. Two-dimensional echocardiography, however, has important limitations in assessing the complex noncircular configuration of the annulus (**Fig. 17.3**). As a matter of fact, transthoracic echocardiography is based on the assumption that the left ventricular outflow tract (LVOT) and annulus are circular structures.

Regarding the LVOT as a circular structure can lead to some error in assessing the severity of aortic stenosis. The echocardiographic diagnosis of aortic stenosis is based on the continuity equation, which has been shown to overestimate the stenosis (or underestimate the aortic valve area) compared with the 3D evaluation provided by CT.

In the context of TAVI, the transthoracic echocardiography measurement of annulus size (distance between the insertions of the leaflets at mid-systole on a parasternal long-axis view) does not reflect its real and variable elliptic shape. Furthermore, this plane does not transect the aortic annulus in its greatest diameter.

In addition, ultrasound cannot assess the vascular access for TAVI.

As a result, CT has become an important imaging modality for assessing the aortic root and aortoiliac arteries in terms of vessel size, tortuosity, degree of calcification, and plaque burden (**Fig. 17.4**).

Vessel assessment is important for including or excluding potential access routes. Retrograde access is possible via femoral or subclavian arteries or, as introduced recently, the ascending aorta through a right anterior minithoracotomy. The femoral artery has been established as the preferred retrograde access, while the antegrade route can be approached transapically in patients with significant iliofemoral disease (**Fig. 17.4C**). Early TAVI delivery systems required 22–24F sheaths to provide access for large valve systems and were associated with a high incidence of major vascular complications. Improved technology and procedural experience has led to current state-of-the art systems, which commonly employ 18F or smaller sheaths (**Table 17.1**) and have significantly lower rates of vascular injury.

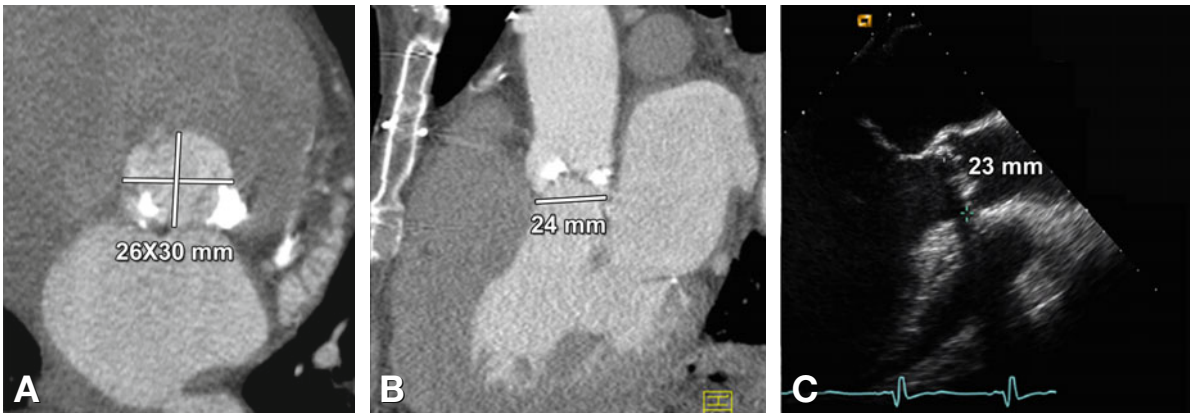

Fig. 17.3 Comparison of three- and two-dimensional annular assessment. Three-dimensional CT evaluation provides volumetric assessment of the annulus. Short-axis view along the annulus aligned at the lowest insertion (hinge) points of the aortic valve cusps (**Panel A**) allows accurate three-dimensional assessment of the dimensions by CT, whereas the three-chamber view (**Panel B**) provides a single measurement only. Transesophageal echocardiographic annulus measurement is also limited by the imaging direction available, which may not be in line with the longest diameter of the annulus (**Panel C**). After implantation of a 23-mm valve, this patient developed grade II paravalvular regurgitation as seen on echocardiography. Based on the CT measurements (**Panels A** and **B**), a larger valve would have been favored. This case illustrates the advantages of valve dimension assessment based on three-dimensional CT as compared with echocardiography alone

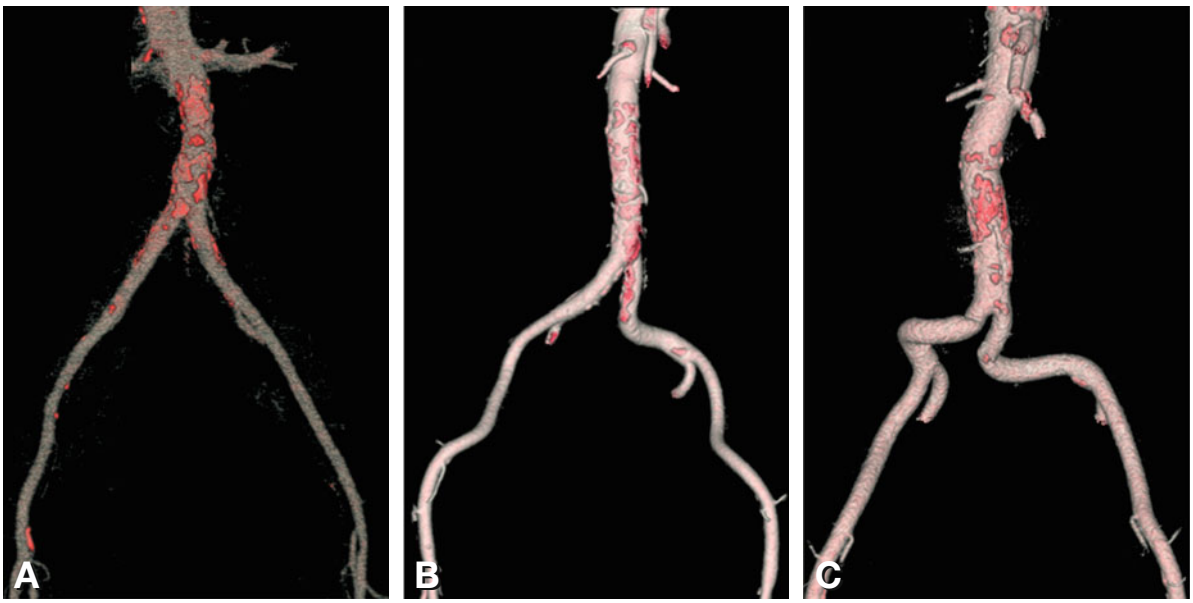

Fig. 17.4 Importance of obtaining pre-TAVI angiography images with CT (shown here are three-dimensional reconstructions of the abdominal aorta and the iliofemoral arteries in three patients). In **Panel A**, vessels are moderately calcified and completely straight. In **Panel B**, tortuosity is moderate. The femoral approach was used in both patients **Panel C** shows iliac artery sections with severe bilateral tortuosity, contraindicating a femoral retrograde approach. A transapical route was therefore chosen

To ensure accuracy, ECG synchronization (either prospective or retrospective) is obligatory for annular and root assessment; however, the vascular access can be evaluated without ECG gating.

For CT to be valuable in TAVI planning, high spatial resolution imaging must be employed for adequate evaluation especially of the aortic root and of the iliofemoral arteries. Image acquisition protocols vary and are very much dependent on the scanner platform used (Chap. 9). The chosen acquisition protocol must allow a reconstructed slice width of 1.0 mm or less throughout the imaging volume. While ECG gating is required for the aortic root to ensure motion suppression, it is not necessary for the imaging of the entire aorta and iliofemoral arteries. As a result, nongated acquisitions are preferred for abdominal and pelvic assessment to lower radiation exposure (owing to the higher helical pitch compared to retrospective ECG-gated techniques). Several protocols can be used, depending on the scanner platform available. When a wide-detector system is used, it is often possible to cover the entire volume with ECG gating. ECG-triggered high-pitch spiral acquisitions can also be helpful as they also allow the required Z-axis coverage to be obtained very rapidly. However, this often makes it difficult to specify the phase of the cardiac cycle in which the annulus is assessed, thus making sizing the annulus for transcatheter heart valve selection less reliable. With routine 64-row CT, it is often more appropriate to perform retrospective gating for the cardiac portion of the study and then to cover the remaining volume with a second nongated acquisition using the same contrast bolus. Recent data suggest that annular assessment in systole is preferable to diastole owing to the dynamic changes of the annulus and slightly larger annular sizes noted in systole. Based on the documented dynamic changes in annular dimensions throughout the cardiac cycle, we recommend systolic annular assessment between 25% and 35% of the cardiac cycle as it will modify transcatheter heart valve selection 15–20% of the time when compared with diastolic imaging. This requires an adequate image quality of the systolic annular images.

A tube voltage of 100 kV should be considered for patients weighing less than 90 kg or with a BMI less than 30 kg/m^2 (the vast majority of TAVI candidates); while a tube potential of 120 kV is usually indicated for the rare patients weighing more than 90 kg and with a BMI above 30 kg/m^2. While proposed for coronary CT angiography we have adopted these recommendations for TAVI assessment. Tube current selection is highly dependent on the CT platform as well as the chosen slice thickness. Tube current should be selected on the basis of patient size with the goal of using the lowest setting ensuring acceptable image noise properties.

Intravenous contrast medium is essential for pre-TAVI assessment. Contrast is needed for accurate access and annular evaluation. Since the patients are elderly and often have reduced kidney function, efforts should be made, if possible, to limit the amount of contrast agent used. One method of reducing contrast volume is to use lower flow rates than is typical for coronary CT angiography. Flow rates of 5 ml/s or greater are currently recommended for coronary CT angiography, while 3 ml/s or less can be adequate in selected patients for annular assessment prior to TAVI. This is still not the preferred contrast protocol but should be considered for patients with borderline renal function.

In order to understand the complex anatomy of the aortic valve and root, several key structures have to be assessed. **List 17.2** gives an overview.

List 17.2. Structures to be assessed for preprocedural planning

1. Aortic annulus for valve sizing
2. Coronary cusp length and degree of calcification
3. Coronary ostia heights
4. Identification of aberrant structures or anomalies (i.e., bicuspid valves)

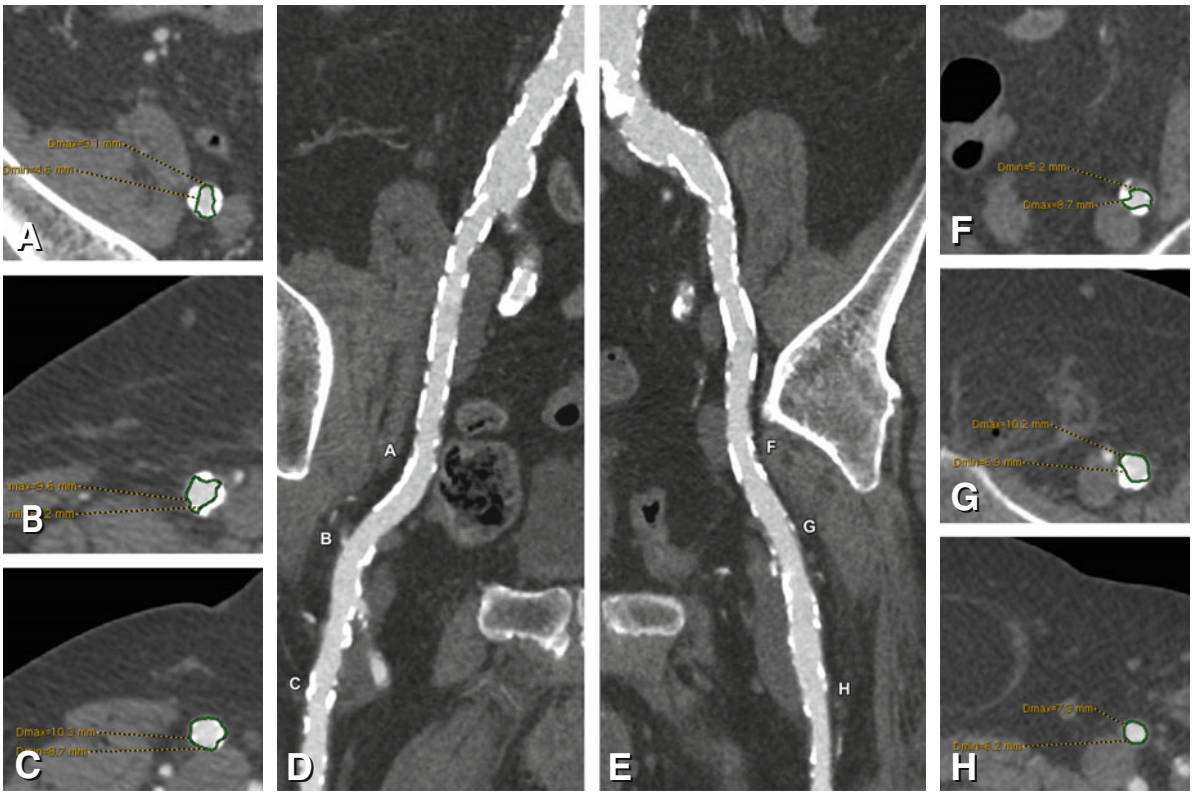

Fig. 17.5 Preprocedural CT assessment for transfemoral access in a 82-year-old male patient with severe aortic stenosis. The iliofemoral arteries are evaluated for stenosis using cross sections (**Panels A–C** and **Panels F–H**) that are orthogonal to curved multiplanar reformations (**Panels D** and **E**) along the right and left iliofemoral arteries. Automated software allows cross-sectional measurement of luminal dimensions (**Panels A–C** and **Panels F–H**). The letters *A–C* and *F–H* (**Panels D** and **E**) indicate the positions of the cross sections on the curved multiplanar reformations. With a minimal lumen diameter of 6 mm and the exclusion of severe kinking, this patient could undergo transfemoral TAVI

17.3 Evaluation

For optimal visualization of the aortoiliac arteries, three-dimensional assessment by CT is recommended (**Fig. 17.4**) and superior to that provided by conventional angiography. Multiplanar and curved multiplanar reformations as well as longitudinal and short-axis (orthogonal to the vessel centerline) cross-section reconstructions are strongly suggested to enable optimal visualization and accurate lumen measurements. These reformations allow comprehensive evaluation of diseased vessels and reduce the risk of stenosis misinterpretation due to tortuosity, artifact, or eccentric calcification (**Figs. 17.5** and **17.6**).

17.3.1 Aortic Annulus: Valve Sizing

Measurement of the aortic annulus dimensions is critical for the success of TAVI. Appropriate transcatheter heart valve selection is essential to reduce paravalvular regurgitation by avoiding undersizing while balancing against the potential risk of root injury from more extreme oversizing. Sizing has been done traditionally by

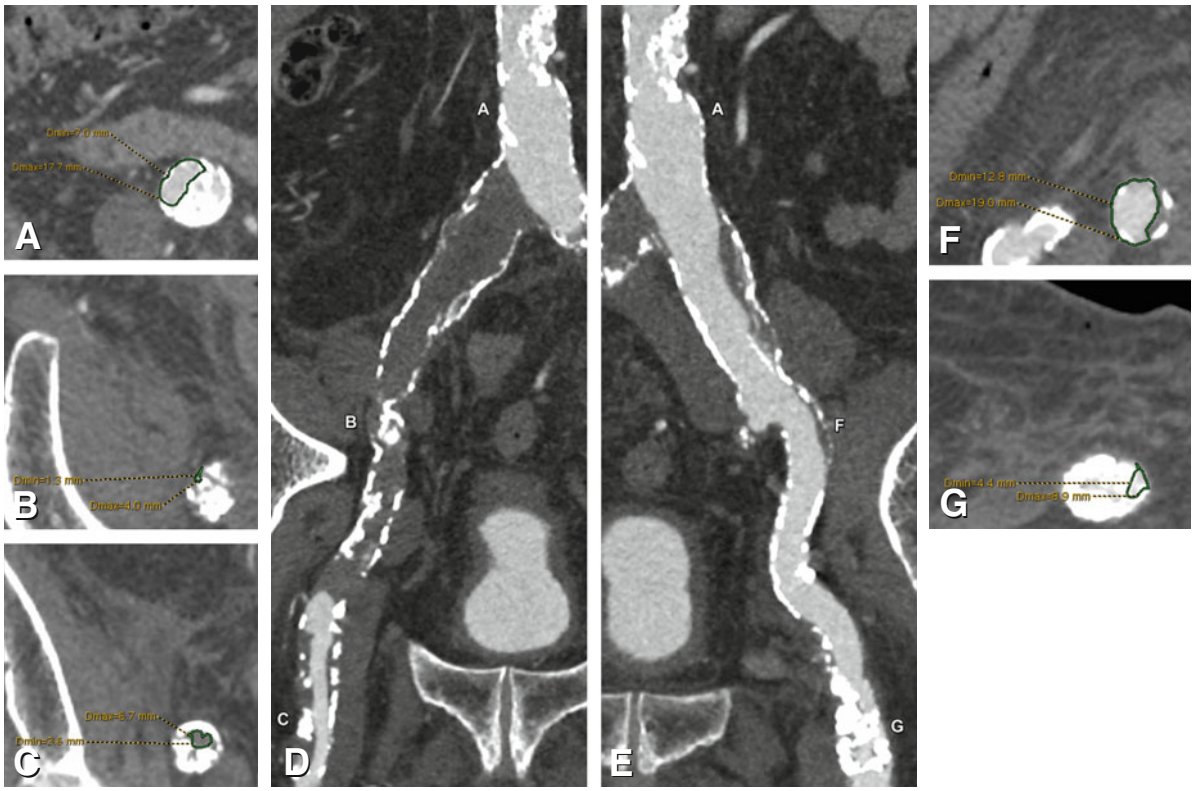

Fig. 17.6 Preprocedural CT assessment of an 80-year-old patient showing findings that precluded a transfemoral approach for TAVI. There was severe plaque burden of the iliofemoral arteries on cross sections (**Panels A**–**C** and **Panels F**–**G**) that were oriented orthogonal to curved multiplanar reformations (**Panel D** and **E**) along the right and left iliofemoral arteries. There was a high-grade stenosis of the abdominal aorta (**Panel A**), and CT also revealed a total occlusion of the right iliac artery (*arrow* in **Panels B** and **D**) with faint retrograde filling of the femoral vessels (**Panel C**). Cross-sectional views also show a subtotal occlusion of the left femoral artery (**Panel G**). Surprisingly, the patient did not suffer from reduced perfusion in his legs and had no related symptoms. The findings precluded a transfemoral access, and the patient underwent transapical TAVI

echocardiography, though several recent studies suggest a benefit of supplementary CT. Annulus dimensions are best assessed using multiplanar cardiac reformations with creation of the annular plane or basal ring defined as the virtual annular ring immediately below the lowest insertion (hinge) point of the aortic valve cusps (**Figs.** 17.7 and 17.8).

Correct prosthesis sizing based on annular measurement is the most important predictor of paravalvular regurgitation and is routinely done with echocardiography. However, two-dimensional transthoracic and/or transesophageal echocardiography tends to underestimate the annulus size, due to its elliptical shape (see Sect. 17.2). Recent studies of annular assessment by CT report higher correlation of three-dimensional measurements with the transcatheter heart valve size, particularly the annular area and mean diameter. These results suggest that outcome can be improved by integrating CT into annular sizing and transcatheter heart valve selection.

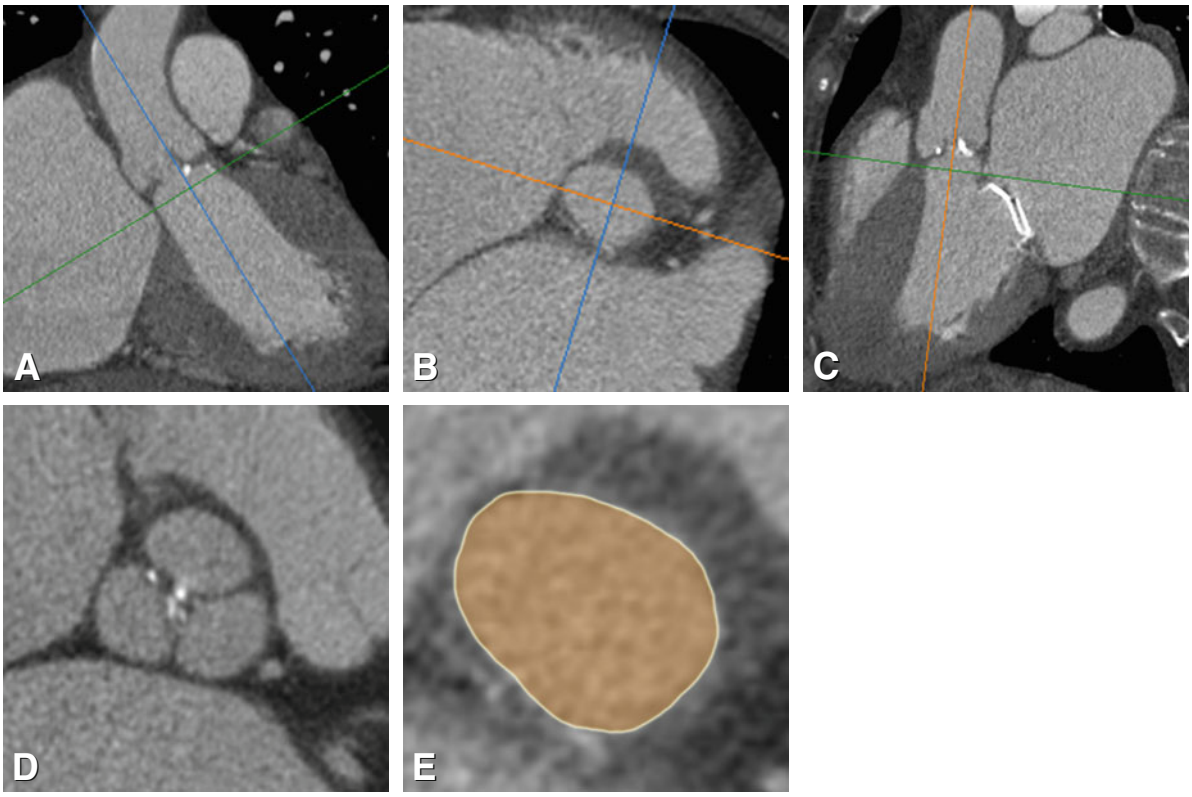

Fig. 17.7 Oblique multiplanar reformation for accurate three-dimensional alignment at the hinge points of the aortic valve and measurement of the "aortic annulus". The aortic annulus is also known as the base of the aortic ring, the so-called basal ring. For correct alignment, one should start with coronal, axial, and sagittal images. These images are manipulated in order to achieve double-oblique multiplanar images in coronal (**Panel A**), axial (**Panel B**), and sagittal orientations (**Panel C**). The colored imaging planes seen as overlays in **Panels A**–**C** are locked orthogonally to ensure exact alignment of the aortic valve (**Panel D**) and measurement of the aortic annulus (**Panel E**). Using the green reference line in the coronal image (**Panel A**) one can turn the axial plane to roughly align with the aortic valvular plane. Then the lowest cusp on the axial image should be identified and the crosshair exactly centered on this cusp's insertion point. By altering the blue reference in **Panel B**, one can manipulate the sagittal orientation (**Panel C**) to align the second cusp on the same level. When two cusps appear in the axial plane, turning the green axial reference line in the coronal image (**Panel A**) will bring the third cusp to appear on the axial view (**Panel D**). Importantly, the plane must be balanced in such a way that all three cusps disappear at the same anatomical level to ensure that the basal ring is correctly reconstructed (**Panel E**). **Panel E** is a magnified view of **Panel B** with an overlay of the measurement of the area and perimeter of the aortic annulus

A new sizing guideline for the balloon-expandable platform has been proposed (**Table 17.2**), recommending a valve prosthesis with a cross-sectional area modestly larger than that of the CT-derived aortic annulus area. A target of 10–15% area oversizing with upper and lower limits of 20–1% is suggested. The Vancouver CT sizing guidelines for Edwards SAPIEN balloon-expandable valves target this range of oversizing, while being mindful that fully deploying currently available balloon-expandable prosthesis sizes (20, 23, 26, 29 mm) would necessitate accepting a broader range of oversizing than is desirable.

The evaluation of other anatomical modifiers, such as LVOT calcification, which represents a risk factor for annulus rupture, shallow sinuses of Valsalva, or a low left main coronary artery may lead to choosing a different transcatheter heart valve size. The three-dimensional capability of CT is currently being employed for sizing the self-expandable Corevalve (Medtronic, Minneapolis. MI). Current guidelines for transcatheter heart valve selection have in fact switched to perimeter-based CT sizing (**Fig. 17.8**) for the self-expanding Medtronic prosthesis. Using this approach, the circumference/perimeter of the annulus is taken into account in valve

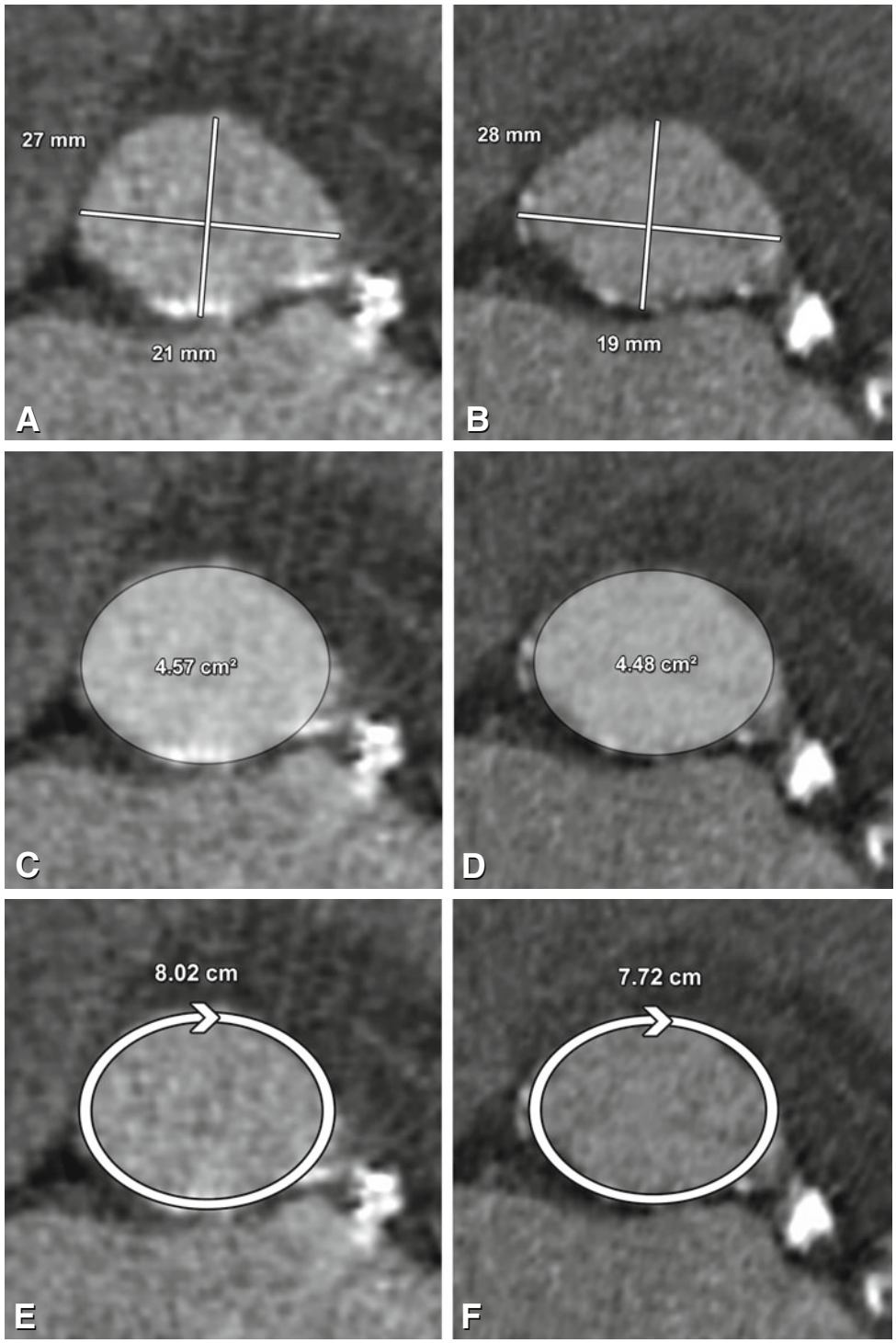

Fig. 17.8 Preprocedural annulus measurements in systole (35% of a cardiac cycle, **Panels A**, **C**, and **E**) and diastole (75% of the cardiac cycle, **Panels B**, **D**, and **F**). Choosing different phases of the cardiac cycle for diameter (**Panels A** and **B**), area (**Panels C** and **D**), or perimeter (**Panels E** and **F**) measurements can result in a difference of 10–20%, due to conformational pulsatile changes of the aortic annulus throughout the cardiac cycle. Hence, end-systole is the best phase for annular measurements, provided adequate image quality is present. Perimeter measurements vary less than diameter or area measurements; however, it is currently less reproducible between different workstations, and appropriate perimeter measurement tools that are available include smoothing algorithms which avoid overestimating perimeters

Table 17.2 The Vancouver CT sizing guidelines for Sapien XT balloon-expandable valves

Annular area (mm²)	20 mm THV (%)	23 mm THV (%)	26 mm THV (%)	29 mm THV (%)
230	NR			
240	NR (30.9)			
250	25.7			
260	20.8			
270	16.4			
280	12.2			
290	8.3			
300	4.7			
310	1.3	NR		
320	NR (−1.9%)	29.8		
330		25.9		
340		22.2		
350		18.7		
360		15.4		
370		12.3		
380		9.3		
390		6.5		
400		3.9	NR	
410		1.3	NR (29.5)	
420		NR (−1.1)	26.4	
430			23.5	
440			20.7	
450			18.0	
460			15.4	
470			13.0	
480			10.6	
490			8.4	
500			6.2	
510			4.1	NR
520			2.1	NR (27.0)
530			0.2	24.6
540				22.3
550				20.1
560				17.9
570				15.9
580				13.9
590				12.0
600				10.1
610				8.3
620				6.5
630				4.8
640				3.2
650				1.6
660				0.1
670				NR

Transcatheter prosthesis selection based on the aortic annulus area measurement by CT compared to the nominal transcatheter valve area. The recommendation is to select a prosthetic valve with a cross-sectional area modestly larger than the aortic annulus. A target of 10–15% area oversizing with upper and lower limits of 1–20% is suggested and balloon underfilling should be considered by the interventionalist when the percentage of oversizing exceeds this (blue-shaded bars)

For example, if a patient's CT annular area is 3.70 cm², a 23-mm valve (area 4.15 cm²) is recommended, resulting in 12% oversizing of the annulus. There are annulus sizes in between prosthesis sizes, however, where it is not possible to oversize by less than 20% (gray-shaded). The recommended approach for these patients is to underfill the transcatheter heart valve balloon. Initial experiences suggest a lowered balloon volume of 2–3 ml, but further refinement is necessary

Alternatively, one could opt to choose a smaller prosthesis model but this approach would be associated with a higher risk of paravalvular leak. Otherwise, consideration might be given to implantation of a self-expanding transcatheter heart valve that may confer a lower risk of annular injury or of surgical valve replacement

THV transcatheter heart valve, *NR* not recommended

Table 17.3 Current sizing recommendations for a self-expanding transcatheter heart valve platform (CoreValve, Medtronic, Minneapolis, Minnesota)

Valve size (mm)	Diameter range (mm)	Perimeter range (mm)	Area range (mm^2)
23	18–20	56.5–62.8	254.5–314.2
26	20–23	62.8–72.3	314.2–415.5
29	23–27	72.3–84.8	415.5–572.6
31	26–29	81.7–91.1	530.9–660.5

selection. The self-expandable prosthesis is then chosen with a target of 10–15% oversizing of the native annular perimeter/circumference in accordance with the official Medtronic guidelines (**Table 17.3**).

The practical application of this CT experience, with both the balloon-expandable and the self-expanding platform, remains somewhat limited at present, owing to the limited valve sizes. Imagers and interventionalists alike should understand and consider the potential implications of CT-based sizing and the increase in transcatheter heart valve nominal area when switching from the smaller to the larger transcatheter heart valves. Taking the balloon-expandable valve for example, upsizing from a 23-mm to a 26-mm balloon-expandable transcatheter heart valve is associated with an exponential 28% increase in external valve area, and a further 25% increase results from using a 29-mm instead of a 26-mm valve. These rather large incremental changes in transcatheter heart valve area make it difficult to appropriately size borderline cases. At present, transcatheter heart valve selection remains a complex decision based on a number of clinical and imaging factors and that imaging tools such as CT or echocardiography can only provide suggestions for transcatheter heart valve selection.

17.3.2 Aortic Root and Coronary Height

Preprocedural evaluation with three-dimensional echocardiography, MRI or CT is indispensible. Although infrequent, coronary ostia occlusion by one of the leaflets may become a life-threatening complication. Though no definite criteria exist to exclude patients, ostia heights >10 mm (above the annular plane/leaflet insertion) are generally considered safe (**Fig. 17.9**). The distance between the annulus and each coronary ostium

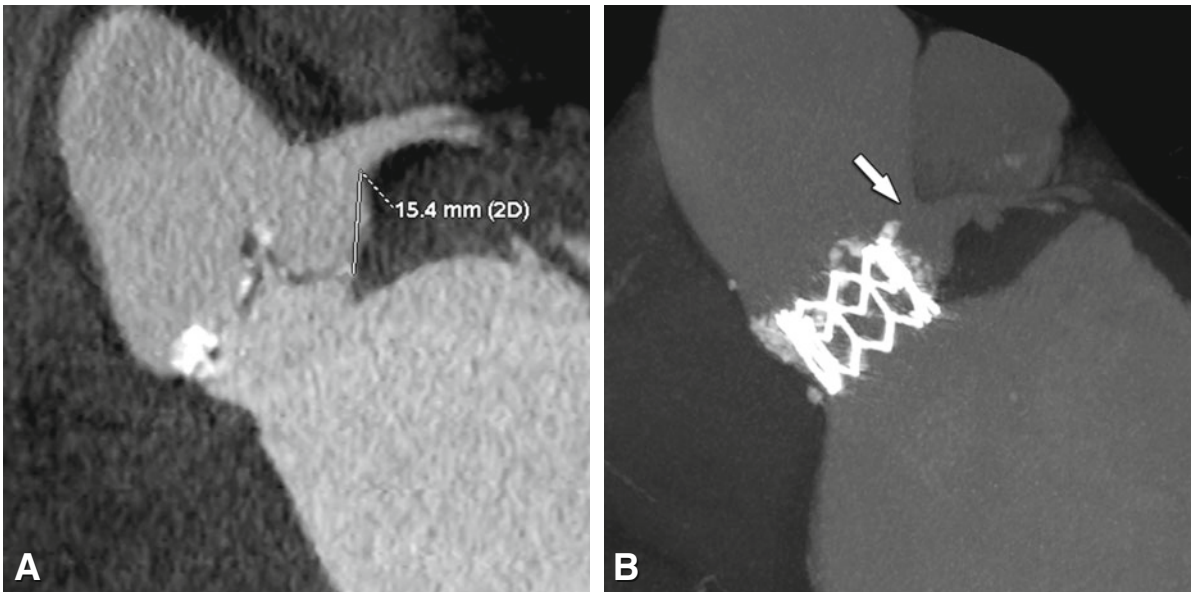

Fig. 17.9 Coronal view of the left main coronary artery and the ascending aorta, showing the relationship between annulus and ostium in the preprocedural (**Panel a**) and postprocedural assessment (**Panel b**). Coronary height is measured from the point of basal leaflet insertion to the inferior aspect of the coronary ostium. Heights above 10–12 mm are considered safe, making the risk of overstenting the coronary ostium negligible for correctly positioned prosthesis. After implanting a balloon-expandable valve in this patient, the coronary ostium was facing the stent. However, coronary perfusion was not compromised due to the depth of the sinus of Valsalva (*arrow* in **Panel b**)

should be assessed along with the morphology of the sinus of Valsalva (**Fig.** 17.10); a shallow sinus combined with a short coronary height and a highly calcified valve carries a high risk of periprocedural coronary occlusion. Comprehensive evaluation of the coronary arteries is not an objective of pre-TAVI CT since invasive coronary angiography is performed preoperatively in all patients.

17.3.3 Structural Assessment

Three-dimensional evaluation including left ventricular geometry, left ventricular aneurysm, coronary artery disease, presence of mobile structures or thrombi, septal hypertrophy with protrusion into the LVOT or mitral regurgitation are important factors in planning a TAVI procedure.

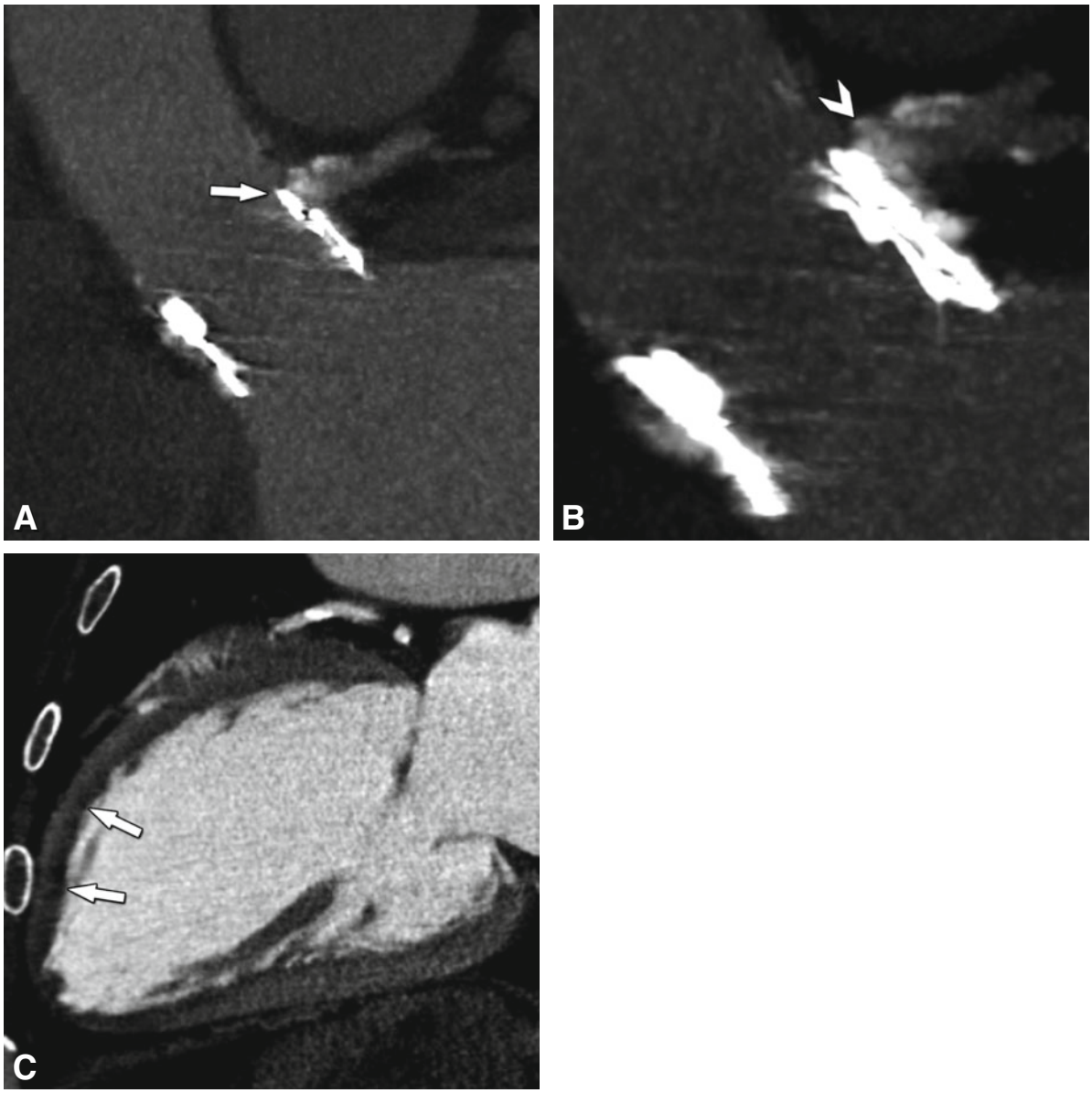

Fig. 17.10 Example of a complicated TAVI in a 75-year-old man. CT demonstrated a relatively low left coronary ostium (10 mm coronary height) and a shallow sinus of Valsalva, which resulted in a close relationship of the implanted valve and the left coronary ostium (*arrow* in **Panel A**). The aortic valve was heavily calcified. The procedure was unremarkable but the patient complained of chest pain in the immediate follow-up. ECG showed ST elevation, and cardiac enzymes were increased. Based on CT, it was suspected that the aortic valve calcification was pushed into the ostium of the left coronary (*arrowhead* in **Panel B**), and anterior subendocardial myocardial ischemia was depicted on a two-chamber long axis view (*arrows* in **Panel C**). The patient received bypass grafts on an emergency basis but died of pulmonary sepsis a few days after surgery

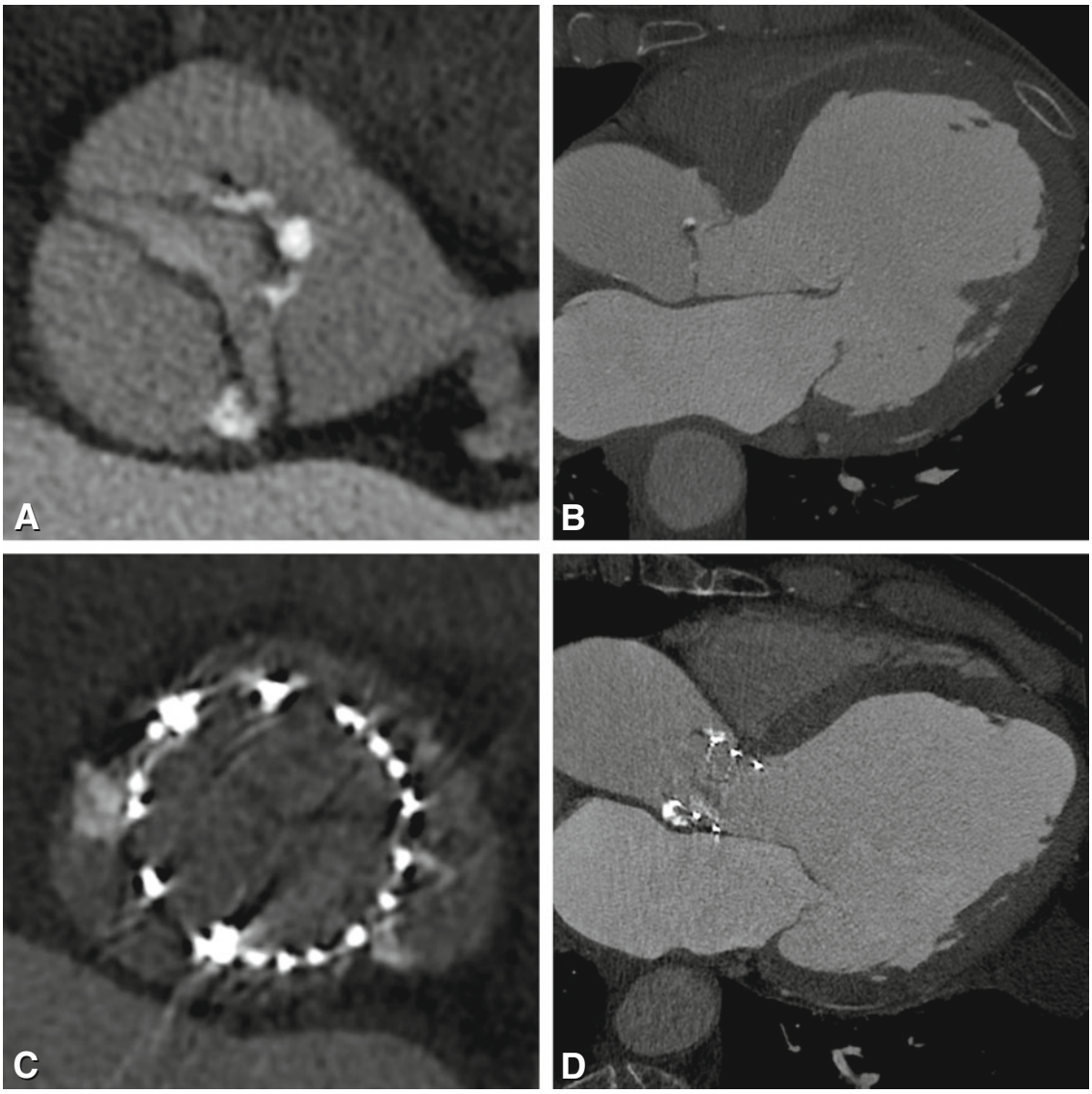

Fig 17.11 Aortic stenosis of a bicuspid aortic valve in a 74-year-old man (**Panel A**). The ascending aorta was dilated with a maximum diameter of 48 mm on a three-chamber view (**Panel B**). Surgery was contraindicated because of cardiac failure. To treat this stenotic bicuspid aortic valve TAVI was performed with a 26-mm Sapien Edwards valve. Postimplantation results are shown on a three-chamber view (**Panel C**) and short-axis view (**Panel D**). Clinical follow-up was unremarkable

17.3.4 Bicuspid Valves

Bicuspid valves are considered a relative contraindication for TAVI due to a theoretically increased risk of paravalvular regurgitation. Despite these concerns, patients with bicuspid aortic stenosis have undergone TAVI with acceptable outcomes (**Fig. 17.11**). CT has a high diagnostic accuracy for bicuspid anatomy, attributed to its excellent spatial resolution. The typical imaging features include a single commissural line in diastole and an elliptic orifice area in systole (Chap. 16). Dynamic imaging is a necessity in the setting of asymmetric bicuspid valve disease to identify the presence of a raphe and to assess cusp opening.

17.4 Complications

Patient selection is crucial to the success of TAVI procedures. This selection is difficult, given the inaccuracy of current risk models to predict outcomes in high-risk patients. A basic criterion for establishing the indication for TAVI is an excessive surgical mortality risk. Traditional surgical risk assessment tools such as the Logistic Euro Score (http://www.euroscore.org) and Society of Thoracic Surgeons Predicted Risk of Mortality score (http://riskcalc.sts.org) have limitations and do not include features such as frailty or porcelain aorta, which make some patients' risk prohibitive for surgery. CT assessment of TAVI candidates has helped identify individuals inappropriate for the procedure.

17.4.1 Paravalvular Regurgitation

Paravalvular regurgitation can be observed in 80–96% of cases (all grades, mostly trivial or mild). In the PARTNER 1B cohort, moderate or severe paravalvular regurgitation occurred in 12% and was associated with higher short- and long-term mortality.

Unlike surgical valve replacement, where the native annulus is directly visualized and sized, TAVI relies exclusively on pre- and periprocedural imaging to size the annulus and to select the correct prosthesis. Undersizing the prosthetic valve relative to the aortic annular size is associated with increased risk of postprocedural paravalvular regurgitation, whereas excessive oversizing may increase the risk of annular rupture, increased conduction system abnormalities requiring pacemaker implantation, or occlusion of the coronary ostia. The noncircular, at times elliptical shape of the aortic annular landing zone also poses challenges for assessment with commonly used two-dimensional imaging techniques. Diverging measurements of two-dimensional echocardiography or calibrated aortic angiography commonly result in undersized prosthetic valves. The increasing precision of three-dimensional modalities, such as CT, MRI, and three-dimensional transesophageal echocardiography provides better insights and allows more granular assessment of the annulus. These modalities have been shown to be powerful in their ability to predict paravalvular regurgitation (**Fig. 17.12**).

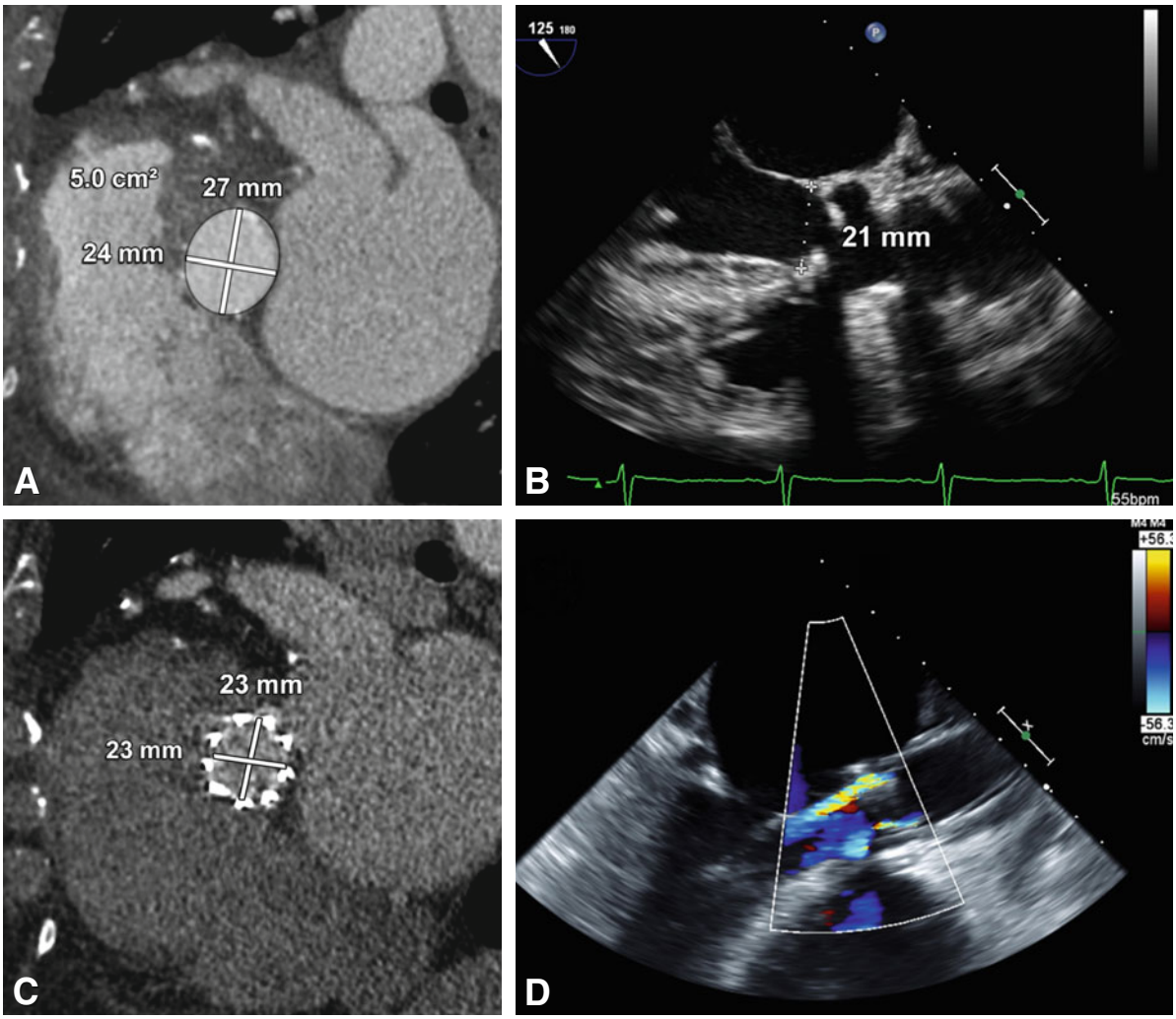

Fig. 17.12 Moderate paravalvular regurgitation post TAVI owing to annular undersizing by echocardiography in an 81-year-old female patient with severe symptomatic aortic stenosis. A double-oblique reconstruction of the basal ring by CT (**Panel A**) shows an annular area of 5.0 cm^2 and dimensions of 24 and 27 mm. The parasternal long-axis transthoracic echocardiography measurement of the annulus was only 21 mm (**Panel B**), which supported the deployment of a 23-mm balloon-expandable transcatheter heart valve. CT after implantation shows a circular 23-mm valve which appears well positioned (**Panel C**). However, postimplantation echocardiography shows moderate paravalvular regurgitation, most likely related to annular undersizing, which might have been avoided with the use of preprocedural CT measurements for valve sizing

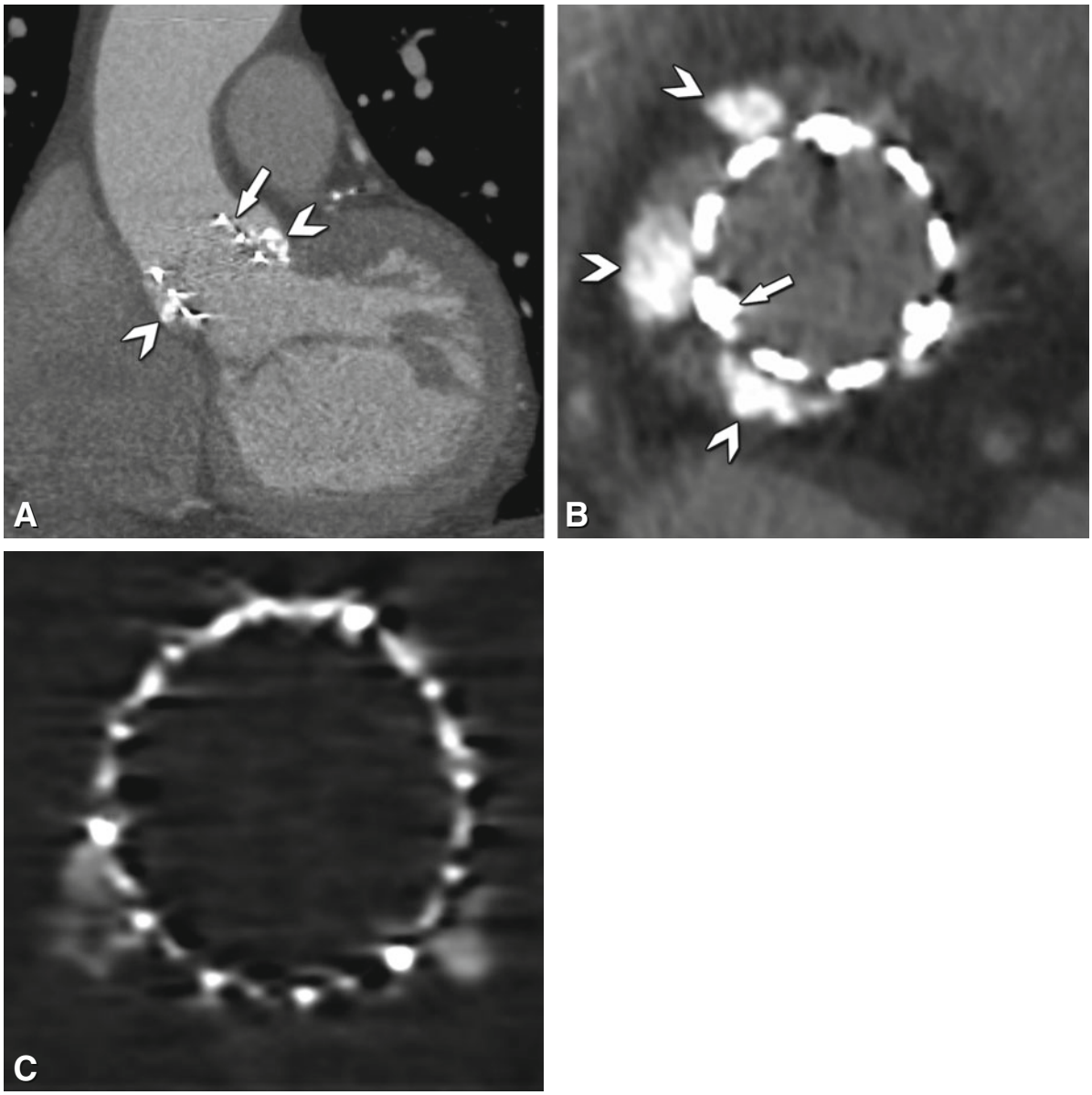

Fig. 17.13 Two examples of CT done for assessing the quality of deployment of the aortic valve. The first patient has a heavily, asymmetrically calcified aortic annulus (*arrowheads*) with incomplete stent adaption (*arrow*, **Panels A** and **B**). Even though this did not result in significant intraprocedural paravalvular leakage, the patient developed grade II regurgitation after 2 years of follow-up. **Panel C** shows a 140 keV monochromatic view of a 29-mm Sapien device in another patient. To evaluate stent circularity (perfect in this case) and positioning of the prosthesis, the examination was performed without contrast agent injection. Dual-energy CT reduces blooming artifact and may improve the differentiation of stent from native calcifications

While undersizing has been identified as a predictor of paravalvular regurgitation, asymmetrically calcified cusps and extensive calcification may also prevent proper sealing of the valve prosthesis. Although there is no consistent definition of total calcific burden or of symmetry or location of plaques, preliminary studies suggest that a higher calcium burden is associated with a significantly increased risk of paravalvular leaks.

Postoperative CT is excellent in depicting the quality of deployment (circularity) of the prosthesis as well as its apposition to the native calcified valve (**Fig. 17.13**).

17.4.2 Major Vascular Complications

Major vascular complications were often reported during the infancy of the transfemoral approach to TAVI, largely contributed by the sheath size, operator inexperience, and inappropriate patient selection. In addition, iliac arteries were assessed by conventional, single-plane angiography, contributing to limited visualization of vessel diameters and obstructions. CT provides three-dimensional assessment of the aortoiliac vessels and allows evaluation of tortuosity, atherosclerosis, calcification, and less frequent dissection or complex atheroma. The current practice for assessing the suitability of patients for the transfemoral route involves a combination of conventional angiography and CT angiography with both imaging modalities providing complimentary information.

Stroke is a known risk in both surgical and transcatheter valve replacement. Given the complexities of the TAVI procedure in these high-risk elderly patients, cerebral embolization may result from a multitude of events. Initial large diameter catheters, device positioning, manipulation at the calcified native valve and the performance of balloon valvuloplasty have all been associated with an increase in embolic events.

A recent meta-analysis reports a stroke rate of 3.5% after 30 days. Rigorous event monitoring in the randomized PARTNER cohorts identified higher rates of cerebrovascular events in TAVI compared to standard therapy and surgical aortic valve replacement. The incidence of non-procedure-related ischemic stroke later than 30 days, however, has been found to be similar to that of medical and surgical aortic valve replacement (2%/year), indicating absence of late ischemic events associated with transcatheter valves.

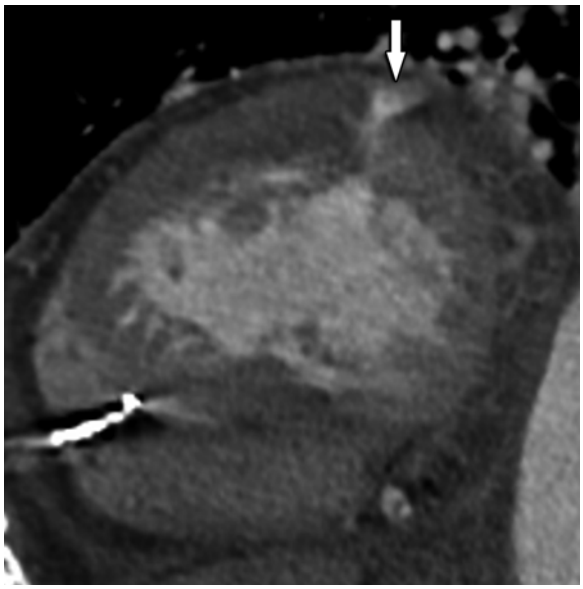

Fig. 17.14 Myocardial injury after transfemoral TAVI (*arrow*) caused by advancement of a stiff guidewire through a catheter into the myocardium

17.4.3 Rare Complications

Rare but potentially fatal complications of TAVI include coronary artery obstruction due to low ostia heights, shallow sinus of Valsalva, and long calcified native leaflets (**Fig. 17.10**). Myocardial injury is associated with transapical approaches and potential pericardial tamponade and abscess have been reported, mainly related to apex incision and suturing (**Figs. 17.14** and **17.15**). Aortic rupture and dissection have also been described,

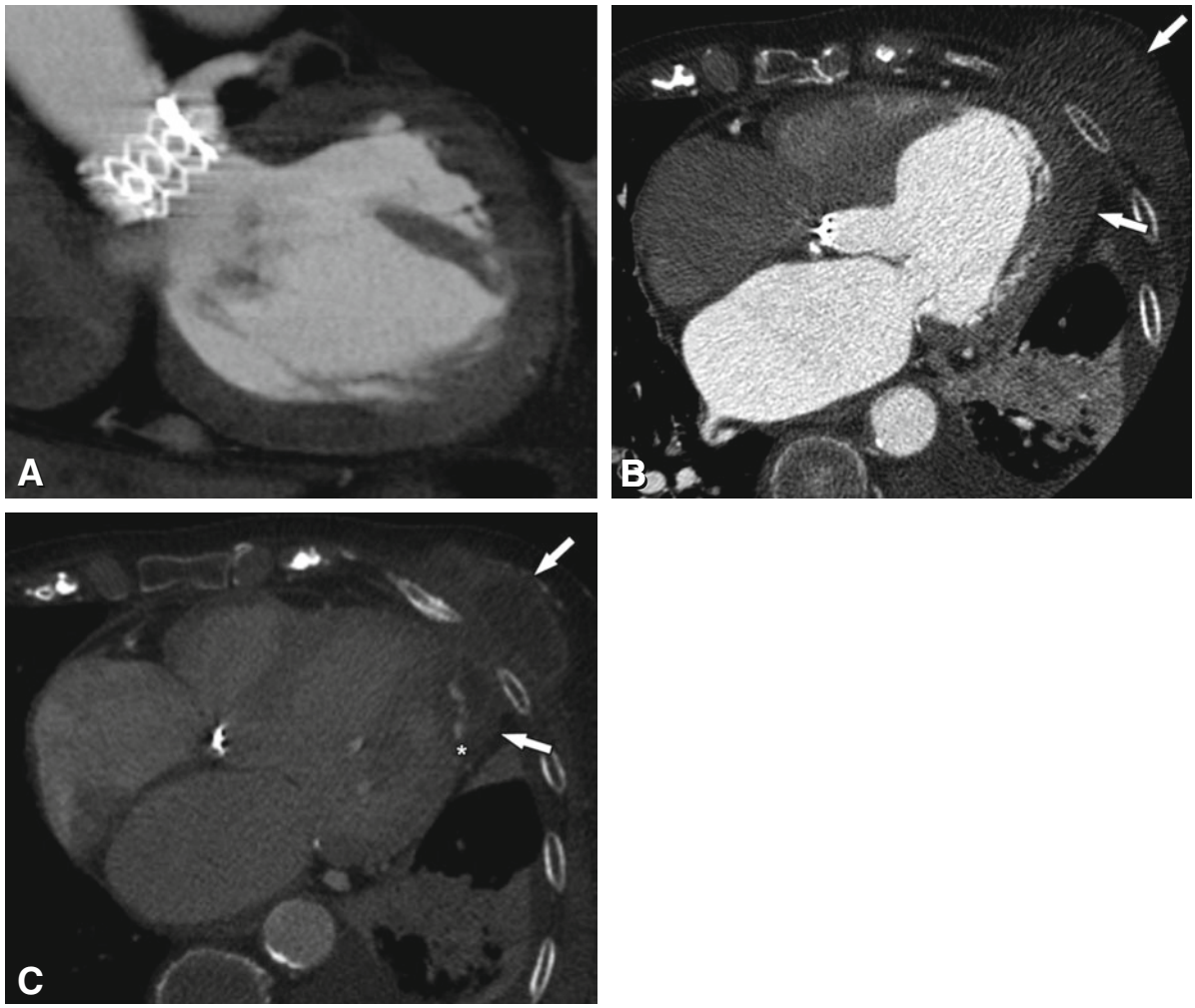

Fig. 17.15 Myocardial injury after transapical TAVI. The heart valve is correctly positioned in this 89-year-old female patient as shown in a left coronal oblique view (**Panel A**). However, the patient presented with fever, and a bicameral abscess facing the apex of the left ventricle (*arrows*) had developed (four-chamber view, **Panels B** and **C**). Note peripheral enhancement and left lung consolidation as signs of infection on these four-chamber views obtained at arterial timing (**Panel B**) and 1 min after contrast agent injection (**Panel C**). Surgical drainage was performed, and the patient was put on intravenous antibiotics. Follow-up was unremarkable. The high-density structure visible along the lateral apical wall of the left ventricle (*asterisk* in **Panel C**) was hemostatic material

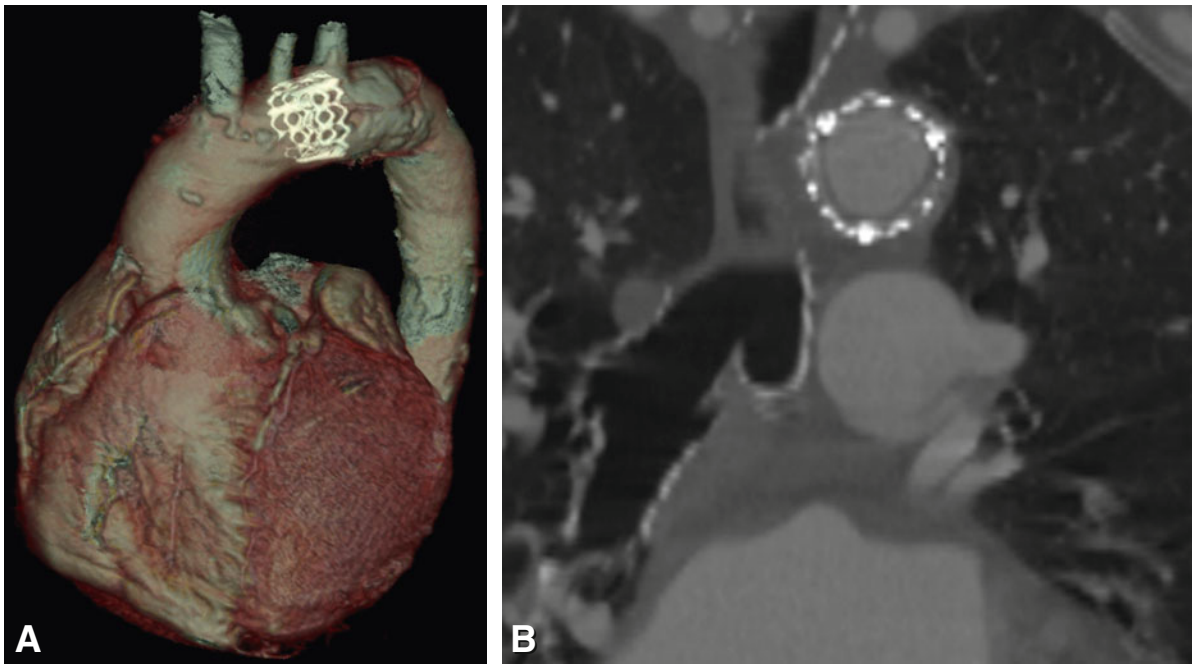

Fig. 17.16 Embolized prosthetic valve. Once embolized the valve is pulled back and positioned in the aorta (**Panel A**). There it functions solely as a stent with the leaflets remaining open during systole and diastole as can be seen in **Panel B**. In a second procedure, another transcatheter aortic valve could be implanted in this patient in the correct position without complications

although they are thankfully rare. Similarly, rare cases of ventricular or aortic embolization of the valve have been reported (**Fig.** 17.16).

17.5 Outlook

A decade after the first implantation, encouraging results from both registries and trials substantiate significant improvements in survival and quality of life for high-risk patients with aortic stenosis. In addition, transcatheter heart valves show excellent durability after 3 years, comparable to that of surgically replaced aortic valves. As technology and procedural experience evolve, there will almost certainly be further advances in technical success and ultimately patient outcome. **List 17.3** summarizes improvements that will enhance patient outcome.

List 17.3. Factors for optimizing patient outcome

1. Better patient selection – identifying patients most likely to benefit from TAVI without unacceptably high rates of complications
2. Reduction in the rate of complications through judicious use of supportive imaging techniques and strict adherence to quality service delivery
3. More accurate valve sizing – device selection tailored to individual clinical indication, patient anatomy, and comorbidities
4. Improved valve design – advances in device design, delivery techniques, and placement optimization will improve overall procedural success
5. Preprocedural planning – road mapping using three-dimensional image fusion in the catheterization lab

17.6 Patient Selection

Individual patient selection still plays a decisive role, making a multidisciplinary cardiology/cardiothoracic surgery/radiology team fundamental for accurate evaluation. TAVI indications are still evolving, and patients are still selected on a case-by-case basis. It should be noted that two thirds of all deaths are noncardiac, suggesting that patient selection is of the utmost importance. It is recommended that all TAVI patients be assessed by a multi-disciplinary team consisting of interventionalists experienced in TAVI, cardiac surgeons who perform a high volume of aortic valve replacement work, radiologists/cardiologists with experience in integrating the specialist imaging modalities (echocardiography/CT), and other supporting team members such as geriatricians, neurologists, and social workers who help guide clinical decision making.

17.6.1 Complications

Preprocedural risk factors and complications in patients with comorbidities limit postprocedural long-term survival. In particular excellent valve durability is emerging as a key factor that indicates that TAVI should not just be available as a palliative procedure but one with long-lasting benefit.

While radiation exposure is not considered a limiting factor in elderly patients eligible for TAVI, reduction of contrast medium volume is of paramount importance for patients in whom renal dysfunction is frequent. New protocols for preprocedural TAVI planning have been described, markedly reducing contrast volume.

High-resolution CT also shows promising results regarding prediction of paravalvular leaks. Both qualitative and quantitative calcification assessment has been related to paravalvular regurgitation.

17.6.2 Road Mapping

Road mapping of the preoperative CT examination in the catheterization laboratory/hybrid operating room to guide and facilitate implantation may improve correct anatomical localization and placement of percutaneous aortic devices. There are various options of how to apply preoperative imaging to enhance procedural success and reduce complication rates.

It has been shown that accurate prediction of the coaxial angle of deployment can reduce fluoroscopic time, reduce contrast requirements, and improve device positioning. Utilizing the same CT data that are acquired for standard preprocedural assessment, fluoroscopic C-arm angulations can be reliably predicted assuming similar patient positioning during CT and TAVI. Different approaches have been previously described by Kurra and Gurvitch. While somewhat different, they share a common goal of projecting all three hinge points of the aortic valve cusps in a single plane. The angulations of this projection can then be recorded across potential fluoroscopic working angles and used for intraoperative fluoroscopic C-arm adjustment for optimal valve deployment (**Fig. 17.17**). Results suggest superior positioning and reduction of the amount of contrast medium.

These preprocedural angles have also been shown to correlate very well with three-dimensional rotational reconstruction acquired at the time of the procedure. Importantly, the accuracy of preprocedural angle prediction relies on the patient being positioned in a similar fashion in the hybrid OR and in the CT scanner. Various CT and angiography suite manufacturers are actively working on hybrid 4-dimensional CT fusion imaging that will hopefully eliminate some of these current limitations (**Fig. 17.18**).

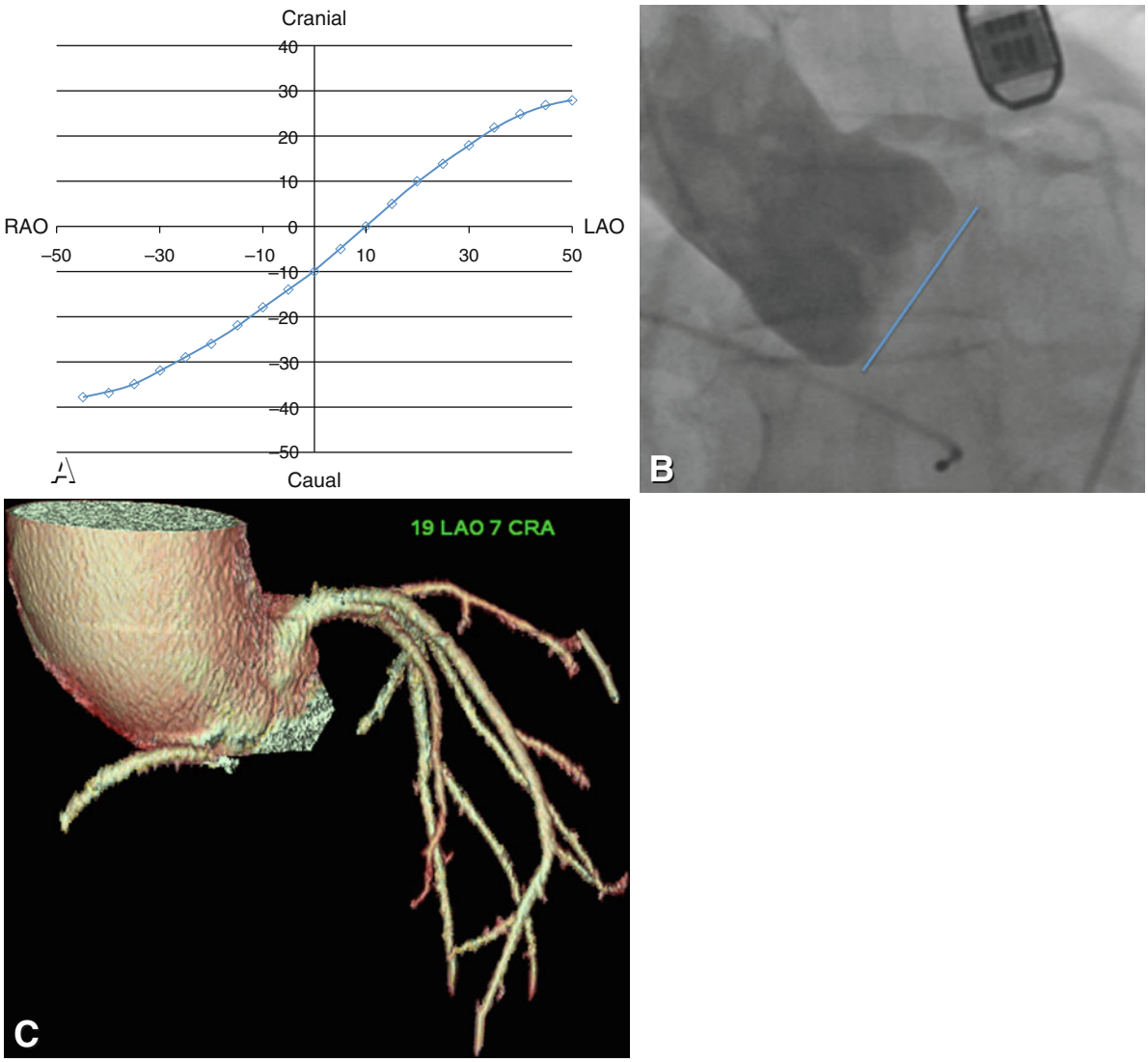

Fig. 17.17 The line of perpendicularity to the aortic annular plane can be reliably and individually measured by CT (**Panel A**). Predicting the optimum fluoroscopic angle by CT (**Panel B**), in this case 19°LAO and 7°CRA, is critical to assist with device positioning and may reduce the risk of device embolization, paravalvular leak, and heart block. **Panel C** shows a resulting fluoroscopic projection that is perpendicular to the annulus with clear separation of the three coronary cusps. In addition to predicting the optimal fluoroscopic angle, CT may help to decrease the volume of contrast agent needed for the intervention

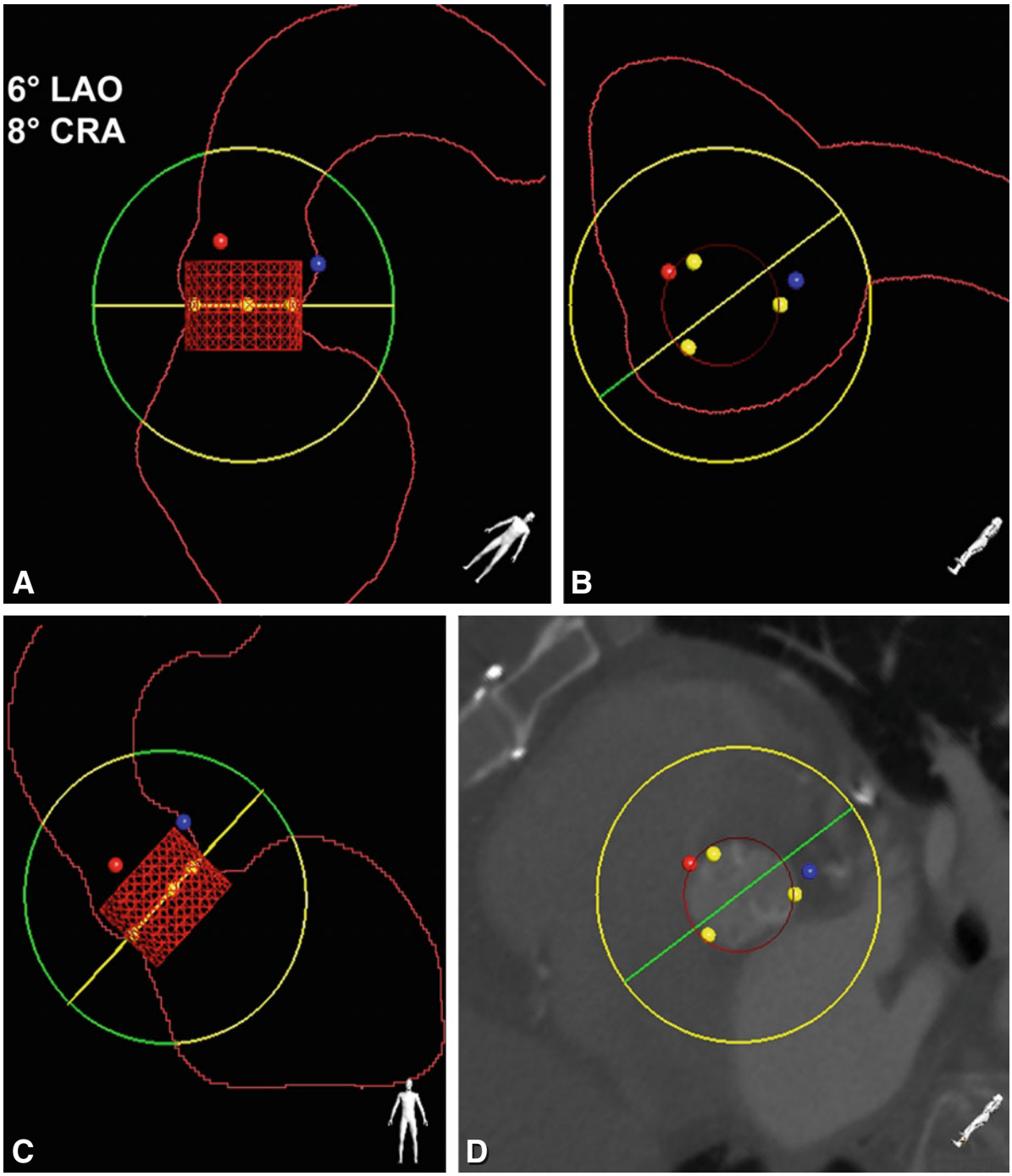

Fig. 17.18 Image fusion to predict the optimal angle for valve deployment and to assess the aortic annulus for device sizing. The CT datasets with the ascending aorta and the left ventricle have been matched to display the aortic arch in 'outline rendering' (**Panel A**). The *red* and *blue* landmarks represent the coronary ostia, while the three *yellow* landmarks indicate the three aortic valve cusps. The *yellow* circle outlines the 'plane of the valve', while the *green circle* is perpendicular to this plane (**Panels B** and **C**). The *red* mesh is a 'virtual device', which is chosen from a library of approved valves and reflects the true dimensions of the expanded aortic valve (**Panel C**). The 'optimal X-ray view' in this particular case was 6°LAO and 8°CRA. The plane of the aortic valve (**Panel B**) can also be viewed on actual CT data (**Panel D**) to see how the virtual devices will fit into the patient's individual anatomy

17.7 Conclusion

CT has significantly contributed to the advancement of TAVI and has become an integral component of the preprocedural workup of patients with symptomatic severe aortic stenosis. The primary role of CT is to guide valve size selection, assess vascular access, risk-stratify for coronary occlusion, and predict the coaxial annular plane to aid in device positioning. The cardiac CT imaging specialist has become a key member of a TAVI program and contributes significantly to its overall success.

Recommended Reading

Barbanti M, Yang TH, Rodés-Cabau J, Tamburino C, Wood DA, Jilaihawi H, Blanke P, Makkar RR, Latib A, Colombo A, Tarantini G, Raju R, Binder RK, Nguyen G, Freeman M, Ribeiro HB, Kapadia S, Min J, Feuchtner G, Gurtvich R, Alqoofi F, Pelletier M, Ussia GP, Napodano M, de Brito FS Jr, Kodali S, Norgaard BL, Hansson NC, Pache G, Canovas SJ, Zhang H, Leon MB, Webb JG, Leipsic J (2013) Anatomical and procedural features associated with aortic root rupture during balloon-expandable transcatheter aortic valve replacement. Circulation 16;128(3):244–253

Binder RK, Leipsic J, Wood D, Moore T, Toggweiler S, Willson A, Gurvitch R, Freeman M, Webb JG (2012) Prediction of optimal deployment projection for transcatheter aortic valve replacement: angiographic 3-dimensional reconstruction of the aortic root versus multidetector computed tomography. Circ Cardiovasc Interv 5:247–252

Binder RK, Webb JG, Willson AB, Urena M, Hansson NC, Norgaard BL, Pibarot P, Barbanti M, Larose E, Freeman M, Dumont E, Thompson C, Wheeler M, Moss RR, Yang TH, Pasian S, Hague C, Nguyen G, Raju R, Toggweiler S, Min JK, Wood DA, Rodés-Cabau J, Leipsic J (2013) The impact of integration of a multidetector computed tomography annulus area sizing algorithm on outcomes of transcatheter aortic valve replacement: a prospective, multicenter, controlled trial. J Am Coll Cardiol. doi: 10.1016/j.jacc.2013.04.036. pii: S0735–1097(13)01878-0. [Epub ahead of print]

Bloomfield GS, Gillam LD, Hahn RT, Kapadia S, Leipsic J, Lerakis S, Tuzcu M, Douglas PS (2012) A practical guide to multimodality imaging of transcatheter aortic valve replacement. JACC Cardiovasc Imaging 5:441–455

Cribier A, Eltchaninoff H, Bash A, Borenstein N, Tron C, Bauer F, Derumeaux G, Anselme F, Laborde F, Leon MB (2002) Percutaneous transcatheter implantation of an aortic valve prosthesis for calcific aortic stenosis: first human case description. Circulation 106(24): 3006–3008

Delgado V, Kapadia S, Schalij MJ, Schuijf JD, Tuzcu EM, Bax JJ (2012) Transcatheter aortic valve implantation: implications of multimodality imaging in patient selection, procedural guidance, and outcomes. Heart 98:743–754

Ewe SH, Ng AC, Schuijf JD, van der Kley F, Colli A, Palmen M, de Weger A, Marsan NA, Holman ER, de Roos A, Schalij MJ, Bax JJ, Delgado V (2011) Location and severity of aortic valve calcium and implications for aortic regurgitation after transcatheter aortic valve implantation. Am J Cardiol 108:1470–1477

Généreux P, Head SJ, Wood DA, Kodali SK, Williams MR, Paradis JM, Spaziano M, Kappetein AP, Webb JG, Cribier A, Leon MB (2012a) Transcatheter aortic valve implantation 10-year anniversary: review of current evidence and clinical implications. Eur Heart J 33(19):2388–2398

Généreux P, Head SJ, Wood DA, Kodali SK, Williams MR, Paradis JM, Spaziano M, Kappetein AP, Webb JG, Cribier A, Leon MB (2012b) Transcatheter aortic valve implantation 10-year anniversary: part II: clinical implications. Eur Heart J 33(19):2399–2402

Gurvitch R, Wood DA, Leipsic J, Tay E, Johnson M, Ye J, Nietlispach F, Wijesinghe N, Cheung A, Webb JG (2010a) Multislice computed tomography for prediction of optimal angiographic deployment projections during transcatheter aortic valve implantation. JACC Cardiovasc Interv 3:1157–1165

Gurvitch R, Wood DA, Tay EL, Leipsic J, Ye J, Lichtenstein SV, Thompson CR, Carere RG, Wijesinghe N, Nietlispach F, Boone RH, Lauck S, Cheung A, Webb JG (2010b) Transcatheter aortic valve implantation: durability of clinical and hemodynamic outcomes beyond 3 years in a large patient cohort. Circulation 122:1319–1327

Gurvitch R, Webb JG, Yuan R, Johnson M, Hague C, Willson AB, Toggweiler S, Wood DA, Ye J, Moss R, Thompson CR, Achenbach S, Min JK, Labounty TM, Cury R, Leipsic J (2011) Aortic annulus diameter determination by multidetector computed tomography: reproducibility, applicability, and implications for transcatheter aortic valve implantation. JACC Cardiovasc Interv 4:1235–1245

Halliburton SS, Abbara S, Chen MY, Gentry R, Mahesh M, Raff GL, Shaw LJ, Hausleiter J, Society of Cardiovascular Computed Tomography (2011) SCCT guidelines on radiation dose and dose-optimization strategies in cardiovascular CT. J Cardiovasc Comput Tomogr 5(4):198–224

Hamdan A, Guetta V, Konen E, Goitein O, Segev A, Raanani E, Spiegelstein D, Hay I, Di Segni E, Eldar M, Schwammenthal E (2012) Deformation dynamics and mechanical properties of the aortic annulus by 4-dimensional computed tomography: insights into the functional anatomy of the aortic valve complex and implications for transcatheter aortic valve therapy. J Am Coll Cardiol 10(59):119–127

Holmes DR Jr, Mack MJ (2011) Transcatheter valve therapy: a professional society overview from the American College of cardiology foundation and the society of thoracic surgeons. Ann Thorac Surg 92:380–389

Holmes DR Jr, Mack MJ, Kaul S, Agnihotri A, Alexander KP, Bailey SR, Calhoon JH, Carabello BA, Desai MY, Edwards FH, Francis GS, Gardner TJ, Kappetein AP, Linderbaum JA, Mukherjee C, Mukherjee D, Otto CM, Ruiz CE, Sacco RL, Smith D, Thomas JD (2012) 2012 ACCF/AATS/SCAI/STS expert consensus document on transcatheter aortic valve replacement. J Am Coll Cardiol 59:1200–1254

Jilaihawi H, Kashif M, Fontana G (2012) Cross-sectional computed tomographic assessment improves accuracy of aortic annular sizing for transcatheter aortic valve replacement and reduces the incidence of paravalvular aortic regurgitation. J Am Coll Cardiol 59:1275–1286

John D, Buellesfeld L, Yuecel S, Mueller R, Latsios G, Beucher H, Gerckens U, Grube E (2010) Correlation of device landing zone calcification and acute procedural success in patients undergoing transcatheter aortic valve implantations with the self-expanding CoreValve prosthesis. JACC Cardiovasc Interv 3:233–243

Kodali SK, Williams MR, Smith CR, Svensson LG, Webb JG, Makkar RR, Fontana GP, Dewey TM, Thourani VH, Pichard AD, Fischbein M, Szeto WY, Lim S, Greason KL, Teirstein PS, Malaisrie SC, Douglas PS, Hahn RT, Whisenant B, Zajarias A, Wang D, Akin JJ, Anderson WN, Leon MB, PARTNER Trial Investigators (2012) Two-year outcomes after transcatheter or surgical aortic-valve replacement. N Engl J Med 366:1686–1695

Kurra V, Schoenhagen P, Roselli EE, Kapadia SR, Tuzcu EM, Greenberg R, Akhtar M, Desai MY, Flamm SD, Halliburton SS, Svensson LG, Sola S (2009) Prevalence of significant peripheral artery disease in patients evaluated for percutaneous aortic valve insertion: preprocedural assessment with multidetector computed tomography. J Thorac Cardiovasc surg 137:1258–1264

Lang RM, Badano LP, Tsang W, Adams DH, Agricola E, Buck T, Faletra FF, Franke A, Hung J, de Isla LP, Kamp O, Kasprzak JD, Lancellotti P, Marwick TH, McCulloch ML, Monaghan MJ, Nihoyannopoulos P, Pandian NG, Pellikka PA, Pepi M, Roberson DA, Shernan SK, Shirali GS, Sugeng L, Ten Cate FJ, Vannan MA, Zamorano JL, Zoghbi WA, American Society of Echocardiography, European Association of Echocardiography (2012) EAE/ASE recommendations for Image acquisition and display using three-dimensional echocardiography. J Am Soc Echocardiogr 25:3–46

Leipsic J, Labounty TM, Min JK, Wood D, Johnson M, Ajlan AM, Wijesinghe N, Webb JG (2011) Multidetector computed tomography in transcatheter aortic valve implantation. JACC Cardiovasc Imaging 4:416–429

Leon MB, Smith CR, Mack M, Miller DC, Moses JW, Svensson LG, Tuzcu EM, Webb JG, Fontana GP, Makkar RR, Brown DL, Block PC, Guyton RA, Pichard AD, Bavaria JE, Herrmann HC, Douglas PS, Petersen JL, Akin JJ, Anderson WN, Wang D, Pocock S, PARTNER Trial Investigators (2010) Transcatheter aortic-valve implantation for aortic stenosis in patients who cannot undergo surgery. N Engl J Med 363:1597–1607

Makkar RR, Fontana GP, Jilaihawi H, Kapadia S, Pichard AD, Douglas PS, Thourani VH, Babaliaros VC, Webb JG, Herrmann HC, Bavaria JE, Kodali S, Brown DL, Bowers B, Dewey TM, Svensson LG, Tuzcu M, Moses JW, Williams MR, Siegel RJ, Akin JJ, Anderson WN, Pocock S, Smith CR, Leon MB, PARTNER Trial Investigators (2012) Transcatheter aortic-valve replacement for inoperable severe aortic stenosis. N Engl J Med 366:1696–1704

Moss RR, Ivens E, Pasupati S, Humphries K, Thompson CR, Munt B, Sinhal A, Webb JG (2008) Role of echocardiography in percutaneous aortic valve implantation. JACC Cardiovasc Imaging 1:15–24

Nietlispach F, Leipsic J, Al-Bugami S, Masson JB, Carere RG, Webb JG (2009) CT of the ilio-femoral arteries using direct aortic contrast injection: proof of feasibility in patients screened towards percutaneous aortic valve replacement. Swiss Med Wkly 139:458–462

Plank F, Friedrich G, Bartel T, Mueller S, Bonaros N, Heinz A, Klauser A, Cartes-Zumelzu F, Grimm M, Feuchtner G (2012) Benefits of high-pitch 128-slice Dual Source Computed Tomography for planning of transcatheter aortic valve implantation: a clinical performance analysis. Ann Thorac Surg 94:1961–1966

Pouleur AC, le Polain de Waroux JB, Pasquet A, Vanoverschelde JL, Gerber BL (2007) Aortic valve area assessment: multidetector CT compared with cine MR imaging and transthoracic and transesophageal echocardiography. Radiology 244:745–54

Ussia GP, Barbanti M, Petronio AS, Tarantini G, Ettori F, Colombo A, Violini R, Ramondo A, Santoro G, Klugmann S, Bedogni F, Maisano F, Marzocchi A, Poli A, De Carlo M, Napodano M, Fiorina C, De Marco F, Antoniucci D, de Cillis E, Capodanno D, Tamburino C, CoreValve Italian Registry Investigators (2012) Transcatheter aortic valve implantation: 3-year outcomes of self-expanding CoreValve prosthesis. Eur Heart J 33:969–976

Willson AB, Webb JG, Labounty TM, Achenbach S, Moss R, Wheeler M, Thompson C, Min JK, Gurvitch R, Norgaard BL, Hague CJ, Toggweiler S, Binder R, Freeman M, Poulter R, Poulsen S, Wood DA, Leipsic J (2012a) 3-dimensional aortic annular assessment by multidetector computed tomography predicts moderate or severe paravalvular regurgitation after transcatheter aortic valve replacement. J Am Coll Cardiol 59:1287–1294

Willson AB, Webb JG, Freeman M, Wood DA, Gurvitch R, Thompson CR, Moss RR, Toggweiler S, Binder RK, Munt B, Cheung A, Hague C, Ye J, Leipsic JA (2012) Computed tomography-based sizing recommendations for transcatheter aortic valve replacement with balloon-expandable valves: comparison with transesophageal echocardiography and rationale for implementation in a prospective trial. J Cardiovasc Comput Tomogr 6(6):406–414

Wuest W, Anders K, Schuhbaeck A, May MS, Gauss S, Marwan M, Arnold M, Ensminger S, Muschiol G, Daniel WG, Uder M, Achenbach S (2012) Dual source multidetector CT-angiography before Transcatheter Aortic Valve Implantation (TAVI) using a high-pitch spiral acquisition mode. Eur Radiol 22:51–58

Pulmonic Valve Implantation, Mitral Valve Repair, and Left Atrial Appendage Closure

V. Delgado

Abstract

Transcatheter procedures for mitral and pulmonic valvular and structural heart disease have increased in the last years. The success of these therapeutic options relies on accurate selection of patients and procedural guidance. CT provides detailed three-dimensional understanding of the operative field for interventional planning.

18.1 Clinical Background

The number of catheter-based interventions for structural heart disease has increased exponentially in the last decade. In addition, more than 8,000 patients with moderate or severe mitral regurgitation have undergone transcatheter mitral valve repair. These interventions are an important therapeutic breakthrough, providing an alternative to patients who are deemed inoperable. Furthermore, percutaneous pulmonic valve implantation has reduced the number of reoperations for failing surgical conduits implanted to treat congenital heart disease involving right ventricular outflow tract obstruction. Finally, percutaneous left atrial appendage closure is a new stroke prevention approach for selected patients with nonvalvular atrial fibrillation and contraindications to anticoagulation. In all these procedures, accurate evaluation of patients, selection of the device and procedural approach, and experience of the operator are key to maximize the success rate and minimize complications. Cardiac imaging, particularly three-dimensional imaging techniques such as computed tomography (CT), plays a central role in selecting patients and planning the procedure. Accurate anatomic characterization of cardiac structures and visualization of anatomic relationships are the strengths of CT (see Chap. 16), and this information is crucial for selecting the device to be implanted, planning the procedural strategy, and anticipating potential complications.

18.2 Percutaneous Pulmonic Valve Implantation

Surgical pulmonic valves or conduits used to treat complex congenital heart disease with right ventricular outflow tract obstruction have a relatively high incidence of failure over the first 4–5 years following implantation. In a series of 205 patients receiving homografts for reconstruction of the right ventricular outflow tract, the incidence of reintervention for homograft failure was 25% at

M. Dewey, *Cardiac CT*,
DOI 10.1007/978-3-642-41883-9_21, © Springer-Verlag Berlin Heidelberg 2014

4- to 5-year follow-up. Stenosis is the most frequent mode of failure of valved conduits or homografts although insufficiency or combined stenosis and insufficiency have also been described. The hemodynamic consequences of failing homografts and valved conduits result in right ventricular failure which, if left untreated, further impairs the long-term outcome of these patients. The development of transcatheter pulmonic valve implantation techniques has provided a therapeutic alternative to patients who may otherwise need repeat surgery.

The Melody valve (Medtronic Inc., Minneapolis, Minnesota, USA) – a bovine jugular vein valve sewn into a platinum iridium stent – has been implanted in the pulmonic valve position in more than 3,000 patients (**Fig. 18.1**). The use of the Melody valve was approved by the United States Food and Drug Administration under the humanitarian device exemption program in 2010. The Edwards SAPIEN valve – a bovine pericardial valve within a stainless-steel frame – is being evaluated in the COMPASSION clinical trial for use in patients with right ventricular outflow tract conduit dysfunction or pulmonary valve stenosis or regurgitation (**Fig. 18.1**). Current recommendations consider transcatheter pulmonic valve implantation as class IIa indication in patients with failing right ventricular-to-pulmonic artery conduit (moderate to severe regurgitation or stenosis) provided that the patients meet the inclusion/exclusion criteria for the available valve types and sizes (**Fig. 18.1**).

Prosthesis dislodgement or migration, coronary artery impingement, and pulmonary artery obstruction are the main complications that can occur during transcatheter pulmonic valve implantation. At follow-up, stent fracture is relatively common and can cause increased right ventricular outflow tract gradient and right ventricular pressure overload. Accurate assessment of the right ventricular outflow tract and pulmonary artery anatomy as well as their spatial relationships prior to the procedure is pivotal to minimize complications. At follow-up, echocardiographic assessment of the valve is mandatory to diagnose potential stent fracture. Accurate follow-up assessment can also be performed using CT (**Table 18.1**).

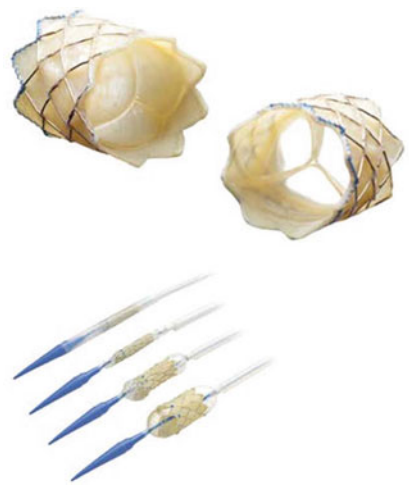

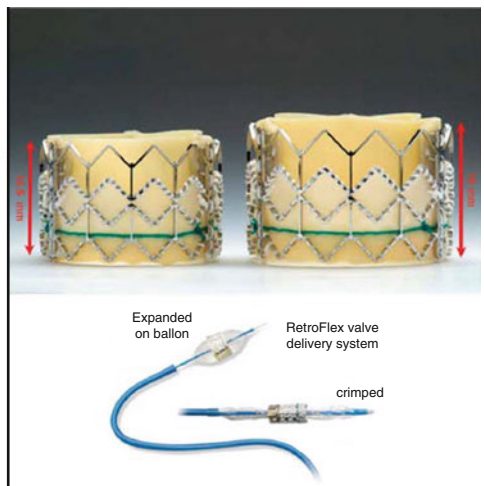

Medtronic Melody Valve	Edwards SAPIEN Valve
Bovine jugular vein value	Bovine pericardial leaflets
Plantinum iridium stent	Stainless steel stent
18, 20 and 22-mm size	23 and 26-mm size
A 22F delivery system	B 24-26F delivery sheath

Fig. 18.1 Percutaneous pulmonic valves. **Panel A** shows the Melody valve, which is implanted through a 22 F balloon catheter delivery system (Ensemble). The valve is crimped onto a balloon of different sizes (18, 20 and 22-mm). **Panel B** shows the Edwards SAPIEN valve, which is mounted onto a balloon of 23 or 26 mm and is implanted through a 24–26 F sheath (Modified and used with permission from Fleming et al. *Progress in Pediatric Cardiology* 2012)

Table 18.1 CT evaluation prior to and after transcatheter pulmonic valve implantation

CT parameters to be assessed	Objective of the assessment
Prior to intervention	
Dimensions of the conduit	Melody valve (18, 20, or 22 mm) for conduits measuring 14–22 mm
	Edwards SAPIEN valve (23 or 26 mm) for conduits measuring 14–25 mm
Conduit calcifications	To anticipate risk of coronary impingement
Coronary artery anatomy and spatial relationship with the right ventricular outflow tract	To anticipate risk of coronary impingement
Distance between the conduit and the origin of the right and left pulmonary arteries	To anticipate risk of pulmonary artery obstruction
After interventions	
Stent fracture	Suspected when increased valve gradients and right ventricular pressure overload

18.2.1 Prior to Intervention

Prior to intervention, the following aspects should be assessed:

- *Dimensions of the valved conduit or homograft*. The Melody valve can be implanted in right ventricular outflow tract conduits with diameters between 14 and 22 mm, whereas the Edwards SAPIEN can be implanted in larger homografts (up to 25 mm). Alignment of the multiplanar reformation planes to obtain the cross-sectional plane of the conduit permits accurate diameter measurement (**Fig. 18.2**). Accurate sizing of the prosthesis will avoid complications such as device migration (if undersized) or homograft rupture (if oversized).
- *Calcification of the valved conduit or homograft*. The extent of valve calcification has been associated with increased risk of coronary artery compression. Prominent bulky calcifications of the conduit may be displaced during ballooning of the percutaneous valve and impinge on a coronary artery even when the internal conduit is far from the coronary artery wall (**Fig. 18.2**). On the other hand, the absence of calcification has been associated with increased risk of stent fracture at follow-up. A calcified conduit or homograft would prevent compressive stress on the percutaneous valve and subsequent stent fracture.

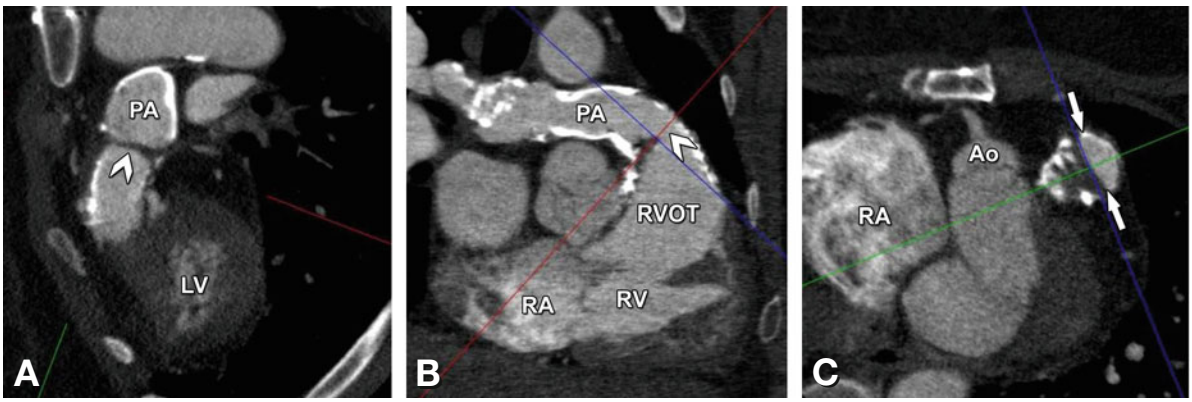

Fig. 18.2 CT evaluation of a stenotic right ventricular outflow tract conduit. The multiplanar reformation planes (**Panels A**–**C**) are aligned orthogonal to the right ventricular outflow tract (*RVOT*) and pulmonary artery (*PA*) at the level of the obstruction (*arrowhead* in **Panels A** and **B**) to obtain the diameters of the conduit (*arrows* in **Panel C**) at the site where the prosthesis will be implanted. *Ao* aorta, *LV* left ventricle, *RA* right atrium, *RV* right ventricle

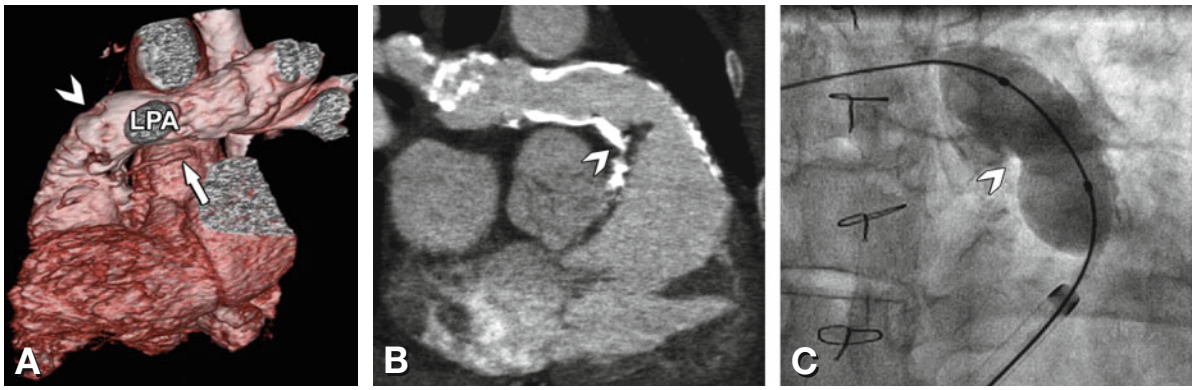

Fig. 18.3 CT evaluation prior to percutaneous pulmonic valve implantation. The spatial relationship between the coronary arteries and the conduit and the distance of the conduit from the main pulmonary artery branches should be evaluated. **Panel A** shows the three-dimensional volume rendering indicating the location of the left anterior descending coronary artery (*arrow*) and the right ventricular outflow tract (RVOT) conduit (*arrowhead*) and left pulmonary artery (*LPA*). The coronary artery is far from the conduit. **Panel B** shows the distance between the main pulmonary artery branches and the site of conduit stenosis (*arrowhead*). **Panel C** shows the fluoroscopic view of the balloon with the arrowhead indicating the area of ingrowth and stenosis within the conduit. *Ao* aorta; *RA* right atrium; *RPA* right pulmonary artery; *RV* right ventricle

- *Relationship with coronary arteries*. Current guidelines advocate the use of CT prior to pulmonic valve implantation to assess the distance between the conduit (and the target position of the percutaneous valve) and the coronary arteries to anticipate the risk of coronary artery impingement (**Fig. 18.3**).
- *Pulmonary artery obstruction*. CT permits accurate assessment of the distance between the conduit and the origin of the right and left pulmonary arteries (**Fig. 18.3**). The Melody valve consists of a 23–26 mm frame that may cause pulmonary artery branch obstruction once deployed. This complication may not occur with the Edwards SAPIEN valve, which has a shorter frame (14–16 mm).

18.2.2 After Interventions

Stent fracture is rather common at follow-up. Recent series have reported an incidence between 21 and 28% at 2-year follow-up. Stent fracture may cause increased pressure gradients and right ventricular failure and, as a consequence, current recommendations advocate surveillance of the percutaneous prosthesis at follow-up. Stent fracture is classified into three categories: type I, with one or more strut fractures without loss of structural integrity; type II, one or more strut fractures with loss of structural integrity; type III, with fragmentation and embolization of stent fragments. The high spatial resolution of current CT scanners allows accurate noninvasive assessment of this complication.

18.3 Transcatheter Mitral Valve Repair

Mitral valve regurgitation is one of the most prevalent valvular heart diseases. Mitral regurgitation is classified according to the underlying pathophysiology: (1) organic mitral regurgitation refers to an intrinsic structural abnormality of any valve component, whereas (2) functional mitral regurgitation is caused by left ventricular remodeling and dysfunction. From the therapeutic point of view, the classification of Carpentier, is frequently used (**Fig. 18.4**). Type I is characterized by normal movement of the mitral leaflets, and mitral

Fig. 18.4 Schematic representation (*left column*) and corresponding CT examples (*right column*) of the functional classification of mitral regurgitation by Carpentier according to the underlying mechanism in a three-chamber view. In type I (**Panels A** and **B**), movement of the leaflets is normal, and mitral regurgitation (*arrow*) results from annulus dilatation or perforation of one of the leaflets (endocarditis). In type II (**Panels C** and **D**), mitral regurgitation is caused by excessive motion of one of the leaflets (P2 prolapse; *asterisk*). In type III (**Panels E** and **F**), restriction of one or both leaflets caused by left ventricular remodeling (*arrowhead*) leads to failure of leaflet coaptation and mitral regurgitation (*arrow*). *AMVL* anterior mitral valve leaflet, *Ao* aorta, *LA* left atrium, *LV* left ventricle, *PMVL* posterior mitral valve leaflet, *RA* right atrium, *RV* right ventricle (Modified and used with permission from Filsoufi et al. *Seminars in Thoracic and Cardiovascular Surgery* 2007 and Wong et al. *Int J Cardiol* 2007)

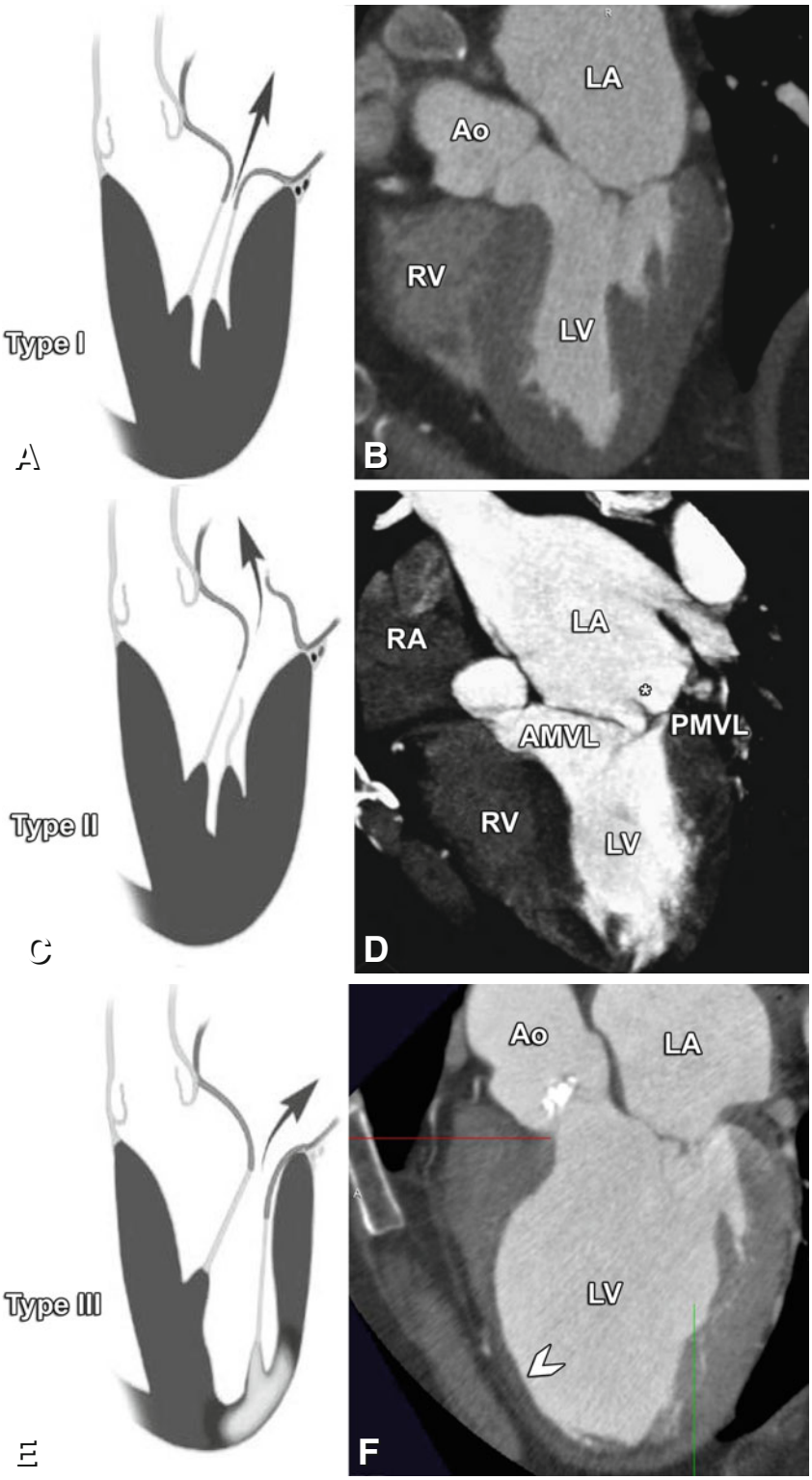
Type I
A
LA
Ao
RV
LV
B
Type II
C
RA
LA
AMVL
PMVL
RV
LV
D
Type III
E
Ao
LA
LV
F

Table 18.2 Percutaneous mitral valve repair techniques

	Device	Study	Required CT assessments
Annuloplasty			
Indirect	CARILLON	AMADEUS	Mitral annulus calcifications
	Monarc	EVOLUTION II	Coronary sinus dimensions and location in relation to mitral annulus and circumflex artery
	Viacor PTMA	PTOLEMY	
Direct	Mitralign	First-in-man	Mitral annulus calcifications
	Guided Delivery Systems	First-in-man	Location of circumflex coronary artery in relation to mitral annulus
Leaflet repair	Mitraclip	EVEREST I-II	Flail gap and width
		REALISM	Coaptation length and depth
	Mobius	MILANO II	Mitral annulus calcifications

regurgitation is caused by isolated mitral annulus dilatation or perforation of one leaflet (endocarditis). Type II is characterized by excessive motion of the leaflets (above the mitral annulus). Type III is characterized by restrictive motion of the leaflets. This category is further subdivided into type IIIa, if the restriction is caused by degeneration of the subvalvular mitral apparatus (rheumatic valve disease), and type IIIb, if restriction is caused by left ventricular dilatation (dilated or ischemic cardiomyopathy). Characterization of the underlying pathophysiology of mitral regurgitation with CT is described in Chap. 16.

Several catheter-based therapies for mitral regurgitation have been developed in the last years. These therapies can be divided into two main groups: mitral annuloplasty and mitral leaflet repair. Other devices aim at restoring left ventricular shape or reducing left atrial size to improve mitral leaflet coaptation. However, the clinical evidence of these therapies is still limited. Percutaneous annuloplasty approaches (indirect and direct) have been developed for functional mitral regurgitation, while percutaneous mitral valve repair has proved successful in patients with organic and functional mitral regurgitation. **Table 18.2** summarizes current percutaneous mitral valve repair technologies that address the mitral valve annulus or the leaflets. The success of these therapies largely relies on accurate selection of patients who may benefit from these therapies and accurate assessment of mitral valve function, anatomy, and geometry with multimodality imaging. Particularly, three-dimensional imaging techniques play a central role in selection of patients and guidance of the procedure. In the following sections, the role of CT in selecting patients for percutaneous mitral valve repair techniques involving mitral annuloplasty or leaflet repair will be reviewed.

18.3.1 Indirect and Direct Percutaneous Mitral Annuloplasty

Percutaneous mitral annuloplasty approaches aim at improving coaptation of mitral leaflets and reduction of regurgitation by restoring the normal dimensions of the mitral annulus in patients with functional mitral regurgitation. Indirect percutaneous mitral annuloplasty techniques use the coronary sinus, whose course parallels the posterior mitral annulus, to deliver a device that partially shrinks the mitral annulus (**Fig. 18.5**). Direct percutaneous mitral annulopasty techniques mimic surgical mitral annuloplasty by implanting a device directly in the mitral annulus (**Fig. 18.5**). Several trials have demonstrated the safety and efficacy of indirect annuloplasty devices in reducing mitral regurgitation and improving symptoms. For the several devices, the procedural feasibility ranges between 60 and 82%. The main

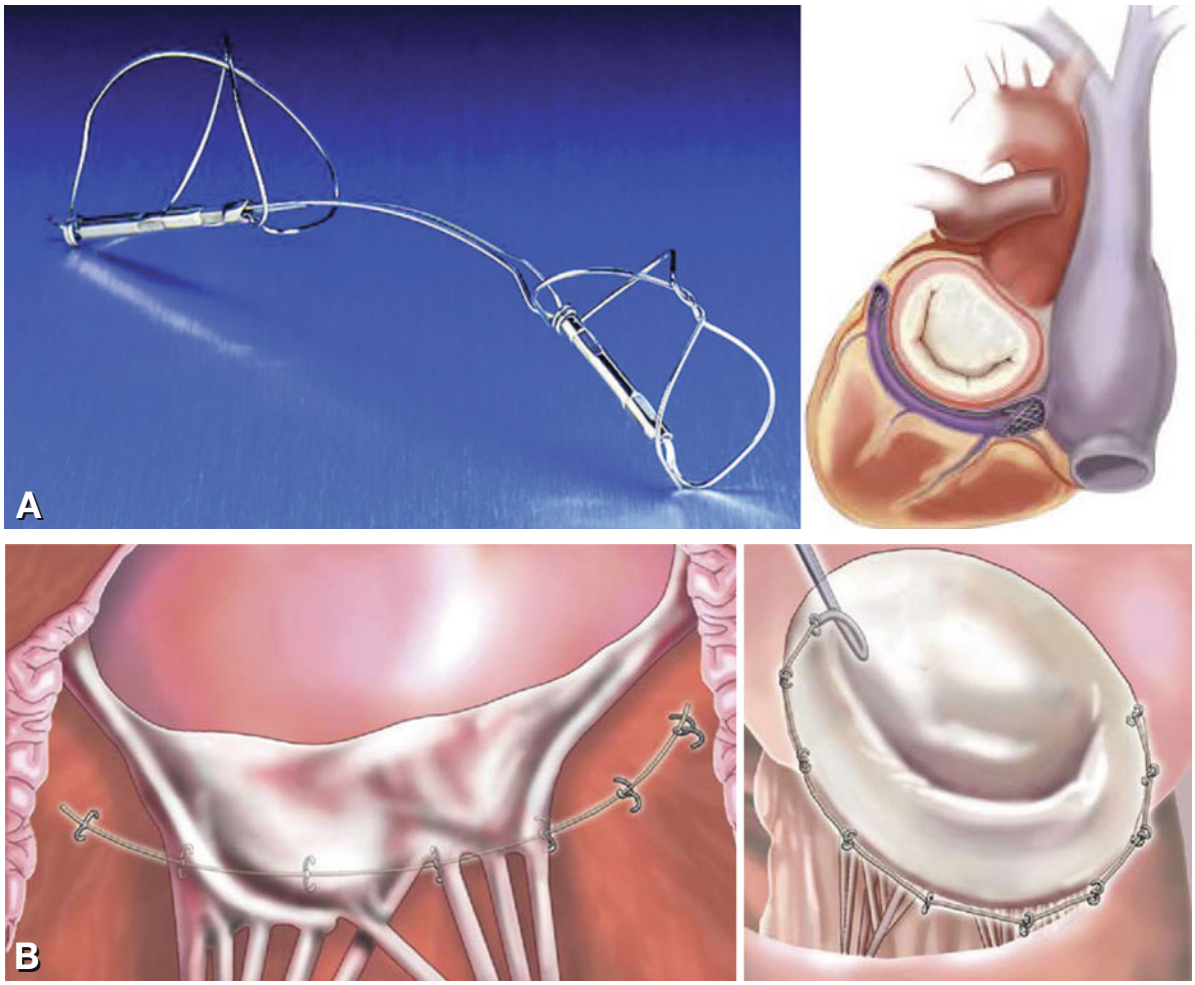

Fig. 18.5 Indirect and direct percutaneous transcatheter mitral valve repair techniques (annuloplasty). The indirect approach (**Panel A**) consists of the implantation of a device (CARILLON device or MONARC device) into the coronary sinus that reduces the anteroposterior diameter of the mitral annulus and improves mitral leaflet coaptation. The direct approach (**Panel B**) with the Guided Delivery System Accucinch places several anchors in the posterior mitral annulus by retrograde catheterization of the left ventricle. These anchors are connected through a drawstring to cinch the mitral annulus (Modified and used with permission from Feldman et al. *J Am Coll Cardiol* 2011 and Harnek et al. *JACC Cardiovasc Intervent* 2011)

reasons for not implanting the device are tortuosity and inappropriate dimensions of the coronary sinus and risk of circumflex coronary artery impingement. In contrast to the indirect percutaneous annuloplasty techniques, the direct annuloplasty techniques are still at early phases of development, and more clinical data demonstrating their safety and effectiveness are needed.

The role of CT prior to percutaneous mitral annuloplasty techniques is focused on analysis of the mitral annulus anatomy and geometry, dimensions of the coronary sinus and anatomical relationship between the mitral annulus, coronary sinus, and circumflex coronary artery.

- *Mitral annulus anatomy*. The mitral annulus is characterized by a three-dimensional saddle-shaped morphology with the peaks located anteriorly and posteriorly and nadirs at the level of the anterolateral and posteromedial commissures. The anterior part of the annulus is reinforced by a fibrous continuity and is in close relationship with the aortic annulus at the level of the left and noncoronary cusps of the aortic valve, whereas the posterior part lacks this fibrous enforcement and is more muscular, which make it more prone to dilatation and calcification. This posterior part of the mitral annulus is in

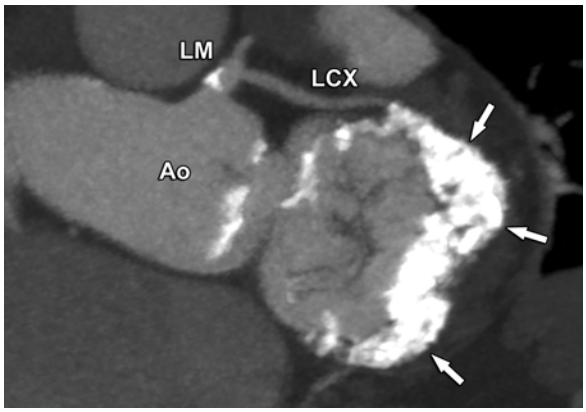

Fig. 18.6 Severe mitral annulus calcification as seen by CT. The posterior part of the mitral annulus is frequently calcified in old patients. The *arrows* indicate large calcifications of the posterior mitral annulus, which may be a contraindication to indirect transcatheter indirect mitral annuloplasty. CT short-axis images are very useful to assess this aspect. *Ao* aorta, *LCX* left circumflex coronary artery, *LM* left main coronary artery

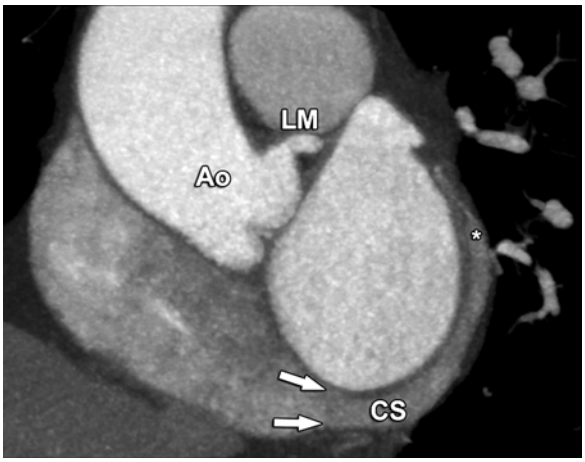

Fig. 18.7 Assessment of the coronary venous system dimensions with CT for transcatheter indirect mitral valve annuloplasty. The ostium of the coronary sinus (*CS*) should be 7–16 mm wide (*arrows*), and the great cardiac vein should be at least 3 mm wide (*asterisk*) to receive the distal anchor of the device. The total length of the coronary venous system should be from 14 to 18 cm. *Ao* aorta, *LM* left main coronary artery

relationship with the coronary sinus – the target structure of percutaneous indirect annuloplasty techniques. Moderate-to-severe mitral annulus calcification has been considered a contraindication for these techniques (**Fig. 18.6**).

- *Coronary sinus*. The dimensions of the coronary sinus and its course along the mitral annulus can be carefully evaluated with CT. In the EVOLUTION trial, the MONARC device required a diameter of the anterior interventricular vein of 3–6 mm, a diameter of the coronary sinus ostium of 7–16 mm, and the length between the great cardiac vein and the coronary sinus ostium should be 14–18 cm (**Fig. 18.7**). Furthermore, several observational studies have shown that the coronary sinus runs superiorly to the mitral valve annulus in the majority of patients, and in 68% of patients the circumflex artery courses between the coronary sinus and the mitral valve annulus with the subsequent risk of arterial occlusion and myocardial infarction during implantation. These aspects are best appreciated on axial images acquired at the level of the mitral annulus and three-dimensional volume renderings of CT (**Fig. 18.8**).

Fig. 18.8 CT assessment of the position of the coronary sinus (*CS*) and great cardiac vein in relation to the mitral annulus and the left circumflex coronary artery before indirect mitral valve repair. **Panel A** shows a CS that runs above the mitral annulus plane (*white line*) on a three-dimensional rendering. The effectiveness of indirect mitral valve repair in this situation may be low. **Panel B** shows, in a different patient, that the CS courses at the same level as the mitral annulus plane but crosses the circumflex artery superiorly (*arrow*). In this situation, an indirect mitral valve annuloplasty would carry the risk of impingement of the coronary artery and myocardial infarction. **Panel C** shows the distal spatial relationship of the coronary venous system with the left circumflex coronary artery. The *arrow* in **Panel C** indicates that the great cardiac vein crosses above the circumflex artery. The main posterolateral vein is indicated by an *asterisk*. With 10-mm maximum-intensity projections along the short-axis, the spatial relationship (*arrow*) between the CS and the left circumflex coronary artery (*LCX*) can also be evaluated (**Panel D**). *Ao* aorta

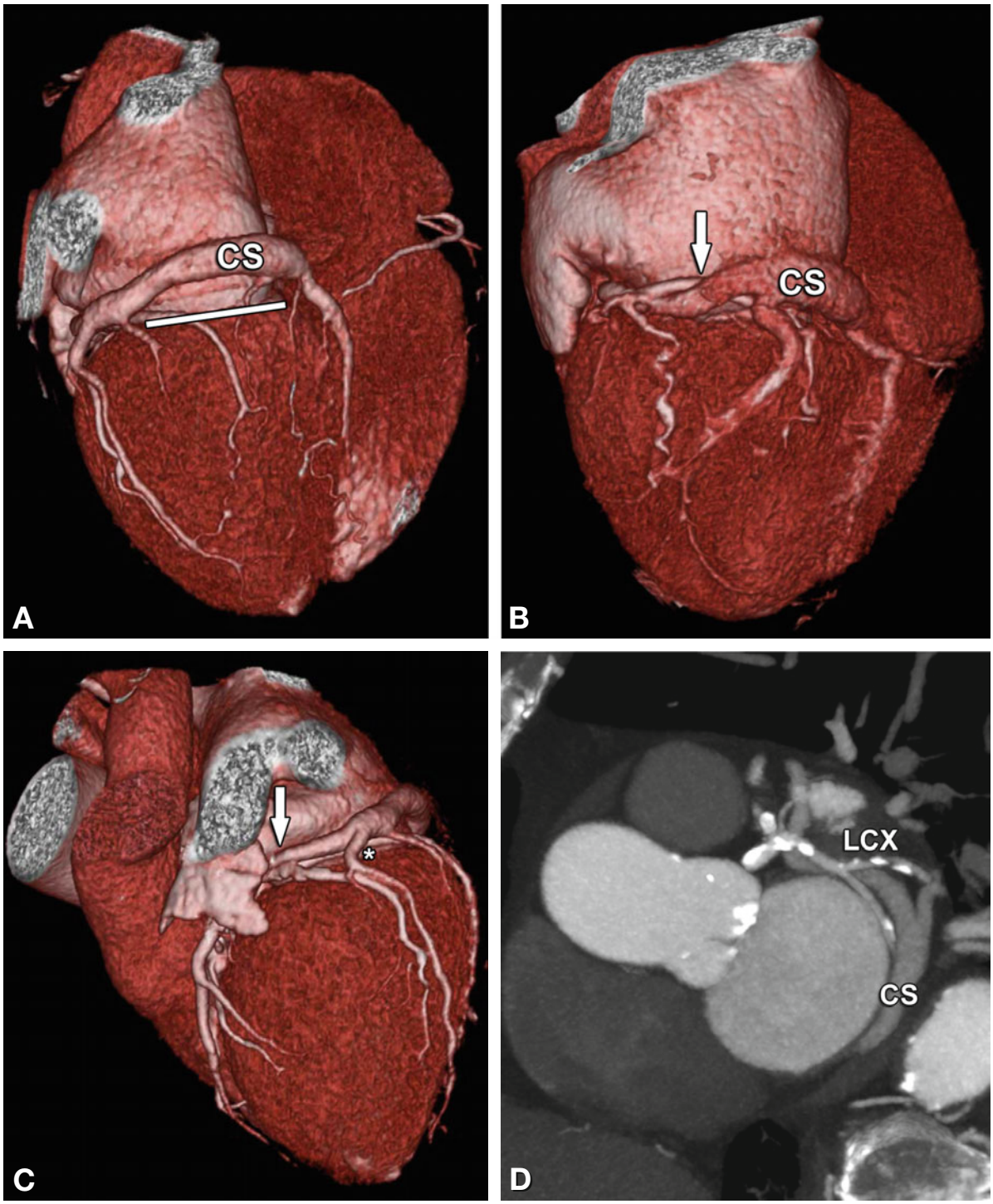
CS
A
CS
B
*
C
LCX
CS
D

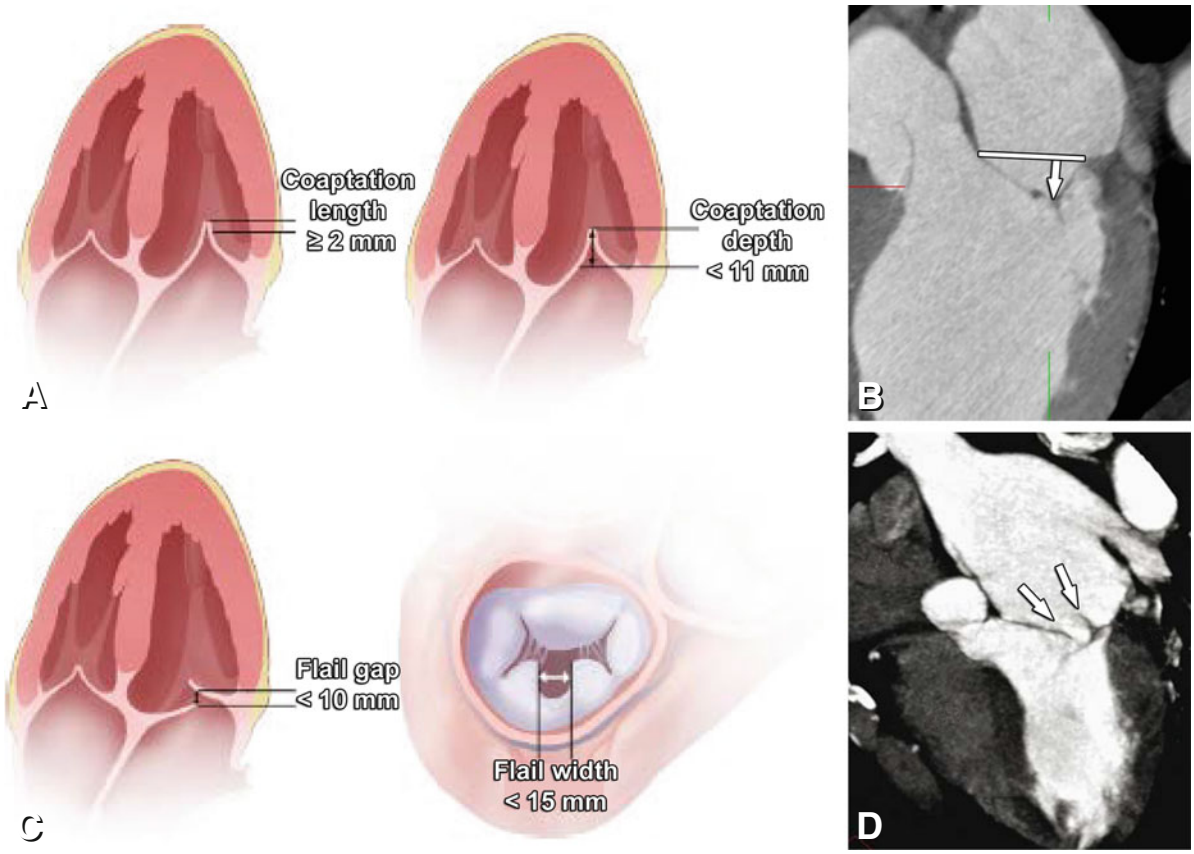

Fig. 18.9 Inclusion criteria for treatment of mitral regurgitation with transcatheter mitral leaflet repair (Mitraclip). **Panel A**: In functional mitral regurgitation, the grade of mitral leaflet tethering can be assessed with CT by measuring the coaptation depth and the coaptation length (*arrow*, **Panel B**). In organic mitral regurgitation, the flail gap and width are important parameters to be assessed (**Panel C**). With CT the flail gap can be measured (*double arrow*, **Panel D**) (Modified and used with permission from Feldman et al. *J Am Coll Cardiol* 2011 and Wong et al. *Int J Cardiol* 2007)

18.3.2 Percutaneous Mitral Leaflet Repair

Percutaneous mitral valve repair with the Mitraclip device (Abbott Park, Illinois, USA) provides the largest clinical data on transcatheter mitral valve repair techniques. Based on the surgical edge-to-edge repair pioneered by Alfieri et al., this approach reduces mitral regurgitation by grasping the two mitral leaflets at the target region with the maximum vena contracta visualized with echocardiography creating an effective double-orifice valve. In some circumstances, two devices may be needed to effectively reduce the regurgitant volume without creating significant mitral stenosis. Candidates for this treatment need to meet several anatomical criteria, which are best assessed using transesophageal echocardiography. However, CT may provide valuable additional information.

In patients with organic mitral regurgitation, the flail gap and width should be <10 and <15 mm, respectively (**Fig. 18.9**). In patients with functional mitral regurgitation, the coaptation length and depth should be >2 and <11 mm, respectively (**Fig. 18.9**). CT data acquired during systole permit accurate assessment of the mitral leaflet scallops that prolapse, the width of the prolapsing scallops, and the location of maximum leaflet tethering. Particularly in patients with functional mitral regurgitation, the angles of the leaflets with the mitral annulus and coaptation depth can be determined with CT and serve as measures of left ventricular remodeling and the amount of tethering exerted on the mitral leaflets (**Fig. 18.10**).

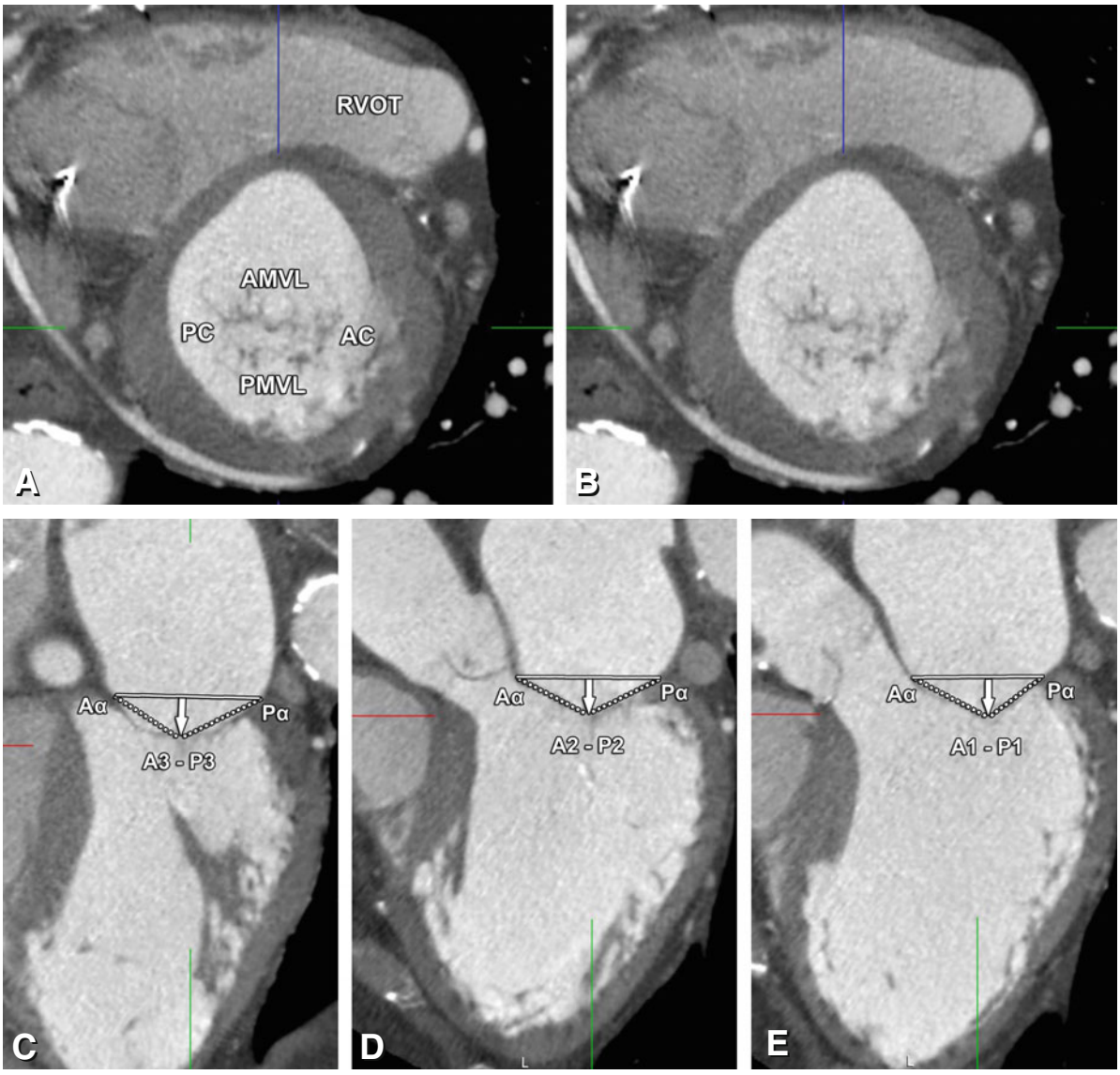

Fig. 18.10 Systematic evaluation of mitral valve geometry with CT. A modified short-axis view of the mitral valve (**Panel A**) shows the anterior and posterior commissures (*AC* and *PC*) as well as the anterior and posterior mitral valve leaflets (*AMVL* and *PMVL*). From this short-axis view, which is again shown in **Panel B** without overlays, three longitudinal parallel planes orthogonal to the mitral valve are displayed in **Panels C**–**E**. The position of these planes parallel to the *blue line* in **Panels A** and **B** are indicated by the letters from *C* to *E* on **Panel B** and define the levels of the mitral valve: posteromedial level (*A3-P3*, **Panel C**), mid level (*A2-P2*, **Panel D**), and anterolateral level (*A1-P1*, **Panel E**). The created longitudinal views (**Panels C**–**E**) of the mitral valve show the anterior and posterior mitral valve leaflets at these three levels, and the mitral valve tenting height (*arrows*) and leaflet angles (*Aα* and *Pα*) can be assessed. *RVOT* right ventricular outflow tract

18.4 Transcatheter Left Atrial Appendage Closure

Atrial fibrillation is the most common cardiac arrhythmia, affecting six million individuals in the United States and causing more than 20% of strokes in the elderly. An estimated 14–44% of patients with atrial fibrillation who are at risk of stroke have contraindications to long-term anticoagulation. Transcatheter left atrial appendage closure techniques are effective alternatives to warfarin for

WATCHMAN	Amplatzer Cardiac Plug	LARIAT
Self-expanding nitinol cage with fixation barbs	Self-expanding nitinol mesh	40-mm pretied radiopaque suture loop
Porous polyethylene membrane on the proximal face of the nitinol cage	Distal lobe with retaining hooks Proximal disk Central polyester patch	Compliant occlusion balloon catheter Magnet-tipped guidewires Suture delivery device
Device size: 21–33 mm for LAA ostium diameter of 17–32 mm	Device size: 16–30 mm for 12.6–28.5 mm maximal orifice width of the LAA	Single-lobed LAA width <40 mm and oriented not superiorly
A	B	C

Fig. 18.11 Left atrial appendage closure technologies

stroke prevention in patients with nonvalvular atrial fibrillation. The results of the PROTECT-AF trial showed that the WATCHMAN device (Boston Scientific, Natick, MA) was not inferior to anticoagulation with warfarin for the composite endpoint (stroke, cardiovascular death, and systemic embolism). Over 3,000 patients with nonvalvular atrial fibrillation have undergone transcatheter left atrial appendage closure. However, implantation of left atrial appendage closure devices requires high operator experience and accurate imaging prior to and during the procedure to minimize complications (pericardial effusion and cardiac tamponade, procedure-related strokes, and device embolization). Currently, transesophageal echocardiography is recommended to size the left atrial appendage and select the device size and to guide the procedure. However, the shape and dimensions of the left atrial appendage are highly variable, and three-dimensional imaging techniques may allow more accurate sizing of the left atrial appendage and procedure guidance. CT is a valuable imaging technique to assist in the procedural steps described in the next sections.

18.4.1 Sizing the Left Atrial Appendage

The different devices available conform to a broad range of left atrial appendage ostium dimensions and shapes. The design of the devices meets different anatomical requirements. The WATCHMAN device consists of a porous polyethylene membrane on the proximal face of a self-expandable nitinol cage with fixation barbs (**Fig. 18.11A**). The size ranges from 21 to 33 mm to accommodate left atrial appendages with ostia of 17–32 mm (measured 1–2 cm from the tip of the left upper pulmonic vein limbus) and a depth that exceeds the width of the left atrial appendage ostium. The Amplatzer Cardiac Plug device (ACP, AGA Medical) consists of a self-expanding flexible nitinol mesh with a distal lobe that retains the hooks for fixation, a proximal disk, and a central polyester patch (**Fig. 18.11B**). This device accommodates left atrial appendages ostia of 12.6–28.5 mm diameter (measured 1 cm below the plane between the left upper pulmonic vein limbus and the circumflex coronary artery). These measurements are based on 2-dimensional

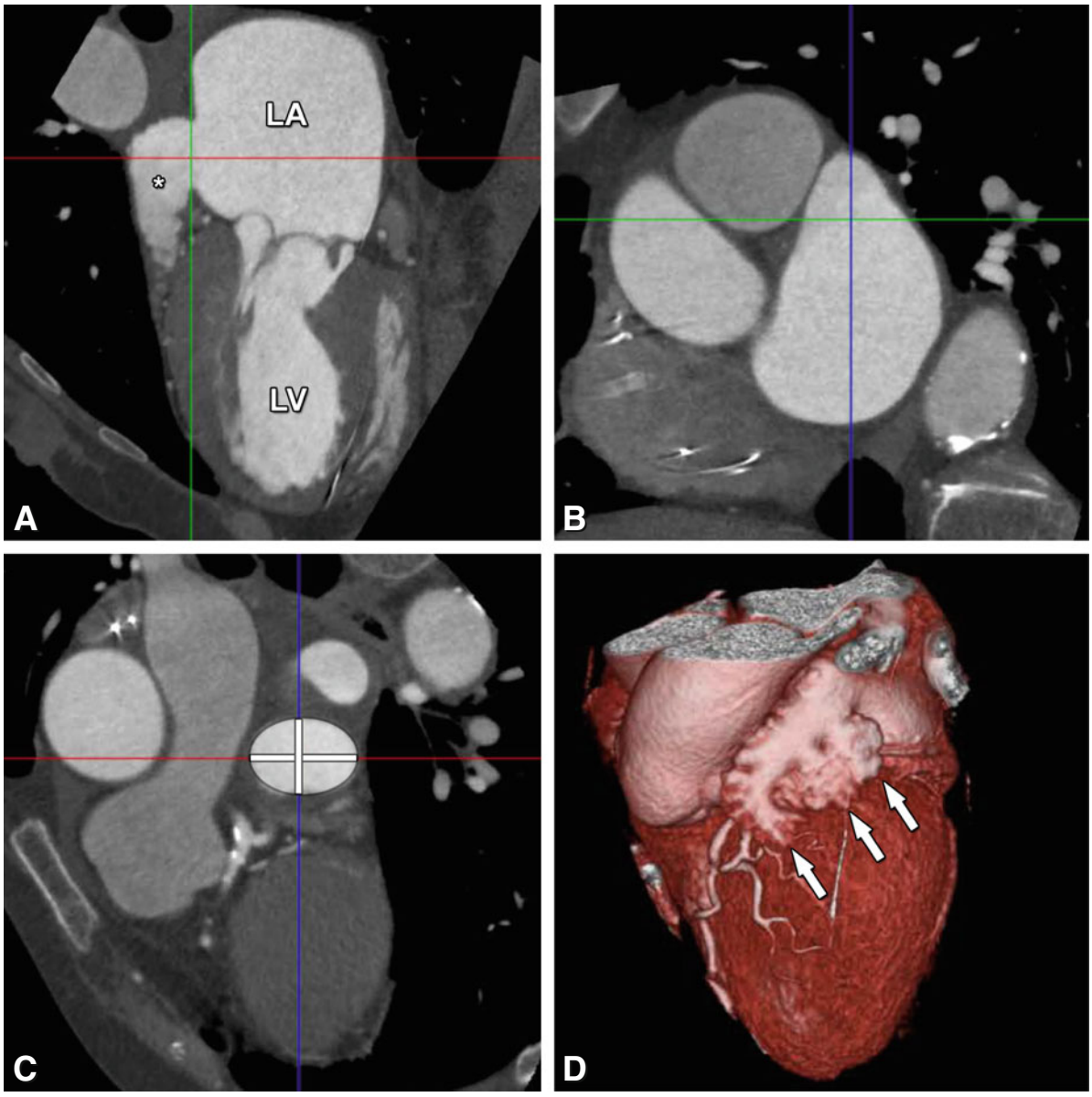

Fig. 18.12 Assessment of left atrial appendage dimensions and shape with CT. **Panels A**–**C** are orthogonally oriented double-oblique multiplanar reformations. **Panel A** is a two-chamber view that corresponds to the position of the *blue line* in **Panels B** and **C**. On **Panel A** the left atrium (*LA*), left ventricle (*LV*), and left atrial appendage (*asterisk*) are seen. **Panel B** is a short-axis view at the level of the ostium of the left atrial appendage that corresponds to the position of the *red line* in **Panels A** and **C**. **Panel C** corresponds to the position of the *green line* in **Panels A** and **B** and allows obtaining the cross-sectional area and the diameters of the ostium of the left atrial appendage. The three-dimensional volume rendering permits accurate visualization of the left atrial appendage with several lobes in this patient (*arrows* in **Panel D**)

transesophageal echocardiography. However, CT is a valuable tool for measuring left atrial appendage dimensions. More recently, the LARIAT Suture delivery device (SentreHEART Inc, Palo Alto, CA) implanted in 100 patients requires CT for sizing the left atrial appendage (**Fig. 18.11C**). This technique combines transeptal placement of a temporary balloon in the left atrial appendage and magnet-tipped guidewires inserted into the left atrial appendage and pericardial space to ligate the left atrial appendage. **Figure 18.11** summarizes the characteristics of the currently available techniques. Multiplanar reformations and three-dimensional volume renderings permit accurate assessment of the diameters and shape of the left atrial appendage, respectively (**Fig. 18.12**).

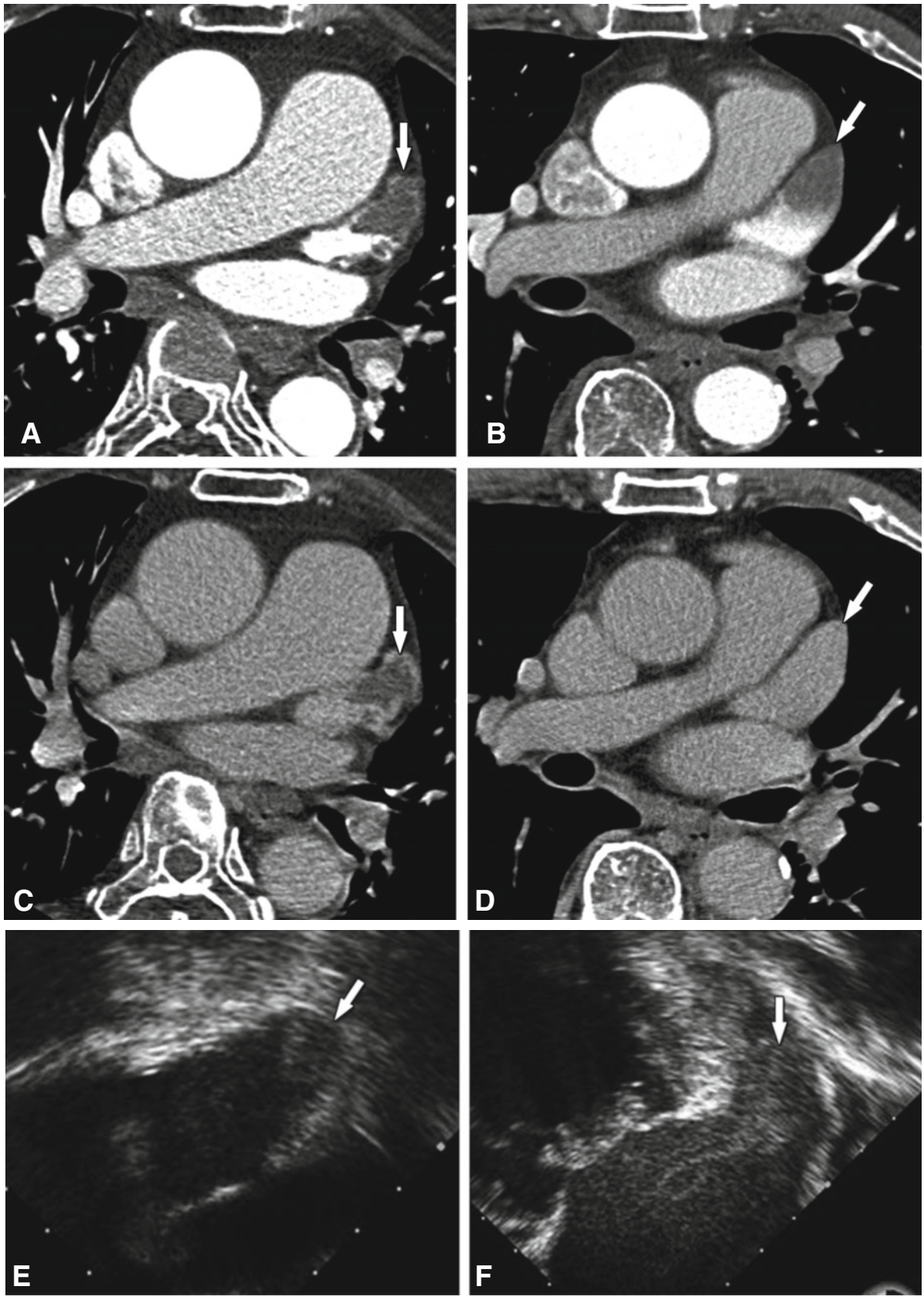
A
B
C
D
E
F

Fig. 18.13 Differentiation between left atrial appendage (LAA) thrombus and arterial-phase filling defects with CT. The left column (**Panels A**, **C** and **E**) shows the example of a 76-year-old woman with stroke. The early-phase angiographic image demonstrates an oval filling defect in the LAA (*arrow* in **Panel A**) that also persists in the late-phase angiographic image (*arrow* in **Panel B**). The transesophageal echocardiographic image shows the oval thrombus in the LAA (*arrow* in **Panel C**). The right column (Panels **B**, **D**, and **F**) shows the example of a 68-year-old man with stroke. The early-phase angiographic image shows a dense triangular filling defect in the LAA (*arrow* in **Panel D**) that is absent in the late-phase image (*arrow* in **Panel E**). The transesophageal echocardiographic image confirms the presence of severe spontaneous echocardiographic contrast but no thrombus was visualized (*arrow* in **Panel F**) (Modified and used with permission from Kim et al. *Am J Cardiol* 2010)

18.4.2 Contraindications

CT can detect left atrial appendage thrombus. However, the presence of low flow on early-phase CT angiography can mimic filling defects. Therefore, acquisition of early- and additional late-phase images or dual-bolus CT may help to differentiate low flow from true thrombus (**Fig. 18.13**). In addition, according to manufacturer's recommendations, the presence of complex atheroma in the aortic arch or descending aorta (with mobile plaques ≥4 mm) is considered a contraindication for the WATCHMAN closure device.

18.4.3 Planning the Procedure

Planning the procedure: CT permits accurate planning of the transeptal puncture and of the angiographic views that will be used to guide the procedure (**Fig. 18.14**). Of particular interest is the anatomy of the interatrial septum. A patent foramen ovale and atrial septal defects are contraindications for the procedure. An example of an Amplatzer device implantation guided by CT. Specifically for the LARIAT Suture delivery device, three-dimensional volume renderings are of interest to evaluate the orientation of the left atrial appendage in relation

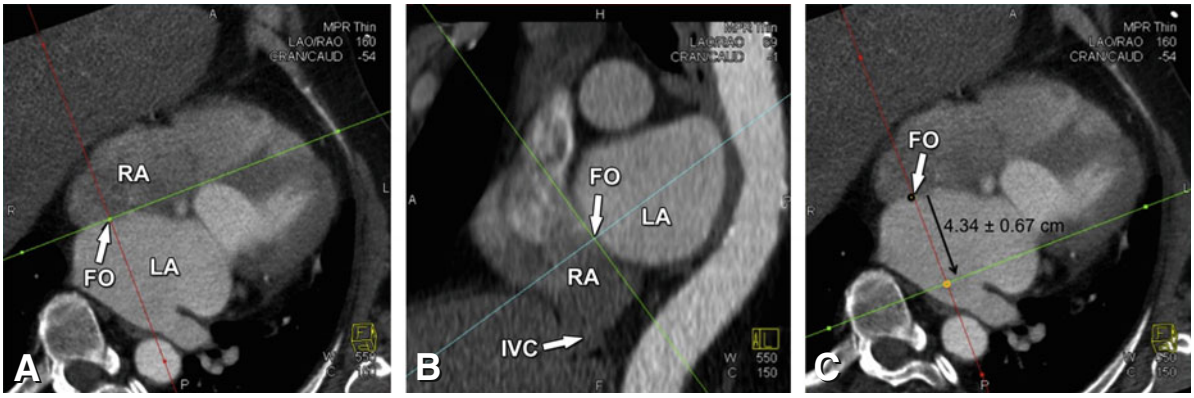

Fig. 18.14 CT evaluation of the fluoroscopy projections during transcatheter left atrial appendage closure using the Watchman or the Amplatzer Cardiac Plug devices. Panels **A**–**C** show alignment of the multiplanar reformation planes to anticipate the fluoroscopy projections during transseptal puncture. The foramen ovale (*FO*) is localized and the angles and distance to the left atrial appendage are assessed. *LA* left atrium, *IVC* inferior vena cava, *RA* right atrium (Modified and used with permission from Krishnaswamy et al. *Int J Cardiol* 2012)

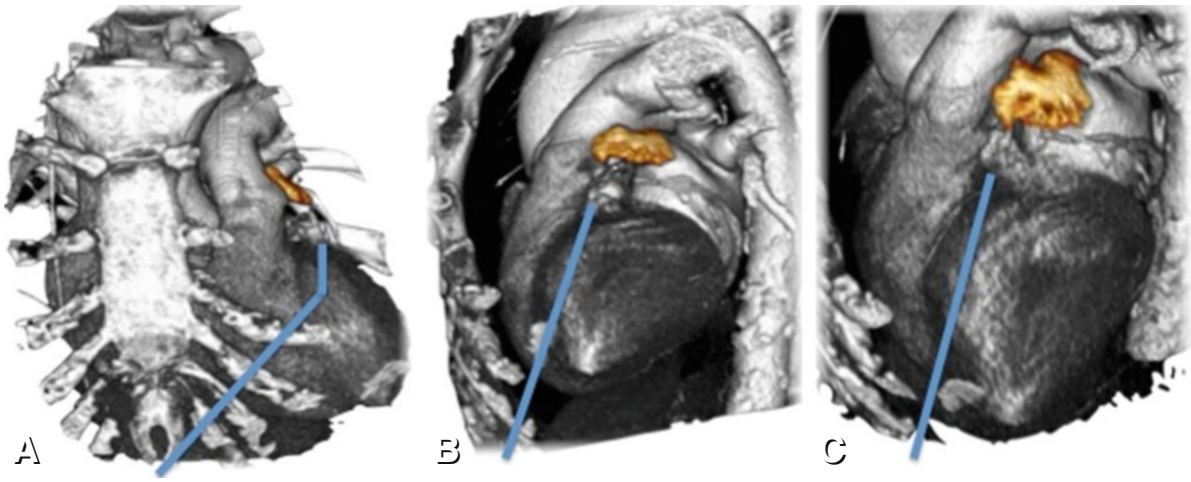

Fig. 18.15 For the LARIAT suture device, three-dimensional volume renderings (**Panels A–C**) permit assessment of the location and orientation of the left atrial appendage in relation to the sternum. The pericardial catheter (*blue catheter*) can be simulated to anticipate the maneuvers during the procedure. The lateral views of the three-dimensional volume renderings show the space between the sternum and the anterior aspect of the myocardium, indicating the steepness of the direction of the pericardial needle (**Panels B** and **C**) (Modified and used with permission from Bartus et al. *J Am Coll Cardiol* 2013)

to the sternum and to anticipate the manipulation of the catheters in the pericardial space (**Fig. 18.15**). The lateral view of the three-dimensional volume renderings shows the space between the sternum and the anterior aspect of the myocardium and indicates the steepness of the direction of the pericardial needle. In the majority of patients, the left atrial appendage is oriented anteriorly. However, in some cases the left atrial appendage can be more posteriorly rotated, which demands more lateral direction of the pericardial needle.

18.5 Conclusions

CT is a valuable imaging technique to select patients for catheter-based cardiac therapies and to plan and guide the procedures. The ability to visualize the structures of interest from unlimited views and to obtain three-dimensional volume renderings improves the selection of the most appropriate device size and procedural approach. Future developments will permit integration of CT and fluoroscopy for procedural guidance.

Recommended Reading

Alfieri O, Elefteriades JA, Chapolini RJ et al (2002) Novel suture device for beating-heart mitral leaflet approximation. Ann Thorac Surg 74(5):1488–1493

Balzer DT (2012) Percutaneous pulmonary valve implantation: fixing the problems and pushing the envelope. Curr Opin Pediatr 24(5):565–568

Bartus K, Han FT, Bednarek J et al (2013) Percutaneous left atrial appendage suture ligation using the LARIAT device in patients with atrial fibrillation: initial clinical experience. J Am Coll Cardiol 62: 108–118

Chatterjee S, Alexander JC, Pearson PJ, Feldman T (2011) Left atrial appendage occlusion: lessons learned from surgical and transcatheter experiences. Ann Thorac Surg 92(6):2283–2292

Delgado V, Tops LF, Schuijf JD et al (2009) Assessment of mitral valve anatomy and geometry with multislice computed tomography. JACC Cardiovasc Imaging 2(5):556–565

Delgado V, Kapadia S, Marsan NA, Schalij MJ, Tuzcu EM, Bax JJ (2011) Multimodality imaging before, during, and after percutaneous mitral valve repair. Heart 97(20):1704–1714

Feldman T, Cilingiroglu M (2011) Percutaneous leaflet repair and annuloplasty for mitral regurgitation. J Am Coll Cardiol 57(5): 529–537

Feltes TF, Bacha E, Beekman RH III et al (2011) Indications for cardiac catheterization and intervention in pediatric cardiac disease: a scientific statement from the American Heart Association. Circulation 123(22):2607–2652

Recommended Reading

Feuchtner GM, Alkadhi H, Karlo C et al (2010) Cardiac CT angiography for the diagnosis of mitral valve prolapse: comparison with echocardiography1. Radiology 254(2):374–383

Filsoufi F, Carpentier A (2007) Principles of reconstructive surgery in degenerative mitral valve disease. Semin Thorac Cardiovasc Surg 19(2):103–110

Fleming GA, Hill KD, Green AS, Rhodes JF (2012) Percutaneous pulmonary valve replacement. Prog Pediatr Cardiol 33:143–150

Haas NA, Moysich A, Mortezaeian H et al (2013) Percutaneous implantation of the Edwards SAPIEN(™) pulmonic valve: initial results in the first 22 patients. Clin Res Cardiol 102:119–128

Harnek J, Webb JG, Kuck KH et al (2011) Transcatheter implantation of the MONARC coronary sinus device for mitral regurgitation: 1-year results from the EVOLUTION phase I study (Clinical Evaluation of the Edwards Lifesciences Percutaneous Mitral Annuloplasty System for the Treatment of Mitral Regurgitation). JACC Cardiovasc Interv 4(1):115–122

Holmes DR, Reddy VY, Turi ZG et al (2009) Percutaneous closure of the left atrial appendage versus warfarin therapy for prevention of stroke in patients with atrial fibrillation: a randomised non-inferiority trial. Lancet 374(9689):534–542

Killeen RP, Arnous S, Martos R, Abbara S, Quinn M, Dodd JD (2010) Chronic mitral regurgitation detected on cardiac MDCT: differentiation between functional and valvular aetiologies. Eur Radiol 20(8):1886–1895

Kim SC, Chun EJ, Choi SI et al (2010) Differentiation between spontaneous echocardiographic contrast and left atrial appendage thrombus in patients with suspected embolic stroke using two-phase multidetector computed tomography. Am J Cardiol 106(8): 1174–1181

Krishnaswamy A, Patel NS, Ozkan A et al (2012) Planning left atrial appendage occlusion using cardiac multidetector computed tomography. Int J Cardiol 158(2):313–317

Landmesser U, Holmes DR Jr (2012) Left atrial appendage closure: a percutaneous transcatheter approach for stroke prevention in atrial fibrillation. Eur Heart J 33(6):698–704

Nkomo VT, Gardin JM, Skelton TN, Gottdiener JS, Scott CG, Enriquez-Sarano M (2006) Burden of valvular heart diseases: a population-based study. Lancet 368(9540):1005–1011

Romero J, Husain SA, Kelesidis I, Sanz J, Medina HM, Garcia MJ (2013) Detection of left atrial appendage thrombus by cardiac computed tomography in patients with atrial fibrillation: a meta-analysis. Circ Cardiovasc Imaging 6(2):185–194

Tops LF, Van de Veire NR, Schuijf JD et al (2007) Noninvasive evaluation of coronary sinus anatomy and its relation to the mitral valve annulus: implications for percutaneous mitral annuloplasty. Circulation 115(11):1426–1432

Wong TW, De LC, Boey HK, Lim MC (2007) Flail P2 cusp of posterior mitral valve leaflet demonstrated on multi-slice computed tomography. Int J Cardiol 115(1):e31–e32

Myocardial Perfusion and Fractional Flow Reserve

K. Kitagawa, A. Erglis, and M. Dewey

Abstract

Myocardial CT perfusion imaging is a rapidly evolving technology that allows assessment of the functional significance of potentially obstructive coronary stenosis. The opportunity for quantification of myocardial perfusion is the greatest potential advantage of CT compared with other perfusion techniques. On the other hand, fractional flow reserve during coronary angiography provides a functional assessment of coronary lesions identified with this modality. Recently, a non-invasive method for estimating fractional flow reserve, based on coronary CT angiography has been introduced. Nevertheless, at present neither CT perfusion nor CT FFR are ready for widespread use in clinical routine.

19.1 Clinical Impact of Myocardial Perfusion Assessment and Fractional Flow Reserve

Recent advancements in CT allow noninvasive assessment of the morphology of coronary artery stenosis. With its high negative predictive value, coronary CT angiography (CTA) has been shown to be most useful for evaluating persons with low to intermediate pretest likelihood of coronary artery disease in whom invasive coronary angiography may otherwise be indicated (Chap. 5). However, the anatomically significant appearance of a coronary stenosis does not always equate with functional significance, and a 50% stenosis identified by coronary CTA is a poor predictor of myocardial ischemia during stress. This is especially true when there are heavily calcified plaques and stents in the coronary arteries. Therefore, patients with obstructive coronary artery disease on CTA

M. Dewey, *Cardiac CT*,
DOI 10.1007/978-3-642-41883-9_22, © Springer-Verlag Berlin Heidelberg 2014

Table 19.1 Comparison of myocardial perfusion imaging modalities

Modality	Advantages	Disadvantages
Nuclear perfusion	Standardized protocol	Radiation exposure
	No nephrotoxicity	Low spatial resolution
	Automated image analysis	Limited sensitivity to triple vessel disease
	Extensive outcome data	
MR perfusion	No radiation exposure	Limited coverage of myocardium
	High in-plane spatial resolution	Nonlinear relationship between contrast medium concentration and signal
	Delayed enhancement available	More physician input needed
		Limited outcome data
CT perfusion	Gapless coverage of entire myocardium with isotropic voxels	No standardized protocol
	Coronary myocardium correlation is easier	Radiation exposure
	Linear relationship between contrast medium concentration and signal	Use of iodinated contrast medium
		No outcome data

may best be investigated using a combined approach with a subsequent functional test such as nuclear stress testing or magnetic resonance (MR) perfusion imaging. CT perfusion (CTP) has recently emerged as a novel technology for assessing the functional significance of coronary stenosis that has certain advantages but also disadvantages over the other myocardial perfusion imaging techniques (**Table 19.1**). Fractional flow reserve (FFR) during invasive coronary angiography is the most accurate and reliable measure of the functional significance of a coronary lesion and is considered the gold standard for deciding whether coronary revascularization will be beneficial. CT estimation of FFR has also shown potential for noninvasively determining whether or not revascularization may be indicated in certain situations. Moreover, it would be convenient and potentially more cost-effective if the patient could be assessed for the functional significance of potentially obstructive coronary stenoses at the time of CTA. More importantly, the patient might benefit from the resulting rapid diagnosis.

19.2 CT Perfusion Imaging Techniques

Myocardial CTP imaging uses the first pass of the iodinated contrast medium in the heart during vasodilator-induced hyperemia to detect ischemic myocardium. The idea has been inspired by MR-based stress myocardial perfusion imaging, which typically monitors the first-pass dynamics of intravenously injected Gd-based contrast media on 3–5 short-axis slices acquired every heart beat over 40–60 heartbeats. However, there are several important differences between CT and MR perfusion imaging that should be carefully considered. First of all, the top priority of cardiac CT is to acquire a high-quality coronary CTA. This is difficult to accomplish during stress-induced tachycardia with the current temporal and spatial resolution of CT. Second, the administration of nitroglycerin for CTA would neutralize the effect of adenosine for CTP, making meaningful perfusion analysis impossible. Therefore, it is necessary to separate resting state coronary CTA (with nitroglycerin) from stress CT myocardial perfusion. Third, in order to minimize radiation CTP should be limited to the necessary acquisitions. Given that radiation exposure from both conventional coronary angiography and SPECT myocardial perfusion imaging is about 5–10 mSv, 15 mSv could be an acceptable maximum radiation dose for a combined stress CTP and rest coronary CTA protocol. There are two major approaches of stress CTP.

19.2.1 Static (Single-Shot) CT Perfusion

Static CTP is defined by the acquisition of images at a predefined single time point during early myocardial perfusion regardless of the imaging technique used

(i.e., retrospective or prospective gating, single- or dual-energy). It has been demonstrated that there is a time frame of approximately 8 s for optimal differentiation of ischemic and nonischemic myocardium for static CTP scans. Early feasibility studies suggest that static CTP can be performed on standard 64-row CT scanners (gantry rotation time of 400 ms and longitudinal coverage of 4 cm) but results in relatively high radiation exposure. In addition, 64-row CTP often suffers from significant motion artifact caused by stress-induced tachycardia.

The breakthrough for stress CTP came with the introduction of second-generation dual-source CT (Siemens Somatom Definition) and wide-area 320-row CT scanners (Toshiba Aquilion ONE). The high temporal resolution of second-generation dual-source CT (75 ms, see Chap. 9b) allows acquisition of motion-free images during vasodilator-stress-induced tachycardia. Moreover, effective doses can be less than 15 mSv by using retrospectively ECG-gated helical acquisition for stress perfusion and prospectively ECG-triggered axial acquisition for rest coronary CTA. One drawback of dual-source CTP is the relatively long scan duration (7–10 s), which is inherent in 64-row CT because it images subvolumes of the entire cardiac volume over 6–10 heartbeats. For acquisition of some subvolumes, dual-source CTP may miss the optimal time frame. Additionally, the resulting temporal inhomogeneity along Z-axis makes quantitative analysis of dual-source CTP difficult. Finally, dual-source CTP may suffer from banding and misalignment artifact.

Volumetric imaging with 320-row CT provides the opportunity to acquire the entire heart as a volume with excellent temporal homogeneity during first-pass myocardial contrast enhancement – the best moment for ischemia detection (temporal resolution of 175 ms with first- and 138 ms with second-generation, see Chap. 9a). An apparent disadvantage of using 320-row CT compared with dual-source CT, on the other hand, is lower temporal resolution in each slice, which may necessitate heart rate control using beta blocker.

The imaging technique of static CTP is basically the same as for rest coronary CTA except for image acquisition timing. Images should be acquired 3–5 s later than for coronary CTA in order to ensure an adequate level of perfusion of contrast material throughout the myocardium. However, since contrast transit time during vasodilator stress may be significantly different from that at rest, we recommend to use the bolus tracking method with a trigger threshold of 200–300 HU in the descending aorta rather than a test bolus method. For static CTP, it is recommended to use retrospectively ECG-gated or prospectively ECG-triggered scans with a widened data acquisition window to implement multiphase reconstruction.

19.2.2 Dynamic CT Perfusion

In dynamic CTP, as with MR perfusion, images are acquired over a predetermined period of time to characterize the wash-in and wash-out of contrast medium in the myocardium, allowing various semi- and fully quantitative analyses of myocardial blood flow (MBF). Although dynamic CTP has so far been limited to animal studies due to the narrow Z-axis coverage and high radiation exposure of conventional 64-row CT, it is now becoming possible to implement dynamic CTP covering the entire left ventricular myocardium in clinical patients with acceptable radiation exposure (**Fig. 19.1**). Dynamic CTP has three major advantages over the static technique. First, noninvasive quantification of MBF may further improve characterization of the hemodynamic relevance of stenosis. Second, differentiation between true perfusion abnormalities and various artifacts is much easier by evaluating the time course of myocardial enhancement. Third, it is less likely to miss the optimal time frame for ischemia detection.

Recently, dynamic CTP using second-generation dual-source CT in the so-called shuttle mode has been implemented. In the shuttle mode, ECG-triggered axial acquisitions will be repeated at two alternating table positions to achieve dynamic acquisition with 7-cm Z-axis coverage. For a heart rate of 63 beats per min or less every single heartbeat and for a heart rate of greater than 63 beats per min every second heartbeat, the other volume is covered. This results in a total of 9–14 datasets of the entire heart (**Fig. 19.1A, B**). Of note, shuttle-mode CTP employs a dedicated image reconstruction technique to minimize variation in CT Hounsfield units (HU) resulting from partial scan reconstruction without sacrificing temporal resolution. Specifically, the algorithm requires acquisition of enough X-ray projections to reconstruct both partial (180° + fan angle) and full (360°) scans. Then, using spatial linear filters, artifact-corrected image data are created by superimposing the low spatial frequency content of the full scan reconstruction (which contains no partial scan reconstruction artifacts but has low spatial resolution and 225 ms temporal resolution) and the high spatial frequency content of the partial scan reconstruction (which contains high spatial frequencies and 75 ms temporal resolution). The radiation exposure of dynamic CTP is 9–10 mSv, which may be substantially reduced in the near future when dose reduction strategies such as automatic exposure control, use of lower tube voltage, and iterative reconstruction can be applied.

There is also an increasing interest in dynamic CTP using second-generation 320-row CT. With maximum detector coverage of 16 cm, dynamic CTP by 320-row CT can easily cover the entire left ventricular

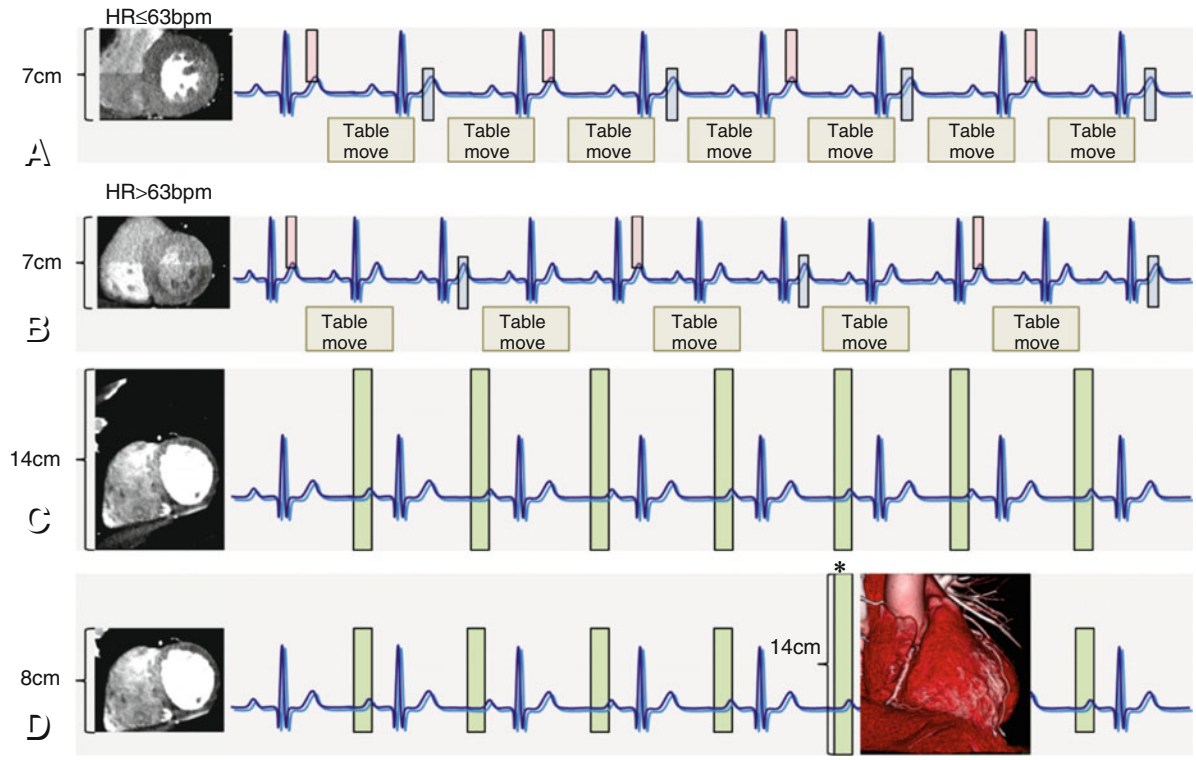

Fig. 19.1 Acquisition of dynamic CTP using dual-source CT (**Panels A** and **B**) and 320-row CT (**Panels C** and **D**). With 4-cm detector coverage, dual-source CT uses "shuttle mode", which scans the heart at two alternate table positions to achieve total Z-axis coverage of 7 cm. Image acquisition occurs every single heartbeat for a heart rate of 63 beats per min or less (**Panel A**) and every second heartbeat for a heart rate of greater than 63 beats per min (**Panel B**). For high heart rates, the same anatomy is therefore covered every fourth heartbeat (**Panel B**). 320-row CT with wide coverage is capable of dynamic CTP of the entire heart without table movement at high temporal sampling rate (**Panel C**). However, wide coverage is not needed and limiting the scan range to 8–10 cm will result in less radiation exposure while covering the entire myocardium (**Panel D**). **Panel D** presents an example of a 320-row CT protocol potentially enabling 8-cm coverage dynamic CTP and 14-cm coverage coronary CTA (*) at a reduced radiation exposure

myocardium without table movement. This results in a higher data sampling rate than the shuttle mode and may therefore improve accuracy of quantitative analysis (**Fig. 19.1C**). Since dynamic CTP using 320-row CT can include the entire coronary artery tree as well, not only the stress scan but also the rest scan can be performed dynamically, so that myocardial perfusion reserve can be calculated. However, this comes at the cost of higher radiation exposure. Although technical improvements are required to reduce radiation exposure further, 320-row CT has potential for dynamic CTP (**Fig. 19.1D**).

To reduce the radiation exposure of dynamic CTP, it is important to minimize the data acquisition window within each RR interval. According to a recent myocardial MR perfusion study, the diagnostic accuracy for detecting significant stenosis is similar in systole and diastole. Advantages of acquiring stress CTP during diastole are: (1) longer quiescent period at lower heart rate, (2) comparison with rest scan is easier, and (3) image fusion with resting coronary CTA can be achieved with less misregistration. On the other hand, systolic acquisition has the following advantages: (1) less sensitive to RR variability and arrhythmia, (2) fewer motion artifacts at higher heart rate, (3) less prone to artifact due to thicker myocardium, and (4) thicker myocardium allows easier contour delineation and evaluation of transmural contrast enhancement. In addition, for platforms with limited coverage such as dual-source CT (73 mm) and 256-slice CT (80 mm; Philips iCT; see Chap. 9c), shorter Z-axis dimensions, which occur during systole, are preferable.

19.3 Patient Preparation

In addition to general preparation for coronary CTA, several special measures are required for stress CTP. It is important to terminate antianginal drugs and caffeine

24 h before the stress test and make sure that the patient has no contraindications to adenosine stress (**List 19.1**). A second intravenous line is required since adenosine and contrast medium should be administered by using separate venous routes in different forearms because rapid injection of adenosine can cause AV block and temporal cardiac arrest. Recording blood pressure, heart rate, and ECG before and after adenosine stress is highly recommended to ensure patient safety. Adenosine is infused intravenously over about 4–5 min with a dose of 140 µg/kg/min. The major safety advantage of adenosine is the ease in its use mainly because of its short half life of below 30 s. Alternatively, the adenosine receptor agonist regadenoson can be used which has the advantage that it can be injected intravenously and that stress tests done with this agent are not influenced by the presence of beta blockers. However, the half life of regadenoson is much longer with about 2–3 min and in case of relevant complications (<1%) the effect may have to be terminated using aminophylline.

To acquire motion-free stress CTP images by first-generation 320-row CT with 175 ms temporal resolution, administration of a beta blocker (e.g., 50–150 mg atenolol) with a target resting heart rate of 60 beats per min is mandatory. Although it has been demonstrated that therapeutic doses of beta blockers do not impair the detection of clinically significant coronary artery disease by vasodilator stress nuclear myocardial perfusion imaging, beta blockers can potentially mask ischemia by increasing hyperemic blood flow. In this regard, platforms with higher temporal resolution have a certain advantage of not requiring beta blockade.

List 19.1. Contraindications to adenosine

1. Myocardial infarction within 24 h
2. Unstable angina
3. Bronchial asthma (relative contraindication)
4. Advanced AV block
5. Decompensated heart failure
6. Sick sinus syndrome
7. Therapy with dipyridamole
8. Long QT syndrome
9. Severe hypotension

19.4 Combined Assessment of Perfusion and Coronary Arteries

19.4.1 Stress First CT Perfusion

Stress CTP first, followed by rest coronary CTA may be preferred when scanners with high temporal resolution such as dual-source CT and second-generation 320-row CT are available (**Figs. 19.2** and **19.3**). The main advantage of a stress-first protocol is that the stress scan is a "clean", uncontaminated acquisition, which facilitates the detection of myocardial ischemia. After the stress scan, beta blockers and sublingual nitroglycerin can be administered to optimize coronary CTA. Drawbacks of this protocol are: (1) a possible image quality degradation of coronary CTA caused by vasodilator stress and increased heart rates and (2) a possible underestimation of perfusion defect on the rest coronary CTA due to the delayed-enhancement phenomenon caused by the contrast medium used for the stress scan.

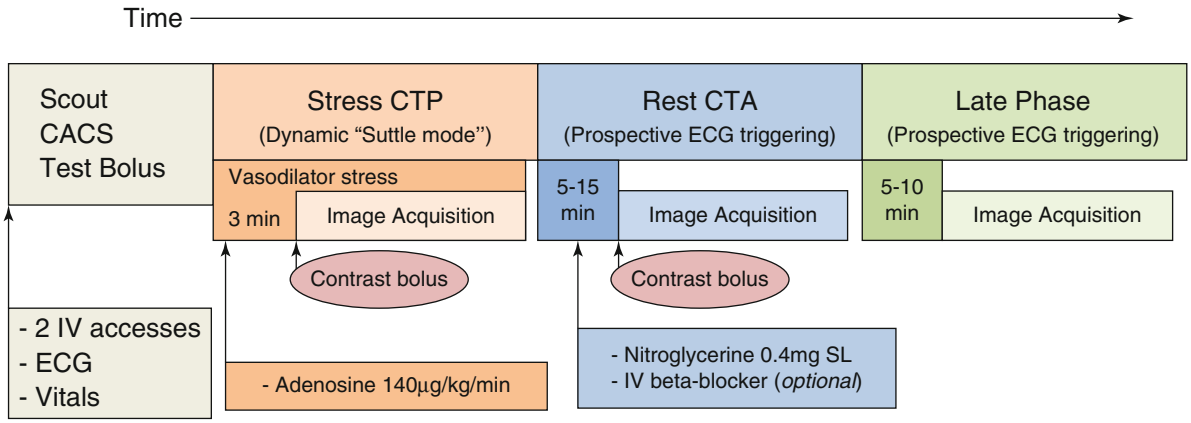

Fig. 19.2 The image acquisition timeline for stress-first comprehensive cardiac CT. In this example, shuttle mode dynamic CT perfusion (*CTP*), rest CT angiography (*CTA*) and delayed enhancement CT are combined. The test bolus is used to optimally time the subsequent CT scans. *CACS* coronary artery calcium scan, *ECG* electrocardiogram, *IV* intravenous, *SL* sublingual

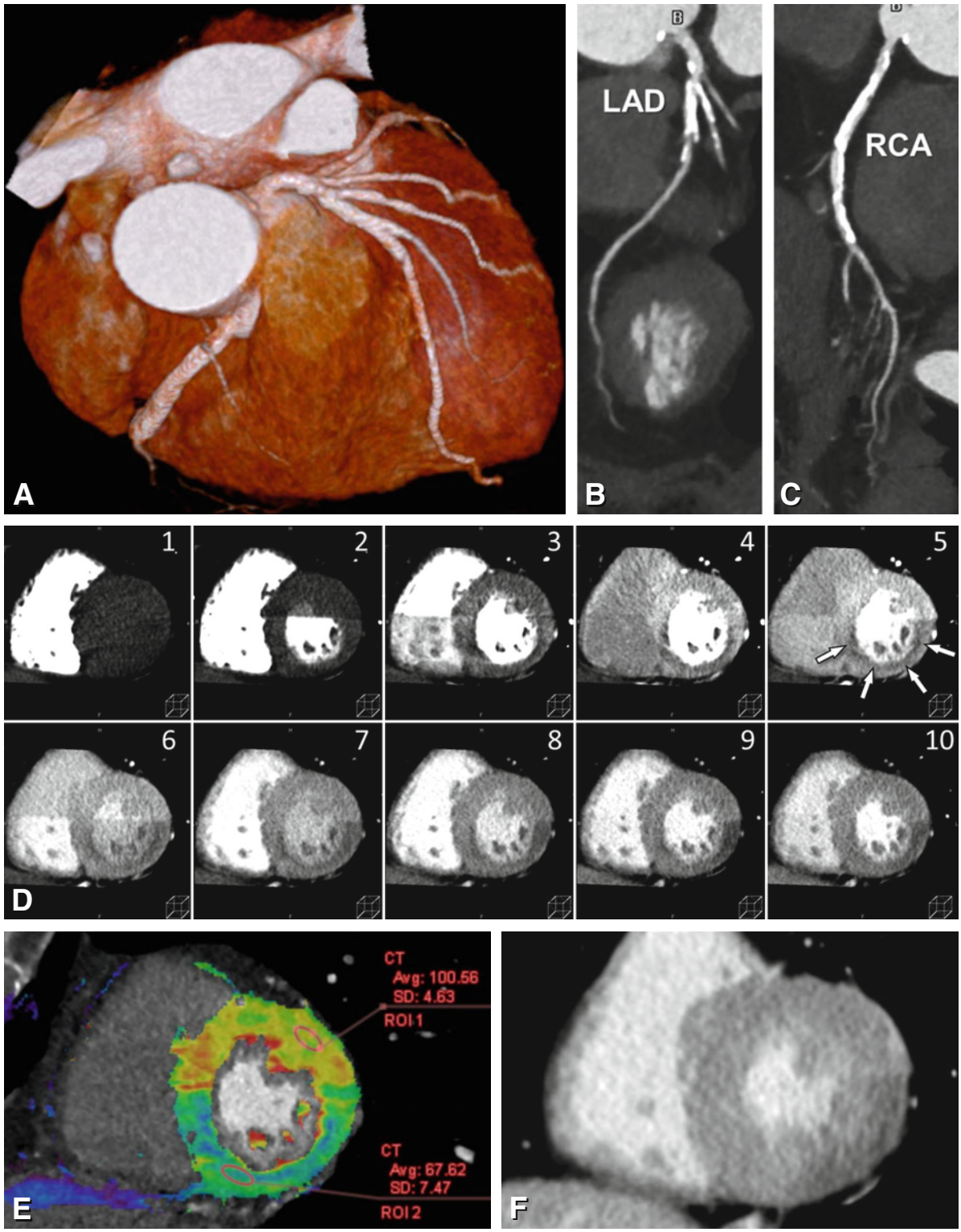

Fig. 19.3 Comprehensive cardiac study using second-generation dual-source CT in a 69-year-old female with diabetes mellitus and angina pectoris. Presence of heavily calcified plaques precluded CT assessment of coronary artery stenosis (**Panels A**–**C**). Stress dynamic CTP of 10 frames acquired intermittently over a period of 30 s demonstrated severe perfusion deficit in the inferior wall (*arrows* in **Panel D**). Quantitative analysis of the dynamic CTP indicated higher myocardial blood flow (100 ml/min/g) in the anterior wall compared with the inferior wall (67 ml/min/g, **Panel E**). There was no delayed enhancement on the late scan (**Panel F**)

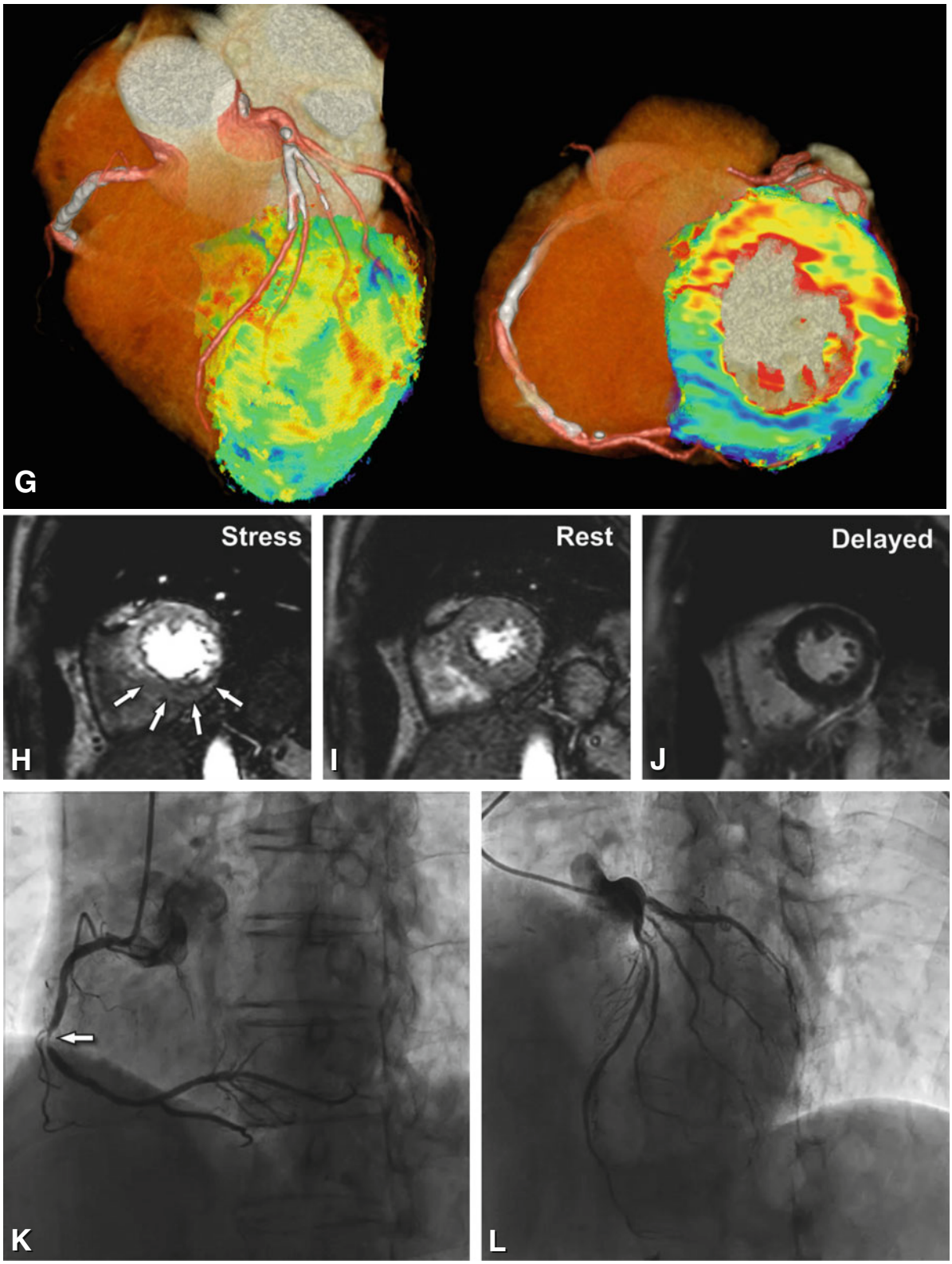

Fig. 19.3 (continued) Fused CTA/stress MBF images can be used to correlate individual coronary artery anatomy and the distribution pattern of MBF (**Panel G**). Presence of extensive inferior ischemia (*arrows*) and absence of infarcted myocardium were confirmed by MRI (**Panels H**–**J**). Conventional coronary angiography revealed high-grade mid-RCA stenosis (*arrow*), which was treated by stenting (**Panel K**). No obstructive disease was seen in the left coronary artery on angiography (**Panel L**)

19.4.2 Rest First CT Perfusion

Performing rest coronary CTA first, followed by stress CTP makes sense from a clinical perspective because stress CTP can be avoided when obstructive coronary artery disease is excluded by coronary CTA (**Figs. 19.4** and **19.5**). The concerns with this approach are: (1) there is cross-contamination of contrast in the stress perfusion scan, potentially masking areas of ischemic myocardium, and (2) beta blockers used to optimize coronary CTA can also potentially mask ischemia. To avoid cross-contamination, it is necessary to have an interval of at least 20–30 min between rest and stress acquisitions. In clinical practice, this interval can be used to assess rest CTA and decide whether or not to proceed to stress CTP with the patient waiting on the scanner bed.

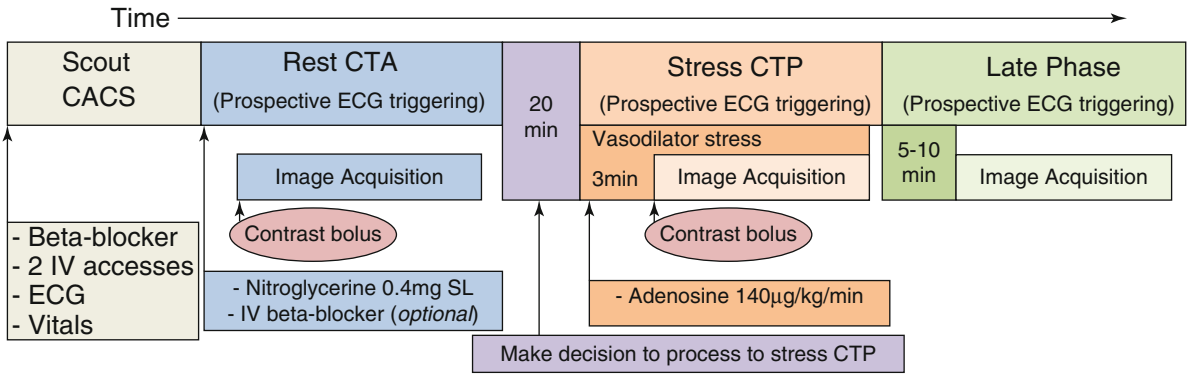

Fig. 19.4 The image acquisition timeline for rest-first CT perfusion (*CTP*) comprehensive cardiac CT using 320-row CT. The most important advantage of this protocol is that we can decide to proceed to stress CTP with knowledge of the results of rest CTA. The CT scans following coronary artery calcium scanning (*CACS*) are initiated with contrast agent bolus tracking. *ECG* electrocardiogram, *IV* intravenous, *SL* sublingual

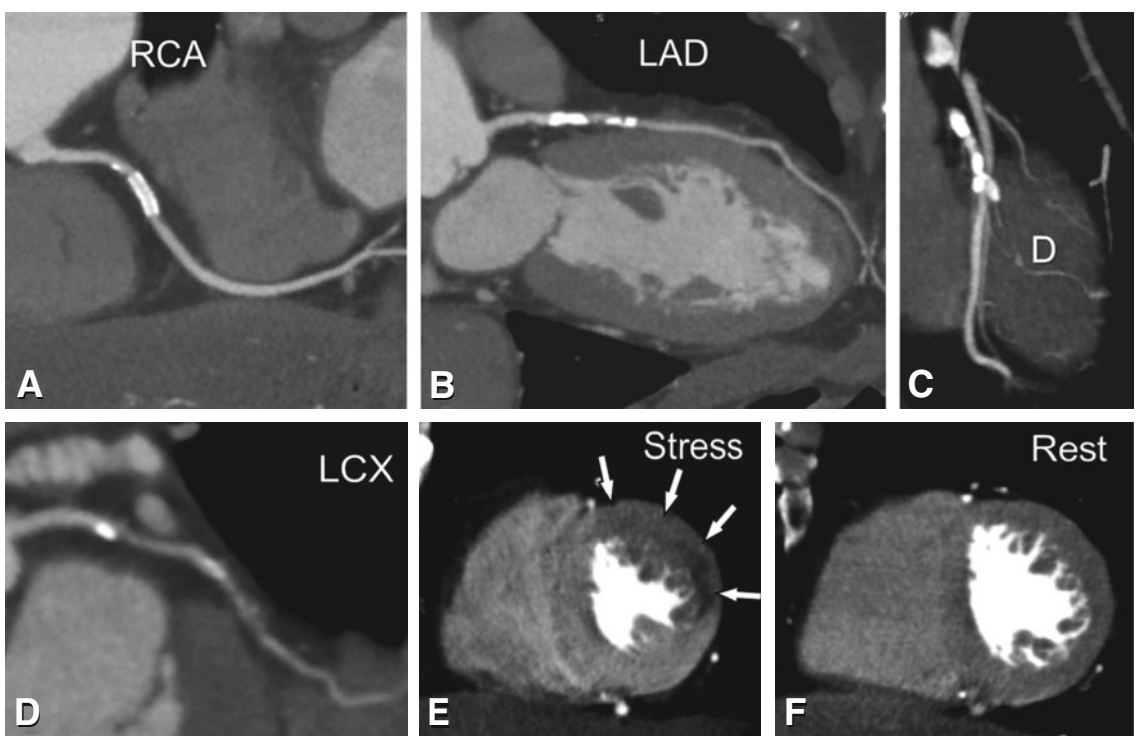

Fig. 19.5 Comprehensive cardiac study using first-generation 320-row CT in a 78-year-old female with a history of lateral myocardial infarction and stent placement into the proximal right coronary artery 6 months earlier. Resting coronary CTA demonstrates a patent right coronary artery stent (**Panel A**). The left anterior descending (*LAD*) coronary artery was not evaluable due to heavy calcifications (**Panels B** and **C**) and there was a diffuse severe stenosis in the left circumflex (*LCX*) coronary artery (**Panel D**). Static (single-shot) stress CTP demonstrated a perfusion deficit in the anterior wall and lateral wall (*arrows* in **Panel E**), which was not evident on rest CTP (**Panel F**)

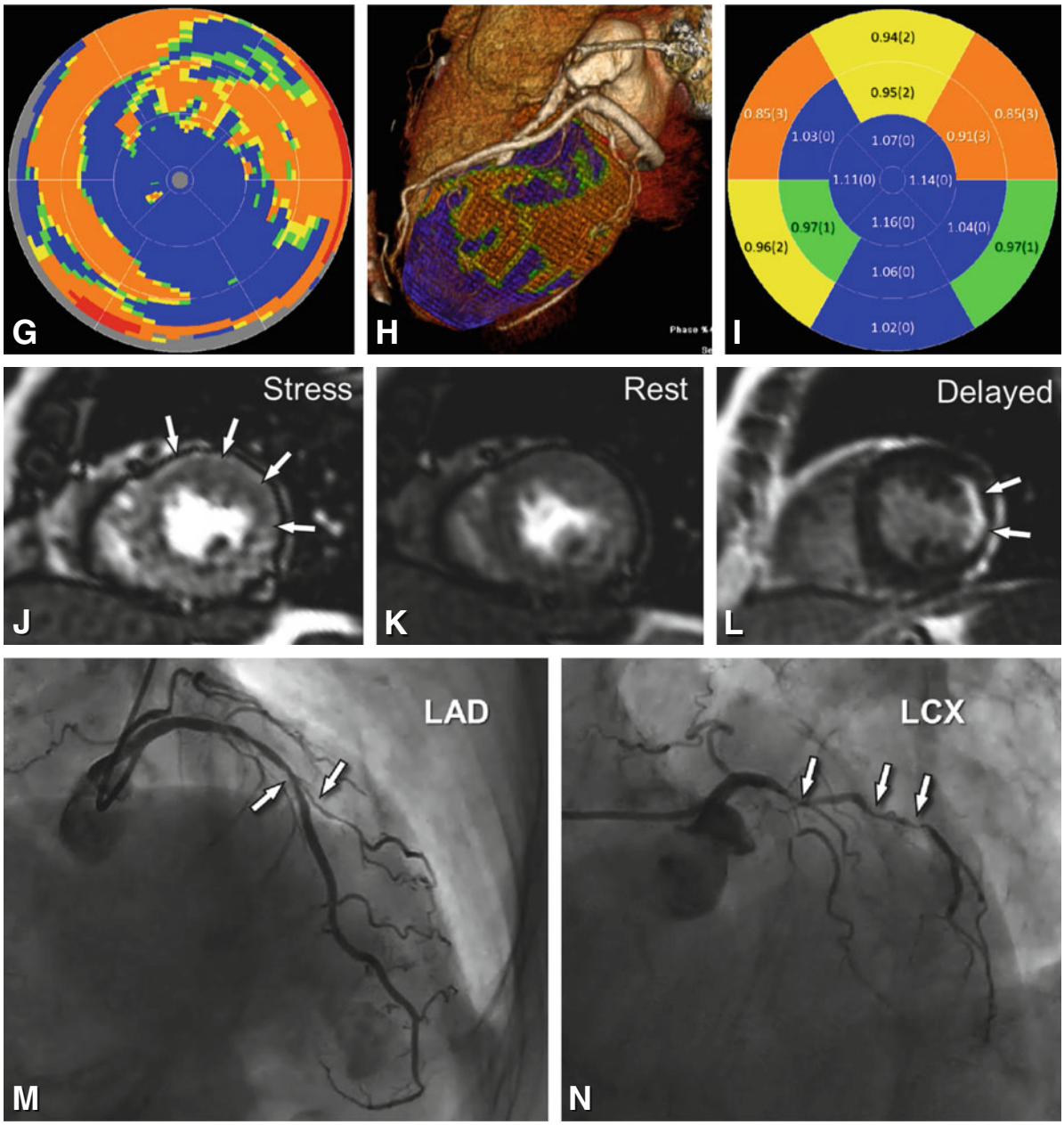

Fig. 19.5 (continued) Polar plot for the transmural perfusion ratio (TPR) demonstrates moderate ischemia (*orange*) in the mid anterior and basal and mid lateral walls and normal perfusion in the remaining walls (*blue*, **Panel G**). Fusion CTA/stress TPR image clearly demonstrates that the ischemic myocardium is supplied by the left circumflex and diagonal branches (**Panel H**). Reduced TPR in the basal septal segments (**Panel I**) was thought to be present due to motion artifacts in this area. TPR in the left circumflex and the diagonal branch territory was 0.85 and 0.94, respectively (**Panel I**). *D* diagonal branch. Stress (**Panel J**) and rest (**Panel K**) myocardial perfusion MRI confirmed the presence of ischemia in the diagonal territory (*arrows* in **Panel J**) and presence of infarcted tissue in the lateral wall (*arrows* in **Panel L**). Conventional coronary angiography revealed moderate mid-LAD stenosis, severe diagonal branch stenosis, and severe proximal-to-mid LCX stenosis (*arrows* in **Panels M** and **N**). There was no in-stent restenosis in the right coronary artery (not shown). Mid-LAD lesion was treated by stent

19.4.3 Delayed-Enhancement Myocardial CT

Myocardial delayed enhancement can be assessed by adding a late-phase scan performed 5–10 min after the second acquisition (either stress CTP or coronary CTA) without or minimal additional contrast administration by employing previously injected contrast medium (total of 100–120 ml for stress and rest). Although assessment of late Gd enhancement is an indispensable component of a comprehensive cardiac MR study, the role of CT is far from being established at this time due to its relatively poor contrast-to-noise ratio and artifacts such as 'band like artifact' (areas of significantly increased or decreased attenuation at the lung-liver interface that compromises assessment of the inferior wall, **Fig. 19.6**). Improvements in image quality are required for CT evaluation of myocardial delayed enhancement to be clinically considered for assessing myocardial viability and fibrosis.

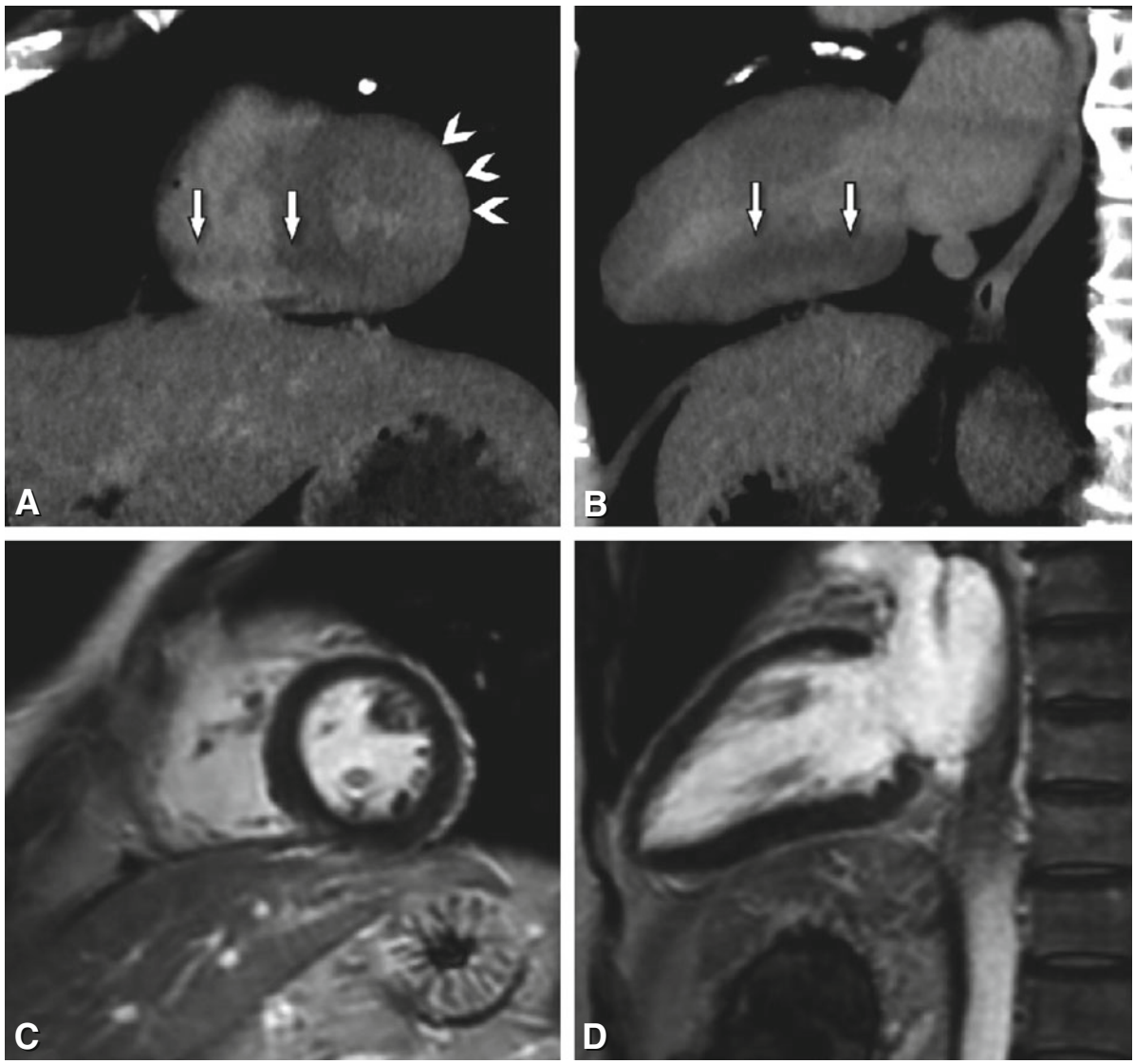

Fig. 19.6 Artifacts on delayed-enhancement CT in a 57-year-old female patient presenting with effort angina. There is a hypoattenuation band in the inferior wall (*arrows*, **Panels A** and **B**). Increased signal in the lateral wall is another frequently encountered artifact on CT for depicting delayed enhancement (*arrowheads*, **Panel A**). The patient had no history of myocardial infarction. These artifacts are likely to be caused by imperfect correction of photon scattering associated with partial scan reconstruction and are not specific to late scans. Magnetic resonance imaging in this patient showed no delayed enhancement on the corresponding short-axis image (**Panel C**) and long-axis image (**Panel D**)

19.5 Reading and Reporting of CT Perfusion Images

19.5.1 Visual Assessment and Pitfalls

As described before, image acquisition timing is of utmost importance for static CTP. Therefore, we recommend to ensure proper acquisition timing by looking at contrast enhancement in the coronary vein for instance (**Fig. 19.7**). If there is no contrast enhancement in the coronary vein, images may have been acquired too early for assessment of myocardial perfusion. Conversely, if enhancement in the coronary vein is greater than that in the coronary artery, the acquisition may have been too late to identify transient perfusion defect (**Fig. 19.7**).

Once proper acquisition timing has been confirmed, datasets should be examined on left ventricular short-axis images using 5- to 10-mm multiplanar reformation with window width and level of 200–300 and 100–150 HU. It would be helpful to display images from 2 or 3 series (stress, rest, and delayed) side by side to screen for any perfusion defect or delayed enhancement.

A reversible perfusion defect – lower attenuation on stress and normal attenuation on rest – indicates the presence of ischemia, while fixed perfusion defects represent infarcted myocardium. However, there are three important CT-related artifacts that can affect CT HU of myocardium during first-pass contrast enhancement, namely beam hardening, motion and cone-beam artifacts.

Beam hardening is a phenomenon that occurs when polychromatic x-ray beams pass through high-density materials (e.g., bone, contrast-filled heart chambers, and great vessels). Preferred absorption of lower-energy beams and increased mean energy of the remaining beams result in areas of hypoattenuation adjacent to high-density materials. Common sites affected by beam-hardening include the basal inferior myocardial wall between the left ventricle and the descending aorta (**Fig. 19.8**). Although it is not difficult to recognize beam hardening in such typical location and appearance, it can mask a true perfusion defect – a phenomenon known as pseudoenhancement. Reconstruction algorithms incorporating beam-hardening correction and dual-energy imaging can minimize the risk of misinterpretation.

Myocardial CT perfusion can be degraded by motion artifacts that also appear as hypoattenuating areas, potentially mimicking true perfusion defects, especially during stress (**Fig. 19.9**). In our experience, the basal septum and basal lateral wall are most often affected by motion. When multiphase reconstruction is available, motion artifacts can be differentiated from true perfusion defects by assessing consistency across different phases of the cardiac cycle (**Fig. 19.9**). Motion artifacts can also be distinguished from perfusion defects by assessing their correlation with coronary artery anatomy.

The third artifact is related to the cone beam and becomes more pronounced as the number of detector rows and therefore the cone angle increases. This artifact arises when the scanner isocenter and projections from the x-ray source onto the multiple detectors do not lie in the same plane. Despite the advent of more sophisticated reconstruction algorithms, this artifact is still quite commonly seen as high- and low-attenuation band interfering with assessment of perfusion in the inferior wall (**Fig. 19.10**).

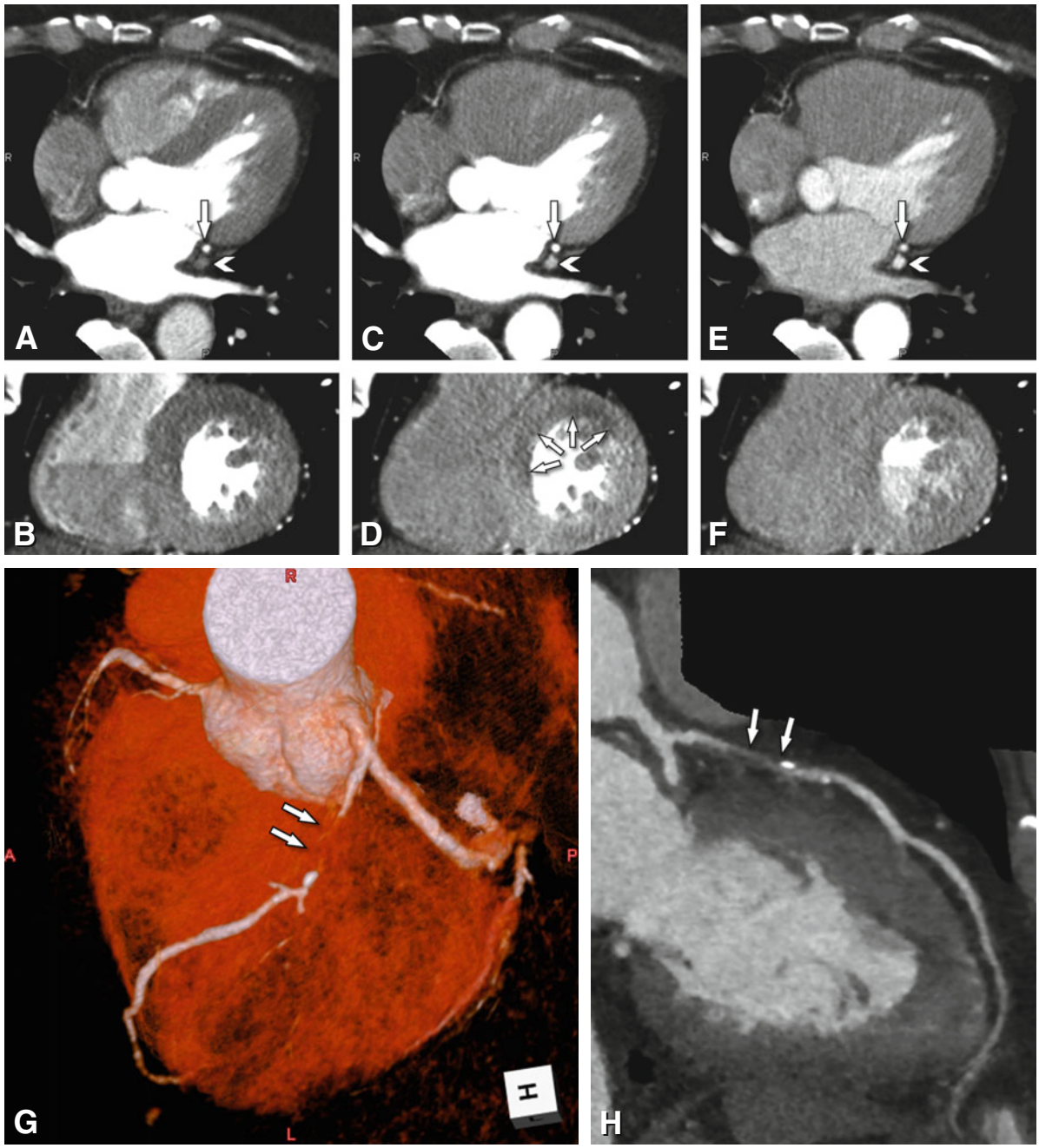

Fig. 19.7 Importance of acquisition timing of CTP as shown in dynamic stress CTP images of a 74-year-old male patient with typical angina pectoris. The axial and short-axis images (**Panels A**–**F**) are from the four-dimensional CTP dataset and represent early (**Panels A** and **B**), mid (**Panels C** and **D**), and late time points of the dynamic acquisition (**Panels E** and **F**). Coronary arteries (*arrow* in **Panel A**) may be best evaluated without contrast medium in the coronary vein (*arrowhead* in **Panel A**). However, it is when there is some contrast medium in the coronary vein (**Panel C**) that myocardial ischemia may be best appreciated as a perfusion deficit with subendocardial predominance (*arrows* in **Panel D**). If contrast enhancement in the coronary vein is greater than or equal to that in the coronary artery (**Panel E**), perfusion deficits may be missed (**Panel F**). A high-grade stenosis of the left anterior descending coronary artery was seen on coronary CTA during rest (*arrows* in **Panels G** and **H**)

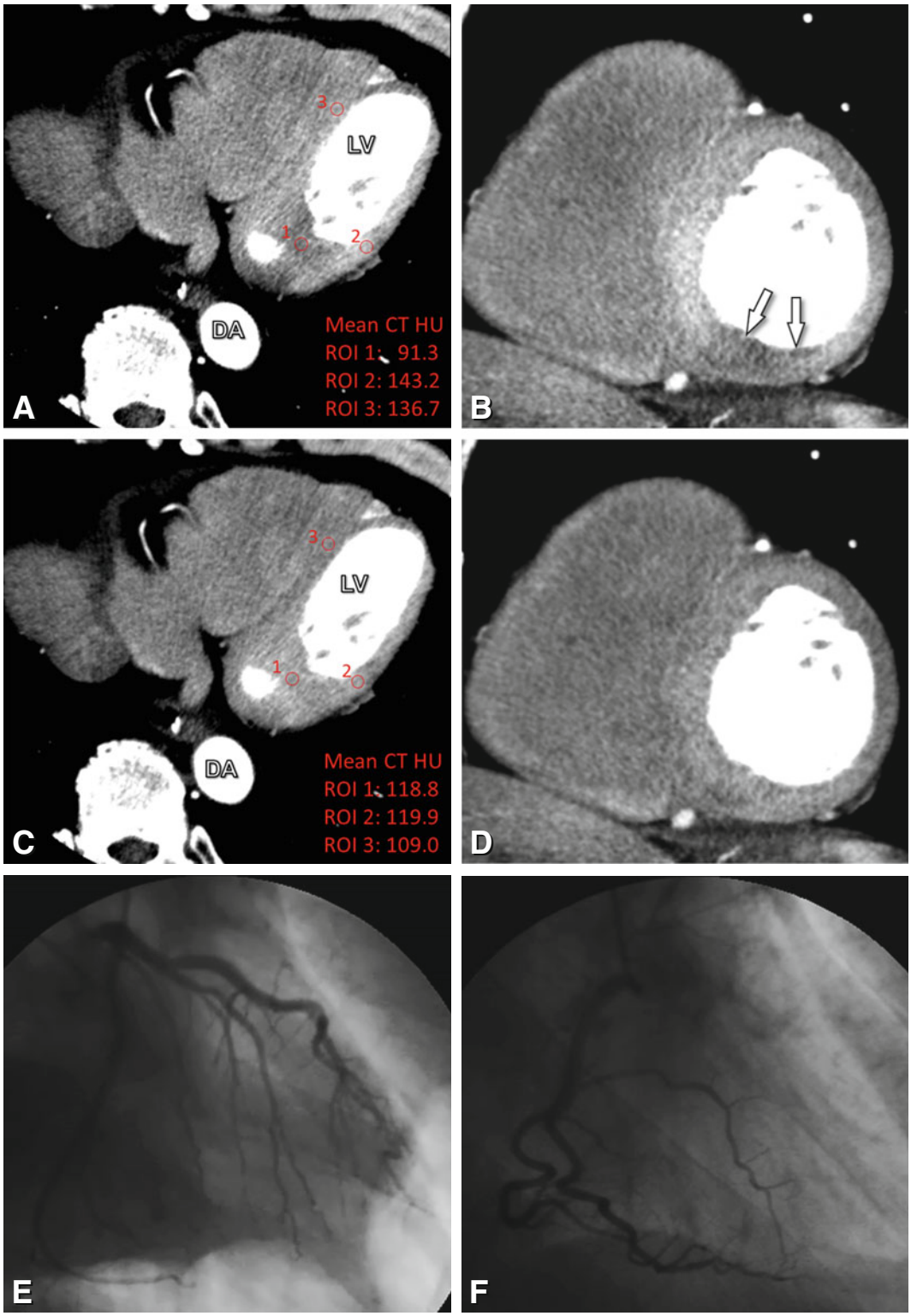

Fig. 19.8 Beam-hardening artifact and the importance of beam-hardening correction. Beam hardening is seen in a 63-year-old male patient with atypical chest pain between the left ventricular (*LV*) cavity and the descending aorta (*DA*) mimicking a perfusion deficit in the inferior wall (**Panels A** and **B**). The artifactual hypoattenuating area disappeared (**Panels C** and **D**) when reconstructed with beam-hardening correction optimized for myocardial perfusion imaging (*ROI 1* in **Panels A** and **C**). Notice that CT Hounsfield units (*HU*) in the lateral wall (*ROI 2* in **Panels A** and **C**) and interventricular septum (*ROI 3* in **Panels A** and **C**) were artifactually increased without beam-hardening correction potentially masking true perfusion deficits. Normal coronary arteries were demonstrated by angiography (**Panels E** and **F**)

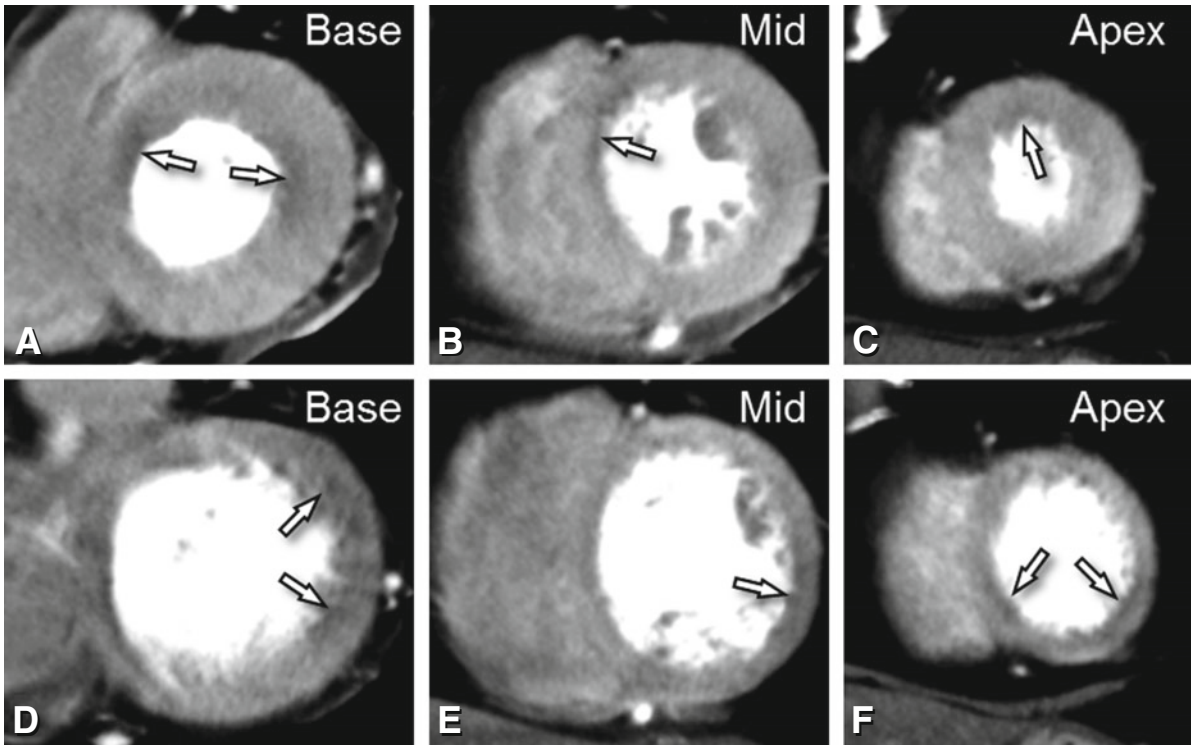

Fig. 19.9 Motion artifacts resulting in myocardial pseudodefects. In this 80-year-old female patient presenting with atypical angina pectoris, multiple low-attenuation areas were observed on systolic (**Panels A**–**C**) and diastolic reconstructions (**Panels D**–**F**) in different locations (*arrows*). These low-attenuation areas changed in shape and location and were considered to be artifacts. Rest coronary CTA demonstrated normal coronary arteries (not shown)

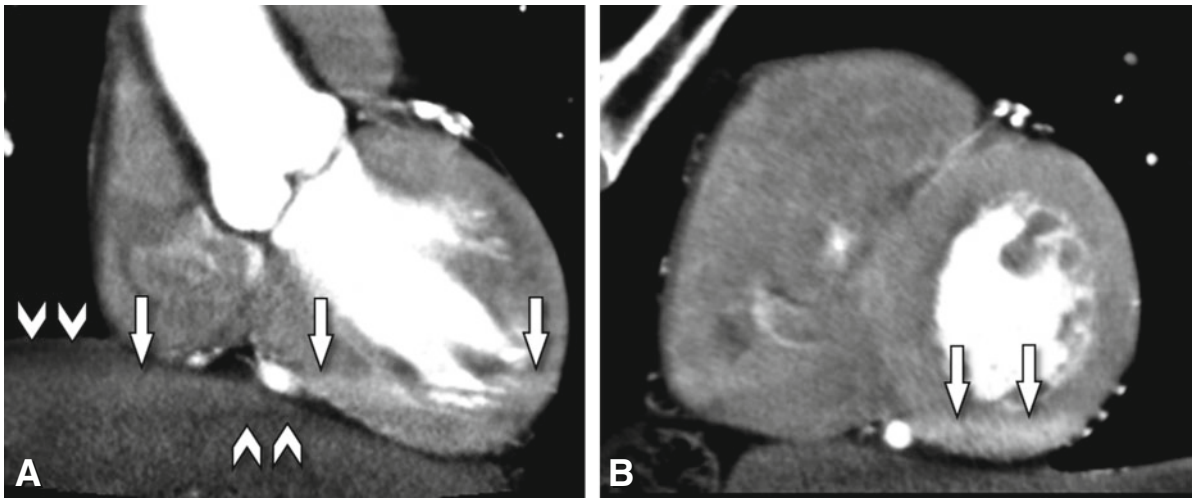

Fig. 19.10 Typical cone-beam artifact. High- (*arrows*) and low- (*arrowheads*) attenuation artifactual bands continuing outside the cardiac silhouette were seen in this 63-year-old patient who presented with angina pectoris in a left coronal oblique two-chamber view (**Panel A**). Assessment of the inferior wall was hampered by the high-density cone-beam artifacts as seen on a short-axis image (*arrows* in **Panel B**). This type of artifact arises when the scanner isocenter and projections from the x-ray source on to the multiple detectors do not lie in the same plane

19.5.2 Semi- and Fully Quantitative Assessment

Various semiquantitative metrics including transmural perfusion ratio (TPR), absolute contrast enhancement, and perfusion index (myocardial contrast enhancement relative to left ventricular enhancement) can be used to analyze static CTP. Of these, TPR – that is the ratio of the subendocardial CT attenuation in HU of one of the 16 myocardial segments (American Heart Association 17-segment model minus the apical segment) to that of the entire subepicardium – inversely correlates with the percent diameter stenosis measured by coronary angiography. TPR reflects transmural perfusion, which is normally higher in the subendocardium and is considered potentially abnormal when it is lower in the subendocardium (**Fig. 19.5G–I**). Since TPR is affected by the reconstruction algorithm used as well as image artifacts and acquisition timing, it should only be used complementary to visual assessment.

Dynamic stress CTP can be evaluated by visual assessment and by semiquantitative approaches, such as upslope analysis of the myocardial time-intensity curve. Fully quantitative analysis of first-pass contrast enhancement allows the absolute quantification of MBF in units of ml/min/g, and may permit more accurate and objective assessment of altered myocardial perfusion. Quantitative analysis of dynamic CTP can be performed using either a deconvolution method or compartment model analysis, similar to MRI. Owing to the linear relationship between the concentration of iodinated contrast medium and CT HU, CTP does not require saturation correction, which is essential for quantitative analysis of MR perfusion (**Table 19.1**).

Specifically for shuttle-mode CTP, a software package for fully quantitative analysis is available. The software uses a dedicated parametric deconvolution technique, which is based on a two-compartment model of intra- and extravascular space, to fit the time-attenuation curves of the LV myocardium. MBF is estimated as the maximum slope of the myocardial time-attenuation curve divided by maximum attenuation of the arterial input function. The resulting perfusion maps can be color-coded and fused with CTA for visual interpretation (**Fig. 19.3E, G**). It has been demonstrated that CT-derived estimates of MBF provide incremental diagnostic value for the detection of hemodynamically significant coronary artery stenosis, as defined by invasive FFR measurement. However, the software consistently underestimates stress MBF in normal myocardium to be 1.1–1.4 ml/min/g with a stress-induced increase of only 40%, which is much lower than expected. Potential explanations for this underestimation include relatively low sampling rate for the myocardial time-attenuation curve and lack of correction for the flow-dependent decrease in the extraction fraction of the iodinated contrast medium. Actually, the equation used to derive MBF in the software is mathematically equal to determination of K1 (the blood-to-myocardium transfer coefficient) of Patlak plot analysis. As K1 is the product of MBF and extraction fraction, the extraction fraction of iodinated contrast medium must be known to quantify absolute MBF from K1. However, the flow-dependent myocardial extraction fraction of iodinated contrast medium has never been determined in vivo in human subjects. Current software requires further refinement of modeling algorithm.

19.5.3 Reporting

Stress myocardial CTP should be included in the structured report of coronary CTA (Chap. 10). To exploit the inherent advantage of combined CTA/CTP study, we recommend matching all potentially obstructive coronary lesions with their downstream myocardial territories to determine their functional significance. Defect severity and extent of each lesion should also be reported. Defect extent can be visually determined by using an ordinal scale, for example: 0 = normal, 1 = mild, perfusion deficit < one-third transmurality; 3 = severe, >50% transmurality; and 4 = thinned chronic infarct. Alternatively, quantitative metrics such as TPR and MBF may be used to communicate the severity of ischemia. Defect extent can be qualitatively reported by describing the myocardial segments involved or by calculating a percentage of ischemic myocardium. It is desirable to include assessment of infarct extent in the assessment of defect extent because it is ischemic but viable myocardium that potentially benefits from intervention.

19.6 Fractional Flow Reserve

FFR provides a lesion-specific index for classifying a coronary lesion as ischemia-causing (functionally significant) versus non-ischemic. It is defined as the ratio of the maximum blood flow through a stenotic artery to maximum blood flow if the artery were normal (**Fig. 19.11**).

19.6.1 Measurement

Measurement of invasive FFR is relatively easy and straightforward using techniques that are in common use in the catheterization laboratory. Generally, a 6 F guiding catheter is used to facilitate wire manipulation, anticoagulation is used as per usual catheterization procedures, and nitroglycerin is administered to maximally dilate the coronary artery. A guidewire with a pressure-sensing transducer located approximately 3 cm from the tip of the wire (St. Jude Medical Systems; Volcano, Inc) is advanced across the stenosis and placed in the distal part of the coronary artery. After induction of maximum coronary hyperemia by intravenous or intracoronary adenosine administration, the pressure gradient across the lesion is recorded and FFR is calculated.

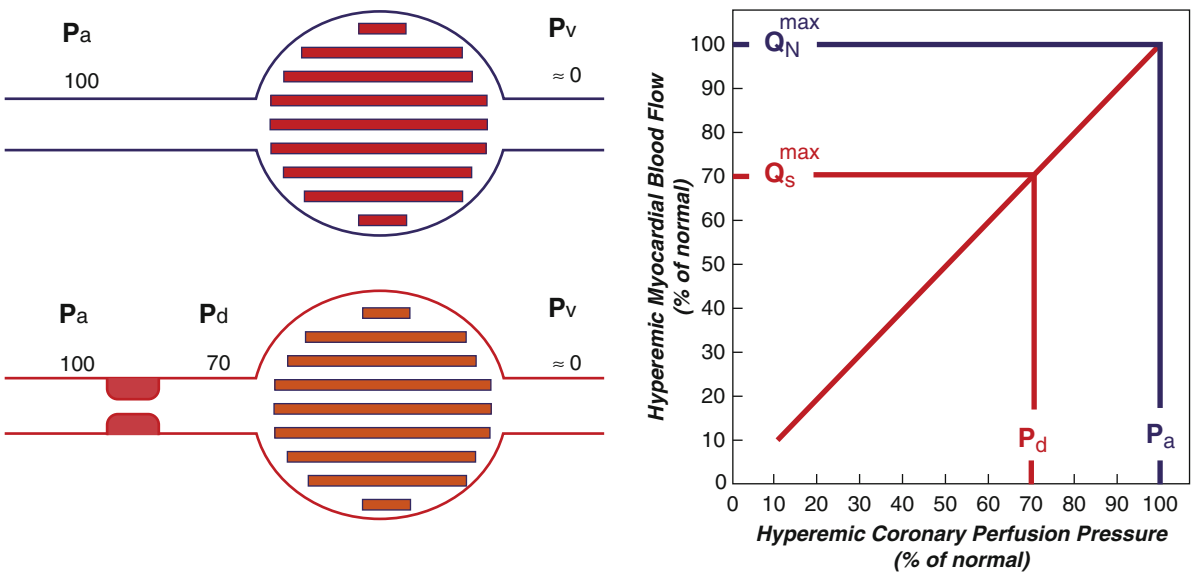

Fig. 19.11 Diagram of the concept of invasive FFR measurements. Numerical example showing how a ratio of 2 pressures (P_d/P_a) corresponds to a ratio of 2 flows ($Q^S max/Q^N max$). The driving pressure, P_a, indicates a normal (100%) maximum myocardial blood flow in the absence of coronary stenosis (*blue lines*). If a stenosis causing a hyperemic pressure gradient of 30 mmHg (*red lines*) is present, the driving pressure will be 70 mmHg (P_d) rather than 100 mmHg. Since the relationship between driving pressure and myocardial blood flow is linear during maximum hyperemia, myocardial blood flow will only reach 70% of its normal value (With permission from Pijls and Sels *J Am Coll Cardiol* 2012)

19.6.2 Clinical Validation

Many studies have shown that tailoring revascularization according to the functional significance of a stenosis rather than its angiographic appearance improves outcomes, reduces costs and, in some patients, avoids the need for revascularization. FFR-guided coronary revascularization improves clinical outcomes of patients with coronary artery disease (**Table 19.2**). Coronary stenoses with FFR < 0.75 are functionally significant and will almost invariably induce ischemia, whereas stenoses with FFR > 0.80 are not functionally significant and are almost never associated with exercise-induced ischemia. This means that the gray zone for FFR spans <10% of the entire range of FFR values and that the best cut-off value for FFR falls within the range of 0.75–0.80 for all subsets studied, including patients with single-vessel disease, multivessel disease, left main stenosis, diabetes mellitus, and previous myocardial infarction.

Table 19.2 Randomized studies of revascularization guided by fractional flow reserve

	DEFER	FAME	FAME 2
Design	International, multicenter, prospective, randomized, parallel groups, open	International, multicenter, prospective, randomized, parallel groups, open	International, multicenter, prospective, randomized, parallel groups, open
Patient	325 patients with moderate, >50%, single-vessel angiographic stenosis with no evidence of reversible ischemia by noninvasive testing	1,005 patients with multivessel coronary artery disease	1,220 patients with stable coronary artery disease and 1-, 2-, 3-vessel disease suitable for percutaneous coronary intervention
FFR cut-off value	0.75	0.80	0.80
Strategies	Deferral group (medical therapy if FFR ≥0.75) Performance group (percutaneous coronary intervention if FFR ≥0.75) Reference group (percutaneous coronary intervention if FFR < 0.75)	Angiography-guided percutaneous coronary intervention FFR-guided percutaneous coronary intervention	Percutaneous coronary intervention plus medical therapy Medical therapy alone
Primary end point definition	Freedom from adverse cardiac events (all-cause mortality, myocardial infarction, coronary artery bypass grafting, coronary angioplasty) after 2 years	Major adverse cardiac events (a composite of death, myocardial infarction, any repeat revascularization) at 1 year	A composite of death from any cause, nonfatal myocardial infarction, unplanned hospitalization leading to urgent revascularization at 2 years
Primary end point results	89% in deferral group, 83% in performance group (P = NS), 78% in reference group	18.3% in angiography group, 13.2% in FFR group (P = 0.02)	4.3% in percutaneous coronary intervention group, 12.7% in medical therapy group, P < 0.001

19.6.3 Clinical Use

Invasive FFR provides a lesion-specific index of the functional significance of coronary lesions. The simplicity of the technique is undisputed, and there is convincing clinical evidence demonstrating the safety and benefit of revascularization guided by FFR. FFR is now considered the standard of care for guiding percutaneous coronary revascularization and has received a class IA recommendation from the European Society of Cardiology and a class IIA recommendation from the American College of Cardiology. Nonetheless, despite overwhelming evidence, supporting the use of FFR to guide clinical decision making, and increasing clinical adoption, FFR is currently used in less than 10% of coronary revascularization procedures in the United States. This may be due to the invasive nature of the procedure and the need for additional instrumentation of the coronary arteries and pharmacologic vasodilation. Therefore, it would be desirable to determine the functional significance of a coronary stenosis non-invasively, using the same underlying principles of FFR, and to thus identify patients who would benefit from coronary revascularization.

19.7 CT Fractional Flow Reserve

Non-invasive myocardial perfusion imaging tests can detect regional differences in coronary flow reserve or wall motion abnormalities as a surrogate marker for ischemia, thereby identifying individuals who may have coronary ischemia. However, information from perfusion imaging is less specific regarding individual vessels because of variations in coronary distribution. CT FFR integrates the anatomic data provided by coronary CTA with computational fluid dynamics to provide information regarding coronary blood flow and the functional significance of individual coronary stenoses. This combined anatomic-physiologic assessment can be performed using standard coronary CTA data, without the need for additional imaging or medication. Total coronary flow under resting conditions is computed from the myocardial mass extracted from CTA data and coronary resistance is calculated from coronary flow and mean aortic pressure. The important boundary condition of maximum hyperemia is modeled by simulating the effect of adenosine in reducing coronary peripheral resistance and thus increasing coronary blood flow. Thus, it is now possible to identify and differentiate functionally significant from physiologically insignificant lesions in a single non-invasive imaging test which requires no additional radiation.

19.7.1 Computation

The scientific basis for computation of FFR from CT has been described in detail by Taylor et al. The process of deriving FFR from coronary CTA involves first constructing an accurate patient-specific anatomic model of the coronary arteries, then producing a mathematical model of coronary physiology by specifying the inflow and outflow boundary conditions and finally computing the numerical solution of the fluid dynamics equations. This combination of anatomy, physiology and computational fluid dynamics enables the calculation of coronary artery blood flow and pressure under conditions of maximum hyperemia. It is important to note that computation of CT FFR is performed using standard coronary CTA without modification of image acquisition protocols and pharmacological stress agents. Coronary CTA DICOM data are uploaded via the web to servers at HeartFlow, Inc. (Redwood City, California) where anatomic image data are extracted and segmented to construct patient-specific computational models of the ascending aorta and coronary arteries. Physiologic models reflecting the boundary conditions at maximal coronary hyperemia are then assigned and the governing equations of blood flow for the entire coronary tree are solved on a supercomputer. This produces a three-dimensional map of velocity and pressure throughout the coronary artery tree and allows interrogation of estimated FFR at any point in the major coronary arteries (**Fig. 19.12**). Reports are provided over the web interface as portable document format images in multiple projections.

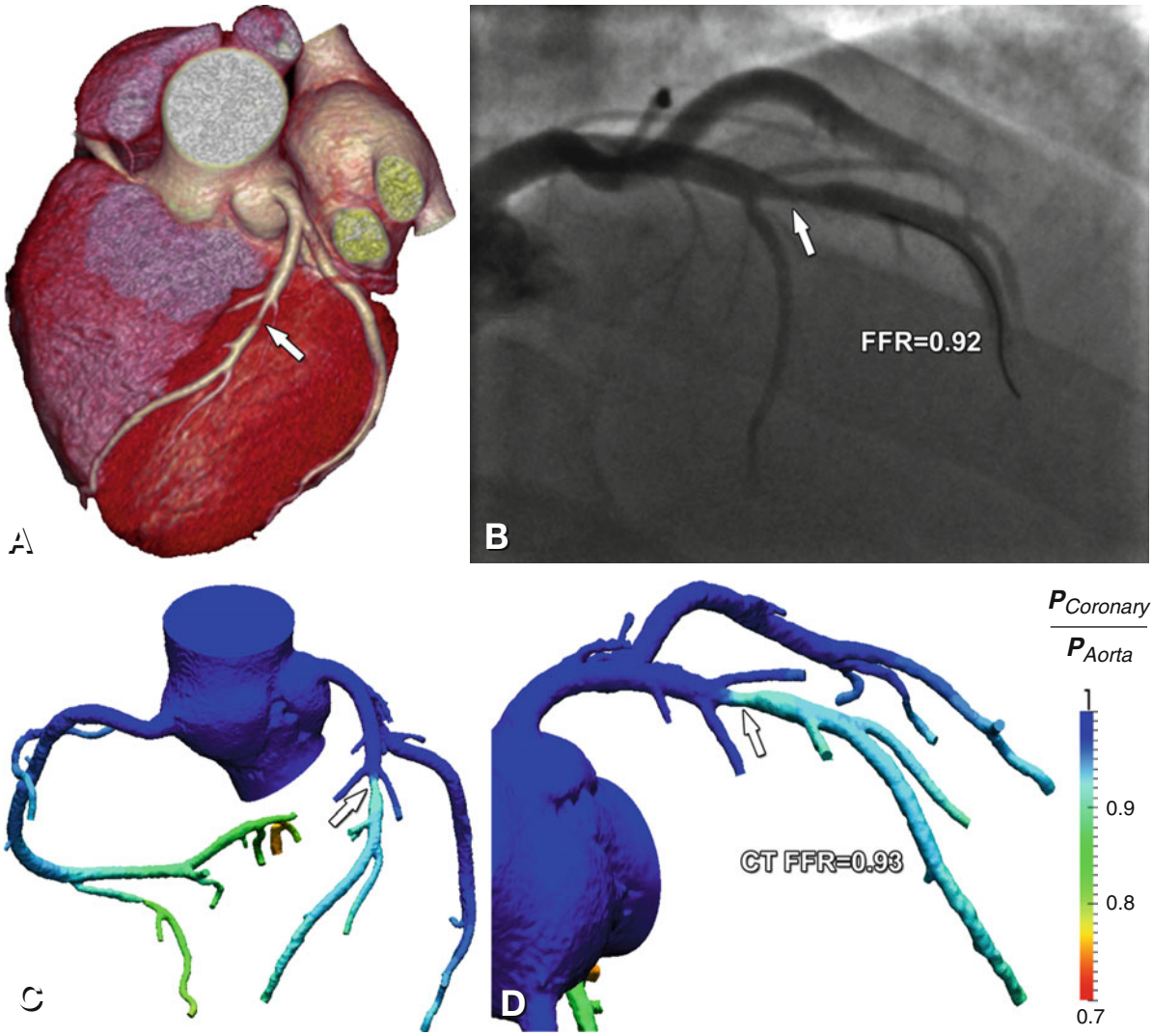

Fig. 19.12 A case example of one of the first patients studied for CT FFR in 2009. This was a 60-year-old man with a 6-month history of intermittent exertional chest pain. Coronary CTA demonstrated a >50% stenosis in the left anterior descending artery (*arrow* in **Panel A**) and diagnostic angiography confirmed a 60% stenosis in the left anterior descending artery (*arrow* in **Panel B**). Computed FFR distal to the lesion was 0.93, indicating that this lesion did not cause ischemia (*arrows* in **Panels C** and **D**). This estimate was in good agreement with measured invasive FFR of 0.92. This patient was treated medically and had no coronary events during 3 years of follow-up

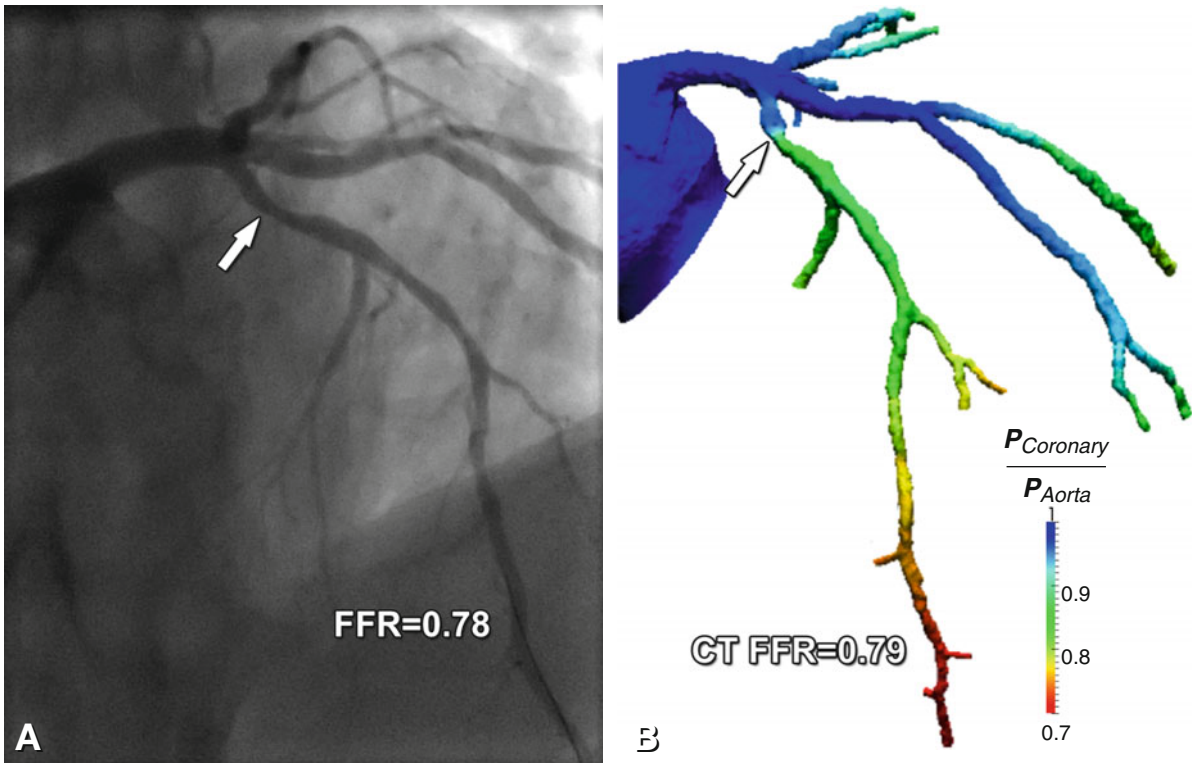

Fig. 19.13 A patient with chest pain and a 60% angiographic stenosis in the proximal left anterior descending artery (*arrow* in **Panel A**). Coronary CTA showed a >50% stenosis, and computed FFR in the left anterior descending artery was 0.79, indicating a functionally significant stenosis (*arrow* in **Panel B**). This was confirmed by an invasively measured FFR of 0.78. The patient underwent successful stenting of the LAD stenosis with relief of angina symptoms and good long-term outcome

19.7.2 Image Quality Requirements

Computation of FFR requires an anatomically accurate model of the coronary arterial tree and the most important requirement is thus a high-quality coronary CTA dataset. CTA should be performed with the goal of achieving a clear, high contrast view of all coronary arteries and plaque, free from artifacts which degrade visibility of the lumen boundary. Prospective and retrospective imaging protocols can be utilized and no protocol modification is required. However, it is important to follow the patient preparation (Chap. 6) and image acquisition recommendations (Chap. 8), particularly with respect to beta blockade for heart rate control and nitroglycerin for coronary dilation. Beta blockade ensures a low heart rate and minimizes heart rate variability with best results if heart rate is <60 beats per min. This will reduce motion artifacts causing blurring and allow use of prospectively gated acquisitions, which will reduce radiation dose (Chap. 7). Sublingual nitrates should be administered in order to dilate the coronary arteries so that CT FFR is computed under the same anatomic conditions as in the catheterization laboratory where nitroglycerin is routinely used when FFR is measured.

19.7.3 Clinical Validation

Clinical validation of CT FFR for the identification or exclusion of functionally significant stenosis has been carried out by comparison of CT FFR with directly measured FFR in the catheterization laboratory. The first in man studies were performed in 2009 in Riga, Latvia and the results of the first 20 patients were presented at the European Society of Cardiology meeting in Stockholm in 2010 (**Figs. 19.12** and **19.13**). Diagnostic accuracy of CT FFR was evaluated in two prospective, multicenter, international studies using measured FFR as the reference standard (**Table 19.3**). The DISCOVER-FLOW study included 103 stable patients

Table 19.3 Per-patient diagnostic performance of CT FFR and CTA alone versus FFR

	DISCOVER-FLOW		DeFACTO	
	CT FFR ≤0.80 (95%CI)	CTA stenosis ≥50% (95% CI)	CT FFR ≤0.80 (95%CI)	CTA stenosis ≥50% (95% CI)
Accuracy	87 (79–93)	61 (51–71)	73 (67–78)	64 (58–70)
Sensitivity	93 (82–98)	94 (85–99)	90 (84–95)	84 (77–90)
Specificity	82 (68–91)	25 (13–39)	54 (46–83)	42 (34–51)
Positive predictive value	85 (73–93)	58 (47–68)	67 (60–74)	61 (53–67)
Negative predictive value	91 (78–98)	80 (52–96)	84 (74–90)	72 (61–81)

with known or suspected coronary artery disease. CT FFR values correlated well with measured FFR with a slight underestimation by CT FFR but relatively wide limits of agreement. The diagnostic performance of CT FFR was significantly better than that of CTA alone. The DeFACTO study involved 252 patients and all studies were interpreted in blinded fashion by independent core laboratories. CT FFR demonstrated significant improvement over CTA in the ability to discriminate patients with and without ischemia (**Table 19.3**).

19.7.4 Potential Limitations

Potential limitations of CT FFR include impaired CT image quality. Since accurate computational models of CT FFR require precise CT definition of the lumen boundary, imaging artifacts (Chap. 10) and increased image noise all can negatively impact the diagnostic accuracy. These artifacts can be minimized by close adherence to image acquisition recommendations (Chaps. 6 and 8), in particular the use of beta blockers to reduce heart rate and heart rate variability and sublingual nitrates to dilate the coronary arteries. A recently published sub-analysis of DISCOVER-FLOW suggests that CT FFR performance is unaffected by a wide range of factors that have shown to degrade image quality. Nonetheless, given the dependence of CT FFR on accurate coronary segmentation for proper image-based modeling, excellent image quality should remain a primary goal to facilitate quantitative interpretation of the lumen boundary. In addition, CT FFR has thus far been evaluated only in patients with stable coronary artery disease and not in patients with acute coronary syndromes or patients with prior coronary artery bypass grafting or percutaneous coronary intervention. Thus, it is still unclear whether the results can be generalized to broader populations of patients. Other companies are working on the development of CTA-based approaches to predict FFR, and studies with outcomes data could help in understanding the clinical utility of patient management based on CT FFR.

19.7.5 Treatment Planning

In addition to the benefits of non-invasive diagnosis of lesion-specific ischemia, computational analysis provides the opportunity to plan and predict the potential benefit of interventional treatments. The computational model, constructed from the CTA obtained prior to angiography and intervention, can be modified to eliminate individual coronary lesions, thus simulating stenting of the stenosis. After modification of the anatomic model, pressure and flow are reestimated under conditions of maximal hyperemia and post-stenting CT FFR can be estimated. Thus one may use this approach to perform "virtual stenting" and predict the expected results of stenting prior to actual stent placement (**Fig. 19.14**).

19.8 Future of Myocardial CT Perfusion and CT Fractional Flow Reserve

The most important perspective of CTP is the potential for absolute quantification of myocardial perfusion, which can be achieved with much higher spatial resolution compared with PET and MRI. Given the rapid progress in hardware and software technologies for dose

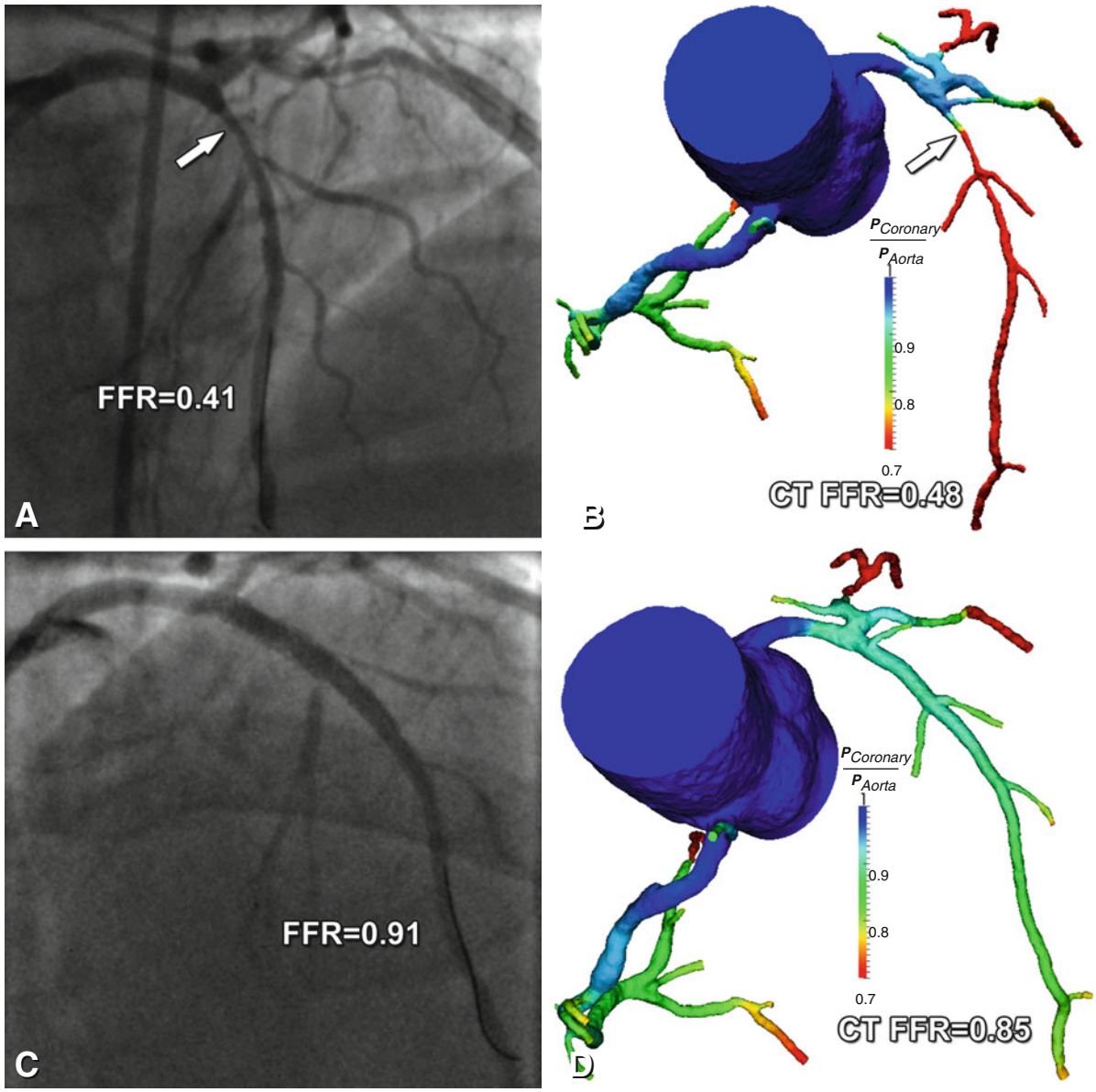

Fig. 19.14 A case example of predictive modeling for percutaneous coronary intervention planning. Angiography demonstrated a significant stenosis in the left anterior descending artery (*arrow* in **Panel A**). The pretreatment model revealed stenosis with a CT FFR 0.48 (*arrow* in **Panel B**), which was in good agreement with invasive FFR (**Panel A**). The actual post-stenting FFR of 0.91 (**Panel C**) was well predicted using modeling based on CTA (**Panel D**)

19

reduction, dynamic CTP and subsequent MBF quantification in ml/min/g should become available on multiple platforms. Improvement of image quality is as important as dose reduction for the future acceptance of CTP. Although performance of myocardial CTP depends on the ability to accurately detect different levels of myocardial enhancement, image acquisition methods and reconstruction algorithms for CTP have not been fully optimized. For example, standard half-scan reconstruction is not ideal for CTP because varying angular position of data acquisition leads to variable myocardial attenuation and other reconstruction artifacts. This limitation might be overcome by using a hybrid of half- and full-scan reconstruction as in shuttle-mode CTP. Further technical improvements are also required for correction of photon scattering and beam hardening.

After feasibility studies both in large animal models and in single-center prospective trials, myocardial CTP is still in the early stages of development with only two multicenter studies conducted until 2013. A technological breakthrough for myocardial CTP would be the potentially very costly combination of dual-source and wide-area detector CT. Until then, more research will focus on improving scan protocols, reconstruction algorithms, and postprocessing methods.

The advantage of CT FFR is its ability to noninvasively diagnose lesion-specific ischemia and thus identify patients who may require coronary angiography and who may benefit from coronary revascularization. Equally important is CT FFR's ability to identify those patients who do not have ischemia and who may be safely and effectively managed medically. Individual lesions which are functionally significant can be readily identified, thus providing a useful platform for treatment planning prior to interventional therapy. It is important to note that computation of FFR is performed using standard coronary CTA without additional radiation, or the administration of pharmacological stress agents. Similarly to CTP, also for CT FFR only tow multicenter studies are currently available. Further research on the two very promising technologies, CTP and CT FFR, is needed before decisions about widespread clinical applications can be made.

Recommended Reading

Abbara S, Arbab-Zadeh A, Callister TQ et al (2009) SCCT guidelines for performance of coronary computed tomographic angiography: a report of the Society of Cardiovascular Computed Tomography Guidelines Committee. J Cardiovasc Comput Tomogr 3:190–204

Bamberg F, Becker A, Schwarz F et al (2011) Detection of hemodynamically significant coronary artery stenosis: incremental diagnostic value of dynamic CT-based myocardial perfusion imaging. Radiology 260:689–698

Bamberg F, Hinkel R, Schwarz F et al (2012) Accuracy of dynamic computed tomography adenosine stress myocardial perfusion imaging in estimating myocardial blood flow at various degrees of coronary artery stenosis using a porcine animal model. Invest Radiol 47:71–77

Bech GJ, De Bruyne B, Pijls NH et al (2001) Fractional flow reserve to determine the appropriateness of angioplasty in moderate coronary stenosis: a randomized trial. Circulation 103:2928–2934

Bischoff B, Bamberg F, Marcus R et al (2013) Optimal timing for first-pass stress CT myocardial perfusion imaging. Int J Cardiovasc Imaging 29:435–442

Blankstein R, Shturman LD, Rogers IS et al (2009) Adenosine-induced stress myocardial perfusion imaging using dual-source cardiac computed tomography. J Am Coll Cardiol 54:1072–1084

Cury RC, Nieman K, Shapiro MD, Nasir K, Cury RC, Brady TJ (2007) Comprehensive cardiac CT study: evaluation of coronary arteries, left ventricular function, and myocardial perfusion – is it possible? J Nucl Cardiol 14:229–243

De Bruyne B, Pijls NH, Kalesan B et al (2012) Fractional flow reserve-guided PCI versus medical therapy in stable coronary disease. N Engl J Med 367:991–1001

Dewey M, Gaemperli O, Schlattmann P (2013) Noninvasive approach to assess coronary artery stenoses and ischemia. JAMA 309(3):233–234

Feuchtner G, Goetti R, Plass A et al (2011) Adenosine stress high-pitch 128-slice dual-source myocardial computed tomography perfusion for imaging of reversible myocardial ischemia/clinical perspective. Circ Cardiovasc Imaging 4:540–549

George RT, Silva C, Cordeiro MA et al (2006) Multidetector computed tomography myocardial perfusion imaging during adenosine stress. J Am Coll Cardiol 48:153–160

George RT, Arbab-Zadeh A, Miller JM et al (2009) Adenosine stress 64- and 256-row detector computed tomography angiography and perfusion imaging: a pilot study evaluating the transmural extent of perfusion abnormalities to predict atherosclerosis causing myocardial ischemia. Circ Cardiovasc Imaging 2:174–182

Ghoshhajra BB, Maurovich-Horvat P, Techasith T et al (2012) Infarct detection with a comprehensive cardiac CT protocol. J Cardiovasc Comput Tomogr 6:14–23

Greenwood JP, Maredia N, Younger JF et al (2012) Cardiovascular magnetic resonance and single-photon emission computed tomography for diagnosis of coronary heart disease (CE-MARC): a prospective trial. Lancet 379:453–460

Ho KT, Chua KC, Klotz E, Panknin C (2010) Stress and rest dynamic myocardial perfusion imaging by evaluation of complete time-attenuation curves with dual-source CT. JACC Cardiovasc Imaging 3:811–820

Ichihara T, Sakuma H, Ishida M et al (2009) Quantitative analysis of first-pass contrast-enhanced myocardial perfusion MRI using a Patlak plot method and blood saturation correction. Magn Reson Med 62:373–383

Ishida M, Sakuma H, Murashima S et al (2009) Absolute blood contrast concentration and blood signal saturation on myocardial perfusion MRI: estimation from CT data. J Magn Reson Imaging 29:205–210

Ishida M, Ichihara T, Nagata M et al (2011) Quantification of myocardial blood flow using model based analysis of first-pass perfusion MRI: extraction fraction of Gd-DTPA varies with myocardial blood flow in human myocardium. Magn Reson Med 66:1391–1399

Kim SM, Kim YN, Choe YH (2013) Adenosine-stress dynamic myocardial perfusion imaging using 128-slice dual-source CT: optimization of the CT protocol to reduce the radiation dose. Int J Cardiovasc Imaging 29:875–884

Kitagawa K, George RT, Arbab-Zadeh A, Lima JA, Lardo AC (2010) Characterization and correction of beam-hardening artifacts during dynamic volume CT assessment of myocardial perfusion. Radiology 256:111–118

Kleiman NS (2011) Bringing it all together: integration of physiology with anatomy during cardiac catheterization. J Am Coll Cardiol 58:1219–1221

Ko S, Choi J, Song M et al (2011) Myocardial perfusion imaging using adenosine-induced stress dual-energy computed tomography of the heart: comparison with cardiac magnetic resonance imaging and conventional coronary angiography. Eur Radiol 21:26–35

Ko BS, Cameron JD, Leung M et al (2012) Combined CT coronary angiography and stress myocardial perfusion imaging for hemodynamically significant stenoses in patients with suspected coronary artery disease: a comparison with fractional flow reserve. JACC Cardiovasc Imaging 5:1097–1111

Koo BK, Erglis A, Doh JH et al (2011) Diagnosis of ischemia-causing coronary stenoses by noninvasive fractional flow reserve computed from coronary computed tomographic angiograms. Results from the prospective multicenter DISCOVER-FLOW (Diagnosis of Ischemia-Causing Stenoses Obtained Via Noninvasive Fractional Flow Reserve) study. J Am Coll Cardiol 58:1989–1997

Lardo AC, Cordeiro MA, Silva C et al (2006) Contrast-enhanced multidetector computed tomography viability imaging after myocardial infarction: characterization of myocyte death, microvascular obstruction, and chronic scar. Circulation 113:394–404

Levine GN, Bates ER, Blankenship JC et al (2011) 2011 ACCF/AHA/SCAI Guideline for Percutaneous Coronary Intervention. A report of the American College of Cardiology Foundation/American Heart Association Task Force on Practice Guidelines and the Society for Cardiovascular Angiography and Interventions. J Am Coll Cardiol 58:e44–e122

Mahnken AH, Klotz E, Pietsch H et al (2010) Quantitative whole heart stress perfusion CT imaging as noninvasive assessment of hemodynamics in coronary artery stenosis: preliminary animal experience. Invest Radiol 45:298–305

Martus P, Schueler S, Dewey M (2012) Fractional flow reserve estimation by coronary computed tomography angiography. J Am Coll Cardiol 59(15):1410–1411

Mehra VC, Valdiviezo C, Arbab-Zadeh A et al (2011) A stepwise approach to the visual interpretation of CT-based myocardial perfusion. J Cardiovasc Comput Tomogr 5:357–369

Min JK, Koo BK, Erglis A et al (2012a) Effect of image quality on diagnostic accuracy of noninvasive fractional flow reserve: results from the prospective multicenter international discover-flow study. J Cardiovasc Comput Tomogr 6:191–199

Min JK, Leipsic J, Pencina MJ et al (2012b) Diagnostic accuracy of fractional flow reserve from anatomic ct angiography. JAMA 308:1237–1245

Motwani M, Fairbairn TA, Larghat A et al (2012) Systolic versus diastolic acquisition in myocardial perfusion MR imaging. Radiology 262:816–823

Nieman K, Shapiro MD, Ferencik M et al (2008) Reperfused myocardial infarction: contrast-enhanced 64-Section CT in comparison to MR imaging. Radiology 247:49–56

Nørgaard BL, Leipsic J, Gaur S, Seneviratne S, Ko BS, Ito H, Jensen JM, Mauri L, De Bruyne B, Bezerra H, Osawa K, Marwan M, Naber C, Erglis A, Park SJ, Christiansen EH, Kaltoft A, Lassen JF, Bøtker HE, Achenbach S; NXT trial study group (2014) Diagnostic performance of non-invasive fractional flow reserve derived from coronary CT angiography in suspected coronary artery disease: The NXT trial. J Am Coll Cardiol pii: S0735-1097(14)00165-X. doi:10.1016/j.jacc.2013.11.043. [Epub ahead of print]

Pijls NH, Sels JW (2012) Functional measurement of coronary stenosis. J Am Coll Cardiol 59:1045–1057

Ramirez-Giraldo JC, Yu L, Kantor B, Ritman EL, McCollough CH (2012) A strategy to decrease partial scan reconstruction artifacts in myocardial perfusion CT: phantom and in vivo evaluation. Med Phys 39:214–223

Rief M, Zimmermann E, Stenzel F, Martus P, Stangl K, Greupner J, Knebel F, Kranz A, Schlattmann P, Laule M, Dewey M (2013) CT angiography and myocardial CT perfusion in patients with coronary stents: prospective intraindividual comparison with conventional coronary angiography. J Am Coll Cardiol 62:1476–1485

So A, Hsieh J, Narayanan S et al (2012) Dual-energy CT and its potential use for quantitative myocardial CT perfusion. J Cardiovasc Comput Tomogr 6:308–317

Taylor CA, Fonte TA, Min JK (2013) Computational fluid dynamics applied to cardiac ct for noninvasive quantification of fractional flow reserve: scientific basis. J Am Coll Cardiol 61(22): 2233–2241

Techasith T, Cury RC (2011) Stress myocardial CT perfusion: an update and future perspective. JACC Cardiovasc Imaging 4:905–916

Tonino PA, De Bruyne B, Pijls NH et al (2009) Fractional flow reserve versus angiography for guiding percutaneous coronary intervention. N Engl J Med 360:213–224

Wijns W, Kolh P, Danchin N et al (2010) Guidelines on myocardial revascularization. Eur Heart J 31:2501–2555

Zoghbi GJ, Dorfman TA, Iskandrian AE (2008) The effects of medications on myocardial perfusion. J Am Coll Cardiol 52:401–416

Hybrid Imaging

O. Gaemperli and P.A. Kaufmann

Abstract

This chapter provides an overview over the role of CT in current hybrid imaging modalities with a special emphasis on technical aspects, clinical indications, and future perspectives.

20.1 Clinical Need for Hybrid Imaging

With their high temporal and spatial resolution, current high-end CT devices are excellent tools for the noninvasive evaluation of normal or abnormal cardiac anatomy. However, while experimental novel techniques such as CT perfusion or CT-derived fractional flow reserve (CT-FFR) are currently under clinical investigation, coronary CT angiography (CTA) remains a purely anatomic technique that does not directly provide functional information on myocardial perfusion. The latter, however, is an important prognostic determinant in patients with stable coronary artery disease (CAD). Recent trials (nuclear substudy of COURAGE, FAME I + II) and current guidelines emphasize the need to assess myocardial perfusion to guide treatment strategies, particularly revascularization, in stable CAD patients. Cardiac hybrid imaging allows combining anatomic information with functional information on myocardial perfusion using noninvasive modalities. By this means, hybrid imaging has the potential to facilitate a comprehensive pathophysiologic understanding of disease extent and severity in stable CAD patients.

20.1.1 Definition of Hybrid Imaging

The term hybrid imaging refers to the combined or fused imaging of two imaging data sets, where both modalities equally contribute to image information. This definition does not include the use of low-dose transmission images for the attenuation correction of cardiac radionuclide studies (single photon emission computed tomography (SPECT), positron emission tomography (PET)).

M. Dewey, *Cardiac CT*,
DOI 10.1007/978-3-642-41883-9_23, © Springer-Verlag Berlin Heidelberg 2014

20.2 Technical Requirements

20.2.1 Coronary CT Angiography

The backbone of cardiac hybrid imaging is noninvasive visualization of coronary arteries, no other technique has yet matched CTA in terms of resolution, accuracy, and clinical robustness (Chap. 4). The fast pace of technological developments in the field of cardiac CT was the main driving force behind the first attempts of cardiac hybrid imaging approximately 10 years ago. Thus, two main factors are the reason why hybrid imaging was accepted in clinical practice and is now a routine technique in many specialized imaging centers: the excellent image quality and high diagnostic accuracy of state-of-the-art multislice CT devices (Chap. 25), and the low radiation exposure of modern cardiac CT acquisition protocols (Chap. 7).

20.2.2 Myocardial Perfusion Imaging

Myocardial perfusion can be assessed using radionuclide imaging studies such as SPECT or (in more specialized centers) PET. Both modalities provide similar three-dimensional (3D) datasets as CTA. These datasets can be easily superimposed onto CT images (after correcting for the lower matrix size and larger voxel size) using dedicated fusion software (**Fig. 20.1**). Other functional modalities (stress echocardiography or magnetic resonance (MR) imaging) are potentially attractive candidates for hybrid imaging. Both modalities avoid ionizing radiation, however, the 2-dimensional (2D) image format of echocardiograms is unsuitable for fusion with CTA. The advent of 3D echocardiography may facilitate fusion imaging with CTA. Stress MR/CTA fusion may be possible using fast perfusion sequences and is currently under clinical investigation (see Sect. 20.5.1).

20.2.3 Software

Dedicated software packages are available from different manufacturers that allow fusion of CTA and radionuclide images (CardIQ Fusion, Advantage Workstation, GE Healthcare; HeartFusion application, Emory University, Atlanta, Georgia; **Fig. 20.1**). A crucial element is a user interface that permits to correct misalignment between datasets. The remaining fusion steps include tracking of the coronary arteries (by methods similar to standard CTA software) and modeling of the perfusion data into a 3D volume-rendering of the left ventricle. Current software packages allow fusion of images from different modalities and even different manufacturers. In experienced hands and with image datasets of reasonable quality, the image fusion process takes no longer than 5 min per patient.

20.2.4 Hybrid Versus Stand-Alone Scanners

The increasing global interest in hybrid imaging from a variety of medical specialties has prompted manufacturers to launch a number of hybrid imaging devices. The best example is the increasing use of hybrid PET/CT scanners for staging of neoplastic disease. The success of PET/CT in oncology has set the stage for a wide dissemination of such hybrid devices and has extended onto other domains. As a result, similar hybrid devices combining SPECT cameras with high-end CT devices and recently also first experimental hybrid PET/MR have been released (**Fig. 20.2**).

Nonetheless, it should be emphasized, that in the setting of *cardiac* hybrid imaging the use of hybrid scanners is not necessarily required, and less crucial than for oncology rectilinear PET/CT. In the latter case, image fusion is accomplished through rapid automated fusion of sequential PET and CT images as the patient is lying still and moved from the PET to the CT gantry. However, in cardiac hybrid imaging, manual superimposition and individual correction of dataset misalignment is crucial

Fig. 20.1 Illustration of the approach to cardiac fusion with software (CardIQ Fusion, Advantage Workstation, GE Healthcare). (**Panels A–D**) *Image coregistration*. This first step is crucial and allows the user to align the often times imperfect correlation (**Panels A** and **C**) on images in three dimensions in order to obtain optimal matching of structural and functional information (**Panels B** and **D**). (**Panel E**) *Definition of left ventricular epicardium*. This protocol displays a view containing the segmented CT left ventricular epicardium using conventional volume-rendering technique, allowing addition or removal of structures from the left ventricular epicardium if needed. Every voxel of the volume has an opacity value and a color. The opacity ramp is based on the Hounsfield units of the CT data. The color of the surface is generated based on the perfusion information. In each point of the surface of the volume-rendered image the color is computed as being the maximum perfusion intensity on a ray going from the particular point to the centre of the heart on CT. (**Panels F** and **G**) *3D volume-rendered fusion images*. As the final step, the hybrid display protocol renders a volume containing the left ventricular epicardial volume, the volume-rendered coronary tree, and the left and right heart chambers acquired by an automatic segmentation algorithm (With permission of Springer from Gaemperli et al. *Eur J Nucl Med Mol Imaging* (2007)

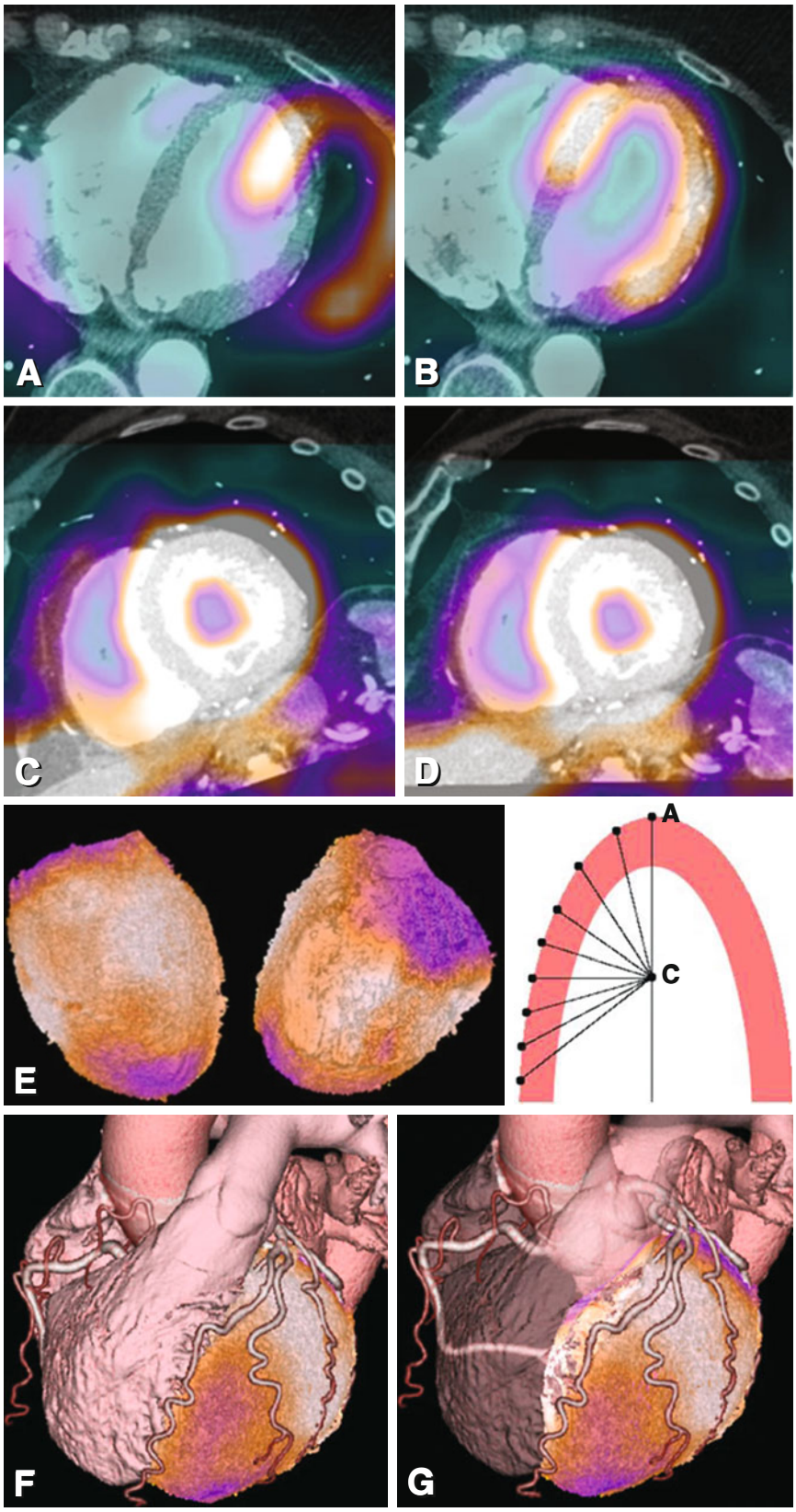
A
B
C
D
E
A
C
F
G

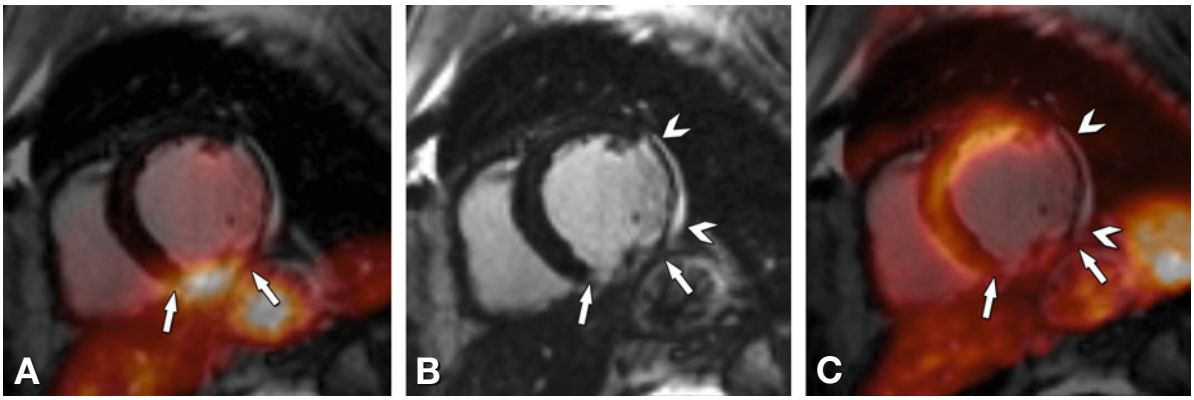

Fig. 20.2 Patient with an acute myocardial infarction after successful revascularization of the right coronary artery undergoing integrated PET/MRI. Fasting ^{18}FDG PET shows focal accumulation in the inferior wall (*arrow* in **Panel A**) with matching diffuse late enhancement on MRI (*arrow* in **Panel B**) and severely reduced PET perfusion (*arrow* in **Panel C**). In addition, there is a chronic infarct of the lateral wall seen by thinning of the myocardium and late enhancement on MRI (*arrowhead* in **Panel B**) with corresponding absent perfusion on $^{13}NH_3$ PET (*arrowhead* in **Panel C**). Although the diagnostic and prognostic impact of hybrid PET/MRI needs to be defined in larger cohorts, this example demonstrates its clinical feasibility (Courtesy of S. Nekolla and C. Rischpler, Munich)

to ensure adequate quality for several reasons: cardiac and respiratory motion, intrinsic disagreement in the size and shape of the left ventricle between nongated SPECT images and diastole-gated CTA, 3D instead of cross-sectional display of fused datasets. Therefore, cardiac hybrid imaging can easily be performed by acquiring datasets on standalone scanners with subsequent software-based fusion, and in fact this set-up may allow exploiting the full capacity of the respective scanners for all kinds of medical purposes rather than having a highly dedicated hybrid device.

20.2.5 Tips

A number of recommendations that should be considered for successful hybrid imaging are summarized in **List 20.1**.

List 20.1. Recommendations for hybrid imaging

1. Use at least 64-row CT scanners (Chap. 2)
2. Fusion of image datasets with a dedicated cardiac fusion software allowing for manual coregistration and correction of dataset misalignment (Fig. 20.1)
3. Perform the perfusion SPECT or PET first as the administration of pre-scan beta-blockers for CTA may otherwise mask small perfusion defects
4. If CTA is performed first with pre-scan administration of intravenous beta blockers, postpone the SPECT study to the following day
5. A hybrid scanner equipped with a high-end CT is desirable as it improves patient comfort and speeds up the total examination
6. Image acquisition is perfectly feasible on standalone scanners, and this approach may be preferable if the scanners are run for other (non-cardiac) examinations

20.3 Clinical Data

A number of small single-center trials assessing the diagnostic accuracy of cardiac hybrid imaging are available and are summarized in **Table 20.1**. Overall, the diagnostic accuracy of hybrid imaging is very high with a sensitivity, specificity, positive and negative predictive value of 88–96%, 92–100%, 77–97%, and 97–99%, respectively. However, a number of limitations apply to these early pilot studies such as the small sample sizes, the heterogeneity of hybrid systems, the varying gold-standard (invasive coronary angiography alone or in

Table 20.1 Added diagnostic accuracy of cardiac hybrid imaging (SPECT/CTA and PET/CTA) (Vessel-based analysis)

Author	Hybrid system	N	Gold standard (definition of significant CAD)	Sens	Spec	PPV	NPV
Namdar et al. (2005)	^{13}N-NH_3 PET/4-slice CTA	25	Flow-limiting coronary stenoses requiring revascularization (ICA + PET)	90	98	82	99
Rispler et al. (2007)	SPECT/16-slice CTA	56	Flow-limiting coronary stenoses (>50% stenosis on ICA + SPECT pos.)	96	95	77	99
Groves et al. (2009)	^{82}Rb PET/64-slice CTA	33	>50% stenosis on ICA	88	100	97	99
Sato et al. (2010)	SPECT/64-slice CTA[a]	130	>50% stenosis on ICA	94	92	85	97
Kajander et al. (2010)	^{15}O-H_2O PET/64-slice CTA	107	Flow-limiting coronary stenosis (>50% stenosis of ICA + FFR)	93	99	96	99

N denotes the number of patients in each study, *SPECT* single photon emission computed tomography, *CTA* coronary CT angiography, *PET* positron emission tomography, *CAD* coronary artery disease, *Sens* sensitivity, *Spec* specificity, *PPV* positive predictive value, *NPV* negative predictive value, *ICA* invasive coronary angiography, *FFR* fractional flow reserve

[a] Hybrid SPECT/CTA only applied for non-evaluable arteries on CTA (14%)

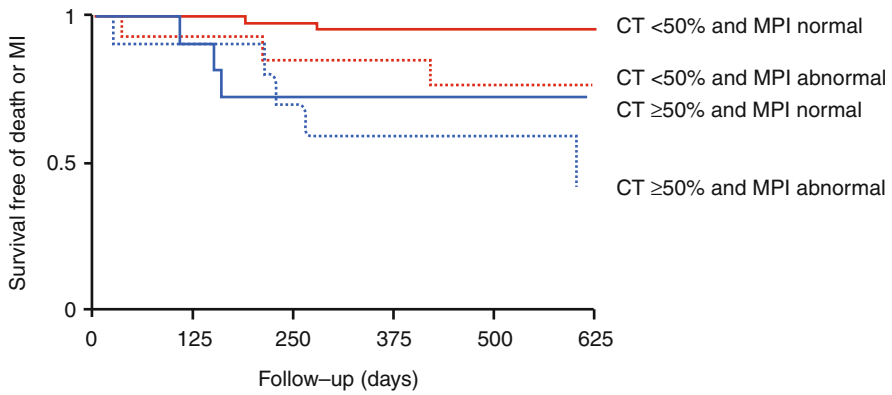

Fig. 20.3 Incremental prognostic value by combining anatomy and function from single photon emission computed tomography (SPECT) and CT. Survival free of death and myocardial infarction in patients with a normal or abnormal myocardial perfusion imaging (MPI) by SPECT and with or without coronary disease on CT. Abnormal MPI was defined as a summed stress score of ≥4 (With permission from van Werkhoven et al. *J Am Coll Cardiol* 2009)

combination with SPECT or FFR, and the single-center design. There is also evidence of an incremental prognostic value from combining functional and anatomic information by SPECT and CTA (**Fig. 20.3**). Larger multi-center trials such as the prospective multimodality European EVINCI study are awaited to confirm these preliminary results.

The synergistic value of cardiac hybrid imaging originates from the exact spatial 3D coregistration of perfusion defects and stenosed coronary arteries, which allows identifying flow-limiting coronary lesions and therefore plan targeted revascularization procedures. A number of small studies suggest that hybrid imaging provides diagnostic information about the hemodynamic relevance of individual coronary lesions beyond the side-by-side analysis of perfusion and CTA datasets (**Table 20.2**). This is particularly true in patients with multivessel disease and patients with inferior or inferolateral perfusion defects.

Table 20.2 Synergistic clinical value of fused hybrid imaging compared to the side-by-side analysis

Author	Hybrid system	Patient population	Incremental value of fused hybrid imaging
Gaemperli et al. (2007)	SPECT/64-slice CTA and 3D image fusion	38 patients with ≥1 SPECT defects	Modification of initial interpretation in 29% of patients. In equivocal lesions, hemodynamic relevance could be confirmed in 35% and excluded in 25%
Santana et al. (2009)	16- and 64-slice CTA and MPI (SPECT or ^{82}Rb PET)	50 patients with suspected CAD	Modification of initial interpretation in 28% of patients. Trend towards increased sensitivity (by 17%) in patients with multivessel disease
Slomka et al. (2009)	Motion frozen SPECT/64-slice CTA (automatic coregistration)	35 patients with suspected CAD	Improved diagnostic performance in RCA- and LCX-territories.

SPECT denotes single photon emission computed tomography, *CTA* coronary CT angiography, *MPI* myocardial perfusion imaging, *PET* positron emission tomography, *CAD* coronary artery disease

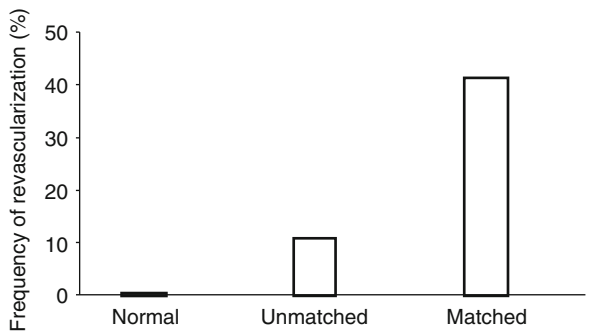

Fig. 20.4 Importance of matched anatomic and perfusion findings for clinical decision making. Data show the frequency of early revascularization among 318 consecutive patients undergoing hybrid SPECT/CT imaging. In the case of a matched finding (i.e. perfusion defect in the territory of a stenosed coronary artery) the revascularization rate was 41%, while it was significantly lower in patients with unmatched (11%) or normal (0%) findings (With permission from Pazhenkottil et al. *Eur Heart J* 2011)

Furthermore, hybrid imaging has been demonstrated to have an impact on downstream resource utilization (**Fig. 20.4**) indicating that hybrid imaging has value for predicting revascularization procedures.

20.4 Potential Indications

Open questions remain as to which patients truly benefit from such integrated hybrid imaging studies. It appears that the vast majority of patients referred for noninvasive cardiac imaging studies to exclude or confirm the presence of CAD are adequately addressed with only one single study (i.e. either CTA or functional imaging test). Additionally, the increased radiation and higher costs of hybrid imaging studies have to be considered as an important factor. Therefore, patients should be carefully selected where an added value of hybrid imaging may be anticipated.

20.4.1 Intermediate Pretest Likelihood

The pretest likelihood of CAD can be assessed based on the age and gender of the subject, the type of chest pain, and the ECG changes on exercise testing (Chap. 5). Patients with intermediate pretest likelihood are more likely to yield intermediate or inconclusive results in one of the imaging studies, e.g. intermediate coronary stenosis on CTA. In this situation an additional perfusion study

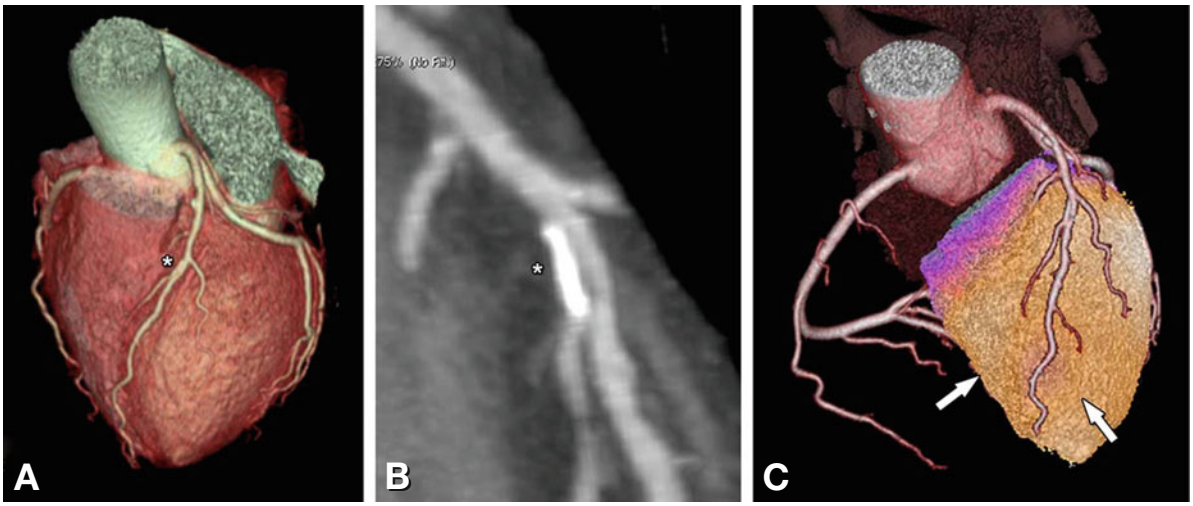

Fig. 20.5 Coronary artery stenosis without hemodynamic relevance on perfusion imaging in a 56-year-old woman with atypical chest pain, family history for coronary artery disease, and ascending1.5-mm ST-segment depression on stress ECG. On CTA using volume rendering (**Panel A**) and thin-slab maximum intensity projection (*arrow* in **Panel B**) a visually quantified 50% mid-left anterior descending (LAD) stenosis was found *asterisk*. In contrast, the sequential hybrid SPECT/CTA revealed normal perfusion of her left ventricular myocardium, particularly in the anterior wall, which excluded hemodynamic relevance of the LAD stenosis (*arrows* in **Panel C**). Therefore, she did not undergo subsequent revascularization

may address the hemodynamic relevance of such lesions and help to decide whether the patient can be treated medically or needs to be referred for invasive angiography with revascularization (**Fig. 20.5**). Such sequential hybrid imaging protocols have been implemented in several centers with hybrid imaging capabilities.

20.4.2 Multivessel Disease

Patients with multivessel disease (MVD) represent a population that is at increased risk for future cardiac events and therefore is often referred for revascularization to improve outcomes. However, the majority of patients with angiographic 3-vessel disease turn out to have considerably less flow-limiting lesions than deemed from the angiograms. Compared to perfusion imaging alone, hybrid imaging may have an incremental diagnostic value particularly in patients with MVD. By this means, hybrid imaging may allow targeted revascularization procedures in MVD patients avoiding stent or bypass overuse with the inherent adverse sequelae of stent or graft reocclusion (**Fig. 20.6**).

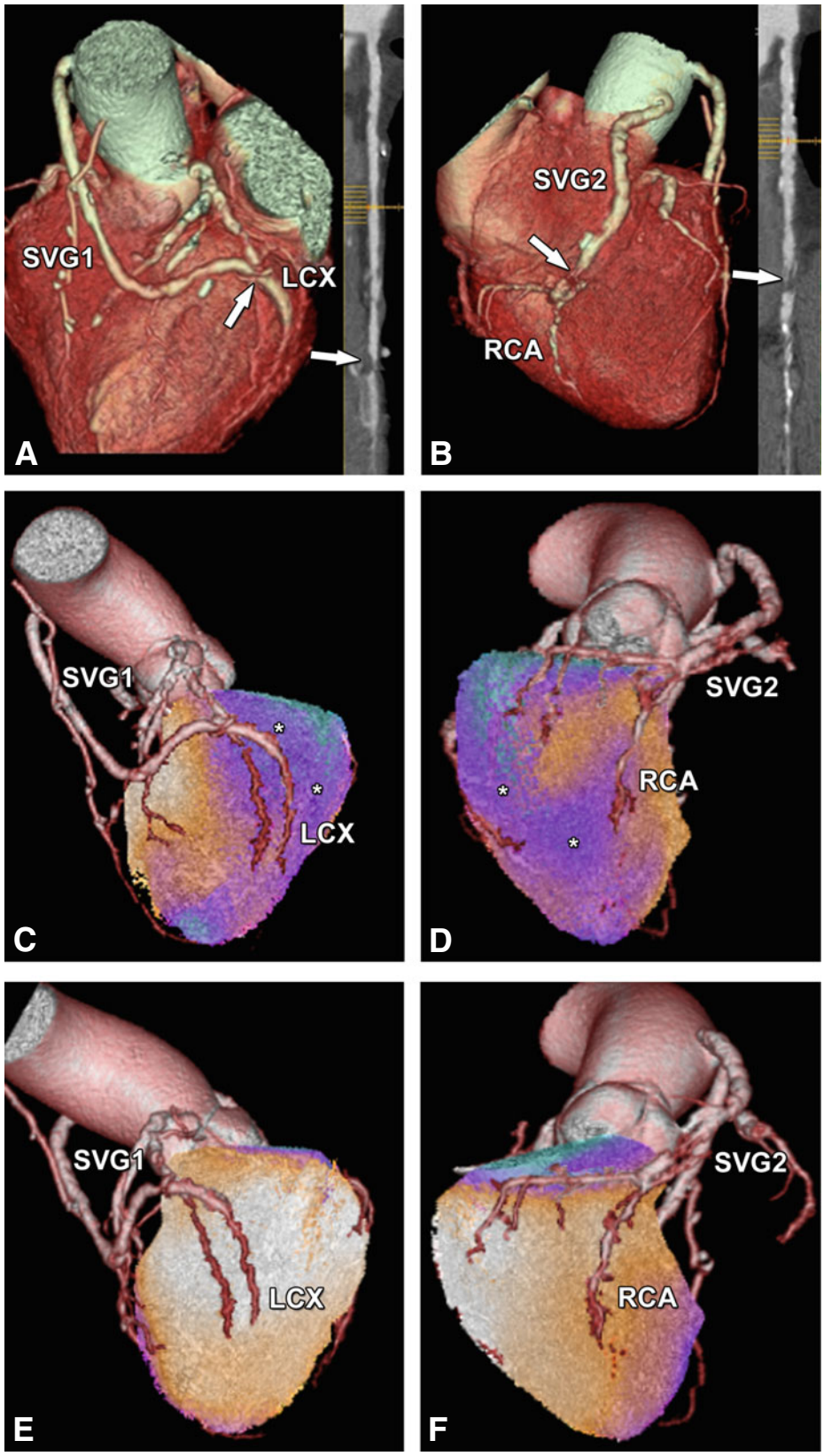
SVG1
LCX
A
SVG2
RCA
B
SVG1
LCX
C
SVG2
RCA
D
SVG1
LCX
E
SVG2
RCA
F

Fig. 20.6 Importance of hybrid imaging in multivessel disease. A 74-year old diabetic patient, who underwent coronary artery bypass grafting 15 years ago, presented with left bundle branch block, new-onset dyspnea, and stress-induced hypotension. CTA documented a high-grade stenosis in the first saphenous vein graft (SVG1) to the left circumflex artery (LCX, *arrows* in **Panel A**) and another high-grade stenosis in the second SVG to the right coronary artery (RCA) (*arrows* in **Panel B**). On hybrid myocardial perfusion PET/CT (with ^{13}N-NH_3) several ischemic areas could be documented in the territory of the LCX (*asterisks* in **Panel C**) and the RCA (*asterisks* in **Panel D**). Importantly, the subsequent viability study using hybrid ^{18}F-fluorodeoxyglucose PET/CT document preserved viability in both territories (Panels **E** and **F**) indicating that revascularization would be beneficial in this patient

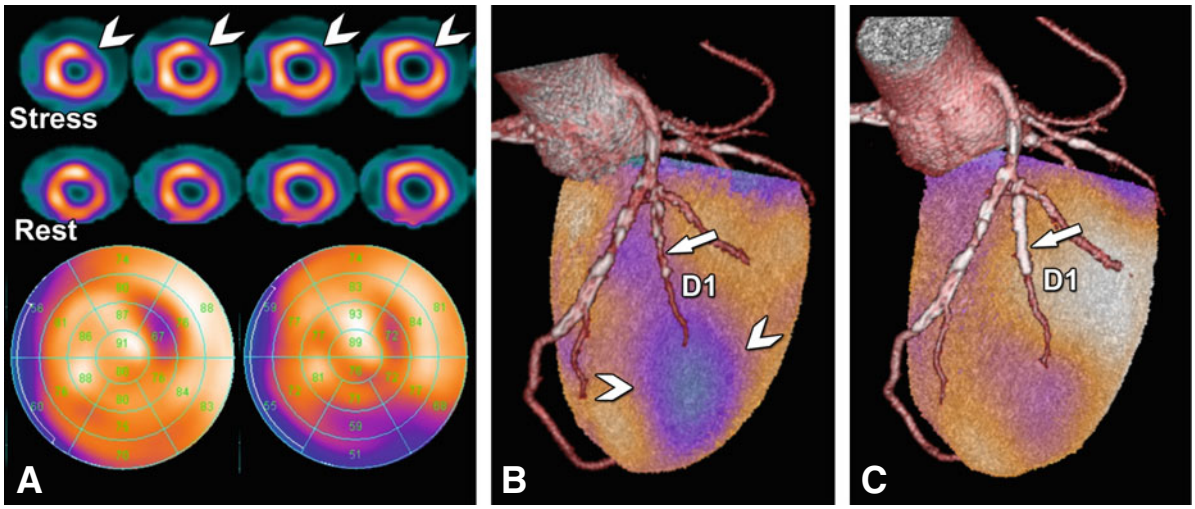

Fig. 20.7 Supporting clinical decision making in side-branch disease using hybrid imaging as illustrated in a 50-year-old man with reduced exercise capacity who was scheduled for hip replacement surgery. A small reversible perfusion defect was noted on SPECT images (*arrowheads* in **Panel A**). On CT angiography, significant changes were observed in all main coronary arteries with a subtotal stenosis of the first diagonal branch (D1) (*arrow* in **Panel B**, not clearly visible on 3D images). Hybrid SPECT/CT images colocalized the perfusion defect (*arrowheads*) with the D1 (**Panel B**), which was therefore the target for revascularization by balloon angioplasty and stenting. On repeat SPECT/CT 3 weeks later, the stent in the D1 can be seen (*arrow* in **Panel C**) along with a normalization of perfusion in the corresponding territory

20.4.3 Significant Side-Branch Disease

Side branches are often regarded as prognostically insignificant but may be associated with significant angina. Although perfusion defects in side branch disease are generally smaller, they may be difficult to distinguish from main branch disease. Hybrid imaging provides accurate coregistration of coronary anatomy and perfusion defects and therefore allows to identify flow-limiting lesions in side branches (diagonal, posterolateral branches) for targeted revascularization procedures (**Fig. 20.7**).

20.4.4 Chronic Total Occlusions

Percutaneous revascularization procedures in patients with chronic total occlusions (CTO) are associated with higher rates of complications and larger contrast media and radiation administration. Therefore, proof of

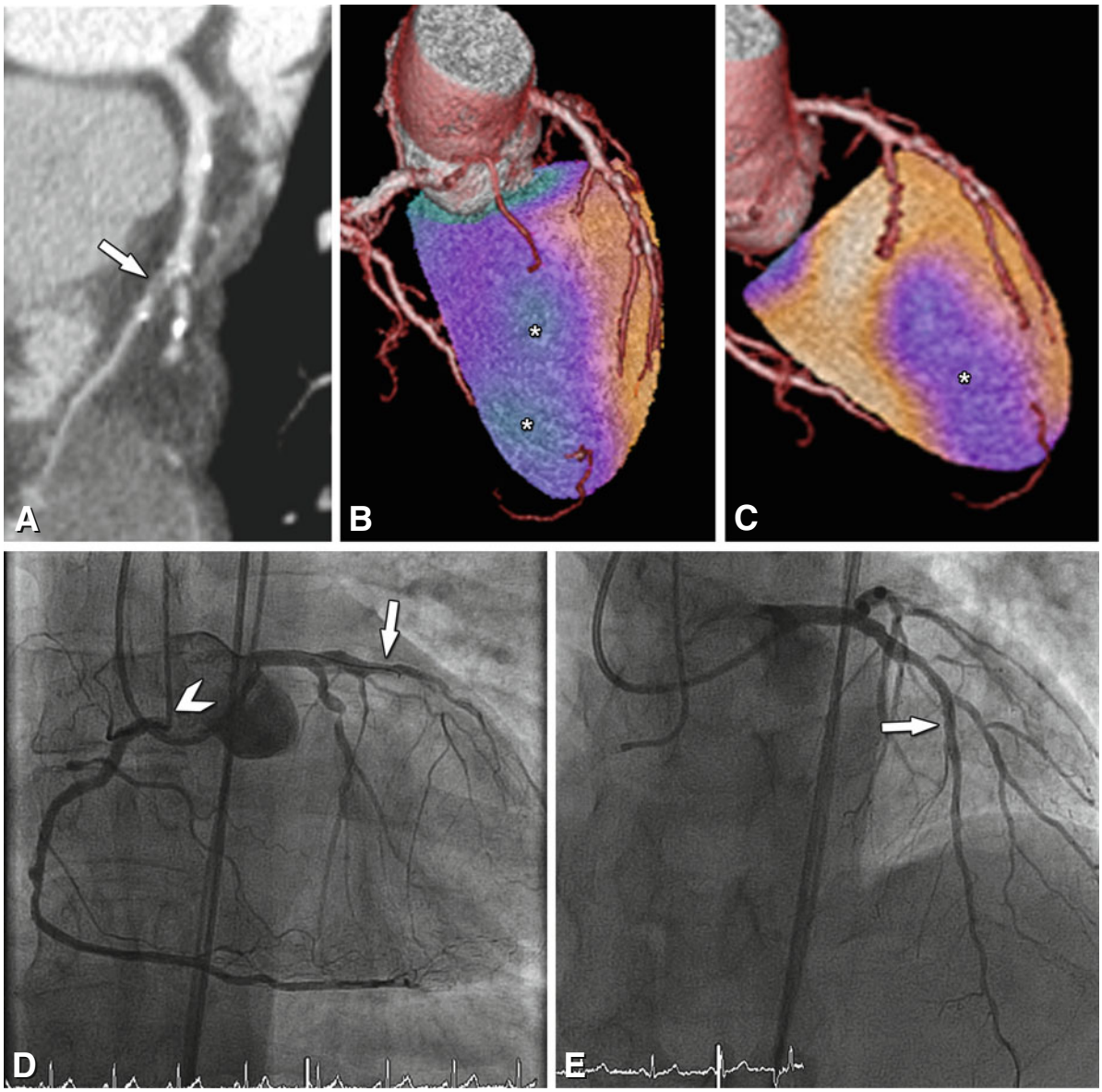

Fig. 20.8 57-year old male patient with stable angina, near-normal ejection fraction with hypokinesia of the anterior wall on echocardiography. His CT angiogram reveals a short mainly noncalcified occlusion of the mid left anterior descending coronary artery (LAD) (*arrows*) with good distal opacification of the lumen indicative of sufficient collaterals (**Panel A**). **Panel B** shows the hybrid myocardial SPECT/CT perfusion study with a large ischemic territory of the anteroseptal wall (*asterisks*). By contrast, the viability study with hybrid ^{18}F-fluorodeoxyglucose PET/CT (**Panel C**) reveals only a small territory of reduced uptake (*asterisk*) at the apical septum indicating significant areas of perfusion-metabolism mismatch which would justify a revascularization procedure. **Panel D** shows the percutaneous procedure with contralateral injection (*arrowhead*) and the guidewire (*arrow*) placed in the mid LAD and a good final angiographic result after stenting of the LAD (*arrow* in **Panel E**). Additionally, there was a 90% left circumflex coronary artery stenosis (**Panel D**) which was revascularized immediately after recanalization of the LAD

myocardial ischemia in the territory of the occluded vessel is mandatory prior to embarking into any potentially harmful intervention. On one hand, hybrid imaging may accurately detect a perfusion defect located in the territory of the CTO vessel. On the other hand, anatomic CT information such as the morphology of the stump, the presence of side vessels, the length of occlusion and/or calcifications are predictors for procedural success (Chap. 10) and may help to decide between antegrade or retrograde revascularization approaches (**Fig. 20.8**).

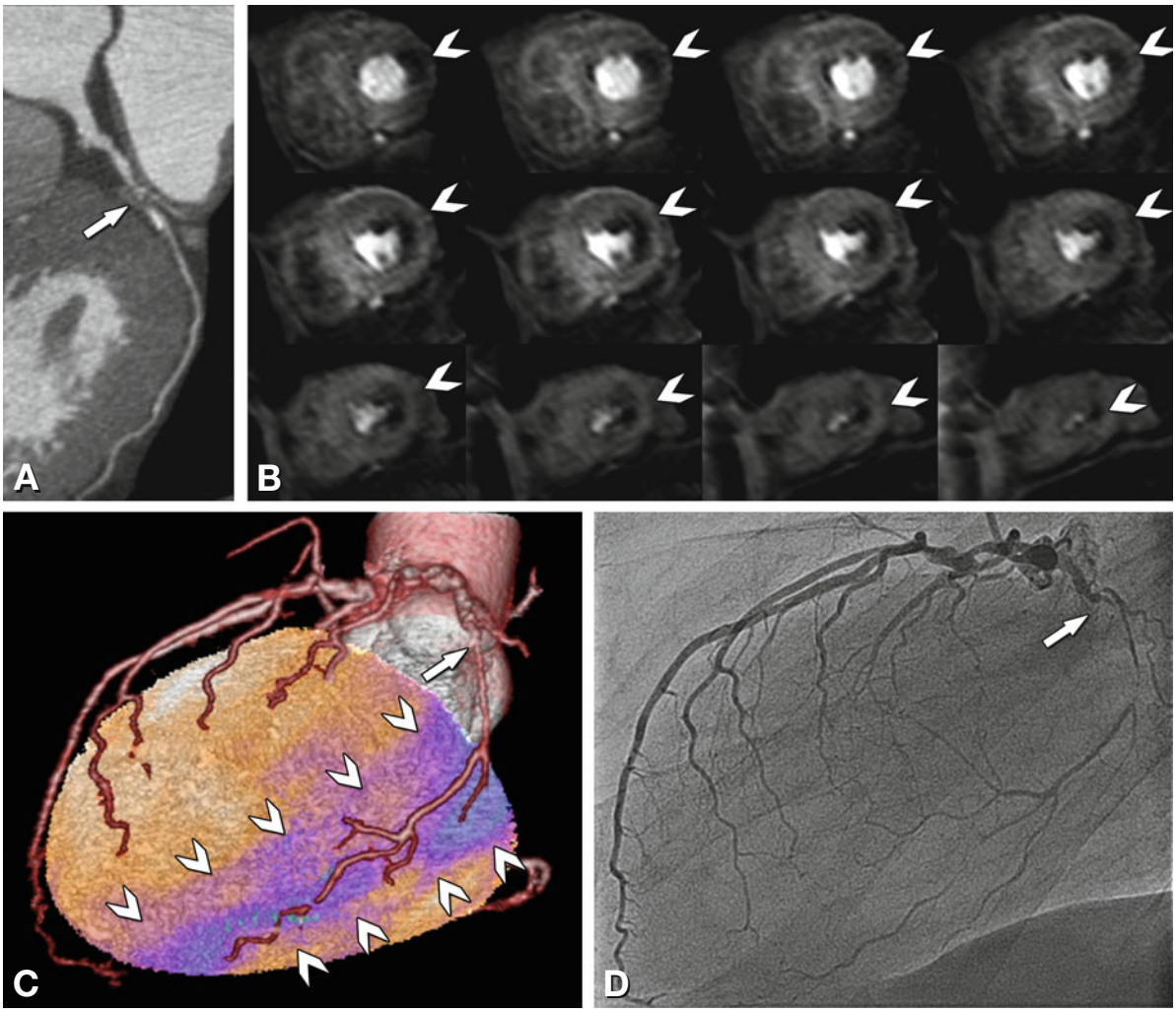

Fig. 20.9 Hybrid stress MR/CTA in a 65-year-old gentleman with typical chest pain. His CT angiography shows a high-grade stenosis/occlusion of the left circumflex artery (LCX, *arrow* in **Panel A**). Stress MR with full 3D coverage of the left ventricle showed a lateral perfusion defect (*arrowheads* in **Panel B**). The hybrid stress MR/CTA documents colocalization of the lateral ischemia (*arrowheads*) with the occluded LCX (*arrow* in **Panel C**) which was later confirmed by invasive angiography (*arrow* in **Panel D**) (With permission from Manka et al. *Eur Heart J* 2011)

20.5 Future Perspectives

Hybrid imaging is increasingly contributing to the development of imaging strategies which go beyond the assessment of myocardial perfusion. Furthermore, the use of other modalities (e.g., cardiac MR) may expand existing indications for hybrid imaging. A number of novel hybrid imaging approaches hold promise to make their way into clinical practice or are used already in very specialized centers.

20.5.1 Hybrid MR/CTA

The use of stress MR instead of SPECT for hybrid imaging has some attractiveness due to the fact that MR has a higher in-plane spatial resolution and avoids ionizing radiation. However, standard first-pass perfusion MR is acquired in three distinct short axes of the left ventricle, not enough to extrapolate onto a volumetric perfusion dataset. Faster perfusion sequences (*kt* SENSE) are now available which allow full coverage of the left ventricle, thereby providing a 3D dataset of perfusion (similar to SPECT) which can be used for fusion with CT. The feasibility of stress MR/CTA hybrid imaging has been demonstrated in first case reports (**Fig. 20.9**).

20.5.2 Cardiac Resynchronization Therapy

Cardiac resynchronization therapy (CRT) has established itself as an important therapeutic option to

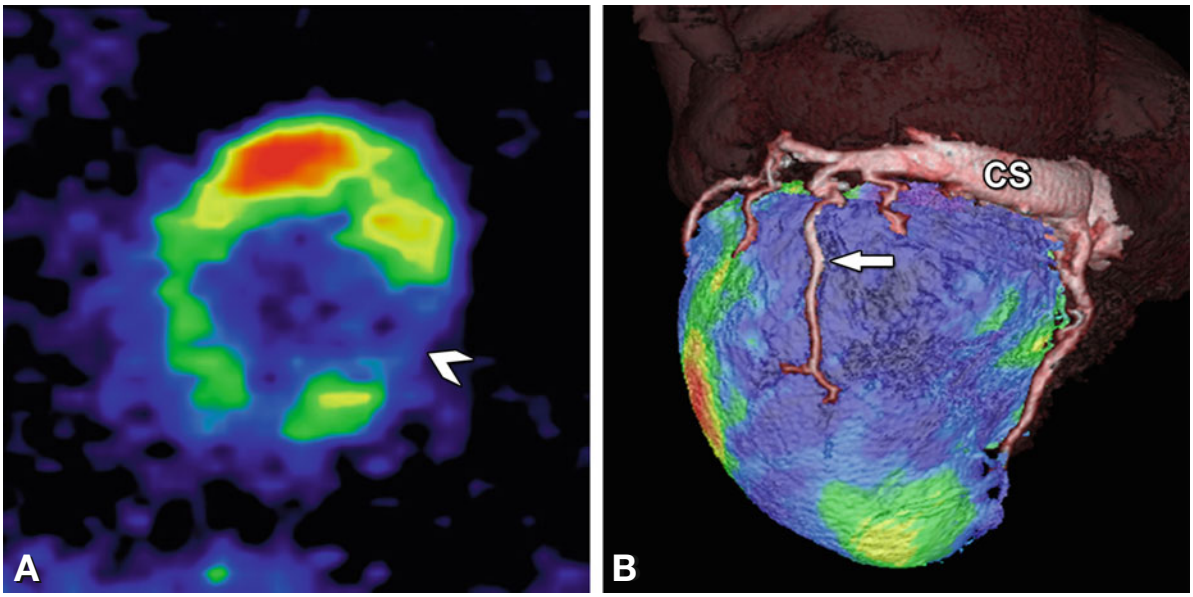

Fig. 20.10 Hybrid FDG PET/CT venous angiogram in a patient with ischemic cardiomyopathy, reduced left ventricular function and congestive heart failure. FDG PET showed a nonviable scar in the inferolateral wall (*arrowhead* in **Panel A**, short-axis slice) while viability in the anterior wall appeared to be preserved. On PET/CT, a large posterolateral vein can be seen which appears suitable for percutaneous lead insertion of a cardiac resynchronization therapy device (*arrow* in **Panel B**, volume rendering view from below), however, viability in the target territory is reduced, questioning whether this particular patient will benefit from such therapy. *CS* coronary sinus

improve symptoms and prognosis in heart failure patients. Unfortunately, CRT non-responder rates are still high (approximately 30%), particularly in patients with ischemic heart disease. Therefore, efficient tools to predict CRT success and improve patient selection are urgently needed. Hybrid imaging may combine venous anatomy from CT (by scanning in the venous phase) with viability information from ^{18}F fluorodeoxyglucose (FDG) PET (**Fig. 20.10**). This approach may allow visualization of venous morphology and identifying candidate veins for percutaneous lead insertion (Chap. 21), while at the same time viability in this territory is ascertained. It is likely that patients in whom the left ventricular lead is placed in a non-viable territory may not respond to CRT.

20

Recommended Reading

Boden WE, O'Rourke RA, Teo KK et al (2007) Optimal medical therapy with or without PCI for stable coronary disease. N Engl J Med 356:1503–1516

De Bruyne B, Pijls NH, Kalesan B et al (2012) Fractional flow reserve-guided PCI versus medical therapy in stable coronary disease. N Engl J Med 367:991–1001

Flotats A, Knuuti J, Gutberlet M et al (2010) Hybrid cardiac imaging: SPECT/CT and PET/CT. A joint position statement by the European Association of Nuclear Medicine (EANM), the European Society of Cardiac Radiology (ESCR) and the European Council of Nuclear Cardiology (ECNC). Eur J Nucl Med Mol Imaging 38:201–212

Gaemperli O, Schepis T, Valenta I et al (2007) Cardiac image fusion from stand-alone SPECT and CT: clinical experience. J Nucl Med 48:696–703

Groves AM, Speechly-Dick ME, Kayani I et al (2009) First experience of combined cardiac PET/64-detector CT angiography with invasive angiographic validation. Eur J Nucl Med Mol Imaging 36:2027–2033

Kajander S, Joutsiniemi E, Saraste M et al (2010) Cardiac positron emission tomography/computed tomography imaging accurately detects anatomically and functionally significant coronary artery disease. Circulation 122:603–613

Manka R, Kuhn FP, Kuest SM, Gaemperli O, Kozerke S, Kaufmann PA (2011) Hybrid cardiac magnetic resonance/computed tomographic imaging: first fusion of three-dimensional magnetic resonance perfusion and low-dose coronary computed tomographic angiography. Eur Heart J 32:2625

Namdar M, Hany TF, Koepfli P et al (2005) Integrated PET/CT for the assessment of coronary artery disease: a feasibility study. J Nucl Med 46:930–935

Pazhenkottil AP, Nkoulou RN, Ghadri JR et al (2011) Impact of cardiac hybrid single-photon emission computed tomography/computed tomography imaging on choice of treatment strategy in coronary artery disease. Eur Heart J 32:2824–2829

Rispler S, Keidar Z, Ghersin E et al (2007) Integrated single-photon emission computed tomography and computed tomography coronary

angiography for the assessment of hemodynamically significant coronary artery lesions. J Am Coll Cardiol 49:1059–1067

Santana CA, Garcia EV, Faber TL et al (2009) Diagnostic performance of fusion of myocardial perfusion imaging (MPI) and computed tomography coronary angiography. J Nucl Cardiol 16:201–211

Sato A, Nozato T, Hikita H et al (2010) Incremental value of combining 64-slice computed tomography angiography with stress nuclear myocardial perfusion imaging to improve noninvasive detection of coronary artery disease. J Nucl Cardiol 17:19–26

Shaw LJ, Berman DS, Maron DJ et al (2008) Optimal medical therapy with or without percutaneous coronary intervention to reduce ischemic burden: results from the Clinical Outcomes Utilizing Revascularization and Aggressive Drug Evaluation (COURAGE) trial nuclear substudy. Circulation 117:1283–1291

Slomka PJ, Cheng VY, Dey D et al (2009) Quantitative analysis of myocardial perfusion SPECT anatomically guided by coregistered 64-slice coronary CT angiography. J Nucl Med 50:1621–1630

Tonino PA, De Bruyne B, Pijls NH et al (2009) Fractional flow reserve versus angiography for guiding percutaneous coronary intervention. N Engl J Med 360:213–224

van der Hoeven BL, Schalij MJ, Delgado V (2012) Multimodality imaging in interventional cardiology. Nat Rev Cardiol 9:333–346

van Werkhoven JM, Schuijf JD, Gaemperli O et al (2009) Prognostic value of multislice computed tomography and gated single-photon emission computed tomography in patients with suspected coronary artery disease. J Am Coll Cardiol 53:623–632

Wijns W, Kolh P, Danchin N et al (2010) Guidelines on myocardial revascularization: the Task Force on Myocardial Revascularization of the European Society of Cardiology (ESC) and the European Association for Cardio-Thoracic Surgery (EACTS). Eur Heart J 31:2501–2555

Electrophysiology Interventions

R.A. Salgado and B. Ghaye

Abstract

The most common CT applications in patients undergoing cardiac electrophysiology interventions are explained, focusing on preprocedural planning and postprocedural follow-up.

21.1 Evolving Role of Electrophysiology Interventions

Interventional cardiac electrophysiology (EP) has evolved into a highly specialized cardiac subspecialty, which is increasingly relying on detailed three-dimensional anatomic visualization of the targeted cardiac and surrounding structures for preprocedural planning, periprocedural guidance, and postprocedural follow-up.

In general, there are two major groups of patients who are candidates for CT prior to EP procedures. The most commonly encountered group includes patients presenting with rhythm disturbances, most notably atrial fibrillation. In this situation, imaging of the left atrium and pulmonary veins by CT can be clinically helpful to guide patient management. Patients with heart failure who are scheduled for cardiac resynchronization therapy form the second group. In this setting, CT has become important for the visualization of the coronary venous system.

21.2 Atrial Fibrillation

Atrial fibrillation is an increasingly encountered supraventricular tachycardia, basically characterized by uncoordinated atrial activation presenting as a chaotic heart rhythm with subsequent deterioration of atrial mechanical function. While some individuals with AF are asymptomatic, others experience varying degrees of discomfort. Atrial fibrillation is a progressive disease which increasingly degrades quality of life over time. It is also associated with important clinical consequences, including diminished cardiac function and an increased risk for atrial cloth formation and thromboembolic stroke.

M. Dewey, *Cardiac CT*,
DOI 10.1007/978-3-642-41883-9_24, © Springer-Verlag Berlin Heidelberg 2014

Studies have shown that, in the majority of patients, atrial fibrillation is initiated by spontaneous electrical discharges originating from arrhythmia-inducing ectopic foci within the pulmonary veins. More specifically, these foci are located near the entrance sites of these veins into the left atrium (atriopulmonary venous junction). Therefore, the rationale behind catheter-based cryo- or radiofrequency transcatheter ablation of these sites is to eliminate the source of abnormal electric signals or to disrupt electrical communication (isolation) between the ectopic foci and the left atrium. During the intervention, the ablation catheter is brought into the left atrium through a percutaneous venous femoral access and subsequent transseptal puncture from right to left atrium (**Fig. 21.1**). While such treatment is generally considered safe in experienced hands, it is nevertheless associated with relatively rare but potentially important complications. Radiofrequency ablation of the pulmonary vein ostia is reserved for patients with symptomatic and drug-refractory paroxysmal or persistent atrial fibrillation.

21.2.1 Role of CT

Both CT and magnetic resonance imaging (MRI) can be used to acquire the required preoperative information. The choice between these two imaging modalities often depends on the local expertise and available equipment. While MRI has the advantage of not involving ionizing radiation and using a generally safe

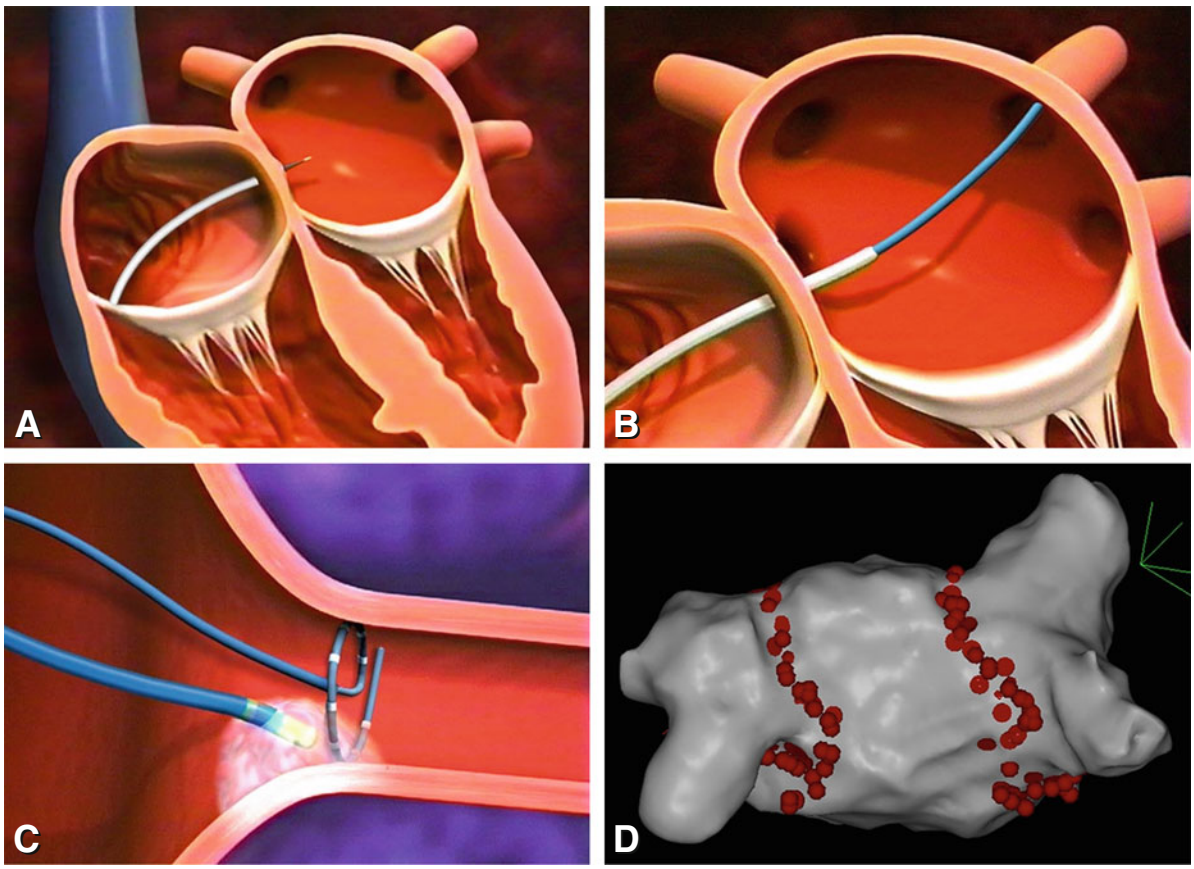

Fig. 21.1 Illustration of the radiofrequency ablation procedure. After traditionally percutaneous venous femoral access, a transseptal catheter puncture is performed to gain access to the left atrium (**Panel A**). Next, the catheter with an ablation electrode at its tip is placed at the level of an atriopulmonary venous junction – in this case the upper left pulmonary vein (**Panel B**). Finally, ablation is performed: a circular Lasso catheter is used for electrical mapping guidance at the atriopulmonary venous junction (the wall of which has myocardial tissue extending from the left atrium), while a linear catheter with ablation electrode performs a radiofrequency ablation at a specific point (**Panel C**). **Panel D** shows a three-dimensional fast anatomic mapping image of the left atrium acquired by dragging a mapping catheter over sites of interest along the atrial endocardial wall. The final ablation points (*red* in **Panel B**) surround the pulmonary vein entrances into the left atrium in a circular fashion, achieving as such electrical isolation (**Panels A**–**C)** (With permission from Ghaye et al., *Radiographics*, 2003)

Table 21.1 Purposes of CT in patients prior to electrophysiology procedures in atrial fibrillation

Item/structure	What to consider
Left atrial wall & cavity	Atrial thrombus: specifically in the left atrial appendage
	Atrial diverticula or other potential obstacles
Pulmonary veins	Number and location
	Size of ostia: specifically the presence of conjoined veins
	Accessory veins or abnormal pulmonary venous return
Interatrial septum	Interatrial shunts: patent foramen ovale, atrial septal defect
	Lipomatous septal hypertrophy
	Septal aneurysm or septal closure device
Periatrial structures	Anatomic relationship with the esophagus
Other ancillary findings	Any finding that could alter the execution of the procedure or influence treatment

Table 21.2 Complications related to radiofrequency ablation of the pulmonary vein ostia

Affected anatomy	Complications
Pulmonary veins	Pulmonary vein stenosis
	Pulmonary vein occlusion
	Pulmonary vein dissection
Lung & pleura	Pulmonary hypertension
	Pulmonary venous infarction
	Pulmonary fibrosis
	Pulmonary embolism
	Pneumothorax
	Hemothorax
	Pleural effusion
Heart & pericardium	Pericarditis
	Hemopericardium & cardiac tamponade
	Cardiac perforation
	Coronary artery spasm & myocardial infarction
	Valve damage
	Atrioesophageal fistula
Other	Systemic thromboembolism
	Phrenic nerve palsy
	Hematoma at puncture site
	Arteriovenous fistula

gadolinium-based contrast agent, it is nevertheless a more complex technique, making its implementation less practical. Therefore, CT has been increasingly used for this purpose, offering exquisite anatomic visualization in a short examination time with little physician input.

An overview of the clinical purpose of CT in the preprocedural evaluation of patients with atrial fibrillation is given in **Table 21.1**. CT is also an excellent tool for detection of short- and long-term procedural complications (**Table 21.2**).

21.2.2 Scan Protocol

One of the most important goals of a preprocedural CT investigation is the acquisition of a high-quality three-dimensional dataset to be used for image integration during the transcatheter ablation procedure. At first glance, this acquisition is similar to a standard cardiac CT protocol for evaluation of the coronary arteries. However, many patients referred prior to EP will have atrial fibrillation at the time of the CT examination, very often causing significant image artifacts on an ECG-triggered CT acquisition. Consequently, while an ECG-triggered acquisition is traditionally preferred for coronary angiography (Chap. 8), a case can be made for non-gated examinations in patients with atrial fibrillation. A non-gated scan can both provide sufficient image quality and reduce radiation exposure (Chap. 7) while shortening the examination time. Nevertheless, in dual-source CT systems using high-pitch protocols and CT systems with large volumetric coverage, ECG-triggered acquisitions can also result in good image quality in patients with atrial fibrillation.

Finally, a major concern raised by (especially prolonged) atrial fibrillation episodes is the formation of thrombi in the left atrium secondary to the altered wall motion, representing one of the most important causes of stroke-related morbidity and mortality. Thrombi predominantly form in the left atrial appendage (LAA) and are often the source of peripheral emboli and consequently the target of appendage occluder devices (**Fig. 21.2**). Since an atrial thrombus is a contraindication

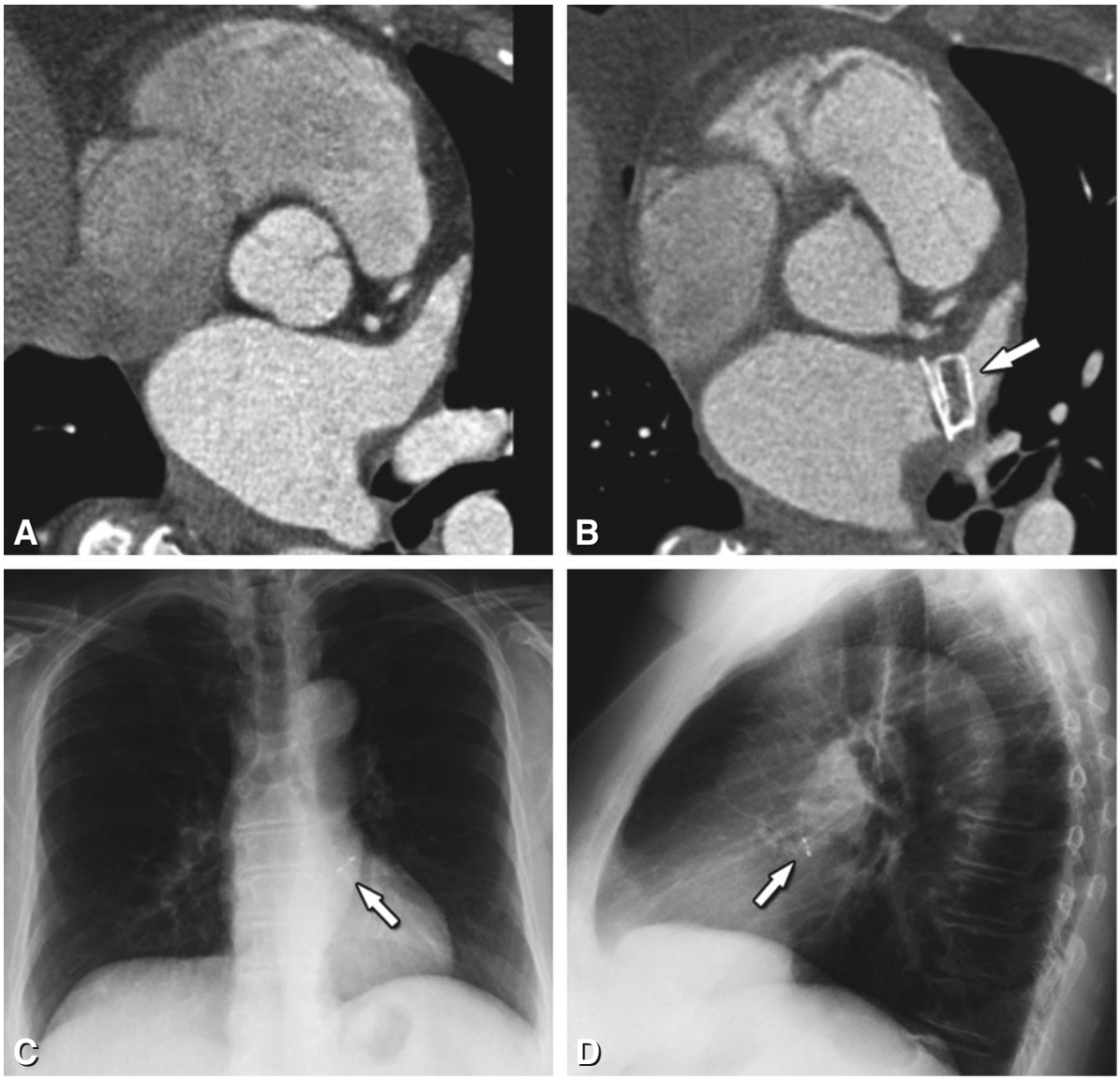

Fig. 21.2 Axial contrast-enhanced CT image in a 67-year-old female before (**Panel A**) and after (**Panel B**) placement of a left atrial appendage occluder device (Amplatzer Cardiac Plug 20 mm, *arrow* in **Panel B**). The device is also seen on frontal (*arrow* in **Panel C**) and lateral (*arrow* in **Panel D**) conventional chest radiographs. Since the left atrial appendage is a major source of thrombus formation due to circulatory stasis, the use of an occluder device here can dramatically reduce the risk of thromboembolic stroke. In this particular patient, anticoagulation therapy could be stopped after device placement. However, this approach is currently controversial, as some investigators argue that there are also other potential sources of emboli, including the atrial septum, left-sided valves, and the aorta. Furthermore, since stroke risk in atrial fibrillation is a systemic problem, occlusion of the left atrial appendage is by some considered only part of the treatment; consequently they continue to promote antithrombotic medication as the standard treatment for preventing stroke in patients with atrial fibrillation

to an EP intervention, a concise evaluation of the LAA is an essential part of every preprocedural CT examination. Caution is however needed as incomplete filling of the LAA is not an infrequent finding in CT scans of the heart performed in the arterial phase, especially when the LAA is enlarged (**Fig. 21.3**). As such, this phenomenon produces a false-positive image with a low-attenuation filling defect mimicking an atrial appendage thrombus due to circulatory stasis. An LAA filling defect therefore needs to be confirmed with an additional delayed-phase scan (albeit at the cost of extra radiation exposure) or with transesophageal echocardiography.

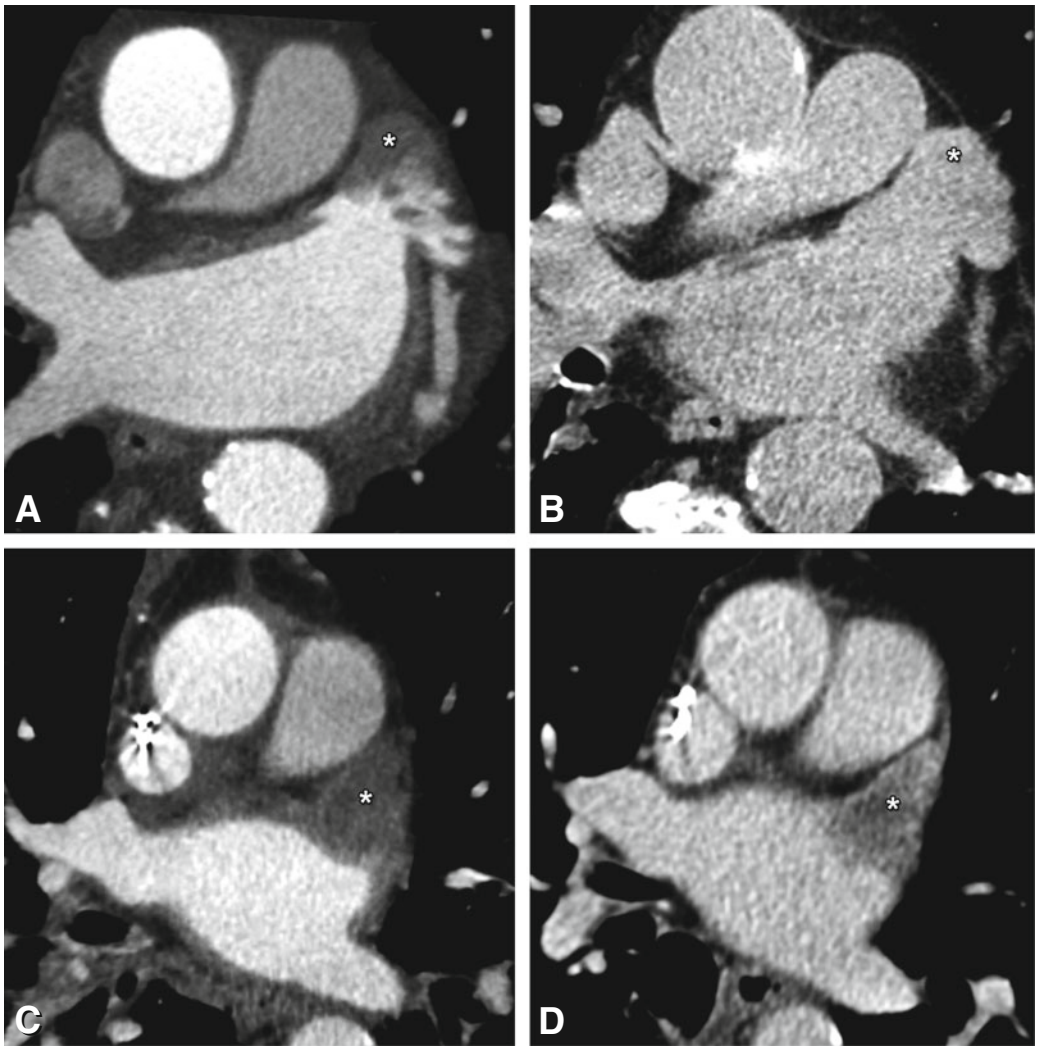

Fig. 21.3 Axial contrast-enhanced CT of two patients with paroxysmal atrial fibrillation prior to radiofrequency ablation, showing a left atrial appendage pseudothrombus (**Panels A** and **B**) and real thrombus (**Panels C** and **D**). Occurring especially in large atria and in patients with atrial fibrillation, slow blood flow can range from moderate to very pronounced (*asterisk* in **Panel A**). In this patient, absence of a thrombus was confirmed by delayed-phase imaging (*asterisk* in **Panel B**). Therefore, diagnosis of a left atrial appendage thrombus should only be retained after a filling defect has been confirmed on delayed-phase imaging or with transesophageal ultrasound. In the second patient, the left atrial appendage is completely filled with a hypodense mass on arterial-phase imaging (*asterisk* in **Panel C**), which persists on delayed-phase imaging (*asterisk* in **Panel D**) with only discrete further opacification surrounding the thrombus. Confirmation of the diagnosis is clinically important, as the presence of a left atrial appendage thrombus is a contraindication to an EP procedure

21.2.3 Postprocessing

After the CT examination, the data are digitally transferred to the EP room for further processing. In our institution, we provide an additional dataset containing only the left atrium and the atriopulmonary junctions of the different veins with a short adjacent vein segment. While this is not strictly necessary, the familiarity of the radiologist with cross-sectional cardiac anatomy, along with solid knowledge of the often-used postprocessing tools on CT workstations, can lead to a more reliable end-result than the use of less specialized software in the EP lab by non-radiologists. We also routinely generate three-dimensional volume-rendered images of the left

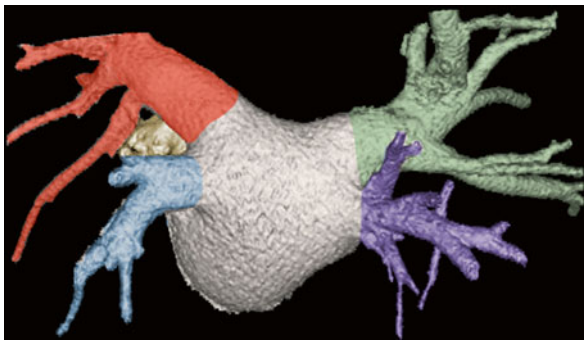

Fig. 21.4 Volume-rendered CT image of the left atrium, atriopulmonary venous junctions, and a short adjacent segment of the pulmonary veins. CT is an excellent tool for anatomic evaluation as echocardiography does not consistently visualize all pulmonary arteries. The normal three-dimensional anatomy of the pulmonary veins is illustrated, which includes the right superior (*green*), right inferior (*purple*), left superior (*red*), and left inferior (*blue*) pulmonary veins. The right superior pulmonary vein drains the right upper and middle lobe, with the left superior pulmonary vein draining the left upper lobe and lingula. The right and left inferior pulmonary veins drain the lower lobes of their respective lungs. This anatomic configuration occurs in 60–70% of patients. A portion of the left atrial appendage (*yellow*) can be seen anterior to the left pulmonary veins

atrium and its pulmonary veins, providing an anatomic overview unmatched by ultrasound (**Fig. 21.4**). Measurement of the size of the pulmonary vein ostia is not routinely done.

21.2.4 Preprocedural Clinically Relevant Anatomy

A correct description of the anatomy of the pulmonary veins and left atrium, specifically mentioning important anatomic variations that can alter the procedural strategy, should always be the first item reported. Typically, a total of four pulmonary veins with four independent ostia can be distinguished on both sides of the left atrium (**Fig. 21.4**). They are appropriately named right superior, right inferior, left superior and left inferior pulmonary vein. The most common anatomic variations are the presence of common (or conjoined) veins and accessory or supernumerary pulmonary veins (**Fig. 21.5**). Other more rare variants must also be reported as they can influence catheter passage (**Fig. 21.6**).

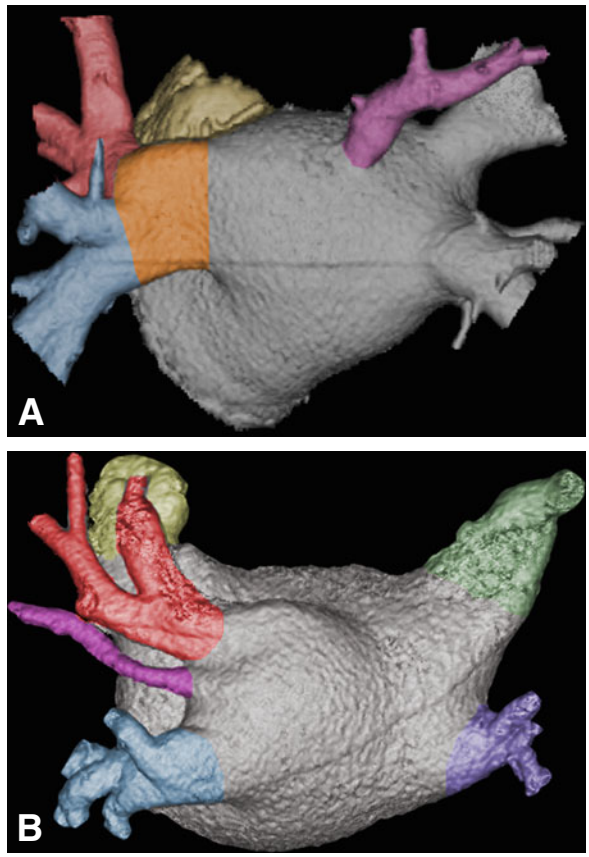

Fig. 21.5 Variant pulmonary vein anatomy in two patients with paroxysmal atrial fibrillation. Volume-rendered CT images are shown. An accessory vein (*purple*) is present in both cases, centered on the posterior atrial wall in **Panel A** and between the upper and lower left pulmonary veins in **Panel B**. Preprocedural detection of these accessory veins is important, since they are easily seen with CT but can be missed on less detailed fast anatomic mapping images acquired during the EP procedure. It is in such cases that integration of CT and EP-derived data can lead to the best roadmap for successful intervention. Furthermore, they have often small ostia (as especially illustrated in **Panel B**), making them more at risk for complications such as stenoses. Additionally, in **Panel A** there is a congenital confluence of the left superior (*red*) and inferior pulmonary vein (*blue*) in one large common trunk (*orange* in **Panel A**). Note the large diameter of this common vein segment, making this a preferred target for electrical isolation. This common variant occurs in 12–25% of the population, mostly on the left side

The presence of large ostia, as sometimes seen in conjoined pulmonary veins, must be reported as they may be prime targets for ablation even without any other

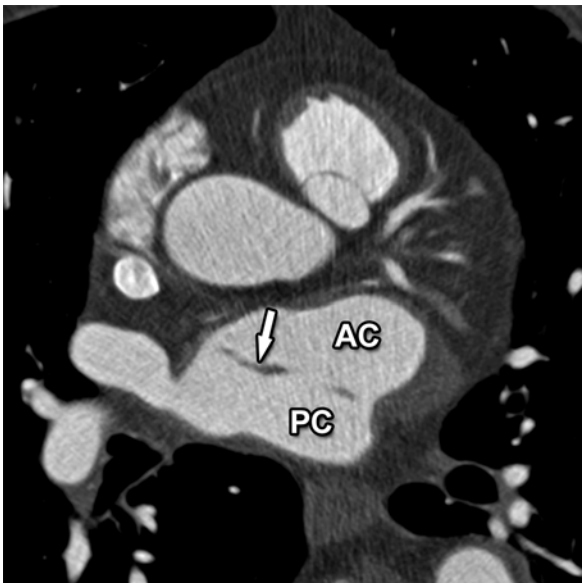

Fig. 21.6 Axial contrast-enhanced CT image in a 70-year-old man revealing an incidentally found cor triatriatum, with a fenestrated fibromuscular membrane (*arrow*) dividing the left atrium into an intercommunicating anterior (*AC*) and posterior chamber (*PC*). This is a rare congenital heart defect of unknown origin, possible secondary to malincorporation of the embryonic common pulmonary vein into the left atrium. Its presence can compromise stable and correct positioning of the ablation catheter during EP interventions and should therefore be reported. Practically, while it increases procedural complexity, a fenestrated membrane will generally not preclude a radiofrequency ablation intervention, as the electrophysiologist will try to use the fenestrations for passage of the catheter between the atrial chambers

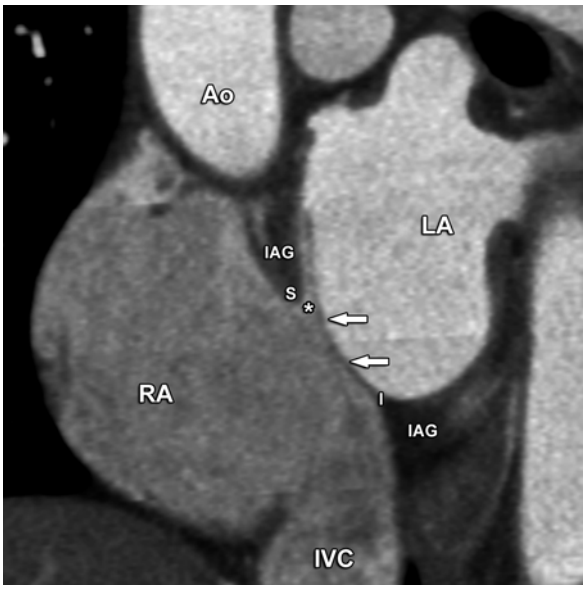

Fig. 21.7 A patent foramen ovale in a young woman. Slightly oblique coronal contrast-enhanced CT image obtained perpendicular to the interatrial septum at the level of the fossa ovalis. The superior (*S*) and inferior (*I*) rims of the fossa ovalis are formed by the septum secundum or interatrial groove (*IAG*). A patent foramen ovale is the result of failed fusion between the septum primum (*arrows*) and the septum secundum at the fossa ovalis, producing a potential communication between left and right atrium (*asterisk*). In this typical case, the septum primum (*arrows*) is fused to the inferior rim of the fossa ovalis (*I*) and extends superiorly as a flap. A patent foramen ovale is a common finding in the general population, with prevalence estimates in autopsy studies ranging from 25 to 35%. Small left-to-right shunts are commonly seen, where the passage of blood is always oblique between the partially overlapping ostium primum and secundum. This is a distinguishing feature compared with atrial septal defects, where the flow direction is perpendicular to the axis of the interatrial septum. Small shunts are of no clinical significance. The presence of a patent foramen ovale facilitates transseptal passage of the catheter during radiofrequency ablation procedures. *Ao* aorta, *RA* right atrium, *LA* left atrium, *IVC* inferior vena cava

evidence of atrial fibrillation foci (**Fig. 21.5**). Overall, both CT and MRI have been reported to deliver more accurate and comparable ostial measurements than transesophageal echocardiography, which often underestimates these dimensions and does not consistently visualize all pulmonary veins.

As positioning of the radiofrequency ablation catheter in the left atrium is achieved through puncture of the interatrial septum from the right atrium, evaluation of this septum is critical. In about 25–35% of patients, transseptal passage might be facilitated by the presence of a patent foramen ovale (PFO), a small potential interatrial shunt secondary to a lack of fusion between the septum primum and septum secundum (**Fig. 21.7**). While a PFO can exist without any detectable shunt, a small left-to-right shunt is common and often of little clinical significance. It can nevertheless become clinically important when left atrial pressure rises as in arterial hypertension for instance. Conversely, any temporary rise of right atrial pressure (e.g. coughing) can provoke a right-to-left shunt with the risk of paradoxical embolism.

A PFO must be distinguished from a true atrial septal defect (ASD), an interatrial communication which is

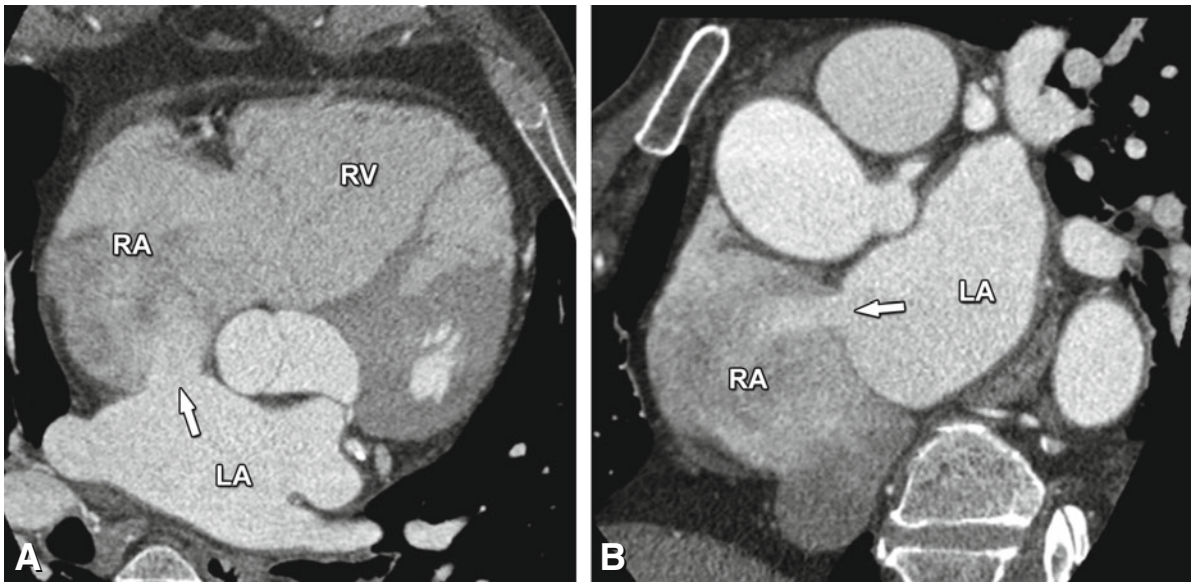

Fig. 21.8 Axial (**Panel A**) and coronal (**Panel B**) contrast-enhanced CT images in a middle-aged woman, illustrating an ostium secundum atrial septal defect as a discontinuity of the interatrial septum of about 1.5 cm length, with a left-to-right shunt illustrated by the passage of contrast-enhanced blood from the left to the right atrium (*arrow* in **Panels A** and **B**). Contrary to a patent foramen ovale, the flow is perpendicular to the axis of the interatrial septum through a septal defect without an overlapping flap. Atrial septal defects constitute 10% of all congenital heart diseases, with an ostium secundum defect being the most common type, accounting for 75% of all cases. In comparison with a patent foramen ovale, an atrial septal defect is a more rare but often clinically more relevant congenital defect. Small defects are usually asymptomatic, especially in the first three decades of life, and often do not require treatment. However, large shunts can initially cause volume and eventually pressure overload of the right heart with atrial and ventricular dilatation (as illustrated in this case), leading to pulmonary hypertension, right ventricular failure, and potentially right-to-left shunting. As a consequence, over 70% of individuals with an atrial septal defect become symptomatic in the fifth decade, or even earlier when the shunt is large. Depending on the characteristics of the atrial septal defect, treatment is endovascular or surgical. *RA* right atrium, *RV* right ventricle, *LA* left atrium

always patent and has greater clinical impact because the shunt tends to be larger in many cases. Three major types of ASD can be distinguished, with an ostium secundum ASD being the most frequently encountered type (**Figs. 21.8**, **21.9,** and **21.10**). One of the distinguishing features between an ASD and a PFO on CT is, besides location, the direction of the shunt flow (compare **Fig. 21.7** with **Fig. 21.8**).

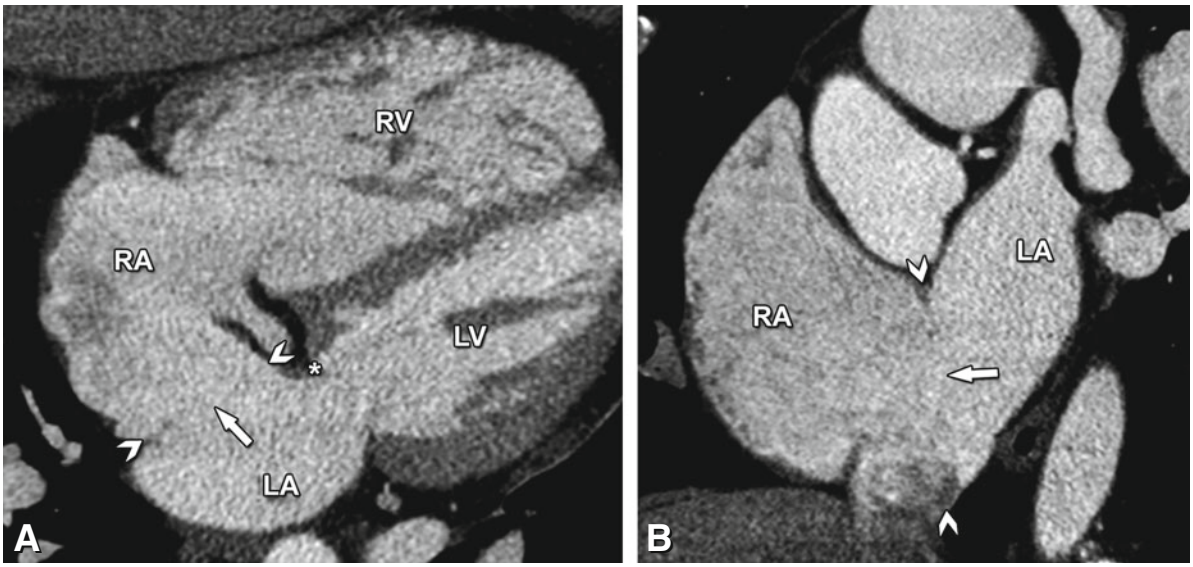

Fig. 21.9 Four-chamber (**Panel A**) and short-axis (**Panel B**) contrast-enhanced CT images in a middle-aged woman illustrating an ostium primum atrial septal defect (*arrowheads* in **Panels A** and **B**). A large communication between the left and right atrium is seen (*arrow* in **Panels A** and **B**), just posterior to the annulus of the mitral valve (*asterisk* in **Panel A**). Note the absence of septal flaps as in a patent foramen ovale and the enlargement of the right ventricle (*RV*) secondary to the shunt-induced volume overload. In contrast to an ostium secundum atrial septal defect, an ostium primum defect is often large and located in the most anterior and inferior part of the interatrial septum, immediately adjacent to the atrioventricular valves. Mostly, it is associated with a cleft in the anterior leaflet of the mitral valve. Ostium primum septal defects account for 15% of all atrial septal defects. *RA* right atrium, *LA* left atrium, *LV* left ventricle

An atrial septal aneurysm is occasionally encountered as a septal outpouching of variable depth and length, mostly from the left into the right atrium (**Fig. 21.11**). It can occur in isolation, but is often associated with other structural abnormalities including mitral valve prolapse and atrial septal defects.

The presence of septal closure devices and a lipomatous septal hypertrophy should be reported prior to an EP intervention because of increase procedural complexity and risk (**Fig. 21.12**).

Left atrial diverticula are common anatomic variants (**Fig. 21.13**). While their presence is in general of little clinical significance, they constitute potential sites of catheter entrapment.

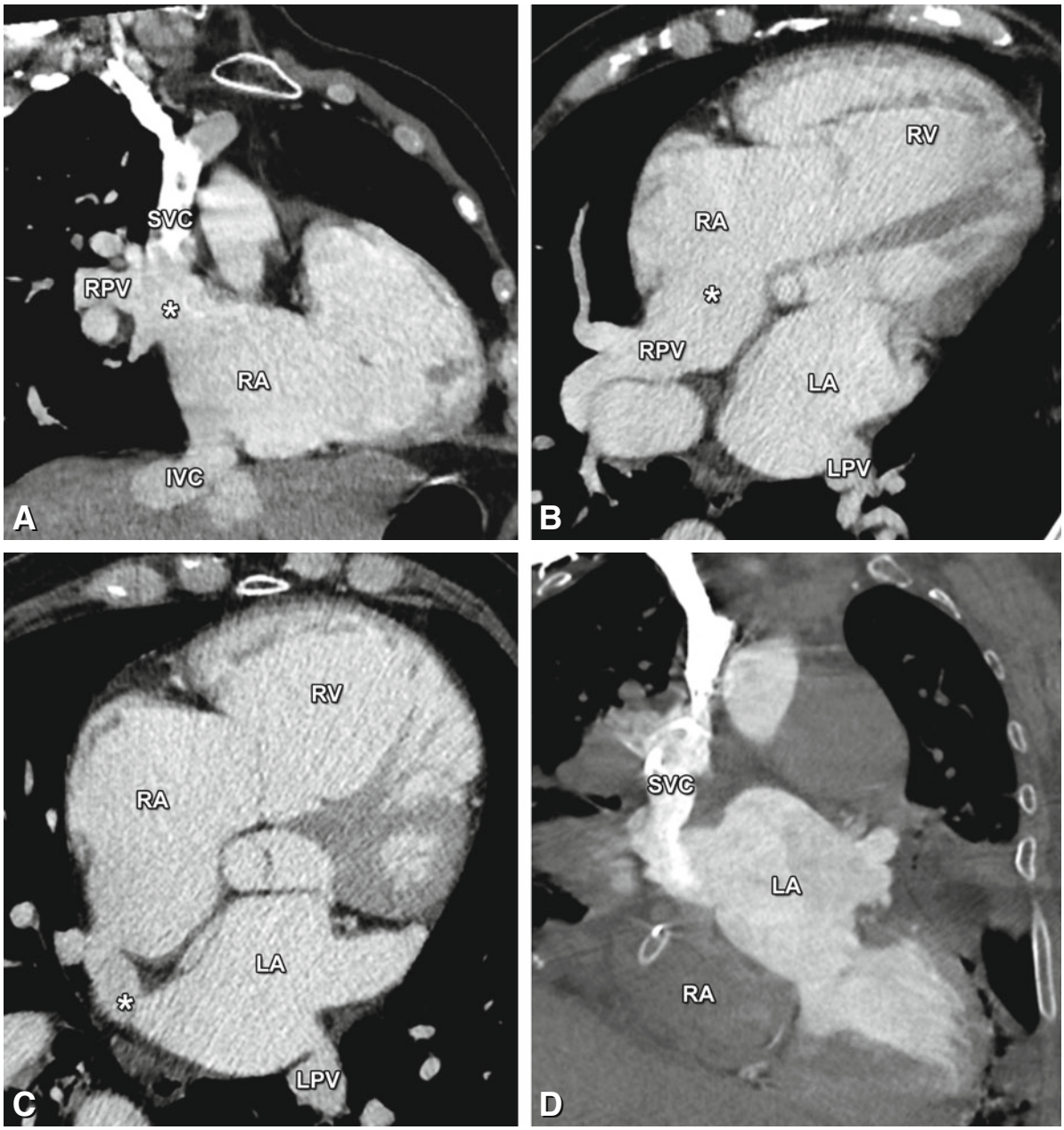

Fig. 21.10 Coronal (**Panel A**) and axial (**Panels B** and **C**) contrast-enhanced CT images in a 72-year-old man with increasing shortness of breath illustrating a sinus venosus defect, a third type of atrial septal defect involving the junction of the superior vena cava (*SVC*) with the right atrium (*RA*). Representing 10% of atrial septal defects, its name is derived from the abnormal fusion between the embryologic sinus venosus and the atrium. Instead of draining into the left atrium (*LA*), the right pulmonary veins (*RPV*) conjoin with the distal SVC into the RA (*asterisk* in **Panels A** and **B**). Additionally, at the same location there is direct communication between the left and right atrium through a short vein segment (*asterisk* in **Panel C**). The lower left pulmonary vein (*LPV*) is seen (**Panels B** and **C**) draining normally into the left atrium. The right heart is enlarged, secondary to a large left-to-right shunt in this case of anomalous pulmonary venous return. This sinus venosus defect was incidentally discovered on CT and surgically corrected. However, follow-up echocardiography in the immediate postoperative period still revealed a substantial shunt (not shown), without being able to determine its origin. A new CT, revealed on a curved multiplanar reformation (**Panel D**) a wrongly connected SVC to the LA with immediate filling of the left heart after intravenous contrast injection through a peripheral antecubital vein and no detectable connection to the RA.

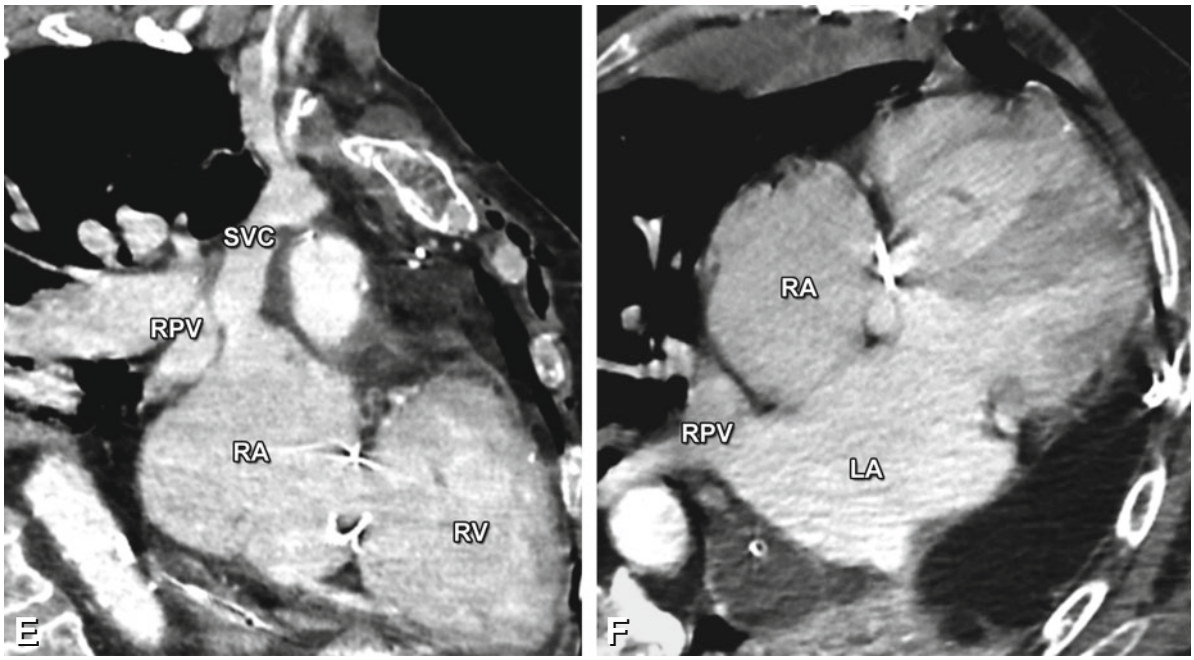

Fig. 21.10 (continued) This was confirmed during promptly performed surgical revision. A final CT examination shows, again on a curved multiplanar reformation (**Panel E**), a restored normal outflow of the SVC into the RA with exclusion of the RPV. The restored connection of the RPV, now communicating correctly with the LA, is further illustrated in **Panel F**. *IVC* inferior vena cava, *RV* right ventricle

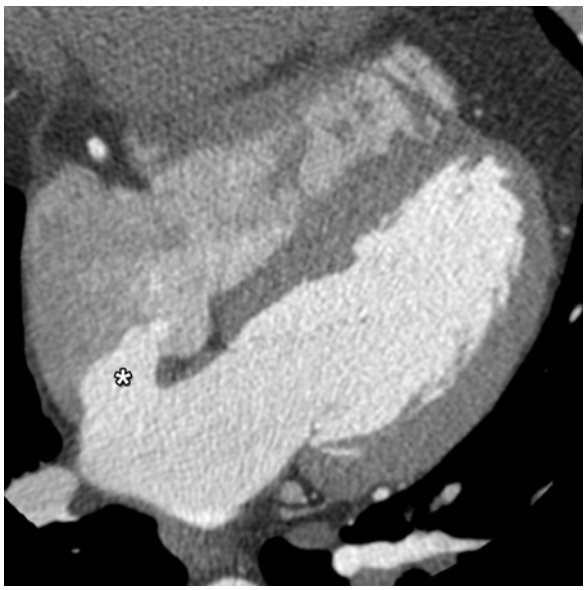

Fig. 21.11 A prominent atrial septal aneurysm (*asterisk*) is seen on a four-chamber view in a 54-year-old male patient. The atrial septal aneurysm bulges about 2 cm into the right atrial cavity. Small aneurysms are of no clinical significance, but thrombus formation in large aneurysms has been reported and is associated with an increased stroke risk. Nevertheless, atrial septal aneurysms pose no formal contraindication to a radiofrequency ablation procedure regardless of their size, as transseptal puncture of this aneurysm is easily achieved without a significantly increased complication risk.

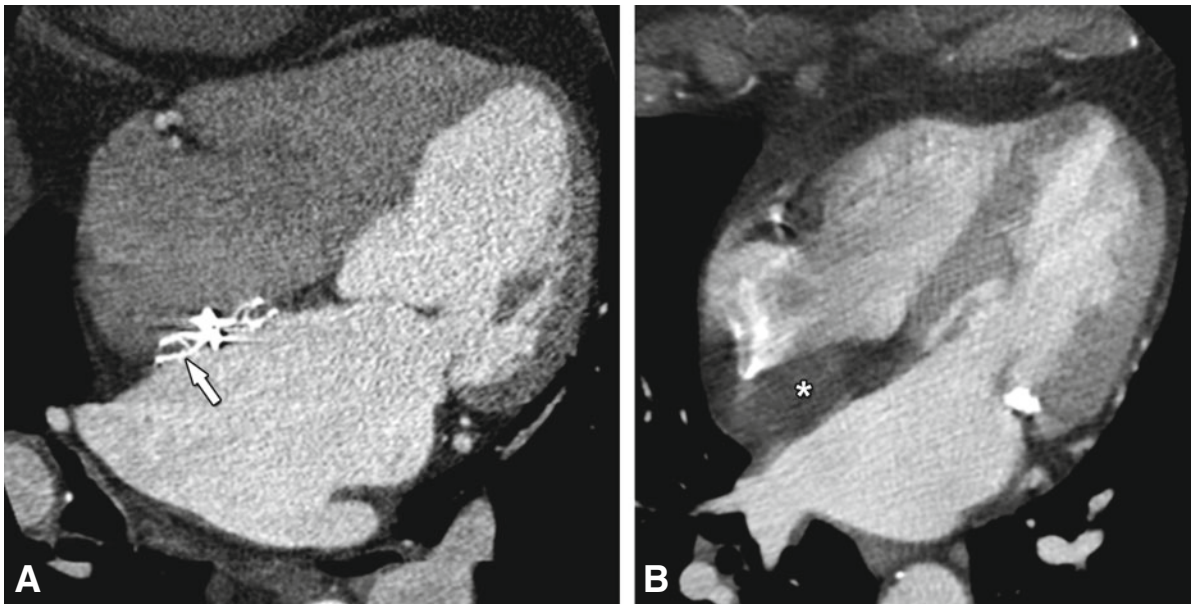

Fig. 21.12 Four-chamber contrast-enhanced CT images in two patients evaluated before radiofrequency ablation for paroxysmal atrial fibrillation. **Panel A** shows an Amplatzer septal closure device in a 57-year-old man after previous patent foramen ovale correction (*arrow* in **Panel A**). The second case illustrates a prominent lipomatous hypertrophic septum in a young woman (*asterisk* in **Panel B**), an entity frequently associated with atrial arrhythmias and atherosclerotic coronary artery disease. The presence of a septal closure device usually does not pose any procedural problems, as a radiofrequency ablation catheter can easily pass through this device without increased complication risk. In contrast, a lipomatous hypertrophic septum may preclude transseptal puncture. Since there are no universal guidelines, each case must be individually assessed. In this specific case (**Panel B**), an unsuccessful attempt at transseptal puncture was made

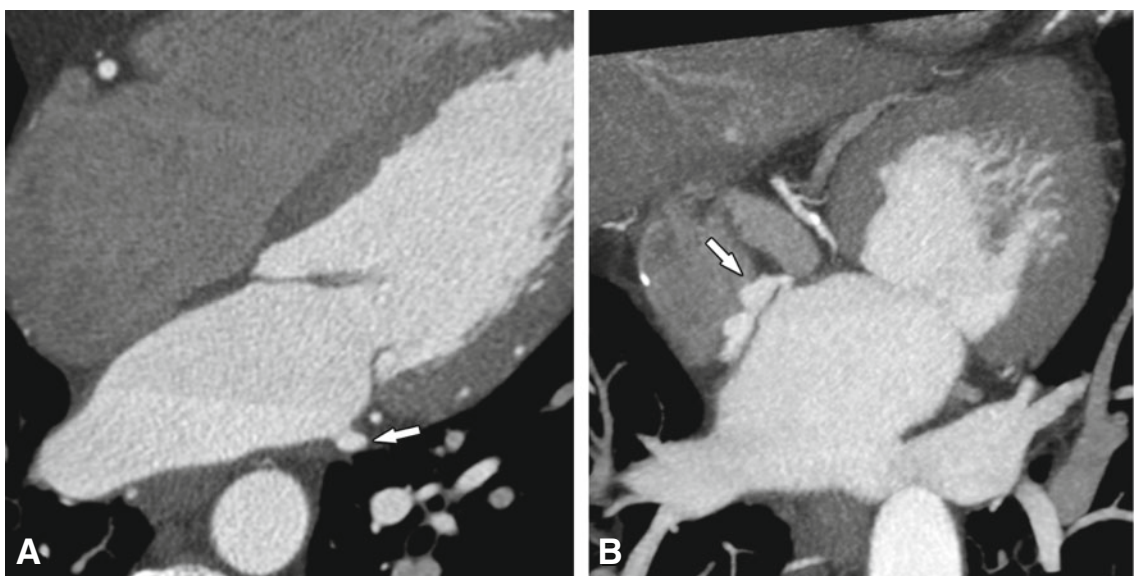

Fig. 21.13 Contrast-enhanced CT in four-chamber view (**Panel A**) and oblique maximum intensity projection (**Panel B**) in two different patients with atrial fibrillation referred for preprocedural anatomy evaluation. Atrial diverticula along the left (*arrow* in **Panel A**) and right atrial wall (*arrow* in **Panel B**) are seen. Small diverticula as in **Panel A** are of no clinical significance. However, thrombus formation in large diverticula, although rare, has been described. The presence and location of diverticula must be reported, as they constitute potential sites of catheter entrapment. Diverticula could give rise to thrombus formation or perforation, since their walls are much thinner than that of the adjacent normal atrium. In practice, atrial diverticula are commonly seen and generally do not cause significant problems during RF ablation procedures

Table 21.3 Rates of complications in radiofrequency ablation procedures of the pulmonary vein ostia

Complication	Rate (%)
Tamponade	1.31
Total femoral pseudoaneurysm	0.93
Transient ischemic attack	0.71
Arteriovenous fistula	0.54
Pulmonary vein stenosis requiring intervention	0.29
Stroke	0.23
Permanent diaphragmatic paralysis	0.17
Death	0.15
Pneumothorax	0.09
Valve damage requiring surgery	0.07
Atrioesophageal fistula	0.04
Hemothorax	0.02
Sepsis, abscesses or endocarditis	0.01
Total	**4.54**

Data from Cappato et al (2010) Updated worldwide survey on the methods, efficacy, and safety of catheter ablation for human atrial fibrillation. Circ Arrhythm Electrophysiol 3:32–38

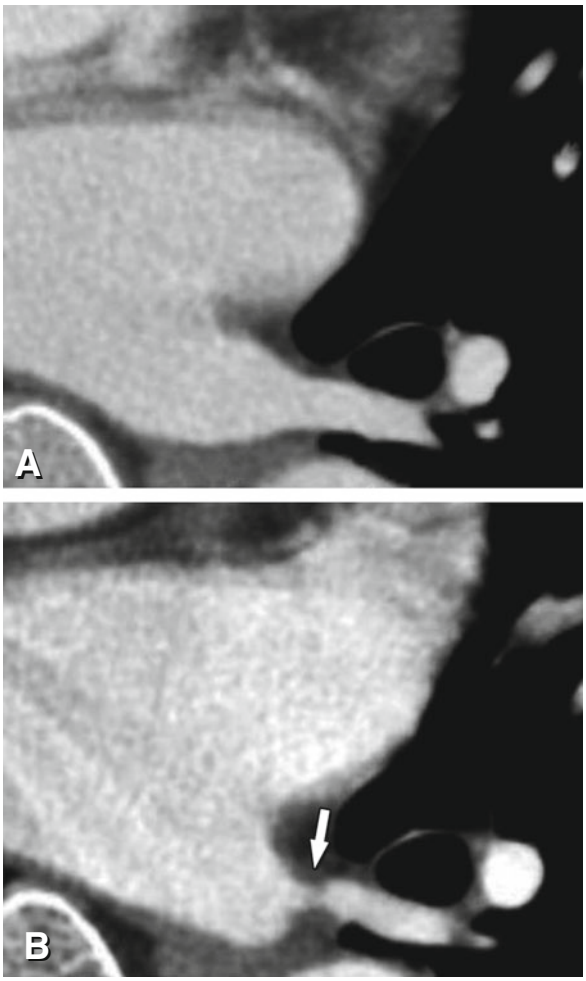

Fig. 21.14 Axial contrast-enhanced CT image in a middle-aged woman before (**Panel A**) and 3 months after radiofrequency ablation procedure for paroxysmal atrial fibrillation. The preprocedural CT examination (**Panel A**) showed a normal left lower pulmonary vein ostium. A repeat examination performed after radiofrequency ablation because the patient complained of progressive shortness of breath revealed a 50–70% stenosis at the ablation site (*arrow* in **Panel B**). Since only one vein acquired a stenosis, hemodynamic repercussions were less severe and could be stabilized with medication, with a subsequently improved clinical condition

21.2.5 Postprocedural Complications

EP-related interventions are generally considered safe in experienced hands, with a reported complication rate of about 4–5% for atrial fibrillation ablation procedures. Nevertheless, several complications can occur (Tables 21.2 and 21.3). We recommend to perform a routine follow-up study within 3–12 months to look for postprocedural complications, or when clinically indicated.

Stenosis of the pulmonary vein at the radiofrequency ablation site is one of the most common complications and is easily detected with CT. Early stenosis is caused by tissue swelling that may regress or progress over time to fibrosis and contraction of the venous wall. While a mild single pulmonary vein stenosis may go unrecognized (**Fig. 21.14**), multiple pulmonary vein stenoses are potentially life-threatening (**Fig. 21.15**). Close scrutiny of the CT images is necessary, since a stenosis can initially be absent or discrete, but evolve over time to a high-degree stenosis or even occlusion (**Fig. 21.16**). With further development of ablation catheters and techniques (including cryoablation) and increasing experience of interventional electrophysiologists, significant postablation stenosis of pulmonary veins has become a rare complication. Treatment remains, however, difficult and not well defined. Successful balloon dilatation

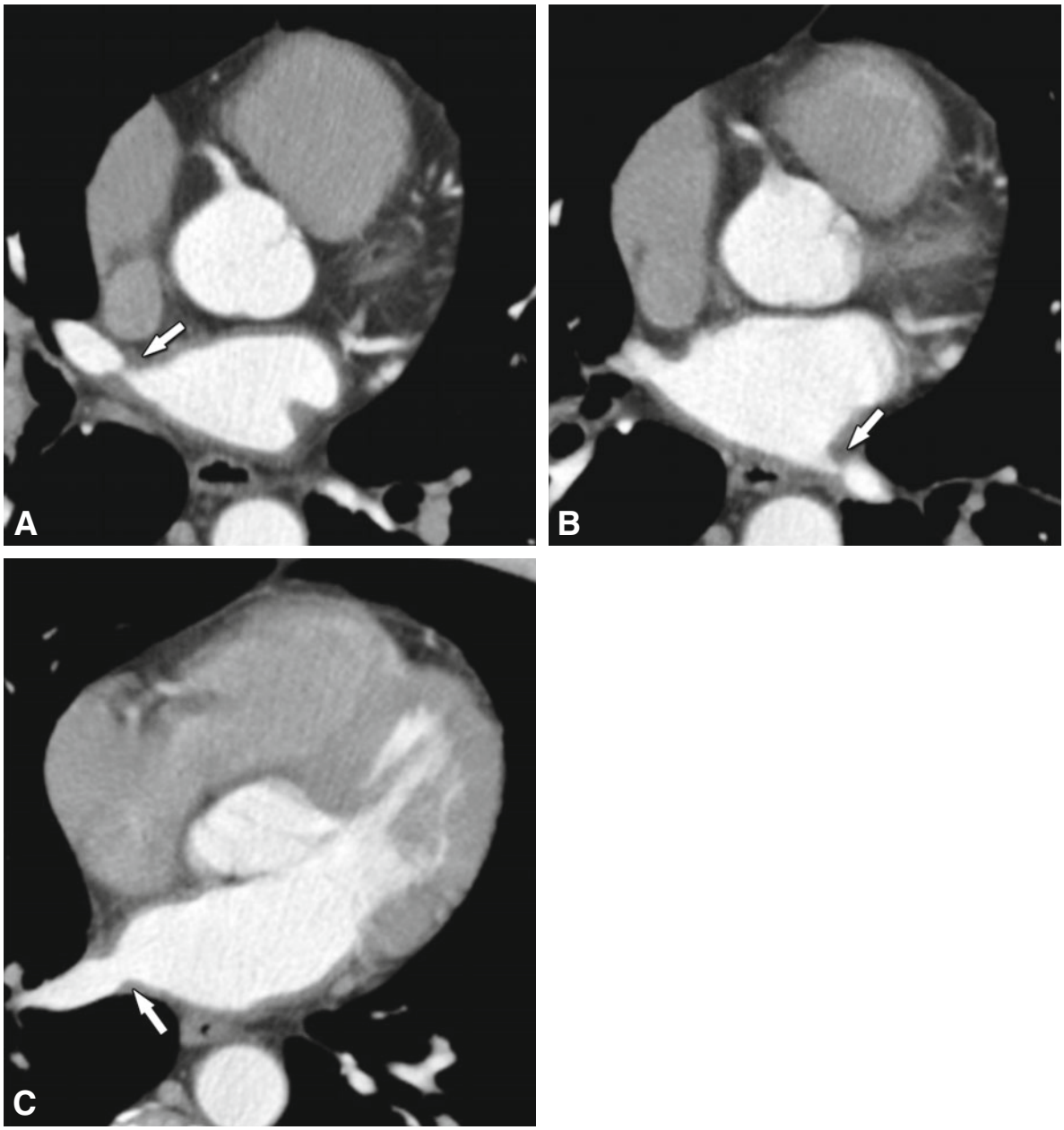

Fig. 21.15 Axial contrast-enhanced CT images in a middle-aged man presenting with increasing shortness of breath after radiofrequency ablation for atrial fibrillation. A total of three pulmonary vein stenoses are seen: two subocclusive stenoses in the upper right (*arrow* in **Panel A**) and lower left (*arrow* in **Panel B**) pulmonary vein and a more moderate stenosis in the lower right pulmonary vein (*arrow* in **Panel C**). While a moderate stenosis in a single pulmonary vein will often have little to no clinical significance, the hemodynamic repercussions increase with the number of affected veins and the degree of stenosis. In this patient, retro-obstructively increased venous pressure caused right heart enlargement and subsequent right heart failure. Direct treatment of pulmonary vein stenoses is very often disappointing or even impossible. In some cases, progressive deterioration of right heart function can eventually lead to heart transplantation as the only possible therapeutic intervention

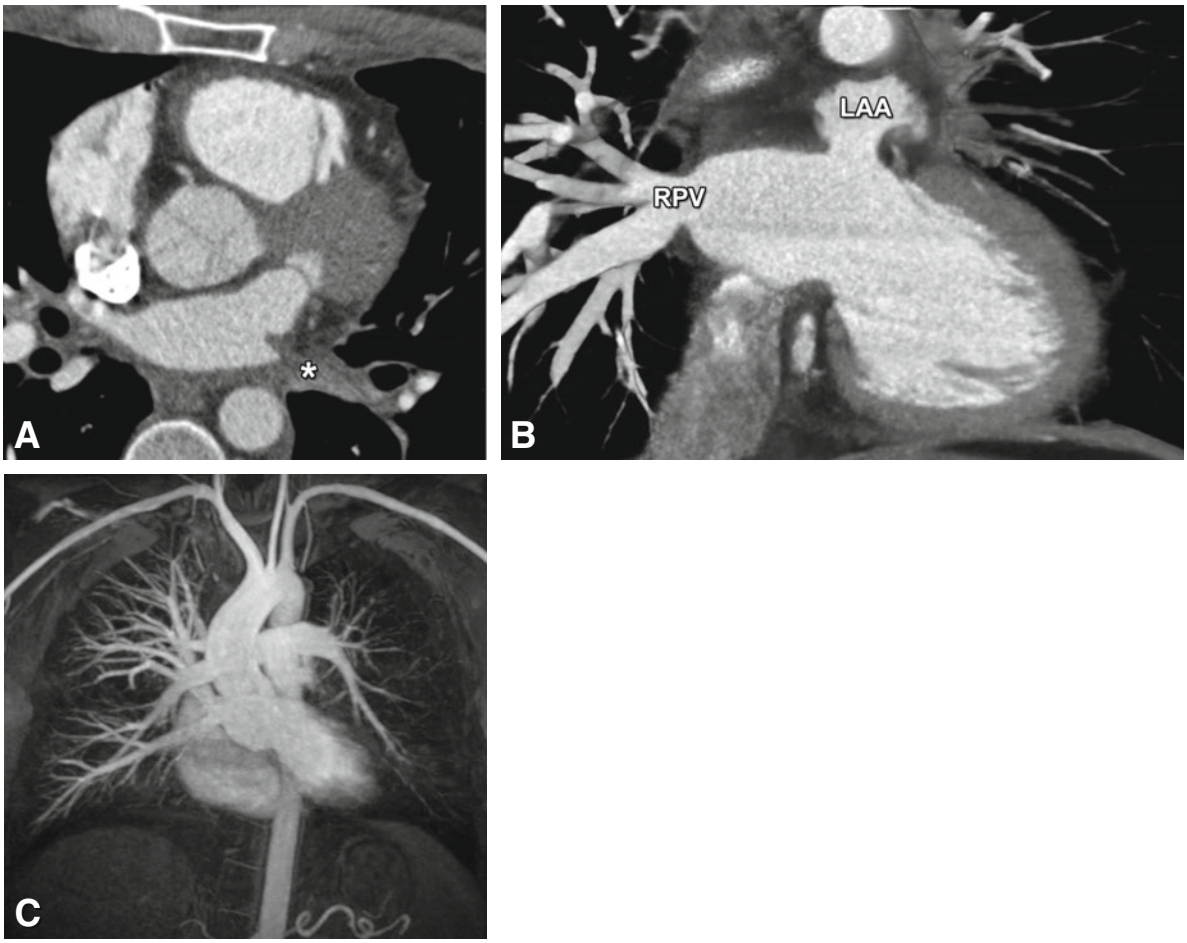

Fig. 21.16 Total occlusion of all left pulmonary veins in a 42-year-old man. Axial contrast-enhanced (**Panel A**) and slight oblique coronal thick-slab volume-rendered (**Panel B**) CT images with a coronal maximum intensity MR angiography image (**Panel C**) are shown. The combination of a presumably wrongly adjusted radiofrequency ablation device (using an unintended higher energy setting for ablation) and repeated ablation procedures in the course of less than 1 year resulted in total occlusion of the left pulmonary veins (*asterisk* in **Panel A**). Perivascular infiltration, probably representing old hemorrhage and fibrosis, is also noted (**Panel A**). The volume-rendered CT image (**Panel B**) and the coronal maximum intensity MR angiography (**Panel C**) examination further illustrate the striking absence of enhancement of the left-sided pulmonary veins and the peripheral tapering of the pulmonary arteries (**Panel C**), reflecting increased venous pressure. This left-sided venous occlusion resulted in a nonfunctioning left lung. A surgical intervention aimed at restoring left pulmonary vein flow was unsuccessful. Further follow-up showed progressive right heart functional deterioration, which eventually will probably lead to combined heart and lung transplantation (Images courtesy of Dr. D. Verdries and Dr. K Tanaka, UZ Brussels). *RPV* right pulmonary veins, *LAA* left atrial appendage

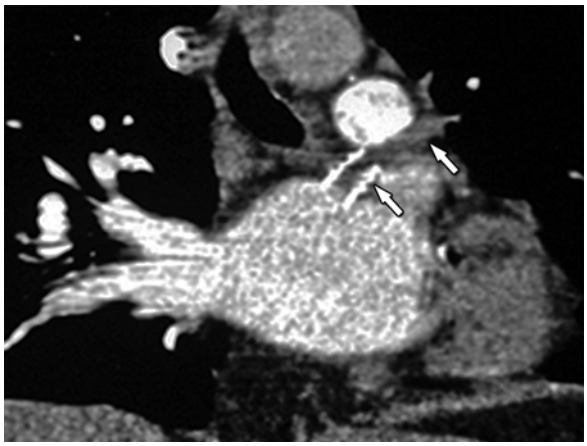

Fig. 21.17 A thrombosed stent at the atriovenous junction of the upper left pulmonary vein (*arrows*) is seen on a slightly oblique coronal reformation image in a middle-aged man. After radiofrequency ablation for paroxysmal atrial fibrillation, the patient developed a significant stenosis in the upper left pulmonary vein. While this was initially successfully corrected with a stent, complete stent thrombosis occurred after just a few weeks. Stent restenosis and thrombosis in a pulmonary vein is a disappointingly frequent finding, occurring in up to 50% of cases. New onset or rapid deterioration of clinical symptoms is the main indication for an intervention. While a mild stenosis may be closely followed with repeat CT examinations at 3–6 months, an approximately 90% stenosis must be treated promptly as it may progress to total occlusion in 3–6 weeks. There are diverse opinions about the need for routine stent implantation in pulmonary vein stenosis, with varying strategies between centers. During the intervention, the hemodynamic significance of a stenosis can be assessed by intracardiac ultrasound-derived transstenotic velocity (usually >1.0–1.6 m/s) and catheter-measured pressure gradient (10–12 mmHg for significant stenosis), with angiography further documenting the stenosis length and morphology. Some centers perform balloon dilation alone as initial treatment with close follow-up using CT. If restenosis occurs, then stent implantation is performed. It is important to realize that pulmonary veins which appear completely occluded on CT can still have a small patent lumen on subselective pulmonary angiography. This is an important difference, as a completely occluded vein markedly decreases the success rate of any intervention

and stent placement have been reported, with restenosis nevertheless occurring in up to 50% (**Fig. 21.17**).

21.2.6 Image Fusion in the EP Room

One of the main goals of preoperative CT in treatment of atrial fibrillation is the fusion of CT anatomy with electrophysiology data of the left atrium and atriopulmonary venous junctions. There have been significant advances in the use of fast anatomic mapping systems in the EP lab. With this technique a three-dimensional model is created with delineation of the left atrium and pulmonary vein ostia, acquired by the dragging of a mapping catheter over sites of interest in the endocardium and epicardium. This allows the sequential acquisition of points, with simultaneous recording of the location of the electrode tip and the local electrogram (electroanatomic mapping) (**Fig. 21.18**). However, since it is only a map with rather rough anatomic contour delineation, it provides no exact anatomic information on the left atrium and pulmonary veins. It is this anatomic information that is imported from the preprocedural CT scan and fused with the (electrical) map to obtain a final image containing both anatomical and electrophysiological information (**Fig. 21.18**)

21.3 Cardiac Resynchronization in Heart Failure

Heart failure is a progressive debilitating condition, with a rising incidence as the age of the general population increases. Its high morbidity and mortality rates are at least in part attributed to electrical conduction defects with delayed activation of the left ventricular free wall, leading to mechanical dyssynchrony and an increased risk of sudden death. In the last decade, several studies have demonstrated that, by stimulating both ventricles simultaneously through biventricular pacing (cardiac resynchronization), the adverse effects of dyssynchrony can be overcome, providing a further therapeutic option in addition to pharmacological treatment in patients with advanced and symptomatic heart failure. In this population, preoperative imaging of the cardiac venous anatomy plays an important role in the guidance of left ventricular lead placement.

21.3.1 Role of CT

The main goal of preoperative imaging is to identify suitable coronary veins for left ventricular lead placement and to provide assistance in defining the optimal position of the lead (**Table 21.4**). Catheter-based venography has been traditionally used for coronary venous imaging. Nevertheless, it can be technically challenging, provides projectional information of complex three-dimensional anatomy, and is associated with a small risk of important complications. Consequently, CT is increasingly used for noninvasive visualization of coronary venous anatomy.

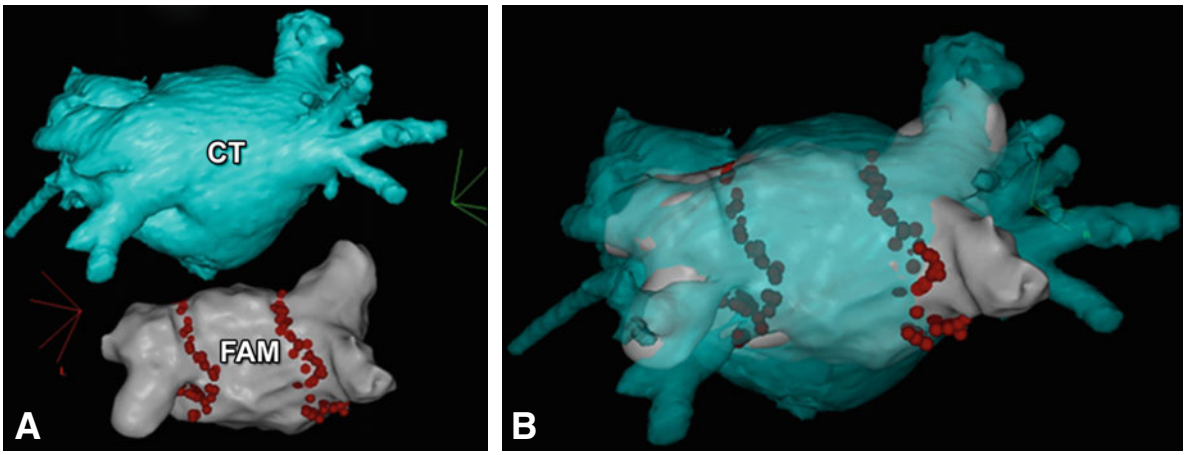

Fig. 21.18 Illustration of fusion between CT and electrophysiology data. At the start of the electrophysiology procedure, a three-dimensional image of the left atrium and atriopulmonary venous junctions is generated through interpolation of several contact points between the catheter electrode and the left atrial wall, a technique called fast anatomical mapping (*FAM*, **Panel A**). The resulting image nevertheless lacks the anatomic detail provided by CT (**Panel A**). Therefore, the combination of both image sources enables a more complete evaluation of the target anatomy (**Panel B**). While this approach is used in many centers, others argue that the time difference between the two image acquisitions can potentially lead to registration errors and mismatching of the anatomic features due to e.g., small interval changes in heart size and fluid status. Consequently, some centers acquire the required three-dimensional image information at the time of the actual intervention using rotational angiography or three-dimensional transesophageal echocardiography

Table 21.4 Purpose of CT in patients prior to resynchronization procedures in heart failure

Target structure	What to consider
Identification of the main coronary veins	Identify the coronary sinus, great cardiac vein, posterolateral vein and the left marginal vein
Presence of important anatomy variations	High insertion of the coronary sinus Hypoplasia, absence or duplication of veins Venous diverticulum
Vein size & other measurements	Size of the coronary sinus for balloon occlusion Distance of target vein from the Thebesian valve Tortuosity and acute angle of target vein confluence Size of first- or large second order tributaries of the coronary sinus for lead implant (minimum 1.5 mm necessary)
Other anatomic barriers & ancillary findings	Anatomic variants of systemic veins Fistulae Any other findings which may limit or inhibit procedural execution

21.3.2 Scan Protocol

The scan technique for coronary venous anatomy is roughly similar to routine coronary CT angiography. A key difference is, however, a longer contrast bolus (an average of 10 s longer than for CT coronary angiography) using a slower injection speed (we typically use 3.5 ml/s). Furthermore, an additional scan delay of 10–15 s after reaching the traditional 180 Hounsfield units in the descending aorta for coronary CT angiography (Chap. 8) is added for better venous opacification.

ECG gating is traditionally advocated for optimal image quality; however, with the short acquisition time of modern CT equipment, good image quality of the venous coronary anatomy can often be obtained with non-gated scans. In practice, we specifically prefer non-gated scans in patients with an irregular heart rhythm to avoid additional artifacts.

21.3.3 Postprocessing

Contrary to imaging of the left atrium and pulmonary veins, no specific three-dimensional postprocessing is required. However, we often generate volume-rendered images of the venous anatomy for better three-dimensional visualization.

21.3.4 Preprocedural Clinically Relevant Anatomy

The coronary venous system is more complex than its arterial counterpart, with frequent variation in the presence, location and size of several vessels. As landmarks for anatomic orientation, we propose to first identify the great cardiac vein, the longest and anatomically most consistent vessel, located in the left atrioventricular groove (**Fig 21.19**). It is often in close proximity to the left circumflex artery, with a superficial position to the arteries in 60–70% of cases. It almost always drains into the coronary sinus, an import anatomic landmark often used as a gateway for device lead placement (**Fig. 21.20**).

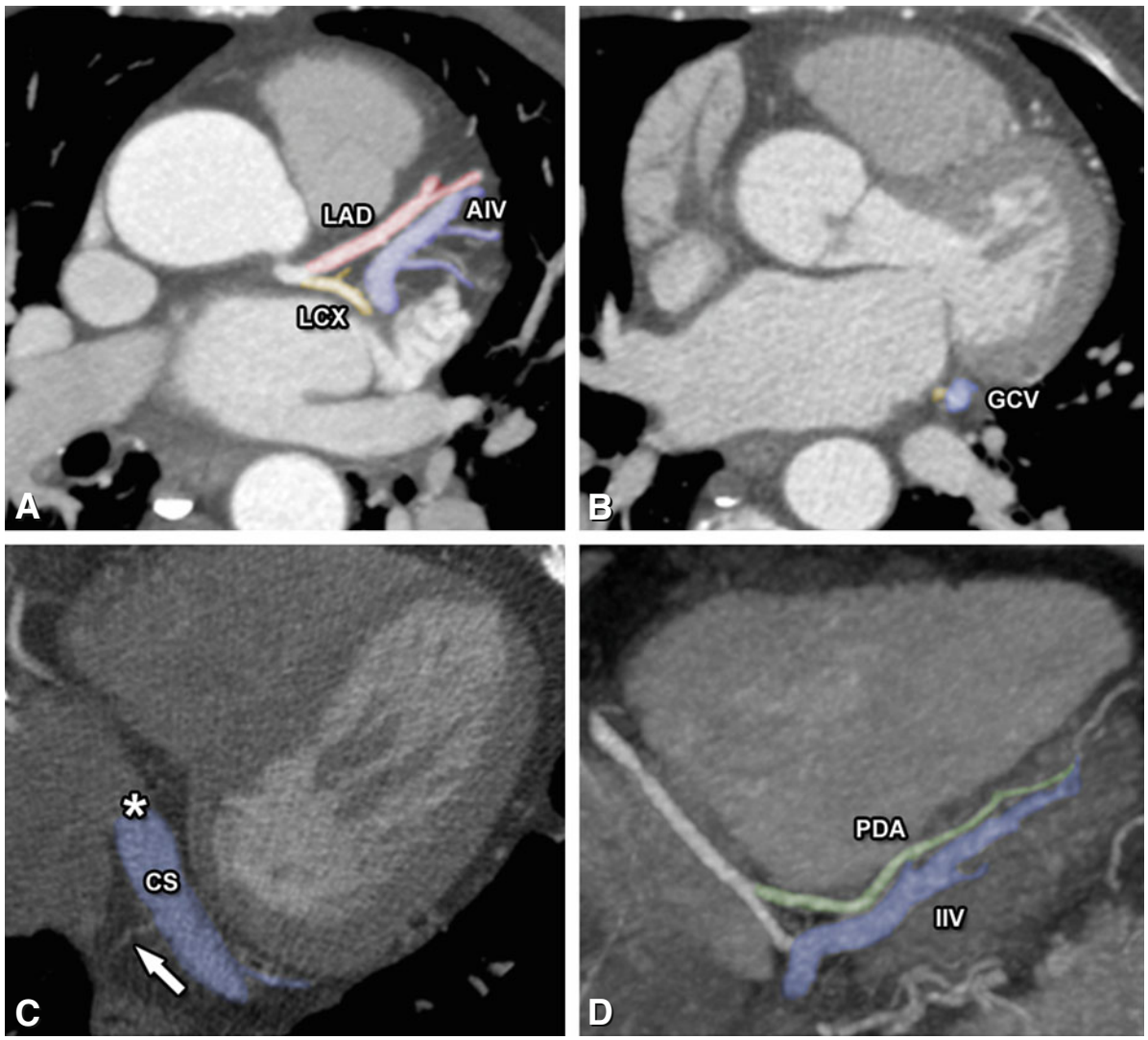

Fig. 21.19 Coronary venous anatomy. The anterior interventricular vein (*AIV*, *blue* in **Panel A**) runs in the anterior interventricular groove, partially parallel with the left anterior descending artery (*LAD*, *red* in **Panel A**). It then enters the left atrioventricular groove, where it is defined as the great cardiac vein (*GCV*, *blue* in **Panel B**). Note the superficial location of the great cardiac vein to the left circumflex artery (*LCX*, *yellow* in **Panels A** and **B**). The GCV drains into the coronary sinus (*CS*, *blue* in **Panel C**), as does the inferior interventricular vein (*IIV*, *blue* in **Panel D**), which is also called the middle cardiac vein. The boundaries of the coronary sinus are formed by the Thebesian valve (*asterisk* in **Panel C**) and the obtuse vein of Marshall (*arrow* in **Panel C**). This small vein has an average diameter of 1 mm, and it is only visible in 40% of CT angiography studies. Note the parallel course of the inferior interventricular vein with the posterior descending artery (*PDA*, *green* in **Panel D**).

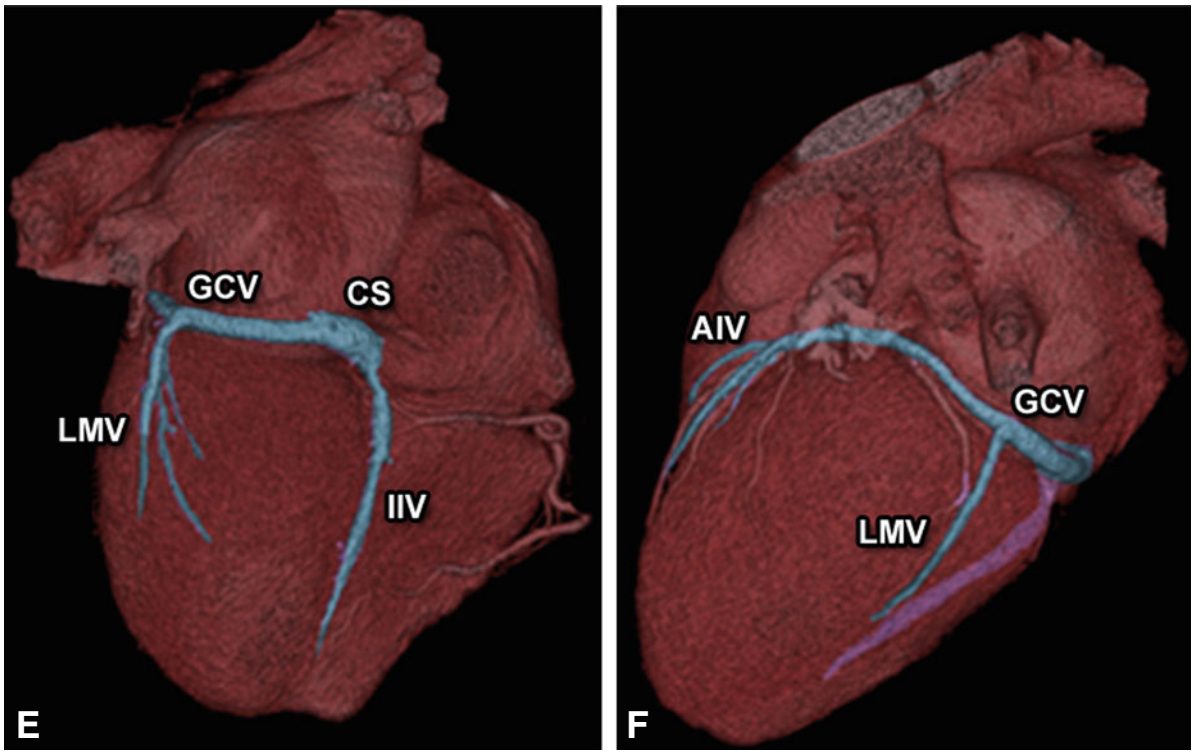

Fig. 21.19 (continued) **Panels E** and **F** further demonstrate the three-dimensional coronary venous anatomy with a large left marginal vein (LMV, **Panels E** and **F**). This vessel can be identified in 70–95% of cases, mostly draining into the great cardiac vein. Along with the posterolateral vein (also seen in **Fig. 21.21**), it is a frequent target for lead placement

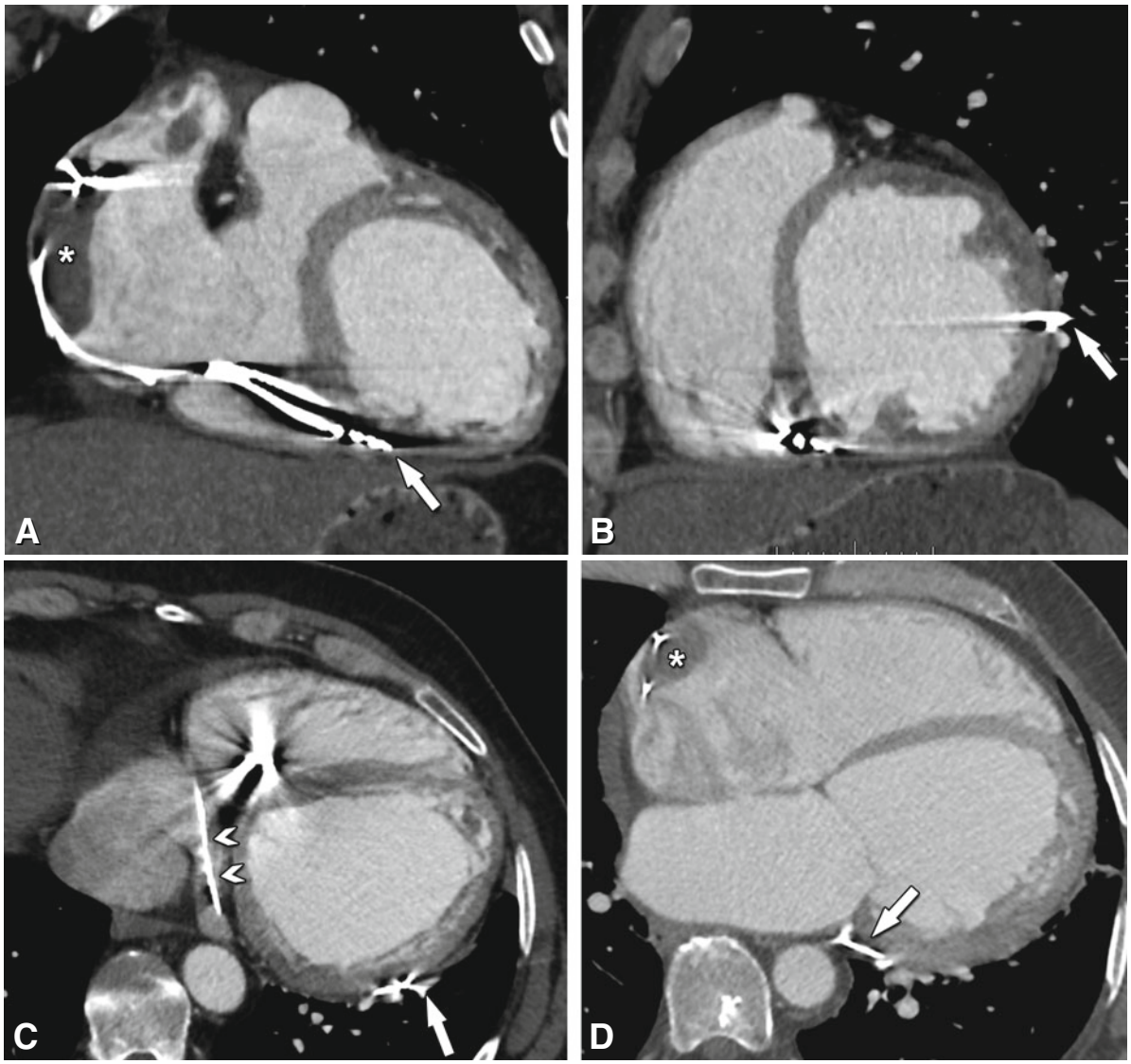

Fig. 21.20 Biventricular device lead placement for cardiac resynchronization therapy in a 33-year-old man with dilated cardiomyopathy. Oblique coronal (**Panel A**), short-axis (**Panel B**), axial (**Panel C**), and four-chamber (**Panel D**) contrast-enhanced CT images are shown. Correct positioning of the leads in the apex of the right ventricle (*arrow* in **Panel A**) and in the left marginal vein (*arrow* in **Panels B–D**) is illustrated. Note the passage of the left ventricular lead through the coronary sinus (*arrowheads* in **Panel C**). In this patient, several intracardiac thrombi were identified along the right ventricular lead (*asterisk* in **Panels A** and **D**), probably due to suboptimal anticoagulative therapy

Veins draining the posterior and lateral wall (left posterior, posterolateral, and marginal veins) must be specifically examined, as they are often used for lead insertion from resynchronization devices. A small diameter (<2 mm) or acute angulation of these veins with the coronary sinus may complicate or preclude safe lead positioning (**Fig. 21.21**). Other anatomic barriers detectable with CT include anatomic variants such as an unroofed coronary sinus (**Fig. 21.22**) or rare arteriovenous fistulae (**Fig. 21.23**). Finally, caution must be taken to avoid placing the lead over infarcted myocardium, as this can significantly limit pacing efficiency.

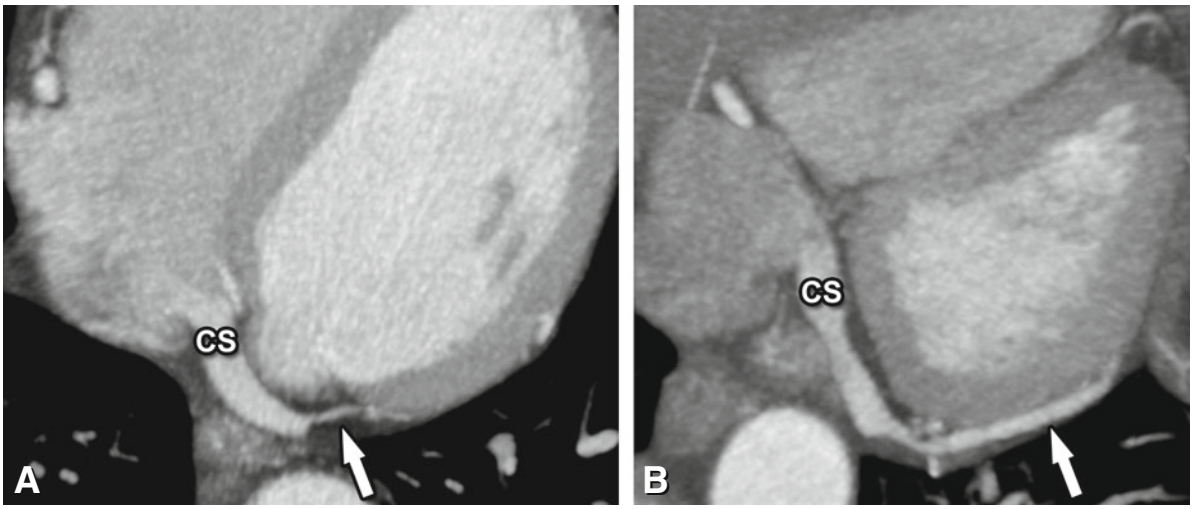

Fig. 21.21 Axial contrast-enhanced CT images in two patients referred for venous anatomy evaluation before cardiac resynchronization therapy left ventricular lead implantation. Variations in size of the posterolateral venous branch, with a small (*arrow* in **Panel A**) and a large vein (*arrow* in **Panel B**) are demonstrated. The latter will be a more suitable vein for lead placement than the first small vein. Veins with a diameter smaller than 2 mm are in general not considered suitable for lead implantation. *CS* coronary sinus

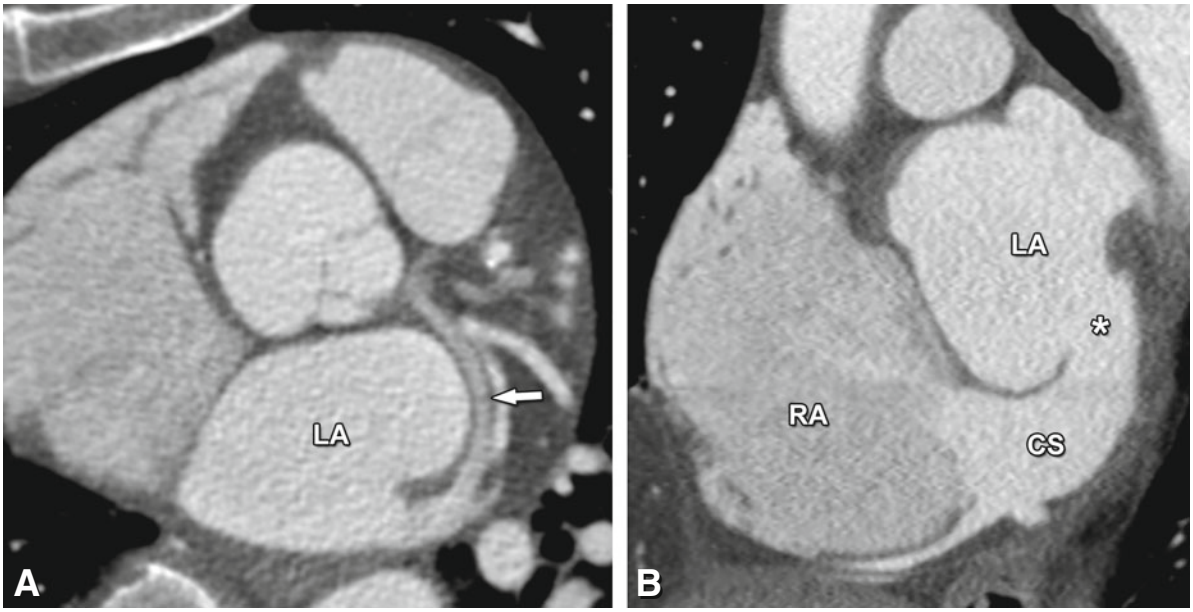

Fig. 21.22 A 43-year-old man with an incidentally discovered unroofed coronary sinus during CT. Contrast-enhanced axial (**Panel A**) and coronal (**Panel B**) CT images are shown. An unroofed coronary sinus is a rare congenital cardiac anomaly in which there is partial (either focal or fenestrated) or complete absence of the roof of the coronary sinus, resulting in a large shunt between the left atrium (*LA*) and the coronary sinus (*CS*). In this case, the great cardiac vein drains directly into the LA (*arrow* in **Panel A**) and there is a large communication between the LA and the CS (*asterisk* in **Panel B**). Surgical correction of this defect was performed, with concomitant perioperative ablation of the pulmonary vein ostia

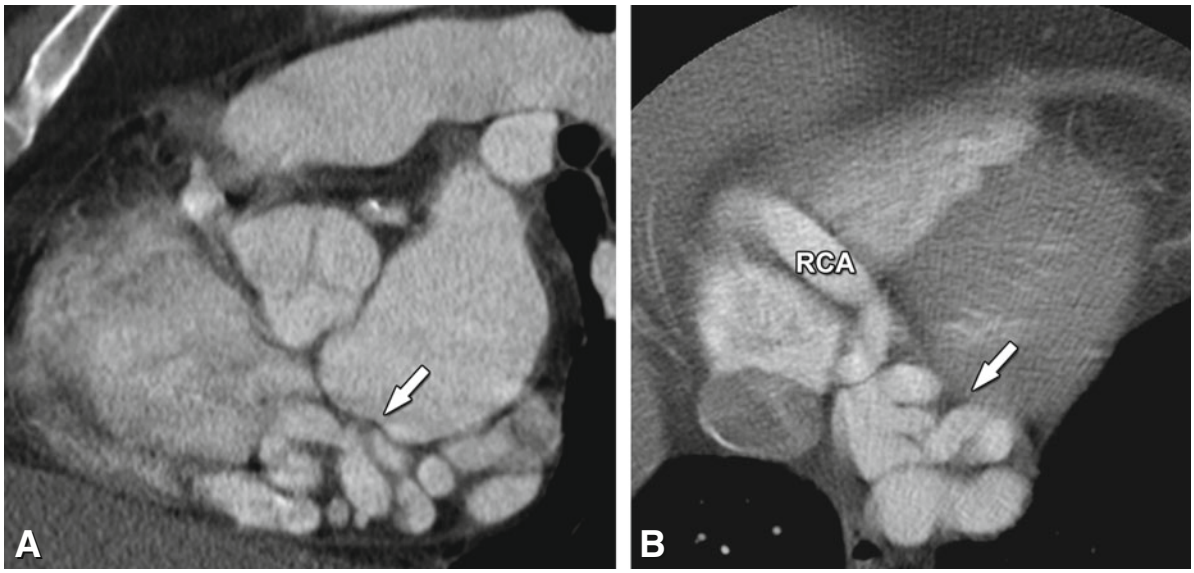

Fig. 21.23 A 54-year-old man with a rare arteriovenous fistula discovered during CT evaluation of the coronary veins. Contrast-enhanced sagittal (**Panel A**) and axial (**Panel B**) CT images are shown. A rare arteriovenous fistula is seen between a dilated right coronary artery (*RCA*, **Panel B**) and enlarged tortuous vessels in the atrioventricular groove (*arrow* in **Panels A** and **B**). The presence of this shunt precluded passage of a left ventricular lead through the coronary sinus. Representing a large shunt between the arterial and venous coronary anatomy, this defect was subsequently surgically corrected

21.3.5 Postprocedural Complications

Despite the increasing number of device implants worldwide and extensive data on the beneficial effect of these devices, little is known about the early and late complications of cardiac resynchronization therapy. Initial reports show pneumothorax, coronary vein dissection and perforation to be the most common complications during the implantation. Implantation of the left ventricular lead seems to be associated with the most complications. Complications on follow-up mostly include infection, hematoma, and lead dislodgement. Currently, it is unknown to which extent CT can be routinely used for the evaluation of these complications. Furthermore, proper visualization of the exact position of the tip of the device leads is sometimes disappointing, as beam-hardening artifacts significantly limit image quality. Therefore, it must be decided on a case-by-case basis whether CT should be used (**Fig. 21.24**).

21.4 Outlook

21.4.1 CT Prior to Atrial Fibrillation Ablation

The continuous development and rising success of EP procedures for atrial fibrillation has stimulated the interdisciplinary communication between cardiologists and radiologists in both preprocedural planning and follow-up of short- and long-term complications. It therefore remains essential for radiologists to know the most common procedures, while cardiologists should have an understanding of the benefits and technical limitations of the used imaging tools.

As CT technology evolves, we can expect to deliver better and more consistent image quality in patients with irregular heart rhythms such as atrial fibrillation as temporal resolution of CT scanners improves. Furthermore, significant advances have been made to achieve this quality with an increasingly low radiation exposure.

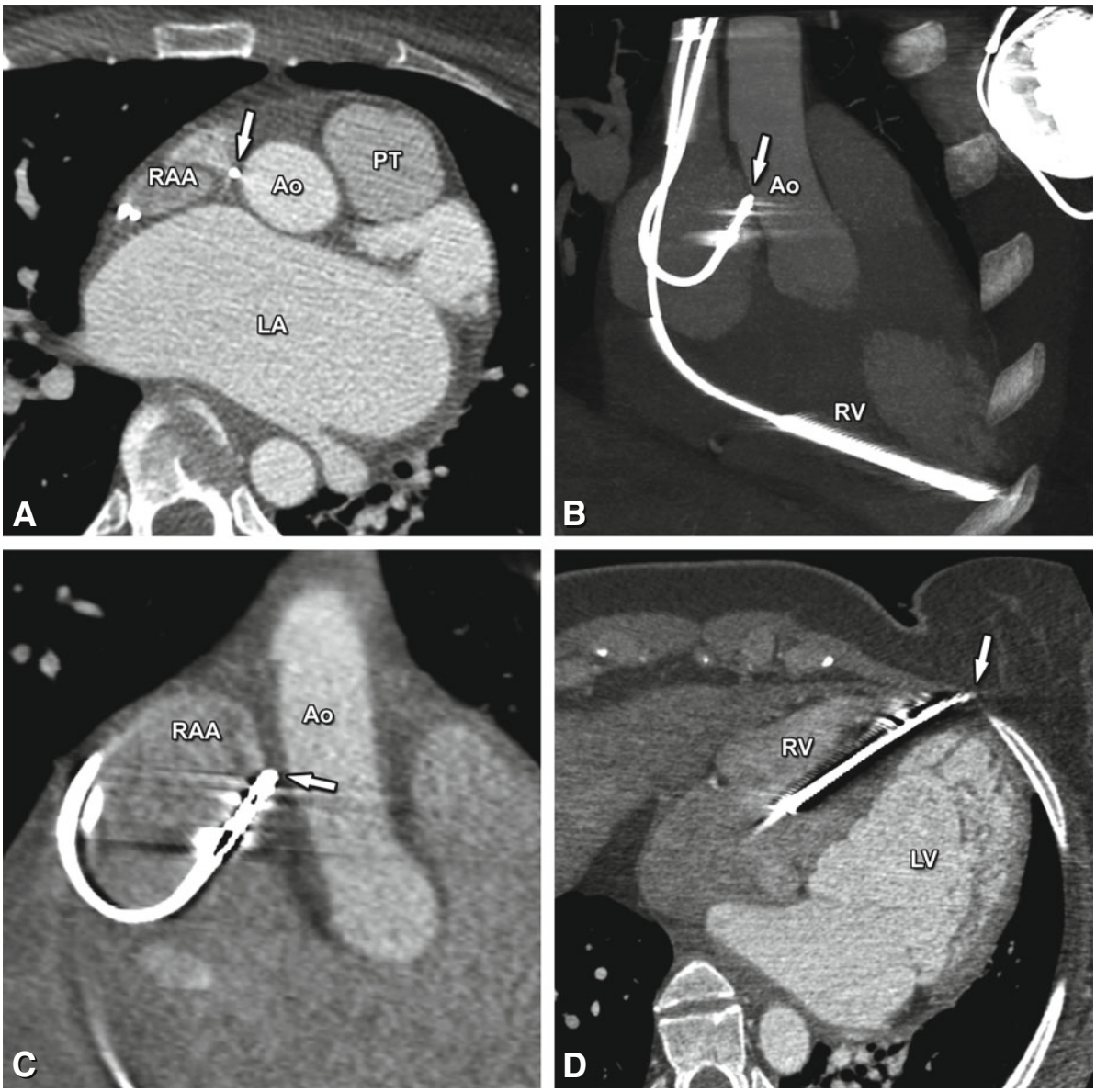

Fig. 21.24 Contrast-enhanced CT of a 34-year-old woman with a dilated non-compaction cardiomyopathy presenting with retrosternal pain after defibrillator implantation. CT was performed to assess the position of the tip of the right atrial lead, as perforation was suspected but could not be conclusively confirmed on echocardiography. An axial CT image (**Panel A**) shows the tip of the right atrial lead (*arrow* in **Panel A**) to be between the right atrial appendage (*RAA*) and the ascending aorta (*Ao*). This is further illustrated on the oblique coronal maximum intensity projection image (*arrow* in **Panel B**) and oblique coronal multiplanar reformatted image (*arrow* in **Panel C**). This is a rare example of correct visualization of the tip of a device lead with CT. The perforated right atrial lead was left in place, as the patient clinically improved with conservative treatment and defibrillator function was not compromised. In general, assessment of correct lead tip positioning is not feasible with CT, as image quality can be severely degraded by beam-hardening artifacts. This is illustrated in **Panel D**, where the tip of the right ventricular lead falsely appears to be located outside the ventricular wall in this completely asymptomatic patient (*arrow* in **Panel D**) because the ventricular wall contour is obscured by artifacts. CT is therefore not generally recommended to assess possible lead perforation, and the decision to use it must be made on a case-by-case basis. *LA* left atrium, *LV* left ventricle

Regarding the fusion of CT and EP data, some authors have pointed out the drawbacks of acquiring the CT and EP anatomic mapping data at different times. These different acquisition times may induce registration errors due to small interval changes in heart size secondary to differences in rhythm, heart rate, myocardial contractility, or fluid status. Therefore, some centers have already reported successful integration of EP data with other imaging methods such as three-dimensional transesophageal echocardiography or rotational angiography, which can be acquired during the ablation procedure for better anatomic consistency.

21.4.2 CT Prior to Cardiac Resynchronization Therapy

At present, CT of the coronary veins remains an often underutilized technique, constituting only a small portion of referrals compared with CT of the coronary arteries. Nevertheless, we can expect that radiologists will increasingly be consulted for preprocedural CT evaluation of the coronary venous anatomy in patients with severe heart failure as resynchronization technology evolves. Knowledge of venous anatomy is critical, as this is less known to many radiologists. Furthermore, CT of the coronary veins will continue to improve, benefiting from advances in CT of the coronary arteries.

Failure rates for left ventricular lead implantation have been reported to be up to 12%. Procedural success is further improved by advances in fusion techniques, during which CT images of the coronary sinus anatomy are overlaid with real-time fluoroscopy images for better guidance and successful lead implantation. Improved outcome of this procedure is likely to further increase the need for preprocedural CT.

Recommended Reading

Abbara S, Cury RC, Nieman K et al (2005) Noninvasive evaluation of cardiac veins with 16-MDCT angiography. AJR Am J Roentgenol 185:1001–1006

Cappato R, Calkins H, Chen SA et al (2010) Updated worldwide survey on the methods, efficacy, and safety of catheter ablation for human atrial fibrillation. Circ Arrhythm Electrophysiol 3:32–38

Douglas PS, Garcia MJ, Haines DE et al (2011) ACCF/ASE/AHA/ASNC/HFSA/HRS/SCAI/SCCM/SCCT/SCMR 2011 Appropriate Use Criteria for Echocardiography. A Report of the American College of Cardiology Foundation Appropriate Use Criteria Task Force, American Society of Echocardiography, American Heart Association, American Society of Nuclear Cardiology, Heart Failure Society of America, Heart Rhythm Society, Society for Cardiovascular Angiography and Interventions, Society of Critical Care Medicine, Society of Cardiovascular Computed Tomography, and Society for Cardiovascular Magnetic Resonance Endorsed by the American College of Chest Physicians. J Am Coll Cardiol 57:1126–1166

Feuchtner GM, Dichtl W, DeFrance T et al (2008) Fusion of multislice computed tomography and electroanatomical mapping data for 3D navigation of left and right atrial catheter ablation. Eur J Radiol 68:456–464

Fink C, Krissak R, Henzler T et al (2011) Radiation dose at coronary CT angiography: second-generation dual-source CT versus single-source 64-MDCT and first-generation dual-source CT. AJR Am J Roentgenol 196:W550–W557

Fuster V, Ryden LE, Cannom DS et al (2011) 2011 ACCF/AHA/HRS focused updates incorporated into the ACC/AHA/ESC 2006 guidelines for the management of patients with atrial fibrillation: a report of the American College of Cardiology Foundation/American Heart Association Task Force on practice guidelines. Circulation 123:e269–e367

Ghaye B, Szapiro D, Dacher JN et al (2003) Percutaneous ablation for atrial fibrillation: the role of cross-sectional imaging. Radiographics 23:S19–S33

Go AS, Hylek EM, Phillips KA et al (2001) Prevalence of diagnosed atrial fibrillation in adults: national implications for rhythm management and stroke prevention: the AnTicoagulation and Risk Factors in Atrial Fibrillation (ATRIA) Study. JAMA 285:2370–2375

Haissaguerre M, Jais P, Shah DC et al (1998) Spontaneous initiation of atrial fibrillation by ectopic beats originating in the pulmonary veins. N Engl J Med 339:659–666

Hamdan A, Charalampos K, Roettgen R (2009) Magnetic resonance imaging versus computed tomography for characterization of pulmonary vein morphology before radiofrequency catheter ablation of atrial fibrillation. Am J Cardiol 104:1540–1546

Handke M, Harloff A, Olschewski M et al (2007) Patent foramen ovale and cryptogenic stroke in older patients. N Engl J Med 357:2262–2268

Hindricks G (1993) The Multicentre European Radiofrequency Survey (MERFS): complications of radiofrequency catheter ablation of arrhythmias. The Multicentre European Radiofrequency Survey (MERFS) investigators of the Working Group on Arrhythmias of the European Society of Cardiology. Eur Heart J 14:1644–1653

Holmes D, Monahan K, Packer D (2009) Pulmonary vein stenosis complicating ablation for atrial fibrillation: clinical spectrum and interventional considerations. JACC Cardiovasc Interv 2:267–276

Hur J, Kim YJ, Lee HJ et al (2011) Dual-enhanced cardiac CT for detection of left atrial appendage thrombus in patients with stroke: a prospective comparison study with transesophageal echocardiography. Stroke 42:2471–2477

Johri AM, Rojas CA, El-Sherief A et al (2011) Imaging of atrial septal defects: echocardiography and CT correlation. Heart 97:1441–1453

Kistler PM, Rajappan K, Jahngir M et al (2006) The impact of CT image integration into an electroanatomic mapping system on clinical outcomes of catheter ablation of atrial fibrillation. J Cardiovasc Electrophysiol 17:1093–1101

Lacomis JM, Wigginton W, Fuhrman C et al (2003) Multi-detector row CT of the left atrium and pulmonary veins before radio-frequency catheter ablation for atrial fibrillation. Radiographics 23:S35–S48

Leipsic J, Labounty TM, Heilbron B et al (2010) Estimated radiation dose reduction using adaptive statistical iterative reconstruction in

coronary CT angiography: the ERASIR study. AJR Am J Roentgenol 195:655–660

Levy S, Camm AJ, Saksena S et al (2003) International consensus on nomenclature and classification of atrial fibrillation: a collaborative project of the Working Group on Arrhythmias and the Working Group of Cardiac Pacing of the European Society of Cardiology and the North American Society of Pacing and Electrophysiology. J Cardiovasc Electrophysiol 14:443–445

Mansour M, Holmvang G, Ruskin J (2004) Role of imaging techniques in preparation for catheter ablation of atrial fibrillation. J Cardiovasc Electrophysiol 15:1107–1108

Nielsen J, Johannessen A, Raatikainen P et al (2012) Radiofrequency ablation as initial therapy in paroxysmal atrial fibrillation. N Engl J Med 367:1587–1595

Packer DL, Keelan P, Munger TM et al (2005) Clinical presentation, investigation, and management of pulmonary vein stenosis complicating ablation for atrial fibrillation. Circulation 111:546–554

Saremi F, Channual S, Raney A (2008) Imaging of patent foramen ovale with 64-section multidetector CT. Radiology 249:483–492

Saremi F, Muresian H, Sánchez-Quintana D (2012) Coronary veins: comprehensive CT-anatomic classification and review of variants and clinical implications. Radiographics 32:E1–E32

Shah SS, Teague SD, LU JC et al (2012) Imaging of the coronary sinus: normal anatomy and congenital abnormalities. Radiographics 32:991–1008

Singh JP, Houser S, Heist EK et al (2005) The coronary venous anatomy: a segmental approach to aid cardiac resynchronization therapy. J Am Coll Cardiol 46:68–74

Stahlberg M, Lund LH, Zabarovskaja S et al (2012) Cardiac resynchronization therapy: a breakthrough in heart failure management. J Intern Med 272:330–343

Thai WE, Wai B, Truong QA (2012) Preprocedural imaging for patients with atrial fibrillation and heart failure. Curr Cardiol Rep 14:584–592

Van Rees JB, De Bie MK, Thijssen J et al (2011) Implantation-related complications of implantable cardioverter-defibrillators and cardiac resynchronization therapy devices: a systematic review of randomized clinical trials. J Am Coll Cardiol 58:995–1000

Wagner M, Butler C, Rief M et al (2010) Comparison of non-gated vs. electrocardiogram-gated 64-detector-row computed tomography for integrated electroanatomic mapping in patients undergoing pulmonary vein isolation. Europace 12:1090–1097

Whitlock R, Healey J, Connolly S (2009) Left atrial appendage occlusion does not eliminate the need for warfarin. Circulation 120: 1927–1932

Yokokawa M, Olgun H, Sundaram B et al (2012) Impact of preprocedural imaging on outcomes of catheter ablation in patients with atrial fibrillation. J Interv Card Electrophysiol 34:255–262

Coronary Artery Anomalies

P.G.C. Begemann, M. Grigoryev, G. Lund, G. Adam, and M. Dewey

Abstract

This chapter gives an overview of coronary anomalies and their development, the course of anomalous coronary arteries, and their classification and clinical importance.

22.1 Embryonic Development

The development of the coronary arteries is a self-organizing process in the subepicardial space, resulting in the formation of a vascular plexus, which connects to the aorta in later stages. This process comprises three major developmental steps: vasculogenesis, angiogenesis, and embryonic arteriogenesis (**Fig. 22.1**).

In the initial stage of embryonic development of the heart, the endocardium and myocardium are being nourished by the blood flowing through the lumen of the heart tube. By the beginning of the third week, as the walls of the developing heart become thicker, diffusion is no longer sufficient to supply the heart tube. At this stage endothelial precursor cells migrate into the myocardium and commence forming the primordial vascular structures (vasculogenesis). The initial channels formed within the epicardial covering are scattered throughout the myocardium, inducing an epicardial-to-endocardial vascular gradient, regulated among others by ventricular epicardial growth factor.

Similar to the first stage, the second stage of development – angiogenesis – also appears to be regulated by hypoxia. There is still no continuity between the separate vascular structures and there is no circulation of systemic blood within them. Later, the vessels coalesce to form the primary vascular plexus. The complex network of the subepicardial primary plexus expands along the dorsal and ventral interventricular sulcus, the atrioventricular sulcus, and then along the base of the truncus arteriosus throughout the myocardium. The vessels sprouting from the primary plexus form new septa and pillars within the vascular lumen, giving rise to the peritruncal ring of capillaries.

Only at the late stages of development will the vascular network gain access to the aortic root (arteriogenesis, **Fig. 22.2**). The vessels from the peritruncal ring sprout preferentially into the aorta, establishing multiple connections to the left and right aortic sinuses and much fewer to the posterior (noncoronary) aortic sinus. The hemodynamic

M. Dewey, *Cardiac CT*,
DOI 10.1007/978-3-642-41883-9_25, © Springer-Verlag Berlin Heidelberg 2014

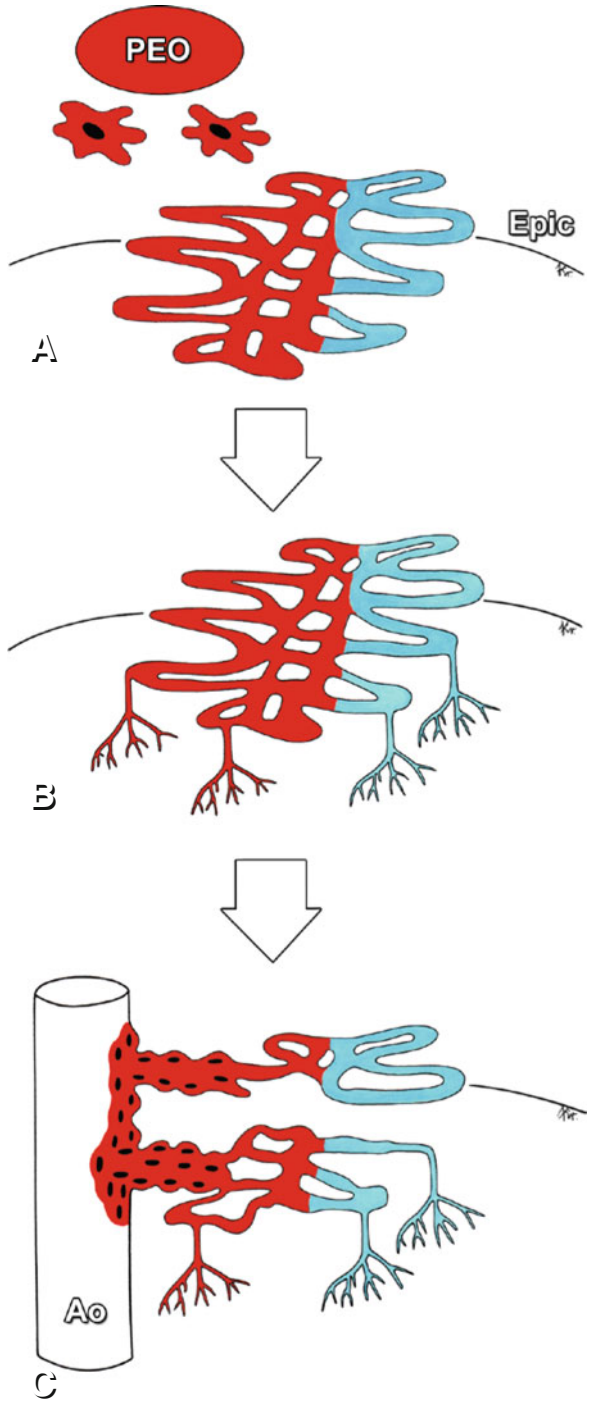

Fig. 22.1 Development of the coronary arteries. Vasculogenesis includes the in situ formation of a primitive capillary plexus in the subepicardial space from immature endothelial precursors partly originating from the proepicardial organ (*PEO* in **Panel A**). This is also the phase during which early differentiation into arterial (*red*) and venous (*blue*) endothelium occurs. Angiogenesis is initiated by the formation of a vascular network via transmyocardial sprouting from preexisting vessels and intussusception, i.e., formation of new pillars and septations within the vascular sprouts (**Panel B**). Subsequent embryonal arteriogenesis begins with the connection of the network to the aorta and continues with extensive remodeling, formation of distinct vascular provinces, recruitment of smooth muscle cells, and vascular stabilization (**Panel C**). For details on arteriogenesis of the coronaries see **Fig. 22.2** (Modified from Y. von Kodolitsch et al. *Zeitschrift für Kardiologie* 2004)

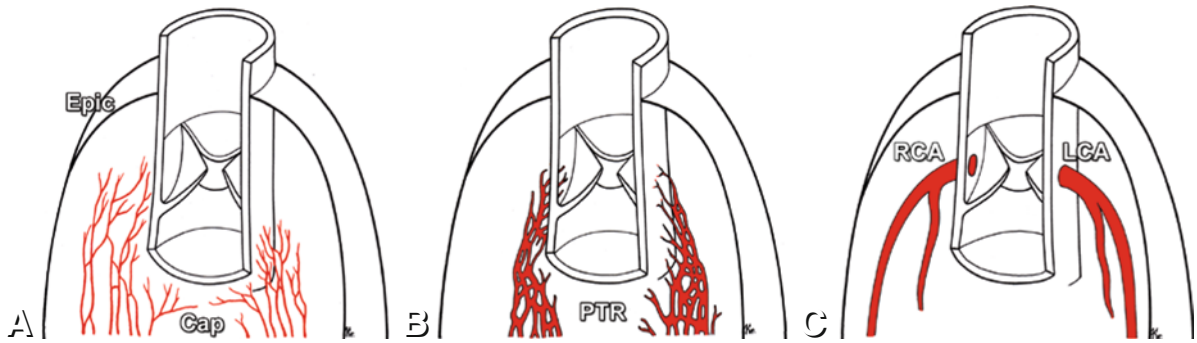

Fig. 22.2 Arteriogenesis of the coronary arteries. Multiple capillaries (*Cap*) form the primary vascular plexus beneath the epicardium (*Epic* in **Panel A**). Around the aorta and pulmonary trunk the capillaries coalesce to form a peritruncal ring (*PTR* in **Panel B**). Subsequently, multiple vessels extend towards the aorta and invade it. The peritruncal ring is reduced to the mainline coronary artery pattern with the right (*RCA*) and left coronary artery (*LCA*) attached to the aorta at the corresponding coronary sinuses (**Panel C**) (Modified from Bernanke et al. *Anat Rec* 2002)

changes associated with this access to the aortic root appear to initiate the vascular maturation of the network and its aortic orifices. The migration of smooth muscle cells and pericytes from the epicardium and the aortic root to the primitive vascular structures and their coalescence with them are the next step of a vascular maturation. As a result, stable arteries are formed; they grow radially and the peritruncal ring with its numerous vessels undergoes partial regression (**Fig. 22.2**). Defects at any stage of this complex development can lead to coronary anomalies.

22.2 Classification

Many different classifications of coronary artery anomalies have been proposed to categorize the enormous number of variations in coronary artery anatomy. This section gives an overview to serve as a basis for an adequate description of coronary anomalies and to facilitate identification of potentially clinically important variants. Most classifications of coronary anomalies rely exclusively on the description of the anatomic variant. The approach favored here is based on the classification proposed by Paolo Angelini (*Circulation* 2007). Other classifications group anomalous coronary arteries according to their origin, course, or termination. Coronary artery anomalies can also be functionally divided into hemodynamically significant (malignant type) and hemodynamically nonsignificant (benign type). The malignant type consists of coronary artery variants that can cause ischemia and even sudden cardiac death.

According to Angelini, coronary anomalies can be anatomically divided into anomalies of origin and course, of intrinsic anatomy, of termination, and anomalous anastomotic vessels (**Table 22.1**). The origin and course of the anomalous coronary artery determine its possible clinical impact to the greatest extent. Instead of an origin from the proper sinus of Valsalva, coronary arteries can arise from the opposite sinus and take different pathways to reach the myocardial area they are supplying. On its course to the opposite site, the coronary artery can pass anterior to the pulmonary artery (**Fig. 22.3**), posterior to the aorta, or interarterially between the aorta and pulmonary trunk, or even intraseptally (subpulmonic course). Coronary anomalies also occur in association with congenital heart disease, for example with tetralogy of Fallot, transposition of the great arteries or pulmonary atresia (Chap. 23).

Table 22.1 Modified classification of coronary anomalies according to Paolo Angelini

A. Anomalies of origin and course
1. Absent LM with split origin of LCA (**Fig. 22.4**).
2. Anomalous location (high, low, commissural) of coronary ostium within aortic root or near proper aortic sinus of Valsalva
3. Anomalous location of coronary ostium outside normal "coronary" aortic sinuses Right posterior aortic sinus, ascending aorta or aortic arch, left or right ventricle, pulmonary artery, etc.
4. Anomalous location of coronary ostium at improper sinus, including joint origin (**Figs. 22.3**, **22.5**–**22.13**)
5. Single coronary artery (**Fig. 22.22**)
B. Anomalies of intrinsic coronary arterial anatomy
1. Congenital ostial stenosis or atresia, coronary ectasia or aneurysm, absence or hypoplasia of coronary artery etc. (**Figs. 22.15** and **22.16**)
2. Intramural (muscular bridge, Chap. 3) or subendocardial course or coronary crossing (**Fig. 22.21**)
3. Anomalous origin of PD, split LAD or RCA, or ectopic origin of first septal branch (**Figs. 22.7**–**22.9**)
C. Anomalies of coronary termination
1. Inadequate arteriolar/capillary ramifications
2. Fistulas from RCA or LCA (**Figs. 22.18**–**22.20**)
D. Anomalous anastomotic vessels

The table and classification was modified from Angelini *Circulation* 2007

LM left main coronary artery, *LCA* left coronary artery, *LAD* left descending coronary artery, *RCA* right coronary artery, *LCX* left circumflex artery, *PD* posterior descending

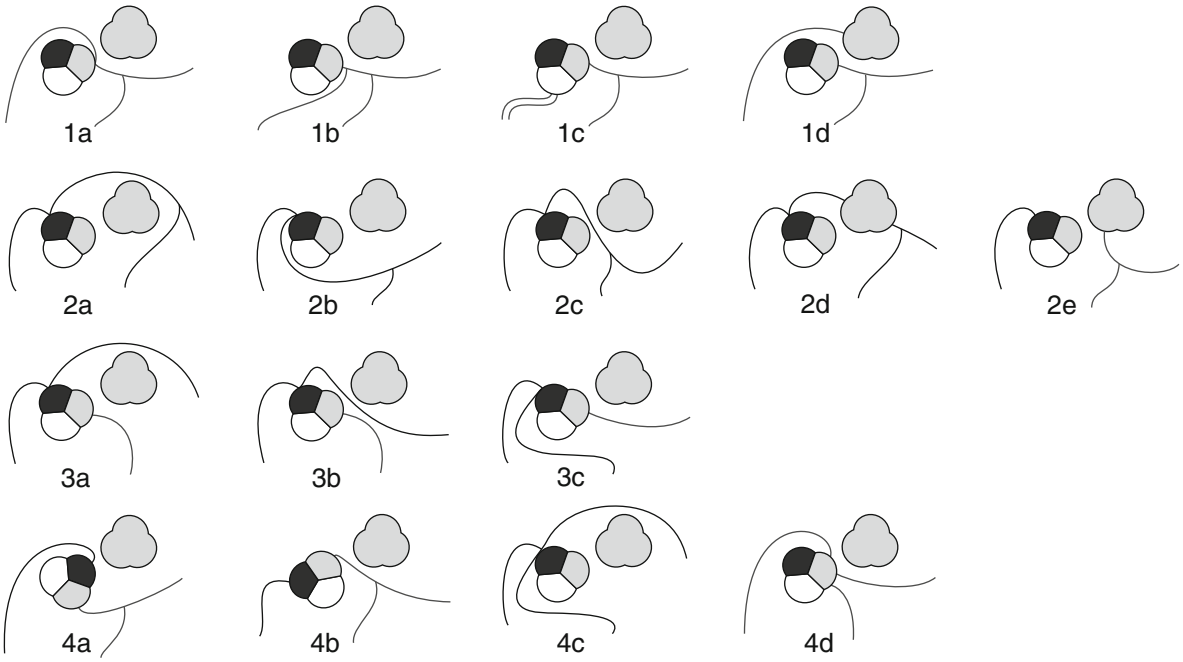

Fig. 22.3 Different courses of anomalously located coronary ostia at improper sinus with *1* showing anomalies of the right coronary artery (*RCA*) (*a*: anterior interarterial course, *b*: posterior course from left sinus of Valsalva, *c*: posterior course from the noncoronary sinus, *d*: anterior course from the pulmonary artery), *2* of the left main coronary artery (*LM*) (*a*: anterior course, *b*: posterior course, *c*: interarterial course, *d*: septal course, *e*: from the pulmonary artery (*Bland–White–Garland syndrome*)), *3* of the central branches of the left coronary artery (*a*: anterior course, *b*: interarterial course, *c*: posterior course), and *4* of both the right and left coronary arteries (*a*: orthotopic origins from clockwise rotated aortic bulb, *b*: orthotopic origins from counter-clockwise rotated aortic bulb, *c*: three origins from the right sinus, *d*: three origins from the left sinus). Aortic root: *black*: right sinus, *grey*: left sinus, *white*: noncoronary sinus. The pulmonary artery is shown completely in grey anterolateral to the aortic root (With permission from Schmitt et al. *European Radiology* 2005)

22.3 Clinical Relevance

The prevalence of coronary anomalies is reported to be 0.3 up to 5.6%, depending on the literature source. In a large study of over 100,000 patients examined by conventional coronary angiography the prevalence of coronary anomalies was found to be around 1.3%. There is also evidence that prevalence varies according to geographic region.

22.3.1 Benign Coronary Anomalies

Coronary anomalies without compromise of blood flow to the myocardium or severe fistulas are considered benign. The simplest coronary anomaly is the absence of the left main coronary artery (split left coronary) with a separate origin of the left anterior descending and left circumflex coronary artery (**Fig. 22.4**). The most common course of a benign anomalous coronary artery is the prepulmonary (**Fig. 22.5**) and retroaortic path (**Figs. 22.6**, **22.7** and **22.8**). Separate origins of diagonal or marginal branches from the aorta are also benign unless their course is compromised (**Fig. 22.9**)

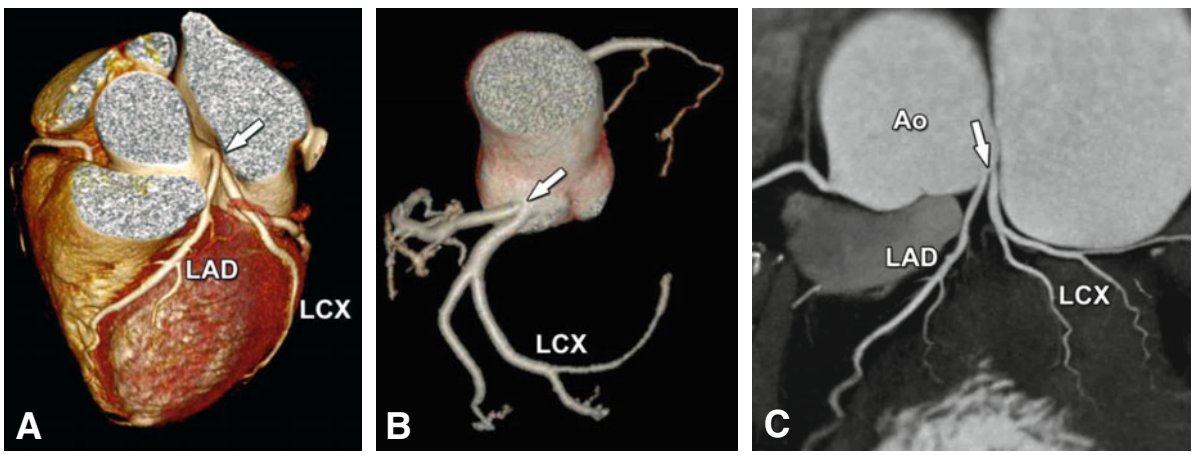

Fig. 22.4 Absence of the left main coronary artery (so-called split left coronary artery). The left anterior descending coronary artery (*LAD*) and the left circumflex coronary artery (*LCX*) arise separately (*arrow*) from the left sinus of Valsalva of the aorta (*Ao*) in a 68-year-old woman who was referred to cardiac CT to exclude coronary artery disease based on atypical chest pain. **Panel A** shows a cranial view of a three-dimensional volume-rendered image. The separate ostia cannot be recognized definitely. Better evaluation is possible on a volume-rendered reconstruction of the coronary tree (**Panel B**) or a two-dimensional map view (**Panel C**)

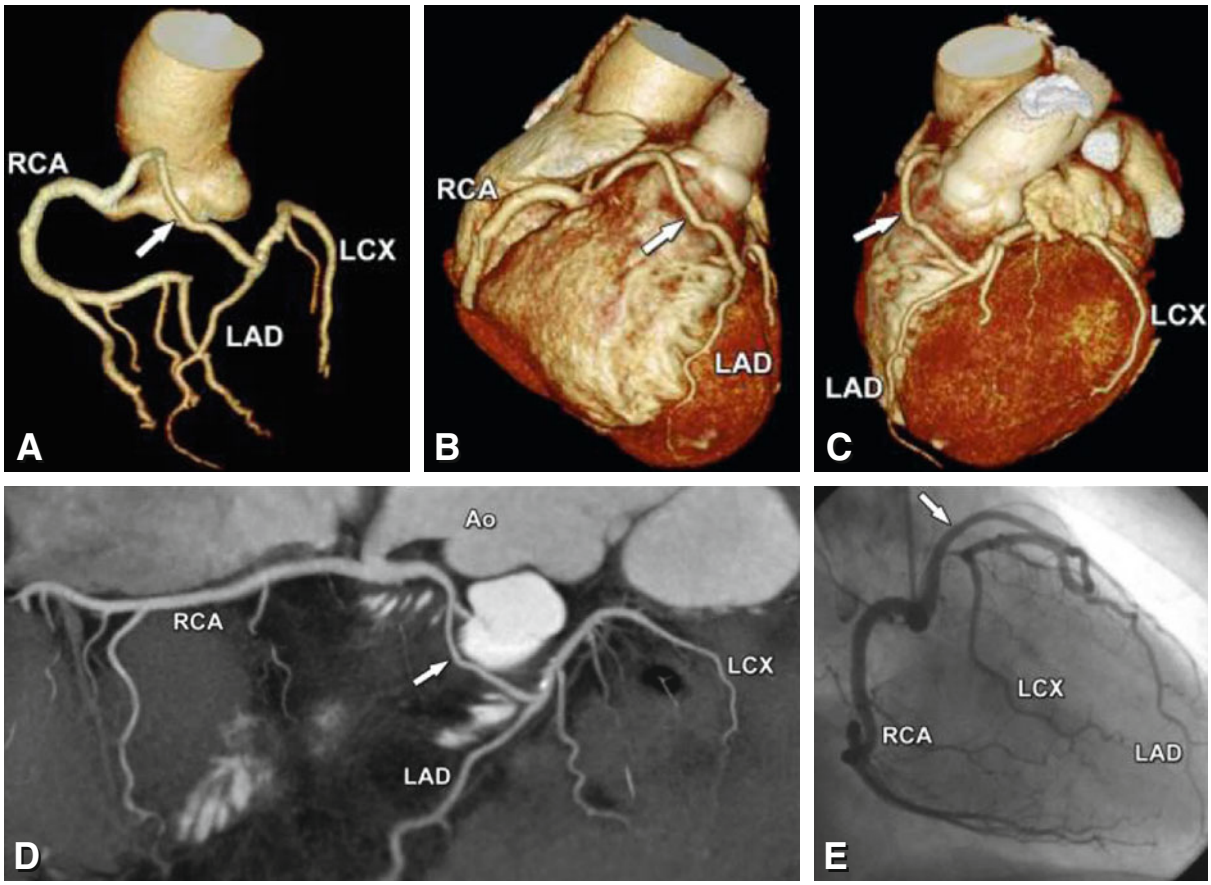

Fig. 22.5 Prepulmonary benign course of the left coronary artery arising from the right coronary artery after a short common trunk, which originates from the right sinus of Valsalva. The anomalously coursing left coronary artery (*arrow* in **Panels A**–**D**) passes anterior to the pulmonary artery to the anterior interventricular sulcus, where it splits into left anterior descending coronary artery (*LAD*) and left circumflex coronary artery (*LCX*). Due to the prepulmonary course of the left coronary artery, this anomaly is considered benign. The CT of this 52-year-old male patient was performed to exclude coronary artery disease based on hypertension and atypical chest pain. Conventional coronary angiography also showed the coronary anomaly, but the course of the proximal part of the left coronary artery was unclear (**Panel E**), therefore, the patient was referred for CT. The patient was medically treated and the further clinical course was uneventful. **Panel A** shows a volume-rendered reconstruction of the coronary tree. **Panels B** and **C** are three-dimensional volume-rendered images from two different views showing the anterior course of the anomalous left coronary artery, while **Panel D** gives an overview on a two-dimensional map view. **Panel E** shows the corresponding invasive angiography. *Ao* aorta

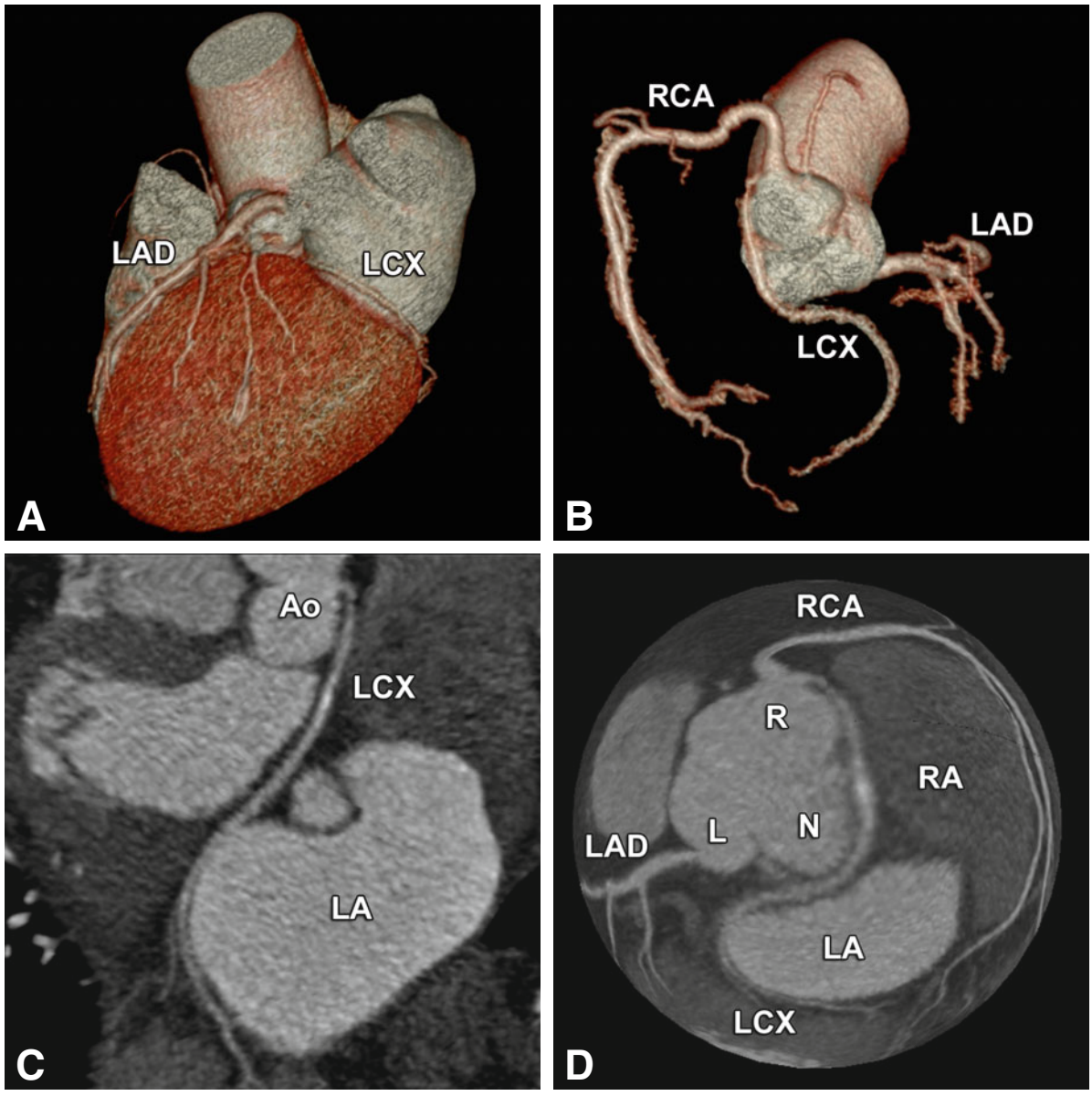

Fig. 22.6 Benign coronary anomaly with a retroaortic course of the left circumflex artery (*LCX*) originating from the right sinus of Valsalva (*R*) next to the ostium of the right coronary artery (*RCA*) in a 72-year-old female patient. CT was performed to exclude coronary artery disease because of chest pain and an abnormality of repolarization on exercise electrocardiography. **Panels A** and **B** show three-dimensional volume renderings of the heart and the coronary tree. The LCX passes retroaortically between the aorta and the right atrium (*RA*) and left atrium (*LA*) to reach the left atrioventricular sulcus as seen on a curved multiplanar reformation of the LCX and a globe view of the coronary tree, respectively (**Panels C** and **D**). Relevant coronary disease could be excluded and a minor artifact was seen in the proximal LCX. *RCA* right coronary artery, *N* noncoronary sinus, *L* left sinus of Valsalva, *Ao* aorta

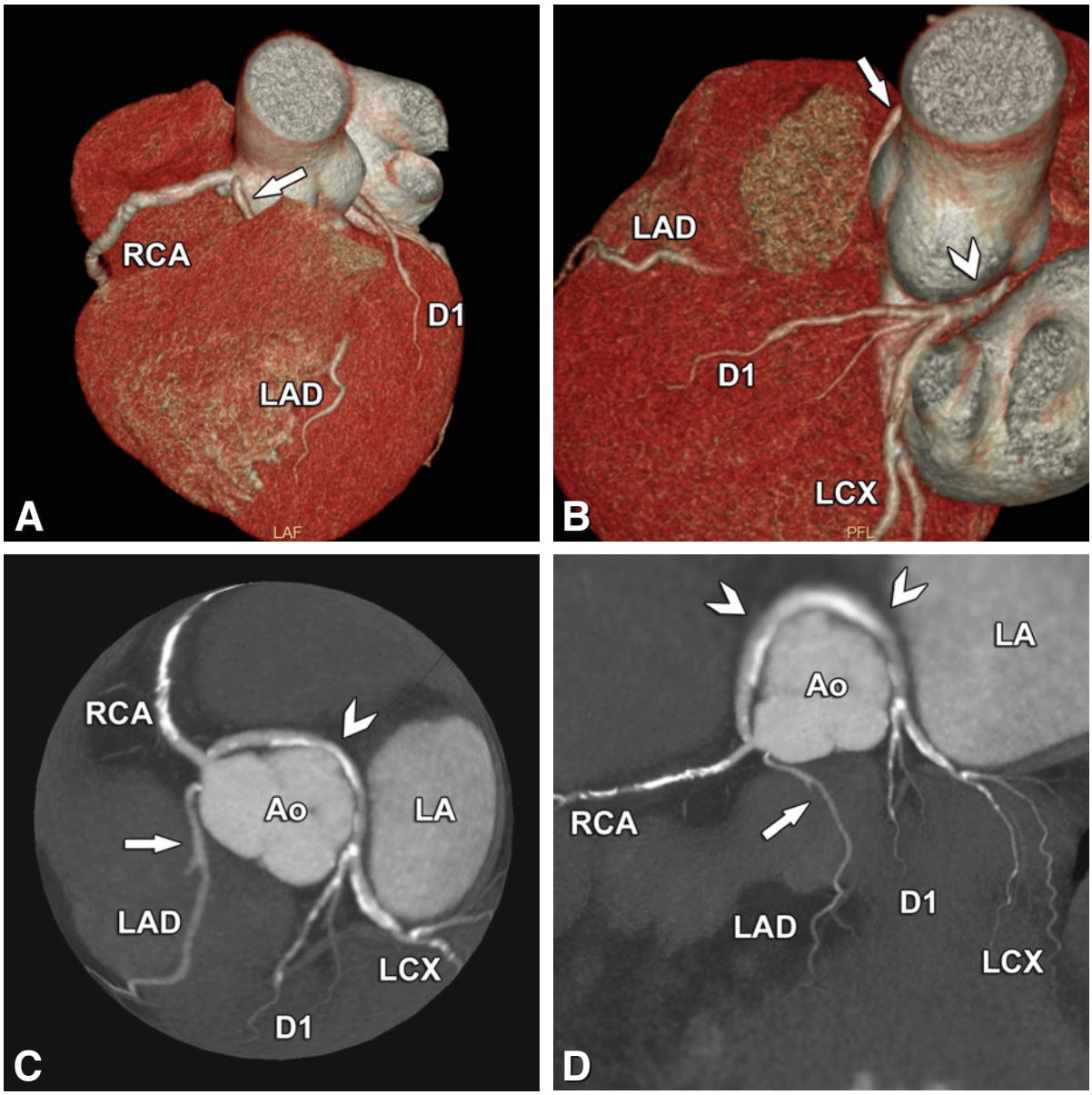

Fig. 22.7 Another complex benign anomaly. The left anterior descending coronary artery (*LAD*) arises from a separate ostium next to the right coronary artery (*RCA*) and takes an intramuscular septal path before it appears in the interventricular sulcus (*arrow*, **Panels A**–**D**). The retroaortic path of the left circumflex coronary artery (*LCX*) and the first diagonal branch (*D1*, *arrowheads*, **Panels B**–**D**) can also be considered benign. **Panels A** and **B** are three-dimensional volume renderings from two different viewing angles, **Panel C** is a globe view, and **Panel D** is a two-dimensional map view, both showing the anomalous course nicely. *Ao* aorta, *LA* left atrium

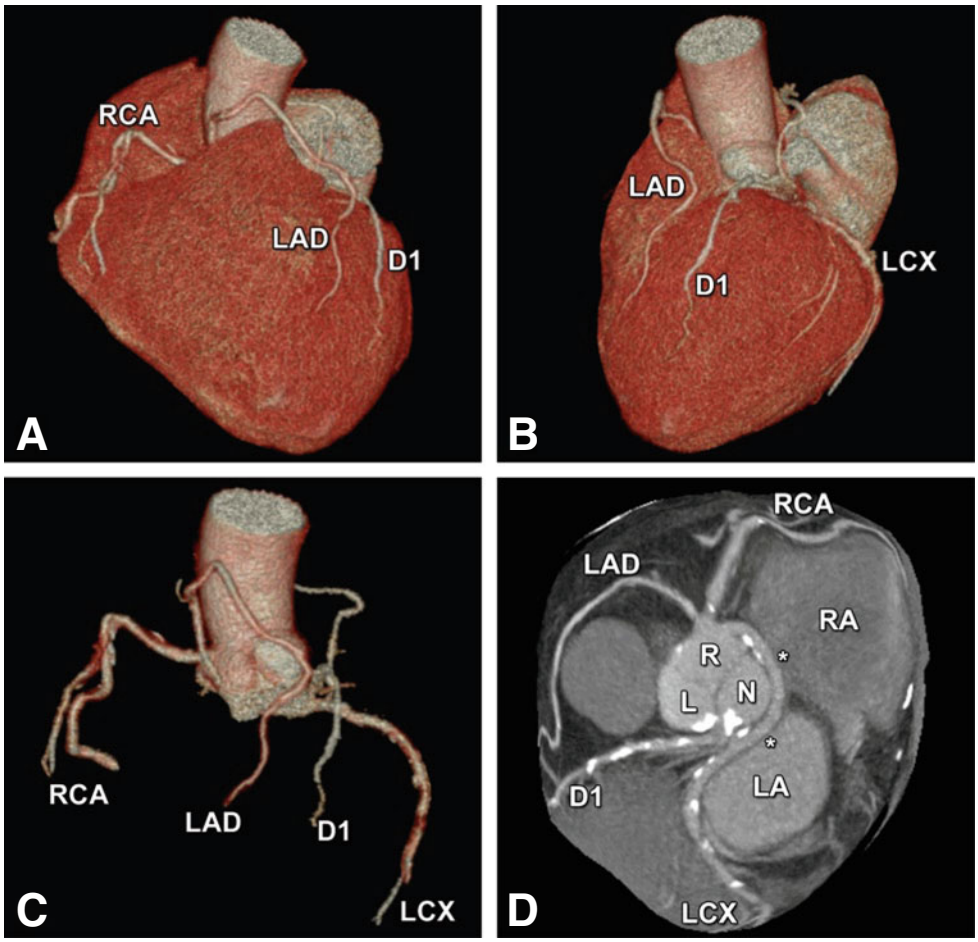

Fig. 22.8 Complex though benign coronary anomaly with two coronary ostia from the right sinus of Valsalva (R) and no coronary ostium on the left sinus of Valsalva (*L*). There are two separate vessels supplying the anterior segments of the myocardium, which were assumed to be the left anterior descending coronary artery (*LAD*) and first diagonal branch (*D1*, **Panels A**–**C**) based on their location (split LAD). The D1 and the left circumflex coronary artery (*LCX*) arise with a common trunk from the right sinus of Valsalva (*R*), which passes retroaortically between the aorta and the right atrium (*RA*) and the left atrium (*LA*) (asterisk in **Panel D**). This common trunk then splits into the D1 and LCX, which then pass to the anterolateral myocardium and the left atrioventricular sulcus, respectively. The right coronary artery (*RCA*) and the LAD arise from a common ostium also from the right sinus of Valsalva (**Panels C** and **D**). The RCA takes the typical course, whereas the LAD takes a prepulmonary course to the anterior interventricular sulcus. Coronary CT angiography of this 64-year-old male patient with known severe coronary artery disease was done after conventional coronary angiography for further imaging of the courses of the anomalous vessels. The patient then received two stents into the LCX due to high grade stenosis. **Panels A** and **B** show three-dimensional volume renderings of the heart from two different viewing angles, which do not allow full identification of the coronary anatomy. The three-dimensional reconstruction of the coronary tree in **Panel C** also fails to clearly show the course of the coronary arteries. The most distinct anatomical depiction is given by the globe view in **Panel D**, which resolves the origins and courses of the anomalous coronary arteries.

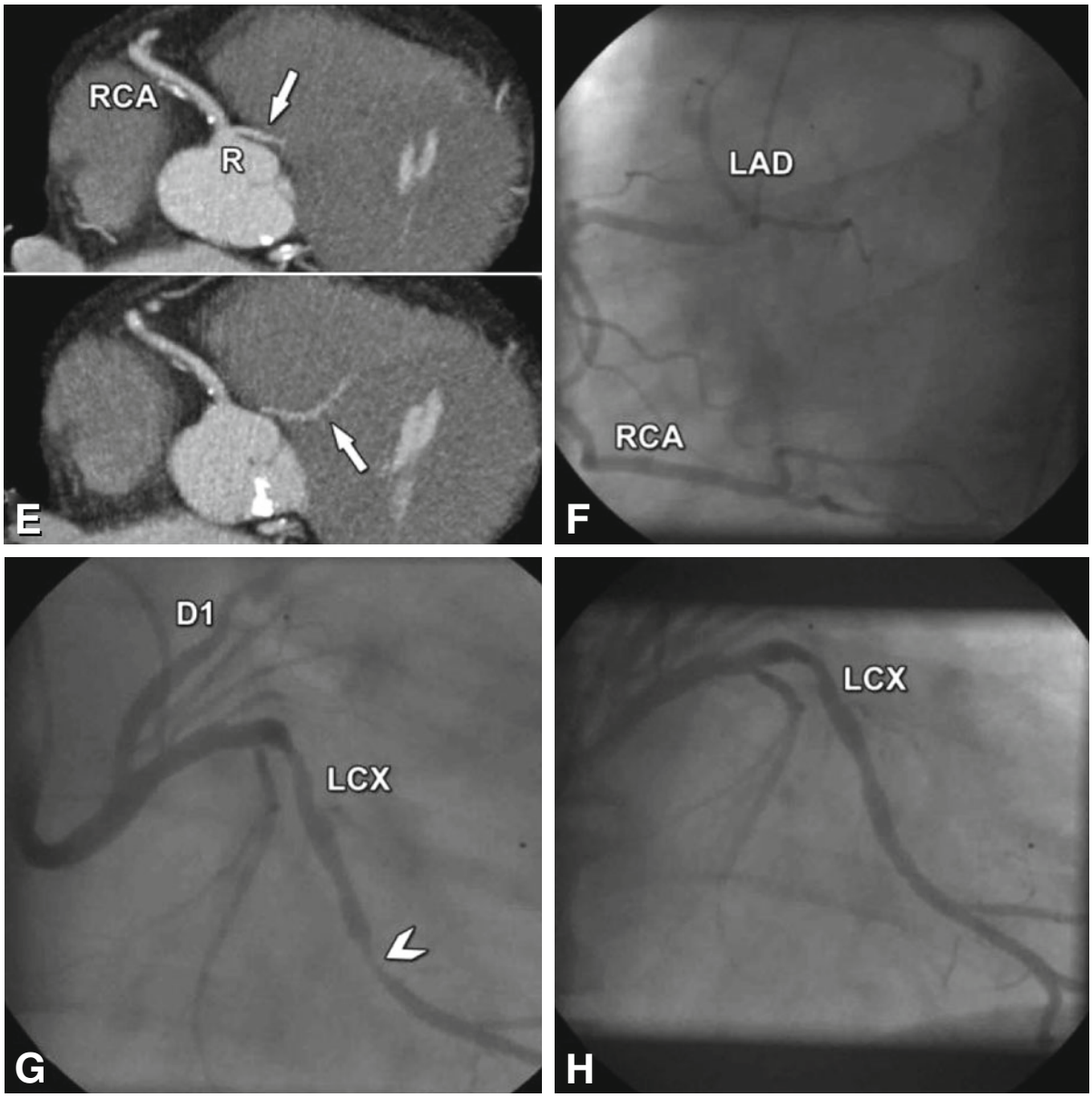

Fig. 22.8 (continued) **Panel E** shows para-axial maximum intensity projections of another small septal branch that originates from the proximal RCA and takes an intramyocardial path into the anterior interventricular septum (*arrow*). **Panels F** and **G** show the corresponding conventional coronary angiography with the coronary stenosis in the LCX (*arrowhead*). **Panel H** demonstrates the LCX after successful stenting of the stenosis. *N* noncoronary sinus

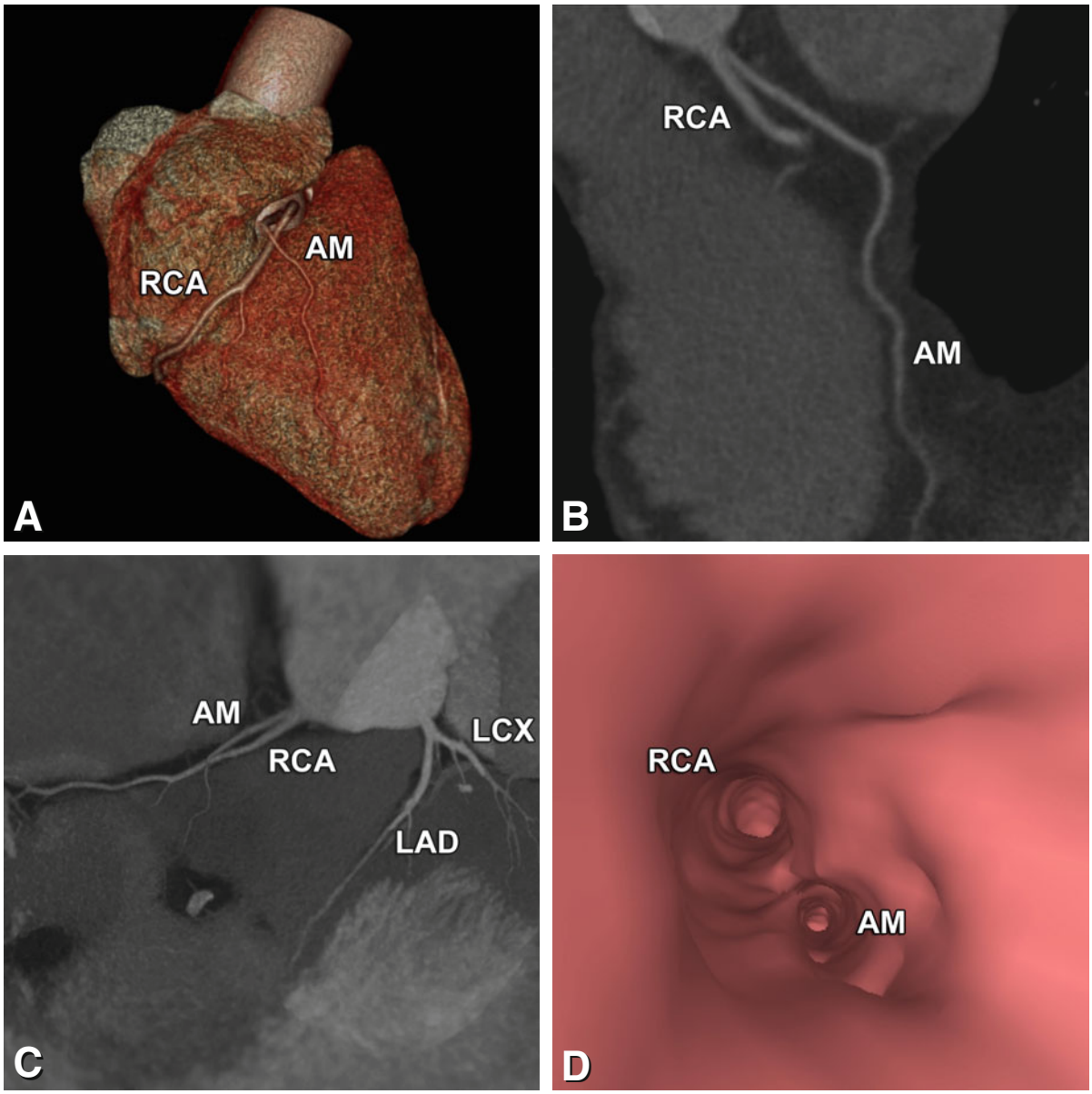

Fig. 22.9 Benign coronary anomaly with a separate origin of a large acute marginal (*AM*) branch from the aorta next to the ostium of the right coronary artery (*RCA*) in a 52-year-old patient with nonspecific ECG-changes and a positive family history for coronary artery disease. An overview of the RCA and AM is seen on a volume-rendered reconstruction (**Panel A**). This benign variant with a separate ostium of the AM next to the ostium of the RCA is shown on a curved multiplanar reformation (**Panel B**), a two-dimensional map view (**Panel C**), and an endoluminal view (**Panel D**). The course of the left anterior descending coronary artery (*LAD*) and the left circumflex coronary artery (*LCX*) were normal and there were no significant stenoses

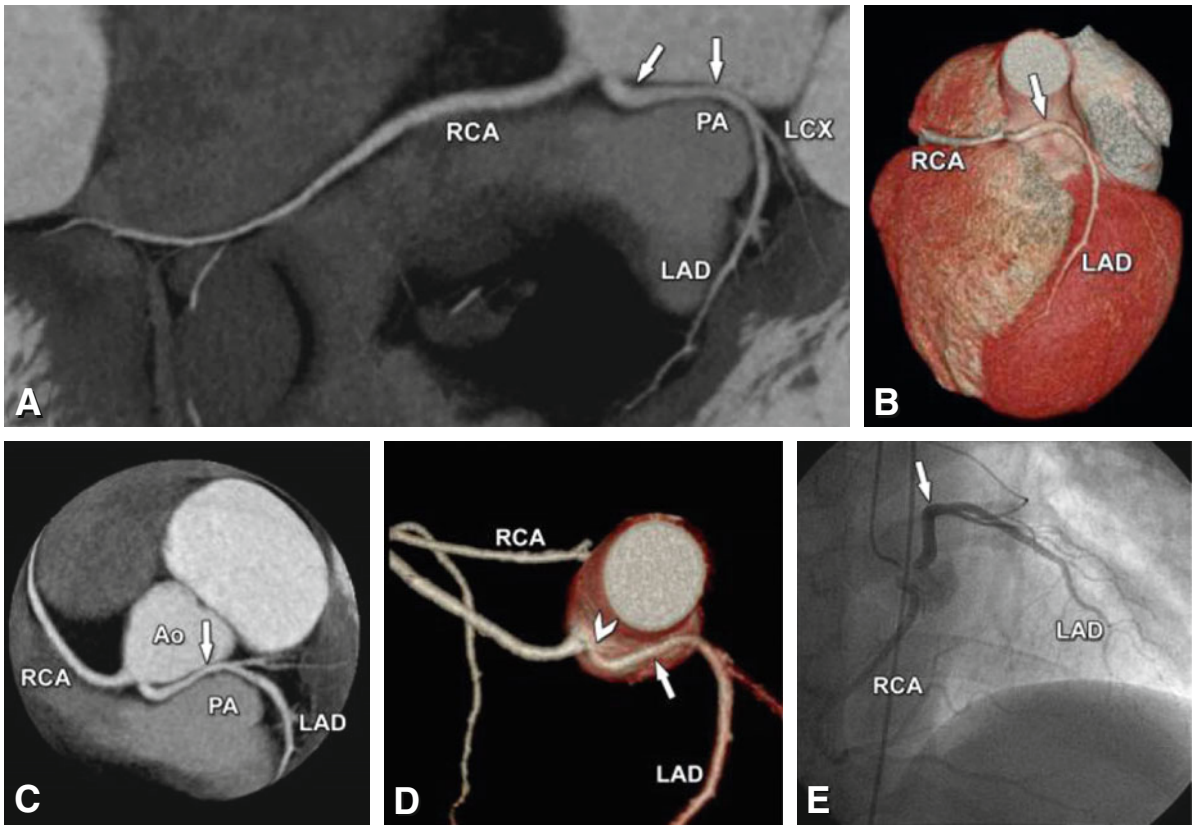

Fig. 22.10 Interarterial (malignant) course of the left coronary artery (*arrow*) with origin from the right sinus of Valsalva next to the ostium of the right coronary artery (*RCA*). After the interarterial course, the anomalous vessel splits into the left anterior descending coronary artery (*LAD*) and left circumflex coronary artery (*LCX*). **Panel A** shows the two-dimensional map view and **Panel B** the corresponding three-dimensional volume-rendered image. **Panel C** presents an additional globe view showing the course similar to the map view while **Panels D** shows the ostium of the left coronary artery (*arrowhead*) next to the one of the RCA. **Panel E** is the conventional coronary angiography which was done in this 36-year-old patient with hypertension because of a positive stress test at high exertion levels with ST-segment depression in the anteroseptal wall. Conventional angiography showed a coronary anomaly with all three coronary arteries arising from the right sinus of Valsalva; however, the course of the left coronary artery was unclear. Therefore CT was performed. Due to the positive stress test the patient received an off-pump single bypass operation connecting the left internal mammary artery (*LIMA*) to the LAD. *Ao* aorta, *PA* pulmonary artery

22.3.2 Malignant Coronary Anomalies

Malignant coronary anomalies with an interarterial course have the highest potential for cardiac events. In those cases the anomalous coronary artery arises from the opposite sinus of Valsalva and takes an interarterial course between the aorta and the pulmonary artery (**Figs.** 22.10, 22.11, 22.12 and 22.13). These anomalies are made responsible for sudden cardiac death, especially in young persons, during or shortly after physical exercise. This is probably due to increased blood flow in the aorta and the pulmonary artery during physical activity, resulting in a compression of the aberrant vessel, thereby inducing myocardial ischemia. Additionally, the origin of the anomalous artery may be narrowed and form an acute angle with the aorta, making it more likely that the blood flow is compromised. An intramural proximal intussusception of the aberrant artery at the

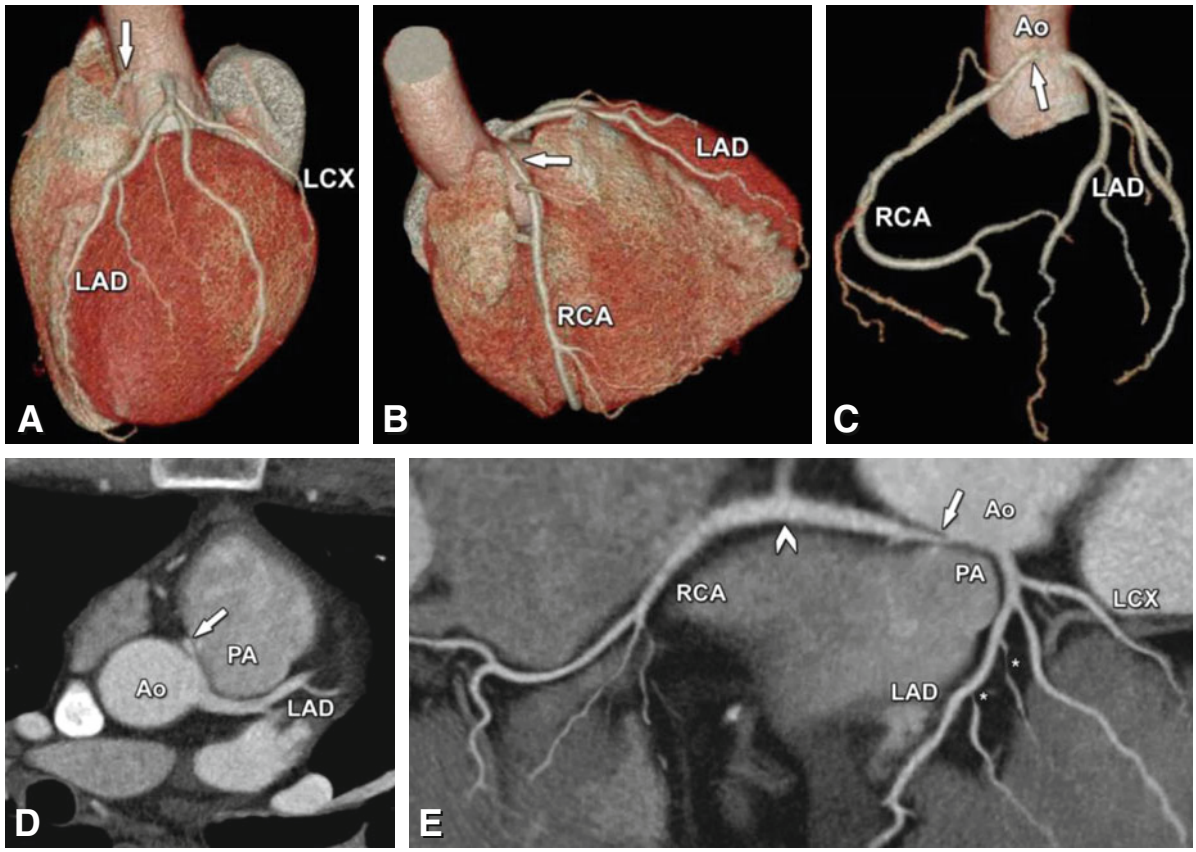

Fig. 22.11 Malignant interarterial course of the right coronary artery (*RCA*), which originates separately from the ostium of the left coronary artery from the left sinus of Valsalva (*arrow* in **Panels A**–**E**). The 31-year-old male patient came for further clarification after conventional coronary angiography, which was performed for atypical chest pain. Stress testing revealed no signs of myocardial ischemia and conservative treatment was recommended. The three-dimensional volume-rendered reconstructions of the heart (**Panels A** and **B**) and the coronary tree (**Panel C**) show the small ostium of the RCA (*arrow*), which forms an acute angle with the aorta (Ao). The maximum intensity projection in **Panel D** shows that already the ostium of the RCA is located between the aorta and the pulmonary artery (PA). An overview is given in the two-dimensional map view (**Panel E**). The narrowings of the diagonal branches (*asterisks*) of the left anterior descending coronary artery (*LAD*) as well as the bulging out of the RCA (*arrowhead*) are artifacts of the map reconstruction (compare with **Panel A**). *LCX*, left circumflex coronary artery

Fig. 22.12 Origin of the left anterior descending coronary artery (*LAD*) and the left circumflex coronary artery (*LCX*) from the right sinus of Valsalva (*arrow*) next to the origin of the right coronary artery (*RCA*) with a malignant course (**Panels A**–**C**). The LCX passes between the aorta (*Ao*) and the pulmonary artery (interarterial), whereas the proximal LAD shows myocardial bridging on its way through the proximal interventricular septum (*arrowheads*) without recognizable compression of the lumen during systole. **Panels A** and **B** show a three-dimensional volume rendering, where the anomalous coronary course cannot be recognized. The volume-rendered coronary tree in **Panel C** gives a good view of the origin of the left coronary artery. The maximum intensity projections in **Panel D** (axial orientation) and **Panel E** (parasagittal orientation) best show the intraseptal course of the LAD (*arrowheads*). The globe view in **Panel F** gives the best overview of the anatomical situation. **Panels G** and **H** show the corresponding conventional coronary angiography in right anterior oblique projections. This 53-year old male patient was sent to CT for further imaging of the coronary anomaly after coronary angiography. Conservative medical treatment was recommended because stress testing revealed no signs of myocardial ischemia and the non-obstructed RCA was the dominant vessel. *R* right sinus of Valsalva, *L* left sinus of Valsalva, *N* noncoronary sinus

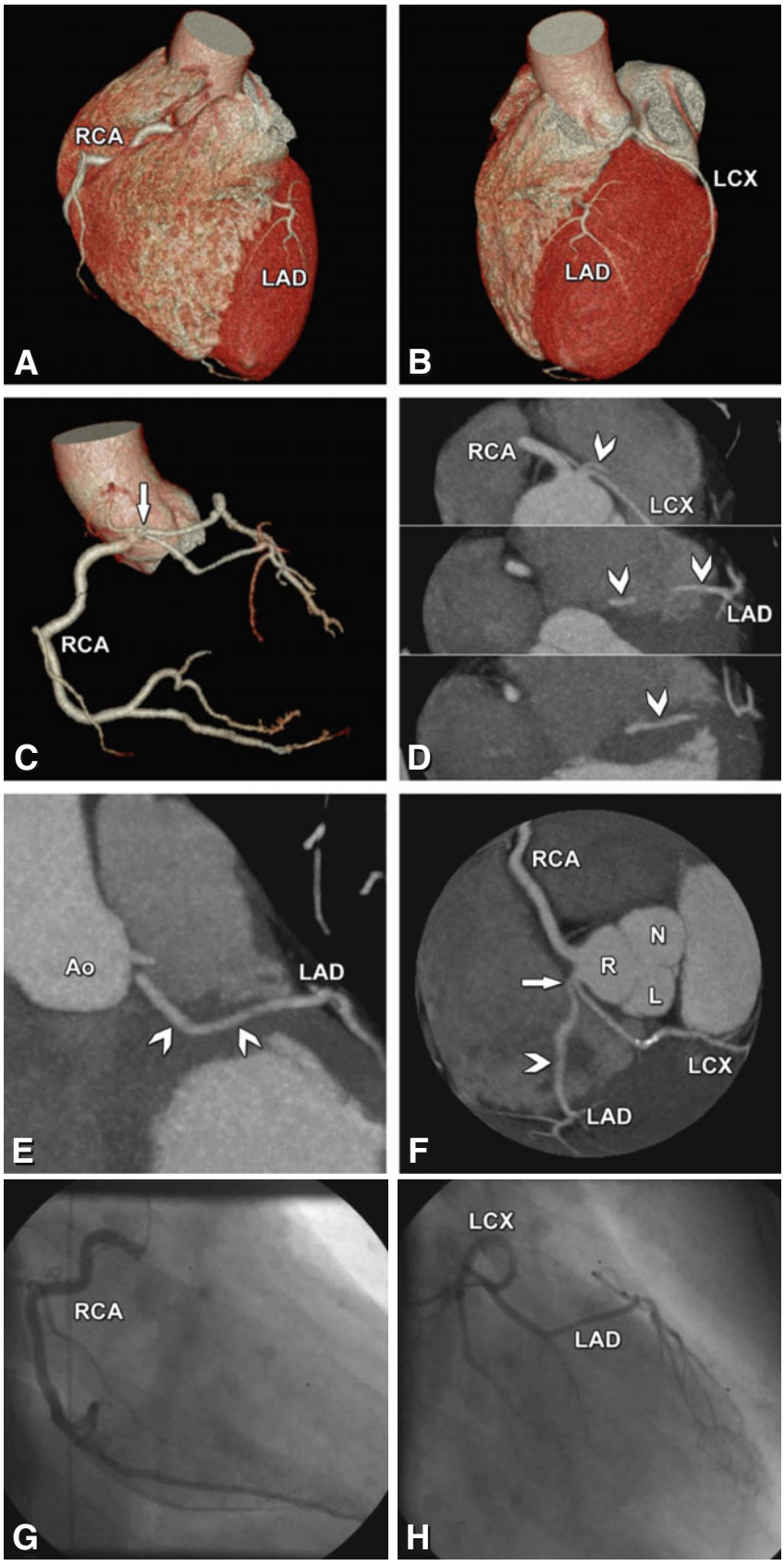
RCA
LAD
A
LCX
LAD
B
RCA
C
RCA
LCX
LAD
D
Ao
LAD
E
RCA
N
R
L
LCX
LAD
F
RCA
G
LCX
LAD
H

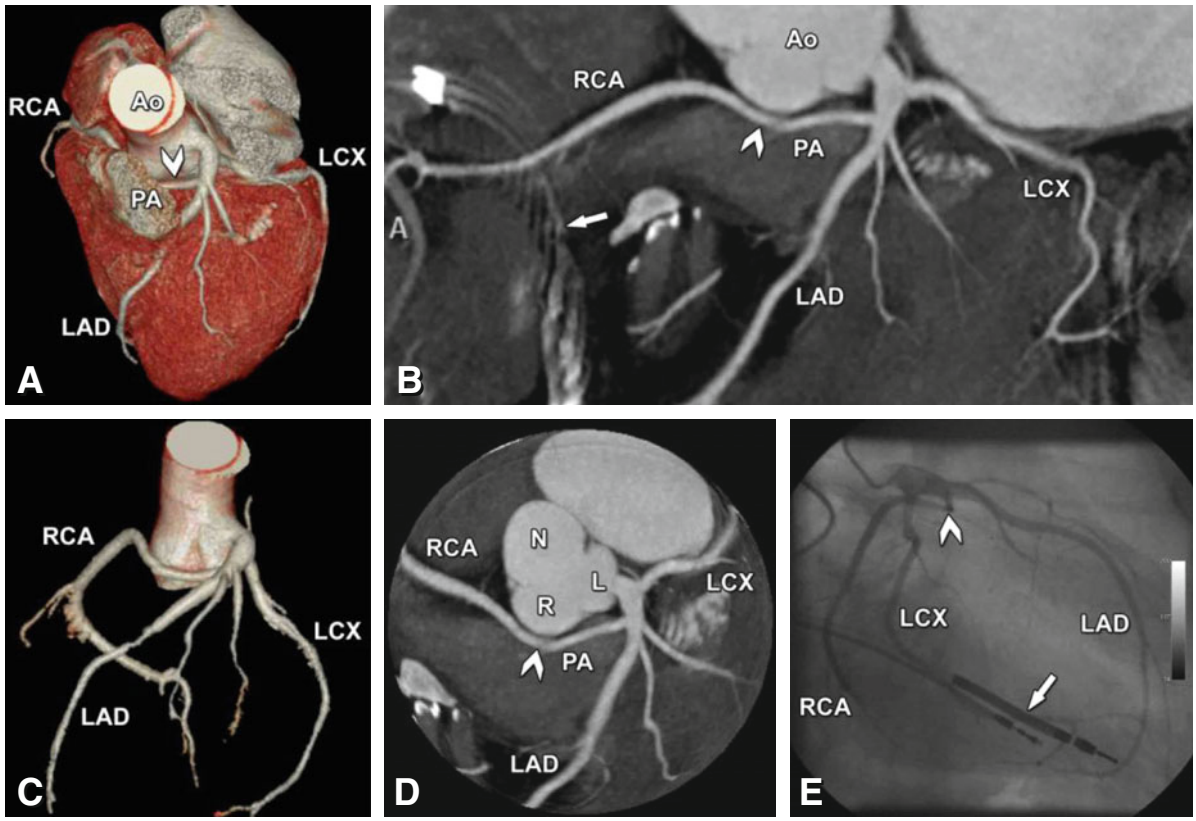

Fig. 22.13 Interarterial (malignant) course of the right coronary artery (*RCA*), which originates from the proximal left anterior descending (*LAD*) and passes between the aorta (*Ao*) and the pulmonary artery (*PA*, *arrowhead* in **Panels A** and **B**). The 45-year-old male patient with known hypertrophic obstructive cardiomyopathy (*HOCM*) came for a second imaging for better depiction of the known coronary anomaly. **Panel A** shows a top view on the three-dimensional volume rendering with the corresponding volume-rendered coronary tree in **Panel C**. The two-dimensional map view (**Panel B**) gives the best overview of the coronary anomaly while the globe view in **Panel D** best shows the aortic valve with its sinuses (*R* right sinus of Valsalva, *L* left sinus of Valsalva, *N* noncoronary sinus). **Panel E** shows the conventional coronary angiography of the patient, confirming the narrowing of the anomalous interarterial vessel (*arrowhead*). The arrow in **Panel B** indicates an artifact of the electrode of the implantable cardioverter-defibrillator (*ICD*) also shown in **Panel E** (*arrow*). The patient was listed for heart transplantation due to HOCM

wall of the aortic root has been reported in intravascular ultrasound studies and might also be an important pathophysiological mechanism.

In a recent publication Lee et al. (*Radiology* 2012) investigated subtypes of right coronary arteries arising from the left sinus of Valsalva and taking an interarterial course. They distinguished a so-called high interarterial coronary artery passing between the aorta and the pulmonary artery and a low interarterial coronary artery passing between the aorta and the right ventricular outflow tract. The high interarterial course turned out to result in a higher prevalence of typical angina and more major adverse cardiac events. This is explained by the compression of the coronary artery between the aorta and the pulmonary artery during systole, which does not occur between the aorta and the right ventricular outflow tract.

Under certain conditions, benign courses of the anomalous coronary arteries that are usually not associated with myocardial ischemia can reduce myocardial blood flow. If for instance the left anterior descending coronary artery (LAD) or right coronary artery (RCA) passes anterior to a dilated right ventricular outflow tract, as in pulmonary hypertension, the anomalous vessel can be stretched and the lumen narrowed. Other coronary anomalies can predispose to clotting, spasm or atherosclerotic build-up.

In a patient with a potentially malignant course of a coronary artery, further treatment is based on the clinical symptoms and the result of stress testing. In symptomatic patients with positive stress testing bypass surgery is usually recommended (**Fig. 22.10**). However, many patients with a potentially malignant course are asymptomatic and have a negative stress test. In these patients conservative treatment is possible. In equivocal cases, intravascular ultrasound is usually recommended for further analysis.

A very rare but severe congenital coronary anomaly is the anomalous left coronary artery off the pulmonary artery (ALCAPA), also called Bland-White-Garland syndrome (**Fig. 22.14**). It occurs in approximately 0.25–0.5% of all congenital heart disease patients (Chap. 23). Most patients show first symptoms of myocardial ischemia or infarction in infancy or early childhood because the entire perfusion territory of the left coronary artery is supplied with venous blood. In untreated cases, mortality within the first year is approximately 90%. Surgical reconstruction is the appropriate treatment.

22.3.3 Further Anomalies

Anomalies of the intrinsic coronary anatomy summarize several anomalies (**Table 22.1**), which do not primarily affect the origin or general course of the coronary arteries, such as congenital stenosis or atresia, aplasia or hypoplasia, or coronary ectasia or aneurysm formation. Aneurysms, however, most commonly develop secondary to atherosclerosis and occur in about 5% of patients with coronary artery disease (**Figs. 22.15** and **22.16**). Angelini did not explicitly mention aneurysms of the coronary ostium or sinus of Valsalva (**Fig. 22.17**) in the intrinsic coronary anatomy group of anomalies but these anomalies best fit into this category. Anomalies of coronary termination (**Table 22.1**) include all kinds of fistulas between coronary arteries and other cardiac vessels or cavities (**Figs. 22.18**, **22.19**, and **22.20**). Intra-atrial courses of coronary arteries have also been described (**Fig. 22.21**). A rather rare and impressively looking coronary anomaly that is most often benign is the so-called single coronary artery (**Fig. 22.22**).

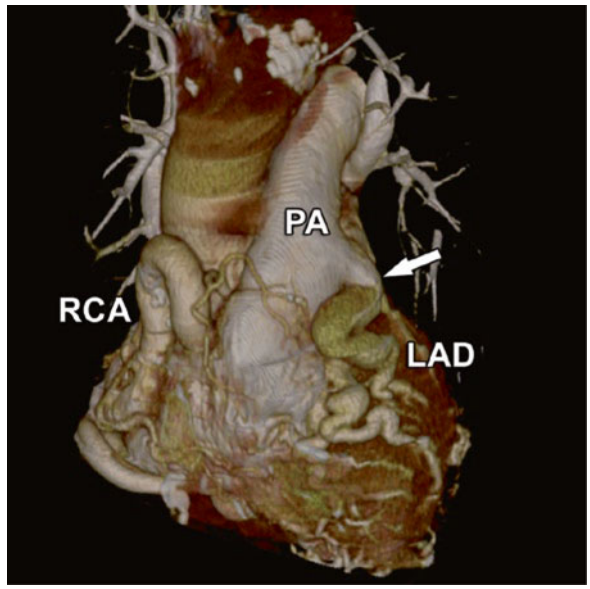

Fig. 22.14 Volume-rendered image of a Bland-White-Garland syndrome in a right anterior oblique view. The right coronary artery (*RCA*) is dilated. The left anterior descending (*LAD*) originates from the pulmonary artery (*arrow*) and is also markedly dilated and tortuous (With permission from Komatsu and Sato et al. *Heart Vessels* 2008)

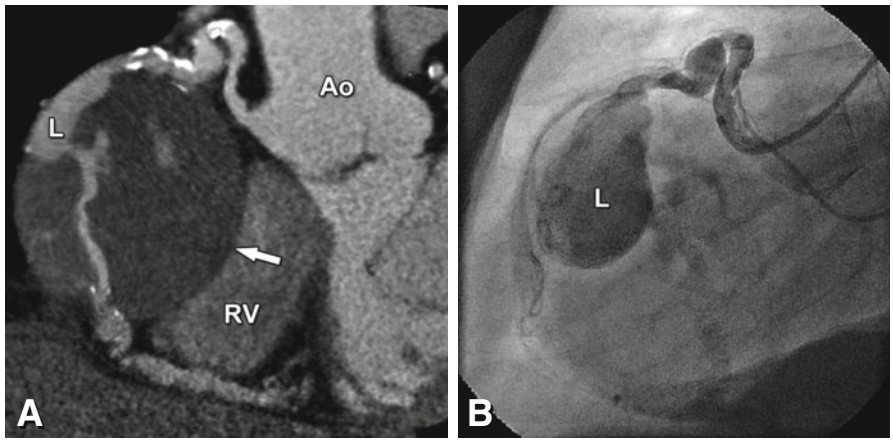

Fig. 22.15 Coronary aneurysm of the right coronary artery (*arrow*) in a 63-year-old male patient who was referred for a right ventricular biopsy after a tentative diagnosis of a malignant tumor of the right ventricular and atrial wall was made. The patient had a history of posterior myocardial infarction. Therefore, cardiac CT (**Panel A**) was performed, which revealed a huge aneurysm of the right coronary artery (*arrow*) measuring 5.6 × 6.6 × 5.8 cm, which was filled with thrombotic material and had a residual lumen (*L*). No significant stenosis was found (the gap in the distal right coronary artery is an artifact from the cath view reconstruction). The aneurysm obstructed the right ventricle (*RV*) from outside. Conventional coronary angiography confirmed the huge aneurysm (*arrow* in **Panel B**) and the patient was sent to surgery

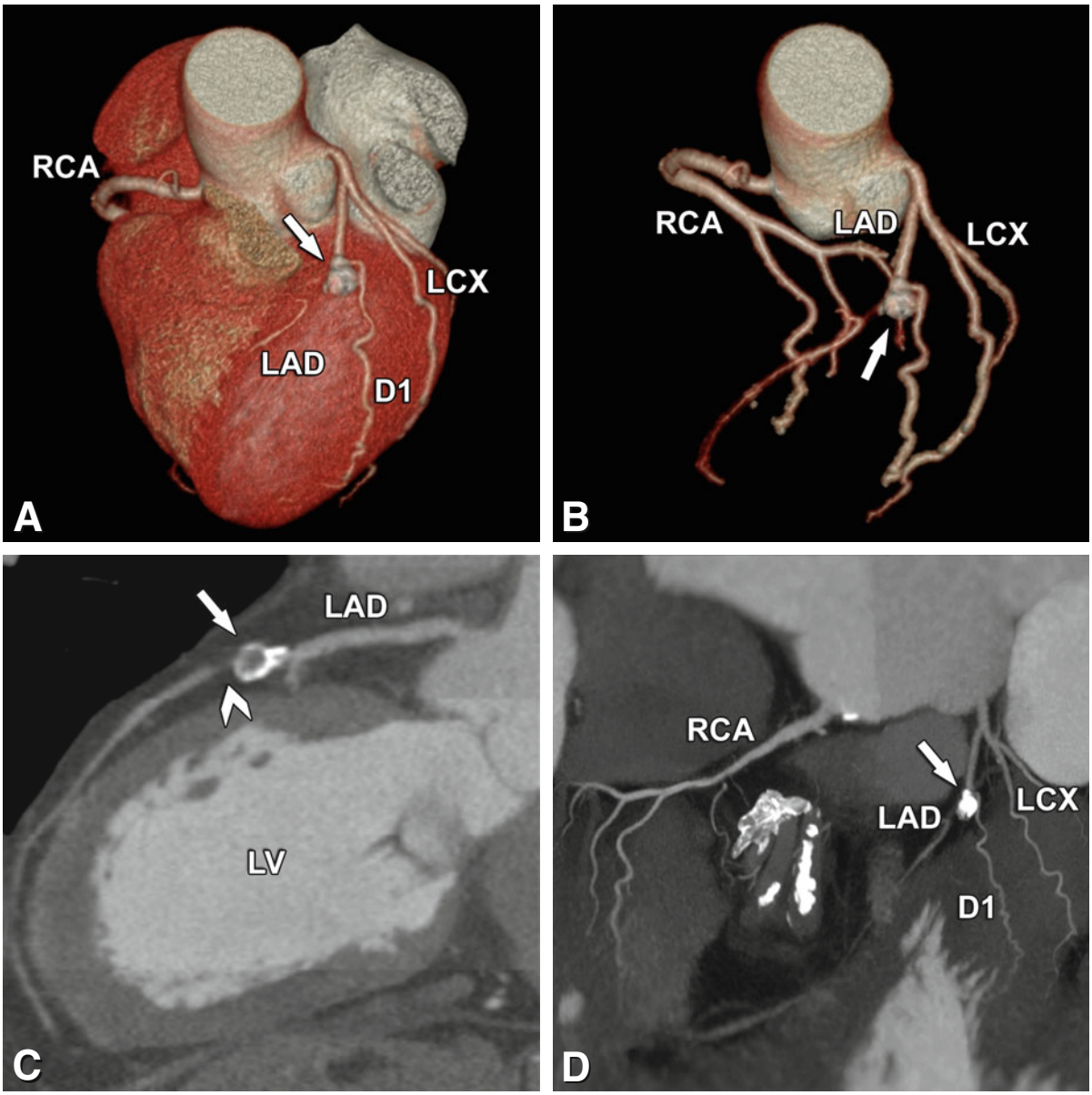

Fig. 22.16 Calcified aneurysm and significant stenosis of the left anterior descending (*LAD*) directly behind the aneurysm in a 69-year-old female patient who presented with atypical angina pectoris of moderate intensity. The most likely etiology is atherosclerosis and single-vessel coronary artery disease. In younger patients, Kawasaki disease must also be considered in the differential diagnosis (Chap. 23). **Panels A** and **B** are a three-dimensional volume-rendered reconstruction of the aneurysm (*arrow*) and the coronary tree, respectively. The curved multiplanar reformation (**Panel C**) shows the aneurysm (*arrow*) and a significant stenosis distal to the aneurysm (*arrowhead*). The two-dimensional map view gives and overview (**Panel D**) and confirms that the first diagonal branch (D1) of the LAD arises proximal to the aneurysm. Coronary angiography and further work up was declined by this patient with moderate clinical symptoms. *RCA* right coronary artery, *LCX* left circumflex coronary artery

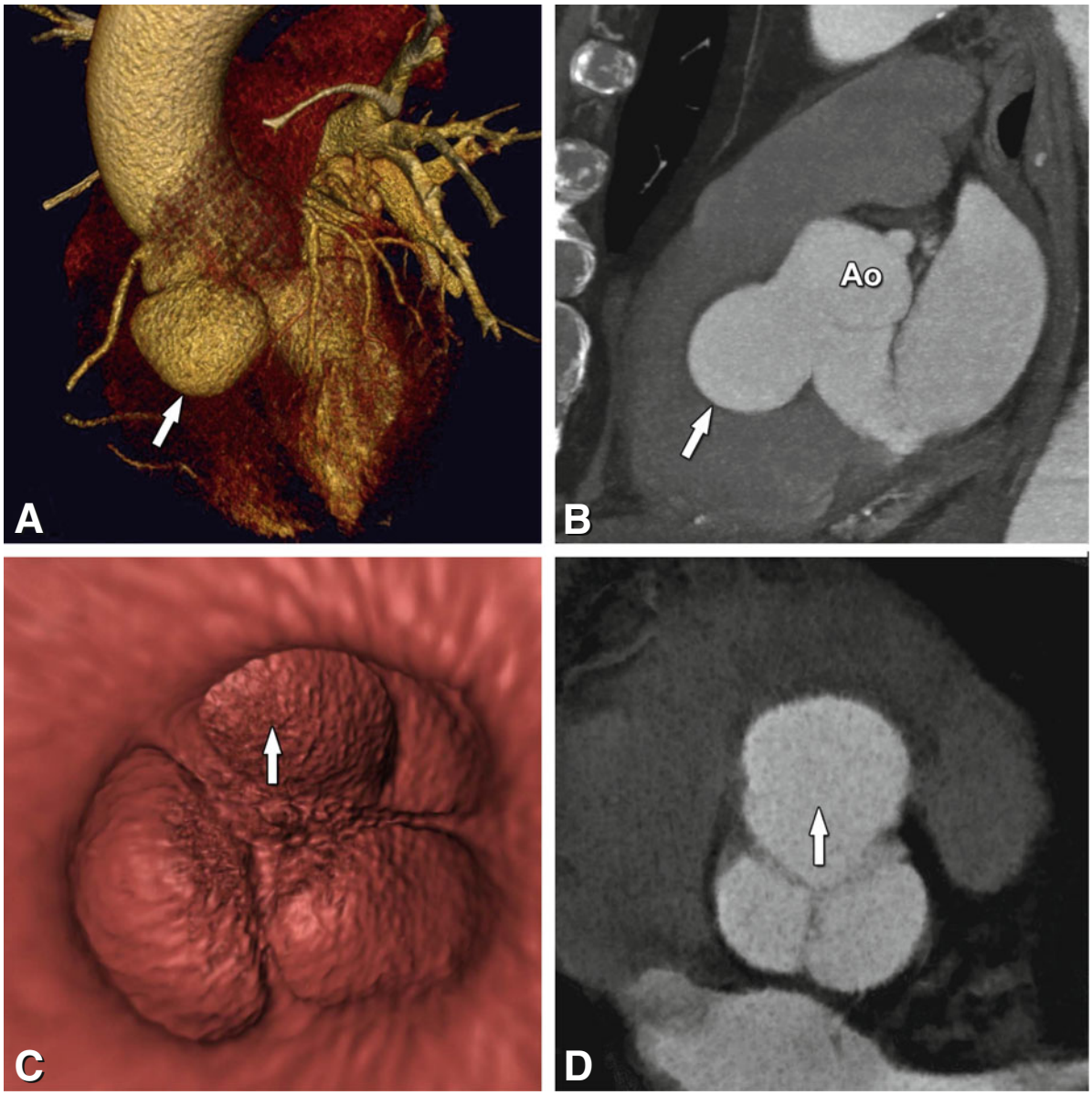

Fig. 22.17 Aneurysm of the right sinus of Valsalva (**Panel A**) in a 79-year-old male patient who was admitted with atypical angina pectoris. This 3.2 cm aneurysm (*arrow*) protrudes into the right ventricle (**Panels A** and **B**). An endoluminal view (**Panel C**) and a minimum intensity projection (**Panel D**) are shown for comparison; CT did not detect any significant coronary artery stenosis. No fistula or pericardial effusion was seen on CT. Because of the patient's age and normal global function on CT and transthoracic echocardiography, surgery was not considered further. *Ao* aorta

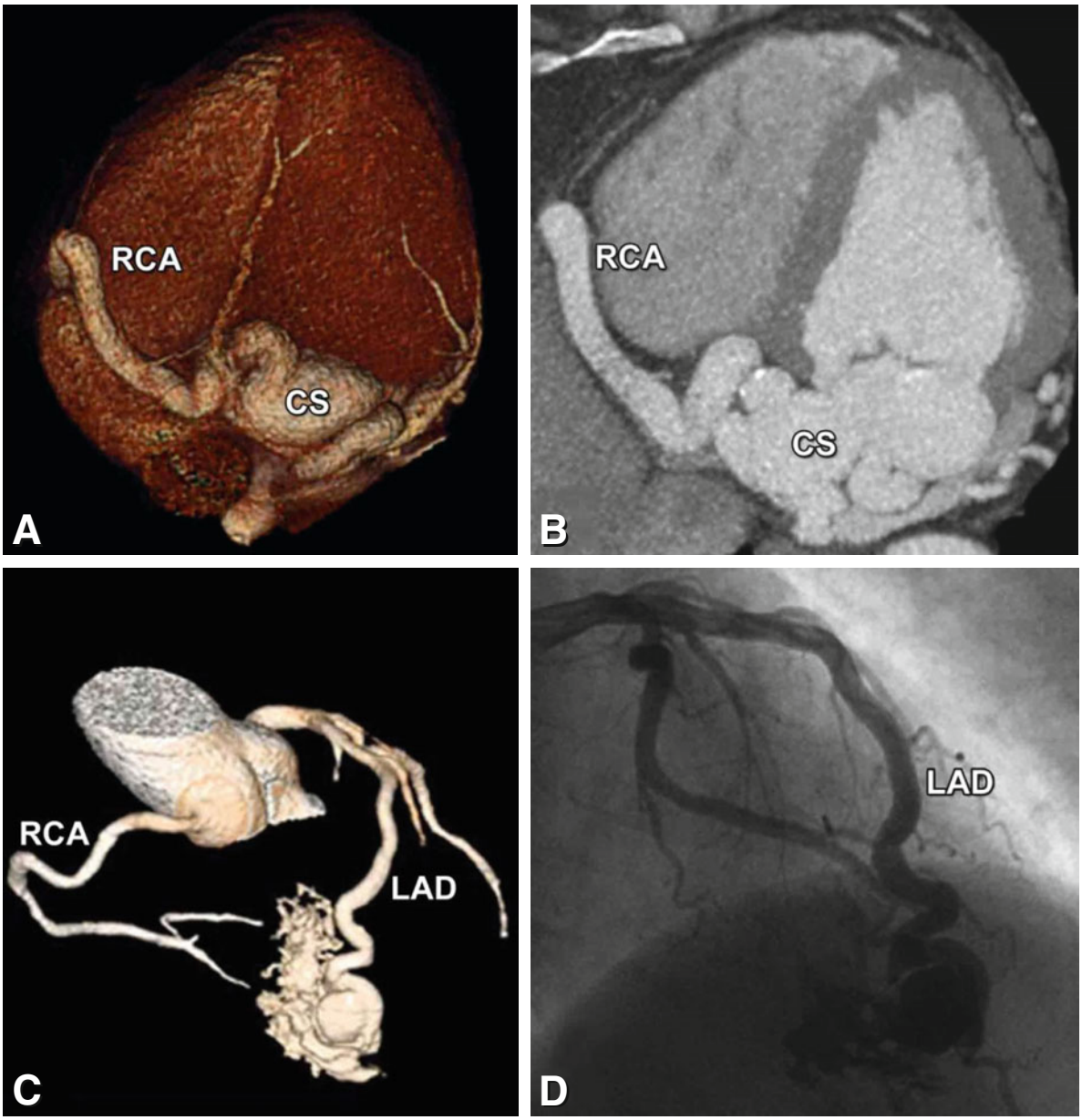

Fig. 22.18 Examples of abnormal termination of coronary arteries. Fistula between the right coronary artery (*RCA*) and the coronary sinus (*CS*) depicted by three-dimensional reconstruction (**Panel A**) and multiplanar reformation (**Panel B**). Fistula in a different patient between the left anterior descending coronary artery (*LAD*) and the right ventricle displayed on three-dimensional reconstructions (**Panel C**) and the corresponding conventional angiogram (**Panel D**) (With permission from Cademartiri et al. *European Radiology* 2007)

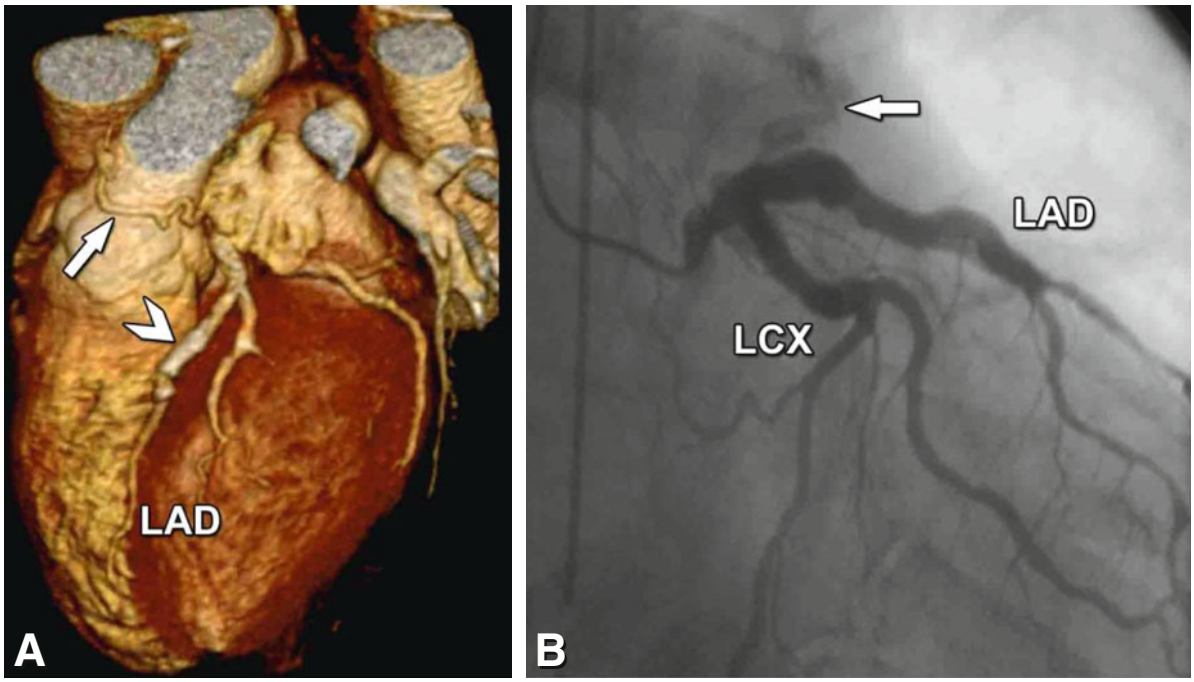

Fig. 22.19 Coronary-pulmonary fistula in a 65-year-old patient who was referred to evaluate the patency of a stent in the proximal left anterior descending coronary artery (LAD) (*arrowhead* in **Panel A**). Additionally, a small shunt vessel between the LAD and pulmonary artery (*arrow*) is seen (**Panel A**), which was verified by conventional coronary angiography (**Panel B**). **Panel A** is a three-dimensional volume rendering. *LCX* left circumflex coronary artery (Images courtesy of T. Bley, Würzburg, Germany)

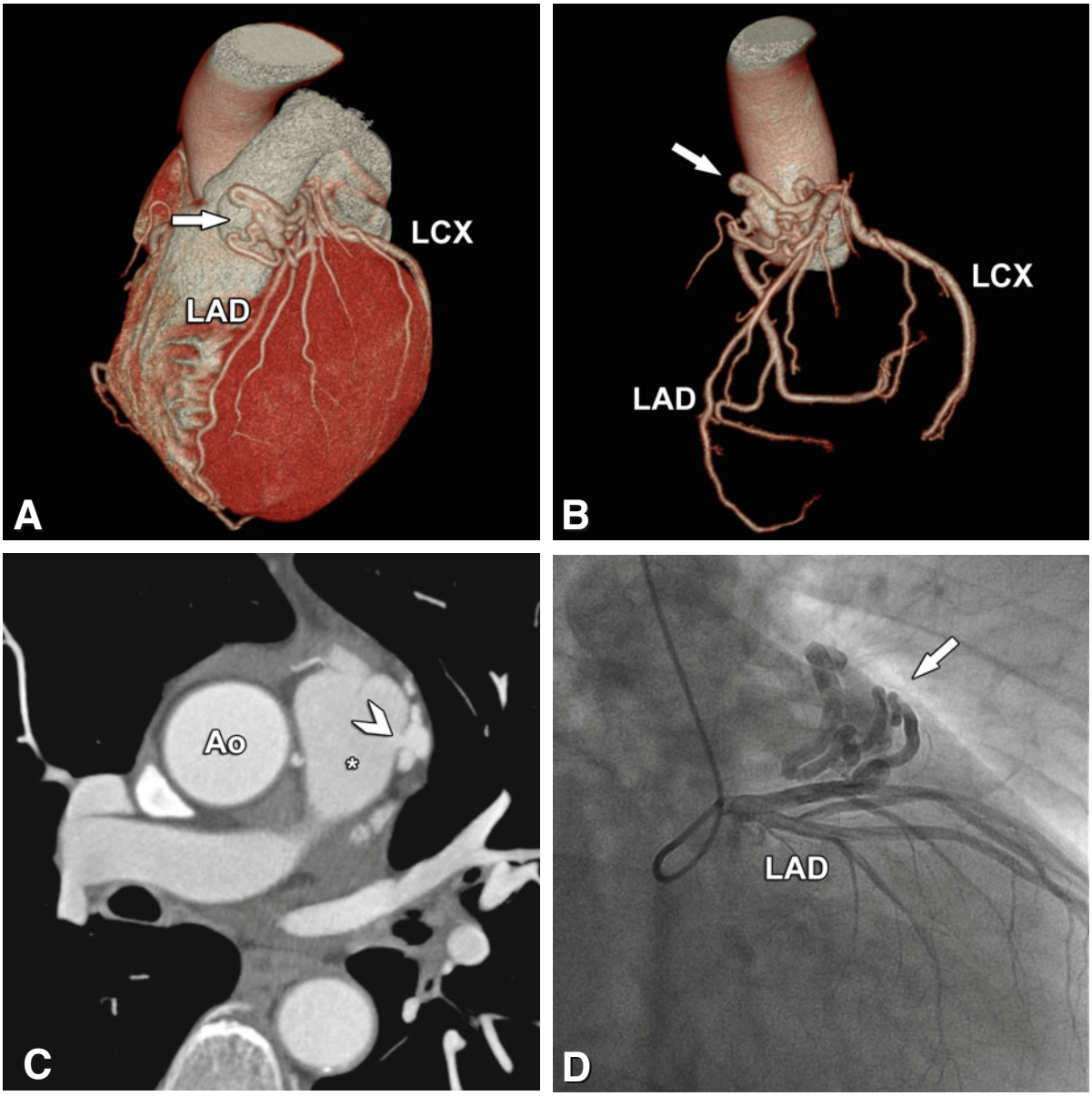

Fig. 22.20 Large fistula between the left anterior descending coronary artery (*LAD*) and the pulmonary trunk in a 59-year-old male patient with suspected coronary artery disease. **Panels A** and **B** are three-dimensional volume-rendered images of the heart and the coronary tree showing the large fistula in the area of the proximal LAD (*arrow*). **Panel C** is an axial maximum-intensity projection, which shows the ostium (*arrowhead*) of the fistula to the pulmonary trunk (*asterisk*). The corresponding coronary angiogram is presented in **Panel D**. Due to the high shunt volume, this fistula was interventionally occluded. *Ao* aorta, *LCX* left circumflex coronary artery

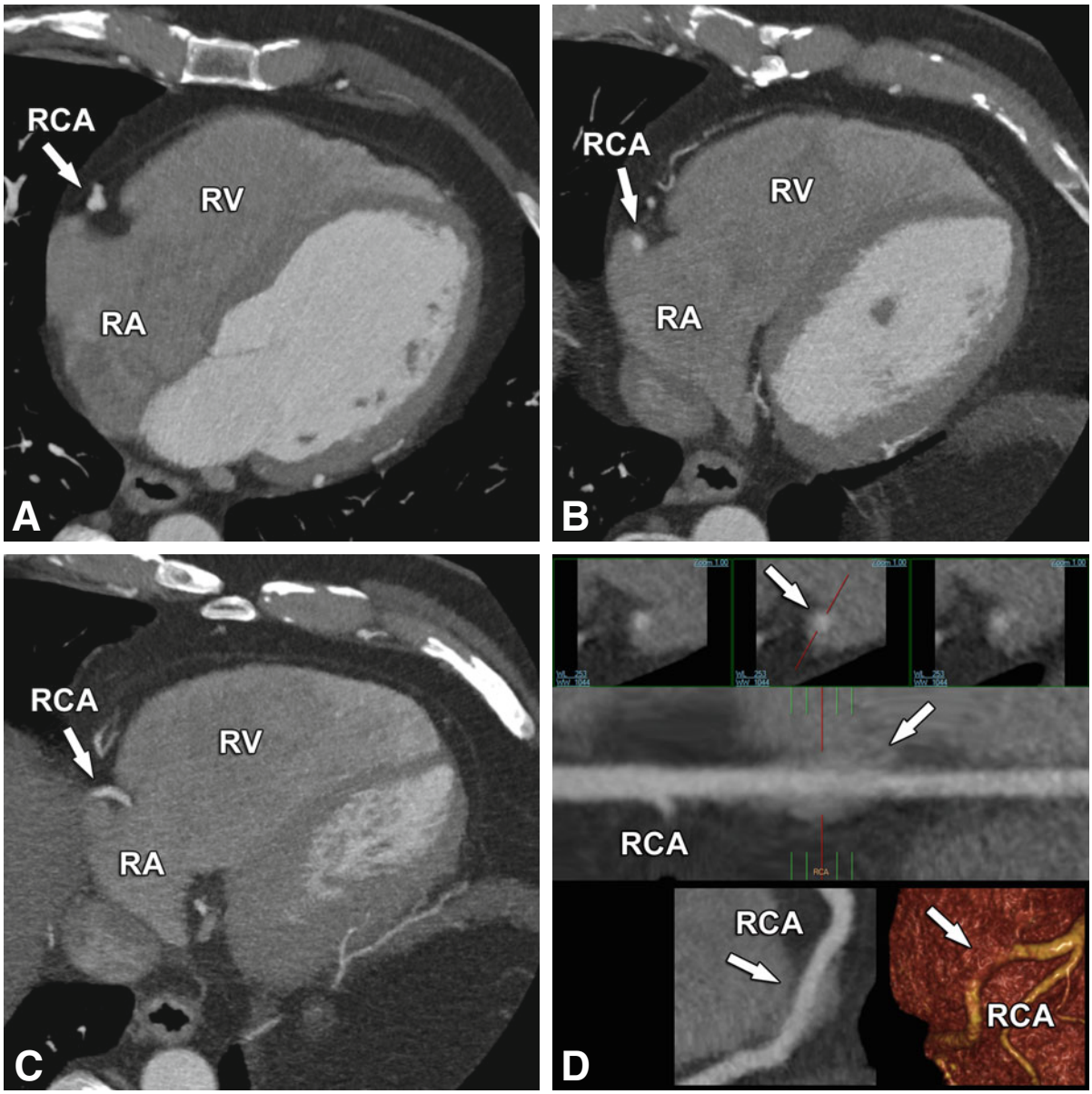

Fig. 22.21 Potential intra-atrial/intramural course of the right coronary artery (*RCA*) through the right atrium (*RA*) in a 46-year-old male patient. **Panels A**–**C** are axial maximum-intensity projections above, at, and below the intra-atrial course, respectively. The cross-sectional views, curved multiplanar reformation, and three-dimensional volume-rendered reconstruction (**Panel D**) show that the mid-RCA is partly covered by tissue (*arrow*). Such an intra-atrial course of a coronary artery without significant obstruction is likely clinically irrelevant, similar to most cases of myocardial bridging. *RV* right ventricle

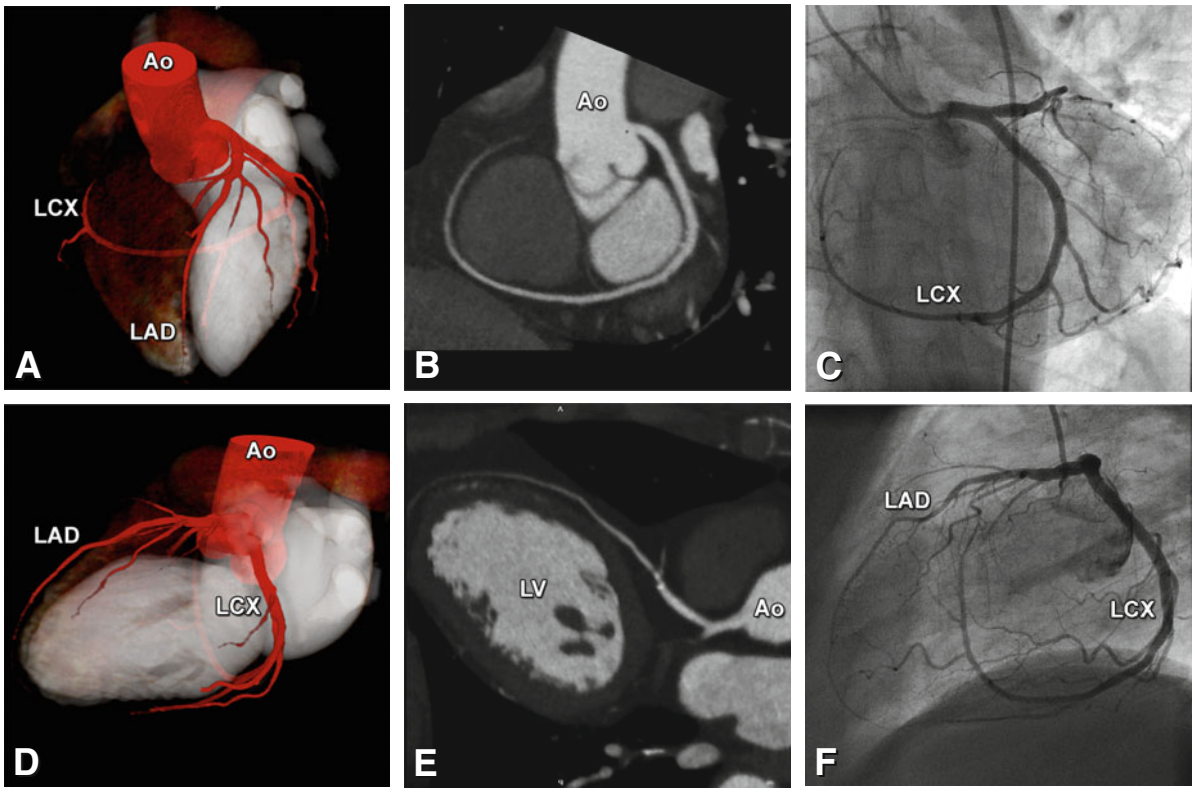

Fig. 22.22 Single coronary artery in a 59-year-old female patient admitted with chest pain radiating into the left arm. **Panel A** shows a three-dimensional CT reconstruction that demonstrates the left coronary artery originating from the left sinus Valsalva with the left circumflex coronary artery (*LCX*) running in both the left and right atrioventricular grooves and supplying the entire inferior segments of the myocardium. Note that there is no right coronary artery. According to Lipton et al. this would be classified as an L-I single coronary. **Panel B** shows a curved multiplanar reformation of LCX. **Panel C** is a caudal view of the LCX obtained by conventional coronary angiography. In the bottom row a three-dimensional CT reconstruction and a curved multiplanar reconstruction of the left descending artery (*LAD*, **Panels D** and **E**) are shown, respectively. Additionally **Panel F** shows a lateral view of both the LAD and LCX during conventional coronary angiography. Coronary artery disease was ruled out on CT and conventional coronary angiography. Further tests including stress electrocardiogram and adenosine stress magnetic resonance imaging ruled out stress induced ischemia. In conclusion, the patient's medication was adjusted (addition of ACE inhibitor and beta blocker) and she was discharged. *Ao* aorta, *LV* left ventricle (Images courtesy of J. Greupner and F. Blaschke, Berlin)

22.4 Cardiac CT

The major advantage of coronary CT in the diagnostic workup of a suspected coronary anomaly is the better anatomic depiction of the origin and course of the coronary arteries. CT is often performed after conventional coronary angiography, either because the latter could not detect a coronary artery or because the course of an anomalous coronary artery did not become absolutely clear.

A CT examination performed for delineation and evaluation of coronary anomalies is similar to standard coronary CT angiography. Emphasis has to be put on secondary reformations, which are important to capture the path of the anomalous vessels, e.g., with double-oblique maximum intensity projections, curved multiplanar reformations, globe views, map views, cath views, and angiographic emulations. In patients with suspected coronary artery anomalies, coronary CT angiography is considered an appropriate indication (Chap. 5). Interestingly, recent publications suggest that coronary anomalies may even be depicted by noncontrast CT, as it is used for coronary artery calcium scoring (Chap. 11). CT is the most accurate and robust noninvasive modality for depicting coronary anomalies. In young patients, magnetic resonance imaging should be preferred though if no contraindications to this test exist.

Recommended Reading

Angelini P (2007) Coronary artery anomalies: an entity in search of an identity. Circulation 115:1296–1305

Angelini P, Velasco JA, Flamm S (2002) Coronary anomalies: incidence, pathophysiology, and clinical relevance. Circulation 105:2449–2454

Bernanke DH, Velkey JM (2002) Development of the coronary blood supply: changing concepts and current ideas. Anat Rec 269:198–208

Borjesson M, Pelliccia A (2009) Incidence and aetiology of sudden cardiac death in young athletes: an international perspective. Br J Sports Med 43:644–648

Cademartiri F, La Grutta L, Malagò R et al (2008) Prevalence of anatomical variants and coronary anomalies in 543 consecutive patients studied with 64-slice CT coronary angiography. Eur Radiol 18:781–791

Cheitlin MD, MacGregor J (2009) Congenital anomalies of coronary arteries: role in the pathogenesis of sudden cardiac death. Herz 34:268–279

Davies JE, Burkhart HM, Dearani JA et al (2009) Surgical management of anomalous aortic origin of a coronary artery. Ann Thorac Surg 88:844–847

Dodd JD, Ferencik M, Liberthson RR et al (2007) Congenital anomalies of coronary artery origin in adults: 64-MDCT appearance. AJR Am J Roentgenol 188:W138–W146

Jappar IA, Chua T, Htoo MMA et al (2012) Diagnosis of anomalous origin and course of coronary arteries using non-contrast cardiac CT scan and detection features. J Cardiovasc Comput Tomogr 6:335–345

Kang JW, Seo JB, Chae EJ et al (2008) Coronary artery anomalies: classification and electrocardiogram-gated multidetector computed tomographic findings. Semin Ultrasound CT MR 29:182–194

Kim SY, Seo JB, Do KH et al (2006) Coronary artery anomalies: classification and ECG-gated multi-detector row CT findings with angiographic correlation. Radiographics 26:317–333; discussion 333–314

Kini S, Bis K, Weaver L (2007) Normal and variant coronary arterial and venous anatomy on high-resolution CT angiography. AJR Am J Roentgenol 188:1665–1674

Lee HJ, Hong YJ, Kim HY, Lee J, Hur J, Choi BW, Chang HJ, Nam JE, Choe KO, Kim YJ (2012) Anomalous origin of the right coronary artery from the left coronary sinus with an interarterial course: subtypes and clinical importance. Radiology 262:101–108

Loukas M, Groat C, Khangura R, Owens DG, Anderson RH (2009) The normal and abnormal anatomy of the coronary arteries. Clin Anat 22:114–128

Maron BJ, Doerer JJ, Haas TS, Tierney DM, Mueller FO (2009) Sudden deaths in young competitive athletes: analysis of 1866 deaths in the United States, 1980–2006. Circulation 119:1085–1092

Schmitt R, Froehner S, Brunn J et al (2005) Congenital anomalies of the coronary arteries: imaging with contrast-enhanced, multidetector computed tomography. Eur Radiol 15:1110–1121

Swaye PS, Fisher LD, Litwin P et al (1983) Aneurysmal coronary artery disease. Circulation 67:134–138

von Kodolitsch Y, Ito WD, Franzen O, Lund GK, Koschyk DH, Meinertz T (2004) Coronary artery anomalies. Part I: Recent insights from molecular embryology. Z Kardiol 93:929–937

Yamanak O, Hobbs RE (1990) Coronary artery anomalies in 126,595 patients undergoing coronary arteriography. Cathet Cardiovasc Diagn 21:28–40

Congenital and Acquired Heart Disease

S. Ley, B.K. Han, R. Arnold, and J.R. Lesser

Abstract

CT has been introduced cautiously in the pediatric and young adult cardiac patient population due to concerns about radiation. Advances in CT technology have resulted in improved spatial and temporal resolution, providing excellent image quality even in neonates with high heart rates. Radiation dose reduction techniques and rapid image acquisition techniques that limit anesthesia needs have decreased the risk of CT for children. CT is an excellent modality for specific congenital cardiac indications when information is needed to supplement echocardiographic findings and when MRI is contraindicated or considered high risk.

23.1 Introduction

Congenital heart disease (CHD) is the most common congenital anomaly. The spectrum of CHD malformations ranges from relatively simple lesions, which are hemodynamically insignificant, to very complex lesions requiring multiple interventions and lifelong surveillance. About two to three out of 1,000 newborns are born with complex congenital heart disease. A majority of patients with even the most complex anomalies are expected to survive to adulthood. There are now more adults with palliated CHD than those followed in the traditional pediatric age range.

Echocardiography remains the most widely used diagnostic modality for patients with CHD, and when additional information is needed, magnetic resonance imaging (MRI) is the procedure most commonly performed. Cardiac CT is primarily used when there are

M. Dewey, *Cardiac CT*,
DOI 10.1007/978-3-642-41883-9_26, © Springer-Verlag Berlin Heidelberg 2014

contraindications to MRI or imaging artifacts degrade diagnostic quality.

CT angiography (CTA) in CHD patients is most commonly indicated for evaluation of arterial and venous anomalies in newborns and for postoperative evaluation of complex disease in older children and adults with contraindications to MRI. This chapter focuses on the most frequent CHD diagnoses referred for CTA and the lesions most commonly found on studies ordered for different indications.

23.2 Technical Considerations

All aspects of CT in the CHD population must be tailored to the size of the patient and the referral indication for imaging. Well-trained CT technicians and direct physician oversight of the exam are required for the complex CHD population due to the variability of patient anatomy and physiology.

23.2.1 Size of Vascular Structures

The submillimeter isotropic resolution of today's CT scanners provides excellent visualization of even small vessels. As children get older, the diameters of all structures increase in size proportionate to growth (**Table 23.1**). Pediatric cardiac structures are often indexed to body surface area from infancy through adolescence. When no CT-specific data are available for indexing a structure to body surface area, echocardiography-based standard deviations (z-score) may be used. A z-score is the number of standard deviations from the 50th percentile for a cardiac structure based on a normal distribution. Thus, a positive standard score represents a deviation above the mean, while a negative standard score represents a deviation below the mean.

23.2.2 Heart Rate and Premedication for Coronary Artery Imaging

The resting heart rates of infants, children, and adolescents are higher than those of adults, and there is more heart rate variability with respiratory changes (sinus arrhythmia, **Table 23.2**). The image acquisition window of current-generation CT scanners is as low as 75 ms, allowing coronary imaging even at higher heart rates. Coronary artery imaging is recommended in pediatric patients for evaluation of potentially malignant coronary artery anomalies, after surgical manipulation or reimplantation, and for evaluation of stenosis or coronary pathology in patients with a history of Kawasaki disease, systemic inflammatory disease, or Williams Beuren syndrome (aortic or pulmonary artery stenosis).

Beta blockade and other medication protocols have been used safely in healthy children to decrease the heart rate and improve the quality of coronary imaging. For patients with chronic heart failure or in those who are critically ill, beta blockade may be clinically

Table 23.1 Age-related diameters and growth rate of great arteries in children

Vessel	Day 1 (mean weight: 2.2 kg)	Three years (mean weight: 20 kg)	Weight-adapted growth per kg weight gain
Ascending aorta (mm)	8.4	14	0.43
Aortic arch (mm)	6.8	14.4	NA
Aortic isthmus (mm)	4.7	8.3	NA
Main pulmonary artery (mm)	7.5	14	0.5
Right pulmonary artery (mm)	4.3	8.6	0.33
Left pulmonary artery (mm)	4.2	8.8	0.35

Data were obtained in 130 normal newborns and infants by Trowitzsch et al.; diameters were measured by echocardiography. Linear growth of the great arteries within the first 3 years of life was found
NA not available

Table 23.2 Age-related heart rates in children

Age (years)	Heart rate (beats per min)
<1	110–160
1–2	100–150
2–5	95–140
5–12	80–120
>12	60–100

contraindicated (Chap. 6). The use of premedication must be tailored to individual patients and their current clinical status.

23.2.3 Respiratory and Motion Artifacts

The newest-generation volumetric or high-pitch scanners can acquire the scan range of a pediatric thorax in one heart beat, or a fraction of a second, which has reduced anesthesia and intubation needs in young patients. Many scans can be performed during free breathing without loss of image quality due to motion artifacts. For some older-generation scanners with image acquisition over several seconds, intubation or sedation may be required to obtain a scan without respiratory motion artifacts. The use of anesthesia and sedation will be dependent on the scanner available at each institution and the amount of detail required from the CT scan.

23.2.4 Intravenous Access and Contrast Agent Injection

Many types of peripheral access can be used for cardiac CT scans in patients with congenital anomalies including peripherally inserted central catheter (PICC) lines, umbilical venous lines, peripheral intravenous (IV) lines, and central venous lines. In the presence of intracardiac shunting, elimination of air bubbles in the injection is particularly important to avoid potential arterial emboli. Low flow rates are recommended when using a 24- or 22-gauge IV access. Careful observation of the IV site during a saline injection is recommended to confirm patency before the contrast agent is injected. Safe power injection through 24–18 gauge IV lines has been reported in pediatric patients. The contrast injection rate through a 24-gauge IV line is typically 0.5–1.0 ml/s and up to 1.5–2 ml/s through a 22-gauge IV access (**Table 23.3**).

23.2.5 IV Line Placement and Injection Protocols

The total contrast agent volume used for pediatric CT angiography is typically 1–2 ml/kg. For pulmonary or arterial angiography without intracardiac mixing, the IV line may be placed in any extremity and an automatic trigger used for image acquisition. A biphasic injection protocol can be used for simultaneous opacification of right- and left-sided cardiac structures.

Table 23.3 Recommended contrast agent injection protocols in children

Age (years)	Preparation
<1	24–22 G venous line as proximal as possible
	0.5–1.0 ml/s for 24 G (<100 psi)
	1–1.5 ml/s for 22 G
	1–2 ml/kg total contrast volume
1–2	22 G venous line as proximal as possible
	1–2 ml/s, psi < 150
	1–2 ml/kg total contrast volume
>2–5	22 G venous line
	2 ml/s
	1–2 ml/kg total contrast volume
>5	18–20 G venous line
	2–5 ml/s
	1–2 ml/kg total contrast volume

23.2.6 Scanning Protocol

Every pediatric CT scan must be adjusted to deliver the lowest radiation dose to obtain a diagnostic image according to the "as low as reasonably achievable" (ALARA) principle. Familiarity with the doses delivered with different scan modes is necessary and allows choosing the scan mode with the least risk for each specific indication. CT scanner output should be adjusted to the patient's size. Using dose reduction techniques allows mSv or sub-mSv imaging for many pediatric indications, including coronary artery imaging.

For anatomic scans, high-pitch or the volumetric scan mode may be used on latest-generation scanners. On older-generation scanners, anatomic scanning is most commonly performed without ECG triggering.

Coronary artery and functional imaging require ECG triggering on all scanner platforms. Several different scan modes are available for coronary artery imaging. The lowest dose technique deemed adequate for the individual patient's heart rate should be used.

For pediatric cardiovascular CT, no general recommendation for kV and mAs settings can be provided. For dose comparison, the dose length product (DLP) should

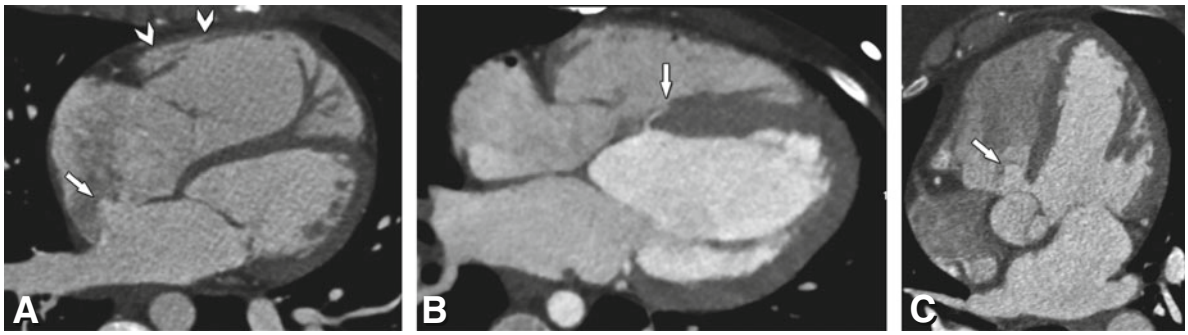

Fig. 23.1 Atrial and ventricular septal wall defects in three patients. **Panel A** shows a centrally located secundum atrial septal defect with contrast shunting from the left to right atrium (*arrow*). Note the right ventricular enlargement in this patient (*arrowheads*). The patient underwent successful device closure of the defect. **Panel B** shows a tiny basal muscular ventricular septal defect (*arrow*). This defect is located just inferior to the perimembranous area; most defects will be located more apically. Note that there was no relevant contrast jet from the left to the right ventricle and the lesion was considered hemodynamically insignificant. **Panel C** shows a large perimembranous ventricular defect located adjacent to the tricuspid valve just inferior to the aortic valve. Note the resulting positive contrast jet from the left to right ventricle in this patient (*arrow*)

be used. In our experience, a DLP as low as 4–8 mGy*cm (70 or 80 kV) is sufficient for imaging a baby weighing 3–4 kg. Only a minor increase in DLP is necessary with increasing weight, as the thoracic diameter stays rather constant during the first years of life. The most common indication for CT angiography in the neonatal CHD population is for evaluation of aortic or pulmonary artery pathology or for characterization of complex systemic and pulmonary venous anomalies prior to intervention. Many postoperative patients will have metallic implants and devices that degrade image quality of MRI. CT is also valuable for coronary artery assessment in patients with a history of Kawasaki disease aneurysm and for assessment of bileaflet mechanical valve function.

23.3 Atrial and Ventricular Septal Defects

The most common congenital anomalies are atrial (7%) and ventricular septal (31%) wall defects (**Fig. 23.1**). However, the role of CT in patients who are referred for preoperative evaluation of ventricular or atrial septal wall defects is limited. Echocardiography and MRI are the main diagnostic modalities for these lesions.

List 23.1. Aortic anomalies and defects

1. Persistent ductus arteriosus (PDA, **Fig. 23.3**)
2. Anomalies of the ascending aorta and of the aortic arch
   - (a) Hypoplastic arch (**Fig. 23.3**)
   - (b) Aortic rings
     - (i) Double aortic arch
     - (ii) Right-sided aortic arch with aberrant left subclavian artery and left-sided ductus arteriosus
     - (iii) Left-sided aortic arch with Lusoria artery
   - (c) Interrupted aortic arch
   - (d) Truncus arteriosus
3. Aortic stenosis and coarctation
   - (a) Coarctation (**Figs. 23.3** and **23.4**)
   - (b) Other aortic stenosis, e.g., subvalvular
4. Rare anomalies, e.g., aneurysm of the ductus arteriosus
5. Complications after interventions and/or surgery (**Fig. 23.4**)
6. Marfan syndrome (development of aortic root dilatation)
7. Ulrich-Turner syndrome (associated with aortic coarctation)

23.4 Aortic Arch

Congenital anomalies of the aorta are one of the most frequent cardiovascular malformations. They include a wide spectrum of diseases (**List 23.1**) ranging from patent ductus arteriosus (**Fig. 23.2**, 5–10% of all CHD) to aortic coarctation (8–10%, **Fig. 23.3**). The initial diagnosis is usually established by echocardiography. Blood pressure difference between the upper and lower extremity

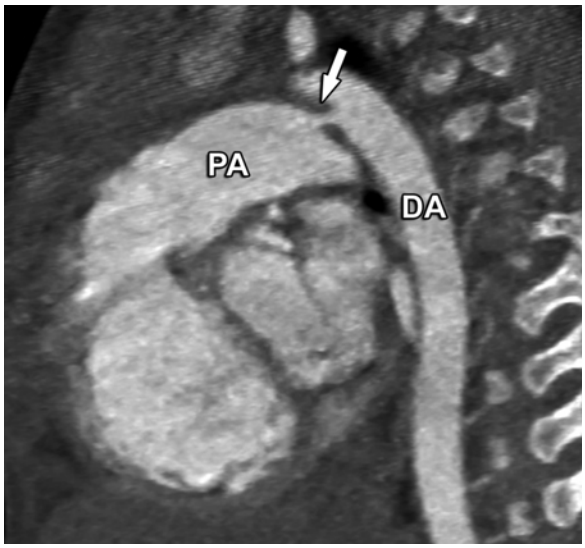

Fig. 23.2 Tiny ductus arteriosus (*arrow*) between the proximal descending aorta (*DA*) and the distal pulmonary artery (*PA*). This was an incidental finding on a CT performed for evaluation of the coronary arteries

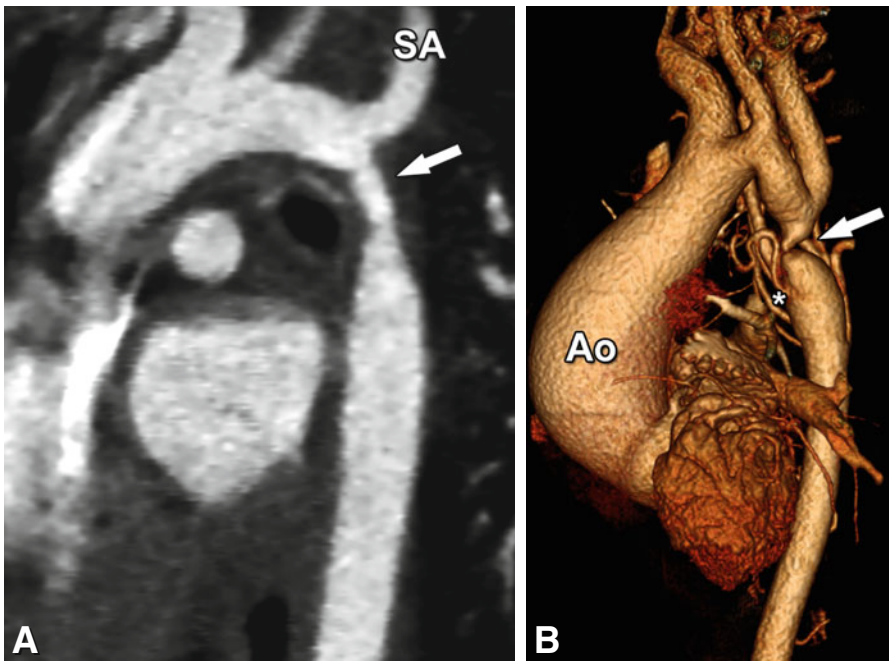

Fig. 23.3 Aortic coarctation in two patients. **Panel A** is a double-oblique image from a prospectively ECG-triggered CT scan showing coarctation in a 2-year-old patient (*arrow*) just distal to the takeoff of the left subclavian artery (*SA*). The high-pitch CT scan was performed during free breathing with an acquisition time of 0.25 s and a dose-length product of 6 Gy.cm. The patient underwent subsequent repair of coarctation with an end-to end anastomosis. **Panel B** shows a three-dimensional reconstruction of a CT scan performed for evaluation of severe aortic coarctation (*arrow*) in an 11-year-old patient who presented for evaluation of a murmur. His ascending aorta (*Ao*) was dilated and the murmur was secondary to aortic insufficiency. He was noted to be hypertensive with a blood pressure gradient of 30 mmHg between the right arm and leg. Note the collateral vessels supplying the descending aorta (*asterisk*). He underwent surgical repair of aortic coarctation and has since been followed clinically for aortic insufficiency and aortic root dilation

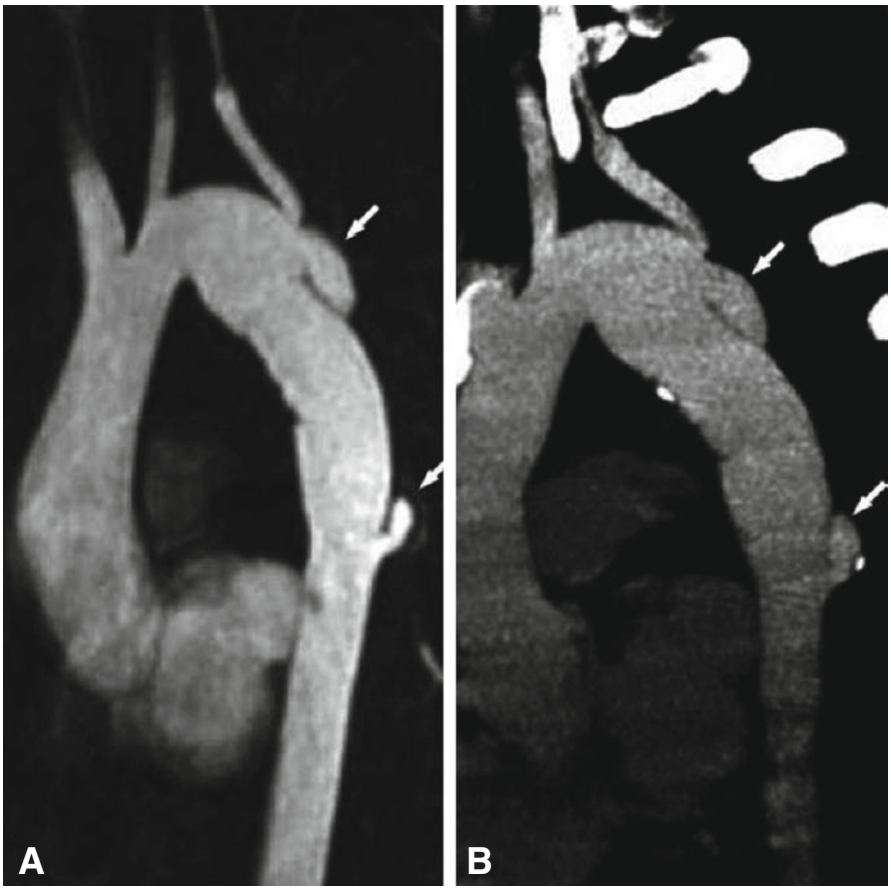

Fig. 23.4 Dissection as a complication after aortic arch operation in a 24-year-old female patient with congenital hypoplasia of the distal aortic arch and patch angioplasty at the age of 2 years. Eight years later a restenosis was diagnosed and a vascular prosthesis (16-mm Hemashield) was implanted. Regular follow-up was performed by MRI. **Panel A** is an MR angiography after intravenous contrast agent administration (10-mm double-oblique maximum intensity projection) that shows new dissections at the proximal and distal anastomosis of the prosthesis (*arrows*). For further surgical planning a nongated CT was performed (**Panel B**, 5-mm maximum intensity projection), which confirmed the MRI findings

is used to determine the pressure gradient unless there is an aberrant subclavian artery that does not allow a pre-coarctation pressure estimate. Doppler echocardiography is helpful in these cases, and catheterization is rarely required prior to surgical intervention for aortic coarctation at most centers. Noncritical stenosis or critical stenosis with well-developed collateral flow to the descending aorta is often detected in grown-ups who present with arterial hypertension and have blood pressure differences between arms and legs. Clinical indications for follow-up examinations are re-coarctation (<3%, higher when operated on in infancy) and postoperative aneurysms (24% after patch angioplasty) or dissection (5–50% after patch angioplasty, **Fig. 23.4**). Because it lacks radiation exposure and allows functional assessment (e.g., flow quantification), MRI is the preferred test in suspected coarctation (**Fig. 23.5**). As patients grow older, MRI may gain an increasing role as the acoustic window for echocardiography becomes poorer with age. CT has an indication in the follow-up of patients with coarctation who have stents, as the intraluminal visualization of stents is excellent (**Fig. 23.6**). In complex aortic arch abnormalities (i.e., double aortic arch), surgeons prefer to have a three-dimensional display of the

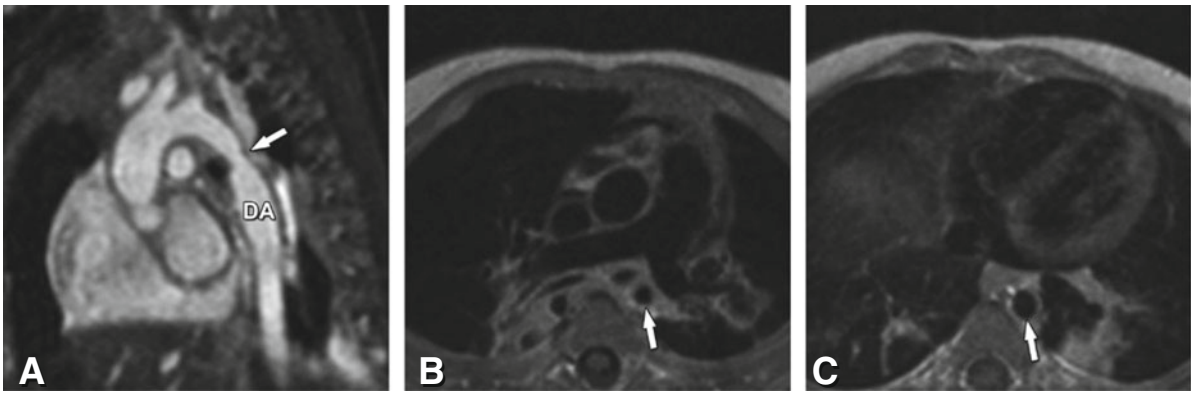

Fig. 23.5 Coarctation of the aorta in a 5-month-old male baby. **Panel A** is an ECG- and respiratory-gated steady-state free precession three-dimensional sequence (MR angiography) without contrast agent administration and demonstrates focal narrowing (*arrow*) of the descending aorta (*DA*). **Panel B** is a spin-echo MRI sequence with dark-blood pulse preparation, which shows the narrowing of the aorta in axial orientation (*arrow*), while **Panel C** shows the normal lumen of the descending aorta (*arrow*) on the same sequence at the level of the diaphragm. Note that the consolidation in the left lower lung seen on **Panel C** is due to a prior pneumonia in this patient

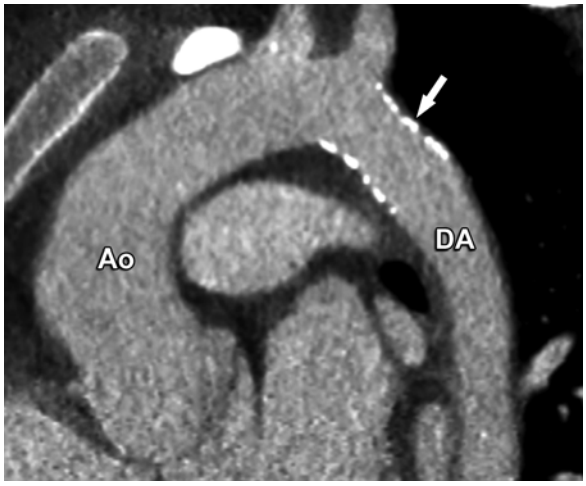

Fig. 23.6 Follow-up CT in an 18-year-old patient after interventions for aortic coarctation. The patient underwent left subclavian flap repair of aortic coarctation as an infant and later required balloon angioplasty of recurrent coarctation with stent placement (*arrow*). The CT was performed with prospective ECG triggering using 80 kV and a scan range limited to the area of interest. Note the absence of a left subclavian artery from the transverse aortic arch due to the initial repair and excellent visualization of the stent and aortic wall. *Ao* aorta, *DA* descending aorta

anatomic relationship between the trachea and the vascular structures. This information can be nicely provided by CT, even in critically ill children. A potential vascular ring associated with a right aortic arch, an aberrant left subclavian artery, and a left-sided ductal ligamentum are common and may be detected incidentally or cause pulmonary pathology. Evaluation of the airways relative to the vessels can be crucial in determining the clinical significance of the finding.

23.4.1 Persistent Ductus Arteriosus

During fetal life the ductus arteriosus connects the main pulmonary artery near its bifurcation to the aorta just beyond the origin of the left subclavian artery. The ductus arteriosus usually closes functionally soon after birth through muscular contractions. A persistent ductus arteriosus (PDA) is encountered in approximately 7% of all congenital heart defects. Echocardiography is the modality of choice for assessment of the ductus arteriosus in infants. CT is only performed if a complex malformation is suspected (**Figs.** 23.2 and 23.7).

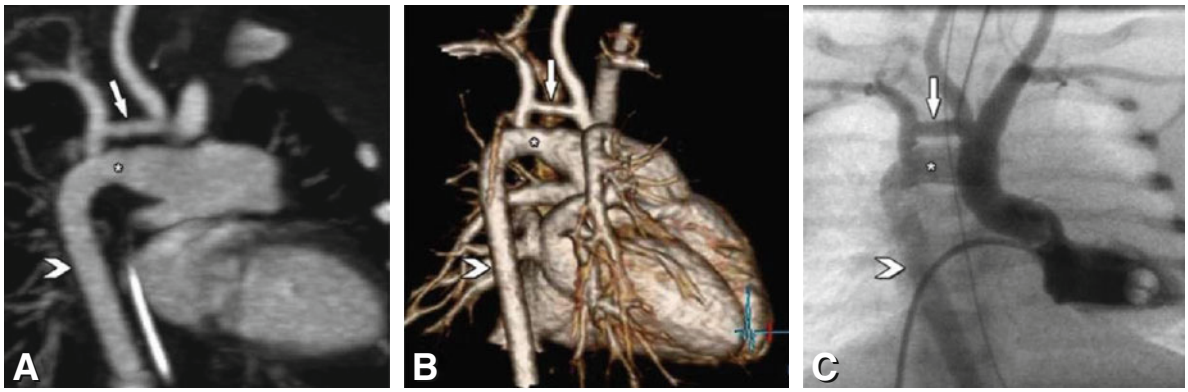

Fig. 23.7 Hypoplastic aortic arch (*arrow*) and large persistent ductus arteriosus Botalli (*asterisk*) in a 2-day-old child prenatally diagnosed with a cardiac malformation. On a double oblique maximum intensity projection (**Panel A**) the large persistent ductus arteriosus and the hypoplastic aortic arch (*arrow*) are shown. The persistent ductus arteriosus connects the main pulmonary artery and the descending aorta (*arrowhead*), which is normal. For operative planning the CT images were additionally presented to the surgeon as three-dimensional volume renderings (**Panel B**). **Panel C** presents the corresponding image from left ventricular catheterization

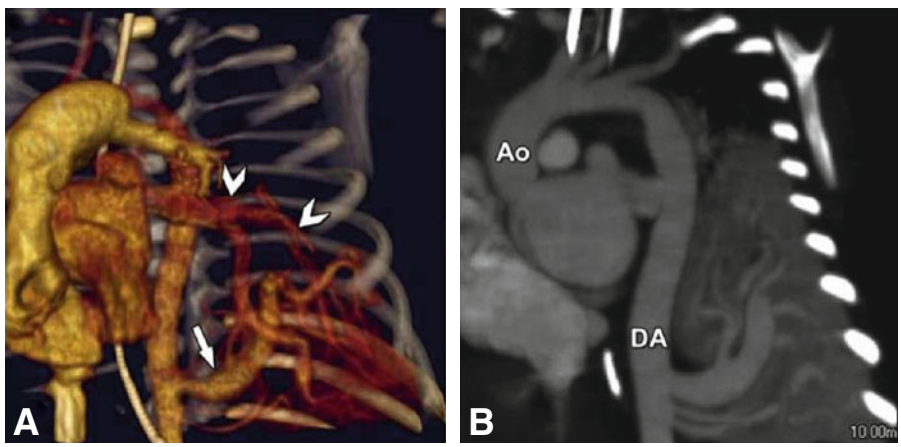

Fig. 23.8 Lung sequestration in a 15-day-old female baby with a prenatally diagnosed anomaly of the left lung. ECG-gated CT was performed using 7 ml contrast agent with 250 mg I/ml at an injection rate of 0.3 ml/s. **Panel A** shows a volume rendering of the arterial supply (three vessels) of the sequestration from the descending aorta (*arrow*). Venous drainage is to the left atrium (*arrowheads*). **Panel B** is a double-oblique maximum intensity projection along the ascending aorta (*Ao*) and descending aorta (*DA*) showing the three arteries supplying the sequestration from the *DA*. Due to the large size of the arterial supply the patient went to surgery for clipping of the arteries

23.4.2 Sequestration

Sequestration is a rare anomaly of the tracheobronchial tree. It has an estimated incidence of 0.15–1.7% in the general population. Sequestrations are classified as intralobar or extralobar. The nonfunctioning lung tissue lacks communication with the tracheobronchial tree and receives its supply from the arterial circulation. Intralobar sequestrations are the most common. The blood supply usually comes from the descending thoracic aorta, but in about 20% of cases, it comes from the upper abdominal aorta, celiac artery, or splenic artery. All pulmonary sequestrations should be treated surgically/interventionally because the high blood flow through the lesion can cause heart failure. Surgical procedures include ligation of the afferent vessels and/or resection of the pulmonary malformation.

In pulmonary sequestrations CT is superior to most other techniques, providing excellent information on both the vessels supporting the malformation (arterial and venous) and the structure of the lung parenchyma inside the malformation (**Fig. 23.8**). The spatial resolution of MR angiography may be too low to achieve adequate visualization of all vascular structures. Also, visualization of the lung parenchyma is difficult using MRI.

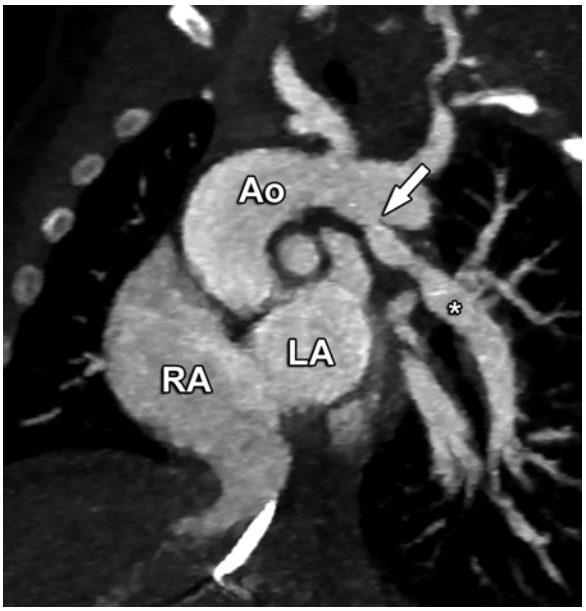

Fig. 23.9 Pulmonary artery arising anomalously from the aorta in a 2-day-old infant. This prospectively ECG-triggered high-pitch CT scan was performed without sedation and with an acquisition time of 0.25 s, 6 ml of contrast agent through a 24-G IV line, and a dose-length product of 5 Gy.cm. The image shows discontinuous pulmonary arteries, with the left pulmonary artery (*asterisk*) arising from the undersurface of the aortic arch (*Ao*, *arrow*). The patient underwent successful reimplantation of the branch pulmonary artery into the main pulmonary artery. *LA* left atrium, *RA* right atrium

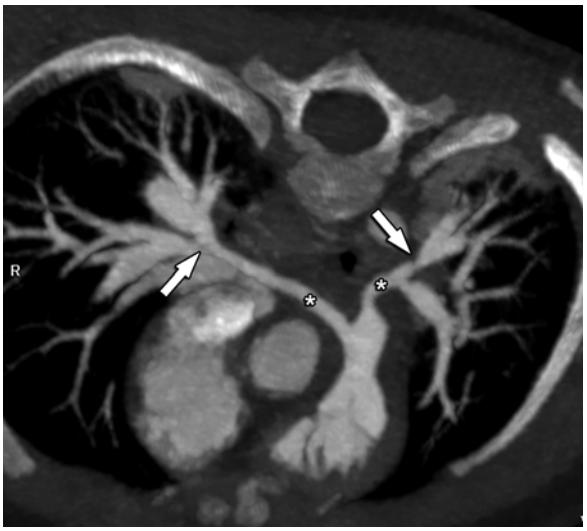

Fig. 23.10 Pulmonary branch hypoplasia in a 5-year-old patient with Williams syndrome. The 5-mm maximum intensity projection shows diffuse proximal branch pulmonary artery hypoplasia (*asterisks*) and focal distal pulmonary arterial narrowing (*arrows*). Because of the diffuse nature of the hypoplasia, no intervention was performed

23.5 Pulmonary Artery Pathology

Echocardiography is excellent for definition of the pulmonary valve and proximal pulmonary arteries, but is inadequate for distal pulmonary artery evaluation. CTA is well suited for detection of an absent pulmonary artery, a pulmonary artery arising anomalously from the aorta (**Fig. 23.9**) or aortopulmonary collateral arteries, and peripheral stenosis associated with certain genetic syndromes (**Fig. 23.10**) and for visualization of both the aortic and pulmonary arterial portions of the ductus arteriosus.

23.5.1 Origin of the Left Pulmonary Artery from the Right Pulmonary Artery (LPA Sling)

The left pulmonary artery arises aberrantly from the right pulmonary artery and runs between the trachea and esophagus to the left side, which either leads to an acute and severe airway compression (infants) or signs of chronic obstructive lung disease (childhood and young adults). Echocardiography is feasible in infants but further visualization of the airways is mandatory. CT is the recommended technique for visualization of the pulmonary arteries and the tracheobronchial tree (**Fig. 23.11**). Surgical correction is always performed with attachment of the left pulmonary artery to the pulmonary trunk anterior to the aorta.

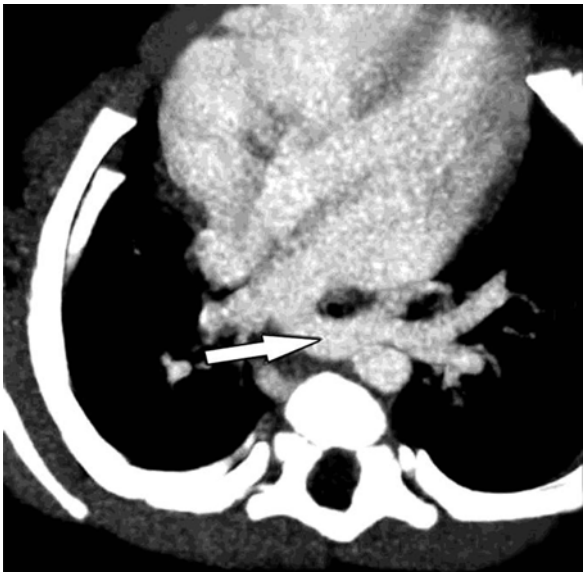

Fig. 23.11 Sling left pulmonary artery in a 5-month-old boy with a history of lower airway obstruction. Maximum intensity projection in the axial plane demonstrates a sling left pulmonary artery (*arrow*) that arises from the right pulmonary artery and courses posterior to the left main bronchus to supply the left lung. The child underwent reimplantation of the sling left pulmonary artery into the main pulmonary artery anterior to the trachea, relieving compression on the left main bronchus (With permission from A.-M. du Plessis et al. *Pediatr Radiol* 2008)

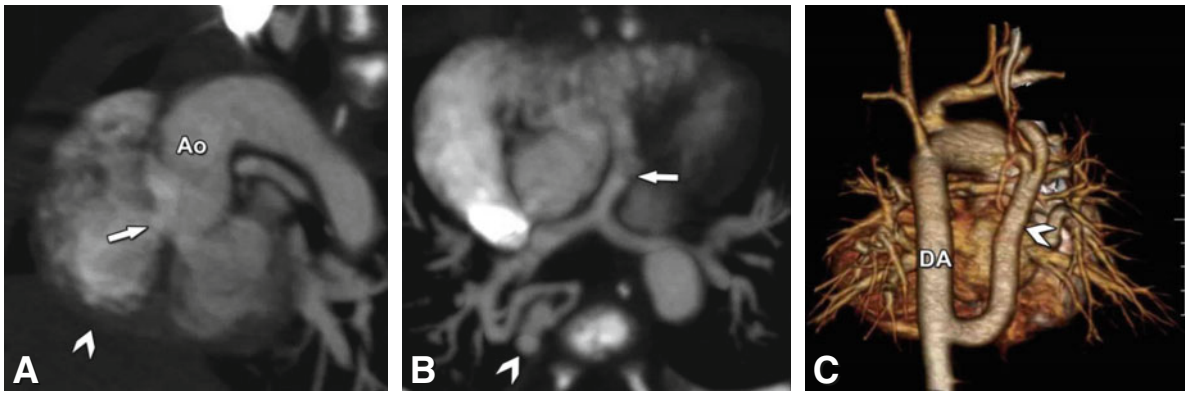

Fig. 23.12 Tetralogy of Fallot in a 1-month-old male baby. ECG-gated 16-row CT was performed using 30 ml of contrast agent with 250 mg I/ml followed by 10 ml saline at an injection rate of 1 ml/s through a venous line at the head. A larger amount of contrast agent was used to opacify the pulmonary arteries as well as the descending aorta and potential collaterals. **Panel A** (double-oblique reformation) shows the ventricular septal defect (*arrow*), the overstriding ascending aorta (*Ao*), and the right ventricular hypertrophy (*arrowhead*). **Panel B** (axial maximum intensity projection) shows the hypoplastic main (*arrow*), right and left pulmonary arteries and a large major aortopulmonary collateral artery (*MAPCA*) draining into the pulmonary arteries (*arrowhead*). The volume rendering (**Panel C**) shows the descending aorta (*DA*) and the large *MAPCA* (*arrowhead*), which is directed upwards. In this case the MAPCAs were too large for embolization and had to be clipped surgically

23.5.2 Tetralogy of Fallot

Tetralogy of Fallot (5–7% of CHD) is the most common right-sided obstructive anomaly. All forms of tetralogy include a large ventricular septal defect and varying degrees of obstruction to pulmonary outflow (**Fig. 23.12**), right ventricular hypertrophy, and aortic override of the ventricular septum. Surgical palliation includes septal defect closure and relief of the right ventricular outflow tract obstruction with a valvotomy, a patch, or a conduit from the right ventricle to the branch pulmonary arteries.

In tetralogy of Fallot with pulmonary artery atresia, lung perfusion is partly or completely provided by collaterals arising from the aortic arch. Defining the architecture of the central pulmonary arteries and aortopulmonary collaterals is essential for determining if the patient is suitable for primary correction. In patients with very small true pulmonary arteries and multiple aortopulmonary collateral vessels, a palliative shunt with unifocalization of the collaterals and pulmonary arteries is typically performed prior to complete repair. Subsequent corrective or palliative operations are usually possible, depending on the growth of the pulmonary arteries. The first aortopulmonary shunt described was the Blalock-Taussig shunt, connecting the subclavian artery to the ipsilateral pulmonary artery in cyanotic patients with tetralogy of Fallot (1944). Modified Blalock-Taussig shunts, central aortopulmonary shunts (using Goretex®), and direct connections of the hypoplastic pulmonary trunk to the aorta are in use today (**Fig. 23.12**). CT has been shown to correlate well with catheterization for evaluation of aortopulmonary collateral anatomy in patients with pulmonary artery atresia (**Fig. 23.12C**).

After complete repair of tetralogy, residual pulmonary stenosis and insufficiency are common and have a detrimental long-term effect on right ventricular function. Reintervention should be timed by evaluation of right ventricular end diastolic volume, end systolic volume, and right ventricular function. This data is most commonly obtained with MRI, but can be obtained with a functional CT dataset in patients with pacemakers or metal artifacts.

The incidence of additional coronary arterial anomalies in patients with tetralogy of Fallot is between 8 and 36%. The following anomalies in the course and/or distribution of the coronary arteries have been described: single coronary ostium, left anterior descending artery arising from the right coronary artery, circumflex artery arising from the right coronary artery, small fistulas between coronary arteries and the pulmonary artery, fistulas between coronary and bronchial arteries or right atrium. For CT in children with tetralogy of Fallot, a high diagnostic accuracy of 95.5% for all disease-related issues (compared to surgical findings) was found in a pilot study. Coronary artery anomalies are significant if they cross the right ventricular outflow tract and affect the planned surgical intervention.

In patients with a previously placed right ventricular outflow tract conduit or stent, CTA can be used to define the dimensions of the proximal and distal conduit, the branch pulmonary arteries, the in-stent luminal dimension, and the coronary artery relationship to the right ventricular outflow tract (**Figs.** 23.13, 23.14, and 23.15).

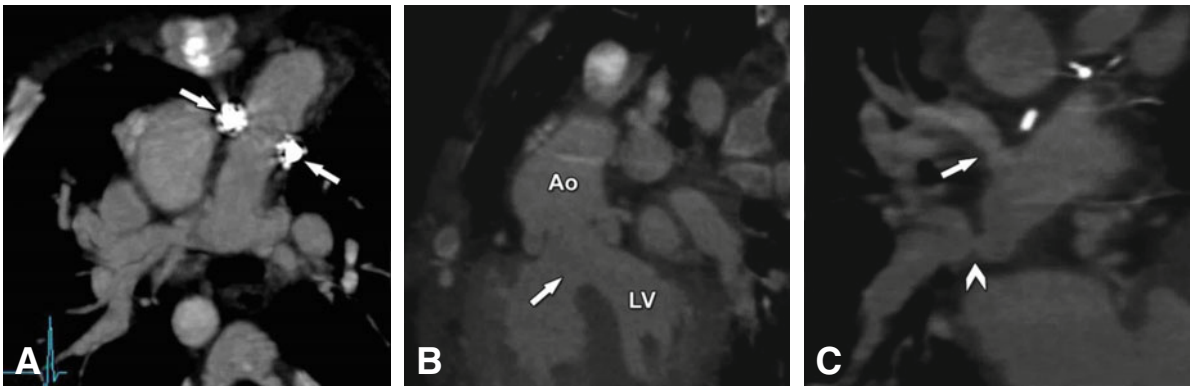

Fig. 23.13 Status post implantation of a pulmonary valve conduit (*arrows*) in a 2-year-old boy with tetralogy of Fallot (**Panel A**). **Panel B** shows the position of the ascending aorta (*Ao*) overstriding the large ventricular septal defect (*arrow*) between the right and left ventricle (*LV*). The examination was indicated to evaluate the anastomosis of the conduit to the native pulmonary arteries (*arrow* and *arrowhead* in **Panel C**). A focal stenosis of the lower lobe pulmonary artery (*arrowhead* in **Panel C**) can be seen. Interestingly, using MRI the spatial resolution was insufficient for precise visualization of the anastomoses, and interpretation was additionally impaired by artifacts from the mediastinal clips

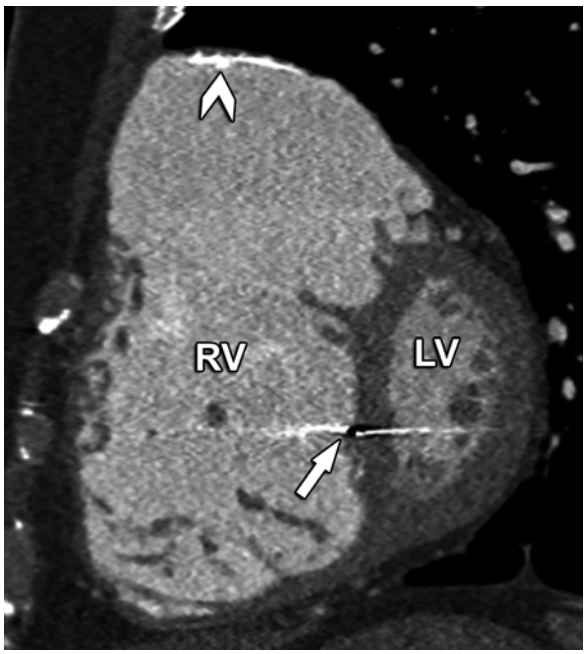

Fig. 23.14 This 30-year-old patient with repaired tetralogy of Fallot had severe pulmonary insufficiency and right ventricular enlargement. The scan was reconstructed in the short axis view from a functional CT scan. Note the transvenous pacer lead beam hardening artifact (*arrow*) and the calcified transannular patch (*arrowhead*). The patient underwent right ventricular outflow tract conduit placement. *LV* left ventricle, *RV* right ventricle

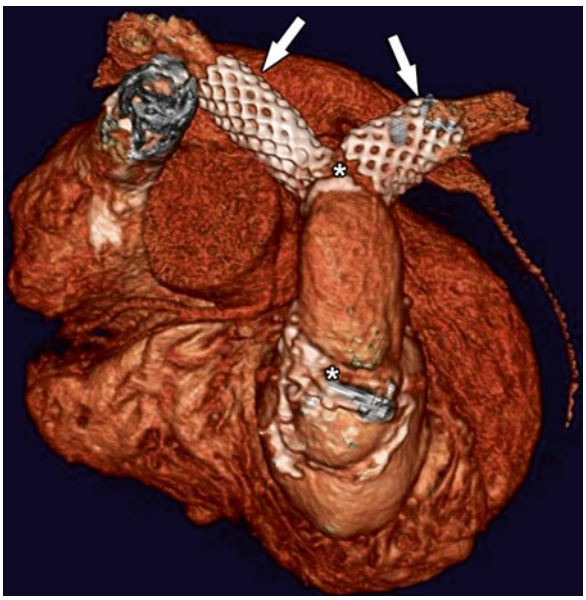

Fig. 23.15 This 20-year-old patient had a right ventricular outflow tract gradient on echocardiography, but the exact site of obstruction was unclear. A CT scan was performed because prior MR images were limited by artifacts. The three-dimensional reconstruction shows bilateral branch pulmonary artery stents (*arrows*) and extensive calcification of the proximal and distal conduit (*asterisks*). The pulmonary artery stents were patent (not shown). The patient underwent subsequent right ventricular outflow tract conduit placement

23.6 Left-Sided Heart Disease

Left-sided obstruction may occur at the level of the pulmonary veins, left atrium (cor triatriatum, Chap. 21), mitral valve, left ventricular outflow tract, or aortic arch (**List 23.2**). Patients may have obstruction at many levels and often have more than one lesion simultaneously. CT is excellent for visualization of total or partial anomalous pulmonary venous return (**Figs. 23.16** and **23.17**) and for complex arch anomalies, but most other lesions are seen very well echocardiographically. CTA is well suited to show the area of anatomic narrowing in cases of obstructed total or partial anomalous pulmonary venous return or the multiple sites of drainage in mixed anomalous pulmonary venous return. A small percentage of patients with obstructed total or partial anomalous pulmonary venous return will go on to develop pulmonary venous stenosis subsequent to repair, and the individual pulmonary vein, site and length of obstruction are well visualized by CTA.

Congenital anomalies of the aortic arch are common. Advanced imaging is usually requested for native arch pathology when there are associated cardiac anomalies or unusual features. CTA can detect aortic aneurysm, recurrent arch obstruction, or stent integrity and in-stent stenosis in patients who have undergone previous catheter-based or surgical intervention. CT can visualize the anatomy of an interrupted aortic arch, unusual ductus arteriosus, or truncus arteriosus to define aortopathy associated with Williams or Marfan syndrome.

List 23.2. Left-sided heart disease

1. Anomalous pulmonary venous return
   - Total anomalous pulmonary venous return (**Fig. 23.16**)
     - Cardiac
     - Infracardiac
     - Supracardiac
     - Mixed
   - Partial anomalous pulmonary venous return (often associated with atrial septal defects)
2. Pulmonary vein stenosis
3. Cortriatriatum (Chap. 21)
4. Aortic coarctation (**Figs. 23.3** and **23.4**)
   - Status post intervention (**Fig. 23.6**)
5. Interrupted aortic arch
6. Hypoplastic left heart syndrome
7. Aortopathy
   - Williams syndrome (**Fig. 23.10**)
   - Marfan syndrome

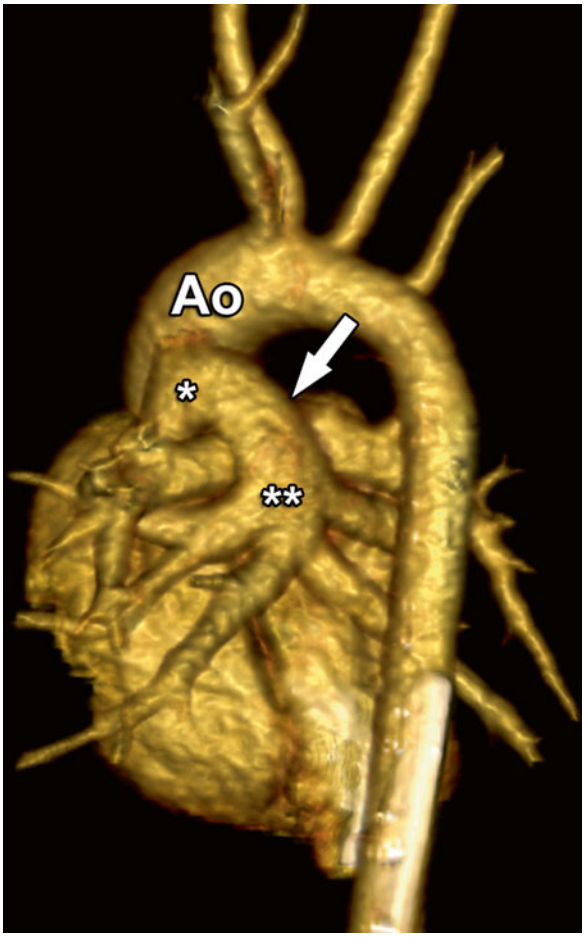

Fig. 23.16 This neonate presented with total anomalous pulmonary venous return (*TAPVR*) to the left superior vena cava (*asterisk*). A free-breathing CT scan was performed using 2 ml/kg of contrast agent injected through a 24-G IV line. The posterior view of a three-dimensional reconstruction shows the vertical vein (*arrow*) coursing over the left pulmonary artery and parallel to the aorta (*Ao*). The pulmonary venous confluence is indicated by two *asterisks*. The patient underwent TAPVR repair with connection of the pulmonary venous confluence to the left atrium

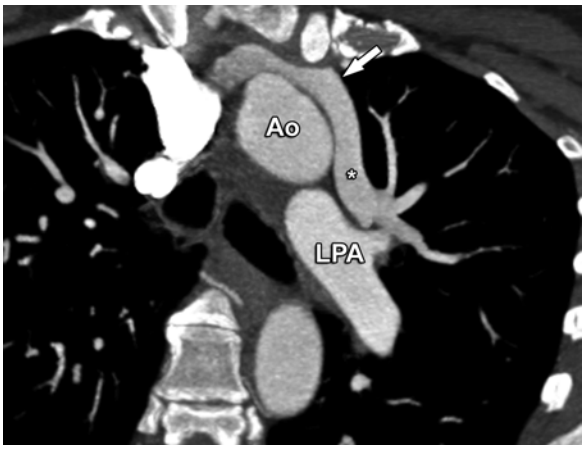

Fig. 23.17 Incidental finding of partial anomalous pulmonary venous return on a CT scan performed for coronary angiography. The axial maximum intensity projection shows the anomalous left upper pulmonary vein (*asterisk*) draining to the innominate vein (*arrow*). Due to the small shunt, no intervention was performed. *Ao* aorta, *LPA* left pulmonary artery

23.7 Transposition of the Great Arteries

Transposition of the great arteries (3–5% of newborn CHD) usually refers to isolated transposition of the great arteries (ventriculoarterial discordance, **Fig. 23.18**). Many older patients will have had an atrial switch, and younger patients will have undergone an arterial switch (**Fig. 23.19**). CTA easily visualizes the systemic and pulmonary venous baffles after atrial switch (**Figs. 23.18** and **23.19**) or the branch pulmonary arteries after the LeCompte maneuver (**Fig. 23.19C**), the reimplanted coronary arteries, and the neoaortic and neopulmonary root after the arterial switch. Although recent surgical outcomes are excellent, long-term follow-up for complications is required and repeat intervention is necessary in a minority of patients. Studies have shown that CTA correctly visualizes significant coronary lesions in these patients compared to catheterization angiography. L-TGA is also called physiologically corrected transposition and refers to both atrioventricular and ventriculoarterial

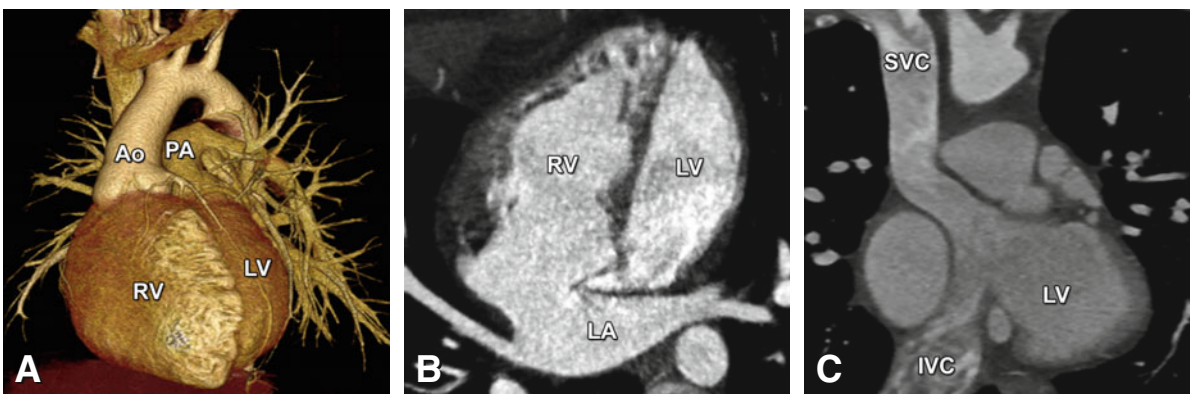

Fig. 23.18 A 27-year-old patient after atrial switch operation performed for transposition of the great arteries in the first year of life. CT images were acquired prospectively using high-pitch helical scanning. The three-dimensional reconstruction shown in **Panel A** illustrates d-transposition of the great arteries, with the anterior and rightward aorta (*Ao*) arising from the right ventricle (*RV*) and the leftward and posterior pulmonary artery (*PA*) arising from the normally positioned left ventricle (*LV*). Follow-up with echocardiography and possibly MRI will be required to screen for systemic right ventricular dysfunction, which is the most common reason for reduced life expectancy of patients with an atrial switch. **Panel B** shows the pulmonary venous baffle to the systemic right ventricle. This baffle is created at the time of the atrial switch to allow pulmonary venous blood to enter the right atrium and then fill the systemic right ventricle. **Panel C** is a coronal maximum intensity projection showing widely patent systemic venous baffles from the superior and inferior vena cava (*SVC* and *IVC*) to the *LV* after the atrial switch. Systemic venous baffle obstruction may occur in the future and is monitored by serial echocardiography or possibly MRI. It is important to assess baffle patency by opacification of the systematic venous system on CT in any patient with prior d-TGA and an atrial switch

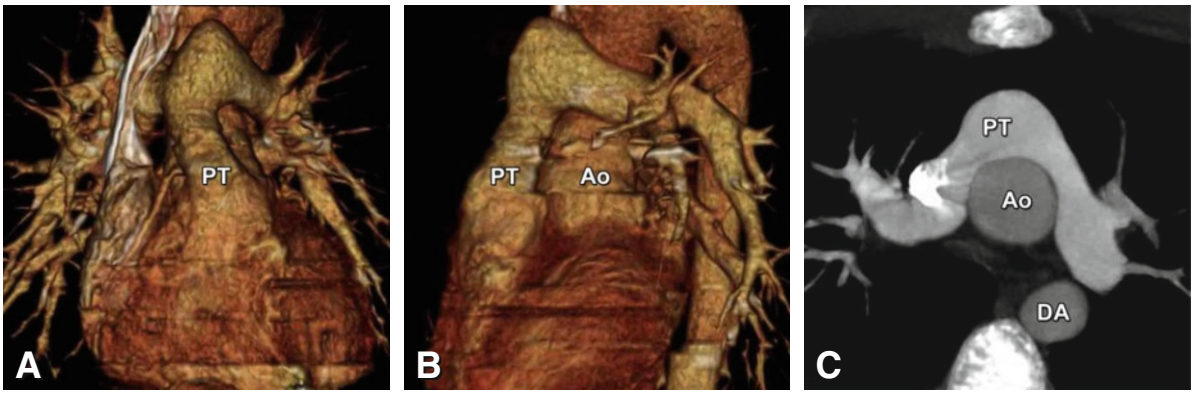

Fig. 23.19 Status post arterial switch operation for dextro-transposition of the great arteries in a 12-year-old boy. **Panels A** and **B** show three-dimensional volume renderings after surgery (anterior and lateral view, *PT* pulmonary trunk, *Ao* ascending aorta). No stenoses or aneurysms were found. An axial maximum intensity projection (**Panel C**) demonstrates the main pulmonary artery anterior to the ascending aorta (*Ao*), whereas there is a normal position of the descending aorta (*DA*)

discordance. Many of these patients have pacemakers due to the high incidence of congenital heart block.

Simultaneous visualization of both sides of the heart in transposition complexes can be accomplished with a biventricular injection protocol. CT of complex transposition must be tailored to the specific patient and operative details.

23.8 Coronary Artery Imaging

Coronary anomalies are classified according to their origin, course, and termination (**Figs.** 23.20 and 23.21). For further details on coronary anomalies pertaining to adults see Chap. 22. An abnormal coronary origin from the opposite sinus of Valsalva is the second most common cause of sudden death on the athletic field in the US. For anomalous left coronary arteries, the high risk interarterial course may be easily differentiated from the different benign courses. Treatment of an anomalous right coronary artery from the left-facing sinus remains a controversial topic.

23.8.1 Anomalous Origin of the Left Coronary Artery from the Pulmonary Artery (ALCAPA or Bland-White-Garland Syndrome)

The anomalous origin of the left coronary artery from the pulmonary artery (ALCAPA) is a rare congenital malformation reported to occur in 0.25–0.5% of all CHD. Most of the times, the anomaly is the only cardiac malformation. Less commonly, the association with other structural abnormalities may conceal the clinical findings and make the diagnosis even more difficult. Chronic myocardial ischemia leads to early progressive left heart failure and cardiac death. Children can survive if enough collaterals between the right coronary artery with a normal origin and the left coronary artery exist (formerly called adult type). This is only the case in 15–20% of patients. The other 80–85% patients do not have adequate collateral supply and develop progressive heart failure with death occurring at the age of 3–6 months. Usually, symptoms

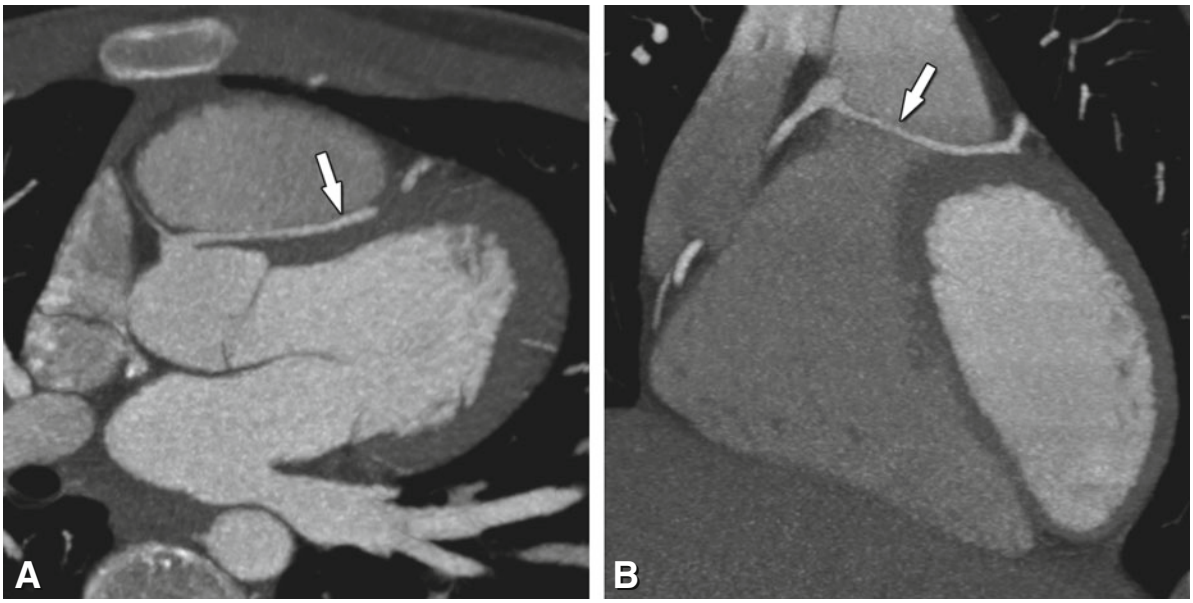

Fig. 23.20 Anomalous left coronary artery in a 10-year-old patient. The intraseptal benign course (Chap. 22) of an anomalous left coronary artery (*arrow*) from the right sinus of Valsalva is shown on maximum intensity projections in the axial (**Panel A**) and coronal orientation (**Panel B**). The course of the anomalous coronary artery is inferior to the pulmonary valve annulus through the septum. Although the patient presented with atypical chest pain, this anomaly is considered benign and unrelated to his symptoms

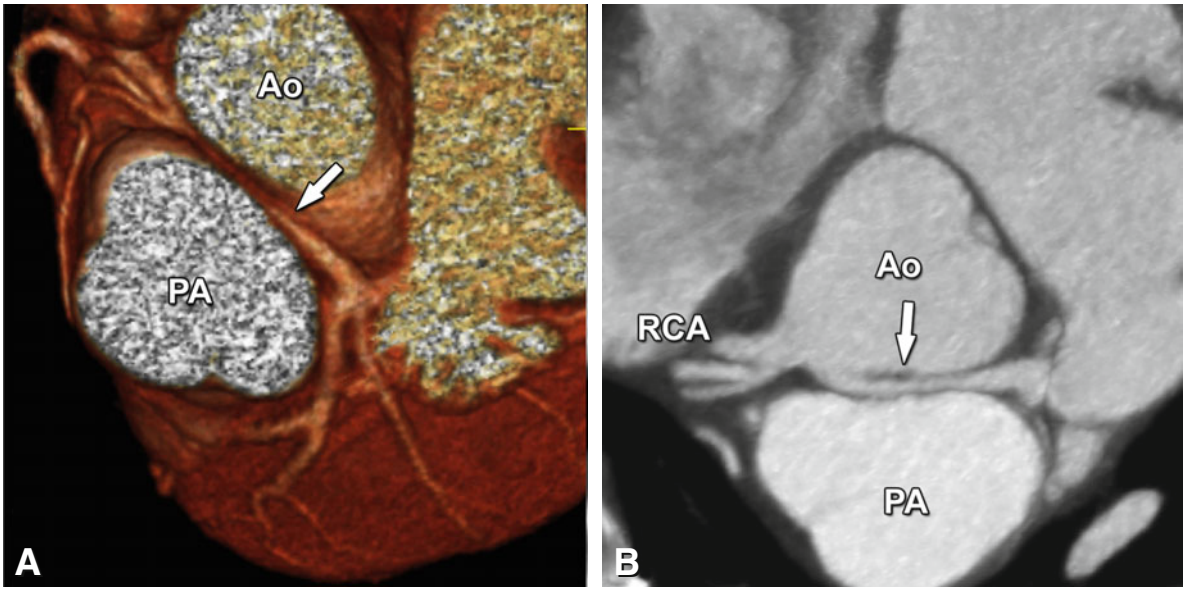

Fig. 23.21 Interarterial left coronary artery arising from the right sinus of Valsalva. This is a potentially malignant anomaly (*arrow*) with increased incidence of sudden death in those without surgical correction (**Panel A**). The maximum intensity projection (**Panel B**) demonstrates where surgical "unroofing" (*arrow*) will be performed to incorporate the left main coronary artery into the aortic sinus and eliminate coronary compression between the aorta (*Ao*) and pulmonary artery (*PA*). Surgical unroofing of the proximal course of the left coronary artery was performed and eliminated the patient's exertional chest pain. *RCA* right coronary artery

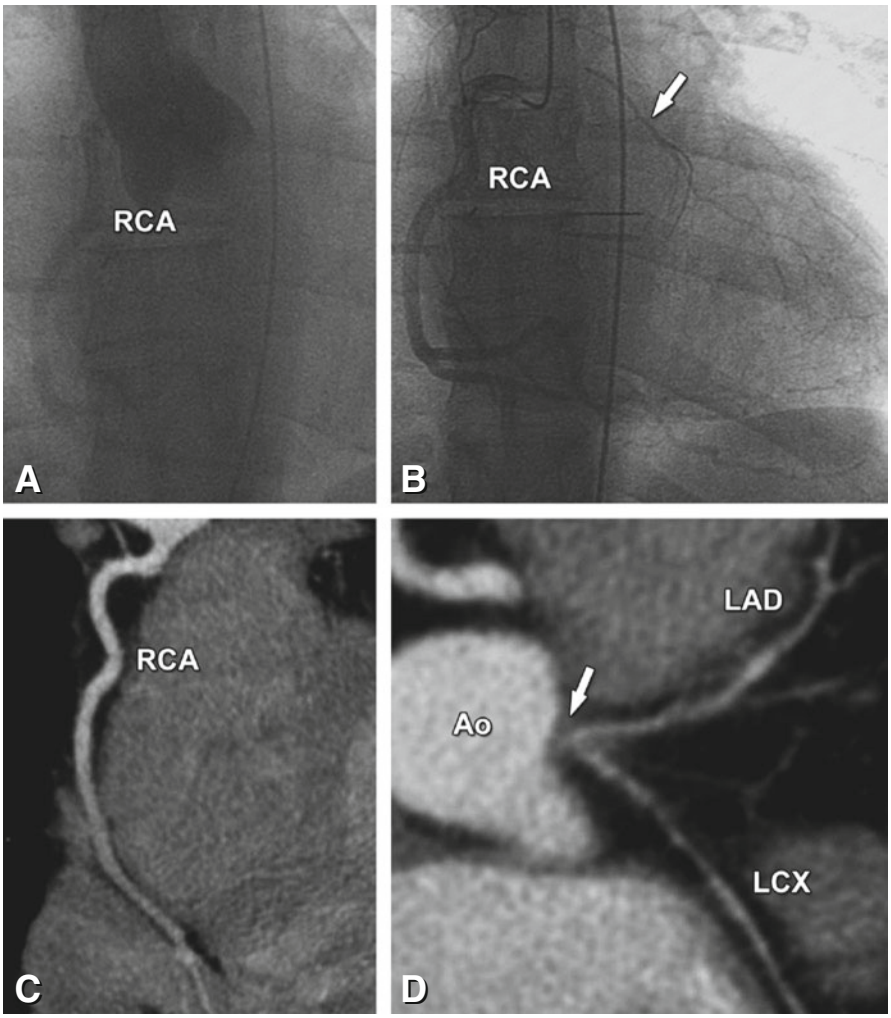

Fig. 23.22 Surgically corrected Bland-White-Garland syndrome in a 16-year-old girl. The left main coronary artery originated from the pulmonary artery and was surgically transferred to the aortic root during infancy to restore normal anatomy. Additionally, a mechanical mitral valve was placed. Conventional angiography (aortography) at follow-up demonstrated the right coronary artery (*RCA*, **Panel A**) but not the ostium of the left coronary artery. A late phase of the dedicated angiography of the *RCA* demonstrated retrograde filling of the left coronary arterial system (*arrow* in **Panel B**) as an indirect sign of left main occlusion. The patient had no clinical symptoms or ECG changes. 16-row CT using adaptive multisegment reconstruction ruled out stenosis of the dominant *RCA* (**Panel C**, curved multiplanar reformation) but also confirmed the occlusion of the reinserted left main coronary artery (*arrow* in **Panel D**, curved multiplanar reformation, *Ao* ascending aorta). Both the left anterior descending (*LAD*) and the left circumflex coronary artery (*LCX*) were opacified on CT due retrograde filling via collaterals from the *RCA*

present late, and the clinical examination is inconspicuous. If there is a clinical suspicion, at this point, CT can reliably detect the anomalous origin of the left coronary artery. It should be kept in mind that scanning should be started when the contrast agent is in the ascending aorta (as usual) as there is retrograde filling of the left coronary artery by the right coronary artery (**Fig. 23.22**).

Coronary artery stenosis is rare in childhood, but has been reported early and late after arterial switch operations, after reimplantation as part of the Ross procedure (a diseased aortic valve is replaced with the person's own pulmonary valve, a pulmonary allograft (valve taken from a cadaver) replaces the patient's own pulmonary valve), and in patients with a history of Kawasaki disease and aneurysms.

23.8.2 Kawasaki Disease

Kawasaki disease is an acute, self-limiting vasculitis of unknown etiology that occurs predominantly in infants and young children. It was first described in 1967 by Dr. Tomisaku Kawasaki in the Japanese literature (Arerugi). The specific cause of the disease is still unknown. Current theories center primarily on immunological causes. Classically, 5 days of fever plus four of five diagnostic criteria must be met to establish the diagnosis. By far the highest incidence of Kawasaki disease occurs in Japan (175 per 100,000 patients under 5 years of age), though its incidence in the US is increasing (approximately 2,000–4,000 cases are identified in the US each year). Kawasaki disease is predominantly a disease of young children, with 80% of patients being younger than 5 years of age. The disease affects more boys than girls.

Cardiac complications are the most important aspect of the disease. Kawasaki disease can cause vasculitis in the coronary arteries and subsequent coronary artery aneurysms. These aneurysms can lead to myocardial infarction even in young children (**Fig. 23.23**). Overall, about 5–20% of children with Kawasaki disease develop coronary artery aneurysms with much higher prevalence among patients who are not treated with intravenous immunoglobulins (IVIG) early in the course of illness (**Fig. 23.24**). Virtually all deaths in patients with Kawasaki disease result from its cardiac sequelae. Mortality peaks 15–45 days after the onset of fever; at this stage, patients have coronary vasculitis with a concomitant marked elevation of the platelet count and a hypercoagulable state. However, sudden death from myocardial infarction may also occur many years later in individuals who develop coronary stenoses following a childhood history of coronary artery aneurysms. Many cases of fatal and nonfatal myocardial infarction in young adults have been attributed to "missed" Kawasaki disease in childhood.

Evaluation of the coronary arteries should include quantitative assessment of internal vessel diameters (**Fig. 23.25**). Aneurysms are at least 1.5 times larger than the surrounding reference vessel diameter and are classified as saccular if axial and lateral diameters are nearly equal or as fusiform if symmetric dilatation with gradual proximal and distal tapering is seen. When a coronary artery is larger than normal without a segmental aneurysm, the vessel is considered ectatic. Standard deviations (called Z-scores) are commonly used to determine if the coronary artery is dilated relative to the patient's body surface area. Care must be taken in making the diagnosis of ectasia because of considerable normal variation in coronary artery distribution and dominance. The Japanese Ministry of Health criteria classify coronary arteries as abnormal (ectatic) if the internal lumen diameter is >3 mm in children <5 years of age or >4 mm in children ≥5 years of age, if the internal diameter of a segment measures ≥1.5 times that of an adjacent segment, or if the coronary lumen is clearly irregular. This is less commonly

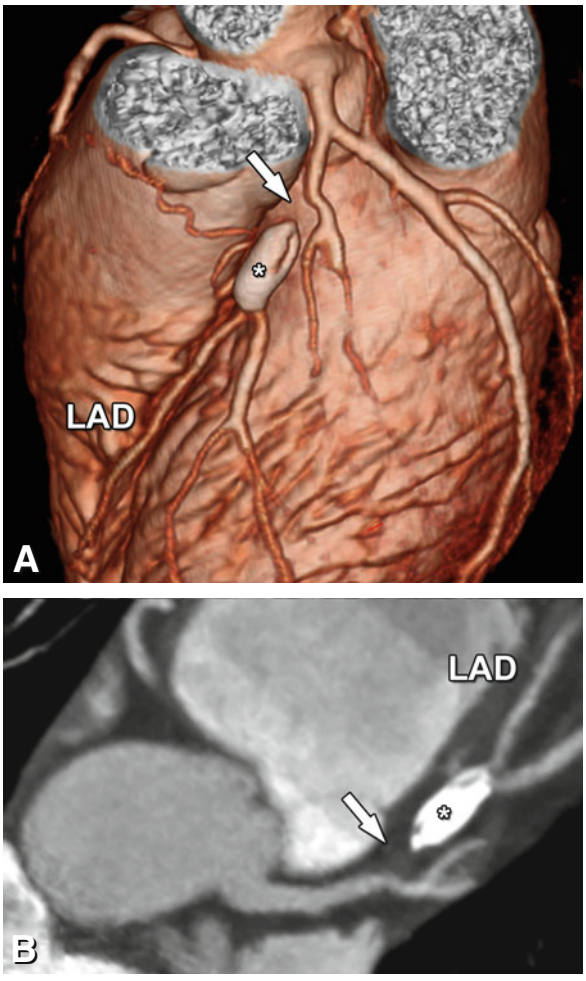

Fig. 23.23 Routine follow-up CT performed in 24-year-old patient who had severe Kawasaki disease at a young age. The three-dimensional reconstruction (**Panel A**) and maximum intensity projection (**Panel B**) show complete occlusion (*arrow*) of the left anterior descending coronary artery (*LAD*) proximal to a calcified aneurysm (*asterisk*). The patient is now managed medically by an adult cardiologist

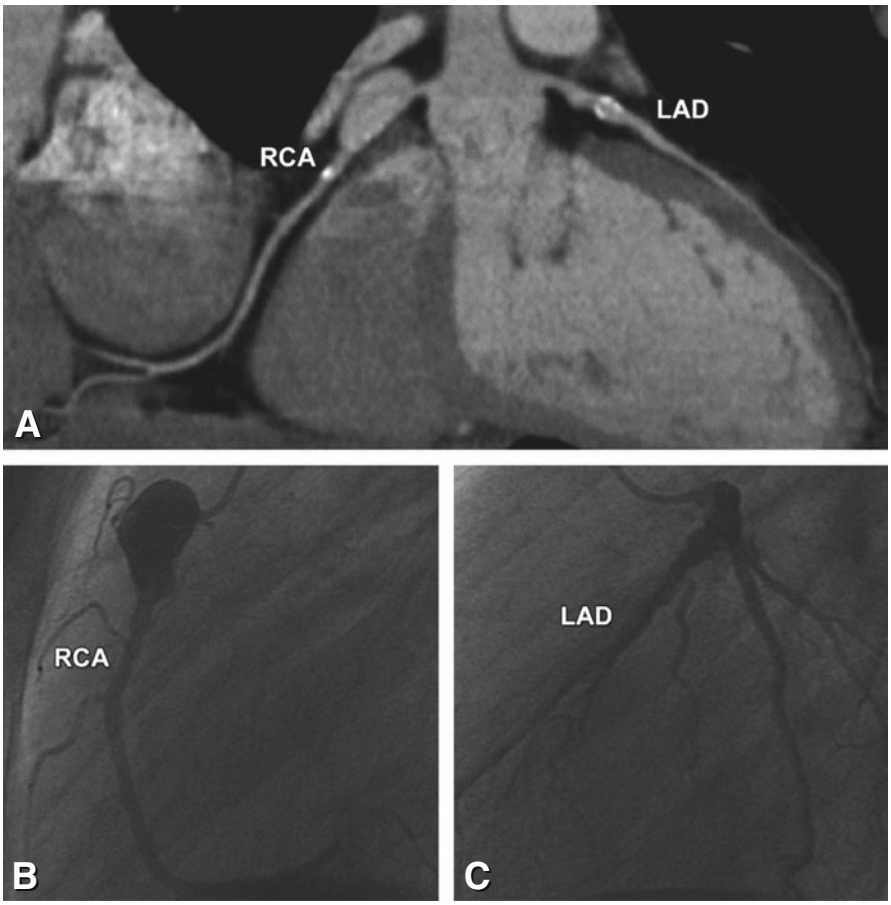

Fig. 23.24 A 25-year-old male patient with Kawasaki disease. The disease occurred at the age of 2 and resulted in a giant aneurysm of the proximal right coronary artery (*RCA*) and a fusiform aneurysm in the left anterior descending coronary artery (*LAD*) seen at CT follow-up (curved multiplanar reformation, **Panel A**). Conventional coronary angiography confirmed these findings in the *RCA* (**Panel B**) and LAD (**Panel C**). The RCA aneurysm was 25 mm long and had a diameter of 12.5 mm on CT (Used with permission from Arnold et al. *Pediatr Radiol* 2007)

Fig. 23.25 A 21-year-old patient with Kawasaki disease and aneurysms of both the left anterior descending coronary artery (*LAD*, **Panels A**–**D**) and the right coronary artery (*RCA*, **Panels E** and **F**). The LAD aneurysm was severely calcified (**Panel B**, curved multiplanar reformation), and stenosis was demonstrated distal to the aneurysm (*arrow* in **Panels A** and **D**). However, the percent diameter stenosis was difficult to evaluate using CT due to the aneurysmal calcification (**Panel D**). There was no stenosis and aneurysm in the left circumflex coronary artery (*LCX*) both on conventional coronary angiography (**Panel A**) and prospectively ECG-gated dual-source CT (**Panel C**). There was no significant stenosis in the *RCA* as seen on conventional coronary angiography (**Panel E**). The CT examination was superior in visualizing the calcifications in the aneurysm and also did not show any stenosis (**Panel F**). However, there was an artifact on CT as seen in **Panels C**, **D**, and **F** (*asterisks*), which was due to arrhythmia

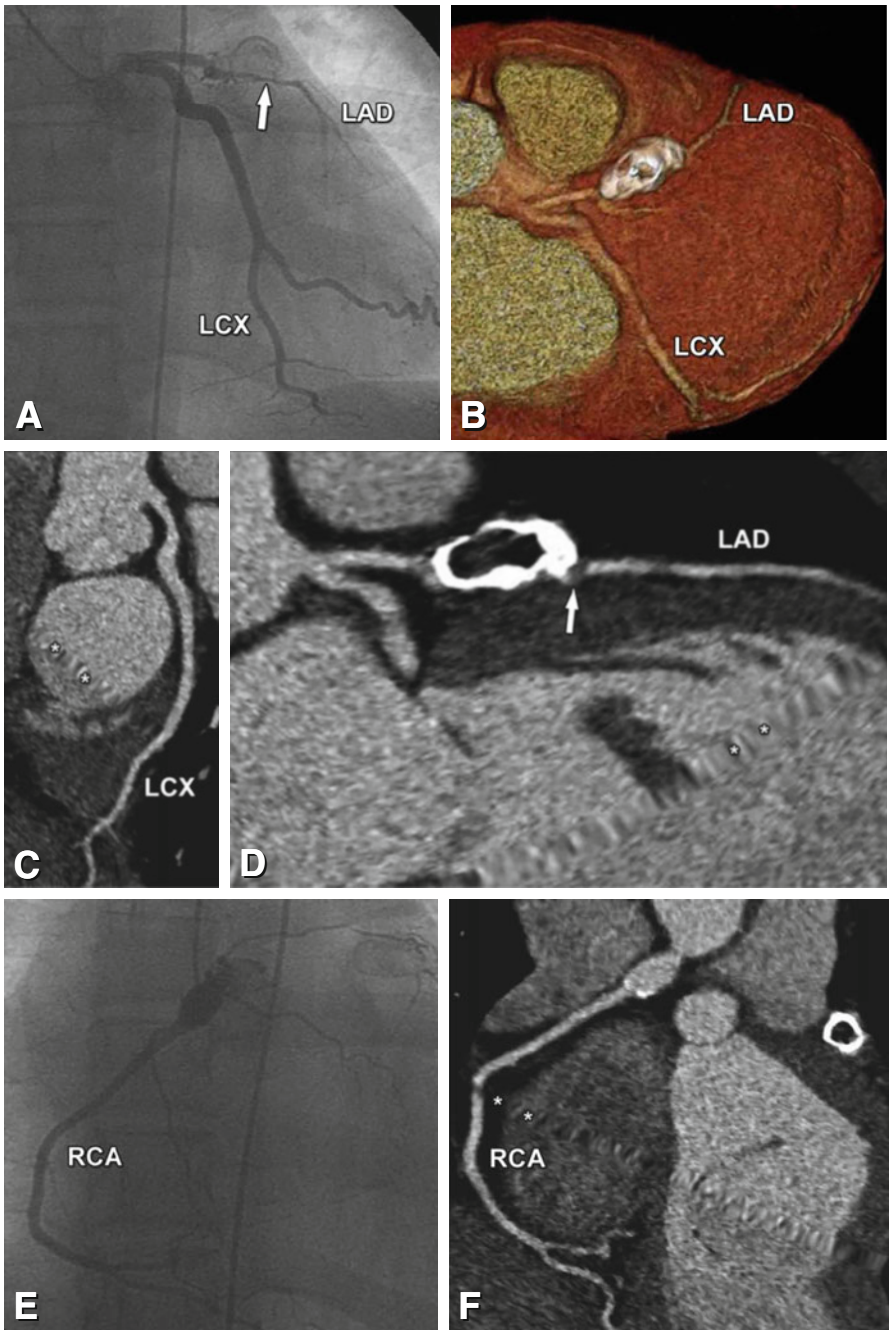
LAD
LCX
A
LAD
LCX
B
LCX
C
LAD
D
RCA
E
RCA
F

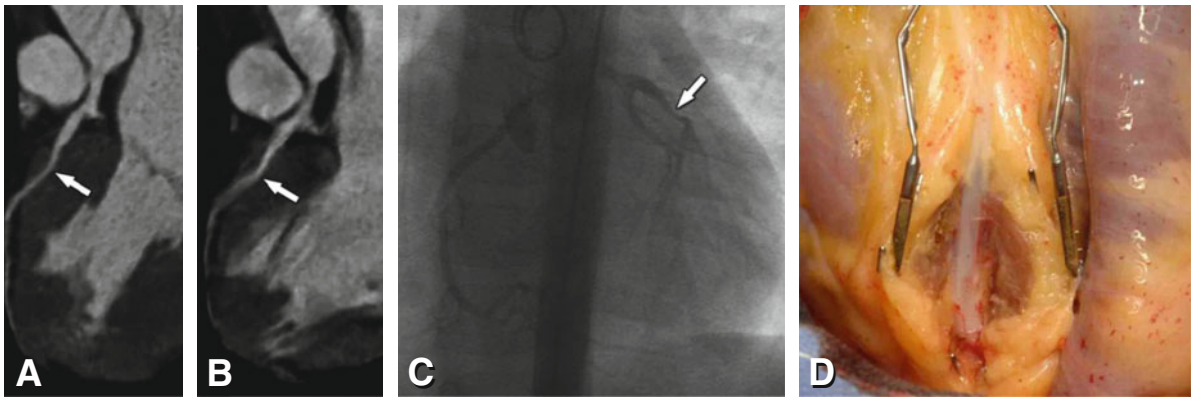

Fig. 23.26 An 11-year-old girl with myocardial bridging of the left anterior descending coronary artery (*LAD*) due to hypertrophic cardiomyopathy. She was admitted to the hospital after a heart attack and resuscitation and was thus referred for CT, which was performed on a dual-source CT scanner at a heart rate of 103 beats per min. The patient showed only limited breath-hold capabilities, leading to artifacts on the reconstructed images. ECG-gated CT angiography using 50 ml of an iodinated contrast agent (370 mg iodine/ml) shows the intramural segment (*arrows*) of the left anterior descending coronary artery displayed as curved multiplanar reformations during systole (**Panel A**) and diastole (**Panel B**). Note the narrow lumen (*arrow*) of the intramural segment during systole and diastole (**Panels A** and **B**). This finding was confirmed on conventional angiography (*arrow* in **Panel C**). **Panel D** shows the intraoperative site after dissection of the myocardium. The further clinical course was uneventful (**Panel D** is courtesy of Dr. C. Sebening, Heidelberg)

used now that the Z-score standard deviations are widely available.

Proximal aneurysm can be evaluated echocardiographically, but the technique is not sensitive enough to exclude coronary stenosis. For evaluation of stenosis or of the more distal coronary segments, either conventional coronary angiography or CT is required. Small studies in follow-up patients (mostly teenagers) have confirmed an almost 100% diagnostic accuracy of CT for detection of aneurysms with conventional coronary angiography as the reference standard. Thus, recent CT scanners can be recommended for noninvasive follow-up after childhood Kawasaki disease, while severe calcifications may still impair estimates of the degree of coronary stenosis.

23.8.3 Myocardial Bridging

Normally, coronary arteries have an epicardial course. A myocardial bridge is a congenital condition in which a segment of coronary artery runs intramurally, through the myocardium, beneath a muscular bridge. The coronary artery segment covered by the myocardial bridge is called a "tunneled" artery. As the heart contracts to pump blood, the muscle exerts pressure across the bridge and may constrict the artery. This can lead to premature ventricular contractions and angina pectoris. There are only case reports on the use of CT for diagnosing myocardial bridging in children. Bridging is most commonly seen in children with hypertrophic cardiomyopathy.

Myocardial bridging most often affects the left anterior descending coronary artery. Mild forms of myocardial bridging (less than 20% diameter stenosis) are often undetectable, as the blood usually flows through the coronary while the heart is relaxing in diastole. Visualization of the coronary arteries during diastole and systole is mandatory to determine the percentage of diameter stenosis and measure the lengths of the tunneled part for planning the surgical strategy in patients with ischemia (**Fig. 23.26**). The effect of myocardial bridging is very controversial and many think it is a normal variant that does not require intervention.

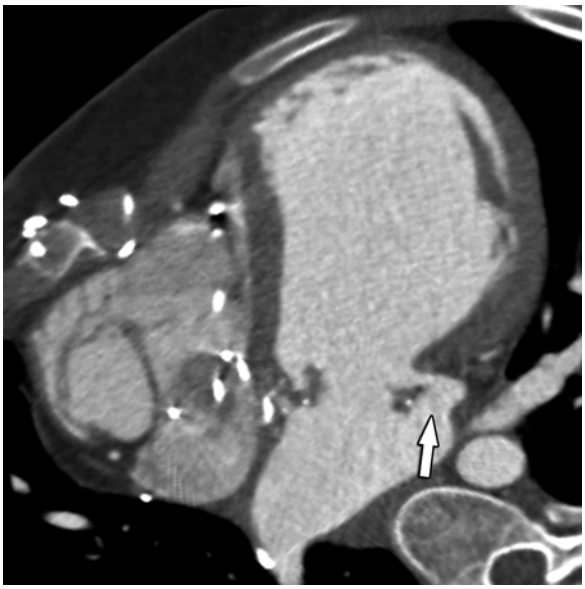

Fig. 23.27 Paravalvular leak after prosthetic mitral valve implantation (*arrow*). This adult patient had undergone multiple prior prosthetic mitral valve placements for her partial atriventricular canal and cleft mitral valve. Approximately 1 year after her last valve replacement, she was found to have an increasing mitral gradient. A functional CT scan was performed for evaluation of left ventricular volumes and regurgitant fraction. A four-chamber view shows a large paravalvular leak of the lateral mitral valve annulus. The severity of insufficiency had been underestimated by transesophageal echocardiography, and increased flow wrongly suggested mitral stenosis with an increased gradient. The valve was subsequently replaced and the patient markedly improved

23.9 Evaluation of Prosthetic Valves

Pediatric patients often have a mechanical (**Fig. 23.13**a) or bioprosthetic valve (**Fig. 23.27**) placed as part of complex palliation. There is an expected gradient through any prosthetic valve, but the gradient can increase due to valve dysfunction, patient-valve size mismatch with somatic growth, or pannus formation. Perivalvar leaks are also seen, and they are difficult to quantify or see by echocardiography due to the artifact from the valve structure itself. CTA is an excellent modality to assess bioprosthetic valve function, pannus formation, and paravalvular leaks (**Fig. 23.27**, Chaps. 16, 17, and 18). For leaks, the regurgitant fraction can be calculated from a function scan based on the stroke volume differences between the right and left ventricle.

Recommended Reading

Angeli E, Formigari R, Pace Napoleone C, Oppido G, Ragni L, Picchio FM et al (2010) Long-term coronary artery outcome after arterial switch operation for transposition of the great arteries. Eur J Cardiothorac Surg 38:714–720

Arnold R, Ley S, Ley-Zaporozhan J et al (2007) Visualization of coronary arteries in patients after childhood Kawasaki syndrome: value of multidetector CT and MR imaging in comparison to conventional coronary catheterization. Pediatr Radiol 37:998–1006

Bland EF, White PD, Garland J (1933) Congenital anomalies of the coronary arteries: report of an unusual case associated with cardiac hypertrophy. Am Heart J 8:787–801

Burns JC, Glode MP (2004) Kawasaki syndrome. Lancet 364:533–544

Daebritz SH, Nollert G, Sachweh JS, Engelhardt W, von Bernuth G, Messmer BJ (2000) Anatomical risk factors for mortality and cardiac morbidity after arterial switch operation. Ann Thorac Surg 69:1880–1886

Ferguson EC, Krishnamurthy R, Oldham SA (2007) Classic imaging signs of congenital cardiovascular abnormalities. Radiographics 27:1323–1334

Frush DP, Siegel MJ, Bisset GS 3rd (1997) From the RSNA refresher courses. Challenges of pediatric spiral CT. Radiographics 17:939–959

Han BK, Lindberg J, Grant K, Schwartz RS, Lesser JR (2011) Accuracy and safety of high pitch computed tomography imaging in young children with complex congenital heart disease. Am J Cardiol 107:1541–1546

Haramati LB, Glickstein JS, Issenberg HJ, Haramati N, Crooke GA (2002) MR imaging and CT of vascular anomalies and connections in patients with congenital heart disease: significance in surgical planning. Radiographics 22:337–347, discussion 48–9

Hayabuchi Y, Inoue M, Watanabe N, Sakata M, Nabo MM, Kitagawa T et al (2010) Assessment of systemic-pulmonary collateral arteries in children with cyanotic congenital heart disease using multidetector-row computed tomography: comparison with conventional angiography. Int J Cardiol 138:266–271

Hoffmann A, Engelfriet P, Mulder B (2007) Radiation exposure during follow-up of adults with congenital heart disease. Int J Cardiol 118:151–153

Hughes D Jr, Siegel MJ (2010) Computed tomography of adult congenital heart disease. Radiol Clin North Am 48:817–835

Jacobs JP, Mavroudis C, Jacobs ML, Maruszewski B, Tchervenkov CI, Lacour-Gayet FG et al (2007) Nomenclature and databases – the past, the present, and the future : a primer for the congenital heart surgeon. Pediatr Cardiol 28:105–115

Jatene AD, Fontes VF, Paulista PP et al (1976) Anatomic correction of transposition of the great vessels. J Thorac Cardiovasc Surg 72:364–370

Konstantinov IE, Alexi-Meskishvili VV, Williams WG, Freedom RM, Van Praagh R (2004) Atrial switch operation: past, present, and future. Ann Thorac Surg 77:2250–2258

Lell MM, May M, Deak P, Alibek S, Kuefner M, Kuettner A et al (2011) High-pitch spiral computed tomography: effect on image quality and radiation dose in pediatric chest computed tomography. Invest Radiol 46:116–123

Ley S, Zaporozhan J, Arnold R et al (2007) Preoperative assessment and follow-up of congenital abnormalities of the pulmonary arteries using CT and MRI. Eur Radiol 17:151–162

Lin MT, Wang JK, Chen YS, Lee WJ, Chiu HH, Chen CA et al (2012) Detection of pulmonary arterial morphology in tetralogy of Fallot with pulmonary atresia by computed tomography: 12 years of experience. Eur J Pediatr 171:579–586

Oh KH, Choo KS, Lim SJ, Lee HD, Park JA, Jo MJ et al (2009) Multidetector CT evaluation of total anomalous pulmonary venous connections: comparison with echocardiography. Pediatr Radiol 39:950–954

Ou P, Celermajer DS, Marini D et al (2008) Safety and accuracy of 64-slice computed tomography coronary angiography in children after the arterial switch operation for transposition of the great arteries. JACC Cardiovasc Imaging 1:331–339

Paul JF, Rohnean A, Elfassy E, Sigal-Cinqualbre A (2011) Radiation dose for thoracic and coronary step-and-shoot CT using a 128-slice dual-source machine in infants and small children with congenital heart disease. Pediatr Radiol 41:244–249

Prakash A, Powell AJ, Geva T (2010) Multimodality noninvasive imaging for assessment of congenital heart disease. Circ Cardiovasc Imaging 3:112–125

Rigsby CK, Gasber E, Seshadri R, Sullivan C, Wyers M, Ben-Ami T (2007) Safety and efficacy of pressure-limited power injection of iodinated contrast medium through central lines in children. AJR Am J Roentgenol 188:726–732

Trowitzsch E, Berger T, Stute M (1991) The diameter of the large arteries in the first 3 years of life. An echocardiography study. Monatsschr Kinderheilkd 139:355–359

Vastel-Amzallag C, Le Bret E, Paul JF, Lambert V, Rohnean A, El Fassy E et al (2011) Diagnostic accuracy of dual-source multislice computed tomographic analysis for the preoperative detection of coronary artery anomalies in 100 patients with tetralogy of Fallot. J Thorac Cardiovasc Surg 142:120–126

Vyas HV, Greenberg SB, Krishnamurthy R (2012) MR imaging and CT evaluation of congenital pulmonary vein abnormalities in neonates and infants. Radiographics 32:87–98

Walhout RJ, Suttorp MJ, Mackaij GJ, Ernst JM, Plokker HW (2009) Long-term outcome after balloon angioplasty of coarctation of the aorta in adolescents and adults: is aneurysm formation an issue? Catheter Cardiovasc Interv 73:549–556

Warnes CA (2006) Transposition of the great arteries. Circulation 114:2699–2709

Warnes CA, Williams RG, Bashore TM, Child JS, Connolly HM, Dearani JA et al (2008) ACC/AHA 2008 guidelines for the management of adults with congenital heart disease: a report of the American College of Cardiology/American Heart Association Task Force on practice guidelines (writing committee to develop guidelines on the management of adults with congenital heart disease). Circulation 118:714–833

Typical Clinical Examples

M. Dewey

Abstract

This chapter presents an overview of the most common clinical examples of cardiac CT.

24.1 Normal Coronary Arteries

The normal anatomy of different coronary artery distribution types as seen with CT is presented in **Figs.** 24.1–24.3.

24.2 Coronary Artery Plaques

Coronary artery plaques of potentially different clinical importance are shown in **Figs.** 24.4–24.7.

24.3 Coronary Artery Stenoses

Significant coronary artery stenoses and occlusions and their variable appearance on cardiac CT, when compared with conventional coronary angiography, are shown in **Figs.** 24.8–24.17. See Chap. 20 for a summary of the diagnostic performance of coronary CT angiography in this application.

24.4 Coronary Artery Bypass Grafts

Arterial and venous coronary artery bypass grafts differ in diameter, but both and are usually evaluable by CT. Examples are shown in **Figs.** 24.18–24.26. See Chap. 25 for a summary of the diagnostic performance of coronary CT angiography in this application.

24.5 Coronary Artery Stents

Evaluation of coronary artery stents is limited using today's technology, and if recommended at all, CT should only be used in patients with a single large-diameter (at least 3.0–3.5 mm) coronary stent. Typical results and issues involved in coronary CT stent imaging are shown in **Figs.** 24.27–24.37. See Chap. 25 for a summary of the diagnostic performance of coronary CT angiography in this application.

24.6 Noncardiac Findings

Noncardiac findings on cardiac CT are not uncommon and must be analyzed as meticulously as possible to ensure that important findings that might be responsible for a patient's symptoms are not missed and that unnecessary follow-up examinations are avoided. Common examples of noncardiac findings are provided in **Figs.** 24.38–24.62.

24.7 Extracoronary Cardiac Findings

Extracoronary cardiac findings are also quite common on cardiac CT and are important, in that they are often associated with the coronary findings and can be responsible for a patient's symptoms. Examples of typical extracoronary cardiac findings are provided in **Figs.** 24.63–24.74.

M. Dewey, *Cardiac CT*,
DOI 10.1007/978-3-642-41883-9_27, © Springer-Verlag Berlin Heidelberg 2014

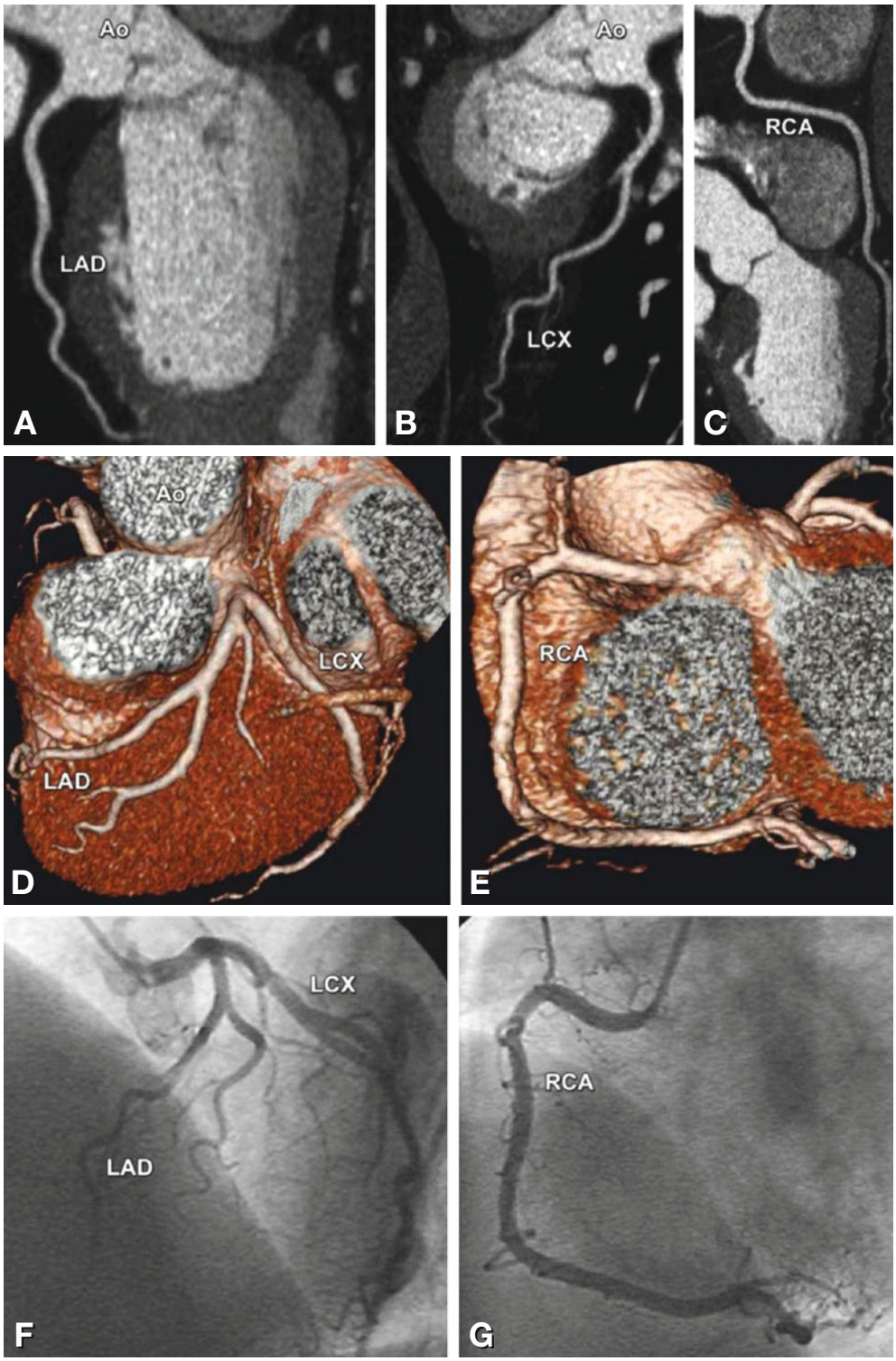

Fig. 24.1 Normal coronary arteries in a 56-year-old female patient presenting with nonanginal chest pain (see Chap. 6 for a description of angina types) and 0.2 mV (2 mm) ST segment depression in II, III, and aVF during stress testing (bicycle). **Panels A–C** show the curved multiplanar reformations along the left anterior descending (*LAD*), left circumflex (*LCX*), and right coronary (*RCA*) artery, respectively. Three-dimensional reconstructions of the left (**Panel D**) and right (**Panel E**) coronary artery are also unremarkable and demonstrate a codominant coronary distribution in this patient, which is found in 7–20% of all individuals. This distribution type is also seen on the corresponding conventional coronary angiograms of the left (**Panel F**) and right coronary artery (**Panel G**). Ruling out coronary artery disease in patients with low-to-intermediate pretest likelihood is the main application of coronary CT angiography. *Ao* aorta

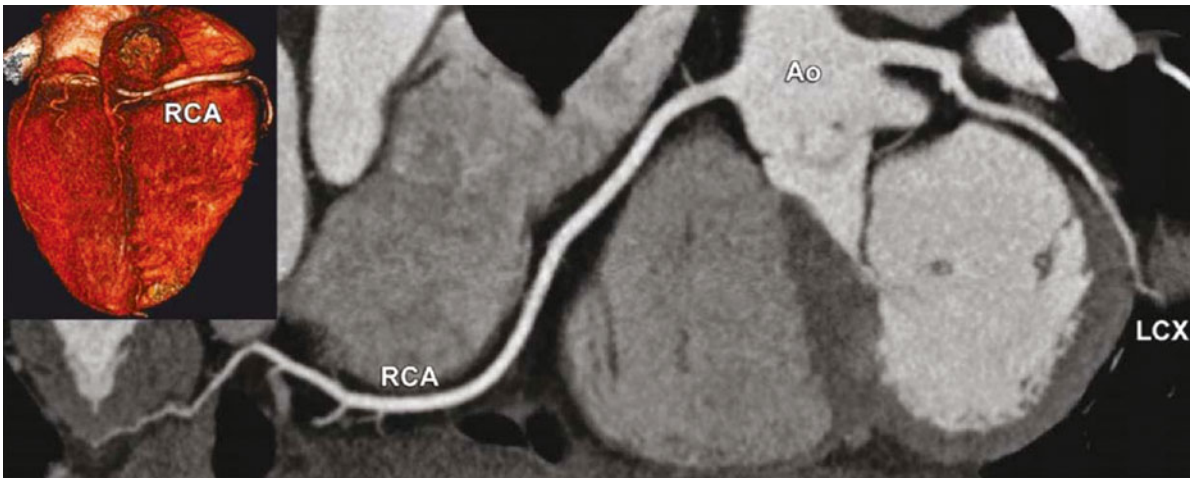

Fig. 24.2 Right coronary artery dominance, which is found in 60–85% of all individuals, as seen with CT using a curved multiplanar reformation along the right coronary (*RCA*) and left circumflex (*LCX*) coronary artery (*inset* shows the base of the heart with RCA dominance). *Ao* aorta

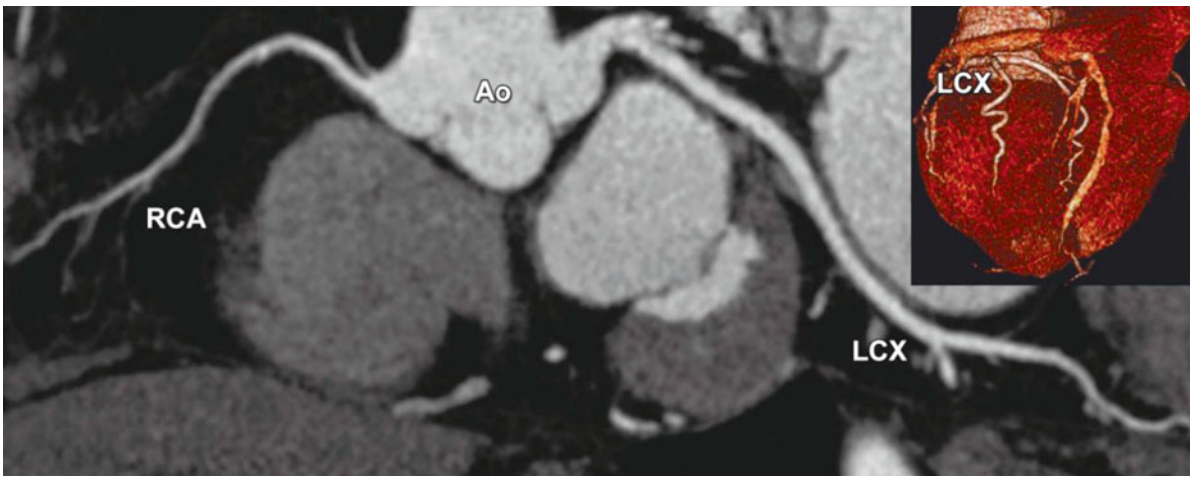

Fig. 24.3 Left coronary artery dominance, which is found in 7–20% of all individuals, as seen with CT using a curved multiplanar reformation along the right coronary (*RCA*) and left circumflex (*LCX*) coronary artery (*inset* shows the base of the heart with dominance of the LCX). *Ao* aorta

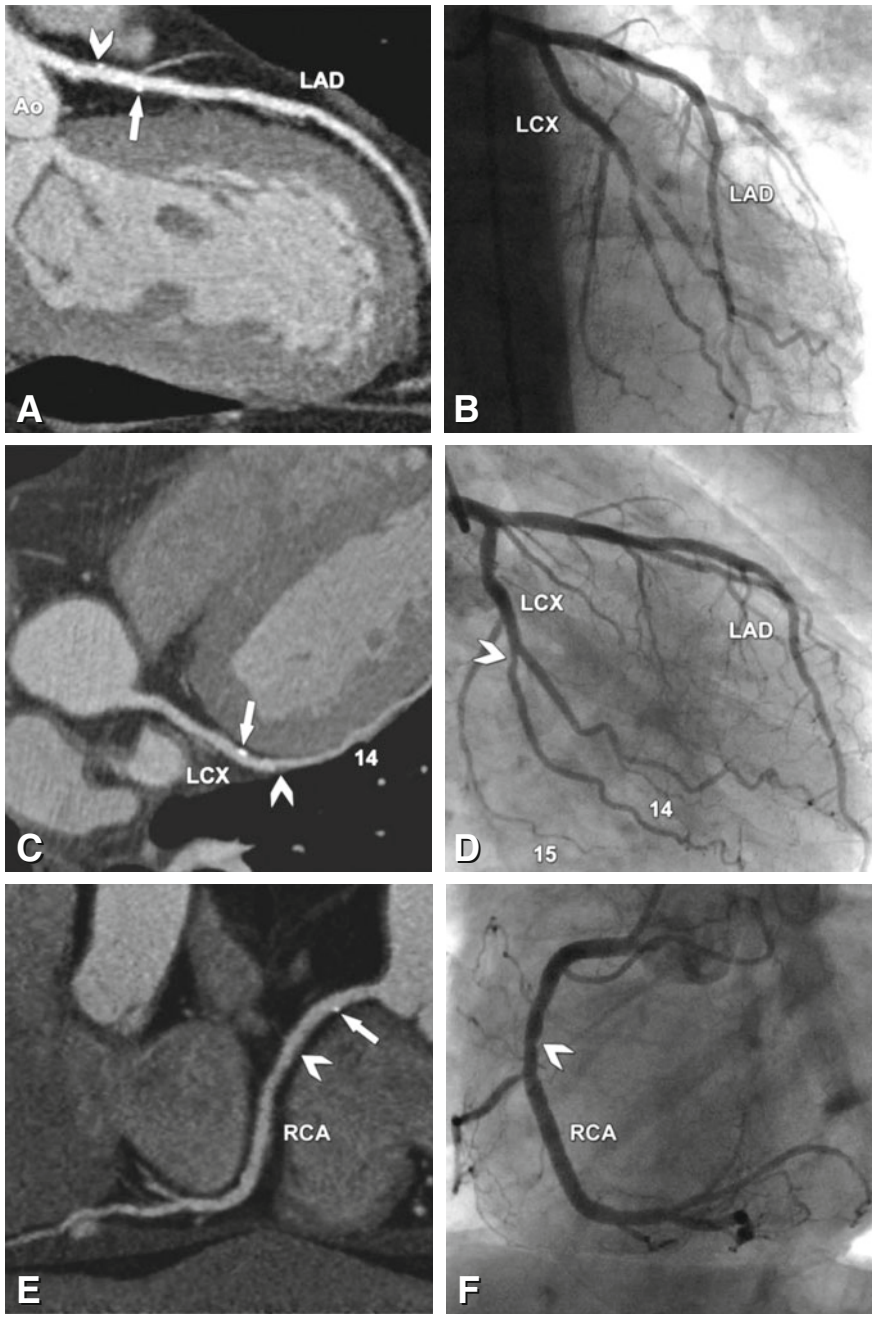

Fig. 24.4 No significant coronary artery stenoses, but small calcified plaques ("calcium spots") and noncalcified plaques in all coronaries in a 65-year-old male patient. The curved multiplanar reformation along the left anterior descending (*LAD*) coronary artery (**Panel A**) shows a calcium spot (*arrow*) and a mixed plaque (consisting of calcified and noncalcified components, *arrowhead*), which do not cause any indentation of the coronary lumen, as demonstrated by conventional coronary angiography (**Panel B**). There is another calcium spot (*arrow*) in the middle segment of the left circumflex coronary artery (*LCX*, **Panel C**) that does not cause any visible luminal narrowing on conventional angiography (**Panel D**), whereas a purely noncalcified plaque in the second obtuse marginal branch (*arrowhead*, segment 14) causes slight indentation of the coronary lumen (*arrowhead* in **Panel D**). The curved multiplanar reformation along the right coronary artery (*RCA*) shows the same findings (**Panel E**) with a calcium spot (*arrow*) not causing luminal narrowing, whereas the more distal noncalcified plaque in segment 2 (*arrowhead* in **Panel E**) is the cause of slight indentation (*arrowhead* in **Panel F**). *Ao* aorta, 15 segment 15 (distal LCX)

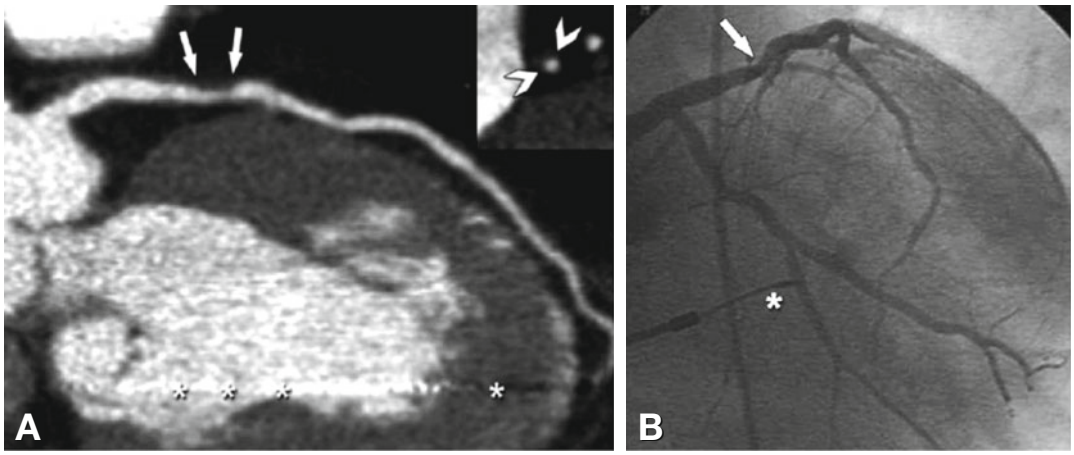

Fig. 24.5 Large noncalcified plaque in the proximal left anterior descending coronary artery (*arrows* in **Panel A**) of a 72-year-old male patient with typical angina pectoris (see Chap. 6 for a description of angina types). The plaque causes positive remodeling of the outer vessel wall (see *inset* in **Panel A**; *arrowheads* demarcate the boundaries of this plaque). The so-called remodeling index is defined as the ratio of the vessel area at the plaque site (including plaque and lumen area) to the mean of the vessel area at the reference site proximal and distal to the plaque. Positive remodeling, as in this case, is present if the index is >1.05 and indicates an increased risk for unstable presentation of patients. However, the value of potential clinical consequences (e.g., initiation or increase in statin therapy) in patients with noncalcified plaques without significant luminal narrowing but positive remodeling has not been established. This plaque (*arrow*) caused a 35% diameter stenosis, as measured with quantitative analysis of coronary angiography (**Panel B**). Note the artifacts in CT (*asterisks* in **Panel A**) arising from the cardiac pacemaker lead (*asterisk* in **Panel B**)

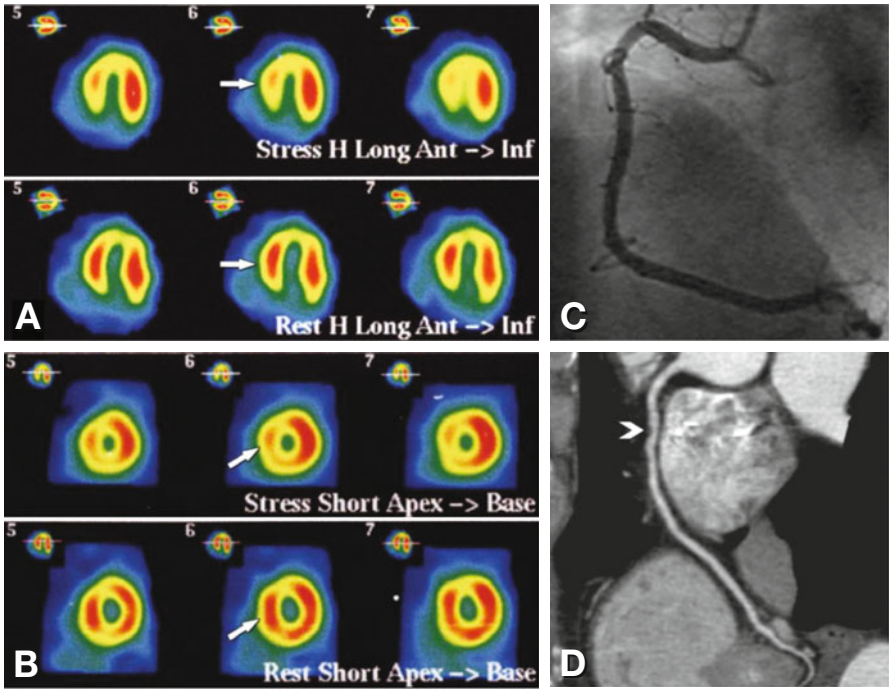

Fig. 24.6 Example of a false-positive single-photon emission computed tomography (SPECT) examination with ^{99m}Tc in a 68-year-old male patient with reduced septal and inferior stress perfusion (*arrows* in **Panels A** and **B**). These findings were suggestive of a significant stenosis in the right coronary artery. The right coronary artery, however, was normal and without signs of significant stenosis on conventional coronary angiography (**Panel C**) or coronary CT angiography (curved multiplanar reformation, **Panel D**). However, there was a noncalcified coronary plaque in the midsegment of the right coronary artery on CT (*arrowhead* in **Panel D**) that was not visible on conventional angiography and might have been responsible for the SPECT findings

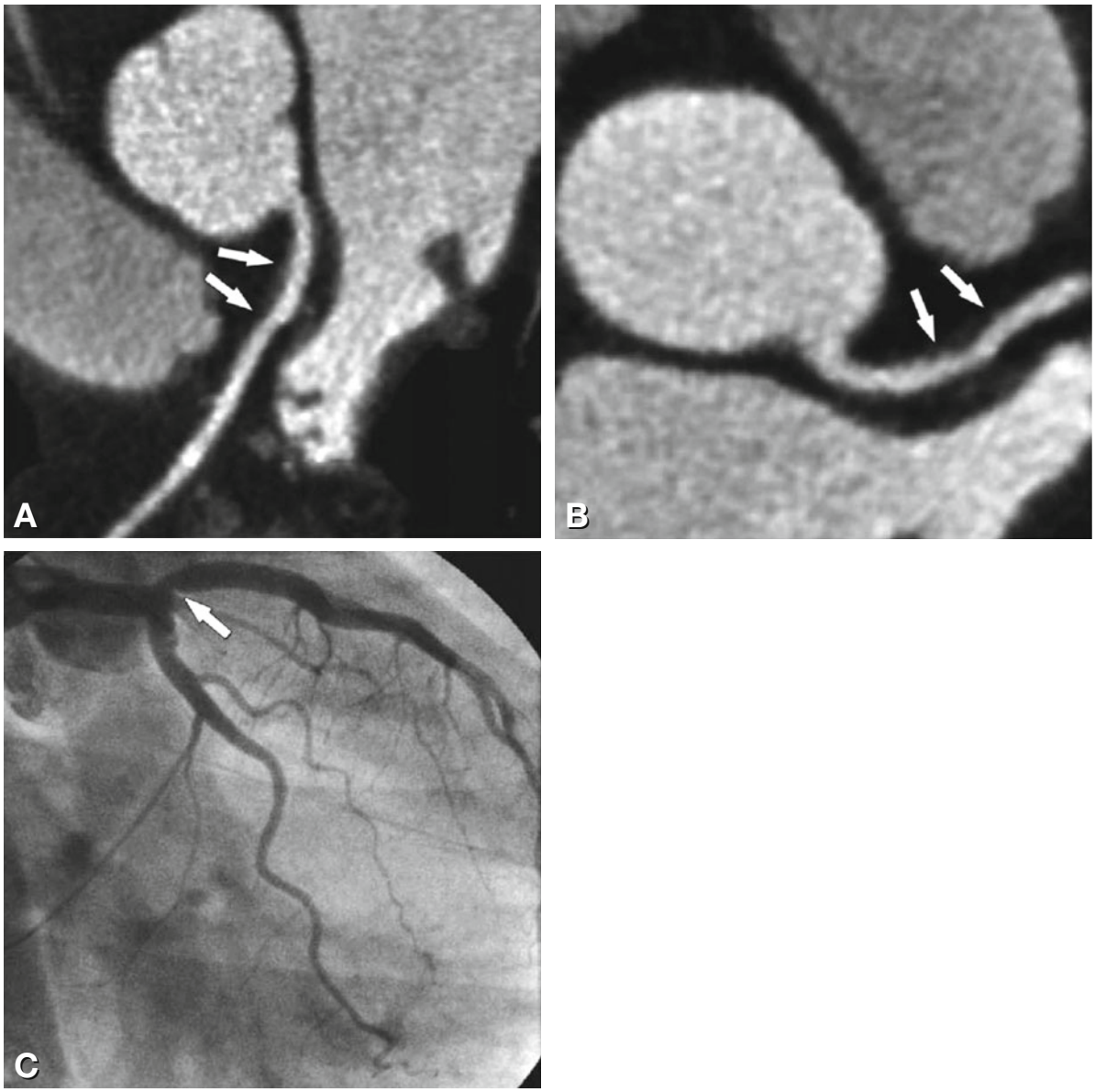

Fig. 24.7 Large noncalcified plaque (*arrows* in **Panels A** and **B**) in the proximal left anterior descending coronary artery in a 58-year-old female patient with typical angina pectoris. The CT results are illustrated using a curved multiplanar reformation (**Panel A**) and maximum-intensity projection (**Panel B**). This plaque also results in positive remodeling (remodeling index of >1.05), but the indentation of the coronary artery lumen (from below, *arrow* in **Panel C**) is not significant (30% diameter stenosis on quantitative analysis)

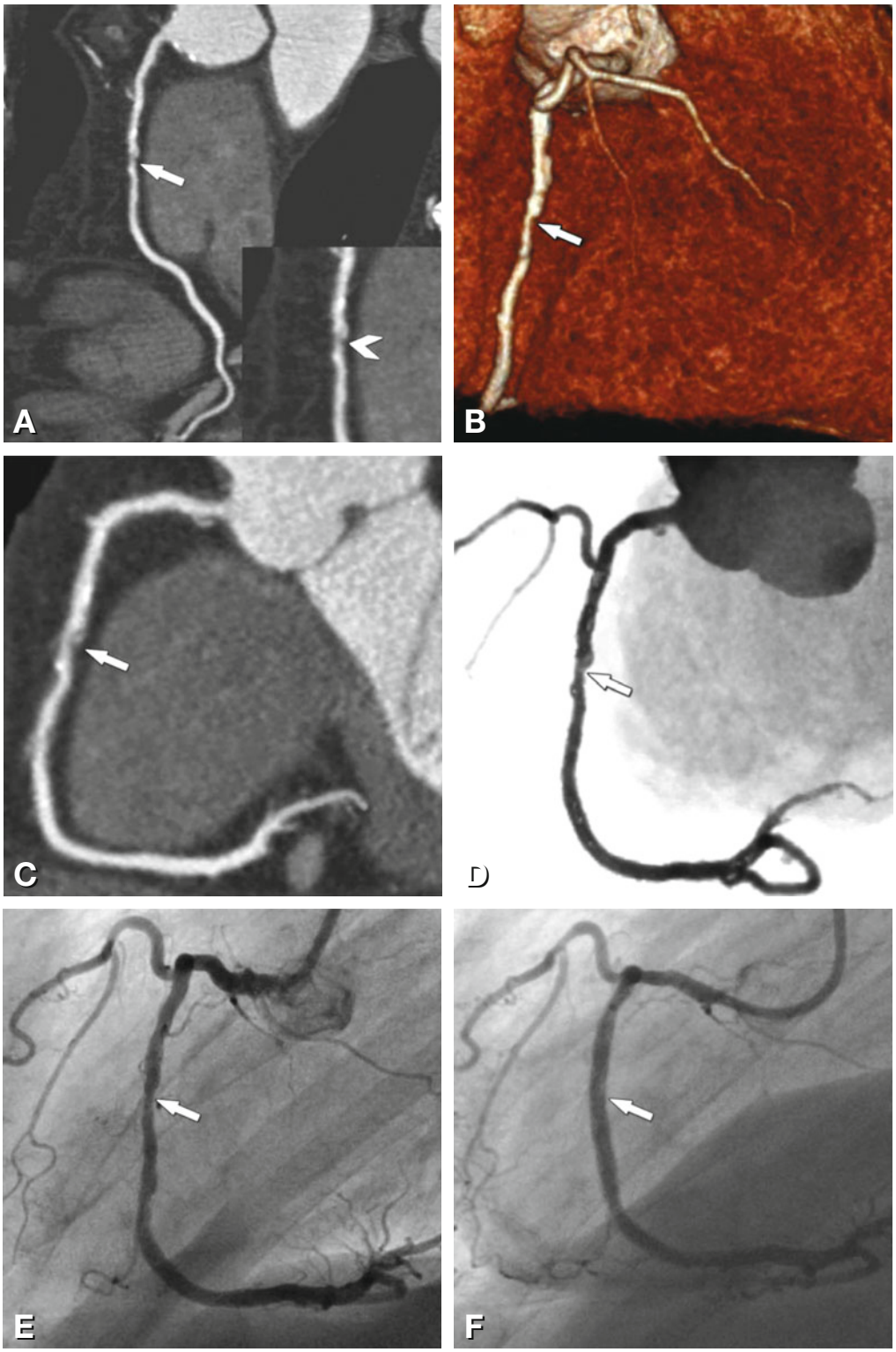

Fig. 24.8 Significant stenosis in the mid-segment of the right coronary artery (*arrows*) on different CT reconstructions (**Panels A**–**D**) in a 62-year-old male patient with typical angina pectoris but unremarkable exercise ECG. Reconstructions of CT include curved multiplanar reformation (**Panel A**, *inset* shows the stenosis (*arrowhead*) in a magnified view), volume-rendered three-dimensional reconstruction (**Panel B**), thin-slab maximum-intensity projection curved along the vessel path (so-called CATH view, **Panel C**), and angiographic emulation (**Panel D**). There was good correlation with the findings on subsequently performed conventional coronary angiography (*arrow* in **Panel E**). During the same invasive angiographic examination, this lesion was treated by stent placement with no residual stenosis (*arrow* in **Panel F**)

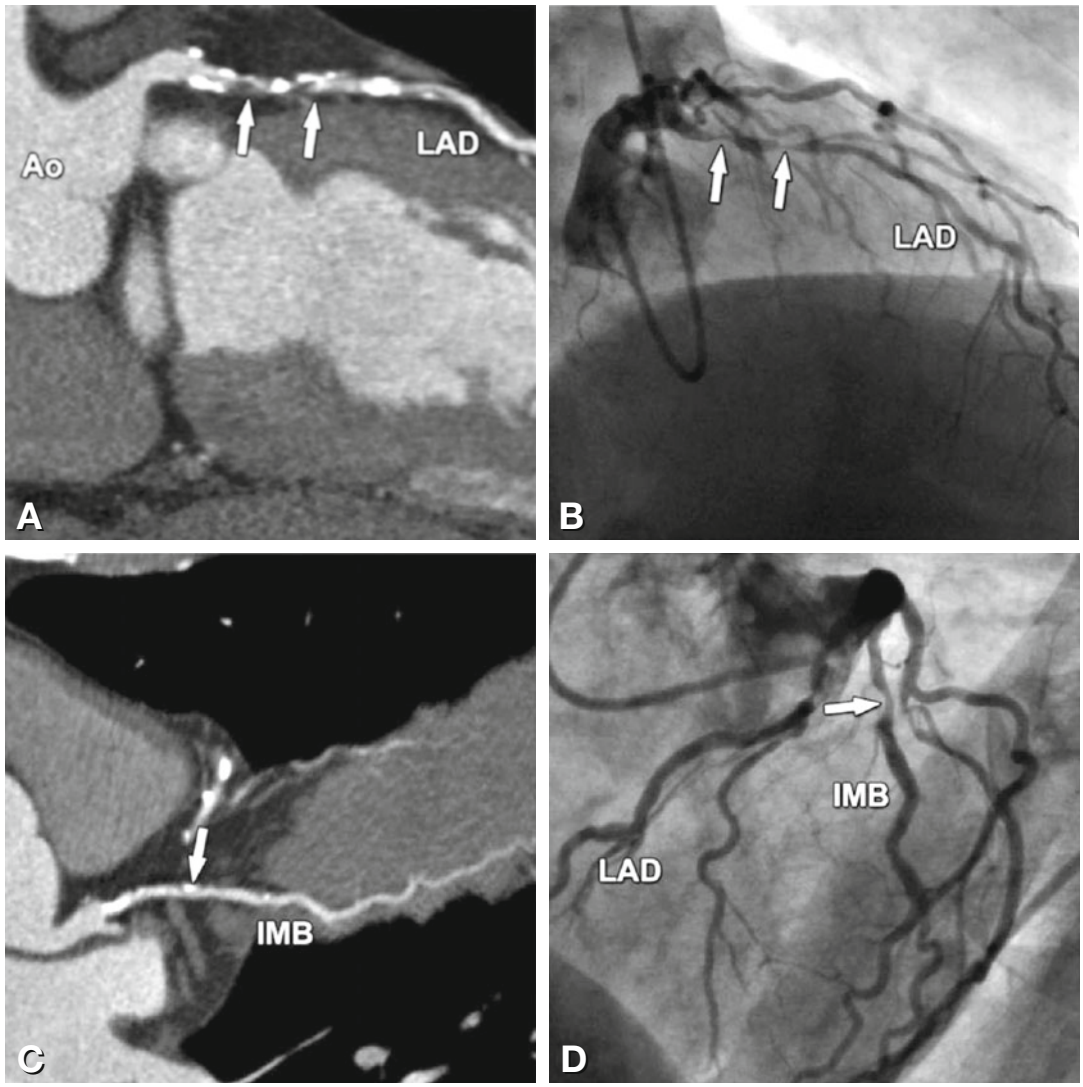

Fig. 24.9 Significant stenoses (*arrows*) in the four main coronary vessels in a 63-year-old male patient with typical angina pectoris and 0.2 mV (2 mm) ST segment depression on exercise ECG in II, III, and aVF indicating posterior ischemia. Coronary CT results are shown as curved multiplanar reformations along the vessels (*left column*) and are directly compared with conventional coronary angiography (*right column*, stenosis degrees obtained with quantitative analysis). There are two 80% diameter stenoses (*arrows*) in the proximal and mid-segment of the left anterior descending coronary artery (*LAD*, **Panels A** and **B**). These result mainly from noncalcified plaques in these two segments (**Panel A**). However, there are also severely calcified plaques that do not result in significant diameter reductions. An intermediate branch (*IMB*) is present in this patient and has a 65% diameter stenosis resulting from a calcified plaque (*arrow* in **Panels C** and **D**).

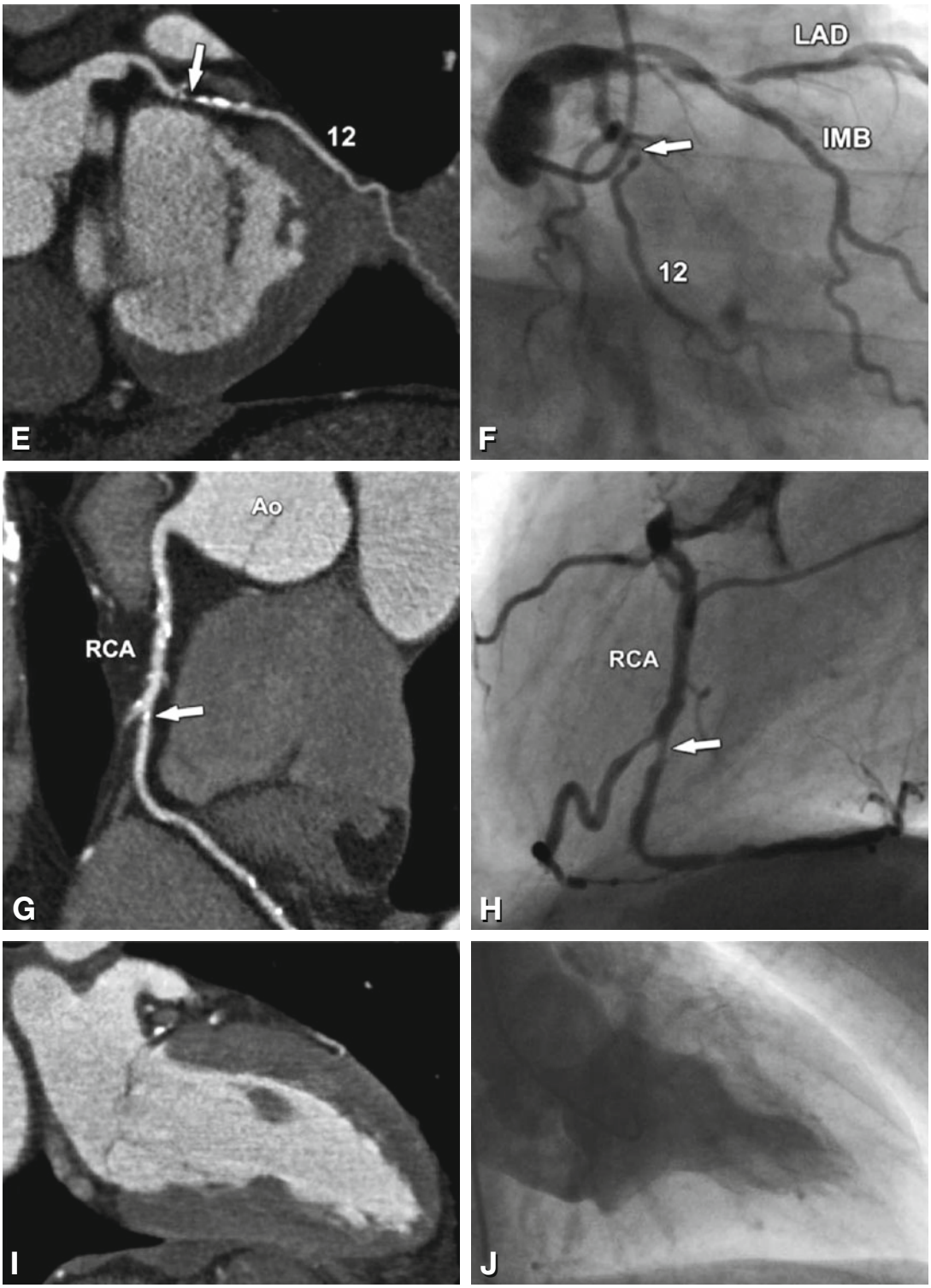

Fig. 24.9 (continued) There is another short significant coronary stenosis resulting from a noncalcified plaque in the first obtuse marginal branch (segment 12, **Panels E** and **F**), with a diameter stenosis on conventional coronary angiography of 75% that was clearly overestimated on CT (90–95%, **Panel E**). In contrast, the 80% diameter stenosis of the mid-right coronary artery (*RCA*, **Panel H**), as determined by quantitative coronary angiography, was underestimated by CT as only 65% (**Panel G**). Global left ventricular ejection fraction was 53% on CT (end-systolic two-chamber view, **Panel I**) and 50% on cineventriculography (end-systolic right anterior oblique view, **Panel J**). Thus, according to guidelines (Chap. 11) percutaneous stenting, rather than coronary bypass grafting, was initiated (beginning with the stenosis in the RCA responsible for the ischemic findings on exercise testing). *Ao* aorta

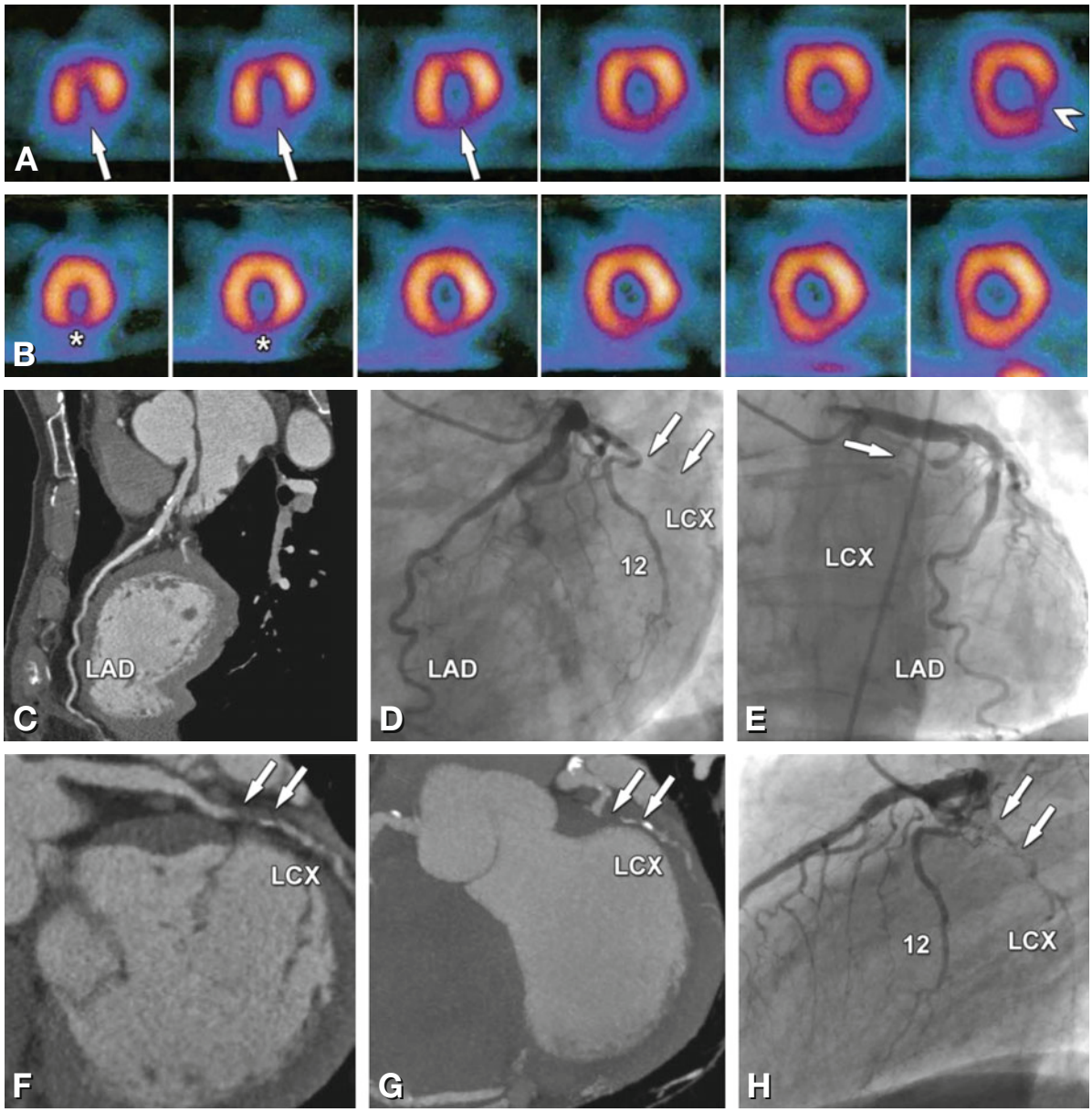

Fig. 24.10 Two-vessel coronary artery disease correctly identified on single-photon emission computed tomography (SPECT) myocardial perfusion imaging (**Panels A** and **B**) and coronary CT angiography (**Panels C**, **F**, **G**, **I**, and **J**) in a 65-year-old male patient with a 1-month history of atypical angina pectoris. SPECT shows ischemia in the apical and mid-inferior segments (*arrows* in **Panel A**, short-axis views) that correlates with less markedly reduced perfusion in the same segments at rest (*asterisks* in **Panel B**). In addition, SPECT shows ischemia in the basal inferolateral segment (*arrowhead* in **Panel A**). Coronary CT angiography shows no significant stenosis in the left anterior descending coronary artery, but only calcified plaques (*LAD*, **Panel C**). This finding is in agreement with conventional angiography (**Panels D** and **E**). However, there is a 10-mm-long occlusion of the mid-left circumflex coronary artery (*LCX*) caused by a mainly noncalcified plaque, as seen with CT (*arrows* in **Panels F** and **G**). **Panel F** is a curved multiplanar reformation along the vessel path, and **Panel G** is a maximum-intensity projection. Conventional coronary angiography confirms the presence of the occlusion but fails to exactly determine the length of the occlusion (*arrows* in **Panels D**, **E**, and **H**),

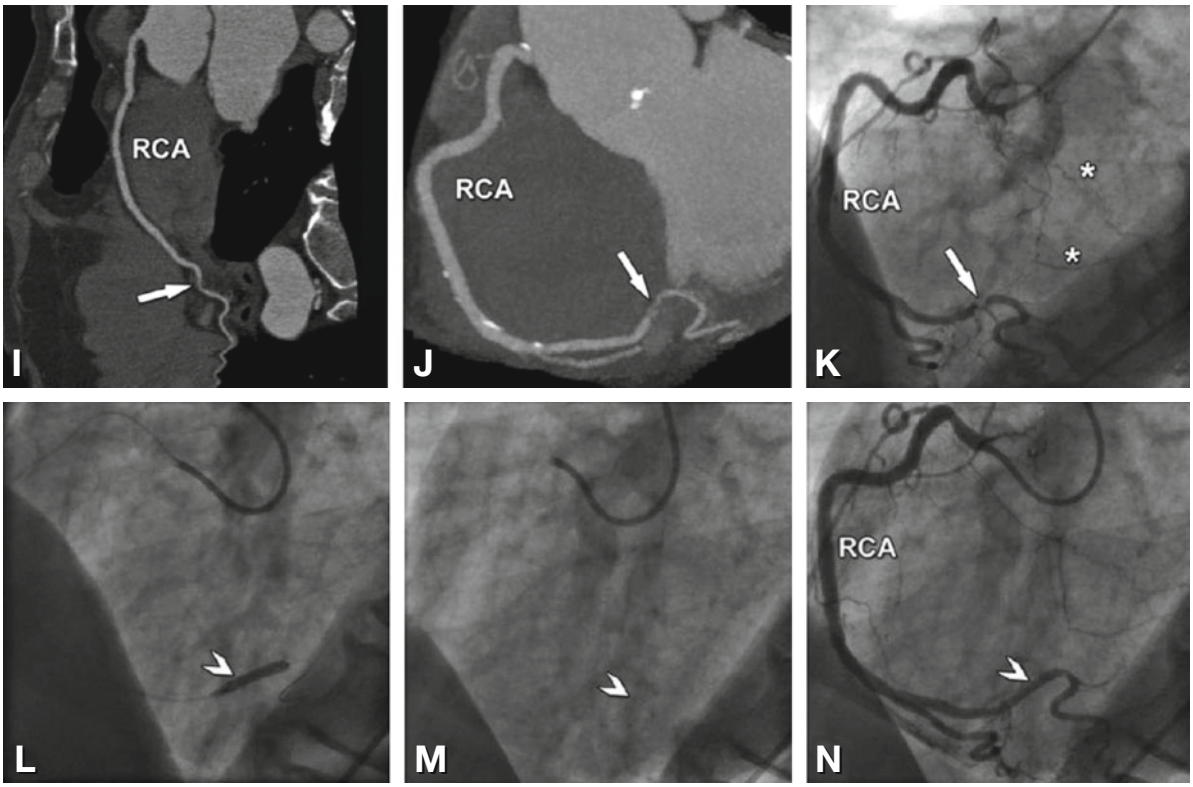

Fig. 24.10 (continued) while it nicely demonstrates the presence of right-to-left collaterals bridging the LCX occlusion (*asterisks* in **Panel K**). Both CT (**Panels I** and **J**) and conventional angiography (**Panel K**) depict a rather short significant 80% diameter stenosis (*arrow*) at the crux cordis in the right coronary artery (*RCA*). Since the occlusion was considered to be a long-standing process, the recent onset of symptoms was most likely due to the reduction in collateral flow to the LCX because of the RCA stenosis. Thus, the RCA stenosis was stented (*arrowheads*) in the same angiographic session, with good technical success (**Panels I**–**N**)

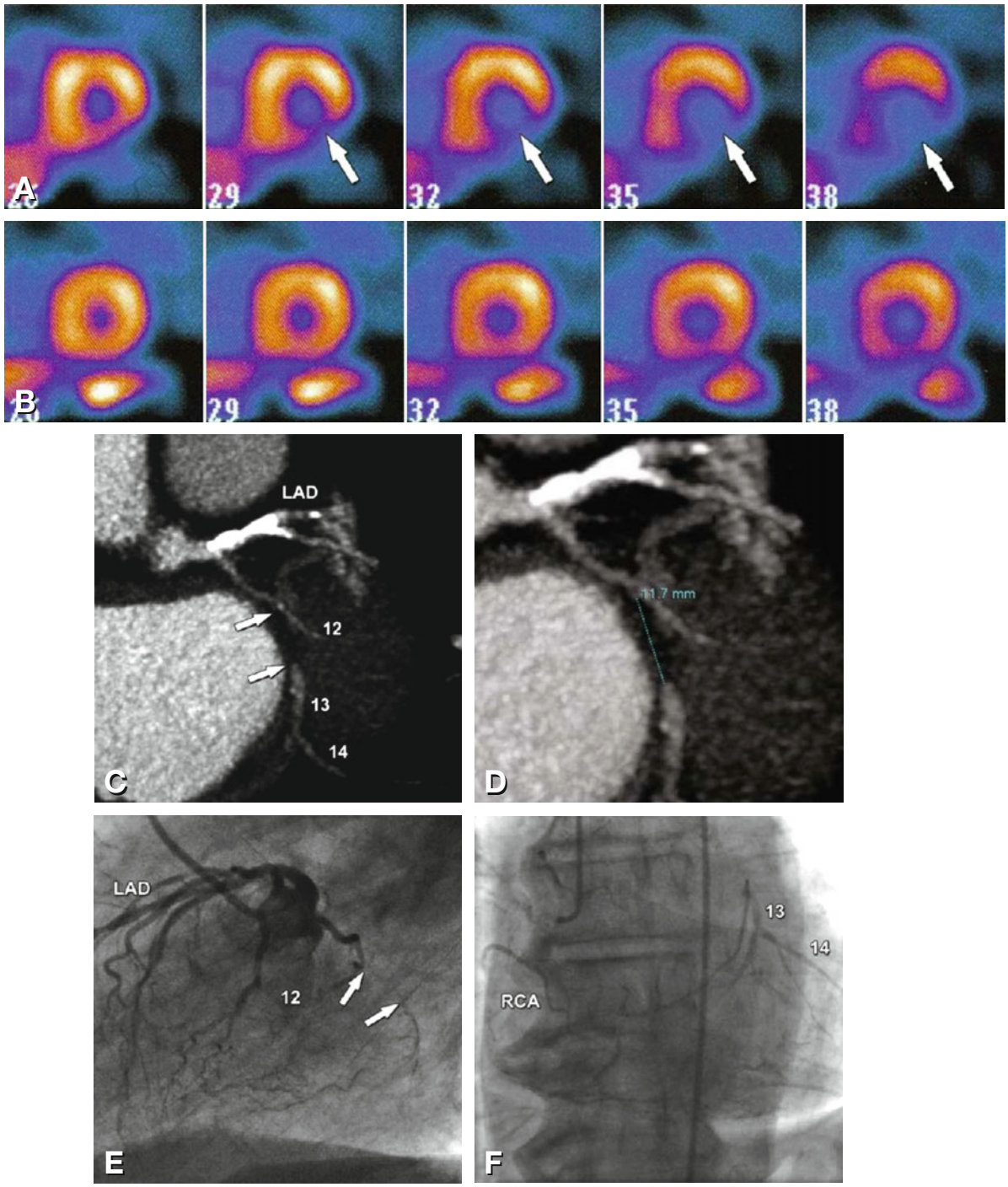

Fig. 24.11 Occlusion of the left circumflex coronary artery (LCX) in a 72-year-old male patient with atypical angina pectoris. There is basal and mid-cavity inferolateral and posterior ischemia (*arrows*) on single-photon emission computed tomography (SPECT) myocardial perfusion imaging (**Panel A**, stress exam). There was no perfusion deficit during the examination of SPECT at rest (**Panel B**). Coronary CT angiography shows a 12 mm-long occlusion (*arrows* and measurement) of the mid-LCX (segment 13) as a result of a noncalcified plaque just distal to the branching of a small obtuse marginal artery (segment 12, **Panels C** and **D**, maximum-intensity projections). Conventional coronary angiography nicely shows the occlusion (*arrows* in **Panel E**) and demonstrates right-to-left collaterals, with filling of the middle and distal left circumflex coronary segments (**Panel F**). Despite the purely noncalcified occlusion, percutaneous revascularization failed, most likely because of the location at a branching obtuse marginal artery. Note that during this angiographic session, the left anterior descending coronary artery (*LAD*) was successfully revascularized. *RCA* right coronary artery

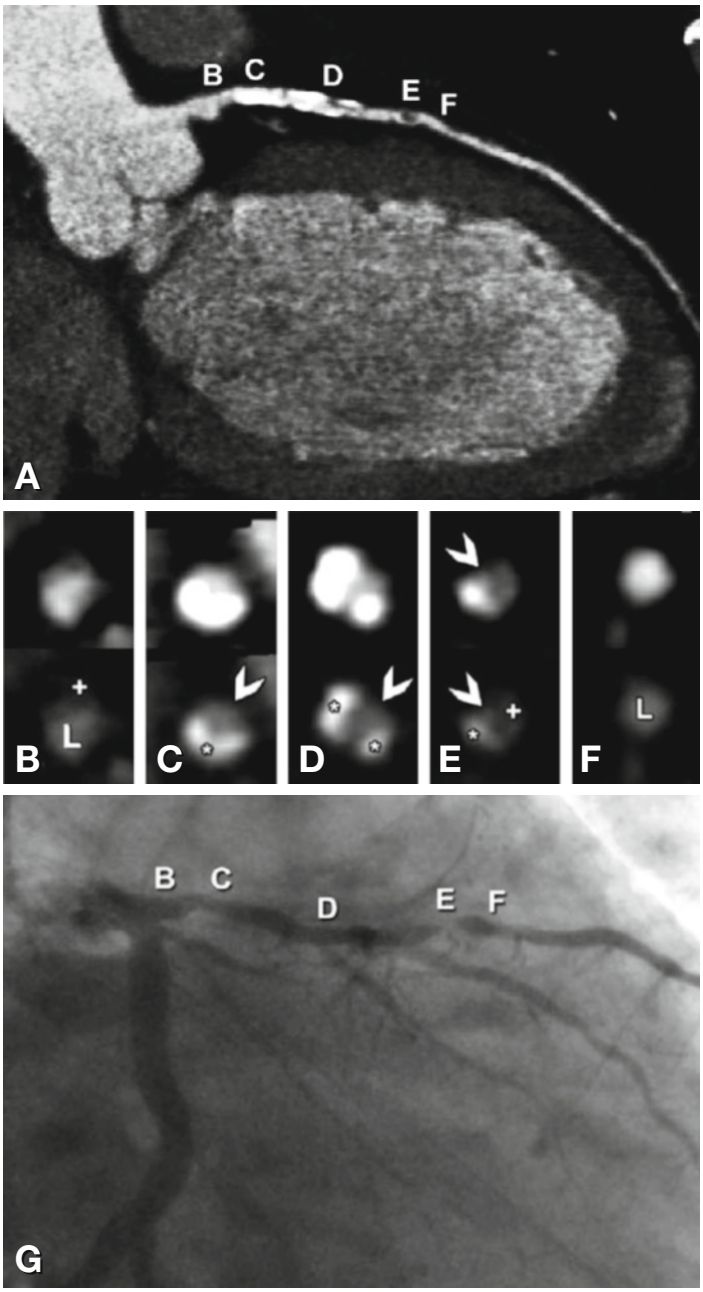

Fig. 24.12 Diffuse atherosclerotic changes in the left anterior descending coronary artery in a 63-year-old male patient with typical angina pectoris (curved multiplanar reformation of CT in **Panel A**). For correlation, cross-sections orthogonal to the curved multiplanar reformation along the vessel obtained by CT (**Panels B**–**F**) and conventional coronary angiography (**Panel G**) are provided. The letters from *B* to *F* indicate matching sites on CT (**Panel A**) and conventional angiography (**Panel G**). The corresponding cross-sections are provided in **Panels B**–**F** using standard coronary artery settings (*top row*) and bone-window-like settings (*bottom row*). Interestingly, despite the diffuse changes, there is only one significant luminal narrowing (90% diameter stenosis) of the coronary artery (*arrowhead* in **Panel E**), which is caused by a noncalcified plaque (*plus* in **Panel E**) and calcified plaque (*asterisk* in **Panel E**). Note that the residual lumen at the site of this plaque is better appreciated using the standard coronary artery window-level settings (*arrowhead* in the *upper row* in **Panel E**). In contrast, the stenosis diameter at the sites of highly calcified coronary artery plaques (*asterisks* in the *bottom row* in **Panels C** and **D**) is more easily evaluated using bone-window settings (*arrowheads* in the *bottom row* in **Panels C** and **D**). The proximal vessel segments (*B* in **Panel G**) and distal vessel segments (*F* in **Panel G**) appear very similar on conventional coronary angiography (**Panel G**). However, CT shows a relevant difference, with a large noncalcified plaque (*plus* in **Panel B**) proximally without luminal narrowing (*L* in **Panel B**), but no such atherosclerotic changes in the distal vessel segment (**Panel F**). This difference underscores the underestimation of the extent of atherosclerosis with conventional coronary angiography, which is well known from necropsy and intravascular ultrasound studies

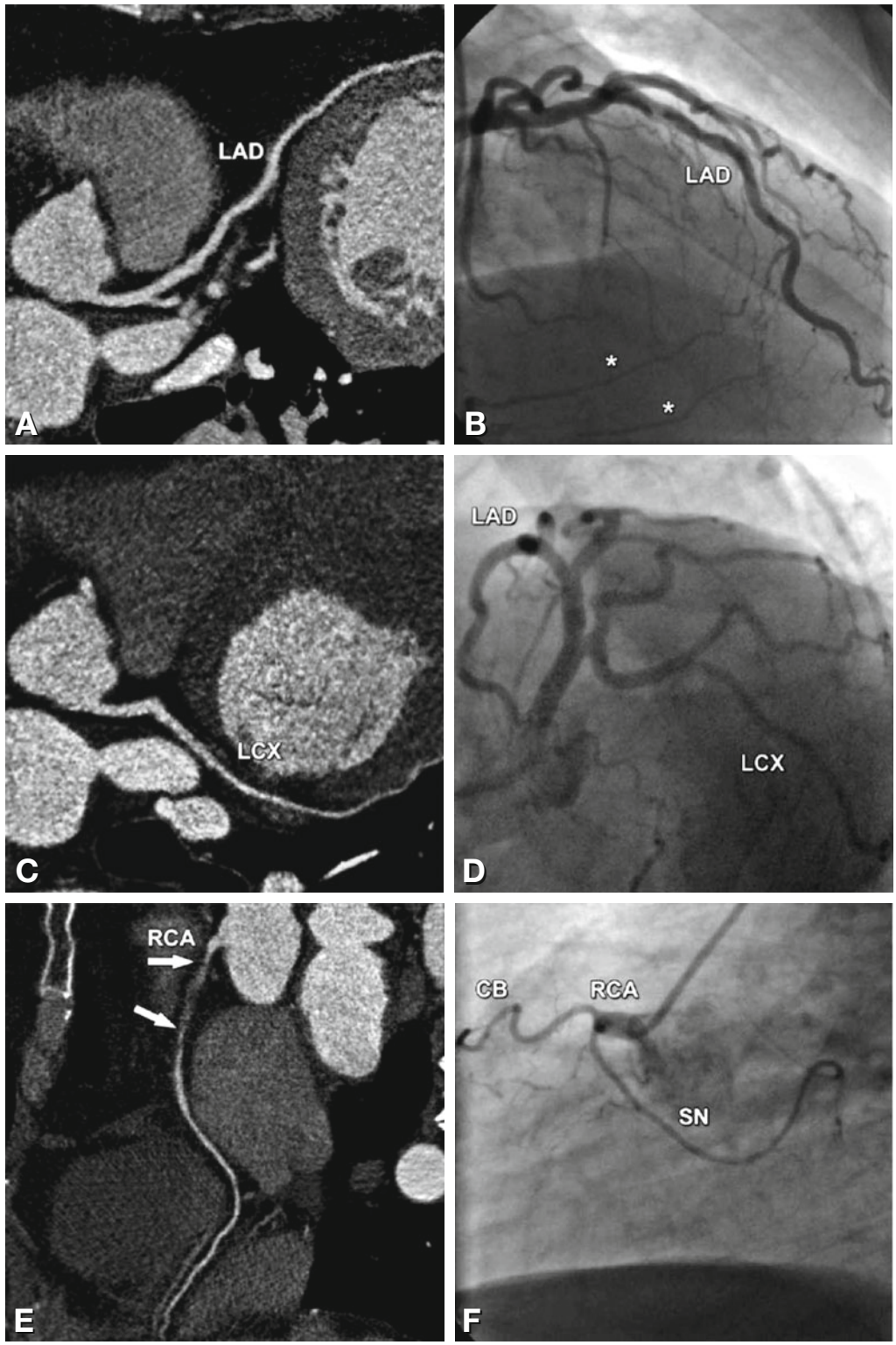
LAD
A
LAD
B
LCX
C
LAD
LCX
D
RCA
E
CB
RCA
SN
F

Fig. 24.13 Occlusion of the right coronary artery (*RCA*) in a 53-year-old male patient with rather atypical presentation (see Chap. 6 for a description of angina types) and 0.05 mV (0.5 mm) ST segment depression during stress testing in II, III, and aVF indicating posterior ischemia. There are no significant stenoses in the left anterior descending (*LAD* in **Panels A** and **B**) and left circumflex coronary artery (*LCX* in **Panels C** and **D**) as seen with coronary CT (curved multiplanar reformations in **Panels A** and **C**) and conventional coronary angiography (**Panels B** and **D**). The occlusion in the proximal and middle segments of the RCA extends over a length of 4 cm and is not calcified (*arrows* in **Panel E**). Because of the short distance from the ostium of the RCA to the beginning of the occlusion (0.5 cm, **Panel F**), percutaneous revascularization was unsuccessful. Note that CT is superior to invasive angiography in identifying the exact length of the occlusion (*arrows* in **Panel E**). Coronary bypass surgery was not considered as an option in this patient because there was good left-to-right collateralization of the occlusion (*asterisks* in **Panel B**), and the patient had only mild symptoms. However, medical therapy was optimized. *CB* conus branch, *SN* sinus node artery

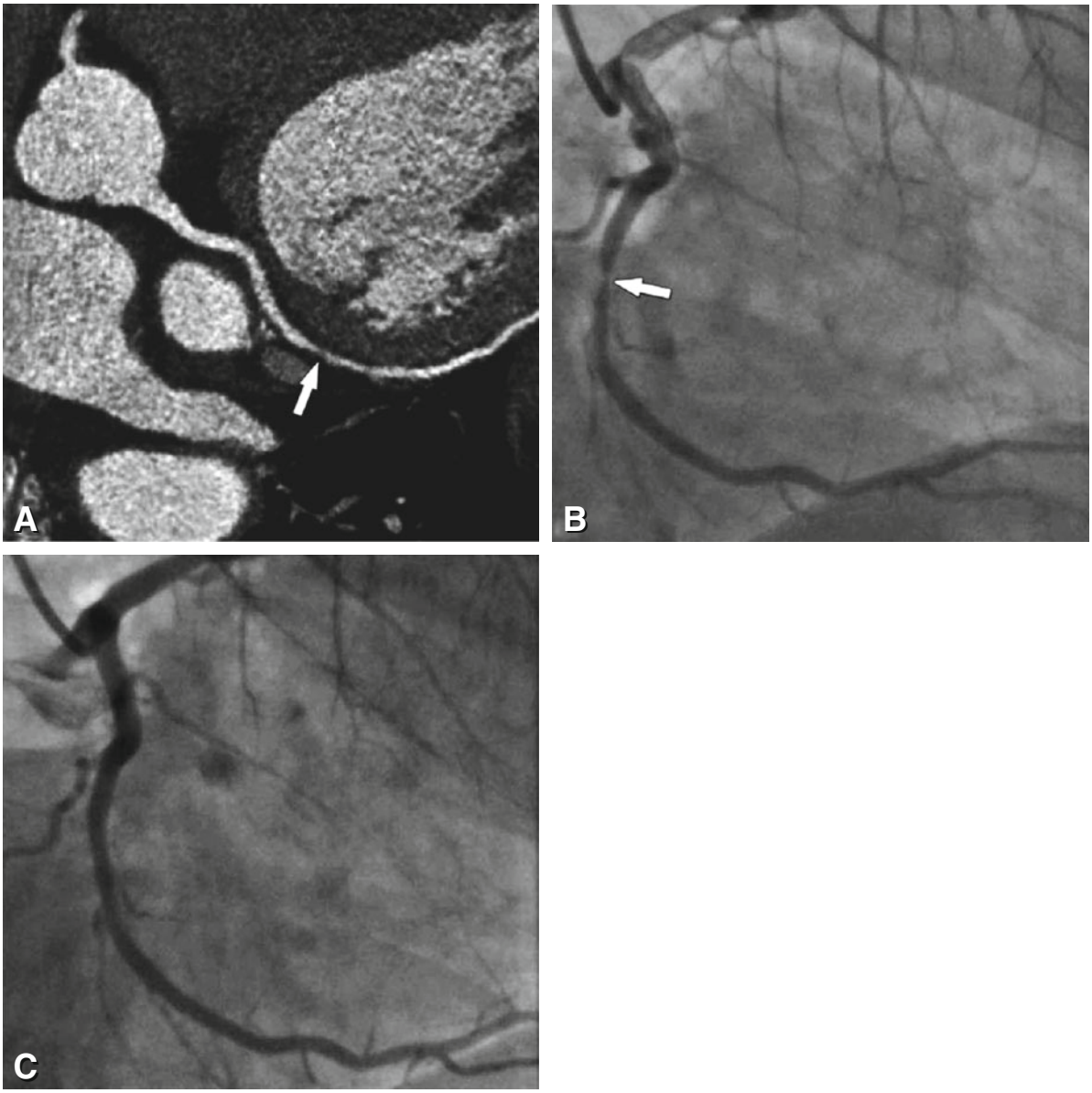

Fig. 24.14 Significant stenosis of the left circumflex coronary artery (*arrows*) in a 76-year-old male patient with typical angina pectoris, as seen with CT (**Panel A**) and conventional coronary angiography (**Panel B**). Measurement of the percent diameter stenosis resulted in values of 70% for CT and 75% for conventional angiography (with quantitative analysis). The stenosis was caused by a noncalcified plaque (*arrow* in **Panel A**). The outcome of percutaneous coronary intervention is shown in **Panel C**

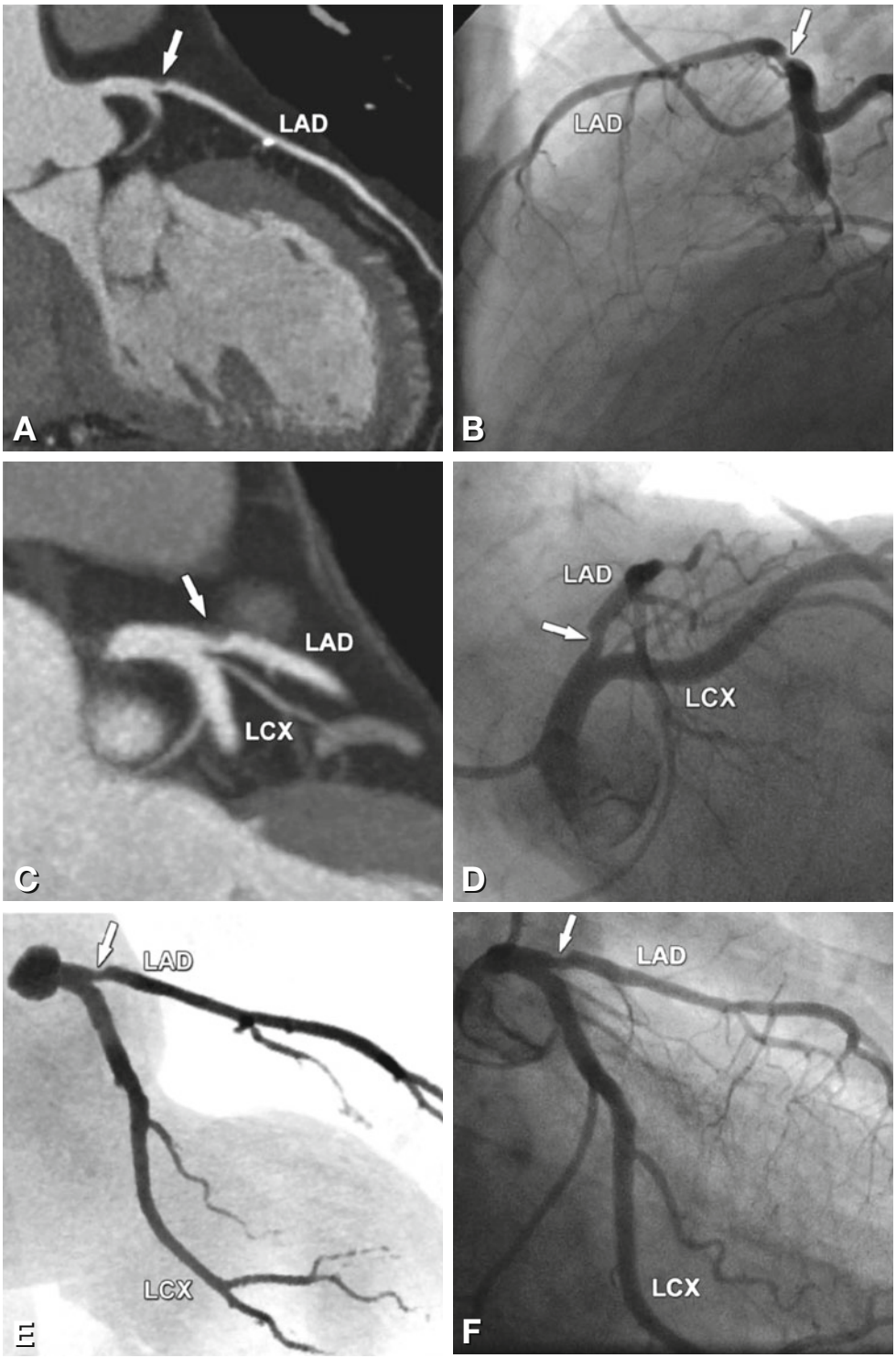

Fig. 24.15 Borderline stenosis (*arrows*) of the proximal left anterior descending coronary artery (*LAD*) in a 62-year-old male patient with typical angina pectoris, as seen with CT (*left column*) and conventional angiography (*right column*). Results of coronary CT angiography are shown as a curved multiplanar reformation (**Panel A**), thin-slab maximum-intensity projection (**Panel C**), and angiographic emulation (**Panel E**). There is good correlation with the corresponding invasive angiogram projections (**Panels B**, **D**, and **F**). Both CT and quantitative conventional coronary angiography estimated a percent diameter stenosis of 50%. Because there were no signs of ischemia on exercise ECG, no revascularization was attempted. With optimized medical management, the patient's angina pectoris resolved. Note that there is a small calcified plaque in the mid-LAD (**Panel A**). *LCX* left circumflex coronary artery

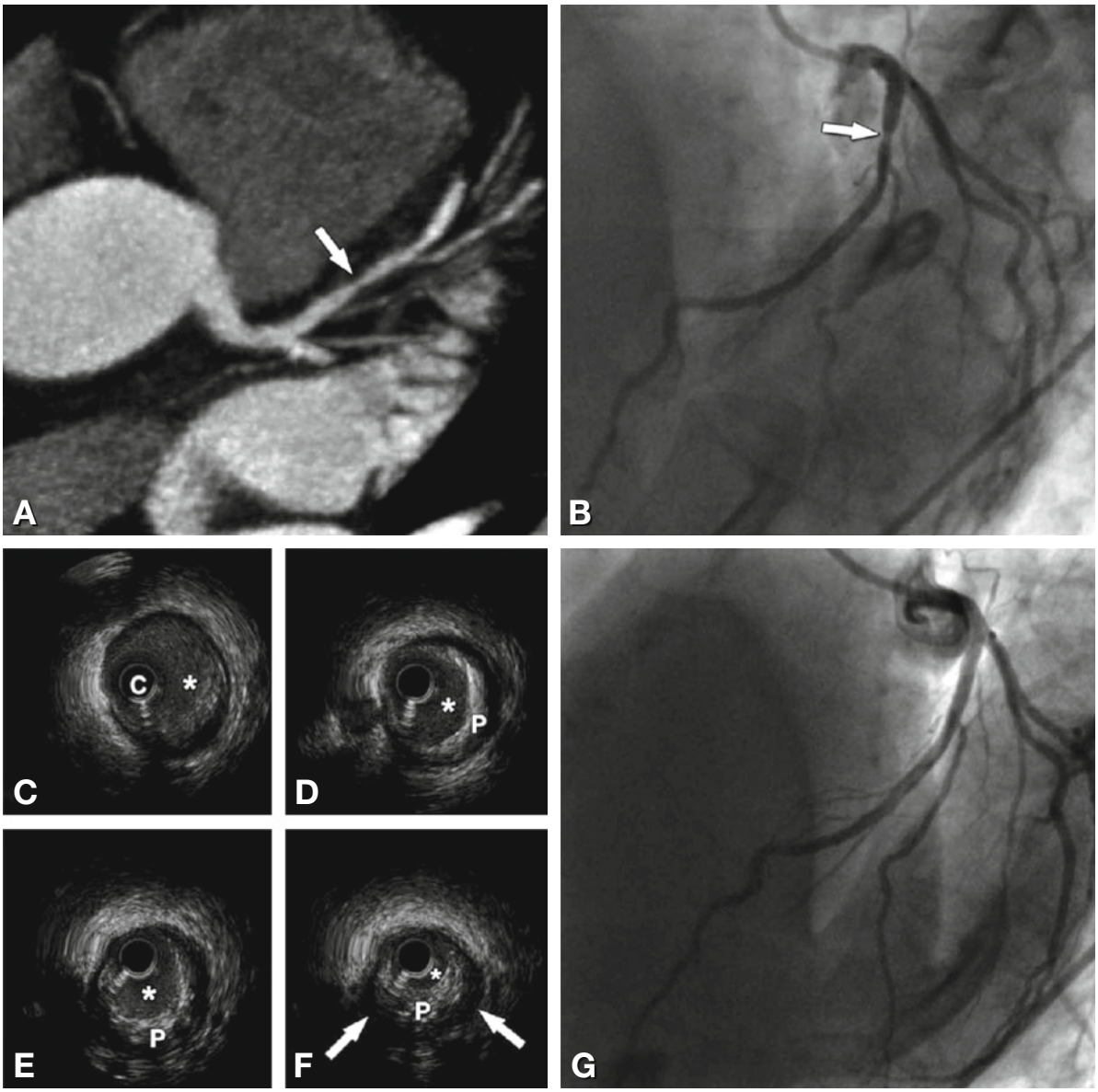

Fig. 24.16 Coronary artery stenosis (*arrow*) in the left anterior descending coronary artery, graded differently by CT (**Panel A**) and invasive angiography (**Panel B**) in a 62-year-old female patient with typical angina pectoris and ST segment depression of 0.15 mV (1.5 mm) in V4-6 during stress testing (bicycle) indicating anterior ischemia. CT shows a short 70% diameter stenosis caused by a noncalcified plaque in the proximal vessel segment with positive remodeling (**Panel A**, maximum-intensity projection), whereas quantitative analysis of conventional angiography shows only a 40% diameter reduction. Because of worsening angina pectoris and the coronary CT findings, repeat angiography, including intravascular ultrasound (**Panels C**–**F**), was performed 6 months later. Intravascular ultrasound (cross-sections), located from proximal LAD to the stenosis, confirmed the presence of the plaque (*P* in **Panels D**–**F**) that caused a short 70% diameter stenosis (*arrows* in **Panel F**) of the lumen (*asterisk* in **Panels C**–**F**). On the basis of these findings, percutaneous coronary intervention was performed (**Panel G**). *C* intravascular ultrasound catheter

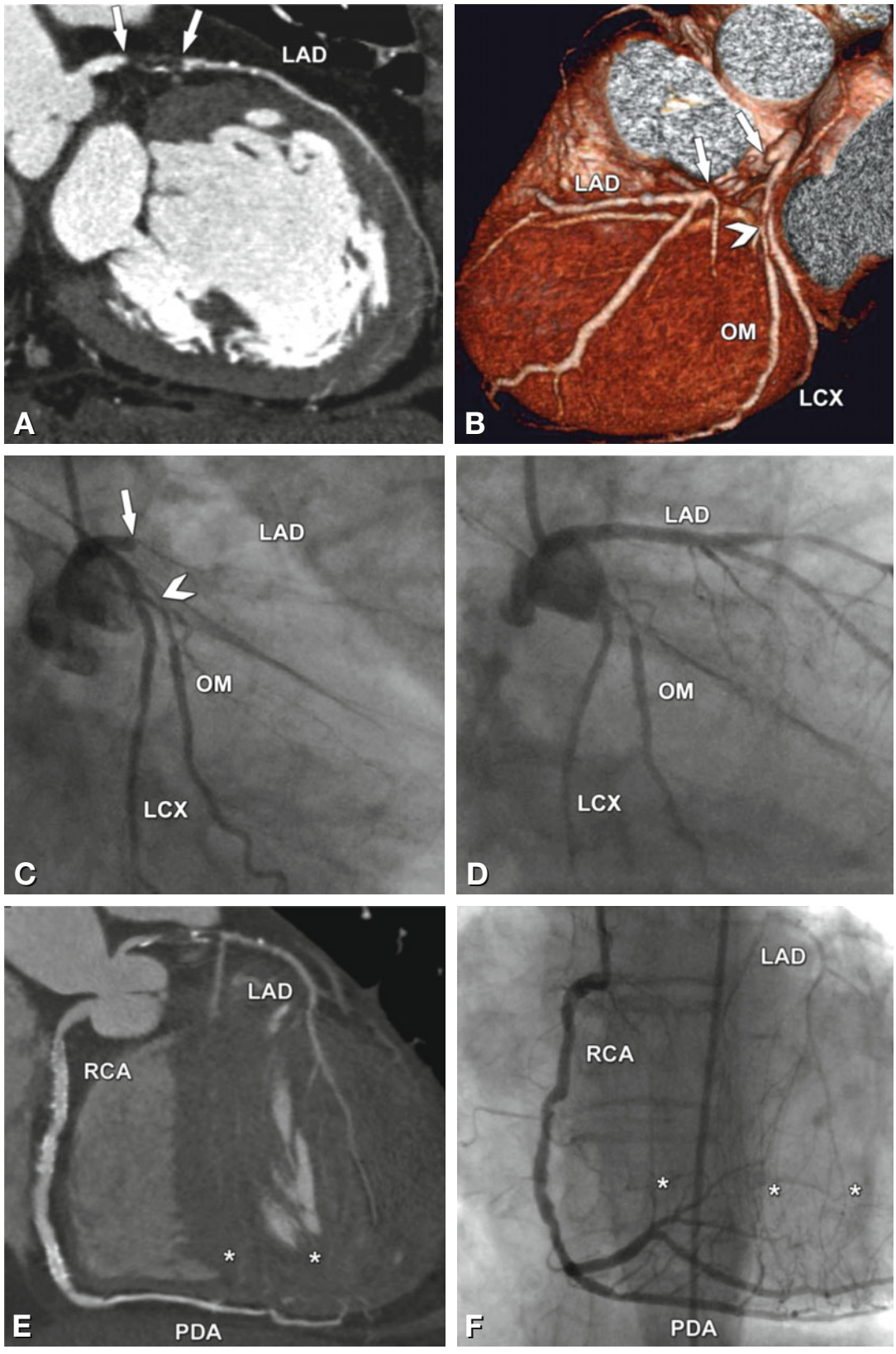
LAD
A
LAD
OM
LCX
B
LAD
OM
LCX
C
LAD
OM
LCX
D
LAD
RCA
*
*
E
PDA
LAD
RCA
*
*
*
F
PDA

Fig. 24.17 Occlusion of the proximal left anterior descending coronary artery (*LAD*) in a 78-year-old female patient with a 2-week history of typical angina pectoris (*arrows* in **Panels A**–**C**). A curved multiplanar reformation of CT is shown in **Panel A**, while **Panel B** is a volume-rendered three-dimensional reconstruction. There is an excellent correlation with conventional coronary angiography, and the length (1.5 cm) of the occlusion, which was mainly caused by a noncalcified plaque, is better seen with CT (*arrows* in **Panel A**). Percutaneous coronary intervention was performed during the same angiographic session, and good revascularization was achieved (compare **Panel D** with **Panel C**). There was also a significant stenosis (*arrowhead* in **Panels B** and **C**) of the obtuse marginal artery (*OM*) of the left circumflex coronary artery (*LCX*). The LAD occlusion was collateralized via septal branches (*asterisks* in **Panels E** and **F**) arising from the posterior descending coronary artery (*PDA*). **Panel E** is a CATH view (curved thin-slab maximum-intensity projection) of coronary CT angiography along the right coronary artery (*RCA*). This CT reconstruction is superior in that it depicts both the RCA with the collaterals (*asterisks*) and the LAD (with the occlusion) in a single image

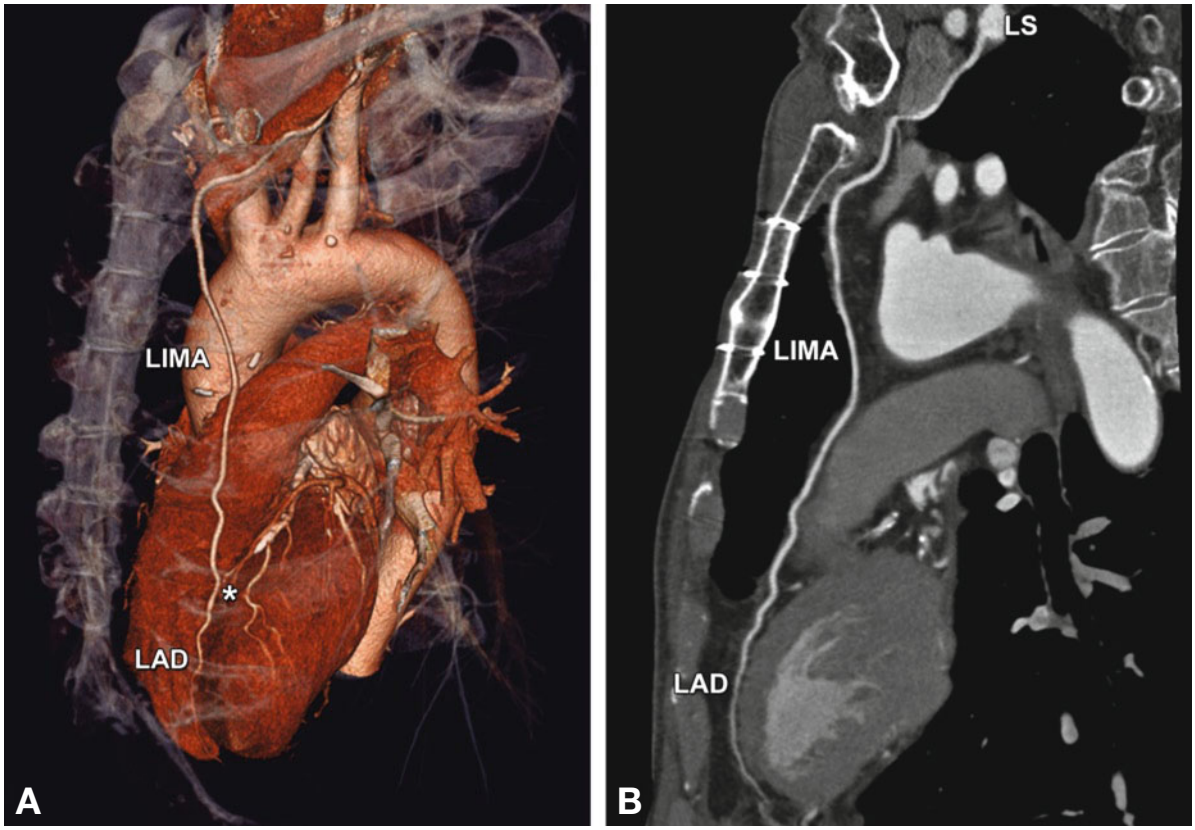

Fig. 24.18 Normal left internal mammary artery (*LIMA*) coronary bypass graft to the left anterior descending coronary artery (*LAD*). The CT data are shown in a three-dimensional volume-rendered reconstruction (left anterosuperior view, **Panel A**), with the distal anastomosis indicated by an *asterisk*. The curved multiplanar reformation along the arterial graft (including its origin from the left subclavian artery, *LS*) is shown in **Panel B**

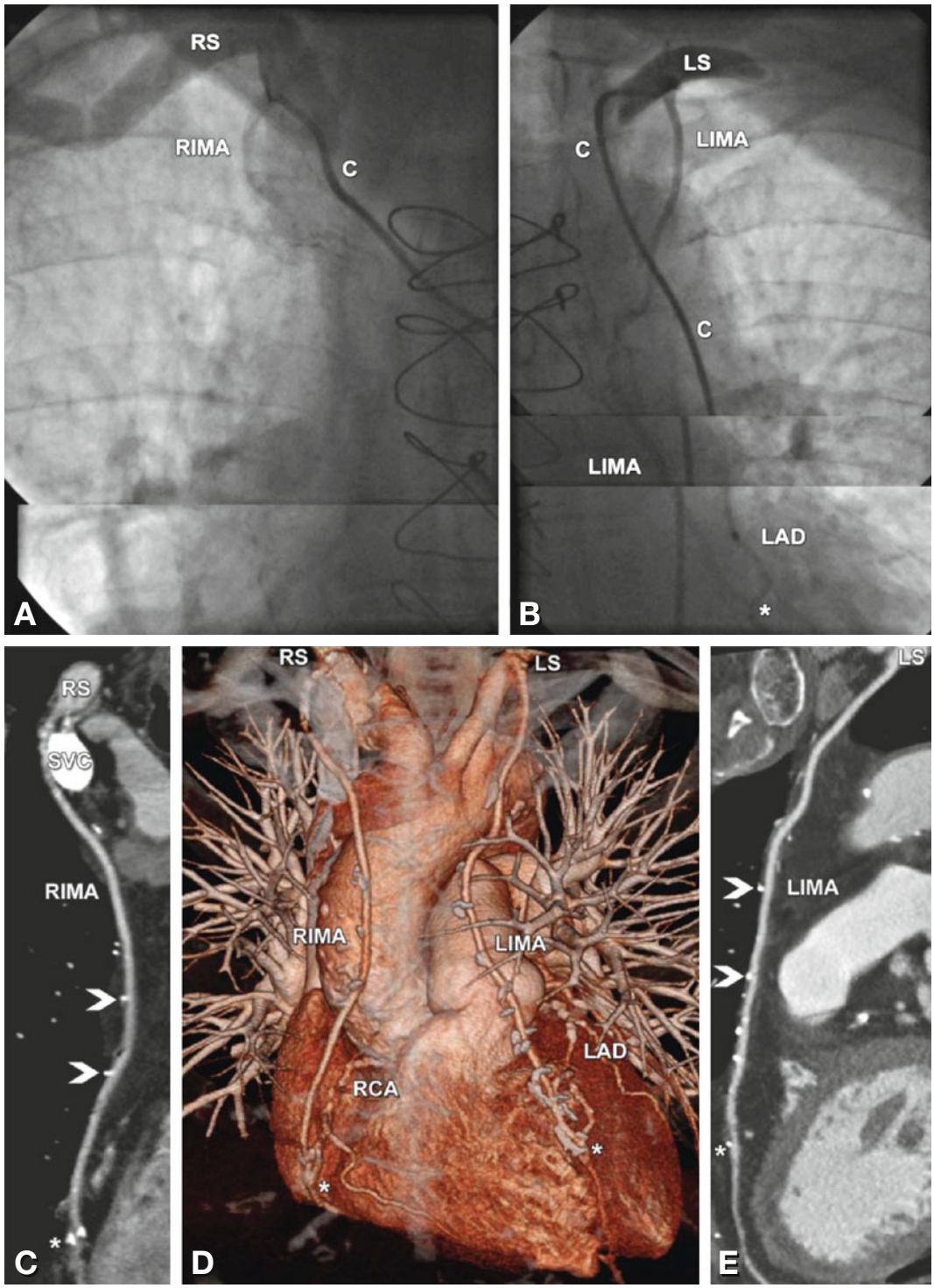
RS
RIMA
C
A
LS
C
LIMA
C
LIMA
LAD
*
B
RS
SVC
RIMA
*
C
RS
LS
RIMA
LIMA
LAD
RCA
*
*
D
LS
LIMA
*
E

Fig. 24.19 Advantages of coronary CT angiography in depicting coronary bypasses. Example of patent coronary arterial bypass grafts in a 68-year-old male patient with typical angina pectoris who underwent bypass grafting 7 years earlier. Conventional coronary angiography failed to demonstrate patency of the graft because it was not possible to selectively insert the catheter into the right internal mammary artery (*RIMA*, **Panel A**). *C* indicates the position of the catheter. The left internal mammary artery (*LIMA*) coronary bypass to the left anterior descending coronary artery (*LAD*) including the distal anastomosis (*asterisk*) was normal on conventional angiography (**Panel B**). CT was initiated, and in contrast to the conventional angiograms, it was able to demonstrate a normal RIMA graft to the right coronary artery (*RCA*) on both a curved multiplanar reformation (**Panel C**) and a three-dimensional volume-rendered reconstruction (*anterior view*, **Panel D**). Coronary CT angiography also confirmed the patency of the LIMA to the LAD (**Panels D** and **E**). Note the metallic surgical clips along the arterial bypass grafts (*arrowheads* in **Panels C** and **E**) and the distal anastomoses (*asterisk* in **Panels C** and **E**). Very dense contrast material is still present in the superior vena cava (*SVC*) because the injection was performed via a right cubital vein. Deviating from the standard procedure of contrast injection into the right arm veins and using left-sided injection instead might have been preferable in this patient. This way, LIMA assessment might have been limited, but CT was primarily performed because conventional angiography was nondiagnostic with regard to the RIMA graft. *C* catheter, *LS* left subclavian artery, *RS* right subclavian artery

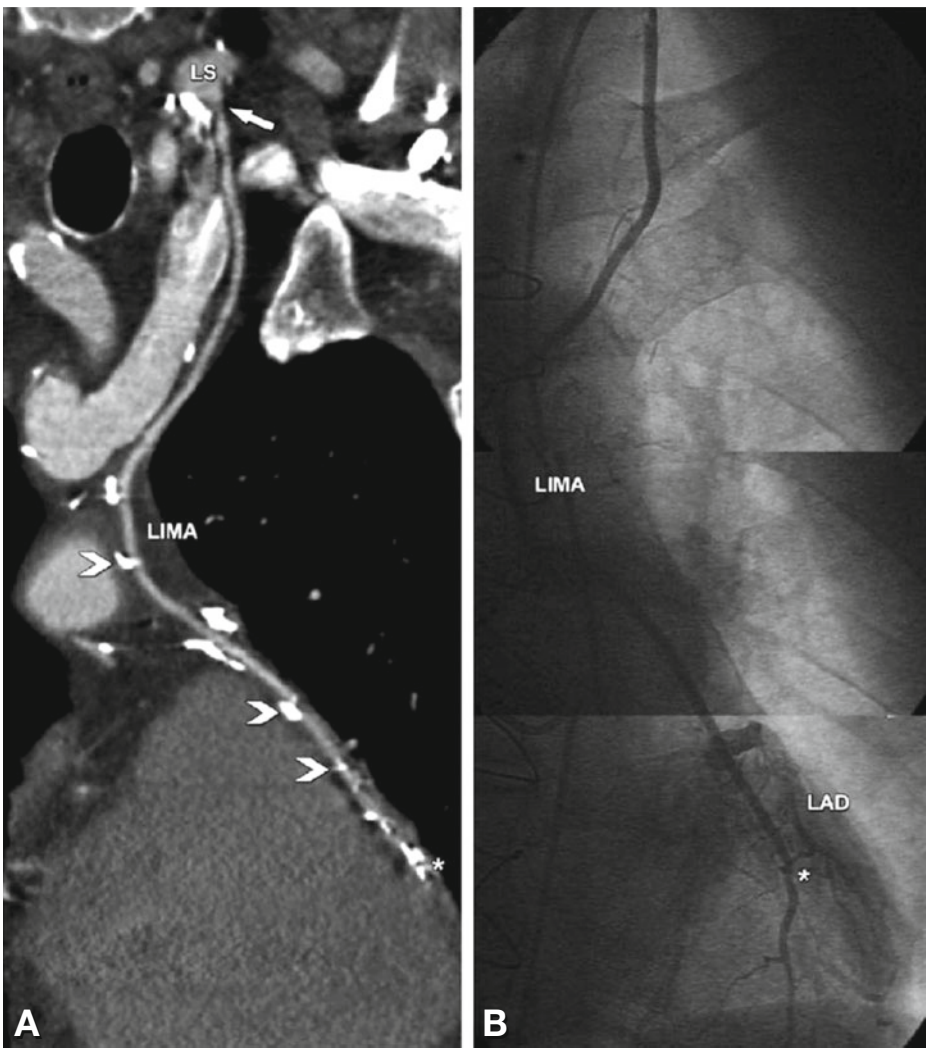

Fig. 24.20 Advantages of conventional coronary angiography in depicting coronary bypasses. In this 74-year-old male patient with atypical angina pectoris who underwent left internal mammary artery (*LIMA*) coronary bypass grafting to the left anterior descending coronary artery (*LAD*) 4 years ago, CT was unable to rule out significant stenoses because of artifacts arising from nearby dense contrast material in the veins (*arrow*) and surgical clips (*arrowheads* in **Panel A**, curved multiplanar reformation). Also, the distal anastomosis (*asterisk*) could not be reliably assessed with CT (**Panel A**). In contrast, subsequently performed conventional angiography shows a patent LIMA to LAD (**Panel B**). Newer surgical clips have a lower metal content and therefore tend to produce fewer artifacts on coronary CT

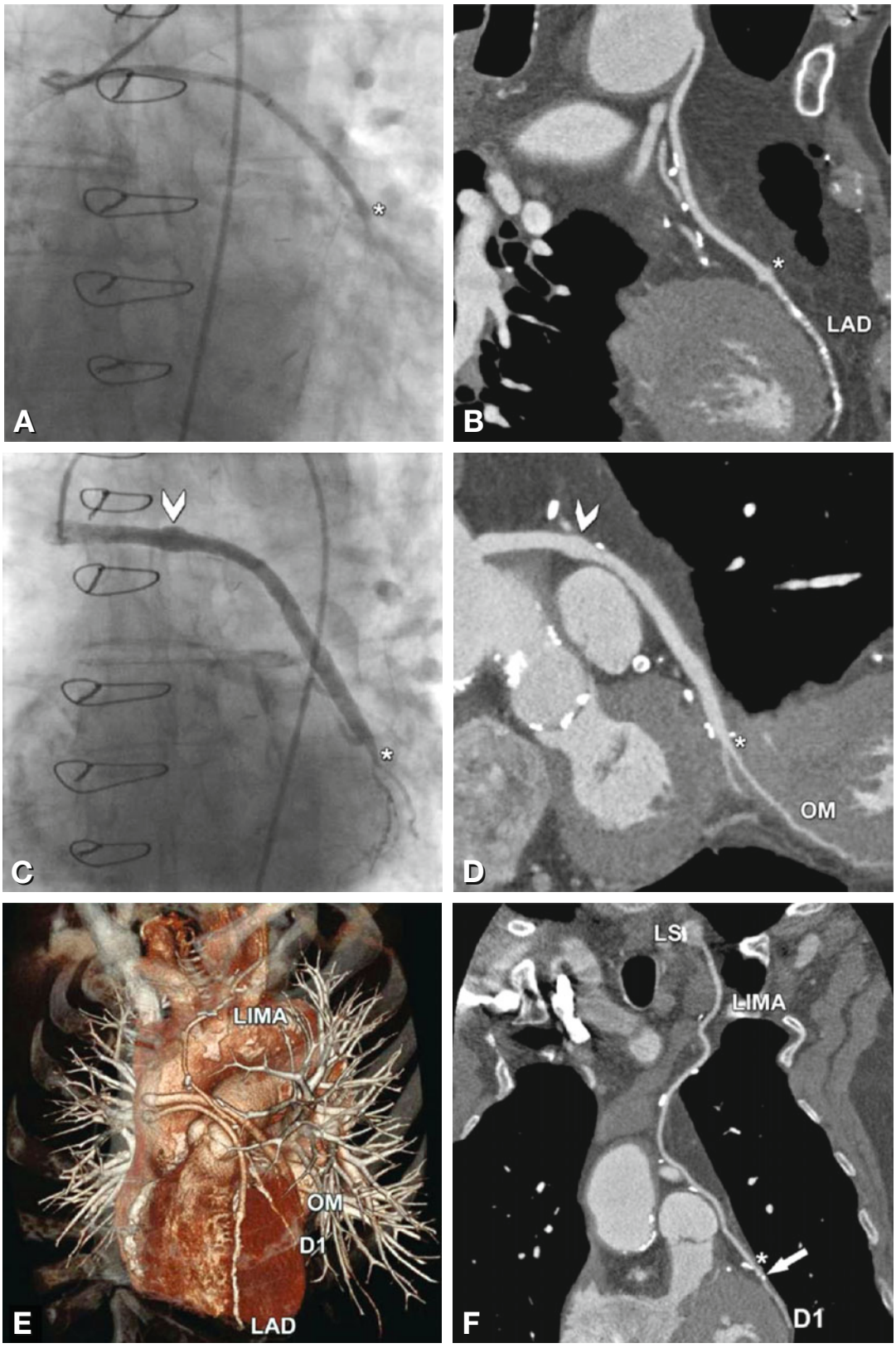
A
B
LAD
C
D
OM
E
LIMA
OM
D1
LAD
F
LSI
LIMA
D1

Fig. 24.21 Normal coronary arterial and venous bypass grafts in a 79-year-old male patient. There is good correlation of conventional angiography (**Panels A** and **C**) and CT (**Panels B** and **D**) in the evaluation of the venous bypass grafts to the left anterior descending coronary artery (*LAD*, **Panels A** and **B**) and the obtuse marginal artery (*OM*, **Panels C** and **D**). There is focal dilatation of the venous graft to the OM due to a venous valve (*arrowhead* in **Panels C** and **D**), while the distal anastomoses (*asterisk*) are unremarkable (**Panels A**–**D**). However, conventional angiography was unsuccessful in aiding the selective insertion of a catheter into the left internal mammary artery (*LIMA*). Thus, CT was initiated and was able to visualize this graft to the first diagonal branch (*D1*). Three-dimensional and curved multiplanar reformations of the LIMA graft are shown in **Panels E** and **F**, respectively. The distal anastomosis of this graft was normal (*asterisk* in **Panel F**), but there was a significant stenosis of the D1 (*arrow* in **Panel F**), which was also seen on conventional coronary angiography. *LS* left subclavian artery

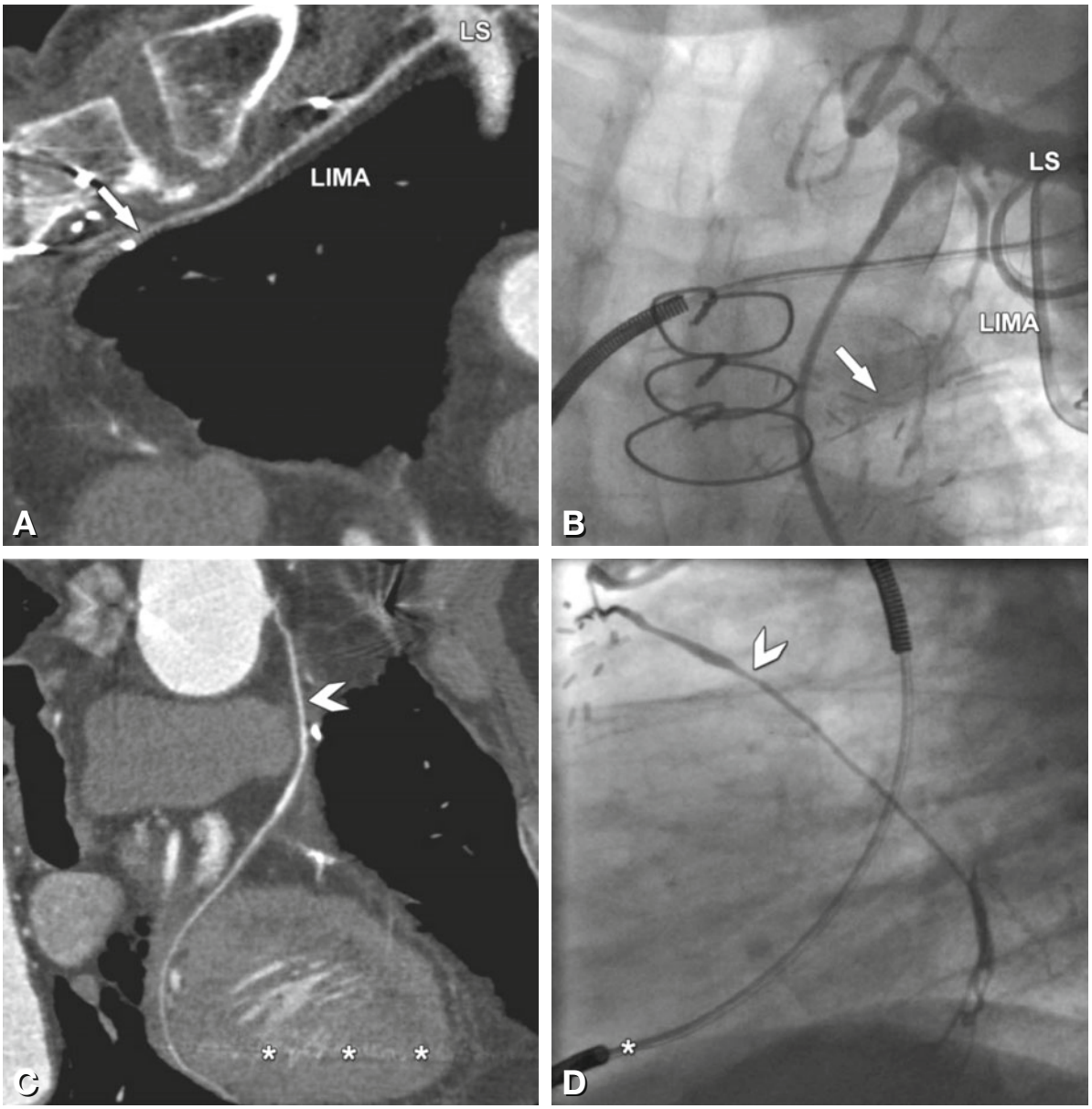

Fig. 24.22 Occluded arterial and functionally occluded venous bypass graft in a 66-year-old male patient without angina but with severe dyspnea. Curved multiplanar reformation along the left internal mammary artery (*LIMA*) shows occlusion about 5–6 cm from the origin (*arrow* in **Panel A**). There is good agreement with the findings from conventional angiography (**Panel B**). The venous bypass graft to the obtuse marginal artery has a very small diameter of only 1 mm (*arrowhead*) and is functionally occluded, as seen on CT (**Panel C**, curved multiplanar reformation) and conventional angiography (**Panel D**). Note that the patient has an implanted cardiac defibrillator (*asterisk* in **Panel D**), which leads to minor artifacts on CT (*asterisks* in **Panel C**). *LS* left subclavian artery

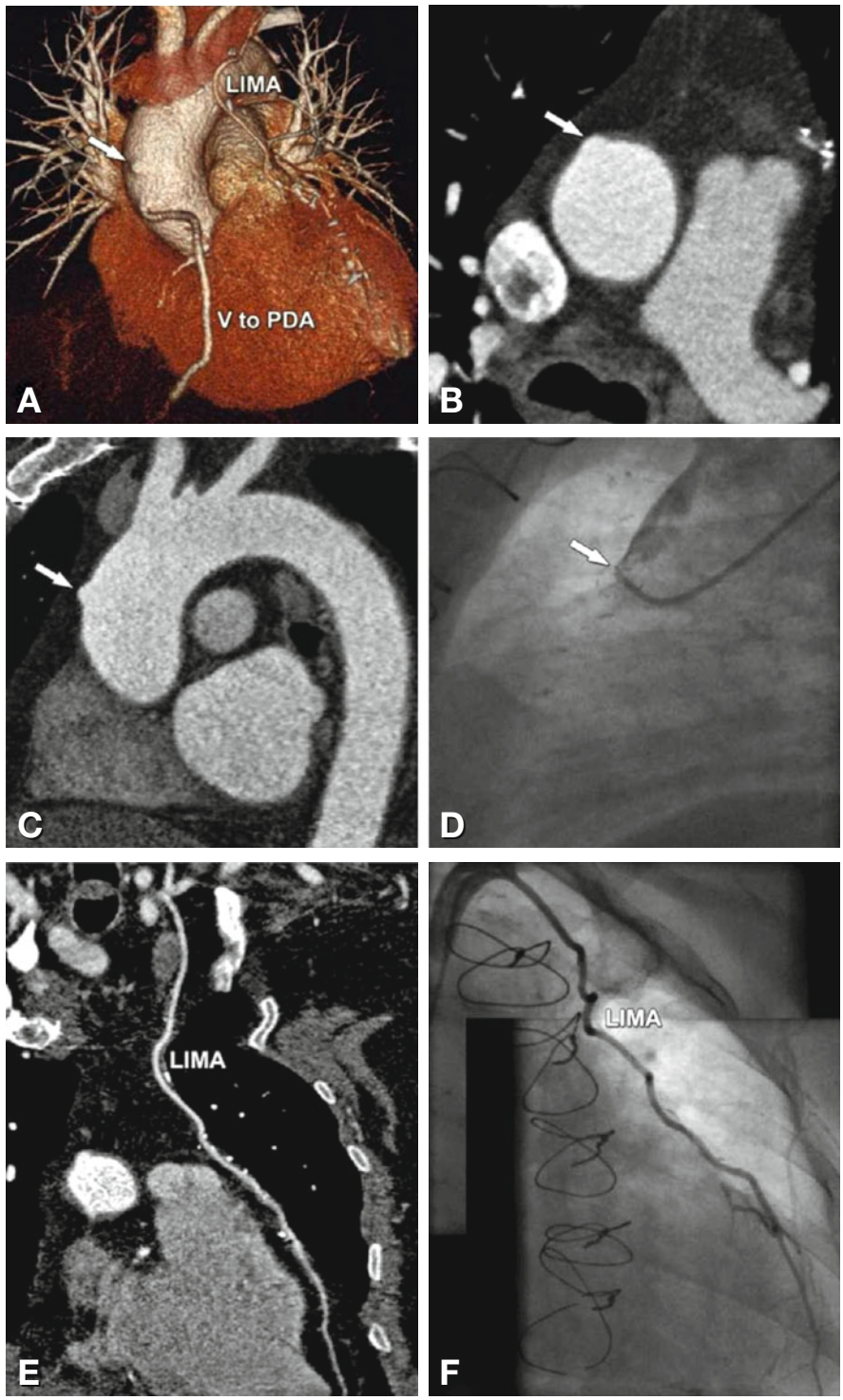

Fig. 24.23 Comprehensive assessment of coronary bypass grafts and native coronary arteries in a 64-year-old female patient with atypical angina pectoris. There is ostial occlusion of the venous bypass graft, which passed to the left circumflex coronary artery, as can be seen in the three-dimensional reconstruction of CT (*arrow* in **Panel A**). In axial source images and a sagittal reconstruction of CT, the occlusion (*arrow*) looks like a small outpouching of the lumen (**Panels B** and **C**). Conventional angiography confirmed the occlusion (*arrow* in **Panel D**). The left internal mammary artery (*LIMA*) is patent to the left anterior descending coronary artery (**Panels E** and **F**).

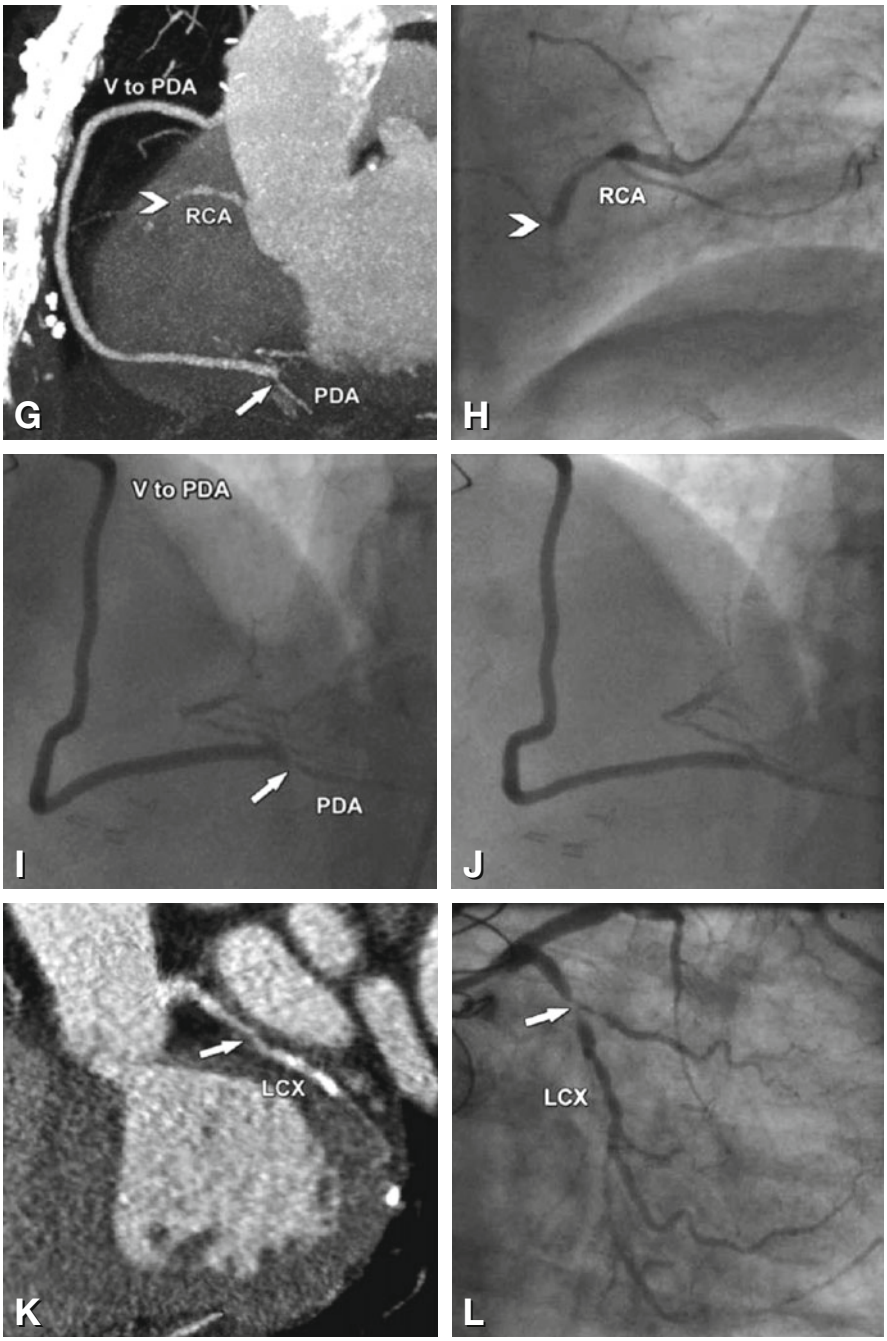

Fig. 24.23 (continued) But CT detected significant stenosis at the distal anastomosis (*arrows*) of the venous bypass graft to the posterior descending coronary artery (*V to PDA*, **Panel G**). **Panel G** is a maximum-intensity projection demonstrating the stenosis at the anastomosis to the PDA (*arrow*). The right coronary artery (*RCA*) is occluded at the junction of segments 1 and 2 (*arrowhead* in **Panel G**). Both the occlusion of the RCA (*arrowhead* in **Panel H**) and the stenosis at the distal anastomosis of the venous bypass graft to the posterior descending coronary artery (*arrow* in **Panel I**) were confirmed by subsequently performed conventional angiography. During the same angiographic session, percutaneous coronary stenting of the stenosis of the distal anastomosis was performed (**Panel J**). CT also found a significant stenosis (*arrow*) of the left circumflex coronary artery (*LCX*, **Panel K**), which was confirmed by conventional angiography (*arrow* in **Panel L**) and was also treated interventionally

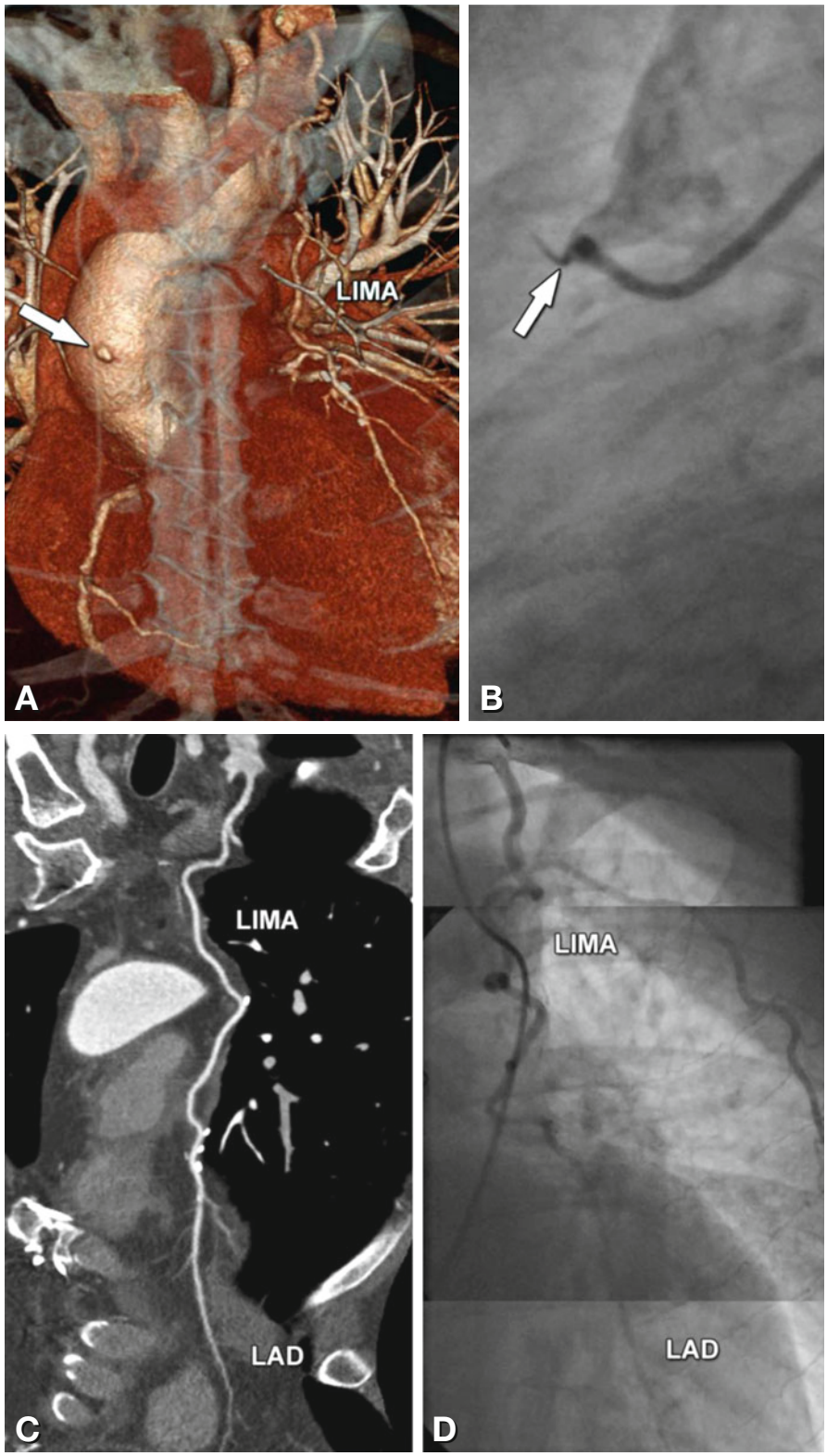

Fig. 24.24 Occluded venous bypass graft and patent left internal mammary artery (*LIMA*) in a 64-year-old male patient with atypical angina. Ostial occlusion of the venous bypass graft (*arrow*) that supplies the left circumflex coronary artery (**Panel A**). **Panel A** is a three-dimensional reconstruction (anterior view). This finding was confirmed by conventional coronary angiography (lateral projection, *arrow* in **Panel B**). The LIMA to the left anterior descending coronary artery (*LAD*) was unremarkable on both CT (curved multiplanar reformation, **Panel C**) and conventional angiography (**Panel D**)

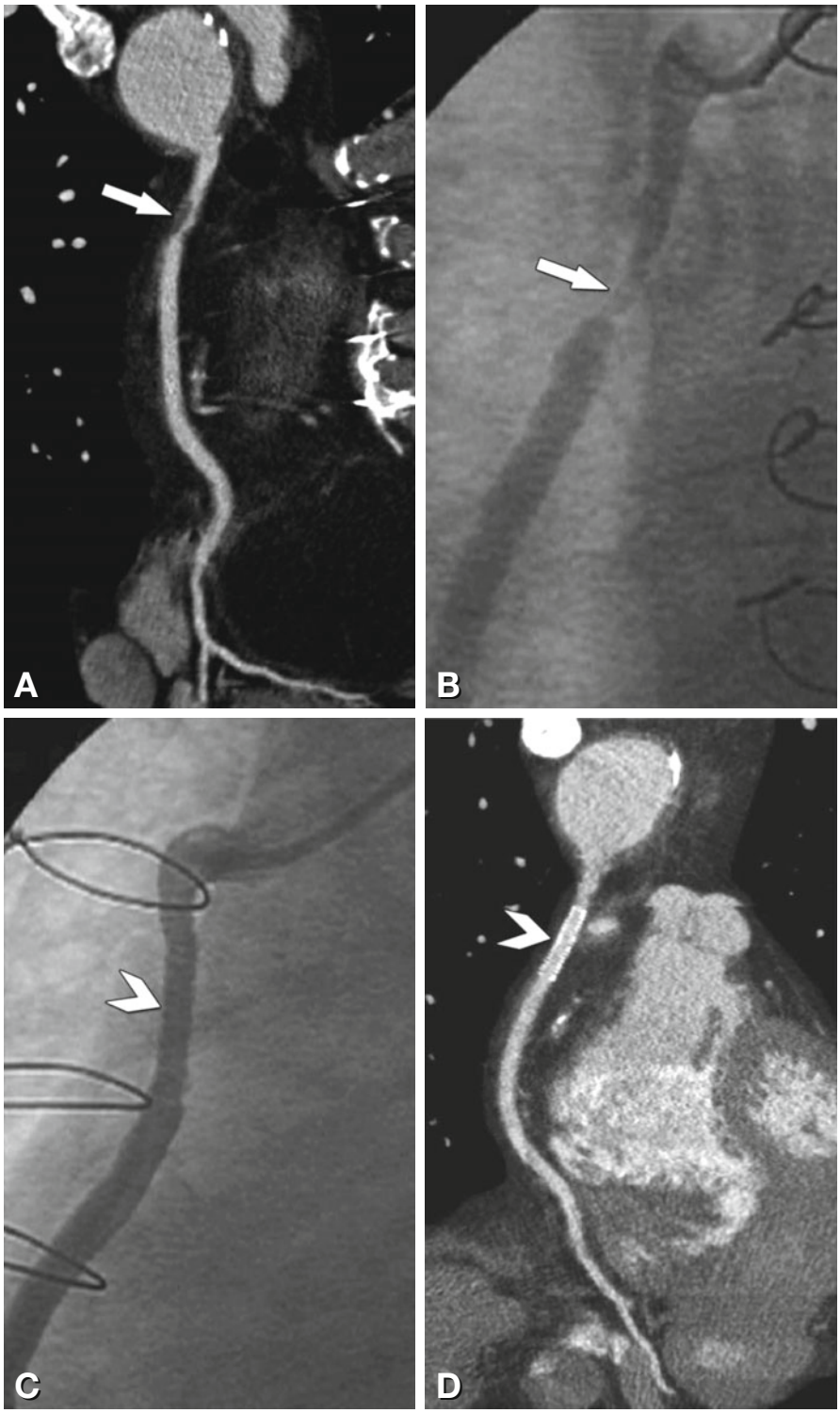

Fig. 24.25 Stenosis of a venous coronary bypass graft in a 69-year-old male patient with typical angina pectoris. Curved multiplanar reformation of CT shows a noncalcified plaque (*arrow*) in the proximal portion of a venous bypass graft to the right coronary artery, resulting in 80% diameter stenosis (**Panel A**) as measured with digital calipers on orthogonal cross-sections. Subsequently performed conventional angiography confirmed this finding (*arrow* in **Panel B**), and during the same angiographic session, percutaneous intervention with a 4.0-mm stent was performed (*arrowhead* in **Panel C**). Follow-up CT demonstrated a patent stent without significant in-stent restenosis (*arrowhead* in **Panel D**)

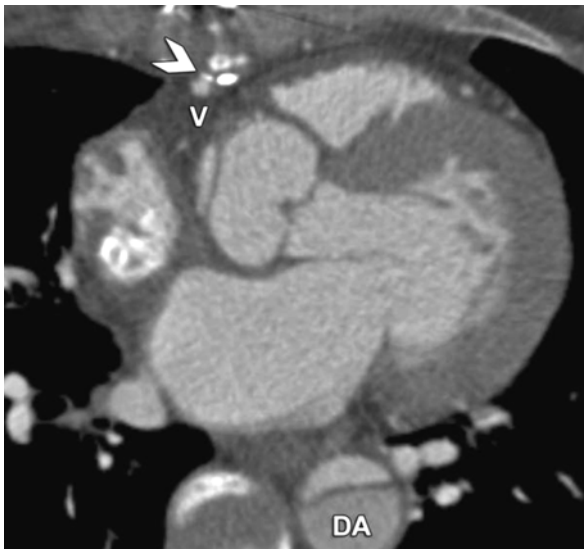

Fig. 24.26 Prior to reoperative cardiac surgery, CT can identify important findings. In this patient, a sternal wire (*arrowhead*) is located near a venous bypass graft (*V*). Also, the distance from the sternum to bypasses can be easily measured using CT before reoperation. In this case, there was also a dissection of the descending aorta (*DA*)

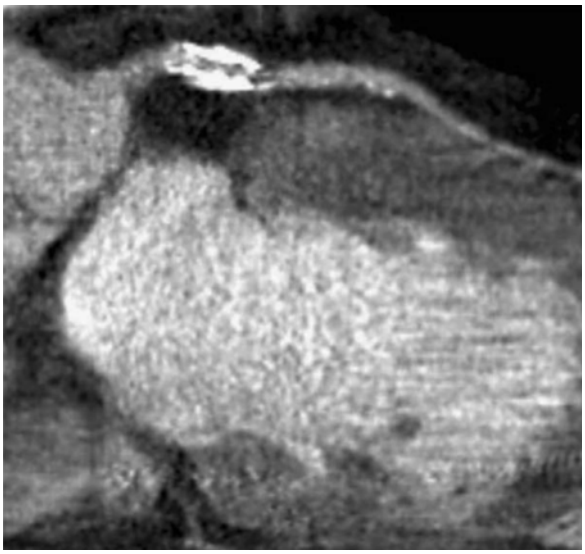

Fig. 24.28 Nondiagnostic coronary artery stent in the proximal left anterior descending coronary artery (curved multiplanar reformation) in a 64-year-old male patient with nonanginal chest pain. Despite the large diameter of the stent (4.0 mm), the lumen was not evaluable because of motion and beam-hardening artifacts. Interestingly, stents as large as this one are implanted in only about a fifth of all cases, and the vast majority of patients receive coronary stents of 2.5 or 3.0 mm in diameter, which can be reliably evaluated by CT in only 50% of the time (Chap. 20)

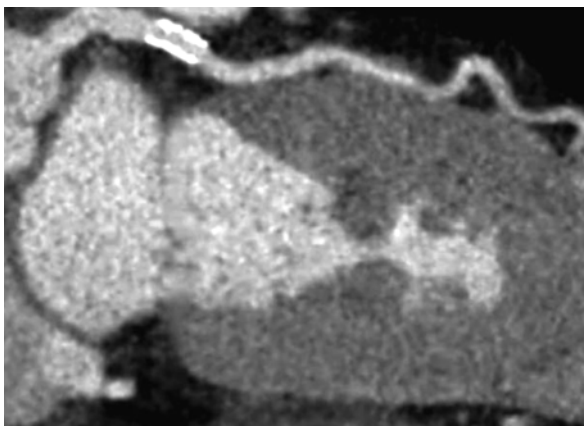

Fig. 24.27 Patent coronary artery stent (3.5-mm diameter) with good runoff in the proximal left anterior descending coronary artery (curved multiplanar reformation) in a 58-year-old female patient presenting with typical angina pectoris

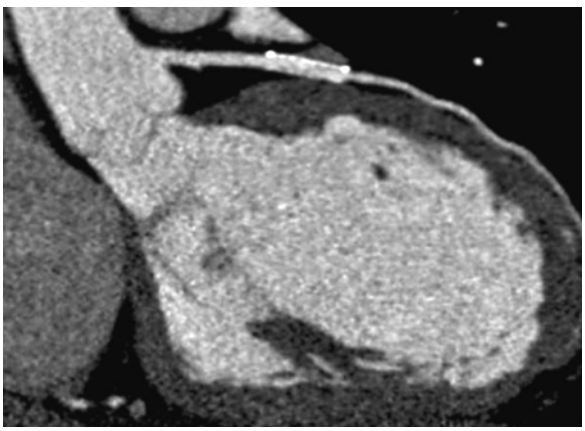

Fig. 24.29 Patent coronary artery stent (3.0-mm diameter) in the proximal left anterior descending coronary artery (curved multiplanar reformation) in a 41-year-old male patient who was asymptomatic but at high risk (history of acute anterior myocardial infarction and stenting at the age of 36). Note the irregular vessel wall immediately distal from the stent that did not result in significant stenosis

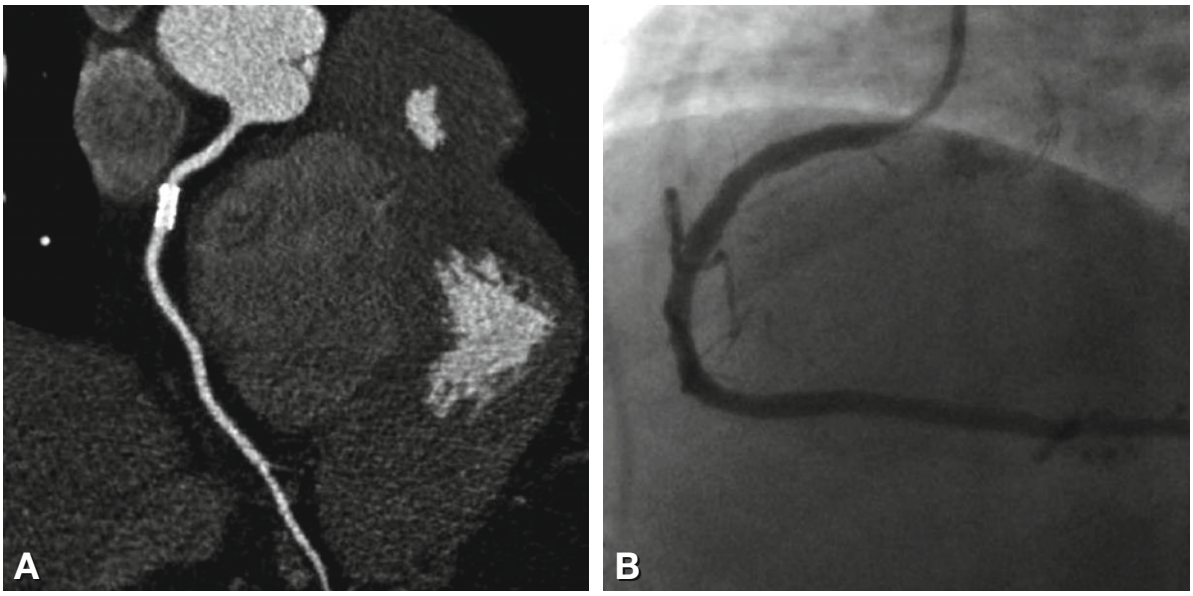

Fig. 24.30 Patent coronary artery stent (4.0 mm diameter) in the mid-right coronary artery without significant restenosis (curved multiplanar reformation, **Panel A**) in a 64-year-old male patient presenting with typical angina pectoris. There is good agreement in this large-diameter stent with conventional coronary angiography (**Panel B**)

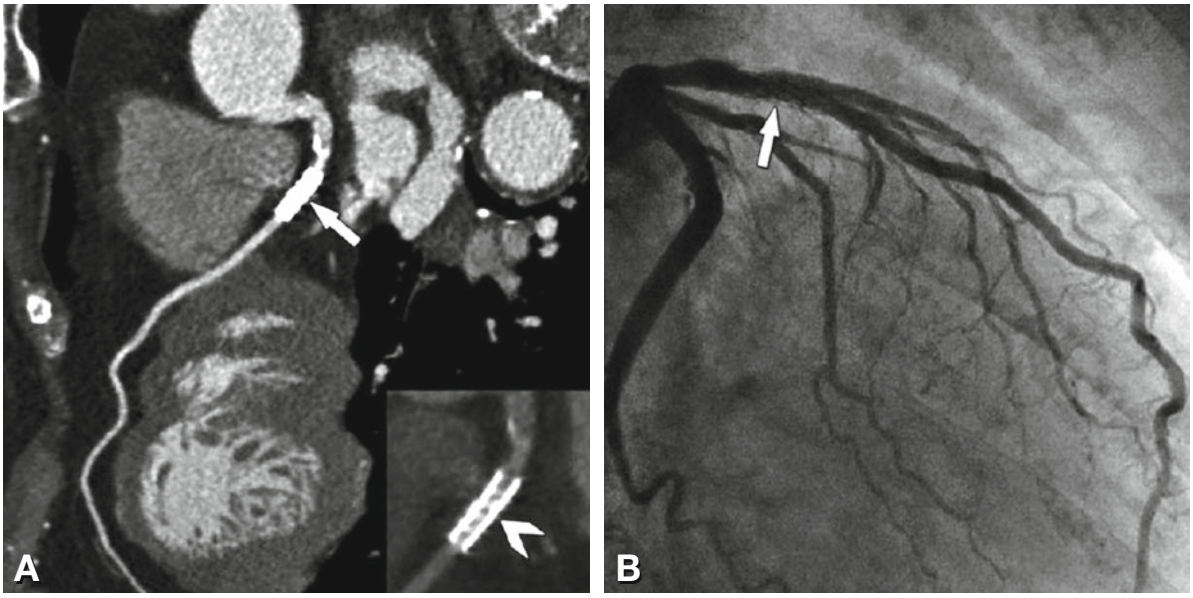

Fig. 24.31 Nondiagnostic small-diameter coronary artery stent (2.5 mm) in the proximal left anterior descending coronary artery (*arrow* in **Panel A**, curved multiplanar reformation) in an 80-year-old female patient presenting with typical angina pectoris. The runoff seems excellent but this is not a reliable sign on its own in excluding significant in-stent restenosis; enhancement may as well be caused by collateral flow that can be overlooked in nondynamic CT imaging. Even stent kernel reconstructions (*inset* in **Panel A**, *arrowhead*, curved multiplanar reformation) did not allow reliable exclusion of significant in-stent restenosis in this case. Conventional coronary angiography (**Panel B**) showed some neointimal proliferation (*arrow*) but no significant in-stent restenosis

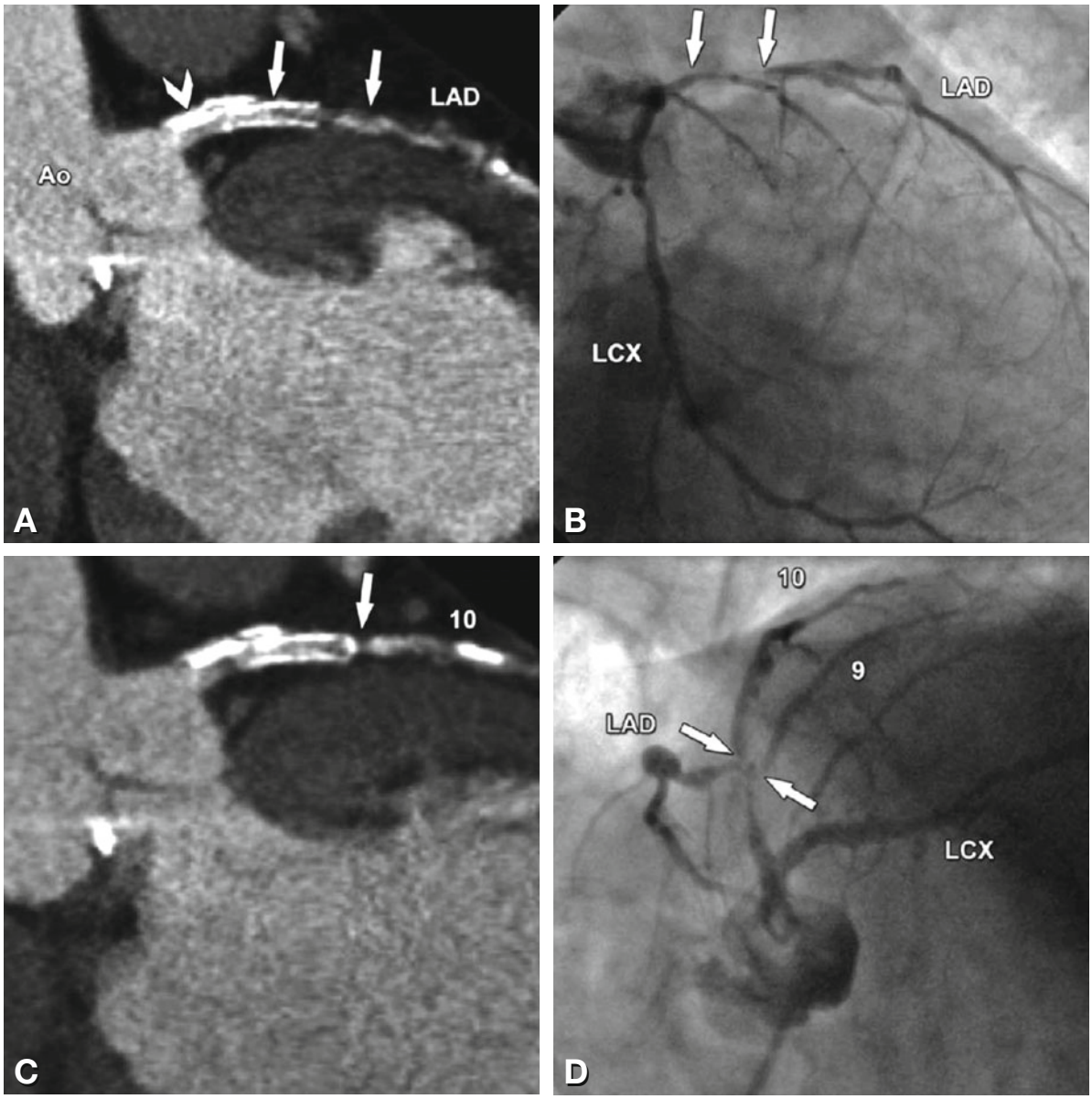

Fig. 24.32 Significant restenosis of a 3.0 mm diameter bare-metal stent in the proximal left anterior descending coronary artery (*LAD*) in a 63-year-old male with typical angina pectoris. Coronary CT angiography suggested occlusion of this stent (*arrows* in **Panel A**, curved multiplanar reformation). There was also a large calcified plaque in the left main coronary artery that did not cause significant luminal narrowing (*arrowhead* in **Panel A**). In contrast, quantitative analysis of conventional coronary angiography demonstrated that there was no occlusion, but 90% in-stent restenosis had occurred (*arrows* in **Panel B**). Because of its lower spatial resolution, CT is often unable to differentiate high-grade stenosis from occlusion. Because of the location of the stent at the branchings of the first (9) and second (10) diagonal branches, a complex situation involving a trifurcation stenosis was present (*arrows* in **Panels C** and **D**). The left circumflex coronary artery (*LCX*) had no significant stenosis (**Panel D**).

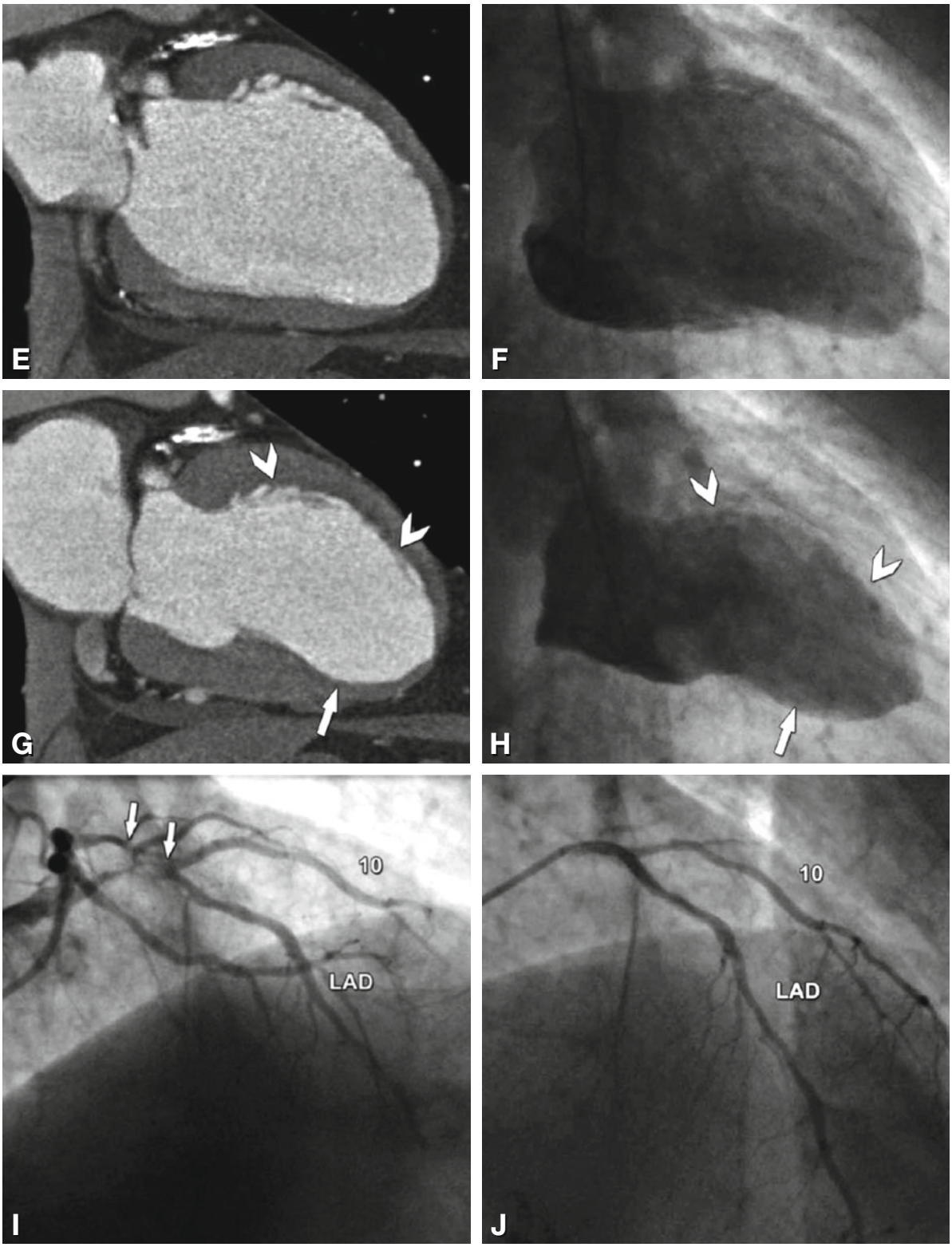

Fig. 24.32 (continued) There was extensive akinesia of the apical inferior segment (*arrow*) and hypokinesia of the midventricular and apical anterior segments (*arrowheads*) in the two-chamber view on CT (**Panels E** and **G**) and in the right anterior oblique projection by cineventriculography (**Panels F** and **H**, with **Panels E** and **F** representing end-diastole and **Panels G** and **H** representing end-systole). During the same angiographic session, successful complex percutaneous intervention of the LAD and the second diagonal branch (10) was performed (**Panels I**–**J**). *Ao* aorta

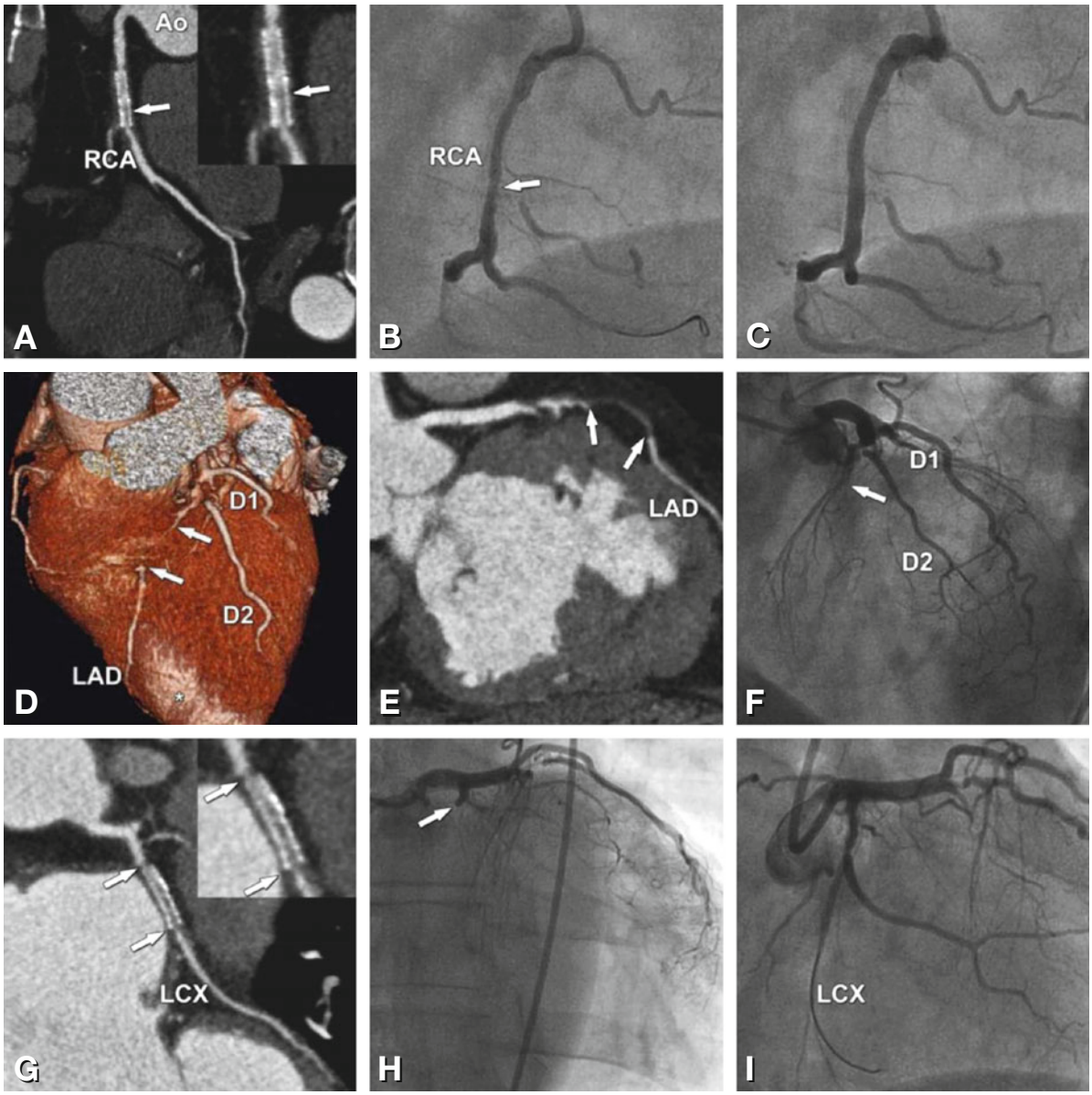

Fig. 24.33 In-stent restenosis and occlusion in a 63-year-old male patient presenting with atypical angina pectoris. The *upper row* (**Panels A**–**C**) shows the results for the right coronary artery (*RCA*), the *middle row* (**Panels D**–**F**) for the left anterior descending coronary artery (*LAD*), and the *bottom row* (**Panels G**–**I**) for the left circumflex coronary artery (*LCX*). Because of the presence of hypodense material in the distal part of the RCA stent (*arrow* in **Panel A**, curved multiplanar reformation), CT suspected significant in-stent restenosis (see *inset* in **Panel A** for a magnified view). Conventional angiography was initiated and confirmed a significant in-stent restenosis in the mid-segment of the RCA (*arrow* in **Panel B**). Percutaneous coronary intervention was performed during the same angiographic session (**Panel C**). CT also showed a known occlusion of the LAD (*arrows*), as depicted here in a three-dimensional volume-rendered reconstruction (**Panel D**), and a curved multiplanar reformation along the vessel (**Panel E**), which was confirmed on conventional angiography (**Panel F**). There were intracoronary LAD collaterals via septal branches that bypassed the occlusion, as seen on CT (**Panels D** and **E**). The LAD occlusion had resulted in apical infarction causing wall thinning (*asterisk* in **Panel D**). The second stent in the proximal left circumflex coronary artery (*LCX*) was filled with hypodense material (*arrows* in **Panel G**, curved multiplanar reformation), and based on coronary CT, occlusion of this stent was suspected (see *inset* in **Panel G** for a magnified view). Conventional angiography also confirmed stent occlusion in the proximal LCX (*arrow* in **Panel H**), and the stent was percutaneously recanalized in the same angiographic session (**Panel I**). *D1* first diagonal branch (segment 9), *D2* second diagonal branch (segment 10)

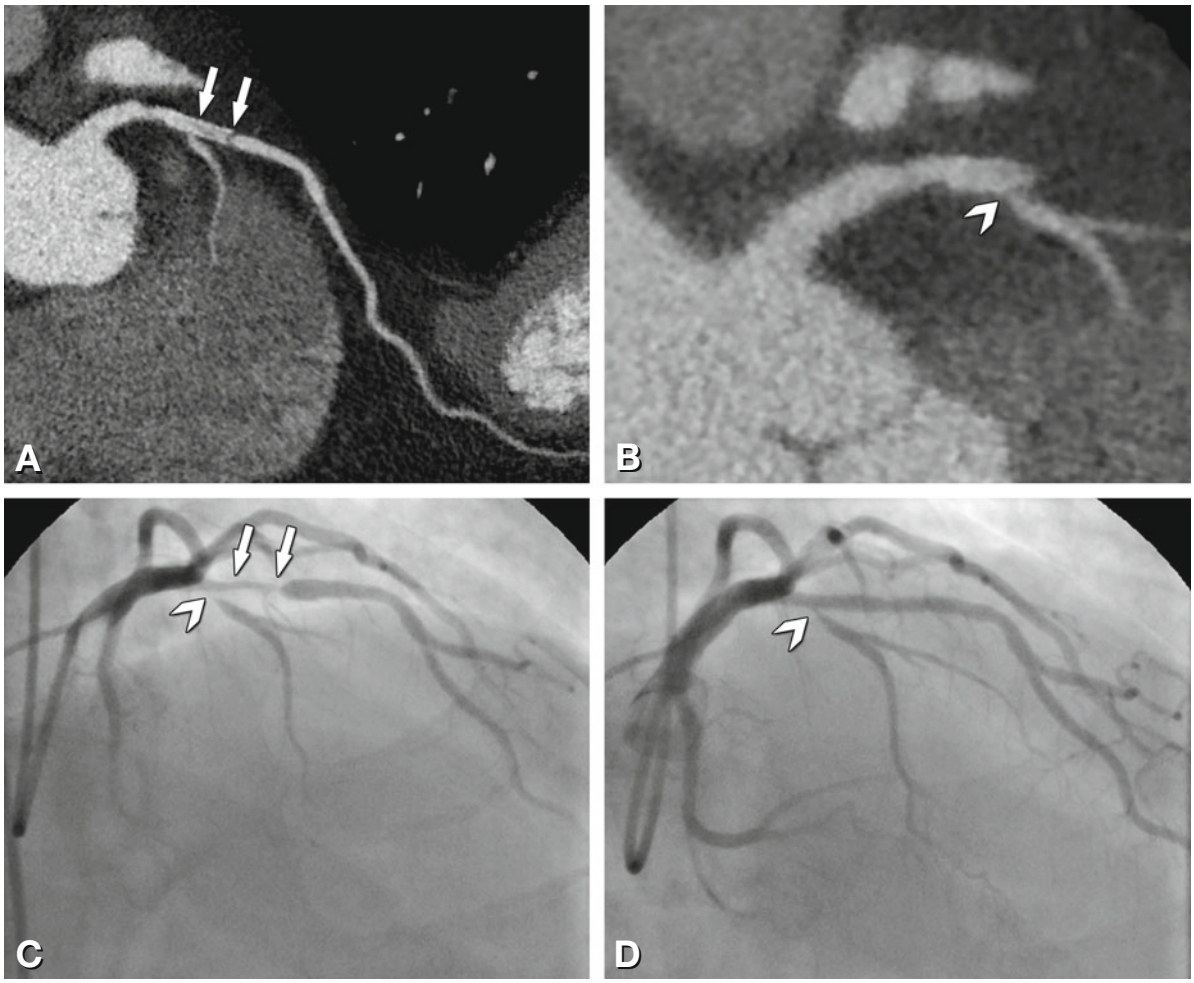

Fig. 24.34 In-stent restenosis of a 3-mm stent in the left anterior descending (*LAD*) coronary artery in a 78-year-old male patient who presented with typical angina pectoris. Cardiac CT (**Panels A** and **B**) and conventional coronary angiography (**Panels C** and **D**) were done as part of a clinical study. Cardiac CT was performed using single-beat 320-row CT, resulting in an effective dose of ca. 3.2 mSv. The effective dose of the diagnostic part of conventional coronary angiography was about 18 mSv. Curved multiplanar reformations along the LAD (**Panel A**) and the first septal branch (**Panel B**) show significant stenoses (*arrows* and *arrowhead*). Conventional coronary angiography (**Panel C**) confirmed these stenoses (*arrows* and *arrowhead*). The in-stent restenosis was treated during the same angiographic session by angioplasty (**Panel D**). The stenosis of the small septal branch was not treated (*arrowhead* in **Panel D**)

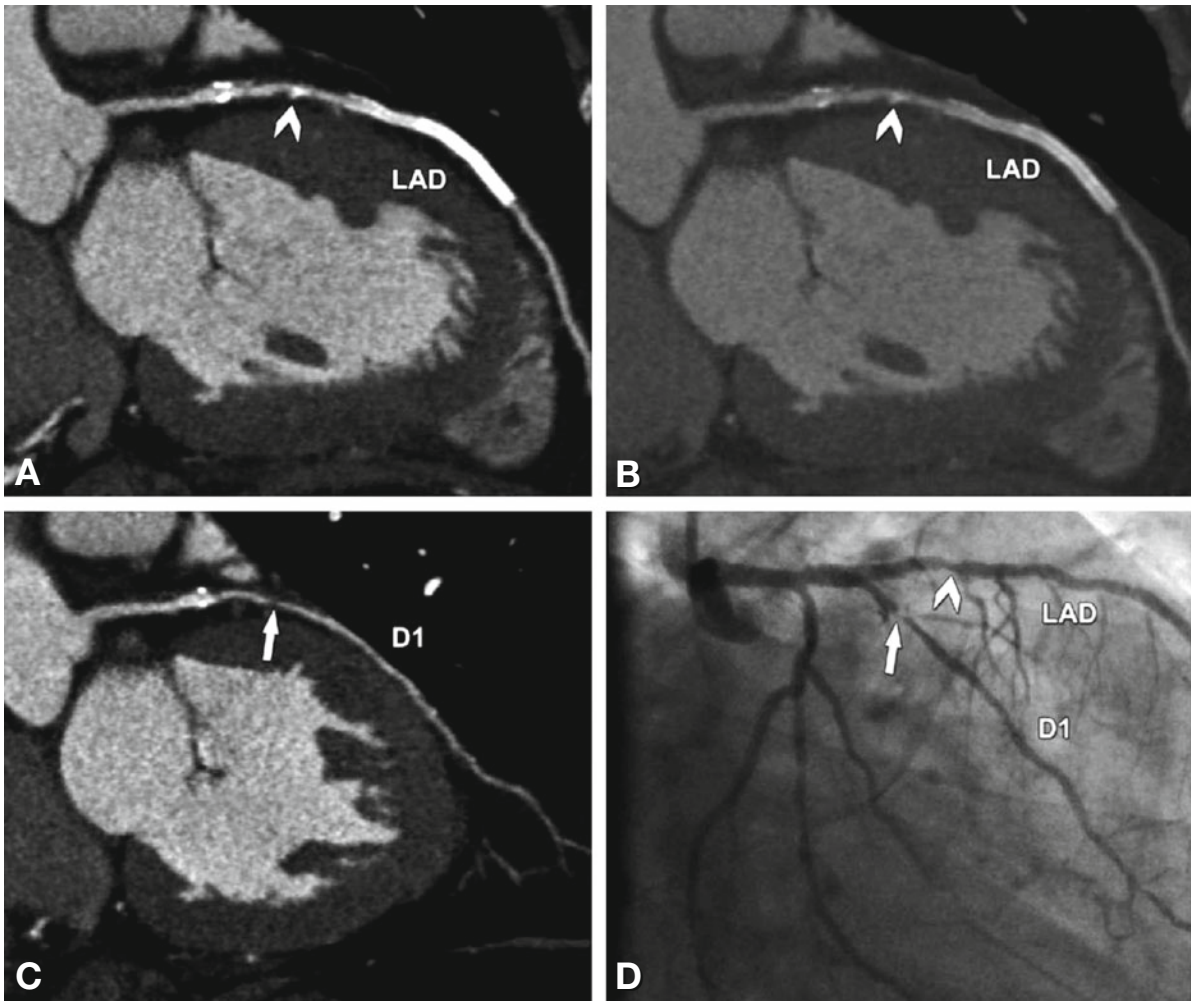

Fig. 24.35 Importance of stent kernels for evaluation of coronary stents. This 53-year-old male patient presenting with typical angina pectoris had a history of stenting of the left anterior descending coronary artery (*LAD*), with two 2.5-mm diameter stents. Curved multiplanar reformation based on standard reconstruction kernel for coronary arteries did not allow reliable assessment of the stent lumen (**Panel A**). Use of stent kernels, however, showed no sign of in-stent restenosis (**Panel B**). Also, the calcified plaque (*arrowhead* in **Panels A** and **B**) was easier to assess using a stent kernel, and significant luminal diameter reduction resulting from this plaque was excluded (**Panel B**). However, a 90% diameter stenosis (*arrow*) of the first diagonal branch (*D1*), caused by a noncalcified plaque (**Panel C**), was confirmed on conventional angiography (*arrow* in **Panel D**). Conventional coronary angiography also confirmed that the calcified plaque in the mid-LAD caused only a nonsignificant reduction in diameter (*arrowhead* in **Panel D**)

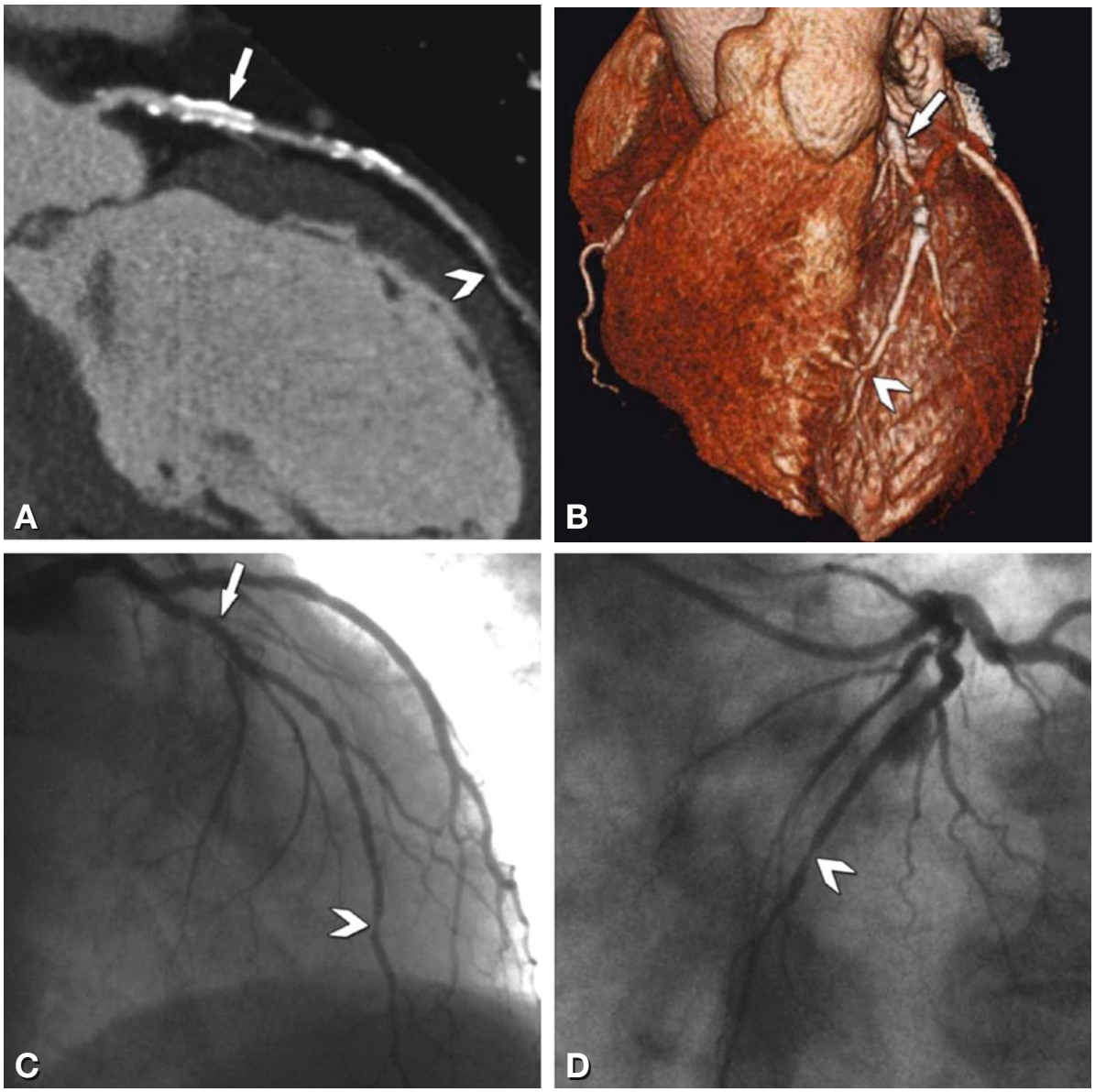

Fig. 24.36 Exclusion of significant in-stent restenosis in the left anterior descending coronary artery in a 70-year-old male patient. The 3.5-mm diameter stent was unremarkable on curved multiplanar reformation of coronary CT (*arrow* in **Panel A**), but a 60% diameter stenosis resulting from a noncalcified plaque was suspected in the distal left anterior descending artery (*arrowhead* in **Panels A** and **B**). Conventional coronary angiography confirmed the patency of the stent (*arrow* in **Panel C**), but the distal stenosis was considered on quantitative analysis to represent a 40% diameter reduction (*arrowhead* in **Panels C** and **D**). This example further illustrates the fact that there is sometimes less-than-perfect agreement between CT and conventional angiography in terms of quantifying coronary artery stenoses. Such disagreements are attributable to the three-dimensional nature of CT, which is advantageous (**Fig. 24.16**) in that it allows a more accurate assessment of diameter reduction, especially in the case of bifurcation lesions; in contrast, the relevantly higher spatial resolution of conventional angiography is a pivotal advantage of this test

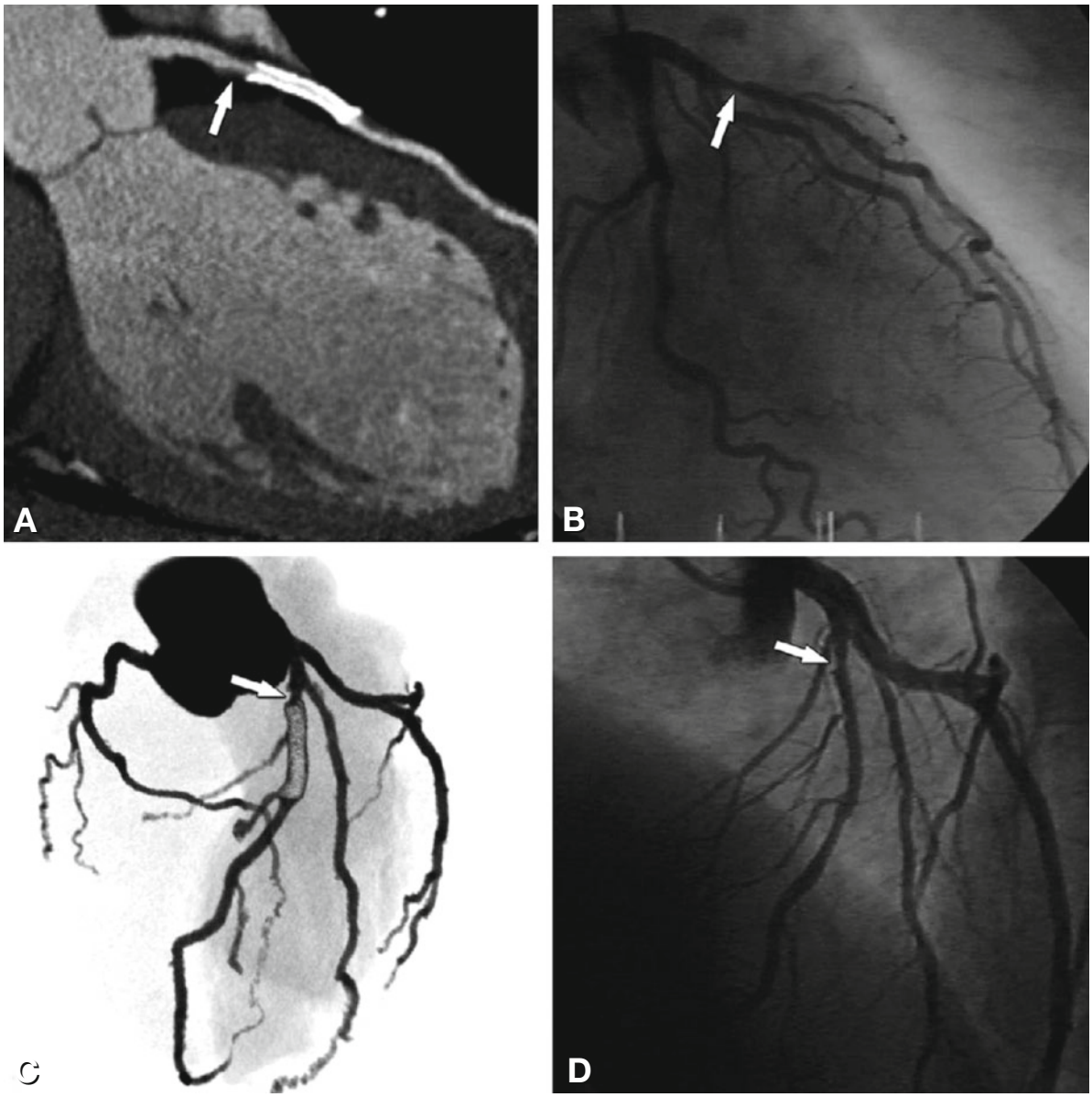

Fig. 24.37 Prestent stenosis in a 45-year-old male patient without symptoms. Curved multiplanar reformation of CT demonstrates a 30% diameter reduction in the lumen immediately proximal to the stent, resulting from a noncalcified plaque (*arrow* in **Panel A**). Significant in-stent restenosis was excluded using stent kernel curved multiplanar reformations (not shown). Conventional angiography also demonstrated the 30% prestent stenosis (*arrow* in **Panel B**). Angiographic emulation of coronary CT angiography nicely demonstrated the stenosis (*arrow* in **Panel C**), with an excellent correlation with conventional angiography (*arrow* in **Panel D**). Note that the angiographic emulation of CT has the advantage of simultaneously depicting the left and right coronary artery

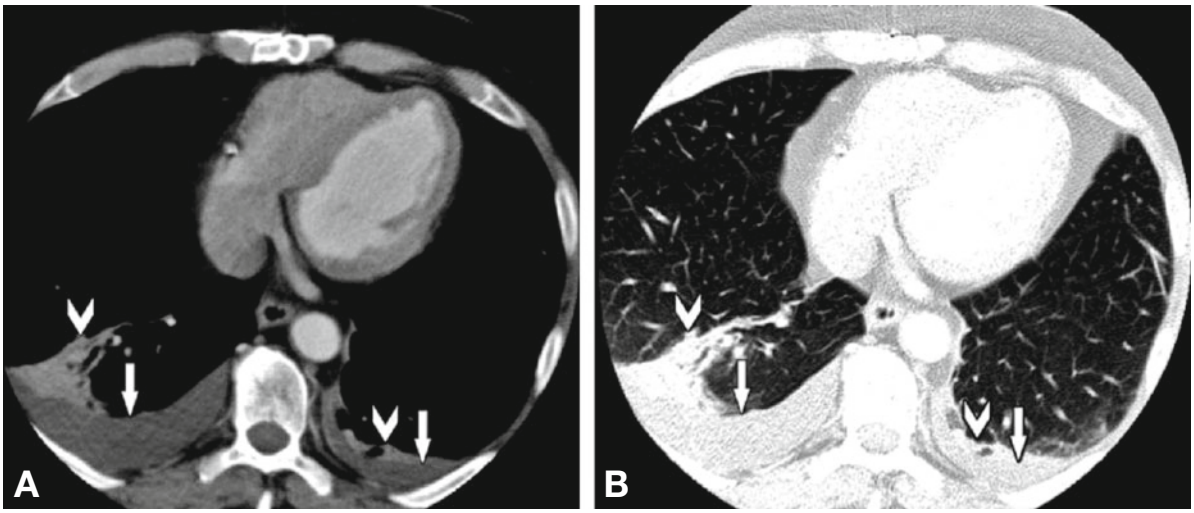

Fig. 24.38 Postoperative bilateral pleural effusion (*arrows*) in a 61-year-old male patient who underwent bypass grafting. Results are shown on large fields of view with soft tissue (**Panel A**) and lung window-level settings (**Panel B**). Note that the effusions cause (nonobstructive) atelectasis in both lower lobes (*arrowheads*)

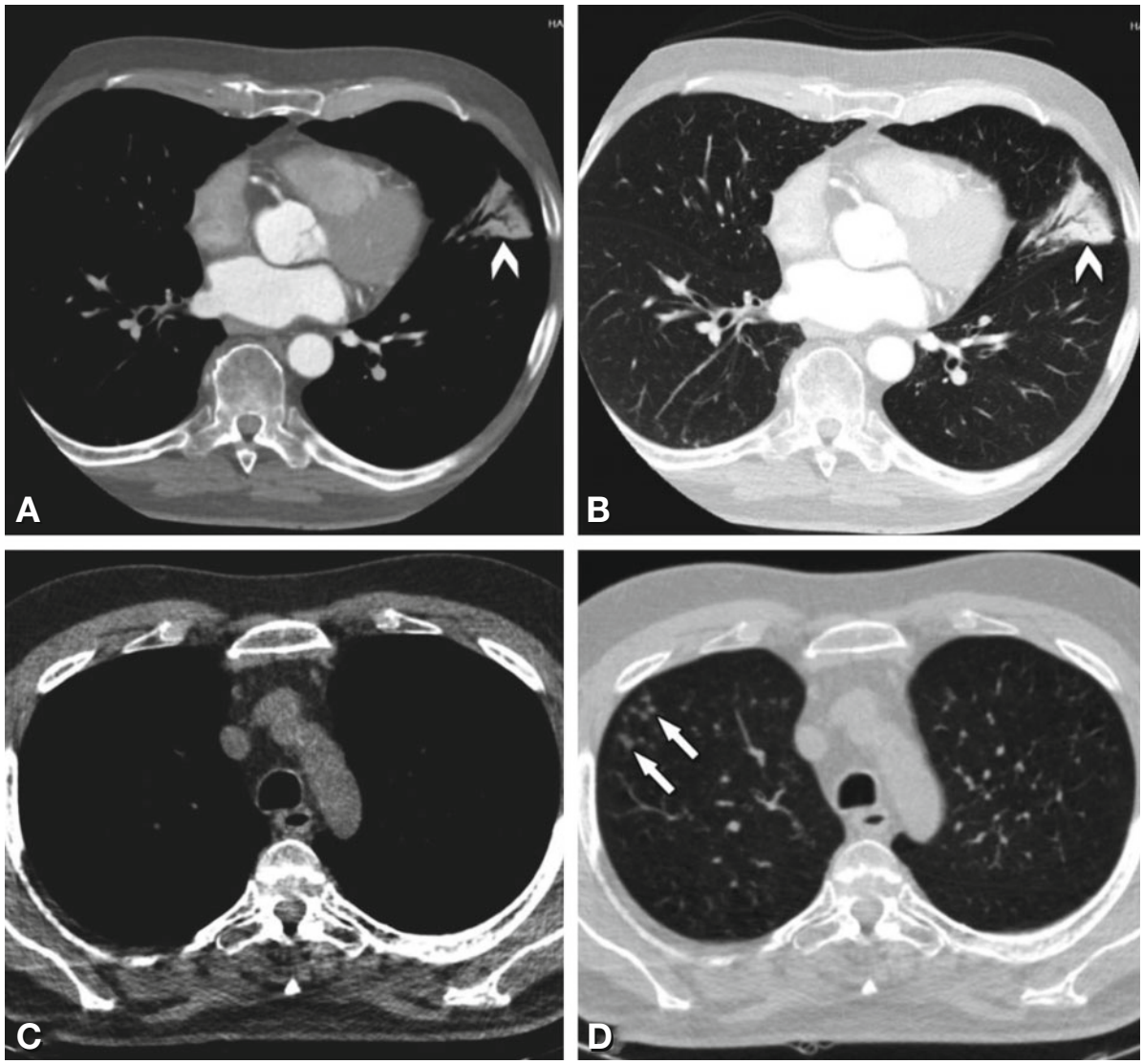

Fig. 24.39 Pneumonia in the left upper lobe in a 65-year-old patient with chronic B-cell lymphocytic leukemia and status post allogenic bone marrow transplantation. Cardiac CT was performed 20 months after bone marrow transplantation because of chest pain and shortness of breath and shows pneumonic consolidation in the left upper lobe (*arrowhead* in **Panels A** and **B**). No coronary artery disease was found on cardiac CT. Chest CT performed 4 months earlier (**Panels C** and **D**) already showed signs of graft-versus-host disease with peripheral tree-in-bud sign compatible with obliterative bronchiolitis in the right upper lobe (*arrows* in **Panel D**) but no pneumonic consolidation at this time (Images courtesy of S. Feger, Berlin)

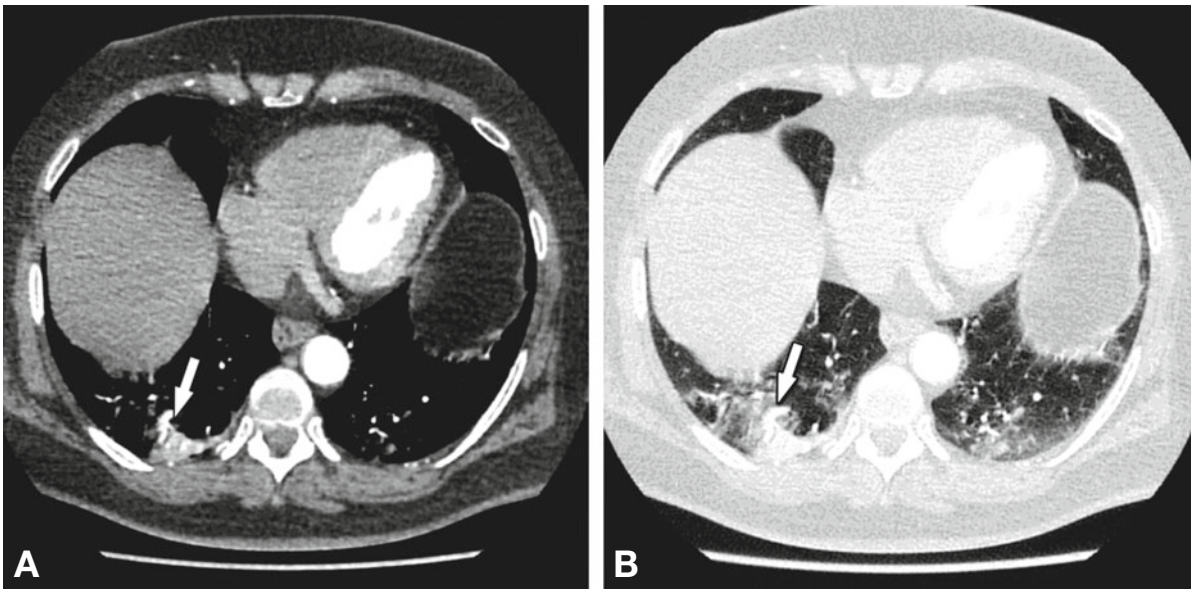

Fig. 24.40 Lung scarring (fibrosis) with partial consolidation of the right lower lobe (*arrow*) in a 60-year-old woman without a history of pneumonia or tuberculosis and without signs of infection. Results are shown on large fields of view with soft tissue (**Panel A**) and lung window-level settings (**Panel B**) and remained unchanged on follow-up (Images courtesy of S. Feger, Berlin)

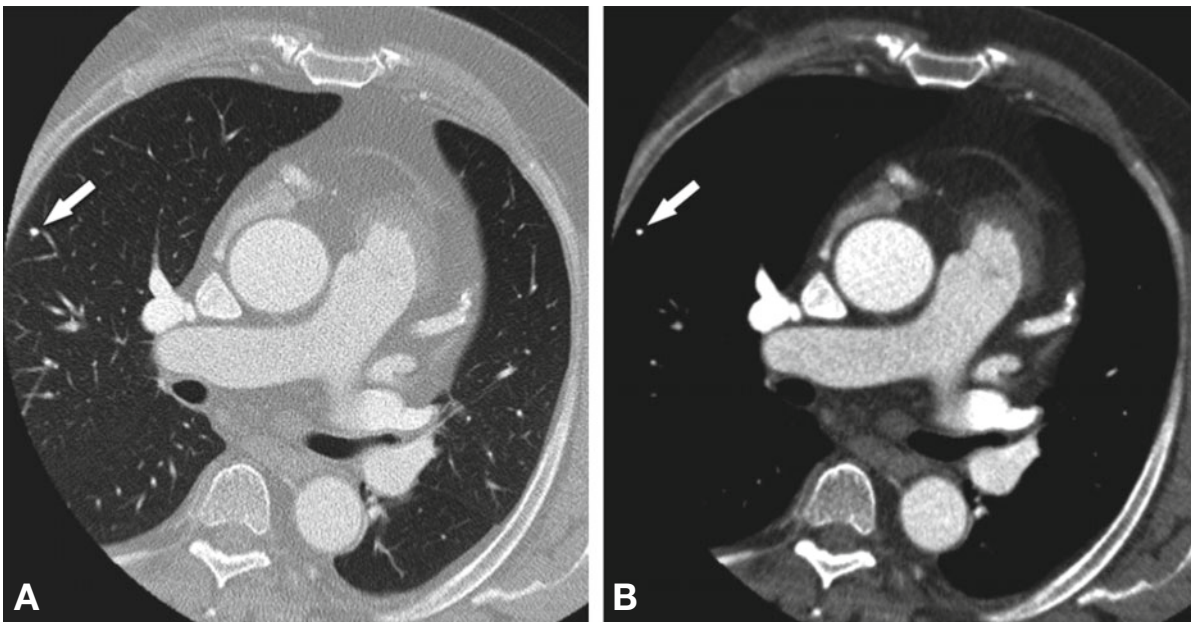

Fig. 24.41 Calcified pulmonary nodule 0.4 cm in diameter (granuloma; lesions ranging in size from 0.3 to 0.5 cm are called "ditzels") in the middle lobe (*arrow* in **Panels A** and **B**) in a 61-year-old male patient without known malignancy. The appearance is characteristic of calcified granuloma and is most likely due to prior infection (e.g., tuberculosis, histoplasmosis)

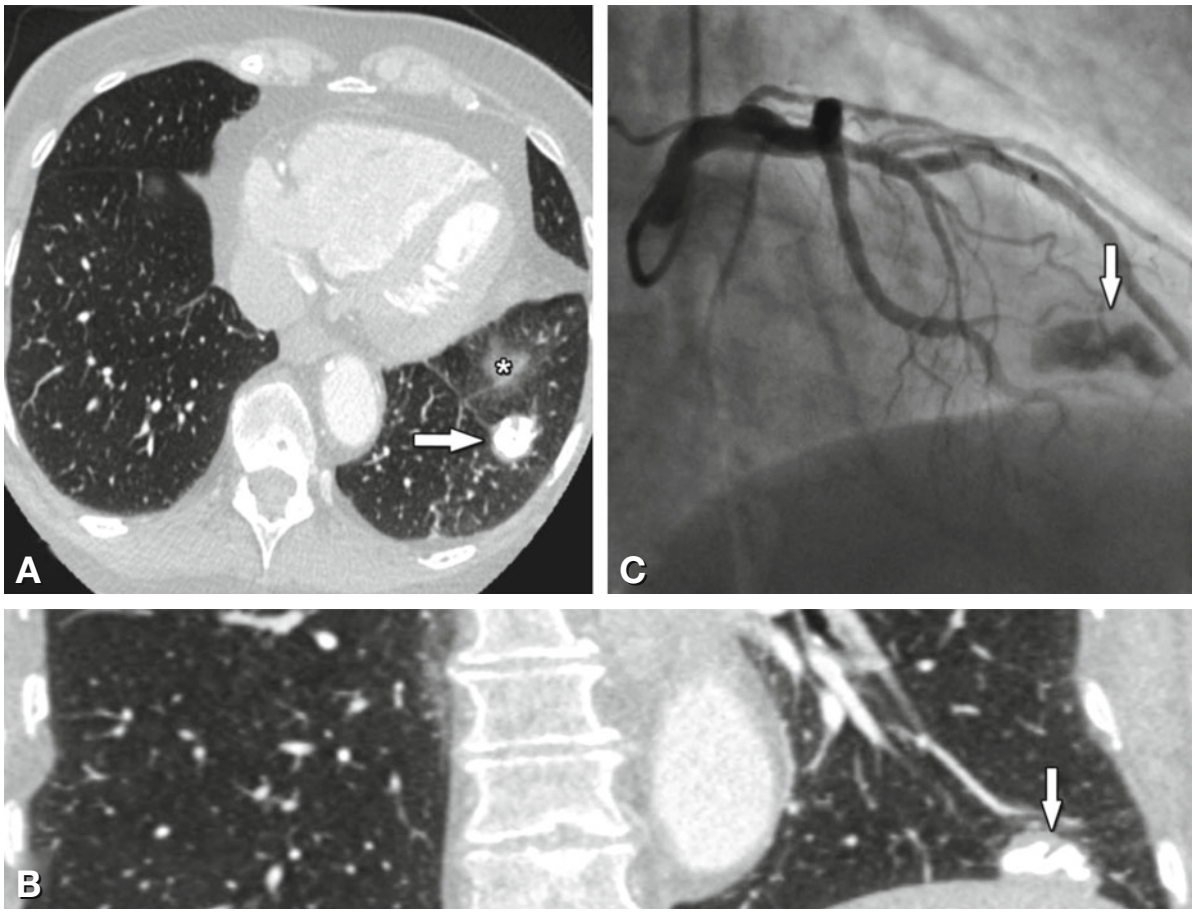

Fig. 24.42 Rather large granuloma (about 2 cm) seen on both cardiac CT (*arrow* in **Panels A** and **B**) and conventional coronary angiogram (*arrow* in **Panel C**) in a 70-year-old female patient with atypical angina pectoris and atrial fibrillation who underwent CT as part of a clinical study. Both CT and conventional coronary angiography ruled out coronary artery disease. The calcified granuloma in the left lower lobe is most likely a remnant of prior tuberculosis. The *asterisk* in **Panel A** indicates part of the diaphragm (Images courtesy of L. Hartmann, Berlin)

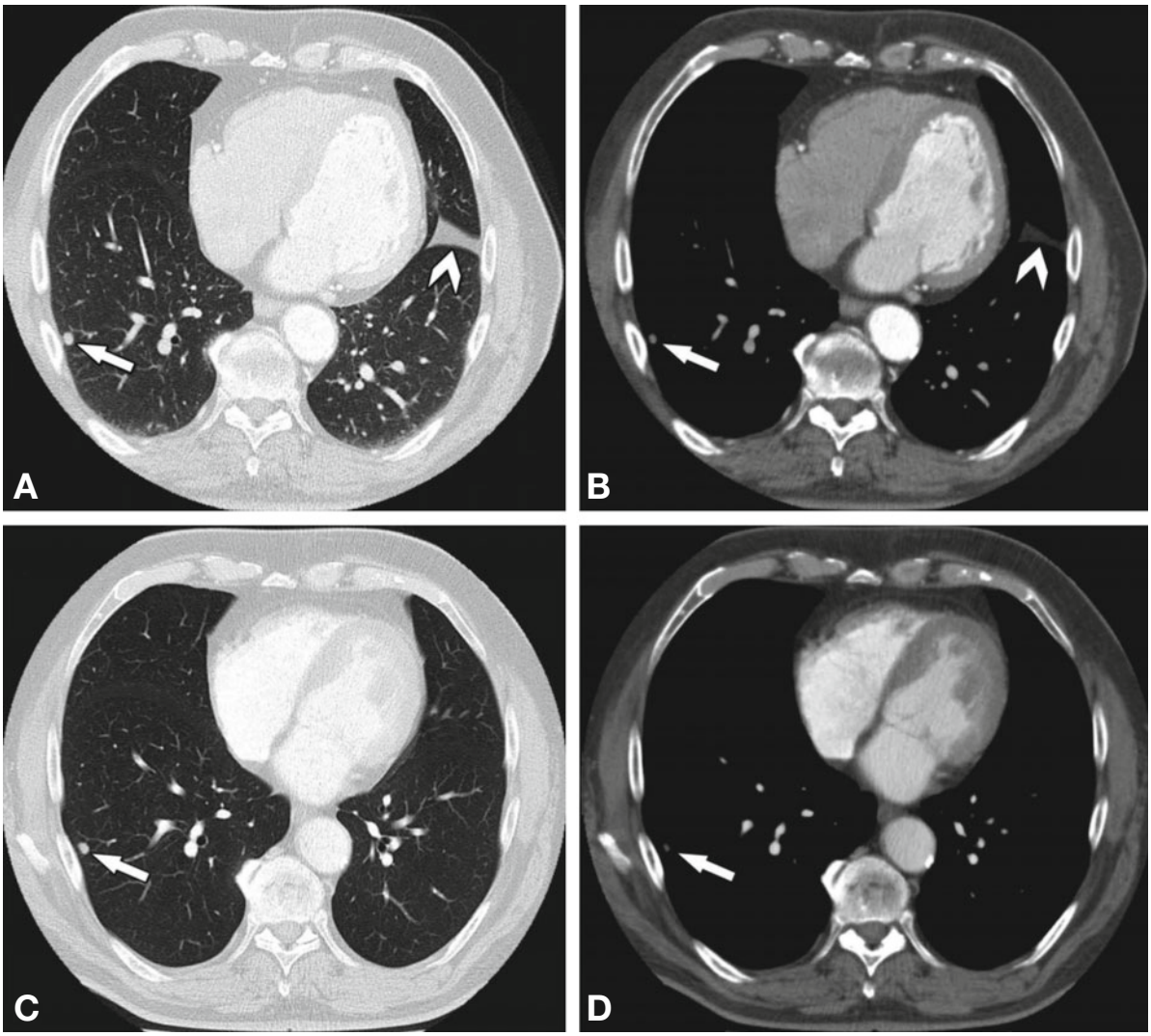

Fig. 24.43 A solitary pulmonary nodule (0.7 cm) in the right lower lobe (*arrow* in **Panels A** and **B**) that is well-circumscribed, predominantly solid, and does not contain any calcifications. There is also an effusion in the left oblique fissure (*arrowhead* in **Panels A** and **B**) Guideline-based 6-month follow-up (According to MacMahon et al. *Radiology* 2005) standard chest CT was performed, which showed a minor decrease in size and ruled out potential malignancy (*arrow* in **Panels C** and **D**). Differential diagnoses for such nodules include benign infectious lesions, atypical adenomatous hyperplasia, metastases, and lung cancer. Follow-up CT scans can serve to differentiate benign and malignant pulmonary nodules in indeterminate cases

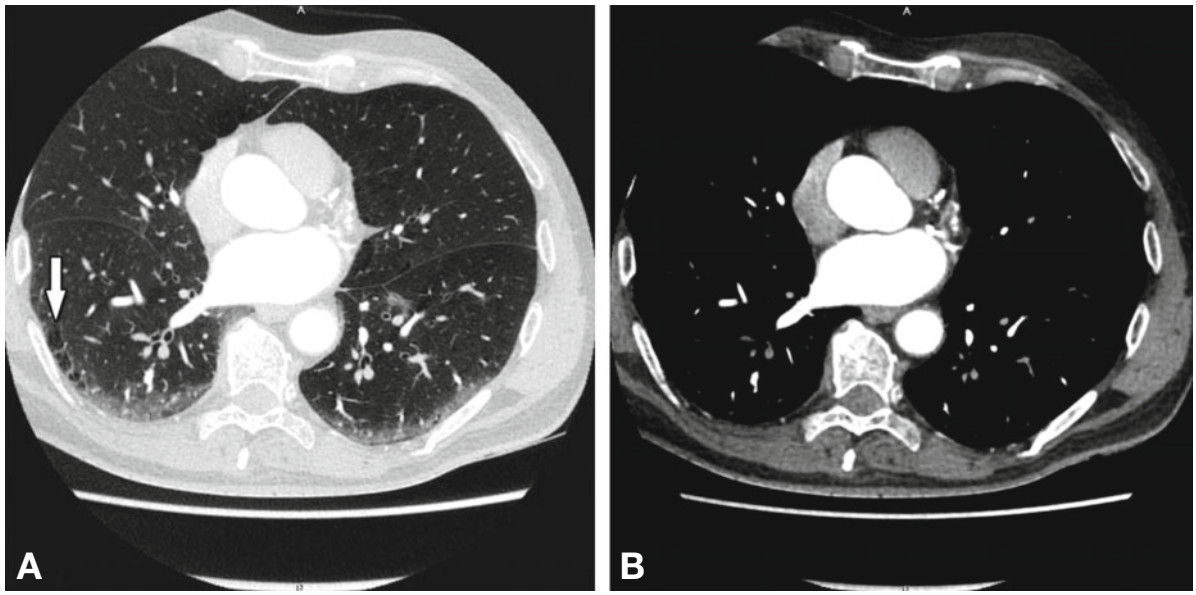

Fig. 24.44 Bullous lung changes (*arrow*) in the periphery of the right lower lobe in a 67-year-old male patient with a long smoking history. Results of cardiac CT are shown on large fields of view with lung (**Panel A**) and soft tissue windowlevel settings (**Panel B**) (Images courtesy of S. Feger, Berlin)

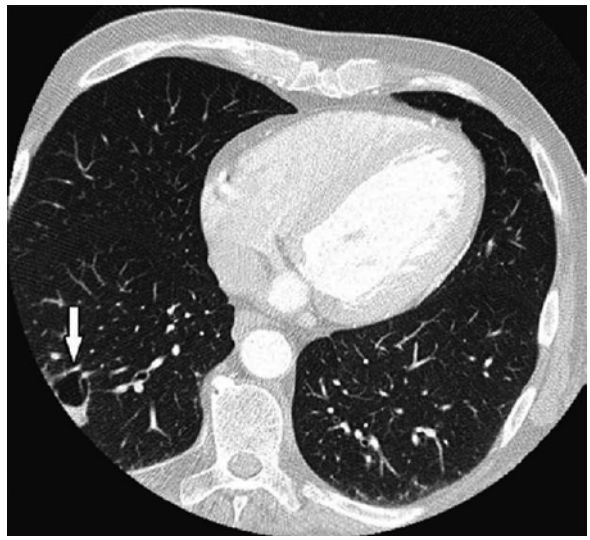

Fig. 24.45 Cavernous lung lesion in the right lower lobe (*arrow*) in a 56-year-old male patient presenting with atypical angina pectoris, who was referred to rule out coronary artery stenoses. There were no significant coronary stenoses, and the nodule with a thin-walled cavity was found on the large fields of view only and was suspected to be due to tuberculosis. Transthoracic biopsy, however, was initiated and revealed a lung carcinoma. Note that because a medium-size scan field of view (320 mm) was chosen for acquisition (to allow using a small focus spot), the reconstruction field of view cannot be larger than 320 mm, and thus the carcinoma is only partially visible

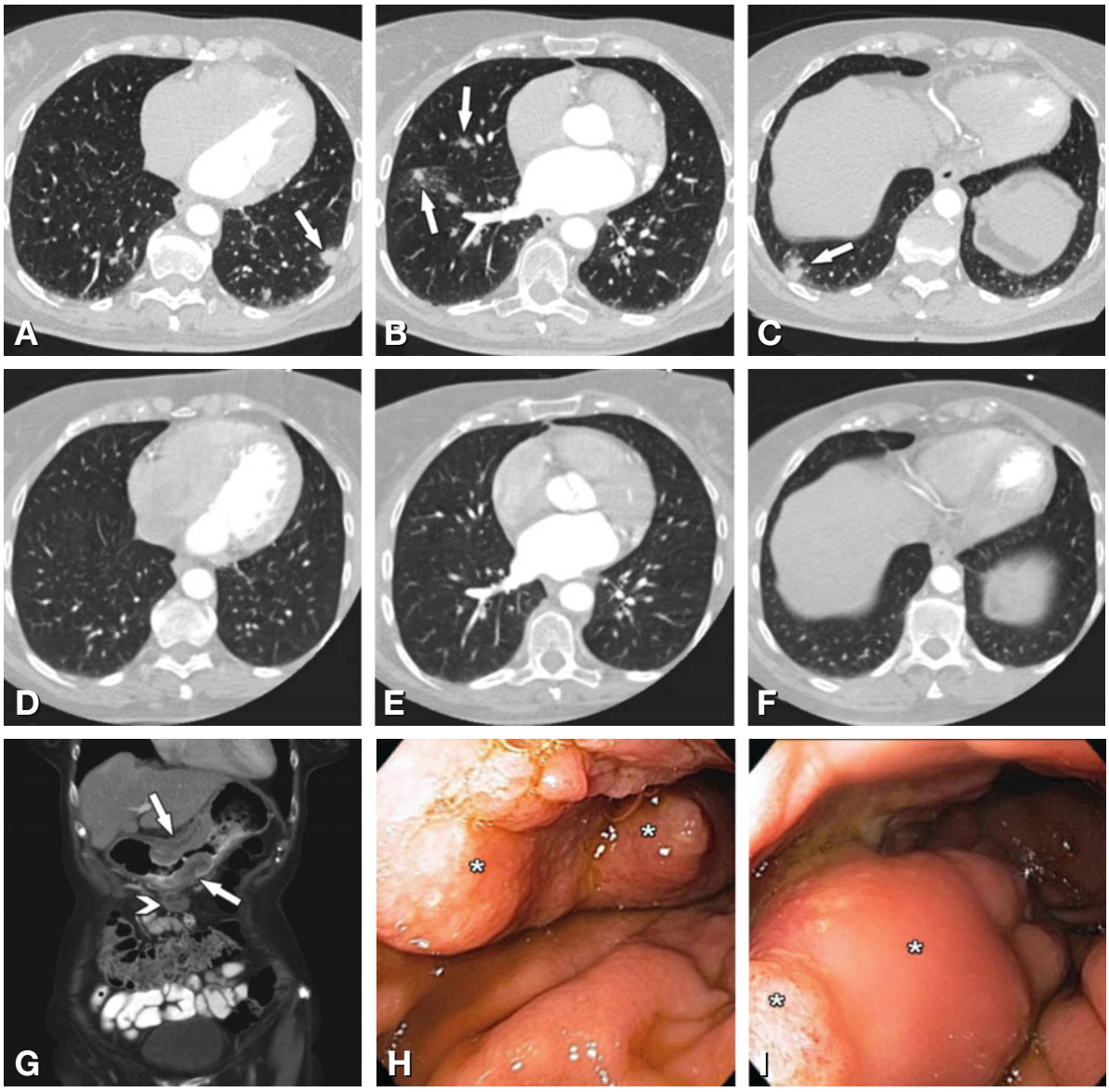

Fig. 24.46 Multiple pulmonary nodules of up to 17 mm seen on cardiac CT (*arrows* in **Panels A**–**C**) in a 71-year-old female patient with atypical angina pectoris and suspected CAD who underwent CT as part of a study in patients with atrial fibrillation. Prior images of the lungs (6 months earlier) showed no lung nodules (**Panels D**–**F**) raising the suspicion of metastases. Subsequent CT of the abdomen revealed a tumor in the stomach (*arrows* in **Panel G**) with local (*arrowhead* in **Panel G**), retroperitoneal, mesenteric, and mediastinal lymph node metastases. Because of suspected gastric carcinoma, gastroscopy including biopsy was performed, showing an ulcerating carcinoma (uT4a N3a M1, *asterisks* in **Panels H** and **I**). The patient underwent palliative chemotherapy with cisplatin, capecitabin, and trastuzumab. Unfortunately, the patient died 1 year later (Images courtesy of C. Jürgensen, E. Zimmermann, and L. Hartmann, Berlin)

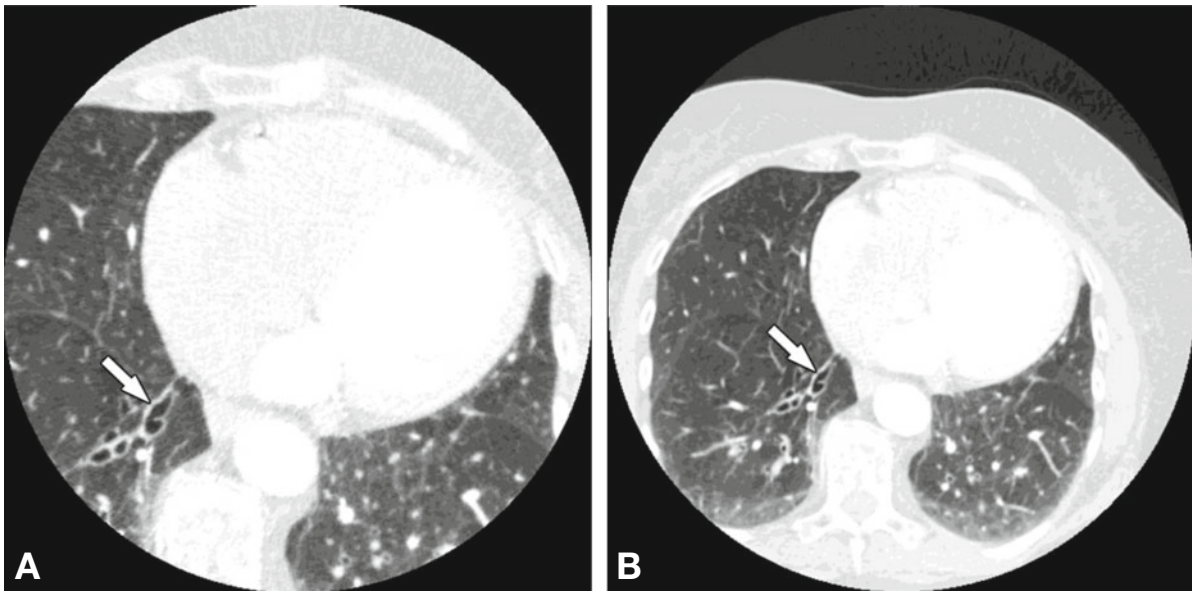

Fig. 24.47 Incidental finding of traction bronchiectasis in the right lower lung due to moderate lung fibrosis in a 73-year-old female patient presenting with atypical angina. Coronary artery disease was ruled out. Both the small cardiac field of view (**Panel A**) and the large lung field of view (**Panel B**) show the bronchiectasis (*arrow*)

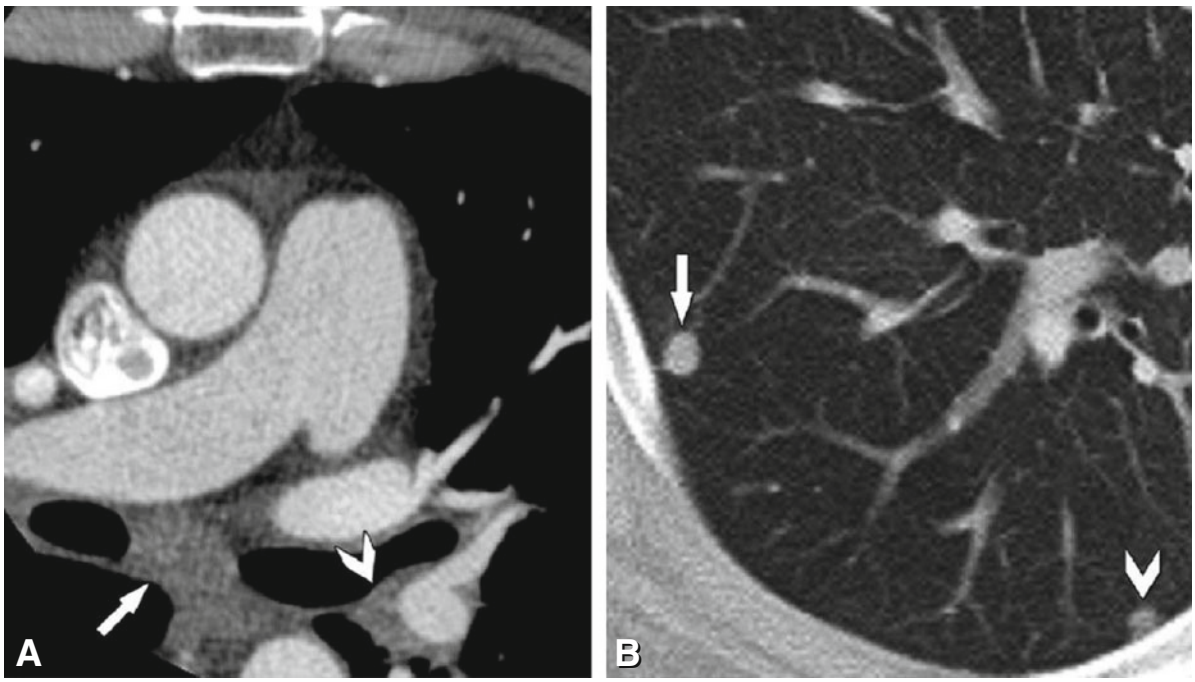

Fig. 24.48 Infracarinal 2 × 1.5 cm mediastinal lymph node (*arrow*) and peribronchial thickening (*arrowhead* in **Panel A**) in a 48-year-old male patient. Pulmonary nodules (*arrow*) and pleural-based opacities were also visible (*arrowhead* in **Panel B**). The final diagnosis was pulmonary sarcoidosis. Common differential diagnoses of mediastinal lymph nodes include lymph node metastases, lymphoma, sarcoidosis, amyloidosis, and silicosis

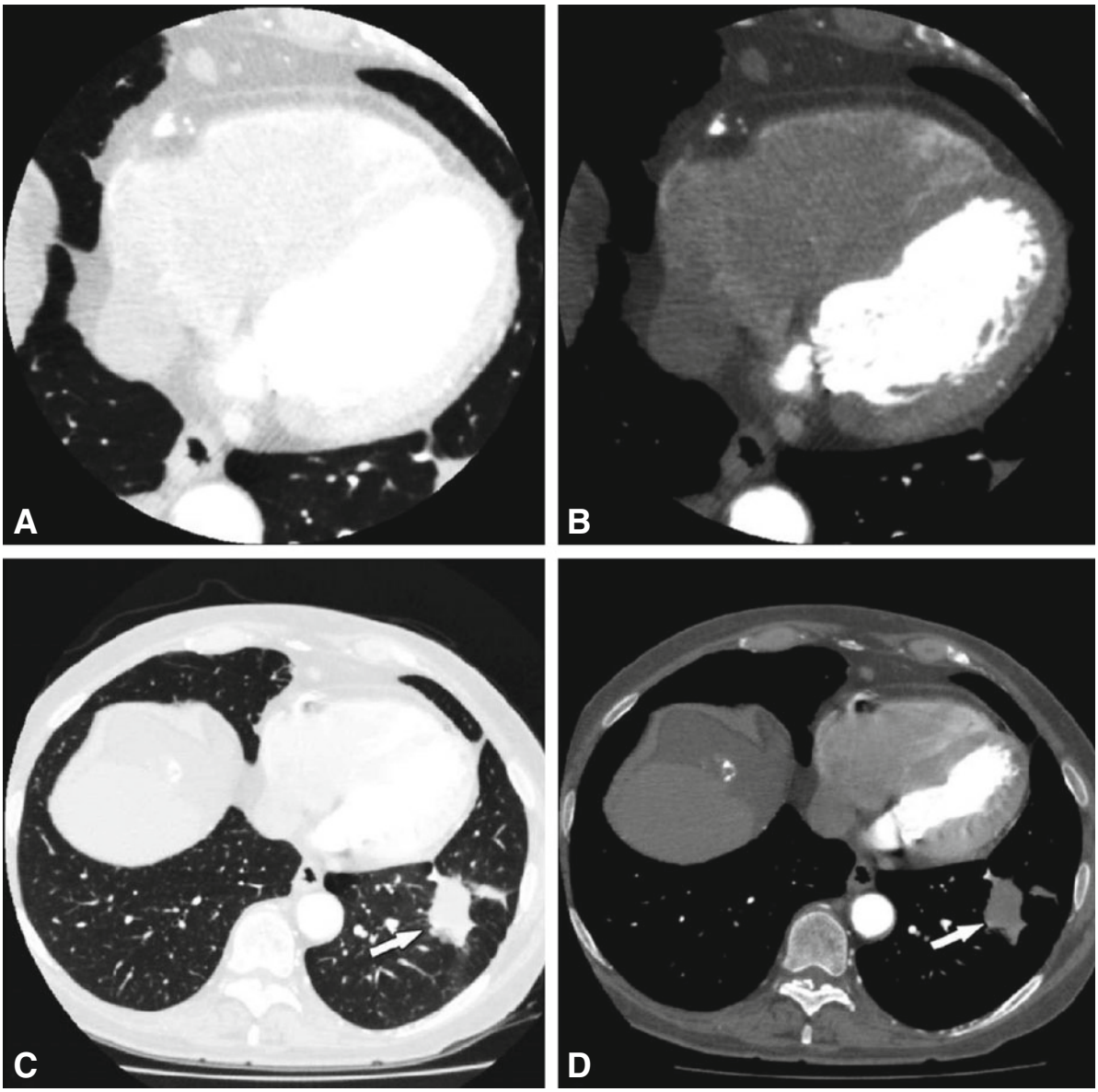

Fig. 24.49 Incidental finding of a lung carcinoma in the left lower lobe not recognized on dedicated small reconstruction fields of view for coronary artery evaluation (**Panels A** and **B**) but visible on the large fields of view with a 320 mm size (*arrow* in **Panels C** and **D**) The *left column* represents lung window-level settings, and the *right column* soft tissue window-level settings. The irregular 2.5 cm mass in the left lower lobe was spiculated and had pleural tails (**Panels C** and **D**), highly suspicious of malignancy. Both bronchoalveolar lavage and transbronchial biopsies were negative (no malignant cells found). However, transthoracic CT-guided lung biopsy resulted in a diagnosis of nonsmall cell lung carcinoma. A positron-emission tomography scan showed no signs of metastasis, and the patient underwent lobectomy of the left lower lobe with partial lingula resection. The final diagnosis was adenocarcinoma, with spread into the lingula and visceral pleura. There were free margins after resection, and no peribronchial metastases (complete resection of a pT2N0M0 tumor). This case underlines how important it is to always reconstruct the lungs on large fields so as to avoid overlooking any pathology. Coronary CT angiography was performed in this 72-year-old female patient before renal transplantation for renal failure resulting from polycystic kidney disease. Note the partially imaged liver cyst with calcification in association with polycystic kidney disease (Images courtesy of L. Kroft)

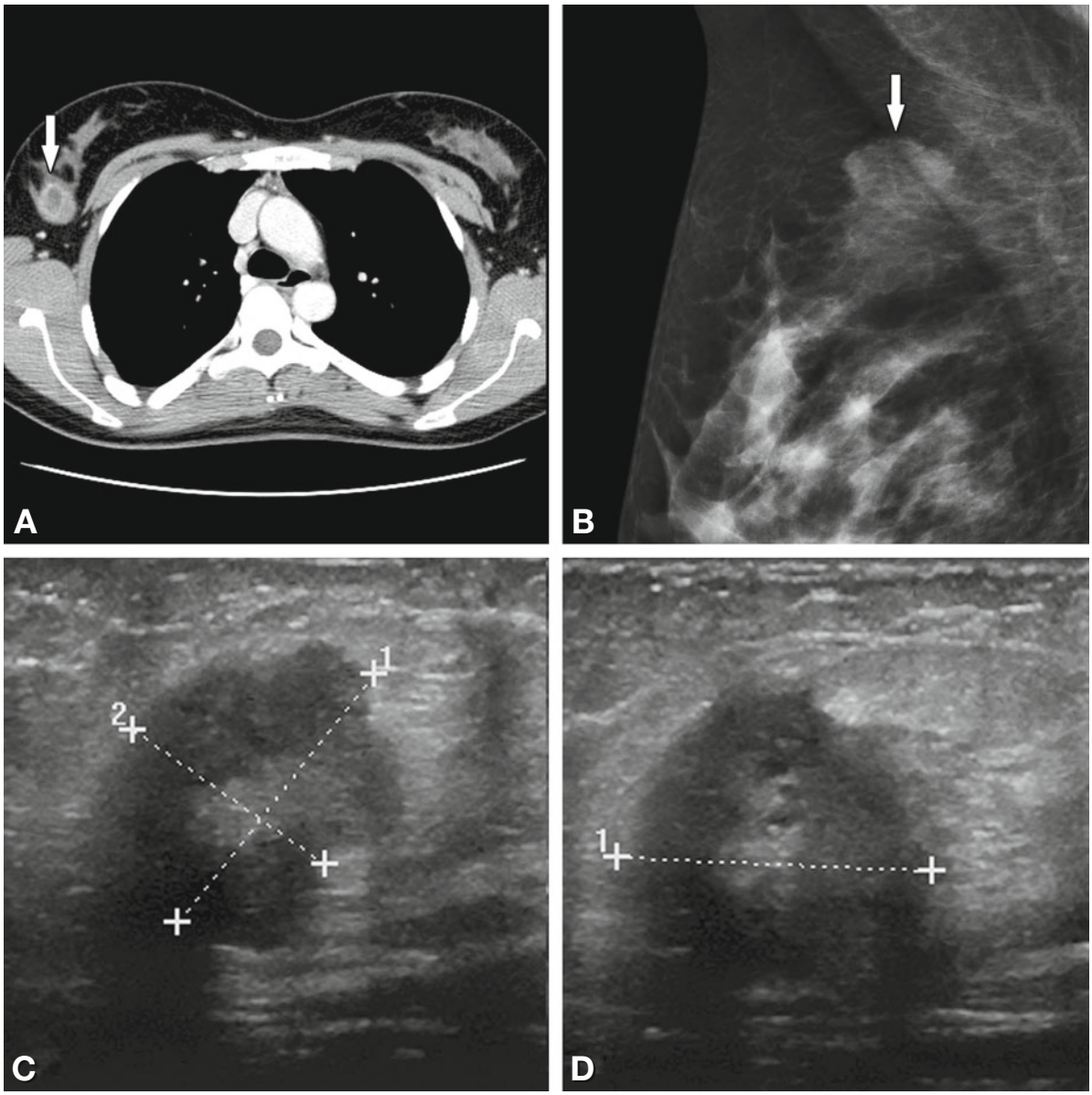

Fig. 24.50 Incidental finding of a well-vascularized 2-cm cancer in the upper outer quadrant of the right breast on chest CT in a 28-year-old female patient who presented with shortness of breath (*arrow* in **Panel A**). **Panel B** shows the tumor (*arrow*) on a magnified mediolateral oblique view mammography. **Panels C** and **D** are sonography images with measurements

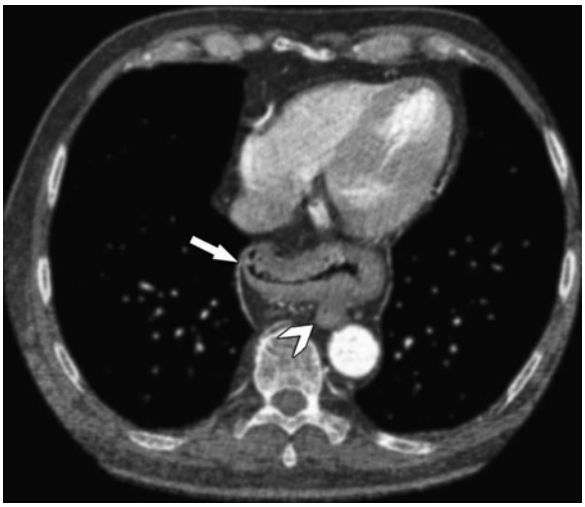

Fig. 24.51 Large hiatal hernia in an 82-year-old male patient (*arrow*). Such hernias can cause chest pain mimicking angina pectoris, and proton pump inhibitors may reduce the symptoms of reflux. The displaced esophagus is located posteriorly (*arrowhead*) to this "upside-down" stomach

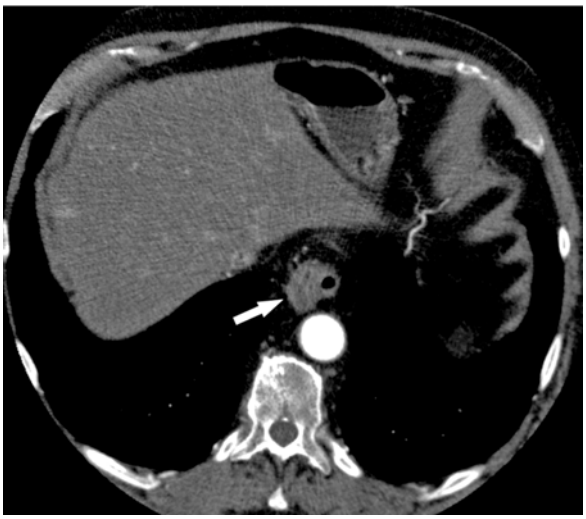

Fig. 24.52 Small hiatal hernia in an 67-year-old male patient (*arrow*) presenting with atypical angina

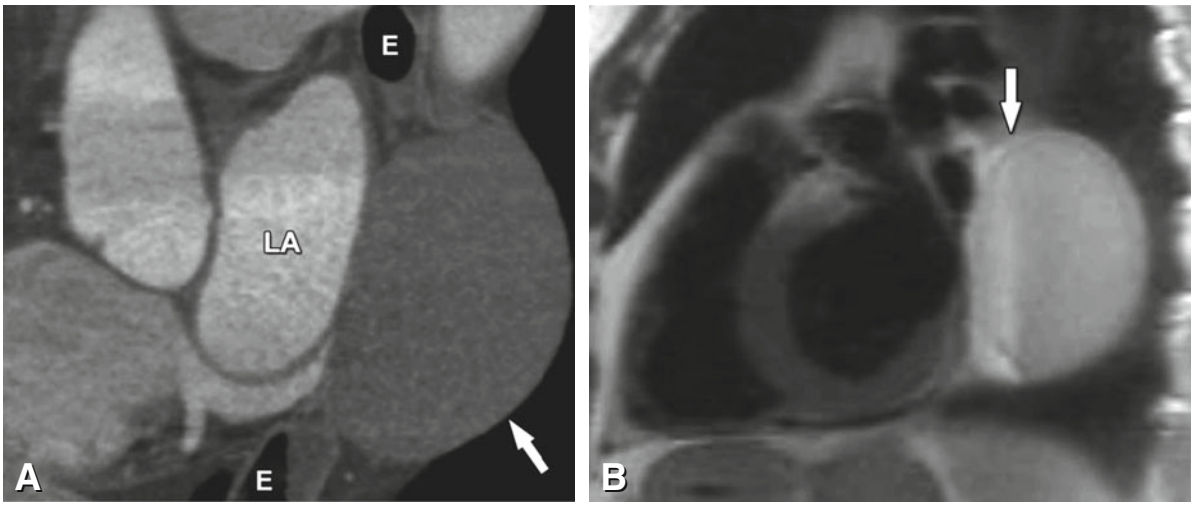

Fig. 24.53 Mediastinal cystic lesion on cardiac CT in a 72-year-old man who presented with dyspnea and atypical angina pectoris (*arrow* in **Panel A**, sagittal reformation). An oval hypoattenuating 8-cm mediastinal tumor was found posterior to the left atrium (*LA*). The differential diagnosis in this situation included a pericardial, bronchogenic, or lymphatic cyst, or less likely, a lymphoma or a malignant tumor arising from a different origin (e.g., the esophagus, **E**). Magnetic resonance imaging was performed for further clarification (**Panel B**) and demonstrated a fluid level (*arrow*). Thus, the lesion was assumed to most likely represent a benign cyst, e.g., of lymphatic origin (lipid-water level) or originating from the pericardium. This case highlights the importance of the availability of different modalities for clarification of noncardiac findings in cardiac CT

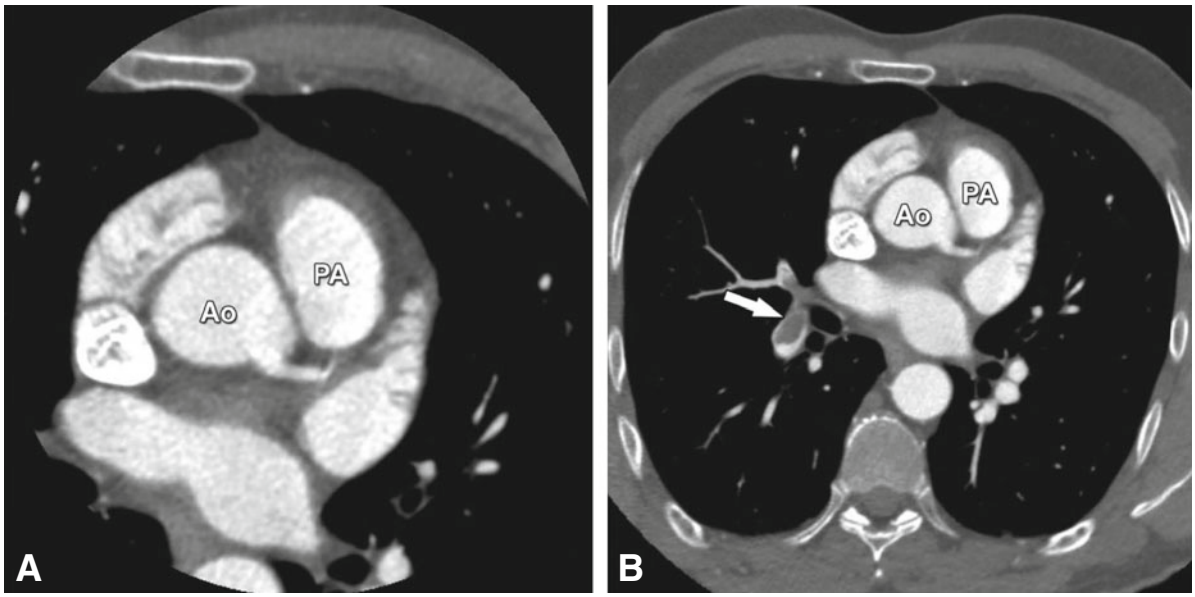

Fig. 24.54 Unexpected pulmonary embolism in a 39-year-old male patient that was not seen on dedicated small reconstruction fields of view for coronary artery evaluation (**Panel A**) but was visible on the large fields of view with 320-mm size (*arrow* in **Panel B**). Note the filling defect in the interlobar pulmonary artery, which was only seen on large-field reconstruction (*arrow* in **Panel B**). Extensive pulmonary embolism was found in the right middle and lower lobes at maximum reconstruction fields-of-view. The patient had to be readmitted for medical treatment of this complication. Coronary CT angiography was performed for evaluation of scar tissue and/or complications after right ventricular radiofrequency ablation therapy of an arrhythmia focus. This case again demonstrates that large fields of view should always be reconstructed and evaluated. *Ao* aorta, *PA* pulmonary artery (Images courtesy of L. Kroft)

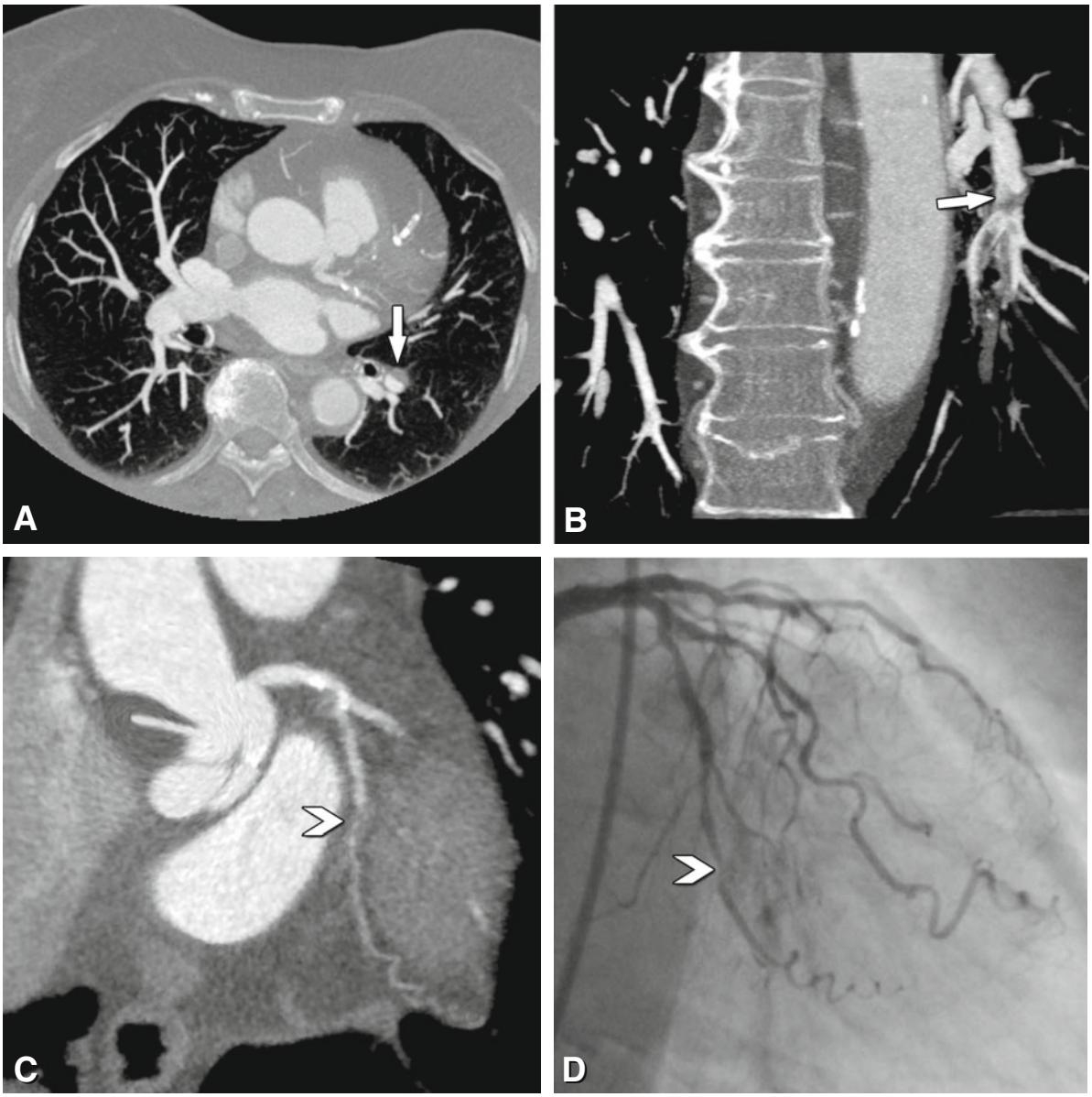

Fig. 24.55 Pulmonary embolism in an 87-year-old patient with progressive shortness of breath and suspected coronary in-stent restenosis (*arrow* in **Panels A** and **B**). CT results are shown in axial (**Panel A**) and coronal maximum-intensity projections (**Panel B**). Anticoagulation was immediately initiated. Cardiac CT also showed a 75% diameter stenosis (*arrowhead*) in a thin-slab maximum-intensity projection curved along the left circumflex coronary artery (so-called CATH view, **Panel C**), which was confirmed on later conventional coronary angiography (*arrowhead* in **Panel D**) (Images courtesy of S. Feger, Berlin)

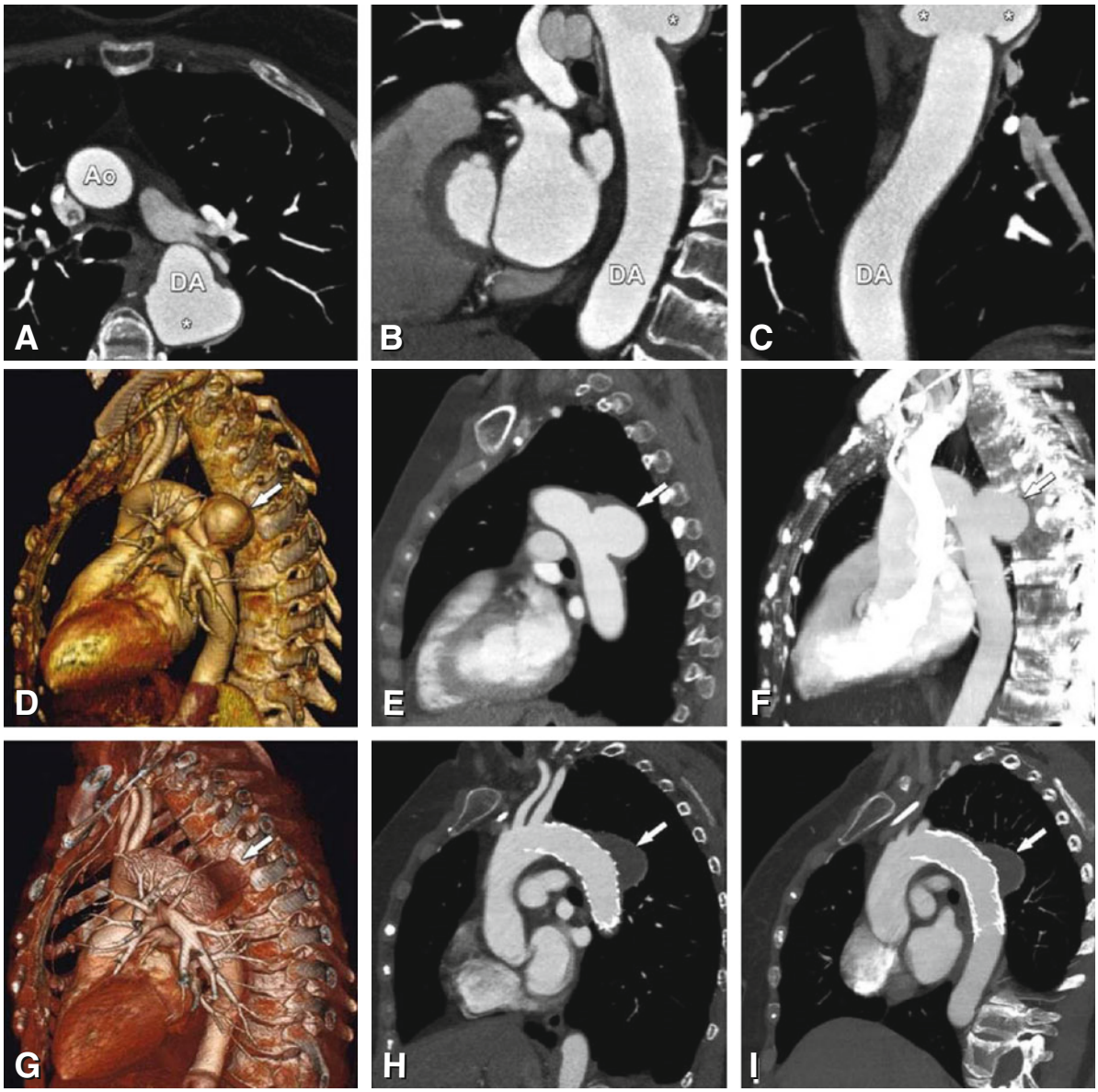

Fig. 24.56 Saccular aneurysm of the descending thoracic aorta in a 65-year-old female patient. On the most cranial slices of coronary CT angiography, a focal excentric dilatation (4.3 cm, *asterisks* in **Panels A**–**C**) of the descending aorta (*DA*) is partially visible. **Panel A** represents an axial source image, and **Panels B** and **C** represent double-oblique sagittal and coronal slices. Because of this extracardiac finding, CT angiography of the thoracic and abdominal aorta was subsequently performed. This test confirmed the focal saccular aneurysm, which did not extend to the aortic arch (*arrow* in **Panels D**–**F**, lateral views). Percutaneous interventional treatment with stenting was performed, and follow-up CT scans showed that the stent excluded the aneurysm well, resulting in thrombosis and exclusion from perfusion of the aneurysm (*arrow* in **Panels G**–**I**, lateral views). The suprarenal location and the absence of atherosclerosis in other vascular territories indicate that this was most likely a mycotic aneurysm. *Ao* aorta

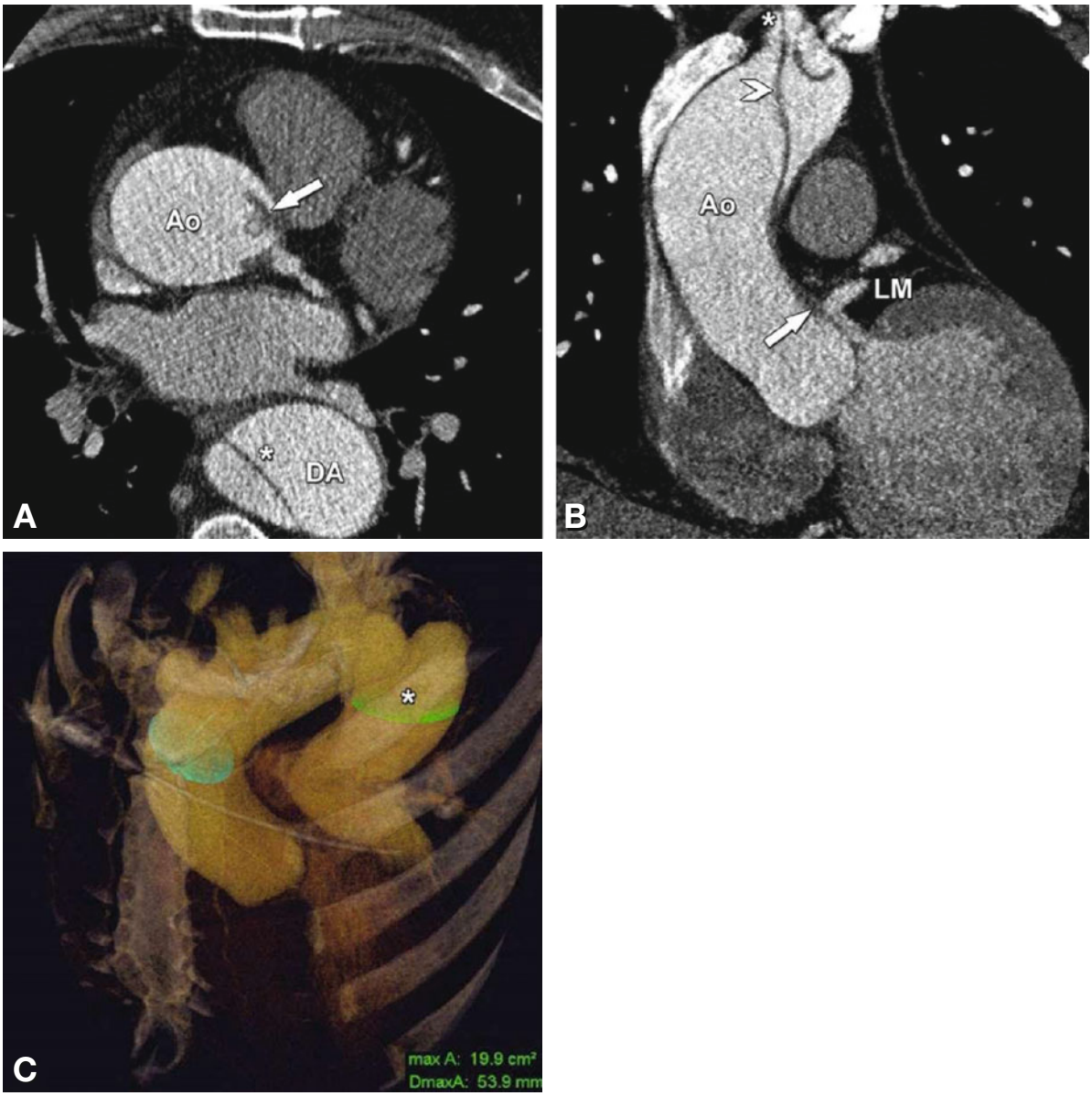

Fig. 24.57 Aortic dissection (Stanford and DeBakey type I) with obstruction of the left main coronary artery ostium and extension into the descending aorta (*DA*) in a 48-year-old male patient presenting with acute thoracic back pain. Axial source images (**Panel A**) and double-oblique coronal images (**Panel B**) demonstrate the dissection membrane in the ascending aorta (*arrowhead* in **Panel B**) and descending aorta (*asterisk* in **Panel A**). The dissection extends into the innominate artery (brachiocephalic trunk, *asterisk* in **Panel B**) and obstructs the left main coronary ostium (*LM*, *arrow* in **Panels A** and **B**). Automatic measurement of the inner diameters of the thoracic aorta was performed (**Panel C**) and revealed a maximum diameter of 5.4 cm (*asterisk* in descending aortic aneurysm). The advantage of this comprehensive ECG-synchronized CT imaging approach is that the coronary arteries can be simultaneously evaluated. Emergency aortic repair and bypass grafting (left internal mammary artery to the left anterior descending and venous bypass graft to the left circumflex) was performed

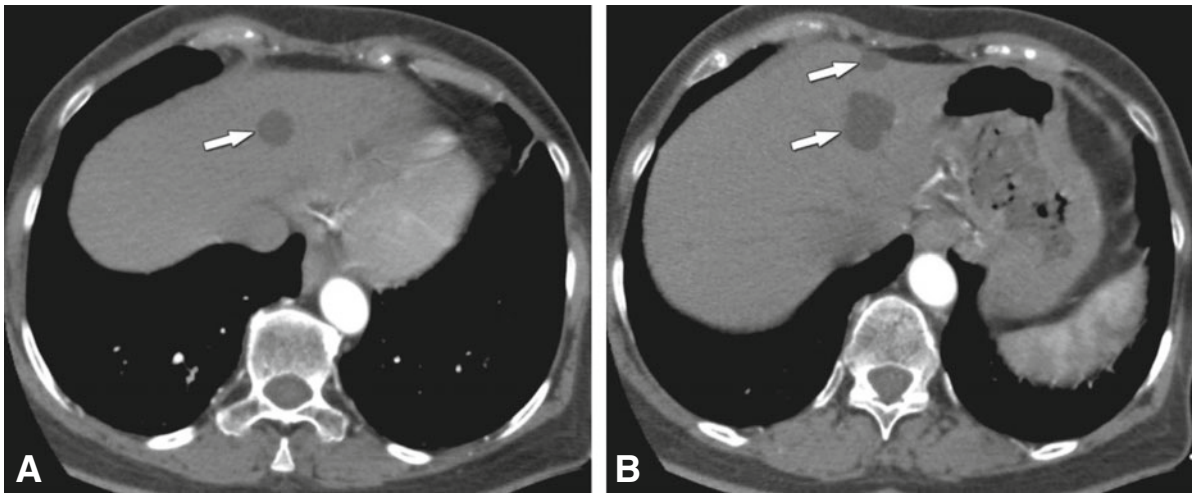

Fig. 24.58 Incidental finding of multiple (up to 2.5 cm) liver cysts (*arrows* in **Panels A** and **B**) in a 66-year-old female patient who underwent coronary CT angiography that excluded significant coronary artery stenoses. Differentiating liver cysts from low-density metastases or liver tumors can be difficult (**Figs. 24.59** and **24.60**) because only the purely arterial phase of liver perfusion is available with coronary CT. Thus, dedicated liver imaging, e.g., using ultrasound, is recommended whenever liver lesions that are suspicious for malignancy or not seen on prior imaging are detected

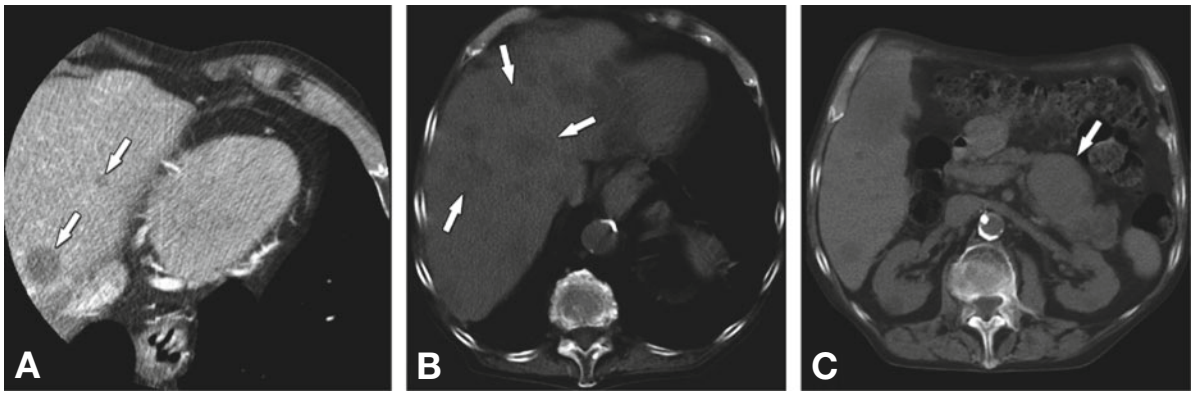

Fig. 24.59 Primarily misinterpreted hepatic metastases. Two round, well-circumscribed hypo-attenuating hepatic lesions were seen on the basal slices of a cardiac CT scan (*arrows* in **Panel A**) in a 78-year-old male patient who was referred for analysis of atypical chest pain. These lesions were reported and thus the referring physician, who had done an ultrasound in this patient a few years ago, recognized that these were new. Thus, abdominal CT (**Panels B** and **C**) was performed for further analysis, confirming that these lesions had already increased size in the short interval since the cardiac CT scan and revealing many more ill-defined lesions (a few of them are marked with *arrows* in **Panel B**), compatible with metastases. Also, a large pancreatic tumor was diagnosed (*arrow* in **Panel C**). Imaging was limited to unenhanced CT because of renal dysfunction. The patient's condition rapidly deteriorated and he died within 2 months. Pancreatic cancer was confirmed at autopsy (From Dewey et al. *Eur Radiol* 2007)

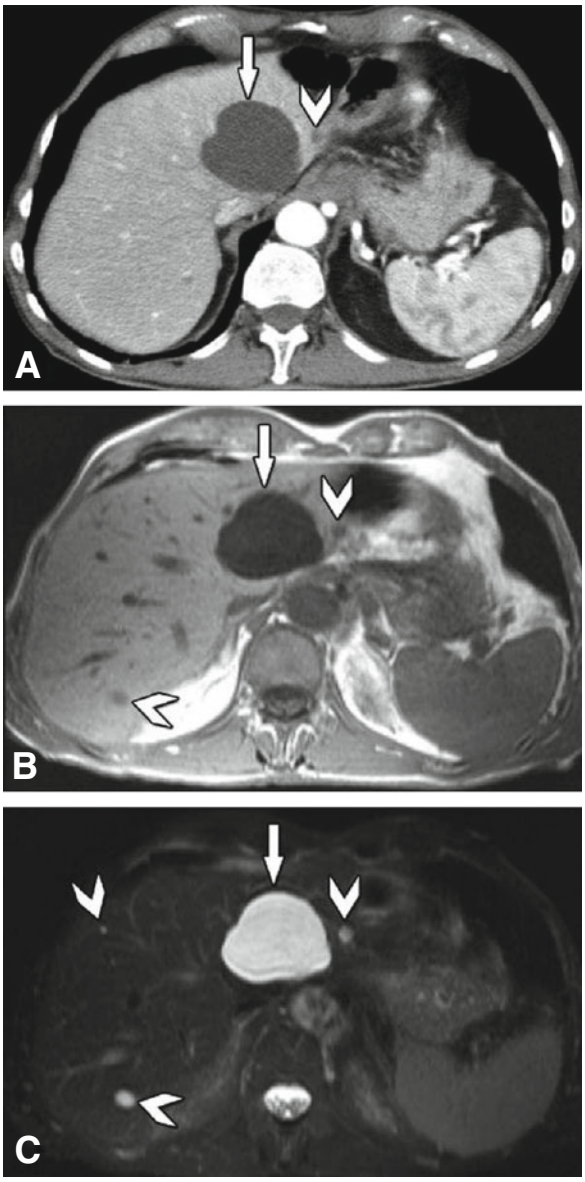

Fig. 24.60 Hepatic cysts confirmed on magnetic resonance imaging. Multiple hypo-attenuating lesions with the largest measuring about 5 cm were incidentally found on cardiac CT of a 76-year-old male patient (*arrow* in **Panel A**). Because of additional smaller lesions (*arrowhead* in **Panel A**) and the fact that cystic liver lesions are not always easy to analyze on the arterial phase images provided by cardiac CT (**Fig. 24.59**), this patient underwent magnetic resonance imaging with T1- (**Panel B**) and T2-weighted (**Panel C**) sequences. These clearly confirmed the benign nature of the liver lesions diagnosed as biliary cysts (*arrow* and *arrowheads* in **Panels B** and **C**)

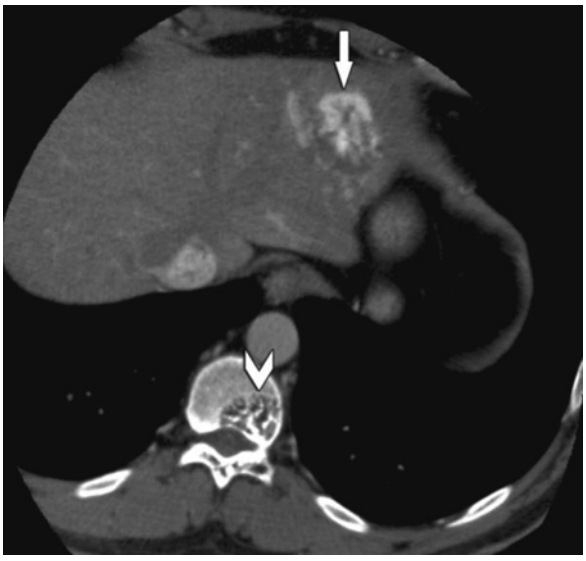

Fig. 24.61 Incidental finding of a hepatic and vertebral body hemangioma in a 52-year-old male patient presenting with atypical angina pectoris. Coronary CT angiography excluded significant coronary artery stenosis and demonstrated a 3.7 cm well-marginated tumor with peripheral globular enhancement in segment II of the liver (*arrow*). Ultrasound confirmed the typical imaging findings of a hepatic hemangioma (not shown). There was also a well-marginated area in a vertebral body (*arrowhead*) with typical trabeculation pattern diagnostic for vertebral body hemangioma

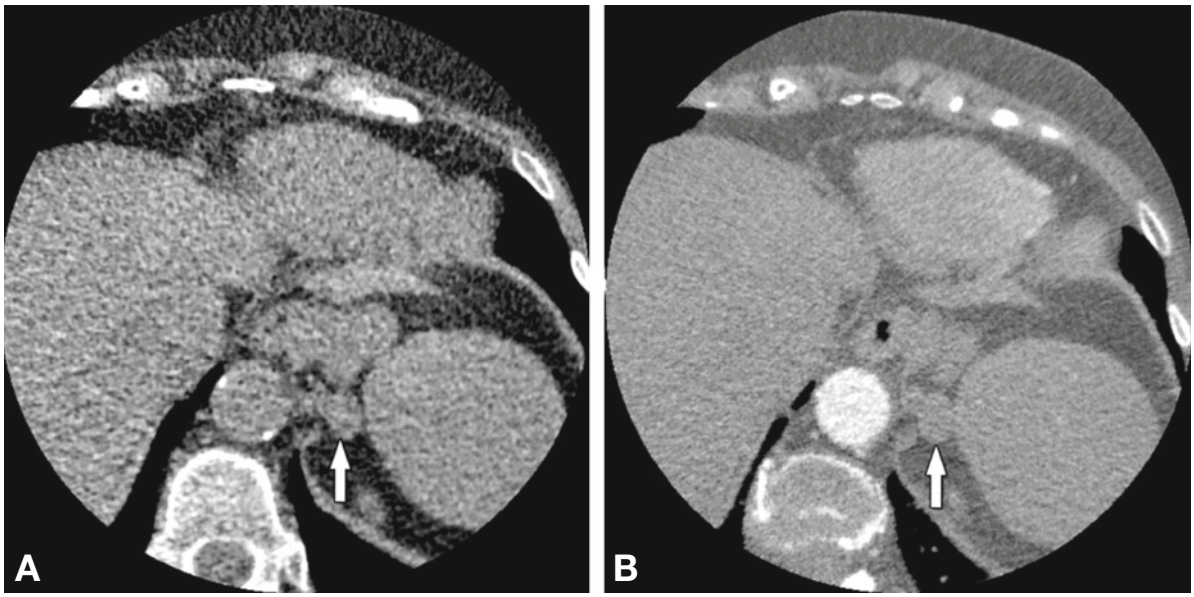

Fig. 24.62 Incidental finding of a 1.7-cm incidentaloma of the left adrenal gland in a 73-year-old female patient. Because of fat isodensities within the lesion on the noncontrast coronary artery calcium scan (*arrow* in **Panel A**) and only minimal enhancement on cardiac CT angiography (*arrow* in **Panel B**) an adrenal adenoma was suspected, and further imaging follow-up was unremarkable

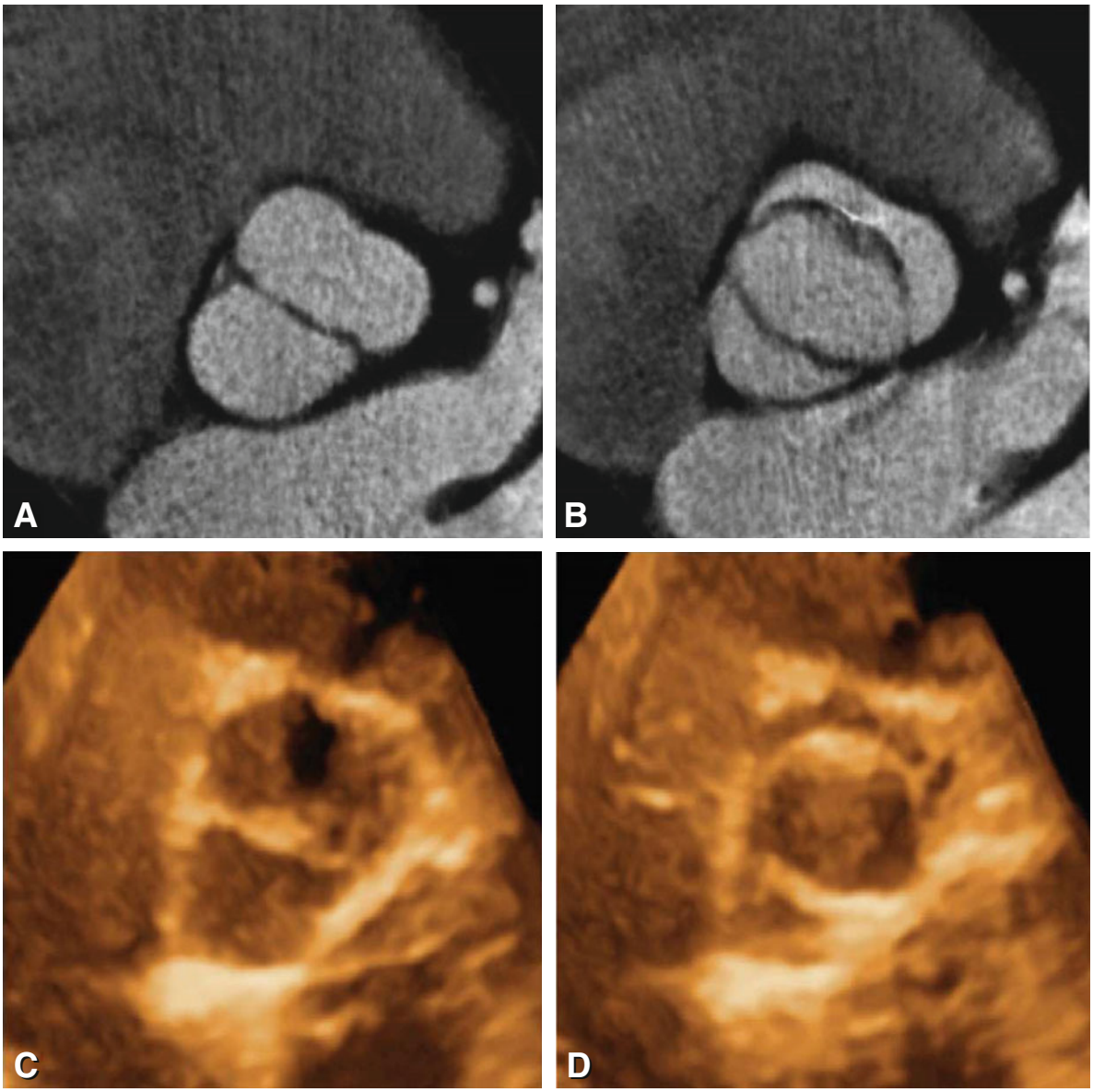

Fig. 24.63 Bicuspid aortic valve in a 48-year-old male patient. There is normal closure (**Panel A**) and opening of the aortic valve (**Panel B**) as seen with CT. CT data are shown as minimum-intensity projections. There is excellent correlation with the findings of three-dimensional transthoracic echocardiography (**Panels C** and **D**) (Echocardiography images courtesy of A.C. Borges)

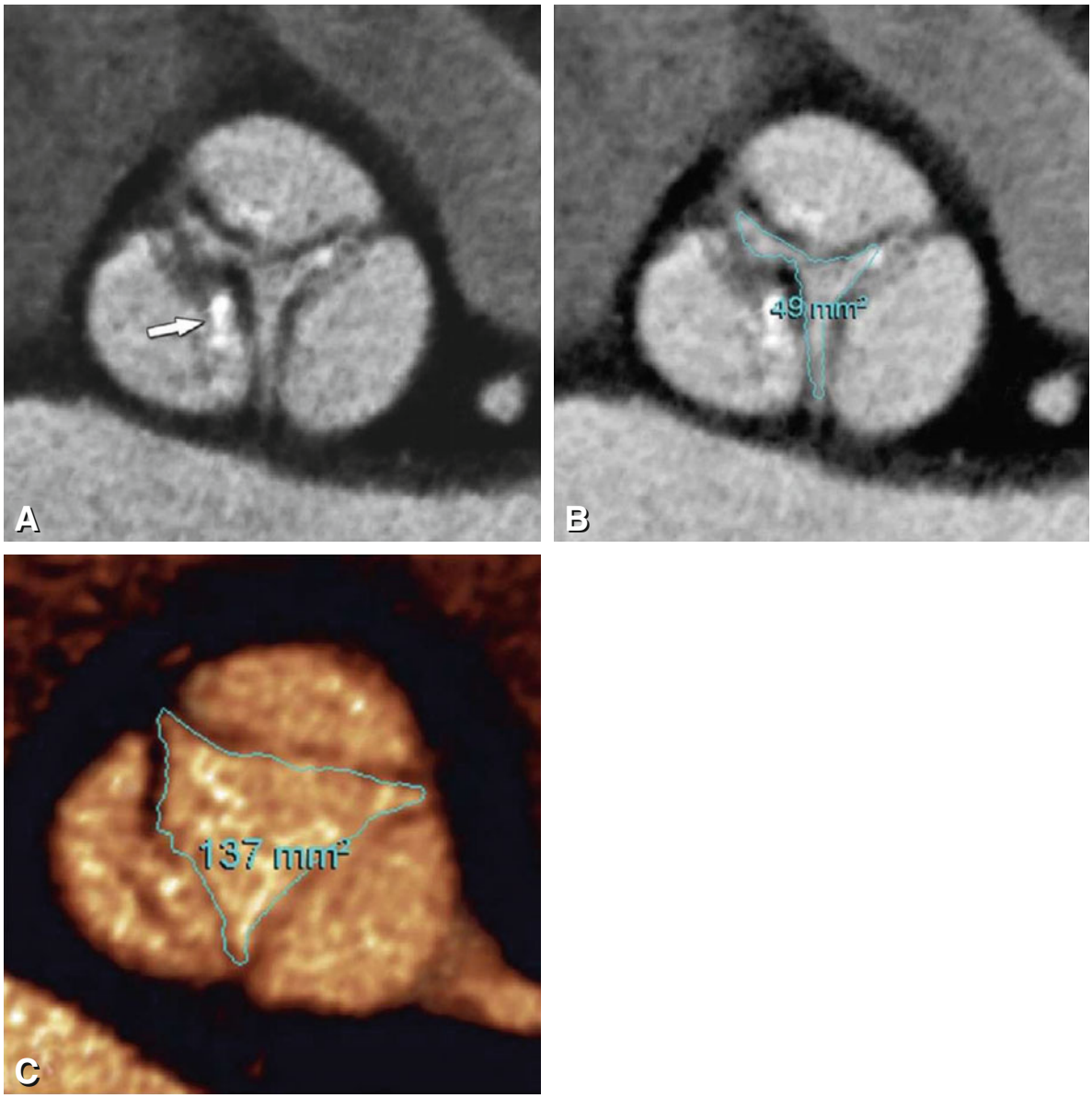

Fig. 24.64 Tricuspid aortic valve in an 83-year-old female patient with stenosis. There are moderate calcifications of the aortic cusps (*arrow* in **Panel A**) that lead to severe (<1.0 cm^2) stenosis of the valve during systole (**Panel A**). Caliper measurement of the aortic valve area during systole (**Panel B**) shows a valve area of 0.49 cm^2. After surgical replacement of the valve, there is marked increase in the systolic aortic valve area (**Panel C**). Mild and moderate aortic valve stenoses are represented by aortic valve areas of >1.5 cm^2 and 1.0–1.5 cm^2, respectively. CT data are shown as minimum-intensity projections

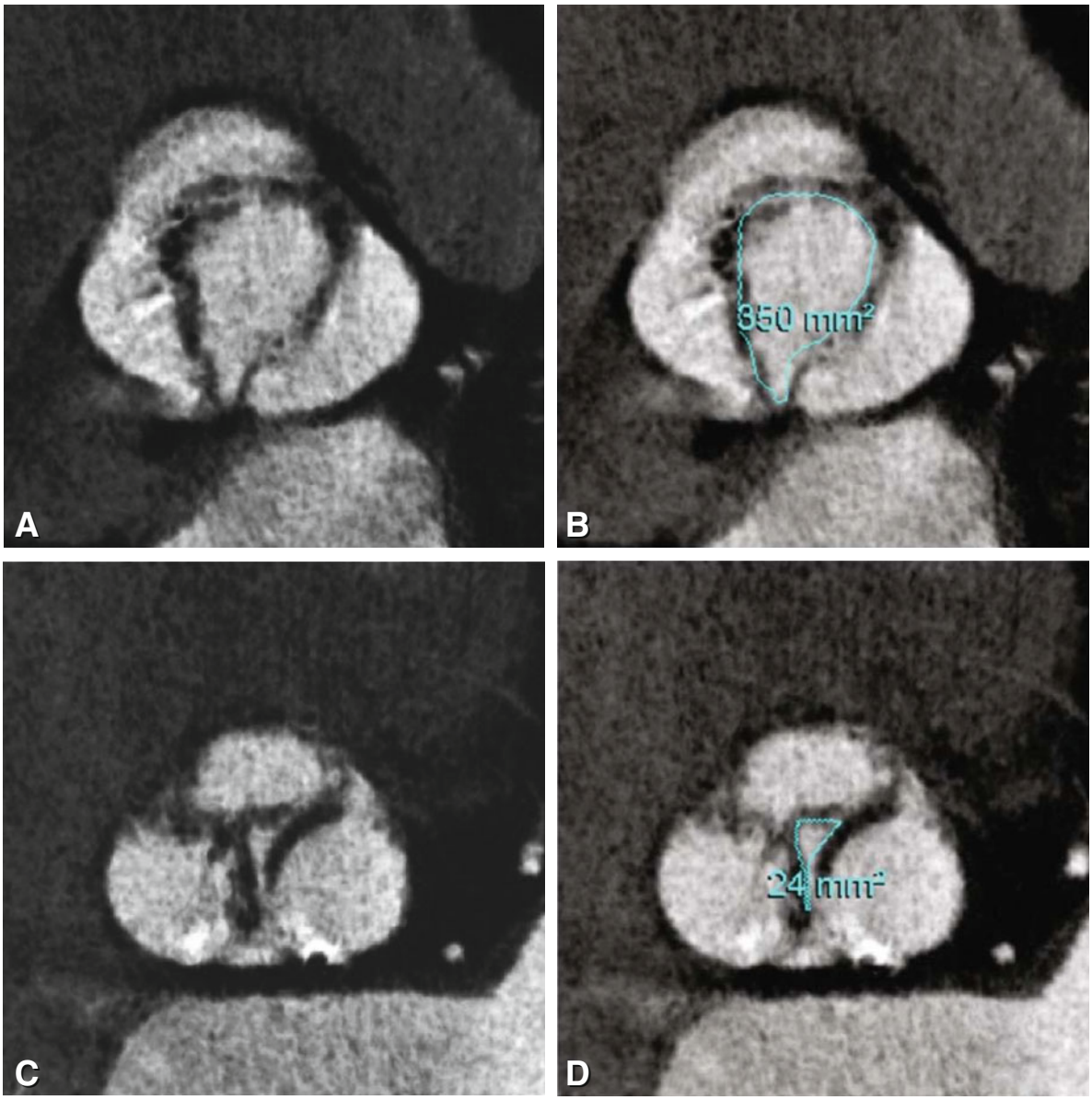

Fig. 24.65 Tricuspid aortic valve with regurgitation in a 48-year-old male patient. **Panels A** and **B** show results of systole with normal opening of the valve cusps, while **Panels C** and **D** show the aortic regurgitation area during diastole (0.24 cm^2). The right column shows the caliper measurements of the aortic valve area. CT data are shown as minimum-intensity projections

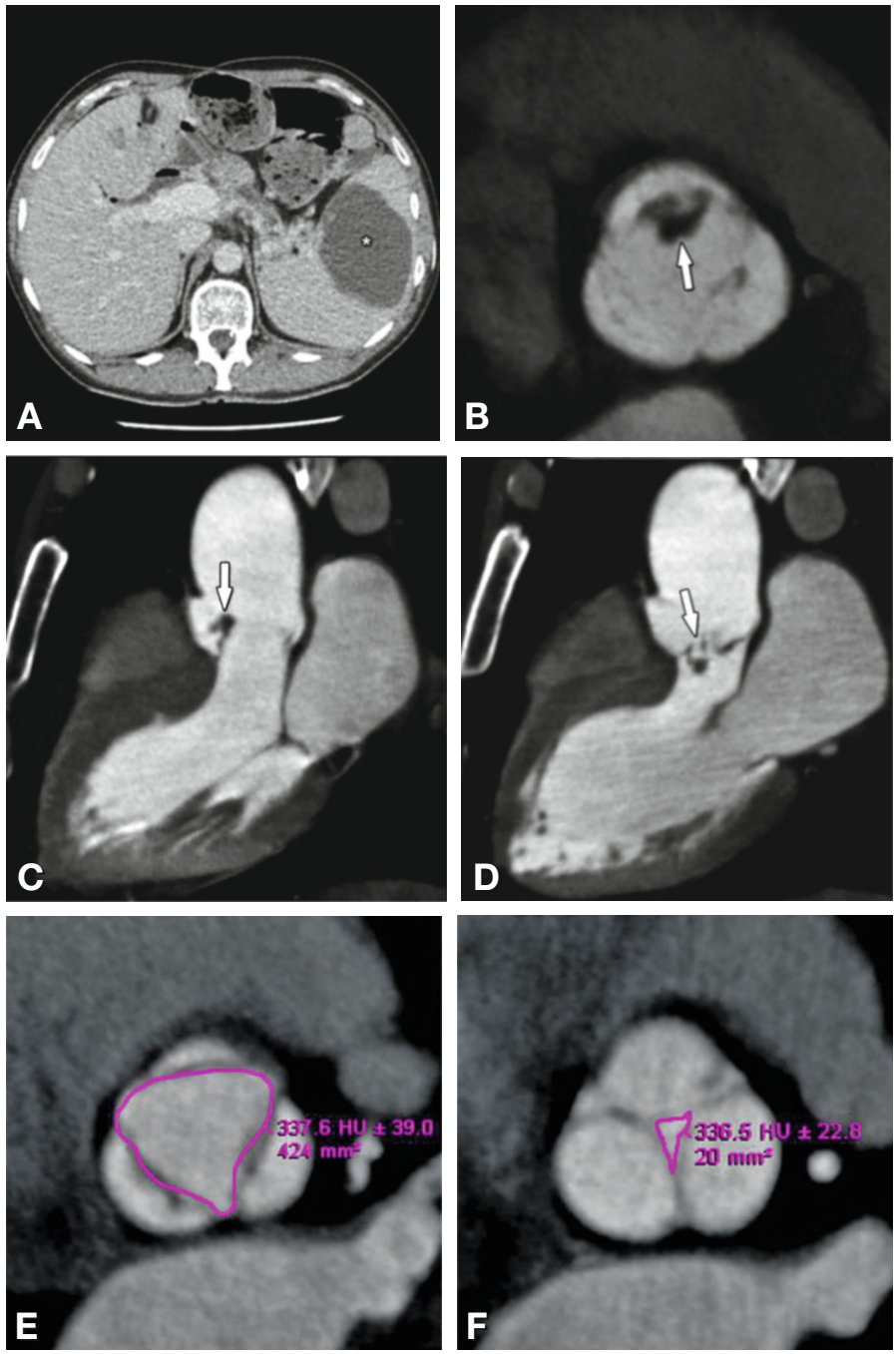

Fig. 24.66 Endocarditis of the aortic valve in a 58-year-old male patient presenting with signs of severe infection. **Panel A** shows a splenic abscess (*asterisk*) on the abdominal CT scan done during the same imaging session as cardiac CT (**Panels B**–**F**). An irregular 11-mm vegetation was found on the right aortic valve cusp on cardiac CT (*arrow* in **Panels B**–**D**). **Panel B** is a minimum-intensity projection of the cross-section of the aortic valve, while **Panels C** and **D** are maximum-intensity projections along the three-chamber view during systole and diastole, respectively. During systole there was unimpaired opening of the aortic valve (**Panel E**), which, however, showed a regurgitation area of 0.2 cm^2 during diastole (**Panel F**).

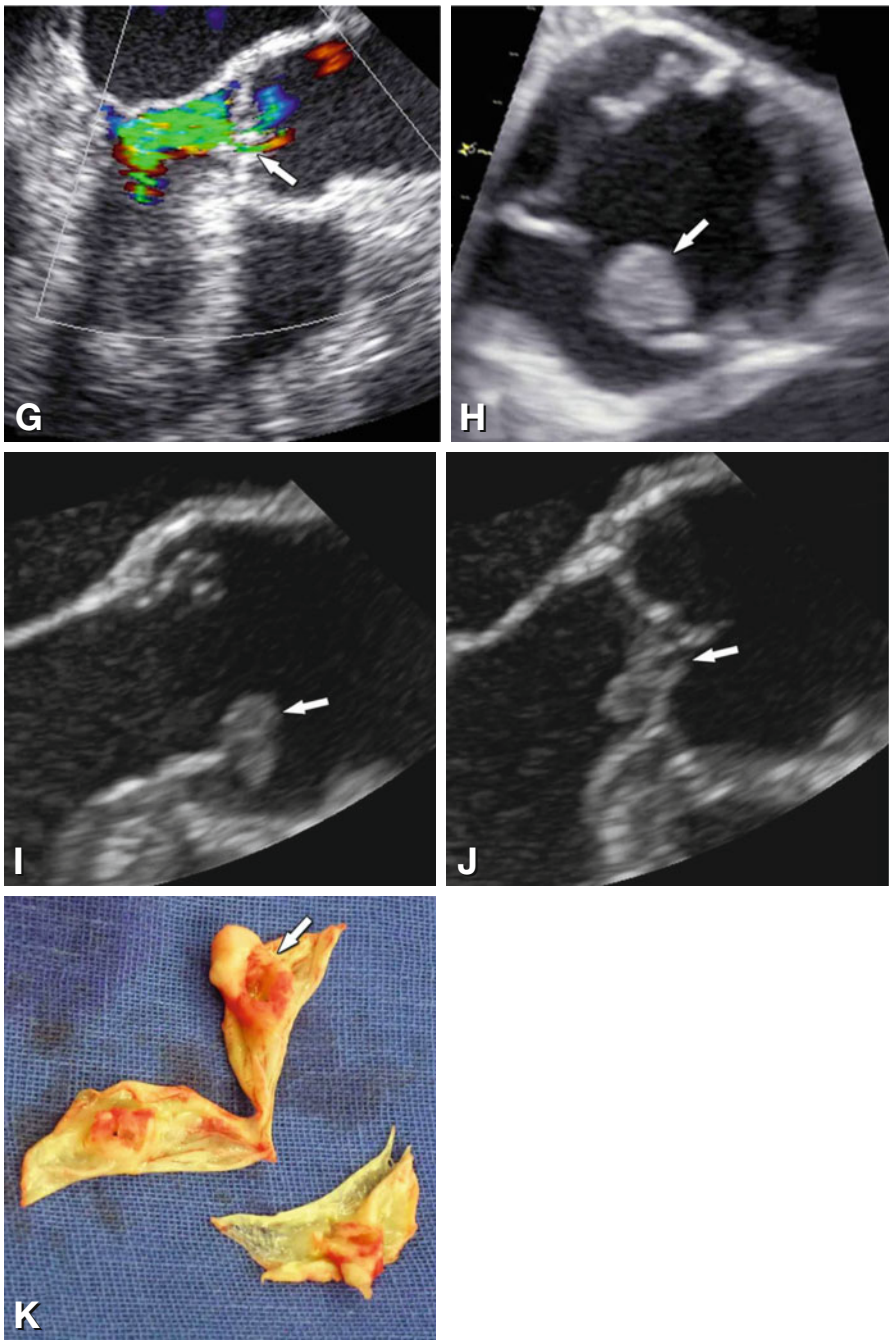

Fig. 24.66 (continued) Transesophageal echocardiography showed a regurgitation jet during diastole (*arrow* in **Panel G**) and confirmed the presence of the vegetation suspicious for aortic valve endocarditis (*arrow* in **Panels H**–**J**). **Panel H** is a cross-sectional view of the aortic valve, while **Panels I** and **J** are three-chamber views during systole and diastole, respectively. After CT, splenectomy was performed first and 2 weeks later a surgical biologic aortic valve implantation was performed after removal of the infected valve. **Panel K** shows the infected aortic valve leaflets after removal with the *arrow* pointing at the vegetation (Echocardiography images are courtesy of W. Poller, Berlin, and cardiac surgery was performed by S. Dushe, Berlin)

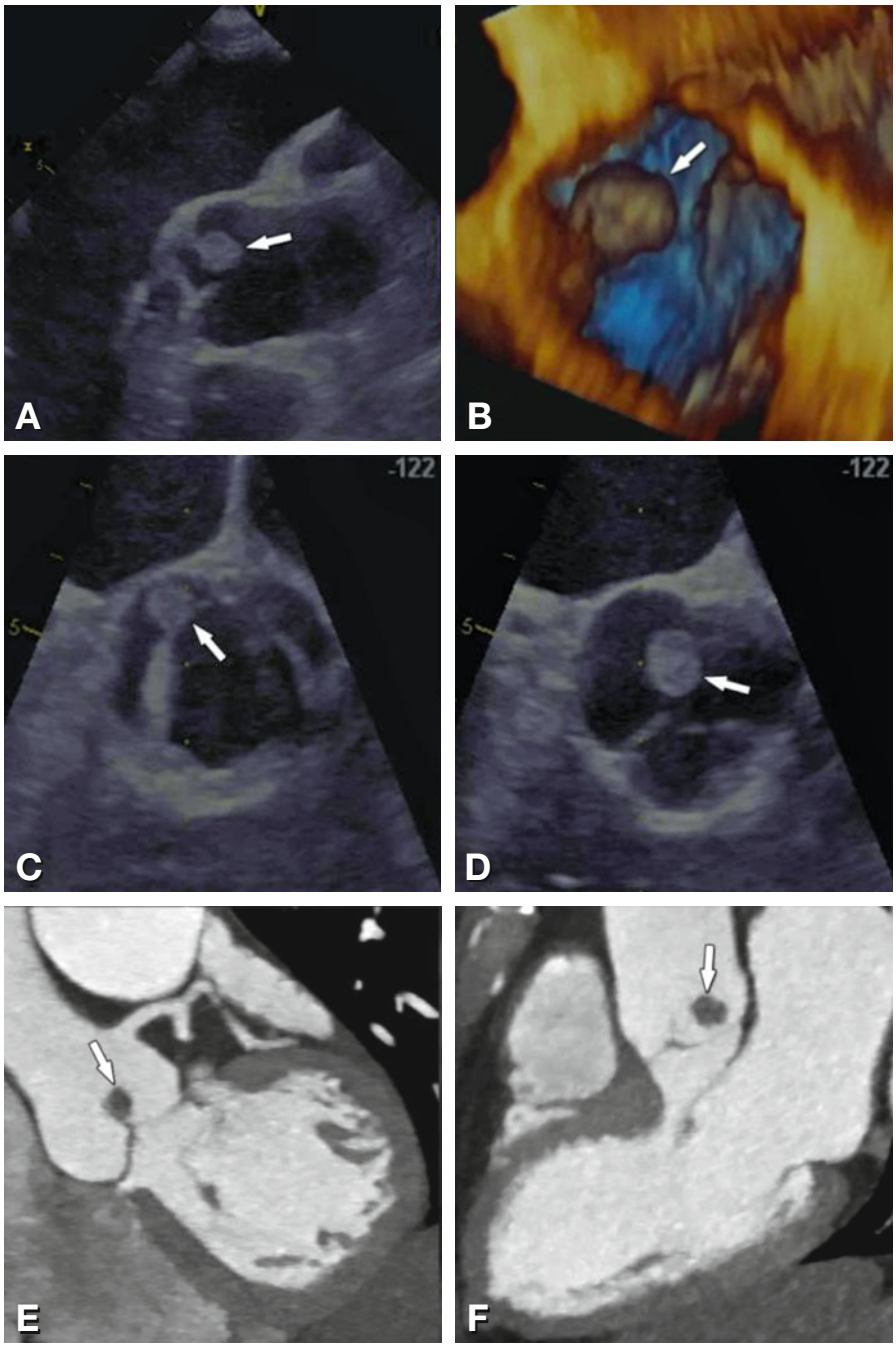

Fig. 24.67 Fibroelastoma of the aortic valve in a 73-year-old female patient. This tumor of the aortic valve was suspected incidentally on transthoracic echocardiography done prior to a dental operation. Transesophageal echocardiography (**Panels A**–**D**) and cardiac CT (**Panels E**–**H**) were performed for confirmation of this 10-mm tumor on the left aortic valve cusp (*arrow*). An oval 11-mm tumor was found on the anterior aortic valve on cardiac CT (*arrow* in **Panels B**–**D**). **Panel A** is a three-chamber view and **Panel B** a three-dimensional view of the aortic valve from transesophageal echocardiography while **Panels C** and **D** are cross-sectional views during systole and diastole, respectively. **Panels E** and **F** are maximum-intensity projections along the left-coronary oblique view and three-chamber view by CT, respectively.

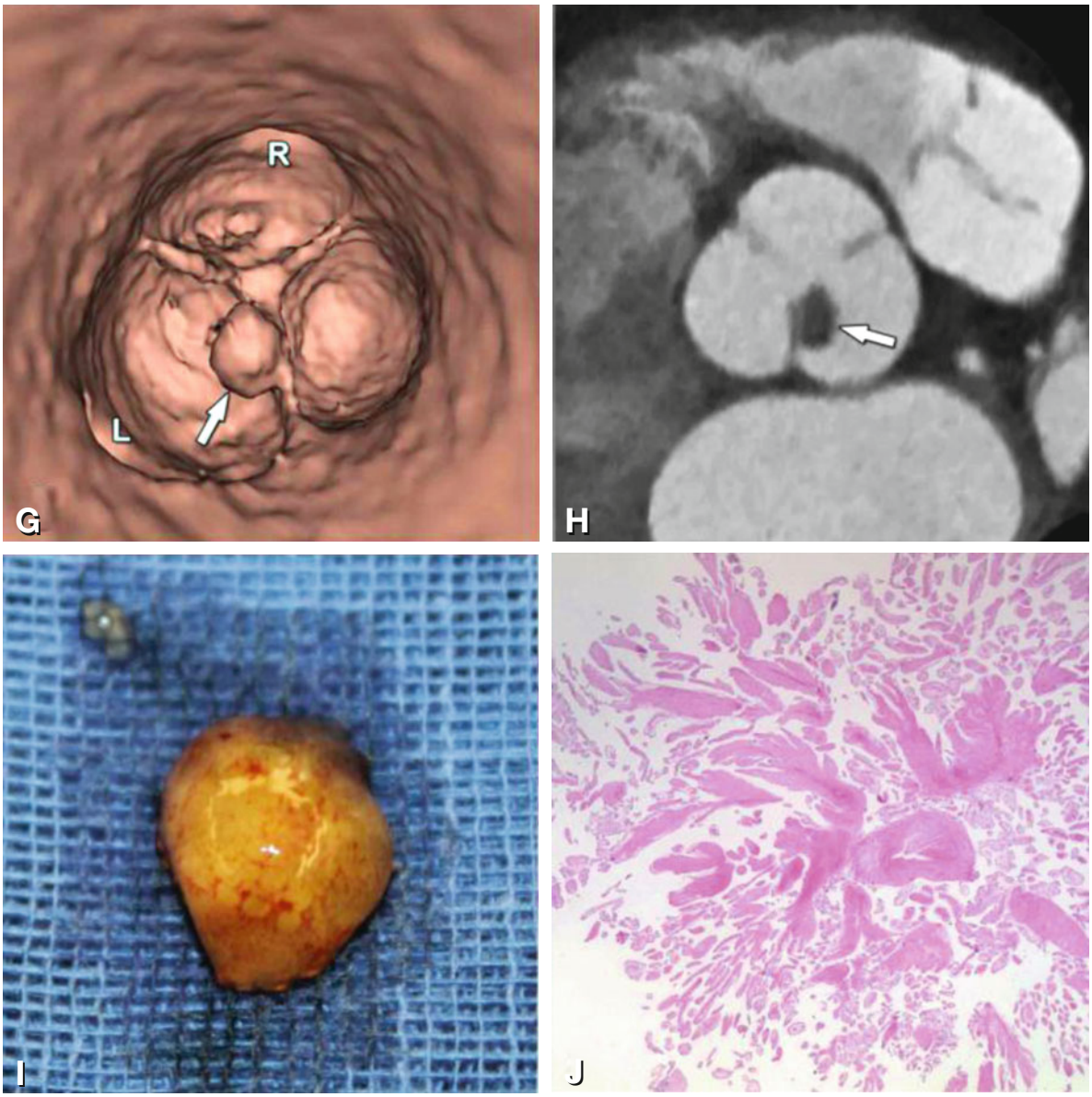

Fig. 24.67 (continued) **Panel G** is a virtual endoscopic view by CT showing the tumor (*arrow*) and the location of the left (*L*) and right (*R*) coronary artery ostia, while **Panel H** is a minimum-intensity projection of the cross-section of the aortic valve. **Panel I** shows the typical appearance of this fibroelastoma after surgical removal, while **Panel J** is the histopathological image confirming a fibroelastoma with partly branching papillary structures, which were covered by a flat endothelial layer and a homogeneous eosinophilic hypocellular matrix without vessels (Echocardiography images are courtesy of F. Knebel, Berlin, the histopathology image is courtesy of M. Rudl, Berlin, and cardiac surgery was performed by S. Holinski, Berlin)

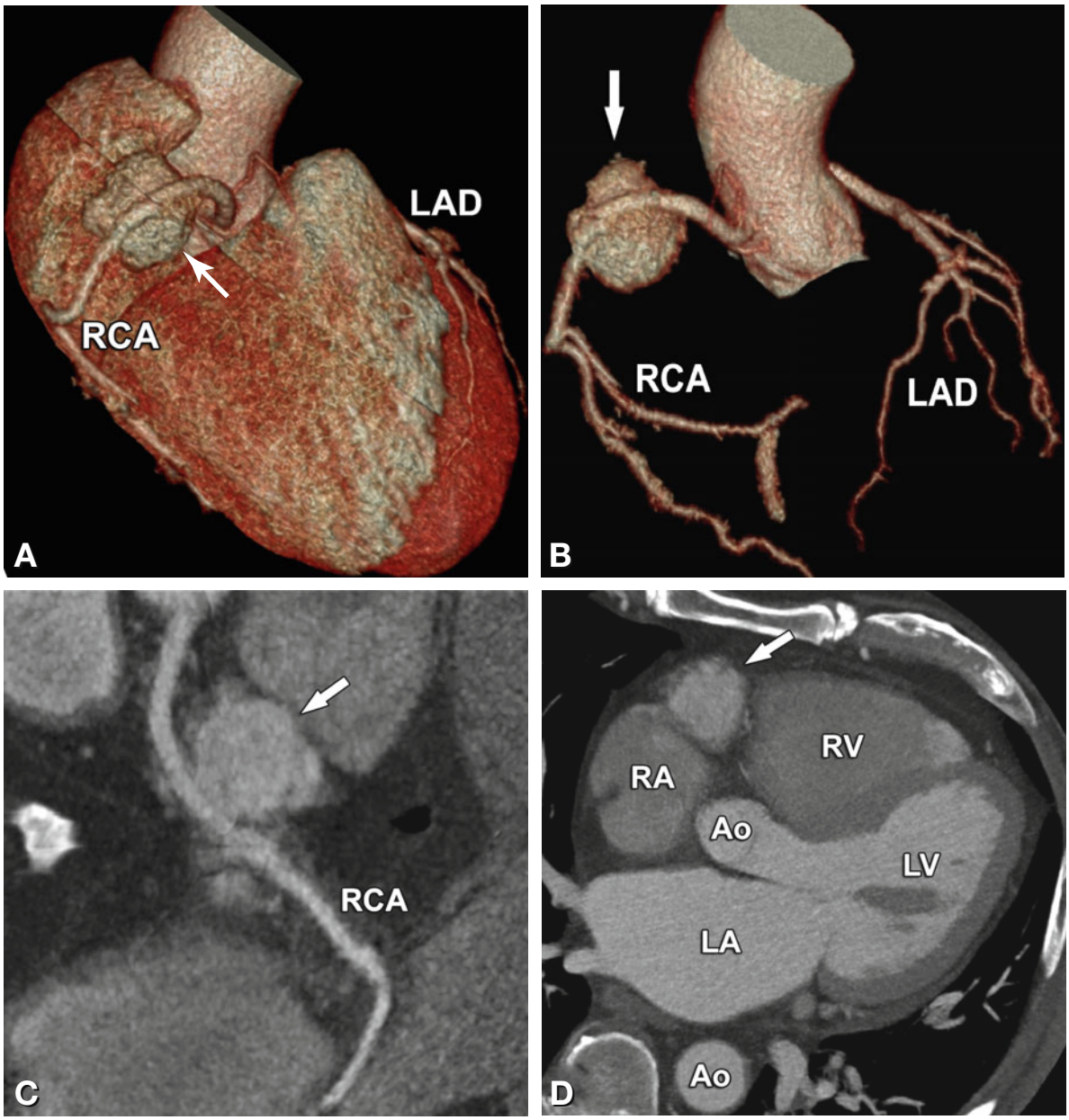

Fig. 24.68 Surprising finding of a well-vascularized 2.2-cm tumor in the right atrioventricular sulcus (*arrow*) in a 65-year-old male patient with suspected coronary artery disease. The tumor is located underneath the course of the right coronary artery (*RCA*) and appears to be supplied by the RCA (**Panels A** and **B**, volume-rendered three-dimensional reconstructions). In **Panels C** and **D** the contact of the RCA to the tumor can be seen on a curved multiplanar reformation and an axial maximum-intensity projection, respectively. Note also that the mass has the same density as the RCA, suggesting an arterial supply.

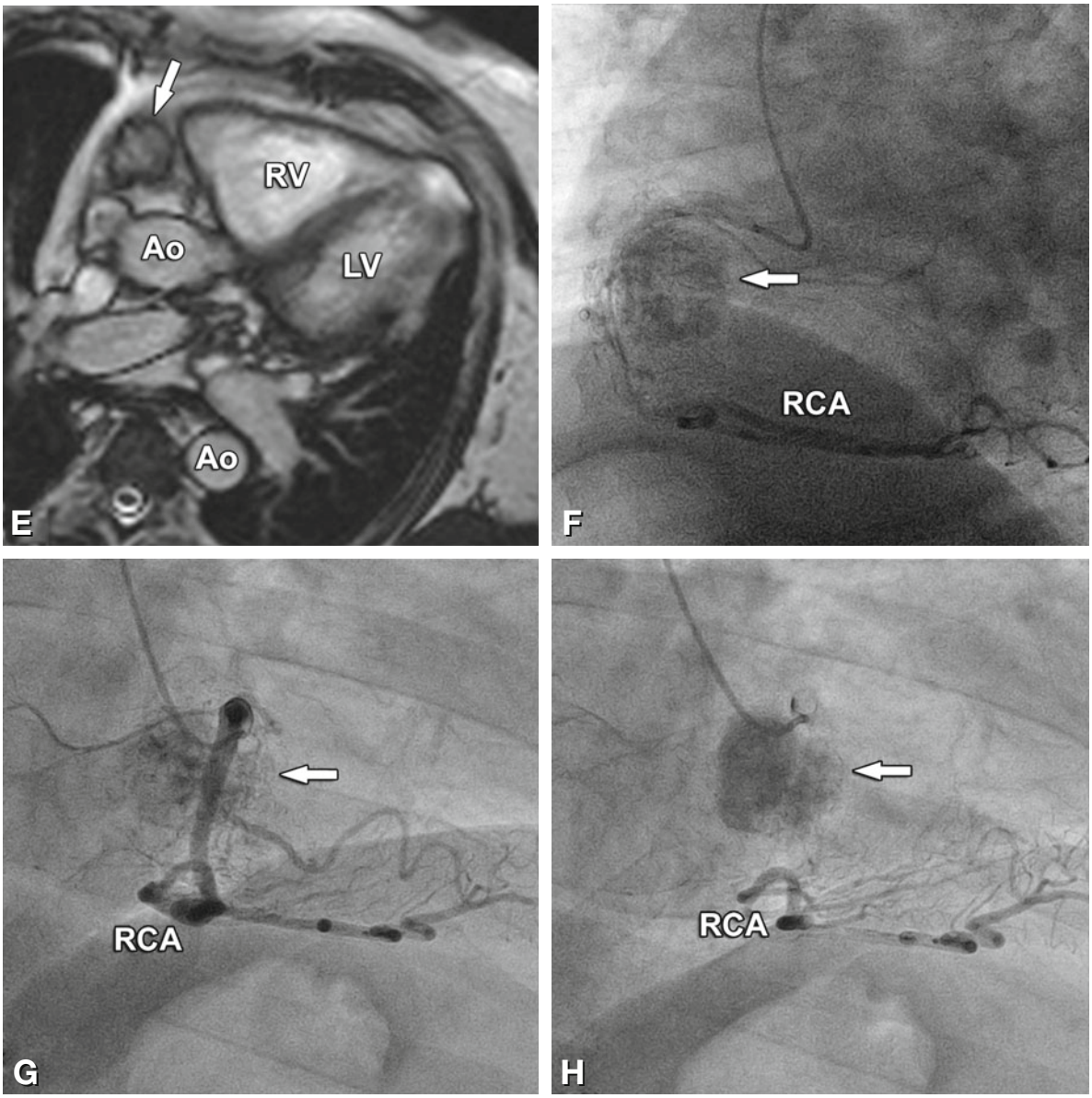

Fig. 24.68 (continued) **Panel E** displays a corresponding axial magnetic resonance image. Conventional coronary angiography (**Panels F**–**H**) revealed an arterial blood supply of the tumor from the RCA (**Panels F** and **G**) and late pooling of contrast material (**Panel H**). A cardiac hemangioma, a rare benign cardiac tumor, was suspected. A follow-up examination after 6 months did not show any growth of the tumor, and open biopsy was done. With the use of immunohistological techniques the pathologist diagnosed an extra-adrenal cardiac paraganglioma without signs of malignancy. Because surgery to completely remove the tumor would have been difficult and risky, it was decided to monitor tumor growth by follow-up studies. *LAD* left anterior descending coronary artery, *RA* right atrium, *RV* right ventricle, *LA* left atrium, *LV* left ventricle, *Ao* Aorta (Images courtesy of P. Begemann except coronary angiography, which is courtesy of S. Berrisch-Rahmel, Düsseldorf, Germany)

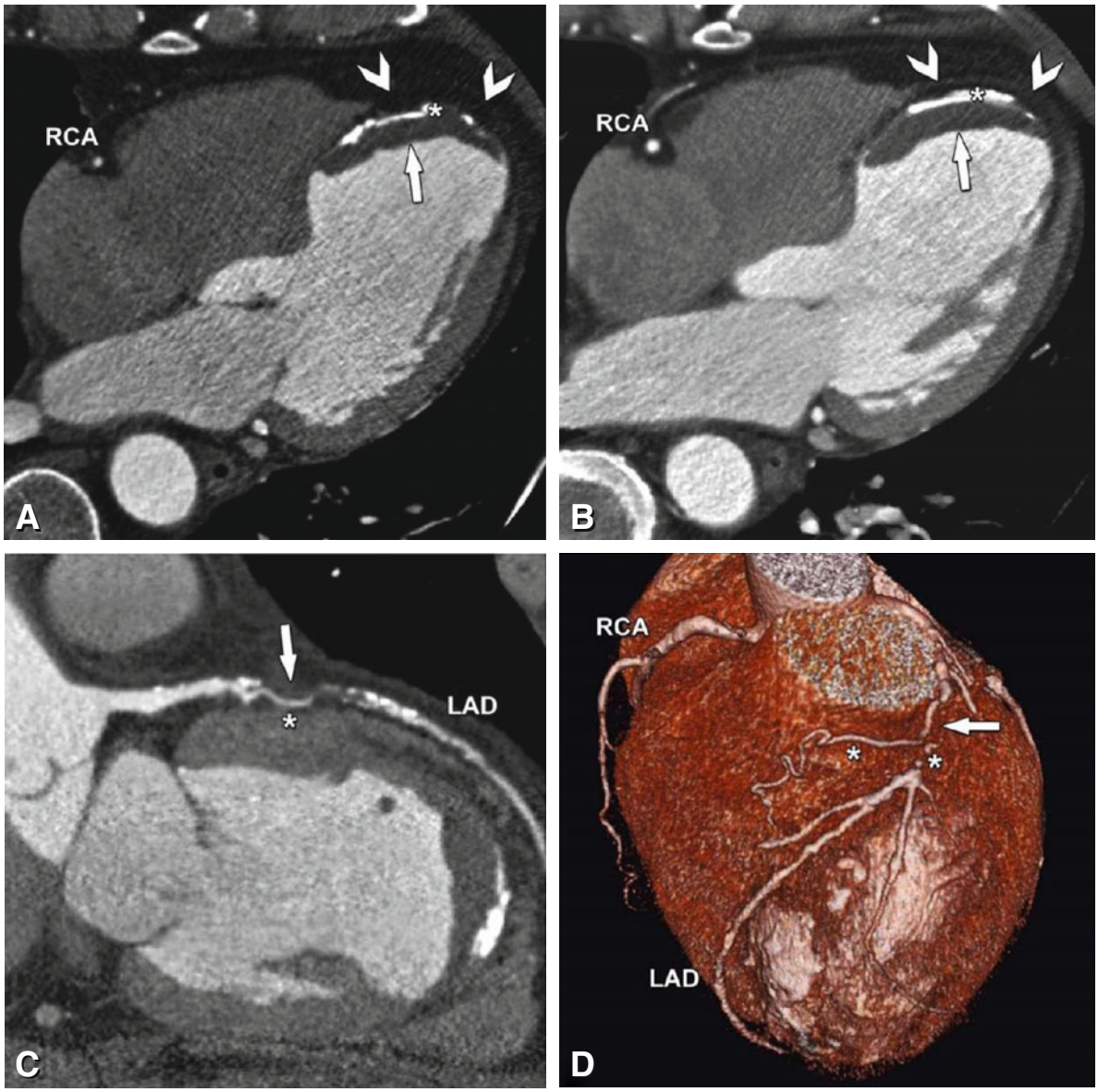

Fig. 24.69 Left ventricular apical aneurysm with thrombus in a 79-year-old male patient with a history of anterior myocardial infarction 19 years ago, who had suspected thrombus on transthoracic echocardiography. There is a left ventricular crescent-filling defect (*arrow* in **Panel A**), representing an apical thrombus. The thrombus is due to stasis of blood in the akinetic apical aneurysm resulting from chronic myocardial infarction. The myocardial infarct has resulted in myocardial calcification (*asterisk* in **Panel A**) and fatty degeneration (*arrowheads* in **Panel A**). The fatty changes in the myocardium are seen as densities similar to those of the pericardial fat. **Panel A** is a four-chamber view of the left ventricle obtained with a 0.5 mm slice thickness. For comparison, the findings are also shown as a 5 mm thin-slab maximum-intensity projection in the four-chamber view (**Panel B**) The myocardial infarction was the result of an occlusion of the left anterior descending coronary artery (*LAD*, *arrow* in **Panels C** and **D**). Left-to-left collaterals (*asterisks* in **Panels C** and **D**) bypass the occlusion. Nevertheless, a large infarction with an apical aneurysm and thrombus formation eventually occurred in this patient. *RCA* right coronary artery

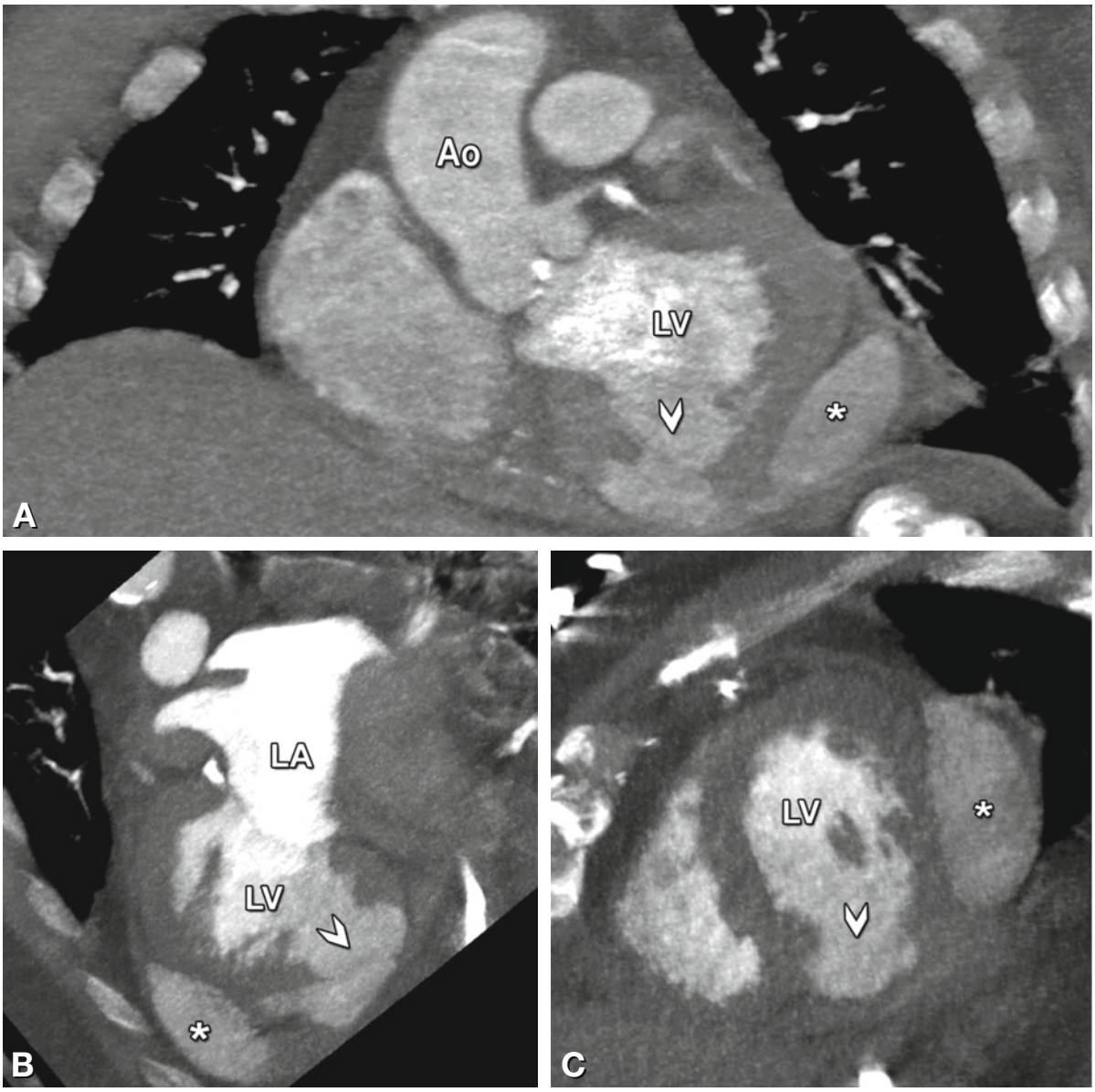

Fig. 24.70 Left ventricular rupture in a 73-year-old male patient with known coronary artery disease 2 days after inferior myocardial infarction. Two days earlier the patient presented with nausea, typical angina pectoris, and ST-segment elevations. Conventional coronary angiography showed an occlusion of the venous bypass graft supplying the right coronary artery. In a complex intervention the native right coronary artery was revascularized with four stents. Within the next 48 h the patient developed acute renal failure, lung edema, and showed a reduced left ventricular ejection fraction of 30%. A transesophageal echocardiography right before cardiac CT showed hypokinesia of the inferior wall and pericardial effusion. Thus, cardiac CT was performed with the suspicion of aortic dissection but showed rupture of the inferior wall of the left ventricle (*arrowhead* in **Panels A**–**C**) with active bleeding into the pericardium (*asterisks* in **Panels A**–**C**). Right after CT the patient became asystolic and died under cardiopulmonary resuscitation. **Panels A**–**C** are maximum-intensity projections in the coronal orientation, two-chamber view, and short axis, respectively. *Ao* ascending aorta, *LA* left atrium, *LV* left ventricle (Images courtesy of E. Zimmermann and L. Hartmann, Berlin)

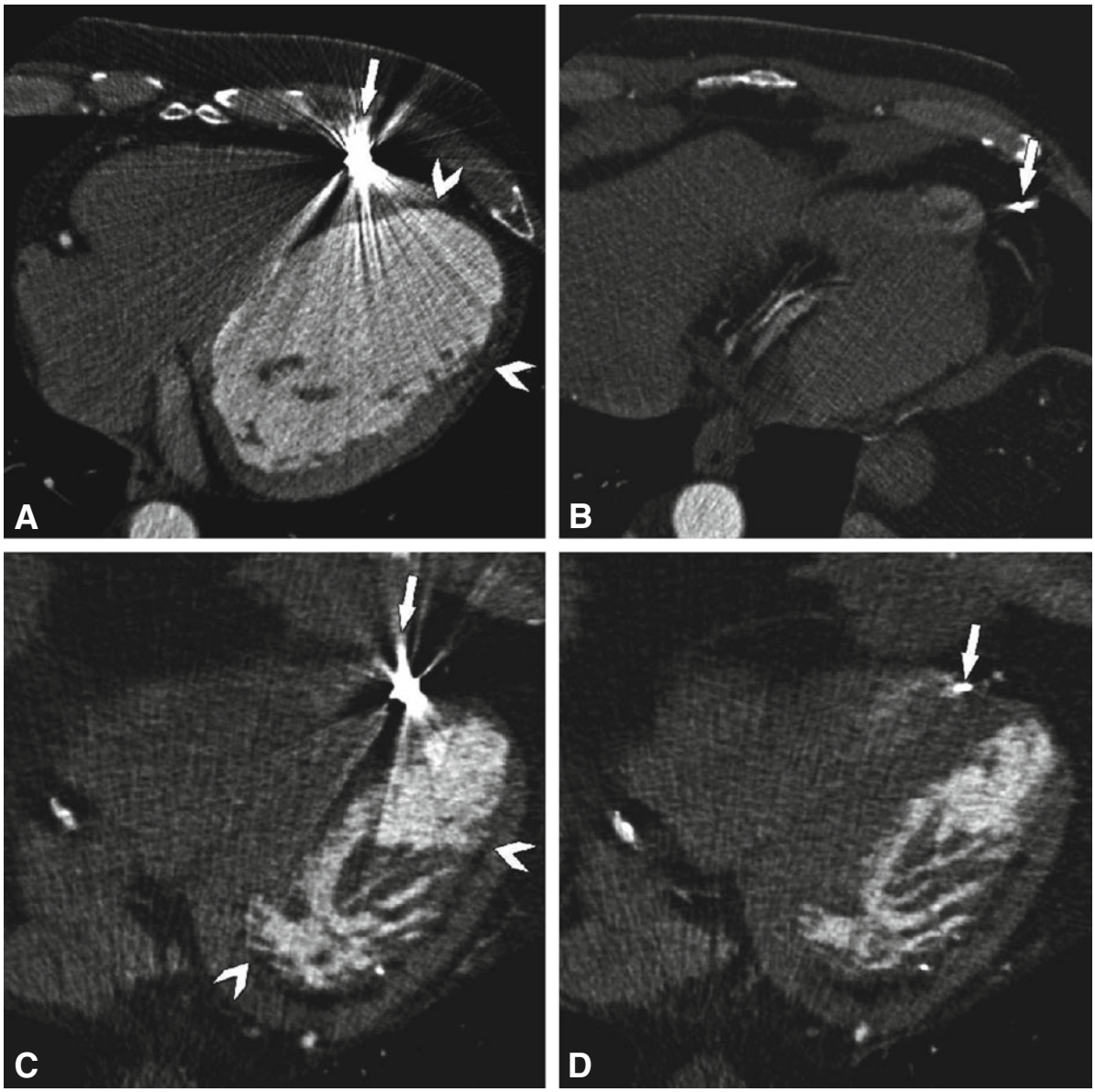

Fig. 24.71 Right ventricular lead perforation of an automated implantable cardioverter defibrillator in a 57-year-old male patient who had pacemaker dysfunction on testing. In **Panel A**, the lead is still in the right ventricle (*arrow*), and an apical infarction (*arrowheads*) is visible. A few slices further caudally, the tip of the lead can be seen penetrating into the pericardial cavity (*arrow* in **Panel B**) For comparison, the same anatomical regions are shown in a different 67-year-old male patient presenting with typical angina pectoris (**Panels C** and **D**). This patient has an inferolateral myocardial infarction (*arrowheads* in **Panel C**), and the tip of the lead is located within the right ventricle (*arrow* in **Panel D**)

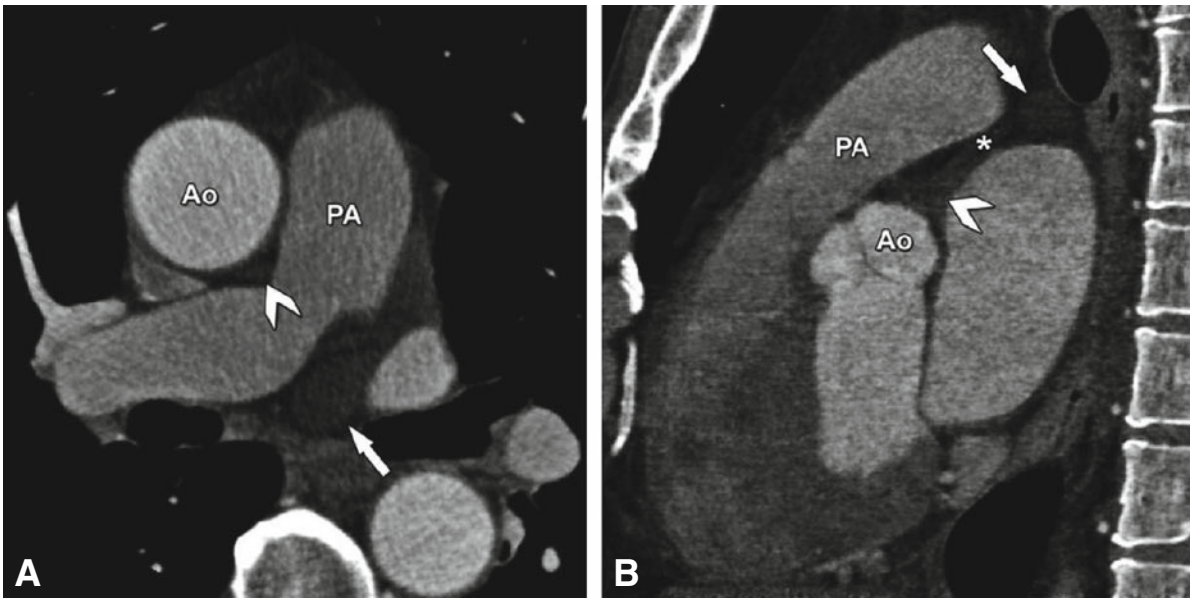

Fig. 24.72 Pericardial recesses and sinuses need to be differentiated from effusions, lymph nodes, and dissections. **Panels A** and **B** show an example of a left pulmonic pericardial recess (*arrow*) in the groove inferior to the left pulmonary artery (*PA*). This recess commonly communicates (*asterisk* in **Panel B**) with the transverse pericardial sinus (*arrowhead* in **Panel B**), which is located posterior to the ascending aorta (*Ao*). Also communicating with the transverse sinus is the superior aortic recess (*arrowhead* in **Panel A**). The posterior pericardial recess (not shown) is also sometimes seen and is located posterior to the right pulmonary artery as part of the oblique pericardial sinus. The typical location and CT appearance (density of water, well-marginated, tapered configuration) allow pericardial recesses to be distinguished from mediastinal lymphadenopathy, pericardial effusions, and aortic dissection

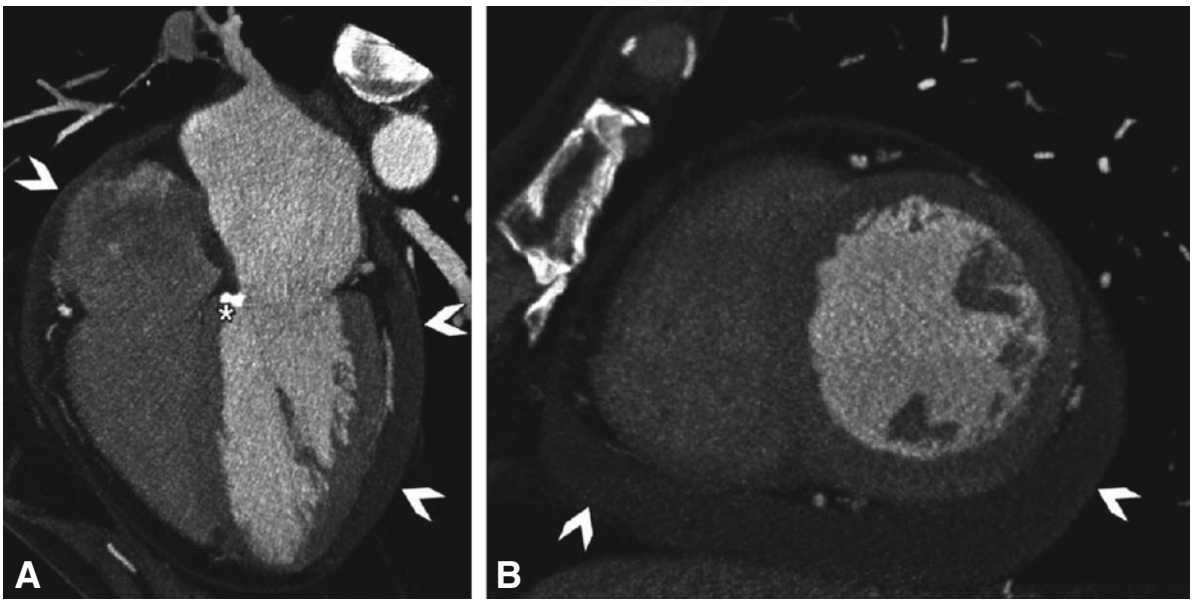

Fig. 24.73 Pericardial effusion (with a 2 cm posterior width) in a 61-year-old male patient 6 months after coronary artery stenting. Both the four-chamber view (**Panel A**) and the cardiac short-axis view (**Panel B**) show the large pericardial effusion (*arrowheads*). There is a small mitral valve annulus calcification (*asterisk* in **Panel A**), another noncoronary cardiac finding. CT data are shown as maximum-intensity projections

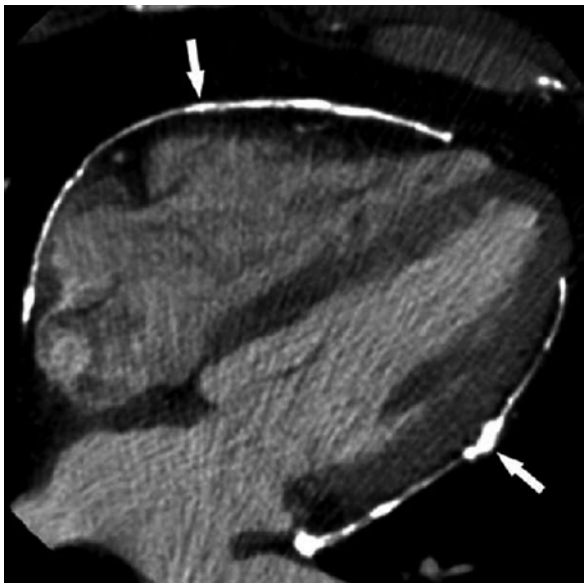

Fig. 24.74 Circumferential calcification of the pericardium (*arrows*) in a four-chamber view. Such calcifications typically cause constrictive pericarditis, which can be associated with elevated right cardiac pressures, dyspnea, exercise intolerance, and even ascites. Most pericardial calcifications have an infectious etiology (e.g., tuberculosis, histoplasmosis)

Results of Clinical Studies

M. Dewey

Abstract

This chapter summarizes the diagnostic performance of cardiac CT. The method has high sensitivity for detecting stenosis in native coronary arteries and can be used to reliably rule out disease in patients with low-to-intermediate pretest likelihood. CT is suited for detecting coronary artery bypass graft occlusion. In patients with stents, high rates of nondiagnostic studies and relatively poor positive predictive value limit the use of cardiac CT. Studies show high agreement of CT with magnetic resonance imaging in cardiac function assessment.

25.1 Coronary Arteries

Noninvasive coronary angiography using multislice CT as a means of ruling out significant stenoses in patients with low-to-intermediate likelihood of disease is the foremost clinical application of this test. Numerous single and multicenter studies have addressed the diagnostic performance of CT in detecting stenoses of the native coronary vessels, and we have summarized the results in terms of per-patient sensitivity and specificity in

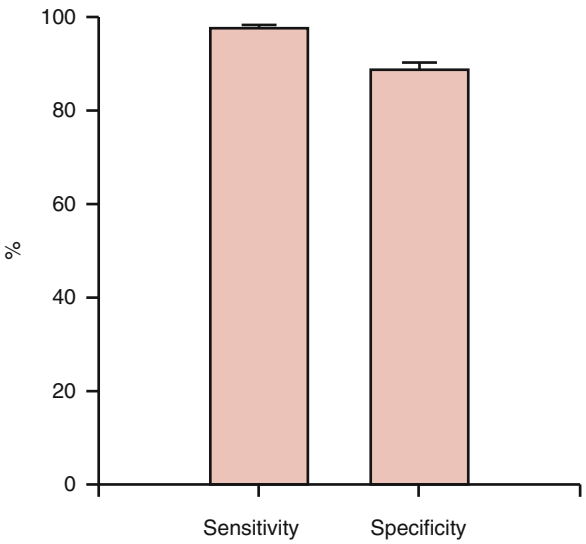

Fig. 25.1 Per-patient diagnostic performance (sensitivity, specificity, and nondiagnostic rate) of coronary CT angiography in native coronary vessels, when compared with conventional coronary angiography as the reference (gold) standard. Results were obtained using all published studies on this topic. *Error bars* represent 95% confidence intervals. Please note that because this figure represents per-patient results, direct comparison with the following figures (per-graft and per-stent results) is not possible

Fig. 25.1. Please note that the negative predictive value of CT is 95% in this analysis (data not shown in the figure) and represents the major advantage of this test (Chaps. 4 and 5).

M. Dewey, *Cardiac CT*,
DOI 10.1007/978-3-642-41883-9_28, © Springer-Verlag Berlin Heidelberg 2014

25.2 Coronary Artery Bypasses

Assessing coronary arterial and venous bypass grafts is an important application of CT in some patients (e.g., patients with recurrent chest pain and equivocal stress results). Numerous single-center studies have addressed the diagnostic performance of CT in coronary artery bypass grafts, and we have summarized the results as per-graft sensitivity and specificity in **Figs.** 25.2 and 25.3.

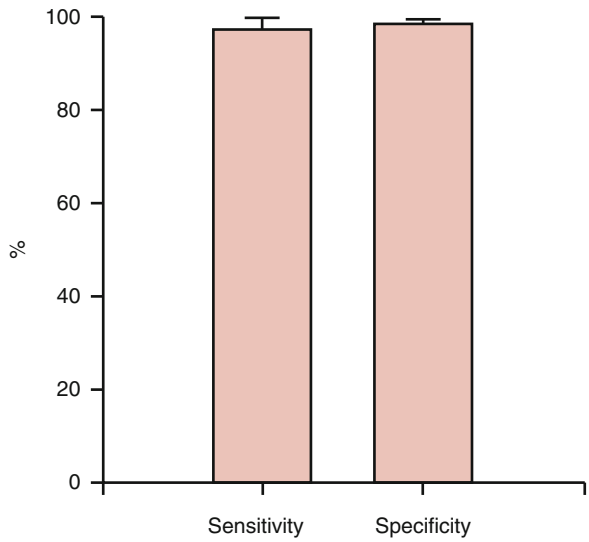

Fig. 25.2 Per-graft diagnostic performance (sensitivity, specificity) of coronary CT angiography in detecting coronary artery bypass graft occlusion, when compared with conventional coronary angiography as the reference (gold) standard. Results were obtained using all published studies on this topic. *Error bars* represent 95% confidence intervals

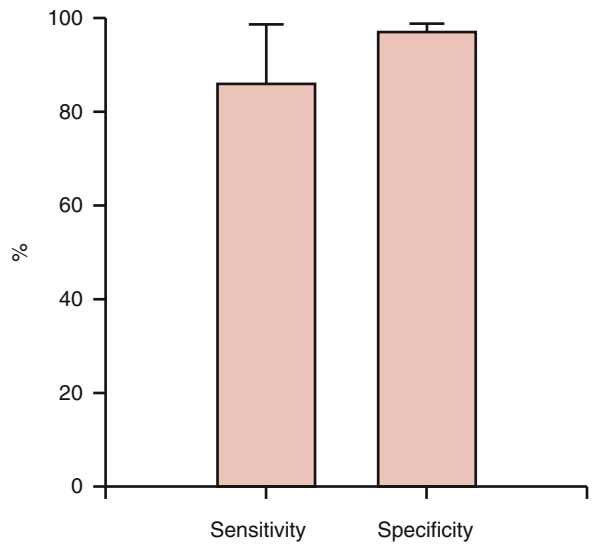

Fig. 25.3 Per-graft diagnostic performance (sensitivity, specificity) of coronary CT angiography in detecting coronary artery bypass graft stenosis, when compared with conventional coronary angiography as the reference (gold) standard. Results were obtained using all published studies on this topic. *Error bars* represent 95% confidence intervals

25.3 Coronary Artery Stents

The successful detection of coronary artery stent stenoses with CT is limited when compared with assessment of the native vessels using current technology. Sufficient image quality and accuracy are, in general, achieved only for large stents (at least 3.5-mm diameter). When smaller stents are present, only about 50% of cases are evaluable. Such nondiagnostic examinations in patients with coronary stents are the major limitation of this indication, which is therefore currently not recommended (Chap. 5). Numerous single-center studies and one multicenter study have addressed the diagnostic performance of CT in detecting in-stent restenoses, and we have summarized the results as per-stent sensitivity and specificity in **Fig. 25.4**. Please note that the positive predictive value is only 70% in this analysis (data not shown in the figure), a major limitation of CT for coronary stent evaluation.

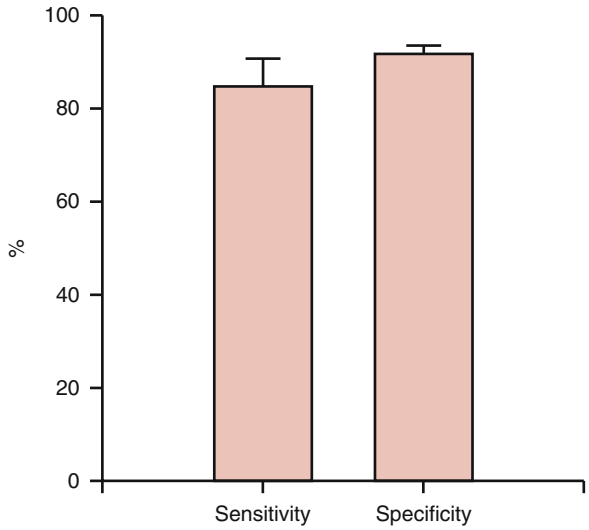

Fig. 25.4 Diagnostic performance (sensitivity and specificity) of coronary CT angiography in detecting coronary artery in-stent restenoses, when compared with conventional coronary angiography as the reference (gold) standard. Results were obtained using all published studies on this topic. Please note that patients with overall nonassessable image quality had to be excluded from this summary, as most studies did not provide detailed information about how many stents were present in these patients. Moreover, in patients with overall acceptable image quality, the per-stent nondiagnostic rate was 15%. *Error bars* represent 95% confidence intervals

25.4 Cardiac Function

Global and regional cardiac function can easily be assessed using the same data that have been acquired for coronary CT angiography on condition that retrospective ECG-gating has been used (Chap. 7). Because cardiac function results have considerable influence on patient management (Chap. 10), left ventricular function should be evaluated in all patients undergoing retrospectively gated cardiac CT (Chap. 15). We have summarized the accuracy of CT in determining left ventricular ejection in **Fig. 25.5**.

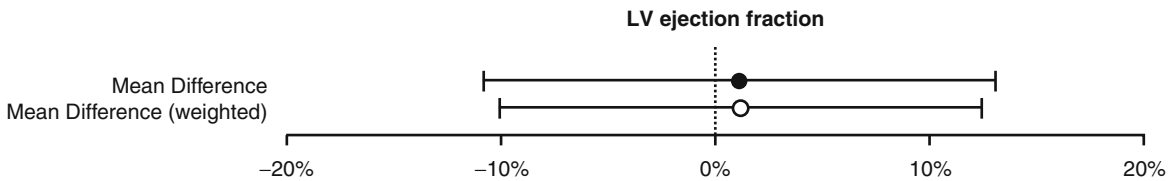

Fig. 25.5 Bland-Altman analysis of the accuracy of CT in determining left ventricular ejection fraction, vs. magnetic resonance imaging as the reference standard. Results are shown as unweighted and weighted (according to study size) mean values and limits of agreement (±95% confidence intervals). The limits of agreement indicate the expected maximum difference between CT and the reference standard and are approximately ±12%. The agreement between cine ventriculography and echocardiography and the reference standard is significantly lower than that of CT, as shown in head-to-head comparisons, indicating the potential advantage of CT over these tests. There is a slight underestimation of the ejection fraction by CT (as identified by the mean of approximately +2%)

Outlook

M. Dewey

Abstract

This chapter discusses anticipated technical and clinical developments with regard to CT.

26.1 Technical Developments

There is an exponential growth in cardiac CT research. Technical developments expected in the near future are summarized in **List 26.1**.

List 26.1. The foremost upcoming technical developments

1. Single-Beat Imaging and Multisource Scanning
2. Further reduction in gantry rotation times
3. Further reduction in slice collimation

26.1.1 Single-Beat Imaging and Multisource Scanning

One important advantage of prospective 320-row volume acquisition is that it may provide more flexibility when extrasystoles occur (Chap. 8) and in patients with atrial fibrillation (**Fig. 26.1**). Dual-source CT has been available for some time now and has been of great value in improving temporal resolution and reducing the dependency on heart rate. It is expected that further technical developments will lead to the availability of clinical multisource CT scanners, which could further reduce the length of the image reconstruction windows within the RR interval. In this way, coronary CT angiography could become fully independent of heart rate. However, scattered radiation also increases when more X-ray tubes are used.

Despite cost issues, it is, therefore, likely that the concepts of wide-area detector and multisource CT will eventually be merged within a single CT scanner, making the advantages of both approaches available for patient care. This may allow solving one of the most important issues in cardiac CT – limited temporal resolution.

26.1.2 Better Temporal Resolution

Further reducing the gantry rotation time (to below the currently achieved 270–350 ms) is an obvious approach to improving temporal resolution and reducing heart rate dependency. However, our ability to shorten the rotation time is limited by the dramatic increase in centrifugal forces that occurs as the rotation time is reduced. For instance, at a 400-ms rotation time, the relative centrifugal force is 18–20 g, which already requires considerable centripetal force to counteract. However, at 200 ms (equal to an

M. Dewey, *Cardiac CT*,
DOI 10.1007/978-3-642-41883-9_29, © Springer-Verlag Berlin Heidelberg 2014

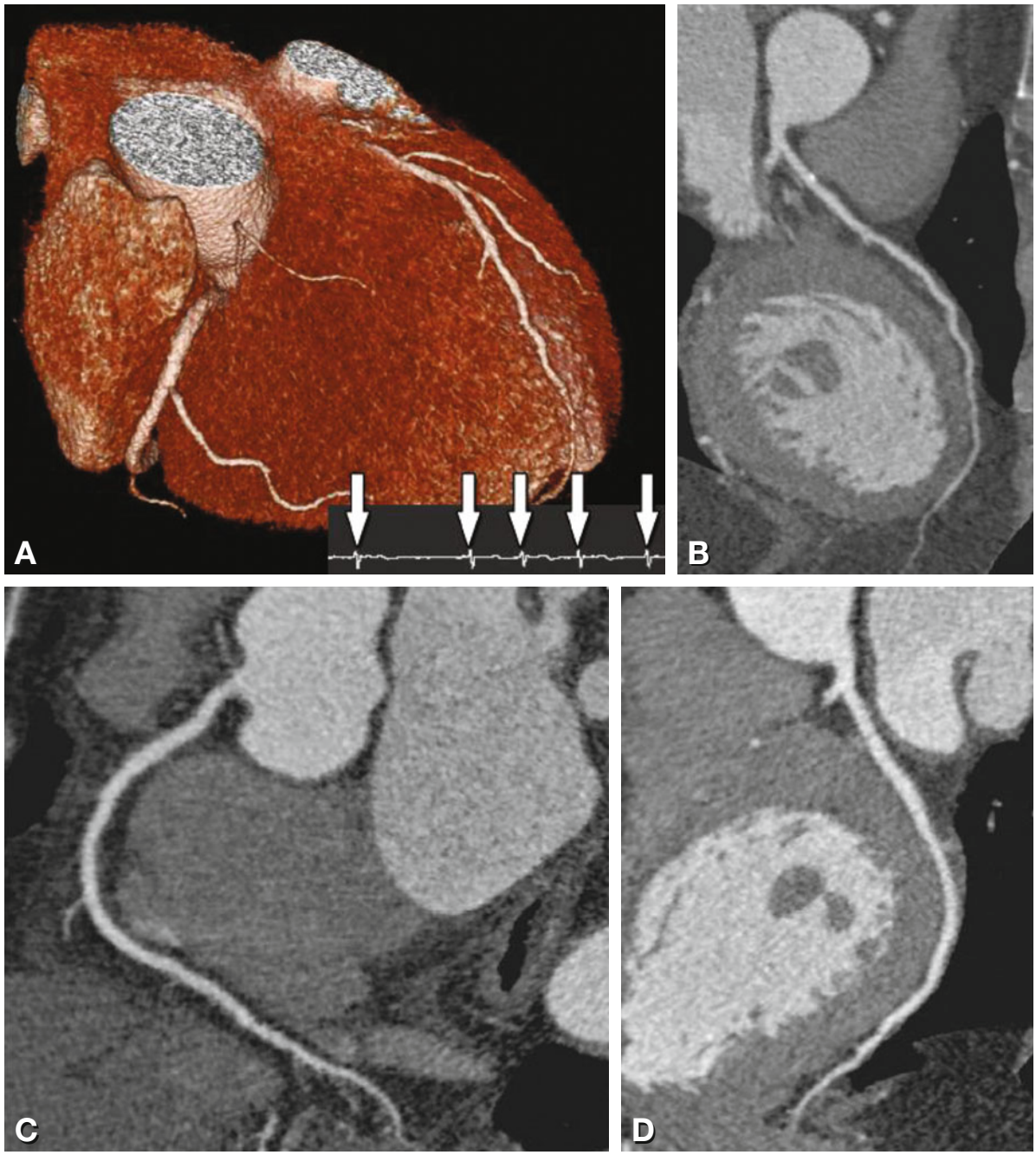

Fig. 26.1 Normal coronary arteries in 320-row CT in a patient with atrial fibrillation. **Panel A** shows the three-dimensional reconstruction and the ECG strip with atrial fibrillation (*arrows* in the inset). **Panels B–D** show curved multiplanar reformations along the left anterior descending, right, and left circumflex coronary artery, respectively, without significant diameter reduction. There is a small artifact in the mid-RCA, but otherwise image quality is very good. Images were acquired during one heartbeat with arrhythmia control using volume CT covering the entire heart in a single gantry rotation

image acquisition window of 100 ms with halfscan reconstruction), the relative centrifugal forces rise to 74–80 g because they are equal to the square of the velocity. New technologies such as an air-bearing CT gantry and faster data transfer systems might alleviate this problem and make it feasible to reduce the rotation time to 200 ms or even shorter. However, it is not very likely that a reduction in the rotation time alone will be pursued as a strategy for

further improving temporal resolution. Instead, it is much more likely that the three concepts of (1) multisource scanning, (2) adaptive multisegment reconstruction and novel intelligent algorithms for improving temporal resolution by reconstruction methods, and (3) shortening the gantry rotation time will be developed further and combined in some fashion to improve temporal resolution.

26.1.3 Better Spatial Resolution

The current slice collimation of coronary CT angiography (between 0.5 and 0.75 mm) limits its application to small structures such as coronary plaque and its internal makeup. Thus, thinner slice collimation (e.g., of 0.2–0.3 mm) or better in-plane resolution (Chap. 9c) have the potential to improve the assessment of plaques and stents and facilitate the quantification of stenoses by coronary CT angiography (**Fig. 26.2**). However, reducing the slice collimation by a factor of 2 requires the radiation exposure to be increased by a factor of 2 (if the same detector technology is used) to keep the image quality constant. Thus, improvements in spatial resolution are not easily achieved using the current technology, and further developments (e.g., detector material) are necessary for clinical applications if one does not wish to increase radiation exposure again.

26.2 Clinical Developments

The expected upcoming clinical developments are summarized in **List 26.2**.

List 26.2. The foremost upcoming clinical developments

1. Reliable coronary artery stent imaging
2. Myocardial perfusion and viability imaging
3. Imaging and follow-up of coronary plaques after medical interventions
4. Application of CT to asymptomatic high-risk patients

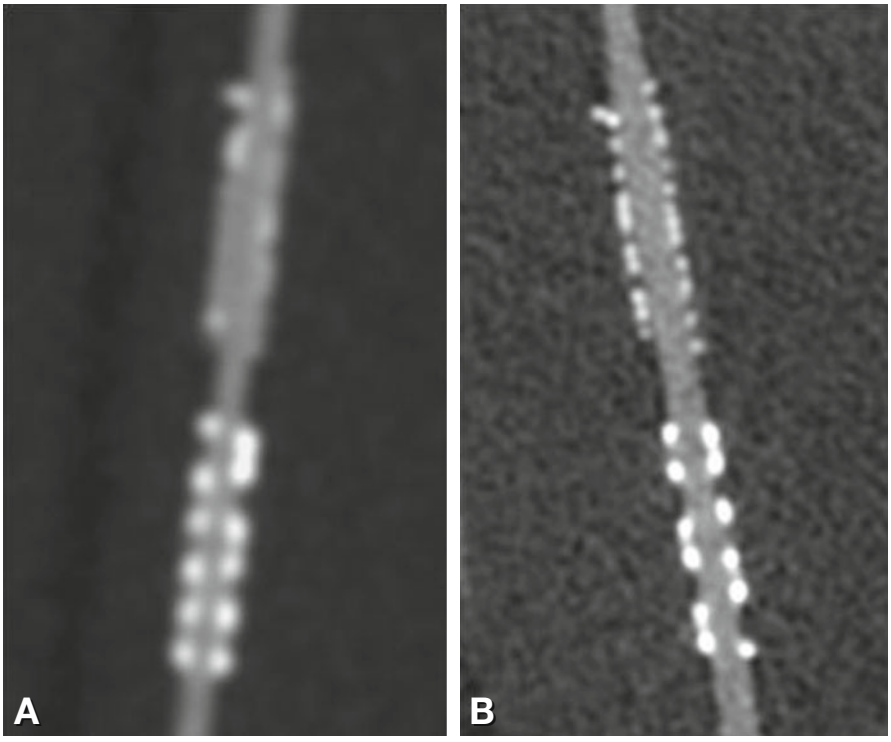

Fig. 26.2 Advantages of high-resolution (fine-cell detector) CT with a ~0.3-mm slice thickness for coronary stent imaging. Multiplanar reformations along a coronary stent with 2.5-mm inner diameter (in a phantom) obtained using 0.625-mm slice collimation and cell width (**Panel A**), and high-resolution CT with 0.3-mm slice collimation and cell width using a 0.3 × 0.3-mm focus size tube (**Panel B**). The opacified lumen within the small stent is more clearly seen, with fewer blooming artifacts, using the thinner slice collimation (Images courtesy of Sachio Kuribayashi. Department of Radiology, Keio University School of Medicine)

26.2.1 Coronary Stent Imaging

The technical innovations described above may make possible the reliable assessment of coronary artery stents for the presence of restenoses. For this purpose, it will be instrumental to add the fourth dimension for myocardial CT perfusion imaging to our analysis and to reduce motion artifacts that are related to ECG irregularities or patients' limited breath-hold capacity. Also, better spatially localized and temporally resolved quantitative measurements of the inner diameter of coronary stents will be pivotal to our efforts to broaden the clinical use of CT and extend it to the follow-up of patients who have undergone coronary stent placement.

26.2.2 Myocardial Perfusion and Viability Imaging

Another advantage of volume CT and second-generation dual-source CT is that a fourth dimension, time, can be added, making it possible to assess myocardial perfusion and coronary blood flow (Chap. 19). With this new option, CT might to some extent replace conventional approaches involving myocardial perfusion imaging, while additionally providing information about the hemodynamic relevance of coronary stenosis in the near future (**Fig. 26.3**). Similar to magnetic resonance imaging, CT can detect late contrast enhancement in the myocardium as a marker of infarction ("viability

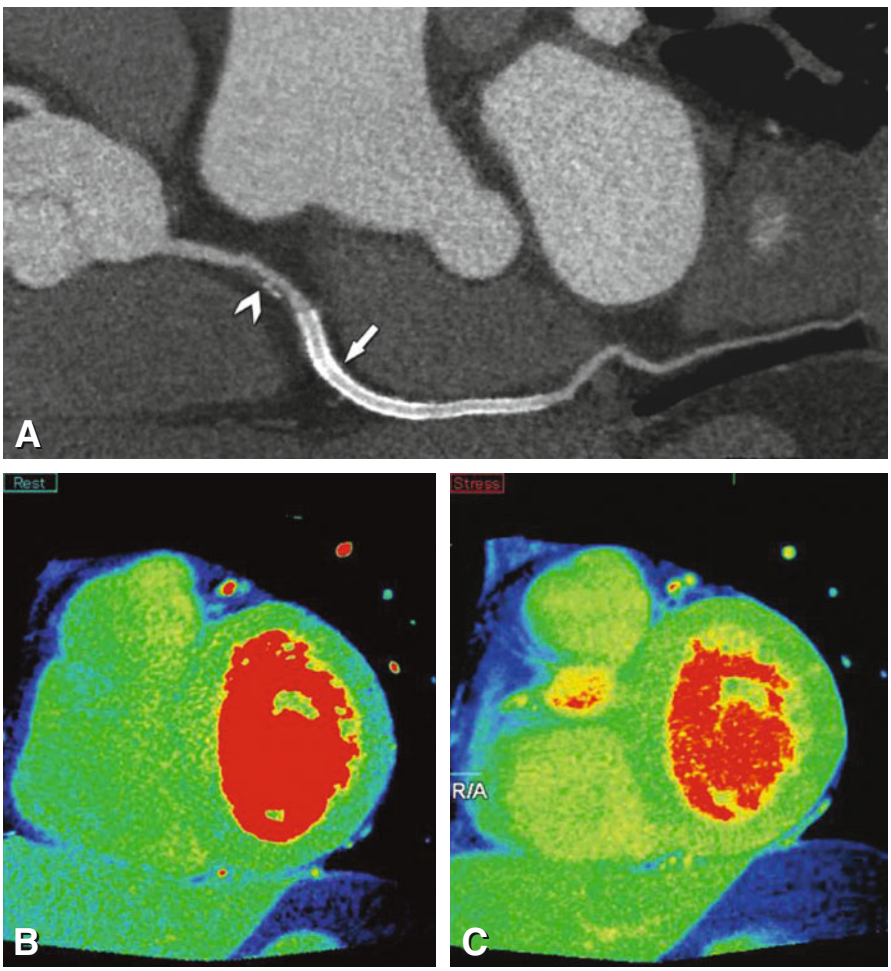

Fig. 26.3 Usefulness of myocardial perfusion imaging using 320-row volume CT in a 67-year-old female patient with atypical symptoms 3 years after stenting of the right coronary artery. Coronary CT angiography shows mostly noncalcified plaque immediately proximal to the stents (*arrowhead* in **Panel A**, curved multiplanar reformation). No significant in-stent restenosis can be identified; however, the small size of the stents (*arrow*, 3 mm diameter) precludes reliable exclusion of significant stenosis. Myocardial perfusion analysis during rest (**Panel B**) and stress (**Panel C**) rules out significant defects

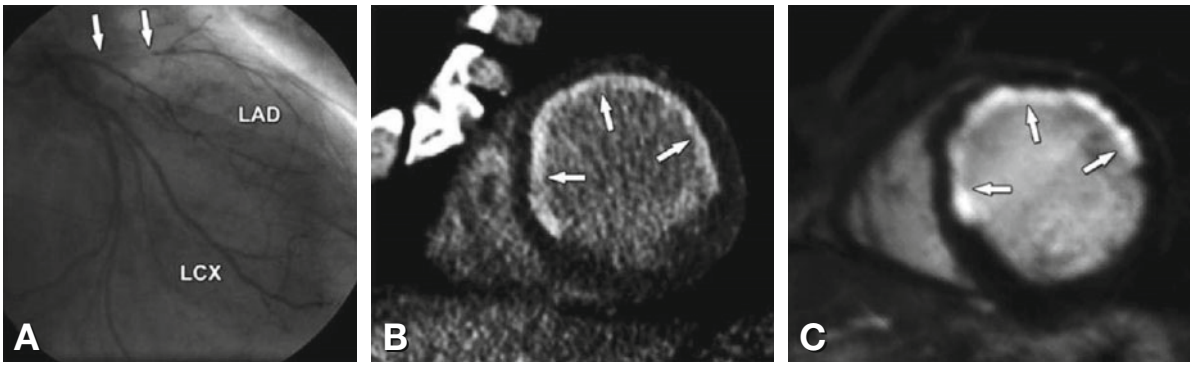

Fig. 26.4 Myocardial viability assessment using CT in a 74-year-old male patient who underwent stenting of a left anterior descending (*LAD*) coronary artery stenosis 2 years earlier. He was now re-admitted to the hospital for recurrent angina. Conventional coronary angiography showed proximal LAD occlusion (*arrows* in **Panel A**) with distal filling via collateral vessels arising from the left circumflex coronary artery (*LCX*). Prospectively ECG-triggered CT immediately following cardiac catheterization (without additional intravenous contrast agent) revealed subendocardial late enhancement (*arrows* in **Panel B**) in the anteroseptal, anterior, and anterolateral segments of the left ventricular wall. These findings were confirmed by delayed contrast-enhanced MR imaging (*arrows* in **Panel C**) (Images courtesy of Andreas Mahnken, Aachen, Germany)

imaging," **Fig. 26.4**). Nevertheless, the required additional contrast agent injection and radiation exposure seriously limit the use of CT for myocardial viability imaging in the near future.

26.2.3 Coronary Plaque Quantification and Characterization

One of the greatest potential advantages of coronary CT angiography is its ability to noninvasively determine the volume, characteristics, and composition of coronary artery plaques (Chap. 14). Since most acute coronary events arise from plaques that cause only a minimal percent stenosis, it is of importance to identify plaque characteristics that are unambiguously associated with a higher risk in individual patients and would be expected to trigger intense medical treatment and preventive measures. However, characteristics such as positive remodeling, noncalcified components, and spotty calcifications, which are more likely to lead to acute events, have not yet been shown to be useful in directing further medical treatment by CT and to thus improve clinical outcome.

One clinically important issue is how to best quantify the diameter reduction resulting from severely calcified coronary plaques. Two approaches have recently been suggested to facilitate this: (1) dual-kVp CT (**Fig. 26.5**) and (2) subtraction of calcium based on noncontrast CT and CT angiography (**Fig. 26.6**).

Although it competes with intravascular ultrasound, CT is also a potential candidate for following up coronary artery plaques after initiation of certain medical therapies. Thus, if further large studies demonstrate its clinical validity and measuring accuracy, coronary CT angiography could become the foremost diagnostic surrogate parameter and test for analyzing the outcome of new drugs in terms of regression of coronary plaques.

26.2.4 Asymptomatic High-Risk Patients

Since 50% of men and 64% of women who die suddenly of coronary heart disease were previously asymptomatic, it is obvious that an ongoing search is necessary to identify parameters that reliably predict such coronary events. The identification of coronary plaques and stenoses in these patients might help optimize further treatment. However, it must be borne in mind that no evidence exists that revascularization of coronary stenoses in asymptomatic patients improves outcomes. Given the radiation dose reduction possible with prospectively triggered acquisition, CT may be used for screening asymptomatic high-risk patients in the future if the clinical usefulness for this indication can be proven. However, large-scale randomized trials that analyze hard and soft events are required before a final decision can be made. Until then, cardiac CT is clearly not indicated in asymptomatic patients for routine clinical screening.

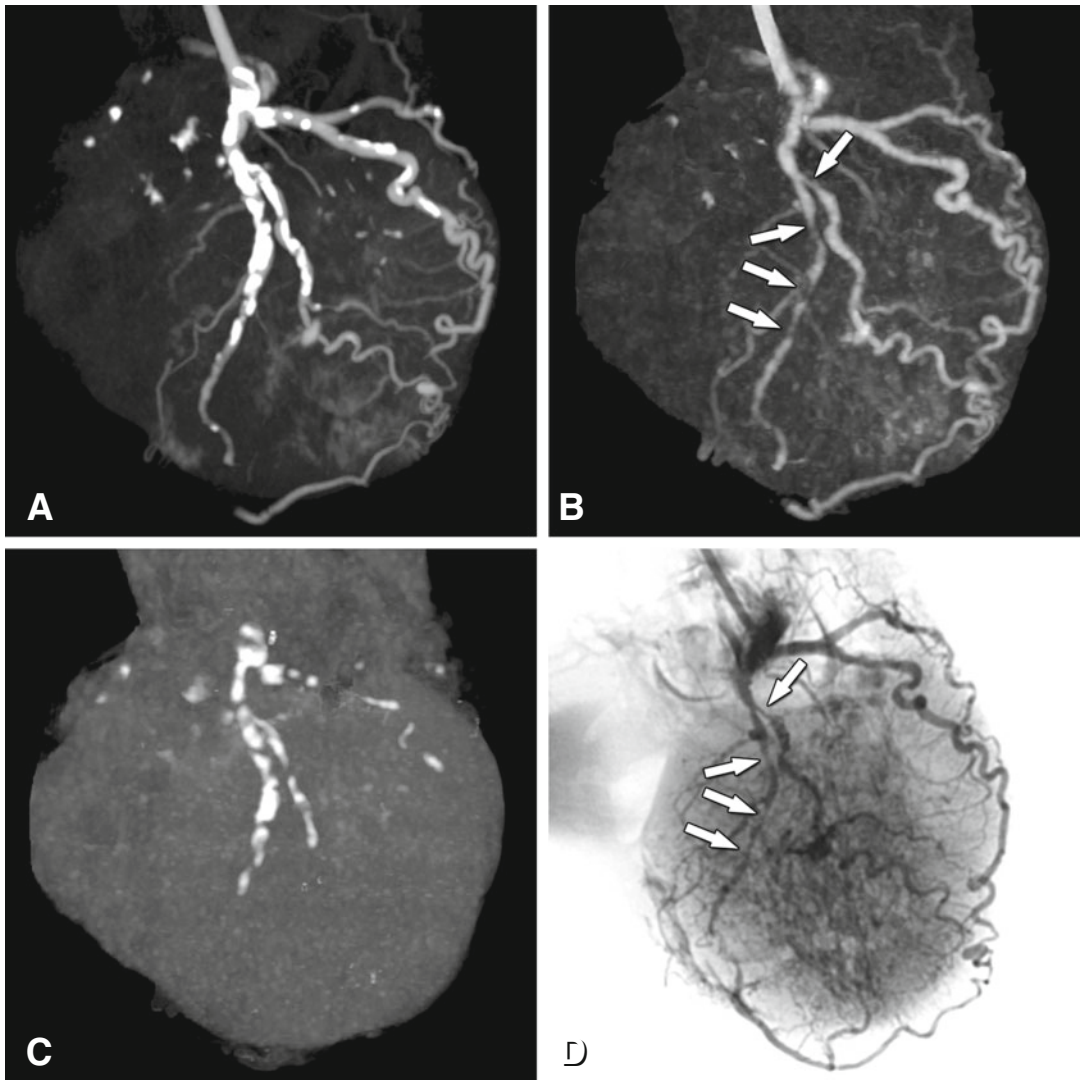

Fig. 26.5 Potential advantages of dual-kVp CT angiography for calcium subtraction shown in an ex-vivo non-beating human heart specimen. **Panel A** is a maximum-intensity projection generated by single-kVpeak (kVp) CT angiography. Evaluation of this dataset for the presence of significant stenosis is severely limited by heavy calcifications. **Panel B** shows the maximum-intensity projection of the iodine-density image generated by fast-switching dual-kVp CT (80 and 140 kVp). The four significant stenoses in the left anterior descending artery and the diagonal branch (*arrows* in **Panel B**) are nicely visualized in this iodine image, while they are obscured by calcium on the standard image (**Panel A**). **Panel C** is the calcium-density maximum-intensity projection generated by fast-switching dual-kVp CT and shows the severe extent of calcium that was removed on the iodine-density image (**Panel B**). Conventional coronary angiography (**Panel D**) confirms the stenoses of the left anterior descending artery and diagonal branch (*arrows*) seen on the iodine-density image (**Panel B**) (With permission from M. Yamada et al. *Circ J* 2011)

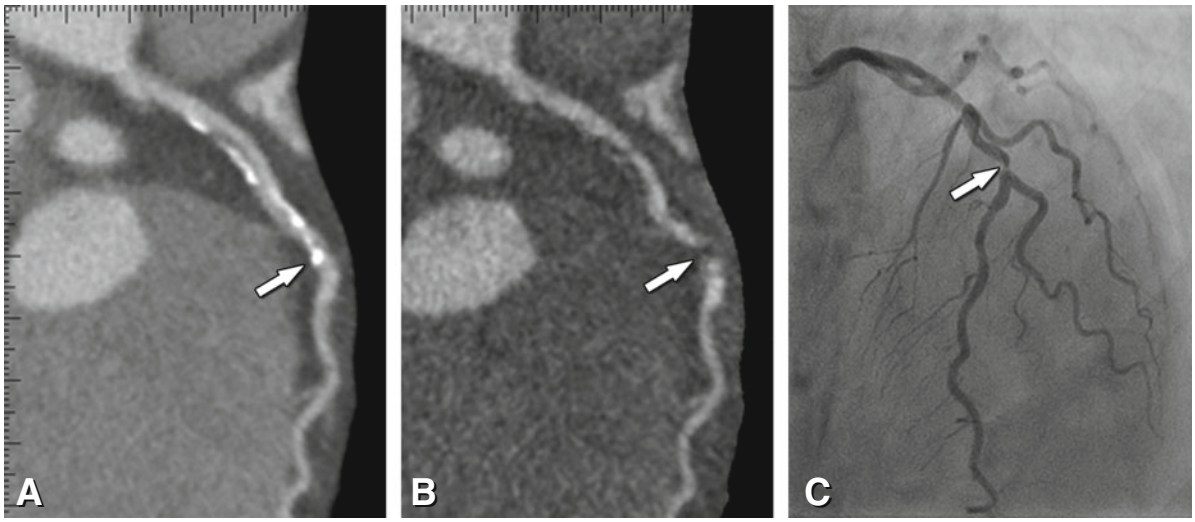

Fig. 26.6 Clinical potential of calcium subtraction by using 320-row CT illustrated in a 75-year-old woman with stable angina pectoris. **Panel A** shows conventional coronary CT angiography without subtraction with a large calcified plaque in the mid left anterior descending coronary artery (LAD, *arrow*) that relevantly limits assessment of this vessel. After subtracting the noncontrast calcium scan data from the CT angiography (**Panel B**) using an algorithm that first incorporates a global non-rigid step followed by local rigid refinement (Volumetric CT Digital Subtraction Angiography), a significant coronary artery stenosis is suspected in this location of the LAD (*arrow*, segment 7). Conventional coronary angiography confirmed the presence of an about 80% stenosis in the mid-LAD (*arrow*, **Panel C**) (Images courtesy of K. Yoshioka, Department of Radiology, Morioka, Japan)

Recommended Reading

Burgstahler C, Brodoefel H, Schroeder S (2009) Cardiac CT in 2009. Minerva Cardioangiol 57:495–509

Choi SI, George RT, Schuleri KH, Chun EJ, Lima JA, Lardo AC (2009) Recent developments in wide-detector cardiac computed tomography. Int J Cardiovasc Imaging 25(Suppl 1):23–29

Dewey M, de Vries H, de Vries L, Haas D, Leidecker C (2010) The present and future of cardiac CT in research and clinical practice: moderated discussion and scientific debate with representatives from the four main vendors. Rofo 182:313–321

Flohr TG, Leng S, Yu L et al (2009a) Dual-source spiral CT with pitch up to 3.2 and 75 ms temporal resolution: image reconstruction and assessment of image quality. Med Phys 36:5641–5653

Flohr TG, Raupach R, Bruder H (2009b) Cardiac CT: how much can temporal resolution, spatial resolution, and volume coverage be improved? J Cardiovasc Comput Tomogr 3:143–152

Gaztanaga J, Garcia MJ (2009) New noninvasive imaging technologies in coronary artery disease. Curr Cardiol Rep 11:252–257

George RT, Ichihara T, Lima JA, Lardo AC (2010) A method for reconstructing the arterial input function during helical CT: implications for myocardial perfusion distribution imaging. Radiology 255(2):396–404

Itagaki MW, Suh RD, Goldin JG (2009) Cardiac CT research: exponential growth. Radiology 252:468–476

Kalra MK, Brady TJ (2008) Current status and future directions in technical developments of cardiac computed tomography. J Cardiovasc Comput Tomogr 2:71–80

Krombach GA, Niendorf T, Gunther RW, Mahnken AH (2007) Characterization of myocardial viability using MR and CT imaging. Eur Radiol 17:1433–1444

Index

M. Dewey, *Cardiac CT*,
DOI 10.1007/978-3-642-41883-9, © Springer-Verlag Berlin Heidelberg 2014